ENCYCLOPEDIA OF
MODERN OPTICS
SECOND EDITION

EDITORS IN CHIEF

Bob D. Guenther

Duke University, Durham, NC, United States

Duncan G. Steel

University of Michigan, Ann Arbor, MI, United States

VOLUME 5

Laser Radar ■ Optical Processing ■ Coherent Control ■ Biomedical: Human Eye ■ BioOptics ■ Microscopy ■ Quantum Optics ■ Organic Materials



ELSEVIER

AMSTERDAM • BOSTON • HEIDELBERG • LONDON • NEW YORK • OXFORD
PARIS • SAN DIEGO • SAN FRANCISCO • SINGAPORE • SYDNEY • TOKYO

Elsevier
Radarweg 29, PO Box 211, 1000 AE Amsterdam, The Netherlands
The Boulevard, Langford Lane, Kidlington, Oxford OX5 1GB
50 Hampshire Street, 5th Floor, Cambridge, MA 02139, United States

Copyright © 2018 Elsevier Ltd. All rights reserved.

No part of this publication may be reproduced or transmitted in any form or by any means, electronic or mechanical, including photocopying, recording, or any information storage and retrieval system, without permission in writing from the publisher. Details on how to seek permission, further information about the Publisher's permissions policies and our arrangements with organizations such as the Copyright Clearance Center and the Copyright Licensing Agency, can be found at our website: www.elsevier.com/permissions.

This book and the individual contributions contained in it are protected under copyright by the Publisher (other than as may be noted herein).

Notices
Knowledge and best practice in this field are constantly changing. As new research and experience broaden our understanding, changes in research methods, professional practices, or medical treatment may become necessary.

Practitioners and researchers may always rely on their own experience and knowledge in evaluating and using any information, methods, compounds, or experiments described herein. In using such information or methods they should be mindful of their own safety and the safety of others, including parties for whom they have a professional responsibility.

To the fullest extent of the law, neither the Publisher nor the authors, contributors, or editors, assume any liability for any injury and/or damage to persons or property as a matter of products liability, negligence or otherwise, or from any use or operation of any methods, products, instructions, or ideas contained in the material herein.

Library of Congress Cataloging-in-Publication Data
A catalog record for this book is available from the Library of Congress

British Library Cataloguing-in-Publication Data
A catalogue record for this book is available from the British Library

ISBN 978-0-12-809283-5

For information on all publications visit our website at http://store.elsevier.com



Publisher: Oliver Walter
Acquisition Editor: Ruth Ireland
Content Project Manager: Sean Simms
Associate Content Project Manager: Marise Willis
Designer: Greg Harris

Printed and bound in the United Kingdom

EDITORIAL BOARD

Jorge Ojeda-Castaneda
Universidad de Guanajuato

Fang-Chung Chen
National Chiao Tung University (NCTU)

Chau-Jern Cheng
National Taiwan Normal University

Lukas Chrostowski
University of British Columbia

Steve Cundiff
University of Michigan

Casimer DeCusatis
Marist College

Hui Deng
University of Michigan

Henry O. Everitt
Duke University

Mike Fiddy
University of North Carolina at Charlotte

Almantas Galvanaskas
University of Michigan

David Gershoni
Technion Institute of Technology

Junsang Kim
Duke University

Mackillo Kira
University of Marburg

Paul McManamon
Ladar and Optical Communications Inst (University of Dayton)

Mary-Ann Mycek
University of Michigan

Xingjie Ni
Penn State University

Christoph Schmidt
University of Göttingen

Mansoor Sheik-Bahae
University of New Mexico

Colin Sheppard
Italian Institute of Technology

Han-Ping David Shieh
National Chiao Tung University

Brian Vohnsen
University College Dublin

Xiushan Zhu
University of Arizona

CONTENTS OF VOLUME 5

Editorial Board v

List of Contributors for Volume 5 ix

Editors in Chief xi

Introduction xiii

VOLUME 5

RF Coherent Detection on Top of Direct Detection Lidar *Barry L. Stann, John F Dammann, Mark M Giza, Brian C Redman, and William C Ruff* 1

Optical Masks Using Walsh Functions *Lakshminarayan Hazra and Pubali Mukherjee* 14

Coherent Control: Theory *H Rabitz* 30

Coherent Control: Experimental *RJ Levis* 39

Optics of the Human Eye *David A Atchison* 43

Measuring Retinal Blood Flow *Alberto de Castro and Stephen A Burns* 64

Adaptive Optics Retinal Imaging Techniques and Clinical Applications *Jessica IW Morgan* 72

Femtosecond Lasers in Retinal Imaging *Christina Schwarz and Jennifer J Hunter* 85

Confocal and Multiphoton Imaging of Cornea *Gopal S Jayabalan and Josef F Bille* 97

Refractive Error and Wavefront Sensing *Larry N Thibos* 108

Methods of Vision Correction *Len Zheleznyak, Ramkumar Sabesan, and Geunyoung Yoon* 116

Laser and Light in Ophthalmology *Michael Mrochen, Nicole Lemanski, and Bojan Pajic* 130

Probing Ocular Mechanics With Light *Susana Marcos, Giuliano Scarcelli, Antoine Ramier, and Seok H Yun* 140

Optical Coherence Tomography and Its Application to Imaging of Skin and Retina *Michael Pircher* 155

TIRF Microscopy and Variants *Daniel Axelrod* 168

Super-Resolution Depth Measurements: Variable Angle TIRF, Super-Critical Angle Fluorescence, MIET *Alexey Chizhik* 175

Overview: Microscopy *CJR Sheppard* 185

Confocal Microscopy *T Wilson* 194

Atom Optics *AD Cronin and DE Pritchard* 203

Organic Semiconductors *Fang-Chung Chen* 220

OLED/Introduction *Dae-Gyu Moon* 232

Harvesting Triplet Excitons in OLED *Gufeng He* 240

Organic Light-Emitting Diodes/Light Extraction *Jiun-Haw Lee* 247

Conjugated Polymer-Based Solar Cells *Gang Li, Widhya Budiawan, Pen-Cheng Wang, and Chih Wei Chu* 256

Dye-Sensitized Solar Cells *Lu-Yin Lin and Kuo-Chuan Ho* 270

Organic Inorganic Hybrid Perovskite Materials and Devices *Yihua Chen, Ning Zhou, and Huanping Zhou* 282

Light Harvesting in Organic Solar cells *Supriya Pillai, Matthew Wright, and Kah H Chan* 292

Organic Lasers *Graham A Turnbull* 309

Organic Photodetectors *Jaehoon Jeong, Hwajeong Kim, and Youngkyoo Kim* 317

Index 331

LIST OF CONTRIBUTORS FOR VOLUME 5

David A Atchison
Queensland University of Technology, Brisbane, QLD, Australia

Daniel Axelrod
University of Michigan, Ann Arbor, MI, United States

Josef F Bille
University of Heidelberg, Heidelberg, Germany

Widhya Budiawan
Research Center for Applied Sciences, Academia Sinica, Taipei, Taiwan (ROC); National Tsing-Hua University, Hsinchu, Taiwan (ROC); and Academia Sinica and National Tsing-Hua University, Hsinchu, Taiwan (ROC)

Stephen A Burns
Indiana University School of Optometry, Bloomington, IN, United States

Kah H Chan
University of New South Wales, Sydney, NSW, Australia

Fang-Chung Chen
National Chiao Tung University, Hsinchu, Taiwan

Yihua Chen
Peking University, Beijing, P.R. China

Alexey Chizhik
University of Göttingen, Göttingen, Germany

AD Cronin
Massachussetts Institute of Technology, Cambridge, MA, USA

John F Dammann
Army Research Laboratory, Adelphi, MD, United States

Alberto de Castro
Indiana University School of Optometry, Bloomington, IN, United States

Mark M Giza
Army Research Laboratory, Adelphi, MD, United States

Lakshminarayan Hazra
University of Calcutta, Kolkata, India

Gufeng He
Shanghai Jiao Tong University, Shanghai, China

Kuo-Chuan Ho
National Taiwan University, Taipei, Taiwan

Jennifer J Hunter
University of Rochester, Rochester, NY, United States

Gopal S Jayabalan
University of Heidelberg, Heidelberg, Germany

Jaehoon Jeong
Kyungpook National University, Daegu, Republic of Korea

Hwajeong Kim
Kyungpook National University, Daegu, Republic of Korea

Youngkyoo Kim
Kyungpook National University, Daegu, Republic of Korea

Jiun-Haw Lee
National Taiwan University, Taipei City, Taiwan

Nicole Lemanski
Mabel Cheng MD PLLC, Albany, NY, United States

RJ Levis
Temple University, Philadelphia, PA, USA

Gang Li
The Hong Kong Polytechnic University, Hong Kong, China

Lu-Yin Lin
National Taipei University of Technology (Taipei Tech), Taipei, Taiwan

Susana Marcos
Instituto de Optica, CSIC, Madrid, Spain

Dae-Gyu Moon
Soonchunhyang University, Asan-si, Chungcheongnam-do, Republic of Korea

Jessica IW Morgan
University of Pennsylvania, Philadelphia, PA, United States

Michael Mrochen
IROC Science AG, Zurich, Switzerland and Swiss Eye Research Foundation, Reinach, Switzerland

Pubali Mukherjee
MCKV Institute of Engineering, Howrah, India

Bojan Pajic
Orasis Ag, Reinach, Switzerland and Swiss Eye Research Foundation, Reinach, Switzerland

Supriya Pillai
University of New South Wales, Sydney, NSW, Australia

Michael Pircher
Medical University of Vienna, Vienna, Austria

DE Pritchard
Massachussetts Institute of Technology, Cambridge, MA, USA

H Rabitz
Princeton University, Princeton, NJ, USA

Antoine Ramier
Massachusetts General Hospital, Boston, MA, United States

Brian C Redman
Army Research Laboratory, Adelphi, MD, United States

William C Ruff
Army Research Laboratory, Adelphi, MD, United States

Ramkumar Sabesan
University of Washington School of Medicine, Seattle, WA, United States

Giuliano Scarcelli
University of Maryland, College Park, MD, United States

Christina Schwarz
University of Rochester, Rochester, NY, United States

CJR Sheppard
National University of Singapore, Singapore

Barry L Stann
Army Research Laboratory, Adelphi, MD, United States

Larry N Thibos
Indiana University, Bloomington, IN, United States

Graham A Turnbull
University of St Andrews, St Andrews, United Kingdom

Pen-Cheng Wang
National Tsing-Hua University, Hsinchu, Taiwan (ROC)

Chih Wei Chu
Research Center for Applied Sciences, Academia Sinica, Taipei, Taiwan (ROC)

T Wilson
University of Oxford, Oxford, UK

Matthew Wright
University of New South Wales, Sydney, NSW, Australia

Geunyoung Yoon
University of Rochester, Rochester, NY, United States

Seok H Yun
Massachusetts General Hospital, Boston, MA, United States

Len Zheleznyak
University of Rochester, Rochester, NY, United States

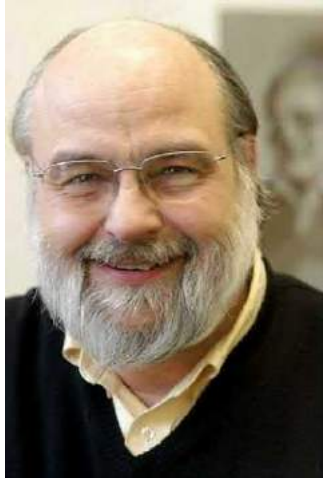
Huanping Zhou
Peking University, Beijing, P.R. China

Ning Zhou
Peking University, Beijing, P.R. China

EDITORS IN CHIEF



Bob D. Guenther received his undergraduate degree from Baylor University and his graduate degrees in Physics from University of Missouri. He has had research experience in condensed matter and optical physics. For 9 years he was active in research management as a Senior Executive in the Army, responsible for the physics research sponsored by the Army. After retiring from the government he held the position of Interim Director of the Free Electron Laser Laboratory and helped establish Duke's Fitzpatrick Center for Photonics and Communication Systems and served as Executive Director of the Center until his retirement. In a continuation of the retirement process, he moved to Applied Quantum Technology and has just retired from that company. He is author of the textbook, *Modern Optics*, second edition. He is now composing an elementary book in optics.



Duncan G. Steel is the Robert J. Hiller Professor of Electrical and Computer Engineering, as well as Professor of Physics and Biophysics. Prior to joining the faculty of the University of Michigan in 1985, he was a senior research scientist at Hughes Aircraft Company at the Hughes Research Laboratories. At the University of Michigan, he was Area Chair and Director of the Optical Sciences Laboratory for 20 years until 2007 when he took over the position of Chair of the Biophysics Research Division during its transition to an academic unit. As an educator and teacher, he has chaired or cochaired over 60 doctoral committees. His research includes coherent optical studies of semiconductors and their application to quantum information. His work also included 30 years of studies on age-related modifications in proteins where he exploited numerous optical techniques including single molecule studies in neurons in his studies on Alzheimer's Disease. He was a Guggenheim Scholar and received the 2010 Isakson Prize from the American Physical Society.

INTRODUCTION

This is the second, updated edition of the *Encyclopedia of Modern Optics*. There are 197 entries, many of them new or updated, reflecting the enormous progress in the optical sciences and technology and the ever-expanding impact since the publication of the first edition. Some of the new topics are:

- Nano-photonics and Plasmonics
- Quantum Optics
- Quantum Information
- Optical Interconnects
- Photonic Crystals and Their Applications
- High Efficiency LED's
- Displays
- Transformation Optics
- Fiber Lasers
- Terahertz
- Multidimensional Spectroscopy
- Organic Optoelectronics
- Gravitational Wave Detectors
- Meta Materials and Plasmonics

Selection of article topics and recruiting authors for those topics in this edition has been the work of the topical editors listed in the prologue. They were able to solicit contributions from internationally recognized leaders in their field.

The entries of the encyclopedia are arranged by subject as best as possible, a task made difficult because the field is now highly interdisciplinary and there are many subjects that have an impact in many different areas. We have added references to other articles so that readers can obtain a deeper understanding of the material or understand how a specific discussion on basic science may impact an application or technology.

RF Coherent Detection on Top of Direct Detection Lidar

Barry L Stann, John F Dammann, Mark M Giza, Brian C Redman, and William C Ruff, Army Research Laboratory, Adelphi, MD, United States

© 2018 Elsevier Ltd. All rights reserved.

Introduction

This article presents research focused on technologies that will lead to low cost, small size, low weight, and low power laser radars (ladar) for applications such as surveillance, and autonomous vehicle navigation. The motivation is to exploit the very high angular and range resolution of ladar and the robust and predictable nature of ladar signatures, which provide true 3-D images that are critical for the aforementioned applications.

The ladar architecture treated here combines the merits of low-cost, rugged, reliable continuous wave (CW) semiconductor lasers and detectors with modern frequency modulation (FM) radar signal processing technology (Stann *et al.*, 1996). In contrast to previous FM/CW ladar concepts, in the architecture to be presented here the FM is applied to a radio-frequency (RF) subcarrier, not the optical carrier. Such an architecture is referred to in this article as incoherent FM/CW ladar. This architecture focuses on the low-altitude, relatively short-range (<1 km) applications where the adverse effects of weather on propagation are minimal.

Presently there are several approaches to semiconductor laser ladar. A classic technique using CW semiconductor lasers or even light-emitting diodes (LEDs) involves measuring the range-dependent phase shift of a constant frequency RF subcarrier; two or more frequencies may be used to eliminate range ambiguities. An innovative embodiment of this technique was recently described by Anthes *et al.* (1993). Another technique investigated by a number of researchers is to modulate the CW source with a pseudorandom code and to cross-correlate the transmitted and returned waveform to determine range. Lee and Ramaswami (1992) recently described an implementation of this architecture with an added resolution-enhancement technique. The incoherent FM/CW ladar architecture discussed here has advantages over these techniques, especially for the low-cost applications. In the following text we discuss the important system aspects and advantages of the incoherent FM/CW ladar architecture and present a short mathematical analysis of the ranging theory. We then show some of the recent experimental results obtained with a breadboard version of the ladar coupled with a two-axis galvanometer-type beam scanner. This includes images of a truck obtained outdoors with a higher-power, improved version of the ladar. This follows previous work we had reported that included images taken in the laboratory with a preliminary version of the ladar. Following this we discuss an adaptation of the incoherent FM/CW ranging technique to a 32×32 pixel focal plane array (FPA) breadboard ladar. Images collected in the laboratory are shown and discussed (Stann *et al.*, 2004).

Incoherent FM/CW Ladar Architecture

Ladar Block Diagram

This section describes the ladar architecture and discusses some of the engineering issues associated with an actual design. Referring to the block diagram of the ladar (**Fig. 1**), a trigger circuit initiates the generation of a linear frequency-modulated (chirp) signal, that is, a signal whose frequency increases linearly as a function of time over period T. Other modulation waveforms are appropriate for this architecture; this one is chosen because the signal processing required to form range gates is readily understood, and the processor has low bandwidth, which makes it easy to implement. For the architecture discussed here, the start frequency of the chirp signal is typically in the tens to low hundreds of megahertz and the stop frequency in the hundreds of megahertz. The difference between the start and stop frequencies, ΔF, is chosen to establish the ladar resolution ΔR according to the usual equation from FM radar theory, $\Delta R = c/2\Delta F$, where c is the velocity of light (Stann *et al.*, 2004). Various commercial devices are available for generating the chirp signal. For short-range, high-resolution applications, commercial oscillators using monolithic microwave integrated circuits (MMICs) or hybrid technologies can be used. For long-range, high-resolution applications, precision linear tuning characteristics are required, which means that YIG-tuned oscillators or direct digital frequency synthesis devices are necessary. For applications where precision oscillators are not affordable, but tuning precision is still required, additional hardware may be built into the ladar that continuously measures the chirp-tuning characteristics. With this information, appropriate compensation techniques can be applied that effectively back out the tuning nonlinearities.

The chirp signal is fed into a wideband power amplifier that modulates the current driving a semiconductor laser diode. A circuit between the power amplifier and the laser diode matches the driving impedance of the amplifier to the laser diode impedance over ΔF. This causes the light beam intensity to remain highly modulated over the chirp bandwidth. Presently, commercial GaAlAs laser diodes are sold that have 2-GHz modulation bandwidths and output powers to 4 W. These specifications support designs with range resolutions less than 0.3 m and ranges to the low kilometers if the processing bandwidth is narrow.

The laser diode converts the chirp current waveform into a light waveform where the power is proportional to the driving current. This light is collected by a lens, collimated, and directed through a hole in a mirror toward a target. The transmitted light that is reflected by the target and propagated back to the ladar is reflected by the mirror and collected by a second lens that focuses

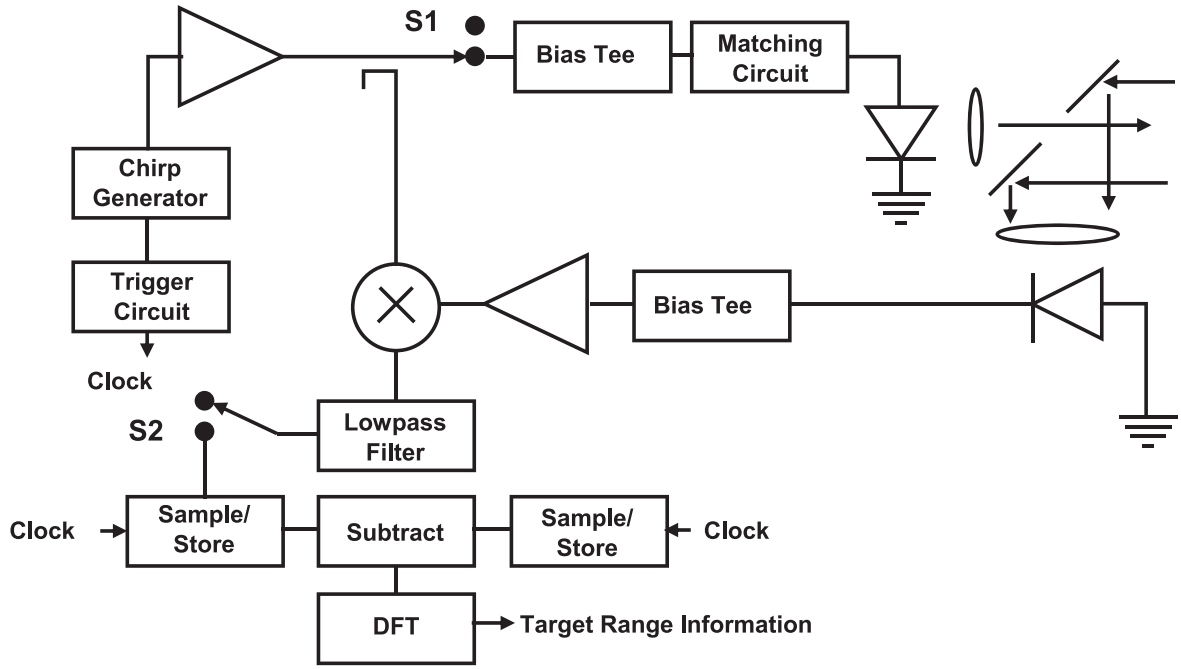


Fig. 1 Block diagram of the incoherent FM/CW ladar. Source: SPIE.

the light onto the active region of a photodiode. This optics design is used in our present breadboard; other optics designs are suitable with this ladar architecture. (Not shown in **Fig. 1** is a two-axis beam scanner placed in the transmit/receive path of the light to facilitate image formation.)

The photodiode effectively converts the received light into a current proportional to the light power; thus it recovers a current waveform identical to the original modulating waveform, except for a reduction in amplitude and a time delay equal to the propagation time from the ladar to the target and return. Commercial photodiodes, readily available for this purpose, have bandwidths to 2 GHz. Current from the photodiode is converted into a voltage with a wideband amplifier. The output of the amplifier is mixed with an undelayed sample of the transmitted chirp waveform, and the output of the mixer is fed into a low-pass filter to recover an intermediate frequency (IF) signal with mean frequency f_{if} given by

$$f_{if} = \Delta F \frac{\tau}{T} \tag{1}$$

where τ is the round-trip time delay for the transmitted signal. For moving targets there is a Doppler shift that is made small relative to f_{if} by proper selection of T. Eq. (1) follows from standard FM radar ranging theory and can be found in any radar textbook. Using $\tau = 2D/c$, where D is the distance from the sensor to the target, and substituting this expression into Eq. (1) yields

$$f_{if} = 2\Delta F \frac{D}{cT} \tag{2}$$

which shows that the frequency of the IF waveform is directly proportional to the range to the target. It follows that the range to the target can be determined by measurement of the frequency of the IF waveform using the Fourier transform or some other technique.

Unfortunately, this straightforward method to obtain target range is not normally effective because the mixer creates a "self-clutter signal" at its IF port that may be larger than the target signal by several orders of magnitude. The self-clutter signal is usually caused by imperfections in the construction of the mixer that allow a detected portion of the local oscillator (LO) to appear at the IF port. Self-clutter signals can also be generated when a small fraction of the LO power leaks over to the receive port, travels toward the first microwave device in the receive path, and is reflected back toward the mixer. The self-clutter signal is an arbitrarily shaped function that is essentially unchanged over many chirp periods. This fact is employed to subtract the clutter signal from the IF signal.

To achieve this, switch S1 is opened to interrupt the transmission of light to the target, therefore leaving only the self-clutter signal present at the low-pass filter output. Switch S2 is closed, thereby directing the clutter signal into a circuit that samples and stores the waveform. For subsequent chirp periods, S1 is closed and S2 is open. The total IF signal is now sampled and stored and then fed into a stage that subtracts the self-clutter signal on a chirp-by-chirp basis. In the last stage, the discrete Fourier transform (DFT) of the subtracted data is performed to map the received time-domain IF signal into the frequency domain, or equivalently, the range domain to indicate distance to the target. The updating rate of the stored self-clutter signal is based on the rate of change of the self-clutter signal and the degree of cancellation required to meet ladar sensitivity requirements.

Advantages

The presented approach to FM/CW ladar contrasts with the traditional approaches where the optical carrier is frequency-modulated and the optical signal is coherently detected. These approaches require highly coherent lasers to detect targets at substantial ranges. The short coherence length of the CW semiconductor lasers used in such designs preclude target detection beyond a few tens of meters or less (Dieckmann, 1994). Even if the coherence length were significantly increased through the use of an external resonator or other techniques, problems resulting from the required precise alignment of return and LO signals, speckle, and large optical Doppler shifts would remain. For these reasons, the incoherent FM/CW ladar can be much less complex and costly, and yet more rugged and reliable.

The incoherent FM/CW ranging approach is a linear system, that is, any number of target and clutter returns will be separated in the range image if they are physically separated by more than ΔR. This is a very important feature if, for instance, the target is partially obscured by foliage or smoke, as one may often expect on battlefields. The phase measurement scheme of Anthes or the superresolution technique of Lee cannot resolve more than one target at a time in the ladar beam. A pulsed system can resolve multiple targets only if its pulse width is less than $2\Delta R/c$ and its receiver bandwidth is sufficient to fully resolve the return pulse, which degrades the Signal-to-noise ratio (SNR). Practical pulsed systems use much longer pulses and corresponding lower bandwidths, and resort to superresolution techniques such as leading-edge detection based on a threshold set at a constant fraction of the peak of the return (Stann *et al.*, 1995). This achieves a high range measurement precision, but requires a high SNR and still cannot resolve closely spaced multiple targets. Thus a target within a smoke cloud may not be discernible even if the ladar power is sufficient to penetrate the smoke. The incoherent FM/CW approach can resolve targets separated by ΔR without requiring a high SNR and with low signal processor bandwidths.

Another advantage of the incoherent FM/CW approach is inherent in its use of CW diode lasers. Diode lasers are limited in peak power by catastrophic damage mechanisms, and, like other semiconductor devices, provide more average power efficiently when operated CW. Most commercial applications of diode lasers, such as for compact disks, barcode scanners, and communications, are for CW devices. Therefore we may expect these devices to improve in performance and especially cost without any Department of Defense (DoD) investment. Finally, the incoherent FM/CW technique can provide Doppler information commensurate with the mean frequency of the AM that gives target velocity and may aid in target detection in a clutter environment.

Mathematical Analysis

This section presents an idealized mathematical analysis to give the reader insights into the formation of range gates by the incoherent FM/CW ladar and the relationship of system parameters to range resolution. This analysis is also instructive in that it shows that the theory is valid when ΔF is as large as or larger than f_0 as in our case, but unlike the case in radar, where ΔF is much smaller than f_0. The discussion here treats only the core theory of the ladar and does not include any analysis of the many other signal processing techniques used in FM radar that can also be exploited to handle problems unique to any real ladar application. Some of the common techniques include the use of alternative modulation waveforms (triangle waves, pseudorandom codes, etc.) to simplify the formation of range cells or inhibit the detection of jamming signals or other operating sensors, the application of weighting on the Intermediate-frequency (IF) waveform to reduce range sidelobes, IF amplifier limiting to effectively normalize the range response to any target return amplitude, the addition of gates to inhibit the detection of clutter and aerosols, Doppler detection to determine target velocity, and methods to determine whether a target is approaching or receding.

FM ranging theory

An analysis of FM ranging theory begins with an expression for the frequency of the transmitted chirp waveform

$$f(t) = f_0 + \frac{\Delta F t}{T}, \quad -\frac{T}{2} \le t \le \frac{T}{2} \tag{3}$$

where f_0 is the center or carrier frequency of the chirp waveform and t is time. The phase of the transmitted chirp waveform is

$$\phi_x(t) = \int_{-\infty}^{t} 2\pi \left(f_0 + \frac{\Delta F}{T} t' \right) \mathrm{d}t' \tag{4}$$

While the phase of the received signal is

$$\phi_r(t) = \int_{-\infty}^{t-\tau} 2\pi \left(f_0 + \frac{\Delta F}{T} t' \right) \mathrm{d}t' \tag{5}$$

The phase difference between the transmitted and the received is

$$\Delta\phi(t) = \phi_x(t) - \phi_r(t) \tag{6}$$

or

$$\Delta\phi(t) = \int_{t-\tau}^{t} 2\pi \left(f_0 + \frac{\Delta F}{T} t' \right) \mathrm{d}t' \tag{7}$$

Performing the integration and inserting the limits yields

$$\Delta\phi(t) = 2\pi\left(f_0 t + \frac{\Delta F}{2T}t^2\right) - 2\pi\left(f_0(t-\tau) + \frac{\Delta F}{2T}\left(t^2 - 2t\tau + \tau^2\right)\right) \tag{8}$$

Canceling the terms and dropping the τ^2 term because τ is set much less than T leaves

$$\Delta\phi(t) = 2\pi f_0\tau + 2\pi\frac{\Delta F}{T}\tau t \tag{9}$$

The mixer and following filtering process yields the IF waveform,

$$V_{\mathrm{m}}(t) = a_{\mathrm{r}}cos(\Delta\phi(t)) \tag{10}$$

or

$$V_{\mathrm{m}}(t) = a_{\mathrm{r}}cos\left(2\pi\left(f_0\tau + \frac{\Delta F}{T}\tau t\right)\right) \tag{11}$$

where a_{r} represents the amplitude of the received signal after considering all propagation, scattering, detection, and mixing losses and amplifier gains.

An examination of Eq. (11) shows that the IF waveform is a cosine function whose argument contains two terms. The first is recognized as a fixed Doppler phase term that is proportional to the carrier frequency and time delay or distance to the target. The second term is a function of time and contains the frequency of $V_{\mathrm{m}}(t)$, $\left(\frac{\Delta F}{T}\right)\tau$, which is proportional to τ or the distance to the target. A plot of this function (**Fig. 2**) as a function of the normalized range $\tau\Delta F$ and normalized t illustrates this behavior. Here the dark regions represent the minimum of $V_{\mathrm{m}}(t)$, and the bright regions represent the maximums. The important feature to notice is that the number of periods observed over normalized time or one sweep of the modulation increases proportionally with the normalized range.

From this, it follows that the target distance can be determined simply by measurement of the frequency of $V_{\mathrm{m}}(t)$ over T. The usual method for determining the frequency content of a waveform requires computing the Fourier transform of the waveform

$$F(f) = a_{\mathrm{r}}/T\int_{-\frac{T}{2}}^{\frac{T}{2}}\cos\left(2\pi\left(f_0\tau + \frac{\Delta F}{T}\tau t\right)\right)\mathrm{e}^{-2\pi ft}\mathrm{d}t \tag{12}$$

Performing the integration yields

$$F(f) = \mathrm{e}^{j2\pi f_0\tau}\left(\frac{\sin\left(\pi\left(\Delta F\frac{\tau}{T} - f\right)T\right)}{\pi\left(\Delta F\frac{\tau}{T} - f\right)T}\right) + \mathrm{e}^{-j2\pi f_0\tau}\left(\frac{\sin\left(\pi\left(\Delta F\frac{\tau}{T} + f\right)T\right)}{\pi\left(\Delta F\frac{\tau}{T} + f\right)T}\right) \tag{13}$$

where the factor a_{r} which modifies the entire equation, has been dropped to effectively normalize the amplitude of the ladar response to a target. For a ladar architecture employing the *DFT* to establish range cells, each complex output sample of the transform represents the magnitude and phase of the respective harmonic frequency components of the input waveform that occur

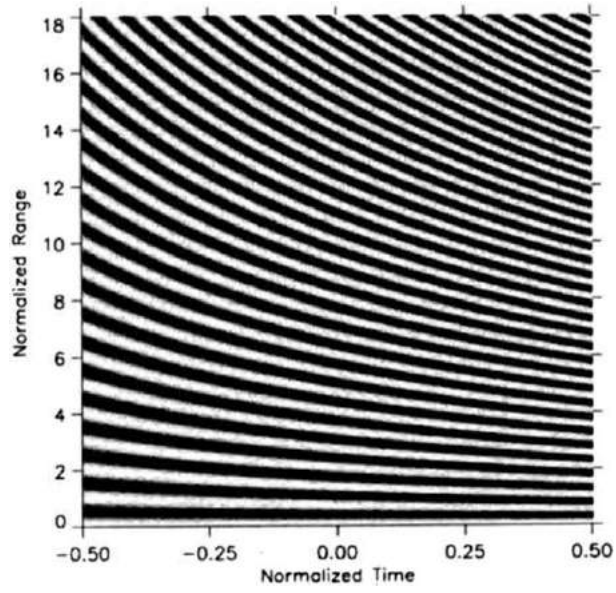


Fig. 2 Intermediate frequency (IF) output waveform as a function of time and normalized range. Source: SPIE.

at integer multiples of $1/T$. This allows f to be replaced in Eq. (13) with n/T, yielding

$$F(n/T) = e^{j2\pi f_0 \tau}\left(\frac{\sin(\pi(\Delta F\tau - n))}{\pi(\Delta F\tau - n)}\right) + e^{-j2\pi f_0 \tau}\left(\frac{\sin(\pi(\Delta F\tau + n))}{\pi(\Delta F\tau + n)}\right) \tag{14}$$

The exponential factors in Eq. (14) represent the Doppler component present in each harmonic line, while the $\sin(x)/x$ factors represent the amplitude of the Doppler components. For n greater than three or four, the second term can be ignored because it is much smaller than the first. Examining the first term shows that each harmonic component of $F\left(\frac{n}{T}\right)$ has a maximum for

$$\Delta F\tau = n \tag{15}$$

which means that the output samples of the discrete Fourier transform have been mapped to normalized range according to Eq. (15). Equivalently, each output sample corresponds to a range gate.

Fig. 3 shows how the amplitude of individual harmonic lines or range gates of Eq. (14) behave as the normalized target range moves from 0 to 18. These plots are called range responses. For instance, the top plot shows the magnitude of the first range gate (harmonic number 0) as a function of target range. As expected, the magnitude of this range gate is maximum at zero range and decreases with increasing range. The rapid modulation in the basic $\sin(x)/x$ shape of the function is caused by the second term in Eq. (14), which is still strong at small n.

The notion of range resolution can now be established from one of the higher-harmonic-number range responses. From these responses, the normalized distance between the 0.64 levels of the mainlobe of the range response is equal to 1, which means that

$$\Delta F\Delta\tau = 1 \tag{16}$$

Using the substitution, $\Delta R = c\Delta\tau/2$, one finds that the range resolution equals

$$\Delta R = \frac{c}{2\Delta F} \tag{17}$$

In the design of an FM radar, ΔF is a small percentage of f_0. Under these conditions, the previous closed-form theory is known to be valid. For a high-resolution design of this ladar, ΔF is a high percentage of f_0, raising the question of whether the theory still holds. To investigate this issue, the ladar was simulated with a brute-force computer code that more closely modeled the processes in an actual system. Comparisons of the results obtained from this model and the closed-form theory showed no significant

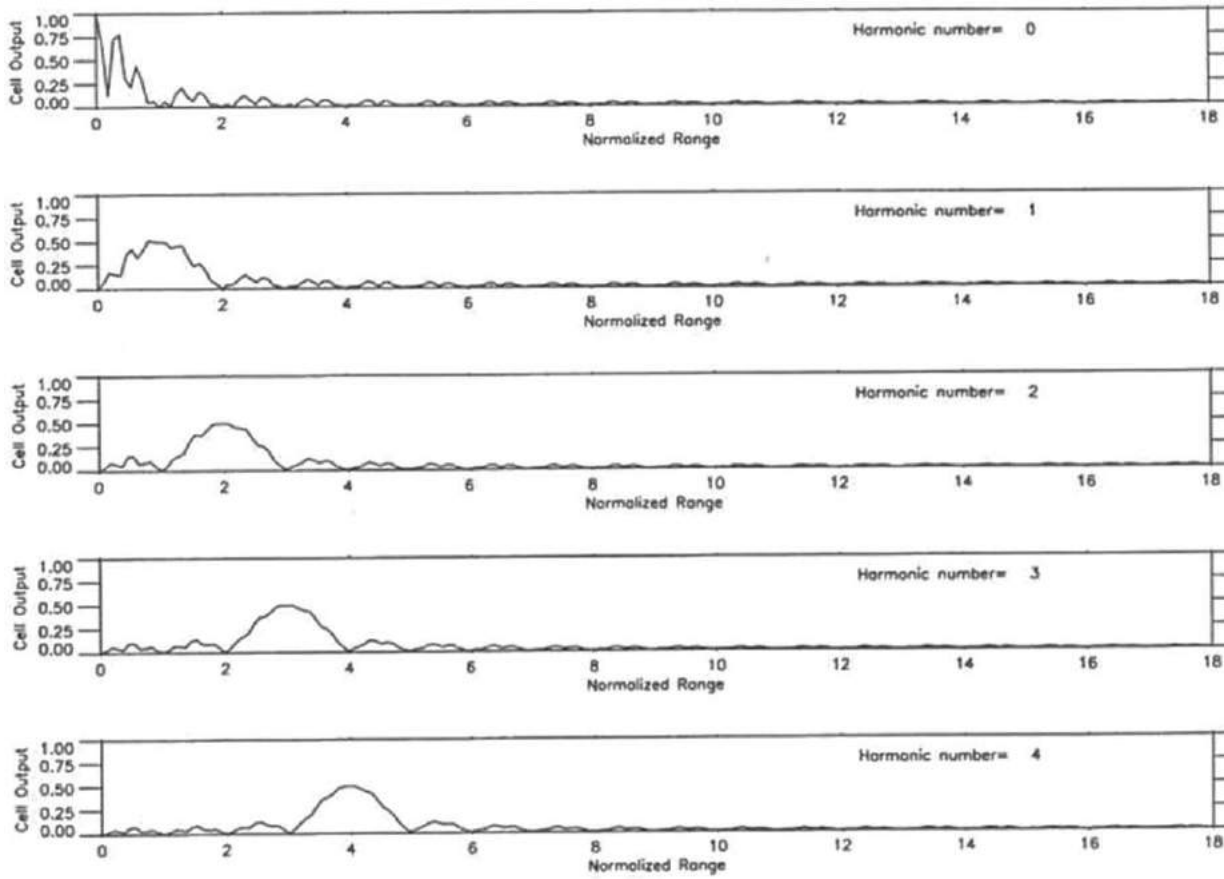


Fig. 3 Range-gate output as a function of normalized target range. Source: SPIE.

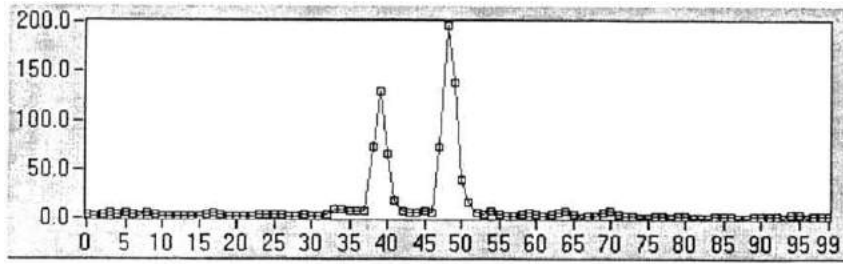


Fig. 4 Discrete Fourier transform (DFT) of intermediate frequency (IF) signal-two targets. Source: SPIE.

differences. Additional verification of the validity of the closed-form theory is evident in the experimental results of the following sections.

Ladar Hardware

A breadboard of the incoherent FM/CW was built to validate the theory and collect high-resolution imagery of targets. The optics and microwave elements of the imaging ladar are organized as shown in the block diagram in **Fig. 1**, except for the placement of a two-axis galvanometer-type beam scanner in the transmit/receive path. Presently, a 100-mW laser diode at 817 nm is employed as the transmitter, and an avalanche photodiode is used for the receiver. The usable bandwidth of the laser and photodiode combination is about 1.3 GHz, and the AM index is approximately 86%. A personal computer (PC) was configured to set the beam pointing direction, trigger chirps, sample the IF data, cancel the self-clutter, form the range gates, and display the data. This system can collect 80×80 pixel image files and display the collected and processed data in several formats.

Point-target measurements

Point-target measurements recovered from tests with the incoherent FM/CW ladar illustrate the theory and some of its performance characteristics. To accomplish this we recorded the IF signal for targets at an approximately 9-m range for a chirp that starts at 600 MHz and ends at 1200 MHz. The DFT is used to map the IF signal into range gates. **Fig. 4** shows when the transform result is used on an IF signal comprised of returns from targets at two different ranges. As discussed earlier, the ladar is a linear system; thus multiple targets can be ranged simultaneously as evidenced by the two impulses present at range-gate 39 and 48. For this test $\Delta F = 600$ MHz thus the distance between range-gate is 0.25 m. This corresponds to 9.75 m for the first target and 12 m for the second target. The first target was deliberately set at 9 m which should correspond to range-gate 36. This error is caused by additional delay in the microwave lines internal to the ladar. When a target is in the middle of a range gate and a Hanning window is used, DFT samples on either side of the maximum should theoretically be 50% of the maximum value, and all others should be substantially suppressed. This is roughly true in the figure. Discrepancies from the theoretical distribution are usually caused by nonlinear FM characteristics in the chirp signal. Other causes may include amplitude modulation of the IF signal due to nonflat amplitude-versus-frequency characteristics of the microwave components, laser diode, and/or detector diode. Nonlinear phase-versus-frequency characteristics of these same devices can also cause spreading of the signal distribution. Additional hardware can be added to the system to measure component errors, and appropriate compensation can be applied to the IF signal to minimize spreading effects. Little effort has been expended so far in reducing these errors in the breadboard ladar.

Imaging measurements

The imaging capabilities of the ladar were tested at an outdoor site on the ARL Adelphi, MD, campus. **Fig. 5** shows the site with an Army pickup truck oriented perpendicular to the ladar at about a 52-m range. All specularly reflective surfaces on the truck were masked with black tape for laser safety reasons. A calibrated standard reflectivity target (18%) is positioned in the lower right of the photograph, and a grassy hill is located about 15 m beyond the truck.

An 80×80 pixel image of the truck was collected with the imaging ladar for aspect angles of approximately 0, 45, and 90 degrees. For brevity, **Fig. 6** shows only the 0 degree result. The uppermost image is formed pixel by pixel by summing outputs from all of the range cells from the front of the truck to beyond the hill. The bottom image sum outputs from the range cells from the front through the rear bumper of the truck only, thereby eliminating the returns from the hill and enhancing the contrast of the truck from the background. The pixel density is sufficient to allow one to determine that the target is indeed a pickup truck. The calibration target appears in each image in the lower right.

32×32 Pixel FPA Ladar Breadboard Using Incoherent Chirped Amplitude Modulation

Introduction

This section presents a FPA ladar architecture that is useful for a variety of applications such as reconnaissance and robotic navigation and is based on the optically incoherent FM/CW ranging architecture reported in the previous section. The incoherent FM/CW ranging architecture is a natural fit to a FPA design because the final system bandwidth is low enough to provide sufficient



Fig. 5 Ladar image site. Source: SPIE.

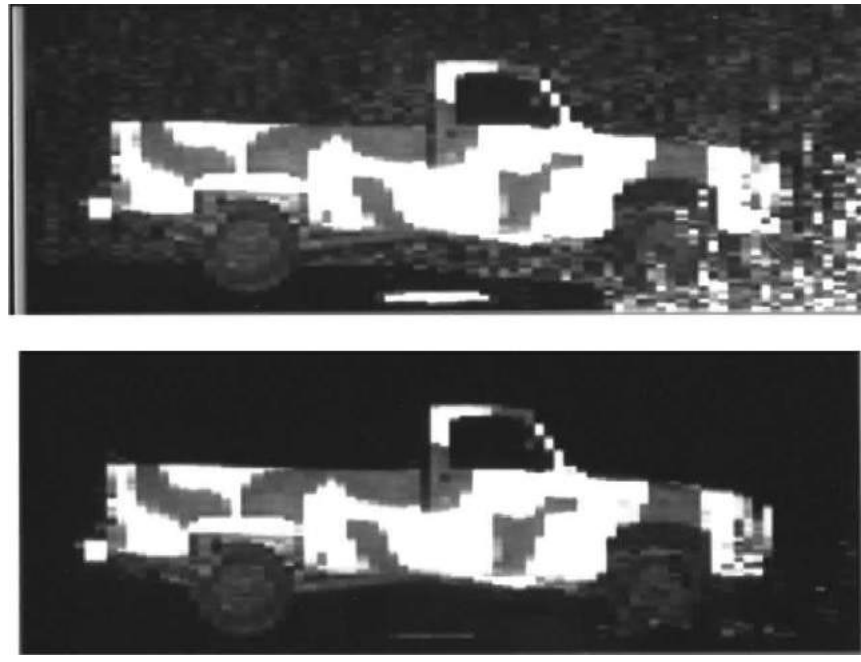


Fig. 6 Ladar images of a pickup truck (All range gates, top, partial). Source: SPIE.

signal-to-noise while using low-cost and low power laser diodes. In the following text we describe the FPA architecture, optoelectronic (OE) detector design, read-out based on code division multiple access (CDMA) techniques, and signal processing. We then summarize work to build a brassboard and related hardware modifications to reduce pixel-to-pixel cross-talk, and the addition of a 32-channel data acquisition system (DAS) and new signal processing and display software. Imagery collected in the lab is displayed along with a discussion of the improvements to image quality achieved with the reduction of pixel-to-pixel cross-talk.

Incoherent FM/CW FPA Breadboard Architecture

In the following text, we briefly describe the operating principles of the 32×32 pixel FPA ladar breadboard using the block diagram shown in Fig. 7. A clock circuit controls the generation of a chirp signal that serves as the laser intensity modulation and RF LO signal. As in the previous section the chirp signal is simply a sinusoidal waveform whose frequency linearly increases over a period T and then flies back to the original start frequency (i.e., sawtooth FM). The chirp signal for our breadboard has a start frequency of 200 MHz and a stop frequency of 800 MHz. FM/CW radar ranging theory supports a rich variety of improvisations to the basic sawtooth modulation format. However, to simplify our present work with the ladar breadboard, we use only the pure sawtooth modulation format, which yields high range resolution with the least amount of ladar signal processing.

To modulate the laser illumination, the chirp signal is fed into a wideband RF power amplifier with a low output driving impedance. Output from the amplifier and a dc current are summed in a bias tee to provide a modulated current drive for a

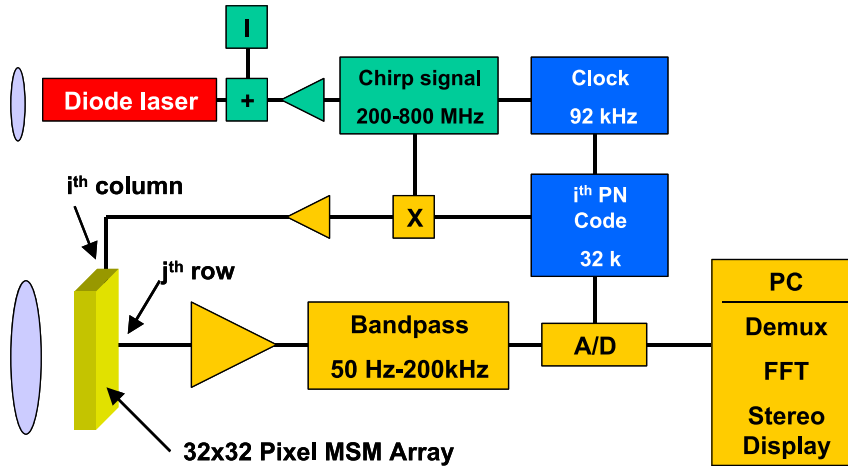


Fig. 7 Laboratory ladar breadboard block diagram. Source: SPIE.

broad-area semiconductor diode laser at 808 nm with a bandwidth at least equal to the bandwidth of the chirp waveform. A high-percentage intensity modulation of the light beam is desirable. The divergent laser beam from the semiconductor laser is collected with a collimator and focused to project a beam sufficiently wide to encompass or floodlight the target scene of interest.

A small portion of the transmitted beam is reflected from the target toward the ladar and collected by the receiver optics. An array of OE-mixing metal-semiconductor-metal (MSM) detectors is located at the focal plane of the receiver optics (Ruff *et al.*, 2000; Shen *et al.*, 2000). When the transmitter RF modulation waveform (LO voltage) is applied across the OE-mixing detectors, a photocurrent response is recovered at each detector that is the product or mixing of the RF LO and the intensity modulated light waveforms. (Note that in contrast to optically coherent detection with an FM-CW waveform, for the chirped AM system the LO is an RF voltage waveform not a laser beam, and the frequency of the intensity modulation of the transmitted laser light is chirped, not the frequency of the laser light's electromagnetic wave.) With sawtooth modulation, the instantaneous transmitted and received chirp waveforms differ in frequency (by the IF) because the round-trip light propagation time delays the received chirp waveform with respect to the LO chirp waveform. Thus, mixing of the LO and return signal in the detectors produces a sinusoidal photocurrent (IF waveform) whose frequency is proportional to range.

To recover the photocurrents from the individual pixels, we employ a unique read-out based on CDMA techniques discussed in more detail in a previous publication (Stann *et al.*, 2003). To implement this technique, we multiply the LO signal for each column of the array by a unique binary code that induces a phase shift on the LO of either 0 or 180 degrees. The net effect is to nearly orthogonalize the photocurrents for all pixels in a row, thus allowing all currents to be combined into a single wire that connects to a transimpedance amplifier (TIA) to the side of the detector array. The TIA converts the photocurrents into a voltage that is then sampled at the code clock rate by an analog-to-digital converter (A/D). The CDMA FPA read-out technique was originally conceived because it allowed us to obtain read-out function with discrete electronic components without having to build a custom read-out integrated circuit (ROIC), which requires substantial development time and is usually expensive. As mentioned, the CDMA technique multiplexes all of the pixel photocurrents in a row onto a single row readout line. This reduces the number of readout lines from 1024 to 32 for the 32×32 pixel FPA. The CDMA readout also requires that different codes modulate the LO drives for each column, so that 32 code modulated LO drive lines are required for the 32×32 pixel array. Thus, the total number of drive and readout lines is 64 for the 32×32 pixel array. In general, an $N \times N$ pixel array will require N readout and N LO lines (a total of 2N) for the CDMA read-out. Demuxing of the data is done digitally in software on a PC. Here the data from each row's A/D is successively multiplied by the codes associated with each pixel, which are generated in software, to recover the IF signal from the respective pixels. The fast Fourier transform (FFT) is taken for each of the demuxed photocurrents, i.e., each of the IF signals, to map the data space into a three-dimensional image space.

32×32 Pixel Laboratory Breadboard Hardware

Fig. 8 shows the front view of our laboratory breadboard. We illuminate with a 3.2-W GaAs multi-stripe diode laser where some of the power is coupled into a fiber cable and directed to allow flood illumination of the receiver field of view (FOV). The receiver lens is 5 cm in diameter, and its position is adjustable to center the FOV on the FPA and to adjust the focus.

A fan-in/fan-out board feeds-in code-modulated LO signals to the FPA columns and feeds-out the photocurrents from each FPA row. Circuitry to apply the codes to the FPA columns are on separate boards that plug-into the rear of the fan-in/fan-out board. Each column driver board supports circuitry to drive two detector array columns. The RF LO signal enters the board from a single input and is immediately fed into a two-way power splitter. Each two-way splitter output is fed into the LO port of a balanced mixer where they are bi-phase modulated by the PN code applied to the IF port. These modulated outputs are then amplified by a pair of MMICs amplifiers that are connected to microstrip lines on the fan-in/fan-out board. CAT5 cables carry the code signals and

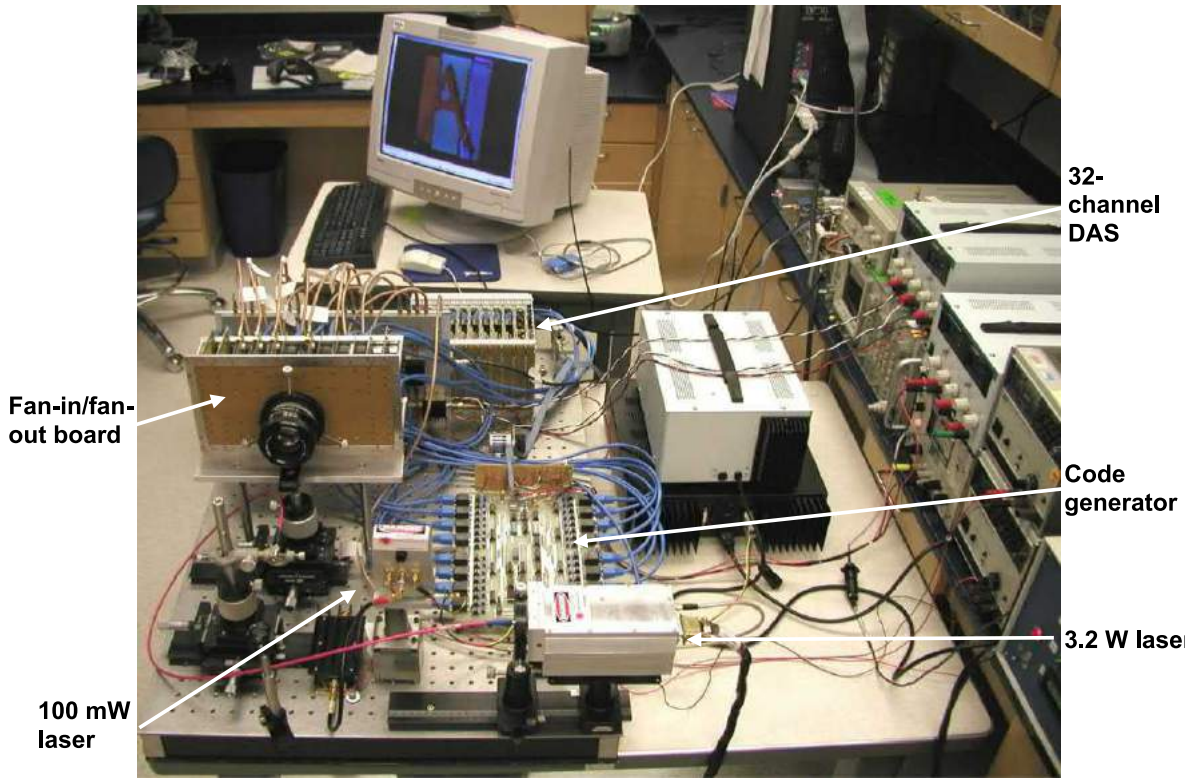


Fig. 8 Front (top) view of 32 × 32 pixel laboratory breadboard. Source: SPIE.

power to the driver board. The RF bandwidth extends from 200 to 800 MHz and each channel can deliver up to 100 mW into a 50-Ω load. This signal level is more than adequate to drive the GaAs detector array and is likely to be adequate to drive an InGaAs array.

The FPA row output currents are fed through the fan-out board to the TIA boards plugged into the back of the fan-in/fan-out board. Each TIA board supports four amplifier channels. Each channel includes a TIA stage based on a new wideband, FET input, operational amplifier that allows high transimpedance gains with wide bandwidths. This capability is especially important for achieving low noise amplification which in-turn increases the ladar's maximum range. The current operating parameters of each amplifier chain are as follows: a transimpedance gain of 300 MΩ, a low-pass cutoff of 200 kHz, and a highpass cutoff of 50 Hz. CAT5 computer patch cables connect the power, grounds, and output signals to a 32-channel DAS that acquires the TIA amplifier outputs. The 32-channel DAS can sample (with 8 bits) each channel at up to a 400 kHz rate; for the current experiments we sample at a 93 kHz rate to facilitate debugging of the ladar.

The code generator appears in the lower middle of the picture. The code generator is based on a classical linear feedback shift register (LFSR) design where the outputs of the fourteenth and fifteenth stages of the LFSR are fed into an exclusive OR, and the resulting output is then fed into the first stage of the LFSR. This process yields a fifteen-bit maximal length binary PN code that repeats every 32,767 ($2^{15}-1$) clock cycles. The code sequence is clocked out at 93 kHz into a series of parallel-out shift registers that provide 32 replicas of the code delayed by two clock periods (i.e., 2 chips). Additional circuitry is included on the board to restart the code sequence at the beginning of each FM chirp, and to inject a seed word into the code generator to insure that the sequence is initialized identically for every chirp. To mitigate transient effects in the driver and TIA boards, the code is run continuously except for a 10-μs period at the beginning of each chirp in which the registers are cleared, and the seed word is injected.

The chirp generator is built around a low-cost, commercial, direct digital synthesizer (DDS) chip (not shown in Fig. 8). Output from the DDS is multiplied-up in frequency by phase-locking to a voltage-controlled microwave oscillator. The basic operating parameters for the chirp generator, including FM deviation, center frequency, and chirp rate, are entered on the ladar control and processing PC which then feeds the data to the chirp generator. The nominal parameter settings are 600 MHz for the FM deviation, 500 MHz for the center frequency, and 3 Hz for the chirp rate. Once the operating parameters are loaded, the chirp generator runs continuously, and sends a digital low-to-high transition at the beginning of each chirp to initialize and start the code generator, and to start the data acquisition process.

Ladar control, signal processing, and display is performed on a PC. A Labview code performs the ladar control and data acquisition functions along with providing display of some intermediate signal processing steps to aid in monitoring system performance. The Labview code captures data from the 32-channel DAS at a 3-Hz frame-rate and stores it on a hard disk. A "C"

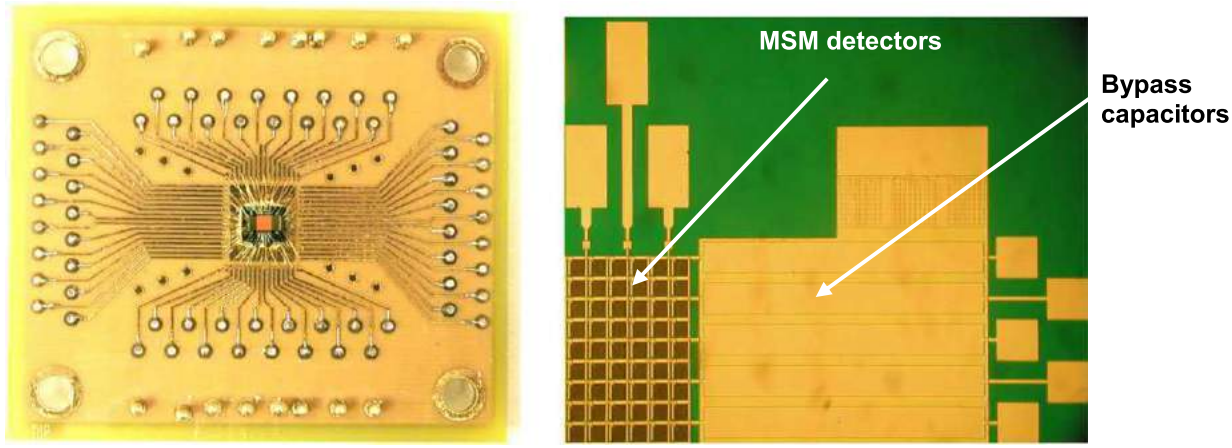


Fig. 9 Metal-semiconductor-metal (MSM) detector array on PC board mount (left), upper right corner of FPA chip showing bypass capacitors (right). Source: SPIE.

code is running concurrently that reads the data from the hard disk, performs the demuxing operations required for the FPA read-out, computes the Fourier transform of the resulting IF signals to range-gate the data, and displays the data in stereo. This process occurs continuously requiring a period of one to two seconds. The interactive 3-D display (stereo display), written at ARL, thresholds the intensity-versus-range signal for each pixel and draws a rectangle at each range where the threshold is exceeded. The size of the rectangle matches the area subtended by the pixel at that range, so a large flat object would be precisely tiled by the rectangles, but rough or very small objects would appear like a point cloud. The display allows a user to zoom and pan around the data and also allows stereoscopic viewing. The depth perception afforded by the stereoscopic viewing and the capability to change perspective enables the user to interpret the data in much the same way as he or she views complex scenes in real life.

MSM Detector Design and Mounting Scheme

The mounting technique for the FPA is shown in the left of Fig. 9. Here LO signals are input from the fan-in/fan-out board to IC socket pins that are soldered into the FPA mount. Microstrip lines (i.e., conductors routed over a ground plane) then carry the LO signals to pads in close proximity to the FPA mounting position; standard wirebonds connect these pads to bonding pads on the FPA chip. The width of the microstrip conductors and the dielectric thickness were made a small as possible but consistent with commercial printed circuit board fabrication techniques to allow maximum distance between lines and therefore achieve minimum cross-talk. This new board also featured IC socket pins that mated with the pins soldered into the FPA mounting board to facilitate changing of the FPA. S_{12} measurements on the new fan-in/fan-out board and FPA mounting board showed that the cross coupling was usually less than -40 db over the ladar's RF bandwidth.

The FPA is 32×32-pixel interdigitated-finger MSM photodetector array with integrated capacitors at the row outputs shown on right of Fig. 9. The integrated capacitors will replace the discrete capacitors mounted on the fan-in/fan-out board. These capacitors bypass the LO signal currents to ground thereby suppressing LO signals that may enter the TIAs and create noise. They additionally prevent the row busses from being modulated by the LO voltages which would create pixel-to-pixel cross-talk. The integrated capacitors perform the bypassing function more effectively than the discrete capacitors because the lead inductance between the FPA row output and ground will be much lower.

The 32×32 FPA of 60 μm pixels is fabricated on semi-insulating GaAs. The thickness of the second silicon nitride layer is such that the capacitance at the end of each row is approximately 15 pf.

Results of Laboratory Breadboard Tests

In this section we briefly discuss our most recent imaging experiments with the breadboard ladar to give the reader some measure of its performance. For these tests, the bandwidth of the modulation is 600 MHz; this establishes a distance of 0.25 m between range cells. All data for a single ladar frame is collected in approximately 0.33 s; this yields a ladar frame rate of 3 Hz that is also the final signal processing bandwidth. The receiver lens diameter is 5.0 cm. As mentioned, some light power from the 3.2-W laser illumination module is coupled into a fiber optic patch cord and light at the output of the cable is then passed through a lens system to form a circular flood illumination field that overlaps the FOV of the receiver. This technique yields a much more uniform illumination field than can be obtained by using the light that is emitted directly out of the laser. The fiber collects 300 mW of laser light; the portion of this light that is in the FOV of the receiver is about 200 mW thus each pixel is illuminated with approximately 0.2 mW of optical power.

The first imaging test examined the ladar performance for a single pixel at one range. Here the collimator of the 100-mW laser illuminator was adjusted so that a small spot (less than the size of a projected pixel) was projected on the wall approximately 11-m

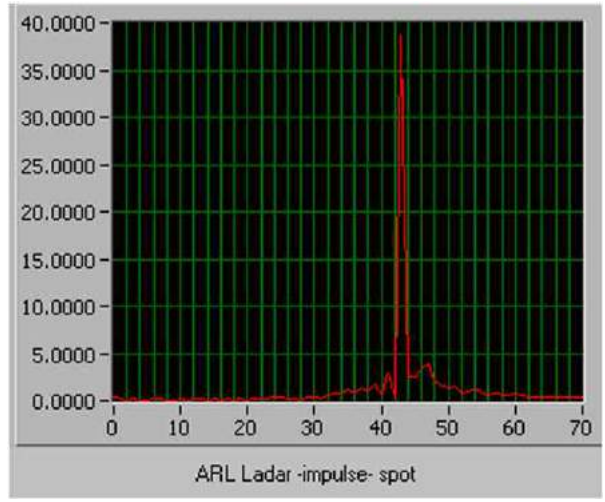


Fig. 10 Ladar impulse response (range dimension). Source: SPIE.

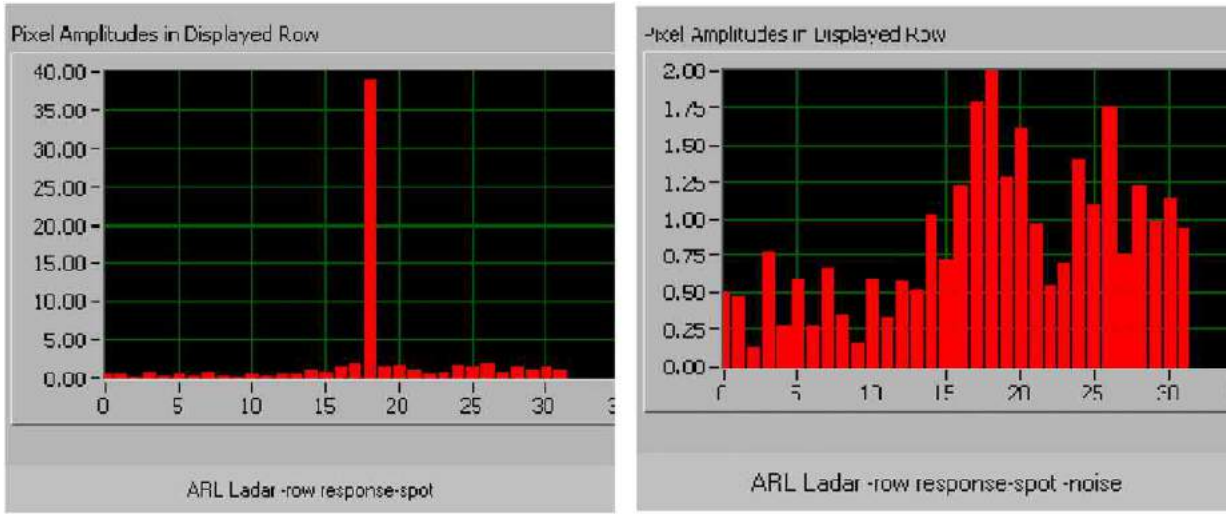


Fig. 11 Impulse response (cross-range dimension; expanded vertical scale on right). Source: SPIE.

distance from the breadboard. The range performance or impulse response in the range dimension is shown in Fig. 10. The horizontal axis is displayed in units of resolution cells which for the amount of FM deviation used (600 MHz) corresponds to 0.25 m; the vertical axis is simply amplitude in arbitrary units. The response peaks at 43 units (11.75 m), as expected, with an amplitude of 38 units; low responses before and after the peak (2.5 and 4 units of amplitude, respectively) are caused by reflections on the microwave transmission lines feeding various components in the breadboard and can be eliminated by improving impedance matching at those points. Overall, the performance in range is acceptable and can be easily improved by more careful attention to the microwave design.

The impulse response in the cross-range or azimuthal dimension is shown in left of Fig. 11. In this figure, the horizontal axis is expressed as pixel number (0 corresponds to pixel number 1) and the vertical axis is again in arbitrary units; the light is positioned on row 21, column 19. As expected, largest amount of signal energy appears at the correct pixel position, however lower values appear at all the other pixel positions. In actuality this will happen because the code read-out concept as implemented here with maximal length pseudorandom sequences will have some non-zero signal level in the other pixel positions. This level of cross-talk is for the most part established by the length of the sequence; other factors such as bandlimiting of any amplifier or filter in the code application or IF signal chain will also affect the cross-talk level (Stann *et al.*, 2003). Considering the situation where the code length (32,767 bits is used in the breadboard) is the only factor, the cross-talk-to-signal ratio should be about –45 db. To better examine the cross-talk level we expanded the vertical scale and displayed the results in the right half of Fig. 11. Here we found that the cross-talk level in pixels to the left of pixel 19 is about –43 db after correcting for the Johnson noise present when the illumination was shut-off. This result is satisfactory considering that any filtering effects in the breadboard will degrade cross-talk

level over the ideal situation. For pixels to the right of pixel 19, the cross-talk level is approximately 10 db higher; this level is expected to degrade image quality particularly in situations where large portions of a target are at a same range. We believe that the cause for this elevated cross-talk level on the right side of the signal is that the LO signals that are routed on the right hand side of the fan-in/fan-out board are coupling to the IF output lines that are also routed on the right hand side of the board and then feeding back to the FPA pixel output bus. This causes a small amount of LO signal from all of the LO lines on the right hand side of the fan-in/fan-out board to be applied to all the detectors in a row. When this happens, the photocurrent in the illuminated pixel becomes modulated at a low level by the codes for other columns. The demuxing step then reports that some signal energy is present in those codes or pixel positions. As mentioned we believe that the problem can be mitigated by improving the RF bypassing of the FPA row output busses by building-in capacitors at the end of each row of the FPA chip. In summary the azimuthal cross-talk is reduced about 20 db over the results achieved in the prior year with the FPA mounted in the leadless chip carrier.

For the imaging test, we set up a scene about 10 m from the breadboard in the back of our lab bay as shown in Fig. 12. Here a cardboard "A" is supported on a pedestal followed by a poster board to the left side of the "A" and 0.25 m further in range. A brown cardboard box is positioned roughly behind the poster board about 0.75 m further in range. A white cardboard box is alongside the brown cardboard box and 0.25 m further in range.

As mentioned earlier, the ladar breadboard can run continuously where a Labview code performs the ladar control and data acquisition functions while a "C" code performs pixel demuxing, range-gate formation, and stereo display. The 3-D image produced by the "C" code updates about every 1–2 s depending on what intermediate data is displayed in the Labview program. This capability is particularly interesting because successive frames are sequentially shown while the viewer can rotate the image to



Fig. 12 Laboratory scene. Source: SPIE.

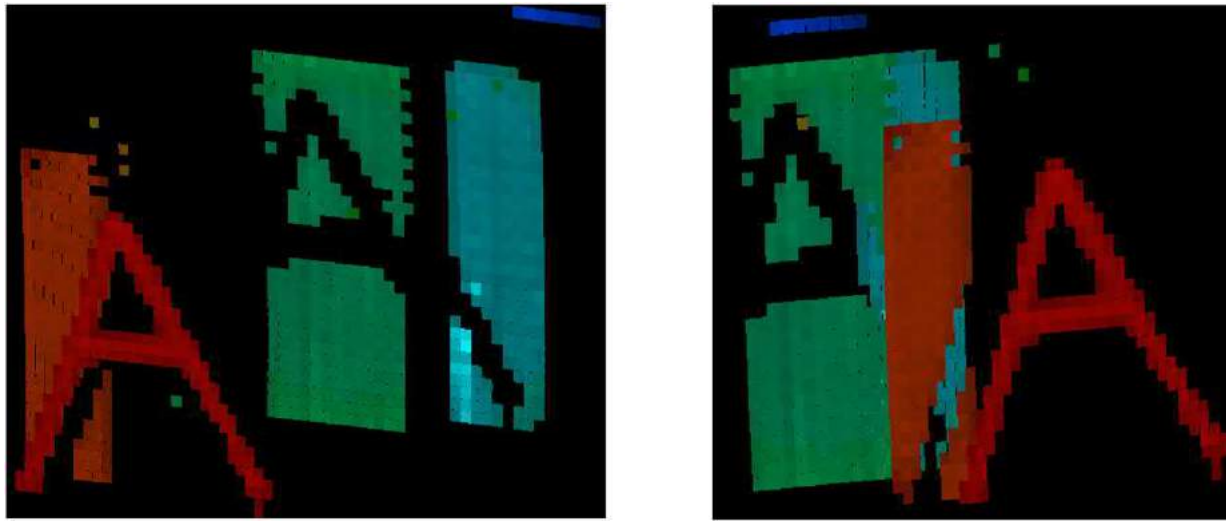


Fig. 13 Breadboard ladar image of laboratory scene. Source: SPIE.

other aspects. In Fig. 13 we show the laboratory scene as imaged from one viewpoint, but displayed at two aspects. The "A" is very well-formed and shows a clear staircase function along the legs as one would expect for an image with pixel-limited resolution. It appears even clearer with the stereo display on the ladar's PC where degradation caused by the screen capture and other processes needed for presentation in a written report are absent. The poster board one resolution cell behind the "A" is clearly separated from the "A" and exhibits the shadow of one leg of the "A." About six artifacts are present in the space between the poster board and the two cardboard boxes. These are the result of somewhat less than theoretical performance of the code-multiplexed read-out. As alluded in the previous section, diagnostic measurements indicate that the cause of this degraded performance is LO signals coupling into the IF output lines and then backing-up into the FPA photocurrent busses. We are reasonably confident that the new FPA design with built-in bypass capacitors at the end of each photocurrent buss is expected to attenuate the LO signals and therefore eliminate the image artifacts. The last two boxes are clearly imaged and show the shadow of the "A" and their respective range displacements. The farthest box has a bright region on its left side; this is caused by a glint return from scotch tape on the box.

Conclusions

We have demonstrated the range measurement capability of an incoherent FM/CW ladar where the FM is applied to an RF subcarrier that AMs the light output, instead of to the optical carrier. We outlined the theory of this approach and proved that it is applicable even when the FM bandwidth is greater than the center frequency of the AM. To mitigate the problems of self-clutter created by mixer imbalances or other processes, we proposed and demonstrated in software a simple subtraction technique that can effectively remove false targets caused by such self-clutter. Measurements made with the breadboard imaging ladar have shown that the range resolution is commensurate with the FM bandwidth. An implementation of the self-clutter cancellation technique in the ladar indeed shows that near-range false targets can be eliminated. Measurements have also shown that the ladar can simultaneously resolve and display multiple targets in the same image pixel that are displaced in range by more than the intrinsic ladar resolution. Finally, images collected of a truck demonstrate the potential of this ladar to enhance the contrast of a target in a clutter background.

Overall, this ladar approach should be advantageous for a number of low-cost short to mid-range commercial and military applications, for a variety of reasons. The use of incoherent light detection should inherently produce a ladar that is less costly and complex, and more rugged and reliable, than ladars that use coherent detection. FM ranging techniques have very low post-mixing signal-processing bandwidths, thus substantially simplifying and reducing the cost of the signal processor. Additionally, the ability to detect multiple targets in one pixel may facilitate signal processing for ladars that may have to function in environments where clutter and aerosols are present. Finally, semiconductor laser diodes provide more average power when they are operated CW; thus acceptable ladar SNRs may be easier to achieve using low-power inexpensive lasers.

We built and successfully tested a 32×32 pixel ladar breadboard using the incoherent FM/CW ranging principles. Also demonstrated was the use of a unique code multiplexing scheme to read-out the FPA post-mixing signals that was built using discrete components. The 32×32 pixel ladar breadboard image quality is substantially improved over image quality obtained with prior work when the FPA was mounted in a standard leadless chip carrier. Now, the images contain clear shadows and completely filled-in backdrops. Currently the system is amplifier noise limited where the noise performance is a factor of roughly 10 worse (in a voltage sense) than the level theoretically achievable. For the future we will need to investigate techniques to improve the signal-to-noise of the receiver. The most desirable method is to develop an OE-mixing detector with a modest amount of gain ($10 \times$). We also believe that the OE mixing detector should be designed using InGaAs that will allow the breadboard to operate at eye-safe wavelengths.

References

Anthes, J.P., Garcia, P., Pierce, J.T., Dressendorfer, P.V., 1993. Nonscanned LADAR imaging and applications. Proceedings of SPIE: Applied Laser Radar Technology 1936, 11–21.
Dieckmann, A., 1994. FMCW-LIDAR with tunable twin-guide laser diode. Proceedings of SPJE 2271, 134–142.
Lee, H.S., Ramaswami, R., 1992. Study of pseudo noise CW diode laser radar for ranging applications. Proceedings of SPIE: Cooperative Intelligent Robotics in Space III 1829, 36–45.
Ruff, W.C., Bruno, J.D., Kennerly, S.W., *et al.*, 2000. Self-mixing detector candidates for an FM/CW ladar architecture. In: Proceedings of SPIE: Laser Radar Technology and Applications V, presented at SPIE AeroSense, vol. 4035.
Shen, P., Stead, M.R., Taysing-Tara, M.A., *et al.*, 2000. Interdigitated finger semiconductor photodetector for optoelectronic mixing. SPIE AeroSense 4028, 426.
Stann, B., Ruff, W., Sztankay, Z., 1995. A practical low-cost high-range-resolution ladar. Proceedings of SPIE: Applied Laser Radar Technology II 2472, 118–129.
Stann, B.L., Abou-Auf, A., Aliberti, K., *et al.*, 2003. Research progress on a focal plane array ladar system using chirped amplitude modulation. Proceedings of SPIE: Laser Radar Technology and Applications VIII 5086, 47.
Stann, B.L., Aliberti, K., Carothers, D, *et al.*, 2004. A 32×32 pixel focal plane array ladar system using chirped amplitude modulation. Proceedings of SPIE: Laser Radar Technology and Applications IX 5412, 264.
Stann, B.L., Ruff, W.C., Sztankay, Z.G., 1996. Intensity-modulated diode laser radar using frequency-modulation/continuous-wave ranging techniques. Optical Engineering 35, 3270–3278.

Further Reading

Skolnik, M.I., 1995. CW and frequency modulated radar. In: Introduction to Radar Systems. New York, NY: McGraw-Hill, pp. 72–112 (Chapter 3).

Optical Masks Using Walsh Functions

Lakshminarayan Hazra, University of Calcutta, Kolkata, India
Pubali Mukherjee, MCKV Institute of Engineering, Howrah, India

© 2018 Elsevier Ltd. All rights reserved.

Introduction

For the sake of developing unambiguous specifications for an optical imaging system, it becomes imperative to define a unique image of an object, and so a one-to-one correspondence between points on the object and image is often assumed. This is an approximate model, and except for a few trivial cases, image formation by real optics can never render a point image corresponding to a point object. This is so, primarily for two reasons. First, the presence of residual aberrations in real optical systems, inhibits transformation of the homocentric bundle of rays, originating from a point object and admitted by the imaging system in the object space, into a homocentric bundle of rays converging to the desired point in the image space. Next, even a completely aberration free system does not form a point image corresponding to a point object on account of the inevitable effects of diffraction arising out of finite size of aperture of any real imaging system.

Fig. 1 shows the schematic of an axially symmetric imaging system forming image of the point object O at the image plane located at O′. The entrance pupil and the exit pupil are located at the points E and E′, respectively.

Let (X, Y) and (ξ, η) be the rectangular Cartesian coordinates of a point on the exit pupil plane and the image plane, respectively. The corresponding origins are taken at E′ and O′. α is the image space semi-angular aperture, and $(n \sin\alpha)$ is the image space numerical aperture, where n is the refractive index of the image space. Normalized coordinates for points on the exit pupil plane are (x, y). They are related to the geometrical coordinates by

$$x = \left(\frac{X}{h}\right) \qquad y = \left(\frac{Y}{h}\right) \tag{1}$$

where h is the radius of the exit pupil. The normalized coordinates (u, v) for points on the image plane are given by

$$u = \left(\frac{n \sin\alpha}{\lambda}\right)\xi \qquad v = \left(\frac{n \sin\alpha}{\lambda}\right)\eta \tag{2}$$

On account of axial symmetry, the normalized distance from the axis of any point with coordinates (X, Y) on the exit pupil plane can be expressed as

$$r = \sqrt{x^2 + y^2} = \frac{\sqrt{X^2 + Y^2}}{h} \tag{3}$$

Similarly the normalized distance p of any point on the image plane with geometrical distance χ from O′ is given by

$$q = \left(\frac{n \sin\alpha}{\lambda}\right)\chi = \left(\frac{n \sin\alpha}{\lambda}\right)\sqrt{\xi^2 + \eta^2} \tag{4}$$

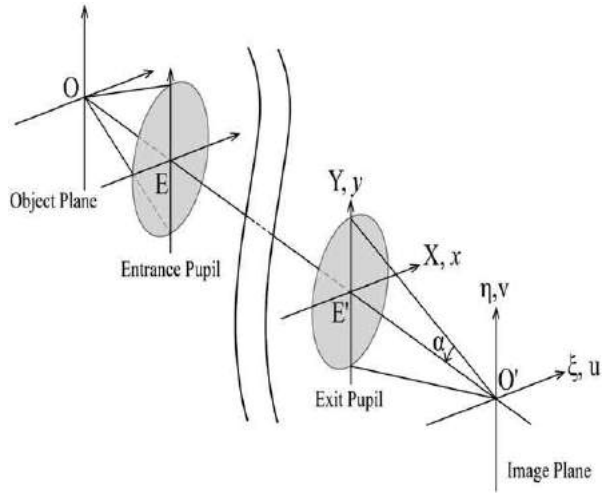


Fig. 1 Object/image planes and entrance/exit pupils of an axially symmetric imaging system.

 doi:10.1016/B978-0-12-803581-8.09379-6

The complex amplitude $F(u,v)$ on the transverse image plane located at O′ is given by the finite Fourier transform of the complex amplitude $f(x,y)$ on the exit pupil at E′, and is given by

$$F(u,v) = \iint f(x,y) e^{i2\pi(ux+vy)} \mathrm{d}x\mathrm{d}y \tag{5}$$

The limits of integration are set by the finite contour of the pupil. The intensity pattern $I(u,v)$ is equal to the squared modulus of the complex amplitude

$$I(u,v) = |F(u,v)|^2 \tag{6}$$

For axially symmetric systems, the intensity distribution on the blur patch is same along any azimuth on the transverse plane at O′, and the two dimensional Fourier transform of Eq. (5) reduces to a Hankel transform of the circularly symmetric pupil function $f(r)$.

$$F(p) = m \int f(r) J_0(pr) r \mathrm{d}r \tag{7}$$

where

$$p = 2\pi q = \frac{2\pi}{\lambda}(n \sin\alpha)\chi \tag{8}$$

and m is a multiplicative constant.

The intensity distribution $I(P)$ is given by

$$I(p) = |F(p)|^2 \tag{9}$$

For aberration free uniform amplitude imaging systems with axially symmetric circular aperture the pupil function $f(r)$ is given by

$$\begin{aligned} f(r) &= 1, \quad 0 \le r \le 1 \\ &= 0, \quad r > 1 \end{aligned} \tag{10}$$

The amplitude distribution $\hat{F}(p)$ in the blur patch on the transverse image plane along any azimuth from the optical axis is given by

$$\hat{F}(p) = m \int_0^1 J_0(pr) r \mathrm{d}r \tag{11}$$

Defining the normalized amplitude $\hat{F}_N(p)$ as $\hat{F}_N(p) = \hat{F}(p)/\hat{F}(0)$, we get

$$\hat{F}_N(p) = 2\frac{J_1(p)}{p} \tag{12}$$

The normalized intensity is given by

$$\hat{I}_N(p) = |\hat{F}_N(p)|^2 = \left[\frac{2J_1(p)}{p}\right]^2 \tag{13}$$

where $J_1(p)$ indicates value of the Bessel function (of the first kind) of order 1 for argument p.

This blur patch consists of a bright central lobe surrounded by bright and dark rings with decreasing intensity, and is known as the Airy pattern. The intensity on the transverse plane along any azimuth from O′ is shown in **Fig. 2**. This pattern is known as the Airy pattern. The uniform amplitude pupil of the imaging system is often called the Airy pupil.

Abbe/Rayleigh limit of two-point resolution on the transverse image plane is based on the intensity distribution in the Airy pattern, and the least resolvable distance $\delta\chi$ on the transverse image plane is proportional to $\{\lambda/n\ (\sin\alpha)\}$, where $n(\sin\alpha)$ is the numerical aperture of the imaging system and λ is the working wavelength. For three dimensional objects, in the two-dimensional image of an axial section of the object the least resolvable distance becomes larger than $\delta\chi$ on account of overlap of defocussed images of neighboring axial sections of the object. The axial distance beyond which this effect becomes insignificant is related with

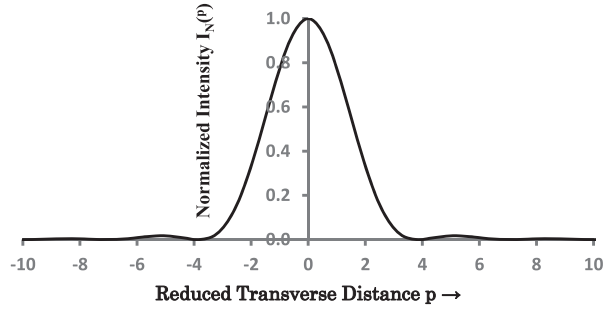


Fig. 2 Airy pattern: the point spread function (PSF) for an aberration-free diffraction limited imaging system.

the location of first zero in the axial distribution of intensity, and this axial resolution $\delta\zeta$ is proportional to $\{\lambda/[n \sin \alpha]^2\}$. It should be noted that both these results refer to aberration-free diffraction limited systems. In presence of aberrations, usually the least resolvable distance obtained in practice is much larger than $\delta\chi$ obtained for aberration free systems.

In order to cater to the needs of diverse applications, it becomes necessary to develop different types of imaging systems with prespecified requirements for $\delta\chi$ and/or $\delta\zeta$; in general, for real time whole field imaging systems, this calls for tailoring of the point spread function (PSF) on the transverse image plane and/or of the distribution of intensity along the axis in the neighborhood of the image plane. In some related applications, sometimes it becomes necessary to tailor the three-dimensional PSF.

Optical Masks

A straightforward approach to tailor the PSF is to use masks over the pupil of the imaging system. From the early days of development of the theories of image formation different types of mask, for example, amplitude, phase and mixed masks are being explored to accomplish the desired goals. Since these three types of mask are lossy, lossless and leaky, respectively, the lossless phase masks are often preferred in practical applications.

Some of the well-known applications of optical masks are:

- apodization
- high frequency enhancement in images
- superresolution
- tailoring the depth of focus
- optical traps.

Apodization is a technique widely used in astronomy for imaging of a faint star in the vicinity of another star that is brighter by several degrees of magnitude, and in spectroscopy for imaging a faint line neighboring a line that is brighter by several degrees of magnitude. This is accomplished with the help of an optical mask on the pupil of the imaging system for lowering down the intensity of the sidelobes in the PSF. It is interesting to note that the name "apodization" is derived from Greek "α" implying "to take away," and "πoδoσ" meaning "feet." In terms of Fourier optics, apodization leads to increase in modulation transfer function (MTF) of the lower spatial frequencies in the image and a concomitant decrease in MTF of the higher spatial frequencies in the image. Optical masks can also be synthesized to accomplish the opposite effect, and this phenomenon is called "High frequency enhancement in images." However, in both cases, the cut-off frequency in the image is not affected by the use of optical masks. As mentioned earlier, the cut-off frequency in an imaging setup is determined by diffraction effects corresponding to the image space numerical aperture and the working wavelength.

Superresolution refers to imaging techniques that can lead to resolution in the image beyond the diffraction limit. Obviously it calls for narrowing down the central lobe of the diffraction limited PSF; but, any attempt to achieve the same is accompanied with increase in intensity of the sidelobes, so much so that the advantages accruing from narrowing of the central lobe cannot be effectively harnessed for increase in resolution. Attempts for superresolution have, therefore, been directed to post-processing of data obtained from scanning techniques for imaging. The narrow central lobe obtained by optical masks can be used for narrow scanning spot, if the noisy sidelobes are eliminated with the help of a suitable spatial filter. On the other hand, if the PSF is tailored by an optical mask in a manner so that at least several sidelobes surrounding the narrow central lobe have low intensity, the imaging set up can be used to obtain resolution beyond the diffraction limit, albeit over a restricted field of view.

Applications of optical imaging can be classified on the basis of requirements for large depth of focus, or small depth of focus. Note that the depth of focus for diffraction limited aberration free systems is determined by the image space numerical aperture, and the working wavelength; also residual aberrations affect the depth of focus considerably. Optical masks can be conveniently used for tailoring the depth of focus.

Single and multiple optical traps have opened up new frontiers in the field of micro and nanotechnology for manipulation of minute particles. Suitable optical masks for tailoring the number, shape and location of optical traps constitute a major challenge.

For the sake of systematic analysis and synthesis of optical masks to be used on the pupil, the pupil function $f(r)$ describing transmission of the mask is expressed in terms of a set of base functions $b_n(r)$ as

$$f(r) \sum_{n=0}^{N-1} a_n b_n(r) \tag{14}$$

Typically, Straubel functions, trigonometric functions, Bessel functions, Chebyshev functions, Zernike polynomials, prolate spheroidal wave functions, etc. have been experimented within search for suitable base functions. Often the convenient amenability of obtaining the finite Fourier or Hankel transforms has weighed in favor of choice of base functions. If the members of the set of base functions are mutually orthogonal, the number of terms to be used in specific applications need not be determined heuristically, for the addition or removal of any term of the series does not affect other terms. With this backdrop in view we explore the use of Walsh functions in analysis and synthesis of optical masks.

Walsh Functions

Walsh functions were introduced by Walsh in 1923 as "a closed set of normal orthogonal functions" defined over the interval (0, 1) and having values $+1$ or -1 within the interval. They are a complete set of normal orthogonal functions over a given finite interval and take on values $+1$ or -1, except at a finite number of points of discontinuity, where they take the value 0. The order of the Walsh function is equal to the number of zero crossings within the specified domain over which the set is defined. The complete set of Walsh functions not only provides a viable alternative but also introduces a significant simplification in the approach of using suitable base functions. They have the interesting property that an approximation of a continuous function over a finite interval by a finite number of base functions of this set leads to a piecewise-constant approximation to the function. Also, the system of Walsh functions possesses some unique properties among all the systems orthonormal in Hilbert space L_2 (0, 1). In fact, the system of Walsh functions may be derived from the character group of the dyadic group which is a topologic group derived from the set of binary representations of the real numbers. This topology of the dyadic group makes properties of the system of Walsh functions strikingly different from those of other systems. Walsh functions have been utilized to a great advantage in the field of signal coding and transmission, in allied problems of information processing and in digital signal processing. Two dimensional Walsh functions in the usual rectangular coordinates have been extensively used in digital image processing applications. For the treatment of problems of image formation where one usually deals with some form of axial symmetry, it is useful to develop Walsh functions in polar coordinates. For systems with rotational symmetry about the axis, it is sufficient to deal only with radial Walsh functions. The latter have been developed as a special case of Walsh functions in polar coordinates and have been found to be quite useful in the treatment of problems of pupil plane filtering and the studies on aberrated optical imagery.

One Dimensional Walsh Functions

A Walsh function of a single variable x is represented as $W_k(x)$ where the subscript k refers to the order of the function. The function takes on values either $+1$ or -1 over a specified domain and the set of Walsh functions is orthogonal and complete in the interval. The same implies the following relation for members of the set of Walsh functions defined over the interval (0, 1)

$$\int_0^1 \mathrm{W}_k(x)\mathrm{W}_{\pounds}(x)dx = \delta_{k\pounds} \tag{15}$$

where $\delta_{k\pounds}$ is the Kronecker delta defined as

$$\delta_{k\pounds} = \begin{cases} 0, & k \neq \pounds \\ 1, & k = \pounds \end{cases} \tag{16}$$

The set has a further specification through the unique definition of the zeroth element of the set as

$$W_0(x) = 1, \quad 0 \leq x \leq 1 \tag{17}$$

Fig. 3 shows the first four one-dimensional Walsh functions $W_k(x)$,k=0, 1, 2, and 3.

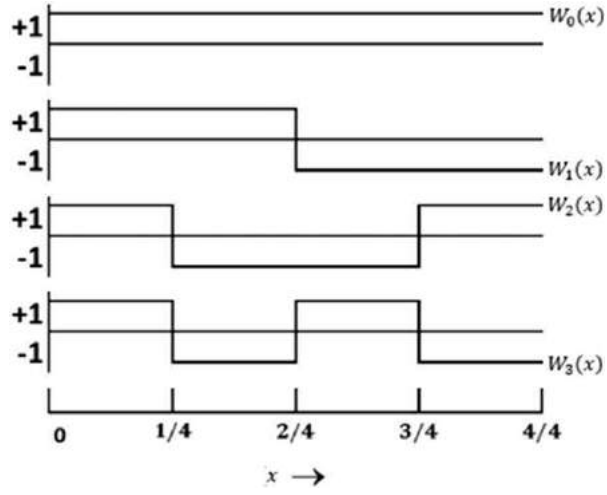


Fig. 3 One dimensional Walsh functions, $W_k(x)$,k=0,1,...,3.

In order to obtain an analytical representation for the unidimensional Walsh functions $W_k(x)$, let the integer k be expressed as

$$k = \sum_{i=0}^{(v)-1} k_i 2^i \tag{18}$$

where k_i are the bits, 0 or 1 of the binary numeral for k, and 2^v is the integral power of 2, whose value just exceeds k. Thus for $k=0$, 1, $v=1$; for $k=0$, 1, 2, 3, $v=2$; for $k=0$, 1, 2, 3, 4, 5, 6, 7, $v=3$, and so on.

For all x in the interval (0, 1) we define

$$W_k(x) = \prod_{i=0}^{(v)-1} \operatorname{sgn}\left[\cos\left(2^i \pi x k_i\right)\right] \tag{19}$$

where

$$\begin{aligned} \operatorname{sgn}(x) &= +1, \quad x>0 \\ &= 0, \quad x=0 \\ &= -1, \quad x<0 \end{aligned} \tag{20}$$

It may be noted from Fig. 3 that the order of the Walsh function is given by the number of zero crossings, i.e., the sign changes of the function in the interval (0, 1).

Two Dimensional Walsh Functions in Rectangular Coordinates

In two dimensions, the orthogonality condition takes the form

$$\int_0^1 \int_0^1 W_k(x) W_{€}(y) W_{£}(x) W_{¥}(y) \mathrm{d}x \mathrm{d}y = \delta_{k£} \delta_{€¥} \tag{21}$$

Fig. 4 depicts a few two dimensional rectangular Walsh functions $W_k(x)W_{€}(y)$, $k=0,1,2,3$, €$=0,1,2,3$.

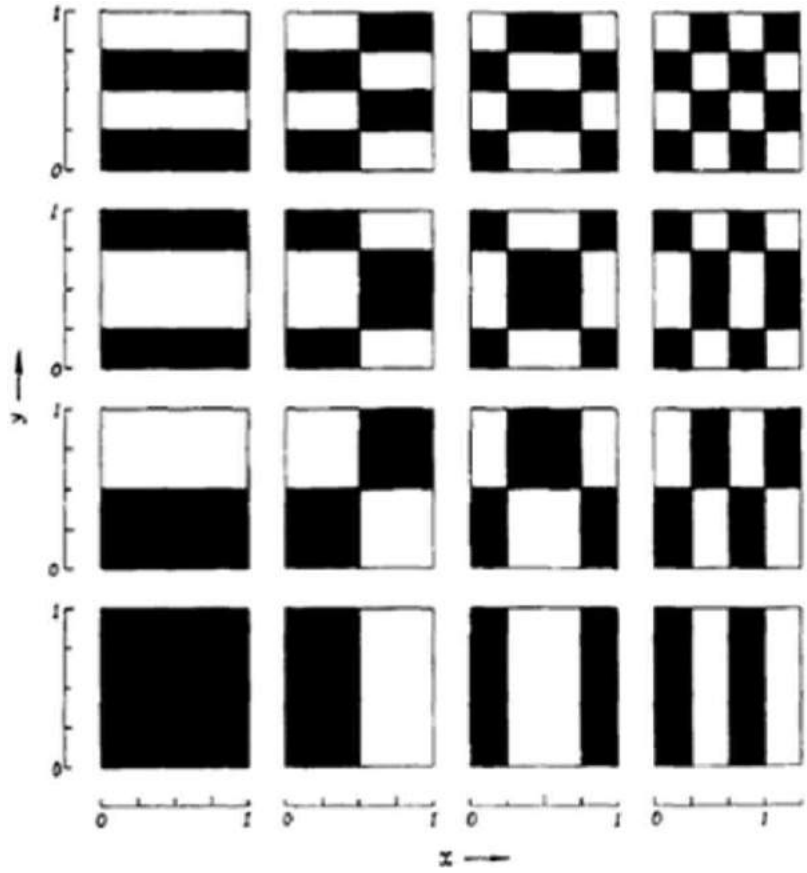


Fig. 4 Two dimensional rectangular Walsh functions $W_k(x)W_{€}(y)$, $k=0,1,2,3$, €$=0,1,2,3$.

Two Dimensional Walsh Functions in Polar Coordinates

In polar coordinates the orthogonality condition reduces to

$$\frac{1}{\pi}\int_0^1\int_0^{2\pi}\varphi_k(r)\mathcal{A}_{€}(\theta)\varphi_{£}(r)\mathcal{A}_{¥}(\theta)r\mathrm{d}r\mathrm{d}\theta=\delta_{k£}\delta_{€¥} \tag{22}$$

where $\varphi_k(r)$ and $\mathcal{A}_{€}\theta$ are the radial Walsh function and azimuthal Walsh function, respectively.

Fig. 5 depicts a few two-dimensional polar Walsh functions $\varphi_k(r)\mathcal{A}_{€}(\theta)$, $k=0,1,2,3$, $€=0,1,2,3$.

Azimuth Invariant Case: Radial Walsh Functions

Alike the case of unidimensional Walsh functions, $W_k(x)$, radial Walsh functions $\varphi_k(r)$ of index $k\geq 0$ and argument r over the interval $(0,1)$ require integer k to be expressed in the form

$$k=\sum_{\mathrm{i}=0}^{\gamma-1}k_{\mathrm{i}}2^{\mathrm{i}} \tag{23}$$

where k_i are the bits, 0 or 1 of the binary numeral for k and 2^{γ} is the integral power of 2 that just exceeds k. Thus for all r in $(0,1)$ we define

$$\varphi_k(r)=\prod_{i=0}^{\gamma-1}\mathrm{sgn}\left[\cos\left(2^i\pi r^2k_{\mathrm{i}}\right)\right]=\prod_{i=0}^{\gamma-1}\mathrm{sgn}\left[\cos\left(2^i\pi tk_{\mathrm{i}}\right)\right]=\varphi_k(t) \tag{24}$$

where $t=r^2$.

The first four radial Walsh functions $\varphi_k(r)$, $k=0,1,2,3$ are shown in (r,θ) space in Fig. 6(a). The corresponding radial variation of $\varphi_k(r)$ along any azimuth is shown in Fig. 6(b).

For azimuth invariant case the orthogonality condition takes the form

$$\int_0^1\varphi_k(r)\varphi_{£}(r)r\mathrm{d}r=\frac{1}{2}\delta_{k£} \tag{25}$$

Note that in $t(=r^2)$ space, the variation of $\varphi_k(t)$ with t is identical as the variation of one dimensional Walsh functions $W_k(x)$ with x.

Walsh Filters as Optical Masks on Pupil

Walsh filters of various orders may be obtained from the corresponding Walsh functions by realizing values of $+1$ or -1 with 0 or π phase, respectively. Note: $e^{i0}=+1$, and $e^{i\pi}=-1$. Radial Walsh filters, derived from radial Walsh functions, form a set of orthogonal phase filters that take on values either 0 or π phase, corresponding to $+1$ or -1 values of the radial Walsh functions over prespecified annular regions of the circular filter. Order of these filters is given by the number of zero-crossings, or equivalently phase transitions within the domain over which the set is defined.

Radial Walsh filters may be used as optical masks on the pupil plane of a rotationally symmetric imaging system for tailoring of the distribution of intensity on and around the focal/image plane of optical imaging systems.

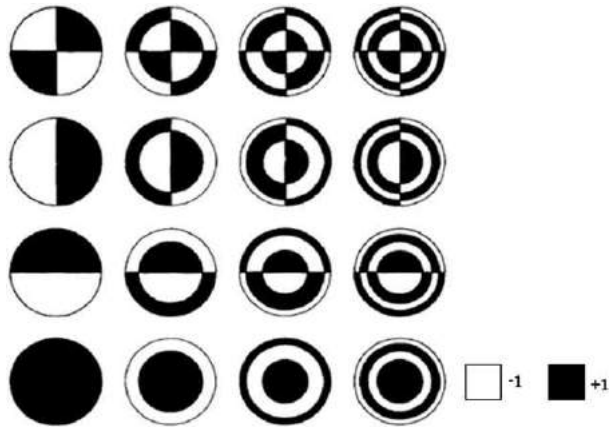


Fig. 5 Two dimensional polar Walsh functions $\varphi_k(r)\mathcal{A}_{€}(\theta)$, $k=0,1,2,3$, $€=0,1,2,3$.

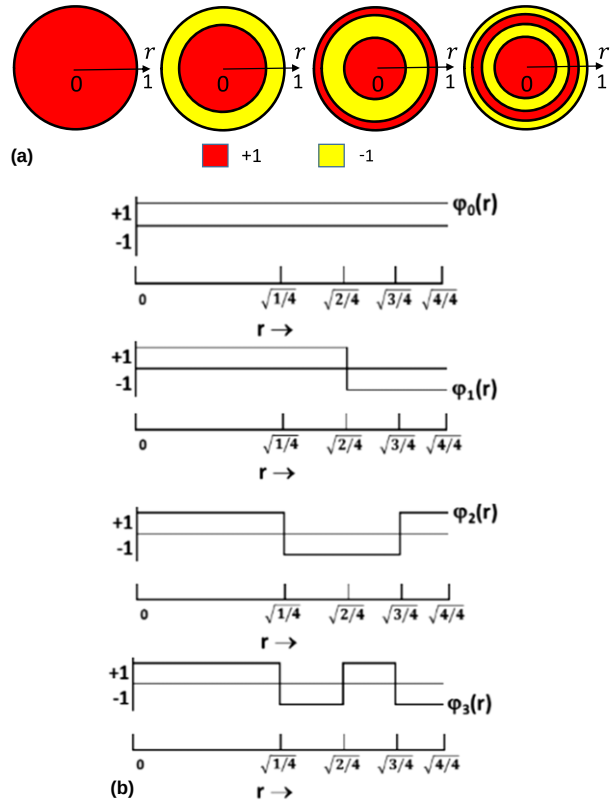


Fig. 6 (a) Radial Walsh functions $\varphi_k(r)$, $k=0,1,\ldots,3$ in (r,θ) space. (b) Radial Walsh functions $\varphi_k(r)$ vs. r along any azimuth θ, $k=0,1,\ldots,3$.

Intensity Distribution on the Transverse Image/Focal Plane With Walsh filters as Optical Masks

For the kth order radial Walsh filter on the pupil, the pupil function may be expressed as

$$f(r)=\varphi_k(r)=\sum_{m=1}^{M} e^{ik\psi_m}B_m(r) \tag{26}$$

where $B_m(r)$ are zero-one functions defined as

$$\begin{aligned} B_m(r)&=1;\ r_{m-1}\le r\le r_m \\ &=0;\ \text{otherwise} \end{aligned} \tag{27}$$

where

$$r_m=\left[\frac{m}{M}\right]^{\frac{1}{2}} \text{ and } r_{m-1}=\left[\frac{m-1}{M}\right]^{\frac{1}{2}} \tag{28}$$

and $M=2^{\gamma}$ is the largest power of 2 that just exceeds k. Over the mth zone of $\varphi_k(r)$, value of $k\psi_m$ is 0 or π, if $\varphi_k(r)=+1$ or -1, respectively, as per the governing relation Eq. (24).

For better accuracy of results each of the M zones of the pupil is divided into J number of equal area subzones such that the whole exit pupil has $T=MJ$ number of equal area concentric zones (**Fig. 7**). The outer and inner radii of the jth subzone of the mth zone are given by

$$r_m^j=\left[\frac{(m-1)J+j}{T}\right]^{\frac{1}{2}} \text{ and } r_m^{j-1}=\left[\frac{(m-1)J+(j-1)}{T}\right]^{\frac{1}{2}} \tag{29}$$

respectively.

The normalized complex amplitude distributions on transverse plane in the farfield for Walsh filters $\varphi_k(r)$ is given by

$$F_N(p)=2\sum_{m=1}^{M}\exp[ik\psi_m]\sum_{j=1}^{J}\int_{r_m^{j-1}}^{r_m^j}J_0(pr)r\mathrm{d}r=2\sum_{m=1}^{M}\exp[ik\psi_m]\sum_{j=1}^{J}\mathcal{J}_m^j(p) \tag{30}$$

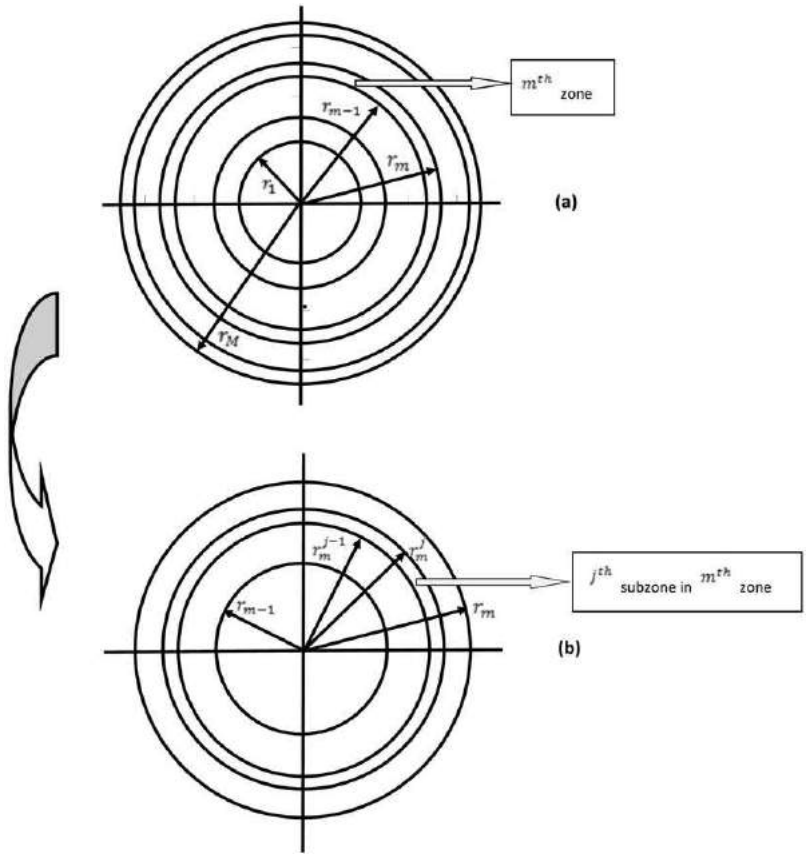


Fig. 7 (a) mth zone in a radial Walsh filter $\varphi_k(r)$ consisting of M concentric equal area zones. (b) jth subzone in the mth zone of the phase filter consisting of J equal area subzones in the mth zone.

where

$$\mathcal{J}_m^j(p) = \left[\frac{r_m^j J_1\left(pr_m^j\right) - r_m^{j-1} J_1\left(pr_m^{j-1}\right)}{p}\right] \tag{31}$$

The normalized intensity distribution on the transverse image plane with radial Walsh filters on $\varphi_k(r)$ the exit pupil is given by

$$I_N(p) = |F_N(p)|^2 = 4 \sum_{m=1}^{M} \sum_{u=1}^{M} \cos[k\psi_m - k\psi_u] \sum_{j=1}^{J} \sum_{v=1}^{J} \mathcal{J}_m^j(p) \mathcal{J}_u^v(p) \tag{32}$$

For a Walsh filter of zero order on the exit pupil, the transverse intensity distribution on the image/focal plane is the Airy pattern where the normalized central intensity at the origin has magnitude one as in **Fig. 4**. For any Walsh filter of nonzero order on the exit pupil, the central intensity is zero. There is no central lobe in the transverse intensity distribution on the focal plane in presence of a radial Walsh filter of any order, except for the order zero. A central dip is surrounded by bright and dark rings for all nonzero orders of radial Walsh filters. **Fig. 8** presents the intensity distribution on the transverse image/focal plane in presence of selected radial Walsh filters $\varphi_k(r)$, $k=1,\ldots,7$ on the pupil. For the sake of comparison, a part of the Airy pattern is also shown superimposed on the intensity distribution for the filter $\varphi_k(r)$.

Distinct characteristics of the PSF corresponding to individual Walsh filters deserve attention, and may be harnessed in emerging applications like optical encryption. On the other hand, a finite set of orthogonal Walsh filters has already been utilized in the design of optimum amplitude filters for Luneburg's third apodization problem. This problem involves determination of the optimum amplitude filter maximizing the fraction of encircled energy within a circle of prespecified radius w with respect to the total energy in the diffraction pattern. The circle is taken as concentric with the center of the PSF. The amplitude transmission of the optimum filter was taken as consisting of a weighted combination of the first weight radial Walsh functions, so that the pupil function is expressed by

$$f(r) = \sum_{k=0}^{7} a_k \varphi_k(r) \tag{33}$$

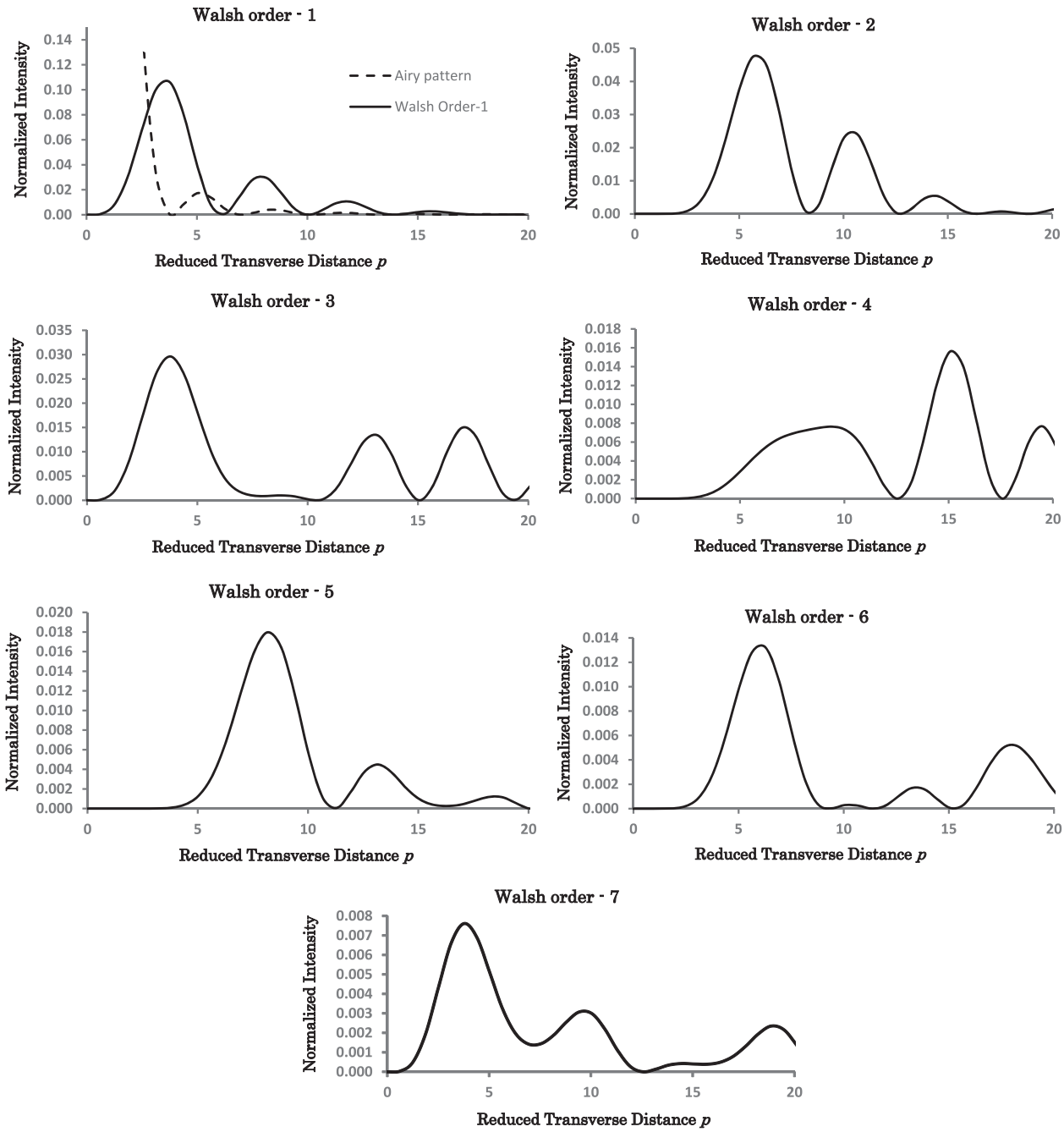


Fig. 8 Normalized intensity distribution on the transverse image/focal plane with radial Walsh filters $\varphi_k(\hat{r})$, $k=1,\ldots,7$.

and the apodizing amplitude filter consists of eight concentric equal area annular zones, amplitude over the whole region of each zone being same. Fig. 9 shows five such filters corresponding to five prespecified values for the radius w. w is expressed in the same dimensionless unit as p. Corresponding PSFs on the image plane are shown in Fig. 10. Note the discerning effects of apodization by the five different filters.

Intensity Distribution Along the Axis Around the Image/Focal Plane

The complex amplitude distribution $F(\chi,\Delta\zeta)$ on the transverse plane located at O'' on the axis needs to be calculated by using Fresnel diffraction formula. With reference to Fig. 11 and Fig. 12, let $E'O' = R_o'$, $E'O'' = R'$ and $O'O'' = R' - R_o' = \Delta\zeta$, where $\Delta\zeta$ refers to the location of the transverse plane with reference to the focal/image plane, and χ refers to the perpendicular distance of a point on the transverse plane from the axis. Detailed derivation of the Fresnel diffraction formula shows that the complex amplitude

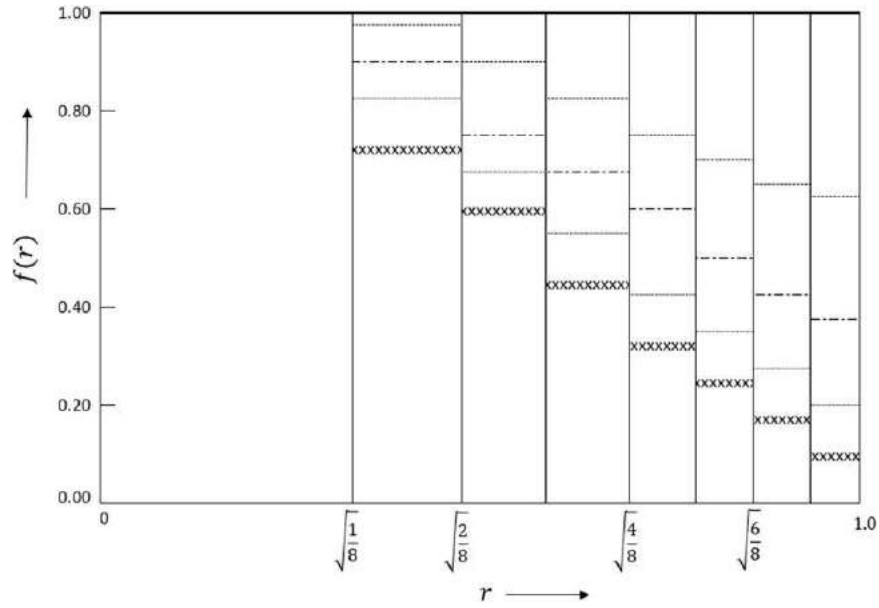


Fig. 9 Optimum eight step apodizing filters corresponding to different values of *w*: —, $w=0$; ——, $w=2.0$; -•-•-, $w=3.0$; •••••, $w=4.0$; xxxx, $w=5.0$. Reprinted with permission from Hazra, L.N., 1977. A new class of optimum amplitude filters. Optics Communications 21, 232–236.

distribution on the transverse plane at O'' is given by a two dimensional Fourier transform of the defocused pupil function of the imaging system. For an axially symmetric pupil function, the 3D distribution of the complex amplitude near the region of the image/focal plane is given by, to a multiplicative factor C,

$$F(\chi,\Delta\zeta)=C\int_0^1 f(r)\exp\left[ikW_{20}r^2\right]J_0(pr)r\mathrm{d}r \tag{34}$$

In Eq. (36) below, the axial shift $\Delta\zeta$ of the transverse plane is expressed in terms of "defocus" aberration W_{20}, where the wave aberration function $W(r)$ is given by

$$W(r)=W_{20}r^2 \tag{35}$$

W_{20} is related to $\Delta\zeta$ by

$$W_{20}=\frac{1}{2}nh^2\left(\frac{1}{R'_o}-\frac{1}{R'}\right)=\frac{1}{2n}(n\sin\alpha)^2\Delta\zeta \tag{36}$$

where h is the maximum semidiameter of the exit pupil.

Instead of actual distances χ and $\Delta\zeta$, expressions for complex amplitude $F(p,a)$ are derived for normalized dimensionless parameters p and a, respectively. p has been already defined in Eq. (8), and the reduced axial coordinate a is related to $\Delta\zeta$ by

$$a=\frac{1}{n\lambda}(n\sin\alpha)^2\Delta\zeta \tag{37}$$

where $\Delta\zeta$ is the actual longitudinal shift representing the axial distance of the transverse plane from the paraxial focal plane, as shown in **Fig.11**. n represents the refractive index of the image space, and $(n\sin\alpha)$ is the image space numerical aperture.

W_{20} is related to a by

$$kW_{20}=a\pi \tag{38}$$

Notwithstanding the use of Hankel transform in evaluation of the complex amplitude on a defocused plane, it should be noted that the numerical results for intensity remain valid even for larger values of a if the oscillatory integral in Eq. (34) is evaluated correctly. Special measures were undertaken in our numerical quadrature algorithm as noted below.

In presence of phase filter $Q(r)$, the defocused pupil function $f(r)$ is given by

$$f(r)=\exp\left[ik\left\{Q(r)+W_{20}r^2\right\}\right] \tag{39}$$

For better accuracy of results each of the M zones of the pupil is divided into J number of equal area subzones as in **Fig. 7** such that the whole exit pupil has $T=MJ$ number of equal area concentric zones. For each of these subzones the outer and inner radii r_m^j

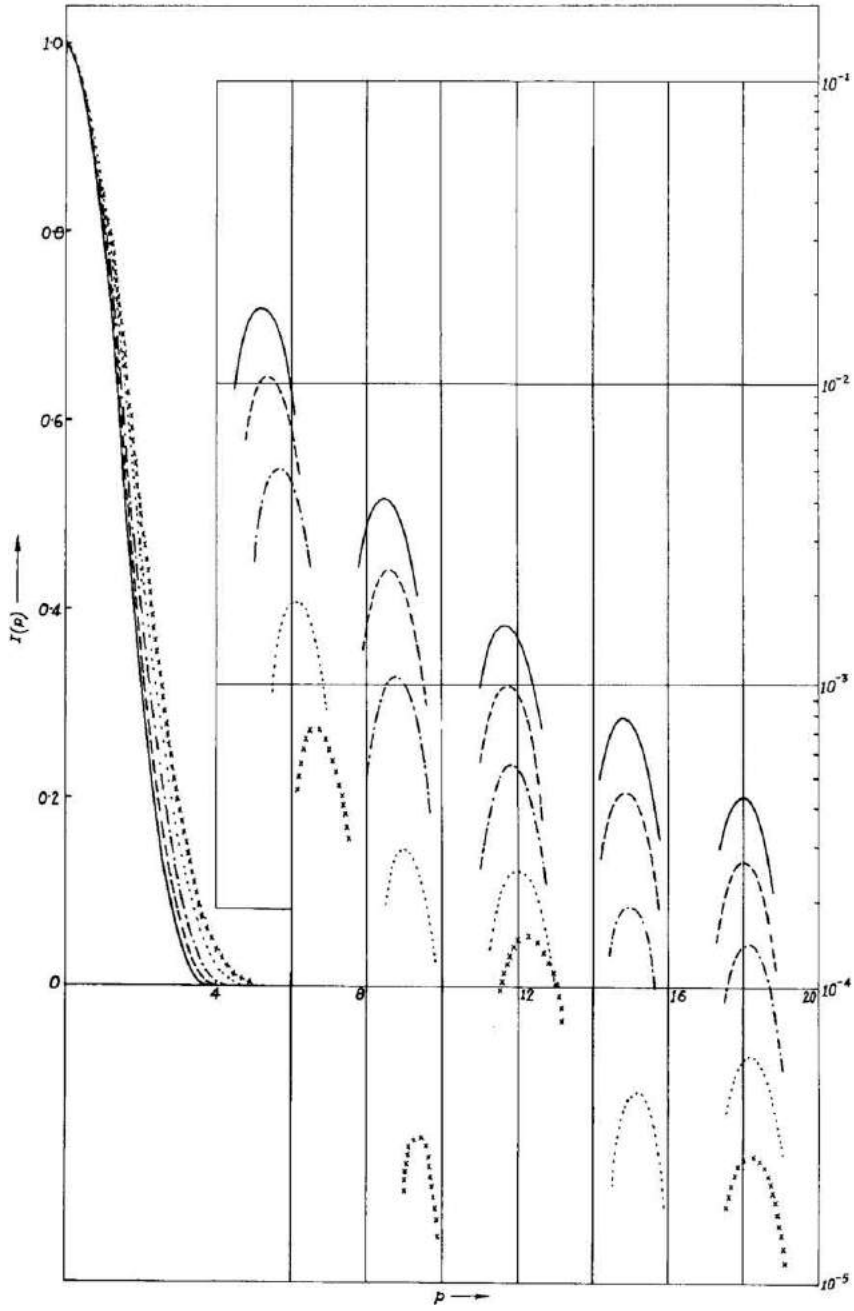


Fig. 10 Point spread functions (PSFs) corresponding to the optimum filters of Fig. 9. The intensity scale is linear up to $p=6.0$; a logarithmic scale is used for $p \geq 4.0$ for better display of the sidelobes. —, $w=0$; ——, $w=2.0$; -•--•-, $w=3.0$; •••••, $w=4.0$; xxx, $w=5.0$. Reprinted with permission from Hazra, L.N., 1977. A new class of optimum amplitude filters. Optics Communications 21, 232–236.

and r_m^{j-1} are given by

$$r_m^j = \left[\frac{(m-1)J+j}{T}\right]^{\frac{1}{2}}$$

$$r_m^{j-1} = \left[\frac{(m-1)J+(j-1)}{T}\right]^{\frac{1}{2}} \tag{40}$$

The normalized complex amplitude at a point O'' on the axis is

$$F_N(a) = F_N(\Delta\zeta) = 2\sum_{m=1}^{M} \exp[ik\psi_m] \sum_{j=1}^{J} \exp\left[ik\overline{W}_m^j\right] \int_{r_m^{j-1}}^{r_m^j} r\,dr \tag{41}$$

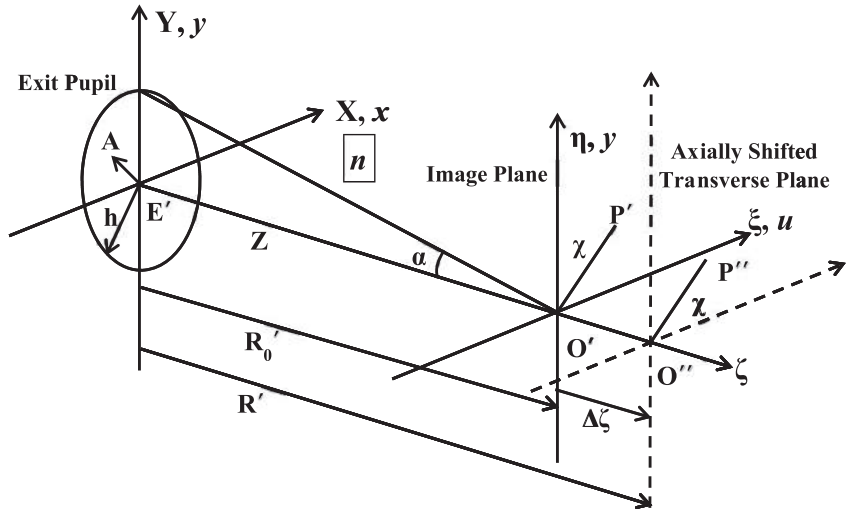


Fig. 11 Exit pupil, image plane and an axially shifted transverse plane in the image space of an axially symmetric imaging system.

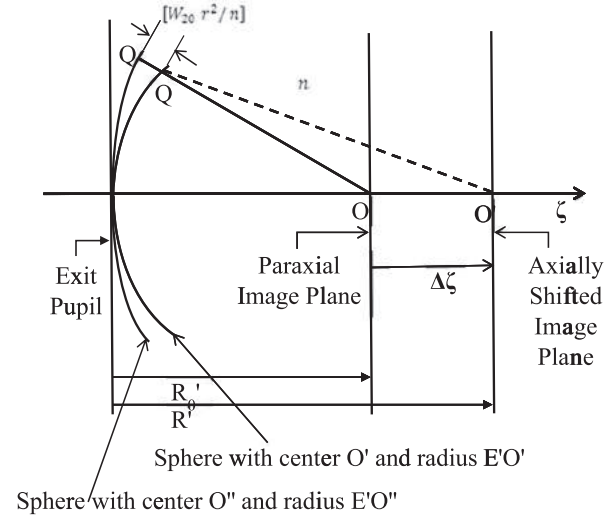


Fig. 12 Shift of image plane by $\Delta\zeta$ gives rise to defocus or "Defect of Focus" aberration [Q″Q′].

The axial shift $O'O'' = \Delta\zeta$ (as in Fig.12). $\overline{W}_m^j$ is the average value of $W(r)$ over the jth subzone of the mth zone and is given by

$$\overline{W}_m^j = \frac{\int_{r_m^{j-1}}^{r_m^j} W(r) r dr}{\int_{r_m^{j-1}}^{r_m^j} r dr} = \frac{W_{20}}{2T}[2(m-1)J + (2j-1)] \tag{42}$$

and

$$\int_{r_m^{j-1}}^{r_m^j} r dr = \Re_j = \left[\frac{\left(r_m^j\right)^2}{2} - \frac{\left(r_m^{j-1}\right)^2}{2}\right] = \left[\frac{1}{2T}\right] \tag{43}$$

In Eq. (26) it is seen that the radial Walsh filter $\varphi_k(r)$ can be expressed as

$$\varphi_k(r) = \sum_{m=1}^{M} e^{ik\psi_m} B_m(r) \tag{44}$$

From the defining relation Eq. (24) the value of $\varphi_k(r)$ over the m-th annular zone with inner and outer radii given by Eq. (28) is either $+1$ or -1; value of $e^{ik\psi m}$ on the m-th annular zone of the corresponding radial Walsh filter is either $+1$ or -1 so that the phase $k\psi_m$ on the m-th zone is either 0 or π, respectively.

From Eqs. (41–44)

$$F_N(a) = \frac{1}{T}\sum_{m=1}^{M} \exp[ik\psi_m] \sum_{j=1}^{J} \exp\left[ik\overline{W}_m^j\right] \tag{45}$$

Therefore, when the radial Walsh filter $\varphi_k(r)$ is used as an optical mask over the exit pupil, the normalized intensity distribution along the axis may be expressed as

$$I_N(a) = |F_N(\Delta\zeta)|^2 = \frac{1}{T^2}\sum_{m=1}^{M}\sum_{u=1}^{M}\sum_{j=1}^{J}\sum_{v=1}^{J} \cos\left[\{k\psi_m - k\psi_u\} + \left\{k\overline{W}_m^j - k\overline{W}_u^v\right\}\right] \tag{46}$$

Illustrative results for variation of normalized axial intensity with the distance from the focal/image plane are presented in Fig. 13 when radial Walsh filters $\varphi_k(r)$ are used as optical masks on the exit pupil. The positive and negative values of a represent axial shifts on either side of the focal/image plane. For the radial Walsh filter $\varphi_0(r)$, which is same as the Airy pupil, the axial intensity on the image plane is maximum. But for all radial Walsh filters of integral order other than zero, the axial intensity on the

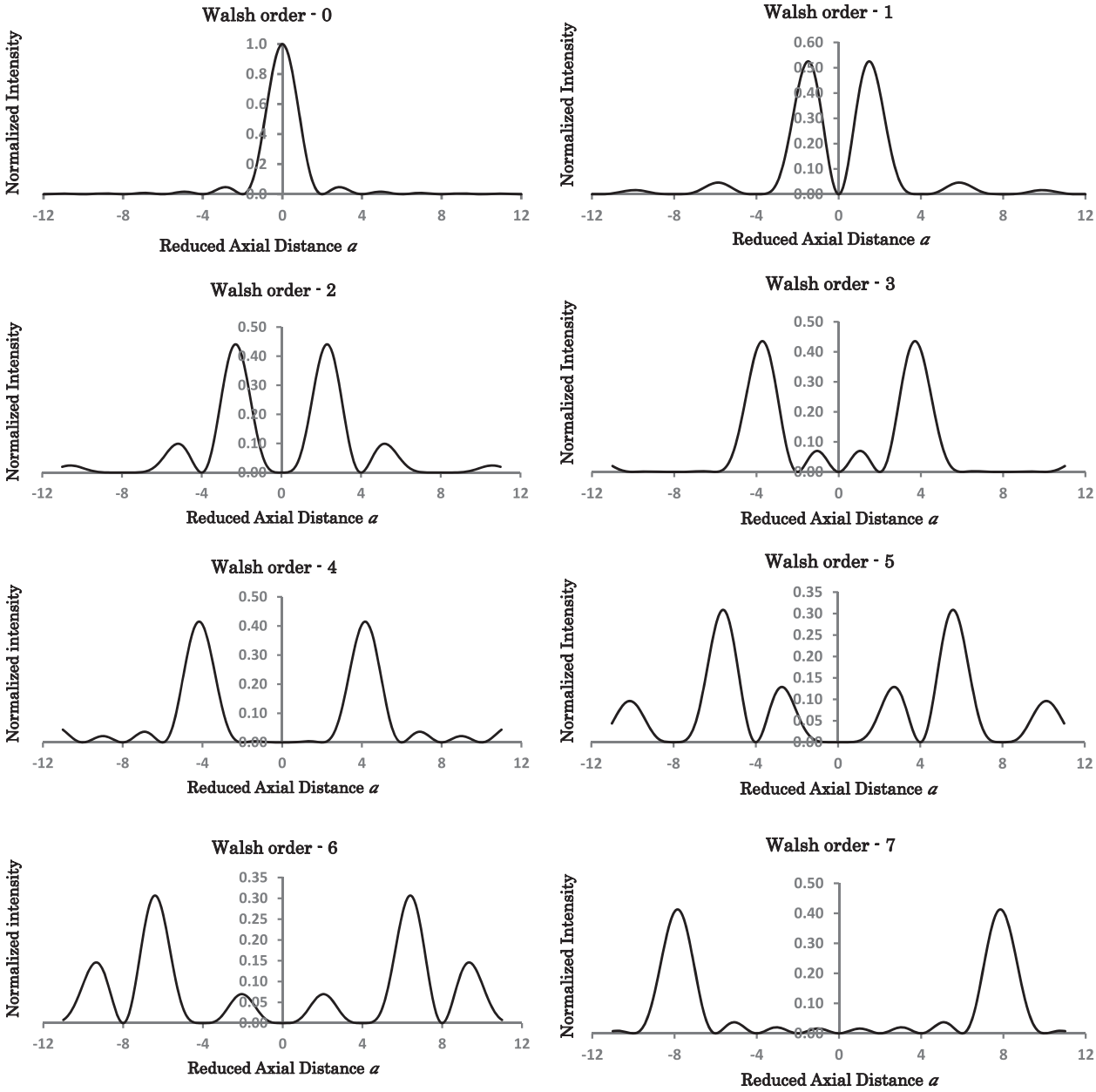


Fig. 13 Normalized intensity distribution along the axis around the transverse image/focal plane with radial Walsh filters $\varphi_k(r)$, k=0,...,7.

image plane is zero. However, for all filters, the intensity along the axis is same for both $+\Delta\zeta$ and $-\Delta\zeta$, where $\Delta\zeta$ represents the distance of the point O'' from O' (Fig. 11).

For Walsh filters of order 0, there is one peak in the axial intensity distribution. In case of radial Walsh filters of lower orders, two distinct peaks are present, and locations and local variation of intensity surrounding the peaks depend on the order of the function. As the order of the radial Walsh filter increases, more peaks of varying intensities appear, but all peaks are located symmetrically with respect to the image plane. Number, location and intensity level in the peaks can be tailored by suitable combination of radial Walsh filters.

Intensity Distribution on Neighboring Transverse Planes Shifted Axially From the Image Plane

Following the analyses presented above, the normalized complex amplitude distribution on a transverse plane located at an axial distance of $\Delta\zeta$ from the image/focal plane (Fig. 11) is given by

$$F_N(p,a) = F_N(\chi,\ \Delta\zeta) = 2\sum_{m=1}^{M}\exp[ik\psi_m]\sum_{j=1}^{J}\exp\left[ik\overline{W}_m^j\right]\int_{r_m^{j-1}}^{r_m^j} J_0(pr)rdr \tag{47}$$

where $\overline{W}_m^j$ is the average value of the wave aberration function over the jth subzone of the mth zone and is given by

$$\overline{W}_m^j = \frac{\int_{r_m^{j-1}}^{r_m^j} W(r)rdr}{\int_{r_m^{j-1}}^{r_m^j} rdr} = \frac{W_{20}}{2T}[2(m-1)J + (2j-1)] \tag{48}$$

and

$$\int_{r_m^{j-1}}^{r_m^j} J_0(pr)r\mathrm{d}r = \mathcal{J}_m^j(p) = \left[\frac{r_m^j J_1\left(pr_m^j\right) - r_m^{j-1}J_1(pr_m^{j-1})}{p}\right] \tag{49}$$

From Eqs. (47)–(49) it follows

$$F_N(p,a) = 2\sum_{m=1}^{M}\exp[ik\psi_m]\sum\nolimits_{j=1}^{J}\exp\left[ik\overline{W}_m^j\right]\mathcal{J}_m^j(p) \tag{50}$$

When a radial Walsh filter $\varphi_k(r)$ is used as an optical mask on the exit pupil, the normalized intensity distribution $I_N(p,a)$ on a neighboring transverse plane located at an axial distance of $\Delta\zeta$ from the image/focal plane is given by squared modulus of $F_N(p,a)$. It follows

$$I_N(p,a) = 4\sum_{m=1}^{M}\sum_{u=1}^{M}\sum_{j=1}^{J}\sum_{v=1}^{J}\cos\left[\{k\psi_m - k\psi_u\} + \left\{k\overline{W}_m^j - k\overline{W}_u^v\right\}\right]\mathcal{J}_m^j(p)\mathcal{J}_u^v(p) \tag{51}$$

A cross section of the three dimensional light distributions around the focal plane produced by some of the radial Walsh filters are presented in Fig. 12. On account of axial symmetry of the imaging system, the intensity distribution is the same along any plane containing the ζ axis. The intensity distribution along (χ,ζ) plane in the focal/image region is presented in Fig. 14 for the radial Walsh filters $\varphi_k(r)$, $k=0,1,2,\ldots,7$. The elliptical blobs or patches of focussed light seen in the figures are the cross sections of the 3D intensity distributions produced near the focus. Except for the case of $\varphi_0(r)$, where a single structure is observed, in all other cases multiple structures are observed. The number and locations of the regions of high light concentration, and the local variation of light intensity in these regions can be tailored by using suitable weighted combination of radial Walsh filters. These regions of high light concentration are effectively multiple optical traps.

Walsh Filters and Self-Similarity

The set of radial Walsh filters can be classified into distinct self-similar groups and subgroups where members of each subgroup possess self-similar structures or phase sequences. The axial and transverse intensity distributions, and also the three dimensional light distribution around the image plane exhibited by one radial filter are similar to the same exhibited by other members of the self-similar group to which the filter belongs. This characteristic of Walsh filters is quite similar to that exhibited by fractal zone plates and other fractal diffracting apertures.

In case of higher order Walsh functions, one or more of the annular zones may become very narrow, so much so that analysis based on scalar diffraction theory may not be valid. Similarly, predictions based on scalar theory are incorrect when optical masks

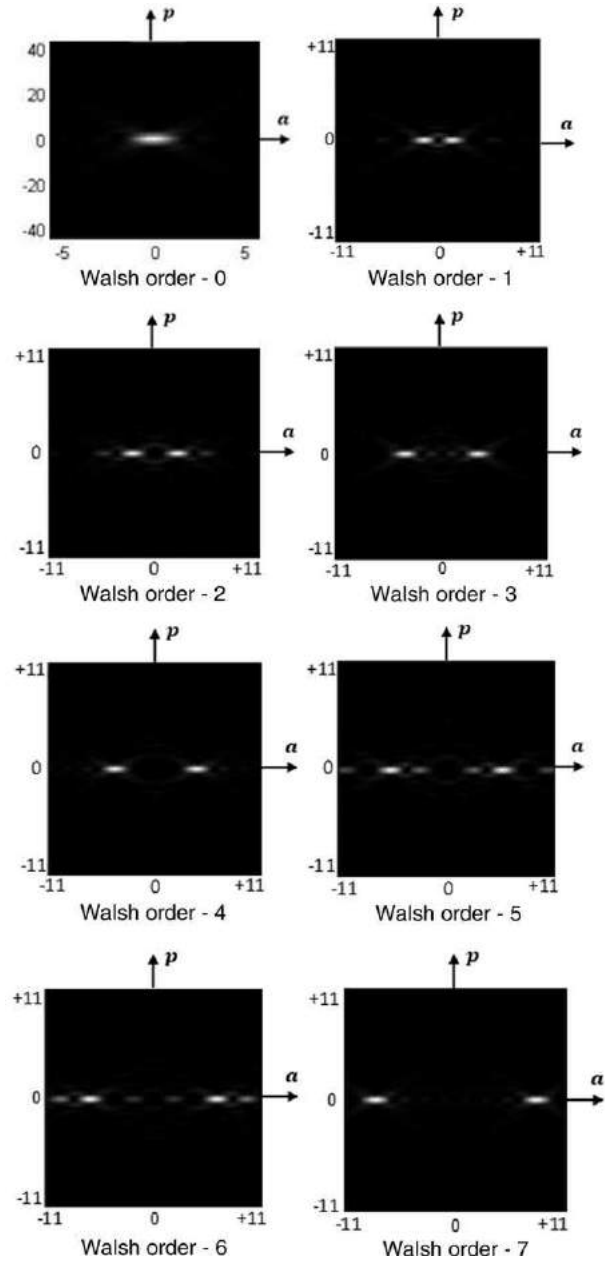


Fig. 14 Intensity distribution along (χ,ζ) plane in the focal/image region with the radial Walsh filters $\varphi_k(r)$, $k=0,1,2,\ldots,7$ on the exit pupil.

using Walsh functions are used in imaging systems of high numerical aperture. Both these challenges can be tackled by using vector diffraction theory.

See also: Fraunhofer Diffraction

Further Reading

Beauchamp, K.G., 1985. Walsh Functions and Their Applications. London: Academic Press.
Boivin, A., 1964. Théorie et calcul des figures de diffraction de revolution. Paris: Gauthier-Villars.
Gu, M., 2000. Advanced Optical Imaging Theory. Berlin: Springer.
Harmuth, H.F., 1972. Transmission of Information by Orthogonal Functions. Berlin: Springer-Verlag.
Hazra, L.N., 1977. A new class of optimum amplitude filters. Optics Communications 21, 232–236.
Hazra, L.N., 2007. Walsh filters in tailoring of resolution in microscopic imagery. Micron 38, 129–135.

Hazra, L.N., Banerjee, A., 1976. Application of Walsh functions in generation of optimum apodizers. Journal of Optics 5, 19–26.
Hazra, L.N., Guha, A., 1986. Far field diffraction properties of radial Walsh filters. Journal of the Optical Society of America A 3, 843–846.
Hazra, L.N., Mukherjee, P., 2015. Self-similarity in radial Walsh filters and axial intensity distributions in the far-field diffraction pattern. Journal of the Optical Society of America A 31, 139–147.
Jacquinot, P., Roizen-Dossier, B., 1964. Apodization. In: Wolf, E. (Ed.), Progress in Optics, vol. III. Amsterdam: North-Holland.
Martinez-Corral, M., Andrés, P., Ojeda-Castañeda, J., Saavedra, G., 1995. Tunable axial superresolution by annular binary filters: Application to confocal microscopy. Optics Communications 119, 491–498.
Neumann, K.C., Block, S.M., 2004. Optical trapping. Review of Scientific Instruments 75, 2787–2809.
Toraldo di Francia, G., 1958. La diffrazione della luce. Torino: Edizioni Scientifiche Einaudi.
Walsh, J.L., 1923. A closed set of normal orthogonal functions. American Journal of Mathematics 45, 5–24.

Coherent Control: Theory

H Rabitz, Princeton University, Princeton, NJ, USA

© 2005 Elsevier Ltd. All rights reserved.

Introduction

Since the inception of quantum mechanics almost a century ago, a prime activity has been the observation of quantum phenomena in virtually all areas of chemistry and physics. However, the natural evolution of science leads to the desire to go beyond passive observation to active manipulation of quantum mechanical processes. Achieving control over quantum phenomena could be viewed as engineering at the atomic scale guided by the principles of quantum mechanics, for the alteration of system properties or dynamic behavior. From this perspective, the construction of quantum mechanically operating solid-state devices through selective material growth would fall into this category. The focus of this article is principally on the manipulation of quantum phenomena through tailored laser pulses. The suggestion of using coherent radiation for the active alteration of microworld processes may be traced to the early 1960s, almost immediately after the discovery of lasers. Since then, the subject has grown enormously to encompass the manipulation of (1) chemical reactions, (2) quantum electron transport in semiconductors, (3) excitons in solids, (4) quantum information systems, (5) atom lasers, and (6) high harmonic generation, amongst other topics. Perhaps the most significant use of these techniques may be their provision of refined tools to ultimately better understand the basic physical interactions operative at the atomic scale.

Regardless of the particular application of laser control over quantum phenomena, there is one basic operating principle involved: active manipulation of constructive and destructive quantum wave interferences. This process is depicted in **Fig. 1**, showing the evolution of a quantum system from the initial state $|\psi_i\rangle$ to the desired final state $|\psi_f\rangle$ along three of possibly many interfering pathways. In general, there may be many possible final accessible states $|\psi_f\rangle$, and often the goal is to achieve a high amplitude in one of these states and low amplitude in all the others. The target state might actually be a superposition of states, and an analogous picture to that in **Fig. 1** would also apply to steering about the density matrix. The process depicted in **Fig. 1** may be thought of as a microscale analog of the classic double-slit experiment for light waves. As the goal is often high-finesse focusing into a particular target quantum state, success may call for the manipulation of many quantum pathways (i.e., the notion of a 'many-slit' experiment). Most applications are concerned with achieving a desirable outcome for the expectation value $\langle\psi_f|O|\psi_f\rangle$ associated with some observable Hermitian operator O.

The practical realization of the task above becomes a control problem when the system is expressed through its Hamiltonian $H=H_0+V_c$, where H_0 is the free Hamiltonian describing the dynamics without explicit control; it is assumed that the free evolutionary dynamics under H_0 will not satisfactorily achieve the physical objective. Thus, a laboratory-accessible control term V_c is introduced in the Hamiltonian to achieve the desired manipulation. Even just considering radiative interactions, the form of V_c could be quite diverse depending on the nature of the system (e.g., nuclear spins, electrons, atoms, molecules, etc.) and the intensity of the radiation field. Many problems may be treated through an electric dipole interaction $V_c = -\boldsymbol{\mu}\cdot\boldsymbol{\varepsilon}(t)$ where $\boldsymbol{\mu}$ is a system dipole moment and $\boldsymbol{\varepsilon}(t)$ is the laser electric field. Where appropriate, this article will consider the interaction in this form, but other suitable radiative control interactions may be equally well treated. Thus, the laser field $\boldsymbol{\varepsilon}(t)$ as a function of time (or frequency) is at our disposal for attempted manipulation of quantum systems.

Before considering any practical issues associated with the identification of shaped laser control fields, a fundamental question concerns whether it is, in principle, possible to steer about any particular quantum system from an arbitrary initial state $|\psi_i\rangle$ to an arbitrary final state $|\psi_f\rangle$. Questions of this sort are addressed by a controllability analysis of Schrödinger's equation

$$i\hbar\frac{\partial|\psi(t)\rangle}{\partial t} = [H_0 - \boldsymbol{\mu}\cdot\boldsymbol{\varepsilon}(t)]|\psi(t)\rangle, \quad |\psi(0)\rangle = |\psi_i\rangle \tag{1}$$

Controllability concerns whether, in principle, some field $\boldsymbol{\varepsilon}(t)$ exists, such that the quantum system described by $H_0=H_0-\boldsymbol{\mu}\cdot\boldsymbol{\varepsilon}(t)$ permits arbitrary degrees of control. For finite-dimensional quantum systems (i.e., those described by evolution amongst a discrete

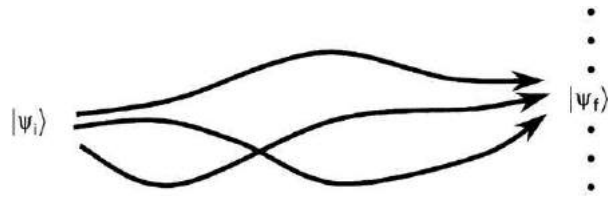


Fig. 1 The evolution of a quantum system under laser control from the initial state $|\psi_i\rangle$ to the final state $|\psi_f\rangle$. The latter state is chosen to have desirable physical properties, and three of possibly many pathways between the states are depicted. Successful control of the process $|\psi_i\rangle \rightarrow |\psi_f\rangle$ by a tailored laser pulse generally requires creating constructive quantum wave interferences in the state $|\psi_f\rangle$ from many pathways, and destructive interferences in all other accessible final states $|\psi_{f'}\rangle \neq |\psi_f\rangle$.

 doi:10.1016/B978-0-12-809283-5.00903-4

set of quantum states), the formal tools for such a controllability analysis exist both for evaluating the controllability of the wave function, as well as the more general time evolution operator $U(t)$, which satisfies

$$i\hbar \frac{\partial U}{\partial t} = [H_0 - \boldsymbol{\mu} \cdot \boldsymbol{\varepsilon}(t)]U, \quad U(0) = 1 \tag{2}$$

Analyses of this type can be quite insightful, but they require detailed knowledge about H_0 and $\boldsymbol{\mu}$. Cases involving quantum information science applications are perhaps the most demanding with regard to achieving total control. Most other physical applications would likely accept much more modest levels of control and still be categorized as excellent achievements.

Theoretical tools and concepts have a number of roles in considering the control of quantum systems, including (1) an exploration of physical/chemical phenomena under active control, (2) the design of viable control fields, (3) the development of algorithms to actively guide laboratory control experiments towards achieving their dynamical objectives, and (4) the introduction of special algorithms to reveal the physical mechanisms operative in the control of quantum phenomena. Activities (1)–(3) have thus far been the primary focus of theoretical studies in this area, and it is anticipated that item (4) will grow in importance in the future.

A few comments on the history of laser control over quantum systems are relevant, as they speak to the special nature of the currently employed successful closed-loop quantum control experiments. Starting in the 1960s and spanning roughly 20 years, it was thought that the design of lasers to manipulate molecular motion could be achieved by the application of simple physical logic and intuition. In particular, the thinking at the time focused on using cw laser fields resonant with one or more local modes of the molecule, as state or energy localization was believed to be the key to successful control. Since quantum dynamics phenomena typically occur on ultrafast time-scales, possibly involving spatially dispersed wave packets, expecting to achieve high quality control with a light source operating at one or two resonant frequencies is generally wishful thinking. Quantum dynamics phenomena occur in a multifrequency domain, and controls with a few frequencies will not suffice. Over approximately the last decade, it became clear that successful control often calls for manipulating multiple interfering quantum pathways (cf., **Fig. 1**). In turn, this recognition led to the need for broad-bandwidth laser sources (i.e., tailored laser pulses). Fortunately, the necessary laser pulse-shaping technologies have become available, and these sources continue to expand into new frequency ranges with enhanced bandwidth capabilities. Many chemical and physical applications of control over quantum phenomena involve performing a significant amount of work (i.e., quantum mechanical action), and sufficient laser field intensity is required. A commonly quoted adage is 'no field, no yield', and at the other extreme, there was much speculation that operating nonlinearly at high field intensities would lead to a loss of control because the quantum system would effectively act as an amplifier of even weak laser field noise. Fortunately, the latter outcome has not occurred, as is evident from a number of successful high field laser control experiments.

Quantum control may be expressed as an inverse problem with a prescribed chemical or physical objective, and the task being the discovery of a suitable control field $\varepsilon(t)$ to meet the objective. Normally, Schrödinger's **Eq. (1)** is viewed as linear, and this perspective is valid if the Hamiltonian is known a priori, leaving the equation to be solved for the wave function. However, in the case of quantum control, neither the wave function nor the control field is known a priori, and the two enter bilinearly on the right-hand side of **Eq. (1)**. Thus, quantum control is mathematically a nonlinear inverse problem. As such, one can anticipate possibly diverse behavior in the process of seeking successful controls, as well as in the ensuing quantum dynamical control behavior. The control must take into account the evolving system dynamics, thereby resulting in the control field being a function (al) of the current state of the system $\varepsilon(\psi)$ in the case of quantum control design, or dependent on the system observations $\varepsilon(\langle O \rangle)$ in the case of laboratory closed-loop field discovery efforts where $\langle O \rangle = \langle \psi | O | \psi \rangle$. Furthermore, the control field at the current time t will depend in some implicit fashion on the future state of the evolving system at the final target time T. It is evident that control field design and laboratory discovery present highly nontrivial tasks.

Although the emphasis in this review is on the theoretical aspects of quantum control theory, the subject exists for its laboratory realizations, and those realizations, in turn, intimately depend on the capabilities of theoretical and algorithmic techniques for their successful implementations. Accordingly, theoretical laser control field design techniques will be discussed, along with algorithmic aspects of current laboratory practice. This material respectively will focus on optimal control theory (OCT) and optimal control experiments (OCEs), as seeking optimality provides the best means to achieve any posed objective. Finally, the last part of the article will present some general conclusions on the state of the quantum control field.

Quantum Optimal Control Theory for Designing Laser Fields

When considering control in any domain of application, a reasonable approach is to computationally design the control for subsequent implementation in the laboratory. Quantum mechanical laser field design has taken on a number of realizations. At one limit is the application of simple intuition for design purposes, and in some special cases (e.g., the weak field perturbation theory regime), this approach may be applicable. Physical insights will always play a central role in laser field design, but to be especially useful, they need to be channeled into the proper mathematical framework. Many of the interesting applications operate in the strong-field nonperturbative regime. In this domain, serious questions arise regarding whether sufficient information is available about the Hamiltonian to execute reliable designs. Regardless of whether the Hamiltonian is known accurately or is an

acknowledged model, the theoretical study of quantum control can provide physical insight into the phenomena involved, as well as possibly yielding trial laser pulses for further refinement in the laboratory.

Achieving control over quantum mechanical phenomena often involves a balance of competing dynamical processes. For example, in the case of aiming to create a particular excitation in a molecule or material, there will always be the concomitant need to minimize other unwanted excitations. Often, there are also limitations on the form, intensity, or other characteristics of the laser controls that must be adhered to. Another goal is for the control outcome to be as robust as possible to the laser field fluctuations and Hamiltonian uncertainties. Overriding all of these issues is merely the desire to achieve the best possible physical result for the posed quantum mechanical objective. In summary, all of these desired extrema conditions translate over to posing the design of control laser fields as an optimization problem. Thus, optimal control theory forms a basic foundation for quantum control field design.

Control field design starts by specification of the Hamiltonian components H_0 and $\boldsymbol{\mu}$ in **Eq. (1)**, with the goal of finding the best control electric field $\boldsymbol{\varepsilon}(t)$ to balance the competing objectives. Schrödinger's equation must be solved as part of this process, but this effort is not merely a forward propagation task, as the control field is not known a priori. As an optimal design is the goal, a cost functional $J=J(\text{objectives, penalties, } \boldsymbol{\varepsilon}(t))$ is prescribed, which contains the information on the physical objectives, competing penalties, and any costs or constraints associated with the structure of the laser field. The functional J could contain many terms if the competing physical goals are highly complex. As a specific simple illustration, consider the common goal of steering the system to achieve an expectation value $\langle\psi(T)|O|\psi(T)\rangle$ as close as possible to the target value O_{target} associated with the observable operator O at time T. An additional cost is imposed to minimize the laser fluence. These criteria may be embodied in a cost functional of the form

$$J=\left(\langle\psi(T)|O|\psi(T)\rangle-O_{\text{target}}\right)^2+\omega\int_0^T\varepsilon^2(t)\mathrm{d}t-2\Im\int_0^T\mathrm{d}t\left\langle\lambda(t)|\mathrm{i}\hbar\frac{\partial}{\partial t}-H_0+\boldsymbol{\mu}\cdot\boldsymbol{\varepsilon}(t)|\psi(t)\right\rangle \tag{3}$$

Here, the parameter $\omega\geq 0$ is a weight to balance the significance of the fluence term relative to achieving the target expectation value, and $|\lambda(t)\rangle$ serves as a Lagrange multiplier, assuring that Schrödinger's equation is satisfied during the variational minimization of J with respect to the control field. Carrying out the latter minimization will lead to **Eq. (1)**, along with the additional relations

$$\mathrm{i}\hbar\frac{\partial}{\partial t}|\lambda(t)\rangle=[H_0-\boldsymbol{\mu}\cdot\boldsymbol{\varepsilon}(t)]|\lambda(t)\rangle,\ |\lambda(T)\rangle=2\sigma O|\lambda(T)\rangle \tag{4}$$

$$\boldsymbol{\varepsilon}(t)=\frac{1}{\omega}\Im\langle\lambda(t)|\boldsymbol{\mu}|\psi(t)\rangle \tag{5}$$

$$\sigma=\langle\psi(T)|O|\psi(T)\rangle-O_{\text{target}} \tag{6}$$

Eqs. (1) and **(4)–(6)** embody the OCT design equations that must be solved to yield the optimal field $\boldsymbol{\varepsilon}(t)$ given in **Eq. (5)**. These design equations have an unusual mathematical structure within quantum mechanics. First, insertion of the field expression in **Eq. (5)** into **Eqs. (1)** and **(4)** produces two cubically nonlinear coupled Schrödinger-like equations. These equations are in the same family as the standard nonlinear Schrödinger equation, and as such, one may expect that unusual dynamical behavior could arise. Although **Eq. (4)** for $|\lambda(t)\rangle$ is identical in form to the Schrödinger **Eq. (1)**, only $|\psi(t)\rangle$ is the true wavefunction, with $|\lambda(t)\rangle$ serving to guide the controlled quantum evolution towards the physical objective. Importantly, **Eq. (1)** is an initial value problem, while **Eq. (4)** is a final value problem. Thus, the two equations together form a two-point boundary value problem in time, which is an inherent feature of temporal engineering optimal control as well. The boundary value nature of these equations typically leads to the existence of multiple solutions, where σ in **Eq. (6)** plays the role of a discrete eigenvalue, specifying the quality of the particular achieved control field design. The fact that there are generally multiple solutions to the laser design equations can be attractive from a physical perspective, as the designs may be sorted through to identify those being most attractive for laboratory implementation.

The overall mathematical structure of **Eqs. (1)** and **(4)–(6)** can be melded together into a single design equation

$$\mathrm{i}\hbar\frac{\partial}{\partial t}|\psi(t)\rangle=[H_0-\boldsymbol{\mu}\cdot\boldsymbol{\varepsilon}(\psi,\sigma,t)]|\psi(t)\rangle,\quad |\psi(0)\rangle=|\psi_{\mathrm{i}}\rangle \tag{7}$$

The structure of this equation embodies the comments in the introduction that control field design is inherently a nonlinear process. The main source of complexity arising in **Eq. (7)** is through the control field $\boldsymbol{\varepsilon}(\psi,\sigma,t)$ depending not only on the wave function at the present time t, but also on the future value of the wavefunction at the target time T contained in σ. This structure again reflects the two-point boundary value nature of the control equations.

Given the typical multiplicity of solutions to Eqs. **(1)** and **(4)–(6)**, or equivalently, **Eq. (7)**, it is attractive to consider approximations to these equations (except perhaps for the inviolate Schrödinger **Eq. (1)**, and much work continues to be done along these lines. One case involves what is referred to as tracking control, whereby a path is specified for $\langle\psi(t)|O|\psi(t)\rangle$ evolving from $t=0$ out to $t=T$. Tracking control eliminates σ to produce a field of the form $\boldsymbol{\varepsilon}(\psi,t)$, thereby permitting the design equations to be explicitly integrated as a forward-marching problem toward the target; the tracking equations are still nonlinear with respect to the evolving state. Many variations on these concepts can be envisioned, and other approximations may also be introduced to deal with special circumstances. One technique appropriate for at least few-level systems is stimulated Raman adiabatic passage (STIRAP), which seeks robust adiabatic passage from an initial state to a particular final state, typically with nearly total destructive interference

occurring in the intermediate states. This design technique can have special attractive robustness characteristics with respect to field errors. STIRAP, tracking, and various perturbation theory-based control design techniques can be expressed as special cases of OCT, with suitable cost functionals and constraints. Further approximation methods will surely be developed, with the rigorous OCT concepts forming the general foundation for control field design.

As the OCT equations are inherently nonlinear, their solution typically requires numerical iteration, and a variety of procedures may be utilized for this purpose. Almost all of the methods employ local search techniques (e.g., gradient methods), and some also show monotonic convergence with respect to each new iteration step. Local techniques typically evolve to the nearest solution in the space of possible control fields. Such optimizations can be numerically efficient, although the quality of the attained result can depend on the initial trial for the control field and the details of the algorithm involved. In contrast, global search techniques, such as simulated annealing or genetic algorithms, can search more broadly for the best solution in the control field space. These more expansive searches are attractive, but at the price of typically requiring more intensive computations. Effort has also gone into seeking global or semiglobal input $\rightarrow$ output maps relating the electric field $\varepsilon(t)$ structure to the observable $O[\varepsilon(t)]$. Such maps may be learned, hopefully, from a modest number of computations with a selected set of fields, and then utilized as high-speed interpolators over the control field space to permit the efficient use of global search algorithms to attain the best control solution possible. At the foundation of all OCT design procedures is the need to solve the Schrödinger equation. Thus, computational technology to improve this basic task is of fundamental importance for designing laser fields.

Many computations have been carried out with OCT to attain control field designs for manipulating a host of phenomena, including rotational, vibrational, electronic, and reactive dynamics of molecules, as well as electron motion in semiconductors. Every system has its own rich details, which in turn, are compounded by the fact that multiple control designs will typically exist in many applications producing comparable physical outcomes. Collectively, these control design studies confirm the manipulation of constructive and destructive quantum wave interferences as the general mechanism for achieving successful control over quantum phenomena. This conclusion may be expressed as the following principle:

Control field–system cooperativity principle: Successful quantum control requires that the field must have the proper structure to take full advantage of all of the dynamical opportunities offered by the system, to best satisfy the physical objective.

This simple statement of system–field cooperativity embodies the richness, as well as the complexity, of seeking control over quantum phenomena, and also speaks to why simple intuition alone has not proved to be a generally viable design technique. Quantum systems can often exhibit highly complex dynamical behavior, including broad dispersion of the wave packet over spatial domains or multitudes of quantum states. Handling such complexity can require fields with subtle structure to interact with the quantum system in a global fashion to manage all of the motions involved. Thus, we may expect that successful control pulses will often have broad bandwidth, including amplitude and phase modulation. Until relatively recently, laser sources with these characteristics were not available, but the technology is now in hand and rapidly evolving (see the discussion later).

The cooperativity principle above is of fundamental importance in the control of all quantum phenomena, and a simple illustration of this principle is shown in Fig. 2 for the control of wave packet motion on an excited state of the NO molecule.

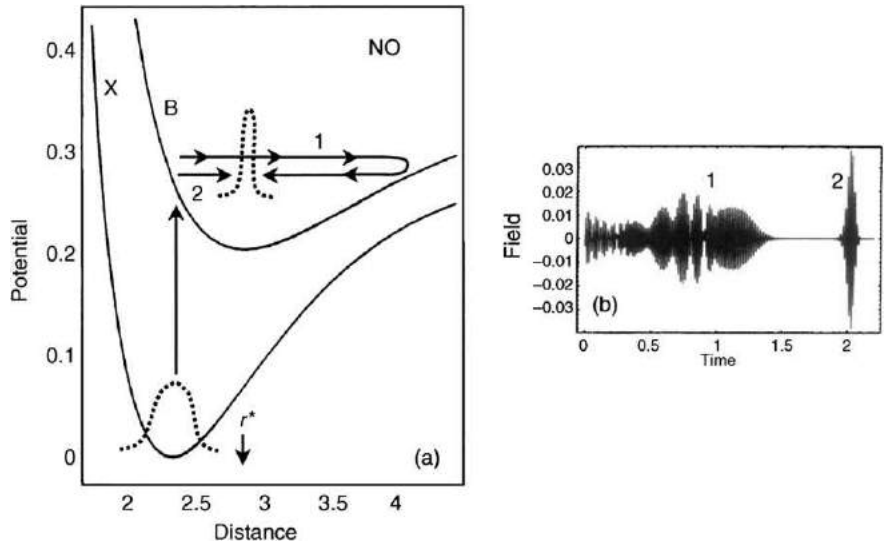


Fig. 2 Control of wave packet evolution on the electronically excited B state of NO, with the goal of creating a narrow final packet over the excited state well. (a) indicates that the ground-state packet is brought up in two pieces using the coordinated dual pulse in (b). The piece of the packet from the first pulse actually passes through the target region, then bounces off the right side of the potential, to finally meet the second piece of the packet at just the right time over the target location r^* for successful control. This behavior is an illustration of the control field–system cooperativity principle stated in the text.

The target for the control is a narrow wave packet located over the well of the excited Bstate. The optimal control field consists of two coordinated pulses, at early and late times, with both features having internal structure. The figure indicates that the ensuing excited state wave packet has two components, one of which actually passes through the target region during the initial evolution, only to return again and meet the second component at just the right place and time, to achieve the target objective as best as possible. Similar cooperativity interpretations can be found in virtually all implementations with OCT.

The main reason for performing quantum field design is to ultimately implement the designs in the laboratory. The design procedures must face laboratory realities, which include the fact that most Hamiltonians are not known to high accuracy (especially for polyatomic molecules and complex solid-state structures), and secondly, a variety of laboratory field imperfections may unwittingly be present. Notwithstanding these comments, OCT has been fundamental to the development of quantum control, including laying out the logic for how to perform the analogous optimal control experiments. Design implementations and further OCT development will continue to play a basic role in the quantum control field. At present, perhaps the most important contribution of OCT has been to (1) highlight the basic control cooperativity principle above, and (2) provide the basis for developing algorithms to successfully guide optimal control experiments, as discussed below.

Algorithms for Implementing Optimal Control Experiments

The ultimate purpose of considering control theory within quantum mechanics is to take the matter into the laboratory for implementation and exploitation of its capabilities. Ideally, theoretical control field designs may be attained using the techniques discussed above, followed by the achievement of successful control upon execution of the designs in the laboratory. This appealing approach is burdened with three difficulties: (1) Hamiltonians are often imprecisely known, (2) accurately solving the design equations can be a significant task, and (3) realization of any given design will likely be imperfect due to laboratory noise or other unaccounted-for systematic errors. Perhaps the most serious of these difficulties is point (1), especially considering that the best quality control will be achieved by maximally drawing on subtle constructive and destructive quantum wave interference effects. Exploiting such subtleties will generally require high-quality control designs that, in turn, depend on having reliable Hamiltonians. Although various designs have been carried out seeking robustness with respect to Hamiltonian uncertainties, the issue in point (1) should remain of significance in the foreseeable future, especially for the most complex (and often, the most interesting!) chemical/physical applications. Mitigating this serious problem is the ability to create shaped laser pulse controls and apply them to a quantum system, followed by a probe of their effects at an unprecedented rate of thousands or more independent trials per minute. This unique capability led to the suggestion of partially, if not totally, sidestepping the design process by performing closed-loop experiments to let the quantum system teach the laser how to achieve its control in the laboratory. Fig. 3 schematically shows this closed loop process, drawing on the following logic:

1. **The molecular view**. Although there may be theoretical uncertainty about the system Hamiltonian, the actual chemical/physical system under study 'knows' its own Hamiltonian precisely! This knowledge would also include any unusual exigencies, perhaps associated with structural or other defects in the particular sample. Furthermore, upon exposure to a control field, the system 'solves' its own Schrödinger equation impeccably accurately and as fast as possible in real time. Considering these points, the aim is to replace the offline arduous digital computer control field design effort with the actual quantum system under study acting as a precise analog computer, solving the true equations of motion.
2. **Control laser technology**. Pulse shaping under full computer control may be carried out using even hundreds of discrete elements in the frequency domain controlling the phase and amplitude structure of the pulse. This technology is readily available and expanding in terms of pulse center frequency flexibility and bandwidth capabilities.
3. **Quantum mechanical objectives**. Many chemical/physical objectives may be simply expressed as the desire to steer a quantum mechanical flux out one clearly defined channel versus another.
4. **Detection of the control action**. Detection of the control outcome can often be carried out by a second laser pulse or any other suitable high duty cycle detection means, such as laser-induced mass spectrometry. The typical circumstance in point (3) implies that little, if any, time-consuming offline data analysis will be necessary beyond that of simple signal averaging.
5. **Fast learning algorithms**. All of the four points above may be slaved together using pattern recognition learning algorithms to identify those control fields which are producing better results, and bias the next sequence of experiments in their favor for further improvement. Although many algorithms may be employed for this purpose, the global search capabilities of genetic algorithms are quite attractive, as they may take full advantage of the high throughput nature of the experiments.

In linking together all of these components into a closed-loop OCE, it is important that no single operational step significantly lags behind any other, for efficiency reasons. Fortunately, this economy is coincident with all the tasks and technologies involved. For achieving control alone, there is no requirement that the actual laser pulse structure be identified on each cycle of the loop. Rather, the laser control 'knob' settings are adequate information for the learning algorithm, as the only criterion is to suitably adjust the knobs to achieve an acceptable value for the chemical/physical objective. The learning algorithm in point (5) operates with a cost functional J, analogous to that used for computational design of fields, but now the cost functional can only depend on those quantities directly observable in the laboratory (i.e., minimally, the current achieved target expectation value). In cases where a physical understanding is sought about the control mechanism, the laser field structure must also be measured. This additional

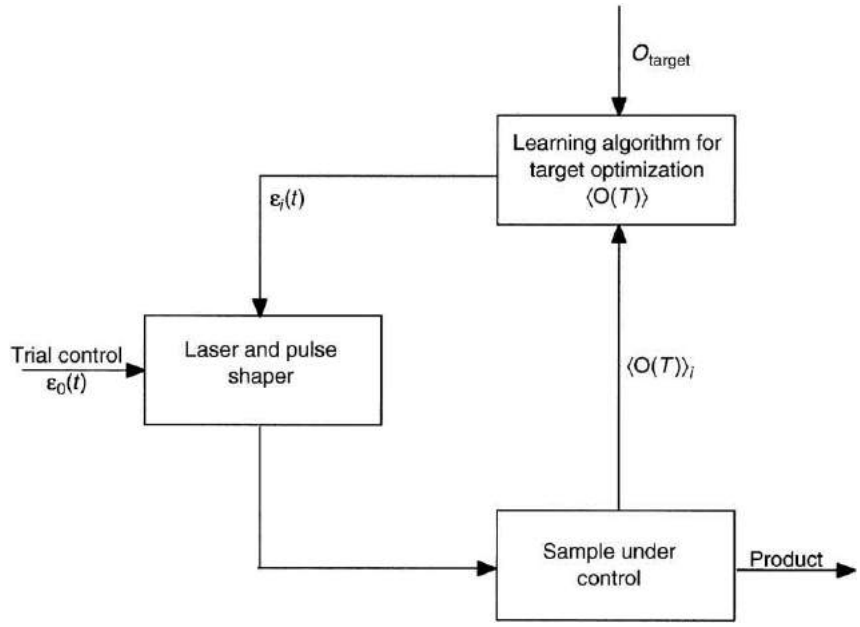


Fig. 3 A schematic of the closed-loop concept for allowing the quantum system to teach the laser how to achieve its control. The actual quantum system under control is in a loop with a laser and pulse shaper all slaved together with a pattern recognition algorithm to guide the excursions around the loop. The success of this concept relies on the ability to perform very large numbers of control experiments in a short period of time. In principle, no knowledge of the system Hamiltonian is required to steer the system to the desired final objective, although a good trial design $\varepsilon_0(t)$ may accelerate the process. The ith cycle around the loop attempts to find a better control field $\varepsilon_i(t)$ such that the system response $\langle O(T)\rangle_i$ for the observable operator O comes closer to the desired value O_{target}.

information is typically also not a burden to attain, as it often is only required for the single best control field at the end of the closed-loop learning experiments.

The OCE process in Fig. 3 and steps (1)–(5) above constitute the laboratory process for achieving optimal quantum control, and exactly the same reasons put forth for OCT motivate the desire for attaining optimal performance: principally, seeking the best control result that can possibly be obtained. Seeking optimal performance also ensures some degree of inherent robustness to field noise, as fleeting observations would not likely survive the signal averaging carried out in the laboratory. Additionally, robustness as a specific criterion may also be included in the laboratory cost functional in item (5). When a detailed physical interpretation of the controlled dynamics is desired, it is essential to remove any extraneous control field features that have little impact on the system manipulations. Without the latter clean-up carried out during the experiments, the final field may be contaminated by structures that have little physical impact. Although quantum dynamics typically occurs on femtosecond or picosecond time-scales, the loop excursions in Fig. 3 need not be carried out on the latter time-scales. Rather, the loop may be traversed as rapidly as convenient, consistent with the capabilities of the apparatus. A new system sample is introduced on each cycle of the loop. This process is referred learning control, to distinguish it from real-time feedback control.

The closed-loop quantum learning control algorithm can be self-starting, requiring no prior control field designs, under favorable circumstances. Virtually all of the current experiments were carried out in this fashion. It remains to be seen if this procedure of 'going in blind' will be generally applicable in highly complex situations where the initial state is far from the target state. Learning control can only proceed if at least a minimal signal is observed in the target state. Presently, this requirement has been met by drawing on the overwhelmingly large number of exploratory experiments that can be carried out, even in a brief few minutes, under full computer control. However, in some situations, the performance of intermediate observations along the way to the target goal may be necessary in order to at least partially guide the quantum dynamics towards the ultimate objective. Beneficial use could also be made from prior theoretical laser control designs $\varepsilon_0(t)$ capable of at least yielding a minimal target signal.

The OCE closed-loop procedure was based on the growing number of successful theoretical OCT design calculations, even with all of their foibles, especially including less than perfect Hamiltonians. The OCT and OCE processes are analogous, with their primary distinction involving precisely what appears in their corresponding cost functionals. Theoretical guidance can aid in identifying the appropriate cost functionals and learning algorithms for OCE, especially for addressing the needs associated with attaining a physical understanding about the mechanisms governing controlled quantum dynamics phenomena.

A central issue is the rate that learning control occurs upon excursions around the loop in Fig. 3. A number of factors control this rate of learning, including the nature of the physical system, the choice of objective, the presence of field uncertainties and measurement errors, the number of control variables, and the capabilities of the learning algorithm employed. Achieving control is a matter of discrimination, and some of these factors, whether inherent to the system or introduced by choice, may work against

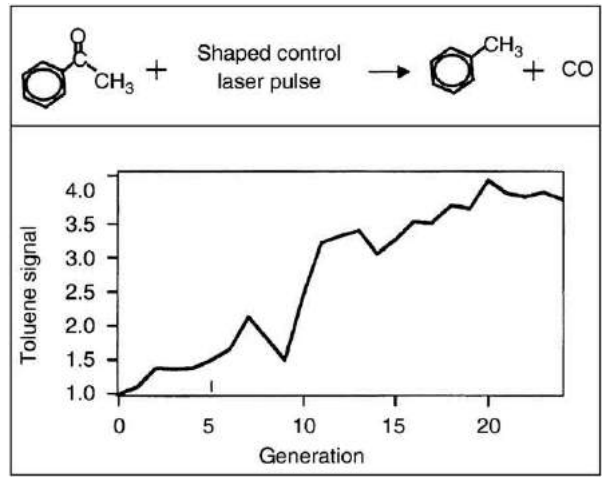


Fig. 4 An illustration of dissociative rearrangement achieved by closed-loop learning control in Fig. 3. The optimally deduced laser pulse broke two bonds in the parent acetophenone molecule and formed a new one to yield the toluene product. The laboratory learning curve is shown for the toluene product signal as a function of the generations in the genetic algorithm guiding the experiments. The fluctuations in the learning curve for optimizing the toluene yield corresponds to the algorithm searching for the optimal yield as the experiments proceed.

attaining good-quality discrimination. At this juncture, little is known quantitatively about the limitations associated with any of these factors.

The latter issues have not prevented the successful performance of a broad variety of quantum control experiments, and at present the ability to carry out massive numbers of closed-loop excursions has overcome any evident difficulties. The number of examples of successful closed-loop quantum control is rapidly growing, with illustrations involving the manipulation of laser dye fluorescence, chemical reactivity, high harmonic generation, semiconductor optical switching, fiber optic pulse transmission, and dynamical discrimination of similar chemical species, amongst others. Perhaps the most interesting cases are those carried out at high field intensities, where prior speculation suggested that such experiments would fail due to even modest laser field noise being amplified by the quantum dynamics. Fortunately, this outcome did not occur, and theoretical studies have indicated that surprising degrees of robustness to field noise may accompany the manipulation of quantum dynamics phenomena. Although the presence of field noise may diminish the beneficial influence of constructive and destructive interferences, evidence shows that field noise does not appear to kill the actual control process, at least in terms of obtaining reasonable values for the control objectives. One illustration of control in the high-field regime is shown in Fig. 4, demonstrating the learning process for the dissociative rearrangement of acetophenone to form toluene. Interestingly, this case involves breaking two bonds, with the formation of a third, indicating that complex dynamics can be managed with suitably tailored laser pulses.

Operating in the strong-field regime, especially for chemical manipulations, also has the important benefit of producing a generic laser tool to control a broad variety of systems by overcoming the long-standing problem of having sufficient bandwidth. For example, the result in Fig. 4 uses a Ti:sapphire laser in the near-infrared regime. Starting with a bandwidth-limited pulse of intensity near $\sim 10^{14}$ W cm^{-2}, in this regime, the dynamic power broadening can easily be on the order of ~ 1 eV or more, thereby effectively converting the otherwise discrete spectrum of the molecule into an effective continuum for ready multiphoton matching by the control laser pulse. Operating under these physical conditions is very attractive, as the apparatus is generic, permitting a single shaped-pulse laser source (e.g., a Ti:sapphire system with phase and amplitude modulation) to be utilized with virtually any chemical system where manipulations are desired. Although every desired physical/chemical goal may not be satisfactorily met (i.e., the goals must be physically attainable!), the means are now available to explore large numbers of systems. Operating under closed loop in the strong-field tailored-pulse regime eliminates the prior serious limitation of first finding a physical system to meet the laser capabilities; now, the structure of the laser pulse can be shaped to meet the molecule's characteristics. Strong field operations may be attractive for these reasons, but other broadband laser sources, possibly working at weaker field intensities, might be essential in some applications (e.g., controlling electron dynamics in semiconductors, where material damage is to be avoided). It is anticipated that additional broadband laser sources will become available for these purposes.

The coming years should be a period of rapid expansion, including a thorough exploration of closed-loop quantum control capabilities. As with the use of any laboratory tool, certain applications may be more amenable than others to attaining successful control. The particular physical/chemical questions need to be well posed, and controls need to have sufficient flexibility to meet the objectives. The experiments ahead should be able to reveal the degree to which drawing on optimality in OCE, combined with the performance of massive numbers of experiments can lead to broad-scale successful control of quantum phenomena. One issue of concern is the richness associated with the large numbers of phase and amplitude control knobs that may be adjusted in the laboratory. Some experiments have already operated with hundreds of knobs, while others have restricted their number in a variety of ways, to simplify the search process. Additional technological and algorithmic advances may be required to manage the

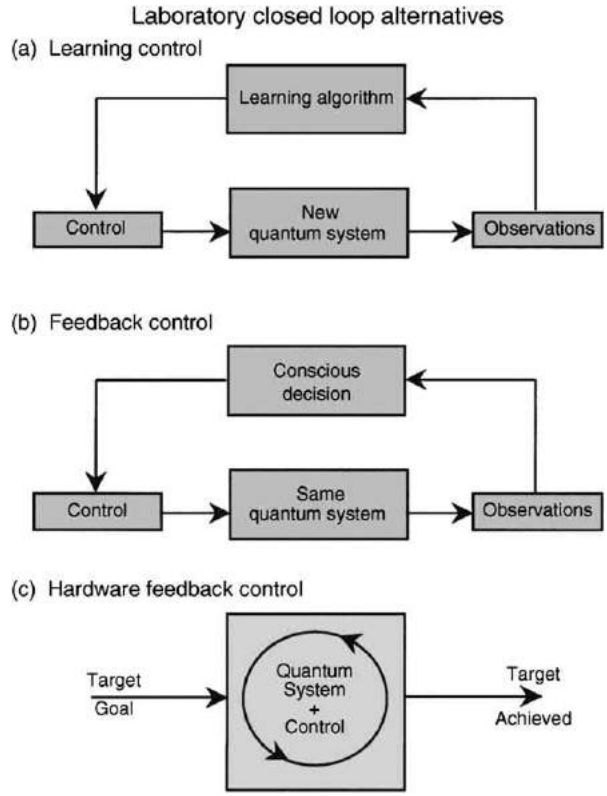


Fig. 5 Three possible closed-loop formulations for attaining laser control over quantum phenomena. (a) is a learning control process where a new system is introduced on each excursion around the loop. (b) utilizes feedback control with the loop being traversed with the same sample, generally calling for an accurate model of the system to adjust the controls on each loop excursion. (c) is, at present, a dream machine where the laser and the sample under control are one unit operating without external algorithmic guidance. The closed-loop learning control procedure in (a) appears to form the most practical means to achieve laser control over quantum phenomena, especially for complex systems.

high-dimensional control space searches. Fortunately, for typical applications, the search does not reduce to seeking a needle in a haystack, as generally there are multiple control solutions, possibly all of very good quality.

As a final comment on OCE, it is useful to appreciate the subtle distinction of the procedure from closed-loop feedback experiments. This distinction is illustrated in **Fig. 5**, pointing to three types of closed-loop quantum control laboratory experiments. The OCE procedure in **Fig. 5(a)** produces a generic laser tool capable of controlling a broad variety of systems with an emphasis in the figure placed on the point that each cycle around the loop starts with a new sample for control. The replacement of the sample on each cycle eliminates a number of difficulties, principally including concerns about sample damage, avoidance of operating the loop at the ultrafast speed of the quantum mechanical processes, and elimination of the effect that 'to observe is to disturb' in quantum mechanics. Thus, learning control provides a generic practical procedure, regardless of the nature of the quantum system. **Fig. 5(b)** has the same structure as that of **Fig. 5(a)**, except the loop is now closed around the same single quantum system, which is followed throughout its evolution. All of the issues mentioned above that are circumvented by operating through laboratory learning control in **Fig. 5(a)** must now be directly faced in the setup of **Fig. 5(b)**. The procedure in **Fig. 5(b)** will likely only be applicable in special circumstances, at least for the reason that many quantum systems operate on timescales far too fast for opto-electronics and computers to keep up with. However, there are certain quantum mechanical processes that are sufficiently slow to meet the criteria. Furthermore, a period of free evolutionary quantum dynamics may be permitted to occur between one control pulse and the next, to make the time issue manageable. While the learning control process in **Figs. 3** and **5(a)** can be performed model-free, the feedback algorithm in **Fig. 5(b)** generally must operate with a sufficiently reliable system Hamiltonian to carry out fast design corrections to the control field, based on the previous control outcome. These are very severe demands, but they may be met under certain circumstances. One reason for considering closed-loop feedback control in **Fig. 5(b)** is to explore the basic physical issue of quantum mechanical limitations inherent in the statement 'to observe is to disturb'. It is suggestive that control over many types of quantum phenomena may fall into the semiclassical regime, lying somewhere between classical engineering behavior and the hard limitations of quantum mechanics. Experiments of the type in **Fig. 5(b)** will be most interesting for exploring this matter. Finally, **Fig. 5(c)** introduces a *gedanken* experiment in the sense that the closed-loop process is literally built into the hardware. That is, the laser control and quantum system act as a single functioning unit operating in a stable fashion, so as to automatically steer the system to the desired target. This process may involve engineering the quantum mechanical system prior to control in cases where that freedom exists, as well as engineering the laser components involved.

The meaning of such a device in Fig. 5(c) can be understood by considering an analogy with airplane flight, where the aircraft is constructed to have an inherent degree of aerodynamic stability and will essentially fly (glide) on its own accord when pushed forward. It is an open question whether closing the loop in the hardware can be attained for quantum control, and an exploration of this concept may require additional laser technologies.

Conclusions

This article presented an overview of theoretical concepts and algorithmic considerations associated with the control of quantum phenomena. Theory has played a central role in this area by revealing the fundamental principles underlying quantum control, as well as by providing algorithms for designing controls and guiding experiments to discover successful controls in the laboratory. The challenge of controlling quantum phenomena, in one sense, is an old subject, going back at least 40 years. However, roughly the first 30 of these years would best be described as a period of frustration, due to a lack of full understanding of the principles involved and the nature of the lasers needed to achieve success. Thus, from another perspective, the subject is quite young, with perhaps the most notable development being the introduction of closed-loop laboratory learning procedures. At the time of writing this article, these procedures are just beginning to be explored for their full capabilities. To appreciate the young nature of this subject, it is useful to note that the analogous engineering control disciplines presently occupy many thousands of engineers worldwide, both theoreticians and practitioners, and have done so for many years. Yet, engineering control is far from considered a mature subject. Armed now with the basic concepts and proper laboratory tools, one may anticipate a thorough exploration of control over quantum phenomena, including its many possible applications.

Acknowledgment

Support for this work has come from the National Science Foundation and the Department of Defense.

See also: Coherent Control: Experimental. Overview: Coherence

Further Reading

Brixner, T., Damrauer, N.H., Gerber, G., 2001. Femtosecond quantum control. Advances in Atomic, Molecular, and Optical Physics 44, 1–54.
Rabitz, H., de Vivie-Riedle, R., Motzkus, M., Kompa, K., 2000. Whither the future of controlling quantum phenomena? Science 288, 824–828.
Rabitz, H., Zhu, W., 2000. Optimal control of molecular motion: Design, implementation and inversion. Accounts of Chemical Research 33, 572–578.
Rice, S.A., Zhao, M., 2000. Optical Control of Molecular Processes. New York: John Wiley.

Coherent Control: Experimental

RJ Levis, Temple University, Philadelphia, PA, USA

© 2005 Elsevier Ltd. All rights reserved.

Introduction

The experimental control of quantum phenomena in atoms, molecules, and condensed phase materials has been a long-standing challenge in the physical sciences. For example, the idea that a laser beam could be used to selectively cleave a chemical bond has been pursued since the demonstration of the laser in the early 1960s. However, it was not until very recent times that one could realize selective bond cleavage. One key to the rapid acceleration of such experiments is the capability of manipulating the relative phases between two or more paths leading to the same final state. This is done in practice by controlling the phase of two (or two thousand!) laser frequencies coupling the initial state to some desired final state. The present interest in phase-related control stems in part from research focusing on quantum information sciences, controlling chemical reactivity, and developing new optical technologies, such as in biophotonics for imaging cellular materials. Ultimately, one would like to identify coherent control applications having impact similar to linear regime applications like compact disk reading (and writing), integrated circuit fabrication, and photodynamic therapy. Note that in each of these the phase of the electromagnetic field is not an important parameter and only the brightness of the laser at a particular frequency is used. While phase is of negligible importance in any one photon process, for excitations involving two or more photons, phase not only becomes a useful characteristic, it can modulate the yield of a desired process between zero and one hundred percent.

The use of optical phase to manipulate atomic and molecular systems rose to the forefront of laser science in the 1980s. Prior to this there was considerable effort directed toward using the intensity and high spectral resolution features of the laser for various applications. For example, the high spectral resolution character was employed in purifying nuclear isotopes. Highly intense beams were also used in the unsuccessful attempt to pump enough energy into a single vibrational resonance to selectively dissociate a molecule. The current revolution in coherent control has been driven in part by the realization that controlling energy deposition into a single degree of freedom (such as selectively breaking a bond in a polyatomic molecule) can not be accomplished by simply driving a resonance with an ever more intense laser source. In the case of laser-induced photo dissociation, such excitation ultimately results in statistical dissociation throughout the molecule due to vibrational mode coupling. In complex systems, controlling energy deposition into a desired quantum state requires a more sophisticated approach and one scheme involves coherent control.

The two distinct regimes for excitation in coherent control, the time and frequency domain experiments, are formally equivalent. While the experimental approach and level of success for each domain is vastly different, both rely on precisely specifying the phase relations for a series of excitation frequencies. The basic idea behind phase control is simple. One emulates the interference effects that can be easily visualized in a water tank experiment with a wave propagating through two slits. In the coherent control experiment, two or more indistinguishable pathways must be excited that connect one quantum state to another. In either water waves, or coherent control, the probability for observing constructive or destructive interference at a target state depends on the phase difference between the paths connecting the two locations in the water tank, or the initial and final states in the quantum system. In the case of coherent control, the final state may have some technological value, for instance, a desirable chemical reaction product or an intermediate in the implementation of quantum computation.

Frequency domain methods concentrate on interfering two excitation routes in a system by controlling the phase difference between two distinct frequencies coupling an initial state to a final state. Perhaps the first mention of the concept of phase control in the optical regime can be traced to investigations in Russia in the early 1960s, where the interference between a one- and three-photon path was theoretically proposed as a means to modulate a two-photon absorption. This two-path interference idea lay dormant until the reality of controlling the relative phase of two distinct frequencies was achieved in 1990 using gas phase pressure modulation for frequency domain experiments. The idea was theoretically extended to the control of nuclear motion in 1988. The first experimental example of two-color phase control over nuclear motion was demonstrated in 1991. It is interesting that the first demonstrations of coherent control did not, however, originate in the frequency domain approach, but came from time domain investigations in the mid-1980s. This was work that grew directly out of the chemical dynamics community and will be described below.

While frequency domain methods were developed exclusively for the observation of quantum interference, the experimental implementation of time-domain methods was first developed for observing nuclear motion in real time. In the time domain, a superposition of multiple states is prepared in a system using a short duration ($\sim$50 fs) laser pulse. The superposition state will subsequently evolve according to the phase relationships of the prepared states and the Hamiltonian of the system. At some later time the evolution must be probed using a second, short-time-duration laser pulse. The time-domain methods for coherent control were first proposed in 1985 and were based on wavepacket propagation methods developed in the 1970s. The first experiments were reported in the mid-1980s.

To determine whether the time or frequency domain implementation is more applicable for a particular control context, one should compare the relevant energy level spacing of the quantum system to the bandwidth of the excitation laser. For instance, control of atomic systems is more suited to frequency domain methods because the characteristic energy level spacing in an atom

(several electron volts) is large compared to the bandwidth of femtosecond laser pulses (millielectron volts). In this case, preparation of a superposition of two or more states is impractical with a single laser pulse at the present time, dictating that the control scheme must employ the initial state and a single excited eigenstate. In practice, quasi-CW nanosecond duration laser pulses are employed for such experiments because current ultrafast (fs duration) laser sources cannot typically prepare a superposition of electronic states. One instructive exception involves the excitation of Rydberg states in atoms. Here the electronic energy level spacing can be small enough that the bandwidth of a femtosecond excitation laser may span several electronic states and thus can create a superposition state. One should also note that the next generation of laser sources in the attosecond regime may permit the preparation of a wavepacket from low-lying electronic states in an atom. In the case of molecules, avoiding a superposition state is nearly impossible. Such experiments employ pico- to femtosecond duration laser pulses, having a bandwidth sufficient to excite many vibrational levels, either in the ground or excited electronic state manifold of a molecule. To complete the time-dependent measurement, the propagation of the wavepacket to the final state of interest must be observed (probed) using a second ultrafast laser pulse that can produce fluorescence, ionization, or stimulated emission in a time-resolved manner. The multiple paths that link the initial and final state via the pump and the probe pulses are the key to the equivalence of the time and frequency domain methods.

There is another useful way to classify experiments that have been performed recently in coherent control, that is into either open-loop or closed-loop techniques. Open-loop signifies that a calculation may be performed to specify the required pulse shape for control before the experiment is attempted. All of the frequency-based, and most of the time-based experiments fall into this category. Closed-loop, on the other hand, signifies that the results from experimental measurements must be used to assist in determining the correct parameters for the next experiment, this pioneering approach was suggested in 1992. It is interesting that in the context of control experiments performed to date, closed-loop experiments represent the only route to determining the optimal laser pulse shape for controlling even moderately complex systems. In this approach, no input from theoretical models is required for coherent control of complex systems. This is unlike typical control engineering environments, where closed-loop signifies the use of experiments to refine parameters used in a theoretical model.

There is one additional distinction that is of value for understanding the state of coherent control at the present time. Experiments may be classified into systems having Hamiltonians that allow calculation of frequencies required for the desired interference patterns (thus enabling open-loop experiments) and those having ill-defined Hamiltonians (requiring closed-loop experiments). The open-loop experiments have demonstrated the utility of various control schemes, but are not amenable to systems having even moderate complexity. The closed-loop experiments are capable of controlling systems of moderate complexity but are not amenable to precalculation of the required control fields. Systems requiring closed-loop methods include propagation of short pulses in an optical fiber, control of high harmonic generation for soft X-ray generation, control of chemical reactions and control of biological systems. In the experimental regime, the value of learning control for dealing with complex systems has been well documented.

The remainder of this article represents an overview of the experimental implementation of coherent control. The earliest phase control experiments involved time-dependent probing of molecular wavepackets, and were followed by two-path interference in an atomic system. The most recent, and general, implementation of control involves tailoring a time-dependent electromagnetic field for a desired objective using closed-loop techniques. Since the use of tailored laser pulses appears to be rather general, a more complete description of the experiment is provided.

Time-Dependent Methods

The first experiments demonstrating the possibility of coherent control were performed to detect nuclear motion in molecules in real time. These investigations were the experimental realization of the pump-dump or pulse-timing control methods as originally described in 1985. The experimental applications have expanded to numerous systems including diatomic and triatomic molecules, small clusters, and even biological molecules. For such experiments, a vibrational coherence is prepared by exciting a superposition of states. These measurements implicitly used phase control both in the generation of the ultrashort pulses and in the coherent probing of the superposition state by varying the time delay between the pump and probe pulses, in effect modulating the outcome of a quantum transition. Since the earliest optical experiment in the mid-1980s, there have been many hundreds of such experiments reported in the literature. The motivation for the very first experiments was not explicitly phase control, but rather the observation of nuclear motion of molecules in real time. In such later measurements, oscillations in the superposition states were observable for many cycles, up to many tens of picoseconds in favorable cases, i.e., diatomic molecules in the gas phase. The loss of signal in the coherent oscillations is ultimately due to passage of the superposition state in to surrounding bath states. This may be due to collision with another molecule, dissociation of the system or redistribution of the excitation energy into other modes of the system not originally excited in the superposition. It is notable that coherence can be maintained in solution phase systems for tens of picoseconds and for the case of resonances having weak coupling to other modes, coherence can even be modulated in large biological systems on the picosecond time scale.

Decoherence represents loss of phase information about a system. In this context, phase information represents our detailed knowledge of the electronic and nuclear coordinates of the system. In the case of vibrational coherence, decoherence may be represented by intramolecular vibrational energy transfer to other modes of the molecule. This can be thought of as the propensity of vibrational modes of a molecule to couple together in a manner that randomizes deposited energy throughout the molecule.

Decoherence in a condensed phase system includes transfer of energy to the solvent modes surrounding the system of interest. For an electronically excited molecule or atom, decoherence can involve spontaneous emission of radiation (fluorescence), or dissociation in the case of molecules. Certain excited states may have high probability for fluorescence and would represent a significant decoherence pathway and an obstacle for coherent control. These states may be called 'lossy' and are often used in optical pumping schemes as well as for stimulated emission pumping. An interesting question arises as to whether one can employ such states in a pathway leading to a desired final state, or must such lossy states be avoided at all costs in coherent control. This question has been answered to some degree by the method of rapid adiabatic passage. In this experiment, an initial state is coupled to a final state by way of a lossy state. The coupling is a coherent process and the preparation involves dressed states that are eigenstates of the system. In this coherent superposition the lossy state is employed, but no population is allowed to build up and thus decoherence is circumvented.

Two-Path Interference Methods

Interference methods form perhaps the most intuitive example of coherent control. The first experimental demonstration was reported in 1990 and involved the modulation of ionization probability in Hg by interfering a one-photon and three-photon excitation pathway to an excited electronic state (followed by two-photon ionization). The long delay between the introduction of the two-path interference concept in 1960 and the demonstration in 1990 was the difficulty in controlling the relative phase of the one- and three-photon paths. The solution involved generating the third harmonic of the fundamental in a nonlinear crystal, and copropagating the two beams through a low-density gas. Changing the pressure of the gas changes the optical phase retardance at different rates for different frequencies, thus allowing relative phase control between two colors. The ionization yield of Hg was clearly modulated as a function of pressure. Such schemes have been extended to diatomic molecular systems and the concept of determining molecular phase has been investigated. While changing the phase of more than two frequencies has not been demonstrated using pressure tuning (because of experimental difficulties), a more flexible method has been developed to alter relative phase of up to 1000 frequency bands, as will be described next.

Closed-Loop Control Methods

Perhaps the most exciting new aspect of control in recent years concerns the prospect for performing closed-loop experiments. In this approach a more complex level of control in matter is achieved in comparison to the two-path interference and pump-probe control methods. In the closed-loop method, an arbitrarily complex time-dependent electromagnetic field is prepared that may have multiple subpulses and up to thousands of interfering frequency bands. The realization of closed-loop control over complex processes relies on the confluence of three technologies: (i) production of large bandwidth ultrafast laser pulses; (ii) spatial modulation methods for manipulating the relative phases and amplitudes of component frequencies of the ultrafast laser pulse; and (iii) closed-loop learning control methods for sorting through the vast number of pulse shapes available as potential control fields. In the closed-loop method, the result of a laser molecule interaction is used to tailor an optimized pulse.

In almost all of the experimental systems used for closed-loop control today, Kerr lens mode-locking in the Ti:sapphire crystal is used to phase lock the wide bandwidth of available frequencies (750–950 nm) to create the ultrafast pulse. In this phenomenon, the intensity variation in the short laser pulse creates a transient lens in the Ti:sapphire lasing medium that discriminates between free lasing and mode-locked pulses. As a result, all of the population inversion available in the lasing medium may be coerced into enhancing the ultrashort traveling wave in the cavity in this way. The wide bandwidth available may then be amplified and tailored into a shaped electromagnetic field. Spatial light modulation is one such method for modulating the relative phases and amplitudes of the component frequencies in the ultrafast laser pulse to tailor the shaped laser pulse. Pulse shaping first involves dispersing the phase-locked frequencies on an optical grating, the dispersed radiation is then collimated using a cylindrical lens and the individual frequencies are focused to a line forming the Fourier plane. At the Fourier plane, the time-dependent laser pulse is transformed into a series of phase-locked continuous wave (CW) laser frequencies, and thus Fourier transformed from time to frequency space. The relative phases and amplitudes may be modulated in the Fourier plane using an array of liquid crystal pixels. After altering the spectral phase and amplitude profile, the frequencies are recombined on a second grating to form the shaped laser pulse. With one degree of phase control and 10 pixels there are an astronomic number (360^{10}) of pulse shapes that may be generated in this manner. (At the present time, pulse shapers have up to 2000 independent elements.) Evolutionary algorithms are employed to manage the available phase space. Realizing that the pulse shape is nothing more than the summation of a series of sine waves, each having an associated phase and amplitude, we find that a certain pulse shape can be represented by a genome consisting of an array of these frequency-dependent phases and amplitudes. This immediately suggests that the methods of evolutionary search strategies may be useful for determining the optimal pulse shape for a desired photoexcitation process.

The method of closed-loop optimal control for experiments was first proposed in 1992 and the first experiments were reported in 1997 regarding optimization of the efficiency of a laser dye molecule in solution. Since that time a number of experiments have been performed in both the weak and strong field regime. In the weak field regime, the intensity of the laser does not alter the field free structure of the excited states of the system under investigation. In the strong field, the field free states of the system are altered by the electric field of the laser. Whether one is in the weak or strong field regime depends on parameters including the

characteristic level spacing of the states of the system to be controlled and the intensity of the laser coupling into those states. Examples of weak field closed-loop control include optimization of laser dye efficiency, compression of an ultrashort laser pulse, dissociation of alkali clusters, optimization of coherent anti-Stokes Raman excitation, and optical pulse propagation in fibers. In the strong field, the laser field is used to manipulate the excited states of the molecule as well as induce population transfer among these states. In this sense, the laser is both creating and exciting resonances, in effect allowing universal excitation with a limited frequency bandwidth of 750–850 nm. For chemical applications, it is worth noting that most molecules do not absorb in this wavelength region in the weak field. Strong field control has been used for controlling bond dissociation, chemical rearrangement, photonic reagents, X-ray generation, molecular centrifuges and the manipulation of mass spectral fragmentation intensities. In the latter case, a new sensing technology has emerged wherein each individual pulse shape represents an independent sensor for a molecule. Given the fact that thousands of pulse shapes can be tested per minute, this represents a new paradigm for molecular analysis.

At the time of this writing, the closed-loop method for adaptively tailoring control fields, has far outstripped our theoretical understanding of the process (particularly in the strong field regime). Adaptive control is presently an active field of investigation, encompassing the fields of physics, engineering, optics, and chemistry. In the coming years, there will be as much work done on the mechanism of control as in the application of the methods. Due to small energy level spacings and complexity of the systems, we anticipate the majority of applications to be in the chemical sciences.

See also: Coherent Control: Theory. Overview: Coherence

Further Reading

Brumer, P.W., Shapiro, M., 2003. Principles of the Quantum Control of Molecular Processes. New York: Wiley Interscience.
Chen, C., Elliott, D.S., 1990. Measurement of optical phase variations using interfering multiphoton ionization processes. Physics Review Letters 65, 1737.
Levis, R.J., Rabitz, H., 2002. Closing the loop on bond selective chemistry using tailored strong field laser pulses. Journal of Physical Chemistry A 106, 6427–6444.
Levis, R.J., Menkir, G.M., Rabitz, H., 2001. Selective bond dissociation and rearrangement with optimally tailored, strong-field laser pulses. Science 292 (5517), 709–713.
Rice, S.A., Zhao, M., 2000. Optical Control of Molecular Dynamics. New York: Wiley Interscience.
Stolow, A., 2003. Femtosecond time-resolved photoelectron spectroscopy of polyatomic molecules. Annual Review of Physical Chemistry 54, 89–119.
Zewail, A.H., Casati, G., Rice, S.A., *et al.*, 1997. Femtochemistry: Chemical reaction dynamics and their control. Chemical Reactions and Their Control on the Femtosecond Time Scale, Solvay Conference on Chemistry 101, 3–45.

Optics of the Human Eye

David A Atchison, Queensland University of Technology, Brisbane, QLD, Australia

© 2018 Elsevier Ltd. All rights reserved.

Basic Optical Structure

The human eye is shown in Fig. 1. The outer layer consists of the cornea at the front and the sclera at the back. The transparent cornea is approximately spherical with a radius of curvature of about 8 mm. The white, opaque sclera is approximately spherical with a radius of curvature of approximately 12 mm. The middle layer of the eye is the uveal tract, which consists of the iris anteriorly, the choroid posteriorly (not shown), and the intermediate ciliary body. Inside the eye, about 3 mm from the cornea, is the transparent lens. The anterior chamber between cornea and iris, and the posterior chamber between iris, ciliary body and lens, contain fluid called the aqueous humor. The vitreous chamber between the lens and the back of the eye contains a transparent, colorless, gelatinous mass called the vitreous humor.

The inner layer of the eye is the light-sensitive tissue called the retina, which is connected to the brain via the optic nerve. Light passes through the inner retinal layers to reach the photoreceptors, where light is absorbed to initiate the electrical and chemical processes involved in vision. Photoreceptors are of two types: rods and cones. Cones are associated with vision in bright (photopic) lighting conditions; there are three types that absorb at different wavelength ranges and initiate color vision. Rods are associated with vision in low (scotopic) light levels, and there is an intermediate (mesopic) light level range where both cones and rods operate. The cones predominate in the fovea, which is 1.5 mm (5 degree field) wide. The fovea is free of rods in its central 1 degree field. When the eye fixates, or "looks at," a small object of interest, the retinal image forms at the foveal center. The inner retinal layers contain ganglion cells, whose axons leave the retina at the optic disk. This is functionally blind because there are no cones or rods here. It is approximately 5 degree horizontally and 7 degree vertically, and its center is approximately 15 degree nasally and 1.5 degree upwards from the foveal center.

Light enters the eye through the cornea, and is refracted by the cornea and lens to focus at the retina. The cornea has the greater power, but the lens power in young eyes can change to allow the eye to focus at different distances – the process of accommodation. The hole in the iris is the aperture stop. When we look at the aperture stop, we see it as the pupil, which is closer to the front of the eye and slightly bigger than the aperture stop. The aperture stop controls how much light reaches the retina and the retinal image quality.

In good quality man-made optical systems, the optical axis is the line that joins the centers of curvatures of the refracting surfaces. However, the eye is not rotationally symmetric; surfaces and the aperture stop are tilted and decentered relative to each other. The optical axis can be defined as the line of best fit through the centers of curvature, which in practice is determined by the best alignment of the images formed by reflection from the surfaces. To complicate matters, the fovea center is about 5 degree from the optical axis as measured at the posterior nodal point of the eye. This lack of symmetry has led to a number of axes being required for the eye. For example, the line-of-sight is the line joining an object of interest and the fovea, and which passes through the center of the aperture stop (see Section Axes and Angles).

Ignoring the lack of symmetry, eyes can be treated like many other optical systems with cardinal points and with an equivalent power. Of more importance than equivalent power in a clinical context is refractive error, which is the error in the equivalent power due to an imbalance between equivalent power and eye length.

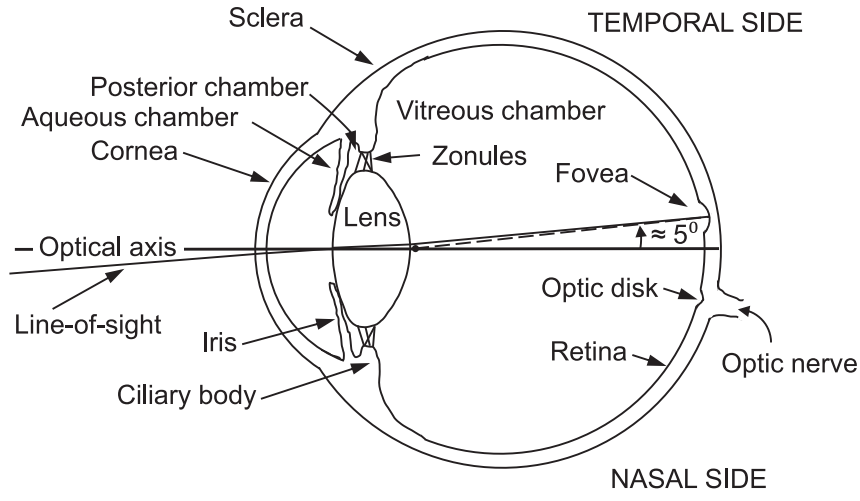


Fig. 1 Horizontal section of a right eye as seen from above.

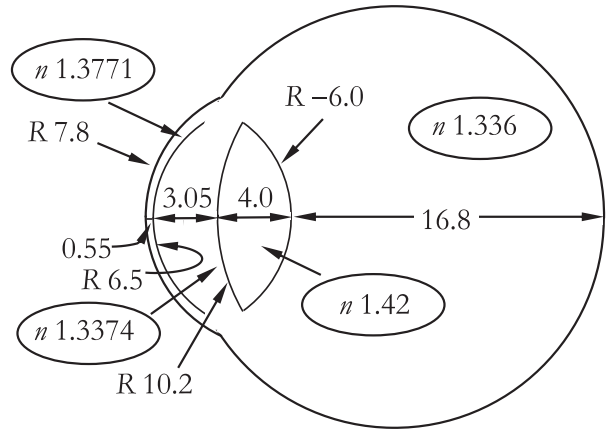


Fig. 2 The Le Grand four-refracting surface schematic eye (Atchison and Smith, 2000), showing dimensions in millimeters and refractive indices. R – surface radius of curvature, n – refractive index.

Dimensions of the eye vary greatly between individuals, and alter with age and accommodation. Average values of populations have been used to construct model (schematic) eyes. These can be made of different complexities, with different number of surfaces. The "paraxial" schematic eyes contain centered, spherical surfaces. These are useful for basic properties, such as component powers, positions of cardinal points, and image size and illuminance calculations, but not for subtle optical effects such as higher-order aberrations. One schematic eye is shown in **Fig. 2** as representative of dimensions in relaxed (non-accommodating) adult eyes. The equivalent power of this eye is approximately 60 m^{-1}. When dealing with powers, the term diopter with symbol "D" is usually used instead of inverse meters, a practice followed in the rest of this article.

The range of angles from the fovea at which perception is possible is referred to as the field-of-vision. Its limits are determined by anatomical, optical, and sensory factors. Field limits are about 100 degree temporally, 90 degree inferiorly, and 40 degree superiorly and nasally. Rotating the eye to remove the upper brow and nose restrictions increases the superior field to about 80 degree and the nasal field to about 60 degree; the latter is now limited by extent of the temporal sensitive retina.

Humans have two eyes which are separated by approximately 60–70 mm in adults. Binocular vision provides slightly improved contrast sensitivity and vision acuity over monocular vision. The total field-of-view is about 210 degree with a 120 degree binocular overlap. The slightly different sizes and/or shapes of the two retinal images of a close object allow three-dimensional perception known as stereopsis. Presenting different images to the two eyes is exploited in a number of circumstances such as enabling near vision at a range of distances where this would otherwise not be possible by putting lenses of different power in front of the two eyes, and having aspects of the object which can only be seen by one eye through filters placed in front of the eyes (e.g., 3-D effects in cinemas). When the eyes accommodate to focus for a near object, they rotate inwards (convergence) to fixate the object.

Cornea

The cornea has about 40 D of power, which about two-thirds of the power of the unaccommodated eye. It contains a tear film (about 4–7 μm thick) at the front, an epithelium, Bowman's membrane, the stroma, Descemet's membrane and the endothelium. The tear film has oily, aqueous and mucous layers, but they are mixed to variable extents during the blinking cycle. Because the tear film is thin and confirms to the shape of the underlying cornea, it is sometimes treated as being optically inert; however it is important in compensating for the roughness of the outer epithelial cells and there are circumstances in which it cannot be ignored optically such as fitting of rigid contact lenses. The stroma has about 90% of the corneal thickness. It contains about 200–250 layers (lamellae) of cylindrical fibrils. The fibrils within a lamella lie parallel to each other and fibrils within a lamella are inclined at large angles to fibrils in adjacent lamellae. While the different layers of the cornea have different refractive indices, the cornea is usually assigned a constant value which of about 1.376.

Estimates of the anterior and posterior surface radii of curvature of the cornea are about 7.8 and 6.3 mm (Atchison and Smith, 2000), respectively, but there are wide ranges. On average males have flatter corneas than females. Corresponding powers for these radii of curvature are approximately 48 and − 6 D; the much smaller power for the posterior cornea is because of the much lower refractive index (0.04) between aqueous and cornea than between cornea and air (0.376). The two radii of curvature are highly correlated (Dunne *et al.*, 1992; Lowe and Clark, 1973; Patel *et al.*, 1993). Some instruments determine a corneal power based on the anterior radius of curvature and an equivalent index such as 1.3375.

The surfaces are not perfectly spherical; they have both toricity and asphericity. Toricity means that the radius of curvature varies with meridian and produces the optical defect of astigmatism (see Section Refractive anomalies/Astigmatism). Most cornea surfaces are also aspheric and are often represented as conics in two dimensions or as conicoids in three dimensions. One way of

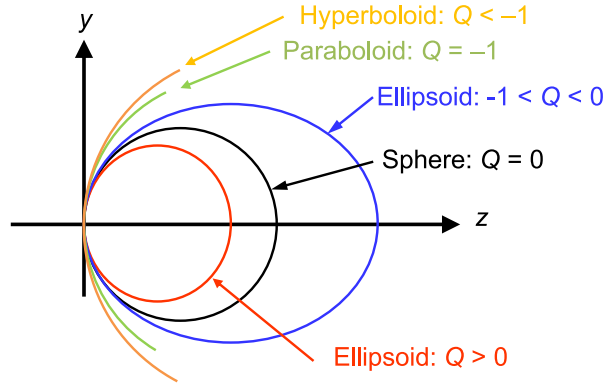


Fig. 3 The *Y–Z* section of conicoids, showing the influence of asphericity on conicoid shape. All surfaces have the same vertex radius of curvature.

expressing a conicoid is

$$z = \frac{c(x^2 + y^2)}{1 + \sqrt{[1 - (1 + Q)(x^2 + y^2)]}}$$

where the coordinates at a point on the surface are (x, y, z) with the z-axis corresponding to the optical axis, c is the vertex curvature (the inverse of the vertex radius of curvature), and Q is the surface asphericity giving different types of conicoids (**Fig. 3**):

$Q < -1$ hyperboloid
$Q = -1$ paraboloid
$-1 < Q < 0$ prolate ellipsoid(z-axis is major axis)
$Q = 0$ sphere
$0 < Q$ ellipsoid with the major axis in the xy plane

Other forms of representing corneal shape include bi-conicoids, in which there are separate x-direction and y-direction vertex curvatures.

Most anterior corneal surfaces can be describe as prolate ellipsoids, i.e., they flatten away from the vertex, with the mean asphericity being about -0.20 (Atchison and Smith, 2000). One consequence of this is that the aberration known as spherical aberration is reduced from that which would occur for spherical corneas. There are fewer estimates of asphericity of the posterior corneal surface than of the anterior corneal surface. Mean estimates of the posterior cornea are negative. These are less likely to be accurate than the anterior corneal estimates because of the issue of imaging the posterior cornea through the anterior cornea.

Corneal thickness is about 0.5 mm near the center, and increases into the periphery because the posterior surface is more curved that the anterior surface.

Aperture Stop and Pupils

The iris forms the aperture stop of the eye. Iris color varies considerably, and this depends upon the amount of pigmentation. The stop position varies between individuals, and with age and accommodation. In young adults it is about 3.5 mm behind the anterior cornea. The aperture size is determined by the balance between the sphincter pupillae and dilator pupillae muscles. The former is a ring around the inner margin of the iris, and its contraction causes the stop to constrict. The latter consists of cells that extend radially from the sphincter, and its contraction causes the stop to dilate.

The entrance pupil is the image of the aperture stop formed in object space by the cornea, and the exit pupil is the image of the aperture stop formed by the lens (**Fig. 4**). Paraxial ray tracing through model eyes, in which it is assumed that the aperture stop lies in the anterior vertex plane of the lens, gives approximate positions and sizes of pupils. While varying between different eyes and with accommodation, the entrance pupil is approximately 13% bigger and 0.5 mm closer to the cornea than the aperture stop, while the exit pupil is about 3% bigger and 0.1 mm behind the aperture stop.

Because the entrance pupil is what we see when we look into the eye, the aperture stop is usually referred to loosely as the pupil. Compared with the entrance pupil, the exit pupil has little significance, and for the rest of this article the term "pupil" will refer to the entrance pupil.

Illumination level is the most important factor affecting pupil size, and pupil diameter may vary between 2 mm at high illuminations to 8 mm in the dark. Watson and Yellott (2012) provided a comprehensive description of the dependence of pupil size on illumination and how this is affected by factors of age, size of adapting field, and whether one of both eyes are adapted. The influence of age on pupil size will be discussed later. Other factors that are important are accommodation and convergence, which usually occur together, and state of arousal. Sometimes effects of these are transient, for example, accommodating from distance to a near target will produce constriction that is usually not sustained.

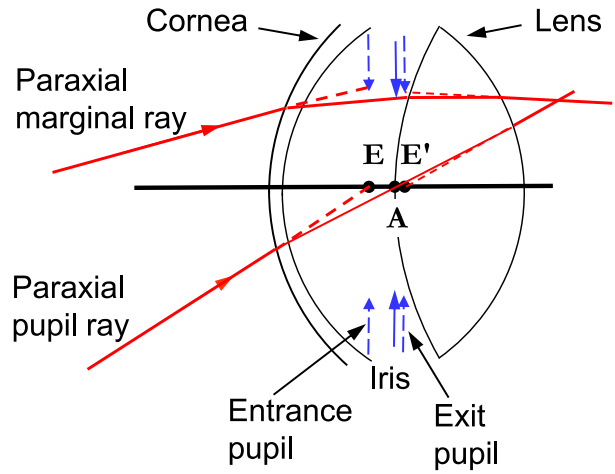


Fig. 4 The aperture stop, the entrance pupil and the exit pupil of the eye. The paraxial pupil ray is directed toward the center of the entrance pupil, by refraction reaches the center of the aperture stop, and is refracted by the lens so that it appears to come from the center of the exit pupil. In a similar fashion, the marginal pupil ray shows the top edges of the aperture stop and the pupils.

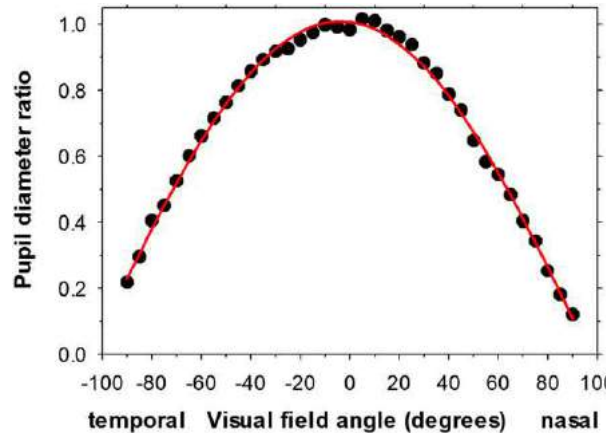


Fig. 5 Pupil diameter ratio as a function of horizontal visual field angle θ for one subject. The data are fitted by $1.009 \cos\left[\frac{(\theta+3.936)}{1.121}\right]$. Unpublished data from the study of Mathur *et al.* (2013).

Drugs can affect pupil size and some are intended for this purpose. Mydriatics cause pupil dilation by either stimulating the sympathetic division of the autonomic nervous system (sympathomimetics) or by blocking its parasympathetic division (parasympatholytics). Miotics cause pupil constriction by either stimulating the parasympathetic division (parasympathomimetics) or by blocking the sympathetic division (sympatholytics).

When the pupil is viewed along the line-of-sight it appears circular in most eyes. When the eye is viewed eccentrically along the horizontal visual field meridian, it becomes elliptical. This is described by a cosine function, flatter by about 12% than the cosine of the viewing angle and decentered by a few degrees into the temporal visual field (Mathur *et al.*, 2013) (**Fig. 5**).

The pupils of most eyes are decentered relative to the center of the limbus, the line demarking the clear cornea from the surrounding sclera. This decentration is about 0.5 mm nasally, and usually becomes more nasal as the pupil constricts. Mean pupil decentration shift across a large range of illuminances is about 0.12 mm, but with individual shifts of up to 0.5 mm (e.g., Mathur *et al.*, 2014).

The pupil size and decentration, particularly the former, have considerable effects on vision. Pupil diameter affects retinal light level and subsequently light adaptation. However, this is not a large effect considering the pupil area can change by a factor of only 16, which is much smaller than the million times range over which the eye operates. The diameter affects the depth-of-focus, which is the range of distances over which the eye cannot detect any change in focus, with the depth-of-focus usually narrowing as pupil size increases. Retinal image quality and visual performance are influenced by pupil size; for large pupil diameters optical defects of the eye known as aberrations cause deterioration in retinal image quality, while for small pupil diameters diffraction limits retinal image quality. Pupil decentration interacts with diameter to affect image quality.

Lens

The lens is a mass of cellular tissue contained within an elastic capsule. An epithelial cell layer underneath the capsule extends from the anterior vertex to the equator. Throughout life, new epithelial cells form near the equator and elongate forwards and backwards as fibers between the epithelium and capsule. These join other fibers at junctions called sutures.

The capsule is attached to the ciliary body by suspensory ligaments called zonules. Contraction of the ciliary body's muscle causes the ciliary body to move forwards and inwards. This reduces tension on the zonules, which in turn reduce tension on the lens and allow the lens to take up a more curved form under the influence of the capsule. Lens power increases because the surfaces increase in power and because of changes of refractive index distribution within the lens. This allows the eye to change focus from distant to close objects. This process is reversible. The ability of the eye to focus on objects at different distances is known as accommodation. This is usually measured as a change in inverse of distances from the eye, rather than change in lens power. As an example if the eye changes its focus from an object 1 m away to 25 cm away, the change in accommodation is $1/0.25-1/1=3.0$ D. The magnitude of possible accommodation is called the amplitude of accommodation. Its peak of about 10 D occurs in the second decade of life, with corresponding "unaccommodated" and "accommodated" equivalent lens powers of about 19 and 30 D, respectively. From the peak, amplitude declines steadily to become zero in about the mid-50s. This is described further in the Section Changes with Age/Accommodation and Presbyopia.

The biometric parameters of the lens vary considerably between people, and with age and accommodation. Some values will be given here which are reasonable estimates for young adults in the unaccommodated state. The radii of curvature for the anterior and posterior surfaces are about 10 mm and -6 mm, respectively, and the central thickness of the lens is about 3.6 mm. The lens diameter is 9–10 mm. During accommodation the radii of curvature decrease, more so for the front surface than for the back surface. This is combined with increase in the axial thickness, most of which occurs in the nucleus of the lens. Both the anterior and vitreous chambers are reduced in depth, and the diameter decreases.

One of the most intriguing things about the lens is its gradient refractive index. There is a plateau of high index (about 1.41) in the central (nucleus) region, but the index reduces toward the periphery where it is about 1.38. This index variation produces continuous refraction of rays, so that there are both surface and internal contributions to the power of the lens. Many model eyes have a constant refractive index rather than a gradient index, and to adequately account for the loss of gradient index power this "equivalent" index must be made higher (e.g., 1.42) than the maximum index of the lens. Gullstrand (1924) referred to the contribution of changes in gradient index during accommodation to changes in power as the "intracapsular mechanism of accommodation."

Axes and Angles

Several axes are required to fully describe the optical properties of the eye, because of a lack of symmetry and the departure of the fovea from a best fit optical axis. The validity of some axes is dependent on idealized eye properties. As well as the axes, names are given to the angles between them. A full treatment of these axes is outside the scope of this article (see Atchison (2017a)).

The most important axes are the optical axis, the line-of-sight, the visual axis and the pupillary axis (**Fig. 6**). The optical axis does not truly exist, but it can be considered to be the line of best fit through the centers of curvature of the intraocular surfaces. The line-of-sight is the line joining the fixation point T and the foveal center T' through the center of the pupil E. This is usually on

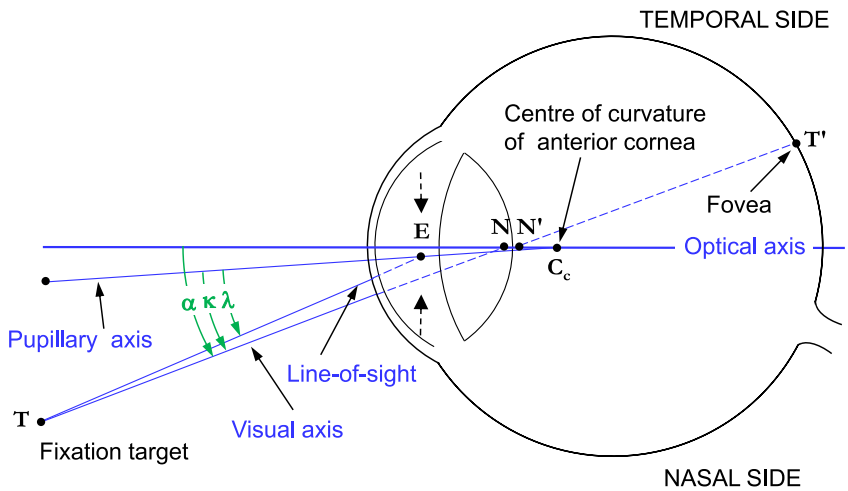


Fig. 6 Some axes and angles of the eye. The object has been shown very close to the eye and the angles are exaggerated for clarity. Adapted from Atchison, D.A., 2017a. Axes and angles of the eye. In: Artal, P. (Ed.), Handbook of Visual Optics. vol. I. Boca Raton, FL: Francis & Taylor Group (Chapter 17).

the nasal side of the optical axis in object space. Because the pupil center moves with accommodation and luminance, this quantity is not fixed. The visual axis is the line joining the fixation point and the fovea center through the nodal points N and N'; it is usually close to the line-of-sight. The pupillary axis is the line passing through the center of the entrance pupil and which is normal to the anterior corneal surface. Usually this lies between the optical axis and the line-of-sight.

The angle between the optical axis and the visual axis is called alpha (or α) and is approximately 5 degree horizontally and 2 degree vertically (visual axis nasal to and above optical axis in object space). The angle between the pupillary axis and line-of-sight is called lambda (or λ) and the angle between the pupillary axis and the visual axis is called kappa (or κ). The angles are of some diagnostic significance, particularly λ which is used to diagnose eccentric fixation and heterotropia (turned eye).

Schematic Eyes

Schematic eyes are models that show optical related biometry of eyes. These have a variety of uses, such as calculating retinal image size, estimating retinal light levels, determining how refractive errors arising from variations in eye dimensions, calculating appropriate powers of intraocular lenses in cataract surgery, estimating aberrations and retinal image quality, and designing ophthalmic instrument and ophthalmic corrections.

Schematic eyes are available in a range of complexity. The paraxial schematic eyes have spherical refractive surfaces that are centered on a common optical axis. Some are not anatomical accurate, for example, the reduced eyes have only one refractive surface. These schematic eyes can describe optics of real eyes accurately only within the paraxial region for which rays are close to the optical axis and subtend small angles to it.

Finite, or wide angle, schematic eyes provide better predictions of aberrations and retinal image quality than the paraxial schematic eyes. They can have various features, such as aspheric surfaces, gradient refractive index, surface tilts and misalignments, media whose refractive indices vary with wavelength, and curved retinas. These eyes require more elaborate calculations than paraxial schematic eyes. Like the paraxial eyes, they are usually based on average values of population values, but can be customized to more accurately describe individual eyes.

An example of a paraxial schematic eye is the Le Grand full theoretical eye (Fig. 7). This contains four-refracting surfaces. It is available in both relaxed and accommodated (7.1 D) forms, but only the former is shown here. It has served as a basis for several paraxial and finite schematic eyes. The figure shows the three pairs of cardinal points. Light leaving the anterior focal point F passes into the eye and is imaged toward infinity. Light passing into the eye from infinity and parallel to the optical axis is imaged at the posterior focal point F'. For light traveling into the eye, the object position can be considered relative to the anterior principal point P and refraction can be treated as if it occurred at the posterior principal point P'. The reverse is true for light traveling from the retina out of the eye. Light traveling into the eye toward the anterior nodal point N appears to pass through the posterior nodal point N' on the image side without the angle of inclination changing.

The constant lens index can be placed by a continuously varying index $N(r)$ described by

$$N(r) = c_0 + c_1 r^2 + c_2 r^4 + c_3 r^6$$

or

$$N(r) = c_0 + c_1 r^p$$

where r is the relative distance from the center of the lens to its edge, and c_0, c_1, c_2, c_3, and p are coefficients. Different levels of sophistication of such modeling have been proposed (Atchison, 2017b).

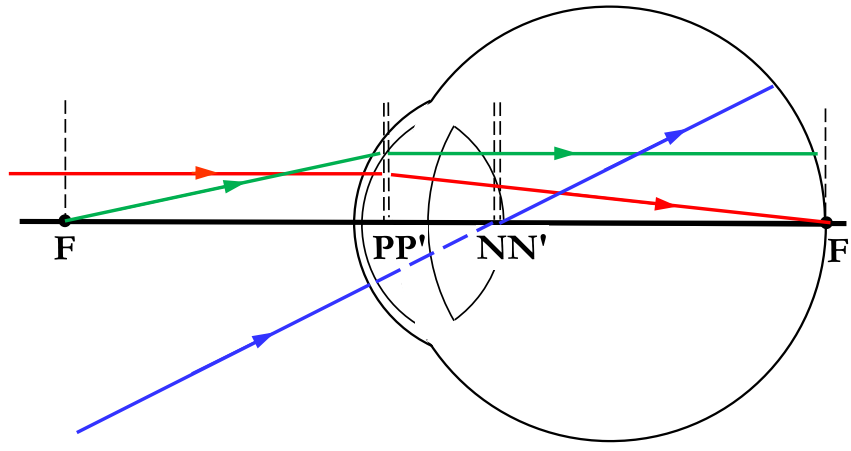


Fig. 7 The unaccommodated version of the Le Grand four-refracting surface schematic eye, showing the cardinal points.

The change in refractive index with wavelength, or chromatic dispersion, of media has been incorporated into some schematic eyes using equations such as Cauchy dispersion equation

$$n(\lambda) = A + B/\lambda^2 + C/\lambda^4 + D/\lambda^6 \ldots$$

and the Cornu dispersion equation

$$n(\lambda) = n_\infty + K/(\lambda - \lambda_0)$$

Here λ is wavelength and A, B, C, D, n_∞, K, and λ_0 are constants for a particular medium.

Most of the well-known schematic eyes are representative of average values in particular populations at the times and places the eyes were devised. Many variations of the common schematic eyes have been proposed to account for changes with age in children and adults, with accommodation and with particular ocular conditions. With increased ocular biometry available, personalized eye models are being developed.

When deciding upon which schematic eye might be employed for one of the applications described in the first paragraph of this section, a good principle is to use the simplest model that is adequate, even if this is anatomically inaccurate.

Light and the Eye

Many regions of the electromagnetic spectrum are important to the eye because they may cause damage to various parts of the eye, but the main region in which we are interested is that producing a visual response and to which we refer as light. The wavelength range of light is approximately 390 to 800 nm, for which the spectral colors we see are violet (~390–450 nm), blue (~450–500 nm), green (~500–560 mm), yellow (~560–600), orange (~600–620 nm), and red (~620–800 nm). The eye response within this range depends upon the luminance. Fig. 8 shows the relative luminous efficiencies under photopic and scotopic conditions, with respective peak sensitivities at 555 and 507 nm. The change in peak between these two values, that occurs under the intermediate mesopic conditions of approximately 3–0.03 cd m^{-2}, is referred to as the Purkinje shift.

Radiometric quantities (radiant flux, radiant intensity, radiance and irradiance) can be converted into the corresponding photometric quantities (luminous flux, luminous intensity, luminance and illuminance) by simple equations that weight the radiometric values at any wavelength by the appropriate relative luminous efficiency.

Passage of Light Into Eye

Not all of light entering the eye reaches the retina. Some is lost by specular reflection at the surfaces of the cornea and lens, by scattering, and by absorption.

The specular reflections are image forming; the virtual images formed by single reflection and by transmission out of the eye are called the Purkinje-Sanson I, II, III and IV images, and correspond to the anterior cornea, posterior cornea, anterior lens and posterior lens surfaces, respectively. These images can be used to estimate lens equivalent refractive index, lens surface radii of

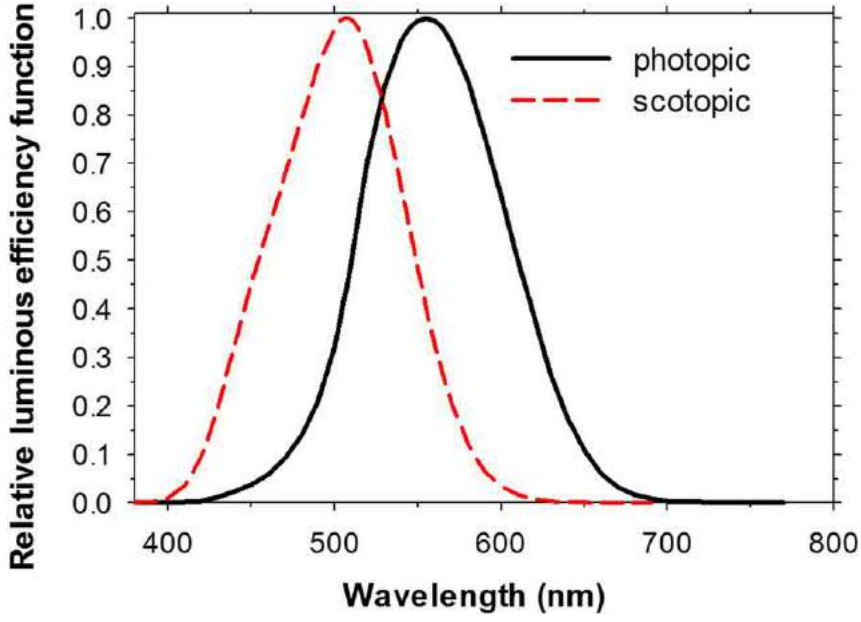


Fig. 8 The relative luminous efficiency functions in photopic and scotopic lighting levels.

curvature, and axes of the eye. Image I is by far the brightest because of the large refractive index between air and the cornea (strictly its tear film) and is located about 3.9 mm inside the eye. Image II is difficult to see because it is in a similar location to image I and is much dimmer because of the low refractive index difference (0.04) between cornea and aqueous. In the unaccommodated eye, Image III is about twice as big as image I and is about 10 mm inside the eye, while image IV is about 4 mm inside the eye, about three-quarters the size of image I and inverted. Both images III and IV change with accommodation, with image III becoming much smaller and moving closer to the cornea.

Transmittance of the eye and its components is highly dependent upon wavelength and age. Of particular interest is the protection given to internal structures from ultraviolet radiation (<380 nm). Considering natural radiation, most ultraviolet below about 288 nm is absorbed by the oxygen and ozone in the atmosphere; 288 nm corresponds approximately to the wavelength at which the cornea starts passing radiation through to the lens. In turn, the lens absorbs nearly all radiation up to 380 nm. Absorption for wavelengths beyond 600 nm is dominated by water, while for shorter wavelengths the spectral absorption is far more absorbing than occurs for water (Atchison and Smith, 2000).

Scatter is caused by spatial variations of refractive index within a medium, usually at the microscopic level, and is a combination of diffraction, reflection, and reflection. The angular distribution of scatter may be complex. Distinction can be made between forward-scattered light which affects retinal imagery and is sometimes called straylight, and back-scattered light directed out of the eye. The forward scatter produces a veiling glare that reduces the contrast of the retinal image and reduces visibility of objects. The backward-scattered light is important for observing intraocular structures in techniques such as slit-lamp biomicroscopy. Given that the cornea and lens contain inhomogeneities on the scale of the wavelength of light, their transparencies in healthy eyes are remarkably high.

An interesting phenomenon related to transmittance is birefringence. This occurs when the velocity of light depends not only on the direction of light travel but also on orientation of the electric field. This results in two refractive indices in a material, and the birefringence is quantified by their difference. Estimates of birefringence have been made for the cornea and retina.

Light at the Retina

Probably about 50–90% of light entering the eye reaches the retina to form images, but there is considerable age and wavelength dependence. Ignoring these factors, a simple measure of retinal illuminance is the troland. The retinal illuminance E_t in trolands is the product of the area A of the pupil in mm^2 and object luminance L in cd m^{-2}:

$$E_t = LA$$

In terms of pupil diameter in millimeter, this is

$$E_t = \pi L D^2/4$$

The luminous efficiency of a beam of light depends upon the entry point of the pupil. This is known as the Stiles–Crawford effect of the first kind (Stiles and Crawford, 1933). This is due to the wave-guide properties of the photoreceptors and can be considered both as an optical and neural phenomenon. A convenient equation for this is

$$\eta/\eta_{max} = e^{-\rho(r-r_{max})^2}$$

where η/η_{max} is relative luminous efficiency for which η is sensitivity at position r from pupil center and η_{max} is peak sensitivity at r_{max}, and with ρ the retinal directionality parameter (**Fig. 9(a)**). The fit can be extended to two dimensions to allow for non-rotational symmetry. Mean foveal ρ is 0.12 ± 0.03 mm^{-1} with horizontal and vertical components for r_{max} of 0.5 ± 0.7 mm nasal and 0.2 ± 0.6 mm superior (Atchison and Smith, 2000). The Stiles–Crawford effect is sometimes factored into retinal illuminance determinations and image quality determinations as a photometric efficiency $S(D)$ for a pupil diameter D as it were a filter at the pupil, which from the previous equation and ignoring the offset of the peak from the pupil center is

$$S(D) = \frac{4\left[1 - e^{-\frac{\rho D^2}{4}}\right]}{\rho D^2}$$

A smaller, but equivalent pupil of diameter D_e without a Stiles–Crawford effect is given by

$$D_e = D\sqrt{[S(D)]}$$

This is shown in **Fig. 9(b)**.

The ρ value of 0.12 mm^{-1} is applicable for subjective measurements not far from the middle of the vision spectrum, and under photopic conditions. It will vary with wavelength and reduce as luminance decreases. Objective methods give much higher values. The Stiles–Crawford effect reduces the effects of aberrations on retinal image quality, although the influence of this is probably small.

Light Interaction With the Back of the Eye

In addition to the absorption of light by the photoreceptors discussed above, there are other interactions with the back of the eye in the retina, choroid and sclera, collectively called the fundus. There are important absorbing pigments: macula pigment in the retina called xanthophyll, the visual pigments in the photoreceptors responsible for initiating the neural process of vision, melanin

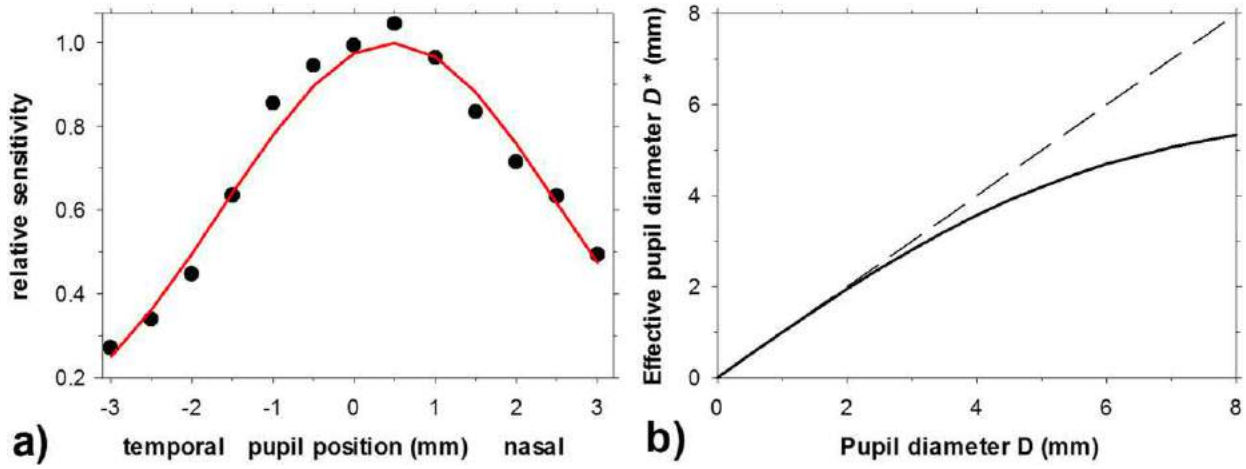


Fig. 9 The Stiles–Crawford effect. (a) Relative sensitivity as a function of position in the pupil, with data fitted by $e^{-0.116(x-0.46)^2}$ and (b) the photometrically equivalent pupil diameter as a function of pupil diameter for a ρ value of 0.12 mm^{-1}.

in the retinal pigment epithelium and choroid, and hemoglobin mainly in the choroid. The sclera backscatters light strongly so that most light reaching it passes back to the retina.

Fundus reflectance, the light reflected and scattered at the fundus and which passes back out of the eye, is used for diagnostic evaluation. Reflectance is low at short wavelengths and gradually increases with increase in wavelength, largely attributable to blood in the choroid. Some of the scattered light will contribute to veiling glare; it is thought that an important role of the Stiles–Crawford effect is to reduce the luminous efficiency of this light.

Refractive Anomalies

When the eye fixates an object of interest, ideally the image is focused at the retina. This may require some accommodation effort of the eye so that the object lies within the far and near points corresponding to minimum and maximum accommodation, respectively.

An eye whose far point is at infinity is referred to as an emmetropic eye, and this is considered the normal eye provided that it has appropriate accommodative amplitude. A refractive anomaly, or refractive error, occurs when the far point is not at infinity. Eyes with far points that are not at infinity are referred to as ametropic eyes. Emmetropia and ametropia might be regarded as opposites, but emmetropia is part of the ametropia distribution.

The departure from emmetropia is often considered to be an error of refraction, and ametropias are referred to also as refractive errors. Refractive anomalies can be corrected with ophthalmic lenses in the form of spectacle, contact, and intraocular lenses. Ophthalmic practitioners do not distinguish between the terms of refractive error and refractive correction, although from a purist perspective they are opposites.

While emmetropia may be defined in terms of the far point being at infinity, within the precision of refractive correction and ophthalmic lens manufacture this is not a practical definition. People with corrections within a range such as -0.25 D to $+0.50$ D may be considered to be emmetropic, but some authorities may give slightly different ranges.

If the range of accommodation is reduced with age so that near objects of interest cannot be seen clearly, it gives a refractive anomaly called presbyopia.

Spherical Refractive Anomalies

In spherical refractive anomalies, the refraction is unaffected by the meridian in the pupil of the eye. These are categorized according to the far point position (the spherical refractive errors) or to the near point position (presbyopia).

For a myopic eye, the far point is in front of the eye (Fig. 10(a)). An object at infinity is focused at the eye's posterior focal point F', which is in front of the retina and consequently the retinal image is blurred. There is a mismatch between the length of the eye and its power, so the eye can be considered as being too powerful for its length or as being too long for its power, although the latter is the better point of view as most myopic eyes have excessive length compared with emmetropic eyes. Clear focus on a distant object can be achieved by placing an ophthalmic lens of appropriate negative power at the front of the eye (Fig. 11(a)). This lens works by forming a virtual image at its back focal plane, which coincides with the far point of the eye.

Myopia has been classified by magnitude (e.g., low, moderate, high), and age of onset (e.g., early onset or late onset). Uncorrected myopes complain of blurred distance vision, which is most noticeable at night when pupils are large and there is a small depth-of-focus. If the level of myopia is sufficient, they may complain that close objects also appear blurred.

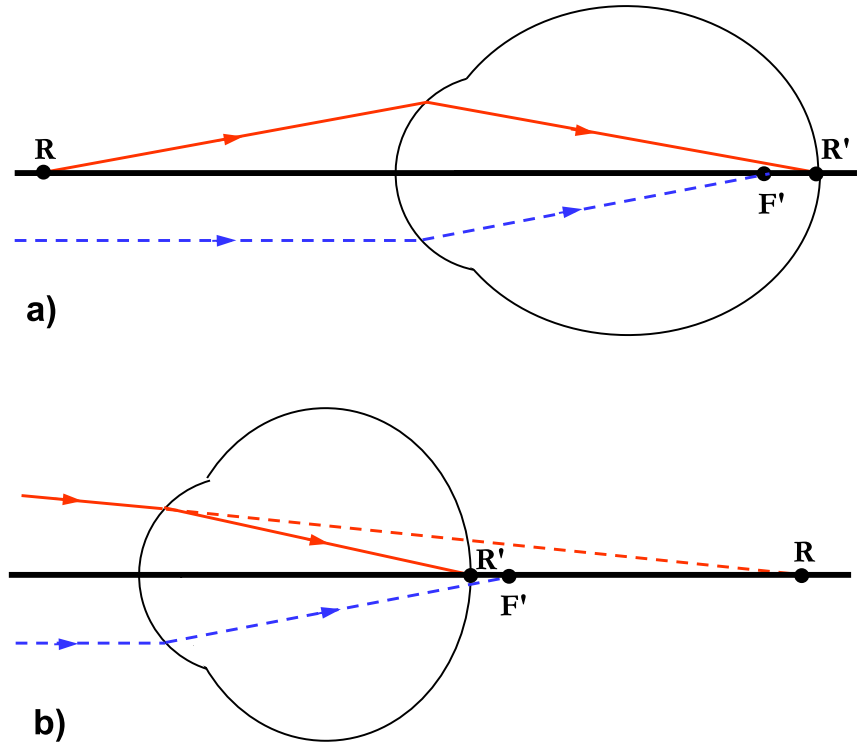


Fig. 10 (a) Myopic and (b) hyperopic eyes, showing the far points at R, retinas at R', and posterior focal points at F'.

For a hyperopic (also hypermetropic) eye, the far point is behind the eye and the posterior focal point F' is behind the retina (Fig. 10(b)). An object at infinity is focused toward this point, and the retinal image is blurred unless the eye has sufficient accommodation amplitude to bring the image into sharp focus. As for myopia, hyperopia can be considered as a mismatch between the length of the eye and its power, but now with the eye being too weak for its length or too short for its power. Clear focus on a distant object can be achieved by placing an ophthalmic lens of appropriate positive power at the front of the eye (Fig. 11(b)). This lens forms a real image at its back focal plane, coinciding with the far point of the eye.

Young hyperopes may have difficulty relaxing accommodation, with residual ciliary muscle tonus producing latent hyperopia. Total hyperopia consists of manifest and latent components, with the portion of the former that can be compensated by accommodative effort being referred to as facultative hyperopia and the remainder as absolute hyperopia. Taking into account the loss of accommodation with age, this can be expressed as

$$\text{Total} = (\text{Facultative}\downarrow + \text{Absolute}\uparrow) + \text{Latent}\downarrow = \text{Manifest}\uparrow + \text{Latent}\downarrow$$

with the directions of the arrows indicating whether a component increases or decreases with aging.

Because uncorrected hyperopes must make more accommodative effort than emmetropes or myopes to view close objects, they tend to complain of sore eyes and headaches associated with effort in near visual tasks. Depending on the level of hyperopia, they may complain of blurred near vision and blurred distance vision, with the former being worse than the latter.

Presbyopia (from the Greek for "old eye") is the difficulty people have in performing near tasks because of the age-related decrease in accommodative amplitude. The near point moves away from the eye to be beyond the near task position. Age of onset is related to the sign and magnitude of refraction, with uncorrected hypermetropes having problems earlier in life than uncorrected myopes. Presbyopia is corrected by ophthalmic lenses that are more positively, or less negatively, powered than the distance correction. Of course, uncorrected presbyopes' main complaint is difficulty performing close tasks.

Astigmatism

Astigmatic refractive errors occur when the refractive error depends upon meridian (Fig. 12). It is usually due to one of more of the refracting surfaces, and particularly the anterior corneal surface, having a toroidal shape. However, it may be due to one or more surfaces being tilted or displaced. The level of astigmatism is the difference being the least and most powerful meridians. Astigmatism is corrected by lenses which have different powers in these meridians, with the power difference being referred to as a cylinder. The cylinder can be given as either positive or negative power, depending upon how the difference is determined. The axis of a positive cylinder will be at 90 degree to its corresponding negative cylinder axis. The axis of a cylinder is specified by an anticlockwise rotation from the right side of an observer looking at the lens in front of a patient's face, to a maximum of 180 degree. The vertical meridian is usually given as 180 degree rather than 0 degree.

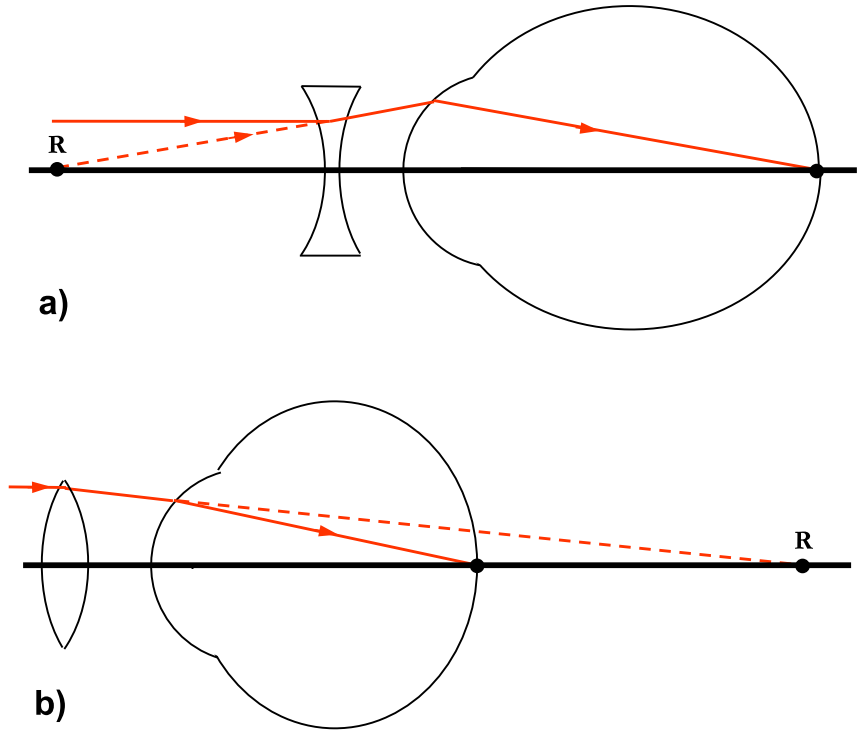


Fig. 11 Ophthalmic corrections for (a) myopia and (b) hyperopia. The posterior focal planes of the correcting lenses coincide with the far points of the eyes at *R*.

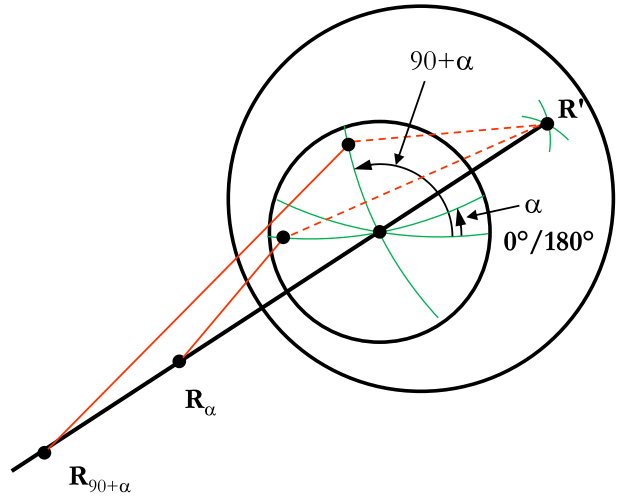


Fig. 12 Astigmatism in the eye. Far points R_α and $R_{\alpha+90}$ are imaged at retinal point R'.

There are different subclassifications of astigmatism. In myopic astigmatism, the eye is too powerful for its length in one (simple myopic astigmatism) or both (compound myopic astigmatism) principal meridians. In hyperopic astigmatism, the eye is too weak for its length in one (simple hyperopic astigmatism) or both (compound hyperopic astigmatism) principal meridians. Mixed astigmatism occurs when one principal meridian is myopic and the other is hyperopic.

Astigmatism may also be classified by axis. With-the-rule astigmatism requires a correcting negative cylinder with an axis within ± 30 degrees of the horizontal meridian; it is usually associated with an anterior cornea that is steeper along the vertical than along the horizontal meridian. Against-the-rule astigmatism requires a correcting negative cylinder lens with an axis within ± 30 degrees of the vertical meridian; it is usually associated with an anterior cornea that is steeper along the horizontal than along the vertical meridian. Oblique astigmatism occurs if the axes are beyond 30 degree from the horizontal and vertical meridians.

Astigmatism causes blurred vision at all distances, although, depending on the type of astigmatism, this may be worse at distance or near. Astigmats may complain of tired and sore eyes and headaches associated with demanding visual tasks.

Ophthalmic lenses to correct astigmatism usually have one spherical surface and one toroidal surface, with the latter generally being the back surface, but are often referred to as sphero-cylindrical lenses. They have the specification

$$S/C \times \alpha$$

where S and C are spherical and cylindrical powers and α is the cylindrical axis. Another specification that is becoming popular is

$$M,\ J_{180},\ J_{45}$$

where M is the mean sphere (also equivalent sphere) and J_{180} and J_{45} are regular and oblique astigmatism components. The two specifications are related by

$$M = S + C/2,\ J_{180} = -C\cos(2\alpha)/2,\ J_{45} = -C\sin(2\alpha)/2$$

and, using negative power cylinders,

$$C = -2\sqrt{\left(J_{180}^2 + J_{45}^2\right)},\ \alpha = \tan^{-1}(J_{45}/J_{180})/2,\ S = M - C/2$$

Some rules have to be used to ensure that α is calculable and is correctly within the range of 0–180 degrees. For calculations of α that do not retain information about signs of J_{180} and J_{45}:

$$\text{If } J_{180} = 0,\ J_{45} < 0,\ \alpha = 135 \text{ degree}$$

$$\text{If } J_{180} = 0,\ J_{45} \geq 0,\ \alpha = 45 \text{ degree}$$

$$\text{If } J_{180} < 0,\ \alpha = \alpha + 90 \text{ degree}$$

This should give an angle between -90 and 90 degrees. To put the angle between 0 and 180, 180 degrees must be added to negative angles to place them in the range 90 to 180 degrees. Either add 180 degree to negative angles or apply the rule:

$$\text{If } J_{180} \geq 0 \text{ and } J_{45} \leq 0,\ \alpha = \alpha + 180 \text{ degree}$$

The M, J_{180}, J_{45} form is useful for averaging a number of readings or for analyzing population data. Such calculations are not valid using the $S/C \times \alpha$ form.

Anisometropia

Here the refractive errors of fellow eyes of a person are different. Subclassifications include anisomyopia when fellow eyes are myopic, anisohyperopia when fellow eyes are hyperopic and antimetropia when one eye is myopic and its fellow eye is hyperopic. Subclassification could extend to consideration of astigmatism. Usually a threshold is set for anisometropia, for example, a person might be considered to have clinically significant anisometropia if it exceeds 1.0 D.

Correction of Refractive Anomalies

As mentioned before, refractive anomalies may be corrected by spectacle, contact and intraocular lenses. Nonsurgical and surgical procedures for the cornea are also available. The former occurs in orthokeratology in which rigid contact lenses are worn overnight to alter the shape of the anterior cornea. Surgical procedures involve removal of tissue from the cornea to alter anterior corneal shape. Future approaches are in development for the noninvasive alteration of the cornea's refractive index, thereby correcting refractive anomalies without the removal of tissue.

Several procedures have been adopted for the correction of presbyopia, where the challenge is to correct vision for different distances. For spectacles, this has meant having different powers in different parts of the lens in the form of multifocal or progressive addition lenses. This approach has also been attempted in contact lenses relying on pressure from the bottom eyelid to move lenses upwards relative to the cornea on downwards eye movement during near tasks. Usually contact lenses and intraocular lenses, and even corneal surgery, use simultaneous vision in which the best compromise between the demands of different distances is attempted; this will reduce image contrast compared with in-focus monofocal corrections as some light must always be out of focus (**Fig. 13**). Modalities include aspheric designs and annuli with different powers. Vision at different distances is highly dependent on pupil size. This dependence is overcome to some extent by using diffractive optics so that light from the entire pupil is concentrated into two orders.

Another modality for correcting presbyopia is a form of simultaneous vision, called monovision, in which different corrections are applied to fellow eyes, for example, one eye corrected for distance tasks and the other for near tasks. This relies on the brain being able to pay attention only to the eye with the clearer image for a particular task. This can be used with contact lenses, intraocular lenses, and corneal refractive surgery.

Another approach to presbyopia is not to modify refraction but to increase depth-of-focus by the use of small apertures in contact lenses, intraocular lenses or in disks implanted into the cornea.

All these correction types come with side effects, for example, spectacle lenses correcting myopia will minify the size of the retinal image. As mentioned above simultaneous vision lenses cannot provide crisp vision at any distance. Spectacle lens correction of anisometropia results in different retinal image sizes and different prismatic effects when looking through lens peripheries, and these may compromise binocular vision.

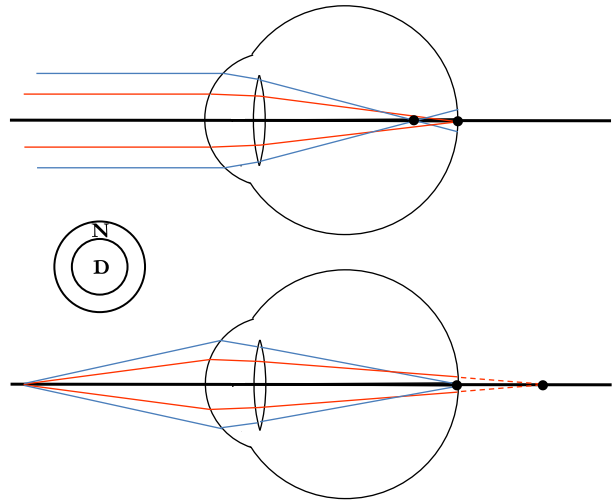


Fig. 13 Imagery with a bifocal contact lens with inner distance and outer near zones. Effects are exaggerated.

Corrections have aberrations that interact with those of the eye. Spectacle lenses do not move with the eye, and their important aberrations are associated with foveal vision and oblique incidence of light on the lens as the eye rotates behind it. Aberrations highly dependent on pupil size, such as spherical aberration, are not important for spectacle lenses as the surface curvatures are too small to affect aberrations. Contact lenses and intraocular lenses move with the eye and have high surface curvatures, and aberrations highly dependent on pupil size are important.

Some ingenious arrangements have been considered for the restoration of accommodation involving moving or altering the shape of intraocular lenses under the influence of the ciliary body during accommodative effort; these rely on the ciliary body's accommodative apparatus being intact. One surgical proposal relies on a maverick theory of accommodation and presbyopia in which the action of the ciliary body is to increase the lens diameter with age, at odds with the argument given here (see Section Changes With Age, Accommodation and Presbyopia), and this is made more difficult by a supposed increase in lens diameter with age. The surgery involves increase in the diameter of the eye so that the ciliary body can once again influence lens shape. At this time, none of these methods has been able to restore more than 2–3 D of accommodation, and usually any improvement is transient.

Aberrations

The refractive anomalies can be considered as optical aberrations of the eye. They reduce retinal image quality, prevent the image from being a perfect replica of an object (disregarding size and luminance effects), and adversely affect visual performance (e.g., visual acuity when reading letter charts). There are other aberrations which can interact with the refractive anomalies. Some of these aberrations become important when the refractive anomalies are corrected. These additional aberrations can be classified as monochromatic aberrations and the chromatic aberrations. Monochromatic aberrations are present at any wavelength and indeed change with wavelength. The chromatic aberrations occur when there is multi-wavelength light, and result from the varying refractive index of a transparent material with wavelength. This latter produces the separation of white light into its colored components known as chromatic dispersion.

Monochromatic Aberrations

There are three common ways of representing monochromatic aberrations (**Fig. 14(a)**). A wave aberration is the departure of the wavefront from the ideal waveform, as measured at the exit pupil. Transverse aberration is the departure of a ray from its ideal location at the image surface. Longitudinal aberration is the departure of the intersection of a ray with a reference axis (the pupil ray) from its ideal intersection; this may not always exist. The monochromatic aberrations must be measured in object space, with the exit pupil becoming the entrance pupil in this description (**Fig. 14(b)**).

In vision science, aberrations are specified as wave aberrations using the ophthalmic optics OSA variant of a Zernike polynomial function series (ANSI, 2010; ISO, 2008). The wave aberration $W(\rho, \theta)$ has the polar representation

$$W(\rho, \theta) = \sum_{n=0}^{k} \sum_{m=2i-n}^{n} c_n^m Z_n^m(\rho, \theta) \tag{1}$$

where Z_n^m is a particular Zernike polynomial and c_n^m is its coefficient (weighting). ρ is the relative distance from the center of the pupil and ranges from 0 to 1 (**Fig. 15**). θ is a meridian in radians and ranges from 0 to 2π. It is measured from the positive X-axis (to an observer's right when he or she looks at an eye) with an anticlockwise angle, as for the cylindrical axis scheme given earlier.

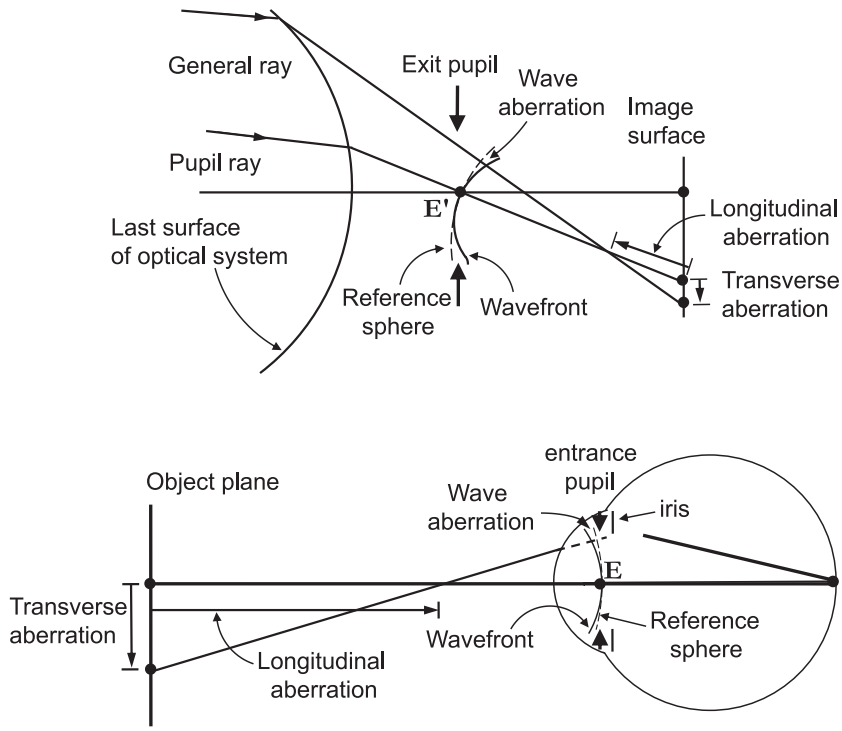


Fig. 14 Wave, transverse and longitudinal aberrations: (a) general optical system and (b) determined in object space as they must be for the eye.

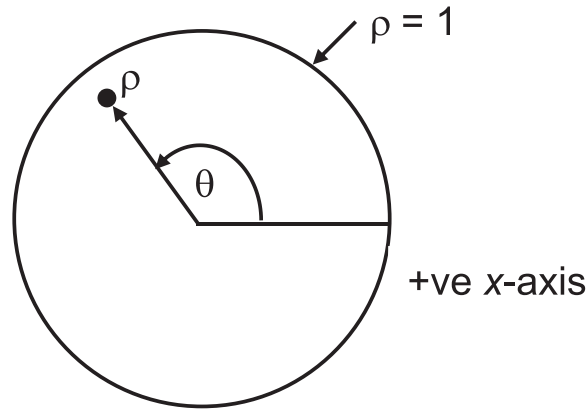


Fig. 15 Pupil coordinate system for specifying ocular aberrations.

i is counted from 0 to n, and k is the maximum order of the polynomial series. The Zernike polynomial function Z_n^m is defined as

$$Z_n^m(\rho,\ \theta) = N_n^m R_n^{|m|}(\rho)\cos(m\theta),\ \textit{for } m \geq 0 \text{ and}$$
$$Z_n^m(\rho,\ \theta) = N_n^m R_n^{|m|}(\rho)\sin(m\theta),\ \textit{for } m < 0$$

where $R_n^{|m|}$ is a radial polynomial that is a function of ρ and $N_n^{|m|}$ is a normalization term. $R_n^{|m|}$ is given by

$$R_n^{|m|}(\rho) = \sum_{s=0}^{(n-|m|)/2} \frac{(-1)^s(n-s)!}{s![0.5(n+|m|)-s]![0.5(n-|m|-s)!\rho^{n-2s}}$$

where the index n is the highest power of the radial polynomial and the index m describes the meridional frequency of the sinusoidal component of the Zernike polynomial. The normalization term N_n^m is given by

$$N_n^m = \sqrt{n+1},\ \text{for } m = 0 \text{ and } N_n^m = \sqrt{2(n+1)},\ \text{for } m \neq 0$$

The normalization means that the variance of each Zernike polynomial function is 1, and so the square of the coefficient of the Zernike polynomial function becomes the contribution of that polynomial function to the variance of the wave aberration.

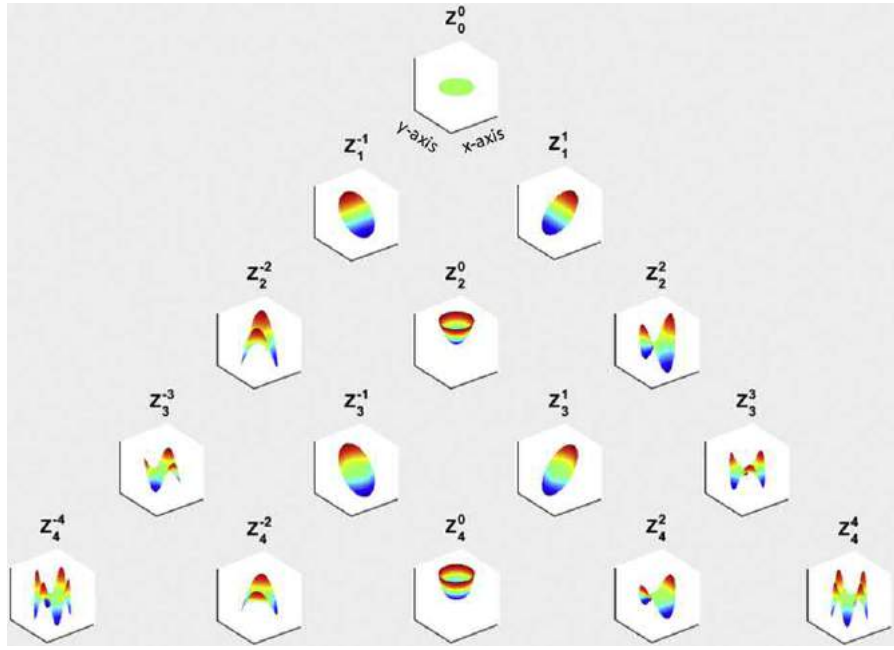


Fig. 16 Three-dimensional representation of the first five orders of the Zernike polynomial functions pyramid.

Summing the squares of the coefficients for Zernike polynomial functions of a particular order n gives the contribution of that order to the wave aberration variance. For the total variance, it is usual to disregard the piston coefficient, whose value is arbitrary, and the tilt coefficients which do not contribute to quality (at least in monochromatic light). The root-mean-square (RMS) of the wave aberration (the square root of its variance) can be used as a measure of image quality. This is given by

$$\mathrm{RMS} = \sqrt{\sum_{n>1,\ \mathrm{all}\ m} \left(c_n^m\right)^2}$$

The coefficients c_n^m are relative to the size of the pupil, and must alter with pupil size. The change is not simple because a Zernike polynomial function of a particular order contains lower order terms, for example, the primary spherical aberration polynomial is $Z_4^0 = \sqrt{5}(6\rho^4 - 6\rho^2 + 1)$. There are various ways by which Zernike coefficients can be recalculated at a new pupil size. Comparing aberration of different eyes, or the aberrations of a particular eye at different times, is valid only if this is done at the same pupil size.

The Zernike polynomial function series is sometimes represented as a pyramid in which order n changes vertically and frequency m changes horizontally **Fig. 16** shows Zernike aberration functions against pupil position for terms up to the 4th-order.

The first row order is $n=0$. The single function is called piston. Its coefficient is usually manipulated to make the wave aberration zero at the pupil center.

The second row order is $n=1$. The terms are tilts or prisms, Z_1^{-1} in the (vertical) y-direction and Z_1^{+1} in the (horizontal) x-direction. They are rotated functions of one another. This rotational nature continues down the pyramid, so that in any row a function with a negative value of the index m is a rotated form of the function with the same, but positive number for m.

The third row order is $n=2$. The terms are the refraction terms. The rotationally symmetric center term is called defocus $\left(Z_2^0\right)$. The side terms are the astigmatisms. Oblique astigmatism $\left(Z_2^{-1}\right)$ with $m=-2$ is on the left; it has a maximum value of $+\sqrt{6}$ along the 45 degree meridian and a minimum value of $-\sqrt{6}$ along the 135 degree meridian. Horizontal/vertical astigmatism $\left(Z_2^{+1}\right)$ with $m=+2$ is on the right; it is rotated by -45 degree from oblique astigmatism to have a maximum value along the horizontal meridian of $+\sqrt{6}$ and a minimum value along the vertical meridian of $-\sqrt{6}$.

The fourth row order is $n=3$. The terms are the first of what are called the higher-order polynomial functions. The two middling terms are the comas, one vertical $\left(Z_3^{-1}\right)$ and one horizontal $\left(Z_3^{+1}\right)$. The fifth-row order is $n=4$, and its rotationally symmetric center term is called spherical aberration $\left(Z_4^0\right)$.

Even order Zernike coefficients can be converted into refraction in the M, J_{180}, J_{45} classification given in the Section Refractive Anomalies according to

$$M = -\frac{4\sqrt{3}c_2^0 - 12\sqrt{5}c_4^0 + 24\sqrt{7}c_6^0 \ldots}{R^2}$$

$$J_{180} = -2\frac{\sqrt{6}c_2^2 - 6\sqrt{10}c_4^2 + 12\sqrt{14}c_6^2 \ldots}{R^2}$$

$$J_{45} = -2\frac{\sqrt{6}c_2^{-2} - 6\sqrt{10}c_4^{-2} + 12\sqrt{14}c_6^{-2} \ldots}{R^2}$$

where is the pupil semidiameter for which coefficients apply. Converting from an error into a correction requires the initial negative signs on the right hand sides of the equations. When doing these calculations, it is convenient to have the coefficients in micrometers and the pupil size in millimeters so that the corrections are in diopters. A lens power minimizing the RMS of the wavefront is determined by using only the first terms on the right hand sides of the equations. As additional terms are added, we come closer to a paraxial refraction, in which we are determining the refraction based on rays traced into/out of the eye for a central part of the pupil.

Most instruments for measuring aberrations use near infrared wavelengths where fundus reflection is much higher than for visible light. This requires corrections ΔM and Δc_2^0 to the spherical equivalent refraction and defocus wave aberration coefficient, respectively. A schematic eye such as the Indiana Chromatic eye can be used for this purpose (Thibos *et al.*, 1992). For the infrared wavelength 840 nm and visible wavelength 550 nm, ΔM is approximately -0.87 D, and from the previous equation for M,

$$\Delta c_2^0 = -\Delta M \cdot \frac{R^2}{4\sqrt{3}} = -0.144 \Delta M \cdot R^2$$

Several investigations have been conducted on the magnitudes and distributions of the higher-order aberrations including how they vary with pupil size, age and refraction, eye side (right versus left), following refractive surgery, in various disease conditions, and the corneal and lenticular contributions to eye aberrations. Concerning pupil size, aberrations increase as pupil size increases and the relative contribution of the higher-order aberrations increases. There is considerable between-eye symmetry, with many higher-order terms being highly correlated between fellow eyes (Hartwig and Atchison, 2012). For on-axis vision, the most important higher-order aberrations are the comas and spherical aberrations. It cannot be overemphasized that the higher-order aberrations become important only when the lower order aberrations are largely corrected.

Aberrations associated with peripheral vision have become of considerable intersect in recent years. The eye has very high peripheral levels of defocus and astigmatism, and there is a shift in the pattern of the former with hyperopia and emmetropia tending toward myopia in the periphery (relative peripheral myopia) and myopes tending toward hyperopia in the periphery (relative peripheral hyperopia), at least along the horizontal vision field (Atchison, 2012). This has led to a consideration that hyperopes and emmetropes with relative peripheral hyperopia might have a tendency to develop myopia, and that compensating for the peripheral refraction might slow the progression of myopia. An alternative view is that the change in peripheral refraction pattern is a consequence rather than a cause of developing myopia.

Accompanying peripheral changes in the second order aberrations are changes in the higher-order aberrations. Most notably, horizontal coma changes approximately linearly with horizontal visual field angle and vertical coma changes approximately linearly with vertical visual field angle.

Chromatic Aberrations

Chromatic dispersion produces two types of aberration, longitudinal and transverse.

Longitudinal chromatic aberration of the eye is shown in **Fig. 17(a)**. A beam of multiwavelength light from an axial target O enters the eye. The refractive indices inside the eye vary with wavelength, so the path followed by a ray depends upon its wavelength. Refractive indices decrease with increase in wavelength, so the eye power decreases as wavelength increases. If the eye is focused at the target for a yellow light, rays of longer wavelength (such as reds) are focused behind the retina and rays of shorter wavelength (such as blues) are focused in front of the retina.

Longitudinal chromatic aberration can be quantified as a "chromatic difference of power" $\Delta F(\lambda)$, which is the difference in power of the eye between a wavelength λ and the reference wavelength $\overline{\lambda}$, i.e.,

$$\Delta F = F(\lambda) - F(\overline{\lambda})$$

It can also be quantified as a "chromatic difference of refraction" $\Delta R_x(\lambda)$, which is the difference between vergences for which a target is focused at the retina for different wavelengths, or more simply is the change in refraction with wavelength; the second way is how the aberration is measured experimentally (**Fig. 17(b)**). In mathematical terms

$$\Delta R_x(\lambda) = L(\lambda) - L(\overline{\lambda})$$

where $L(\lambda)$ and $L(\overline{\lambda})$ are the object vergences required at λ and $\overline{\lambda}$, respectively. For the situation shown in the figure, these vergences are both negative.

The relationship between chromatic difference of refraction and chromatic difference of power is (Atchison and Smith, 2000)

$$\Delta R_x(\lambda) = \frac{[n'(\lambda) - n'(\overline{\lambda})]\,[F(\overline{\lambda}) + L(\overline{\lambda})]}{n'(\overline{\lambda})} - \Delta F(\lambda)$$

where $n'(\lambda)$ and $n'(\overline{\lambda})$ are vitreous refractive indices at λ and $\overline{\lambda}$, respectively.

For an emmetropic eye focused at infinity, $L(\overline{\lambda}) = 0$, and the equation reduces to

$$\Delta R_x(\lambda) = \frac{[n'(\lambda) - n'(\overline{\lambda})]\,F(\overline{\lambda})}{n'(\overline{\lambda})} - \Delta F(\lambda)$$

The range of chromatic difference of refraction is about 2.1 D between 400 and 700 nm, and is slightly higher than that for a reduced eye filled with water. There are minor differences between studies and between participants within studies. Despite the

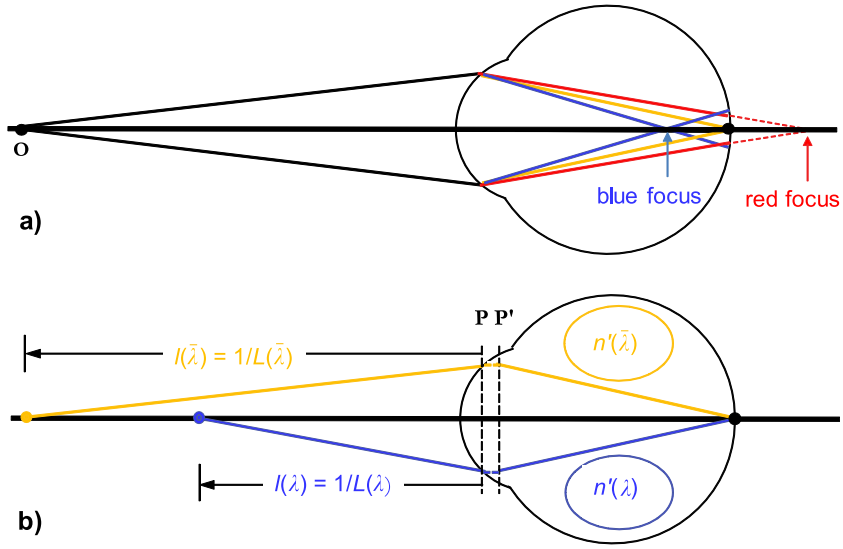


Fig. 17 Longitudinal chromatic aberration (greatly exaggerated). (a) Imagery at the eye for blue, yellow and red lights when the yellow light is focused at the retina and (b) determining chromatic difference of refraction. Object distances are specified relative to the anterior principal plane of the eye.

large magnitude, longitudinal chromatic aberration has little deleterious effect on vision, largely because its effects are attenuated by the variable sensitivity of the eye to different wavelengths (**Fig. 8**).

Transverse chromatic aberration of the eye is shown in **Fig. 18(a)** for an eye which is a centered optical system and for off-axis object point Q. The different wavelength images are at different depths because of the longitudinal chromatic aberration. Also, because the power is less for long wavelengths than for short wavelengths, longer wavelength rays are deviated less than shorter wavelength rays to reach the retina further away from the optical axis.

Like longitudinal chromatic aberration, transverse chromatic aberration must be measured outside the eye, where it is quantified as a "chromatic difference of position" (**Fig. 18(b)**). Rays of wavelength λ and $\bar{\lambda}$ originate from different positions in object space, but pass through the same point in the pupil to intersect at the retina. The chromatic difference of position $t(\lambda)$ for height h of the rays in the pupil, relative to the visual axis ray (ray passing through the nodal points) is

$$t(\lambda) = a_{\lambda} - a_{\bar{\lambda}}$$

where a_{λ} and $a_{\bar{\lambda}}$ are angles subtended by the rays with the visual axis in object space.

The transverse chromatic aberration and longitudinal chromatic aberration, or more specifically the chromatic difference of position and the chromatic difference of refraction, are related by the equation (Atchison and Smith, 2000)

$$t(\lambda) \approx h\,\Delta R_x(\lambda)$$

Because the eye is a decentered optical system, there is transverse chromatic aberration associated with foveal vision, and the foveal chromatic difference of position is

$$t(\lambda) \approx d\,\Delta R_x(\lambda)$$

where d is the departure of the line-of-sight, the axis joining the fixation target and the center of the pupil, from the visual axis (**Fig. 18(b)**).

The range of foveal chromatic difference of position across the visible spectrum can be higher than 1 min of arc. Usually the line-of-sight is nasal to the visual axis in object space (**Fig. 6**). In binocular vision, this can give rise to the phenomenon of chromostereopsis in which reddish objects appear to be closer than bluish objects at the same distance. Potentially transverse chromatic aberration can have deleterious effects on vision because it produces wavelength-dependent changes in spatial phase of images. This may be a problem for highly decentered natural or artificial pupils. Two-thirds loss of resolution may result for 3 mm displacement of small artificial pupils (Green, 1967; Thibos *et al.*, 1991).

Retinal Image Quality

Retinal image quality can be determined in different ways. One way is to use the wave aberrations themselves or a metric based on them such as the root-mean-squared aberrations. Another common quality measure is the point spread function, which is the shape and dimension of the image of a point object. The optical transfer function measures changes, from object to image, in the contrast and phase of sinusoidal varying luminance patterns. The wave aberration is related to the point spread function and optical transfer function by Fourier transforms, but this overestimates the quality of the retinal image as it does not take into account scatter within the media and the fundus. The point spread function can be measured by a double pass method (light

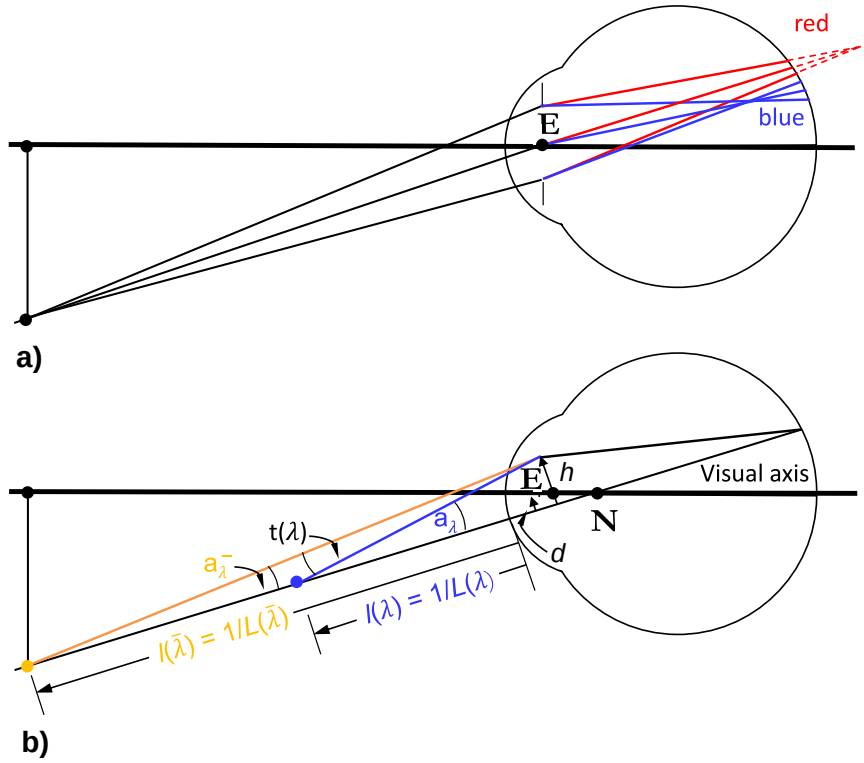


Fig. 18 Transverse chromatic aberration (greatly exaggerated). (a) Centered pupil and an off-axis object and (b) determining chromatic difference of position (for simplicity, the nodal points are assumed to be at a common point).

passes into the eye and is reflected out), and the contrast aspect of the optical transfer function can be estimated by comparing contrast sensitivities of the eye obtained with screen-based equipment and with an interferometric method in which the optics are effectively by-passed (Atchison and Smith, 2000).

Several metrics based on wave aberrations have been used to estimate objective refractions. They involve manipulating refraction to minimize or maximize some aspect of the aberrations or of image quality, for example, maximizing the Strehl intensity ratio which is the height of the point spread function relative to its aberration-free height.

Changes With Age

Pathological changes that occur in the optics of the eye with age, such as cataract, will not be considered here.

Cornea

As age increases, there is fiber degeneration, decreased spacing between collagen fibrils of the stroma, and increases in the cross-sectional area of collagen fibers. Descemet's membrane increases in thickness with age and the size of endothelial cells becomes more variable. Endothelial function may become impaired, with the aqueous humor seeping into the cornea, disrupting structural order and increasing light scatter.

The anterior surface radius of curvature is usually greater along the horizontal than along the vertical meridian in young eyes, but this trend reverses with age. There is little variation in transmittance with age, but Boettner and Wolter (1962) found a decrease in the direct (non-scattered) light with increased age.

Aperture Stop and Iris

The natural pupil becomes smaller with increase in age, a process known as senile miosis, and this is accompanied by decreases in speed and magnitude of pupil reactions.

Lens

The human lens grows throughout life with considerable changes in size, shape, mass, and stiffness. The young lens is soft and easy to deform, while the old lens is stiff and unable to be deformed. With age, the lens becomes thicker along its axis with

corresponding decrease in anterior chamber depth. Its surfaces become more curved, with greater change for the anterior than for the posterior surface. Equatorial thickness either does not change or increases slowly with age. There are changes in refractive index distribution such that the refractive index change is restricted to a smaller proportion of the peripheral lens, accompanied by a reduction in the equivalent index (Kasthurirangan *et al.*, 2008).

Light Loss at the Retina

Retinal illumination decreases with age due to senile miosis and decrease in ocular transmittance. Decrease is much more rapid for shorter than for longer wavelengths (e.g., van de Kraats and van Norren, 2007) (**Fig. 19**). As a consequence, the lens becomes more yellow with increase in age. With aging, there is increase in both forward and backward-scattered light.

Refraction

The distribution of refraction is strongly age-dependent. Newly-born children have a normal distribution whose mean is considerably hyperopic with a distribution range to approximately ± 10 D (Grosvenor, 2002). The growth of ocular components is coordinated so that emmetropia can be achieved by 6 years of age, a process known as emmetropization, but emmetropia is not always subsequently maintained. By 6–8 years the mean refraction is slightly hyperopic and the distribution is steeper than a normal distribution (leptokurtosis). A pronounced tail in the myopic direction develops after this and is observed in data of 20-year olds. The distribution is stable between the ages of 20 and 40 years, after which the distribution becomes less leptokurtic and then there is usually a hyperopic shift (Grosvenor, 2002). The age-related formation of cataracts can alter the refraction.

Most studies of refraction have been cross-sectional, meaning the measurements of people of different ages occurred within a limited time span. These can mask intergenerational (longitudinal) changes. In particular they do not pick up changes in the direction of myopia that have been occurring in the last few decades (e.g., Edwards and Lam, 2004) (**Fig. 20**). Myopia prevalence is correlated with increasing urbanization (Ip *et al.*, 2008; Zhan *et al.*, 2000) and its prevalence in East Asian countries is now in excess of 80% by early adulthood (He *et al.*, 2004; Lin *et al.*, 2004; Wu *et al.*, 2001). Myopia is a leading cause of blindness in later life, as having severe myopia doubles the risk of developing serious eye problems, such as cataract and retinal detachment. There is no "safe" level of myopia, with even low levels increasing the risk of other ocular diseases (Flitcroft, 2012).

The age-related changes mentioned above for corneal toricity affect astigmatism of the eye. Considerable astigmatism, usually against-the-rule, exists in the first year, but decreases quickly during early infancy. Astigmatism is usually with-the-rule up to 40 years, after which the prevalence of against-the-rule astigmatism increases.

Accommodation and Presbyopia

Presbyopia is the name given to the loss of clear and comfort near vision which occurs because of the age-related loss of accommodation amplitude. Onset for most people is the early to mid-40s, but is affected by the amplitude, the nature and duration of close work, and other refractive conditions. The decline in amplitude of accommodation might be affected by a number of factors including diet, race, exposure to ultraviolet radiation, and temperature. As an example of the influence of refractive conditions, in the absence of a distant correction, a low myope would need a lesser amplitude of accommodation than a hyperope to perform near tasks and would become presbyopic later in life.

Previously it was mentioned that, after peaking early in life, accommodation amplitude gradually reduces to become zero by mid-50s. Many clinically related studies suggest that some accommodation remains into older age (**Fig. 21**). This is an artefact of subjective measurement (the participants' judgement is involved) involving depth-of-focus.

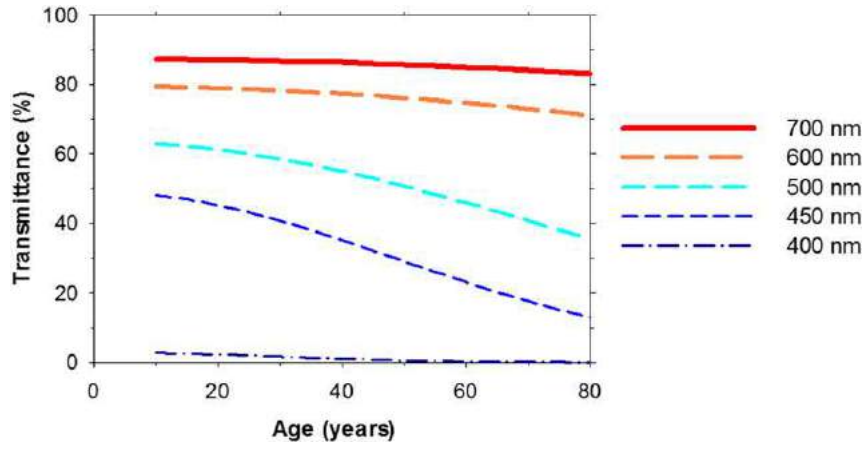


Fig. 19 Transmittance of the eye as a function of age at different wavelengths according to the fit given by Eq. (8) of van de Kraats and van Norren (2007).

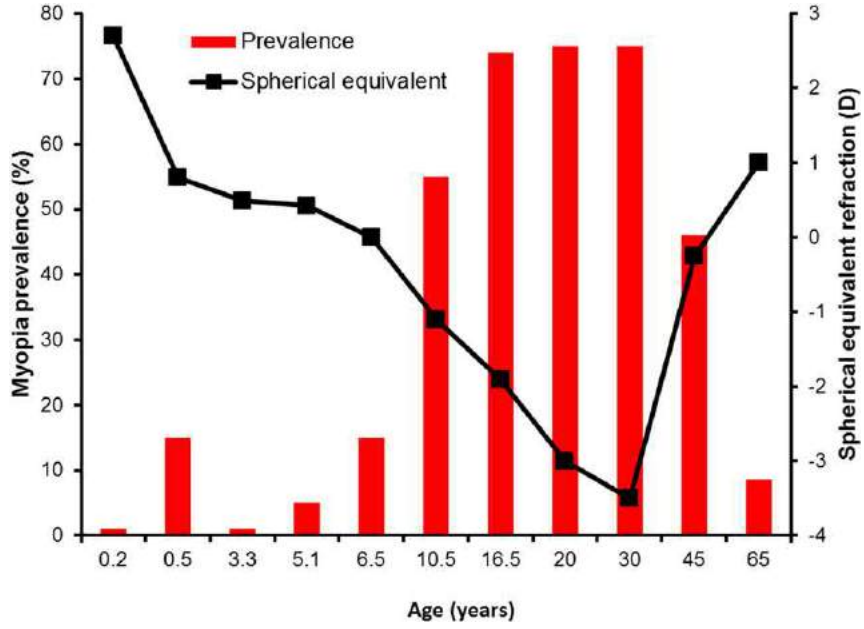


Fig. 20 Mean spherical equivalent refraction (*D*) as a function of age in a Hong Kong population. Data of Edwards, M.H., Lam, C.S., 2004. The epidemiology of myopia in Hong Kong. Annals Academy of Medicine, Singapore 33 (1), 34–38.

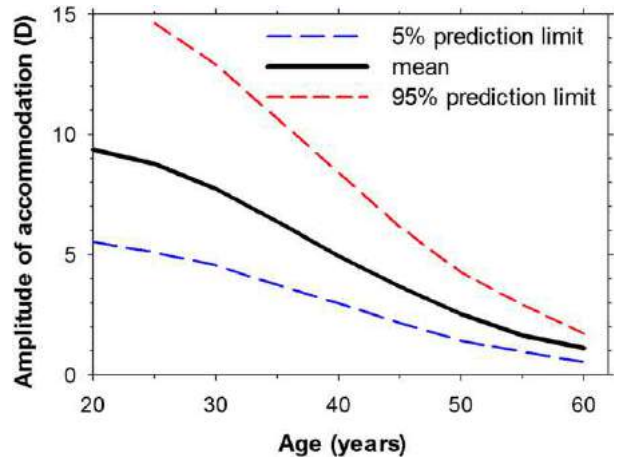


Fig. 21 Subjective amplitude of accommodation as a function of age from the study of Ungerer (1986).

Aberrations

Taking into account normal age-related pupillary miosis, there is reduction in higher-order aberrations with increase in age (Applegate *et al.*, 2007). Considering fixed pupil sizes, total higher-order aberrations increase throughout adulthood and spherical aberration becomes more positive with increase in age (Applegate *et al.*, 2007).

See also: Lenses and Mirrors

References

American National Standards Institute (ANSI), 2010. American National Standard Z80.28 for Ophthalmics – Methods for Reporting Optical Aberrations of Eyes. Washington, DC: American National Standards Institute.

Applegate, R.A., Donnelly 3rd, W.J., Marsack, J.D., Koenig, D.E., Pesudovs, K., 2007. Three-dimensional relationship between high-order root-mean-square wavefront error, pupil diameter, and aging. Journal of the Optical Society of America A 24 (3), 578–587.

Atchison, D.A., 2012. The Glenn A. Fry Award Lecture 2011: Peripheral optics of the human eye. Optometry and Vision Science 89 (7), 954–966.
Atchison, D.A., 2017a. Axes and angles of the eye. In: Artal, P. (Ed.), Handbook of Visual Optics, vol. I. Boca Raton, FL: Francis & Taylor Group.Chapter 17.
Atchison, D.A., 2017b. Paraxial schematic eyes. In: Artal, P. (Ed.), Handbook of Visual Optics, vol. I. Boca Raton, FL: Francis & Taylor Group.Chapter 16.
Atchison, D.A., Smith, G., 2000. Optics of the Human Eye. Oxford: Butterworth-Heinemann.
Boettner, E.A., Wolter, J.R., 1962. Transmission of the ocular media. Investigative Ophthalmology 1, 776–783.
Dunne, M.C., Royston, J.M., Barnes, D.A., 1992. Normal variations of the posterior corneal surface. Acta Ophthalmology 70 (2), 255–261.
Edwards, M.H., Lam, C.S., 2004. The epidemiology of myopia in Hong Kong. Annals, Academy of Medicine, Singapore 33 (1), 34–38.
Flitcroft, D.I., 2012. The complex interactions of retinal, optical and environmental factors in myopia aetiology. Progress in Retinal Eye Reseach 31, 622–660.
Green, D.G., 1967. Effect of ocular chromatic aberration on monocular visual performance. Journal of Physiology 190, 583–593.
Grosvenor, T.P., 2002. Primary Care Optometry, fourth ed. Boston: Butterworth-Heinemann.
Gullstrand, A., 1924. Appendix IV. Mechanism of accommodation. In: Southall, J.P.C. (Ed.), Helmholtz, H. H. (1909) Handbuch der Physiological Optik. Translated From the Third German Edition, vol. 1. Washington, DC: Optical Society of America, pp. 382–415.
Hartwig, A., Atchison, D.A., 2012. Analysis of higher-order aberrations in a large clinical population. Investigative Ophthalmology and Vision Science 53 (12), 7862–7870.
He, M., Zeng, J., Liu, Y., *et al*., 2004. Refractive error and visual impairment in urban children in southern China. Investigative Ophthalmology and Vision Science 45 (3), 793–799.
Ip, J.M., Huynh, S.C., Robaei, D., *et al*., 2008. Ethnic differences in refraction and ocular biometry in a population-based sample of 11–15-year-old Australian children. Eye (London) 22 (5), 649–656.
International Standards Organisation (ISO), 2008. Ophthalmic Optics and Instruments – Reporting Aberrations of the Human Eye. Geneva, Switzerland: ISO, (ISO 24157: 2008).
Kasthurirangan, S., Markwell, E.L., Atchison, D.A., Pope, J.M., 2008. In vivo study of changes in refractive index distribution in the human crystalline lens with age and accommodation. Investigative Ophthalmology and Visual Science 49 (6), 2531–2540.
Lin, L.L., Shih, Y.F., Hsiao, C.K., Chen, C.J., 2004. Prevalence of myopia in Taiwanese schoolchildren: 1983 to 2000. Annals, Academy of Medicine, Singapore 33 (1), 27–33.
Lowe, R.F., Clark, B.A., 1973. Posterior corneal curvature. Correlations in normal eyes and in eyes involved with primary angle-closure glaucoma. British Journal of Ophthalmology 57 (7), 464–470.
Mathur, A., Gehrmann, J., Atchison, D.A., 2013. Pupil shape as viewed along the horizontal visual field. Journal of Vision 3, 1–8.
Mathur, A., Gehrmann, J., Atchison, D.A., 2014. Influences of luminance and accommodation stimuli on pupil size and pupil center location. Investigative Ophthalmology and Visual Science 55 (4), 2166–2172.
Patel, S., Marshall, J., Fitzke, F.W., 1993. Shape and radius of posterior corneal surface. Refractive and Corneal Surgery 9 (3), 173–181.
Stiles, W.S., Crawford, B.H., 1933. The luminous efficiency of rays entering the eye pupil at different points. Proceedings of the Royal Society of London Series B: Biological Sciences 112, 428–450.
Thibos, L.N., Bradley, A., Zhang, X., 1991. Effect of ocular chromatic aberration on monocular visual performance. Optometry and Vision Science 68, 599–607.
Thibos, L.N., Ye, M., Zhang, X., Bradley, A., 1992. The chromatic eye: A new reduced-eye model of ocular chromatic aberration in humans. Applied Optics 31, 3594–3600.
Ungerer, J., 1986. The Optometric management of presbyopic airline pilots. Unpublished PhD Thesis, University of Melbourne.
van de Kraats, J., van Norren, D., 2007. Optical density of the aging human ocular media in the visible and the UV. Journal of the Optical Society of America A 24 (7), 1842–1857.
Watson, A.B., Yellott, J.I., 2012. A unified formula for light-adapted pupil size. Journal of Vision 12, 1–16.
Wu, H.M., Seet, B., Yap, E.P., *et al*., 2001. Does education explain ethnic differences in myopia prevalence? A population-based study of young adult males in Singapore. Optometry and Vision Science 78 (4), 234–239.
Zhan, M.Z., Saw, S.M., Hong, R.Z., *et al*., 2000. Refractive errors in Singapore and Xiamen, China – A comparative study in school children aged 6 to 7 years. Optometry and Vision Science 77 (6), 302–308.

Measuring Retinal Blood Flow

Alberto de Castro and Stephen A Burns, Indiana University School of Optometry, Bloomington, IN, United States

© 2018 Elsevier Ltd. All rights reserved.

Introduction

The retina of the eye, in addition to being one of our most vital sensory organs, is the most accessible portion of the central nervous system (CNS). This has led to an array of noninvasive approaches to measuring its structure and function. It is uniquely accessible for optical measurements, since evolution has resulted in an optical window that lets us probe more than 2 cm into the body. While early optical measurements of the retina were primarily structural and based on photography, it was quickly realized that the blood supply of the retina, which enters and exits the eye through the optic nerve head and courses across the surface, provides a unique window into the CNS. The retina has the added advantage that the circulation is laid out in a layered form, with most of the vessels lying in a series of layers parallel to the walls of the eye (Snodderly *et al.*, 1992), an arrangement which parallels the neural layers of the retina. This arrangement allows ready optical access to the vessels and is simpler than the layout in the cortex, which can be quite complex. Thus the eye was an early target for measurements of blood flow and its regulation. The techniques used included measures of the flow of fluorescein dye (Wessing, 1974; Jung *et al.*, 1983; Wolf *et al.*, 1989, 1990), speckle decorrelation (Fercher and Briers, 1981; Suzuki *et al.*, 1991), and laser Doppler velocimetry (Riva *et al.*, 1972, 1979; Feke and Riva, 1978) or Doppler optical coherence tomography (OCT) (Chen *et al.*, 1997; Westphal *et al.*, 2002). Measurements have included blood velocity, total flow, and have incorporated the regulation of blood flow, allowing measures of both the metabolic demands of the retina and body, as well as how the oxygen supply is driven by neuronal tissue. That is, when a visual stimulus is presented to the eye, the blood flow must change to meet the increased metabolic demand of the neural tissue, a process referred to as neurovascular coupling (Riva *et al.*, 2001; Pournaras *et al.*, 2008; Kur *et al.*, 2012). Some retinal diseases, such as diabetic retinopathy (DR), have a severe impact on both the structure of the retinal vasculature and the regulation of blood flow (Grunwald *et al.*, 1986, 1990; Kohner *et al.*, 1995; Garhöfer *et al.*, 2004; Deak and Schmidt-Erfurth, 2013).

Most of the blood flow in the posterior pole of the eye is supplied by the central retinal artery and exits the eye through central retinal vein, both of which traverse the optic nerve. For this reason measurements near the optic nerve can capture a large proportion of the blood supply to the neural retina as it enters and exits the eye. These measurements therefore can provide a tool for understanding the total retinal metabolic demand. These vessels are relatively large, typically on the order of 100 μm or larger, and thus are easily resolved and carry large volumes of blood, providing a high signal:noise ratio (SNR) for measurements. However, vascular control (Villringer and Dirnagl, 1995; Riva *et al.*, 2001, 2005; Pournaras *et al.*, 2008) is performed at a more local level (Zhong *et al.*, 2012), and in fact it is not known how local the control of retinal blood flow is, nor the area over which it is regulated. In recent years there has been increasing interest in making more local measurements of retinal blood flow driven in part by the growing availability of adaptive optics in retinal imaging.

This article provides a brief overview of current optical techniques for measuring retinal blood flow and then concentrates on approaches to measure the cell velocity in the capillaries of the human retina.

Total Retinal Blood Flow

Early measurements of blood flow depended on injecting fluorescein into the body and then using photographic and video techniques to measure the transit time (Jung *et al.*, 1983). These dye methods improved with the development of techniques based on the scanning laser ophthalmoscope (SLO) (Wolf *et al.*, 1989, 1990) and because they measured the transit of blood moving from the central retinal artery to the draining veins, they gave an estimate of the total transit time of the retina. By combining this with the approximate size of the vessels, and making assumptions about the nature of the flow based on parabolic velocity distribution (Pouiselle's law), an estimate of total blood delivered to the eye could be obtained. These techniques are mostly based on plasma velocity, since fluorescein is a small molecule and is present in the plasma fraction of the blood. The advent of the laser allowed development of laser Doppler velocimetry measurements (Feke and Riva, 1978; Riva *et al.*, 1979), and by making these measurements from two points in the pupil, variations due to angle and bulk movements could be accounted for, improving the accuracy. More recently, OCT has been used to make Doppler measurements (White *et al.*, 2003; Leitgeb *et al.*, 2004; Dai *et al.*, 2013; Doblhoff-Dier *et al.*, 2014; Aschinger *et al.*, 2015). In both techniques the Doppler shift arising from red blood cells is used to provide a measurement of the velocity of the cells. Typically the centerline velocity has been measured, since this provides a maximum frequency shift on the impinging light. It is becoming increasingly apparent that the flow in the retina is not parabolic (Bishop *et al.*, 2001; Logean *et al.*, 2003; Zhong *et al.*, 2011; Willerslev *et al.*, 2014) and the advances in both axial and lateral resolution are allowing more accurate estimates of total blood flow (Baumann *et al.*, 2011).

The movement of cells in the vasculature can also be used to generate flowmetry estimates. In these it is the variation over time, rather than the Doppler shift, that is used to estimate perfusion of the tissue. This was first attempted using speckle decorrelation (Fercher *et al.*, 1985) and flowmetry (Riva *et al.*, 1992) and the motion alone has been used to qualitatively separate vessels according to their speed (Ferguson *et al.*, 2004). OCT also can be combined with this technique, and this is generally called OCT

 doi:10.1016/B978-0-12-803581-8.09774-5

angiography (or OCT-A) although there are a number of variants (Makita *et al.*, 2006; Wang *et al.*, 2007; Tokayer *et al.*, 2013). Finally the motion can be directly tracked by imaging a single line repeatedly over a larger vessel with an adaptive optics scanning laser ophthalmoscope (AOSLO). In this method, by stopping the slow scanner, streaks created by the erythrocytes passing through are visible in the spatiotemporal image and its slope can be related directly to speed (Zhong *et al.*, 2008, 2011).

Capillary Blood Flow

Why Measure Blood Flow in Capillaries

Noninvasive access to capillaries and capillary flow is of increasing interest in the retina. Capillary velocities have mainly been measured in the area surrounding the fovea, where there is one or two capillary layers and one can easily assume that these are perpendicular to the retina, i.e., in the imaging plane. There are a number of purposes for such measurements, ranging from the understanding of the local control of blood flow, to biological parameters governing flow, such as the interaction of blood with the vascular walls, to the impact of disease on both the physical properties of the vascular system and the regulation of flow. Techniques for measuring flow at the capillary level depend on the ability to measure the movement of cells on an individual basis. A number of techniques have been devised for this, including psychophysics, fluorescent detection techniques, and, most recently, adaptive optics (**Fig. 1**). Some general patterns emerge from these techniques, however, it is important to note that different techniques measure different aspects of the blood, ranging from the relatively large leukocytes (psychophysics and recently, AO imaging), to cell aggregates interspersed with plasma (fluorescein), to red blood cells (direct imaging with adaptive optics). Because of this heterogeneity in the measuring techniques, differences in velocities obtained using different techniques are not surprising. The small diameters of the capillaries and the need for cells to deform as they move through them can cause differences in velocity for different blood fractions. However, understanding the differences between the methods and the velocities being measured remains an important topic of research as will be an understanding of the variability of the normal retina, since this provides the background upon which clinical measurements need to be compared. The next section of this article compares results obtained with six different methods, most having very different assumptions.

Blue Field Entoptic Phenomenon

The retina itself can be used as a detector for measuring retinal blood flow. This is what is done with the blue field entoptoscope (Kato, 1952; Riva and Petrig, 1980). When looking at a relatively bright blue field (including a clear blue sky), bright dots can be observed moving in an erratic manner in the observer's visual field. These dots are believed to be white blood cells moving in the capillaries of the eye. White blood cells do not absorb blue light and thus, when crossing over a region of retina the cells are detected by the photoreceptors giving the appearance of a bright dot. By comparing the perceived motion of these dots to a simulation on a computer monitor the apparent speed can be matched (Riva and Petrig, 1980). The blue field technique gives an average velocity of 0.77 mm s^{-1} and this varies with exercise (Kato, 1952). Velocity estimates are pulsatile, changing with the heart beat (Riva and Petrig, 1980) and the mean velocity decreases with age by 20% (Grunwald *et al.*, 1993). The measured pulsatility, defined as (Vmax-Vmin)/Vmean, is 0.98 (Riva and Petrig, 1980). The impact of diabetes on capillary flow is non-monotonic; in diabetics with no retinopathy. Fallon *et al.* (1986) observed average velocities similar to those in non diabetics

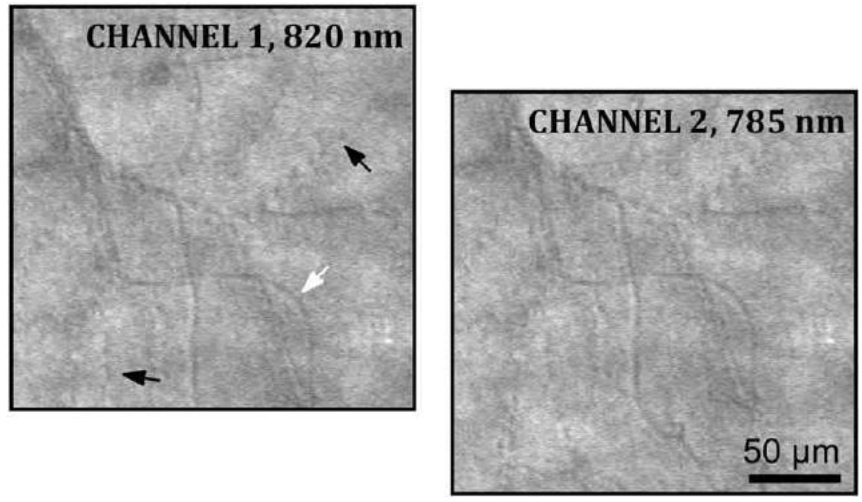


Fig. 1 Adaptive optics scanning laser ophthalmoscope (AOSLO) images of capillaries in the perifoveal area of a healthy subject. The use of multiply scattered light has allowed direct visualization of leukocytes (passing through the capillary marked with the white arrow) and erythrocytes (black arrow) in the capillaries in the retina (individual video frames).

Table 1 Average velocities measured in the blood cells. The different measurement techniques target different cells type. Numerical values are the average value found in each study, the standard deviation of the measurement when this was reported in between parenthesis, the range of velocities measured

Author	*Cell type*	*Velocity (mm mm s^{-1})*	*Measurement method*
Kato (1952)	Leukocyte	0.77	Entoptic phenomenon
Riva and Petrig (1980)	Leukocyte	0.74 (0.25–1.33)	Entoptic phenomenon
Fallon *et al.* (1986)	Leukocyte	0.54 ± 0.19 Non diabetic 0.51 ± 0.24 No retinopathy 0.74 ± 0.32 Background DR 0.37 ± 0.20 Preproliferative DR 0.56 ± 0.27 Proliferative DR 0.42 ± 0.14 Photocoagulated	Entoptic phenomenon
Wolf *et al.* (1991)	Erythrocyte	3.28 ± 0.45 Non diabetics 2.89 ± 0.57 Diabetics	Fluorescein, scanning laser ophthalmoscope (SLO)
Arend *et al.* (1991)	Erythrocyte	3.28 ± 0.45 Healthy 2.51 ± 0.88 No retinopathy 2.42 ± 0.40 Background DR 2.28 ± 0.16 Preproliferative DR 2.27 ± 0.58 Proliferative DR	Fluorescein, SLO
Grunwald *et al.* (1993)	Leukocyte	0.92 ± 0.12 for 20–50 y.o. 0.61 ± 0.21 for 50–70 y.o.	Entoptic phenomenon
Scheiner *et al.* (1994)	Leukocyte	0.60 ± 0.07 No flickering 1.01 ± 0.11 16 s Flickering	Entoptic phenomenon
Arend *et al.* (1995)	Erythrocyte Leukocyte	2.68 ± 0.30 0.89 ± 0.20	Fluorescein, SLO Entoptic phenomenon
Yang *et al.* (1997)	Leukocyte	1.37 ± 0.35 1.41 ± 0.29	Fluorescein, SLO Labeled leukocytes, SLO
Paques *et al.* (2000)	Leukocyte	1.43 ± 1.30 In macula 1.82 ± 1.40 In peripapillary area	Labeled leukocytes, SLO
Martin and Roorda (2005)	Leukocyte	1.37 ± 0.29 (0.77–2.10)	Adaptive optics scanning laser ophthalmoscope (AOSLO)
Martin and Roorda (2009)	Leukocyte	1.30 ± 0.40 (0.49–2.31)	AOSLO
Tam and Roorda (2011)	Leukocyte Plasma gap	1.80 ± 0.22 (1.1–2.5) 1.30 ± 0.55 (0.4–1.6)	AOSLO
Tam *et al.* (2011)	Leukocyte	1.82 ± 0.42	AOSLO
Bedggood and Metha (2012)	Erythrocytes	1.30 (0.3–3.3)	AO fundus imaging
de Castro *et al.* (2016)	Erythorcytes	1.14 (0.3–2.23)	Dual channel AOSLO

Abbreviation: DR, diabetic retinopathy.

(0.51 and 0.54 mm s^{-1}, respectively), but reported an increase of velocity in patients with background retinopathy (0.74 mm s^{-1}), and a decrease in the preproliferative stage (0.37 mm s^{-1}), to increase again after photocoagulation (0.42 mm s^{-1}). Additionally, the velocity of the leukocytes is sensitive to neural activity, increasing in the presence of flickering background lights. This velocity increase (Scheiner *et al.*, 1994) occurs about 15 s after the onset of the flickering stimulus and under the conditions used increased more than 50% (from 0.60 to 1.01 mm s^{-1}). In general, velocities measured with the blue field entoptoscope are some of the lower velocity values obtained (**Table 1**), but it is important to note that these are almost certainly leukocytes moving through the capillaries near the foveal avascular zone, which are some of the smallest capillaries, and the slower values may reflect the mechanical constraints on fitting large cells through small capillaries.

Fluorescein Angiography

Fluorescein angiography is a common clinical technique for investigating the health of the retinal vasculature. During fluorescein angiography the fluorescein dye is injected (typically in the arm) and arrives as a dye front at the eye. Because the early phases of the fluorescein angiogram have high contrast it is possible to obtain excellent images of the vascular network. If fluorescein angiograms are collected using video techniques, segments of low and high fluorescence can be observed moving through the capillaries in the parafoveal region of the retina. The segments of low fluorescence are thought to correspond to erythrocytes in rouleaux formation (that is strings of red blood cells closely packed to each other). The cells are not stained by the fluorescein and thus are dark and the more fluorescent segments then correspond to cell-free plasma (Arend *et al.*, 1994). The velocity of the hypofluorescent segments, which are sparse enough to be readily identified, can be determined by measuring

the distance traveled between two frames. Using videos captured with a SLO, an average speed in the perifovea of 3.28 mm s^{-1} was obtained in normal subjects and a lower value (2.89 mm s^{-1}) was observed in diabetics (Arend *et al.*, 1991; Wolf *et al.*, 1991).

While the hypofluorescent segments were assumed to be rouleaux, Yang *et al.* (1997) made measurements on two types of hyperfluorescent signals: hyperfluorescent dots and hyperfluorescent segments. He considered the dots to be leukocytes and measured a speed of 1.37 mm s^{-1} and, similar to Wolf *et al.* (1991), hypothesized that the segments might be the plasma gaps located between erythrocyte rouleaux. The segments moved at a lower velocity that the dots, consistent with the size difference of the particles being tracked. The velocities measured with fluorescein angiography are higher than those obtained with the blue field entoptoscope. This could be because they measure slightly different parts of the retina since with an SLO measurements can be performed at higher eccentricity than when using the blue field entoptic phenomenon (Arend *et al.*, 1995), or perhaps because the visual backgrounds are different leading to a different demand on retinal blood flow. Both techniques provided a background, but that of the SLO is very bright and is actually flickering due to the sequential scan with local intensity varying at approximately 30 frames per second.

Fluorescently Stained Leukocytes

A variant of the fluorescein method involves the use of labeled leukocytes. In this method blood is withdrawn from a subject, leukocytes are separated from the plasma and erythrocytes by centrifugation, and they are stained with fluorescein. When reinjected into the same patient from whom they were extracted the externally stained leukocytes can be observed passing through the capillaries of the retina, providing a very high contrast signal. The velocity can be determined without the risk of aliasing due to the sparse number of stained cells. Thus a single cell can be followed as it changes position over several frames of a video. Yang *et al.* (1997) measured leukocyte velocity using an SLO and measured an average value of 1.41 mm s^{-1}. Paques *et al.* (2000) used a similar method and reported a mean velocity of 1.43 mm s^{-1} in the macula and 1.82 mm s^{-1} in the peripapillary area. This technique is very powerful, and since the subject's own cells are used as a low risk of complications, however, it is not possible in some regions to obtain approvals for its use in humans.

Leukocyte Imaging With AOSLO

Adaptive optics has now enabled imaging at cellular scale in the living human retina (Liang *et al.*, 1997). The first applications to measuring blood flow with adaptive optics used a confocal AOSLO focused on the cone photoreceptors. Under these conditions, dark shadows can be visualized moving across the retina. This motion is most evident in the capillaries close to the fovea. Martin and Roorda (2005) argued that they should be leukocytes and calculated their speed by measuring the distance traveled between several frames giving an average velocity of 1.37 mm s^{-1}, similar to previous studies of leukocytes velocity as discussed above. The velocity of these shadows varies with the cardiac pulse (Martin and Roorda, 2009) with an average minimum speed of 1.0 mm s^{-1} and an average maximum speed of 1.58 mm s^{-1}, resulting in a pulsatility of 0.45. The speed of the leukocytes was also determined by computationally straightening the capillaries and calculating the slope of the changes of intensity along a capillary as a function of time (Tam *et al.*, 2011). In this spatiotemporal plot thick, high contrast and sparse traces and thin, low contrast and dense traces were observed. This pattern of results is consistent with the thick traces being leukocytes and the thin traces corresponding to erythrocytes or plasma gaps between erythrocytes. However, contrary to expectations, the velocity of the leukocytes was found to be higher than the velocity found in plasma gaps (1.80 vs. 1.30 mm s^{-1}) suggesting that either these traces are not a good proxy for erythrocyte velocity or that leukocytes and erythrocytes travel at similar velocities when restricted to single-file capillaries (Tam *et al.*, 2011).

Erythrocyte Imaging With AOSLO

Adaptive optics also allows directly imaging cells in the retinal vessels. If a confocal AOSLO is focused on the small vessels and capillaries, bright moving dots are seen. These can move quite quickly. It is possible to sample these moving cells more densely by momentarily halting the slow direction of the scan. The retinal image at this point become a position versus time image, and the cells are seen as diagonal streaks, with the angle of the streak representing the component of the cell's velocity in the direction of the scan (Zhong *et al.*, 2008). This approach works well for vessels ranging in size from about 15–20 μm in diameter upwards, but at the small end is limited by eye movements, since to capture the entire cardiac cycle the scanning line should remain on the vessel for about 1 s, and micro-saccades and ocular drift can move it off. In animals under anesthesia this or similar techniques (Guevara-Torres *et al.*, 2016) work relatively well, and the advent of highly stabilized AOSLO's hold promise for capillary measurements (Vogel *et al.*, 2006; Burns *et al.*, 2007; Yang *et al.*, 2014). In addition to the eye movements there are other disadvantages of this technique in that not all of the cells are easily seen. Visibility of the cells in a confocal imaging mode is highly dependent on the orientation of the cells and thus brightness can vary rapidly. In addition, there are so many cells that great care needs to be taken to avoid aliasing. The contrast issue can be dealt with by imaging using multiply scattered light imaging (Elsner *et al.*, 2000). This form of imaging improves contrast of vasculature and allows red blood cells to be directly imaged, while traveling through the capillaries (Chui *et al.*, 2012). The potential for aliasing has recently been solved by using two image wavelengths and a scanning system to collect images from the two channels with a slight offset between them

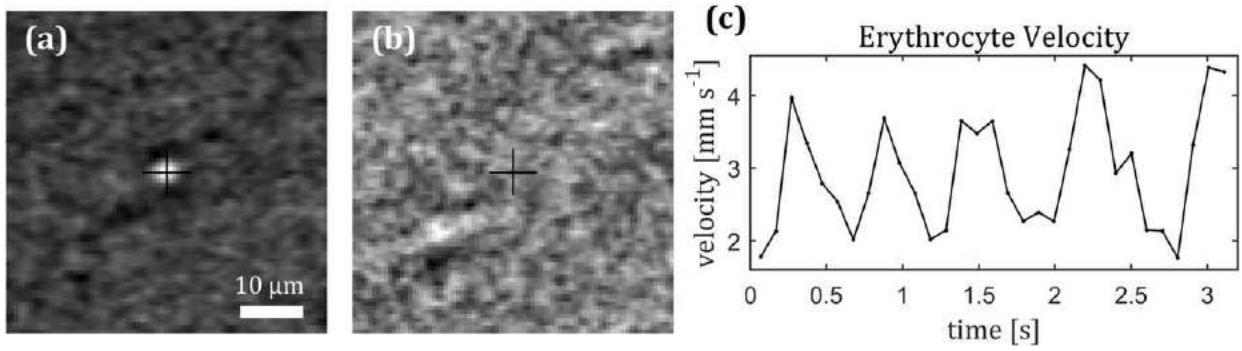


Fig. 2 The erythrocyte position was detected in one of the channels (a) and when studying the same region in the other channel (b) the one with the temporal shift, a displaced image of the same cell was observed. In the figure, the shift of the image of the average cell is used to calculate the velocity at different times (c).

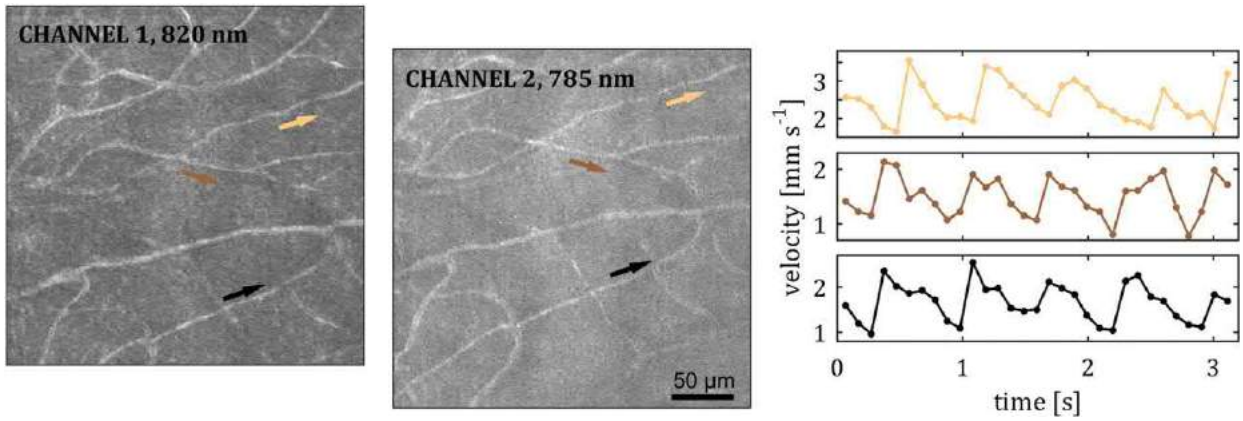


Fig. 3 Using a dual channel scanning laser ophthalmoscope, the velocity of the red blood cells passing through three capillaries was measured simultaneously.

(de Castro *et al.*, 2016). This spatial offset is equivalent to a temporal separation, because the same retinal region is imaged at slightly different times in each channel. By varying the spatial misalignment, the temporal offset can be varied over a wide range of values to match the imaging task. If the displacement is made in a pupil conjugate plane, then it becomes possible to rapidly adjust the temporal separation between channels. Thus by using multiply scattered light imaging and a separation of 71 lines (which corresponds to 4.7 ms, since the frequency of the fast scan was 15.1 kHz), de Castro *et al.* (2016) were able to measure the velocity of the red blood cells in the capillaries of the foveal and parafoveal region (**Fig. 2**). The velocity measurements were pulsatile, with peak values ranging from 0.70 to 3.98 mm s^{-1}. The average velocities of three different subjects, 10 capillaries each, ranged from 0.30 to 2.23 mm s^{-1} with a mean value of 1.14 mm s^{-1}, similar to estimates of other methods although lower than the fluorescein methods (**Table 1**).

To obtain a better signal to noise ratio de Castro *et al.* averaged cell images from three consecutive frames, i.e., one measurement every 107 ms. They were able, under good conditions to determine the velocity at the frame rate of the imaging system, 36 ms. The technique also allowed simultaneous measurements of multiple capillaries within a single field of view, typically between 1.2 and 1.8 degrees. One striking feature of the measurements is that different capillaries within the same video and of the same size have different red blood cell velocities (**Fig. 3**).

Erythrocyte Imaging With Flood Illuminated Adaptive Optics. Particle Image Velocimetry

Adaptive optics can also be used in non-scanning system. Using a flood illuminated adaptive optics ophthalmoscope with a high temporal resolution camera, Bedggood and Metha (2012) were successful in imaging erythrocytes traveling through the capillaries and velocities could be determined with particle image velocimetry methods. To achieve a frame rate of 460 frames per second, the vertical extent of the imaged regions was reduced to 70 μm and images were captured during sequences of 130 ms (60 frames). They found a wide range of velocities (from 0.3 to 3.3 mm s^{-1}, mean 1.3 mm s^{-1}) and a general increase in velocity during the captured time sequences. They reported that the same capillary segments showed different velocities when

imaged several times and also that, within the same sequence, while some capillary segments increased their velocity, others did not. The authors argued that the reason for the increase in velocity during imaging was not neurovascular coupling, since the reaction time in capillaries in animal models as well as the human eye is typically longer (Scheiner *et al.*, 1994) than their imaging time. The advantage of the flood illuminated approach is that image rates can be very high, and corrections for timing arising from the nature of scanning systems are not needed. However, image quality is not as good as with the AOSLO methods due to the lower contrast, and the applicability of this approach to image blood cells in clinical or older populations is not yet known.

Discussion

The literature on blood velocity and blood flow in the eye is very large, and as we have shown, interpretation requires understanding not only the measurement technology, but the biophysical properties of blood flow within different size blood vessels and indeed under different physiological and pathological conditions. However, because flow measurements can be combined with other optical measurements such as oximetry (Delori, 1988) to determine metabolic activity (Blair *et al.*, 2016) the promise to use these techniques for understanding both the normal and abnormal properties of the CNS is great. It is also important to note that most of the techniques have different advantages and disadvantages, and so one particular method may not be ideal to answer all questions.

The different techniques do seem to give different estimates of velocity, and some of these differences may reflect the different components of the blood being used to measure velocity as well as where in the retina they are measured. However, many of the techniques use leukocytes, and while these can be expected to move more slowly through capillaries, since they are much larger, the values found in erythrocytes (Bedggood and Metha, 2012; de Castro *et al.*, 2016) are comparable to those measured on leukocytes using the entoptic phenomenon (Kato, 1952; Riva and Petrig, 1980; Fallon *et al.*, 1986; Grunwald *et al.*, 1993), labeling with fluorescein (Yang *et al.*, 1997; Paques *et al.*, 2000), or direct imaging with AOSLO (Martin and Roorda, 2005, 2009; Tam and Roorda, 2011). However, the peak velocities found with higher temporal resolution using the dual channel AOSLO (de Castro *et al.*, 2016) are only comparable to those obtained injecting intravenous fluorescein (Arend *et al.*, 1991, 1995; Wolf *et al.*, 1991).

Finally, it is clear that there is a lot of variability in the measurements. **Table 1** summarizes measurements of capillary blood velocity. And within any cell class the variability in the velocity measurements is large and this may reflect more than measurement variability, since different capillaries have different speeds and composition of cells (Tam *et al.*, 2011; de Castro *et al.*, 2016; Guevara-Torres *et al.*, 2016).

This natural variation may place a fundamental limit on the simple application of these techniques to clinical measurements, since it will be necessary to obtain sufficient sample sizes to understand the cause of differences. However, it should not be a problem when testing the response of the retina to different conditions within an eye (such as exercise or visual stimulation) since in this case the response of several individual vessels can be compared. Finally, it is important to note that the eye now provides a tissue in which it is possible to measure the entire vascular tree ranging from vessels larger than 100 μm to the smallest capillaries. This will allow improved understanding of the biophysical properties of the entire vascular network and how it responds to stress and disease.

References

Arend, O., Harris, A., Sponsel, W.E., *et al.*, 1995. Macular capillary particle velocities: A blue field and scanning laser comparison. Graefe's Archive for Clinical and Experimental Ophthalmology 233, 244–249.

Arend, O., Harris, A., Wolf, S., 1994. Capillary blood flow velocity measurements in cystoid macular edema with the scanning laser ophthalmoscope. American Journal of Ophthalmology 117, 819–820.

Arend, O., Wolf, S., Jung, F., *et al.*, 1991. Retinal microcirculation in patients with diabetes mellitus: Dynamic and morphological analysis of perifoveal capillary network. British Journal of Ophthalmology 75, 514–518.

Aschinger, G.C., Schmetterer, L., Doblhoff-Dier, V., *et al.*, 2015. Blood flow velocity vector field reconstruction from dual-beam bidirectional doppler oct measurements in retinal veins. Biomedical Optics Express 6, 1599–1615.

Baumann, B., Potsaid, B., Kraus, M.F., *et al.*, 2011. Total retinal blood flow measurement with ultrahigh speed swept source/Fourier domain oct. Biomedical Optics Express 2, 1539–1552.

Bedggood, P., Metha, A., 2012. Direct visualization and characterization of erythrocyte flow in human retinal capillaries. Biomedical Optics Express 3, 3264–3277.

Bishop, J.J., Nance, P.R., Popel, A.S., Intaglietta, M., Johnson, P.C., 2001. Effect of erythrocyte aggregation on velocity profiles in venules. American Journal of Physiology 280, H222–H236.

Blair, N.P., Wanek, J., Felder, A.E., *et al.*, 2016. Inner retinal oxygen delivery, metabolism, and extraction fraction in Ins2akita diabetic mice. Investigative Ophthalmology & Visual Science 57, 5903–5909.

Burns, S.A., Tumbar, R., Elsner, A.E., Ferguson, D., Hammer, D.X., 2007. Large-field-of-view, modular, stabilized, adaptive-optics-based scanning laser ophthalmoscope. Journal of the Optical Society of America A, Optics, Image Science, and Vision 24, 1313–1326.

Chen, Z.P., Milner, T.E., Srinivas, S., *et al.*, 1997. Noninvasive imaging of in vivo blood flow velocity using optical doppler tomography. Optics Letters 22, 1119–1121.

Chui, T.Y.P., Vannasdale, D.A., Burns, S.A., 2012. The use of forward scatter to improve retinal vascular imaging with an adaptive optics scanning laser ophthalmoscope. Biomedical Optics Express 3, 2537–2549.

Dai, C.X., Liu, X.J., Zhang, H.F., Puliafito, C.A., Jiao, S.L., 2013. Absolute retinal blood flow measurement with a dual-beam doppler optical coherence tomography. Investigative Ophthalmology & Visual Science 54, 7998–8003.

Deak, G.G., Schmidt-Erfurth, U., 2013. Imaging of the parafoveal capillary network in diabetes. Current Diabetes Reports 13, 469–475.

de Castro, A., Huang, G., Sawides, L., Luo, T., Burns, S.A., 2016. Rapid high resolution imaging with a dual-channel scanning technique. Optics Letters 41, 1881–1884.
Delori, F.C., 1988. Noninvasive technique for oximetry of blood in retinal vessels. Applied Optics 27, 1113.
Doblhoff-Dier, V., Schmetterer, L., Vilser, W., *et al.*, 2014. Measurement of the total retinal blood flow using dual beam Fourier-domain doppler optical coherence tomography with orthogonal detection planes. Biomedical Optics Express 5, 630–642.
Elsner, A.E., Miura, M., Burns, S.A., *et al.*, 2000. Multiply scattered light tomography and confocal imaging: Detecting neovascularization in age-related macular degeneration. Optics Express 7, 95–106.
Fallon, T.J., Chowiencyzk, P., Kohner, E.M., 1986. Measurement of retinal blood flow in diabetes by the blue-light entoptic phenomenon. British Journal of Ophthalmology 70, 43–46.
Feke, G.T., Riva, C.E., 1978. Laser doppler measurements of blood velocity in human retinal-vessels. Journal of the Optical Society of America 68, 526–531.
Fercher, A.F., Briers, J.D., 1981. Flow visualization by means of single-exposure speckle photography. Optics Communications 37, 326–330.
Fercher, A.F., Hu, H.Z., Vry, U., 1985. Rough surface interferometry with a two-wavelength heterodyne speckle interferometer. Applied Optics 24, 2181–2188.
Ferguson, R.D., Hammer, D.X., Elsner, A.E., Webb, R.H., Burns, S.A., 2004. Wide-field retinal hemodynamic imaging with the tracking scanning laser ophthalmoscope. Optics Express 12, 5198–5208.
Garhöfer, G., Zawinka, C., Resch, H., *et al.*, 2004. Reduced response of retinal vessel diameters to flicker stimulation in patients with diabetes. British Journal of Ophthalmology 88, 887–891.
Grunwald, J.E., Brucker, A.J., Schwartz, S.S., *et al.*, 1990. Diabetic glycemic control and retinal blood-flow. Diabetes 39, 602–607.
Grunwald, J.E., Piltz, J., Patel, N., Bose, S., Riva, C.E., 1993. Effect of aging on retinal macular microcirculation: A blue field simulation study. Investigative Ophthalmology & Visual Science 34, 3609–3613.
Grunwald, J.E., Riva, C.E., Sinclair, S.H., Brucker, A.J., Petrig, B.L., 1986. Laser doppler velocimetry study of retinal circulation in diabetes mellitus. Archives of Ophthalmology 104, 991–996.
Guevara-Torres, A., Joseph, A., Schallek, J.B., 2016. Label free measurement of retinal blood cell flux, velocity, hematocrit and capillary width in the living mouse eye. Biomedical Optics Express 7, 4228–4249.
Jung, F., Kiesewetter, H., Körber, N., *et al.*, 1983. Quantification of characteristic blood-flow parameters in the vessels of the retina with a picture analysis system for video-fluorescence angiograms: Initial findings. Graefe's Archive for Clinical and Experimental Ophthalmology 221, 133–136.
Kato, K., 1952. Studies on the velocity of the blood stream in the retinal capillaries. The Keio Journal of Medicine 1, 251–268.
Kohner, E.M., Patel, V., Rassam, S.M.B., 1995. Role of blood-flow and impaired autoregulation in the pathogenesis of diabetic-retinopathy. Diabetes 44, 603–607.
Kur, J., Newman, E.A., Chan-Ling, T., 2012. Cellular and physiological mechanisms underlying blood flow regulation in the retina and choroid in health and disease. Progress in Retinal and Eye Research 31, 377–406.
Leitgeb, R.A., Schmetterer, L., Hitzenberger, C.K., *et al.*, 2004. Real-time measurement of in vitro flow by Fourier-domain color doppler optical coherence tomography. Optics Letters 29, 171–173.
Liang, J., Williams, D.R., Miller, D.T., 1997. Supernormal vision and high-resolution retinal imaging through adaptive optics. Journal of the Optical Society of America A 14, 2884–2892.
Logean, E., Schmetterer, L., Riva, C.E., 2003. Velocity profile of red blood cells in human retinal vessels by confocal scanning laser Doppler velocimetry. Laser Physics 13, 45–51.
Makita, S., Hong, Y., Yamanari, M., Yatagai, T., Yasuno, Y., 2006. Optical coherence angiography. Optics Express 14, 7821–7840.
Martin, J.A., Roorda, A., 2005. Direct and noninvasive assessment of parafoveal capillary leukocyte velocity. Ophthalmology 112, 2219–2224.
Martin, J.A., Roorda, A., 2009. Pulsatility of parafoveal capillary leukocytes. Experimental Eye Research 88, 356–360.
Paques, M., Boval, B., Richard, S., *et al.*, 2000. Evaluation of fluorescein-labeled autologous leukocytes for examination of retinal circulation in humans. Current Eye Research 21, 560–565.
Pournaras, C.J., Rungger-Brändle, E., Riva, C.E., Hardarson, S.H., Stefansson, E., 2008. Regulation of retinal blood flow in health and disease. Progress in Retinal and Eye Research 27, 284–330.
Riva, C., Benedek, G.B., Ross, B., 1972. Laser Doppler measurements of blood-flow in capillary tubes and retinal arteries. Investigative Ophthalmology 11, 936.
Riva, C.E., Falsini, B., Logean, E., 2001. Flicker-evoked responses of human optic nerve head blood flow: Luminance versus chromatic modulation. Investigative Ophthalmology & Visual Science 42, 756–762.
Riva, C.E., Feke, G.T., Eberli, B., Benary, V., 1979. Bidirectional LDV system for absolute measurement of blood speed in retinal vessels. Applied Optics 18, 2301–2306.
Riva, C.E., Harino, S., Petrig, B.L., Shonat, R.D., 1992. Laser Doppler flowmetry in the optic-nerve. Experimental Eye Research 55, 499–506.
Riva, C.E., Logean, E., Falsini, B., 2005. Visually evoked hemodynamical response and assessment of neurovascular coupling in the optic nerve and retina. Progress in Retinal and Eye Research 24, 183–215.
Riva, C.E., Petrig, B., 1980. Blue field entoptic phenomenon and blood velocity in the retinal capillaries. Journal of the Optical Society of America 70, 1234–1238.
Scheiner, A.J., Riva, C.E., Kazahaya, K., Petrig, B.L., 1994. Effect of flicker on macular blood flow assessed by the blue field simulation technique. Investigative Ophthalmology & Visual Science 35, 3436–3441.
Snodderly, D.M., Weinhaus, R.S., Choi, J.C., 1992. Neural vascular relationships in central retina of macaque monkeys (*Macaca fascicularis*). Journal of Neuroscience 12, 1169–1193.
Suzuki, Y., Masuda, K., Ogino, K., *et al.*, 1991. Measurement of blood-flow velocity in retinal-vessels utilizing laser speckle phenomenon. Japanese Journal of Ophthalmology 35, 4–15.
Tam, J., Roorda, A., 2011. Speed quantification and tracking of moving objects in adaptive optics scanning laser ophthalmoscopy. Journal of Biomedical Optics 16, 036002.
Tam, J., Tiruveedhula, P., Roorda, A., 2011. Characterization of single-file flow through human retinal parafoveal capillaries using an adaptive optics scanning laser ophthalmoscope. Biomedical Optics Express 2, 781–793.
Tokayer, J., Jia, Y., Dhalla, A.H., Huang, D., 2013. Blood flow velocity quantification using split-spectrum amplitude-decorrelation angiography with optical coherence tomography. Biomedical Optics Express 4, 1909–1924.
Villringer, A., Dirnagl, U., 1995. Coupling of brain activity and cerebral blood-flow – Basis of functional neuroimaging. Cerebrovascular and Brain Metabolism Reviews 7, 240–276.
Vogel, C.R., Arathorn, D.W., Roorda, A., Parker, A., 2006. Retinal motion estimation in adaptive optics scanning laser ophthalmoscopy. Optics Express 14, 487–497.
Wang, R.K., Jacques, S.L., Ma, Z., *et al.*, 2007. Three dimensional optical angiography. Optics Express 15, 4083–4097.
Wessing, A., 1974. Fluorescence-television-angiography of retina and anterior segments of eye with highly sensitive television photographic valves. Klinische Monatsblatter Fur Augenheilkunde 165, 817–822.
Westphal, V., Yazdanfar, S., Rollins, A.M., Izatt, J.A., 2002. Real-time, high velocity-resolution color doppler optical coherence tomography. Optics Letters 27, 34–36.
White, B.R., Pierce, M.C., Nassif, N., *et al.*, 2003. In vivo dynamic human retinal blood flow imaging using ultra-high-speed spectral domain optical doppler tomography. Optics Express 11, 3490–3497.
Willerslev, A., Li, X.Q., Munch, I.C., Larsen, M., 2014. Flow patterns on spectral-domain optical coherence tomography reveal flow directions at retinal vessel bifurcations. Acta Ophthalmologica 92, 461–464.
Wolf, S., Arend, O., Toonen, H., *et al.*, 1991. Retinal capillary blood flow measurement with a scanning laser ophthalmoscope. Preliminary Results. Ophthalmology 98, 996–1000.

Wolf, S., Jung, F., Kiesewetter, H., Korber, N., Reim, M., 1989. Video fluorescein angiography – Method and clinical-application. Graefes Archive for Clinical and Experimental Ophthalmology 227, 145–151.

Wolf, S., Toonen, H., Arend, O., *et al.*, 1990. Retinal capillary bloodflow measurement by means of a scanning laser ophthalmoscope. Biomedizinische Technik 35, 131–134.

Yang, Q., Zhang, J., Nozato, K., *et al.*, 2014. Closed-loop optical stabilization and digital image registration in adaptive optics scanning light ophthalmoscopy. Biomedical Optics Express 5, 3174–3191.

Yang, Y., Kim, S., Kim, J., 1997. Fluorescent dots in fluorescein angiography and fluorescein leukocyte angiography using a scanning laser ophthalmoscope in humans. Ophthalmology 104, 1670–1676.

Zhong, Z., Huang, G., Chui, T.Y.P., Petrig, B.L., Burns, S.A., 2012. Local flicker stimulation evokes local retinal blood velocity changes. Journal of Vision 12, 3.

Zhong, Z., Petrig, B.L., Qi, X., Burns, S.A., 2008. In vivo measurement of erythrocyte velocity and retinal blood flow using adaptive optics scanning laser ophthalmoscopy. Optics Express 16, 12746–12756.

Zhong, Z., Song, H., Chui, T.Y.P., Petrig, B.L., Burns, S.A., 2011. Noninvasive measurements and analysis of blood velocity profiles in human retinal vessels. Investigative Ophthalmology & Visual Science 52, 4151–4157.

Adaptive Optics Retinal Imaging Techniques and Clinical Applications

Jessica IW Morgan, University of Pennsylvania, Philadelphia, PA, United States

© 2018 Elsevier Ltd. All rights reserved.

Introduction

Ophthalmoscopy is a fundamental part of a fundus exam, because it allows observation of the retina through the natural optics of the eye. Since the first fundus photograph was taken in 1886 (Jackman and Webster, 1886), numerous modalities for ocular imaging have been developed. However, the overarching goal of these imaging techniques remains stationary: to understand the structure and function of the normal visual system and to assist in the diagnosis, prognosis, and treatment of the diseased visual system. The purpose of this current article is to describe state-of-the-art adaptive optics (AO) high-resolution ophthalmic imaging, the detection schemes used in different AO imaging modalities, the current analysis methods utilized for interpreting high-resolution AO images of the outer retina, and a brief discussion of the current and future clinical applications for this technology.

Optical Limitations for Imaging in the Eye

One can think of retinal imaging in the same terms as imaging with a microscope, where the retina is the sample to be imaged and the optical components of the eye provide the final objective lens in front of the sample. All optical systems, including the eye, are limited in resolution by their point spread function (psf), which is defined as the volume of space over which a focused point of light extends. Therefore the resolution of a retinal image, regardless of which imaging modality or detection scheme is employed, will be limited by the size of the eye's psf. The eye's psf in turn is dependent upon the quality of the optical components of the eye (the cornea and lens) as well as the limiting aperture of the eye (the pupil). For an ideal, aberration-free eye, the psf would be determined by diffraction through the pupil. In the diffraction limit, the spatial extent of the psf decreases with increasing pupil diameter, leading to the resolution limit:

$$l_{\text{transverse}} = \frac{1.22 f \lambda_0}{D}$$

where f is the focal length of the eye, λ is the central imaging wavelength, and D is the pupil diameter. Unfortunately, the cornea and lens of the real eye are not ideal optical elements; these elements impose optical aberrations on light entering (or reflected out of) the eye, and thereby increase the size of the psf beyond that of the diffraction limit. For real eyes with pupil diameters that are 2 mm or smaller, the size of the psf is dominated mainly by diffraction. However, for pupil diameters larger than 2 mm, ocular aberrations become the dominant factor for determining the extent of the psf (Packer and Williams, 2003). In theory, eliminating the optical aberrations imposed on light entering or exiting the eye by the cornea and lens would reduce the size of the psf to that observed in the diffraction limiting case, even at large pupil sizes. Optically compensating for the eye's optical aberrations thus becomes the main concept behind high-resolution AO ophthalmoscopy.

AO

AO is a technique first proposed by astronomers to measure and correct for optical aberrations imposed by turbulence in earth's atmosphere (Babcock, 1953). Incorporating this technique into ground-based telescopes resulted in improvements in transverse resolution and contrast of astrological images. The same concept was applied to ophthalmoscopy by Liang *et al.* (1997). The goal of AO ophthalmoscopy is straightforward: first measure, then correct for the optical aberrations of the living eye in order to attain diffraction limited resolution through large pupil sizes.

Ophthalmic AO systems typically use a Shack–Hartman wavefront sensor to measure the optical aberrations of the eye. This consists of a lenslet array and a two-dimensional (2D) camera. The lenslet array is placed at a plane optically conjugate with the eye's pupil. Each lenslet of the array focuses a small section of the wavefront to a single spot on the camera. For an ideal, aberration-free optical system, the result is a perfectly spaced 2D grid of focused spots, called the reference. For an aberrated system, such as the real eye, the arrangement of focused spots will be distorted from the perfectly spaced reference grid, and the x and y displacement of each focused spot from its ideal reference location allows a direct calculation of the wave aberration at the location of the lenslet within the pupil plane (Liang *et al.*, 1994).

After the wavefront sensor, the second critical component for an AO system is the wavefront corrector. This optical element also is placed optically conjugate with the eye's pupil and therefore the lenslet array of the Shack–Hartman wavefront sensor. Ophthalmic AO systems typically use a deformable mirror for this purpose, but other techniques, such as liquid crystal spatial light modulators, also can be used. The shape of the deformable mirror is adjusted to be one half of the amplitude of the wave

 doi:10.1016/B978-0-12-803581-8.09777-0

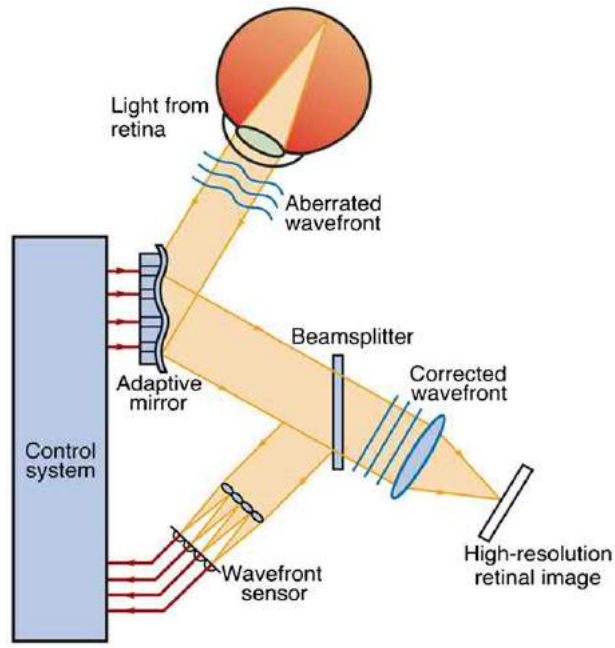


Fig. 1 Schematic diagram of wavefront measurement and adaptive optics (AO) correction. Reprinted from Carroll, J., Gray, D.C., Roorda, A., Williams, D.R., 2005. Recent advances in retinal imaging with adaptive optics. Optics and Photonics News 16, 36–42 with permission from Joseph Carroll.

aberration at each point in the pupil, such that the imposed phase delay at each point in the pupil results in a (close-to) aberration-free wavefront that when measured using the Shack–Hartman wavefront sensor approaches the reference grid of focus spots. This AO correction yields an aberration corrected psf for the eye, which is thus close to that of the diffraction limit, even for dilated pupils. A schematic diagram of wavefront measurement and AO correction is shown in **Fig. 1** (Carroll *et al.*, 2005). Most state-of-the-art AO systems run in closed loop with real-time AO correction occurring multiple times per second, as has been shown to provide improved AO quality in comparison with open loop systems (Hofer *et al.*, 2001). Retinal imaging with a visible or near infrared light source (400–900 nm) incorporating AO correction over a dilated pupil (7 mm) provides sufficient transverse resolution for observing individual cells in the living retina, noninvasively.

AO Retinal Imaging

It is important to note that AO on its own is not a method of retinal imaging. Rather, AO is a tool used to increase the transverse resolution of a given imaging modality by correcting the optical aberrations of the eye. To obtain an AO retinal image, AO must be incorporated with technologies that encompass retinal image acquisition techniques. Here we describe three such retinal imaging modalities, AO flood-illuminated ophthalmoscopy, AO scanning laser/light ophthalmoscopy (AOSLO), and AO-optical coherence tomography (AO-OCT), and discuss applications of these three imaging techniques for studying the structure and function of the normal and diseased retina.

AO Flood-Illuminated Ophthalmoscopy

The first application of AO to ophthalmoscopy occurred when Liang, Williams, and Miller incorporated AO correction into a flood-illuminated fundus camera (Liang *et al.*, 1997). A fundus camera system involves using a light source to uniformly illuminate a patch of retina and a 2D science camera to record the backscattered light from that same retinal patch. Considerations for imaging include ensuring investigators use only non-phototoxic (ocularly safe) amounts of light to illuminate the retina and a camera sensitive enough to capture the low reflective signal returning back from the retina and through the pupil of the eye. The first report of AO corrected fundus photography showed improvement in both contrast and resolution in images of the cone photoreceptors in comparison to non-AO corrected images of the same retinal patch. Since this early work, improvements in both light sources and the speed of digital cameras have made possible high frame acquisition rates using AO corrected flood-illumination retinal imaging.

An important consideration for flood-illuminated retinal imaging systems is the image exposure time. One property of flood-illuminated systems is that all pixels within the 2D image are acquired at the same time. This is an advantage in that the retinal

image incorporates few distortions and thus the spatial relationship between features in the image represents true retinal anatomy. On the other hand, the eye is continually undergoing fixational eye motion, and thus, any eye motion that occurs during the image exposure/acquisition time will result in a blurring of retinal features. For imaging microscopic features, such as the individual cones in the photoreceptor mosaic, even small eye movements can result in blurring out the contrast between neighboring cones. By limiting the exposure time of a single image to less than 10 msec, Rha *et al.* (2006) found most retinal images exhibited cone mosaic structure, and thus concluded that blurring from fixational eye motion was minimal when using this short exposure duration. Early applications of AO flood-illumination ophthalmoscopy demonstrated the arrangement and variability of the three cone classes in the trichromatic cone mosaic (Roorda and Williams, 1999) and loss of waveguiding cones in a dichromat (Carroll *et al.*, 2004) and in patients with inherited retinal degenerations (Wolfing *et al.*, 2006). In addition, AO flood-illumination ophthalmoscopy has been used to examine the reflectance of cones over time both in the absence and presence of visual stimuli (Pallikaris *et al.*, 2003; Jonnal *et al.*, 2007).

AO Scanning Laser/Light Ophthalmoscopy

Scanning laser/light ophthalmoscopy (SLO) was the second retinal imaging modality to incorporate AO correction (Roorda *et al.*, 2002). SLO operates by focusing a point source of light (a laser or super-luminescent diode) to the retina, and using a point detector, such as a photomultiplier tube (PMT), to detect the backscattered (or emitted) light from that point. The point source on the retina is then repeatedly raster scanned in 2D, and the time-sync between the scanners and the point detector is used to construct a 2D image sequence based on the x, y position of the scanned beam on the retina. A feature of this image collection paradigm is that each pixel of the image sequence is obtained at a different point in time, yielding real-time movies of the retina, but including in the raw data all eye movements. Even when asked to hold the eye perfectly still, subjects experience involuntary eye movements; this involuntary motion exists not only between frames of the image sequence (inter-frame motion), but also within frames of the image sequence (intra-frame motion). Intra-frame motion complicates the registration and averaging of multiple frames together, but results in precise measurements of fixational eye motion (Sheehy *et al.*, 2015). Again, the transverse resolution of an SLO is limited by the eye's psf, which is improved when using AO aberration correction.

Most AOSLO imaging systems place a pinhole in front of the photodetector that is confocal with the retinal layer of interest in order to reduce the amount of backscattered light detected from retinal layers other than the plane of focus. This results in improved contrast in the retinal image in comparison with flood-illuminated AO systems. Using a confocal pinhole also provides coarse axial sectioning through the retinal layers. While the psf provides the transverse resolution, the size of the confocal pinhole provides the axial resolution for an AOSLO system. Close-to diffraction limited systems with just over 1 Airy disk-sized confocal pinholes have demonstrated axial resolutions of $\sim$50 μm (Venkateswaran *et al.*, 2004). The first application of confocal AOSLO by Roorda *et al.* (2002) demonstrated the coarse axial sectioning obtained by imaging waveguiding photoreceptor reflectance, blood flow through the retinal capillaries, and reflectance of the nerve fiber layer at the same retinal location. Confocal AOSLO imaging is the most often applied AO imaging modality to date. Among numerous other applications, this imaging paradigm has enabled routine observation of the cone and rod photoreceptor waveguiding reflectance mosaic in normal sighted individuals (**Fig. 2**) and

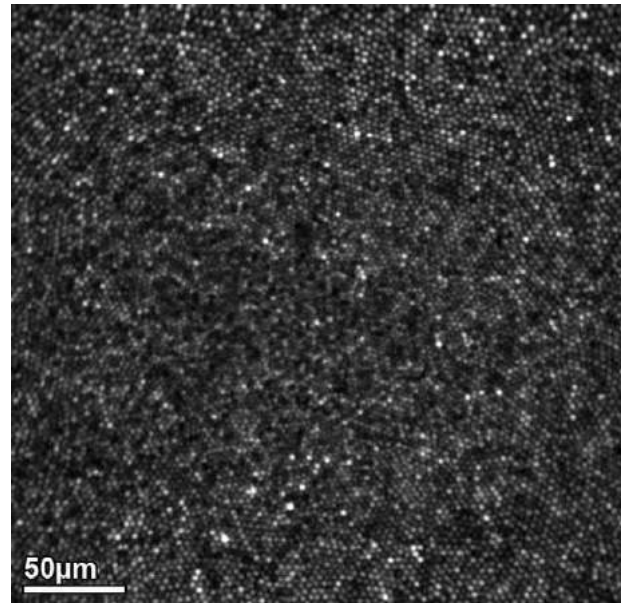


Fig. 2 Confocal adaptive optics scanning laser/light ophthalmoscopy (AOSLO) image of the foveal cone mosaic from a normal sighted control.

in patients with retinal disease, visualization of the parafoveal capillaries, the retinal vascular network and blood flow in normal sighted individuals and in patients with diabetes, and examination of the lamina cribrosa (for a recent review describing AOSLO image findings in disease, see Morgan, 2016).

Again, the AOSLO is analogous to a scanning microscope, so just as in microscopy, one can manipulate the illumination and the detection beams in the system to attain different views of the retinal structure other than those obtained from confocal reflectance. One demonstration of this came from combining autofluorescence imaging with AOSLO to visualize the retinal pigment epithelium (RPE) in human and nonhuman primates (Morgan *et al.*, 2009). The RPE cytoplasm contains inherently fluorescent lipofuscin, a byproduct of the natural processes of phototransduction and phagocytosis. Lipofuscin granules consist of a conglomeration of multiple molecules that when excited with a short wavelength in the visible spectrum (blue/green) emit with a longer visible wavelength (red). Unfortunately, the autofluorescence signal from lipofuscin is low – too low to observe cellular structure in an individual autofluorescence AOSLO frame and too low for using the autofluorescence signal to register multiple frames together. Safety limits for ocular light exposures prevent simply increasing the excitation irradiance until a usable signal is obtained. To overcome these problems, Morgan *et al.* (2009) used simultaneous autofluorescence and confocal reflectance imaging to obtain two temporally and spatially synced retinal images, one with the low signal to noise autofluorescence signal and the other with the high signal to noise confocal reflectance signal. The high signal to noise reflectance images were used to determine the fixational eye motion present from frame to frame, and thus the lateral translation required to stabilize the image sequence. Since the autofluorescence image was acquired simultaneously, the fixational eye motion present in the autofluorescence image sequence was the same as the fixational eye motion present in the reflectance image sequence. Morgan *et al.* then applied the same lateral translations needed to stabilize the reflectance image to the autofluorescence image sequence and integrated the autofluorescence signal over the full image series. This novel image processing technique enabled visualization of the RPE cell mosaic in living humans (**Fig. 3**) and nonhuman primates and is routinely used to co-register simultaneously captured image sequences regardless of signal strength.

Autofluorescence imaging of the RPE lipofuscin was a natural extension from confocal AOSLO reflectance imaging because of the intrinsic contrast provided by the autofluorescent material in the retina. However, fluorescent imaging in the retina is not limited to autofluorescence of lipofuscin, but rather can be extended to other fluorescent markers as well. The general technique is to use the appropriate excitation and emission wavelengths for the fluorophore of interest, and attain a signal with enough spatial contrast to allow observation of the feature of interest in the final image. Fluorescence imaging with AOSLO has been demonstrated using both fluorescein (Chui *et al.*, 2014) and indocyanine green (ICG), both of which are fluorescent dyes approved for injection to the bloodstream, and which are generally used in ophthalmic imaging to elucidate abnormalities in the retinal and choroidal blood vessels. ICG has also been shown to provide additional contrast for viewing RPE cells (Tam *et al.*, 2016). Other fluorophores in the retina can provide the needed signal and contrast; fluorescence of cells tagged with fluorescent markers have been demonstrated in nonhuman primates and rodents (Geng *et al.*, 2012), two photon fluorescence has been demonstrated in nonhuman primates (Sharma *et al.*, 2016), and single photon intrinsic infrared autofluorescence of melanin in humans and other species holds promise. Regardless of the fluorophore being excited, successful AOSLO (or AO flood illumination) fluorescence imaging requires: (1) the presence of a fluorophore with spatial contrast; (2) an excitation and emission spectra that will pass

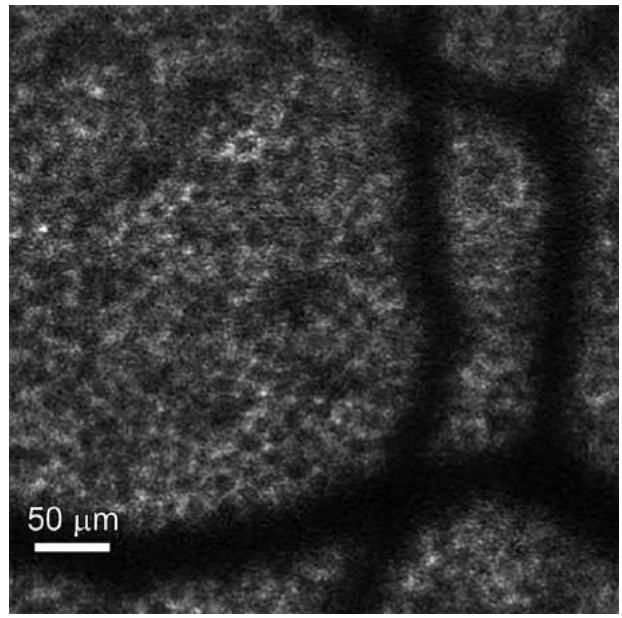


Fig. 3 Autofluorescence image of the retinal pigment epithelium (RPE) mosaic at approximately 20 degrees superior to fixation in a normal sighted control.

through the optics of the eye; (3) safe (non-phototoxic) excitation; and (4) sufficient quantity of emitted signal which is captured by the detector.

For more than the first decade following the invention of AOSLO, both reflectance and fluorescence imaging was done using a confocal pinhole in front of the point detector as described above. Then, in 2012, Chui *et al.* (2012) published a study in which the authors offset the pinhole from its central position, effectively blocking confocal reflectance and capturing a portion of the non-confocal multiply scattered light from the retina. This study demonstrated the advantage of this method for imaging retinal vasculature, and became the first of a series of imaging innovations using non-confocal AOSLO detection techniques (**Fig. 4**), each of which showed distinct advantages for elucidating various retinal structures. The second non-confocal AOSLO detection technique described, termed dark-field (Scoles *et al.*, 2013), involved excluding the light that would normally pass through the confocal pinhole and detecting the light passing through an annulus surrounding the blocked pinhole. This technique captured the non-confocal multiply scattered light in the retina, and allowed visualization of the RPE cells in normal retina at some locations without using fluorescence techniques (**Fig. 5**). Non-confocal "split detection" shortly followed in which the dark-field signal was split in half using a knife edge and two images (one from each side of the knife edge) were captured simultaneously using two separate detectors. The two images were then recombined using the following equation:

$$I_{x,y_{\text{split}}} = \frac{I_{x,y_{\text{det}_1}} - I_{x,y_{\text{det}_2}}}{I_{x,y_{\text{det}_1}} + I_{x,y_{\text{det}_2}}} + 128$$

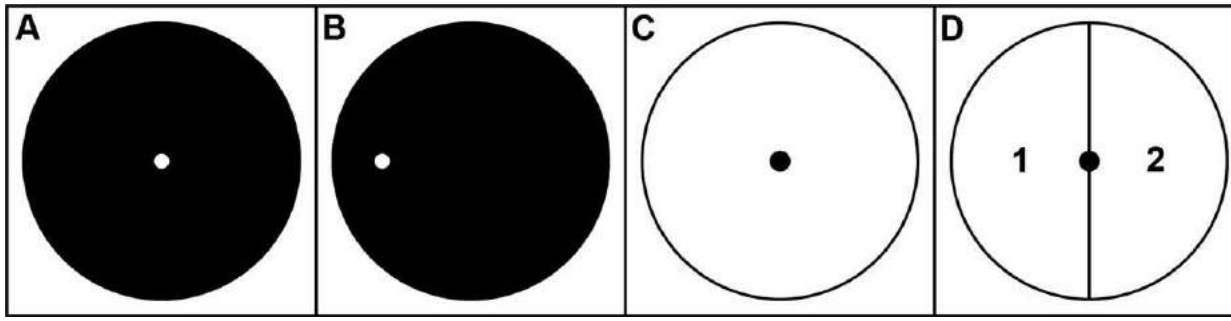


Fig. 4 Adaptive optics scanning laser/light ophthalmoscopy (AOSLO) detection schemes showing the spatial extent of the retinal plane over which light is blocked from (black) or captured by (white) the point detector. (A) Confocal. (B) Offset pinhole. (C) Dark-field. (D) Non-confocal split detection, where two point detectors are used and the two images are recombined using their difference divided by their sum to form the non-confocal split detection image.

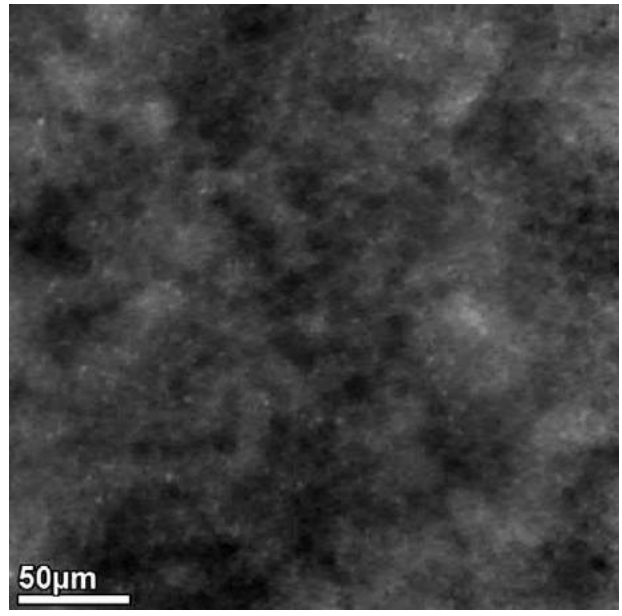


Fig. 5 Dark-field adaptive optics scanning laser/light ophthalmoscopy (AOSLO) image of the retinal pigment epithelium (RPE) mosaic from a normal sighted control.

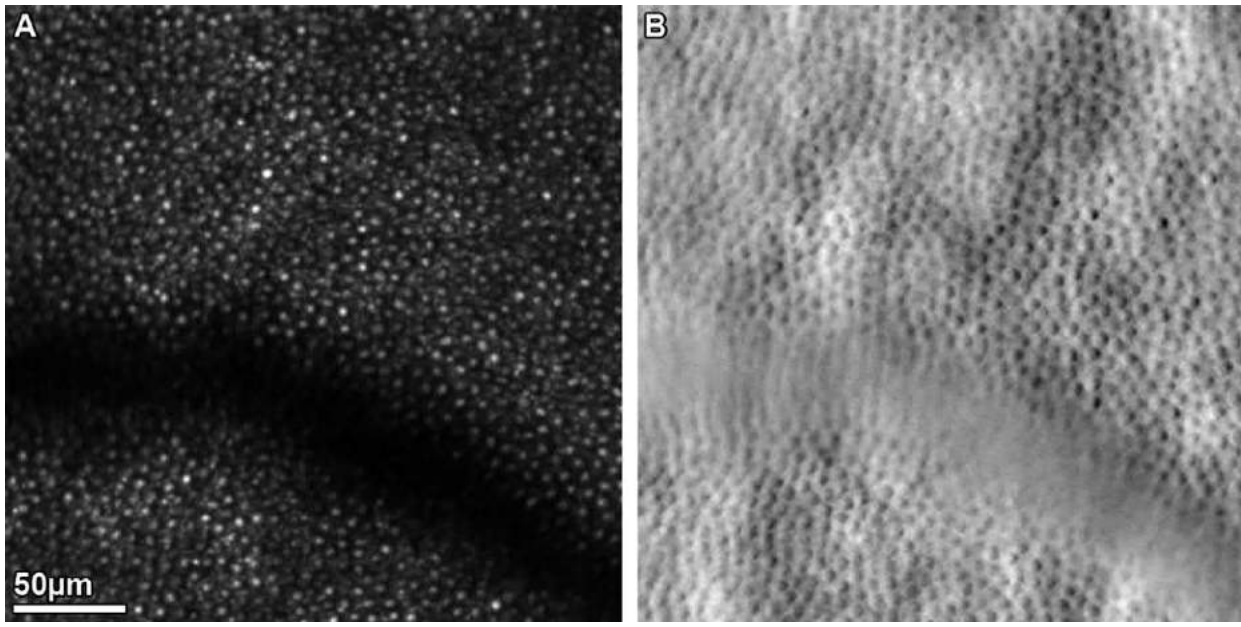


Fig. 6 Confocal (A) and non-confocal split detection (B) adaptive optics scanning laser/light ophthalmoscopy (AOSLO) image of the photoreceptor mosaic from a normal sighted control.

where $I_{x,y}$ is the image intensity at each pixel in the images from the two non-confocal detectors. This detection scheme resulted in the first in vivo images of the photoreceptor inner segment mosaic (**Fig. 6**; Scoles *et al.*, 2014). The technique also showed improvements in contrast of vasculature, with greater improvements visible in blood vessels running parallel to the direction of the knife edge. Noteworthy is that the denominator of the split detection equation above is simply the dark-field image. Thus one significant advantage of combining non-confocal split detection with confocal AOSLO imaging is that by using three separate point detectors, the confocal, non-confocal split detection, and dark-field images all can be acquired simultaneously. In theory, this allows investigators to observe the photoreceptor waveguided reflectance mosaic, the inner segment mosaic, and the RPE mosaic at the same location at the same time. In practice, slight differences in the optimal focus level for each cell class sometimes requires sequential imaging of the multiple retinal layers. In addition, RPE imaging with dark-field to date has not proven 100% successful, since there can be significant cross-talk between the photoreceptor mosaic images and the RPE (Scoles *et al.*, 2013). Regardless, the technique of simultaneously collecting multiple images under these difference detection configurations holds promise for studying retina structure at the cellular level in normal sighted individuals and in patients with retinal disease. Finally, other configurations of knife edge and offset pinhole arrangements have led to the first in vivo images of inner retinal neurons in mice (Guevara-Torres *et al.*, 2015), nonhuman primates and humans (Rossi *et al.*, 2017). Innovation surrounding AOSLO illumination and detection schemes have clearly provided methods to elucidate contrast between cells that are transparent under standard reflectance and confocal detection techniques. Undoubtedly, investigators will continue to explore novel methods for noninvasive imaging of additional retinal cell types, and work to optimize imaging conditions to allow routine observation of multiple cell types in the presence and absence of disease.

AO-OCT

While AO provides high transverse resolution as described above, optical coherence tomography (OCT) provides high axial resolution. Time-domain OCT (without AO) was first demonstrated by Huang *et al.* (1991). In time-domain OCT, interference signals are measured between the retina and reflections from a reference arm of an interferometer as it is translated in depth. The inference signal generated using this paradigm is used to create a one-dimensional (1D) cross-sectional image (A-scan) showing the relative depth of each backscattering layer in the retina. Following the acquisition of a single A-scan, the OCT beam is laterally translated on the retina so that the location of the subsequent A-scan is adjacent to the previous one, thereby creating a 2D cross-sectional image (B-scan) of the retina, built up over time. Raster scanning the location of the A-scan in 2D creates a three-dimensional (3D) volumetric OCT data set.

Applications for time-domain OCT were limited by the A-scan acquisition rate, which in turn was limited by the time needed to physically move the reference arm through the depth corresponding to the dimension of each A-scan. Keeping the reference arm static during the A-scan acquisition would in part overcome the limitation imposed by acquisition time but required further technological innovation within the OCT imaging technique. Spectral domain OCT and swept source OCT provided this needed innovation by operating in the spectral regime and utilizing a stationary detector (using a spectrometer to detect the OCT signal or

a tunable light source that is rapidly swept through a broad band, respectively). State-of-the-art OCT systems all take advantage of the increased imaging speeds and higher sensitivity afforded by spectral domain OCT methods in comparison to time-domain OCT (Choma *et al.*, 2003).

The properties governing the transverse and axial resolution in OCT are independent, making OCT a perfect complement for AO. As described above, the transverse resolution of OCT is governed by the eye's psf. The axial resolution, however, is dependent only on the central imaging wavelength (λ_0) and the bandwidth of the imaging source ($\Delta\lambda$).

$$l_{\text{axial}_{\text{OCT}}} \propto \frac{{\lambda_0}^2}{\Delta\lambda}$$

Combining AO with OCT yields subcellular resolution in all dimensions, in theory enabling subcellular volumetric imaging in the living retina. The first application of AO-OCT was by Hermann *et al.* (2004). Since that time numerous groups have utilized AO-OCT to acquire volume data sets of the retina with increased resolution, in particular, showing axial reflections arising from the inner/outer segment junction (also termed ellipsoid layer) and cone/rod outer segment tips. More recently, improvements in software to allow intra-scan registration and hardware to use multiple synchronized detectors to further increase scan acquisition speed (Kocaoglu *et al.*, 2014) have led to AO-OCT images showing the inner/outer segment junctions of the cones, the cone outer segment tips, the RPE mosaic, and the choroicapillaris (Kocaoglu *et al.*, 2016; Liu *et al.*, 2016). AO-OCT imaging has also enabled visualization of the individual cells within the retinal volume corresponding to the ganglion cell bodies, showing not only the individual ganglion cells in a monolayer, but also the individual ganglion cells piled on top of each other in depth (Liu *et al.*, 2017). Applications for AO-OCT imaging abound, especially now that the technology has reached a point where the inner retinal cells can be visualized. To date, however, AO-OCT technology has not been as widely adopted as the AOSLO or AO flood-illumination imaging techniques.

Post Processing and AO Image Analysis

Each of the AO imaging modalities described above results in the acquisition of a retinal image with cellular resolution. Regardless of the imaging modality used, the signal to noise ratio of the retinal image can be improved by averaging multiple images together. Other applications gain an increase in contrast (e.g., motion contrast) by comparing retinal features between sequentially acquired images. Both averaging and comparing sequential images require co-registration of the images. Further, the images obtained using AO imaging systems generally span a field of view of two degrees per side or less (with some exceptions, that then sacrifice sampling density by enlarging pixel size). To cover a larger field of view, investigators typically acquire multiple images adjacent to one another, and in post-processing analysis stitch them together to observe a larger portion of the retina. The result of both multi-frame averaging and multi-image location montaging, means that post processing of AO images regularly occurs. While the concept of averaging and montaging is valid for all the imaging modalities discussed, the image processing steps undertaken must take into account the nature and properties of the acquisition modality being used. For example, a series of frames acquired using a flood-illuminated system at nominally the same retinal location may show translation and rotation between frames, though each frame individually should be free from motion artifacts (assuming the involuntary eye motions of the subject are minimal over the acquisition time of the image as was shown for most images acquired in less than 10 ms). Thus co-alignment of multiple images can be accomplished by finding the optimal transformation to account for the translation and rotation between individual frames using cross-correlation or other comparative algorithms, such as the scale invariant features transform (SIFT). Once the individual images are transformed to be co-aligned, a simple average of the aligned frames provides a higher signal to noise retinal image than an individual frame, and this averaged image from flood-illuminated AO systems is mostly free of motion artifacts.

In comparison, the image processing for both AOSLO and AO-OCT images is more involved, since both techniques are acquired over a period of time throughout which the eye is continually undergoing involuntary eye motions. This results not only in the inter-frame/inter-scan translation and rotation motion described in the flood illumination acquisition condition but also motion within a frame/scan, considered intra-frame/intra-scan motion. An added complication for scanning systems comes from any nonlinearities in the scanner velocity. For example, most AOSLO systems use a fast resonant scanner with a sinusoidal velocity. Evenly sampled pixels in time then result in a sinusoidal distortion in the pixel scale across the frame along the direction parallel to the scanner motion, with pixels on the edges of the image elongated in comparison with pixels closer to the middle of the frame, which are more compressed. These same types of lateral distortions are present in OCT images acquired with systems that also use a nonlinear scanner. The first step of image post-processing is to de-warp the images to remove any effect from a nonlinear scan velocity. The second step is to average together multiple dewarped frames. This is routinely done using an intra-frame registration algorithm, which involves first choosing a reference frame (in the ideal case free from intra-frame motion), second dividing the remaining frames into strips (along the fast scan direction), and third, registering each of these strips to the reference frame (Dubra and Harvey, 2010). The product of this intra-frame 2D registration is to allow averaging of multiple frames to increase the signal to noise ratio of the final registered image, while removing the intra-frame motion from frames other than the reference, which would otherwise blur the features in the image. Unfortunately, this technique does not correct intra-frame motion contained within the selected reference image, and thus the final averaged image will necessarily contain the same spatial distortions that exist within the reference image. At present there is no widely accepted technique for correcting the intra-frame motion within the reference frame, though solutions for using multiple reference frames to identify the ground truth for the image have been proposed

(Cooper *et al.*, 2016a,b; Bedggood and Metha, 2017). In comparison with AOSLO, AO-OCT image registration and averaging has the added complication that the retina is moving in 3D, so registering adjacent A-scans to account for axial movements throughout a B-scan and volumetric data set is also required.

Following multi-frame registration and averaging, adjacent images or volumetric data sets must be montaged to expand the field of view from the small field acquired over a single imaging location to a larger field covering a bigger portion of the retina. Most montaging to date has been done manually, however, an automated montaging algorithm was recently described and validated at the cellular level by Chen *et al.* (2016). The automated algorithm was based on feature matching between images using a combination of SIFT and random sample consensus (RANSAC) functions and the resultant automated montage was of comparable quality to manual montages made from the same image sets. While the software was only validated using images acquired from an AOSLO, the authors speculated that the algorithm would also work on *en face* images acquired under other AO imaging modalities.

Metrics to Analyze Cell Mosaics

AO imaging has enabled visualization of many layers and cell types in the retina, and with this visualization comes the desire to quantify metrics within the image to assess retinal health. To date the most studied feature of AO images remains the waveguided reflectance of the cone photoreceptors. As a result, the most quantification of AO images has been done on the cone mosaic. The discussion of AO metrics below describes what has been done to date and therefore is heavily focused on analysis of the cone mosaic. However, the techniques described here could be applied to any cell mosaic visualized, and almost assuredly will be applied to other cell classes beyond the cone mosaic as they become imaged more routinely.

As described above, AO ophthalmoscopy has enabled routine imaging of the cone mosaic both in normal sighted individuals and in patients with retinal disease. With the ability to observe waveguiding cones, comes the ability to identify cone locations and then quantify parameters of the cone mosaic as a function of retinal eccentricity. Numerous metrics have been used to quantify the structure of the cone mosaic including: cone density, average cone spacing, cone size, mosaic regularity, number of neighbors, nearest/farthest neighbor spacing, cone orientation, and others (Cooper *et al.*, 2016a,b). Each metric has its own set of advantages and disadvantages, and thus the best characterization of a mosaic may be a combination of multiple metrics. However, all mosaic metrics share one thing in common: prior to quantification, investigators must first determine the location of each cone in the mosaic. In addition, regardless of which metric is used, all contiguous cones within the analyzed region must be identified in order to obtain the most accurate results.

Determining the cone locations is many times done in a semi-automated fashion. Initially, cone locations are found by automated algorithms, such as the one described by Li and Roorda (2007), which identify local intensity maxima in an image, while also imposing restrictions on the location of the local maxima (such as a minimum spacing between maxima to eliminate false positives from noise and multiple counts for a single cone). Generally, automated cone selections are then manually reviewed to allow an operator to add cone locations (correct false negatives from the automated algorithm), and remove or move cone locations (correct false positives from the automated algorithm). To date, no automated cone identification software has proven itself superior enough to eliminate the need for manual review. In addition, there are many times when automated algorithms currently will fail, in particular, in cases of disease where cones may not exhibit normal reflectance or spacing patterns. Since automated algorithms are just searching for local maxima within an image, the algorithms at present will find "cones" in any image, so operators must inspect images prior to using automated cone selection algorithms and must review the algorithm's output in order to maintain high quality cone identifications. Automated algorithms have also been presented for identifying the cone inner segments in split detection images and the RPE cells in autofluorescence images. Regardless of the imaging modality or automated algorithm, manual inspection of the results remains necessary. Manually/semi-automated grading of normal cone locations has been shown to be repeatable and reliable between graders (**Fig. 7**).

Once cone (or other cell) locations are identified, a number of metrics can be applied to determine parameters of the mosaic at a given retinal location, both in normal and diseased eyes. The two most commonly used mosaic parameters are cone density and cone spacing. Cone density simply counts the number of cells identified over a given area. Typically, cell spacing is found by the density recovery profile (DRP) algorithm, which first measures the distance between each pair of identified cones in an image, second determines a histogram of distances by placing the paired distances into bins, and third identifies the distance at which the first peak of the histogram occurs. Distances between cells can also be used to identify the average nearest/farthest neighbor spacing. In a perfectly regular triangularly packed mosaic, the nearest, farthest, and DRP cone spacing would all be the same. Thus the width of the DRP histogram, or the variability in any of the cell spacing metrics gives information regarding the regularity of the cell mosaic.

Regularity can also be assessed through calculation of the Voronoi diagram, which assigns each pixel in the image to its nearest cell center; boundaries of the Voronoi diagram correspond to midpoints between cell locations and vertices correspond to locations equidistant to three cell centers. This type of analysis allows quantification of the average and standard deviation of the number of Voronoi neighbors, where in a perfectly regular triangularly packed mosaic all cells have exactly six neighbors. Each Voronoi cell area is the inverse of cell density at a particular cell location, and the average Voronoi cell area is the inverse of the cell density over the image.

Regardless of which mosaic metric is used (density, spacing, regularity, or other), the Voronoi diagram is useful for identifying the boundaries over which a metric should be calculated (**Fig. 8**). Cone/cell metrics are currently only calculated over small regions

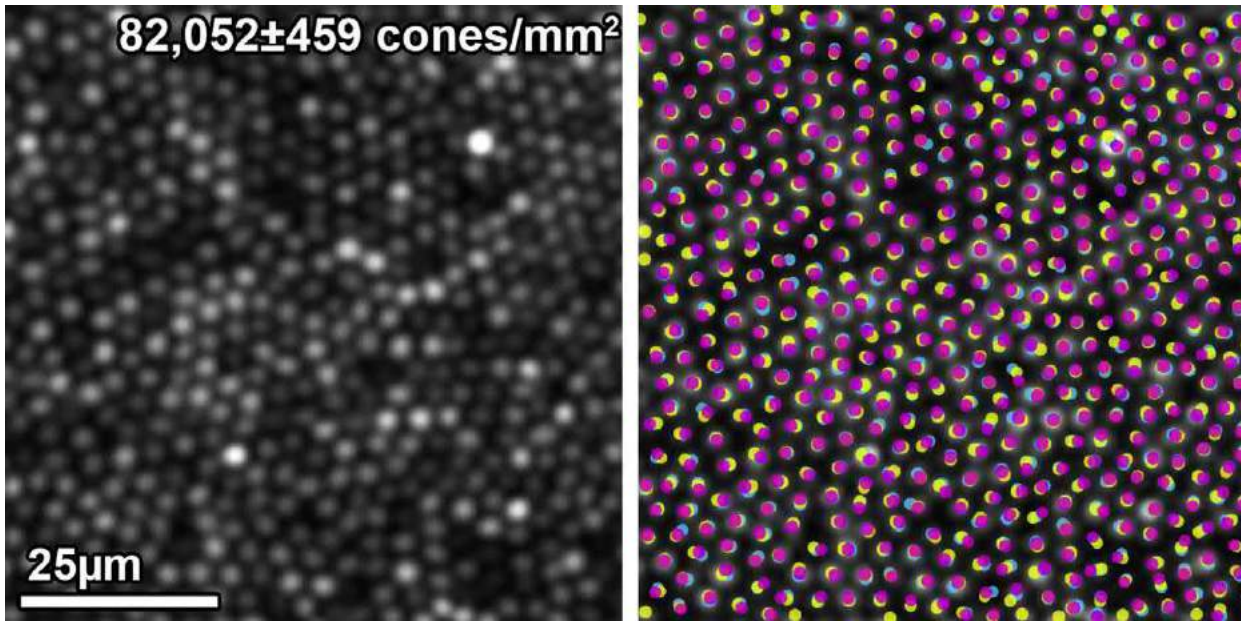


Fig. 7 Confocal adaptive optics scanning laser/light ophthalmoscopy (AOSLO) image of a normal sighted control (left). Three-trained observers manually identified cones (colored points overlaid on the cone mosaic image, right). Mean ± standard deviation of the cone density measurements from the three observers is shown.

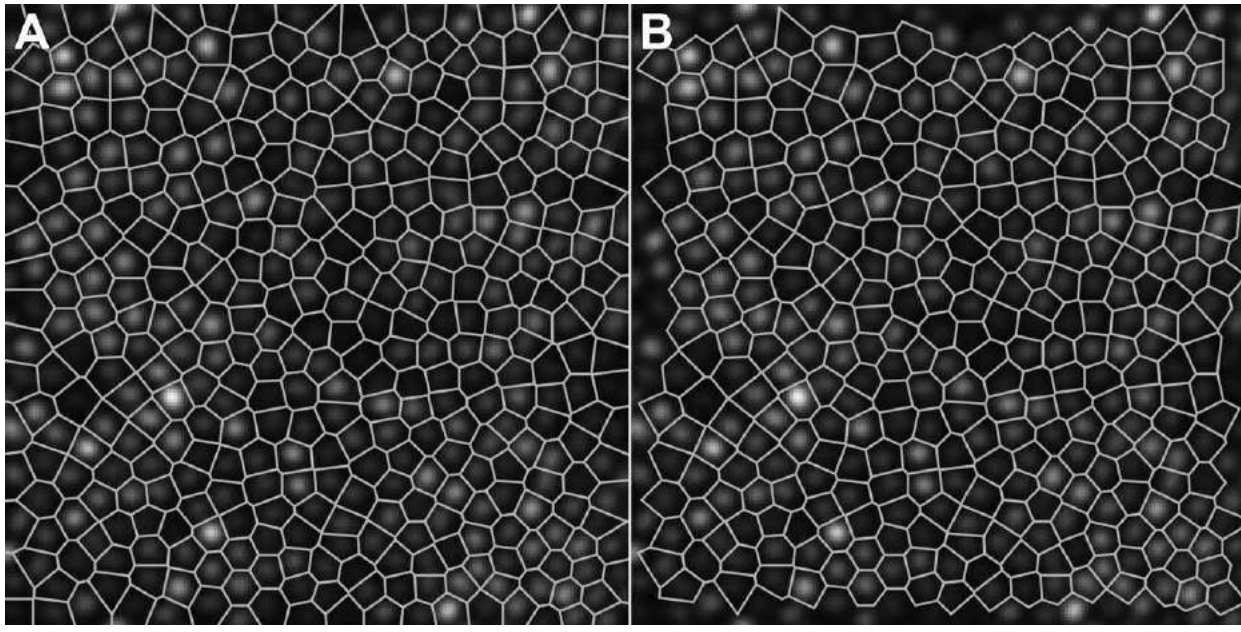


Fig. 8 Voronoi diagram overlaid on a confocal adaptive optics scanning laser/light ophthalmoscopy (AOSLO) image of the cone mosaic (A). The edge of the image shows the cells that are not bounded within the Voronoi diagram. Image metrics should be calculated over only bound Voronoi cells (B) to reduce edge effect errors. Even within the bound Voronoi mosaic, error from edge effects are still present, for example, the bound but pointed Voronoi cells at the top of the image (B).

of interest selected throughout the larger montage, and the borders of those regions of interest can lead to errors in mosaic metrics (As an example, consider a border cell, whose nearest/farthest neighbor is outside of the region of interest and therefore is not identified.). To reduce boundary error, only cells who are fully bound within the Voronoi diagram (i.e., have no open Voronoi edges) should be included in summary metrics from an image.

One of the advantages of in vivo imaging is that the same cells can be followed over time. AO imaging has enabled longitudinal tracking of cells, though despite two decades of research, the number of studies that evaluate longitudinal cone mosaic metrics is

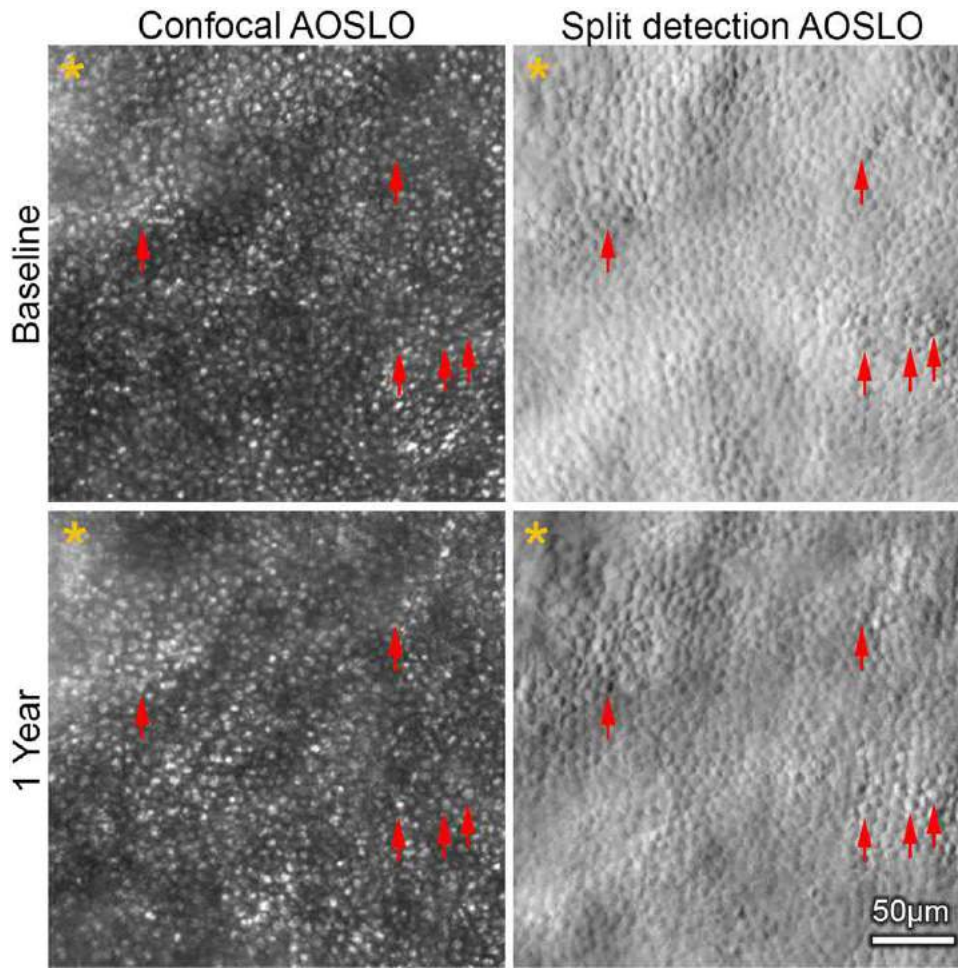


Fig. 9 Longitudinal confocal and non-confocal split detection AOSLO images at baseline and 1 year in a patient with Choroidermia, an X-linked inherited retinal degeneration. The cone photoreceptor mosaic is visible in both the confocal and split detection images, though the confocal reflectance from the cones of the Choroideremia patient appears "smudged" in comparison to the confocal reflectance of normal cones as seen in Figs. 1 and 5(A). Cell-by-cell alignment is demonstrated over the 1 year time period, with the red arrows showing the same cells visible in each imaging modality at each time point. The yellow asterisk marks the sharp border between intact retina and atrophy in this patient. Mild inward progression of the border can be observed over the 1 year time period.

limited. This is in part due to the complicated analysis process of ensuring that the same cells are followed. First, the small field of view of most AO imaging systems requires that longitudinal montaging be performed. For patients, this means any change in the preferred location of fixation will complicate longitudinal alignment. Second, the reflectance profiles of cones changes on time scales of minutes, hours, and days. Thus while cones are expected to remain stationary in the mosaic, the reflectance pattern over the mosaic will change from time point to time point. This means intensity matching will not successfully align images from different time points, and that pattern matching between time points will be more difficult. Third, for scanning systems, any distortions caused by eye motion will be different between images from different time points. This will further complicate alignment between images from different imaging sessions. Finally, in cases of pathology, true changes in retinal structure may make cell-by-cell alignment impossible. Despite these difficulties, longitudinal imaging can be performed and alignment with cellular precision can be achieved (Fig. 9). At present this process is tedious and time-consuming, and more robust and reliable algorithms are needed before the technique will be widely used.

Applications to Clinical Trials

Before any new technology is accepted into routine medical care, it must demonstrate clinical utility by changing currently accepted standards of care. Investigators have long touted the potential for AO to influence patient care, both by enabling earlier detection of disease and by assessing treatment outcomes. However, to date most clinical studies utilizing AO imaging have been limited to cross-sectional studies investigating affected patients' cone densities (or other metric/AO feature) in comparison to

normal. Nonetheless, AO imaging is now entering a phase where investigators are increasingly including AO imaging as a secondary/exploratory outcome measure in clinical trials testing the safety and efficacy of experimental interventions.

There are at least two conceivable mechanisms through which AO imaging could influence clinical trials. First, AO imaging could identify patients most amenable to a particular treatment. Second, AO could inform assessments of the safety and efficacy of treatment at the cellular level. As just one example, recent advances have led to an era where gene therapy approaches are conceivable for treating inherited retinal degenerations. Gene therapy aims to restore cellular function to dysfunctional or non-functional cells but its success requires that the target cells are present prior to treatment. Therefore, in theory, AO imaging could identify which patients, and which areas of their retinas, structurally retain dysfunctional cells that would be amenable to gene therapy treatment. In addition, longitudinal AO imaging of the treated patients could provide evidence of retinal changes (either positive or negative) following intervention at the same cellular scale. This type of clinical application for AO is not limited to gene therapy, but could also benefit any treatment option that targets cellular structure or function, including stem cell therapies, small molecular therapies and optogenetics.

Despite the high potential for AO to provide cellular level insight to the treatment of retinal disease, there remains only one study utilizing AO imaging to assess an experimental therapy. Talcott *et al.* (2011) applied AOSLO imaging to assess longitudinal changes in cone density in eyes treated with ciliary neuro-trophic factor (CNTF) implants in comparison to sham-treated fellow eyes in three patients (two with retinitis pigmentosa and one with Usher's syndrome). The authors found that eyes treated with CNTF retained higher cone densities over 2–3 years than sham-treated control eyes. Despite this AO finding, the larger Phase 2 trial investigating the efficacy of CNTF found no visual acuity or visual field benefit for CNTF-treated eyes compared to sham-treated eyes (Birch *et al.*, 2013). Together these results beg the question: is cone density an earlier biomarker of CNTF treatment efficacy than visual acuity or visual fields? One possibility is that longer trials assessing visual acuity and visual fields might show a benefit from CNTF implants, as better visual acuity and/or larger visual fields would ultimately be expected in eyes that retain more cones. Alternatively, retaining visible cones in AO images might not correspond to a functional benefit in these tested patients.

The study by Talcott *et al.* (2011) for CNTF implants highlights critical considerations for clinical trials. As a practical matter, the structure and economics of clinical trials for experimental therapies mean that a high value is placed on outcome measures that can reveal safety and efficacy (or lack thereof) reasonably soon after application of a therapy. Such outcome measures are best formulated in the context of the most precise characterizations of disease presentation and progression. Because of its increased resolution, cellular imaging capabilities and quantifiable analysis, AO retinal imaging has high potential to yield this precise characterization. Here, AO imaging is already playing a clinical role, and numerous studies have characterized retinal diseases at the cellular level (Morgan, 2016). However, before AO metrics can become accepted outcome measures for therapeutic clinical trials, investigators must transition from cross-sectional observational studies to longitudinal studies, which utilize cellular metrics to investigate the effect a given treatment has on the natural progression of a disease. Subsequently, the investigators must relate altered disease progression found from AO imaging to altered disease progression measured clinically. While it seems intuitive that patients who retain more cone structure will experience higher visual function, this correlation remains to be demonstrated in a treated patient population.

Functional Assessment in Conjunction With AO Imaging

As described above, most clinical applications of AO have been cross-sectional observational studies, intended to characterize diseased retinal structure. However, interest abounds and capabilities exist for measuring cellular function at the same resolution with which investigators image the retina. There are two methods for investigating function at the cellular level: psychophysical measures and physiological measures.

Psychophysical measures of vision involve recording a patient's subjective response to the presentation of a visual stimulus, such as is done in clinical microperimetry. AO-assisted microperimetry enables the presentation of visual stimuli to the retina with the same cellular resolution (same spatial extent of the psf) as attained for retinal imaging. This, in combination with retinal tracking through AOSLO imaging, has allowed repeated presentations of a visual stimulus targeted to the same photoreceptor or group of photoreceptors, thereby enabling measurements of single cell visual thresholds (Harmening *et al.*, 2014). For a full review on AO psychophysical testing, see Tuten *et al.* (2012).

While psychophysical testing remains the gold standard for assessing visual function, measuring function one cell at a time is not practical for testing either high volumes of cells within a patient or for testing high volumes of patients. Instead, objective, validated, and high-throughput biomarkers of function are needed. Physiological biomarkers of cellular function through imaging could provide this high-throughput alternative to single cell psychophysical measures. As one example, investigators have shown that cone near infrared reflectance (Jonnal *et al.*, 2007; Grieve and Roorda, 2008; Rha *et al.*, 2009) and optical path length (Hillmann *et al.*, 2016) can change following a visible stimulus. These stimulus-evoked intrinsic reflectance responses hold promise as biomarkers for cone function, though further study demonstrating that these measures correlate with functional vision are needed.

Conclusions

AO is a tool through which investigators can measure and correct for the optical aberrations of the living eye and thereby improve the resolution of retinal imaging devices. AO in combination with numerous retinal imaging modalities and detection schemes

has enabled observation of single cells in the living retina. Clinical applications abound, especially as investigators transition from cross-sectional observational studies to longitudinal studies of retinal disease and its treatment.

Conflict of Interest

JIWM holds US Patent 8226236 on material related to this article.

Acknowledgments

This article was supported by NIH U01EY025477, NIH U01EY025864, the Foundation Fighting Blindness, Research to Prevent Blindness, the F.M. Kirby Foundation, and the Paul and Evanina Mackall Foundation Trust. The content is solely the responsibility of the author and does not necessarily represent the official views of the National Institutes of Health.

See also: Confocal Microscopy. Optics of the Human Eye

References

Babcock, H.W., 1953. The possibility of compensating astronomical seeing. Publications of the Astronomical Society of the Pacific 65,229–236.
Bedggood, P., Metha, A., 2017. De-warping of images and improved eye tracking for the scanning laser ophthalmoscope. PLOS ONE 12 (4), e0174617.
Birch, D.G., Weleber, R.G., Duncan, J.L., Jaffe, G.J., Tao, W., 2013. Randomized trial of ciliary neurotrophic factor delivered by encapsulated cell intraocular implants for retinitis pigmentosa. American Journal of Ophthalmology 156,283–292.
Carroll, J., Gray, D.C., Roorda, A., Williams, D.R., 2005. Recent advances in retinal imaging with adaptive optics. Optics and Photonics News 16,36–42.
Carroll, J., Neitz, M., Hofer, H., Neitz, J., Williams, D.R., 2004. Functional photoreceptor loss revealed with adaptive optics: An alternate cause for color blindness. Proceedings of the National Academy of Sciences of the United States of America 101,8461–8466.
Chen, M., Cooper, R.F., Han, G.K., *et al*., 2016. Multi-modal automatic montaging of adaptive optics retinal images. Biomedical Optics Express 7,4899–4918.
Choma, M., Sarunic, M., Yang, C., Izatt, J., 2003. Sensitivity advantage of swept source and Fourier domain optical coherence tomography. Optics Express 11,2183–2189.
Chui, T.Y., Dubow, M., Pinhas, A., *et al*., 2014. Comparison of adaptive optics scanning light ophthalmoscopic fluorescein angiography and offset pinhole imaging. Biomedical Optics Express 5,1173–1189.
Chui, T.Y., Vannasdale, D.A., Burns, S.A., 2012. The use of forward scatter to improve retinal vascular imaging with an adaptive optics scanning laser ophthalmoscope. Biomedical Optics Express 3,2537–2549.
Cooper, R.F., Sulai, Y.N., Dubis, A.M., *et al*., 2016a. Effects of intraframe distortion on measures of cone mosaic geometry from adaptive optics scanning light ophthalmoscopy. Translational Vision Science and Technology 5,10.
Cooper, R.F., Wilk, M.A., Tarima, S., Carroll, J., 2016b. Evaluating descriptive metrics of the human cone mosaic. Investigative Ophthalmology & Visual Science 57,2992–3001.
Dubra, A., Harvey, Z., 2010. Registration of 2D images from fast scanning ophthalmic instruments. Lecture Notes in Computer Science 6204,60–71.
Geng, Y., Dubra, A., Yin, L., *et al*., 2012. Adaptive optics retinal imaging in the living mouse eye. Biomedical Optics Express 3,715–734.
Grieve, K., Roorda, A., 2008. Intrinsic signals from human cone photoreceptors. Investigative Ophthalmology & Visual Science 49,713–719.
Guevara-Torres, A., Williams, D.R., Schallek, J.B., 2015. Imaging translucent cell bodies in the living mouse retina without contrast agents. Biomedical Optics Express 6,2106–2119.
Harmening, W.M., Tuten, W.S., Roorda, A., Sincich, L.C., 2014. Mapping the perceptual grain of the human retina. Journal of Neuroscience 34,5667–5677.
Hermann, B., Fernandez, E.J., Unterhuber, A., *et al*., 2004. Adaptive-optics ultrahigh-resolution optical coherence tomography. Optics Letters 29,2142–2144.
Hillmann, D., Spahr, H., Pfaffle, C., *et al*., 2016. In vivo optical imaging of physiological responses to photostimulation in human photoreceptors. Proceedings of the National Academy of Sciences of the United States of America 113,13138–13143.
Hofer, H., Chen, L., Yoon, G.Y., *et al*., 2001. Improvement in retinal image quality with dynamic correction of the eye's aberrations. Optics Express 8,631–643.
Huang, D., Swanson, E.A., Lin, C.P., *et al*., 1991. Optical coherence tomography. Science 254,1178–1181.
Jackman, W., Webster, J., 1886. Photographing the retina of the living human eye. Photographic News 23,340–341.
Jonnal, R.S., Rha, J., Zhang, Y., *et al*., 2007. In vivo functional imaging of human cone photoreceptors. Optics Express 15,16141–16160.
Kocaoglu, O.P., Liu, Z., Zhang, F., *et al*., 2016. Photoreceptor disc shedding in the living human eye. Biomedical Optics Express 7,4554–4568.
Kocaoglu, O.P., Turner, T.L., Liu, Z., Miller, D.T., 2014. Adaptive optics optical coherence tomography at 1 MHz. Biomedical Optics Express 5,4186–4200.
Liang, J., Grimm, B., Goelz, S., Bille, J., 1994. Objective measurement of the wave aberrations of the human eye using a Hartmann–Shack wavefront sensor. Journal of the Optical Society of America A 11,1949–1957.
Liang, J., Williams, D.R., Miller, D.T., 1997. Supernormal vision and high-resolution retinal imaging through adaptive optics. Journal of the Optical Society of America A 14,2884–2892.
Li, K.Y., Roorda, A., 2007. Automated identification of cone photoreceptors in adaptive optics retinal images. Journal of the Optical Society of America A 24,1358–1363.
Liu, Z., Kocaoglu, O.P., Miller, D.T., 2016. 3D imaging of retinal pigment epithelial cells in the living human retina. Investigative Ophthalmology & Visual Science 57, OCT533–OCT543.
Liu, Z., Kurokawa, K., Zhang, F., Miller, D., 2017. In vivo imaging of human retinal ganglion cells with AO-OCT. IOVS. 58: ARVO E-Abstract 3430.
Morgan, J.I., 2016. The fundus photo has met its match: Optical coherence tomography and adaptive optics ophthalmoscopy are here to stay. Ophthalmic and Physiological Optics 36,218–239.
Morgan, J.I.W., Dubra, A., Wolfe, R., Merigan, W.H., Williams, D.R., 2009. In vivo autofluorescence imaging of the human and macaque retinal pigment epithelial cell mosaic. Investigative Ophthalmology & Visual Science 50,1350–1359.
Packer, O., Williams, D.R., 2003. Light, the retinal image, and photoreceptors. In: Shevell, S. (Ed.), The Science of Color. Oxford: Elsevier Science Publishing Company.
Pallikaris, A., Williams, D.R., Hofer, H., 2003. The reflectance of single cones in the living human eye. Investigative Ophthalmology & Visual Science 44,4580–4592.
Rha, J., Jonnal, R.S., Thorn, K.E., *et al*., 2006. Adaptive optics flood-illumination camera for high speed retinal imaging. Optics Express 14,4552–4569.

Rha, J., Schroeder, B., Godara, P., Carroll, J., 2009. Variable optical activation of human cone photoreceptors visualized using a short coherence light source. Optics Letters 34,3782–3784.
Roorda, A., Romero-Borja, F., Donnelly III, W.J., *et al*., 2002. Adaptive optics scanning laser ophthalmoscopy. Optics Express 10,405–412.
Roorda, A., Williams, D.R., 1999. The arrangement of the three cone classes in the living human eye. Nature 397,520–522.
Rossi, E.A., Granger, C.E., Sharma, R., *et al*., 2017. Imaging individual neurons in the retinal ganglion cell layer of the living eye. Proceedings of the National Academy of Sciences of the United States of America 114,586–591.
Scoles, D., Sulai, Y.N., Dubra, A., 2013. In vivo dark-field imaging of the retinal pigment epithelium cell mosaic. Biomedical Optics Express 4,1710–1723.
Scoles, D., Sulai, Y.N., Langlo, C.S., *et al*., 2014. In vivo imaging of human cone photoreceptor inner segments. Investigative Ophthalmology & Visual Science 55,4244–4251.
Sharma, R., Schwarz, C., Williams, D.R., *et al*., 2016. In vivo two-photon fluorescence kinetics of primate rods and cones. Investigative Ophthalmology & Visual Science 57,647–657.
Sheehy, C.K., Tiruveedhula, P., Sabesan, R., Roorda, A., 2015. Active eye-tracking for an adaptive optics scanning laser ophthalmoscope. Biomedical Optics Express 6,2412–2423.
Talcott, K.E., Ratnam, K., Sundquist, S.M., *et al*., 2011. Longitudinal study of cone photoreceptors during retinal degeneration and in response to ciliary neurotrophic factor treatment. Investigative Ophthalmology & Visual Science 52,2219–2226.
Tam, J., Liu, J., Dubra, A., Fariss, R., 2016. In vivo imaging of the human retinal pigment epithelial mosaic using adaptive optics enhanced indocyanine green ophthalmoscopy. Investigative Ophthalmology & Visual Science 57,4376–4384.
Tuten, W.S., Tiruveedhula, P., Roorda, A., 2012. Adaptive optics scanning laser ophthalmoscope-based microperimetry. Optometry and Vision Science 89,563–574.
Venkateswaran, K., Roorda, A., Romero-Borja, F., 2004. Theoretical modeling and evaluation of the axial resolution of the adaptive optics scanning laser ophthalmoscope. Journal of Biomedical Optics 9,132–138.
Wolfing, J.I., Chung, M., Carroll, J., Roorda, A., Williams, D.R., 2006. High-resolution retinal imaging of cone-rod dystrophy. Ophthalmology 113,1014–1019.

Femtosecond Lasers in Retinal Imaging

Christina Schwarz and Jennifer J Hunter, University of Rochester, Rochester, NY, United States

© 2018 Elsevier Inc. All rights reserved.

Introduction

Early diagnosis and timely therapeutic intervention is critical to avoid blindness in retinal disease. While clinical symptoms often manifest late in the disease course, structural changes are visible on a microscopic scale long before onset of clinical disease. State-of-the-art adaptive optics scanning light ophthalmoscopes (AOSLO) capture reflected or scattered light from the fundus of the eye and provide exquisite resolution in *en face* dimensions (<2 μm), which is suited to observe changes in cellular structure (Roorda and Duncan, 2015). In unhealthy retina, cellular metabolism and function are altered prior to structural changes and cell death. Detecting these early changes may provide an opportunity for treatment to prevent vision loss. The most promising imaging modalities are those that can interrogate the retina's molecular composition and biochemical pathways, providing thus information on the tissue's anatomy and physiology.

Fluorescence imaging has great potential because it can spectrally target particular fluorophores, either endogenous or exogenous, offering the possibility of high contrast imagery of specific molecular species. A milestone for biological imaging was achieved in 1990, when Denk and colleagues applied two-photon excited fluorescence (TPEF) to microscopy (Denk *et al.*, 1990). TPEF microscopy is based on the fact that two photons arriving at a fluorescent molecule closely in time can behave like a single photon of half the wavelength (Göppert-Mayer, 1931; Göppert, 1929). Great strides have been made since in cell biology and neuroscience thanks to the technique's optical sectioning capability in highly scattering tissue and its ability to provide structural and functional information (Campagnola *et al.*, 1999; Denk and Detwiler, 1999; Denk *et al.*, 1995; Helmchen, 2009; Svoboda *et al.*1997; Svoboda and Yasuda, 2006; Yuste and Denk, 1995). TPEF offers yet another advantage when applied to the eye: a host of endogenous fluorophores excitable in the ultraviolet (UV) can be studied in the living primate eye for the first time. Fluorophores with valuable diagnostic potential, such as NAD(P)H (Huang *et al.*, 2002; Shuttleworth, 2010; Zipfel *et al.*, 2003) and all-*trans*-retinol (Imanishi *et al.*, 2004; Kaplan, 1985), are normally inaccessible because their excitation requires UV light that is blocked by the cornea and crystalline lens (Boettner and Wolter, 1962). However, as illustrated in **Fig. 1**, infrared (IR) light is readily transmitted by the eye's optics and can excite these fluorophores via two-photon absorption. Fluorescence is emitted in the visible spectrum, which exits the eye relatively unattenuated and can be collected for image formation.

This article reviews the current state of in vivo nonlinear retinal imaging. It treats the theory of nonlinear ophthalmoscopy, which is generally performed with a nonlinear microscope where the anterior optics of the eye is used instead of an optimized microscope objective to investigate the back of the eye. Further, it discusses its practical implementation as well as light safety aspects. Finally, an outlook on promising future research is given. Due to the fast growth of this area and the multidisciplinary nature of it, this chapter is not intended to be self-contained. Other reviews on nonlinear microscopy (Diaspro, 2002; Diaspro and

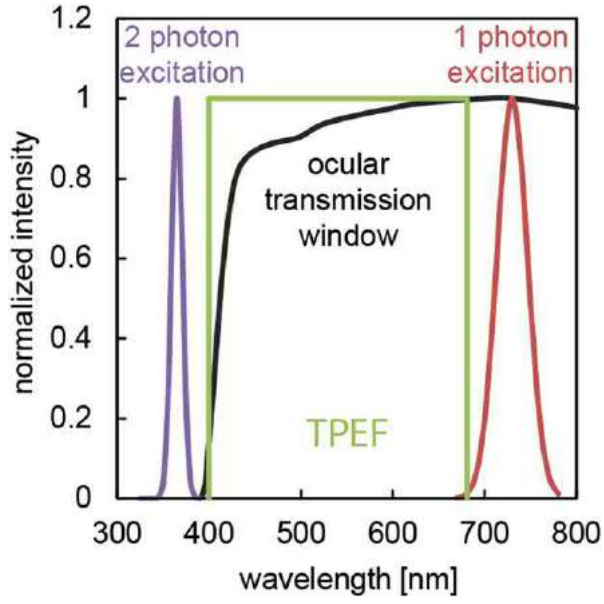


Fig. 1 Many key fluorophores are only excitable in the UV outside the ocular transmission window (Boettner and Wolter, 1962). However, infrared photons can excite these molecules via two-photon absorption.

Chirico, 2003; Diaspro *et al.*, 2005; Masters and So, 2008; Svoboda and Yasuda, 2006; Xu and Webb, 1997) and multiphoton imaging of the eye (Imanishi *et al.*, 2007; Sharma and Hunter, 2017) are highly recommended.

In Vivo Multiphoton Retinal Imaging With Adaptive Optics

By nature the retina is a multilayered tissue that is highly transparent for visible light. While this property is beneficial for vision, it becomes a challenge when the goal is to visualize individual retinal layers. Photoreceptors, nerve fiber layer and retinal vessels can readily be imaged in the visible or IR by capturing reflected light in a confocal detection scheme. Visible or IR light also excites single-photon fluorescence from lipofuscin or melanin, which can be harnessed to reveal the retinal pigment epithelium (Delori *et al.*, 1995; Granger *et al.*, 2017; Morgan *et al.*, 2009). Other retinal layers have so far been impossible to visualize with confocal reflectance or single-photon fluorescence methods, although offset aperture techniques show promise (Scoles *et al.*, 2014; Guevara-Torres *et al.*, 2016; Rossi *et al.*, 2017). Advantageously, autofluorescent molecules, which in the living eye are excitable via multiphoton absorption in the UV, are present throughout the retina. The occurrence and distribution of these molecules may be directly associated with retinal health and physiology. Valuable information can be gained by capitalizing on the fluorescence properties of these molecules, such as the absorption and emission spectra, the fluorescence lifetime, anisotropy, etc. By measuring these characteristics, cells and their organelles can be studied and information about the composition of the cells themselves as well as their surrounding environment can be gained.

Structural In Vivo Multiphoton Ophthalmoscopy

The retina contains many UV-excitable fluorophores that are abundant in different cell classes or cell compartments: Photoreceptors and retinal pigment epithelial cells contain retinoids (Chen *et al.*, 2005; Imanishi *et al.*, 2004; Kaplan, 1985) that take part in the visual cycle. Lipofuscin accumulates within the retinal pigment epithelium (Bindewald-Wittich *et al.*, 2006), especially at advanced age (Kennedy *et al.*, 1995a). Collagen is present in basement membranes and extracellular matrix and is, along with elastin, an integral component of vessel walls (Zoumi *et al.*, 2002, 2004). As precursor molecules for hemoglobin, porphyrins are present in blood and tissue fluids (Zheng *et al.*, 2011). Additionally, all living cells contain NAD(P)H (Chen *et al.*, 2005) and flavoproteins (Zhao *et al.*, 2007), because these molecules are involved in cellular metabolism. NAD(P)H is highly concentrated in the mitochondria, but is also present in the cytosol in the cell. Flavoproteins are almost exclusively present in the mitochondria.

These fluorophores provide intrinsic optical contrast from cells throughout the retina (Gualda *et al.*, 2010), even though their efficiency is relatively poor compared to specifically designed exogenous fluorophores. Nowadays two-photon excited fluorescence ophthalmoscopy (TPEFO) can be performed routinely in the living eye of mouse (Palczewska *et al.*, 2010, 2014a) and primate (Hunter *et al.*, 2011). **Fig. 2** shows near-foveal cones in the living macaque eye imaged in 730 nm confocal reflectance and TPEF modality. While the reflectance of single cones differs considerably between cones, the amount of emitted fluorescence is similar. Using an AOSLO, cellular mosaics in many retinal layers other than the photoreceptor layer have been imaged non-invasively at 730 nm and ~900 nm excitation wavelength (Sharma *et al.*, 2016b). RPE cells appeared dark in the center and bright along the cell wall. At the nerve fiber layer, bright streaks, probably the Müller cells, were visible between the darker nerve fibers. Fluorescence was also captured from vessel walls. A major breakthrough was the visualization of cell layers that are invisible in confocal reflectance imaging methods, such as the nuclear layers (Sharma *et al.*, 2016b). Of particular interest are thereby the ganglion cells because these are the primary output neurons of the retina, which degenerate in glaucoma, the second leading cause of blindness worldwide (Quigley, 2011). Capitalizing on experience gained with two-photon ophthalmoscopy in monkey to find the best focal depth and retinal location for ganglion cell imaging, parameters could be optimized to obtain the first in vivo

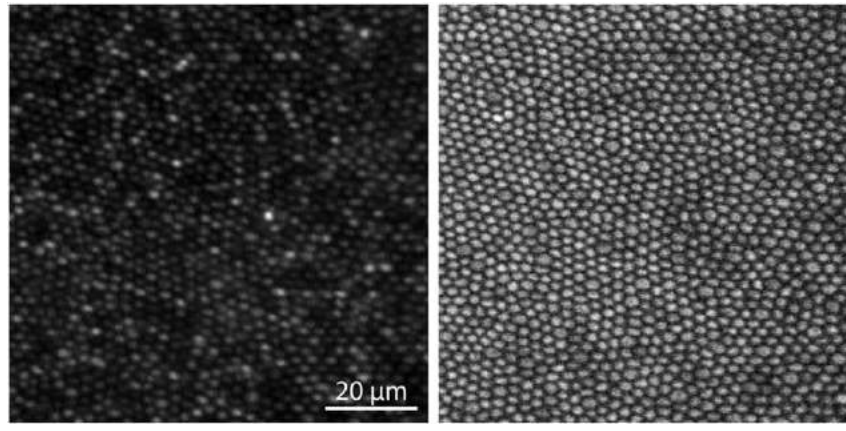


Fig. 2 Reflectance (left) and TPEF (right) image of near-foveal cones in the living macaque eye.

images of ganglion cells with offset aperture reflectance imaging at light levels that are safe for use in the living human eye (Rossi *et al.*, 2017).

Functional In Vivo Multiphoton Ophthalmoscopy

Recording autofluorescence from retinoids and NADH over time has the potential to track functional activity at a cellular scale (Chen *et al.*, 2005; Imanishi *et al.*, 2004; Kaplan, 1985). TPEF from photoreceptors has been shown to increase in response to photopigment bleaching and decline again in the dark (Sharma *et al.*, 2016a), offering the possibility of monitoring photoreceptor function in vivo. The prevailing view is that the dominant source of time-varying TPEF from photoreceptor outer segments is all-*trans*-retinol, an intermediate component of the visual cycle (Ala-Laurila *et al.*, 2006; Chen *et al.*, 2005; Kaplan, 1985; Liebman, 1969, 1973; Tsina *et al.*, 2004). The visual cycle (see **Fig. 3** for a schematic of the canonical visual cycle) occurs in several steps involving numerous enzymes and chaperone proteins (Kiser *et al.*, 2012, 2014; Lamb and Pugh, 2004; Saari, 2000). TPEF imaging quantifies an intermediate step or steps inside the visual cycle and might therefore prove to be a valuable tool for optically dissecting the normal visual cycle. The kinetics of the normally functioning visual cycle in nonhuman primates have been characterized in rod photoreceptors using TPEF (Sharma *et al.*, 2017). **Fig. 3** shows the time course of TPEF during adaptation to the imaging laser and the response to a brief flash intended to instantaneously bleach the visual pigment with subsequent recovery.

Insufficiencies can occur in any step of the visual cycle due to genetic mutation, dietary factors, or age, which will result in slowed pigment regeneration or even blindness (Lamb and Pugh, 2004). Multiphoton retinal imaging could thus give diagnostic and prognostic insight into retinal diseases such as Stargardt macular dystrophy, retinitis pigmentosa, Leber congenital amaurosis, fundus albipunctatus, Sorsby fundus dystrophy, and Bothnia dystrophy (Lamb and Pugh, 2004; Thompson and Gal, 2003; Travis *et al.*, 2007). Previous techniques to quantify visual cycle kinetics by measuring dark adaptation and/or rhodopsin regeneration have relied on psychophysics, the electroretinogram, or rhodopsin densitometry. There are a number of limitations to using these methods: Psychophysical measurements are subjective and time consuming. Electroretinograms, although objective, are based on global voltage variations generated by many circuits in the retina and are thus highly susceptible to eye movements. While rhodopsin densitometry estimates the kinetics of rhodopsin regeneration directly, it is subject to artifacts such as reflectance changes associated with neural responses or vascular changes (Grieve and Roorda, 2008; Masella *et al.*, 2014a). So far, such contamination from intrinsic optical signals has not been observed in TPEF ophthalmoscopy, and only further experimentation will reveal whether there are important additional components to the TPEF signal.

In addition to endogenous fluorophores, TPEF of extrinsic fluorophores, such as genetically encoded calcium indicators (GECIs) can provide important functional information at the cellular scale. GECIs can be delivered to specific cells or cell compartments within living animals via transgenesis or viral constructs. **Fig. 4** shows a retinal ganglion cell labeled with GCaMP5 that was imaged with a two-photon AOSLO in the living macaque eye. For GECIs in retinal cells, the advantage of two-photon over single-photon excitation lies in the use of near-infrared light, which provides reduced visual stimulation and the intrinsic optical sectioning of TPEF. In addition, at these long wavelengths, extrapolating from the trend at 900 nm, axial chromatic aberration and ocular dispersion is expected to be minimal (Atchison and Smith, 2000) which can improve efficiency and further reduce visual interference from the imaging beam. In mouse, in vivo functional responses to visible stimulation have been recorded using TPEF imaging (without adaptive optics correction) of the GECI GCaMP6 (Bar-Noam *et al.*, 2016).

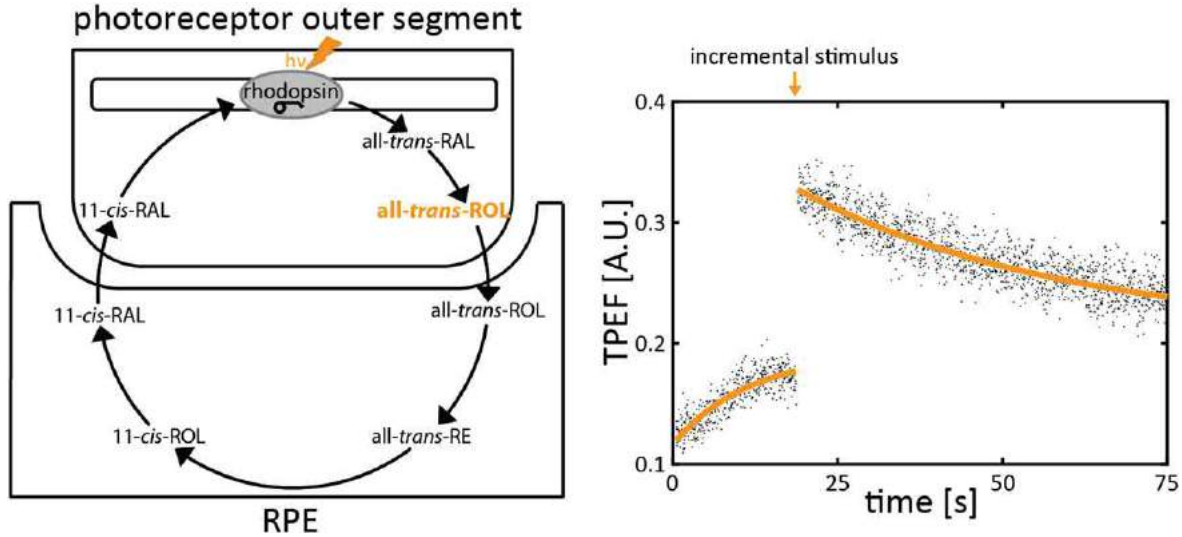


Fig. 3 (left) Schematic of the canonical visual cycle regenerating bleached rhodopsin. All-trans-retinol is the strongest candidate for fluorescence changes in response to stimulation. (right) Time course of TPEF. The initial fluorescence increase is due to stimulation by the imaging laser. After an instantaneous full bleach, fluorescence increases abruptly and gradually declines.

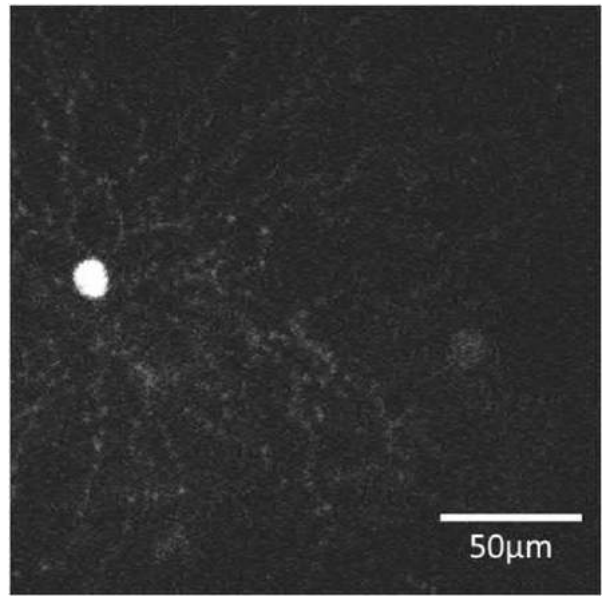


Fig. 4 Retinal ganglion cell labeled with GCaMP5 in the living macaque eye. The highly fluorescent cell nucleus is visible as well as the large dendritic arbor. In collaboration with Robin Sharma, Lu Yin, and William Merigan.

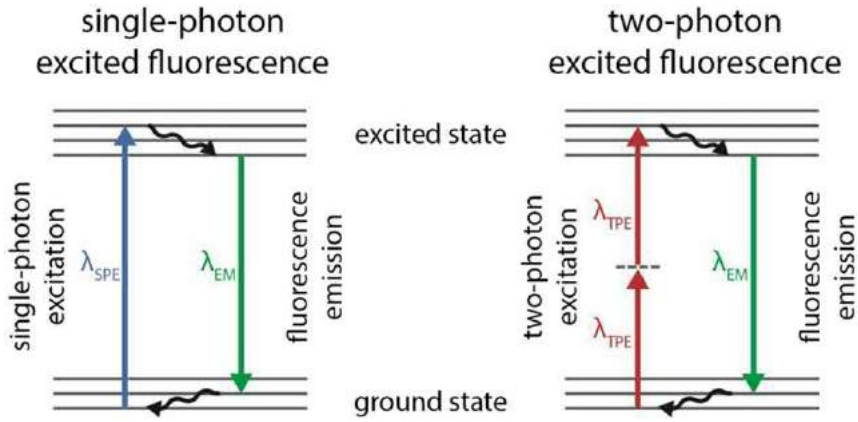


Fig. 5 Jablonski diagram illustrating the excitation of a fluorophore via a single-photon and a two-photon process.

Theory of Multiphoton Retinal Imaging

A number of books and articles on the theory of multiphoton imaging have been published over the years (Denk *et al.*, 2006; Diaspro, 2002; So *et al.*, 2000; Xu and Webb, 1997). Only the most important aspects for retinal imaging are specified here.

The mechanisms of single-photon excitation (SPE) and two-photon excitation (TPE) are illustrated in the Jablonski diagrams in Fig. 5. In single-photon excitation, a fluorescent molecule absorbs a photon and is raised to an excited electronic state. The photon energy must match the energy gap between ground and excited state. As the molecule relaxes back to the ground state, energy can be lost through fluorescence, that is, emission of photons. The emitted photons are of longer wavelength (less energy) than the photons used for excitation due to non-radiative energy loss in the form of heat or vibration within the molecule. The energy difference between fluorescence excitation and emission is referred to as Stokes shift.

Fluorescent molecules can also be excited via a multiphoton process, where two or more photons are absorbed quasi-simultaneously (Göppert-Mayer, 1931; Göppert, 1929). The total energy of the absorbed photons must equal the energy required for conventional single-photon excitation. For two-photon excited fluorescence, the excitation wavelength is approximately twice the wavelength for single-photon excitation.

$$\lambda_{SPE} \approx \left(\frac{1}{\lambda_1} + \frac{1}{\lambda_2}\right)^{-1} \approx \frac{\lambda_{TPE}}{2}$$

The temporal window for two-photon absorption can be calculated via the energy-time uncertainty (Louisell, 1973), taking into account the photon energy $\Delta E = \frac{h \cdot c}{\lambda_{TPE}}$ at the wavelength for two-photon excitation λ_{TPE} in the UV or visible range

$$\Delta t \approx \frac{\hbar}{2\Delta E} = \frac{\lambda_{TPE}}{4\pi c} \approx 10^{-16} s$$

where $\hbar = \frac{h}{2\pi}$ with Planck's constant $h \approx 6.63 \times 10^{-34} \frac{m^2 kg}{s}$ and the speed of light $c \approx 3 \times 10^8 \frac{m}{s}$.

For multiphoton excitation, ultrafast lasers emitting very short pulses ($\sim$fs) are required. Such lasers produce high peak powers, while the average power is low. The peak power can be calculated via

$$P_{peak} = \frac{\langle P(t) \rangle}{f_{rep} \cdot \tau_P} = g^{(1)} \cdot \frac{P_{avg}}{f_{rep} \cdot \tau_P}$$

where P_{avg} is the average power, f_{rep} is the pulse repetition frequency and τ_P the pulse duration. The factor $g^{(1)}$ depends on the pulse shape and is 0.94 and 0.88 for Gaussian and Hyperbolic-secant-squared pulse shapes respectively.

Because time and frequency domain are related via the Fourier transform, pulse duration and spectral bandwidth are linked. This behavior is expressed in the time-bandwidth product. The time-bandwidth product of a non-chirped, transform-limited Gaussian pulse is $\tau_P \cdot \Delta\lambda = \frac{2ln2 \cdot \lambda^2}{\pi \cdot c}$. It can be derived by calculating the FWHM of the Fourier transform of a Gaussian function as $\tau_P \cdot \Delta f = \frac{2ln2}{\pi} \approx 0.44$, where $\Delta f = \frac{c \cdot \Delta\lambda}{\lambda^2}$ with λ being the center wavelength. The shorter the pulse durations, the broader is the spectral bandwidth, and the more challenging it becomes to focus the beam in both space and time.

The response of fluorescent molecules to excitation depends on two parameters: The absorption cross section δ_2 quantifies the affinity to absorb photons at a certain wavelength λ and the quantum yield η specifies the efficiency in the conversion of absorbed energy into light emission. The quantum yield is preserved in single-photon and multi-photon excitation; however, absorption cross sections differ. Two-photon absorption cross sections are usually broader and blue shifted from what would be expected from single-photon absorption cross sections (Huang *et al.*, 2002). One advantage of the broader absorption cross sections for two-photon excitation is that a single laser can simultaneously excite multiple fluorophores. In honor of Maria Göppert-Mayer, the widely used yet unofficial unit of the two-photon absorption cross section is the GM, corresponding to 10^{-50} cm^4 s^1 $photon^{-1}$. Two-photon absorption cross sections are about two orders of magnitude greater for exogenous than endogenous fluorophores. For instance, the two-photon absorption cross section is $\sim$6 GM for GFP (Diaspro *et al.*, 2005) and 0.02 GM for NADH (So *et al.*, 2000) at a wavelength of 700 nm.

The fluorescence intensity of molecules that are excited via a two-photon effect is proportional to the absorption cross section δ_2, the quantum yield η and the intensity I squared of incident light (Diaspro and Chirico, 2003):

$$I_f(t) \propto \delta_2(\lambda_{TPE}) \cdot \eta \cdot I^2(t) = \delta_2(\lambda_{TPE}) \cdot \eta \cdot \frac{P^2(t) \cdot NA^4}{\pi^2 \cdot {\lambda_{TPE}}^4}$$

taking into account that intensity is defined as power per area $I(t) = \frac{P(t)}{A}$ and the illuminated area at the focal plane of a diffraction-limited system in the paraxial approximation $A \approx \pi \frac{{\lambda_{TPE}}^2}{NA^2}$ (Born and Wolf, 1999). For lasers with pulse repetition rate f_{rep} and pulse width τ_P, the time-averaged power squared depends on the peak power P_{Peak} and the pulse shape $\langle P^2(t) \rangle = g^{(2)} \cdot \langle P(t)^2 \rangle = g^{(2)} \cdot \frac{{P_{avg}}^2}{\tau_P \cdot f_{rep}}$. The factor $g^{(2)}$ is related to the energy contained within one pulse and is 0.66 and 0.59 for Gaussian and Hyperbolic-secant-squared pulses respectively. The average number of photons that the fluorescing medium emits per second is therefore:

$$\langle n_f(t) \rangle \propto \delta_2(\lambda_{TPE}) \cdot \eta \cdot g^{(2)} \cdot \frac{{P_{avg}}^2}{\tau_P \cdot f_{rep}} \left(\frac{NA^2}{\pi \cdot h \cdot c \cdot \lambda_{TPE}} \right)^2$$

where, P_{avg} is the time-averaged laser power, λ_{TPE} is the two-photon excitation wavelength, NA is the numerical aperture of the objective, τ_P is the pulse duration and f_{rep} is the laser repetition rate, h is Planck's constant and c the speed of light. It can be seen that the efficiency of TPEF is dependent on the spatial focusing as well as the temporal pulse shape. These parameters must be optimized for successful TPEF imaging.

If the excitation rate exceeds the de-excitation rate, ground state depletion occurs. In other words, if the fluorescence lifetime of the fluorescent molecule ($\sim 10^{-9}$ s for biological molecules) is greater than the fluorescence emission rate $\frac{1}{\langle n_f(t) \rangle}$, fluorescence emission eventually saturates. This means that increasing the imaging laser power is only beneficial up to a certain value. For greater laser powers, it is likely that the targeted molecules are raised to even higher excited states.

Second harmonic generation (SHG) is also a second order nonlinear process but differs from two-photon absorption in several aspects. In contrast to two-photon absorption, SHG involves an electron transition to a virtual (not a real) state, energy is conserved, and the SHG pulses are temporally synchronous with the laser excitation pulses. The emitted photon has twice the energy (half the wavelength) of the absorbed photons. SHG can only arise from media lacking a center of symmetry. In biological samples, SHG imaging has proven valuable for visualization of highly ordered structural proteins such as collagen without the need for exogenous fluorophores (Campagnola *et al.*, 2001). SHG and TPEF imaging can be performed with the very same microscope or ophthalmoscope. Both techniques provide complementary information.

Considerations, Artifacts and Implementation of Two-Photon Excited Fluorescence Ophthalmoscopy

Any imaging system is fundamentally limited in the smallest detail it can resolve. The resolution of an optical system is related to the full width at half maximum (FWHM) of its intensity point spread function (PSF) (Born and Wolf, 1999). The intensity I in the focal region of an aberration-free lens of circular aperture and numerical aperture $NA = n \sin \alpha$ is given as

$$I(u,v) = \left| 2 \int_0^1 J_0(v\varrho) \exp\left(\frac{1}{2} i u \varrho^2\right) \varrho d\varrho \right|^2$$

where J_0 is the zero-order Bessel function of the first kind, ϱ is the radial coordinate in the pupil plane and u and v are axial and radial normalized coordinates given by

$$u = \frac{8\pi}{\lambda} z\, n \sin^2\left(\frac{\alpha}{2}\right) \text{ and } v = \frac{2\pi}{\lambda} r\, n \sin \alpha$$

where λ is the imaging wavelength, and z and r are the axial and lateral distance from the focus.

Intensity PSFs in the paraxial approximation are listed for different types of microscopes in **Table 1** (Gu and Sheppard, 1995; Sheppard and Gu, 1990).

For simplicity, we consider that detection in a single-photon microscope occurs at a wavelength that is greater than the excitation wavelength $\lambda_{SPEF} = g \cdot \lambda_{SPE}$ $(g > 1)$ and that the illuminating light in a two-photon microscope is of twice the wavelength of that used in a single-photon microscope $\lambda_{TPE} = 2\lambda_{SPE}$ to image the same fluorophore.

In a conventional single-photon microscope, the entrance aperture of the objective lens is uniformly illuminated and the detection is performed pointwise. The imaging PSF is only determined by the illumination PSF: $I_{SP} = I(u,v)$.

In a confocal single-photon microscope, both illumination and detection are performed pointwise. The imaging PSF is determined only by the illumination and the detection PSF: $I_{SP} = I^2(u,v)$.

To increase signal detection efficiency, most two-photon microscopes are built in the conventional, not the confocal configuration. Due to the quadratic dependence of a two-photon event on the excitation intensity, the PSF of such a conventional two-photon microscope is: $I_{TP} = I^2\left(\frac{u}{2}, \frac{v}{2}\right)$

The lateral resolution for point-like objects can be calculated from the intensity distributions in the focal plane $z = 0$, whereas the axial resolution for such objects is calculated from the intensity distribution along the optical axis $(r = 0)$.

Based on this assessment, the shorter the imaging wavelength and the greater the numerical aperture of the objective, the better is the resolution. For in vivo ophthalmoscopy, the NA is limited by the maximum diameter of the dilated pupil of the eye and therefore small compared to common microscope objectives. When the pupil has been dilated, the human and macaque eye has a numerical aperture of ~ 0.2, whereas the mouse eye has a numerical aperture of ~ 0.5 (Geng *et al.*, 2011). Therefore, the small angle approximation holds for ophthalmoscopy.

The lateral resolution of a conventional single-photon microscope is:

$$d_{SP_r} = \frac{3 \cdot 83}{2\pi} \frac{\lambda}{NA} \approx 0.61 \frac{\lambda}{NA}$$

The axial resolution is:

$$d_{SP_z} = \frac{\lambda}{2\, n \sin^2 \frac{\alpha}{2}} = \frac{\lambda}{n(1 - \cos\alpha)} = \frac{\lambda}{n\left(1 - \sqrt{1 - \sin^2\alpha}\right)} \approx \frac{2\lambda n}{NA^2}$$

With the Taylor series for $\sin^2\alpha \ll 1$, $\sqrt{1 - \sin^2\alpha} \approx 1 - \frac{1}{2}\sin^2\alpha$ and $NA = n \sin\alpha$. From the given PSFs in **Table 1**, it can be easily seen that spatial resolution when imaging point-like objects in a confocal single-photon microscope is improved by factor of $\frac{1}{\sqrt{2}}$, whereas in a conventional two-photon microscope it is worse by a factor of $\sqrt{2}$ with respect to a conventional single-photon microscope.

For a typical excitation wavelength of 365 nm when targeting retinol and the numerical aperture of the human eye, the spatial resolution limits for an optically-perfect eye would be 1.1 μm in a conventional and 0.8 μm in a confocal single-photon ophthalmoscope and 1.6 μm in a two-photon ophthalmoscope. Taking into account the refractive index of the vitreous of

Table 1 Comparison of PSFs for different types of microscopes.

	Conventional single-photon microscope	*Confocal single-photon microscope*	*Conventional two-photon microscope*
PSF	$I_{SP} = I(u,v)$	$I_{cSP} = I^2(u,v)$	$I_{TP} = I^2\left(\frac{u}{2}, \frac{v}{2}\right)$
Radial PSF (z = 0)	$I_{SP_r}(v) = \left[\frac{2J_1(v)}{v}\right]^2$	$I_{cSP_r}(v) = \left[\frac{2J_1(v)}{v}\right]^4$	$I_{TP_r}(v) = \left[\frac{2J_1\left(\frac{v}{2}\right)}{\frac{v}{2}}\right]^4$
Axial PSF (r = 0)	$I_{SP_a}(u) = \left[\frac{\sin\left(\frac{u}{4}\right)}{\frac{u}{4}}\right]^2$	$I_{cSP_a}(u) = \left[\frac{\sin\left(\frac{u}{4}\right)}{\frac{u}{4}}\right]^4$	$I_{TP_a}(u) = \left[\frac{\sin\left(\frac{u}{8}\right)}{\frac{u}{8}}\right]^2$

$n_0 = 1.336$, the axial resolution is 24 μm in a conventional and 17 μm in confocal single-photon ophthalmoscope and 34 μm in a two-photon ophthalmoscope. Even though lateral and axial resolution when imaging point-like objects in a two-photon microscope are worse compared to other microscope types discussed here, the real advantage is due to the optical sectioning when imaging thick specimens, because the background is greatly reduced.

In general, all optical systems exhibit some optical imperfections. Optical materials such as glass elements can greatly reduce the system efficiency if their optical properties are not adequately taken into account. In addition, the optics of the eye is far from being perfect. The most deleterious imperfections for nonlinear ophthalmoscopy are monochromatic aberrations, chromatic aberrations and material dispersion. Understanding and correcting for these optical aberrations is essential when optimizing the imaging system. Monochromatic aberrations are imperfections that are present even for a single wavelength. These aberrations result from imperfections in surface shape of the optical elements and local refractive index changes. Monochromatic aberrations of lower orders can be corrected for with spherical and cylindrical lenses, whereas the real-time correction of higher order aberrations requires adaptive optics (AO). This technique makes it possible to routinely resolve single photoreceptors with scanning light ophthalmoscopes (Dubra *et al.*, 2011). Excellent reviews on AO for vision science have been published (Porter *et al.*, 2006; Roorda and Duncan, 2015).

If the spectral bandwidth of the imaging light is broad, the overall optical quality of the system is affected by the wavelength-dependent refractive indices of the optical elements. The refractive index of the eye is greater for shorter than for longer wavelengths. Transverse chromatic aberration causes a change in magnification with wavelength. When imaging close to the optical axis or in the temporal near-periphery, transverse chromatic aberration is generally small (Winter *et al.*, 2016). Longitudinal chromatic aberration causes light of different wavelengths to focus at different distances from the lens (Thibos *et al.*, 1992; Vinas *et al.*, 2015) and can be statically corrected with an achromatizing lens, emitting the opposite chromatic aberration of the eye (Fernández *et al.*, 2006). The simplest design is a symmetrical triplet compensating for the chromatic aberration of the eye to be imaged, when placed in a conjugate pupil plane. Proper alignment of the achromatizing lens with the pupil of the eye is important to avoid introducing additional transverse chromatic aberration.

Furthermore, the speed of light in the ocular media changes with wavelength, which results in light from a broadband source not arriving at the same time on the retina, and therefore in an increase in pulse duration. The broadened pulse duration can be estimated via $\tau_{out} = \tau_{in}\sqrt{1 + 7.68\left(\frac{D \cdot L}{\tau_{in}^2}\right)^2}$, where L is the distance traversed within the optical media and D is the optical dispersion parameter. At 725 nm, the optical dispersion value of the vitreous humor is $32.2\frac{fs^2}{mm}$, whereas that of the cornea-lens complex is $183\frac{fs^2}{mm}$, for instance (Coello *et al.*, 2007).

Several approaches exist for dispersion correction. Second-order dispersion can be corrected by a prism pair, which is sufficient for pulses with a bandwidth of less than 30 nm. For lasers with larger bandwidths additional correction of higher-order dispersion may considerably increase TPEF efficiency. For this purpose, commercial 4 f pulse shapers that optimize dispersion pre-compensation via multiphoton intrapulse interference phase scan (MIIPS) (Lozovoy *et al.*, 2004; Pestov *et al.*, 2010) have been used with microscopes. MIIPS relies on a high-precision grating in combination with a spatial light modulator (SLM). The grating spectrally disperses the beam on the way to the SLM and recombines the spectral components on the way back. At the SLM, every pixel corresponds to a different spectral range and the phase of the pulse can be independently modulated for different wavelengths. In this way, the SLM has the capability to shape the temporal profile of the pulse. Traditionally, the SHG signal after transmission through a thin nonlinear crystal is used for optimization of two-photon microscopes. In the case of a two-photon ophthalmoscope, only second-order dispersion has been corrected using the TPEF signal from the retina as feedback (Hunter *et al.*, 2011).

Effects of Femtosecond Lasers on the Retina

A disadvantage of fluorescence imaging, and especially TPEF, is that the in vivo retina must be exposed to much higher light levels than are used in conventional reflectance imaging. Roughly speaking, in vivo single photon imaging generally requires exposures that are ~1 order of magnitude and TPEF requires ~4 orders of magnitude more light than reflectance imaging. The need to address safety in TPEFO is all the more pressing given the indication that diseased retina might be more susceptible to light damage than healthy retina, which is based on a study in dogs suffering a rhodopsin mutation as a model for retinitis pigmentosa (Cideciyan *et al.*, 2005). Efficient two-photon imaging currently requires the use of sub-100 fs pulsed lasers, but due to a lack of data, safety standards for these light exposures are not well established (ANSI Z136.1-2014). The use of a pulsed light source for non-linear retinal imaging generates peak powers that have the potential to cause thermal, mechanical, and photochemical damage (Boulton *et al.*, 2001; Rockwell *et al.*, 2010) or some combination of these mechanisms as well as transient effects.

Thermal Damage

Excess heating of the tissue (>20°C) leads to immediate thermal damage, seen as local coagulation and an inflammation response. Thermal lesions usually occur with exposure durations on the time scale of μs up to 10 s with a time$^{2/3}$ dependence of the damage threshold upon exposure duration for visible and near infrared laser exposures (Lund and Edsall, 1999). Cell death may be attributed to protein denaturation (Mellerio, 1994). In the retina, the action spectrum for minimal thermal damage is

consistent with the absorption spectrum of melanin (Lund *et al.*, 2008). The time for heat dissipation from a melanin granule in the retina is treated as 5 μs (ANSI Z136.1-2014). The ultrashort femtosecond lasers used for TPE have a pulse repetition frequency faster than that cooling time and are often treated as continuous-wave (CW) lasers at the average power for the purposes of safety calculations in addition to considering the safety of an individual pulse corrected by the multiple pulse correction factor. Specific safety standard calculations are outside the scope of this review.

Mechanical Damage

Ultrashort pulse lasers emit peak powers that have the potential to cause mechanical damage. Mechanical (or acoustic) damage is due to compression or tension within the tissue (Youssef *et al.*, 2011) after energy deposition that occurs more rapidly than dissipation is possible. On the one hand, the nonlinear dependence of the refractive index on irradiance can cause self-focusing of the laser beam. In the extreme case, the beam diameter is decreased below the diffraction limit. On the other hand, high peak powers can cause ionization and thus plasma formation. Plasma has absorptive properties different from those of ordinary gases. The critical power for self-focusing and plasma formation can be calculated and compared to ensure they are above the estimated peak power for an ocular exposure at a given wavelength.

Self-focusing

When a short pulse propagates through a nonlinear medium, the Kerr effect leads to a phase delay which is largest on the beam axis (where the optical density is highest) and smaller outside the axis. This is similar to the action of a lens. Self-focusing occurs if the laser peak power approaches the critical power (Boyd *et al.*, 2009; Marburger, 1975) defined by:

$$P_{cr} = \frac{0.148 \cdot \lambda^2}{n_0 \cdot n_2}$$

where the linear and nonlinear refractive indices for vitreous humor are $n_0 = 1.336$ and $n_2 = 43.9 \cdot 10^{-21} \frac{m^2}{W}$ (Rockwell *et al.*, 1993), respectively.

Plasma Formation

Laser-induced breakdown (LIB) is the partial or complete ionization of a solid, liquid or gas through absorption of laser energy. The ionization results in a gas of charged particles, a plasma, which absorbs optical radiation much more strongly than ordinary matter. The plasma can thus be rapidly heated by the laser beam to very high temperatures, producing plasma expansion, an audible acoustic signature and a visible plasma emission. There are two mechanisms which can lead to LIB: direct ionization of the medium by multiphoton absorption or cascade ionization where free electron(s) have to be present at the beginning of the pulse. In the femtosecond regime only "pure" multiphoton ionization is fast enough to allow breakdown to occur over the duration of the pulse. For laser-induced breakdown with subsequent bubble formation, a critical electron density of 10^{24} electrons cm^{-3} is needed, whereas for laser-induced breakdown without subsequent bubble formation, a critical electron density of 10^{22} electrons cm^{-3} is sufficient. Low-density plasmas may also be a mechanism for femtosecond pulse tissue damage (Vogel *et al.*, 2002a,b). The critical electron density associated with significant optical absorption in the plasma is 10^{18} electrons per cm^3.

The irradiance threshold for plasma formation in the femtosecond laser pulse regime in vitreous humor can be calculated (Schwarz *et al.*, 2016) following the example of Cain *et al.* (2005). Calculations are based on the first order model of Kennedy (Kennedy, 1995; Kennedy *et al.*, 1995b), with special attention to Kennedy (1995) sections IV D and V F. For the ultrashort pulse regime, this model relies on the theory of multiphoton ionization in condensed media (Keldysh, 1965). The irradiance threshold for multiphoton breakdown as derived by Kennedy is:

$$I_{cr} = \frac{\left(\frac{\rho_{cr}}{A \cdot 0.5 \cdot \tau_P}\right)^{1/K}}{B}$$

with ρ_{cr} being the critical free electron density explained below, $K = \langle 1 + \frac{\Delta}{\hbar \cdot \omega} \rangle = 4$ the number of photons required to ionize the medium when $\Delta = 6.5$ eV is the ionization energy of the medium and $\omega = \frac{2 \cdot \pi \cdot c}{\lambda}$ the optical frequency where $c = 3.10^8 \frac{m}{s}$ is the vacuum speed of light, λ the wavelength and the parameters

$$A = \left(\frac{2}{9 \cdot \pi}\right) \cdot \omega \cdot \left(\frac{m' \cdot \omega}{\hbar}\right)^{\frac{3}{2}} \cdot e^{2K} \cdot \Phi(z) \cdot \left(\frac{1}{16}\right)^K$$

and

$$B = \frac{q^2}{m' \cdot \Delta \cdot \omega^2 \cdot c \cdot \varepsilon_0 \cdot n_0}$$

where ω, K and Δ are the same as above, $\varepsilon_0 = 8.85 \cdot 10^{-12} \frac{C}{Vm}$ is the permittivity of free space, $n_0 = 1.336$ the index of refraction of the medium at frequency ω, $m' = 4.55 \cdot 10^{-31}$ kg the exciton reduced mass, $\hbar = 6.58 \cdot 10^{-16}$ *eVs* the reduced Planck constant, $q = 1.6 \cdot 10^{-19}$ *C* the electron charge, and $\Phi(z) = e^{-z^2} \cdot \sum_0^\infty \frac{z^{2n+1}}{n!(2n+1)}$ represents Dawson's Integral with $z = \sqrt{2 \cdot K - \frac{2 \cdot \Delta}{\hbar \cdot \omega}}$.

Photochemical Damage

Photochemical damage occurs when the energy in a photon of light is strong enough to break chemical bonds in the irradiated molecules. The bond breakage can result in conformational changes to a molecule or in the formation of free radicals and reactive oxygen species. These molecular changes can eventually result in cell damage or death. Photochemical damage is usually observed with visible light exposures longer than a second. However, recent results suggest photochemical damage to the RPE is also possible using near infrared light (Zhang *et al.*, 2016). The particular molecules involved in photochemical damage are expected to vary with exposure wavelength.

As a consequence of the nonlinear optical process underlying two-photon excitation, light in the UV range of wavelengths that is usually blocked by the ocular media (Boettner and Wolter, 1962) can be generated at the retina. This is observed in the sensitivity to and color appearance of near-infrared pulsed lasers as compared to CW sources of the same wavelength (Palczewska *et al.*, 2014b). It is not known what impact the increased proportion of UV and visible light in combination with IR light might have on retinal structure and function. Recent evidence suggests that threshold damage as a result of sub-100 fs light at 730 nm 5 times above the ANSI standard (ANSI Z136.1-2014) corresponds to a loss of S-cones (Schwarz *et al.*, 2017), possibly via a photochemical mechanism.

Infrared Autofluorescence Reduction

Exposure to infrared illumination required for TPEFO causes a long-lasting reduction in infrared autofluorescence (IRAF) (Masella *et al.*, 2014b). Fundus IRAF is thought to originate mainly from the choroid and RPE with a slightly higher relative contribution of the choroid in older and darkly pigmented subjects. Candidate fluorophores are oxidized melanin and components closely related to melanin. IRAF reduction can occur with pulsed and CW infrared light exposures (Schwarz *et al.*, 2016) and appears to be consistent with a photochemical mechanism. In non-human primate, partial recovery was seen at 1 month, with full recovery within 21 months. This long-lasting effect of infrared illumination in both humans and monkeys occurs at exposure levels four to five times below current safety limits. Possible explanations are therefore the bleaching of melanin or changes in fluorescence efficiency of oxidized melanin secondary to changes in the environment. To date, there is no evidence of IRAF reduction causing a clinically significant impact on retinal health or visual function.

Outlook

In vivo multiphoton fluorescence ophthalmoscopy is a growing field for retinal imaging of intrinsic and extrinsic fluorophores because of its ability to provide insight into both retinal structure and function. The ability to image fluorescence from both NAD(P)H and FAD opens the possibility for reduction–oxidation (redox) measurements (Chance and Thorell, 1959; Skala *et al.*, 2007), an indication as to the state of cellular respiration. Whether a cell is favoring aerobic or anaerobic metabolism can be an indication of its health. Further insight can be gained by tracking of fluorescent properties such as emission spectra and fluorescence lifetime. The composition of fluorophores contributing to the emission signal may be identified by their spectral contribution. Fluorescence lifetime is a measure of the average delay between fluorescence excitation and the time at which photons are emitted (Venetta, 1959). The lifetime varies with the conformational state of the fluorophore and its microenvironment, which may provide a means to distinguish healthy from unhealthy cells. For example, NADH exists in both free and protein-bound forms with identical emission spectra, but different fluorescence lifetimes (0.3 ns and 2.36 ns, respectively) (Skala *et al.*, 2007). Altered lifetimes of NADH and FAD have been demonstrated in precancerous cells, likely related to the increased reliance on glycolysis in cancer cells (Skala *et al.*, 2007). Using non-cellular scale single-photon fluorescence lifetime imaging ophthalmoscopy (Schweitzer *et al.*, 2004), differences from control in ocular fluorescence lifetime have been reported for AMD (Schweitzer *et al.*, 2009), Stargardt disease (Dysli *et al.*, 2016), Alzheimer's disease (Jentsch *et al.*, 2015) and diabetes (Schweitzer *et al.*, 2011). However, measurements of fluorescence lifetime using TPEF ophthalmoscopy of the non-human primate photoreceptor mosaic have only recently been reported (Feeks *et al.*, 2017). Furthermore, fluorescence lifetime of extrinsic fluorescent markers can provide insight into particular cellular properties such as pH or the ratio of cytosolic NADH: NAD + (Mongeon *et al.*, 2016; Yellen and Mongeon, 2015).

TPEF ophthalmoscopy has the potential to be an effective clinical measure of photoreceptor and RPE health and provide early detection of outer retinal dysfunction. This requires the safe translation of this imaging modality for use in humans. Schwarz *et al.* (2016) have demonstrated in macaque that TPEF measurements of photoreceptor function are feasible at light levels within safety standards. Using a variety of clinical and high resolution imaging methods, such as fundus photography, reflectance and fluorescence cSLO, OCT, fluorescein angiography, and AO imaging of photoreceptors and RPE, IRAF reduction was the only significant effect. No other structural or functional changes were detected for any of the exposures, though of course we cannot exclude the possibility that changes could be detected with more sensitive tests or longer follow-up. No effect of repeated exposures on TPEF time course could be detected, suggesting that visual cycle function is maintained. Photoreceptors and RPE appeared normal in adaptive optics images. This safety study suggests that TPEF ophthalmoscopy will soon be feasible in people.

Acknowledgements

The authors wish to thank Robin Sharma, Sarah Walters, James Feeks, Grazyna Palczewska, Krzysztof Palczewski and David R. Williams. This work was funded by grants NIH/NEI P30-EY001319, R01-EY022371, R01-EY004367, U01-EY025497, and EY007125, and an Unrestricted Grant to the University of Rochester, Department of Ophthalmology from Research to Prevent Blindness, New York, NY, the Beckman-Argyros Award and the Alcon Research Award.

See also: Probing Ocular Mechanics With Light

References

Ala-Laurila, P., Kolesnikov, A.V., Crouch, R.K., *et al.*, 2006. Visual cycle: Dependence of retinol production and removal on photoproduct decay and cell morphology. The Journal of General Physiology 128 (2), 153–169. http://doi.org/10.1085/jgp.200609557.

Atchison, D.A., Smith, G., 2000. Optics of the Human Eye. Butterworth Heinemann.

Bar-Noam, A.S., Farah, N., Shoham, S., 2016. Correction-free remotely scanned two-photon in vivo mouse retinal imaging. Light: Science & Applications 5 (1), e16007. http://doi.org/10.1038/lsa.2016.7.

Bindewald-Wittich, A., Han, M., Schmitz-Valckenberg, S., *et al.*, 2006. Two-photon-excited fluorescence imaging of human RPE cells with a femtosecond Ti: Sapphire laser. Investigative Ophthalmology & Visual Science 47 (10), 4553–4557. http://doi.org/10.1167/iovs.05-1562.

Boettner, E.A., Wolter, J.R., 1962. Transmission of the ocular media. Investigative Ophthalmology & Visual Science 1 (6), 776–783.

Born, M., Wolf, E., 1999. Principles of Optics. Cambridge University Press.

Boulton, M., Rózanowska, M., Rózanowski, B., 2001. Retinal photodamage. Journal of Photochemistry and Photobiology B: Biology 64 (2–3), 144–161. http://doi.org/10.1016/S1011-1344(01)00227-5.

Boyd, R.W., Lukishova, S.G., Shen, Y.R., 2009. Self-focusing: Past and Present: Fundamentals and Prospects.

Cain, C.P., Thomas, R.J., Noojin, G.D., *et al.*, 2005. Sub-50-fs laser retinal damage thresholds in primate eyes with group velocity dispersion, self-focusing and low-density plasmas. Graefe's Archive for Clinical and Experimental Ophthalmology 243 (2), 101–112. http://doi.org/10.1007/s00417-004-0924-9.

Campagnola, P.J., Clark, H.A., Mohler, W.A., Lewis, A., Loew, L.M., 2001. Second-harmonic imaging microscopy of living cells. Journal of Biomedical Optics 6 (3), 277–286. http://doi.org/10.1117/1.1383294.

Campagnola, P.J., Wei, M.D., Lewis, A., Loew, L.M., 1999. High-resolution nonlinear optical imaging of live cells by second harmonic generation. Biophysical Journal 77 (6), 3341–3349. http://doi.org/10.1016/S0006-3495(99)77165-1.

Chance, B., Thorell, B., 1959. Localization and kinetics in living of reduced pyridine by microfluorometry. The Journal of Biological Chemistry 234 (11), 3044–3050.

Chen, C., Tsina, E., Cornwall, M.C., *et al.*, 2005. Reduction of all-trans retinal to all-trans retinol in the outer segments of frog and mouse rod photoreceptors. Biophysical Journal 88 (3), 2278–2287. http://doi.org/10.1529/biophysj.104.054254.

Cideciyan, A.V., Jacobson, S.G., Aleman, T.S., *et al.*, 2005. In vivo dynamics of retinal injury and repair in the rhodopsin mutant dog model of human retinitis pigmentosa. Proceedings of the National Academy of Sciences of the United States of America 102 (14), 5233–5238. http://doi.org/10.1073/pnas.0408892102.

Coello, Y., Xu, B., Miller, T.L., Lozovoy, V.V., Dantus, M., 2007. Group-velocity dispersion measurements of water, seawater, and ocular components using multiphoton intrapulse interference phase scan. Applied Optics 46 (35), 8394–8401.

Delori, F.C., Dorey, C.K., Staurenghi, G., *et al.*, 1995. In vivo fluorescence of the ocular fundus exhibits retinal pigment epithelium lipofuscin characteristics. Investigative Ophthalmology & Visual Science 36 (3), 718–729.

Denk, W., Detwiler, P.B., 1999. Optical recording of light-evoked calcium signals in the functionally intact retina. Proceedings of the National Academy of Sciences of the United States of America 96 (12), 7035–7040. http://doi.org/10.1073/pnas.96.12.7035.

Denk, W., Piston, D.W., Webb, W.W., 2006. Multi-photon molecular excitation in laser-scanning microscopy. Handbook of Biological Confocal Microscopy: Third Edition. 535–549. http://doi.org/10.1007/978-0-387-45524-2_28.

Denk, W., Strickler, J.H., Webb, W.W., 1990. Two-photon laser scanning fluorescence microscopy. Science (New York, N. Y.) 248 (4951), 73–76. http://doi.org/10.1126/science.2321027.

Denk, W., Sugi.mori, M., Llinás, R., 1995. Two types of calcium response limited to single spines in cerebellar Purkinje cells. Proceedings of the National Academy of Sciences of the United States of America 92 (18), 8279–8282. http://doi.org/10.1073/pnas.92.18.8279.

Diaspro, A., 2002. Confocal and Two-Photon Microscopy: Foundations, Applications and Advances.

Diaspro, A., Chirico, G., 2003. Two-photon excitation microscopy. Advances in Imaging and Electron Physics 126,195–286.

Diaspro, A., Chirico, G., Collini, M., 2005. Two-photon fluorescence excitation and related techniques in biological microscopy. Quarterly Reviews of Biophysics 38 (2), 97–166. http://doi.org/10.1017/S0033583505004129.

Dubra, A., Sulai, Y., Norris, J.L., *et al.*, 2011. Noninvasive imaging of the human rod photoreceptor mosaic using a confocal adaptive optics scanning ophthalmoscope. Biomedical Optics Express 2 (7), 1864–1876. http://doi.org/10.1364/BOE.2.001864.

Dysli, C., Wolf, S., Hatz, K., Zinkernagel, M.S., 2016. Fluorescence lifetime imaging in Stargardt disease: Potential marker for disease progression. Investigative Opthalmology & Visual Science 57 (3), 832. http://doi.org/10.1167/iovs.15-18033.

Feeks, J.A., Walters, S., Schwarz, C., Hunter, J.J., 2017. Two-photon fluorescence lifetime ophthalmoscopy of intrinsic fluorophores on a cellular scale in the living macaque. In: ARVO Meeting 2017.

Fernández, E.J., Unterhuber, A., Povazay, B., *et al.*, 2006. Chromatic aberration correction of the human eye for retinal imaging in the near infrared. Optics Express 14 (13), 6213–6225.

Geng, Y., Schery, L.A., Sharma, R., *et al.*, 2011. Optical properties of the mouse eye. Biomedical Optics Express 2 (4), 717–738. http://doi.org/10.1364/BOE.2.000717.

Göppert, M., 1929. Über die Wahrscheinlichkeit des Zusammenwirkens zweier Lichtquanten in einem Elementarakt. Die Naturwissenschaften 17 (48), 932. http://doi.org/10.1007/BF01506585.

Göppert-Mayer, M., 1931. Über Elementarakte mit zwei Quantensprüngen. Annalen Der Physik 114,273–294.

Granger, C., Williams, D.R., Rossi, E.A., 2017. Near-infrared autofluorescence imaging reveals the retinal pigment epithelial mosaic in the living human eye. In: ARVO Meeting 2017.

Grieve, K., Roorda, A., 2008. Intrinsic signals from human cone photoreceptors. Investigative Ophthalmology and Visual Science 49 (2), 713–719. http://doi.org/10.1167/iovs.07-0837.

Gualda, E.J., Bueno, J.M., Artal, P., 2010. Wavefront optimized nonlinear microscopy of ex vivo human retinas. Journal of Biomedical Optics 15 (2), 26007. http://doi.org/10.1117/1.3369001.

Gu, M., Sheppard, C.J.R., 1995. Comparison of three-dimensional imaging properties between two-photon and single-photon fluorescence microscopy. Journal of Microscopy 177 (2), 128–137. http://doi.org/10.1111/j.1365-2818.1995.tb03543.x.
Guevara-Torres, A., Joseph, A., Schallek, J.B., 2016. Label free measurement of retinal blood cell flux, velocity, hematocrit and capillary width in the living mouse eye. Biomedical Optics Express (BOE) 7, 4228–4249.
Helmchen, F., 2009. Two-photon functional imaging of neuronal activity. In: Frostig, R.D. (Ed.), In Vivo Optical Imaging of Brain Function. CRC Press, p. 428.
Huang, S., Heikal, A.A., Webb, W.W., 2002. Two-photon fluorescence spectroscopy and microscopy of NAD(P)H and flavoprotein. Biophysical Journal 82 (5), 2811–2825. http://doi.org/10.1016/S0006-3495(02)75621-X.
Hunter, J.J., Masella, B., Dubra, A., *et al.*, 2011. Images of photoreceptors in living primate eyes using adaptive optics two-photon ophthalmoscopy. Biomedical Optics Express 2 (1), 139–148. http://doi.org/10.1364/BOE.2.000139.
Imanishi, Y., Batten, M.L., Piston, D.W., Baehr, W., Palczewski, K., 2004. Noninvasive two-photon imaging reveals retinyl ester storage structures in the eye. The Journal of Cell Biology 164 (3), 373–383. http://doi.org/10.1083/jcb.200311079.
Imanishi, Y., Lodowski, K., Koutalos, Y., 2007. Two-photon microscopy: Shedding light on the chemistry of vision. Biochemistry 46 (34), 9674–9684. http://doi.org/10.1021/bi701055g.Two-photon.
Jentsch, S., Schweitzer, D., Schmidtke, K.U., *et al.*, 2015. Retinal fluorescence lifetime imaging ophthalmoscopy measures depend on the severity of Alzheimer's disease. Acta Ophthalmologica 93 (4), e241–e247. http://doi.org/10.1111/aos.12609.
Kaplan, M.W., 1985. Distribution and axial diffusion of retinol in bleached rod outer segments of frogs (Rana pipiens). Experimental Eye Research 40 (5), 721–729. http://doi.org/10.1016/0014-4835(85)90141-1.
Keldysh, L.V., 1965. Ionization in the field of a strong electromagnetic wave. Soviet Physics JETP 20 (5), 1307–1314. http://doi.org/10.1234/12345678.
Kennedy, C.J., Rakoczy, P.E., Constable, I.J., 1995a. Lipofuscin of the retinal pigment epithelium: A review. Eye (London, England) 9, 763–771. http://doi.org/10.1038/eye.1995.192.
Kennedy, P.K., 1995. A first-order model for computation of laser-induced breakdown thresholds in ocular and aqueous media: Part I – Theory. IEEE Journal of Quantum Electronics 31 (12), 2241–2249.
Kennedy, P.K., Boppart, S.A., Hammer, D.X., *et al.*, 1995b. A first-order model for computation of laser-induced breakdown thresholds in ocular and aqueous media: ii – Comparison to experiment. IEEE Journal of Quantum Electronic 31 (12), 2250–2257.
Kiser, P.D., Golczak, M., Maeda, A., Palczewski, K., 2012. Key enzymes of the retinoid (visual) cycle in vertebrate retina. Biochimica et Biophysica Acta – Molecular and Cell Biology of Lipids 1821 (1), 137–151. http://doi.org/10.1016/j.bbalip.2011.03.005.
Kiser, P.D., Golczak, M., Palczewski, K., 2014. Chemistry of the retinoid (visual) cycle. Chemical Reviews 114, 194–232. http://doi.org/10.1021/cr400107q.
Lamb, T.D., Pugh, E.N., 2004. Dark adaptation and the retinoid cycle of vision. Progress in Retinal and Eye Research 23 (3), 307–380. http://doi.org/10.1016/j.preteyeres.2004.03.001.
Liebman, P.A., 1969. Microspectrophotometry of retinal cells. Annals of the New York Academy of Sciences 157,250–264.
Liebman, P.A., 1973. Microspectrophotometry of visual receptors. In: Langer, H. (Ed.), Biochemistry and Physiology of Visual Pigments. Berlin: Springer-Verlag, pp. 299–305.
Louisell, W.H., 1973. Quantum Statistical Properties of Radiation.
Lozovoy, V.V., Pastirk, I., Dantus, M., 2004. Multiphoton intrapulse interference. IV. Ultrashort laser pulse spectral phase characterization and compensation. Optics Letters 29 (7), 775–777.
Lund, D.J., Edsall, P., 1999. Action spectrum for retinal thermal injury. SPIE 3591,324–334.
Lund, D.J., Edsall, P., Stuck, B.E., 2008. Spectral dependence of retinal thermal injury. Journal of Laser Applications 20 (2), 76. http://doi.org/10.2351/1.2900534.
Marburger, J.H., 1975. Self-focusing: Theory. Progress in Quantum Electronics 4,35–110.
Masella, B.D., Hunter, J.J., Williams, D.R., 2014a. New wrinkles in retinal densitometry. Investigative Ophthalmology & Visual Science 55 (11), 7525–7534. http://doi.org/10.1167/iovs.13-13795.
Masella, B.D., Williams, D.R., Fischer, W.S., Rossi, E.A., Hunter, J.J., 2014b. Long-term reduction in infrared autofluorescence caused by infrared light below the maximum permissible exposure. Investigative Ophthalmology and Visual Science 55 (6), 3929–3938. http://doi.org/10.1167/iovs.13-12562.
Masters, B.R., So, P.T.C., 2008. Handbook of Biomedical Nonlinear Optical Microscopy.
Mellerio, J., 1994. Light effects on the retina. Principles and Practice of Ophthalmology. 1–23.
Mongeon, R., Venkatachalam, V., Yellen, G., 2016. Cytosolic NADH-NAD^+ redox visualized in brain slices by two-photon fluorescence lifetime biosensor imaging. Antioxidants & Redox Signaling 25 (10), 553–563. http://doi.org/10.1089/ars.2015.6593.
Morgan, J.I.W., Dubra, A., Wolfe, R., Merigan, W.H., Williams, D.R., 2009. In vivo autofluorescence imaging of the human and macaque retinal pigment epithelial cell mosaic. Investigative Ophthalmology & Visual Science 50 (3), 1350–1359. http://doi.org/10.1167/iovs.08-2618.
Palczewska, G., Dong, Z., Golczak, M., *et al.*, 2014a. Noninvasive two-photon microscopy imaging of mouse retina and retinal pigment epithelium through the pupil of the eye. Nature Medicine 20 (7), 785–789. http://doi.org/10.1038/nm.3590.
Palczewska, G., Maeda, T., Imanishi, Y., *et al.*, 2010. Noninvasive multiphoton fluorescence microscopy resolves retinol and retinal condensation products in mouse eyes. Nature Medicine 16 (12), 1444–1449. http://doi.org/10.1038/nm.2260.
Palczewska, G.,, Vinberg, F.,, Stremplewski, P.,, *et al.*, 2014b. Human infrared vision is triggered by two-photon chromophore isomerization. Proceedings of the National Academy of Sciences. doi:10.1073/pnas.1410162111.
Pestov, D., Lozovoy, V.V., Dantus, M., 2010. Single-beam shaper-based pulse characterization and compression using MIIPS sonogram. Optics Letters 35 (9), 1422–1424.
Porter, J., Queener, H., Lin, J., Thorn, K., Awwal, A., 2006. Adaptive Optics for Vision Science: Principles, Practices, Design and Applications.
Quigley, H.A., 2011. Glaucoma. The Lancet 377 (9774), 1367–1377. http://doi.org/10.1016/S0140-6736(10)61423-7.
Rockwell, B.A., Roach, W.P., Rogers, M.E., *et al.*, 1993. Nonlinear refraction in vitreous humor. Optics Letters 18 (21), 1792–1794. http://doi.org/10.1364/OL.18.001792.
Rockwell, B.A., Thomas, R.J., Vogel, A., 2010. Ultrashort laser pulse retinal damage mechanisms and their impact on thresholds. Medical Laser Application 25 (704), 84–92. http://doi.org/10.1016/j.mla.2010.02.002.
Roorda, A., Duncan, J.L., 2015. Adaptive optics ophthalmoscopy. Annual Review of Vision Science 1 (1), 19–50. http://doi.org/10.1146/annurev-vision-082114-035357.
Rossi, E.A., Granger, C.E., Sharma, R., *et al.*, 2017. Imaging individual neurons in the retinal ganglion cell layer of the living eye. Proceedings of the National Academy of Sciences 114 (3), 201613445. http://doi.org/10.1073/pnas.1613445114.
Saari, J.C., 2000. Biochemistry of visual pigment regeneration – The Friedenwald Lecture. Investigative Ophthalmology 41 (2).
Schwarz, C., Sharma, R., Fischer, W.S., *et al.*, 2016. Safety assessment in macaques of light exposures for functional two-photon ophthalmoscopy in humans. Biomedical Optics Express 7 (12), 5148–5169.
Schwarz, C., Sharma, R., Keller, M., Williams, D.R., Hunter, J.J., 2017. Intense ultrashort pulsed light in the infrared selectively damages putative S cones. In: ARVO Meeting 2017.
Schweitzer, D., Hammer, M., Schweitzer, F., *et al.*, 2004. In vivo measurement of time-resolved autofluorescence at the human fundus. Journal of Biomedical Optics 9 (6), 1214. http://doi.org/10.1117/1.1806833.
Schweitzer, D., Klemm, M., Quick, S., *et al.*, 2011. Detection of early metabolic alterations in the ocular fundus of diabetic patients by time-resolved autofluorescence of endogenous fluorophores. Proceedings of SPIE 8087, 1–9. http://doi.org/10.1117/12.889109.
Schweitzer, D., Quick, S., Schenke, S., *et al.*, 2009. Comparison of parameters of time-resolved autofluorescence between healthy subjects and patients suffering from early AMD. Der Ophthalmologe 106 (8), 714–722.

Scoles, D., Sulai, Y.N., Langlo, C.S., *et al*., 2014. *In vivo* imaging of human cone photoreceptor inner segments. Investigative Ophthalmology and Visual Science 55 (7), 4244–4251.

Sharma, R., Hunter, J.J., 2017. Multiphoton imaging of the retina. Handbook of Visual Optics, Volume Two: Instrumentation and Vision Correction. 392.

Sharma, R., Schwarz, C., Hunter, J.J., *et al*., 2017. Formation and clearance of all- *trans* -retinol in rods investigated in the living primate eye with two-photon ophthalmoscopy. Investigative Opthalmology & Visual Science 58 (1), 604. http://doi.org/10.1167/iovs.16-20061.

Sharma, R., Schwarz, C., Williams, D.R., *et al*., 2016a. In vivo two-photon fluorescence kinetics of primate rods and cones. Investigative Opthalmology & Visual Science 57 (2), 647–657. http://doi.org/10.1167/iovs.15-17946.

Sharma, R., Williams, D.R., Palczewska, G., Palczewski, K., Hunter, J.J., 2016b. Two-photon autofluorescence imaging reveals cellular structures throughout the retina of the living primate eye. Investigative Opthalmology & Visual Science 57 (2), 632. http://doi.org/10.1167/iovs.15-17961.

Sheppard, C.J.R., Gu, M., 1990. Image formation in two-photon fluorescence microscopy. Optik 86 (3),

Shuttleworth, C.W., 2010. Use of NAD(P)H and flavoprotein autofluorescence transients to probe neuron and astrocyte responses to synaptic activation. Neurochemistry International 56 (3), 379–386. http://doi.org/10.1016/j.neuint.2009.12.015.

Skala, M.C., Riching, K.M., Gendron-Fitzpatrick, A., *et al*., 2007. In vivo multiphoton microscopy of NADH and FAD redox states, fluorescence lifetimes, and cellular morphology in precancerous epithelia. Proceedings of the National Academy of Sciences 104 (49), 19494–19499. http://doi.org/10.1073/pnas.0708425104.

So, P.T.C., Dong, C.Y., Masters, B.R., Berland, K.M., 2000. Two-photon excitation fluorescence microscopy. Annual Review of Biomedical Engineering 2,399–429.

Svoboda, K., Denk, W., Kleinfeld, D., Tank, D.W., 1997. In vivo dendritic calcium dynamics in neocortical pyramidal neurons. Nature 385 (6612), 161–165. http://doi.org/10.1038/385161a0.

Svoboda, K., Yasuda, R., 2006. Principles of two-photon excitation microscopy and its applications to neuroscience. Neuron 50 (6), 823–839. http://doi.org/10.1016/j.neuron.2006.05.019.

Thibos, L.N., Ye, M., Zhang, X., Bradley, A., 1992. The chromatic eye: A new reduced-eye model of ocular chromatic aberration in humans. Applied Optics 31 (19), 3594–3600.

Thompson, D.A., Gal, A., 2003. Vitamin A metabolism in the retinal pigment epithelium: Genes, mutations, and diseases. Progress in Retinal and Eye Research 22 (5), 683–703. http://doi.org/10.1016/S1350-9462(03)00051-X.

Travis, G.H., Golczak, M., Moise, A.R., Palczewski, K., 2007. Diseases caused by defects in the visual cycle: Retinoids as potential therapeutic agents. Annual Review of Pharmacology and Toxicology 47, 469–512. http://doi.org/DOI 10.1146/annurev.pharmtox.47.120505.105225.

Tsina, E., Chen, C., Koutalos, Y., *et al*., 2004. Physiological and microfluorometric studies of reduction and clearance of retinal in bleached rod photoreceptors. The Journal of General Physiology 124 (4), 429–443. http://doi.org/10.1085/jgp.200409078.

Venetta, B.D., 1959. Microscope phase fluorometer for determining the fluorescence lifetimes of fluorochromes. Review of Scientific Instruments 30 (6), 450–457. http://doi.org/10.1063/1.1716652.

Vinas, M., Dorronsoro, C., Cortes, D., Pascual, D., Marcos, S., 2015. Longitudinal chromatic aberration of the human eye in the visible and near infrared from wavefront sensing, double-pass and psychophysics. Biomedical Optics Express 23 (4), 513–522. http://doi.org/10.1364/OE.23.00948.

Vogel, A., Huttmann, G., Paltauf, G., Noack, J., 2002a. Femtosecond-laser-produced low-density plasmas in transparent biological media: A tool for the creation of chemical, thermal and thermomechanical effects below the optical breakdown threshold. SPIE Photonics West 4633,23–37.

Vogel, A., Noack, J., Huettmann, G., Paltauf, G., 2002b. Low-density plasmas below the optical breakdown threshold: potential hazard for multiphoton microscopy, and a tool for the manipulation of intracellular events. SPIE Photonics West 4620, 202–216. http://doi.org/10.1117/12.470693.

Winter, S., Sabesan, R., Tiruveedhula, P., *et al*., 2016. Transverse chromatic aberration across the visual field of the human eye. Journal of Vision 16 (14), 1–10. http://doi.org/10.1167/16.14.9.

Xu, C., Webb, W.W., 1997. Multiphoton excitation of molecular fluorophores and nonlinear laser microscopy. Topics in Fluorescence Spectroscopy 5, 471–540. (ST–Multiphoton excitation of molecular).

Yellen, G., Mongeon, R., 2015. Quantitative two-photon imaging of fluorescent biosensors. Current Opinion in Chemical Biology 27, 24–30. http://doi.org/10.1016/j.cbpa.2015.05.024.

Youssef, P.N., Sheibani, N., Albert, D.M., 2011. Retinal light toxicity. Eye (London, England) 25 (1), 1–14. [http://doi.org/10.1038/eye.2010.149.]

Yuste, R., Denk, W., 1995. Dendritic spines as basic functional units of neuronal integration. Nature. http://doi.org/10.1038/375682a0.

Zhang, J., Sabarinathan, R., Bubel, T., Williams, D.R., Hunter, J.J., 2016. Action spectrum for photochemical retinal pigment epithelium (RPE) disruption in an in vivo monkey model. Proceedings of SPIE 9706, 1–6. http://doi.org/10.1117/12.2213615.

Zhao, L., Qu, J., Niu, H., 2007. Identification of endogenous fluorophores in the photoreceptors using autofluorescence spectroscopy. Proceedings of SPIE 6826, 1–7. http://doi.org/10.1117/12.760139.

Zheng, W., Li, D., Zeng, Y., Luo, Y., Qu, J.Y., 2011. Two-photon excited hemoglobin fluorescence. Biomedical Optics Express 2 (1), 71–79. http://doi.org/10.1364/BOE.2.000071.

Zipfel, W.R., Williams, R.M., Christie, R., *et al*., 2003. Live tissue intrinsic emission microscopy using multiphoton-excited native fluorescence and second harmonic generation. Proceedings of the National Academy of Sciences of the United States of America 100 (12), 7075–7080. http://doi.org/10.1073/pnas.0832308100.

Zoumi, A., Lu, X., Kassab, G.S., Tromberg, B.J., 2004. Imaging coronary artery microstructure using second-harmonic and two-photon fluorescence microscopy. Biophysical Journal 87 (4), 2778–2786. http://doi.org/10.1529/biophysj.104.042887.

Zoumi, A., Yeh, A., Tromberg, B.J., 2002. Imaging cells and extracellular matrix in vivo by using second-harmonic generation and two-photon excited fluorescence. Proceedings of the National Academy of Sciences of the United States of America 99 (17), 11014–11019. http://doi.org/10.1073/pnas.172368799.

Confocal and Multiphoton Imaging of Cornea

Gopal S Jayabalan and Josef F Bille, University of Heidelberg, Heidelberg, Germany

© 2018 Elsevier Ltd. All rights reserved.

Introduction

Most of our daily activities depend on a proper vision, and any loss in the visual acuity will strongly influence our quality of life. Preserving vision throughout an individual's lifetime is of a major concern in ophthalmology. The reliable diagnoses in ophthalmology are determined by detecting and monitoring the infinitesimal changes in tissue structures. The ophthalmologists mostly rely on slit-lamp biomicroscopy that was developed over a century ago in the 1890s. Subjective slit-lamp biomicroscopy remains as the backbone of clinical examination; however, objective tools and technologies are needed in order to provide a comprehensive understanding of structural alterations at a cellular level. Corneal disease is one of the leading causes of blindness worldwide, and a prompt and accurate diagnosis of corneal diseases is a milestone for successful treatment and followup.

Since the invention of the first ophthalmoscope by Hermann von Helmholtz in 1851, the quest for quantitative in vivo imaging of ocular surfaces for diagnostic and monitoring purposes was initiated. Recently, a number of imaging technologies were developed for research and clinical purposes. Boosted by the newest developments in microscopy, confocal microscopy has been widely employed in clinics and research for corneal diagnosis. Confocal microscopy has emerged as a powerful technique to study the corneal structure (Fig. 1) with high spatial and contrast images compared to conventional microscopy.

With the introduction of ultrafast pulsed laser sources, multiphoton microscopy practically became feasible and experienced a tremendous success in biological microscopy. Multiphoton microscopy allows three-dimensional (3D) tissue imaging over time, and it is an important asset in investigational imaging. Intrinsic tissue fluorescence, called autofluorescence, which is initiated by collagen, elastin, NAD(P)H etc., can be imaged by multiphoton microscopy and provides structural and functional information of the cornea. In this article, we will discuss the principles and the potential use and limitations of confocal and multiphoton microscopy for corneal imaging.

Principles of Confocal and Multiphoton Microscopy

Confocal Microscopy

The principle of confocal microscopy was patented in 1957 by Marvin Minsky, in order to overcome the limitations of conventional wide-field microscopy. In a conventional wide-field microscope, the entire specimen (i.e., cornea) will be illuminated evenly by a light source, and the specimens in the optical path are all excited at the same time. The resulting fluorescence (i.e., emitted light) from the specimen will be detected by the photodetector or camera including a largely unfocused background part. In contrast, confocal microscopy uses a point illumination source with a pinhole in front of the detector to eliminate the out of

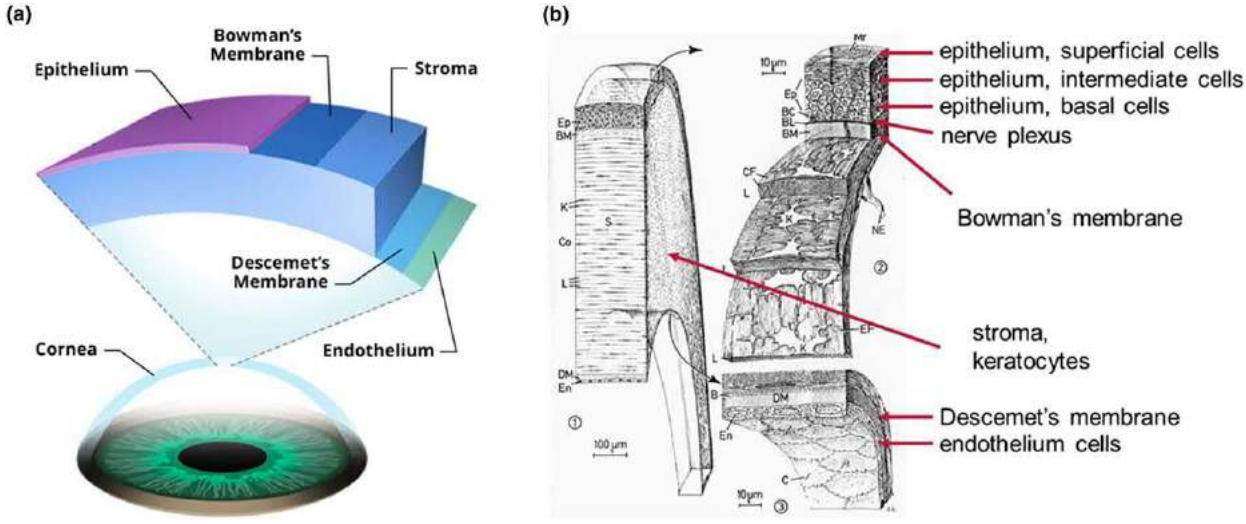


Fig. 1 Anatomical structure of cornea: (a) schematic presentation of a cornea (http://www.allaboutvision.com/visionsurgery/corneal-inlays-onlays.htm) and (b) layers of cornea (courtesy from the slide Krstic, R.V., 1991. Human microscopic anatomy. Springer).

focus light or glare. The optical resolution of confocal microscopy images is better than conventional wide-field microscopy, since the fluorescence is produced very close to the focal plane.

Multiphoton Microscopy

Multiphoton microscopy includes two-photon excited fluorescence (TPEF), second harmonic generation (SHG) and third harmonic generation (THG) imaging (Fig. 2). In 1931, the theoretical basis of two-photon excitation was established by Maria Göppert-Mayer, and then the photophysical effect of two-photon excitation was experimentally verified by Kaiser and Garret in 1963. Two-photon excitation is a fluorescence process in which a fluorophore (a molecule that fluoresces) is excited by simultaneous absorption of two photons. The familiar single-photon (i.e., confocal) fluorescence process involves exciting a fluorophore from the electronic ground state to an excited state by a single photon. This single-photon process typically requires photons in the ultraviolet or blue/green spectral range. However, the same excitation process can be generated by the simultaneous absorption of two less energetic photons (typically in the infrared spectral range) under sufficiently intense laser illumination. This nonlinear process occurs if the sum of energies of the two photons is greater than the energy gap between the molecule's ground and excited states. Since this process depends on the simultaneous absorption of two infrared photons, the probability of two-photon absorption by a fluorescent molecule is a quadratic function of the excitation radiance. Under sufficient intense excitation, three-photon and higher photon excitation are also possible. This process is similar to two-photon excitation wherein three photons or higher number of photons must interact with the fluorophore simultaneously to produce the fluorescence.

Almost all multiphoton microscopy is based on ultrashort pulsed lasers, because the multiphoton efficiency of an n-photon process depends on the peak power P according to P^n relation. The use of pulsed lasers enables efficient fluorophore excitation at a fast scanning rate. Moreover, focusing a pulsed laser into a specimen can generate a harmonic upconversion as well. Although the nonlinear optical effect known as SHG has been recognized in early days of laser physics, the use of SHG and its three-photon variant third (THG) is fairly new in research. Harmonic generation is a nonlinear process in which photons with the same frequency interact with a nonlinear material and generate a new photon with twice the energy. SHG is useful for investigating the ordered structural protein assemblies such as collagen fibers in the cornea.

Confocal Laser Scanning Microscopy

Confocal laser scanning microscopy (CLSM) has been widely implemented in clinics for diagnostic purposes. It is based on a conventional optical microscope, instead of a lamp a laser is used as a light source. The laser is focused on the cornea through the objective lens to a single spot in the focal plane. The laser beam is scanned in a raster pattern using the scanning mirrors in x–y direction and an entire image of the cornea at a certain focal plane will be reconstructed. The emitted light generated from the cornea at the focal plane will be collected by the same objective lens and the collected signals will be recorded using a photomultiplier tube (PMT). This scanning principle does not improve the spatial resolution over conventional optical microscopy, because the excitation is produced throughout the entire beam path of the laser in the cornea, i.e., above and below the focal plane. However, the spatial resolution can be improved by placing a pinhole in front of the detector to eliminate the out of focus light. This leads to an excellent spatial resolution and enables serial optical sections from thick specimens (Fig. 3(a)).

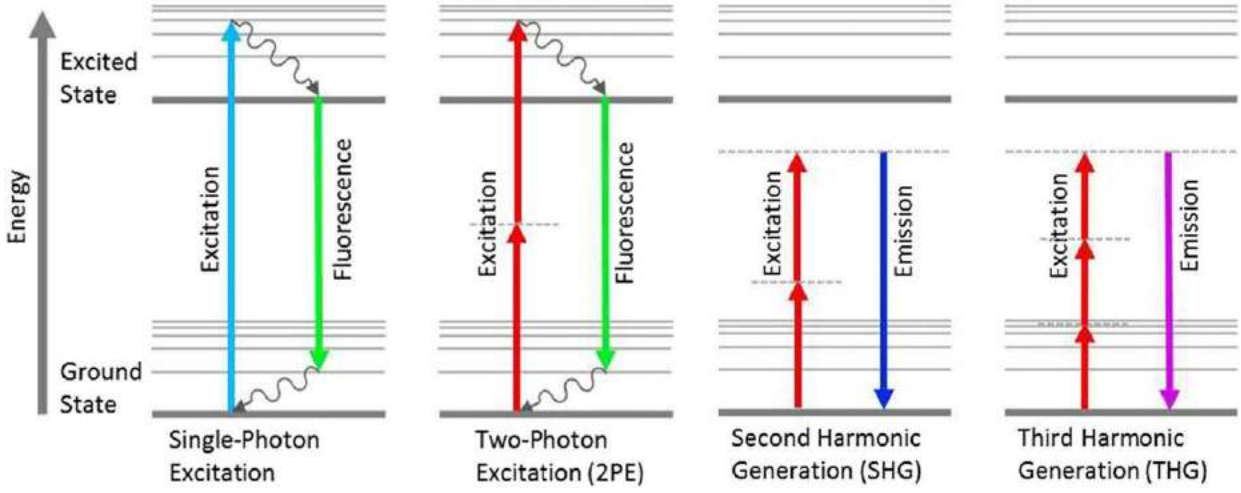


Fig. 2 Jablonski diagram of single-photon excitation, two-photon excitation (2PE), second harmonic generation (SHG), and third harmonic generation (THG). (http://www.azooptics.com/Article.aspx?ArticleID=1175)

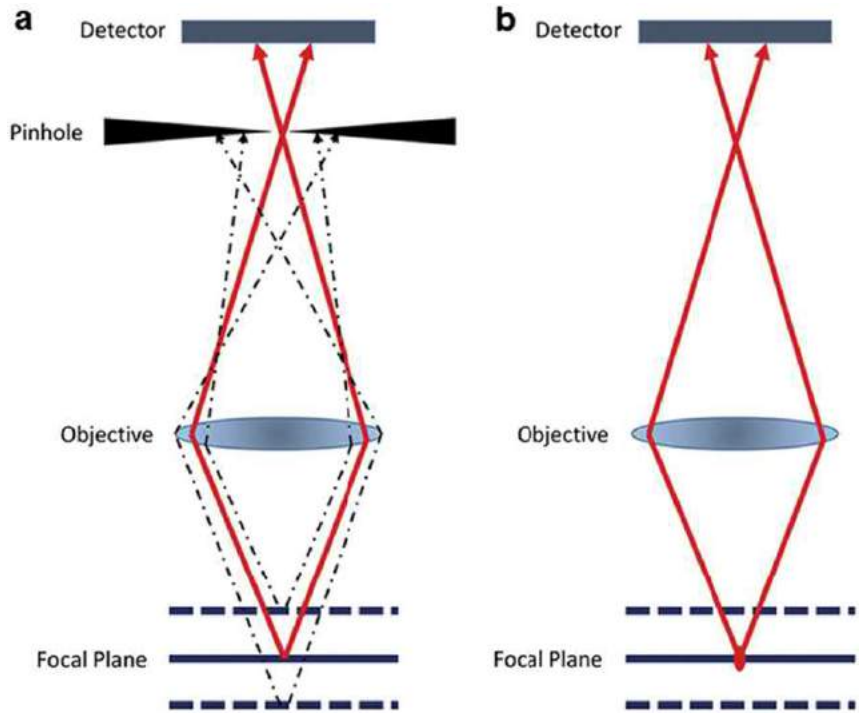


Fig. 3 The principle of confocal and two-photon microscopy. (a) In confocal microscopy, the emitted fluorescent light from the focal plane will pass through the pinhole and the out of focus light will be blocked by the pinhole and (b) in multiphoton microscopy, the two-photon excitation generates fluorescence only at the focal plane, so a pinhole is not required since no background fluorescence is produced. Reproduced from Allocca, G., Kusumbe, A.P., Ramasamy, S.K., Wang, N., 2016. Confocal/two-photon microscopy in studying colonisation of cancer cells in bone using xenograft mouse models. BoneKEy Reports 5. doi:10.1038/bonekey.2016.84.

Two-Photon Laser Scanning Microscopy

The invention of two-photon fluorescence light microscopy by Denk, Webb, and coworkers revolutionized the in vivo 3D cellular imaging. By focusing an ultrashort pulsed laser through the objective lens sufficient excitation intensity can be generated on the focal plane (Fig. 3(b)). When the laser beam is focused on the specimen, the photons become crowded and the probability of two photons interacting simultaneously will be increased.

The significant advantage of two-photon excitation over single-photon (confocal) excitation is the narrow localization. In confocal microscopy, although the fluorescence is excited throughout the illuminated volume of the specimen, the signal originating from the focal plane will pass through the pinhole. In two-photon excitation, the fluorescence will be generated only at the focal plane, and no background fluorescence will be produced. Therefore, a pinhole is not required for two-photon microscopy. Due to the localized excitation of two-photon excitation, the 3D resolution of the images can be achieved identically to confocal microscopy. Since there is no absorption in out of focus specimen area, the excitation light can penetrate much deeper through the specimen to the focal plane. This results in greater penetration compared to confocal microscopy. Also, two-photon microscopy minimizes photobleaching and photodamage.

Confocal and Multiphoton Microscopy of Cornea

Three types of confocal microscopes are available for corneal imaging:

- Tandem scanning microscopy.
- Slit scanning microscopy.
- Laser scanning microscopy.

Tandem scanning microscopy sheds the light of high intensity through a pinhole and generates a two-dimensional (2D) image. However, tandem scanning microscopy for confocal imaging is not produced anymore. In contrast to tandem scanning, slit scanning microscopy has been employed in clinics with reduced scanning and examination time with high contrast imaging. Slit scanning has the ability to scan many points in parallel to the axis of the slit. Laser scanning microscopy is the latest addition to corneal imaging, where the laser beam is scanned over the back of the microscope objective through scanning mirrors. The Heidelberg Retina Tomograph (HRT) in combination with the Rostock Cornea Module (RCM) is a commercially available

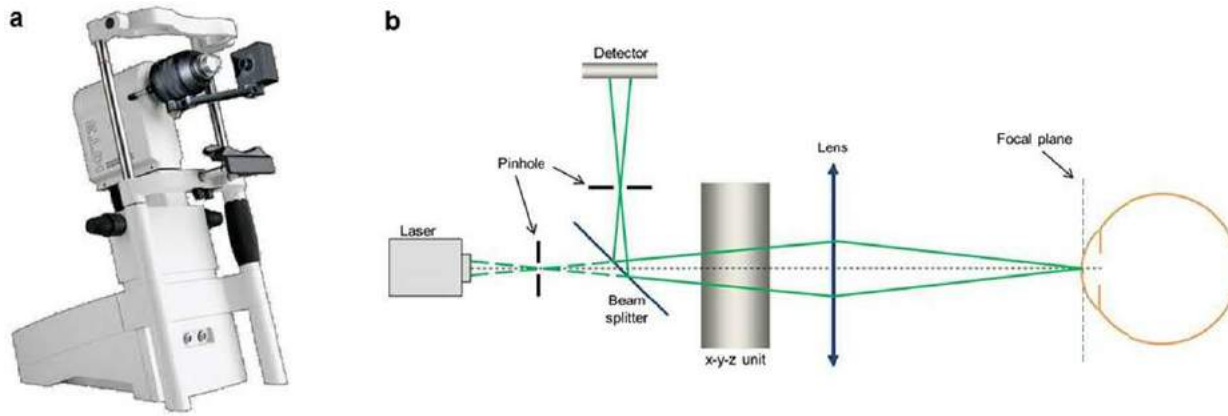


Fig. 4 (a) Heidelberg Engineering Heidelberg retinal tomograph-rostock cornea module (HRT-RCM) confocal microscopy and (b) schematic diagram of the optical set up of the HRT-RCM. Heidelberg Engineering Brochure.

confocal microscope that has been widely used in clinics for corneal imaging. The HRT-RCM uses a class I laser and this laser poses no risk of ocular injury.

Heidelberg Retinal Tomograph-RCM

The Heidelberg Retinal Tomograph-RCM (HRT-RCM) (Fig. 4(a)) was developed by Heidelberg Engineering GmbH in cooperation with Rostock Eye clinic for in vivo investigation of the cornea. A 670-nm laser is used as light source and the laser is focused on the cornea with a high numerical aperture objective lens (63 × /0.95 NA or 60 × /0.90 NA; interchangeable). The laser is raster scanned by the scanning mirrors and is focused on the cornea by the objective lens. The emitted fluorescent light from the cornea is captured using a detector. The confocal pinhole is used in front of the detector to eliminate the out of focus light (Fig. 4(b)). The confocal imaging of the cornea can be acquired with the field of view 250 μm × 250 μm, 400 μm × 400 μm, and 500 μm × 500 μm with a 63 × objective lens. A viscous sterile gel is interposed between the objective lens and cornea to eliminate the optical interface between two different refractive indices. The depth of the focus can be adjusted manually relative to the cornea in a plane parallel to the corneal surface, to scan the cornea from epithelium to endothelium.

Confocal Imaging of Normal Cornea

The HRT-RCM provides excellent resolution with sufficient contrast at different layers of the cornea, and distinct corneal layers from epithelium to endothelium can be visualized. The corneal epithelium is composed of five to six layers (Fig. 5(a)–(d)), as superficial cells, intermediate cells, and basal cells. The superficial cells are flat polygonal cells with well-defined border, prominent nuclei and uniform density of cytoplasm. It is about 40–50 μm in diameter and approximately 5 μm thick. The intermediate cells also known as wing cells are similar to superficial cells, but the nuclei are not evident. It is typically about 30–45 μm in size and characterized by the cell borders. Basal cells are approximately 10–15 μm and smaller in size. The basal cells appear denser than the superficial and wing cells.

The subbasal nerve plexus (Fig. 5(e)) is characterized by the presence of hyper-reflective fibers of 4–8 mm length, and connected with anastomoses and organized in a vortex pattern in the lower nasal quadrant of the paracentral cornea. The visualization of corneal nerve plexus was not possible until the introduction of confocal microscopy. The nerve fibers appear bright and well contrasted against a dark background.

Corneal stroma accounts for 90% of total corneal thickness and the keratocytes density is much higher in anterior stroma than in posterior stroma. The keratocyte counts are 1000 cells/mm^2 in the anterior stroma and 700 cells/mm^2 in the posterior stroma. The confocal image of the stroma exhibits multiple irregular oval, round or bean shaped bright structures representing keratocytes (Fig. 5(f) and (g)). The collagen fibers cannot be visualized by confocal microscopy in normal cornea.

Corneal endothelium is composed of a single layer of cells that are 4–6 μm thick and approximately 20 μm in diameter. The endothelial cells progressively decline with age, and the normal endothelial cell count amounts to 3000 cells/mm^2 in a healthy cornea. The endothelial cells appear as bright hexagonal and polygonal cells with unrecognizable nuclei (Fig. 5(h)).

Confocal Microscopy in Corneal Pathologies

Confocal microscopy has been an effective tool in clinical diagnosis, and it is widely used to assess corneal infections, corneal dystrophies, pre and postsurgical assessment of laser-assisted in situ keratomileusis (LASIK), photorefractive keratectomy (PRK), keratoconus and infectious keratitis. Also, it is used to monitor the cornea after injuries, and for differential diagnosis of

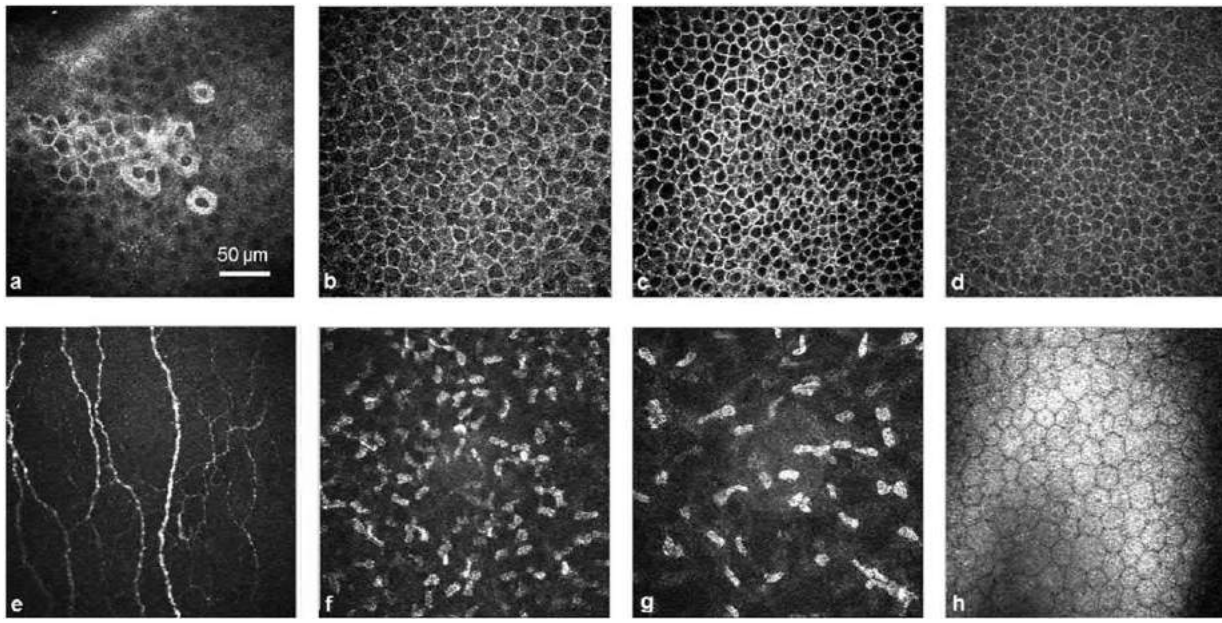


Fig. 5 In vivo confocal microscopy images of the corneal layers in normal human subject from epithelium to endothelium. (a)–(d) Epithelium, (e) subbasal nerve plexus, (f) and (g) anterior and posterior stroma, and (h) endothelium. Courtesy of Prof. R. Guthoff, Prof. J. Stave, Dr. A. Zhivov, University of Rostock (from Heidelberg PowerPoint).

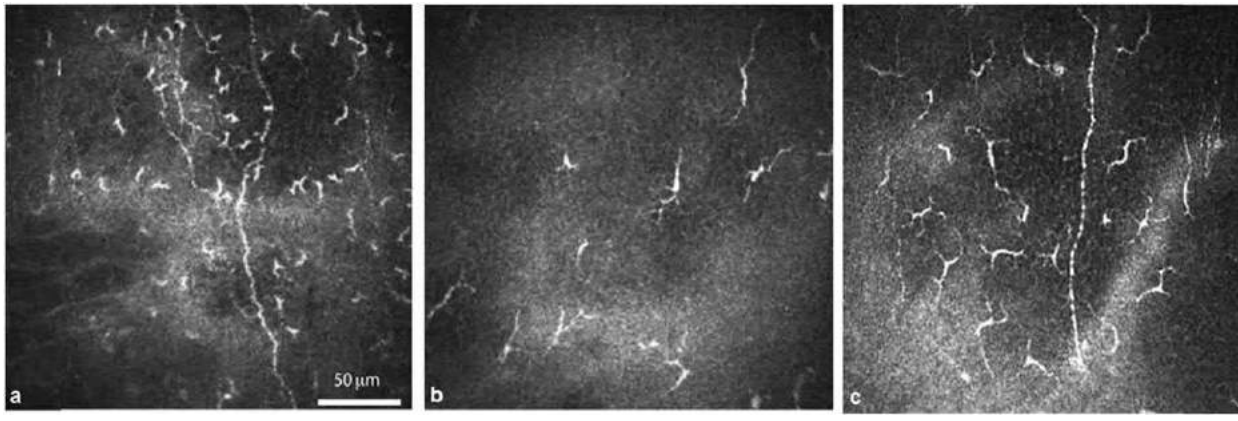


Fig. 6 In vivo confocal microscopy images demonstrating different forms of Langerhans cells. (a) Individual cell bodies without processes; (b) cells bearing dendrites; and (c) cells arranged in a meshwork via long interdigitating dendrites. Reproduced from Guthoff, R.F., Baudouin, C., Stave, J., 2006. Atlas of Confocal Laser Scanning In-Vivo Microscopy in Ophthalmology. Springer: Germany.

conjunctival tumors and conjunctivitis. As an example for clinical confocal imaging of the cornea, the Langerhans cell distribution and postsurgical assessment of LASIK using the HRT-RCM is shown in **Figs. 6** and **7**.

Langerhans Cells

Langerhans cells can be evaluated using confocal microscopy with emphasis on cell morphology and cell distribution. In confocal microscopy, the Langerhans cells are visualized typically as bright corpuscular particles with dendritic morphology. These cells are distributed in low numbers at the center of the cornea and higher densities at the periphery of the cornea. Confocal microscopy helps in differentiating the Langerhans cells bodies that lack dendrites, Langerhans cells with small dendritic process form a local network, and Langerhans cells forming a meshwork via long interdigitating dendrites (**Fig. 6(a)–(c)**). The average density of Langerhans cells in normal subjects is 34 ± 3 cells/mm^2 (range 0–64 cells/mm^2) in the center of the cornea, and 98 ± 8 cells/mm^2 (range 0–208 cells/mm^2) in the periphery. Langerhans cells contribute to the immune and inflammatory responses, and determine the cell-mediated immunity.

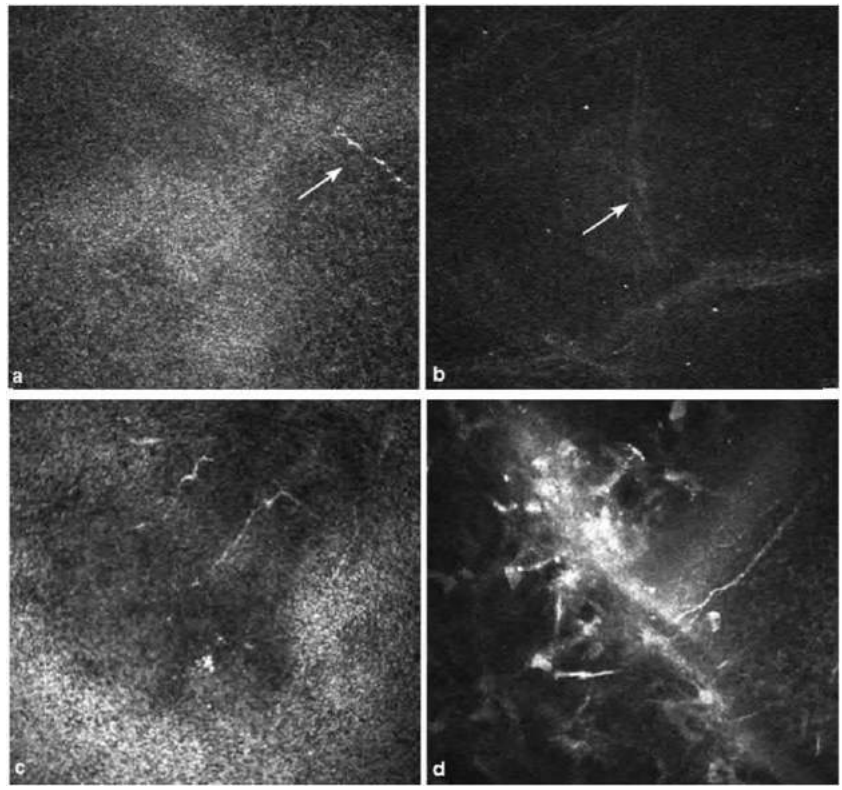


Fig. 7 Innervation after refractive surgery. (a) Nerve fibers near subbasal layer; (b) nerve fibers near Bowman's membrane; (c) two months after LASIK – small regenerating nerve fibers in the central cornea; and (d) nine months after LASIK – new nerve fiber growing from the edge of flap region to center. Reproduced from Guthoff, R.F., Baudouin, C., Stave, J., 2006. Atlas of Confocal Laser Scanning In-Vivo Microscopy in Ophthalmology. Springer: Germany.

Postsurgical Assessment of LASIK

LASIK is an excimer laser-based refractive surgical procedure that is currently being successfully used by surgeons to correct refractive errors (myopia, hyperopia etc.). After LASIK surgery, the cornea is typically evaluated by slit-lamp biomicroscopy and computerized corneal topography. The confocal microscopy evaluation of LASIK pre- and postsurgery adds new aspects in corneal diagnosis. The distribution of the corneal nerves and degeneration of the nerve structures can be visualized by confocal microscopy, and thus a direct comparison between innervation and sensitivity or symptom severity of the dry eye can be provided (Fig. 7).

Two-Photon Laser Scanning Microscopy

Two-photon laser scanning microscopy based on the HRT was developed to investigate the cornea (Fig. 8). A compact femtosecond laser was employed in the system as the light source and an additional detection path for the two-photon mode was implemented. Both the confocal and two-photon images can be captured using the same instrument. An electronic switch facilitates the switching between the two imaging modes, while both detection modes are synchronized with the scanning unit. The laser beam is deflected in x- and y-direction via two scanning mirrors (scan unit, Fig. 8(b)) to trace out a square raster of 300×300 μm², 200×200 μm², or 150×150 μm² at a frame rate up to 16 Hz. The laser is focused on the cornea with a high numerical aperture objective lens ($40 \times /0.80$ NA or $16 \times /0.80$ NA; interchangeable). The wide field of view can be achieved by using the $16 \times$ objective lens with less distinct cell morphology. Like confocal microscopy (HRT-RCM) the focus can be adjusted manually and different layers of the cornea can be visualized. A viscous sterile gel has to be placed between the objective lens and the cornea to eliminate the optical interface between two different indices.

Two-Photon Imaging of Normal Cornea

The TPEF imaging of cornea has been extensively employed in preclinical studies, but has not been implemented in clinics yet. Although confocal microscopy has been used in clinical diagnosis, the collagen fiber orientation in the stroma cannot be visualized, and it provides only morphological information rather than the tissue's functional state. With two-photon imaging

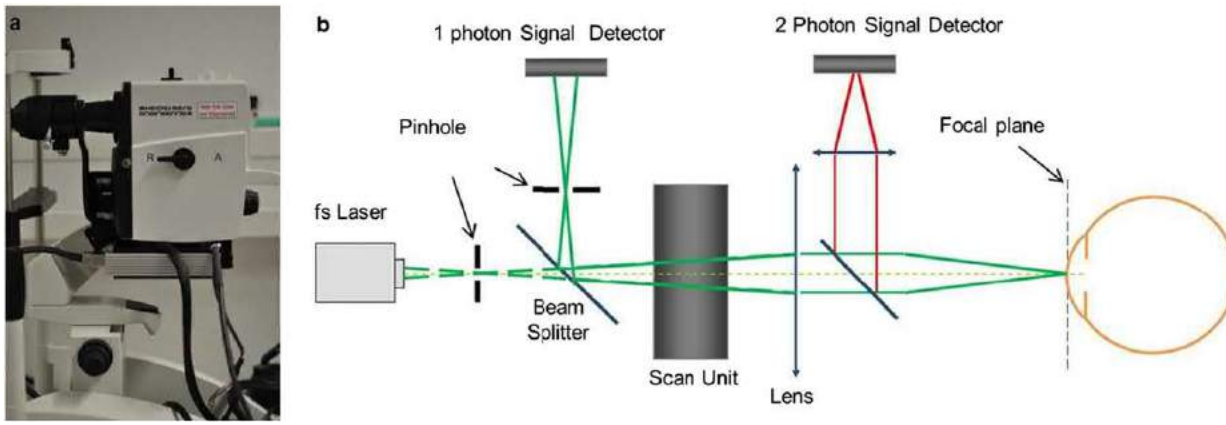


Fig. 8 (a) Heidelberg Engineering two-photon microscopy and (b) schematic diagram of the optical set up of two-photon microscopy based on HRT. Reproduced from Qu, Y., Thomas, K.E., Vola, M.E., *et al.*, 2012. Rapid identification of microorganisms using the two-photon ophthalmoscope. Investigative Ophthalmology and Visual Science 53 (14), 6175; Qu, Y., Thomas, K.E., Schuster, A.K., *et al.*, 2011. Identification of microorganisms utilizing the two-photon ophthalmoscope. Investigative Ophthalmology and Visual Science 52 (14), 5823.

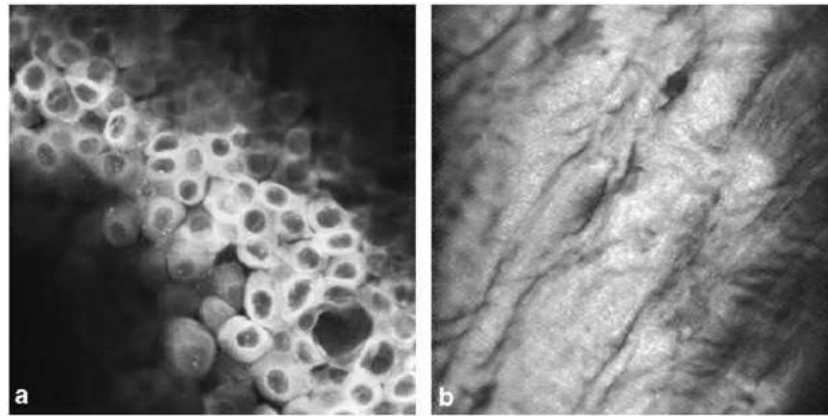


Fig. 9 Two-photon imaging of corneal epithelial cells (a) and stromal collagen fibers (b) of human cornea. Reproduced from Qu, Y., Thomas, K. E., Vola, M.E., *et al.*, 2012. Rapid identification of microorganisms using the two-photon ophthalmoscope. Investigative Ophthalmology and Visual Science 53 (14), 6175; Qu, Y., Thomas, K.E., Schuster, A.K., *et al.*, 2011. Identification of microorganisms utilizing the two-photon ophthalmoscope. Investigative Ophthalmology and Visual Science 52 (14), 5823.

both the tissue structures and the metabolic state can be well addressed. Two-photon microscopy provides excellent resolution and high contrast images of the cornea similar to confocal microscopy. High resolution two-photon images of the corneal epithelium and the collagen fibers from the human corneal buttons are shown in **Fig. 9**. The collagen fibers in the stroma can be well established with TPEF and SHG imaging.

Two-Photon Imaging of Limbal Stem Cells

The limbal stem cells are located in the basal layer of the corneal limbus, and the proliferation of the limbal cells maintains the cornea by replacing the lost cells by tears. Limbal stem cells also prevent the conjunctival epithelial cells from migrating onto the surface of the cornea. The limbal stem cells have never been visualized with confocal microscopy and with the use of two-photon microscopy the limbal stem cells have been identified in mice. The limbal stem cells are smaller in size and it is shown by two-photon microscopy (**Fig. 10**). The two-photon imaging of limbal stem cells would help in the diagnosis of limbal stem cell deficiency and also differentiate and explore the nature of the limbal stem cells in a precise way.

Two-Photon Imaging of Infectious Keratitis

Confocal microscopy plays a significant role in detecting the microorganisms causing corneal infections. It is difficult to identify the microorganisms like *Acanthamoeba* on the ocular surfaces since the appearance can impersonate as herpetic or bacterial keratitis. In most cases, the *Acanthamoeba* keratitis is diagnosed either by tissue culture or corneal biopsy, and histological analysis.

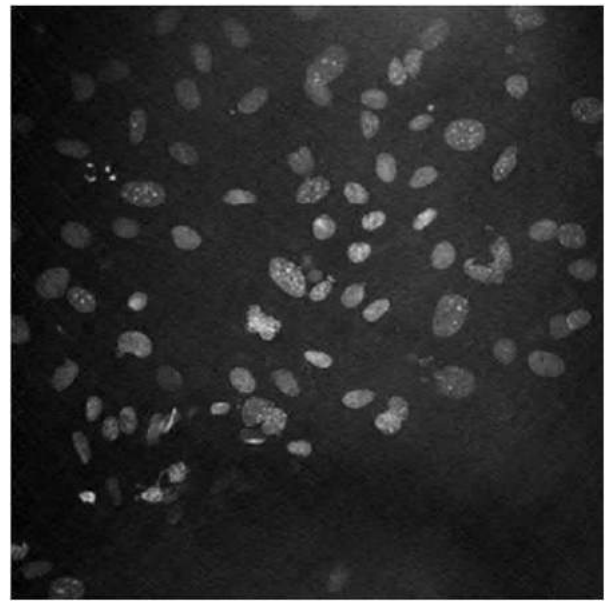


Fig. 10 Two-photon imaging of mice limbal stem cells. Reproduced from Qu, Y., Thomas, K.E., Vola, M.E., *et al.*, 2012. Rapid identification of microorganisms using the two-photon ophthalmoscope. Investativе Ophthalmology and Visual Science 53 (14), 6175; Qu, Y., Thomas, K.E., Schuster, A.K., *et al.*, 2011. Identification of microorganisms utilizing the two-photon ophthalmoscope. Investigative Ophthalmology and Visual Science 52 (14), 5823.

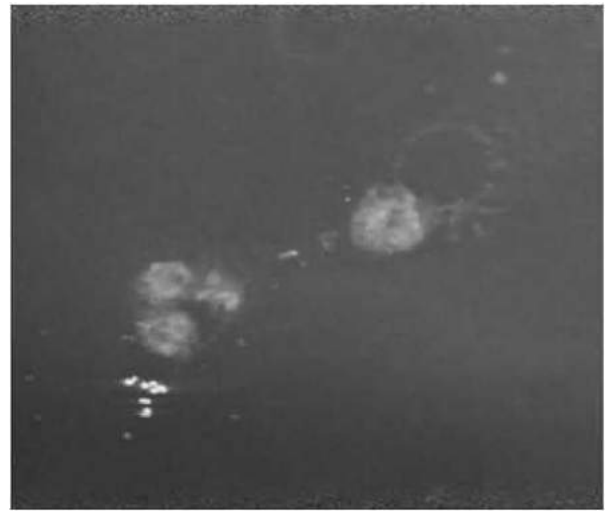


Fig. 11 Two-photon imaging of *Acanthamoeba* keratitis. Reproduced from Qu, Y., Thomas, K.E., Vola, M.E., *et al.*, 2012. Rapid identification of microorganisms using the two-photon ophthalmoscope. Investigative Ophthalmology and Visual Science 53 (14), 6175; Qu, Y., Thomas, K.E., Schuster, A.K., *et al.*, 2011. Identification of microorganisms utilizing the two-photon ophthalmoscope. Investigative Ophthalmology and Visual Science 52 (14), 5823.

Although confocal microscopy lacks sufficient resolution in detecting the *Acanthamoeba* keratitis, it is used for diagnostic purposes since confocal microscopy is the only available diagnostic tool for patients. In confocal microscopy, the *Acanthamoeba* is visualized as round or ovoid highly reflective structures and the same is depicted by the two-photon microscopy (**Fig. 11**).

Second Harmonic Imaging of Cornea

Collagen is the major component of connective tissues including cornea, and due to its transparency to visual and near infrared light the human eye is ideal for laser-based diagnostic and imaging applications. Among different multiphoton implementations, SHG imaging is particularly suitable to investigate non-centrosymmetric structures like collagen fibrils (**Figs. 12** and **13**). The basic structure of the collagen fibril is a triple helix composed of three proteins chains, which gives collagen the intrinsic ability of SHG

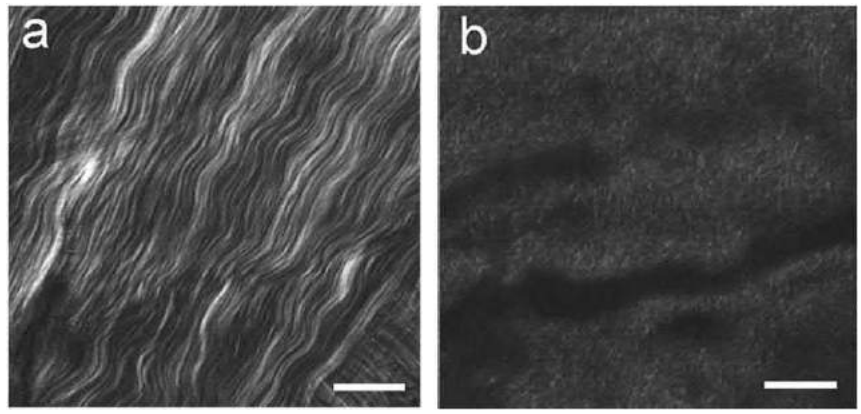


Fig. 12 SHG imaging of corneal collagen fibrils in (a) forward and (b) backward directions from porcine cornea. The fibrillar structures resolved in (a) correspond to collagen bundles which are composed of regularly packed collagen fibrils. Scale = 10 mm. Reproduced from Han, M., Giese, G., Bille, J., 2005. Second harmonic generation imaging of collagen fibrils in cornea and sclera. Optics Express 13, 5791–5797.

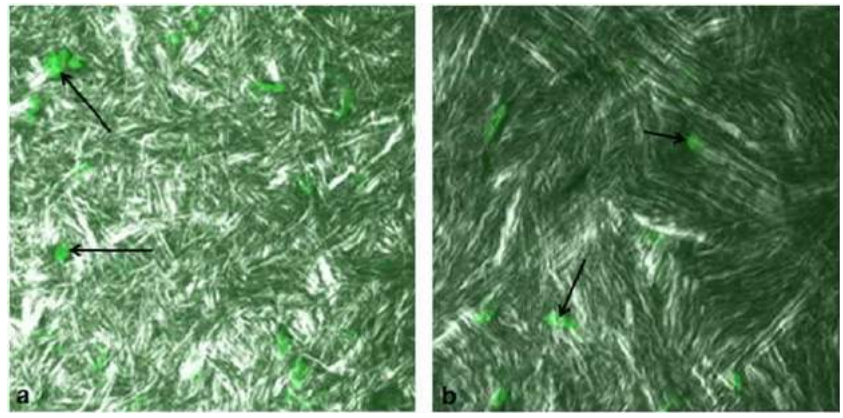


Fig. 13 SHG imaging and two-photon imaging of human cornea from (a) Bowman's membrane and (b) corneal stroma. The collagen fibers were visualized using the SHG imaging and the keratocytes (arrows) were visualized with the two-photon imaging. Reproduced from Han, M., Giese, G., Bille, J., 2005. Second harmonic generation imaging of collagen fibrils in cornea and sclera. Optics Express 13, 5791–5797.

imaging. Similar to TPEF, SHG is produced in only a small focal volume, permitting high resolution 3D optical sectioning of thick tissues. In contrast to TPEF, SHG from collagen is an intrinsic and a coherent process. Intrinsic imaging avoids the complications of slicing and labeling, and samples can be investigated under physiological conditions. Coherent constructive or destructive interference of SHG provides extra hints to the ultrastructure of collagen fibrils and their organizations.

The collagen fibrils of the porcine cornea using SHG imaging are shown in **Fig. 12**. Most collagen fibrils run parallel to the cornea surface and share similar orientations with their neighbors. One of the unique features of SHG is that the geometry of the SHG emission field reflects the size and shape of the collagen fibrils. The SHG radiation pattern is mainly determined by the phase matching condition and the objects with the axial size on the order of the second harmonic wavelength exhibit forward directed SHG, while objects with a axial size less than $\lambda/10$ (approx. 40 nm) are estimated to produce nearly equal backward and forward SHG signals.

In **Fig. 12(b)**, the backward SHG from cornea was extremely weak and there was no correlation between the structures revealed by forward and backward SHG imaging. The predominant forward SHG implies that the corneal collagen fibrils are not randomly distributed. It's worth mentioning that the fibrillar structures revealed in **Fig. 12(b)** actually correspond to collagen bundles composed of many corneal collagen fibrils. In cornea, the collage fibrils ($n = 1.47$) and the extrafibrillar matrix ($n = 1.35$) have different refractive indices, thus the collagen fibrils have to be treated as individual scatters. Since the dimension of the collagen bundle (approximately 0.5 μm) is close to the second harmonic wavelength (400 nm), the phase correlation of SHG from neighboring collagen fibrils should be taken into account. The forward predominant SHG radiation from cornea indicates the regular arrangement of the collagen fibrils, at least in the domain of the collagen bundles.

In **Fig. 13**, SHG and two-photon imaging of human cornea from Bowman's membrane (**Fig. 13(a)**) and corneal stroma (**Fig. 13 (b)**) is depicted. The collagen fibers were visualized using the SHG imaging and the keratocytes (arrows) were imaged with TPEF imaging.

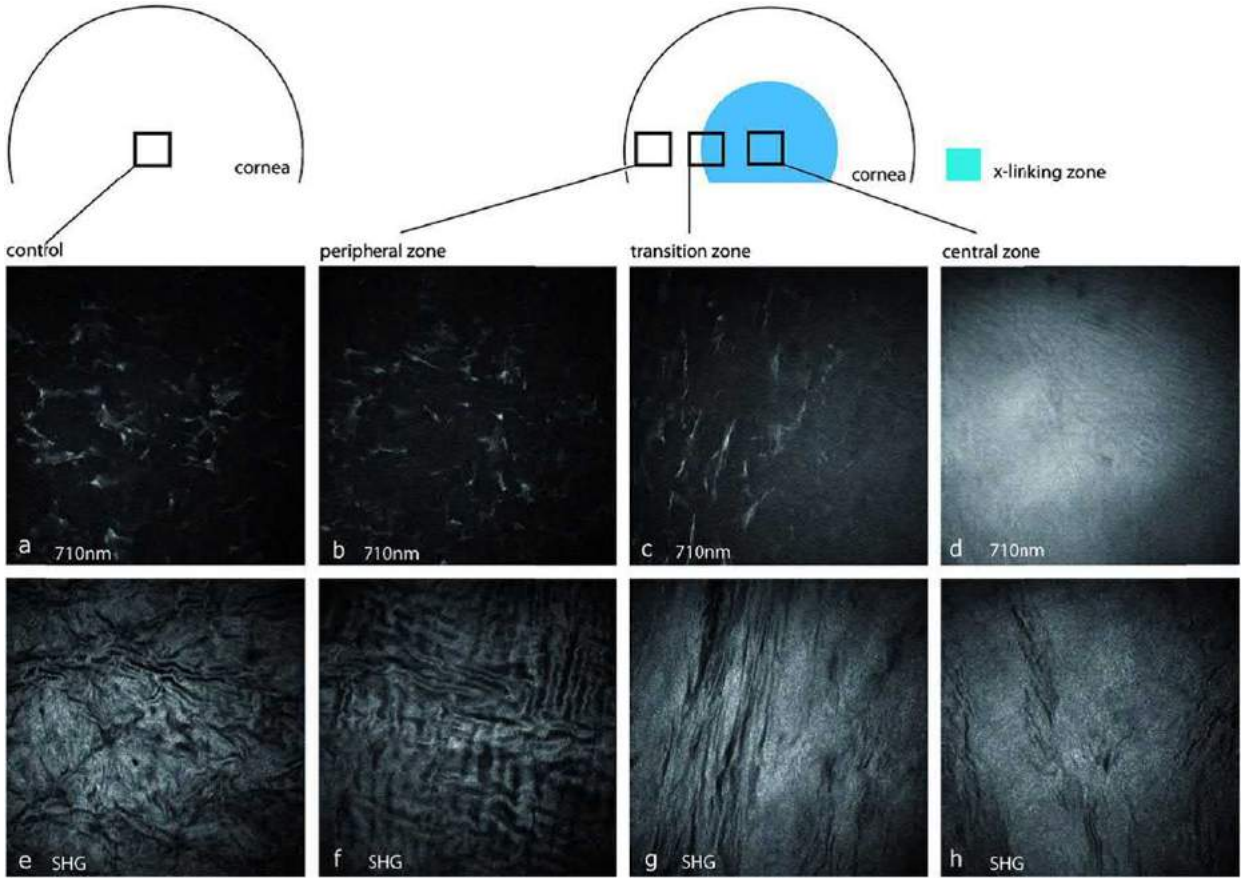


Fig. 14 Two-photon microscopy of enucleated rabbit eyes 2 weeks after standard corneal CXL, upper row: two-photon imaging at 710 nm excitation light and lower row: second harmonic generation. (a) Two-photon imaging of the central zone of control cornea; (b) the peripheral zone of the treated cornea shows keratocytes in a dense network; (c) at the tangential zone, there is a sharp transition between the treated area and the untreated area, as shown by diminished keratocytes and a strong autofluorescence signal toward the central zone; (d) in the central zone, there are no keratocytes and the autofluorescence signal is uniform and strong; (e) and (f) second harmonic generation of stromal collagen in the control zone and the peripheral zone of the treated cornea shows a wavelike pattern; (g) at the transition zone toward the treated area, the wavelike pattern changes to a uniform signal; (h**)** in the central zone, a uniform SHG signal is visible. Reproduced from Steven, P., Hovakimyan, M., Guthoff, R.F., Hüttmann, G., Stachs, O., 2010. Imaging corneal crosslinking by autofluorescence 2-photon microscopy, second harmonic generation, and fluorescence lifetime measurements. Journal of Cataract Refractive Surgery 36 (12), 2150–2159.

Two-Photon Imaging of Corneal Cross-linking

Keratoconus is a progressive, noninflammatory and bilateral ectatic corneal disease characterized by corneal thinning and weakening. The thinning is most apparent at the apex of the cornea, and the steep conical protrusion leads to high myopia with irregular astigmatism. The visual loss occurs primarily from irregular astigmatism and myopia, and secondarily from the corneal scarring. Computerized corneal topography has become a gold standard for the early identification of keratoconus and recently confocal microscopy has also been used to assess the keratoconus cornea. Corneal cross-linking (CXL) is an invasive treatment procedure for keratoconus in order to stop or delay the process. The CXL procedure increases the mechanical and biomechanical stability of the cornea by application of ultraviolet-A light of 370 nm and riboflavin (vitamin B2). The assessment of cornea after cross-linking is limited because the treatment effect cannot be visualized by slit-lamp biomicroscopy. Confocal microscopy can detect the side effects like stromal edema and rarefication, the reappearance of stromal keratocytes over time. However, the effect of crosslinks between the collagen fibers after CXL cannot be visualized by confocal microscopy. Two-photon imaging with SHG is effective in measuring the crosslinks between collagen fibers as shown in Fig. 14.

Laser Safety Considerations of Two-Photon Microscopy

The safe use of lasers has been a primary consideration since lasers are widely used for treatments and in research laboratories. The American National Standards Institute (ANSI) has specific standards for eye safety that take into account many of the important experimental variables such as laser power delivered at the cornea, viewing time, beam diameter or full-field viewing, the exposure area on the retina, and the wavelength. Near infrared radiation (NIR) relative to visible wavelength is considered to be less

phototoxic and has deeper penetration in thick biological tissues, which is one of the key reasons for its widespread use in imaging devices. Compared to retinal imaging, the safety standards for illuminating the cornea and anterior structures of the eye are tolerant. The laser safety limits for corneal imaging can be calculated by the maximum permissible exposures (MPE) according to the ANSI standards as follows:

$$\text{Recommended MP corneal irradiance} = 25 \times t - 0.75 \left(\text{W/cm}^2\right) \text{ for } t < 10\text{s}$$

$$\text{Recommended MP corneal irradiance} = 4.0 \left(\text{W/cm}^2\right) \text{ for } t > 10\text{s}$$

For example, if the irradiated area is described by 1536 μm × 1536 μm = 0.0236 cm^2, the MPE should be 94.4 mW for longer exposure time ($t > 10$s) and should be 515 mW for shorter exposure time.

Future Directions

Before implementing multiphoton microscopy for in vivo imaging of the human cornea, the shortcomings of these nonlinear microscopy techniques have to be addressed. For TPEF imaging, the drawback of depositing the energy into the tissue has to be evaluated to prevent photodamage. Although SHG and THG are absorption-free and can be used without photobleaching effects, harmonic imaging has another disadvantage that currently obstructs its use in ophthalmic practice. The harmonic signals are emitted predominantly in forward direction, whereas in backward direction the harmonic signals are weak. This limits SHG imaging for in vivo applications, and the backscattered signal might be enhanced using an absorbing dye. Also, new optical techniques such as wavefront aberration optimization and adaptive optics may be a key for future in vivo applications. Until these restrictions of multiphoton microscopy are eliminated, confocal microscopy remains exclusive in the assessment of cellular morphology in living human cornea.

Acknowledgment

The authors like to thank Heidelberg Engineering GmbH (Heidelberg, Germany) for providing equipment support.

See also: Optical Coherence Tomography and Its Application to Imaging of Skin and Retina. Optics of the Human Eye

Further Reading

Denk, W., Strickler, J.H., Webb, W.W., 1990. Two-photon laser scanning fluorescence microscopy. Science 248, 73–76.
Guthoff, R.F., Baudouin, C., Stave, J., 2006. Atlas of Confocal Laser Scanning In-Vivo Microscopy in Opthalmology. Germany: Springer.
Guthoff, R.F., Zhivov, A., Stachs, O., 2009. In vivo confocal microscopy, an inner vision of the cornea – A major review. Clinical and Experimental Ophthalmology 37, 100–117.
Han, M., Giese, G., Bille, J., 2005. Second harmonic generation imaging of collagen fibrils in cornea and sclera. Optics Express 13, 5791–5797.
Hao, M., Flynn, K., Nien-Shy, C., *et al*., 2010. In vivo non linear optical (NLO) imaging in live rabbit eyes using the heidelberg two-photon laser ophthalmoscope. Experimental Eye Research 91 (2), 308–314.
Mantopoulos, D., Cruzat, A., Hamrah, P., 2010. In vivo imaging of corneal inflammation: New tools for clinical practice and research. Seminars in Ophthalmology 25 (5-6), 178–185.
Steven, P., Hovakimyan, M., Guthoff, R.F., Hüttmann, G., Stachs, O., 2010. Imaging corneal crosslinking by autofluorescence 2-photon microscopy, second harmonic generation, and fluorescence lifetime measurements. Journal of Cataract & Refractive Surgery 36 (12), 2150–2159.

Refractive Error and Wavefront Sensing

Larry N Thibos, Indiana University, Bloomington, IN, United States

© 2018 Elsevier Ltd. All rights reserved.

Definitions and Conventions

Refractive Error, Refractive Correction, and Their Physical Units

The purpose of the eye's optical system is to cast an image of the external world onto the photoreceptor layer of rods and cones in the retina. If the system were perfect it would focus all rays of light from a point source into a single image point on the retina. Real eyes, however, suffer from aberrations, which are optical imperfections that degrade the quality of the retinal image and hamper vision. Since aberrations are flaws in the refraction of light, one might presume that the terms aberrations and refractive errors are synonymous. However, in the field of ophthalmic and visual optics, the term refractive error is restricted to two specific types of aberrations: defocus and astigmatism. Historically, these are the only two aberrations that could be measured routinely in a clinical environment and then corrected easily with spectacles or contact lenses. Although the existence of other ocular aberrations (e.g., coma, spherical aberration, etc.) has been known since the time of Newton, those aberrations could not easily be measured or corrected clinically. Since these "higher-order" aberrations fell outside the domain of conventional clinical practice, they were excluded from the traditional definition of refractive error. Depending on context, astigmatism may also be excluded leaving just defocus as the only aberration implied by the term refractive error.

The sign convention for specifying refractive errors of eyes can appear confusing. Although scientists may be inclined to describe the refractive errors of the eye, per se, clinicians prefer to specify the lens needed to correct the eye's refractive errors. As illustrated in Fig. 1, the ideal condition of emmetropia exists when distant objects produce well-focused retinal images.

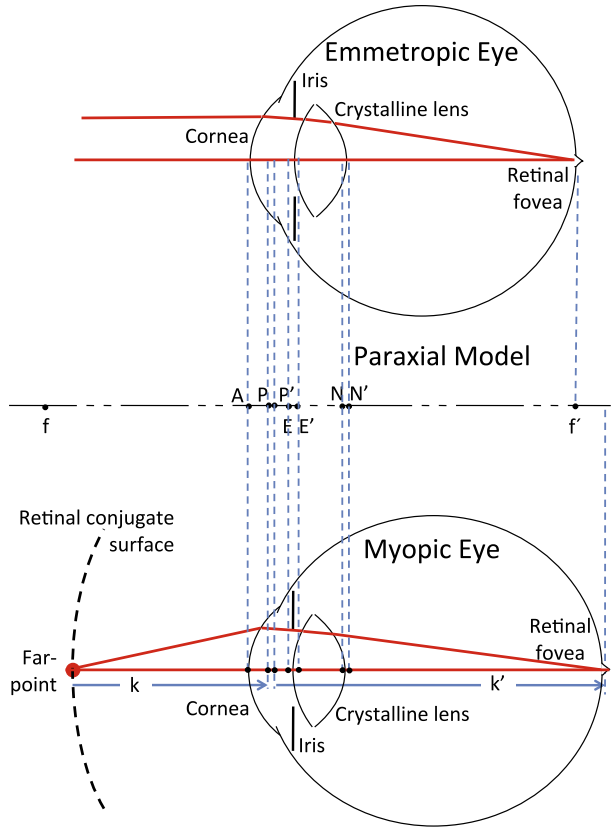


Fig. 1 Schematic optical diagrams of the eye. Upper panel shows an emmetropic eye focusing rays from a distant point source onto the retinal photoreceptors in the fovea. Lower panel shows a myopic eye focusing rays from a point source at finite distance onto the retinal photoreceptors. Middle panel is a Gaussian paraxial model for both eyes showing cardinal points (f,f' – focal points; P,P' – principal points; N,N' – nodal points), the entrance and exit pupils (E,E') and the corneal apex (A).

 doi:10.1016/B978-0-12-803581-8.09780-0

However, a short-sighted (i.e., myopic) eye has too much refractive power to clearly focus the retinal image of a distant object, and therefore requires a correcting spectacle or contact lens of negative power. Thus, the sign of the defocus component of refractive error for myopic eyes is negative by standard clinical conventions. Conversely, a hyperopic eye has too little power to focus on distant objects and therefore requires a positive correcting lens, so hyperopic refractive error is positive.

Refractive errors and viewing distance of objects are both specified in units of inverse meters, more commonly referred to as diopters (D). Diopters is the preferred unit in ophthalmic and visual optics because practical problems are more easily solved when the Gaussian conjugate equation of paraxial optics

$$n'/k' = n/k + (n' - n)/r \tag{1}$$

where k is the object distance, k' is the image distance, n is the refractive index of object space, n' is the refractive index of image space, and r is the radius of curvature of the refracting surface, is rewritten as

$$K' = K + F \tag{2}$$

where K is the object vergence, K' is the image vergence, and F is the refracting power of the surface attributed to the Gaussian principal planes. All three quantities in this linear equation have physical units of diopters. The situation here is analogous to electrical circuits involving parallel resisters, for which solutions are most easily obtained by introducing the term conductance when referring to the inverse of resistance. That maneuver requires a corresponding change of physical units of resistance (ohms) to inverse units of conductance (mhos). In the present optical analogy, inverse distance from object or image points to their respective principal points is called vergence, which has units of diopters. Thus, the Gaussian conjugate Eq. (2) reads "the vergence K' of light leaving a refracting surface (or thin lens) is equal to the incident vergence of light K plus the refracting power F of the lens". If the lens is astigmatic, this same equation applies to refraction in any meridian but the refracting power F varies sinusoidally with meridian angle. A simple mnemonic for distinguishing the closely related terms power and vergence is: "lenses have the power to change the vergence of light".

Given the terminology introduced above, the defocus component of refractive error may be defined three equivalent ways that are mutually consistent but have different interpretations. They may be understood by considering **Fig. 1**, which illustrates a simple case of myopia caused by axial elongation of the eye. Thus, the myopic optical system in this example has the same paraxial cardinal points as the illustrated emmetropic eye, but axial elongation causes the retinal conjugate surface to move from infinity to a finite distance from the eye. The myopic eye's far point, which is the point in object space that is optically conjugate to the retinal fovea, is located at some finite distance k from the first principal point P. So the first interpretation of refractive error occurs in object space: it is the vergence of the eye's far point,

$$\text{Refractive error} = K = n/k \tag{3}$$

The second interpretation is in image space: it is the focusing error for a distant object point. Since $K=0$ for objects at infinity, the focusing error is computed from Eq. (2) as the difference between the required power K' (sometimes called the dioptric length of the eye) and the eye's available power F,

$$\text{Refractive error} = K = K' - F \tag{4}$$

The third interpretation conceives of refractive error as a lens prescription: it is the power of the correcting lens needed to focus a distant target on the retina. Again $K=0$, so the required correcting lens has to make up the difference between the eye's dioptric length and its power, as indicated in Eq. (4). In principle, the correcting lens should be placed in the eye's first principal plane but in practice it is placed on the cornea (i.e., a contact lens, which requires only a small adjustment in power), or in the spectacle plane (which requires a larger adjustment in lens power to compensate for the significant separation of the lens from the eye's first principal point).

Specification of Sphero-Cylindrical Lenses and Refractive Errors

Several conventions are in common use for specifying the sphero-cylindrical lens needed to fully correct an eye's refractive errors. Differences between these conventions arise from alternative ways of envisioning how a prescribed sphero-cylindrical lens is constructed from component lenses. Two of these conventions presuppose that the correcting lens is the combination of a spherical lens of power S juxtaposed with a cylindrical lens of power C oriented with the axis of the cylinder at some angle α. The difference between these two conventions is the sign of C. Optometrists typically prefer to think of C as a negative number, whereas ophthalmologists typically prefer to think of C as a positive number. Simple transposition formulae allow conversion from one convention to another. A third convention preferred by many researchers replaces S with M, the so-called mean spherical-equivalent power. If one imagines correcting an eye with sphero-cylindrical refractive error using only a spherical lens of power M, the eye would remain astigmatic by some amount J. The value of J refers to the power of a so-called Jackson crossed-cylinder, which is constructed from two conventional cylinder lenses of equal but opposite powers oriented with their axes mutually perpendicular.

All three of the conventions described above may be said to be in polar form since the astigmatic component of the correction is given in terms of a magnitude (lens power) and an angle (the orientation of the lens axis). For computational purposes, conversion from polar form to rectangular form is usually advantageous. This is easily accomplished for the cross-cylinder

convention using the following transposition formulae:

$$\begin{aligned} M &= S + C/2 \\ J_0 &= -\frac{C}{2}\cos 2\alpha \\ J_{45} &= -\frac{C}{2}\sin 2\alpha \end{aligned} \tag{5}$$

The three-dimensional vector $[M, J_0, J_{45}]$ is known in the ophthalmic optics literature as a power vector and the length of a power vector is called blur strength. Blur strength quantifies the overall blurring effect of sphero-cylindrical refractive error on image quality according to geometrical optics. The components of a power vector may be converted to second-order Zernike aberration coefficients using the following formulae:

$$\begin{aligned} M &= \frac{-c_2^0 4\sqrt{3}}{r^2} \\ J_0 &= \frac{-c_2^2 2\sqrt{6}}{r^2} \\ J_{45} &= \frac{-c_2^{-2} 2\sqrt{6}}{r^2} \end{aligned} \tag{6}$$

where c_n^m is the nth order Zernike coefficient of meridional frequency m and r is the pupil radius. If Zernike coefficients are specified in microns (10^{-6} m) and pupil radius is specified in millimeters (10^{-3} m) then the computed values of M, J_0 and J_{45} will have units of diopters (m^{-1}).

Specification of Higher-Order Aberrations of Eyes

The accepted convention for reporting Zernike aberration coefficients in the ophthalmic optics field is given in ANSI standard Z80.28. (ANSI, 2010) The normalization scheme used in this standard allows an interpretation of individual Zernike coefficients as the RMS wavefront error of the corresponding aberration mode. Accordingly, we may infer from Eq. (6) that defocus (M) and astigmatism (J_0, J_{45}) in diopters are proportional to the ratio of RMS wavefront error to pupil area.

Zernike polynomials Z_n^m are indexed according to their radial order n and their meridional frequency m. Historically, the attention of clinical practitioners has been directed at the lower Zernike orders 1–2 but increasing attention to the higher orders ($n > 2$) has occurred in recent years due to the technological development of wavefront aberrometers (see Section Aberrometry and Wavefront Sensing). The mathematical formula describing individual Zernike basis functions, or modes, is given by the equation

$$Z_n^m = N_n^m R_n^{|m|}(\rho) M(m\theta) \tag{7}$$

which is separable into a function of pupil-plane coordinates ρ (the normalized radial coordinate) and θ (meridian angle, measured counterclockwise from the horizontal when viewing the patient). The radial term for the Zernike polynomial function with indices n and m is given by the equation

$$R_n^{|m|}(\rho) = \sum_{s=0}^{0.5(n-|m|)} \frac{(-1)^s (n-s)!}{s!(0.5(n+|m|)-s)!\ (0.5(n-|m|)-s)!}\ \rho^{n-2s} \tag{8}$$

where s is an integer summation index incremented by one unit. The meridional (or azimuthal) term for a Zernike polynomial function with index m is given by the equations

$$\begin{aligned} M(m\theta) &= \cos(m\theta) \quad \text{if } m \geq 0 \\ M(m\theta) &= \sin(|m|\theta) \quad \text{if } m < 0 \end{aligned} \tag{9}$$

The normalization term N in Eq. (7) makes every Zernike mode have unit variance over the unit circle and is defined by the equation

$$N_n^m = \sqrt{(2-\delta_{0,m})(n+1)} \quad \text{where } \delta_{0,m} = 1 \text{ if } m = 0, \quad \delta_{0,m} = 0 \text{ if } m \neq 0 \tag{10}$$

Zernike aberration coefficients provide the weighting factors needed to reconstruct a wavefront aberration for an individual eye with a weighted sum of orthonormal basis functions. The circle polynomials of Zernike were selected over the traditional Seidel series for the ANSI standard because they are a complete set that can be used to represent any continuous, smooth function over a circular domain. Moreover, individual basis functions in the set correspond to common aberrations found in optical systems (e.g., defocus, coma, spherical aberration). One disadvantage of Zernike basis functions is that their spatial derivatives are not orthogonal, which hampers the accurate calculation of coefficients from wavefront slope measurements. This disadvantage is overcome by fitting slope data with Zernike radial slope polynomials (Nam *et al.*, 2009).

Another disadvantage stems from the fact that Zernike basis functions of a given order are balanced with basis functions of lower orders to achieve orthogonality and minimize RMS variation. For example, the basis function for Zernike spherical aberration is constructed by subtracting an amount of defocus (which varies as ρ^2) from Seidel spherical aberration (which varies as ρ^4). Thus the total amount of defocus (in the ρ^2 sense) is distributed across multiple Zernike modes, a fact that can hamper interpretation and complicates the calculation of power vector description of refractive errors when higher-order aberrations are present. These problems are reduced by an alternative set of basis functions (Stephenson, 2009) that combine the benefits of Zernike polynomials (completeness) and Seidel polynomials (un-balanced).

Methods for Determining Refractive Error and Refractive State

Refraction is a clinical process for determining the refractive error of an eye. Refractions can be performed objectively with a clinical autorefractor, an instrument that determines spherical and astigmatic focusing errors of the eye, or with an aberrometer, an instrument that also measures higher-order aberrations. Traditionally, refractive errors are measured subjectively by clinicians using psychophysical methods to determine the best combination of spherical and cylindrical correcting lens for optimizing vision and therefore, by implication, optimizing focusing of the retinal image. Clinicians generally regard the subjective refraction as definitive since it includes the patient's judgment of optical focus based on their own visual perception using their own retina and brain. However, other considerations (e.g., matching image size in the two eyes) may lead the clinician to prescribe correcting lenses that are somewhat suboptimal optically in order to achieve overall objectives of visual comfort and performance. Consequently, the prescribed lens is often different from that indicated by the refraction procedure.

Locating the Eye's Far Point With Optical Measurements

The far point of an eye is that point in object space which is optically conjugate to the entrance apertures of the foveal photoreceptors when accommodation is relaxed. Since refractive error is equal to the vergence of the far point according to Eq. (3), locating an eye's far point is a straightforward means of determining refractive error. Unfortunately, an unambiguous far point exists only for an ideal eye which is free of all optical aberrations except defocus. Real eyes invariably suffer from other aberrations besides defocus, and therefore an operational definition of the far point is required. For example, an astigmatic eye may be described as having two far points, one for line objects oriented parallel to the axis of astigmatism and another for the orthogonal orientation. The point midway between these two extremes is a widely accepted approximation for the far point of an astigmatic eye since this is where the far point would be located if the astigmatism were corrected by a lens. This approximation assumes higher-order aberrations are negligible, in which case refractive errors may be computed directly from second-order Zernike coefficients using Eqs. (5) and (6).

One reasonable approximation for the far point of an eye with higher-order aberrations is that location in object space where an object must be located in order to maximize the quality of its retinal image. Unfortunately, this approximation does not locate the far point uniquely for several reasons. Firstly, image quality depends on the characteristics of the visual stimulus (e.g., luminance, size, spatial frequency spectrum, wavelength spectrum) and therefore may change as the stimulus changes. Secondly, there are many ways to define and measure image quality (Thibos *et al.*, 2004), none of which are universally endorsed by the clinical or vision science communities. Thirdly, the psychophysical judgment of optimum focus by an observer depends on factors other than optical image quality, such as neural sampling of the retinal image, cortical neural processing, and perceptual weighting given to the various features of optical blur (e.g., contrast attenuation, loss of sharpness, and doubling or ghosting of the image). Moreover, the selection of an objective method for locating the nominal far point of an eye is likely to depend on the intended application.

Definition of the Eye's Refractive State

The human eye is an active optical system that responds to changes in viewing distance by changing its refractive power, a process called accommodation. At any given state of accommodation, each point on the retinal surface is optically conjugate (at least approximately) to some location in visual space. The locus of all such points is called the retinal conjugate surface. Refractive state is defined as the vergence of the retinal conjugate surface, which in general will vary across the visual field. Thus, refractive state is essentially the same concept as refractive error defined above, but extended to apply to the accommodating eye. Although it would seem reasonable to use the general term "refractive state" for an eye in any state of accommodation, the historical precedent is to use the term "refractive error" for the special case of relaxed accommodation (i.e., minimum power). Clearly, the same difficulty in establishing a universally accepted method for specifying refractive error described above applies equally to specifying refractive state.

Methods for Estimating Refractive State From Zernike Aberration Coefficients

Wavefront aberrometers make comprehensive measurements of an eye's aberrations reported in the form of Zernike aberration coefficients, C_n^m. From these measurements one may compute the eye's wavefront aberration function $W(\rho,\theta)$ as a weighted sum of

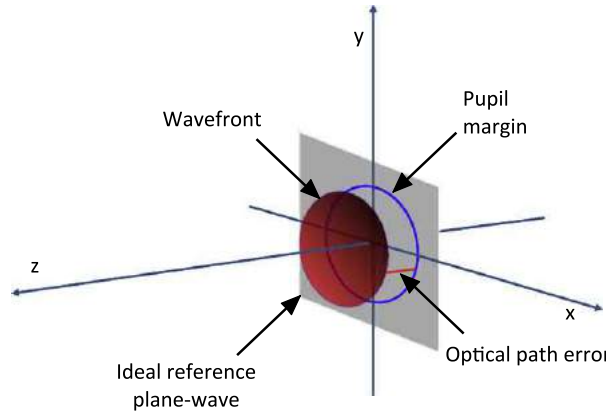


Fig. 2 A reference coordinate system for specifying wavefront errors. A right-hand (*x*,*y*,*z*) coordinate reference frame is constructed such that the *z*-axis is the chief ray and the (*x*, *y*) plane is perpendicular to the *z*-axis at the center of the exit pupil.

Zernike polynomials,

$$W(\rho,\theta)=\sum_{n,m}c_n^m Z_n^m \tag{11}$$

A given aberration function refers to a specific visual direction, which is typically the foveal line of sight defined by the path of the chief ray in object space joining the point of regard (i.e., the fixation point) with the center of the eye's entrance pupil. More generally, the chief ray for any point in visual space defines a line-of-sight along which an aberration function may be specified.

Wavefront aberration functions, or maps, have a variety of physical, mathematical, and practical interpretations and uses. Physically, the map describes the optical distance from an object point to the corresponding retinal image point through different parts of the pupil, relative to the optical distance along a path through the center of the pupil (i.e., along the chief ray). An equivalent interpretation, illustrated in **Fig. 2**, is the sag (relative to an ideal plane-wave) in the *z*-direction of a wavefront reflected from the eye produced by a point source on the retina. These differential errors in optical path length cause phase errors in light arriving at the image point, which in turn degrades image quality. Mathematically, the aberration map $W(\rho,\theta)$ is the phase portion of the generalized pupil function $P(\rho,\theta)$ defined in optical theory as

$$P(\rho,\theta)=A(\rho,\theta)\exp(-\mathrm{i}kW(\rho,\theta)) \tag{12}$$

where $A(\rho,\theta)$ is the corresponding amplitude function and $k=2\pi/\lambda$. The generalized pupil function is a fundamental description of an optical system that enables calculation of the optical point spread function (PSF) and optical transfer function (OTF) (Goodman, 2005), both of which are functional measures of optical quality. Scalar metrics of image quality computed from the PSF or OTF are useful in practical optimization problems, such as determining refractive state or prescribing lenses to correct the eye's aberrations.

Aberrometry and Wavefront Sensing

Wavefront sensors, the core technology used in ocular aberrometers, are both new and old. In the clinical literature, the first applications of aberrometry to refractive surgery (Applegate and Howland, 1997) and to ocular disease (Thibos and Hong, 1999) appeared near the end of the 20th century years. However, the fundamental principle by which modern aberrometers measure ocular wave-front aberrations of eye was discovered 400 years ago by the celebrated Jesuit philosopher-astronomer, Christopher Scheiner (Scheiner, 1619), a contemporary of Galileo and Kepler. All three astronomers conceived of the eye as an optical instrument that forms retinal images in the same way that a telescope forms images. However, it was Scheiner who first demonstrated how to measure the refractive error of the human eye using a simple device that is known today as Scheiner's disk. Although Scheiner used his invention to measure and study only spherical refractive error (i.e., defocus, which is the simplest and most prevalent of all ocular aberrations), the basic idea was generalized by Thomas Young at the beginning of the 19th century to measure astigmatism in his own eye (Young, 1801), and eventually by Liang *et al.* at the end of the 20th century to measure higher-order aberrations (Liang *et al.*, 1994). Thus, Scheiner's disk is the prototype of the modern Shack–Hartman wavefront sensor for measuring ocular aberrations.

Determining Optical Path Lengths From Ray Deflections

The challenge of using a Shack–Hartmann sensor with a living eye is that the eye is a closed system, so it can be measured only by reflecting light off the patient's retina as illustrated in **Fig. 3**. Thus, for measurement purposes, object space is inside the eye and image space is the external world. To make measurements, a narrow laser beam is introduced into the eye using a beam-splitter to produce a source of reflected light, a so-called retinal beacon. Light reflected out of the eye passes through an array of small,

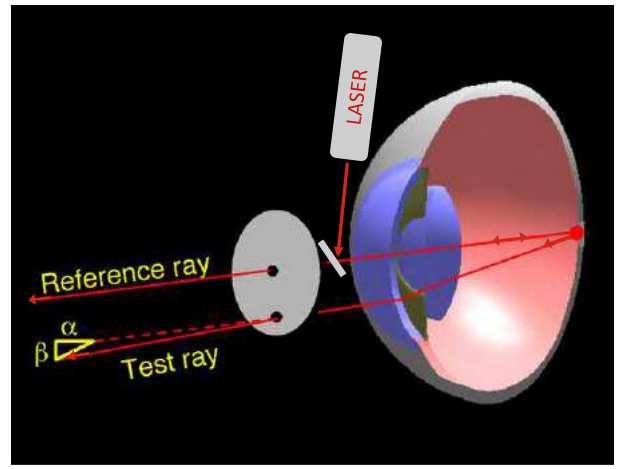


Fig. 3 Principle of operation of the Scheiner–Hartmann–Shack wavefront aberrometer. A laser beam injected into the eye produces a retinal beacon that reflects light out of the eye for measurement. Angular deviation of an isolated test ray relative to the direction of the reference ray is a measurement of local wavefront slope. In a practical instrument, multiple apertures defined by a micro-lenslet array produce simultaneous measurements at many points in the eye's pupil.

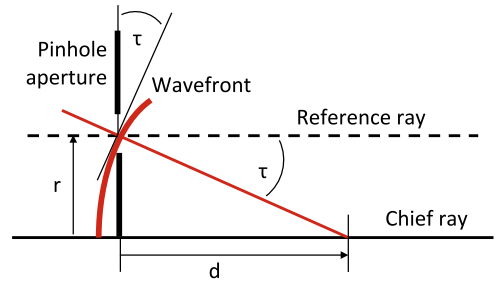


Fig. 4 Geometry for defining wavefront vergence. A pinhole aperture located distance r from the z-axis isolates a ray perpendicular to the wavefront and intersecting the z-axis at some distance Z from the aperture plane. Skew rays that do not intersect the chief ray are projected into the plane of the diagram to determine the radial component of vergence.

pinhole apertures (i.e., Scheiner's disk or a Hartmann screen) to isolated rays exiting through specific locations in the eye's pupil. The ray's direction of propagation relative to the chief ray is specified by (α,β), the angles of deviation from a secondary reference ray (dashed line) parallel to the chief ray and passing through the aperture. In a modern device, the array of pinholes is replaced by an array of micro-lenslets that subdivides the beam of light reflected out of the eye from the retinal beacon. Each lenslet forms a spot image that deviates horizontally and vertically from the optical axis of the lenslet by an amount that is directly proportional to the angular deviations (α,β). Since rays are, by definition, normal to the exiting wavefront, the sensor is essentially a mechanism for measuring wavefront slope, from which wavefront shape is recovered by integration.

Converting Ray Aberrations to Wavefront Aberrations

As described in Section Determining Optical Path Lengths From Ray Deflections, the principle of operation of the Shack–Hartman wavefront sensor used in ocular aberrometers is to measure the deviation of individual rays of light passing through various locations in the eye's pupil. From the geometry of Fig. 4 we see that, for small angles of deviation of the ray from the reference direction, angle τ and wavefront slope are approximately equal,

$$\text{wavefront slope} = \tan(\tau) \cong \tau = \text{deviation angle} \tag{13}$$

In general, the aberrated ray does not lie in the meridional plane defined by the optical axis of the system and a point on the wavefront located at the foot of the ray. However, if we project the ray onto the meridional plane of Fig. 4, then another useful relationship can be deduced from the geometry:

$$\frac{\text{wavefront slope}}{\text{location in pupil}} = \frac{\partial W(\rho,\theta)/\partial\rho}{\rho} = \frac{\tan(\tau)}{r} = \frac{1}{d} = \text{wavefront vergence} \tag{14}$$

This equation says that, for any meridian θ, the radial component of wavefront vergence (in diopters) is equal to the ratio of radial wavefront slope (in radians) to pupil location (in meters). So, although wavefront vergence is a vector quantity with

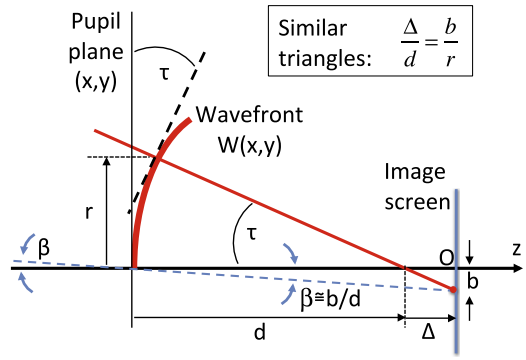


Fig. 5 Geometry for expressing the relationship between wavefront aberrations and the size of blurred images. The diagram depicts a cross-section of a reflected wavefront of light emerging from the eye produced by a point source on the retinal fovea. The plane of the diagram is perpendicular to the eye's entrance pupil and contains the foveal line of sight (i.e., the *z*-axis). An isolated ray passing through the pupil plane at distance *r* from the pupil center intersects the image screen at distance *b* from the *z*-axis and thus contributes one point to the blurred image. (For simplicity, we assume the ray is in the plane of the diagram but in general this is not necessarily true.) The angular size (in radians, subtended at the pupil center) of this blurred point is approximately equal to the focusing error *E* (in diopters) of the aberrated ray (which depends on the axial location of the image screen) and radial distance *r* (in meters).

orthogonal components proportional to (α,β), the radial component is a scalar quantity that may be used to recover wavefront phase by integration (Nam *et al.*, 2009).

A similar geometrical analysis reveals the relationship between wavefront aberrations and the size of blurred images. Although we are ultimately interested in blurring of the retinal image, aberration measurements are performed on the reflected wavefront emerging from the eye as illustrated in **Fig. 5**. Consider an image screen that is placed some small distance Δ from the focused plane where an isolated ray intersects the chief ray (i.e., the *z*-axis). This focusing error causes the image point contributed by the illustrated ray to be displaced by amount b from the image point O contributed by the chief ray. In other branches of optics, this linear displacement in the image plane is of primary concern. However, in vision science we are typically interested more in the angle β subtended by b at the pupil center. If we assume the pupil is near the eye's nodal point then the angles of blur subtended in image and object space are the same. The extent of this angular blur is easily computed if we express ray aberrations as a vergence error in diopters. That is, let the vergence of the image screen be $1/(d+\Delta)$ and the vergence of the ray in this example be $1/d$, so the vergence error E is

$$E = \frac{1}{d+\Delta} - \frac{1}{d} = -\frac{\Delta}{d^2+d\Delta} \cong -\frac{\Delta}{d^2} \quad \text{for } \Delta \ll d \tag{15}$$

The negative sign in this result means a negative correcting lens would be required to focus this aberrant ray. A negative sign also means the ray crosses the optical axis before striking the image surface.

From the geometry of similar triangles in **Fig. 5**, $\Delta/d = b/r$ and for small values of defocus, $\beta \cong b/d$. Substituting these two relationships into Eq. (15) reveals that the angular subtense β of the blurred image point (in rad) produced by the aberrated ray is the product of focusing error E (in diopters) and radial position r of the ray in the pupil plane (in meters),

$$E = -\frac{b}{rd}, \quad -Er = \frac{b}{d} \cong \beta \tag{16}$$

The minus sign in Eq. (16) indicates that the ray intersected the chief ray before arriving on the opposite side of the image screen in this example. Although the derivation described the deviated ray as a focusing error for simplicity, Eq. (16) applies even when higher-order aberrations are present if E is computed from wavefront vergence as defined by Eq. (14).

The three fundamental concepts of wavefront phase, wavefront slope, and wavefront curvature can each be used to assess optical quality of the eye and determine the optimum sphero-cylindrical correcting lens as described in Section Optimizing Retinal Image Quality by Correcting Refractive Errors. These properties of a wavefront are linked together by geometry and calculus in a manner directly analogous to distance, velocity, and acceleration. Slope is the spatial derivative of wavefront phase and curvature is the spatial derivative of slope. Conversely, slope is the integral of curvature and phase is the integral of slope. Thus, measurements of wavefront slope provided by a wavefront sensor may be mathematically integrated to retrieve the shape of the aberrated wavefront. Just as distance, velocity, and acceleration each have different physical units, wavefront phase, slope, and curvature have different units. Wavefront phase is measured in microns, which is perhaps more easily interpreted if normalized by the wavelength of light to yield waves of phase shift. Wavefront slope is specified in micrometer per millimeter, which is the same as milliradians (1 mrad = 3.438 arcmin) and wavefront curvature is specified in micrometer per square millimeter which is the same as inverse meters or diopters.

An important practical application of Eq. (14) is to derive a formula for paraxial refractive error that takes into account the fact that 2nd order Zernike modes are included in higher-order modes for the purpose of building an orthogonal set of basis functions with minimum variance. Thus to determine paraxial refractive errors, it is necessary to apply Eq. (14) to the Zernike expansion given by Eq. (11) and evaluate the result at the pupil center. Since all terms in ρ^n with $n>2$ have zero slope when $\rho=0$, they make no contribution to paraxial wavefront vergence according to Eq. (14). For a 6th order Zernike expansion, the resulting formula for paraxial refractive error reduces to

$$\begin{aligned} M &= \frac{-c_2^0 4\sqrt{3} + c_4^0 12\sqrt{5} - c_6^0 24\sqrt{7}}{r^2} \\ J_0 &= \frac{-c_2^2 2\sqrt{6} + c_4^2 6\sqrt{10} - c_6^2 12\sqrt{14}}{r^2} \\ J_{45} &= \frac{-c_2^{-2} 2\sqrt{6} + c_4^{-2} 6\sqrt{10} - c_6^{-2} 12\sqrt{14}}{r^2} \end{aligned} \tag{17}$$

Optimizing Retinal Image Quality by Correcting Refractive Errors

The ultimate decision of whether a retinal image is optimally focused by a sphero-cylindrical correcting lens is complicated by the presence of higher-order aberrations and by how the question is framed. If the decision is an esthetic judgment, the observer's subjective criterion for making the decision may be unknown or difficult to articulate. If the decision is based on performance of an objective task, then optimum focus may depend on the nature of the task (e.g., reading printed text versus detecting a target) or on stimulus parameters (e.g., size, velocity, intensity, etc.). Experiments on human observers have shown that, for the task of reading small letters, refractive corrections based on Eq. (6) tend to leave the eye slightly myopic whereas corrections based on Eq. (17) tend to leave the eye slightly hyperopic (Martin *et al.*, 2011). The optimum correction lies between these limits, suggesting that optimization of some metric of retinal image is a better way to compute refractive error from wavefront aberration measurements. Numerous metrics have been evaluated for this purpose, several of which provide unbiased measures of optimum focus. One widely used unbiased metric called the visual Strehl ratio is analogous to the common Strehl ratio but is determined for a neutrally weighted optical PSF obtained by convolving the optical PSF with a neural weighting function that represents the spatial filtering properties of the visual system.

See also: Interferometric Imaging

References

ANSI, 2010. American national standard Z80.28 for ophthalmics – Methods for reporting optical aberrations of eyes, ANSI Z80.28, American National Standards Institute.
Applegate, R.A., Howland, H.C., 1997. Refractive surgery, optical aberrations, and visual performance. Journal of Refractive Surgery 13 (3), 295–299.
Goodman, J.W., 2005. Introduction to Fourier Optics. Greenwood Village, CO: Roberts & Co.
Liang, J., Brimm, B., Goelz, S., Bille, J.F., 1994. Objective measurement of the wave aberrations of the human eye with the use of a Hartmann–Shack wave-front sensor. Journal of the Optical Society of America, A 11, 1949–1957.
Martin, J., Vasudevan, B., Himebaugh, N., Bradley, A., Thibos, L., 2011. Unbiased estimation of refractive state of aberrated eyes. Vision Research 51 (17), 1932–1940.
Nam, J., Thibos, L.N., Iskander, D.R., 2009. Zernike radial slope polynomials for wavefront reconstruction and refraction. Journal of the Optical Society of America A Optics, Image Science, and Vision 26 (4), 1035–1048.
Scheiner, C., 1619. Oculus, Sive Fundamentum Opticum. Innspruk: Agricola.
Stephenson, P.C., 2009. Optical aberrations described by an alternative series expansion. Journal of the Optical Society of America A Optics, Image Science, and Vision 26 (2), 265–273.
Thibos, L.N., Hong, X., 1999. Clinical applications of the Shack–Hartmann aberrometer. Optometry and Vision Science 76, 817–825.
Thibos, L.N., Hong, X., Bradley, A., Applegate, R.A., 2004. Accuracy and precision of objective refraction from wavefront aberrations. Journal of Vision 4 (4), 329–351.
Young, T., 1801. The Bakerian lecture: On the mechanism of the eye. Philosophical Transactions of the Royal Society of London 91, 23–88.

Methods of Vision Correction

Len Zheleznyak, University of Rochester, Rochester, NY, United States
Ramkumar Sabesan, University of Washington School of Medicine, Seattle, WA, United States
Geunyoung Yoon, University of Rochester, Rochester, NY, United States

© 2018 Elsevier Ltd. All rights reserved.

Introduction

For centuries humans have been inventing technologies to correct the eye's optical aberrations. As our understanding of the eye's optical defects has evolved, so too has the complexity of correction methods. But despite technological advances, from the medieval looking-stone to the modern-day femtosecond laser, aberration-free vision remains out of reach for most of the population.

Two primary approaches to correcting the eye's refractive error are wide-spread:

1. Introducing corrective lenses in front of the eye (e.g., spectacles or contact lenses).
2. Altering the eye's optical properties by modifying the cornea (e.g., refractive surgery) or replacing the crystalline lens with an intraocular lens.

In this article, we will review both approaches to correcting the eye's optical aberrations to improve visual performance. Finally, we consider promising future approaches to vision correction.

Background

Spectacles

The inventor of spectacles is unknown, however, it is thought that spectacles were invented in the late 1200s (Dreyfus, 1988). The earliest known depiction of spectacles in a painted work of art is the portrait of Cardinal Hugo of Providence, painted by Tommaso de Modena in 1352 (**Fig. 1**).

Spectacle technology has advanced in terms of lightweight optical materials and anti-reflection coatings, but their main function of correcting the eye's lower order aberrations (sphere and cylinder) has remained relatively unchanged.

Fig. 2 illustrates a myopic (i.e., near-sighted) eye before and after correction with a spectacle lens. In the case of myopia, the eye has access refractive power (sphere), resulting in a focus in front of the retina (**Fig. 2(a)**) for light coming from infinity (i.e., a collimated beam). Therefore, the required corrective lens has negative defocus, which pushes the focus posteriorly towards the retina (**Fig. 2(b)**).

Despite the efficacy and convenience of spectacles, their limitations for certain optical corrections are significant. For example, as the eye's directional gaze changes, a different area of the spectacle is used. This is akin to a decentration, or misalignment of the correction-lens' wavefront from the eye's wavefront. This is not an issue for conventional lenses that only correct lower order aberrations, however it does prevent efficacious higher-order aberration correction in spectacles.

Contact lenses

While the initial ideas behind contact lenses can be traced back to the 16th century to Leonardo da Vinci, it was not until 1888 that a German ophthalmologist, Adolf Fick, successfully fit the first contact lens. Fick used glass blowing to create lenses which rested on the sclera of the eye and neutralized the refractive power of the cornea by filling the space between with dextrose. The solution, given its similarity in refractive index to the cornea, would minimize the power arising from the corneal front surface, otherwise exposed to air. Indeed, the same refractive index matching approach to alter the corneal power was proposed earlier by Leonardo da Vinci, and later used by Thomas Young to confirm the presence of astigmatism in the cornea (**Fig. 3**).

Since their inception, contact lenses have taken different forms varying in their size, material properties, oxygen permeability and optical characteristics. Their growth is marked by two key inventions. First, the development of polymethyl methacrylate (PMMA) made lenses lighter and smaller than those made from glass, leading to contacts which could be worn on the cornea as opposed to earlier glass sclerals. These plastic polymers were later refined to allow for better oxygen permeability and led to a class of lenses which are now more commonly called rigid gas permeable (RGP) contact lenses. The second revolutionary advance came with the development of soft hydrogel materials (Wichterle and Lim, 1960) which substantially increased the wear time of contacts by improving oxygen permeability and led to the conventional "soft" contact lenses. While the permeability characteristics of such hydrogels were advanced following their invention, a major breakthrough came about from the development of silicone hydrogels in the 1990s that allowed for extremely high oxygen permeability leading to extended wear times and wearing comfort. Note however that all the aforementioned types and materials (except for glass) of contacts are still in use today for varying degree of abnormalities in the cornea and the ocular surface. In addition to optical correction discussed below, some applications of contact lenses pertain to non-refractive cases also. Scleral lenses ranging in diameter from 13 to 24

 doi:10.1016/B978-0-12-803581-8.09781-2



Fig. 1 Earliest depiction of spectacles in art: Cardinal Hugo of Providence. Painted by Tommaso de Modena, 1352.

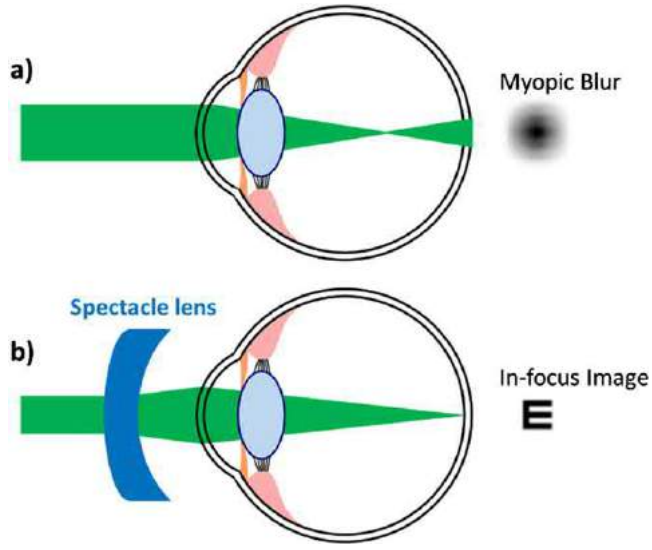


Fig. 2 Schematic of an (a) un-corrected and (b) corrected myopic eye with a negative diopter spectacle lens.

mm rest on the sclera of the eye and create a reservoir tear layer between the cornea and the lens. By virtue of being placed on the sclera and not the sensitive corneal tissue, these lenses are often used to provide relief in patients with corneal disease or following injury- for instance in extreme cases of dry eye, corneal ectasia, post-LASIK or corneal transplant complications, Stevens–Johnson syndrome and Sjogren's syndrome. A similar protective role for the cornea is met by bandage soft contact lenses as well.

Contact lenses provide a unique vehicle for delivering optical corrections to the eye – both for conventional refraction (sphere and cylinder) and for those corneas affected by higher order aberrations beyond sphero-cylindrical errors. The advantage of contacts in providing optical correction arises mainly because the lenses sit in close axial proximity to the eye's optical and physical pupil leading to two key desirable features. First, when the eyeball moves, the contacts move in unison, thereby continuously providing the requisite optical correction despite large changes in gaze. Second, the accessible field of view remains large and consistent across a variety of viewing conditions. Conversely, spectacles, by virtue of being stationary, do not align the eye's optical axis when the gaze changes. Furthermore, by being displaced axially from the eye's pupil, the isoplanatic patch (the field of view over which the aberrations remain relatively constant) shrinks and leads to a smaller effective field of view when using spectacles.

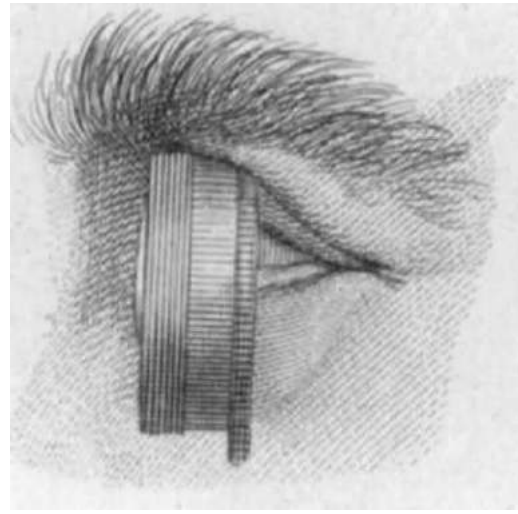


Fig. 3 Thomas Young's illustration of neutralizing the cornea by refractive index matching by applying a lens with water reservoir. Reproduced figure from 1801 publication.

These two factors are less critical for conventional sphero-cylindrical corrections however pose a significant challenge for compensating large magnitudes of asymmetric optical aberrations.

The overall principle of a contact lens in providing refractive error correction is similar to that of spectacles, albeit with a few key differences. Similar to a spectacle prescription, a positive/negative powered lens is used to correct for hyperopia/myopia, while unequal spherical powers across the horizontal and vertical meridians are used to correct for cylinder. However, the magnitude of refraction needs to accommodate for the different axial locations of the spectacle and contact lens corrections. In a clinical setting, prescriptions are sought using trial lenses placed at the spectacle plane. To convert the spectacle prescription to contact lens power at the cornea, the following equation is used, where K: refraction at the corneal/contact lens plane, F: refraction at the spectacle plane, d: vertex distance or the distance between the spectacle and the corneal plane (typically 12–13 mm).

$$K = \frac{F}{1 - dF}$$

In addition to the optical considerations, contacts are designed to accommodate for the physiological demand of supporting metabolism in the cornea via replenishing the supply of the tear film. The physical characteristics (curvature, diameter, edge profile, thickness) are thus optimized for the lens to move with every blink and realign with the visual axis afterwards. The alignment is less critical for pure spherical error correction compared to cylindrical and higher order aberration. This is because spherically asymmetric errors are not corrected optimally when the optical axes of the eye and the corrective optics are not co-aligned. Common strategies to align the lens include prism-ballast or double slab-off wherein different thickness profiles across the surface of the lens help in its optimum interaction with the eyelids and stabilizing it post-blink (Holden, 1975).

The efforts to compensate for higher order aberrations using ophthalmic lenses received a major boost mainly due to the advent of wavefront sensing techniques (Liang *et al.*, 1994). Using these advanced techniques, the corneal abnormality of keratoconus (KC) and its optical consequences have been evaluated (Pantanelli *et al.*, 2007; Maeda *et al.*, 2002). Given the large magnitude of higher order aberrations found in KC, it was immediately appreciated that these patients stand to benefit greatly from an optical correction aimed at minimizing these aberrations.

Soft contact lenses with wavefront-guided surface profiles have been shown to have potential in correcting HOA and improving vision in KC (López-Gil *et al.*, 2003; Sabesan *et al.*, 2007; Marsack *et al.*, 2008). In such a scheme of correction in two eyes with KC shown by López-Gil *et al.*, the lens was designed according to the aberration profile of the eye, but the reduction in higher order aberration and improvement in vision were relatively small (López-Gil *et al.*, 2003). One possible explanation for the small average reduction in higher order aberration could be the failure to account for the decentration and rotation of the contact lens on the eye. Static and dynamic contact lens movements critically affect correction performance of HOA, as the lens is not aligned to the center of the visual axis, especially in eyes with abnormal corneal surface profiles (Navarro *et al.*, 2000; Guirao *et al.*, 2001). Sabesan *et al.* demonstrated a scheme of correction in KC using soft contact lenses where the lens was designed by accounting for both the eye's aberration profile and the static lens decentration and rotation on eye (Sabesan *et al.*, 2007). Using these wavefront-guided customized soft contact lenses, an improvement in optical quality by a factor of 3 in HOA with respect to the conventional lens on average in 3 KC patients was demonstrated. The improved optics resulted in an average improvement of 2.1 lines in visual acuity over the conventional correction of defocus and astigmatism alone. However, the residual higher order wavefront error was still nearly double of what is observed in normal eyes. This residual error was explained to a reasonable extent by the manufacturing error and lens movement. To reduce the variability of lens position by conferring mechanical stability between blinks, Chen *et al.* (2007) employed back surface customized soft contact lenses whose posterior surface profiles were sculpted to match

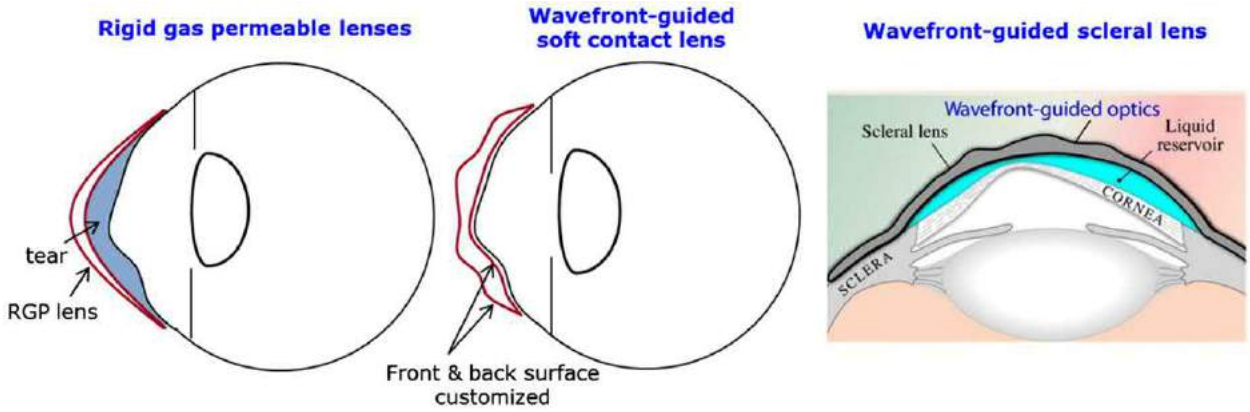


Fig. 4 Different contact lens strategies to overcome corneal higher order aberrations in highly aberrated eyes, such as keratoconus.

the anterior corneal surface in KC. On-eye performance of the back surface customized soft contact lens demonstrated that the lens stability was improved by a factor of 2 for horizontal and vertical decentration, and a factor of 5 in rotational orientation over conventional lens. However, significant residual HOA induced by internal optics, especially posterior corneal surface still degraded retinal image quality. Additional customization of the front surface of the lens thus has the potential to further correct these residual aberrations.

Clinically, RGPs and scleral lenses are considered the standard of correction in KC. These lenses achieve correction by masking corneal irregularities with the tear lens between the posterior lens surface and the anterior corneal surface, in the same manner as the first attempts of fitting contacts. RGP corneal contact lenses are 8.5–10.5 mm in diameter and cover only 75–80% of the cornea. Mini-scleral, corneo-scleral and scleral lenses which range in diameter from 13–24 mm, depending on type or fit, may rest partly on the cornea. A scleral lens prosthetic device (SLPD) with diameters ranging from 17.5–24 mm is designed and fit to vault the cornea entirely. A noteworthy difference between RGP corneal lens and SLPD is the dynamic movement of these corrective devices on the eye. A well-fitted corneal RGP lens slides with each blink to allow for tear exchange necessary for physiological tolerance at the corneal surfaces where contact is made. Optical correction in an RGP corneal lens is thus inherently unstable. A carefully fitted SLPD is expected to exhibit minimal movement because the bearing haptic aligns with a large area of conjunctiva overlying the sclera. Suction is avoided by precise alignment with the sclera or by creation of channels on the posterior surface (Rosenthal, 2009, 2010). The clinical benefits of an SLPD in terms of improvement in visual acuity and visual function across a wide range of diagnoses including KC have been established (Stason *et al.*, 2010). By virtue of their larger diameter and broader bearing zone, these devices have been employed in the treatment of various other forms of corneal ectasia, corneal irregularity following transplant, ulcers, dry eye syndrome, ocular surface disease and others (Pullum *et al.*, 2005; Segal *et al.*, 2003). Reduction of HOA has been reported in normal and KC eyes with corneal RGP lens (Hong and Himebaugh, 2001; Dorronsoro *et al.*, 2003; Marsack *et al.*, 2007; Negishi *et al.*, 2007) and SLPD (Gumus *et al.*, 2011). However, since these lenses minimize only anterior corneal aberrations, significant posterior corneal aberrations remain uncompensated (Chen and Yoon, 2008). In addition, aberrations such as coma and astigmatism are induced due to RGP corneal lens rotation and decentration, further degrading retinal image quality. The positional stability between blinks due to the large surface coverage in SLPD makes it an ideal platform for wavefront-guided correction of HOA in KC. Sabesan *et al.* demonstrated significant reduction in root-mean-square of HOA and improvement in vision in 11 advanced KC eyes wearing wavefront-guided SLPD (Sabesan *et al.*, 2007). HOA were effectively corrected by the customized SLPD with wavefront-guided optics and RMS was reduced 3.1 times on average to 0.37 ± 0.19 μm for a 6 mm pupil, comparable to normal levels. This correction resulted in significant improvement of 1.9 lines in mean visual acuity ($P < 0.05$). Contrast sensitivity was also significantly improved by a factor of 2.4, 1.8 and 1.4 on average for 4, 8 and 12 cycles/degree, respectively ($P < 0.05$ for all frequencies). Interestingly, although the residual aberration was comparable to that of normal eyes, the average visual acuity in logMAR with the customized SLPD was 0.21, substantially worse than normal acuity. This implicates the role of chronic exposure to poor retinal image quality that may restrict the visual benefit achievable immediately after wavefront-guided customized treatment in these eyes (**Fig. 4**).

Visual Benefit of Correcting Higher Order Aberrations

The amount of benefit to be gained from correcting the eye's higher order aberrations depends on subjects' native wavefront profiles and pupil size. However, the visual benefit has been shown to be significant for various visual tasks (e.g., visual acuity, contrast sensitivity), especially in low light levels where pupils are large or in ocular pathologies such as KC. Higher order aberration correction in the human eye has been demonstrated with several methods, such as soft contact lenses (Chen *et al.*, 2007; Sabesan *et al.*, 2007), scleral lenses (Sabesan *et al.*, 2013; Marsack *et al.*, 2014), phase plates (Yoon *et al.*, 2004; Allen and Raasch, 2005) and adaptive optics (Yoon and Williams, 2002; Legras and Rouger, 2008; Rossi *et al.*, 2007; Sabesan *et al.*, 2007, 2012). However, the degree of visual benefit can vary widely depending on the individual subjects.

In a seminal population study ($n = 109$ eyes) by Williams *et al.* (2000), it was found that contrast sensitivity was expected to improve by a factor between 1 (no improvement) and 8 times (16 cyc/deg, 5.7 mm pupil) after higher order aberration correction. The variability in visual benefit indicates that some subjects are more suited for higher order aberration correction than others. Patients with large amounts of higher order aberrations or abnormal eyes (e.g., KC, high spherical aberration post-laser refractive surgery) would clearly stand to benefit from higher order aberration correction. However, aside from the magnitude of aberrations, other factors such as subjects' native pupil size should also be considered. As pointed out by Williams *et al.*, visual benefit is minimal in bright light conditions (i.e., when the pupil is small) or in the presence of focusing error, which is commonplace due accommodative lag (Williams *et al.*, 2000).

Furthermore, the vast majority of studies on the impact of higher order aberration correction have been monocular. Using a binocular adaptive optics vision simulator, Sabesan *et al.* (2012) showed that binocular summation decreased when subjects' native higher order aberrations were corrected. Therefore, monocular estimates of visual benefit tend to overestimate in the case of binocular correction.

While individual higher order aberrations vary randomly from patient to patient, the exception is primary spherical aberration (Porter *et al.*, 2001; Thibos *et al.*, 2002), the correction of which has been shown to lead to significant improvements in both visual acuity and contrast sensitivity (Sabesan *et al.*, 2012; Piers *et al.*, 2004, 2007; Schwarz *et al.*, 2014). The primary source of the eye's spherical aberration is the cornea (Artal *et al.*, 2002), and thus intraocular lenses have been a natural platform for its correction (Holladay *et al.*, 2002; Muñoz *et al.*, 2006). However, it is important to note that depth of focus suffers with the correction of spherical aberration (Piers *et al.*, 2004). This is particularly important in regard to intraocular lenses, as cataract surgery leaves patients unable to accommodate.

Chromatic Aberration

Longitudinal chromatic aberration of the human eye is approximately 2 diopters across the visible spectrum (Thibos *et al.*, 1992; Atchison and Smith, 2005). Due to the dispersion of ocular media (i.e., positive Abbe number), the longer wavelengths are relatively hyperopic compared to shorter wavelengths. Because this is caused by the inherent material properties of the eye's anatomy, chromatic aberration is more consistent across the population relative to the monochromatic aberrations (e.g., sphere, cylinder and higher order aberrations). With advances in diffractive intraocular lens technology, there has been a renewed interest in correcting ocular chromatic aberration (Schwarz *et al.*, 2014; López-Gil and Montés-Micó, 2007; Artal *et al.*, 2010). However, as discussed by Lopez-Gil and Bradley, the clinical benefit of correcting spherical and chromatic aberrations may be modest (López-Gil and Bradley, 2012), especially under photopic conditions. In addition, misaligned intraocular lenses providing spherical and chromatic aberration correction lead to unwanted aberrations, such as transverse chromatic aberration, coma and astigmatism (López-Gil and Montés-Micó, 2007; Cheng *et al.*, 2010).

Presbyopia

Past the age of approximately 40 years, even emmetropic eyes require vision aids. As the eye ages, it loses its ability to accommodate (i.e., change focus from far to near objects) due to lifelong crystalline lens growth and loss of elasticity. The age-related loss of accommodation is known as *presbyopia*. As first measured by Donders in 1864 (Donders and Moore, 1864) and later by Duane in 1912 (Duane, 1912), the eye's amplitude of accommodation suffers a steady decline, starting in childhood until a plateau is reached at approximately 50 years (**Fig. 5**).

Evidence of visual aids can be traced to magnifying lenses known as "reading stones" developed in the 9th century, CE. The English friar Roger Bacon wrote in 1250 CE of such devices to correct for his presbyopia:

> *"It may be observed that old people hold objects they wish to examine further from the eye. …If anyone examines letters or other minute objects through the medium of crystal or glass or other transparent substance, if it be shaped like the lesser segment of a sphere, with the convex side being towards the eye, and the eye being in the air, he will see the letters far better, and they will seem larger to him. …For this reason, such an instrument is useful to old persons…"* (James, 1928).

Until the 18th century invention of Benjamin Franklin's bifocal spectacles, little progress was made for correcting presbyopia. However, the last several decades have experienced a tremendous increase in research and development devoted to presbyopia correction. As a result, there are currently a wide variety of strategies available, which are outlined in **Table 1**.

The field of presbyopia correction can be segmented into two categories: (1) the restoration of the eye's ability to accommodate, i.e., change focal length and (2) increase the eye's depth of focus.

Restoring Accommodation

The majority of accommodation restoration techniques have focused on using eye's lens as the engine for dynamic optical power change. For example, pharmacological agents (Renna *et al.*, 2016; Crawford *et al.*, 2014) and femtosecond laser induced micro-incisions (Holzer *et al.*, 2009; Ripken *et al.*, 2008) are currently in development for restoring elasticity to the presbyopic crystalline lens.

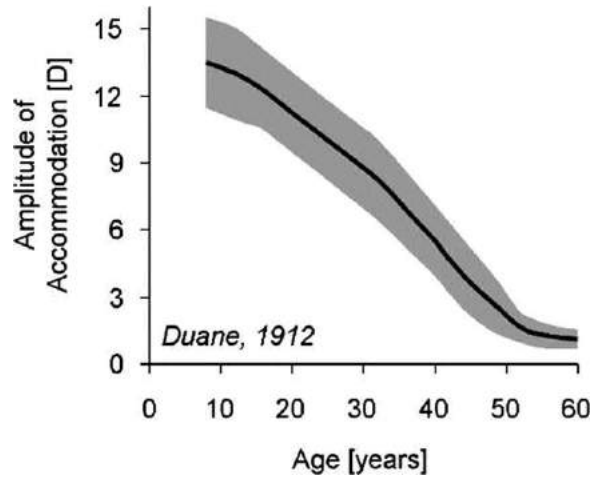


Fig. 5 Amplitude of accommodation as a function of age. Average and upper and lower limits are indicated by black line and grey area, respectively. Figure adapted from Duane, A., 1912. Normal values of the accommodation at all ages. Journal of the American Medical Association 59 (12), 1010–1013.

Table 1 Methods for correcting presbyopia

	Method *Spectacles*	*Description* *Reading glasses* *Bifocals, trifocals, progressives*	*Mechansim* *Single vision* *Change of gaze*
Restoring Dynamic Accommodation (*pseudophakic accommodation*)	Intraocular Lenses	Accommodating IOL	Positional and shape changes induced by ciliary body
Extending Depth of Focus (*pseudoaccommdation*)	Contact Lenses	Bifocal, multifocal	Wavefront aberrations
	Corneal Surgery	Tissue removal: LASIK, PRK	Wavefront aberrations
		Implantable refractive corneal inlay	Wavefront aberrations
		Implantable small-aperture inlay	Pinhole effect
	Intraocular Lenses	Multifocal IOL	Wavefront aberrations and/or diffraction
	Monovision	Dominant eye corrected for distance, non-dominant eye corrected for near	Binocular combination of two eyes' retinal images

Otherwise, novel accommodating intraocular lens (IOL) designs have be proposed to restore accommodation (Pepose *et al.*, 2017). Such lenses are designed to change surface curvature or shift axially within the eye during accommodative effort. One such curvature-change design is the Powervision (Belmont, CA) FluidVision IOL, which is comprised of a hollow lens and liquid-filled reservoir haptics. When the eye is in its relaxed state, the liquid resides within the haptics and the lens rests in a relatively flat shape, defining the geometry for viewing distant objects. As the eye exerts accommodative effort, the ciliary muscle contracts, decreasing the equatorial diameter of the capsular bag. This forces the fluid from the haptic reservoir into the central lens cavity, increasing its curvature and optical power, thereby providing near vision (Sheppard *et al.*, 2010).

Alternatively, accommodating IOLs may function on axial displacement, such as the Crystalens (Bausch and Lomb, Rochester, NY). The Crystalens is a single-optic IOL mounted on hinged haptics, allowing the lens to vault anteriorly during accommodative effort, as illustrated in **Fig. 6**. However, in a theoretical analysis by Hunter *et al.*, it was shown that a 1 mm axial shift of a 20D IOL induces a 1.2D optical change. Therefore, single-optic accommodating IOLs must travel an excessive distance through the anterior chamber to provide a meaningful optical change for presbyopia correction.

Several investigators (Koeppl *et al.*, 2005; Marcos *et al.*, 2014; Zheleznyak, 2014) have assessed accommodative IOL movement by measuring changes in anterior chamber depth during accommodative effort. They have found that on average, the single-optic accommodating IOL (Crystalens, Bausch + Lomb) undergoes a posterior shift during accommodative effort by approximately 0.15 mm. Similarly, studies measuring changes in wavefront aberrations during accommodative effort show inconsistent changes in defocus, and in some cases, an incorrect change in the eye's power (Zheleznyak, 2014; Pérez-Merino *et al.*, 2014).

To overcome this limitation, dual-optic IOL designs have been proposed (e.g., Synchrony IOL, Abbott Medical Optics, Santa Clara, CA). In comparison to single-optic designs, the dual-optic accommodating IOL achieves approximately 2.2D increase in power with a 1 mm shift of the anterior lens (McLeod *et al.*, 2007). However, the expected benefit of the dual-optic design over the

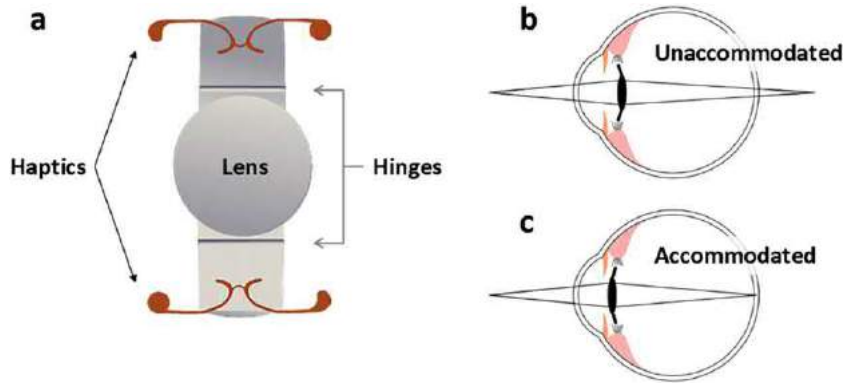


Fig. 6 (a) Single-optic accommodating intraocular lens (Crystalens, Bausch + Lomb, Rochester, NY). Illustration of the intended axial movement of a single-optic accommodating IOL in the (b) unaccommodated and (c) accommodated states of the pseudophakic eye.

single-optic accommodating IOL has not been reflected clinically (Alió *et al.*, 2012) and may be due to capsular bag fibrosis limiting IOL movement (Koeppl *et al.*, 2005).

Extending the Eye's Depth of Focus

In the absence of true accommodation restoration, extending the eye's depth of focus has been a common path taken by clinicians to alleviate the symptoms of presbyopia. This can be achieved by reducing pupil size or introducing multifocality to the wavefront aberrations via aspheric refractive surfaces, diffractive optical elements, or both.

The Pinhole Effect

Reducing the pupil size of the eye is the easiest way to lessen the impact of presbyopic blur. For example, eyelid squinting is a common means of truncating the pupil, albeit only vertically, to improve acuity in the presence of refractive error (Sheedy *et al.*, 2003). Pupil size also effects aberration-free image quality at 0D of defocus. The cutoff frequency of the modulation transfer function (MTF) is linearly dependent upon the pupil size, as shown below.

$$f_{cutoff} = \frac{d}{\lambda}$$

Where f_{cutoff}, r and λ represent cutoff frequency (in cycles/radian), pupil diameter and wavelength, respectively. Therefore, as pupil size decreases, so does the cutoff frequency of the MTF and the spatial bandwidth of the image, thereby degrading distance image quality. Therefore, decreasing pupil size for extended depth of focus is a trade-off with distance optical quality. This concept is illustrated below in **Fig. 7**.

Extended depth of focus via small pupils has been implemented with pinhole corneal inlay (KAMRA, AcuFocus, Irvine, CA). The inlay is implanted within the corneal stroma and has a 1.6 mm inner diameter. Although significant improvements in near vision have been demonstrated (Yılmaz *et al.*, 2011), it may only be implanted monocularly (typically the non-dominant eye), due to the reduction in retinal illuminance.

Multifocal Wavefront Aberrations

In contrast with the pinhole effect, manipulating the wavefront aberrations is a means of extending depth of focus without reducing retinal image brightness. However, wavefront multifocality is also accompanied by the trade-off with distance optical quality. As shown in **Fig. 8(a)**, monofocal wavefronts result in all rays across the pupil converging to a single point, or a single focus. An example of a refractive bifocal with a central add power for near vision is illustrated in **Fig. 8(b)**. In this case, when the blue ray bundle is in focus on the retina, the red ray bundle is out of focus. Thus, the out of focus (red) ray bundle degrades retinal image quality and is commonly referred to as halo or glare. An example of a continuous distribution of refractive powers across the pupil is spherical aberration (**Fig. 8(c)**). Although spherical aberration is known to increase depth of focus, efforts of mitigating negative side-effects (e.g., degraded distance vision) have included incorporating higher order spherical aberrations (Yi *et al.*, 2011; Benard *et al.*, 2011) and pupil amplitude apodization (Zheleznyak *et al.*, 2014).

A novel concept in multifocal wavefront design segmenting the wavefront angularly into zones of refractive power, also known as a *light-sword* wavefront (Petelczyc *et al.*, 2009, 2011; de Gracia *et al.*, 2013; Mira-Agudelo *et al.*, 2016). A benefit of this technique is that the relative energy allocated to far and near vision is unaffected by pupil size. Recent theoretical (Petelczyc *et al.*, 2011; de Gracia *et al.*, 2013) and psychophysical (Mira-Agudelo *et al.*, 2016) studies have shown that angular multifocal designs have promise in offering superior through-focus image quality over traditional radial designs (e.g., **Fig. 8(b)**).

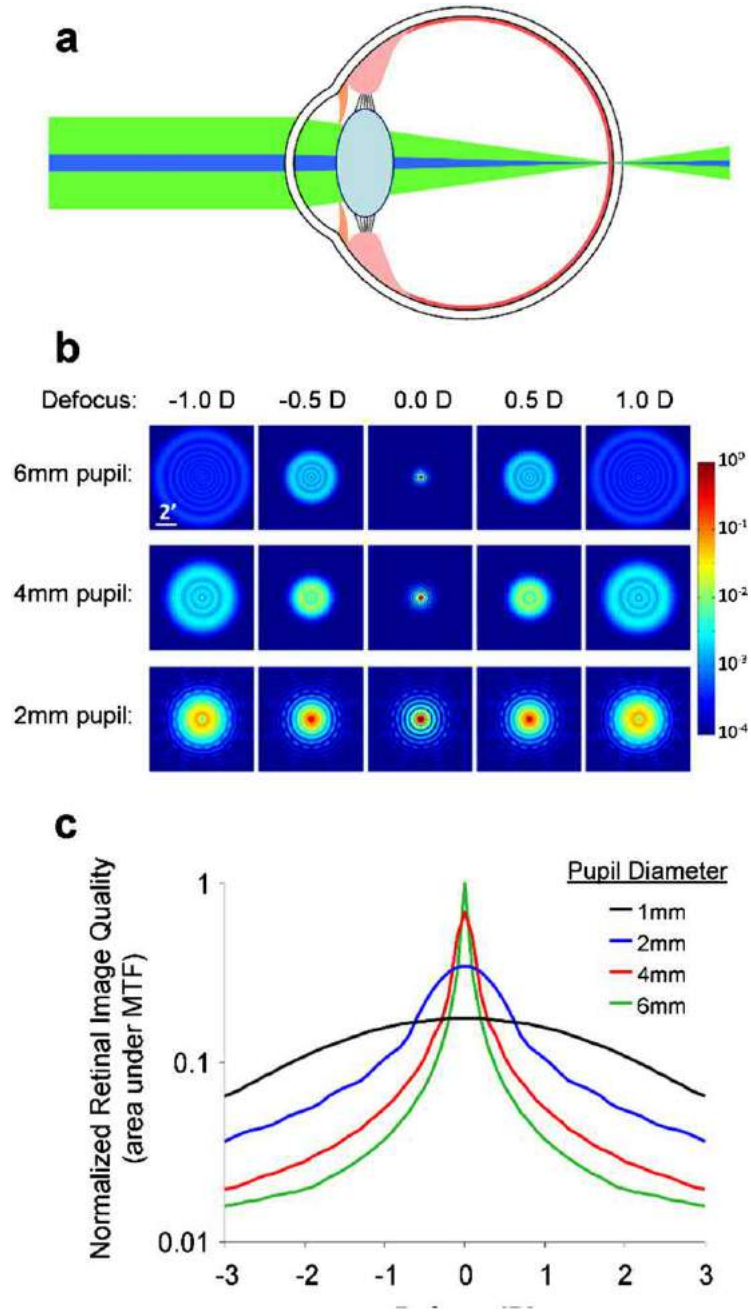


Fig. 7 (a) Schematic eye with ray bundle from a distant object for large and small pupils. Through-focus blur circles are shown for comparison. (b) Through-focus point spread functions with 6, 4 and 2 mm pupil diameters. (c) Through-focus normalized retinal image quality in monochromatic light (550 nm) of an aberration-free eye with various pupil sizes.

In addition to refractive multifocal wavefronts, diffractive multifocals also offer a means of increasing the eye's depth of focus. Typically implemented in intraocular lenses, diffractive multifocals consists of a radially symmetric diffractive structure which separate the light into several orders of diffraction. The phase height (in multiples of the design wavelength, λ) determines the diffraction efficiency, or the amount of energy allocated to far or near image quality. Three diffractive multifocals with various phase heights exhibiting (a) an emphasis on far vision, (b) equal energy to both far and near vision or (c) and emphasis on near vision are shown in **Fig. 9**. Diffraction efficiency may also be modified by means of apodizing the phase height as a function of pupil radius, as in the case of the ReSTOR (Alcon) apodized multifocal intraocular lens (Davison and Simpson, 2006). Recent advances in diffractive multifocal design have also resulted in trifocal intraocular lenses aimed at improving vision for intermediate object distances (Gatinel *et al.*, 2011).

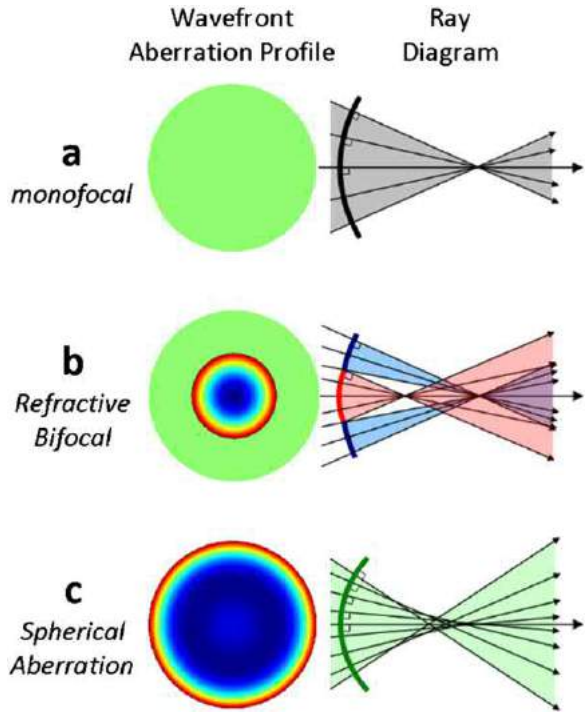


Fig. 8 Wavefront aberration maps and ray diagrams of (a) monofocal, (b) refractive bifocal and (c) spherical aberration wavefronts.

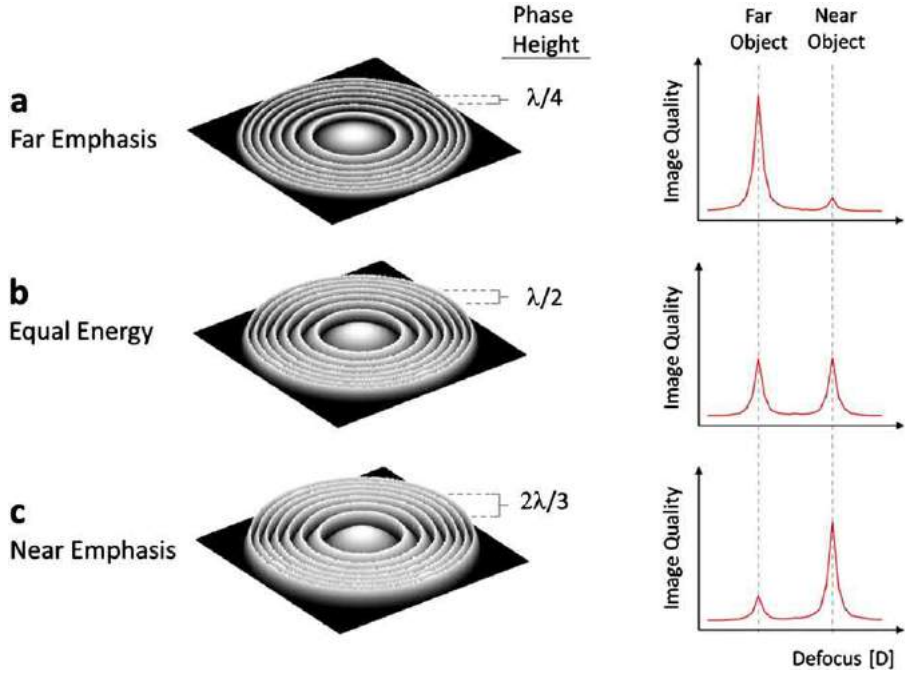


Fig. 9 Diffractive multifocal wavefronts and their associated through-focus image quality are shown for designs with (a) an emphasis on far vision, (b) equal energy to both far and near vision or (c) and emphasis on near vision.

Through-focus image quality (in-vitro) of a monofocal and various multifocal IOLs is shown in **Fig. 10**. In this case, retinal image quality is defined as the fidelity of a resolution target, which has been shown to correlate well with clinically measured visual acuity in pseudophakic patients (Plaza-Puche *et al.*, 2015). Optical bench metrology of IOLs is critical to understanding their optical performance. Alternatively, while Shack–Hartmann wavefront sensing measure the wavefront, it does not typically quantify

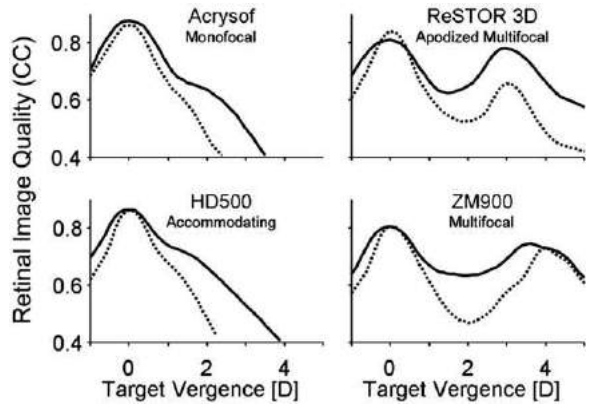


Fig. 10 Through-focus retinal image quality of a monofocal and various diffractive multifocal IOLs. Adapted from Zheleznyak, L., Kim, M.J., MacRae, S., Yoon, G., 2012. Impact of corneal aberrations on through-focus image quality of presbyopia-correcting intraocular lenses using an adaptive optics bench system. Journal of Cataract & Refractive Surgery 38 (10), 1724–1733.

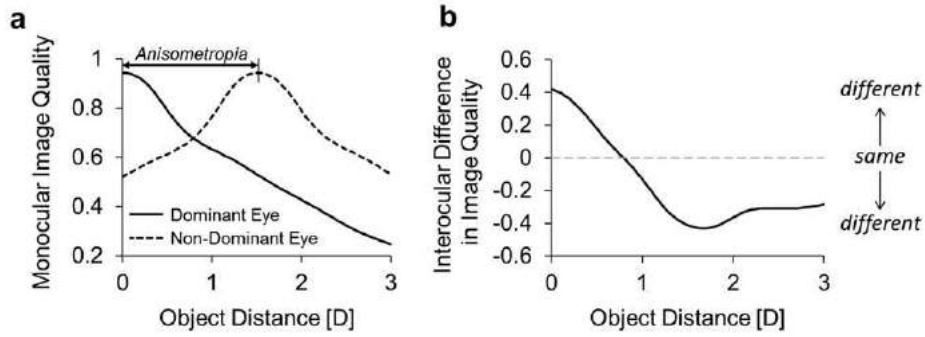


Fig. 11 (a) Through-focus monocular image quality for the dominant and non-dominant eyes in traditional monovision. The magnitude of anisometropia is defined as the dioptric difference in peak monocular image quality. (b) Through-focus interocular difference in monocular image quality.

scatter and its measurement may be confounded by diffractive multifocal designs. By observing a point-spread function or resolution target through a pseudophakic model eye, the eye's optics may be more fully understood. An important side note: optical bench tests are not conclusive in their representation of a patient's perception. A combination of optical and neural factors, such as the Stiles–Crawford effect (Applegate and Lakshminarayanan, 1993), retinal sampling (Hirsch and Curcio, 1989) and cortical processing inform a patient's perception of the visual world.

Binocular Approaches to Presbyopia Correction

Monovision is a paradigm of presbyopia correction which capitalizes on the binocularity of the visual system. In traditional monovision, the dominant eye is corrected for distance vision, whereas the fellow non-dominant eye is corrected for near vision by introducing positive defocus. To illustrate the impact of anisometropia on optical quality of the two eyes, through-focus monocular image quality in the presence of 1.5 diopters (D) of anisometropia is shown in **Fig. 11(a)**. Typical amounts of anisometropia induced clinically in traditional monovision vary from 1D to 2D (Evans, 2007; Jain *et al.*, 1996; Johannsdottir and Stelmach, 2001).

Traditional monovision requires patients to suppress the image from the blurred eye and to rely solely on the eye with superior image quality for high acuity tasks. While this technique does improve presbyopic visual performance at near object distances, binocular visual functions such as binocular summation (Pardhan and Gilchristt, 1990; Legras *et al.*, 2001) and stereopsis (Lovasik and Szymkiw, 1985) are sacrificed. As shown in **Fig. 11(b)**, anisometropia leads to a large difference in interocular image quality. In this example, the largest interocular difference occurred at distance (0D) and intermediate (1.5D) object distances.

To overcome the limitations of traditional monovision, it has been proposed to ease the large difference in interocular image quality by increasing each eye's depth of focus. This technique, also known as modified monovision, may be implemented with spherical aberration (Vandermeer *et al.*, 2015; Zheleznyak *et al.*, 2013, 2015), multifocal intraocular lenses (Ravikumar *et al.*, 2016) or by constricting the eye's entrance pupil diameter, as with a small-aperture corneal inlay (Fernández *et al.*, 2013).

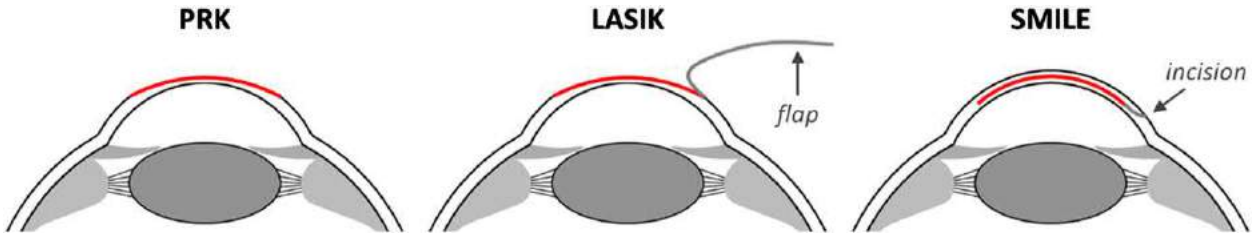


Fig. 12 Illustrations of PRK, LASIK and SMILE laser refractive surgeries. The red segment in each figure indicates the ablation zone.

Refractive Surgery

In 1948, Jose I. Barraquer Moner introduced a surgical procedure to correct the eye's refractive error by sculpting the cornea's topography, a procedure he named *keratomileusis*. Almost 70 years later, laser vision correction is among the most widely performed elective surgical procedures worldwide (Reinstein *et al.*, 2012).

The premise behind refractive surgery is the reshaping of the cornea's topography to control the eye's wavefront aberrations. This can be achieved in a variety of ways, although currently there are three primary techniques: PRK, LASIK and SMILE (illustrated in **Fig. 12**).

In *photorefractive keratectomy*, or PRK, the cornea's epithelial layer is removed, exposing the underlying stroma. An excimer laser (193 nm wavelength) is subsequently used to ablate undesired tissue, resulting in a new thickness profile of stroma (Seiler *et al.*, 2000). The epithelial layer regrows on the newly sculpted stromal bed within a week of the procedure (Caldwell and Reilly, 2008; Lee *et al.*, 2005).

Alternatively, in *laser-assisted* in situ *keratomileusis*, or LASIK, the epithelial layer is not removed. Instead, to expose the stromal bed for laser sculpting, a flap is created in the cornea with a microkeratome blade, or more recently, with a femtosecond laser ($\sim$1040 nm wavelength). The flap is cut such that a section of tissue remains, serving as a hinge for the folding of the flap to expose the underlying stroma. After excimer laser ablation is complete on the stroma (similar to PRK), the flap is folded back into place.

The desire for less-invasive refractive surgery has ushered in a relatively new procedure known as *small incision lenticule extraction*, or SMILE, which avoids both epithelial removal or creating a flap. This is achieved via femtosecond laser used to remove a section of tissue (i.e., the *lenticule*) from within the cornea's stroma through a small incision outside the optical zone.

Due to the invasive nature of these procedures, which inherently sever collagen fibrils in the stromal bed, there may be unintended consequences, such as dry eye (due to nerve damage) and ectasia (due to biomechanical instability) (Randleman *et al.*, 2008).

A common patient complaint after refractive surgery is poor visual quality, especially under low light conditions (e.g., starburst, halos and glare during night driving) (Villa *et al.*, 2007; Hammond *et al.*, 2004). The root of most of these visual symptoms is the unintended induction of higher order aberrations that accompanies the correction of myopia and hyperopia with refractive surgery due to the corneas biological response and ablation efficiency (Yoon *et al.*, 2005). For example, several studies have shown a significant correlation between the diopters of correction (i.e., myopia or hyperopia) and induction of spherical aberration (Yoon *et al.*, 2005; Marcos *et al.*, 2001), subsequently degrading contrast and visual quality. Decentration of the ablation zone has also been shown to induce unwanted optical aberrations (Mrochen *et al.*, 2001).

The Future of Vision Correction

To address the limitations of ablative refractive surgery, several less invasive procedures are under development, such as corneal collagen crosslinking and femtosecond laser induced refractive index correction.

Corneal collagen crosslinking is a technique in which ultra-violet radiation, when paired with doping agents such as riboflavin, cross-links the corneal collagen, thereby increasing the mechanical strength of the corneal tissue (Snibson, 2010). A challenge of this technique however is accurate doping of the cornea. Because the epithelial cell layer acts as a barrier, the most common application (e.g., the *Dresden protocol*) requires epithelial cell debridement (similar to PRK). While this procedure is invasive, the subsequent radiation is non-ablative and tissue-sparing. Corneal crosslinking is typically used for mechanically stabilizing the progression of keratoconus or ectasia, and research and development are underway to transition this method to refractive error (Kanellopoulos and Asimellis, 2014) and presbyopia (Kanellopoulos and Asimellis, 2015) correction by way of targeted ultra-violet radiation.

Another recent advance in non-invasive vision correction includes the use of femtosecond lasers to alter the refractive index of corneal stroma (Savage *et al.*, 2014; Ding *et al.*, 2008; Xu *et al.*, 2011; Wozniak *et al.*, 2017). This procedure does not require any epithelial cell layer debridement and is non-ablative and tissue-sparing. In this technique, a pulsed laser is focused into the cornea, triggering a multiphoton absorption process which results in a highly localized refractive index change, limited to a voxel of several micrometers. Due to the multiphoton nature of this process, the laser focus is scanned throughout the optical zone of the

treatment. The short pulse duration (~100 femtoseconds) and high repetition rate of laser pulses (MHz regime) allows for relatively little energy required to alter the cornea's refractive index, as compared to femtosecond lasers specifically designed for cutting tissue (e.g., flap cutting). By varying laser parameters such as pulse energy and scan speed, the magnitude of refractive index change is highly controlled during scanning. This approach has also been demonstrated in intraocular lens material (Sahler *et al.*, 2016), and contact lens material (Gandara-Montano *et al.*, 2015). In addition, visual performance has been demonstrated with phase plates modified by the laser induced refractive index correction technique (Zheleznyak *et al.*, 2017).

Summary

Methods of vision correction have come a long way, from medieval looking-stones to advances in modern technology, such as surgical implants and laser refractive surgery. Whether it is sphero/cylindrical error, or the more subtle higher order and chromatic aberrations, all eyes suffer from some degree of optical aberrations. Thus, the need for a robust, non-invasive means of providing clear vision persists. While many methods for correction exist, they are each limited in their efficacy for reasons detailed above. Therefore, advances in technology and our fundamental understanding of vision are critical to ushering in the future of vision correction.

See also: Aberrations

References

Alió, J.L., Plaza-Puche, A.B., Montalban, R., Ortega, P., 2012. Near visual outcomes with single-optic and dual-optic accommodating intraocular lenses. Journal of Cataract & Refractive Surgery 38 (9), 1568–1575.

Allen, Y.Y., Raasch, T.W., 2005. Design and fabrication of a freeform phase plate for high-order ocular aberration correction. Applied Optics 44 (32), 6869–6876.

Applegate, R.A., Lakshminarayanan, V., 1993. Parametric representation of Stiles–Crawford functions: Normal variation of peak location and directionality. JOSA A 10 (7), 1611–1623.

Artal, P., Berrio, E., Guirao, A., Piers, P., 2002. Contribution of the cornea and internal surfaces to the change of ocular aberrations with age. JOSA A 19 (1), 137–143.

Artal, P., Manzanera, S., Piers, P., Weeber, H., 2010. Visual effect of the combined correction of spherical and longitudinal chromatic aberrations. Optics Express 18 (2), 1637–1648.

Atchison, D.A., Smith, G., 2005. Chromatic dispersions of the ocular media of human eyes. JOSA A 22 (1), 29–37.

Benard, Y., Lopez-Gil, N., Legras, R., 2011. Optimizing the subjective depth-of-focus with combinations of fourth-and sixth-order spherical aberration. Vision Research 51 (23), 2471–2477.

Caldwell, M., Reilly, C., 2008. Effects of topical nepafenac on corneal epithelial healing time and postoperative pain after PRK: A bilateral, prospective, randomized, masked trial. Journal of Refractive Surgery 24 (4), 377–382.

Cheng, X., Bradley, A., Ravikumar, S., Thibos, L.N., 2010. The visual impact of Zernike and Seidel forms of monochromatic aberrations. Optometry and Vision Science: Official Publication of the American Academy of Optometry 87 (5), 300.

Chen, M., Sabesan, R., Ahmad, K., Yoon, G., 2007. Correcting anterior corneal aberration and variability of lens movements in keratoconic eyes with back-surface customized soft contact lenses. Optics Letters 32 (21), 3203–3205.

Chen, M., Yoon, G., 2008. Posterior corneal aberrations and their compensation effects on anterior corneal aberrations in keratoconic eyes. Investigative Ophthalmology & Visual Science 49 (12), 5645.

Christina, K., Oliver, F., Rupert, M., *et al.*, 2005. Pilocarpine-induced shift of an accommodating intraocular lens: At-45 Crystalens. Journal of Cataract & Refractive Surgery 31 (7), 1290–1297.

Crawford, K.S., Garner, W.H., Burns, W., 2014. Dioptin™: A novel pharmaceutical formulation for restoration of accommodation in presbyopes. Investigative Ophthalmology & Visual Science 55 (13), 3765.

Davison, J.A., Simpson, M.J., 2006. History and development of the apodized diffractive intraocular lens. Journal of Cataract & Refractive Surgery 32 (5), 849–858.

de Gracia, P., Dorronsoro, C., Marcos, S., 2013. Multiple zone multifocal phase designs. Optics Letters 38 (18), 3526–3529.

Ding, L., Knox, W.H., Bühren, J., Nagy, L.J., Huxlin, K.R., 2008. Intratissue refractive index shaping (IRIS) of the cornea and lens using a low-pulse-energy femtosecond laser oscillator. Investigative Ophthalmology & Visual Science 49 (12), 5332–5339.

Donders, F.C., Moore, W.D., 1864. On the Anomalies of Accommodation and Refraction of the Eye: With a Preliminary Essay on Physiological Dioptrics. vol. 22. London: New Sydenham Society.

Dorronsoro, C., Barbero, S., Llorente, L., Marcos, S., 2003. On-eye measurement of optical performance of rigid gas permeable contact lenses based on ocular and corneal aberrometry. Optometry and Vision Science 80 (2), 115–125.

Dreyfus, J., 1988. The invention of spectacles and the advent of printing a revised version of paper given to the bibliographical society 20 January 1987. The Library 6 (2), 93–106.

Duane, A., 1912. Normal values of the accommodation at all ages. Journal of the American Medical Association 59 (12), 1010–1013.

Evans, B.J., 2007. Monovision: A review. Ophthalmic and Physiological Optics 27 (5), 417–439.

Fernández, E.J., Schwarz, C., Prieto, P.M., Manzanera, S., Artal, P., 2013. Impact on stereo-acuity of two presbyopia correction approaches: monovision and small aperture inlay. Biomedical Optics Express 4 (6), 822–830.

Gandara-Montano, G.A., Ivansky, A., Savage, D.E., Ellis, J.D., Knox, W.H., 2015. Femtosecond laser writing of freeform gradient index microlenses in hydrogel-based contact lenses. Optical Materials Express 5 (10), 2257–2271.

Gatinel, D., Pagnoulle, C., Houbrechts, Y., Gobin, L., 2011. Design and qualification of a diffractive trifocal optical profile for intraocular lenses. Journal of Cataract & Refractive Surgery 37 (11), 2060–2067.

Guirao, A., Williams, D.R., Cox, I.G., 2001. Effect of rotation and translation on the expected benefit of an ideal method to correct the eye's higher-order aberrations. Journal of the Optical Society of America A-Optics Image Science and Vision 18 (5), 1003–1015.

Gumus, K., Gire, A., Pflugfelder, S.C., 2011. The Impact of the Boston ocular surface prosthesis on wavefront higher-order aberrations. American Journal of Ophthalmology 151 (4), 682–690.

Hammond, S.D., Puri, A.K., Ambati, B.K., 2004. Quality of vision and patient satisfaction after LASIK. Current Opinion in Ophthalmology 15 (4), 328–332.
Hirsch, J., Curcio, C.A., 1989. The spatial resolution capacity of human foveal retina. Vision Research 29 (9), 1095–1101.
Holden, B.A., 1975. The principles and practice of correcting astigmatism with soft contact lenses. Clinical and Experimental Optometry 58 (8), 279–299.
Holladay, J.T., Piers, P.A., Koranyi, G., van der Mooren, M, Norrby, N.E.S., 2002. A new intraocular lens design to reduce spherical aberration of pseudophakic eyes. Journal of Refractive Surgery 18 (6), 683–691.
Holzer, M.P., Mannsfeld, A., Ehmer, A., Auffarth, G.U., 2009. Early outcomes of INTRACOR femtosecond laser treatment for presbyopia. Journal of Refractive Surgery 25 (10), 855–861.
Hong, X., Himebaugh, N., 2001. On-eye evaluation of optical performance of rigid and soft contact lenses. Optometry & Vision Science 78 (12), 872.
Jain, S., Arora, I., Azar, D.T., 1996. Success of monovision in presbyopes: Review of the literature and potential applications to refractive surgery. Survey of Ophthalmology 40 (6), 491–499.
James, R., 1928. The father of british optics: Roger bacon, c. 1214–1294. The British Journal of Ophthalmology 12 (1), 1.
Johannsdottir, K.R., Stelmach, L.B., 2001. Monovision: A review of the scientific literature. Optometry & Vision Science 78 (9), 646–651.
Kanellopoulos, A.J., Asimellis, G., 2014. Hyperopic correction: Clinical validation with epithelium-on and epithelium-off protocols, using variable fluence and topographically customized collagen corneal crosslinking. Clinical ophthalmology (Auckland, NZ) 8, 2425.
Kanellopoulos, A.J., Asimellis, G., 2015. Presbyopic PiXL cross-linking. Current Ophthalmology Reports 3 (1), 1–8.
Hyung, K.L., Kyung, S.L., Jin, K.K., *et al.*, 2005. Epithelial healing and clinical outcomes in excimer laser photorefractive surgery following three epithelial removal techniques: Mechanical, alcohol, and excimer laser. American Journal of Ophthalmology 139 (1), 56–63.
Legras, R., Hornain, V., Monot, A., Chateau, N., 2001. Effect of induced anisometropia on binocular through-focus contrast sensitivity. Optometry & Vision Science 78 (7), 503–509.
Legras, R., Rouger, H., 2008. Calculations and measurements of the visual benefit of correcting the higher-order aberrations using adaptive optics technology. Journal of Optometry 1 (1), 22–29.
Liang, J., Williams, D.R., 1994. Objective measurement of wave aberrations of the human eye with the use of a Hartmann–Shack wave-front sensor. Journal of the Optical Society of America A, Optics, Image Science, and Vision 11 (7), 1949–1957.
López-Gil, N., Bradley, A., 2012. The Potential for and Challenges of Spherical and Chromatic Aberration Correction With New IOL Designs. BMJ Publishing Group Ltd.
López-Gil, N., Montés-Micó, R., 2003. Correcting ocular aberrations by soft contact lenses. South African Optometric Association 62, 173–177.
López-Gil, N., Montés-Micó, R., 2007. New intraocular lens for achromatizing the human eye. Journal of Cataract & Refractive Surgery 33 (7), 1296–1302.
Lovasik, J.V., Szymkiw, M., 1985. Effects of aniseikonia, anisometropia, accommodation, retinal illuminance, and pupil size on stereopsis. Investigative Ophthalmology & Visual Science 26 (5), 741–750.
Maeda, N., Fujikado, T., Kuroda, T., *et al.*, 2002. Wavefront aberrations measured with Hartmann–Shack sensor in patients with keratoconus. Ophthalmology 109 (11), 1996–2003.
Marcos, S., Barbero, S., Llorente, L., Merayo-Lloves, J., 2001. Optical response to LASIK surgery for myopia from total and corneal aberration measurements. Investigative Ophthalmology & Visual Science 42 (13), 3349–3356.
Marcos, S., Ortiz, S., Pérez-Merino, P., *et al.*, 2014. Three-dimensional evaluation of accommodating intraocular lens shift and alignment in vivo. Ophthalmology 121 (1), 45–55.
Marsack, J.D., Parker, K.E., Applegate, R.A., *et al.*, 2008. Performance of wavefront-guided soft lenses in three keratoconus subjects. Optometry and Vision Science: Official Publication of the American Academy of Optometry 85 (12), E1172.
Marsack, J.D., Parker, K.E., Pesudovs, K., Donnelly III, W.J., Applegate, R.A., 2007. Uncorrected wavefront error and visual performance during RGP wear in keratoconus. Optometry & Vision Science 84 (6), 463.
Marsack, J.D., Ravikumar, A., Nguyen, C., *et al.*, 2014. Wavefront-guided scleral lens correction in keratoconus. Optometry and Vision Science: Official Publication of the American Academy of Optometry 91 (10), 1221–1230.
McLeod, S.D., Vargas, L.G, Portney, V., Ting, A., 2007. Synchrony dual-optic accommodating intraocular lens: part 1: Optical and biomechanical principles and design considerations. Journal of Cataract & Refractive Surgery 33 (1), 37–46.
Mira-Agudelo, A., *et al.*, 2016. Compensation of presbyopia with the light sword lenscompensation of presbyopia with the light sword lens. Investigative Ophthalmology & Visual Science 57 (15), 6870–6877.
Mrochen, M., Kaemmerer, M., Mierdel, P., Seiler, T., 2001. Increased higher-order optical aberrations after laser refractive surgery: A problem of subclinical decentration. Journal of Cataract & Refractive Surgery 27 (3), 362–369.
Muñoz, G., Albarrán-Diego, C., Montés-Micó, R., Rodríguez-Galietero, A., Alió, J.L., 2006. Spherical aberration and contrast sensitivity after cataract surgery with the Tecnis Z9000 intraocular lens. Journal of Cataract & Refractive Surgery 32 (8), 1320–1327.
Navarro, R., Moreno, E., Dorronsoro, C., 2000. Phase plates for wave-aberration compensation in the human eye. Optics Letters 25 (4), 236–238.
Negishi, K., Kumanomido, T., Utsumi, Y., Tsubota, K., 2007. Effect of higher-order aberrations on visual function in keratoconic eyes with a rigid gas permeable contact lens. American Journal of Ophthalmology 144 (6), 924–929.
Pantanelli, S., MacRae, S., Jeong, T.M., Yoon, G., 2007. Characterizing the wave aberration in eyes with keratoconus or penetrating keratoplasty using a high-dynamic range wavefront sensor. Ophthalmology 114 (11), 2013–2021.
Pardhan, S., Gilchristt, J., 1990. The effect of monocular defocus on binocular contrast sensitivity. Ophthalmic and Physiological Optics 10 (1), 33–36.
Pepose, J.S., Burke, J., Qazi, M.A., 2017. Benefits and barriers of accommodating intraocular lenses. Current Opinion in Ophthalmology 28 (1), 3–8.
Pérez-Merino, P., Birkenfeld, J., Dorronsoro, C., *et al.*, 2014. Aberrometry in patients implanted with accommodative intraocular lenses. American Journal of Ophthalmology 157 (5), 1077–1089.
Petelczyc, K., Garcia, J.A., Bará, S., *et al.*, 2009. Presbyopia compensation with a light sword optical element of a variable diameter. Photonics Letters of Poland 1 (2), 55–57.
Petelczyc, K., Ares García, J., Bará, S., *et al.*, 2011. Strehl ratios characterizing optical elements designed for presbyopia compensation. Optics Express 19 (9), 8693–8699.
Piers, P.A, Fernandez, E.J, Manzanera, S., Norrby, S., Artal, P., 2004. Adaptive optics simulation of intraocular lenses with modified spherical aberration. Investigative Ophthalmology & Visual Science 45 (12), 4601–4610.
Piers, P.A., Manzanera, S., Prieto, P.M., Gorceix, N., Artal, P., 2007. Use of adaptive optics to determine the optimal ocular spherical aberration. Journal of Cataract & Refractive Surgery 33 (10), 1721–1726.
Plaza-Puche, A.B., Alió, J.L., MacRae, S., *et al.*, 2015. Correlating optical bench performance with clinical defocus curves in varifocal and trifocal intraocular lenses. Journal of Refractive Surgery 31 (5), 300–307.
Porter, J., Guirao, A., Cox, I.G, Williams, D.R., 2001. Monochromatic aberrations of the human eye in a large population. JOSA A 18 (8), 1793–1803.
Pullum, K.W., Whiting, M.A., Buckley, R.J., 2005. Scleral contact lenses: The expanding role. Cornea 24 (3), 269.
Randleman, J.B., Woodward, M., Lynn, M.J., Stulting, R.D., 2008. Risk assessment for ectasia after corneal refractive surgery. Ophthalmology 115 (1), 37–50.
Ravikumar, S., Bradley, A., Bharadwaj, S., Thibos, L.N., 2016. Expanding binocular depth of focus by combining monovision with diffractive bifocal intraocular lenses. Journal of Cataract & Refractive Surgery 42 (9), 1288–1296.
Reinstein, D.Z., Archer, T.J., Gobbe, M., 2012. The history of LASIK. Journal of Refractive Surgery 28 (4), 291–298.
Renna, A., Vejarano, L.F., Cruz, E., Alió, J.L., 2016. Pharmacological treatment of presbyopia by novel binocularly instilled eye drops: A pilot study. Ophthalmology and Therapy. 1–11.

Ripken, T., Oberheide, U., Fromm, M., 2008. fs-Laser induced elasticity changes to improve presbyopic lens accommodation. Graefe's Archive for Clinical and Experimental Ophthalmology 246 (6), 897–906.
Rosenthal, P., 2010. Scleral lens with scalloped channels or circumferential fenestrated channels. US Patent 7,695,135.
Rosenthal, P., 2009. Scleral contact lens with grooves and method of making lens. US Patent 7,591,556.
Rossi, E.A, Weiser, P., Tarrant, J., Roorda, A., 2007. Visual performance in emmetropia and low myopia after correction of high-order aberrations. Journal of Vision 7 (8), 14.
Sabesan, R., Ahmad, K., Yoon, G., 2007. Correcting highly aberrated eyes using large-stroke adaptive optics. Journal of Refractive Surgery 23 (9), 947–952.
Sabesan, R., Johns, L., Tomashevskaya, O., *et al*., 2013. Wavefront-guided scleral lens prosthetic device for keratoconus. Optometry and Vision Science: Official Publication of the American Academy of Optometry 90 (4), 314.
Sabesan, R., Moon Jeong, T., Carvalho, L., 2007. Vision improvement by correcting higher-order aberrations with customized soft contact lenses in keratoconic eyes. Optics Letters 32 (8), 1000–1002.
Sabesan, R., Zheleznyak, L., Yoon, G., 2012. Binocular visual performance and summation after correcting higher order aberrations. Biomedical Optics Express 3 (12), 3176–3189.
Sahler, R., Bille, J.F, Enright, S., Chhoeung, S., Chan, K., 2016. Creation of a refractive lens within an existing intraocular lens using a femtosecond laser. Journal of Cataract & Refractive Surgery 42 (8), 1207–1215.
Savage, D.E., Brooks, D.R., DeMagistris, M., *et al*., 2014. First demonstration of ocular refractive change using blue-IRIS in live catsrefractive changes using blue-IRIS. Investigative Ophthalmology & Visual Science 55 (7), 4603–4612.
Schwarz, C., Cánovas, C., Manzanera, S., *et al*., 2014. Binocular visual acuity for the correction of spherical aberration in polychromatic and monochromatic light. Journal of Vision 14 (2), 8.
Segal, O., Barkana, Y., Hourovitz, D., *et al*., 2003. Scleral contact lenses may help where other modalities fail. Cornea 22 (4), 308.
Seiler, T., Kaemmerer, M., Mierdel, P., Krinke, H.-E., 2000. Ocular optical aberrations after photorefractive keratectomy for myopia and myopic astigmatism. Archives of Ophthalmology 118 (1), 17–21.
Sheedy, J.E., Truong, S.D., Hayes, J.R., 2003. What are the visual benefits of eyelid squinting? Optometry & Vision Science 80 (11), 740–744.
Sheppard, A.L., Bashir, A., Wolffsohn, J.S., Davies, L.N., 2010. Accommodating intraocular lenses: A review of design concepts, usage and assessment methods. Clinical and Experimental Optometry 93 (6), 441–452.
Snibson, G.R., 2010. Collagen cross-linking: A new treatment paradigm in corneal disease–a review. Clinical & Experimental Ophthalmology 38 (2), 141–153.
Stason W.B., Razavi M., Jacobs D.S., *et al*., 2010. Clinical benefits of the boston ocular surface prosthesis. American Journal of Ophthalmology 149 (1),54–61.
Thibos, L.N., Hong, X., Bradley, A., Cheng, X., 2002. Statistical variation of aberration structure and image quality in a normal population of healthy eyes. JOSA A 19 (12), 2329–2348.
Thibos, L.N., Ye, M., Zhang, X., Bradley, A., 1992. The chromatic eye: A new reduced-eye model of ocular chromatic aberration in humans. Applied Optics 31 (19), 3594–3600.
Vandermeer, G., Rio, D., Gicquel, J.-J., Pisella, P.-J., Legras, R., 2015. Subjective through-focus quality of vision with various versions of modified monovision. British Journal of Ophthalmology 99 (7), 997–1003.
Villa, C., Gutiérrez, R., Jiménez, J.R., Gonzalez-Méijome, J.M., 2007. Night vision disturbances after successful LASIK surgery. British Journal of Ophthalmology 91 (8), 1031–1037.
Wichterle, O., Lim, D., 1960. Hydrophilic gels for biological use. Nature 185 (4706), 117–118.
Williams, D., Yoon, G.Y., Porter, J., *et al*., 2000. Visual benefit of correcting higher order aberrations of the eye. Journal of Refractive Surgery 16 (5), S554–S559.
Wozniak, K.T., Gearhart, S.M., Savage, D.E, *et al*., 2017. Comparable change in stromal refractive index of cat and human corneas following blue-IRIS. Journal of Biomedical Optics 22 (5). doi:10.1117/1.JBO.22.5.055007.
Xu, L., Knox, W.H, DeMagistris, M., Wang, N., Huxlin, K.R., 2011. Noninvasive intratissue refractive index shaping (IRIS) of the cornea with blue femtosecond laser light. Investigative Ophthalmology & Visual Science 52 (11), 8148–8155.
Yi, F., Iskander, D.R., Collins, M., 2011. Depth of focus and visual acuity with primary and secondary spherical aberration. Vision Research 51 (14), 1648–1658.
Yılmaz, O.F., Alagöz, N., Pekel, G., *et al*., 2011. Intracorneal inlay to correct presbyopia: Long-term results. Journal of Cataract & Refractive Surgery 37 (7), 1275–1281.
Yoon, G., Jeong, T.M., Cox, I.G., Williams, D.R., 2004. Vision improvement by correcting higher-order aberrations with phase plates in normal eyes. Journal of Refractive Surgery 20 (5), S523–S527.
Yoon, G., MacRae, S., Williams, D.R., Cox, I.G., 2005. Causes of spherical aberration induced by laser refractive surgery. Journal of Cataract & Refractive Surgery 31 (1), 127–135.
Yoon, G.-Y., Williams, D.R., 2002. Visual performance after correcting the monochromatic and chromatic aberrations of the eye. JOSA A 19 (2), 266–275.
Zheleznyak, L., Alarcon, A., Dieter, K.C., Tadin, D., Yoon, G., 2015. The role of sensory ocular dominance on through-focus visual performance in monovision presbyopia corrections. Journal of Vision 15 (17), 1–12.
Zheleznyak, L., Gandara-Montano, G., MacRae, S., *et al*., 2017. First demonstration of human visual performance through refractive-index-modified ophthalmic devices written in hydrogels [ARVO E-ABSTRACT 1274]. Investigative Ophthalmology & Visual Science 58, 1274.
Zheleznyak, L., Sabesan, R., Oh, J.-S., MacRae, S., Yoon, G., 2013. Modified monovision with spherical aberration to improve presbyopic through-focus visual performance. Investigative Ophthalmology & Visual Science 54 (5), 3157–3165.
Zheleznyak, L.A., 2014. Overcoming Presbyopia by Manipulating the Eyes' Optics. University of Rochester.
Zheleznyak, L., Jung, H., Yoon, G., 2014. Impact of pupil transmission apodization on presbyopic through-focus visual performance with spherical aberration. Investigative Ophthalmology & Visual Science 55 (1), 70–77.

Laser and Light in Ophthalmology

Michael Mrochen, IROC Science AG, Zurich, Switzerland and Swiss Eye Research Foundation, Reinach, Switzerland
Nicole Lemanski, Mabel Cheng MD PLLC, Albany, NY, United States
Bojan Pajic, Orasis Ag, Reinach, Switzerland and Swiss Eye Research Foundation, Reinach, Switzerland

© 2018 Elsevier Ltd. All rights reserved.

The human eye is a complex transparent optical system that receives light in the electromagnetic spectrum. The key structures of the eye include the pupil, iris, lens, cornea, conjunctiva, sclera, conjunctiva, fovea, choroid, optic nerve, optic disc, cilary body, macula and retina, the latter of which contain photoreceptors responsible for light perception and vision including color differentiation and the perception of depth. The eye can be divided into three layers: the outermost fibrous layer comprised of the cornea and sclera; the middle layer, which consists of the choroid, ciliary body, pigmented epithelium and the iris; and, the retina which represents the innermost layer. A transparent, watery fluid, called aqueous humour occupies the anterior and posterior chambers, i.e., between the cornea and the iris and between the iris and the lens, respectively, while vitreous humour, with a more jelly like consistency, fills the posterior cavity behind the lens. The ciliary body connects the iris to the choroid and is responsible for focusing the crystalline lens and secreting aqueous humour. The lens is attached to ciliary body by the Zonule of Zinn.

In order for the eye to operate correctly, each structure of the eye must function correctly. Given the complexity of the eye it is perhaps not surprising that it may be affected by numerous and systemic disorders, ranging from conjunctivitis and dry eye syndrome to age-related disease including macular degeneration and cataracts. Additionally, refractive disorders including hyperopia, myopia, astigmatism and presbyopia are thought to affect more than two billion of the world population; the World Health Authority estimates that 153 million people worldwide have uncorrected refractive errors, excluding presbyopia (World Health Organization, 2009).

Light and Laser Therapy

Lasers and light technologies have become important diagnostic and therapeutic tools in ophthalmology. They can be used for imaging the eye and can also be used to treat eye conditions, including glaucoma and retinal disease as well as refractive conditions involving the cornea and lens.

Laser and light treatments used in ophthalmology have photochemical, photothermal and photomechanical mechanisms. The Interactions of light with biological tissues depend on its wavelength, pulse duration and irradiance (**Fig. 1**). However, all are caused primarily by the interaction of photons with the molecules and the molecular compounds of the tissue.

Reducing the illumination time (micro- to millisecond range) and increasing the intensities the tissue temperature can be increased and thermal processes might occur. As temperature rises, the cellular and tissue structural proteins undergo denaturation and conformational changes a process defined as thermal coagulation. Increasing the temperature up to 100°C or more, may cause

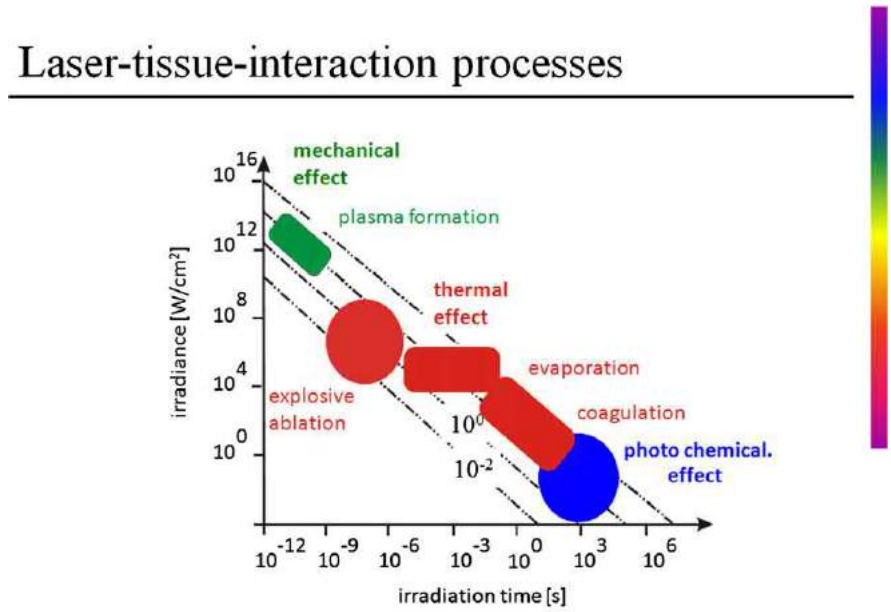


Fig. 1 The interaction between laser and biological tissue.

 doi:10.1016/B978-0-12-803581-8.09782-4

vaporization of the liquid within the tissue. Further reduction of the illumination time might finally lead to an explosive tissue removal (photoablation).

Photochemical Interaction

The primary interaction mechanism between tissue and laser light are mainly depending on the wavelength, irradiation time (pulse duration) and the intensity or energy dose. For long irradiation times (seconds to minutes) and low intensities one can observe mainly photochemical processes. Photochemical interactions are the basis for cross linking of corneal collagen (CXL).

Therapeutic photochemical interactions are typically performed at low irradiances (<1 W/cm^2) for long durations, i.e., tens of seconds, to avoid tissue heating. During photochemical interactions, a photon of a specific wavelength is absorbed by a photosensitizer which transforms the molecule (e.g., porphyrin, riboflavin) into the exited singlet state. The molecule decays back to the ground state, or it can be converted into the excited triplet state which in turn is able to transfer energy to a triplet ground state of oxygen. This energy transfer results in highly toxic singlet oxygen. This toxic singlet oxygen in turn produce irreversible oxidation of the cell structures in the areas to which the photosensitizer has been concentrated (Palanker, 2014).

As noted earlier, CXL is an example of a photochemical reaction. It involves four important factors: energy dose of the applied ultraviolet (UV) light, concentration or formulation of riboflavin, oxygen concentration within the tissue, timing of riboflavin diffusion, oxygen diffusion, and light exposure. Riboflavin acts as a photosensitizer that is activated by the absorbed UV light to create reactive oxygen species (ROS) which help to produce bonds between molecules in the stroma, thus increasing the biomechanical strength of the cornea.

The Dresden Protocol uses a 0.1%–0.15% aqueous solution of riboflavin-5-phosphate (vitamin B2) that provides a high absorption and, therefore, good shielding-effect at a wavelength of 360–370 nm. The typically used radiant exposure (energy does) of 5.4 J/cm² allows for biomechanical stiffening of the cornea following treatment.

CXL is an established treatment for keratoconus and post-LASIK ectasia with numerous clinical studies showing that it is helps to slow disease progression, regularize the cornea and improve visual acuity in patients with these disorders. Other indications include pellucid marginal degeneration, iatrogenic keratectasia after refractive laser surgery and corneal melting that does not respond to conventional therapy. More recently, CXL has also been investigated as a treatment for refractive errors including myopia, hyperopia and astigmatism (Kanellopoulos, 2014) and for infectious keratitis.

It is known that upon photochemical activation, oxygen species are released from each of the carboxylic groups present in riboflavin, leading to the generation of a light activated riboflavin and single reactive oxygens in solution (O^{2-}). As there are two by-products of the photochemical activation, there are two mechanisms available to interact with the collagen structure. In the direct mechanism (Type I), the light activated riboflavin interacts directly with the collagen molecule by hydrogen abstraction of amines to stabilize its own carbon double bonds therefore enabling intermolecular covalent crosslinks to form in the collagen. In the indirect mechanism (Type II), single reactive oxygens form hydrogen peroxide (H_2O_2) and free radicals (e.g., superoxide anion O^{2-}) which in turn oxidize the collagen molecule and therefore enable the formation of indirect covalent crosslinks. Most cross-linking occurs through Type I photochemical reactions (Lichtman and Conchello, 2005; Rich *et al.*, 2014; Balasubramanian *et al.*, 1990).

It seems to be of relevance that when an anaerobic solution of riboflavin is exposed to blue or ultraviolet light in the presence of an electron donor, the yellow color of the solution is reduced in intensity. The spectrum of the resulting solution is identical to that of chemically reduced riboflavin and aeration of the solution results in a complete return of the color such that the spectrum of the original and aerated solutions. The photoreaction of riboflavin in the presence of an electron donor would appear to be a photoreduction. In aqueous media, photoreduction in the presence of an electron donor is considered to be more efficient than photobleaching (Carr, 1960; Smith, 1963; Cairns, 1970).

As a result of Type I and Type II reactions, are two reaction mechanisms competing for oxygen in the cornea: excited riboflavin and reduced-state riboflavin. Consequently oxygen is rapidly consumed in the cornea. Unfortunately, reduced-state riboflavin is not reactive and does not act as a photosensitizer. Only new oxygen molecules that diffuse into cornea from atmosphere can lead to further crosslinking activities. The depletion of oxygen during CXL suggests a combined Type I and Type II mechanism after several minutes as oxygen begins to replenish itself. Of note, Herekar (2007) reported on the depletion of oxygen during corneal cross linking and found a significant reduction of oxygen available for Type II reactions within the first 3–5 min at an intensity of 3 mW/cm^2. At an intensity of 16 mW/cm^2, the depletion occurred in less than 1 min. Thus, during CXL, both anaerobic and aerobic conditions are created in the cornea. Anaerobic conditions occur where reduced state riboflavin is formed and all oxygen is consumed. Aerobic conditions occur when oxygen from the air diffuses into the cornea. It is reasonable to conclude then that it is the oxygen diffusion time might be primary driver for the depth and effectiveness of CXL. Specifically, reducing the diffusion time will create a thinner aerobic layer, producing a CXL effect only at anterior part of cornea. Higher diffusion of oxygen will cause deeper CXL effects and higher efficacy (**Fig. 2**).

Photothermal Interactions

Photothermal interactions are the basis for treatments such as panretinal photocoagulation (PRP). Simply speaking, when tissue absorbs laser energy, a photothermal interaction occurs. Tissue temperature changes both during and after the laser irradiation are crucial. Depending on the temperature change and duration of exposure, different effects may occur, i.e., necrosis, coagulation and

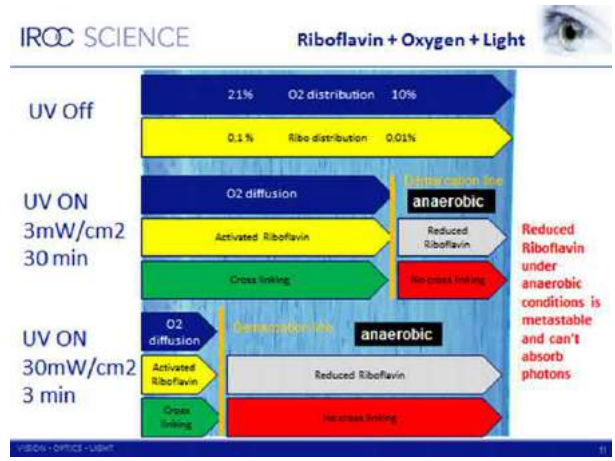


Fig. 2 The photochemical relationship between oxygen, riboflavin and UVA light.

vaporization. Daniel Palanker Department of Ophthalmology and Hansen Experimental Physics Laboratory, Stanford University, Stanford, CA, notes that heat diffusion during the laser pulse becomes significant when the pulse duration exceeds the time it takes for heat to spread over the distance equal to the laser penetration depth in tissue. For pulses shorter than the characteristic diffusion time across the light absorption zone, the heat cannot escape from the energy deposition zone during the pulse; this results in the most efficient heating (Palanker, 2014).

Panretinal photocoagulation was first evaluated in the 1970s using both xenon arc laser and argon laser treatments on patients with proliferative diabetic retinopathy (PDR). The study found that while both laser types were similarly effective, the argon laser was associated with fewer adverse effects.

Panretinal photocoagulation for the treatment of PDR typically uses visible light to create a thermal burn in the retinal tissue. When the retinal pigment epithelium ((RPE) which overlays the choroid, just below the retina) absorbs laser light, localized coagulation necrosis occurs, i.e., the laser coagulates the RPE and adjacent photoreceptors, but the retina remains intact. As a result, PRP reduces the area of ischemic tissue, which in turn reduces total vascular endothelial growth factor (VEGF) production in the eye. This in turn helps to reduce neovascularization (American Academy of Ophthalmology).

Ischemic diseases, namely diabetic retinopathy, retinal vein occlusions and sickle cell retinopathy, are the main therapeutic targets for PRP. Indications for focal photocoagulation treatments include retinal breaks, ocular tumors, extrafoveal choroidal neovascular membrane, and microaneurysms.

The overall goal of panretinal photocoagulation is to reduce the oxygen consumption of the outer retina and re-establish a balance between the oxygen supply and demand. PRP typically employs or PRP, typically yellow, green, or red laser light to create micro burns. Specifically, absorbed laser energy is converted into thermal energy, raising the tissue temperature to 20°C–30°C. Tissue burns denature tissue proteins leading to local cell death and coagulative necrosis. An average PRP treatment administers 1200–1500 burns across an area 0.5 mm diameter. This number of burns/area may help to reduce the number of photoreceptors and oxygen consumption of the outer retina by around 20%.

There are several PRP protocols including long duration and short duration protocols. A short duration protocol uses pattern scanning that delivers a pattern of multiple burns in roughly the same time it takes for a conventional laser to deliver one burn. Consequently, the pulse duration is approximately 10–30 ms per spot and the number of spots administered is approximately 3000–5000. As the name suggests, the long duration protocol is more time consuming because the burns are delivered individually. The pulse duration is usually 100 ms with a large spot size (200–500 μ). A power of 200–250 mW is typically applied (American Academy of Ophthalmology).

Photomechanical Interactions

Photomechanical interactions (photodisruption) form the basis for precise tissue cutting, useful in refractive and cataract surgery. Photodisruption occur when absorption of the laser intensity results in an optical break down due to the high electric field strength beyond the binding energy of molecules. The created electron plasma requires more space leading to fast expansion of the plasma. Expanding and collapsing cavitation bubbles can rupture nearby tissue or eject tissue fragments from the exposed surface. To avoid heat diffusing away from the laser absorption site, energy should be delivered within the thermal confinement time accounting for the use of relatively short pulse durations, i.e., in femto- to picosecond range (Palanker, 2014).

The Small Incision Lenticule Extraction (SMILE) procedure, which is a minimally invasive procedure, designed to correct higher degrees of myopia is an example of photomechanical laser application. Specifically, a femtosecond laser is used to create a 3 mm corneal micro-tunnel through which the lenticule is extracted. SMILE received FDA approval in 2016.

SMILE is indicated for myopia (− 1.0 D to − 8 D) – and may be particularly useful for myopic patients with dry eye because there is less disruption of corneal surface, and in turn, the tear film, as compared with LASIK. Patients should also have ≤ − 0.50 D cylinder and MRSE − 8.25 D in the affected eye. SMILE is unsuitable for patients with astigmatism.

The SMILE procedure employs a femtosecond laser. During the procedure, the individually calibrated curved glass of the femtosecond laser is placed against the cornea, Formation of a meniscus tear film allows the patient to see the fixation target because the vergence of the fixation beam is focused according to the patient's refraction, The patient to looks at the fixation target and corneal suction ports are activated to fixate the eye. The lower interface of the intrastromal lenticule is created first, followed by the upper interface of the lenticule (which is known as a cap). The laser is then used to create a 2–3 mm tunnel incision that links the cap interface to the corneal surface (Reinstein *et al.*, 2014).

An applanation-free femtosecond laser has also been proposed by Pajic and colleagues and is designed to circumvent the problems associated with weak and strong applanation, respectively. In the case of weak applanation on one hand, an adaption piece of almost the same curvature as the cornea is brought onto the eye. In the case of strong applanation on the other hand, a painful applanation is generated by pressing the eye down with a glass plate. In an applanation-free procedure, physiological saline with a refractive index (n = 1.338) close to that of the cornea (regularly n = 1.376) is brought on top of the eye into the suction ring. This liquid ensures a very good refractive index matching and thus minimizes the wave front distortion of the fs-laser pulses upon entrance into cornea. The thickness of the liquid can be varied from a few hundred μm to 1 mm. In this way, an applanation-free processing of the cornea becomes possible (Pajic and Hafezi, 2011).

Laser and Light Interaction and Ocular Target Tissue

Cornea

Laser and light technology play an important role in the treatment of corneal conditions, such as keratoconus. Keratoconus is a bilateral disorder characterized by steepening and thinning of the central cornea, which leads to loss of visual acuity. In early stages keratoconus is treated with contact lenses; however, traditionally, when patients become contact lens-intolerant, keratoplasty, or corneal transplant surgery is performed. Advances in lasers and light, decreased the need for keratoplasty. For example, CXL helps to increase the biomechanical strength of the cornea, with the goal of avoiding corneal transplant.

The procedure utilizes a 0.1%–0.15% aqueous solution of riboflavin-5-phosphate (vitamin B2) and UVA light at a wavelength of 360–370 nm (intensity 3 mW/cm^2), usually for 30 min. This is known as the Dresden Protocol. The typically used radiant exposure (energy does) of 5.4 J/cm² allows for biomechanical stiffening of the cornea following treatment. Newer accelerated protocols with shorter treatment times are currently under development.

Findings from a meta-analysis of randomized controlled trials that assessed the effect of CXL in slowing progression of keratoconus show that CXL significantly decreased mean keratometry, maximum keratometry and minimum keratometry. There were also significant improvements in best spectacle-corrected visual acuity (BCVA). Manifest cylinder error decreased significantly in patients undergoing CXL procedure compared with control patients in sensitivity analysis. Thus, CXL appears to be an effective option in stabilizing the cornea in keratoconus (Li *et al.*, 2015; Cummings *et al.*, 2016; Choi *et al.*, 2017). Some authors found that the accelerated CXL protocol with higher UV intensity and reduced irradiation time showed a smaller topographic flattening effect when compared to the standard Dresden protocol. Sadoughi *et al.* (2016) also compared the Dresden protocol with accelerated CXL (9 mW/cm^2 for 10 min) in patients with progressive keratoconus. Like Cummings *et al.*'s study, they found that accelerated CXL had similar refractive, visual, keratometric, and aberrometric results and significant less adverse effects on the corneal thickness and endothelial cells as compared with the conventional method after 12 months follow-up.

There is a large body of published studies describing outcomes in the treatment of keratoconus. Collagen corneal cross-linking was first pre-clinically evaluated as a conservative treatment for keratectasia in 1998 bySpoerl *et al.* (1998). Enucleated porcine eyes were treated with UV-light (lambda = 254 nm), 0.5% riboflavin, 0.5% riboflavin and UV-light (365 nm) blue light (436 nm) and sunlight, and the chemical agents, glutaraldehyde (1% and 0.1%, 10 min) and Karnovsky's solution (0.1%, 10 min), and were then compared with untreated corneas. They found that compared to untreated corneas treatment with riboflavin and UV-irradiation as well as weak glutaraldehyde or Karnovsky's solutions significantly increased corneal stiffness (Spoerl *et al.*, 1998). This early in vitro study paved the way for Wollensak *et al.*'s prospective, nonrandomized clinical pilot study in 23 eyes with moderate or advanced progressive keratoconus. Data from this study showed that treatment with riboflavin and ultraviolet-A (UVA) irradiation (370 nm, 3 mW/cm^2 for 30 min) halted the progression of keratoconus in all eyes and caused disease regression in 16 eyes (70%) (Wollensak *et al.*, 2003).

The initial clinical results have been confirmed and reproduced during the past 15 years in multiple clinical studies and have lead to regulatory approvals around the world including FDA approval of the Dresden protocol in 2016. Overall, it appears that CXL's main benefit is in halting, or at least slowing, disease progression. However, it may also help to improve visual acuity. A systemic literature review and meta-analysis of ocular functional and structural parameters of patients with keratoconus undergoing cross-linking procedures found an improvement in visual acuity of 1–2 Snellen lines 3 months or more after undergoing CXL; changes were more pronounced in uncorrected visual acuity. Some topography parameters were found to be improved (0.6–1 diopters) 12–24 months after CXL (Meiri *et al.*, 2016). According to a study by Greenstein and Hersh, outcomes following CXL may be predicted by preoperative patient characteristics. Results of the study, which comprised 104 eyes (66 keratoconus;

38 corneal ectasia), showed that patients with worse preoperative CDVA and higher K values, (particularly with a CDVA of 20/40 or worse or a maximum K of 55.0 D or more), were most likely to have improvement after CXL. However, the authors noted that no preoperative characteristics were predictive of CXL failure (Greenstein and Hersh, 2013).

Lens

Lasers play a key role in modern-day cataract surgery. For many cataract surgeons, femtosecond lasers have replaced hand-held tools for creating the corneal incision and anterior capsulotomy as well as lens and cataract fragmentation. It is also possible to correct astigmatism through corresponding arcuate incisions. It has been suggested that use of femtosecond laser may help to improve safety and precision and reduce postoperative complications versus traditional cataract surgery. A study by Abell and colleagues of outcomes and safety in more than 4000 cases at a single center, however, showed that the two cataract surgery techniques appear to be equally safe. The authors reported that the safety of femtosecond-assisted cataract surgery (FLACS) in terms of posterior capsule complications was equal to that of phacoemulsification, and that anterior capsule tears was a concern in both groups (Abell *et al.*, 2015). A meta analysis of 14,567 eyes that also compared FLACS to manual cataract surgery similarly found that there were no statistically-significant differences between groups in terms of patient-important visual and refractive outcomes and overall complications (Popovic *et al.*, 2016).

Lasers are often also use post-cataract surgery. The neodymium: yttrium-aluminum-garnet (Nd: YAG) laser is used to perform postoperative opacification, and has largely replaced surgical cutting or polishing of the posterior capsule in the management of opacification. The Nd: YAG laser is a solid-state laser with a wavelength of 1064 nm and has a photomechanical effect (Steinert, 2013).

Vitreoretinal

Light is also employed in the treatment of vitreoretinal disorders. Retinal laser photocoagulation is used to treat retinal tears (laser retinopexy) in order to inhibit progression to a retinal detachment. For this indication, green light is the wavelength typically because it is well absorbed by melanin and hemoglobin but is poorly absorbed by xanthophylls thus limiting the potential of macular damage. Red wavelengths are also used and are particularly helpful in patients with media opacity such as cataracts. However, since red light has a longer wavelength than green light, there may be more unpredictable and more heterogeneous absorption by the choroid; this in turn may increase pain and may also lead to focal damage to Bruch's membrane (Silva and Blumenkranz, 2013).

Panretinal photocoagulation is used to treat diabetic retinopathy; it may also be used to retinal ischemia and retinal neovascularization of avascular areas. A number of lasers have been used in panretinal photocoagulation including ruby lasers (694-nm wavelength), argon lasers which can use the blue (488-nm wavelength) and green (514-nm wavelength) light emission, and dye lasers. In the 1990s diode lasers (810-nm wavelength) and micropulsed diode lasers, and later, transpupillary thermotherapy (TTT) using a near-infrared (810-nm wavelength) laser were introduced. Newer developments include pattern scan laser photocoagulator with a 532-nm laser and 532-nm pattern-type eye-tracking lasers (Kozak and Luttrull, 2015).

There are a number of landmark studies describing PRP outcomes in diabetic retinopathy. These include the Diabetes Control and Complications Trial, the Diabetic Retinopathy Study, the Early Treatment Diabetic Retinopathy Study (ETDRS) and the Diabetic Retinopathy Vitrectomy Study Research Group trial (Royle *et al.*, 2015).

These studies highlighted a number of points. The randomized, controlled DRS trial, undertaken by the National Eye Institute in the 1970s, compared the efficacy of PRP (versus no treatment) in delaying the progression of PDR and preventing vision loss. The study included 1700 patients with non-proliferative PDR in both eyes or PDR in at least one eye. Patients received PRP treatment in one eye, and no treatment in the fellow eye. Patients were randomly assigned to receive either xenon arc treatment or argon treatment. Findings showed that PRP reduced the risk of severe visual loss by more than 50%. The vision loss rate was 16.3% in untreated eyes versus 6.4% in treated eyes over two years. The study also showed that argon laser was more effective than the xenon arc laser. Importantly, the DRS study also showed that at 2 years, 11% of treated eyes versus 26% of untreated eyes with high-risk retinopathy developed severe visual loss. At 4 years, 20% of treated eyes and 44% of untreated eyes developed severe visual loss ($>5/200$). In patients with early proliferative retinopathy – 3% of treated eyes and 7% of untreated eyes developed severe visual loss at 2 years. At 4 years 7% of treated eyes and 21% of untreated eyes developed severe visual loss. The ETDRS group subsequently examined whether early PRP was more effective than delayed PRP treatment. The ETDRS study group concluded that scatter photocoagulation should not be offered in mild cases of PDR as the potential adverse effects and relative risks of treatment may outweigh minimal benefits gained by treatment at early stages. They advised that PRP treatment should commence when non-proliferative PDR becomes severe or progresses into PDR (American Academy of Ophthalmology; Royle *et al.*, 2015).

Lasers are also being increasingly used to reduce symptomatic vitreous floaters. Vitreous floaters are deposits of various size, shape, consistency, refractive index, and motility within the eye's vitreous humour, which is normally transparent. Previously, neodymium–yttrium-aluminum-garnet (Nd: YAG) were employed which was associated with mixed success. More recently, modified YAG lasers have been used. The Ultra Q Reflex™ system (Ellex Medical Lasers, Australia,) is a Q-switched Nd: YAG laser that vaporizes floaters at lower energy levels and with fewer shots than older laser systems. Unlike traditional Nd: YAG lasers, this modified laser is focused onto the front surface of the floater. The laser emits a short and small burst of energy that provides a

potent power density (10^9 J/cm^2). This energy converts collagen and hyaluronic molecules found in a floater into a gas, which is then reabsorbed into the eye (The Ultra Q Reflex). Findings from a retrospective, observational study by Inder Paul Singh, MD (Cummings *et al.*, 2016) of 168 eyes of 124 patients (mean age, 66 years (range, 42–89 years)) who underwent YAG vitreolysis (laser power range 2.0–5.5 mJ) demonstrated that 92% of patients were satisfied with the procedure. There was one case of intraocular pressure (IOP) spike, and two phakic lenses were damaged, one of which required cataract surgery. No retinal detachment or other retinal complications were seen and there was no anterior chamber or vitreous reactions (Singh, 2014).

Refractive

Lasers and light therapy has perhaps received the widest recognition in the treatment of refractive errors, in particular the use of excimer lasers.

Excimer laser (PRK and LASIK)

Excimer lasers are used in the treatment of myopia, hyperopia and astigmatism; operates in the ultraviolet spectral region. Laser-assisted in situ keratomileusis (LASIK) and PRK both employ this type of laser technology. While PRK uses an excimer to reshape the surface of the cornea, LASIK uses an excimer laser reshapes the cornea under a corneal flap at the stromal level.

Excimer lasers typically operate in the UV spectrum and use a gas mixture (known as the excimer gain medium) containing a noble gas such as argon, and a halogen, e.g., chlorine or fluorine. When a high voltage electric discharge is delivered into the laser cavity these gases combine to form a high energy excited gas state (excited dimer). When this high-energy compound subsequently dissociates, a photon of energy is released corresponding to the energy of the noble gas-halogen molecule. This light energy is amplified in the laser system resulting in the production of a high-energy discrete pulse of laser energy which disrupts chemical bonds of proteins, glycosaminoglycans, and nucleic acids in the cornea. Importantly, laser energy is absorbed by these compounds but with minimal damage to surrounding tissue because of a high energy density and short pulse duration (Manche *et al.*, 1998).

The efficacy of LASIK and PRK is well established. However, a literature analysis that included randomized controlled trials comparing LASIK and PRK for the correction of any degree of myopia (1135 participants, 1923 eyes) concluded that LASIK gives a faster visual recovery and is a less painful technique than PRK. Nevertheless, the authors added that the two techniques appear to give similar outcomes 1 year after surgery (Shortt *et al.*, 2013).

Photorefractive keratectomy (PRK) is a laser that utilizes excimer laser technology, and is typically used in the treatment of keratoconus. Current regimes for PRK utilize topography-guided ablation profiles designed to help reduce corneal surface irregularities with the goal of improving vision. In a retrospective follow-up study by Tambe *et al.* (2015), 28 eyes of 23 patients (age 17–60) with grade 1–3 keratoconus received topography-guided PRK between 1998 and 2013. Of the 28 eyes, 18% underwent corneal transplantation at a median of 7 years (range 3–10) after PRK, four eyes were not available for follow-up, and in the remaining 19 eyes, corrected distance visual acuity (CDVA) was improved in 16 eyes (84.3%), reduced in 2 eyes (10.5%), and unchanged in 1 eye (5.2%). The mean spherical equivalent was reduced from -6.2 to -3.7 diopters (D) after 3 months and to -2.1 D at the late follow-up visit. Similarly, the mean cylinder was reduced from -4.2 to -3.0 D after 3 months and at the late follow-up. The authors suggested, therefore, that topography-guided PRK in keratoconus may help to reduce myopia and astigmatism and may offer a temporary or permanent alternative to keratoplasty in contact lens-intolerant keratoconus.

Femtosecond laser

Femtosecond laser technology is now also being employed in LASIK. Known as femtosecond laser-assisted LASIK (FS-LASIK), the femtosecond laser is used for flap creation while the excimer laser is used for stromal bed ablation. Thus the femtosecond laser allows the surgeon to create a thin-hinged corneal flap and a significant less deviation in flap thickness without using a microkeratome. An analysis published in 2017 concluded that FS-LASIK yielded more predictable corneal flaps, lesser ocular aberrations, better uncorrected visual acuity, less variations in IOP and a reduced risk of developing dry eye. However, FS-LASIK may cause transient light sensitivity, diffuse lamellar keratitis, opaque bubble layer, corneal haze and rainbow glare (Bashir *et al.*, 2017).

The SMILE procedure also uses femtosecond laser technology. SMILE evolved from Femtosecond Lenticule Extraction (FLEx) and has been shown to be safe and effective treatment for myopia (Vestergaard *et al.*, 2012; Wang *et al.*, 2013; Kamiya *et al.*, 2014). The procedure involves cutting a small lenticule in the corneal stroma with a femtosecond laser. The lenticule is subsequently removed through a small incision.

There are number of published studies describing SMILE visual and refractive outcomes (Vestergaard *et al.*, 2012; Wang *et al.*, 2013; Kamiya *et al.*, 2014; Sekundo *et al.*, 2014; Agca *et al.*, 2014; Lin *et al.*, 2014). A systematic review and meta-analysis that compared (SMILE) with (FS-LASIK) for treating myopia concluded that both FS-LASIK and SMILE are safe, effective and predictable surgical options for treating myopia. However, they also found that dry eye symptoms and loss of corneal sensitivity may occur less frequently after SMILE than after FS-LASIK (Shen *et al.*, 2016). Nevertheless, limitations of SMILE have been identified. A literature analysis published by Seiler *et al.* noted that the visual rehabilitation after SMILE takes significantly longer (weeks) compared to LASIK (days). They added that the refractive success rate of SMILE is still not as good as that of LASIK (88% vs. 95% within $\pm$ 0.5 D) (Seiler *et al.*, 2017). The disadvantage of SMILE is that a rest refractive error it is said an enhancement is not possible with the FS laser. Thus for this procedure an excimer laser is needed.

Femtosecond lasers are also used in the treatment of keratoconus. The femtosecond laser is a near-infrared laser that works at a wavelength of 1053 nm. This laser is utilized to cut small precise channels in the cornea, for implantation of intrastromal corneal ring segments (ICRS). ICRS are thin curved pieces of plastic that are inserted into the cornea in order to provide biomechanical stability in keratoconus. Historically these channels were made with a handheld instrument, but this often resulted in the instrument inadvertently puncturing through the already thinned corneal stroma. The femtosecond laser is now used to cut precise channels prior to implantation of ICRS. The laser has an ultra-short-pulse duration (in the range of 10^{-15} s), allowing it to produce smaller shock waves which helps to minimize collateral damage (Kullman and Pineda, 2010; Mamalis, 2011). There are only a few studies comparing the effectiveness of femtosecond versus manual channel creation; however, published data suggest that femtosecond laser channel creation is safe with few complications. Coskunseven *et al.* (2011) conducted a retrospective chart review of 531 patients (850 eyes) who underwent ICRS using a femtosecond laser for channel creation. They noted that the overall complication rate was 5.7% (49 cases out of 850 eyes). The main complication was incomplete channel formation (2.7% cases).

Other

Lasers also play an important role in the treatment of glaucoma (**Table 1**) and include selective laser trabeculoplasty (SLT), argon laser trabeculoplasty (ALT) (both of which target the trabecular meshwork and are used in the treatment of open-angel glaucoma) and laser iridotomy, which targets the outer edge of the iris and is used to treat closed-angle glaucoma. Lasers are also used in cyclophotocoagulation (targeting the ciliary body) and for suture lysis.

Selective laser trabeculoplasty has largely replaced ALT, mainly due to its improved safety profile. The improved safety of SLT versus ALT is due to the former's very short pulse duration of three nanoseconds. This permits selective photothermolysis, i.e., the laser selectively targets cells of the trabecular meshwork. Unlike ALT, it does not cause coagulative damage to the trabecular meshwork and reduces collateral damage to surrounding tissues (Song, 2016).

Future Applications

There is a large variety of application developments and new technologies under development in ophthalmology. In this article we are highlighting some of the current developments that might affect the current standard of care for treating patients with vision disorders.

Photochemical– Corneal cross linking for refractive procedures

Encouragingly, CXL is also emerging as a treatment for pathologies other than corneal ectasia. As noted, CXL is being evaluated as a treatment for refractive errors. Known as photorefractive intrastromal corneal collagen cross-linking (PiXL™), the procedure uses riboflavin and a ultraviolet-A (UVA) 365 nm wavelength light source with programmable illumination pattern delivered by a proprietary device to cause differential corneal tissue "stiffening" to reshape the cornea. A key advantage of this approach is that, unlike tissue ablation/removal in current corneal refractive procedures, there is no removal of stromal tissue. Early study findings are encouraging.

Thus far, studies have focused on the use of PiXL as a treatment for low myopia. Feasibility study findings published in 2014 (Kanellopoulos, 2014) showed that application of 12 J/cm^2 applied transepithelially in a predetermined pattern led to an average improvement of 2.3 diopters (D) 1 week postoperative. Findings from a 6-month prospective study of 14 patients with myopia or myopic astigmatism undertaken by Matthias Elling, FEBO, showed statistically-significant improvement in UCVA at 1, 3 and 6 months postoperatively. A significant improvement in BCVA was also observed. Data also improvements in mean manifest sphere and manifest refractive spherical equivalent at all visits versus baseline (Elling *et al.*, 2017). Data presented at XXXIV Congress of the European Society of Cataract and Refractive Surgeons (ESCRS) from a 12-month study of 39 eyes, also undertaken by Matthias Elling showed significant improvements in UCVA and no loss of BCVA. In a 9-month study of eight patients, a mean myopia reduction of 0.75 D with no loss of BCVA was noted (Primary Care Optometry News, 2017).

Photochemical – Corneal cross linking for corneal infections

Collagen corneal cross-linking is also being investigated as a treatment of infectious keratitis. Known in this context as PACK-CXL (photo activated chromophore for infectious keratitis), the procedure may provide an alternative to standard antibiotic therapy in treating infectious corneal disorders (Tabibian *et al.*, 2015). The antimicrobial effect occurs due to the effect of UV light interacting with riboflavin. The resulting reactive oxygen species damage the pathogen cell walls; riboflavin may also interact with the nucleic acids of the pathogen, preventing replication.

Larger randomized prospective clinical trials are few for PACK-CXL thus far, but smaller case reports findings from small series prove promising. Makdoumi and colleagues reported a series of 16 patients with culture proven bacterial ulcers who all improved after being treated with CXL alone. All eyes achieved epithelial healing and less inflammation, although two patients required antibiotic therapy to completely resolve their infection (Makdoumi *et al.*, 2012). Said *et al.* (2014) compared PACK-CXL with standard anti-microbial therapy in 40 eyes of 40 patients with advanced infectious keratitis and coexisting corneal melting. Twenty-one patients underwent PACK-CXL and antimicrobial therapy while 19 patients received antimicrobial therapy only.

Table 1 Application of laser and light technologies according to tissue type/indication

Intended use	*Application*	*Tissue structure*	*Laser/light source*	*Wavelength*	*Interaction mechanism*
Treatment of corneal ectasia	Corneal cross linking	Cornea	UV-LED (continuous wave or pulsed)	365 nm	Photochemical
Corneal scars or other corneal disorders	Phototherapeutic keratectomy (PTK)	Cornea	ArF Excimer laser	193 nm	Photoablation
Treatment of refractive errors	Photorefractive keratectomy (PRK) and Laser assisted in-situ keratomileusis (LASIK)	Cornea	ArF Excimer laser	193 nm	Photoablation
	LASIK- Flaps and Small Incision Lenticule Extraction (SMILE)	Cornea	Femtosecond lasers (pulse duration 220–580 fs)	1043 nm	Photomechanical/ photodisruption
Treatment of glaucoma	Laser trabeculoplasty	Trabecular mesh work	2w-Nd: YAG Argon laser	532 nm 515 nm	Photothermal
	Laser iridotomy/laser peripheral iridoplasty	Iris	Nd:YAG (2w) Argon	532 nm 1064 nm 515 nm	Photothermal/ photomechanical
	Cyclophotocoagulation	Ciliary body	Nd:YAG Diode laser	1064 nm 810 nm	Photothermal
	Glaucoma laser suture lysis	Cutting a suture of trabecular ectomy scleral flap	2w-Nd:YAG Argon laser	532 nm 515 nm	Photothermal
Treatment of cataract	Femtosecond laser-assisted cataract surgery (FLACS)	Cataractous lens fragmentation and incisions for cataract surgery	Neodymium: glass (pulse duration 300 – 500 fs)	1053 nm	Photomechanical/ photodisruption
	Posterior Capsulotomy	Turbid posterior lens capsule after intra-ocular lens implantation	Nd:YAG (Q-switched)	1064 nm	Photomechanical/ photodisruption
Treatment retinal or choroidal pathology	Retinal ischemic processes (e.g., diabetes, retinopathy of prematurity)	Retina	2w-Nd: YAG Argon laser	532 nm 515 nm	Photothermal
	Retinal tears	Retina	2w-Nd: YAG Argon laser	532 nm 515 nm	Photothermal
	Focal macular laser therapy for focal macular oedema	Retina	2w-Nd: YAG Argon laser	532 nm 515 nm	Photothermal
	Photodynamic therapy for choroidal neovascularization	Choroid	Diode laser	690 nm	Photochemical
	Transpupillary thermotherapy (TTT)	Malignant choroidal melanoma	Diode laser	810 nm	Photothermal
Treatment of vitreous disorders	Vitreous strand in the anterior chamber, posterior vitreous detachment and vitreous floaters	Vitreous	Nd: YAG (Q-switched)	1064 nm	Photomechanical
Treatment of lid and orbit	Blepharoplasty	Upper and lower eye lid	CO_2 laser	10,600 nm	Photoablation

Although PACK-CXL did not shorten the time to corneal healing, the complication rate was 21% in the antimicrobial group, whereas there was no incidence of corneal perforation or recurrence of the infection in the PACK-CXL group.

Photothermal – Computer guided treatments

Studies of PRP in diabetic macular edema (DME) using conventional slit-lamp based laser application have shown low success rates in terms of either visual acuity gains or reductions in anti-VEGF use burden, likely due to inadequate accuracy and completeness associated with conventional laser therapy (ETDRS Study Group, 1985; Michael *et al.*, 2011; Mitchell *et al.*, 2011; Brown *et al.*, 2013). Consequently, technology has been developed to improve laser spot accuracy. Computer-guided technology for navigated laser photocoagulation offers significantly greater accuracy in laser spot application to areas of edema than traditional laser treatment. Study findings also show that navigated laser photocoagulation reduces the retreatment rate (as compared with conventional laser therapy) by almost half in patients with DME (Neubauer *et al.*, 2013). An additional development is subthreshold diode micropulse laser. This was developed with the treatment of DME in mind, but it may also be affective in the treatment of PDR.

Photomechanical – The SMILE procedure

As noted earlier, SMILE is indicated for myopia with clinically-insignificant astigmatism. However, trials are underway to evaluate SMILE in myopic patients with astigmatism and hyperopic patients. Use of 345 nm UV femtosecond laser pulses, which may have applications in SMILE, but also flap creation and ultrathin Descemet-stripping endothelial keratoplasty has also been tested in vivo by Hammer and colleagues (Hammer *et al.*, 2015). The Laser energy levels required by a ultraviolet femtosecond laser to disrupt corneal tissue are tenfold lower than those required by an infrared laser offering significant safety advantages. Additionally, light of shorter wavelength can be focused more precisely and may therefore allow more precise photodisruption of the corneal stroma. Clinical studies are needed to determine the safety and efficacy of 345 nm UV femtosecond laser.

Conclusion

Laser and light therapy continues to play a key role in the management of many ophthalmic disorders. Ongoing developments suggest that improvements may be made to existing treatments, and may even provide new ways of treating problems, for example, guided crosslinking in the treatment of myopia. Although, a greater body of evidence is needed to ascertain whether these new technologies will have a clinically-significant impact, it appears likely that lasers and light therapies will have a growing role in ophthalmology.

References

Abell, R.G., Darian-Smith, E., Kan, J.B., *et al.*, 2015. Femtosecond laser-assisted cataract surgery versus standard phacoemulsification cataract surgery: Outcomes and safety in more than 4000 cases at a single center. J Cataract Refract Surg. 41 (1), 47–52.

Agca, A., Demirok, A., Cankaya, K.I., *et al.*, 2014. Comparison of visual acuity and higher-order aberrations after femtosecond lenticule extraction and small-incision lenticule extraction. Cont Lens Anterior Eye 37 (4), 292–296.

American Academy of Ophthalmology, Panretinal photocoagulation. Available at: http://eyewiki.aao.org/Panretinal_Photocoagulation.

Balasubramanian, D., Du, X., Zigler, J.S., 1990. The reaction of singlet oxygen with proteins, with special reference to crystallins. Photochem Photobiol. 52, 761–768.

Bashir, Z.S., Ali, M.H., Anwar, A., Ayub, M.H., Butt, N.H., 2017. Femto-LASIK: The recent innovation in laser assisted refractive surgery. J Pak Med Assoc. 67 (4), 609–615.

Brown, D.M., Nguyen, Q.D., Marcus, D.M., *et al.* RIDE and RISE Research Group, 2013. Long-term outcomes of ranibizumab therapy for diabetic macular edema: The 36-month results from two phase III trials: Rise and RIDE. Ophthalmology 120 (10), 2013–2022.

Cairns, W.L., 1970. Products of riboflavin photodegradation, Iowa State University. Available at: http://lib.dr.iastate.edu/rtd/4214/.

Carr, D.O., 1960. Mechanism of riboflavin-catalyzed oxidations, Iowa State University. Available at: http://lib.dr.iastate.edu/rtd/2813/.

Choi, M., Kim, J., Kim, E.K., Seo, K.Y., Kim, T.I., 2017. Comparison of the conventional dresden protocol and accelerated protocol with higher ultraviolet intensity in corneal collagen cross-linking for keratoconus. Cornea 36 (5), 523–529.

Coskunseven, E., Kymionis, G.D., Tsiklis, N.S., *et al.*, 2011. Complications of intrastromal corneal ring segment implantation using a femtosecond laser for channel creation: A survey of 850 eyes with keratoconus. Acta Ophthalmol 89 (1), 54–57.

Cummings, A.B., McQuaid, R., Naughton, S., Brennan, E., Mrochen, M., 2016. Optimizing corneal cross-linking in the treatment of keratoconus: A comparison of outcomes after standard- and high-intensity protocols. Cornea 35 (6), 814–822.

Elling, M., Kersten-Gomez, I., Dick, H.B., 2017. Photorefractive intrastromal corneal cross-linking for the treatment of myopic refractive error: Six month interim findings of an ongoing 12-month prospective study. J Cataract Refract Surg 43 (6), 789–795.

Elman, M.J., Bressler, N.M., Qin, H., *et al.*, 2011. Expanded 2-year follow-up of Ranibizumab plus prompt or deferred laser or triamcinolone plus prompt laser for diabetic macular edema. Ophthalmology 118 (4), 609–614.

ETDRS Study Group, 1985. Photocoagulation for diabetic macular edema. Early Treatment Diabetic Retinopathy Study report number 1. Early Treatment Diabetic Retinopathy Study research group. Arch Ophthalmol. 103 (12), 1796–1806.

Greenstein, S.A., Hersh, P.A., 2013. Characteristics influencing outcomes of corneal collagen crosslinking for keratoconus and ectasia: Implications for patient selection. J Cataract Refract Surg. 39 (8), 1133–1140.

Hammer, C.M., Petsch, C., Klenke, J., *et al.*, 2015. Corneal tissue interactions of a new 345 nm ultraviolet femtosecond laser. J Cataract Refract Surg. 41 (6), 1279–1288.

Herekar, S., 2007. Fractionated cross-linking: Preliminary lab investigation. In: 3rd International Congress on Corneal Cross Linking, Zurich, Switzerland (accessed 08.12.07).

Kamiya, K., Shimizu, K., Igarashi, A., Kobashi, H., 2014. Visual and refractive outcomes of femtosecond lenticule extraction and small-incision lenticule extraction for myopia. Am J Ophthalmol 157 (128–134), e122.

Kanellopoulos, A.J., 2014. Novel myopic refractive correction with transepithelial very high-fluence collagen cross-linking applied in a customized pattern: Early clinical results of a feasibility study. Clin Ophthalmol (Auckland, NZ) 8, 697–702.
Kozak, I., Luttrull, J.K., 2015. Modern retinal laser therapy. Saudi Journal of Ophthalmology 29 (2), 137–146.
Kullman, G., Pineda 2nd, R., 2010. Alternative applications of the femtosecond laser in ophthalmology. Semin Ophthalmol 25, 256–264.
Li, J., Ji, P., Lin, X.L., 2015. Efficacy of corneal collagen cross-linking for treatment of keratoconus: A meta-analysis of randomized controlled trials. PLOS ONE 10 (5), e0127079. doi:10.1371/journal.pone.0127079.
Lichtman, J.W., Conchello, J.A., 2005. Fluorescence microscopy: Review. Nature Methods 2, 910–919.
Lin, F., Xu, Y., Yang, Y., 2014. Comparison of the visual results after SMILE and femtosecond laser-assisted LASIK for myopia. J Refract Surg 30, 248–254.
Makdoumi, K., Mortensen, J., Sorkhabi, O., Malmvall, B.E., Crafoord, S., 2012. UVA-riboflavin photochemical therapy of bacterial keratitis: A pilot study. Graefes Arch Clin Exp Ophthalmol. 250, 95–102.
Mamalis, M., 2011. Femtosecond laser: The future of cataract surgery? J Cataract Refract Surg 37, 1177–1178.
Manche, E.E., Carr, J.D., Haw, W.W., Hersh, P.S., 1998. Excimer laser refractive surgery. Western Journal of Medicine 169 (1), 30–38.
Meiri, Z., Keren, S., Rosenblatt, A., *et al*., 2016. Efficacy of corneal collagen cross-linking for the treatment of keratoconus: A systematic review and meta-analysis. Cornea 35 (3), 417–428.
Mitchell, P., Bandello, F., Schmidt-Erfurth, U., *et al*. RESTORE Study Group, 2011. The RESTORE study: Ranibizumab monotherapy or combined with laser versus laser monotherapy for diabetic macular edema. Ophthalmology 118 (4), 615–625.
Neubauer, A.S., Langer, J., Liegl, R., *et al*., 2013. Navigated macular laser decreases retreatment rate for diabetic macular edema: A comparison with conventional macular laser. Clin Ophthalmol. 7, 121–128.
Pajic, B.,Hafezi, F., 2011. Applanation-free femtosecond laser processing of the cornea. In: Pajic-Eggspuehler, B. (Ed.),Femtosecond Laser Techniques and Technology, OSA Publishing.
Palanker, D., 2014. Ophthalmic laser therapy: Mechanisms and applications. Available at: https://web.stanford.edu/~palanker/publications/Ophthalmic_Laser_Therapy.pdf.
Popovic, M., Campos-Möller, X., Schlenker, M.B., Ahmed, I.I., 2016. Efficacy and safety of femtosecond laser-assisted cataract surgery compared with manual cataract surgery: A meta-analysis of 14,567 eyes. Ophthalmology 123 (10), 2113–2126.
Primary Care Optometry News, 2017. Studies show promising results for PiXL procedure in low myopia.
Reinstein, D.Z., Archer, T.J., Gobbe, M., 2014. Small incision lenticule extraction (SMILE) history, fundamentals of a new refractive surgery technique and clinical outcomes. Eye and Vision 1, 3. doi:10.1186/s40662-014-0003-1.
Rich, H., Odlyha, M., Cheema, U., Mudera, V., Bozec, L., 2014. Effects of photochemical riboflavin-mediated crosslinks on the physical properties of collagen constructs and fibrils. Journal of Materials Science Materials in Medicine 25 (1), 11–21.
Royle, P., Mistry, H., Auguste, P., *et al*., 2015. Pan-retinal photocoagulation and other forms of laser treatment and drug therapies for non-proliferative diabetic retinopathy: Systematic review and economic evaluation. Southampton (UK): NIHR Journals Library. doi:10.3310/hta19510.
Sadoughi, M.M., Einollahi, B., Baradaran-Rafii, A., *et al*., 2016. Accelerated versus conventional corneal collagen cross-linking in patients with keratoconus: An intrapatient comparative study. Int Ophthalmol. doi:10.1007/s10792-016-0423-0.
Said, D.G., Elalfy, M.S., Gatzioufas, Z., *et al*., 2014. Collagen cross-linking with photoactivated riboflavin (PACK-CXL) for the treatment of advanced infectious keratitis with corneal melting. Ophthalmology 121 (7), 1377–1382.
Seiler, T., Koller, T., Wittwer, V.V., 2017. Limitations of SMILE (Small Incision Lenticule Extraction). Klin Monbl Augenheilkd 234 (1), 125–129.
Sekundo, W., Gertnere, J., Bertelmann, T., Solomatin, I., 2014. One-year refractive results, contrast sensitivity, high-order aberrations and complications after myopic small-incision lenticule extraction (ReLEx SMILE). Graefes Arch Clin Exp Ophthalmol. 252 (5), 837–843.
Shen, Z., Shi, K., Yu, Y., *et al*., 2016. Small incision lenticule extraction (SMILE) versus femtosecond laser-assisted in situ keratomileusis (FS-LASIK) for myopia: A systematic review and meta-analysis. (Virgili G, ed.) PLOS ONE 11 (7), e0158176. doi:10.1371/journal.pone.0158176.
Shortt, A.J., Allan, B.D., Evans, J.R., 2013. Laser-assisted in-situ keratomileusis (LASIK) versus photorefractive keratectomy (PRK) for myopia. Cochrane Database Syst Rev. 1), CD005135.
Silva, R.A., Blumenkranz, M.S., 2013. Prophylaxis for retinal detachments. American Academny of Ophthalmology. Available at: https://www.aao.org/munnerlyn-laser-surgery-center/prophylaxis-retinal-detachments.
Singh, I.P., 2014. How YAG Laser Vitreolysis can be Used in Practice for Treatment of Floaters. Ophthalmology Times.
Smith, E.C., 1963. The photochemical degradation of riboflavin, Iowa State University. Available at: http://lib.dr.iastate.edu/rtd/2947/.
Song, J., 2016. Complications of selective laser trabeculoplasty: A review. Clinical Ophthalmology (Auckland, NZ) 10, 137–143.
Spoerl, E., Huhle, M., Seiler, T., 1998. Induction of cross-links in corneal tissue. Exp Eye Res. 66 (1), 97–103.
Steinert, R.F., 2013. Nd:YAG laser posterior capsulotomy. Available at: https://www.aao.org/munnerlyn-laser-surgery-center/ndyag-laser-posterior-capsulotomy-3.
Tabibian, D., Richoz, O., Hafezi, F., 2015. PACK-CXL: Corneal cross-linking for treatment of infectious keratitis. Journal of Ophthalmic & Vision Research 10 (1), 77–80.
Tambe, D.S., Ivarsen, A., Hjortdal, J., 2015. Photorefractive keratectomy in keratoconus. Case Reports in Ophthalmology 6 (2), 260–268.
The Ultra Q Reflex. Ellex medical lasers. Available at: http://www.ellex.com/physicians/product-portfolio/laser-floater-removal/ultra-q-reflex/.
Vestergaard, A., Ivarsen, A.R., Asp, S., Hjortdal, J.O., 2012. Small-incision lenticule extraction for moderate to high myopia: predictability, safety, and patient satisfaction. J Cataract Refract Surg 38, 2003–2010.
Wang, Y., Bao, X.L., Tang, X., *et al*., 2013. Clinical study of femtosecond laser corneal small incision lenticule extraction for correction of myopia and myopic astigmatism. Zhonghua Yan Ke Za Zhi 49 (292–298), 19.
Wollensak, G., Spoerl, E., Seiler, T., 2003. Riboflavin/ultraviolet-a-induced collagen crosslinking for the treatment of keratoconus. Am J Ophthalmol. 135 (5), 620–627.
World Health Organization, 2013.What is refractive error?Available at: http://www.who.int/features/qa/45/en/.

Probing Ocular Mechanics With Light

Susana Marcos, Instituto de Optica, CSIC, Madrid, Spain
Giuliano Scarcelli, University of Maryland, College Park, MD, United States
Antoine Ramier and Seok H Yun, Massachusetts General Hospital, Boston, MA, United States

© 2018 Elsevier Ltd. All rights reserved.

Nomenclature

FEM Finite Element Model
OCT Optical Coherence Tomography
sOCT Spectral OCT
ssOCT Swept Source OCT
CXL Cross-Linking
UVX Riboflavin Ultraviolet Light CXL
RGX Rose Bengal Green Light CXL
IOP Intraocular Pressure
FP Fabry–Perot
VIPA Virtually Imaged Phased Array
DSEK Descemet's stripping endothelial keratoplasty
DALK Deep anterior lamellar keratoplasty
LASIK Laser-assisted in situ keratomileusis
OCE Optical coherence elastography
SNR Signal to noise ratio
ARF Acoustic radiation force
λ Wavelength of light in vacuum
ρ Density
ν Poisson's ratio
E Young's modulus
c_g Group velocity
$\Delta\phi$ Phase difference
ΔL Optical path length difference
Δu_z Geometric displacement (component along the optical axis z)
n Refractive index
$\sigma_{\Delta L}$ Sensitivity (noise floor) for the optical path length difference

Glossary

Acoustic radiation force Physical force exerted by acoustic waves.
Brillouin Scattering Inelastic light scattering phenomenon where incident light interacts with acoustic phonons within a material to produce scattered light with different color (wavelength or frequency).
Corneal Refractive Surgery Surgical reshaping of the cornea (generally using laser ablation or corneal lenticule extraction) to produce a refractive change to correct refractive errors.
Corneal Videokeratography Technique to measure anterior corneal surface topography, generally base on the projection of rings onto the cornea and analysis of the acquired image.
Cross-Linking Surgical treatment of keratoconus using a photosensitizer and a light irradiation to produce chemical bonds between collagen fiber and increase corneal stiffness.
Ectasia Posterior corneal bulging resulting from reduced corneal thining in corneal refractive surgery or disease.
Elastography Imaging modality that maps the elastic properties of tissues.
Etalon Transparent slab with two reflecting surfaces used to separate light components of different colors based on multi-pass interference.
Glaucoma Ocular disease in which damage is produced in the optic nerve head (generally due to increased Intraocular Pressure), resulting in nerve fiber loss and peripheral vision loss.
Gonioscopy lens Specialized lens used in ophthalmology placed on the surface of the cornea for visualizing the anterior segment angle.
Interference (of light) Physical phenomenon where two light waves are superposed and form a resultant wave of larger or smaller amplitude depending on the relative delay of the two.
Intrastromal Corneal Ring Segments Surgical treatment of keratoconus consisting on sections of ring segments (with triangular or hexagonal section) implanted in the corneal periphery through a manual or femto-second laser channel in order to flatten the cornea and increase surface regularity.
Keratoconus Ocular disease produced in which corneal weakening leads to corneal bulging and degraded optical quality and vision.
Modulus (of elasticity) Parameter that quantifies the resistance of a sample to be deformed.
Myopia Ocular condition in which distant objects are focused in front of the retina resulting in a blurred image.
Optical Coherence Tomography Low coherence interferometric imaging technique allowing high resolution tomographic images of the eye. Common modalities (Fourier domain) include spectral and swept source operation principles.
Presbyopia Age-related loss of accommodation capacity with age, associated to increased stiffness in the crystalline lens.
Rayleigh surface waves Elastic waves propagating at the surface of a solid, comprising both longitudinal and transverse components, solutions of the elastic wave equation for a semi-infinite medium.
Scheimpflug Imaging Eye anterior segment imaging modality in which a slit is projected onto the eye and cross-section images of the eye from the anterior cornea to the posterior cornea (or to the posterior lens) are collected. The

 doi:10.1016/B978-0-12-803581-8.09783-6

camera axis is tilted 45° with respect to the optical axis in order to increase the depth of focus. Geometrical and optical distortion needs to be corrected for proper quantification.

Spectrometer Instrument capable of splitting incident light in its sub-components of different color (wavelength or frequency).

Introduction

The cornea and crystalline lens of the eye are optical elements that project images of the outside world onto the retina. Although primarily regarded as lenses and investigated in terms of their optical performance, understanding the mechanical properties of the ocular elements is also crucial. The mechanical structure of the cornea determines its shape, which in turn determines its optical quality. A compromise of the corneal mechanical structure will therefore highly impact vision of the patient (Dupps and Wilson, 2006). On the other hand, the crystalline lens in the young eye has the capability of changing its shape to focus near and far objects, so called accommodation. Increased in the crystalline lens stiffness results in the loss of accommodation capacity (Weeber *et al.*, 2007), a condition called presbyopia, affecting 100% of the population beyond the age of 45. The quest for a treatment restoring crystalline lens elasticity, or alternatively, accommodating intraocular lens with the mechanical capacity to respond to an accommodative stimulus would be the ultimate solutions for presbyopia. The mechanical properties of another ocular tissue, the sclera, have also been linked with the development of myopia, which results from the excessive elongation of the eyeball. It has been acknowledged that understanding the matrix and cellular factors contributing to a weakened sclera in myopes may aid in the development of a clinically appropriate treatment for myopia (McBrien and Jobling, 2009). Finally, because pressure is a mechanical phenomenon, and because of elevated intraocular pressure (IOP) is a risk factor for glaucoma, the role of ocular biomechanics in understanding the development and progression of glaucomatous optics neuropathy has long been recognized. On the one hand, standard measurements of IOP are largely affected by corneal biomechanics (Liu and Roberts, 2005). On the other hand, the mechanical effects of IOP on the optical nerve head, and the contribution of the tissue mechanical properties to the susceptibility of IOP insult are key to understand individual differences in the mechanical, ischemic and cellular events occurring in glaucoma (Sigal and Grimm, 2012).

While the implication of ocular tissue mechanics in presbyopia, myopia and glaucoma is clear, the cornea has been a primary focus of attention to the investigation and clinical measurement of biomechanics. Knowledge of the corneal biomechanical properties is key in the understanding of the progression of certain corneal diseases (such as keratoconus) or the corneal response to treatments. Certain corneal treatments such as surgeries involving incisions (cataract, incisional refractive surgery) (Denoyer *et al.*, 2013) or intrastromal corneal ring segment implantation to treat keratoconus rely specifically on the mechanical response of the cornea (Ortiz *et al.*, 2012; Pérez-Merino *et al.*, 2013, 2014). Emerging treatments of keratoconus, such as corneal collagen cross-linking, aim at increasing corneal stiffness, therefore changing the corneal mechanical response.

Despite the agreement on the clinical need to monitor the mechanical properties of the cornea, most knowledge of the inherent constituent properties of the cornea comes from tests in vitro (uniaxial extensiometry, two-dimension flap extensiometry, or corneal or whole eye inflation) (Andreassen *et al.*, 1980; Wollensak *et al.*, 2003; Kling *et al.*, 2010, 2012; Boyce *et al.*, 2007; Elsheikh *et al.*, 2007; Kling and Marcos, 2013a,b,c). The reports of the corneal Young modulus in the literature span almost two orders of magnitude. The differences across studies likely arise from the differences across methods, the relative complexity of the corneal structure, and the differences in the experimental conditions across studies (Andreassen *et al.*, 1980; Wollensak *et al.*, 2003; Kling *et al.*, 2010, 2012; Boyce *et al.*, 2007; Elsheikh *et al.*, 2007; Kling and Marcos, 2013a,b,c). Some methods attempt to reproduce the geometry and the integrity of the cornea of an intact eye (i.e., whole eye inflation), however it is likely that the effect of hydration and post-mortem time in experiments ex vivo are an important source of variability in the measurements (Kling and Marcos, 2013a,b,c). Besides, there is a clinical need for in vivo evaluation of corneal biomechanical parameters, at the patient level, for diagnostics and monitoring of disease and treatment. The availability of a method to quantify the corneal biomechanical properties of a patient in the clinic will allow to identify the risk of post-LASIK ectasia in a refractive surgery candidate (Ambrosio *et al.*, 2011). A clinical tool will also aid in the diagnosis of keratoconus, which at present is solely based on topographic and geometrical evaluation of the patient's cornea. State-of-the-art treatment techniques for keratocous will also largely benefit for quantification of corneal biomechanics. The selection of the appropriate Intrastromal Ring Segment (ICRS) design in refractive or keratoconus treatment (Kling and Marcos, 2013a,b,c) can be guided by individual assessment of the corneal biomechanical response. On the other hand, quantitative biomechanical parameters will help to monitor the effect of collagen cross-linking (Bak-Nielsen *et al.*, 2013), a new treatment for keratoconus aiming at stiffening corneal tissue.

Requirements of in vivo measurements of corneal mechanics include non-invasiveness, rapid acquisition times, and the availability of data allowing direct reconstruction of the inherent mechanical properties of the cornea, in isolation from other factors. The use of optical imaging methods fulfills most of those requirements, and is ideal for in vivo assessment. Several approaches have been suggested to measure corneal biomechanical properties in vivo, either using optical, acoustic or magnetic imaging. These include: corneal videokeratography upon stepwise central indentation with a cantilever that measures corneal bending-resistance (Grabner *et al.*, 2005); ultrasonic and magnetic resonance techniques that use the shear wave propagation velocity to map corneal elasticity in vivo (Litwiller *et al.*, 2010); corneal optical coherence elastography producing a strain mapping based on speckle tracking (Muthupillai *et al.*, 1995; Ford *et al.*, 2006); air-puff corneal deformation imaging; phase-sensitive

Optical Coherence Tomography based on phase changes of successive corneal cross-sectional images (Chang *et al.*, 2002); and Brillouin microscopy providing a spatially resolved map of corneal Brillouin modulus, which is correlated to the local relative values of corneal elastic modulus, upon induction of quasi-static oscillations (GHz) in the tissue (Scarcelli *et al.*, 2007a,b). A drawback of several of these techniques is that they are slow (magnetic imaging), show a relatively low spatial resolution (ultrasonic/magnetic resonance imaging) or require contact of a probe with the patient's corneal surface and hence the use of anesthetics (physical applanation and ultrasound based techniques). The current article will address the three last based techniques, given the advantages of using light to capture mechanical information.

Besides, imaging techniques track corneal deformation, but quantification is needed to retrieve the inherent corneal biomechanical properties from the acquired images. Corneal tissue is a complex mechanical biomaterial, frequently described as a non-isotropic viscoelastic material. As in most soft-biological tissues, viscoelastic properties arise from the time-dependent nature of the biomechanical properties, are expected to be of major importance. For example, progressive deformation of the cornea (ectasia) occurring in keratoconus, and after some LASIK procedures, is a result of a viscoelastic phenomenon. Nevertheless, ex vivo techniques have primarily quantified the elastic properties (Young's modulus), which is in fact non-linear. Most in vivo techniques describe corneal deformation parameters, which are only partially dependent on the mechanical properties (other factors such as corneal thickness and IOP play a role in deformation). Besides, the corneal properties vary across corneal depth, which is directly addressed by the depth-resolved nature of Brillouin Microscopy.

The full power of light-based imaging techniques to quantify inherent mechanical properties is only achieved when those are combined with Finite Element Modeling (FEM). Assuming a certain material model and an accurate knowledge of the applied forces it is possible to retrieve the material variables through inverse optimization. Applied forces can be an air puff (which dynamically changes through a deformation event) or an acoustic stimulus. In Brillouin microscopy it is necessary to assume relationships between the Brillouin modulus and the modulus of elasticity and values for tissue density and index of refraction. Relationships between the shear modulus and the Brillouin modulus can also be validated with the aid of FEM analysis.

While these techniques have been primarily used to analyze the cornea, some of them are also suited to study mechanical properties of other tissues such as the crystalline lens (Brillouin microscopy) or the sclera (air puff deformation or OCT vibrography).

This article describes three optical imaging techniques to measure ocular biomechanics: (1) Air Puff Corneal Dynamic Imaging, using Scheimplug imaging or Ocular Coherence Tomography (OCT); (2) Phase-sensitive OCT Elastography (3) Brillouin Microscopy; also known as OCT Vibrography. Special emphasis will be made on applications in corneal tissue. Inherent corneal properties in human and animal models obtained from FEM analysis and Inverse Optimization using input data from imaging techniques will be presented.

Air Puff Corneal Dynamic Imaging

High-speed corneal imaging in combination with an air puff combines the advantages of non-invasiveness and high-speed acquisition suitable for measurements in vivo. This concept, using Scheimpflug imaging has been recently commercialized by Oculus (Corvis ST system by Oculus). Air puff OCT has been demonstrated by groups at Copernicus University (Torun, Poland) and at the Institute of Optics CSIC (Madrid, Spain). This system is FDA approved as a tonometer, but provides also quantitative analysis of corneal deformation parameters (but not inherent material properties). Previous attempts (Ocular Response Analyzer by Reichert) to use air-puff applanation measurements to derive corneal mechanical properties were limited by the collection of relatively indirect data.

Direct imaging of the temporal and spatial corneal deformation profile during the air-puff event allows quantitative analysis and, through the use of Finite-Element modeling, retrieval of corneal elasticity moduli. In addition, the selected time for deformation (in the order of miliseconds) allows quantification of viscoelastic properties (relative viscoelasticity modulus and relaxation time constant) in a regime of interest for characterization of the corneal mechanical response to disease and treatments.

Air Puff Scheimpflug Imaging

The Corvis instrument by Oculus operates under the principle of Scheimplfug imaging. In Scheimpflug imaging a slit is projected onto the eye. A tilt of the imaging plane with respect to the optical axis of the instrument allows for a large depth-of-focus. While this generates geometrical distortions, these can be corrected by software. In the Corvis, the Ultra High Speed Scheimpflug camera takes over 4300 frames per second to monitor corneal response to a metered collimated air puff with fixed profile that has symmetrical configuration and fixed maximal internal pump pressure of 25 kPa. The Scheimpflug camera has blue light LED (455 nm) and covers 8.5 mm horizontally of a single slit. Recording measurement time is 30 ms, which allows for acquiring 140 digital frames. Each image has 576 measuring points.

Air Puff OCT Imaging

Direct OCT measurements of the human corneal dynamics during an air-puff induced deformation were first presented in 2011 (Alonso-Caneiro *et al.*, 2011). The authors reported a novel apparatus that combined swept source OCT (ssOCT) system

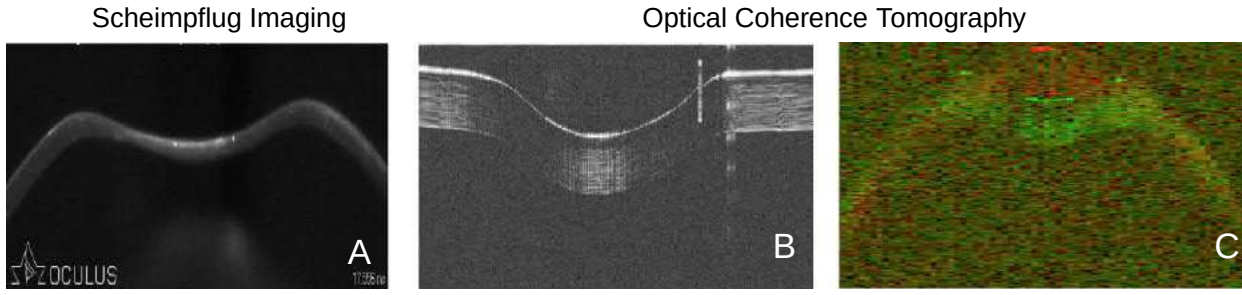


Fig. 1 Air-puff corneal deformation imaging (porcine eyes ex vivo). A. Spatial deformation from Scheimpflug-based imaging, Corvis ST by Oculus; B. Temporal deformation (A-scan of apex as a function of time) from air-puff ssOCT imaging (Nicolaus Copernicus University); C. Spatial deformation imaging (B-scan) from air-puff sOCT imaging (Instituto de Optica, CSIC). Merged undeformed cornea and maximally deformed cornea. Air-puff deformation event ≈20 ms in all cases. Images are from Alonso-Caneiro, D., Karnowski, K., Kaluzny, B.J., *et al.*, 2011. Assessment of corneal dynamics with high-speed swept source optical coherence tomography combined with an air puff system. Optics Express 19 (15), 14188–14199 and Dorronsoro, C., Pascual, D., Pérez-Merino, P., Kling, S., Marcos, S., 2012. Dynamic OCT measurement of corneal deformation by an air puff in normal and cross-linked corneas. Biomedical Optics Express 3 (3), 473–487.

(Karnowski *et al.*, 2011) with an air-puff chamber adapted from a commercial non-contact tonometer (**Fig. 1(A)**). A commercial prototype of swept source laser (AXSUN Technologies Inc., Billerica, MA) was used as a light source (50 kHz; 1300 nm; 110 nm optical bandwidth centered at 1300 nm, axial resolution of 9 μm in air; 0.9 mm imaging depth range; 102 dB; for 2.5 mW average optical power at the cornea). The module of an air-puff pressure chamber was extracted from a clinically approved tonometer (XPert NCT; Reichert Inc., Buffalo, NY) and was built into the imaging head of ssOCT system (**Fig. 1(B)**). A custom designed electrical circuit was used to power the air-puff chamber motor with high-voltage pulse. Additionally during the air-puff the induced corneal deformation reference pressure signal is obtained via pressure sensor originally built in the chamber.

Single A-scans are collected in time during the corneal deformation from the single/central point on the cornea where air stream is applied (*M*-scan). As a result the direct measurement of air induced deformation of the corneal surfaces and the anterior surface of the lens is presented. The corneal applanation/recovery time is approximately 20 ms.

The combination of an air-puff with a sOCT system was presented by Dorronsoro *et al.* (2012). In this configuration, a tilted mirror was used to couple a commercial non-contact tonometer (NT 2000, Nidek, Hiroishi, Japan) with a custom spectral domain OCT system (Alonso-Caneiro *et al.*, 2011). The tube of the tonometer providing the air puff passes through the center of the tilted mirror through a drilled hole. This configuration allows both instruments, the OCT system and the tonometer, point at the corneal apex in an almost normal orientation. This configuration allows dynamic imaging of corneal cross-sections during the air puff deformation event. The OCT imaging axis and the axis of air puff tube are perpendicularly oriented, and lying in a horizontal plane, with the tilted mirror located at the point of intersection between these two axes, at 45 (See **Fig. 1(C)**). In the vertical direction the mirror an additional tilt of 8° was imposed to avoid the horizontal scanning beam of the sOCT to overlay the mirror hole (tube tip) and therefore vignet the image. As in conventional non-contact corneal tonometry, the air puff impacts the cornea directly and produces a fast deformation event (<30 ms). The distance from the non-contact tonometer tube tip to the corneal apex was set to 11-mm. This distance is the identical configuration to that used in the standard use for corneal applanation tonometry of the instrument. The air puff configuration was manually set, in order to obtain the same standard air puff spatio-temporal profile in all measurements. The full air pressure provided by the instrument was used in the experiments, and delivery timing was electronically triggered, in synchronization with the image acquisition by the OCT.

Corneal Deformation Parameters

This Corvis processing software allows dynamic inspection of the actual deformation process during deformation. Advanced algorithms for edge detection of the corneal contours are applied for every frame. The recording starts with the cornea at the natural convex shape. The air puff forces the cornea inwards (ingoing phase) through applanation (first or ingoing applanation) into a concavity phase until it achieves the highest concavity. There is an oscillation period before the outgoing or returning phase. The cornea undergoes a second applanation before achieving its natural shape when there is a possible oscillation. The Corvis ST commercial system identifies the timing and corresponding pressure of the air puff at the first and second applanations and at the moments of highest concavity in the spatial deformation images. Intraocular pressure (IOP) is calculated based on the timing of the first applanation event. This initial IOP measurement is dependent of corneal resistance. The deformation amplitude is determined as the highest displacement of the apex in the highest concavity moment image. Other measured parameters are: the radius of curvature at highest concavity; applanation lengths and corneal velocities during ingoing and outgoing phases (**Fig. 2**).

Quantitative parameters can also be extracted from the captured set of OCT images, using custom routines (Dorronsoro *et al.*, 2012). These routines involve corneal edge detection algorithms and numerical computations of temporal and spatial deformation parameters (deformation amplitude, speeds and durations of deformation) to extract the parameters, the stable non-deformed cornea immediately before the deformation event is compared with the deformed cornea during the air puff event. A subset of used descriptive parameters are graphically illustrated in **Fig. 3**: *corneal thickness* (1, red) at the corneal apex before and

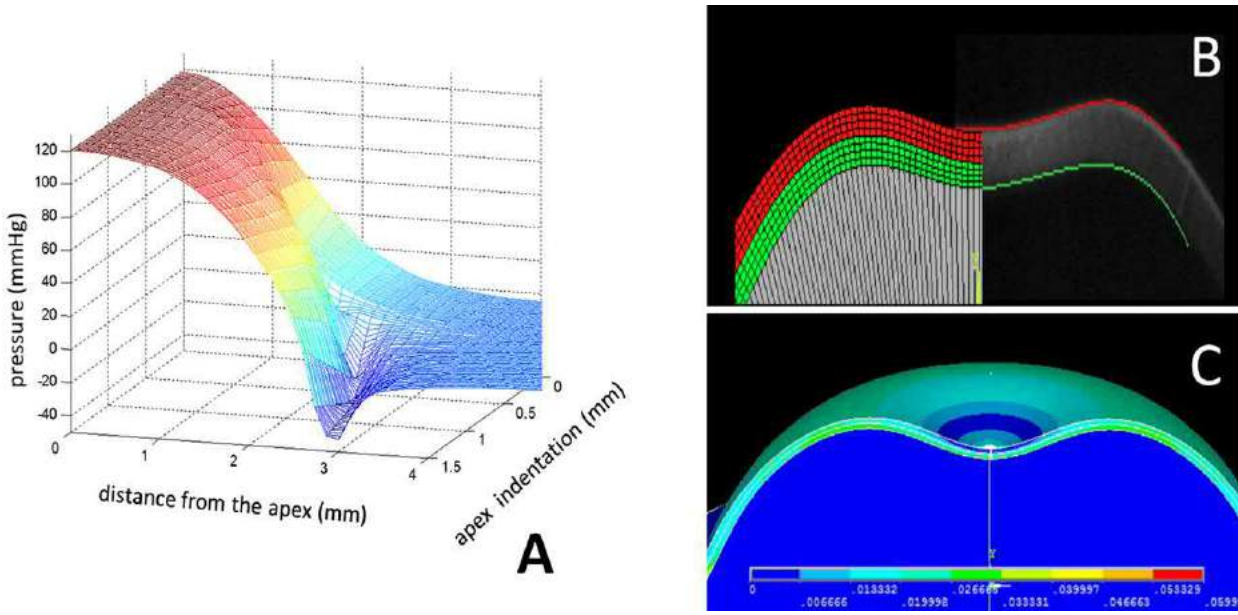


Fig. 2 A. Air-puff spatio-temporal profile (from pressure measurements and hydrodynamics calculations); B. Cornea at maximum air-puff spatial deformation: Experimental and Fine-Element model in inverse optimization. C. Simulated corneal deformation with retrieved biomechanical parameters. Data are from Kling, S., Bekesi, N., Dorronsoro, C., *et al.*, 2014. Corneal viscoelastic properties from finite-element analysis of in vivo air-puff deformation. PLOS ONE 9 (8), e104904.

after the deformation, and during maximum deformation; *deformation amplitude* (4, red) at the corneal apex (representing the maximum deformation depth); *overall deformation period* (9); *increasing deformation period* (7); *decreasing deformation period* (8); *mean increasing and decreasing deformation speeds* (2 and 6, black); *peak increasing and decreasing deformation speeds* (3 and 5, orange) (maximum positive and negative slopes of the deformation curve, represented as orange lines).

The parameters above were obtained from high-speed A-scan measurements at the corneal apex, a measurement mode available in both described approaches. Additional information can be extracted from the dynamic B-scan measurements (along the horizontal meridian; **Fig. 3**), providing a direct view of the dynamic spatial deformation of the cornea. Analysis of the B-scans during the deformation event could theoretically provide similar results on the apex dynamics than the A-scan measurements. However, the temporal sampling in those measurements is lower resulting in a lower precision of the extracted temporal parameters. The B-scans were also used to obtain additional deformation parameters at maximum deformation: *diameter of the deformed zone* (10, green), *displaced corneal volume* at the moment of peak deformation (11, gray), *non-deformed corneal radius* (12) and *peak deformed corneal radius* (13).

Corneal Mechanical Properties From Air Puff Corneal Dynamic Imaging

Although the air puff corneal deformation can be characterized using several temporal and spatial deformation parameters deformation is affected not only by mechanical properties, but also by geometrical parameters (corneal thickness and, to a lesser extent, corneal curvature) as well as Intraocular Pressure (IOP) (Kling and Marcos, 2013a,b,c). Finite-Element-Models (FEM) have been recently been applied to reconstruct the inherent mechanical parameters of corneal tissue from Scheimpflug-based temporal and spatial deformation imaging, and on measurements of the temporal and spatial properties of the air-puff (**Fig. 1**) (Marcos *et al.*, 2014). To simulate the experimental conditions accordingly, the pressure characteristics provided by the air-puff system were determined. The temporal pressure profile was measured experimentally using a pressure sensor and then a computational fluid dynamics simulation was performed to determine the spatial pressure profile, and its change during the deformation event. The corneal tissue was modeled as a linear viscoelastic material, in 2-D. Inverse modeling, with a multi-step optimization procedure, was performed in order to find the biomechanical parameter set that best represented the different experimental conditions. Retrieved parameters include the modulus of elasticity, viscoelastic relative modulus and relaxation constant, and represent the suitable descriptive parameters to monitor corneal biomechanical properties and to predict the mechanical response to modeling.

The reconstruction of the inherent material properties from air-puff corneal deformation has been validated using phantom corneas of different hydrogel polymer materials and thicknesses and on porcine corneas, at a constant IOP of 15 mmHg (Bekesi *et al.*, 2016a,b). Uniaxial tensile tests were performed on the model cornea materials as well as on corneal strips, and the results were compared to stress-strain simulations assuming the reconstructed material parameters. The simulated stress-strain curves of the studied hydrogel corneal materials fitted well the experimental stress-strain curves from uniaxial extensiometry. Equivalent Young´s moduli of the reconstructed material properties from air-puff were 0.31, 0.58 and 0.48 MPa for the three polymer materials respectively which differed $<1\%$ from those obtained from extensiometry. The simulations of the same material but

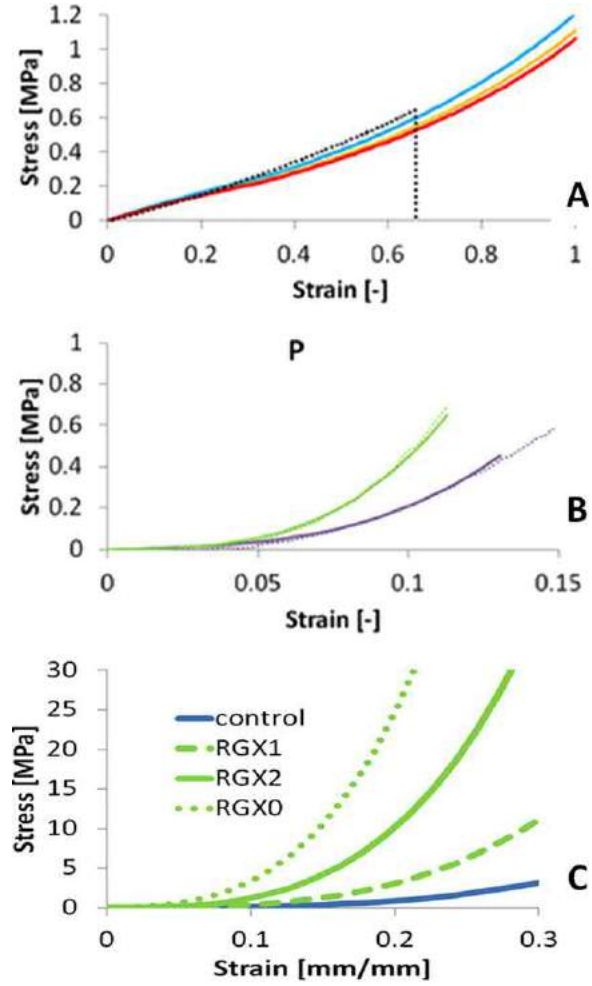


Fig. 3 Stress-strain curves in phantom, porcine corneas and rabbit corneas. A. Obtained from extensiometry on polymer strips (dotted line) and from air-puff corneal deformation imaging and inverse optimization. Red, Yellow and Red lines correspond to phantom corneas (mounted in an artificial eye) of the same material but different thicknesses B. Obtained from extensiometry on corneal strips, and from air-puff corneal deformation imaging and inverse optimization. Green and Purple correspond to two different corneas. C. Obtained from air-puff corneal deformation imaging and inverse optimization in untreated rabbit corneas, rabbit corneas 1-month and 2-month following cross-linking treatment (RGX, Rose Bengal Cross Linking) in vivo, rabbit corneas following cross-linking ex vivo (measurements immediately after enucleation and treatment). Data are from Bekesi, N., Kochevar, I.E., Marcos, S., *et al.*, 2016a. Corneal biomechanical response following collagen cross-linking with rose bengal–green light and riboflavin-UVA. Investigative Ophthalmology & Visual Science 57, 992–1001; Bekesi, N., Dorronsoro, C., de la Hoz, A., Marcos, S., 2016b. Material properties from air puff corneal deformation by numerical simulations on model corneas. PLOS ONE 11 (10), e0165669 and Bekesi, N., *et al.*, 2017. Biomechanical changes after in vivo collagen cross-linking with rose bengal–green light and riboflavin-UVA. Investigative Ophthalmology & Visual Science 58, 1612–1620.

different thickness resulted in similar reconstructed material properties. The air-puff reconstructed average equivalent Young´s modulus of the porcine corneas was 1.3 MPa, within 18% of that obtained from extensiometry.

Clinical and Experimental Applications of Air Puff Deformation Imaging: Cross-Linking

Corneal cross-linking (CXL) is an emerging treatment to halt the progression of ectatic disorders by crosslinking collagen fibrils and glycoproteins in the corneal stroma. Reconstruction of corneal mechanical parameters from air puff corneal deformation has been applied to the characterization of different modalities of CXL (Riboflavin UVA UVX and Rose Bengal Green light RGX) on rabbit eyes ex vivo and in vivo (under constant IOP) (Bekesi *et al.*, 2016b, 2017) as well as in a human eye in vivo (Kling *et al.*, 2014).

Corneal deformation amplitude decreased significantly after both CXL methods. The material parameters obtained from inverse modeling were consistent with corneal stiffening after both RGX and UVX. Within the treated corneal volume, the elasticity was found to decrease by a factor of 11 after RGX and by a factor of 6.25 after UVX following treatments ex vivo. Conversely, elasticity increased by factors of 3.4 (RGX) and 1.7 (UVX) 1 month and by factors of 10.7 (RGX) and 7.3 (UVX)

2 months after treatment in vivo. The equivalent modulus of elasticity of rabbits eye ranged from 1.43 MPa (untreated eyes) and 15 MPa (2-month post RGX, treated area). The estimated equivalent modulus of elasticity in a human eye was 0.45 MPa. Other estimates include viscoelastic properties, such as relative modulus and time relaxation constants. The viscoelastic effect was evidenced by the remaining deformation (between 18.7% and 24.1% of the overall deformation at different IOPs), which gradually decreased with time after the air-puff event. The viscoelasticity of the cross-linked porcine corneas ex vivo was described by a relative modulus of 0.7 and a relaxation time constant of 1.5 ms, and contributed with 46% to the maximal apex indentation.

Phase-Sensitive Optical Coherence Elastography

Principles and Implementations of Optical Coherence Elastography

The interferometric nature of OCT allows phase measurement for the detection of tissue deformation at micro- and nano-scales in amplitude and from static to ultrasound frequencies in the time scale. This capability has been harnessed for elastography, also known as optical coherence elastography (OCE), by employing appropriate mechanical stimuli. In the previous section, we have described an air-puff stimulus designed to induce macroscopic corneal deformation. Stimulus with reduced amplitudes can induce microscopic corneal deformation, which can be readily measured by phase-sensitive OCT. Compared to macroscopic air-puff, microscopic perturbation involves proportionally smaller strain changes in the tissue and less IOP changes. The smaller perturbations avoid the need of nonlinear mechanical analysis and minimize secondary effects, such as corneal tension and scleral expansion, induced by the IOP change. In this section, we describe a variety of elastography techniques based on phase measurement in OCT.

Early OCE studies used intensity-based measurement to track displacement of structures under an applied load. Intensity-based OCE has been applied for ophthalmic applications (Ford *et al.*, 2006, 2011, 2014; Torricelli *et al.*, 2014; Armstrong *et al.*, 2013), in which displacement vector is calculated from cross-correlation between initial and mechanically perturbed images. However, nowadays phase-sensitive detection has become a far more popular choice for OCE because it provides better displacement sensitivity compared to the intensity-based method.

In Fourier domain OCT, the phase of each image pixel is readily measured from the Fourier transform of the measured interferometric signal. The phase change $\Delta\phi$ can be directly related to the change in optical path length delay ΔL by a simple relationship: $\Delta\phi(z,t) = \frac{4\pi}{\lambda}\Delta L(z,t)$. Converting the optical delay to a true geometrical displacement requires knowledge of or assumptions about the refractive index distribution $n(z)$. It is also important to take into account the discontinuity of the refractive index at the corneal surface (Song *et al.*, 2013). The cornea is generally simplified as a two-layer structure consisting of a coupling medium of index n_0 (often the air) and a tissue layer of index n_1. Then, the geometrical displacement is calculated from the phase profile within the tissue with respect to the phase at the corneal surface $\Delta\phi_0$ (Wang and Larin, 2014):

$$\Delta u_z(z,t) = \frac{\lambda}{4\pi n_1}\left(\Delta\phi(z,t) + \Delta\phi_0(t)\frac{n_1 - n_0}{n_0}\right)$$

The amplitude sensitivity, $\sigma_{\Delta L}$, of shot-noise-limited, phase-sensitive measurement is given by the signal-to-noise ratio (SNR) via $\sigma_{\Delta L} = \frac{\lambda}{4\pi}\frac{1}{\sqrt{SNR}}$. For example, for regions with SNR of 40 dB in OCT images, a displacement sensitivity better than a thousandth of the optical wavelength (i.e., sub-nanometer) is achieved.

Other noise sources, such as mechanical vibrations of optical components in an OCT system can increase the phase noise above the fundamental SNR limit. Some of the noise may be reduced by common-path interferometer designs (Choma *et al.*, 2005). Wavelength swept lasers in swept-source OCT tend to introduce additional noise to due phase jitter between wavelength sweep cycles and a data acquisition clock. A calibration mirror (Vakoc *et al.*, 2005) and real-time interferometeric clock generation (Braaf *et al.*, 2011) have been developed to mitigate the swept laser-induced noise. Phase-sensitive detection can only measure the axial component of the displacement parallel to the axis of an OCT beam, and phase measurement may present phase-wrapping errors when the displacement amplitude is greater than the optical wavelength. Techniques to get around these problems have also been put forward.

Depending on the type of mechanical perturbations the applied stimuli induce on the cornea, we may sort elastography techniques in three categories: static, standing waves (i.e., vibrational resonance), and traveling (acoustic) waves, which are illustrated in **Fig. 4**. All approaches share common steps in operation. First, a mechanical force is applied to the tissue to induce deformation. Second, OCT is used to measure the deformation. And, finally a biomechanical model is applied to relate the observed deformation to tissue stiffness.

Static OCE was the first proposed approach for general OCE (Schmitt, 1998) and for ophthalmic applications (Ford *et al.*, 2006). It is based on the simple concept that softer areas deform more than stiffer areas. The well-known static mechanics is applied to derive tissue elasticity from measured strain for given external stress. Typically, the external stress is applied by compressing the tissue with a contact device, such as an objective lens or a transparent plate. Although this simple mechanical method is widely used for general measurements of ex vivo tissue samples, it is not as commonly used for applications to the eye because a noncontact approach is preferred for clinical diagnosis in patients. Nonetheless, several studies using ex vivo rabbit and human eyes showed the proof of concept by using a gonioscopy lens to compress the cornea (Ford *et al.*, 2011, 2014). Another

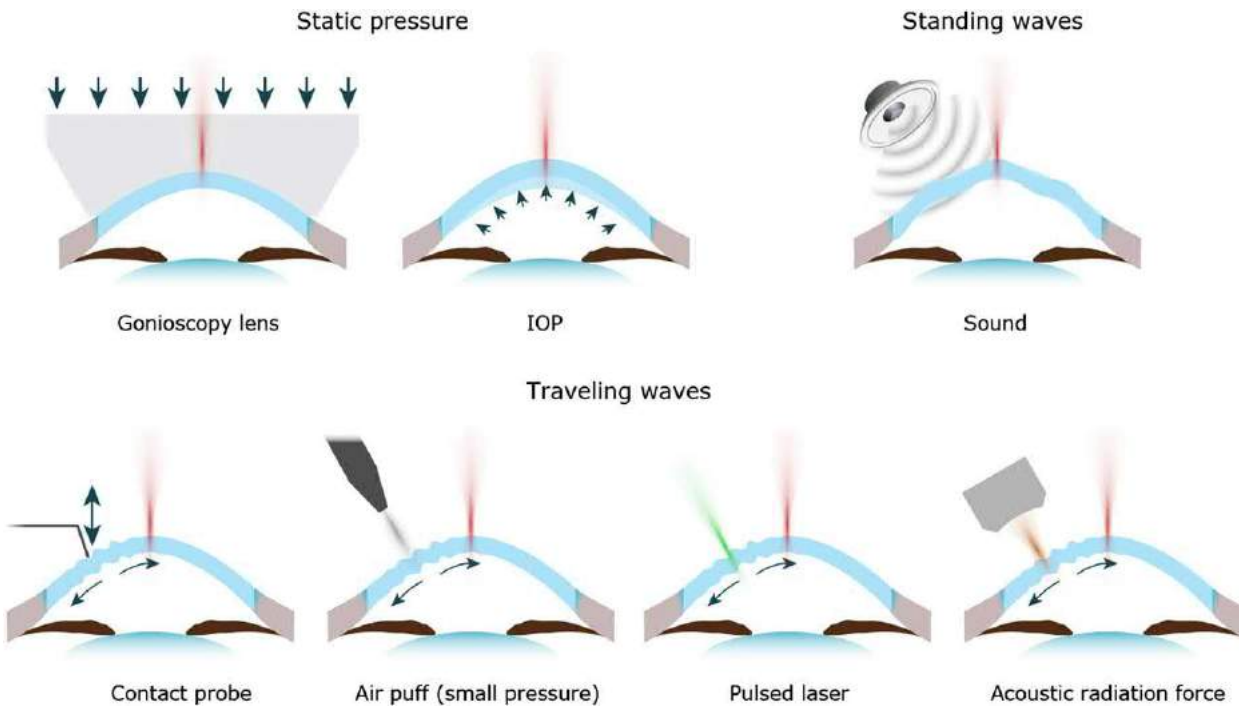


Fig. 4 OCT elastography techniques. Various mechanical loading methods have been employed to induce different types of perturbations ranging from static deformation and vibrational resonance to propagating acoustic waves.

variant of static OCE is to externally modulate IOP as a loading mechanism for cornea elastography. Proof-of-concept experiments were performed on ex vivo corneal explants (Ford *et al.*, 2006, 2016). Although this invasive technique is unlikely to be applicable in clinical settings, it could be useful for ex vivo measurements and animal studies.

Traveling wave OCE has been extensively used for ocular elastography. The basic principle of operation was adapted from shear wave elastography in ultrasound imaging. It uses a localized energy source to excite mechanical acoustic waves, which then propagate in the tissue. The wave parameters, such as the amplitude, velocity, and decay rate, are extracted from OCT measurements and related to the mechanical properties of the tissue. Various non-contact approaches are available to excite the traveling waves in the eye. As a direct analogue of ultrasound shear wave elastography, amplitude-modulated ultrasound was used to excite shear waves via acoustic radiation force (ARF), which are then detected by phase-sensitive OCT (Nguyen *et al.*, 2015). Intense pulsed laser light can excite acoustic waves via the photo-acoustic effect (Li *et al.*, 2012). However, both of these techniques require high ultrasound and optical energy to generate measurable acoustic amplitudes, raising safety concern to the eye. Some techniques to mitigate this issue have been proposed, such as numerical ultrasound pulse compression (Nguyen *et al.*, 2015) and surface reflection-induced ARF (Ambroziński *et al.*, 2016).

As described in the previous section, large-amplitude air puffs can induce millimeter-scale deformations in the cornea but such large deformations involve the non-linear response of collagen fibrils in the corneal stroma and thus add complexity to the mechanical analysis. Air puffs with a significantly lowered amplitude and shorter duration have been introduced to OCE as a way to excite traveling acoustic waves in the cornea (Wang *et al.*, 2013) and have extensively been investigated.

An advantage of traveling-wave OCE is that analytical relationships between Young's modulus and the acoustic wave velocity can be established. A few expressions have been derived, which are valid under different circumstances depending on the frequency and location of the excitation force. Vibrations generated at the surface of the cornea were often modeled as Rayleigh surface waves (Li *et al.*, 2012; Wang *et al.*, 2013), and Young's modulus E is obtained from the wave group velocity c_g, using $E = \frac{2\rho(1+(v))^3}{(0.87+1.12(v))^2} c_g^2$. This formula is accurate only in a high-frequency limit in which the acoustic wavelength is much smaller than the corneal thickness. In more general cases, the impact of the thickness and curvature of the cornea, as well as the aqueous humor, have been investigated in detail (Han *et al.*, 2015b,c; Aglyamov *et al.*, 2015). A modified Rayleigh–Lamb wave model that accounts for the layered structure and viscosity of the cornea has been developed (Han *et al.*, 2015a, 2017).

Standing wave OCE is based on modal analysis, with the rationale that for a given structure geometry, a stiffer material will cause a higher resonance frequency. A frequency-domain method using sound wave stimulus has been proposed, in which the vibrational modes of the cornea or the whole eye globe are analyzed by sweeping the acoustic frequency. The eye has a fundamental resonance frequency of about 100 Hz (Akca *et al.*, 2015). As in the case of the air-puff methods, to extract elastic modulus numerical simulations would be necessary, which takes into account the entire eye globe as well as the cornea.

Applications of Optical Coherence Elastography in Ocular Tissues

Corneal biomechanics has been the major application area of OCE. This is in part because cornea is readily accessible for the induction of a mechanical stimulus but more due to the fact that the mechanical properties of the cornea are involved in number of pathological processes and are considered an important factor to consider in refractive surgeries and some vision treatments. The first demonstrations of cornea OCE were performed in the mid-2000s (Ford *et al.*, 2006; De La Torre-Ibarra *et al.*, 2006). But the interest for ophthalmic OCE increased considerably in the early 2010s with the progress of phase-sensitive OCE (Li *et al.*, 2012; Manapuram *et al.*, 2012; Ford *et al.*, 2011).

OCE can measure the biomechanical changes induced by CXL (Ford *et al.*, 2014; Singh *et al.*, 2016). In particular, OCE has been used to quantify the effects of standard epithelium-off CXL procedures for various transepithelial crosslinking reagents and femtosecond laser-assisted riboflavin-UVA CXL (Armstrong *et al.*, 2013). A follow-up study (Torricelli *et al.*, 2014) showed that benzalkonium chloride-ethylenediaminetetraacetic acid (BKC-EDTA) induced a larger stiffening effect than the standard epithelium-off riboflavin-UVA procedure. More recently, stiffness mapping of customized CXL treated corneas has been demonstrated (Singh *et al.*, 2017).

The age dependence of corneal stiffness was examined by using an oscillating tip as the source of mechanical waves on live mice (Manapuram *et al.*, 2012). The observed age-related increase in corneal stiffness with age was in agreement with previous measurements done by conventional mechanical measurements (Cartwright *et al.*, 2011; Elsheikh *et al.*, 2007). The relaxation rate after a mechanical stimulus was also shown to increase with age (Li *et al.*, 2014).

Besides the cornea, phase-sensitive OCE has been used to characterize the mechanical properties of the posterior sclera in ex vivo porcine eyes (Singh *et al.*, 2017) and measure the mechanical properties of crystalline lens in rabbit eyes (Wu *et al.*, 2015). Similarly, retinal OCE was performed on ex vivo porcine eyeballs (Song *et al.*, 2015).

Brillouin Microscopy

Brillouin Microscopy Technique

Brillouin microscopy takes advantage of a light scattering phenomenon first described by Brillouin (1922). When incident light hits a sample, it interacts with microscopic sound waves (acoustic phonons) within the material so that the scattered light has a slightly different frequency than the incidence light. Such acoustic phonons are inherently present in any material and are specific to the mechanical properties of the material. As such, the Brillouin frequency shift between incident and scattered light, can provide local mechanical information of the sample (**Fig. 5**). The Brillouin frequency shift is described by the equation:

$$(v)_B = \pm \frac{2n}{\lambda_P}\sqrt{\frac{M'}{\rho}}\cos\left(\frac{\theta}{2}\right) \tag{1}$$

In Eq. (1), n is the refractive index of the sampled material, M′ is the real part of the longitudinal elastic modulus of the material, ρ is the density of the material and θ is the angle between incident and scattered optical radiation; importantly.

Because the light scattering is driven by acoustic waves, the changes in wavelength between incident and scattered light are in the 1–10 picometer wavelength range, or GHz frequency range. This is more than 1000 times smaller than changes observed with Raman scattering or fluorescence. Thus, to detect Brillouin signals, ordinary spectrometers cannot be used as they lack the spectral resolution to resolve Brillouin signal from input laser light and the spectral extinction to detect Brillouin scattered light in the presence of strong light with similar wavelength. A solution to this problem was first developed by JR Sandercock who developed a spectrometer using multiple-pass scanning Fabry–Perot (FP) interferometers (Sandercock, 1975). Sandercock's spectrometer has been used since the 1970s enabling noncontact mechanical analysis of materials in a variety of fields (Dil, 1982) including the first

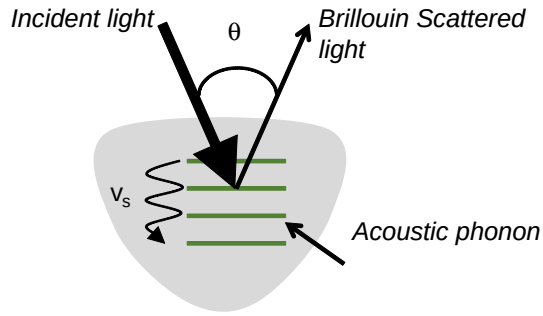


Fig. 5 Brillouin Principle: When incident light hits a sample, it interacts with microscopic sound waves (acoustic phonons) within the material so that the scattered light has a slightly different frequency than the incidence light. Such acoustic phonons are inherently present in any material and are specific to the mechanical properties of the material.

characterization of ocular tissue (Vaughan and Randall, 1980). However, FP spectrometers are characterized by slow acquisition times (~10 min to hours per spectrum), therefore their applications to biomedical sciences is difficult.

In 2008, the introduction of virtually-imaged phased array (VIPA) etalons (Shirasaki, 1996) in lieu of FP interferometers greatly improved acquisition time (Scarcelli *et al.*, 2008). The VIPA etalon is similar to a FP etalon with few key differences: (1) the etalon is tilted and input light is diverging so that different incidence angle find different resonances; this enables to collect all the spectrum in one shot (Koski *et al.*, 2002); (2) the first surface of a VIPA is totally reflective and only allows light to enter the interferometer through a narrow anti-reflection-coated window; this prevents the formation of a reflected interference pattern which translates in about two-order of magnitude higher throughput. VIPA-based Brillouin spectrometers have been further improved in recent years thus enabling the transition from single-point Brillouin spectroscopy to an imaging modality through the combination with confocal microscopes (Scarcelli *et al.*, 2007a,b, 2008, 2011). This configuration has now been used for several years to measure tissue, cells and sub-cellular structures (Scarcelli *et al.*, 2015a; Scarcelli and Yun, 2012; Zhang *et al.* 2017a,b).

Brillouin modulus and relationship with standard mechanical properties

From a mechanical standpoint, Brillouin spectroscopy probes the response of a sample to a one-dimensional oscillatory strain of hypersonic (~GHz) frequency. The measured frequency shift is related to the longitudinal modulus of material, as shown in Eq. (1). However, in Eq. (1) both index of refraction and density of material are not constant within a sample and from sample to sample therefore the extraction of Brillouin longitudinal modulus needs to be carefully examined. In biological material such as cells and tissues, density and refractive index are strongly correlated; for ocular tissues approximating density and index to constant values yields only a small percentage error. Therefore, local, three-dimensional, direct measurement of the longitudinal elastic modulus of material can be obtained by measuring the Brillouin spectrum. In crystalline materials, the longitudinal modulus (M') is related to traditional Young's modulus (E') in a straightforward manner through the Poisson's ratio (σ) via $M' = E'(1-\sigma)/(1+\sigma)(1-2\sigma)$. However, in biological material the fundamental relationship to Young's or shear moduli is not yet established because of the large difference in frequency of the test (quasi-static vs GHz) which is relevant due to the frequency-dependent moduli of most biomaterials (Mofrad and Kamm, 2006) and because of the near incompressibility of biological tissue due to the high water content.

For both cornea and lens tissue, an empirical correlation between Brillouin modulus and traditional Young's or shear modulus has been established experimentally. Such correlation has been found to be linear in log-log scale (Scarcelli *et al.*, 2011), which suggests a power-law relationship, consistent with what was previously found in tissue, polymers and cells (Deng *et al.*, 2006; Fabry *et al.*, 2001; Gittes and MacKintosh, 1998; Jonas *et al.*, 2008; Duck, 1990; Holm and Sinkus, 2010).

This offers the possibility of quantitatively measure cornea and lens mechanical properties after proper calibration. Specifically, for a given material we can write: $\log(M') = a\log(E') + b$, where the coefficients a and b are intrinsic properties of material that have a fundamental basis on atomic and molecular interactions. We can also write $\frac{\Delta M'}{M'} = a\frac{\Delta E'}{E'}$ where $\Delta M'$, $\Delta E'$ are respective derivatives or variations. This allows to estimate the sensitivity of the instrument to actual variations in Young's modulus. Current Brillouin instruments reach frequency sensitivity of ± 1 MHz/$\sqrt{\text{Hz}}$, which corresponds to a relative error in longitudinal moduli, $\Delta M'/M' \approx +/-0.3\%$ for an integration time of 0.1 s. Using for example $a = 0.03$ measured with porcine corneal tissues, we determine that the Brillouin measurement can detect a difference in Young's modulus, $\Delta E'/E'$ of about 9% at an integration time of 0.1 s.

Applications of Brillouin Microscopy in the Cornea

Recent Brillouin measurements for the analysis of keratoconus, corneal collagen crosslinking and refractive surgery are promising (**Fig. 6**) (Scarcelli *et al.*, 2014, 2015b). For keratoconus, both ex vivo and in vivo human experiments were performed. For ex vivo

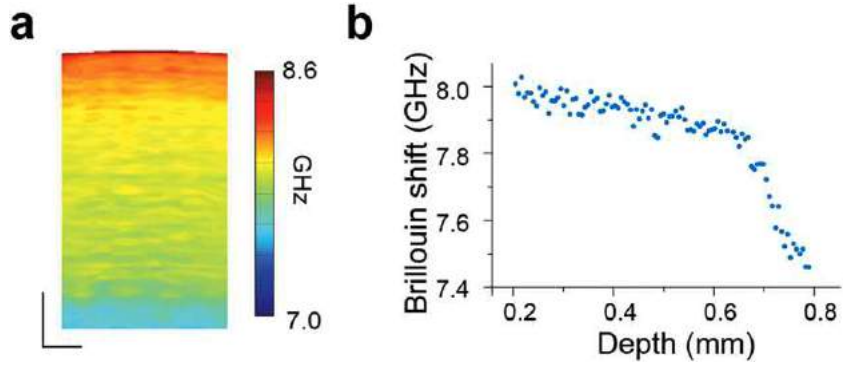


Fig. 6 Cornea Applications: (a) Representative Brillouin cross-section of a bovine cornea ex vivo reveals depth-dependence of Brillouin shift. Scale Bar 200 μm. (b) Representative depth profile of a bovine cornea ex vivo. A high correlation in depth is observed between regions of higher Brillouin shift and regions with higher content and more branching of corneal collagen.

analysis, normal tissue samples were obtained from donor corneas used in Descemet's stripping endothelial keratoplasty (DSEK); keratoconic tissue samples were obtained from deep anterior lamellar keratoplasty (DALK) procedure in advanced keratoconus patients. For the in vivo study, patients with advanced keratoconus were measured just before undergoing DALK surgery and compared to healthy volunteers. Ex vivo and in vivo analysis are consistent with each other: keratoconic corneas had overall lower Brillouin shift, thus lower elastic modulus. Thanks to Brillouin spatial resolution, we performed a spatially resolved analysis: the Brillouin shift of the normal corneas was observed to be relatively uniform across the central region of the cornea; while in keratoconus patients a strong spatial variation was measured with the cone showing the lowest Brillouin shift and indicating a large (up to ~70%) focal reduction in Young's modulus. Interestingly, away from the cone, the elastic modulus was very similar to normal cornea in both ex vivo and in vivo investigations.

For the analysis of corneal crosslinking, Brillouin has the potential to quantify the mechanical efficacy of various procedures. Because a universally recognized standard CXL protocol (Dresden) exists, we can use the log-log correlation to relate the changes of elastic modulus induced by CXL without calibration by comparing the unknown procedure to the standard Dresden protocol via the following equation:

$$\frac{\Delta M'_X}{\Delta M'_{Dresden}} = \frac{\Delta E'_X}{\Delta E'_{Dresden}}$$

Thus far, we have been able to use demonstrate Brillouin's ability to assess the efficacy of several cross-linking protocols while varying parameters of the CXL procedure (Reiss *et al.*, 2011). For example, corneal cross-linking currently requires an epithelium debridement prior to exposure to Riboflavin and UV-A. However, recent efforts have been given towards assessing the efficacy of the procedure without removing the epithelium (epi-On CXL) and, thereby, decreasing patient discomfort. The epi-on CXL procedure was estimated to induce about 33% of the stiffening done by the standard Dresden procedure. For comparison, the mechanical stiffening of the epi-on procedure was tested with gold-standard quasi-static rheology and was found to induce approximately 39% of the stiffening of epi-off CXL. Prior studies (Wollensak and Iomdina, 2009) found the mechanical efficacy of transepithelial CXL to be approximately 20% of standard CXL.

For the analysis of refractive surgery, we recently tested Brillouin's ability to assess corneal mechanical changes associated with LASIK surgery. LASIK surgery is expected to decrease the stiffness of the cornea due to the creation of a flap and the subsequent corneal ablation. To revert this potentially harmful effect, an accelerated CXL procedure has begun to be tested in combination with LASIK surgery. We used Brillouin microscopy to observe the properties of the cornea during the various stages of the LASIK/CXL combined procedure. After the LASIK flap was created, the cornea showed lower stiffness, especially in the anterior and central portions, where the flap was created. However, we observed no statistically significant difference after the flap-induced cornea was exposed to accelerated CXL. Therefore, using Brillouin microscopy, we were able to conclude the accelerated CXL procedure commonly paired with LASIK did not yield significant benefits towards increasing the compromised stiffness.

Applications of Brillouin Microscopy in the Crystalline Lens

The condition commonly known as presbyopia is related to the age-related loss of accommodation. Accommodation is the crucial biomechanical process of human vision that enables young persons to see near and distant objects by dynamically adjusting the focusing power of the eye. As age increases, the accommodation power drops. From a biomechanical point of view, this process is

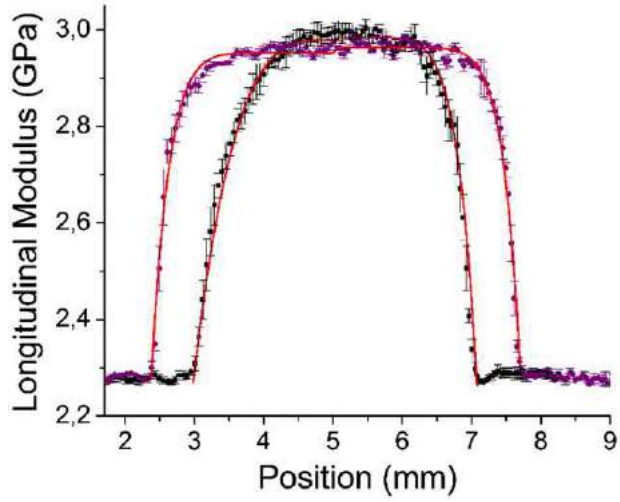


Fig. 7 Lens Applications: Brillouin microscopy can detect the crystalline lens longitudinal modulus with high-spatial resolution in vivo. Here shown the mean sagittal longitudinal elastic modulus in 28-(black square) and 60-(purple dot) year-old human lenses (n = 3). The red curves are power fits of the lens profiles.

due to the inability of the eye muscles to significantly change the shape of the crystalline lens. It has long been suspected that the loss of accommodation power is due to the diminished capacity of ciliary muscles to contract the lens with age. However, recent data indicate that ciliary muscles maintain ability to contract after the loss of accommodation (Ostrin and Glasser, 2007). Other potential candidate factors for presbyopia onset are age-dependent changes of the capsule and zonular fibers; but experiments have found too little changes to account for the decrease in accommodation power (Brian and Melinda, 2009; Fisher, 1969). Thus, the crystalline lens seems to be the main factor in the loss of accommodation; specifically age-related increased stiffness of the crystalline lens is suspected as the primary cause of presbyopia: as age progresses, the lens tissue stiffen which diminishes its ability to change shape (Glasser and Campbell, 1998, 1999).

Brillouin microscopy is a promising technique to characterize lens mechanical properties. In particular, the high 3D spatial resolution of Brillouin microscopy enables to characterize the spatial distribution of the longitudinal modulus within the crystalline lens (**Fig. 7**). In animal lenses, Brillouin microscopy revealed a dramatic age-dependent increase in the longitudinal modulus of the murine lens in vivo (Scarcelli *et al.*, 2011) and in porcine/bovine lenses ex vivo. In human lens, both the spatial distribution and the age dependence have been characterized (Besner *et al.*, 2016). In terms of spatial distribution, at all ages, the central portion of the lens was stiffer than the periphery, a result that was confirmed by ex vivo experiments using traditional standard shear rheometry. This result is consistent with some previous studies (Scarcelli *et al.*, 2011; Reiss *et al.*, 2011, 2012; Randall and Vaughan, 1982; Bailey *et al.*, 2010; Yoon *et al.*, 2013; Hollman *et al.*, 2007; Pau and Kranz, 1991) but not others (Fisher, 1971; Heys *et al.*, 2004; Weeber *et al.*, 2007; Wilde *et al.*, 2012). In terms of age dependence, Brillouin analysis did not find a statistically significant change of the peak longitudinal modulus with age, which confirmed previous Brillouin analysis performed ex vivo with FP interferometers (Bailey *et al.*, 2010). The most prominent age-related feature revealed by Brillouin was the increase of the stiff portion of the lens. Thus, Brillouin analysis does not support the previously reported "massive" increase of lens modulus as main factor to loss of accommodation (Fisher, 1971; Heys *et al.*, 2004; Weeber *et al.*, 2007; Wilde *et al.*, 2012). However, although more calibration mechanical studies are needed, with the given profiles and log-log correlation, the increase of the stiff portion of the lens would yield a 2-fold increase in the overall stiffness of the lens with age, which is consistent with previous ex vivo data (Glasser and Campbell, 1999; Augusteyn *et al.*, 2011).

Towards a Clinical Brillouin Microscopy System

A widely-available clinical Brillouin device that could measure biomechanical properties of the cornea and lens could find widespread application in both ophthalmic research and in the clinic. Currently available Brillouin microscopes have reached the performance levels to enable clinical testing and clinical studies to test the potential of Brillouin microscopy for keratoconus, crosslinking and presbyopia are currently on-going. For both cornea and lens applications, Brillouin microscopy has already shown biologically- and clinically-relevant information.

However, the success of Brillouin microscopy is highly dependent on its technology development. At the current mechanical sensitivities of in vivo instruments, Brillouin technology offers only ~10 discernable values for the stratification of patients of varying keratoconus stages. Also, current imaging sessions to collect a full Brillouin map of cornea or lens tissue may take 10–30 min. Finally, both the cost of the Brillouin microscope and the complexity of the setup represent an obstacle for widespread adoption in the clinic. Technological improvements are needed to address all of these issues. On this front, significant improvements have been shown already, although still at proof-of-principle stages: improved spectral selection at low loss has the potential to increase the throughput of Brillouin spectrometers (Fiore *et al.*, 2016; Shao *et al.*, 2016; Edrei *et al.*, 2017; Berghaus *et al.*, 2015a,b); novel multiplexed geometries could potentially speed-up the acquisition time by one to two order of magnitudes (Zhang *et al.*, 2016); standardized procedures for spectrometer alignment have been developed (Berghaus *et al.*, 2015a,b); the sensitivity of clinical instruments is currently limited by drifts due to temperature changes or laser instabilities, which could be removed with frequency locking or absolute frequency standards. Finally, improved speed and sensitivity could come from using higher laser power as all the experiments reported so far have used smaller illumination levels than the ones used in other clinical ophthalmic instruments. As a result, there is reason for optimism that Brillouin technology could be adopted in the clinic, focused engineering efforts aimed at making Brillouin microscopy faster, more sensitive, portable and easy to operate by non-experts will be crucial for the widespread use of the technology.

See also: Optical Coherence Tomography and Its Application to Imaging of Skin and Retina

References

Aglyamov, S.R., *et al.*, 2015. The dynamic deformation of a layered viscoelastic medium under surface excitation. Physics in Medicine and Biology 60 (11), 4295–4312.
Akca, B.I., *et al.*, 2015. Observation of sound-induced corneal vibrational modes by optical coherence tomography. Biomedical Optics Express 6 (9), 3313.
Alonso-Caneiro, D., Karnowski, K., Kaluzny, B.J., *et al.*, 2011. Assessment of corneal dynamics with high-speed swept source optical coherence tomography combined with an air puff system. Optics Express 19 (15), 14188–14199.
Ambrosio, J.R., *et al.*, 2011. Evaluation of corneal shape and biomechanics before lasik. International Ophthalmology Clinics 51 (2), 11–38.
Ambroziński, Ł., *et al.*, 2016. Air-coupled acoustic radiation force for non-contact generation of broadband mechanical waves in soft media. Applied Physics Letters 109 (4), 43701.
Andreassen, T.T., Simonsen, A.H., Oxlund, H., 1980. Biomechanical properties of keratoconus and normal corneas. Experimental Eye Research 31 (4), 435–441.

Armstrong, B.K., *et al*., 2013. Biological and biomechanical responses to traditional epithelium-off and transepithelial riboflavin-UVA CXL techniques in rabbits. Journal of Refractive Surgery 29 (5), 332–341.
Augusteyn, R., *et al*., 2011. Age-dependence of the optomechanical responses of ex vivo human lenses from India and the USA, and the force required to produce these in a lens stretcher: The similarity to in vivo disaccommodation. Vision Research 51 (14), 1667–1745.
Bailey, S.T., *et al*., 2010. Light-scattering study of the normal human eye lens: Elastic properties and age dependence. Transactions on Biomedical Engineering 57 (12), 2910–2917.
Bak-Nielsen, S., *et al*., 2013. The rigidity of corneas before and after corneal cross-linking – As measured by Corvis® ST. Investigative Ophthalmology & Visual Science 54, 1613. (E-Abstract).
Bekesi, N., *et al*., 2017. Biomechanical changes after in vivo collagen cross-linking with rose bengal–green light and riboflavin-UVA. Investigative Ophthalmology & Visual Science 58,1612–1620.
Bekesi, N., Dorronsoro, C., de la Hoz, A., Marcos, S., 2016b. Material properties from air puff corneal deformation by numerical simulations on model corneas. PLOS ONE 11 (10), e0165669.
Bekesi, N., Kochevar, I.E., Marcos, S., 2016a. Corneal biomechanical response following collagen cross-linking with rose bengal–green light and riboflavin-UVA. Investigative Ophthalmology & Visual Science 57,992–1001.
Berghaus, K.V., Yun, S.H., Scarcelli, G., 2015a. High speed sub-GHz spectrometer for Brillouin scattering analysis. Jove-Journal of Visualized Experiments 106, e53468.
Berghaus, K., Zhang, J., Yun, S.H., Scarcelli, G., 2015b. High-finesse sub-GHz-resolution spectrometer employing VIPA etalons of different dispersion. Optics Letters 40 (19), 4436–4439.
Besner, S., Scarcelli, G., Pineda, R., Yun, S.H., 2016. In vivo Brillouin analysis of the aging crystalline lens. Investigative Ophthalmology & Visual Science 57 (13), 5093–5100.
Boyce, B.L., Jones, R.E., Nguyen, T.D., Grazier, J.M., 2007. Stress-controlled viscoelastic tensile response of bovine cornea. Journal of Biomechanics 40 (11), 2367–2376.
Braaf, B., *et al*., 2011. Phase-stabilized optical frequency domain imaging at 1-μm for the measurement of blood flow in the human choroid. Optics Express 19 (22), 20886.
Brian, P.D., Melinda, K.D., 2009. The lens capsule. Experimental Eye Research 88.
Brillouin, L., 1922. Diffusion de la lumiere et des rayonnes X par un corps transparent homogene influence del'agitation thermique. Annals of Physics 17,88–122.
Cartwright, N.E.K., Tyrer, J.R., Marshall, J., 2011. Age-related differences in the elasticity of the human cornea. Investigative Ophthalmology and Visual Science 52 (7), 4324–4329.
Chang, E.W., Kobler, J.B., Yun, S.H., 2002. Subnanometer optical coherence tomographic vibrography. Optics Letters 37 (17), 3678–3680.
Choma, M.A., *et al*., 2005. Spectral-domain phase microscopy. Optics Letters 30 (10), 1162–1164.
De La Torre-Ibarra, M.H., Ruiz, P.D., Huntley, J.M., 2006. Double-shot depth-resolved displacement field measurement using phase-contrast spectral optical coherence tomography. Optics Express 14 (21), 9643–9656.
Deng, L.H., *et al*., 2006. Fast and slow dynamics of the cytoskeleton. Nature Materials 5 (8), 636–640.
Denoyer, A., Ricaud, X., Van Went, C., Labbé, A., Baudouin, C., 2013. Influence of corneal biomechanical properties on surgically induced astigmatism in cataract surgery. Journal of Cataract & Refractive Surgery 39 (8), 1204–1210.
Dil, J.G., 1982. Brillouin-scattering in condensed matter. Reports on Progress in Physics 45 (3), 285–334.
Dorronsoro, C., Pascual, D., Pérez-Merino, P., Kling, S., Marcos, S., 2012. Dynamic OCT measurement of corneal deformation by an air puff in normal and cross-linked corneas. Biomedical Optics Express 3 (3), 473–487.
Duck, F.A., 1990. Physical Properties of Tissue. London: Academic.
Dupps, W.J., Wilson, S.E., 2006. Biomechanics and wound healing in the cornea. Experimental Eye Research 83 (4), 709–720.
Edrei, E., Gather, M., Scarcelli, G., 2017. Integration of spectral coronagraphy within VIPA-based spectrometers for high extinction Brillouin imaging. Optics Express 25,6895.
Elsheikh, A., *et al*., 2007. Assessment of corneal biomechanical properties and their variation with age. Current Eye Research 32 (1), 11–19.
Fabry, B., Maksym, G.N., Butler, J.P., *et al*., 2001. Scaling the microrheology of living cells. Physical Review Letters 87 (14), 1481021–1481024.
Fiore, A., Zhang, J., Shao, P., Yun, S., Scarcelli, G., 2016. High-extinction virtually imaged phased array-based Brillouin spectroscopy of turbid biological media. Applied Physics Letters 108 (20), (ARTN 203701).
Fisher, R., 1969. Elastic constants of the human lens capsule. The Journal of Physiology 201 (1), 1–20.
Fisher, R.F., 1971. Elastic constants of human lens. Journal of Physiology-London 212 (1), 147–180.
Ford, M., *et al*., 2006. OCT corneal elastography by pressure-induced optical feature flow. In: SPIE Proceedings 6138, Ophthalmic Technologies XVI, 61380P.
Ford, M.R., *et al*., 2011. Method for optical coherence elastography of the cornea. Journal of Biomedical Optics. 16005.
Ford, M.R., *et al*., 2014. Serial biomechanical comparison of edematous, normal, and collagen crosslinked human donor corneas using optical coherence elastography. Journal of Cataract & Refractive Surgery 40 (6), 1041–1047.
Fu, J., *et al*., 2016. Depth-resolved full-field measurement of corneal deformation by optical coherence tomography and digital volume correlation. Experimental Mechanics.
Gittes, F., MacKintosh, F.C., 1998. Dynamic shear modulus of a semiflexible polymer network. Physical Review E 58 (2), R1241–R1244.
Glasser, A., Campbell, M., 1998. Presbyopia and the optical changes in the human crystalline lens with age. Vision Research 38 (2), 209–238.
Glasser, A., Campbell, M., 1999. Biometric, optical and physical changes in the isolated human crystalline lens with age in relation to presbyopia. Vision Research 39 (11), 1991–4006.
Grabner, G., *et al*., 2005. Dynamic corneal imaging. Journal of Cataract & Refractive Surgery 31,163–174.
Han, Z., *et al*., 2017. Optical coherence elastography assessment of corneal viscoelasticity with a modified Rayleigh–Lamb wave model. Journal of the Mechanical Behavior of Biomedical Materials 66,87–94.
Han, Z., Aglyamov, S.R., *et al*., 2015a. Quantitative assessment of corneal viscoelasticity using optical coherence elastography and a modified Rayleigh–Lamb equation. Journal of Biomedical Optics 20 (2), 20501.
Han, Z., Li, J., Singh, M., Aglyamov, S.R., *et al*., 2015b. Analysis of the effects of curvature and thickness on elastic wave velocity in cornea-like structures by finite element modeling and optical coherence elastography. Applied Physics Letters 106 (23), 1–5.
Han, Z., Li, J., Singh, M., Wu, C., *et al*., 2015c. Quantitative methods for reconstructing tissue biomechanical properties in optical coherence elastography: A comparison study. Physics in Medicine and Biology 60 (9), 3531–3547.
Heys, K.R., Cram, S.L., Truscott, R.J.W., 2004. Massive increase in the stiffness of the human lens nucleus with age: The basis for presbyopia. Molecular Vision 10,956–963.
Hollman, K.W., O'Donnell, M., Erpelding, T.N., 2007. Mapping elasticity in human lenses using bubble-based acoustic radiation force. Experimental Eye Research 85 (6), 890–893.
Holm, S., Sinkus, R., 2010. A unifying fractional wave equation for compressional and shear waves. Journal of the Acoustical Society of America 127 (1), 542–548.
Jonas, M., Huang, H.D., Kamm, R.D., So, P.T.C., 2008. Fast fluorescence laser tracking microrheometry, II: Quantitative studies of cytoskeletal mechanotransduction. Biophysical Journal 95 (2), 895–909.
Karnowski, K., Kaluzny, B.J., Szkulmowski, M., *et al*., 2011. Corneal topography with high-speed swept source OCT in clinical examination. Biomedical Optics Express 2 (9), 2709–2720.
Kling, S., Bekesi, N., Dorronsoro, C., Pascual, D., Marcos, S., 2014. Corneal viscoelastic properties from finite-element analysis of in vivo air-puff deformation. PLOS ONE 9 (8), e104904.
Kling, S., Ginis, H., Marcos, S., 2012. Corneal biomechanical properties from two-dimensional corneal flap extensiometry: Application to UV-Riboflavin cross-linking. Investigative Ophthalmology and Vision Sciences 53 (8), 5010–5015.

Kling, S., Marcos, S., 2013a. Effect of hydration state and storage media on corneal biomechanical response from in vitro inflation tests. Journal of Refractive Surgery 29 (7), 490–497.
Kling, S., Marcos, S., 2013b. Finite element modeling of intrastromal ring segment implantation into a hyperelastic cornea. Investigative Ophthalmology and Vision Sciences 54 (1), 881–889.
Kling, S., Marcos, S., 2013c. Contributing factors to corneal deformation in air puff measurements. Investigative Ophthalmology and Vision Sciences 54 (7),
Kling, S., Remón, L., Pérez-Escudero, A., *et al.*, 2010. Corneal biomechanical changes after collagen cross-linking from porcine eye inflation. Investigative Ophthalmology and Vision Sciences 51 (8), 3961–3968.
Koski, K.J., Muller, J., Hochheimer, H.D., Yarger, J.L., 2002. High pressure angle-dispersive Brillouin spectroscopy: A technique for determining acoustic velocities and attenuations in liquids and solids. Review of Scientific Instruments 73 (3), 1235–1241.
Li, C., *et al.*, 2012. Noncontact all-optical measurement of corneal elasticity. Optics Letters 37 (10), 1625–1627.
Li, J., *et al.*, 2014. Air-pulse OCE for assessment of age-related changes in mouse cornea in vivo. Laser Physics Letters 11 (6), 65601.
Litwiller, D., Lee, S., Kolipaka, A., Mariappan, Y., Glaser, K., *et al.*, 2010. MR elastography of the ex vivo bovine globe. Journal of Magnetic Resonance Imaging 32 (1), 44–51.
Liu, J., Roberts, C.J., 2005. Influence of corneal biomechanical properties on intraocular pressure measurement: Quantitative analysis. Journal of Cataract & Refractive Surgery 31 (1), 146–155.
Manapuram, R.K., *et al.*, 2012. In vivo estimation of elastic wave parameters using phase-stabilized swept source optical coherence elastography. JBO Letters 17 (10), 15–18. Available at: https://biomedicaloptics.spiedigitallibrary.org/article.aspx?articleid=1367083.
Marcos, S., Kling, S., Bekesi, N., Dorronsoro, C., 2014. Corneal biomechanical properties from air-puff corneal deformation imaging. In: SPIE Proceedings 8946, Optical Elastography and Tissue Biomechanics, 894609.
McBrien, N.A., Jobling, A.I., 2009. Biomechanics of the sclera in myopia: Extracellular and cellular factors. Optometry and Vision Science 86 (1), E23–E30.
Mofrad, M.R.K., Kamm, R.D., 2006. Cytoskeletal Mechanics. New York: Cambridge University Press.
Muthupillai, R., *et al.*, 1995. Magnetic resonance elastography by direct visualization of propagating acoustic strain waves. Science 269 (5232), 1854–1857.
Nguyen, T.-M., *et al.*, 2015. Shear wave elastography using amplitude-modulated acoustic radiation force and phase-sensitive optical coherence tomography. Journal of Biomedical Optics 20 (1), 16001.
Ortiz, S., Perez-Merino, P., Alejandre, N., *et al.*, 2012. Quantitative OCT-based corneal topography in keratoconus with intracorneal ring segments. Biomedical Optics Express 3, 814–882.
Ostrin, L.A., Glasser, A., 2007. Edinger-Westphal and pharmacologically stimulated accommodative refractive changes and lens and ciliary process movements in rhesus monkeys. Experimental Eye Research 84 (2), 302–313.
Pau, H., Kranz, J., 1991. The increasing sclerosis of the human lens with age and its relevance to accommodation and presbyopia. Graefes Archive for Clinical and Experimental Ophthalmology 229 (3), 294–296.
Perez-Merino, P., Ortiz, S., Alejandre, N., *et al.*, 2014. Ocular and optical coherence tomography-based corneal aberrometry in keratoconic eyes treated by intracorneal ring segments. American Journal of Ophthalmology 157,116–127.
Pérez-Merino, P., Ortiz, S., Alejandre, N., Jiménez-Alfaro, I., Marcos, S., 2013. Quantitative OCT-based longitudinal evaluation of intracorneal ring segment implantation in keratoconus. Investigative Ophthalmology & Visual Science 54, 6040–6051.
Randall, J., Vaughan, J.M., 1982. The measurement and interpretation of Brillouin scattering in the lens of the eye. Proceedings of the Royal Society of London Series B – Biological Sciences 214 (1197), 449–470.
Reiss, S., *et al.*, 2012. Ex vivo measurement of postmortem tissue changes in the crystalline lens by brillouin spectroscopy and confocal reflectance microscopy. Transactions on Biomedical Engineering 59 (8), 2348–2354.
Reiss, S., Burau, G., Stachs, O., Guthoff, R., Stolz, H., 2011. Spatially resolved Brillouin spectroscopy to determine the rheological properties of the eye lens. Biomedical Optics Express 2 (8), 2144–2159.
Sandercock, J.R., 1975. Some recent developments in Brillouin scattering. RCA Review 36 (1), 89–107.
Scarcelli, G., *et al.*, 2015a. Noncontact three-dimensional mapping of intracellular hydromechanical properties by Brillouin microscopy. Nature Methods 12 (12), 1132.
Scarcelli, G., Besner, S., Pineda, R., Kalout, P., Yun, S.H., 2015b. In vivo biomechanical mapping of normal and keratoconus corneas. JAMA Ophthalmology 133 (4), 480–482.
Scarcelli, G., Besner, S., Pineda, R., Yun, S.H., 2014. Biomechanical characterization of keratoconus corneas ex vivo with Brillouin microscopy. Investigative Ophthalmology & Visual Science 55 (7), 4490–4495.
Scarcelli, G., Kim, P., Yun, S., 2011. In vivo measurement of age-related stiffening in the crystalline lens by brillouin optical microscopy. Biophysical Journal 101 (6), 1539–1584.
Scarcelli, G., Kim, P., Yun, S.H., 2008. Cross-axis cascading of spectral dispersion. Optics Letters 33 (24), 2979–2981.
Scarcelli, G., Yun, S.H., 2007a. Confocal Brillouin microscopy for three-dimensional mechanical imaging. Nature Photonics 9 (2), 39–43.
Scarcelli, G., Yun, S.H., 2007b. Three-dimensional brillouin confocal microscopy. In: Conference on Lasers and Electro-Optics/Quantum Electronics and Laser Science Conference and Photonic Applications Systems Technologies, OSA Technical Digest Series (CD), paper CTuV5.
Scarcelli, G., Yun, S.H., 2012. In vivo Brillouin optical microscopy of the human eye. Optics Express 20,9197.
Schmitt, J.M., 1998. OCT elastography: Imaging microscopic deformation and strain of tissue. Optics Express 3 (6), 199.
Shao, P., *et al.*, 2016. Etalon filters for Brillouin microscopy of highly scattering tissues. Optics Express 24 (19), 22232–22238.
Shirasaki, M., 1996. Large angular dispersion by a virtually imaged phased array and its application to a wavelength demultiplexer. Optics Letters 21 (5), 366–368.
Sigal, I.A., Grimm, J.L., 2012. A few good responses: Which mechanical effects of IOP on the ONH to study? Investigative Ophthalmology & Visual Science 53 (7), 4270–4278.
Singh, M., *et al.*, 2016. Noncontact elastic wave imaging optical coherence elastography for evaluating changes in corneal elasticity due to crosslinking. IEEE Journal of Selected Topics in Quantum Electronics 22 (3), 266–276.
Singh, M., Li, J., *et al.*, 2017. Optical coherence elastography for evaluating customized riboflavin/UV-A corneal collagen crosslinking. Journal of Biomedical Optics 22 (9), 91504.
Singh, M., Nair, A., Aglyamov, S.R., *et al.*, 2017. Noncontact optical coherence elastography of the posterior porcine sclera in situ as a function of IOP. In:Manns, F., Söderberg, P.G., Ho, A. (Eds.), Proceedings SPIE 10045, Opthalmic Technologies XXVII. p. 1004524.
Song, S., *et al.*, 2015. Quantitative shear-wave optical coherence elastography with a programmable phased array ultrasound as the wave source. Optics Letters 40 (21), 5007.
Song, S., Huang, Z., Wang, R.K., 2013. Tracking mechanical wave propagation within tissue using phase-sensitive optical coherence tomography: Motion artifact and its compensation. Journal of Biomedical Optics 18 (12), 121505.
Torricelli, A.A.M., *et al.*, 2014. BAC-EDTA transepithelial riboflavin-UVA crosslinking has greater biomechanical stiffening effect than standard epithelium-off in rabbit corneas. Experimental Eye Research 125,114–117.
Vakoc, B., *et al.*, 2005. Phase-resolved optical frequency domain imaging. Optics Express 13 (14), 5483–5493.
Vaughan, J.M., Randall, J.T., 1980. Brillouin scattering, density and elastic properties of the lens and cornea of the eye. Nature 284 (5755), 489–491.
Wang, S., *et al.*, 2013. A focused air-pulse system for optical-coherence-tomography-based measurements of tissue elasticity. Laser Physics Letters 10 (7), 75605.
Wang, S., Larin, K.V., 2014. Noncontact depth-resolved micro-scale optical coherence elastography of the cornea. Biomedical Optics Express 5 (11), 3807–3821.
Weeber, H.A., Eckert, G., Pechhold, W., *et al.*, 2007. Stiffness gradient in the crystalline lens. Graefe's Archive for Clinical and Experimental Ophthalmology 245 (9), 1357–1366.
Wilde, G.S., Burd, H.J., Judge, S.J., 2012. Shear modulus data for the human lens determined from a spinning lens test. Experimental Eye Research 97 (1), 36–48.

Wollensak, G., Iomdina, E., 2009. Biomechanical and histological changes after corneal crosslinking with and without epithelial debridement. Journal of Cataract and Refractive Surgery 35 (3), 540–546.
Wollensak, G., Spoerl, E., Seiler, T., 2003. Stress-strain measurements of human and porcine corneas after riboflavinultraviolet-a-induced cross-linking. Journal of Cataract & Refractive Surgery 29,1780–1785.
Wu, C., *et al*., 2015. Assessing age-related changes in the biomechanical properties of rabbit lens using a coaligned ultrasound and optical coherence elastography system. Investigative Ophthalmology & Visual Science 56 (2), 1292–1300.
Yoon, S., Aglyamov, S., Karpiouk, A., Emelianov, S., 2013. The mechanical properties of ex vivo bovine and porcine crystalline lenses: Age-related changes and location-dependent variations. Ultrasound in Medicine and Biology 39 (6), 1120–1127.
Zhang, J., Fiore, A., Yun, S.H., *et al*., 2016. Line-scanning Brillouin microscopy for rapid non-invasive mechanical imaging. Scientific Reports, 6, ARTN 35398.
Zhang, J., Nou, X., Kim, H., Scarcelli, G., 2017a. Brillouin flow cytometry for label-free mechanical phenotyping of the nucleus. Lab on a Chip 17,663–670.
Zhang, J., Wu, C., Raghunathan, R., Larin, K.V., Scarcelli, G., 2017b. Non-invasive structural and biomechanical imaging of the developing embryos using OCT and Brillouin microscopy. In: SPIE Proceedings 10067, Optical Elastography and Tissue Biomechanics IV, 100670W.

Further Reading

Ortiz, S., Siedlecki, D., Perez-Merino, P., *et al*., 2011. Corneal topography from spectral optical coherence tomography. Optics Express 2 (12), 3232–3247.
Scarcelli, G., Yun, S.H., 2008. Confocal Brillouin microscopy for three-dimensional mechanical imaging. Nature Photonics 2 (1), 39–43.
Scarcelli, G., Yun, S.H., 2011. Multistage VIPA etalons for high-extinction parallel Brillouin spectroscopy. Optics Express 19 (11), 10913–10922.

Optical Coherence Tomography and Its Application to Imaging of Skin and Retina

Michael Pircher, Medical University of Vienna, Vienna, Austria

© 2018 Elsevier Ltd. All rights reserved.

Abbreviations

AMD Age related macular degeneration
BCC Basal cell carcinoma
CNV Choroidal neovascularization
DOF Depth of focus
FWHM Full width at half maximum
OCT Optical coherence tomography
SLO Scanning laser ophthalmoscope
UHR Ultra high resolution

Nomenclature

A-scan Depth profile recorded with OCT
B-scan Cross-sectional image consisting of several laterally displaced A-scans
C-scan En-face image extracted from an OCT volume scan

Introduction

Optical coherence tomography (OCT) provides cross-sectional images of tissue with high axial resolution. Thereby the sample is probed using light in the infrared range. Image acquisition is performed noninvasively and nondestructively. The axial resolution of OCT lies in the micrometer range and is decoupled from the transverse resolution. This overcomes limitations associated with the numerical aperture of the objective and allows imaging with high axial resolution despite a moderate transverse resolution. Thus layered structures, such as human skin or the human retina, are well suited to be investigated with OCT. The penetration depth in tissue depends on the corresponding scattering properties and typically lies in the order of 1–2 mm. Structures that lie deeper within tissue can be visualized either because of overlying transparent tissue (as is the case in the human eye) or because of endoscopic probes that can be moved inside the body. OCT can be regarded as bridge between microscopic imaging technologies such as confocal microscopy (with limited depth penetration) to macroscopic imaging technologies such as ultrasound or computer tomography.

OCT is a highly sensitive technique and can achieve sensitivities ranging up to 110 dB or more. This allows detection of light even from weak backscattering samples. Image acquisition in OCT is done through recording of depth profiles (A-scans). Several laterally displaced A-scans form a cross-sectional image or B-scan. In a volume scan of the sample several laterally displaced B-scans are recorded. Another advantage of OCT is the high imaging speed. A-scan rates of several megahertz have been reported. Thus highly sampled volumes or several volumes per second can be recorded.

The highest impact of OCT certainly lies in the field of ophthalmology. No other imaging modality is capable to provide three-dimensional (3D) information of retinal tissue. Diagnosis and treatment control of retinal diseases are strongly depending on OCT images and the impact to the field can be compared with the invention of the direct ophthalmoscope more than 200 years ago. Many instruments are commercially available and OCT imaging has found a wide range of applications. Apart from ophthalmology OCT imaging can be found in dermatology, cardiovascular research, pulmonology, and many more. In addition to the biomedical field OCT has been applied to material sciences and art preservation (Stifter, 2007).

Basic Principle of OCT

The technique evolved from low coherence interferometry and was initially intended to measure axial distances in the eye. The basic principle is similar to ultrasound technology. However, instead of sound waves light is used to generate an image. The speed of light is much higher than that of sound waves. Thus, an interferometric technique is needed in order to distinguish between light that has traveled different distances in the micrometer range. **Fig. 1(A)** shows a scheme of an OCT interferometer. Light is emitted from an OCT light source and is split by the beam splitter into two arms, the reference arm and the sample arm, respectively. In the reference arm, the light is back reflected by the reference arm mirror. In the sample arm the beam is deflected on a scanning unit (for x- and y-scanning) before the light is sent to the sample. The light is backscattered from the sample, de-scanned and brought to interference with light from the reference arm at the beam splitter. The interfering light is then detected by the detector. It is very common to use fiber optics for the interferometer part. This eliminates the need for interferometer alignment and enables the fabrication of very compact systems. There are several techniques available for OCT.

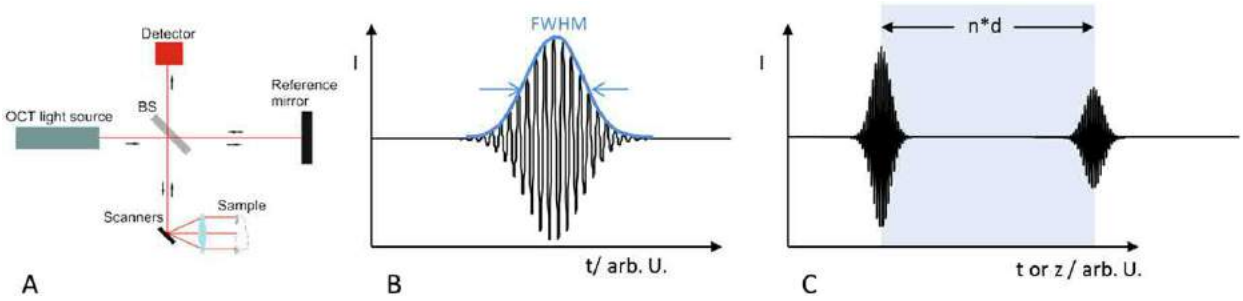


Fig. 1 (A) Scheme of an optical coherence tomography (OCT) interferometer. BS denotes the beam splitter of the interferometer. For time domain optical coherence tomography (TD-OCT) the reference mirror is mounted on a translation stage. (B) Measured intensity *I* at the detector (interference pattern) when the mirror is moved in axial direction (reflectivity in sample and reference arm are equal) full width at half maximum (FWHM) denotes the full width at half maximum of the coherence function which is defined as axial resolution in OCT. (C) Measured interference pattern when a glass plate with thickness *d* is measured (*n* denotes the refractive index of the glass plate).

Timed Domain OCT

Initially the so-called time domain OCT (TD-OCT) technique has been used. In this technique the interferometer is illuminated with a broadband light source. To generate an A-scan (depth profile) the reference mirror is moved axially. In the case of a mirror in the sample arm, the detector will record an intensity pattern that is shown in **Fig. 1(B)**. Due to the broad bandwidth of the source, interference fringes will only be visible if sample and reference arm lengths are matched (within the coherence gate). Thus light originating from different depths can be separated. In the case of a glass plate the light will be backscattered (or back reflected) at the front and back surface of the plate. During axial scanning of the reference arm mirror two coherence functions (arising at the surface and back surface of the glass plate) as illustrated in **Fig. 1(C)** will be detected. The distance between the two signals corresponds to the optical thickness of the plate (i.e., the geometrical thickness multiplied with the refractive index of the plate). The full width at half maximum (FWHM) of the coherence function is defined as the axial resolution of OCT and equals the round trip coherence length ($=1/2$ of the coherence length) of the light source.

The A-scan rate of this technique is limited by the inertia of the mirror to a few 100 Hz. However, the method can be highly sensitive. Motion of the mirror will introduce a Doppler frequency shift for each wavelength. Thus, a carrier frequency for the OCT signal is generated which allows for band pass filtering of the signal. This procedure filters 1/f noise out and increases the sensitivity. Depending on the bandwidth of the light source and the speed of motion a certain electronic signal bandwidth needs to be detected. Faster speeds will require larger electronic bandwidths (of the detector and amplifying electronics) and thus lower system sensitivity.

To overcome the limitation given by the inertia of the mirror, a galvanometer scanning mirror and a grating (rapid scanning optical delay line) can be placed in the reference arm. Instead of a translational motion in spatial domain, this configuration allows for a rotational motion in wavelength domain. The method has the advantage that the group delay (axial scanning of the sample) and the phase delay (modulation frequency of the OCT signal) can be adjusted independently. Therefore the imaging speed can be improved up to a few kilohertz. TD-OCT detects only light backscattered from within the coherence volume of the sample. The coherence volume is defined through the round trip coherence length and the transverse resolution of the system. Light from other depths (outside the coherence volume) is rejected which limits the sensitivity of the method. However, the depth range of the system depends on the travel range of the reference mirror. Thus, in principle very long axial distances without loss in sensitivity can be scanned with TD-OCT.

Fourier Domain OCT

With the development of Fourier domain (FD) OCT the sensitivity could be greatly improved. The gain in sensitivity can be directly translated into imaging speed that allows A-scan rates an order of magnitude higher than in TD-OCT. Two different FD-OCT schemes are possible. The spectral domain (SD) OCT technique uses a similar broadband light source as in TD-OCT. However, instead of a single detector at the interferometer exit the light is spectrally dispersed trough a grating and detected with a line scan camera (cf. **Fig. 2(A)**). Thereby, the reference arm mirror is kept stationary. In this way light from the entire sample depth is recorded simultaneously which results in a sensitivity advantage compared to TD-OCT.

In case of a mirror in the sample arm (same light power returning from sample and reference arm) the spectrometer camera will detect an interference pattern that is displayed in **Fig. 2(B)**. The modulation of the spectrum arises from constructive and destructive interference for each wavelength and depends on the path length difference between sample and reference arm beam. Thus the frequency of the modulation depends on the amount of path length difference. Smaller differences result in low frequencies, while larger differences cause higher frequencies. In addition, the spectrum (and the interference pattern) is detected in the wavelength domain. Thus, each modulation frequency that corresponds to a certain depth will have a chirp along the spectrum. To remove this chirp, the spectrum needs to be transformed into k-space ($=1/\lambda$-space). Associated with this chirp will

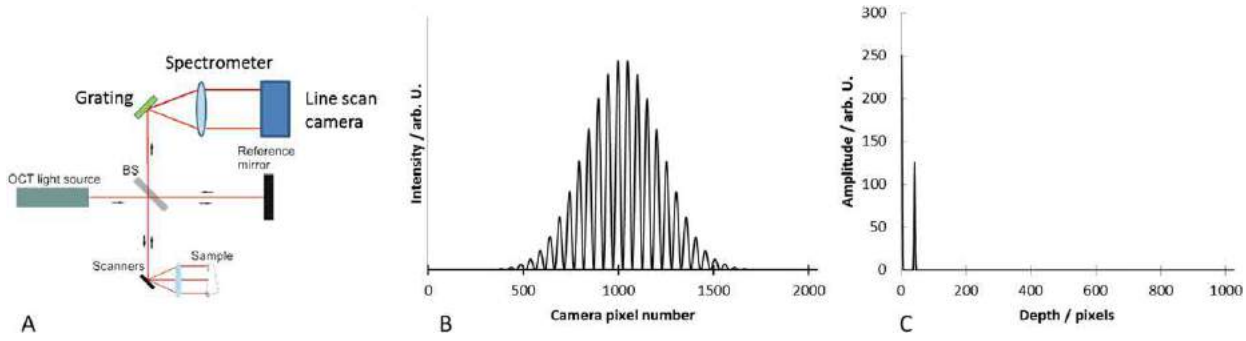


Fig. 2 (A) Scheme of a spectral domain optical coherence tomography (SD-OCT) instrument using a spectrometer in the detection arm (BS, beam splitter). (B) Measured interference pattern when a mirror is placed in the sample arm (light power returning from sample and reference arm are equal). (C) Fast Fourier transformation of the spectrum measured in (B) corresponding to a depth profile.

be a drop of sensitivity (sensitivity fall off) with depth because of the finite width of the detector elements (camera pixels). Higher frequency components (constructive and destructive interference of neighboring wavelengths) will therefore be detected by a single detector element and thus not be visible. It should be noted that FD-OCT requires a minimum detection speed. Jitter within the interferometer or axial movement of the sample (in case of in vivo imaging) will cause a change (phase shift) in the interference pattern which degrades the visibility of the interference pattern when this change occurs during the exposure time of the camera. In order to avoid this "fringe washout" the exposure time should be shorter than 1 ms.

In the case displayed in **Fig. 2(B)** one arm is only slightly longer than the other. At this point it should be noted that it is not possible to distinguish (without any other means) between positive (reference arm is longer) or negative (sample arm is longer) path length differences because both will result in the same frequency modulation of the spectrum. In order to generate an A-scan the interference pattern (modulated spectrum) needs to be Fourier transformed. The corresponding depth profile is plotted in **Fig. 2(C)**. Because of the inability to distinguish between positive and negative frequencies, the transformation of the spectrum yields in fact two depth profiles that are mirrored around zero delay. Zero delay refers to the position where sample and reference arm lengths are exactly matched. The total number of sample points after Fourier transformation stays constant. However, this means that the number of sample points per A-scan is only half the number of camera pixels. Because the mirrored A-scan does not contain additional information it is very common in OCT to simply omit this part as is done in **Fig. 2(C)**.

The depth range of a SD-OCT system depends on the spectral resolution of the spectrometer as increasing depth is associated with higher modulation frequencies that need to be sampled according to the Nyquist theorem. This resolution is determined by the dispersion properties of the grating (number of lines that are illuminated on the grating), the spectrometer optics and the number of pixels that are available on the line scan camera. According to Leitgeb *et al.* (2003) the maximum depth range can be calculated via

$$z_{\max} = \frac{\lambda^2}{4\delta\lambda} \tag{1}$$

where λ and $\delta\lambda$ denote the wavelength and the spectral resolution, respectively. A typical OCT configuration uses a light source with a central wavelength of 840 nm, a bandwidth of 50 nm, and a 2048 pixel camera. Assuming that 150 nm bandwidth is imaged onto the camera and that the separation between spectral lines (corresponding to the resolution provided by the grating) is smaller than the size of a pixel an imaging depth of 2.4 mm is achieved. Back reflections from larger imaging depths will appear attenuated as aliasing frequencies and may cause unwanted artifacts inside an OCT image.

Another technique for realizing FD-OCT is swept source (SS) OCT. SS-OCT uses fast (wavelength) tunable lasers as light source in combination with a single (fast) photo detector. During a laser sweep the interference pattern is recorded depending on wavelength and separated in time. The pattern will be similar to the one displayed in **Fig. 2(B)**. It should be noted that the instantaneous power at each wavelength can be higher compared to SD-OCT which compensates for the nonparallel data acquisition scheme of SS-OCT compared to SD-OCT. Similar as in SD-OCT, light backscattered from the entire sample depth contributes to the interference pattern and the depth profile is reconstructed in a similar way via Fourier transformation of the recorded spectral information. The instantaneous linewidth of the source determines the instantaneous coherence length and defines the depth range of the system. The instantaneous linewidth thus plays an equivalent role as the spectral resolution of SD-OCT. Within this range light from the reference arm and sample arm are coherent and can interfere. However, the instantaneous line width is a completely different measure as the round trip coherence length. The latter is defined by the FWHM of the laser sweep, while the former is the width of a laser line emitted at a certain wavelength within the sweep. **Fig. 3(A)** illustrates the emission of a SS laser.

The output power of many swept laser sources fluctuates. In order to compensate for this fluctuations balanced photo detection is employed. **Fig. 3(B)** shows a schematic of a fiber-based SS-OCT instrument. The light emitted from the SS is already confined in a single mode fiber. Before the entrance of the interferometer the light traverses a fiberized circulator and is split thereafter by a 50:50 beam splitter into reference and sample beam, respectively. The light back reflected from both arms is recombined by the 50:50

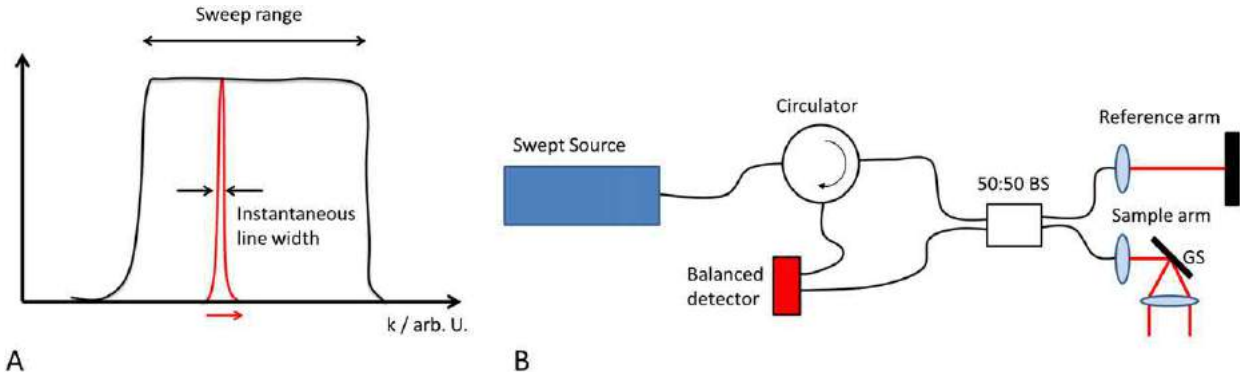


Fig. 3 (A) Illustration of a swept source (SS) laser sweep. The sweep range determines the axial resolution of the system. The instantaneous line width (drawn not to scale) determines the imaging depth provided by the light source. (B) Representative scheme of a SS optical coherence tomography (OCT) instrument based on fiber optics and balanced photo detection. BS 50:50, fiber beam splitter; GS, galvanometer scanner.

beam splitter and is detected with a balanced photo detector. The circulator ideally transmits nearly 100% of the light from the light source to the interferometer, while nearly 100% of the light coming from the interferometer is transmitted to the detector. There are several advantages of SS-OCT compared to SD-OCT. In SD-OCT the light is detected with a spectrometer. The efficiency of the spectrometer cannot be 100% which results in a lower sensitivity compared to SD-OCT. In addition the wavelength sweep can be performed in $1/\lambda$ space which results in an elimination of the frequency chirp that is present in spectrometer-based systems and correspondingly into an elimination of the sensitivity drop with depth. Finally, the spectrometer needs to be perfectly aligned in order to achieve a high sensitivity which sets high demands, from a technical point of view, on the spectrometer design in commercial instruments. No such alignment is required for SS-OCT instruments.

Resolution

The FWHM of the interference pattern (cf. **Fig. 1(B)**) defines the axial resolution of OCT and is inversely proportional to the bandwidth of the light source. In case of a Gaussian-shaped spectrum the resolution can be calculated via following equation (Drexler and Fujimoto, 2015):

$$\Delta z = \frac{2\ln(2)\overline{\lambda}^2}{n\pi\Delta\lambda} \tag{2}$$

where λ denotes the central wavelength, $\Delta\lambda$ the bandwidth, and n the refractive index of the medium. As can be seen from this equation, the resolution in OCT depends on the central wavelength of the light source and the corresponding bandwidth. **Fig. 4** shows the axial resolutions for three wavelength regions that are commonly used in OCT. Standard OCT resolution refers to bandwidths around 50 nm corresponding to an axial resolution between 5 and 15 μm. The use of larger bandwidths (100 nm or more) is known as ultrahigh resolution OCT and requires ultra-broadband light sources, such as titanium sapphire laser or supercontinuum light sources. Important for achieving the resolution in OCT that is provided by the light source is a sufficient optical transparency of the optical components and matching of dispersion (see below) introduced in reference and sample arm, respectively. Especially fiberized interferometers may cause unwanted effects because single mode propagation (multimode propagation results in coherent image artifacts) depends on the size of the core diameter in respect to the wavelength. Thus larger wavelengths will be stronger attenuated if the core size is chosen to ensure single mode propagation for the shortest wavelengths.

The transverse resolution mainly depends on the imaging optics in the sample arm. In order to achieve maximum fringe visibility it is common in OCT to use light with high spatial coherence. Light emitted from a single mode fiber has this property. Because of its directionality, divergence, and Gaussian intensity profile, the beam propagation can be described using Gaussian optics. In many OCT systems the objective lens is not the limiting aperture as the beam is scanned over this lens in order to achieve transverse scanning of the sample. Hence, the beam remains Gaussian and the resolution can be calculated via the FWHM of the Gaussian beam waist ω_0 and the angular spread θ_S of the Gaussian beam (Fercher, 2010):

$$\Delta x = 2\sqrt{\ln 2}\omega_0 = 2\sqrt{\ln 2}\frac{\overline{\lambda}}{\pi\theta_S} \tag{3}$$

$\overline{\lambda}$ denotes the central wavelength of the beam. Strictly speaking, this resolution can be obtained only at the focal (or certain depth) plane. Outside this focal plane the resolution is degraded. A measure for the imaging depth where the resolution is degraded only by a factor of $\sqrt{2}$ is the Rayleigh range z_R Twice this range defines the depth of focus (DOF), which can be calculated with

$$2z_R = \mathrm{DOF} = 2\frac{\overline{\lambda}}{\pi\theta_S^2} \tag{4}$$

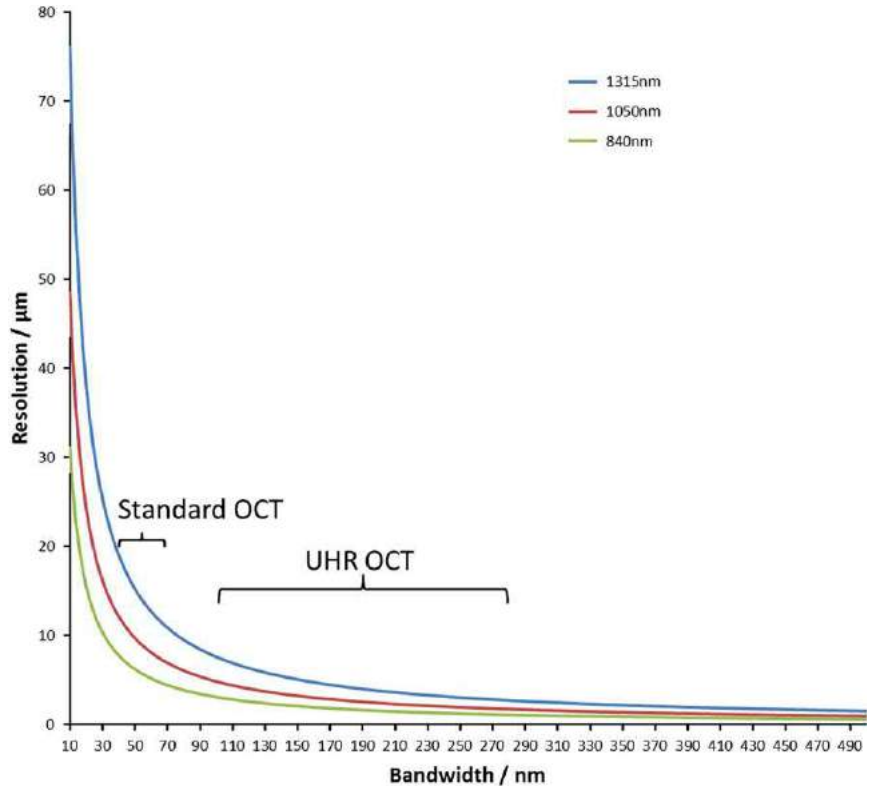


Fig. 4 Axial resolution of an optical coherence tomography (OCT) system depending on the bandwidth and the central wavelength for three commonly used wavelength regions. Standard OCT uses a bandwidth between 30 and 70 nm, which results in a resolution below 20 μm. Ultrahigh resolution (UHR) OCT refers to the use of larger bandwidths (>100 nm) and corresponding resolutions that are below 5 μm.

Thus for high-resolution systems only part of the imaged volume will be in focus and imaged sharply. For an OCT system at 1300 nm and 20 μm transverse resolution the DOF will be 2 mm. This DOF will be reduced to 20 μm in the case of 2 μm transverse resolution. Hence, the imaging optics needs to be carefully designed in order to optimize the OCT performance. Several methods have been proposed to maintain high transverse resolution throughout the imaging depth. These are based on a dynamic shift of focus with the coherence gate (only possible for TD-OCT) or on the use of special illumination techniques (such as Bessel beams).

Sensitivity

Several noise sources influence the sensitivity in OCT. Receiver noise from the photo detectors, excess noise arising from fluctuations in light power, and shot noise that originates from the quantum nature (and random arrival) of photons. Ideally, an OCT system is limited by shot noise only. This limit can be reached through the coherent amplification process inherent to OCT as the light power returning from the reference arm greatly exceeds the power returning from the sample. In the case of sufficient light power from the light source, the amount of light returning from the reference arm can be optimized in order to reach the shot noise limit. In TD-OCT the shot noise limited sensitivity depends on the detection bandwidth and the power efficiency of the interferometer (Izatt *et al.*, 2015):

$$\text{Sensitivity} = \frac{\rho P_S}{2e\Delta B_{TD}} \tag{5}$$

where ρ denotes the quantum efficiency of the detector, P_S is the light power returning from the sample arm (with a 100% reflective mirror as sample), e is the electron charge ($e = 1.6\ 10^{-19}$ °C), and ΔB_{TD} is the electronic detection bandwidth of the TD-OCT systems. The light power returning from the sample depends on the power incident on the sample, the interferometer configuration, and the optical losses within the system. Let us consider a fiber-based Michelson interferometer with a 50/50 splitting ratio and 4 mW of optical power (central wavelength at 1300 nm with a bandwidth of 50 nm) on the sample. The light is emitted from a single mode fiber. Thus the coupling efficiency (of the light returning from the sample) will be ~50%. Another 50% of the light is lost due to the fiber beam splitter which results in an optical power returning from the sample arm (with a 100% reflective mirror as sample) of 1 mW. When the above mentioned TD-OCT instrument is operated at 1 kHz A-scan rate and 3 mm depth range a minimum electronic bandwidth of 800 kHz will be required. This results in a sensitivity of the OCT system (assuming 0.8 quantum efficiency of the detector) of 103 dB.

In FD-OCT the sensitivity can be expressed in a similar way (Leitgeb *et al.*, 2003):

$$\text{Sensitivity} = \frac{\rho P_S}{4e\Delta B_{FD}} M \tag{6}$$

with ΔB_{FD} the electronic bandwidth of FD-OCT systems (inversely proportional to the exposure time of the camera in SD-OCT) and M the number of spectral channels of the FD-OCT systems. By comparing this equation with Eq. (5) we can see that the sensitivity of FD-OCT is a factor of M/2 larger than in TD-OCT. Thus, for a FD-OCT instrument operating with the same light source and interferometer as before will have an improved sensitivity. Nevertheless, following issues need to be considered. The light returning from the sample will be slightly attenuated by the efficiency of the spectrometer (this typically lies in the range of 60%) and the exposure time of the camera will be shorter than the time corresponding to the A-scan rate because the camera requires a certain readout time. For an A-scan rate of 70 kHz we assume that 1000 pixels on the camera are (equally) illuminated and that the camera requires 4 μs for readout. This results in an exposure time of ~10 μs. The detection bandwidth B of FD-OCT is given by (Leitgeb *et al.*, 2003)

$$B_{FD-OCT} = \frac{2z_R}{l_c \tau} \tag{7}$$

with z_R denoting the depth range of the system and l_c the double pass coherence length. τ is the exposure time of the camera. In our case ($z_R = 6$ mm, $l_c = 15$ μm, and $\tau = 10$ μs) the detection bandwidth is 80 Mhz which results in a shot noise limited sensitivity of 108 dB. Thus, a higher sensitivity can be achieved with this SD-OCT system although the imaging speed is increased by a factor of 70.

Dispersion

Dispersion describes the effect of a wavelength dependent refractive index of a medium. For example, the refractive index of water (cf. **Fig. 5**) is not constant and decreases with wavelength. For OCT dispersion mismatch between the interferometer arms results in a degradation of the axial point spread function. This is associated with a degradation of axial resolution and sensitivity. Thus the interferometer arms need to be balanced which is normally achieved by inserting corresponding materials that are present in the sample arm (such as lenses for scanning optics) into the reference arm of the interferometer. For compensating dispersion of the eye cuvettes that are filled with water are commonly used. FD-OCT records spectral data. Therefore it is possible to compensate for dispersion in post-processing.

Wavelength Range

The choice of imaging wavelength in OCT depends on the investigated sample as well as on the availability of light sources. For a high penetration depth the total attenuation coefficient of tissue at the imaging wavelength should be minimal. Both, absorption and scattering contribute to the total attenuation coefficient. Water is the main constituent of tissue (apart from teeth

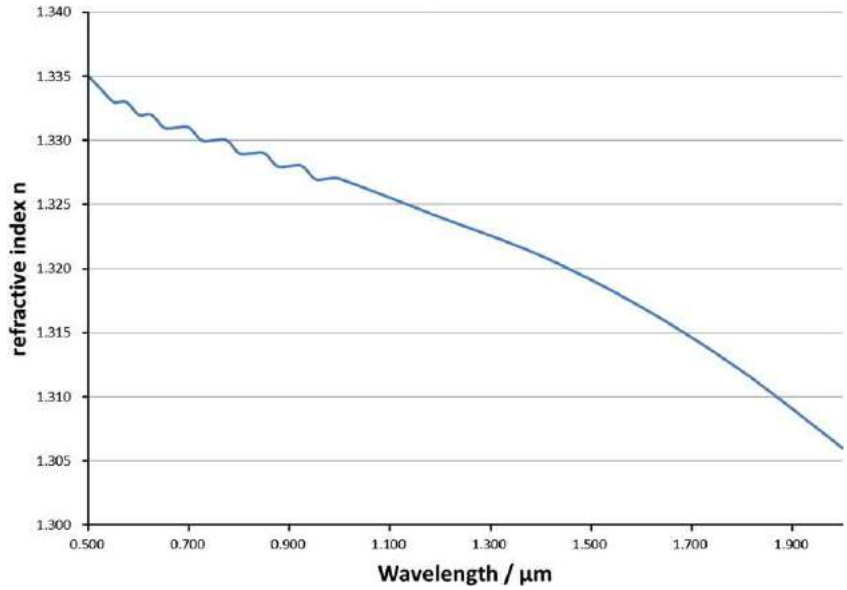


Fig. 5 The wavelength dependence of the refractive index of water in the visible and near-infrared (NIR) region. Data from Hale, G.M., Querry, M. R., 1973. Optical-constants of water in 200-nm to 200-μm wavelength region. Applied Optics 12(3), 555–563.

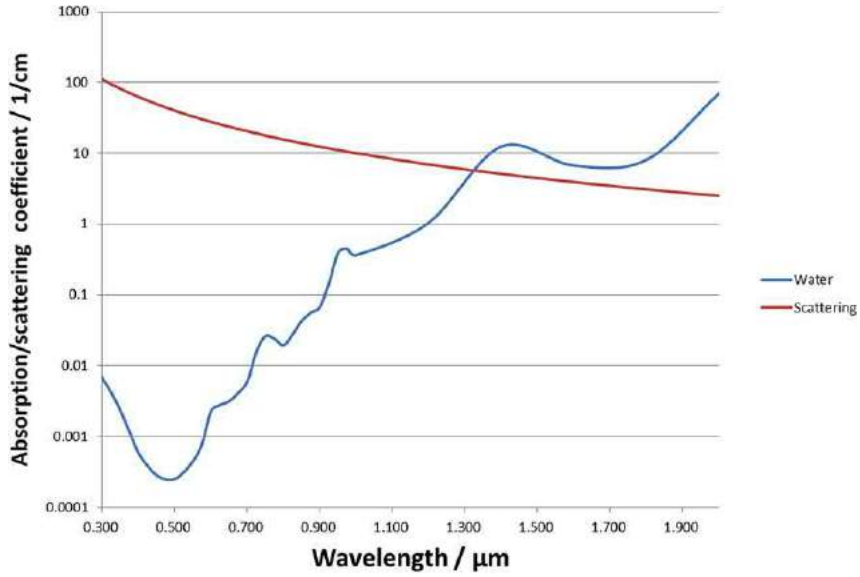


Fig. 6 Absorption coefficient of water and scattering coefficient of dense tissue. The three main optical coherence tomography (OCT) imaging wavelengths (840, 1060, 1300 nm) are outlined in the graph. Data from Hale, G.M., Querry, M.R., 1973. Optical-constants of water in 200-nm to 200-μm wavelength region. Applied Optics 12(3), 555–563.

or bones) and its absorption properties will be dominating. As can be seen in Fig. 6 the absorption coefficient of water strongly increases from visible light to infrared light. On the other hand, scattering gradually decreases in this wavelength range. At the 1300 nm wavelength region the contribution of scattering and absorption are largely within the same range. Thus, this wavelength region is the preferred choice for imaging dense tissue such as human skin as for shorter wavelengths the penetration will be limited by scattering, while for longer wavelengths absorption will be dominating. Imaging at 1300 nm requires detector materials that are sensitive in this region. These are much more expensive than comparable materials that are sensitive in the visible range. As such the preferred OCT imaging technology will be based on SS-OCT because this technology requires a single-balanced detector (instead of a detector array as in SD-OCT) and provides some benefits (as outlined above) compared to the SD-OCT counterpart.

For imaging the retina, the light has to traverse the ocular media (eye length of $\sim$2 cm) twice which significantly changes the situation. The scattering properties of the retina are of less importance compared to the transmittance of the light through the eye. Ocular media are very weakly scattering (apart from pathologies such as cataract). Thus the imaging wavelength should be as close to the visible range as possible to minimize absorption by water. However, for highly sensitive measurements the quantum efficiency of the detector should be high. The used detector material, silicon, has a peak around 900 nm and levels off toward shorter wavelength. Thus imaging wavelength close to the maximum of the quantum efficiency of the detector is desirable. An additional aspect is that in the visible range the photoreceptors of the retina will be very sensitive to light (tails of the absorption spectra reach into the infrared region). Hence, the subjective perception of the light power will increase rapidly at wavelength regions that are close or within the visible range. This is associated with increasing subject discomfort during imaging, even though the light levels that are sent to the eye have to be below the limits for safe exposure. In addition dispersion is more pronounced for shorter wavelength regions. Because of these issues the wavelength region around 840 nm has been found as compromise and is widely used in OCT for retinal imaging. Since line scan cameras in this wavelength region are easily available and relatively cheap, the preferred imaging technique in this wavelength region is SD-OCT.

Nevertheless, another wavelength region at 1060 nm which is around a local minimum of the water absorption spectrum (cf. Fig. 6) has gained interest in recent years. Due to the longer wavelength region the penetration depth within the retina can be increased and the influence of media opacities (such as cataract) on the image quality will be lower. Another advantage of this wavelength region is the availability of fast SSs. Thus high sensitivity can be maintained throughout the imaging depth which further improves the retinal image quality. Due to technical issues (dispersion introduced by fiber optics), SSs at 840 nm are relatively slow compared to their counterparts at 1060 or 1300 nm.

OCT Angiography

In recent years, OCT angiography (OCTA), a method to visualize vessel structure within tissue, has gained increasing interest. There are many different approaches to realize OCTA. The underlying basic principle, however, is the same for all methods. The idea is that two (or more) measurements (A-scans or B-scans) are taken at the same location but separated in time. By comparing these measurements changes (intensity or phase or both) caused by blood flow can be detected. The time separation between these

measurements needs to be short enough in order to minimize the influence of sample motion and long enough in order to ensure sufficient changes introduced by blood flow. With A-scan rates of 100 kHz or more the most common OCTA technique is based on recording several B-scans at the same location. This, however, increases the overall measurement time.

The major benefit of OCTA is that it provides information on the microvascular perfusion of tissue noninvasively. In addition, due to the spatial separation of capillaries, these can be visualized even though the lateral extension lies below the transverse resolution of the system. Other techniques that are capable to provide information on the vascular structure require the application of contrast agents. Some subjects may show allergic reactions or other complications after administration of such contrast agents. Thus state of the art angiographic imaging is always associated with residual risk factors. Another benefit of OCTA lies in the fact that depth resolved information on the vasculature is provided. This allows for a separation between individual vascular beds and thus an improved image contrast. It should be noted, however, that OCTA is not able to detect vessel leakages because the technique relies on motion contrast. Within leakages motion occurring between individual B-scan recordings will be too slow compared to subject motion to be detected in vivo. However, in vitro experiments have shown that without bulk sample motion slow fluid motion (such as Brownian motion) can be visualize with OCTA techniques.

Imaging of Human Skin

The human skin is easily accessible with optical methods. In clinical routine, lesions will be first inspected visually with high magnification using a microscope (dermatoscope). In the case of suspicious lesions a biopsy will be taken which will be sliced and prepared for histologic examination. The cellular details provided by this histologic examination can then be used to determine the malign or benign status of a lesion and finally determines the further clinical procedure. OCT may represent an alternative to the histologic examination as it provides in vivo and noninvasively cross-sectional images of skin. Current studies focus on improving the sensitivity and specificity of OCT methods for detecting malign tissue (Ulrich *et al.*, 2016). Thereby, additional contrast mechanism such as polarization sensitive OCT or OCTA are used to gather additional information. Especially OCTA provides essential additional information as tumors, such as basal cell carcinoma (BCC) are known to present with increased vascularization.

Using fiber-based or handheld systems practically every location can also be reached with OCT. In order to minimize scattering and absorption, the preferred imaging wavelength for human skin will be in the 1300 nm range. The penetration depth of OCT in skin is in the order of 1–2 mm. **Fig. 7** shows a representative B-scan image of a finger recorded with a 1310 nm SD-OCT instrument. The A-scan rate of the instrument was 91 kHz. The image consists of 500 A-scans and was recorded in ~5 ms. The bandwidth of the light source was 50 nm which results in an axial resolution of 10 μm in tissue (assuming a refractive index of 1.4). The power onto the skin was 8 mW. Individual layers of the skin can be clearly seen in **Fig. 7** and are labeled in the image.

Supplementary material related to this article can be found online at http://dx.doi.org/10.1016/B978-0-12-803581-8.09787-3.

An interesting skin region is the nail fold of a finger. In this region capillaries are close to the surface (close to the nail some capillaries extend parallel to the surface) and can be investigated with optical methods. In order to assess the status of the capillary network, capillaroscopy is used in clinical routine. This method examines the skin with a microscope after applying a contrast agent (such as oil) to the skin region. Using OCTA this network can be visualized completely noninvasively and without the

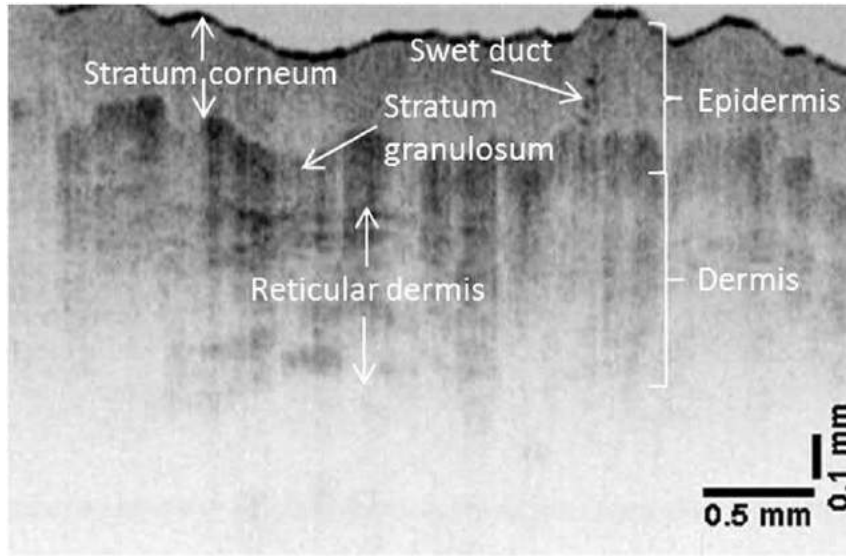


Fig. 7 Representative B-scan image recorded at 1300 nm of the inner side of a finger. Superficial layers down to deeper layers of the dermis can be visualized. The multimedia file (media 1) shows a fly through of B-scans of the entire three-dimensional (3D) data set.

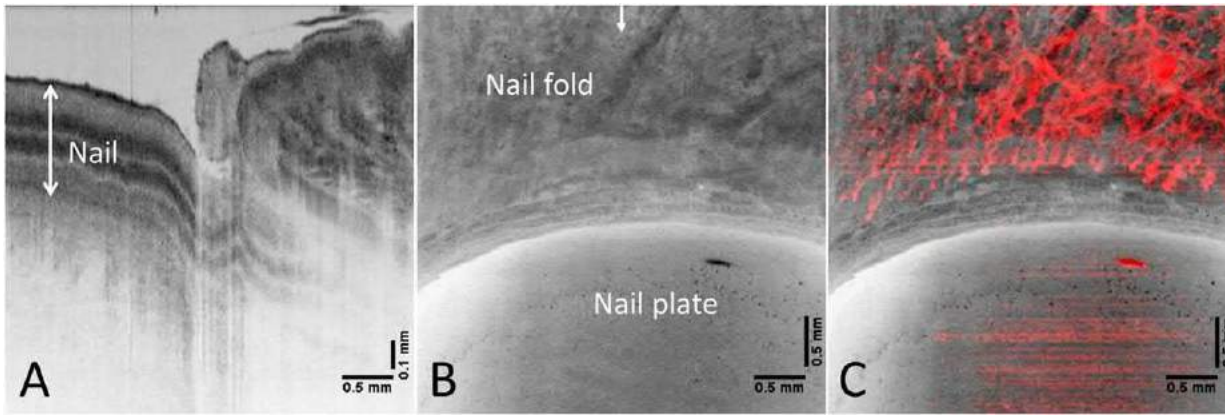


Fig. 8 Representative optical coherence tomography (OCT) images recorded in the nail fold region of a healthy volunteer. (A) OCT-intensity B-scan (averaged over 5 B-scans). (B) Depth integrated en-face intensity image. The arrow indicates the location of the B-scan displayed in (A). (C) Depth integrated en-face intensity image and overlaid (red) vessel map.

application of a contrast agent. **Fig. 8** shows representative image data recorded with the SD-OCT instrument described above. The intensity B-scan (**Fig. 8(A)**) clearly shows different structures such as the nail plate and different skin layers of the nail fold. The banding structure within the nail plate is an artifact that originates from birefringence of the plate. The sensitivity of the system is sufficient to penetrate through the nail plate as structures underneath the plate can be seen. The axial displacement of the nail plate beneath the nail fold (cf. right hand side in **Fig. 8(A)**) is caused by the increased optical path length that is introduced by light propagation through the overlying nail fold tissue. The en-face intensity projection clearly shows the different regions of the nail fold and nail plate. **Fig. 8(C)** shows a composite image where the depth integrated vessel structure is overlaid to the intensity image of **Fig. 8(B)**. In this image the capillary network can be clearly seen. Close to the nail plate individual capillary loops can be seen which are typical for this skin region.

Imaging of Human Retina

The human retina consists of several layers and represents an essential part for the vision process. All layers that can be seen in histology can be visualized with OCT. **Fig. 9** shows a representative OCT B-scan image of the fovea region with a labeling of the different retinal layers. In healthy subjects the fovea is the location of best visual acuity. In this region the highest density of cone photoreceptors can be found. These cells are responsible for photopic vision and can be distinguished into three types (sensitive in the short, medium, and long wavelength region). In the fovea no rod photoreceptors (responsible for scotopic vision) are present. The light is incident from the top of this image and has to penetrate different retinal layers until it is detected by the photoreceptors. The pigments of the photoreceptors are located within the outer segments of cones and rods. The image was recorded with a research grade prototype SD-OCT instrument operating at 863 nm with a bandwidth of 60 nm which resulted in an axial resolution of $\sim$4 μm in tissue (assuming a refractive index of 1.4). The A-scan rate was 70 kHz and one B-scan consisting of 1024 A-scans was recorded in $\sim$15 ms. Although the axial resolution is sufficient to resolve individual retinal layers, individual cells (such as photoreceptors) cannot be visualized. In order to increase the transverse resolution, aberrations that are introduced by imperfections of the eye optics need to be compensated for. This can be done with the implementation of adaptive optics, a technology known from astronomy (Pircher and Zawadzki, 2007).

Many commercial OCT devices for imaging the retina are available. **Fig. 10** shows representative data recorded with a commercial SD-OCT instrument. The instrument provides a scanning laser ophthalmoscope (SLO) overview mode that is used for retinal tracking. The location of the recorded B-scan is marked with a green line in the SLO image. The image quality is very similar to the previous image. The entire 3D data set can be viewed in media 2.

Supplementary material related to this article can be found online at http://dx.doi.org/10.1016/B978-0-12-803581-8.09787-3.

In order to outline the difference of retinal images recorded at different wavelengths, **Fig. 11** shows a retinal image recorded at 1040 nm. Compared to the previous images enhanced penetration into the choroid and even into the sclera can be seen. Otherwise all retinal layers can be seen with similar quality. The image was recorded with a research grade SS-OCT instrument operating at 100 kHz A-scan rate and 20 × 20 field of view. The axial resolution of the system was 5.6 μm in tissue.

Through a change in the scanning pattern (recording of several B-scans at the same location) angiographic data can be retrieved. **Fig. 12** shows representative data of a healthy volunteer recorded with a commercial instrument. The en-face projection images were generated through depth integration over the depth extension indicated with white arrows in **Fig. 12(A)**). **Fig. 12(B)**) shows cross-sectional angiographic data (red) overlaid to the intensity image. The contrast of retinal vessels is greatly increased using the angiographic data evaluation. The en-face projection of the intensity images (cf. **Fig. 12(C)**) shows larger vessels as shadows.

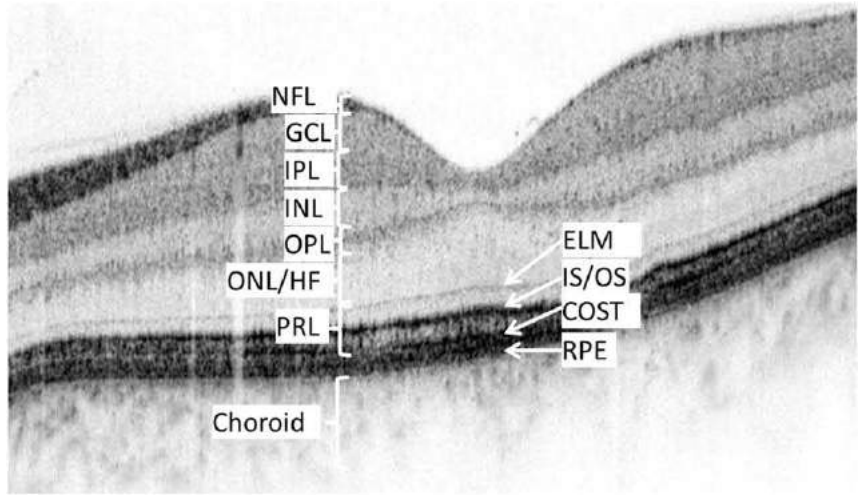


Fig. 9 Optical coherence tomography (OCT) image of the retina with a labeling of the different layers (the image spans an angle of 28 degree which corresponds to ~8 mm on the retina). COST, cone outer segment tips; ELM, external limiting membrane; GCL, ganglion cell layer; INL, inner nuclear layer; IPL, inner plexiform layer; IS/OS, junction between inner and outer segments of cone photoreceptors; ONL/HF, outer nuclear layer/Henle's fiber layer; OPL, outer plexiform layer; PRL photoreceptor layer; RNFL, retinal nerve fiber layer; RPE, retinal pigment epithelium.

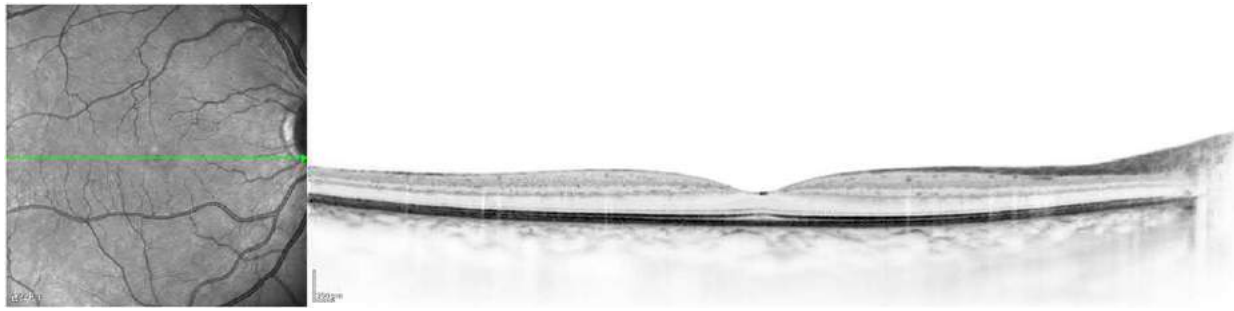


Fig. 10 Representative retinal image data of the fovea of a healthy volunteer recorded with a commercial instrument (imaging wavelength = 840 nm). Left: overview scanning laser ophthalmoscope (SLO) image. Right: optical coherence tomography (OCT) B-scan recorded at the location indicated in the left image with the green arrow. The multimedia file (media 2) shows a fly through of B-scans of the entire 3D data set.

However, the entire vascular structure can be seen in the corresponding OCTA projection map. This map clearly shows the avascular zone of the fovea region. From these maps deteriorations (such as non-perfused areas) from the normal vasculature structure can be easily determined.

Fig. 13 shows representative image data of patients with age related macular degeneration (AMD). AMD is regarded as one of the major causes of blindness in the industrialized world. The disease mainly affects the macula region (containing the fovea) of subjects that are older than 60 years. AMD can be differentiated into several forms: dry AMD and wet AMD. The latter is the most severe form which results (untreated) into a rapid degradation of visual acuity. An early indicator of AMD is the presence of Drusen. Drusen are elevations of the retinal pigment epithelium (RPE)/photoreceptor bands because of accumulation of retinal debris underneath these layers. Fig. 13(A) shows a typical example of OCT images recorded in a patient with Drusen. The elevations of the photoreceptors cause image distortions and degradation in visual acuity of the patient. At locations of the Drusen an additional layer (Bruch's membrane) can be seen. In the healthy case, this layer is obscured by the overlying RPE. Due to the highly scattering of the pigments within the RPE, this layer appears as broadened diffuse layer although it is a mono cellular layer. The 3D visualization of Drusen allows for a quantitative assessment of the size and volume of the Drusen. As such the effect of therapeutic interventions on the Drusen size can be precisely monitored.

The most severe form of AMD is choroidal neovascularization (CNV). In this case new vasculature is generated within the retina and leakages of these lead to damage of the sensitive neural tissue of the retina. Fig. 13(B) shows a representative B-scan of the fovea region of a patient with CNV. Scarring of retinal tissue and associated disintegration of photoreceptors is very often accompanied by this disease. Using OCT the size of edema or cysts can be quantified. In addition vascular growth can be determined using OCTA. Therapeutic intervention (such as anti-vascular endothelial growth factor (anti-VEGF) therapy) can be easily monitored and the technology can be meanwhile regarded as gold standard for this kind of diagnosis and for treatment control.

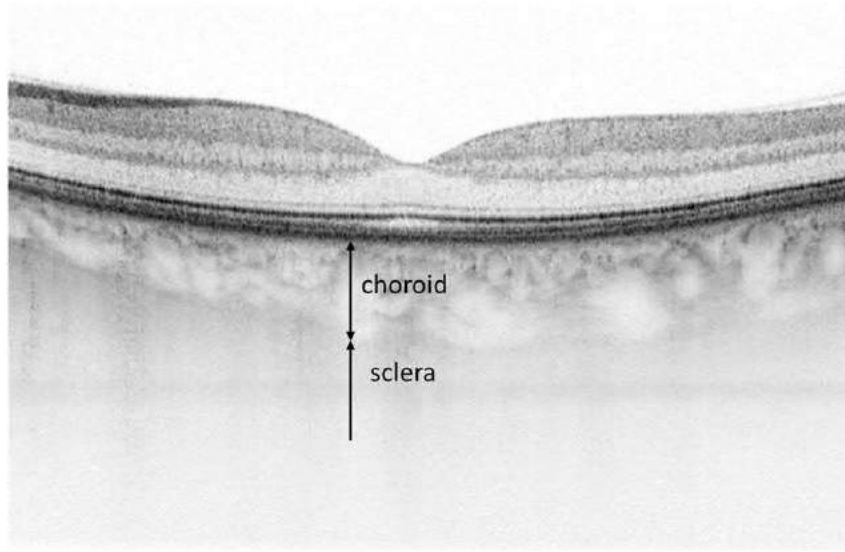


Fig. 11 Retinal image of the fovea of a healthy volunteer recorded with a swept source optical coherence tomography (SS-OCT) instrument at 1040 nm. Enhanced penetration into the choroid and sclera can be observed.

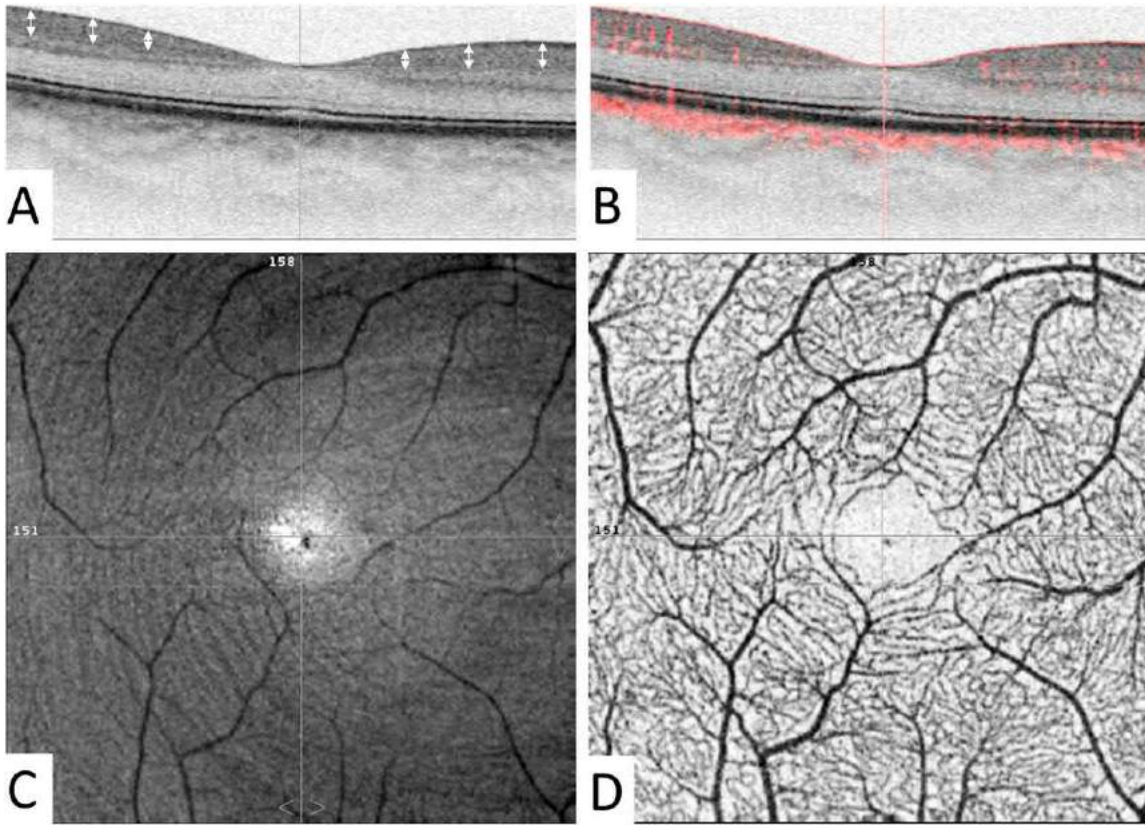


Fig. 12 Retinal images of the fovea of a healthy volunteer recorded with a commercial instrument. (A) Central B-scan of the volume scan. The arrows indicate the image depth that was used to generate the en-face images in (C) and (D). (B) Central B-scan of the volume scan and overlaid vessel structure (in red) retrieved with the angiography algorithm. (C) En-face intensity image (white = high intensity, black = low intensity) generated through depth integration over the area indicated in (A). En-face vessel map generated through maximum intensity projection of the angiographic data within the area indicated in (A).

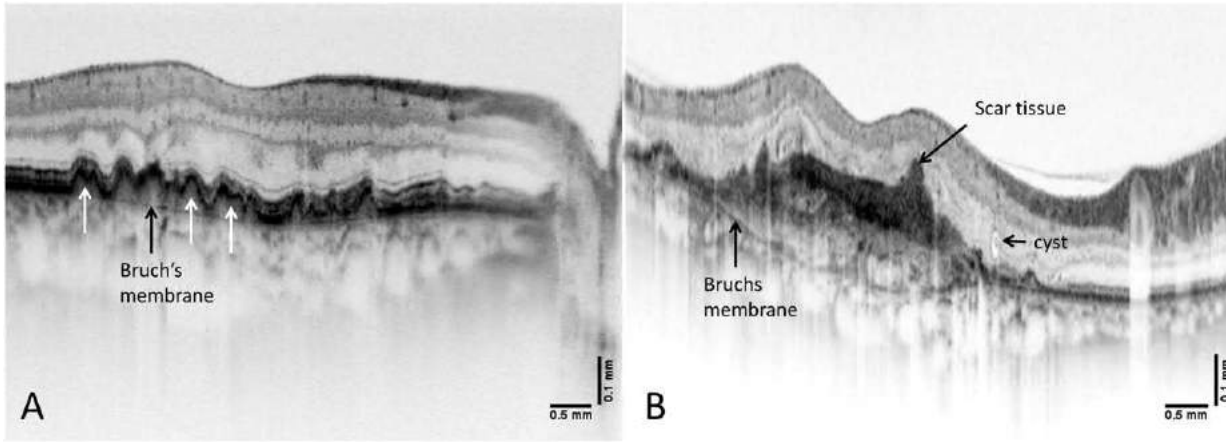


Fig. 13 Representative optical coherence tomography (OCT) B-scans (averaged over 50 frames) at 840 nm of patients with age related macular degeneration (AMD). (A) OCT B-scan image of Drusen (some are indicated by white arrows). The black arrow indicates Bruch's membrane. (B) OCT B-scan image of a choroidal neovascularization (CNV). Images are displayed on a logarithmic intensity scale.

There are many other retinal diseases where OCT plays a key role in diagnosis. A summary of the impact of OCT to all these diseases will be beyond the scope of this article. Nevertheless, one specific example should be mentioned: Glaucoma, a disease that is associated with visual field defects and one of the major causes for blindness worldwide. At an early stage of the disease, these defects occur in the periphery of the retina which is not easily noticeable by patients themselves because for reading etc. only the fovea region is used. Before changes in the visual field can be detected, a loss of retinal nerve fiber tissue (loss in layer thickness) will occur. The 3D imaging capabilities of OCT enable a precise measurement of the retinal nerve fiber layer thickness. Thus OCT provides an excellent indicator for early signs of Glaucoma and for monitoring therapeutic success.

Conclusion and Outlook

OCT is a very powerful imaging technology. With the development of FD-OCT imaging speed could be greatly improved and A-scan rates in the megahertz range have become possible. This paved the way for many new applications of OCT. This article focused on skin and retinal imaging but many more applications of OCT are available. Associated with the improved imaging speed is the possibility to investigate dynamic processes or to increase the contrast through the introduction of angiographic evaluation of OCT data. The noninvasive visualization of capillaries in tissue, such as skin or retina, opens completely new perspectives for clinical research. The high clinical demand of this technology manifests itself through the rapid commercialization of OCTA for both, skin, and retinal imaging. Thereby, OCT certainly plays a key role for accurate diagnosis especially in ophthalmic routine. Nevertheless, there are new developments in the field. Currently new SSs are developed that provide higher speeds (A-scan rates) and very long coherence lengths. Meanwhile, imaging depth ranges of some meters have been demonstrated with OCT. This opens new possibilities such as imaging of the whole eye (from the cornea to the retina) with a single SS-OCT system. In addition further parallelization of OCT is investigated. Line field OCT, for example, records one B-scan in parallel. Thereby SD-OCT (this requires an area detector in the spectrometer) or SS-OCT can be used. The latter uses a SS in combination with a line scan camera. Very high speeds (several volumes per second) can be achieved using a full-field illumination in combination with a SS and a very fast area camera. The demands on the camera are very high because the phase stability (to avoid "fringe washout") requires the recording of a volume within a short time frame (ideally below 1 ms). In order to have sufficient sampling points in depth (determined by the number of spectral lines) the frame rate of the camera needs to be in the order of 50 kHz. Apart from the high imaging speeds that are possible and that have been demonstrated for in vivo retinal imaging, the full-field technique provides phase stability over the entire field of view (in lateral direction). OCT provides direct access to the phase of the electric light field and computational techniques can be applied in order to compensate for aberrations introduced, for example, by the eye. Thus high resolution can be achieved even without the use of hardware-based adaptive optics. In addition, the focal plane of the image can be adjusted in post-processing. As such, an entirely sharp volume can be obtained with high transverse resolution despite of a limited DOF.

Apart from these developments, OCT has become a valuable tool in cardiovascular research. Using fiberized probes, OCT imaging can be done from inside the body, for example, within a coronary artery. As such plaques, deposits, or stents within the artery can be visualized in vivo. Key element for this development is the high imaging speed provided by OCT. Currently clinical trials are performed to demonstrate the benefit of cardiovascular OCT compared to state of the art examination tools.

Another development in the field is the combination of OCT with other imaging technologies. For example, the combination of OCT with photo acoustics has gained increasing interest. The photo acoustic technique relies on absorption of the probing light beam and provides a higher penetration depth but lower resolution than OCT. Therefore vasculature that is located deeper within

tissue can be visualized. The combination with OCTA enables the visualization of the entire vascular network as superficial capillaries are detected with OCT, while the deeper vascular structure is detected with photo acoustics.

Acknowledgments

The author likes to thank following people from the Medical University of Vienna for their assistance: Christoph K. Hitzenberger, Matthias Salas, Martin Fürst, Mitsuro Sugita, Teresa Torzicky, and Ursula Schmidt-Erfurth.

See also: Interferometric Imaging. Overview: Coherence

References

Drexler, W., Fujimoto, J., 2015. Optical Coherence Tomography, Heidelber. New York, NY: Springer.
Fercher, A.F., 2010. Optical coherence tomography – Development, principles, applications. Zeitschrift Fur Medizinische Physik 20, 251–276.
Izatt, J.A., Choma, M.A., Dhalla, A., 2015. Theory of optical coherence tomography. In: Drexler, W., Fujimoto, J.G. (Eds.), Optical Coherence Tomography. Heidelberg; New York, NY; Dordrecht; London: Springer.
Leitgeb, R., Hitzenberger, C.K., Fercher, A.F., 2003. Performance of Fourier domain vs. time domain optical coherence tomography. Optics Express 11, 889–894.
Pircher, M., Zawadzki, R., 2007. Combining adaptive optics with optical coherence tomography: Unveiling the cellular structure of the human retina in vivo. Expert Review of Ophthalmology 2, 16.
Stifter, D., 2007. Beyond biomedicine: A review of alternative applications and developments for optical coherence tomography. Applied Physics B-Lasers and Optics 88, 337–357.
Ulrich, M., Themstrup, L., De Carvalho, N., *et al.*, 2016. Dynamic optical coherence tomography in dermatology. Dermatology 232, 298–311.

TIRF Microscopy and Variants

Daniel Axelrod, University of Michigan, Ann Arbor, MI, United States

© 2018 Elsevier Ltd. All rights reserved.

Introduction

Total internal reflection fluorescence microscopy (TIRFM) is a method of illuminating a fluorescent sample so that only the zone proximal to the solid support (the "substrate") will be excited. This high excitation selectivity greatly reduces background fluorescence from regions farther from the substrate. TIRFM has found many applications in studies of cell/substrate contact, intercellular organelles near those contact regions, and exo-and endocytosis, as well as single molecules studies where out-of-focus background would otherwise make detection difficult.

Numerous reviews of TIRFM have been written (Schneckenburger, 2005; Axelrod, 2014), including a chapter in the Encyclopedia of Cell Biology, also published by Elsevier/Academic Press (Axelrod, 2016). Those works (and their references) and the references in this article should be consulted for mathematical details of the basic theory and optical configurations. The emphasis here is on qualitative effects and intuitive explanations, with no equations presented. This chapter will focus on TIR-related issues of lateral and axial resolution, polarization, multiphoton variations, refractive index measurement, scattering, and combinations of TIRFM with other optical techniques.

Qualitative Basic Principles

TIR occurs at a planar interface between two dielectrics (defined as $z=0$) of different refractive index when the angle of incidence as measured from the direction normal to the interface in the higher index material exceeds some critical angle. From the viewpoint of simple ray optics and Snell's Law, at that critical angle, the refracted beam propagating into the lower index material refracts away from the normal and skims along the surface. At higher angles, the beam reflects 100% back into the higher index material. From the viewpoint of wave optics, the incident plane waves approaching the interface at subcritical angles change direction at the interface due to their increased speed in the lower index medium. However, the spacing of the wavefronts on both sides of the interface, as they intersect the surface, must be equal. That requirement, along with the fixed wavelength for propagation in the low index medium (set by the frequency and speed of light there) determines the orientation of wavefronts in the low index medium. At the critical angle, the wavefronts in the lower index material are oriented normal to the interface. At higher incidence angles, the geometry would force the spacing of the wavefronts to be closer than can be supported as propagating light in the lower index material, so instead, the wavefronts becoming exponentially decaying in amplitude with distance along the normal direction (the "z-direction") to the substrate (Axelrod, 2013). This spatially-decaying field in z is called the "evanescent field" of TIR. It still has wavefronts moving along the surface with an amplitude at $z=0$ at least as large as the incident field's amplitude (and usually higher), and those sinusoidal electric field fluctuations are fully capable of exciting light-absorbing (and possibly fluorescing) molecules. The evanescent field can also be scattered by refractive index variations in the low index material and thereby partially converted back into propagating light. Those two mechanisms – absorption and scattering – of the evanescent field, decrease the amplitude of the reflected beam to less than 100%, but that decrement typically is very small.

Lateral Resolution

In its standard, high aperture microscope objective-based form, TIRF is made possible by focusing the incident beam to a small spot at the objective's back focal plane, sufficiently far off-axis so the beam emerges collimated from the objective, and heads toward the sample at greater than the critical angle. For this to work, the objective aperture must be greater than the refractive index of the medium on the low density side of the interface (1.33 for water) and preferably at least 1.4. In the space between the BFP and final emergence, the beam expands from its focus, so TIRF is necessarily a wide-field method, possibly illuminating the entire field of view. Reducing the area of illumination is certainly possible (by decreasing the angle of convergence/divergence) while retaining the incident beam's focus at the objective back focal plane (BFP). But as that convergence angle decreases, the size of the focal spot at the BFP necessarily increases by diffraction. The result is that the angle of incidence starts to spread, and some light may even spread into sub-critical angles, thereby polluting the purity of the evanescence.

But for some purposes, a very small lateral area of illumination at the TIR/sample plane is desirable. One such purpose is improve lateral resolution by combining TIRF with structured illumination microscopy (SIM). In standard SIM (Gustafsson *et al.*, 2000; Hirvonen *et al.*, 2009), excitation field is given a periodic illumination (in one or two dimensions). Then at least three successive images are recorded, each with the periodicity shifted by 120 deg in phase; a computer algorithm then recombines these images into a rendition of the original image with substantially increased resolution. (Qualitatively, this works because two fluorescent points spaced apart by a sub-resolution distance will "see" different excitation intensities on the steep slopes of the

 doi:10.1016/B978-0-12-803581-8.09481-9

periodic illumination, and that difference will change or even reverse as the phase is shifted.) One commercially-available way of producing a periodicity is simply to project onto the sample the shadow of a grating positioned at an equivalent sample plane in the excitation path. But the finer the periodic spacing, the higher will be the ultimate reconstructed resolution. By interfering pairs of oppositely directed and mutually coherent TIR beams (Chung *et al.*, 2007; Kner *et al.*, 2009; Fiolka *et al.*, 2012; Beach *et al.*, 2014), a striped interference pattern in the evanescent field can generated with a spacing that is significantly smaller than any that could be produced by either a projected grating or by interfering subcritical propagating beams.

This TIR-SIM procedure produces resolution improvement in one dimension only, the dimension transverse to the interference stripes. But two additional oppositely-directed coherent TIR beams (all split from the same laser source) can be introduced from the orthogonal direction, producing an interference checkerboard. This leads to improved resolution in both dimensions in the sample plane.

Conceptually extending this approach, evanescent fields could be configured to approach from many azimuthal directions simultaneously. These would all constructively interfere completely in only one location: at the very center of the field. In the most extreme case, an azimuthal circular ring of supercritical illumination will form a very tiny evanescent spot in the center, with a radius only about 2/3 of that obtainable by focusing subcritical laser beam (Axelrod, 2013). That spot would have not only the thin $\lambda/5$ to $\lambda/10$ axial decay length of standard wide-area TIRF but also an extremely small lateral size, thereby defining an illumination volume of only $\sim 0.005\ \mu m^3$. Such a small volume could be used for scanning (Chon and Gu, 2004; Terakado *et al.*, 2009), for highly confined FRAP, and for FCS.

To create this highly concentrated TIR illumination pattern, the incident light must be confined to a supercritical radius ring at the back focal plane. If the light is focused to a sharp annulus in that BFP region, the polar angle of incidence at the sample (and thereby the evanescent field depth at the sample) will be a well defined value. If the light is merely limited to that region but not focused there, the polar incidence angle (and evanescent field depth) will span a range of values. This is the approach used by Chon and Gu (2004); Terakado *et al.* (2009). The polarization of the ring at the BFP should be such that any azimuthal direction will produce an evanescent field polarization that can interfere with that of every other azimuthal direction, as done by Terakado *et al.* (2009); otherwise, the smallest possible spot at the sample plane will not be produced. The only possible BFP polarization that can do this is radial polarization, which can be implemented by commercially available circular grating plates (Beresna *et al.*, 2011).

In standard intersecting beam TIR-SIM pairs with a finite number of azimuthal angles, the best resolution depends on how small can be the spacing of the interference fringes. Use of the highest refractive index substrate helps, because that decreases the wavelength of the incident light in the substrate. Another approaches is to use a substrate that is imprinted with a periodic pattern spacing even smaller than the spacing of intersecting TIR beams. This can improve the resolution even farther. A grating also gives the optical system a resonance that increases the amplitude of the evanescent field for particular incidence angles and wavelengths. This occurs, for example, if the periodic grating spacing is an integral multiple of the incident light wavelength as measured along the TIR surface (Sentenac *et al.*, 2009).

TIR Polarization

The evanescent field is polarized according to the polarization of the incident beam. S-pol incident light (say, in the y direction, for incident light in the x-z plane) gives rise to s-pol evanescence (in this case, the y direction). P-pol incident light (say, in the x-z plane of incidence) gives rise to a p-pol evanescent field. The p-pol takes the form of an elliptical polarization, mainly along the z-direction but with some amplitude in the x-direction at a 90 deg phase difference. The characteristic decay distance of the evanescent electric field in the axial (z) direction is the same regardless of polarization.

The p-pol ability to produce a polarization in the z-direction is unique: standard EPI-illumination with excitation light directed along the axial direction produces only polarizations oriented in the sample plane, the x-y directions. That z-direction polarization cannot excite fluorophores whose dipoles lie parallel to the sample plane. But any deviation from parallelism can be excited. For example, a planar membrane labeled with a fluorophore (such as a carbocyanine dye with a double hydrocarbon tails such as diI or diD coupled by a conjugated bridge) whose excitation dipole lies in the local plane of the membrane will not be excited if the membrane itself lies parallel to the TIR substrate. But if the membrane is wavy or folded or has protrusions or indentations, those region will selectively "light up" under p-pol TIRF, against a dark background. This effect has been used to detect sites of endo- and exocytosis as they occur on living secretory cells (Steyer and Almers, 1999), and also to study the interaction and kinetics of fusion between lipid vesicles and planar supported membranes (Oreopoulos and Yip, 2009; Kiessling *et al.*, 2010). The technique requires that two images be recorded, one with p-pol, and one with s-pol for normalization. Optical designs to speed the switching and image acquisition have been devised (Johnson *et al.*, 2014).

Variable Polar Angle Illumination, Including Subcritical

The depth of the evanescent field is a function of incidence polar angle, decreasing rapidly from (theoretically) infinite right at the critical angle, down to about a single wavelength of light at about one degree higher than the critical angle, and farther down to about a tenth of the wavelength at skimming (90 deg) polar incidence angle. (However, the intensity of the evanescent field drops

monotonically with increasing incidence angle.) Another chapter in this Encyclopedia describes how this variation may be used to determine z-distance separation of a single fluorophore from a TIR surface, and previous reviews contain mathematical details. In principle, the z-dependent concentration C(z) of a fluorophore near a substrate could be inferred by performing an inverse Laplace transform to the TIRF intensity vs. polar incidence angle I vs. θ profile. In practice, various reasonable guesses for C(z) are tested by comparing their predicted I vs. θ profiles against actual measured profiles (Olveczky *et al.*, 1997; Oheim *et al.*, 1998). Variable-angle TIRF has also been used to measure the distribution of z-distances of whole secretory granules from the cell/substrate contact region (Rohrbach, 2000).

If the polar incidence angle is made to be slightly less than the critical angle, the incident beam refracts into the sample at a very high (but less than 90 deg) polar angle. If the subcritical incident beam were truly an infinitely-broad plane wave, as generally assumed in basic optical theory for TIR, then the z-depth in the lower index medium would be infinite. But in practice, a refracted beam skimming along the surface above the substrate has a finite depth. That depth is not easily controlled in commercial TIRF setups. But it can be estimated by viewing a fluorescent sample under epi-illumination with the angle of incidence adjusted to zero degrees (i.e., straight up in an inverted microscope, called "EPI-fluorescence"). The illuminated region will be roughly circular with fuzzy edges but with some characteristic radius on the sample. That radius (usually many micrometers) will be the approximate z-depth of the field of a barely subcritical beam when viewed at its position of emergence from the substrate. The emerging beam will form a "pencil" of light slowly diverging up from the substrate. By viewing the illuminated region "downbeam", several micrometers from where it emerged from the substrate, the full diameter of the beam propagates in the lower density medium. By laterally shifting the emergence location from the region under observation, the height of that pencil above the substrate can adjusted. This allows the ability to explore fluorescence from regions in that shaft of light at user-controllable varying depths into the sample, depths that are inaccessible to standard TIRF and yet do not excite as much out-of-focus background as does standard "straight-up" EPI. With a custom setup based around a free laser beam, rather than commercial setup based around an optical fiber, the radius of the illumination region can be controlled by changing the angle of convergence/divergence of the incident beam at the objective BFP: the smaller that angle, the smaller the radius and consequently the smaller the depth of the subcritical refracted beam. It should be possible to increase the lateral extent of the illumination without increasing the z-depth (i.e., to produce a sheet rather than a pencil) by use of a cylindrical lens.

Barely subcritical illumination has been given a variety of names in the literature: leaky TIRF, quasi-TIRF, pseudo-TIRF, and Highly Inclined and Laminated Optical sheet (HILO), and Variable Angle Epifluorescence microscopy, the last two of which are the most scientifically accurate since subcritical illumination is not TIR at all (Konopka and Bednarek, 2008; Lu *et al.*, 2013; Sun *et al.*, 2011; Tokunaga *et al.*, 2008).

Somewhat related to high angle subcritical illumination is "Light Sheet Microscopy", in that a relatively thin sheet of illumination (but not as thin as in TIR) is imposed on the sample at an adjustable height from the substrate. The optical setup can be elaborate, involving two objectives trained upon the sample from orthogonal directions, one for sheet illumination, the other for detection, with a specially configured sample holder at the intersection of the two objectives' focal planes (Weber *et al.*, 2014). Light-sheet microscopy has also been adapted for two-photon excitation, which produces a thinner effective sheet with less background (Zong *et al.*, 2015).

Even without varying the incidence angle, but just by setting it a slightly supercritical angle (to achieve a fairly deep evanescent field), the z-position of discrete sources can be deduced (at least over a couple of wavelength distance range), by analyzing the height and breadth of point spread function of the source (Mondal and Hess, 2017).

Two Photon TIRF

All of the above variants of TIRF are in the realm of linear optics (except for the very last one), in which the observed fluorescence is proportional to the first power of the illumination intensity. Multiphoton microscopy, by producing emission proportional to at least the second power of the illumination, has been used to greatly improve axial resolution in scanning focal-spot microscopies. It is reasonable to think that two-photon TIRF excitation should have the ability to halve the effective evanescent field depth and thereby produce even more z-selectivity than standard TIRF. In practice, the standard multiphoton illumination source is a pulsed laser with a near IR emission. In linear mode, that would produce a deeper evanescent field than would visible light, because the evanescent field depth is proportional to wavelength. In two-photon mode, the evanescent field depth is indeed halved, but that only brings it back down to what would have been obtained from single photon visible light.

The real advantage of multiphoton TIRF is further suppression of background scattering. Scattering from a variety of sources (see sections below) can be significant, but generally it is less intense than the evanescent field itself (at least near $z=0$). With its non-linear favoring of the brightest places, multiphoton techniques give an advantage to the pure evanescent field over background scattering (Oheim and Schapper, 2005; Lane *et al.*, 2012).

The Reflected Beam in TIR

The depth of the evanescent field is a function of the local refractive index on the low-index side of the interface. For any fixed supercritical incidence angle and particular substrate, the depth increases as the refractive index increases, and the dependence is

rather steep for barely supercritical angles. Unfortunately, the sample's refractive index is usually not known accurately, and may even vary laterally with heterogeneous samples. TIR itself, without the fluorescence, can provide the unknown information.

In TIRF, attention is on the evanescent field, and upon the detection of fluorescence that it excites. But the (nonfluorescent) reflected beam itself contains information about the sample. By replacing the standard dichroic mirror (used to reflect the incident beam up though the objective to the sample and block the transmission of the reflected beam) with a standard 100% mirror positioned only partway across the aperture, the reflected beam can be captured. The microscope/detector optical system that normally would image the fluorescence will now image the reflected beam itself. The image is not sharp (because only a fraction of the objective aperture is used), but it has an interesting feature. At image locations corresponding to locations in the sample where the refractive index is low (say, off-cell on a cell culture), TIR is achieved and the reflection is bright whereas locations with low refractive index are subcritical and the reflection is dim. As the incidence angle is increased stepwise over a stack of images, the transition from subcritical to supercritical is quite distinct, and the transition occurs over a specific narrow range of angles that is very sensitive to local refractive index. By analyzing the image stack, the spatially-resolved refractive indices of a cell culture's contact regions with the substrate can be calculated. A bonus result is a measure of the separation between the bottom of the cell and the substrate because increased separation affects the steepness of the local reflected intensity increase with angle (Bohannon *et al.*, 2017).

In principle, the reflected beam's polarization also contains information about sample refractive index. If the incident beam is linear polarized at 45 deg (i.e., half s-pol and half p-pol), the two polarizations suffer different phase delays upon TIR. The reflected beam then will be elliptically polarized, to an extent that depends on local refractive index of the sample.

A coherent collimated supercritical angle incident beam before the TIR surface is a plane wave, but interaction with the laterally variable sample index sample distorts the wavefront flatness. By interfering the reflected beam with a plane wave reference beam from the same source, a hologram of the sample can be recorded digitally (Ash *et al.*, 2010).

Supercritical Angle Emission

As discussed in another article in this Encyclopedia, an excited fluorophore embedded in a low refractive index near a higher index planar substrate will produce an emission pattern that is very different from what it would produce in isolation: see Axelrod (2013) for mathematical details. Part of this effect is simple refraction of the emitted light into the substrate, thereby changing its propagation direction. All of the propagating emission light is bent into angles that are "subcritical", leaving higher polar emission "supercritical" angles dark. But a major part of the effect is due to the existence of the fluorophore's "near field", evanescent light that does not propagate away from the fluorophore vicinity. If the substrate is close enough (within about a wavelength), it will capture some of the near field, convert it to propagating light, and send it into those high supercritical polar angles in the substrate material. In fact, the brightest emission propagates exactly at the border between sub and supercritical, at the "critical" angle itself. The exact critical angle is quantitatively related to the refractive index of the material in which the fluorophore is embedded.

To measure that critical angle, the sample's emission is collected with a high aperture objective, often the same as one that would be used for TIR excitation (i.e., NA generally greater than 1.4). The objective's back focal plane reveals a one-to-one mapping of emission angles into radial positions. By recording images of the brightest ring in the back focal plane, and measuring its radius, the sample' refractive index can be computed (Brunstein *et al.*, 2017). Unfortunately, spatial information is lost, because emission light from any location in the image plane passes through all areas of the back focal plane. However, if the excitation region on the sample could be restricted and scanned, then spatially-localized refractive index information could be recovered.

TIR Scattering

An important limitation of TIRF is scattering of the incident light. Part of this scattering originates in the excitation path of the optical system itself, particular in objective-based TIRF. Mattheyses and Axelrod (2005) found this to constitute about 10% of the intensity at $z=0$. This is probably much less in prism-type TIRF because the excitation path there is largely out of the field of view. Brunstein *et al.* (2014a,b) found that the scattering originating in the optical system is generally larger than the scattering of evanescent light by a cell culture sample, at least for flat and confluent cultures. However, for thicker or denser cells, sample-induced scattering could be greater. This is a problem because the scattered light can excite fluorescence at z-distances well beyond the reach of the evanescent field itself.

One kind of scattering is generated when an "object", a portion of the sample generally larger than one wavelength, has a refractive index too high to support TIR at the incidence angle used. That higher refractive index can be spaced away from the TIR surface within about a wavelength, and still capture some of the evanescent field energy and convert it to propagating light: this is called "frustrated TIR". That propagating light can then scatter or even become trapped in structures that cause it to total reflect multiple times (such as in spherical beads). Another complication occurs because frustrated TIR disrupts the evanescent field, leaving downbeam objects in the sample in a shadow. It also can lead to multiple reflections between the sample object and the TIR surface, so that the object no longer "sees" a pure exponentially decaying field.

Of particular interest is scattering resulting from refractive index gradients in the sample, even if all regions have a low enough refractive index to support TIR at the given incidence angle. The simplest case is a sphere residing in an evanescent field. (The

sphere may be considered a simplified model of a biological cell in a TIRF experiment.) This is a special case of Mie scattering, which results from a propagating plane wave hitting a dielectric object larger than a small fraction of the wavelength. The results of such a calculation (Ganic *et al.*, 2002) show that the scattering pattern is very different for propagating plane wave scattering vs. evanescent scattering; much of the symmetry is lost in the evanescent case. The angular pattern is also very dependent on the incident polarization. An alternative calculation (Bekshaev *et al.*, 2013) recasts the plane wave to have an imaginary incidence angle; this is equivalent to an evanescent wave. In both cases, the results explicitly shown are for the case where the refractive index of the spheres is high enough to cause "frustrated" TIR, but the mathematical techniques should be valid also for spheres with much lower index. Neither approach accounts for optical interactions with the TIR surface (such as multiple reflections, capture of evanescent fields on the surface of the sphere by the TIR substrate, etc.), nor for multiple scattering, refocusing, and shadowing among nearby spheres. There is room for useful theoretical work in this area.

Interactions between the TIR surface and the sphere are taken into account by Liu *et al.* (2000). The radius of the sphere, in combination with the wavelength, leads to sharp resonances in the intensity of scattering, which also depends on separation distance of the sphere to the substrate compared to the radius. The calculations, however, assumed that the sphere was made of the same material as the planar substrate, and therefore is not directly relevant to practical TIRF, where the biological cell under view has a refractive index much lower than the TIR substrate so that an evanescent field can exist inside the cell.

An alternative approach to the TIR scattering problem dispenses with the single sphere and instead postulates a rough surface (Nieto-Vesperinas and Sanchez-Gil, 1992). In the theory, the roughness could be periodic, or a known function, or a randomly generated function. However, predicting scattering in practical TIRF is a somewhat different case, because the "roughness" is not in the (high index) substrate, but in a lower index layer (the cells) adhered to a smooth substrate.

TIR fluorescence microscopy was originally an outgrowth of prism-based TIR illumination in which the (non-fluorescent) scattering was collected and imaged through a microscope (Ambrose, 1956). TIR scattering, both static and dynamic (in which coherent scattered light from multiple scattering centers interferes and causes random intensity fluctuations), ca be used to observe the behavior – positions and motions – of small objects or colloidal particles near the TIR surface (Sigel, 2009).

TIR Combined With FRAP or FCS or FLIM

A very early application of TIRF microscopy was actually not for imaging at all, but for measuring the dynamics of biomolecules at surfaces: on/off chemical kinetic rates and surface diffusion. When looking at a fluorescent solution with subcritical angle illumination ("EPI") through a microscope, the fluorescence looks unchanging and uniform (apart from interference fringes if a coherent laser source is used). But when the incidence angle is increased to the critical angle and beyond, the view quickly changes to a more speckly appearance that also "twinkles" as molecules diffuse in and out of the thin evanescent region. By measuring the amplitude and rapidity of these fluctuations in a small lateral region (by autocorrelation of the fluorescence intensity), the absolute concentration, the reversible binding rates, and any surface diffusion can all be inferred (Thompson *et al.*, 1981, 2009; Thompson and Steele, 2007), a technique called TIR-Fluorescence Correlation Spectroscopy (TIR-FCS).

A different but related procedure, called TIR-Fluoresence Recovery After Photobleaching (TIR-FRAP) also measures kinetic rates and diffusion but calls for photobleaching the region near the substrate with a bright flash of TIR "bleach" illumination and then monitoring the post-bleach fluorescence recovery with a much dimmer TIR "probe" illumination. To see diffusion in a short experimental time, it is useful to reduce the area of illumination. One way is to shape it into a line (Burghardt and Axelrod, 1981). Another is to intersect two TIR beams, forming interference stripes, much in the manner of structured illumination but for a different purpose (Fulbright and Axelrod, 1993).

TIR-FRAP has been applied to measuring the diffusion of fluorescent-marked proteins inside secretory granules of living cells (Ngatchou-Weiss *et al.*, 2014) These spherical granules are small ($\sim$ 300 nm in diameter), but the evanescent field depth is even smaller (usually $<$100 nm). Therefore, the TIR bleaching flash will photobleaching mainly those proteins in the part of the granule most proximal to the TIR substrate. Recovery will occur during the probe phase of the experiment due to diffusive redistribution of protein within the granule, and its rate can be interpreted in terms of a diffusion coefficient. Care must be taken, as in all FRAP experiments, to account for spontaneous "reversible" recovery after photobleaching that may occur in the millisecond to tens of millisecond time scale, even in the absence of diffusion.

The nearby presence of a dielectric surface can affect the fluorescence lifetime of a fluorophore. This occurs by several possible mechanisms. One of them is the interaction of the surface with the fluorophore's near field. This provides an additional path for energy to be drained from the excited state, shortening the lifetimes. Another mechanism is the change in the chemical environment near a surface: viscosity, ionic strength, accessibility of quenchers, etc. Since much biological fluorescence microscopy observes cells very near a supporting substrate (the coverslip), fluorescence lifetime imaging microscopy (FLIM) techniques have been combined with TIRF to specifically study the surface effects. The setup and applications are reviewed in Gadella (2009).

TIRF on Single Molecules

Detection of single molecules with single attached fluorophores is challenging in part because the number of photons available from a single fluorescent molecule before it photobleaches away is quite limited, typically less than one million, and many of these

photons may be absorbed or may miss the detector system. With few available photons, shot noise in the signal (due to the randomness of photon emission and detection) makes it imperative that other extraneous noise sources be reduced. One of the most common features in fluorescence microscopy is background, and even if it is constant in intensity, it can still produce its own shot noise that will bury the signal from the single fluorophore. TIRF has been effective in suppressing background, so it is used commonly in single molecule fluorescence detection. For reviews of the single molecule field in general, see Lord *et al.* (2010) and for a theoretical focus on the optical aspects, see Axelrod (2012).

A particularly unique aspect of single molecule studies is the ability to "see" the orientation of an immobilized molecule, not just to detect its existence. Some information about orientation can be gleaned from viewing the emission focused at the sample plane with polarizing filters, but the information can be ambiguous. As an alternative, analysis of the azimuthal distribution of emission at the back focal plane (BFP) of the objective (Burghardt and Ajtai, 2009) removes the ambiguity.

See also: Overview: Microscopy

References

Ambrose, E.J., 1956. A surface contact microscope for the study of cell movements. Nature 178, 1194.

Ash III, W.M., Clark, D., Lo, C.-M., Kim, M.K., 2010. Total internal reflection holographic microscopy for quantitative phase characterization of cellular adhesion. Proc. of SPIE 7568. doi:10.1117/12.842470.

Axelrod, D., 2012. Fluorescence excitation and imaging of single molecules near dielectric-coated and bare surfaces: A theoretical study. J. Microscopy 247, 147–160.

Axelrod, D., 2013. Evanescent excitation and emission in fluorescence microscopy. (Invited review) Biophys. J. 104, 1401–1409. (Correction, 104:2321).

Axelrod, D., 2014. Evanescent excitation and emission. In: Cornea, A., Conn, P.M. (Eds.), Fluorescence Microscopy: Super-Resolution and Other Novel Techniques. Elsevier, pp. 1–14.

Axelrod, D., 2016. Total internal reflection fluorescence microscopy. In: Bradshaw, R.A., Stahl, P.D. (Eds.), Encyclopedia of Cell Biology 2. Academic Press, pp. 62–69.

Beach, J.R., Shao, L., Remmert, K., *et al.*, 2014. Nonmuscle myosin II isoforms coassemble in living cells. Curr. Biol. 24, 1160–1166.

Bekshaev, A.Y., Bliokh, K.Y., Nori, F., 2013. Mie scattering and optical forces from evanescent fields: A complex-angle approach. Opt. Express 21, 7082–7095.

Beresna, M., Gecevičius, M., Kazansky, P.G., Gertus, T., 2011. Radially polarized optical vortex converter created by femtosecond laser nanostructuring of glass. Appl. Phys. Lett. 98. doi:10.1063/1.3590716.

Bohannon, K.P., Holz, R.W., Axelrod, D., 2017. Refractive index imaging of cells with variable-angle near-TIR microscopy. Microsc. Microanal. 1–11. doi:10.1017/S1431927617012570.

Brunstein, M., He'rault, K., Oheim, M., 2014b. Eliminating unwanted far field excitation in objective-type tirf. Part II. Combined evanescent-wave excitation and supercritical-angle fluorescence detection improves optical sectioning. Biophys. J. 106, 1044–1056.

Brunstein, M., Roy, L., Oheim, M., 2017. Near-membrane refractometry using supercritical angle fluorescence. Biophys. J. 112, 1940–1948.

Brunstein, M., Teremetz, M., He'rault, K., Tourain, C., Oheim, M., 2014a. Eliminating unwanted far-field excitation in objective-type TIRF. Part I. Identifying sources of nonevanescent excitation light. Biophys. J. 106, 1020–1032.

Burghardt, T.P., Ajtai, K., 2009. Mapping microscope object polarized emission to the back focal plane pattern. J. Biomed. Opt. 14, 034036.

Burghardt, T.P., Axelrod, D., 1981. Total internal reflection/fluorescence photobleaching recovery study of serum albumin adsorption dynamics. Biophys. J. 33, 455–468.

Chon, J.W.M., Gu, M., 2004. Scanning total internal reflection fluorescence microscopy under one-photon and two-photon excitation: Image formation. Appl. Opt. 43, 1063–1071.

Chung, E., Kim, D., Cui, Y., Kim, Y.-H., So, P.T.C., 2007. Two-dimensional standing wave total internal reflection fluorescence microscopy: Superresolution imaging of single molecular and biological specimens. Biophys. J. 93, 1747–1757.

Fiolka, R., Shao, L., Rego, E.H., Davidson, M.W., Gustafsson, M.G., 2012. Time-lapse two-color 3D imaging of live cells with doubled resolution using structured illumination. Proc. Natl. Acad. Sci. USA 109, 5311–5315.

Fulbright, R.M., Axelrod, D., 1993. Dynamics of nonspecific adsorption of insulin to erythrocyte membrane. J. Fluor. 3, 1–16.

Gadella, T.W.J., Jr., (Ed.), 2009. Total internal reflection fluorescence lifetime imaging microscopy. In: Laboratory Techniques in Biochemistry and Molecular Biology, 33.

Ganic, D., Gan, X., Gu, M., 2002. Three-dimensional evanescent wave scattering by dielectric particles. Optik 113, 135–141.

Gustafsson, M.G.L., Agard, D.A., Sedat, J.W., 2000. Doubling the lateral resolution of wide-field fluorescence microscopy using structured illumination. Proc. SPIE 3919, 141–150.

Hirvonen, L.M., Wicker, K., Mandula, O., Heintzmann, R., 2009. Structured illumination microscopy of a living cell. Eur. Biophys. J. 38, 807–812.

Johnson, D.S., Toledo-Crow, R., Mattheyses, A.L., Simon, S.M., 2014. Polarization-controlled TIRFM with focal drift and spatial field intensity correction. Biophys. J. 106, 1008–1019.

Kiessling, V., Domanska, M.K., Tamm, L.K., 2010. Single SNARE-mediated vesicle fusion observed in vitro by polarized TIRFM. Biophys. J. 99, 4047–4055.

Kner, P., Chhun, B.B., Griffis, E.R., Winoto, L., Gustafsson, M.G.L., 2009. Super-resolution video microscopy of live cells by structured illumination. Nat. Methods 6, 339–342.

Konopka, C.A., Bednarek, S.Y., 2008. Variable-angle epifluorescence microscopy: A new way to look at protein dynamics in the plant cell cortex. Plant J. 53, 186–196.

Lane, R.S.K., Macpherson, A.N., Magennis, S.W., 2012. Signal enhancement in multiphoton TIRF microscopy by shaping of broadband femtosecond pulses. Opt. Express. 25948–25959.

Liu, C., Weigel, T., Schweiger, G., 2000. Structural resonances in a dielectric sphere on a dielectric surface illuminated by an evanescent wave. Opt. Commun. 185, 249–261.

Lord, S.J., Lee, H.-L.D., Moerner, W.E., 2010. Single-molecule spectroscopy and imaging of biomolecules in living cells. Anal. Chem. 82, 2192–2203.

Lu, W., Xia, T., Xu, L., Chen, Y.-G., Fang, X., 2013. Visualization of the post-Golgi vesicle mediated transportation of TGF-β receptor II by quasi-TIRFM. J. Biophotonics 7, 788–798.

Mattheyses, A., Axelrod, D., 2005. Direct measurement of evanescent field profile and depth in TIRF microscopy. J. Biomed. Opt. 11, 014006.

Mondal, P.P., Hess, S.T., 2017. Total internal reflection fluorescence based multiplane localization microscopy enables super-resolved volume imaging. Appl. Phys. Lett.. doi:10.1063/1.4983786.

Ngatchou-Weiss, A., Bittner, M.A., Holz, R.W., Axelrod, D., 2014. Protein mobility within secretory granules. Biophys. J. 107, 16–25.

Nieto-Vesperinas, M., Sanchez-Gil, J.A., 1992. Light scattering from a random rough interface with total internal reflection. J. Opt. Soc. Am. A 9, 424–436.

Oheim, M., Loerke, D., Preitz, B., Stuhmer, W., 1998. A simple optical configuration for depth-resolved imaging using variable angle evanescent-wave microscopy. "Optical Microscopy". SPIE 3568, 131–140.

Oheim, M., Schapper, F., 2005. Non-linear evanescent-field imaging. J. Phys. D Appl. Phys. 38, R185–R197.

Olveczky, B.P., Periasamy, N., Verkman, A.S., 1997. Mapping fluorophore distributions in three dimensions by quantitative multiple angle-total internal reflection fluorescence microscopy. Biophys. J. 73, 2836–2847.
Oreopoulos, J., Yip, C.M., 2009. Combinatorial microscopy for the study of protein–membrane interactions in supported lipid bilayers: Order parameter measurements by combined polarized TIRFM/AFM. J. Struct. Biol. 168, 21–36.
Rohrbach, A., 2000. Observing secretory granules with a multiangle evanescent wave microscope. Biophys. J. 78, 2641–2654.
Schneckenburger, H., 2005. Total internal reflection fluorescence microscopy: Technical innovations and novel applications. Curr. Opin. Biotechnol. 16, 13–18.
Sentenac, A., Belkebir, K., Giovannini, H., Chaumet, P.C., 2009. High-resolution total internal-reflection fluorescence microscopy using periodically nanostructured glass slides. J. Opt. Soc. Am. A 26, 2550–2557.
Sigel, R., 2009. Light scattering near and from interfaces using evanescent wave and ellipsometric light scattering. Curr. Opin. Colloid Interface Sci. 14, 426–437.
Steyer, J.A., Almers, W., 1999. Tracking single secretory granules in live chromaffin cells by evanescent-field fluorescence microscopy. Biophys. J. 76, 2262–2271.
Sun, W., Xu, A., Marchuk, K., Wang, G., Fang, N., 2011. Whole-cell scan using automatic variable-angle and variable-illumination-depth pseudo-total internal reflection fluorescence microscopy. J. Lab. Autom.. 255–262.
Terakado, G., Watanabe, K., Kano, H., 2009. Scanning confocal total internal reflection fluorescence microscopy by using radial polarization in the illumination system. Appl. Opt. 48, 1114–1118.
Thompson, N.L., Burghardt, T.P., Axelrod, D., 1981. Measuring surface dynamics of biomolecules by total internal reflection with photobleaching recovery or correlation spectroscopy. Biophys. J. 33, 435–454.
Thompson, N.L., Steele, B.L., 2007. Total internal reflection with fluorescence correlation spectroscopy. Nat. Protocols 2, 878–890.
Thompson, N.L., Wang, X., Navaratnarajah, P., 2009. Total internal reflection with fluorescence correlation spectroscopy: Applications to substrate-supported planar membranes. J. Struct. Biol. 168, 95–106.
Tokunaga, M., Imamoto, N., Sakata-Sogawa, K., 2008. Highly inclined thin illumination enables clear single-molecule imaging in cells. Nat. Methods 5, 159–161. (Addendum, 455).
Weber, M., Mickoleit, M., Huisken, J., 2014. Light sheet microscopy. Methods Cell Biol. 123, 193–215.
Zong, W., Zhao, J., Chen, X., *et al*., 2015. Large-field high-resolution two-photon digital scanned light-sheet microscopy. Cell Res. 25, 254–257.

Further Reading

Axelrod, D., 2007. Total internal reflection fluorescence microscopy. In: Török, P., Kao, F.-J. (Eds.), Optical Imaging and Microscopy: Techniques and Advanced Systems, Springer Series in Optical Sciences., second ed., Berlin: Springer, pp. 195–236.

Super-Resolution Depth Measurements: Variable Angle TIRF, Super-Critical Angle Fluorescence, MIET

Alexey Chizhik, University of Göttingen, Göttingen, Germany

© 2018 Elsevier Ltd. All rights reserved.

Introduction

Fluorescence microscopy is one of the most commonly used techniques for studying biological samples. It allows one to observe live samples in real time; the technical simplicity of fluorescence imaging techniques makes it accessible for a broad community of life-science researchers; and finally, specific labelling allows one to directly visualize sub-cellular structures. Moreover, in contrast to X-ray, electron, or atomic force microscopy, optical microscopy allows one to perform 3D imaging of thick samples up to hundreds of micrometers. However, the wave nature of light limits the spatial resolution of a conventional fluorescence microscope, i.e., it cannot resolve structures smaller than the diffraction limit. In the visible spectral range, this corresponds to a spatial resolution of roughly half a micrometer along the optical (z-) axis, and of about a quarter of a micrometer in the x-y plane. Abbe's equation,

$$d = \frac{\lambda}{2n\sin\alpha} \tag{1}$$

which was formulated in 1873, relates the resolution d of a lens with its numerical aperture $\mathrm{NA} = n \cdot \sin(\alpha)$, and with the wavelength λ of light. **Fig. 1** shows a simulated diffraction limited focal spot formed by focusing a linearly polarized light of 488 nm with a perfectly designed lens of 1.2 NA into water. These are the parameters of a typical microscope that is used for the biological imaging, and the size of the shown focal spot defines the resolution of the system.

For more than a century, the diffraction barrier imposed by the wave nature of light seemed to be insurmountable. The fundamental step towards a change of perception of optical resolution was made only by the end of the 20th century, when 4Pi microscopy enhanced the axial (along optical axis) resolution by almost a factor of 7 (Hell and Stelzer, 1992). This invention was followed by the invention of numerous fluorescence imaging techniques, which meanwhile allow one to achieve nearly nanometer resolution (Hell, 2003, 2009; Huang *et al.*, 2009). All existing super-resolution microscopy methods can be mostly divided into the two general groups according to their fundamental principle of resolution enhancement: deterministic, and stochastic techniques (Hell, 2003, 2009; Huang *et al.*, 2009). Increase of optical resolution in deterministic methods is based on the nonlinearity of fluorescence excitation. This group of methods includes STED, I^5M, RESOLFT, SIM and their derivatives. The second group of super-resolution imaging techniques employs reversible stochastic photo-switching of fluorophores between photo-active and inactive states, which can be partially tuned using various physico-chemical parameters. Among these methods are STORM, dSTORM, PALM, GSD, SPDM, SOFI and variants thereof.

Whereas some of the above techniques squeeze the lateral resolution down to some tens of nanometers, the much less axial resolution remains a key limiting factor for applications where z-sectioning of a sample is required. This drawback of almost all super-resolution microscopy methods stimulated the appearance of another class of high-resolution axial imaging methods, either independent or complementary to the methods that enhance lateral resolution.

To avoid confusion, it should be noted that not all of the high-resolution axial imaging methods, which will be discussed below, can be technically attributed to the family of super-resolution microscopy. Whereas the term "super-resolution microscopy" implies a resolution of two or more closely located emitters located *on the same* axis, these techniques axially localize *single*

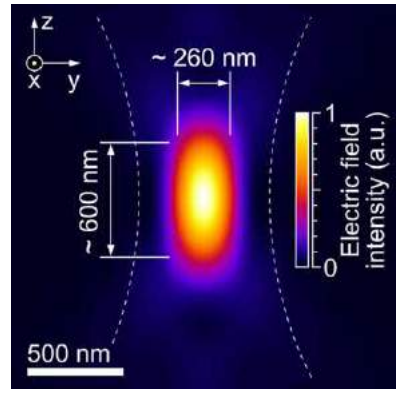


Fig. 1 The side view of the simulated diffraction limited focal spot created by 488 nm linearly polarized light when focused in water with a 1.2 NA objective lens. The dashed curves schematically show the direction of light focusing. Calculations are done by the methods of Jörg Enderlein, see Ref. Enderlein *et al.* (1999).

fluorophores (or in more general case fine structures) with nanometer accuracy. Later in the text, we will not emphasize this difference; however, it is important to keep it in mind to understand the limitations of the techniques discussed below.

Existing high-resolution axial imaging methods are based on several general approaches. First, the axial localization of a fluorophore can be determined by detecting it with different positions of the focal plane (biplane imaging (Juette *et al.*, 2008)), or by tailoring the shape of the point spread function (PSF) (astigmatic imaging (Huang *et al.*, 2008), helical wavefront shaping (Pavani *et al.*, 2009)). With such methods, one achieves ca. 70 nm axial resolution and ca. 30 nm lateral resolution. In all cases, the axial resolution is typically worse by a factor of 3–5 than the lateral one.

The second general approach is deducing the axial position of an emitter from relative intensities of single-fluorophore images when employing an interferometric detection system. Interferometric PALM (iPALM) (Shtengel *et al.*, 2009) and 4pi-STORM (Aquino *et al.*, 2011) approach single nanometer *z*-localization accuracy. However, the high technical complexity of the required optical system, and the need for tedious sample preparation and adjustment limit their applicability for routine microscopy measurements. Technically simpler coherent optical microscopy methods such as RICM (Limozin and Sengupta, 2009), or iSCAT (Kukura *et al.*, 2009) routinely achieve nanometer or even sub-nanometer localization accuracy of scattering/reflecting objects along the optical axis. However, the drawbacks of these methods are the lack of specificity of the imaged structures, and the reduced sensitivity when compared with most fluorescence-based methods.

In this article, we will focus on three distinct techniques for high resolution axial imaging, which combine unprecedented nanometer resolution with technical simplicity: Supercritical Angle Fluorescence (SAF) (Ruckstuhl and Verdes, 2004; Deschamps *et al.*, 2014), variable-angle Total Internal Reflection Fluorescence (TIRF) (Cardoso Dos Santos *et al.*, 2016; Stock *et al.*, 2003), and Metal Induced Energy Transfer (MIET) (Chizhik *et al.*, 2014; Karedla *et al.*, 2014; Baronsky *et al.*, 2017) microscopy. Despite the differences in their technical principle, all three methods are based on the same common effect of evanescence of light close to an interface. This general principle is in contrast to all other super-resolution microscopy techniques, which achieve resolution enhancement by reversible switching between different states of fluorescence emitters (either stochastically or deterministically). The axial localization methods discussed here are based on evanescent light, either in emission (SAF and MIET), or in excitation (variable angle TIRF).

In this article, we will discuss the physical principle of these methods, their technical implementation, applications, advantages, limitations, and potential future perspectives. In view of the numerous excellent articles and comprehensive reviews about each of these techniques, we will here not focus much on the mathematical formalism of the methods, but rather on recent technical implementations and an overview of recent applications that have not been discussed in other reviews.

Variable-Angle Total Internal Reflection Fluorescence Microscopy

In contrast to standard epifluorescence microscopy, in total internal reflection fluorescence (TIRF) microscopy the incident angle of the plane-wave excitation light is chosen above the critical angle of total internal reflection between the coverslide and the sample medium (see **Fig. 2**). Due to the fact that the refractive index n_2 of an aqueous solution is lower than that of glass, i.e., $n_1 > n_2$, this results in total internal reflection of the incident light at all angles that are greater than the critical angle

$$\Theta_c = \arcsin(n_2/n_1) \tag{2}$$

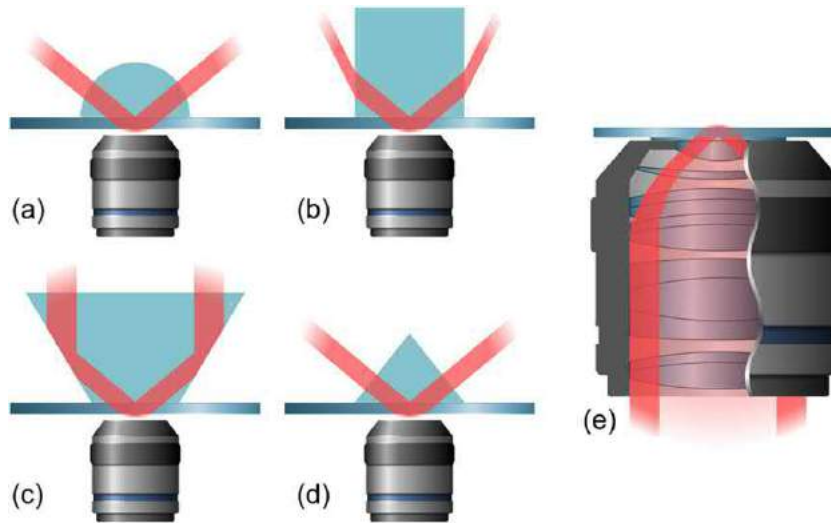


Fig. 2 (a)–(d) Schematic of various prism-based TIRF excitation/detection systems. (e) Schematic of prismless TIRF excitation/detection scheme, where a high NA objective lens is used for transmitting both excitation and emission light. The optical components inside the objective lens are not shown; the light path is shown schematically.

Despite being totally reflected, the incident light generates an evanescent electromagnetic field that extends into the sample and decays exponentially with the distance from the interface according to

$$I(z) = I_0 \exp[-z/d(\Theta)] \tag{3}$$

The penetration depth $d(\Theta)$ of the electric field $I(z)$ at wavelength λ is given byAxelrod *et al.* (1984)

$$d(\Theta) = \frac{\lambda/4\pi}{\sqrt{n_1^2 \sin^2\Theta - n_2^2}} \tag{4}$$

Exponential decay of the filed intensity results in a confinement of the excitation volume within ca. the first 100 nm above the sample surface. Confining illumination of a sample within a narrow region allows one to enhance the signal-to-noise ratio by suppressing the background signal and out of focus fluorescence and to limit the photo-damage of the specimen, thus making TIRF an ideal tool for imaging cellular structures near the sample surface. The idea of using TIRF to illuminate cells in close contact with the sample surface was first proposed byAmbrose (1956) and later developed by Axelrod (1981). We will omit here further details on TIRF microscopy and its variants, which are extensively described in the article by Daniel Axelrod. In the current article, we will focus on one of its advanced varieties that allow for extracting the fluorophore-substrate separation distance with axial resolution of 10 nm for certain types of samples.

The exponential decrease of the evanescent field upon TIRF illumination of the sample allows one to estimate the axial localization of a fluorophore by measuring its relative brightness. However, quantitative interpretation of a TIRF image for extracting the distance between an emitter and the substrate surface is far from being trivial (Cardoso Dos Santos *et al.*, 2016). The contrast of TIRF images depends on several parameters, such as the local concentration of fluorophores, their orientation, absorption cross section, and angular emission distribution, as well as on local variations of the fluorophore's quantum yield and the sample's refractive index (Chizhik *et al.*, 2011; Mertz, 2000).

The situation becomes even more complicated by the fact that some of these parameters can vary as a function of height (Chizhik *et al.*, 2014; Mertz, 2000; Enderlein *et al.*, 1999; Enderlein, 1999). This complication can be addressed by recording a series of TIRF images at different incident angles of the incident light. Since all the above parameters do not depend on Θ, their values will not change by varying the angle of incidence. By including all the unknown parameters in a new factor $\chi(x, y, z)$, one can rewrite Eq. (3) as

$$I(x, y, z, \Theta_i) = \chi(x, y, z)\gamma(\Theta_i)\exp(-z/d(\Theta_i)) \tag{5}$$

where $\gamma(\Theta_i)$ is the correction factor that takes into account the variation of the field intensity at the substrate-sample interface as a function of the angle of incidence Θ_i (Axelrod *et al.*, 2002). Taking the logarithm of Eq. (5), one obtains

$$\ln\frac{I(x, y, z, \Theta_i)}{\gamma(\Theta_i) - \gamma(\Theta_1)} = \ln[\chi(x, y, z)\gamma(\Theta_1)] - \frac{z}{d(\Theta_i)} \tag{6}$$

The logarithm on the left side of Eq. (6) depends linearly on $d^{-1}(\Theta_i)$. Therefore, by using a linear fit in each pixel of the fluorescence image measured at different angles of incidence, one can retrieve the fluorophore-substrate distance, without requiring any information on parameters related to the molecular parameters, such as quantum yield, absorption cross-section, or concentration. This technique, known as variable-angle TIRF (vaTIRF), was introduced in the mid-eighties (Lanni *et al.*, 1985; Gingell *et al.*, 1985) for studies of sub-cellular structures.

One of the advantages of vaTIRF is that it allows one to simultaneously determine the value of the effective refractive index (n_2 in Eq. (4)) of the sample, which includes the combined influence of any water gap between a cell membrane and the substrate surface, and the cytoplasma inside the cell. This index determines the penetration depth $d(\Theta)$ of the evanescent field (Cardoso Dos Santos *et al.*, 2016).

VaTIRF was used for quantification of the membrane height on focal adhesion zones (Burmeister *et al.*, 1994), for mapping the topography of cells above a substrate (Olveczky *et al.*, 1997), for studying axial motion of secretory granules in the ventral side of living cells (Loerke *et al.*, 2002), and to investigate the influence of 5-aminolevulinic acid on the adhesion of tumor cells (Lassalle *et al.*, 2007).

Experimentally, the first realizations of vaTIRF were based on an optical coupling of the substrate to a glass or quartz prism of cubic, trapezoidal, hemi-cylindrical or hemi-spherical shape (**Fig. 2(a–b)**). One of the key challenges is to keep the position of the illuminating light spot on the sample constant while changing the angle of incidence. This is possible only when using a hemi-spherical or hemi-cylindrical prism or a multiple focus laser scanning system (Stock *et al.*, 2003). A drawback of all these vaTIRFM systems is that when a prism is used to generate the evanescent wave, the microscope objective is then mounted on the opposite side of the sample for fluorescence collection, which often diminishes the image quality, for instance in case of low sample transparency or strong light scattering. To address this issue, a prism-less approach in TIRF has been proposed (Axelrod, 2001). Indeed, a prism-less setup based on an inverted microscope equipped with a high numerical aperture (NA) objective (NA > 1.4) allows for obtaining images with the full resolution defined by the NA. In this configuration, the objective is used both to create the evanescent excitation and to collect the signal (**Fig. 2(e)**). The prism-less approach simplifies installation and adjustment of the optical system which is required for tuning incidence angle of the excitation light. Recently, Boulanger *et al.* (2014) demonstrated the superior capability of a prism-less setup in vaTIRFM by imaging the cortical actin network. Jaffiol and co-workers used a similar system for studying adhesion of MDA-MB-231 cancer cells to a glass substrate (Cardoso Dos Santos *et al.*, 2016). By recording a

series of 10 TIRF images with different incidence angles of excitation light, the authors achieved an axial resolution close to 10–20 nm that makes vaTIRF suitable for quantifying cell adhesion structures or cell topography. Sequential vaTIRF imaging with selective photobleaching of molecules within the lower layers close to the interface can be used for straightforward observation of deeper structures within a sample without masking signals from farther distances by the brighter signals closer to the substrate (Fu *et al.*, 2016).

Super-Critical Angle Fluorescence Microscopy

Almost all fluorophores can be considered as ideal electric dipole emitters. Along with the far-field component, the dipole also has a near-field part which is not connected to far-field radiation, but which can strongly interact with nearby structure and interfaces. Let us consider a fluorophore that is located in close proximity to an interface separating two media with different refractive indices n_1 and n_2. The electric field of the emitting fluorophore can be represented as a superposition of plane waves, where each of these plane waves is refracted according to Snell's law when travelling from medium with refractive index n_2 into the medium with refractive index n_1 ($n_2 < n_1$). As a result, the emission into medium 1 is restricted within a cone limited by the critical angle

$$\Theta_c = \arcsin(n_2/n_1) \tag{7}$$

This component is referred to as under-critical angle fluorescence (UAF). However, if the fluorophore-interface distance is smaller than the fluorescence wavelength, then additional super-critical angle fluorescence (SAF) emission is observed (Enderlein *et al.*, 1999) due to the coupling of evanescent near-field components of the dipole field into medium 1. As a result, one can now also observe, in medium 1, emission along angles larger than the critical angle Θ_c.

Fig. 3(a) and **(b)** show the angular distribution of emission for an isotropically oriented molecule that is located directly at the glass-water interface (a), or separated by a third of its emission wavelength (b). Thus, displacing the fluorophore by only a few tens of nanometers away from the interface leads to a strong angular redistribution of emission, a large part of which can be found

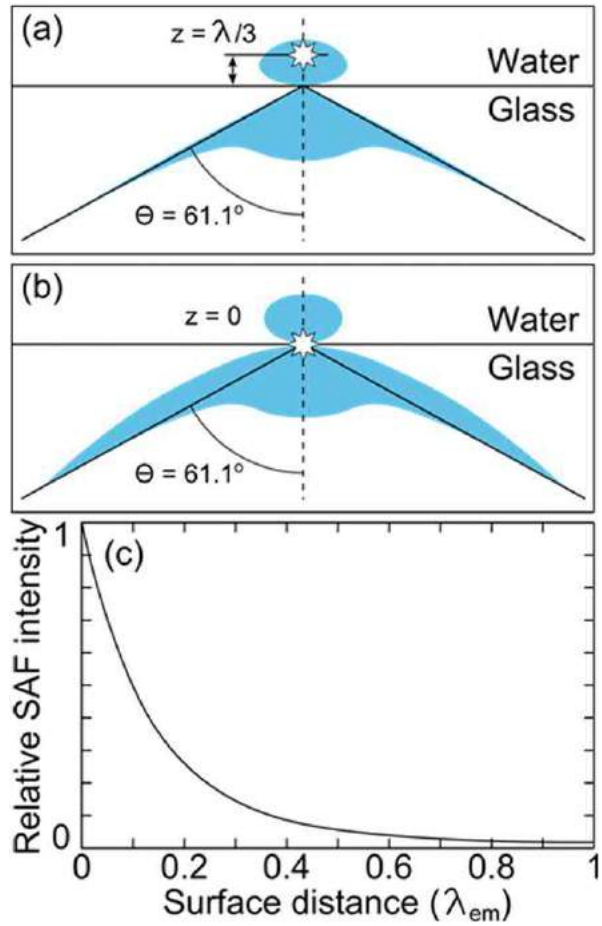


Fig. 3 Polar plots of the emission direction of molecules with isotropically oriented transition dipole (a) at the water/glass interface and (b) a surface distance equal to a third of the emission wavelength. (c) Dependence of SAF emission on the molecule's axial position. Calculations are done by the methods of Jörg Enderlein, see Ref. Enderlein *et al.* (1999).

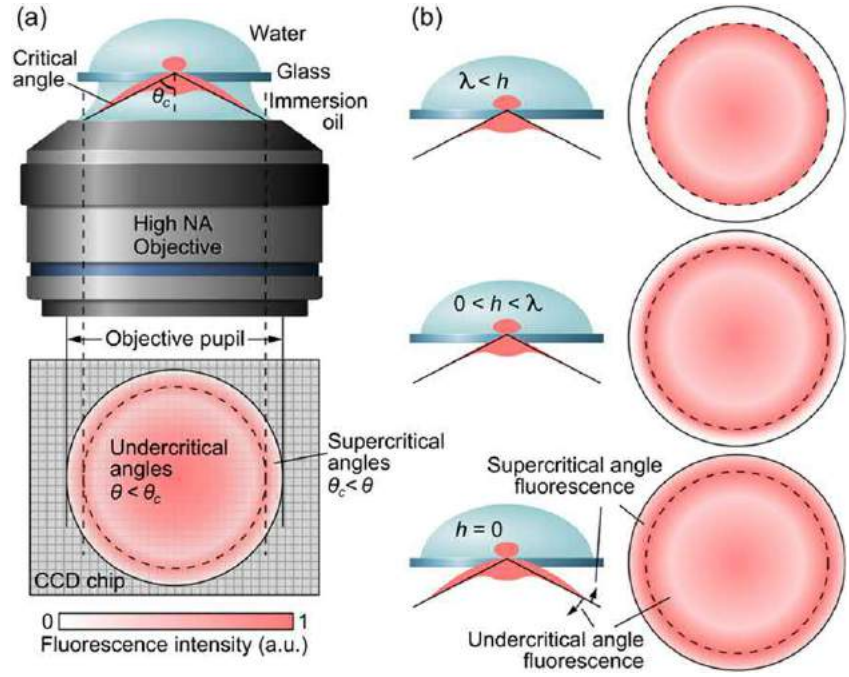


Fig. 4 (a) Schematic of the SAF and UAF fluorescence detection system. (b) Angular distribution of emission of a fluorophore at different axial positions and the corresponding distributions of the SAF and UAF at the back focal plane of the objective lens. Calculations are done by the methods of Jörg Enderlein, see Ref. Enderlein *et al.* (1999).

above the critical angle of 61.1° for the given ratio if refractive indices. This modulation of emission can be directly visualized by collecting the fluorescence with a high NA objective lens and measuring the profile of the collimated beam with a sensitive EMCCD chip. **Fig. 4(a)** shows a schematic of such a measurement. The dashed ring corresponds to the photons emitted at the critical angle. All the light which is detected inside this ring is the under-critical fluorescence. The light that is detected beyond the dashed ring corresponds to the super-critical fluorescence. Depending on the axial position of the emitter, the ratio of the super- and under-critical fluorescence changes (**Fig. 4(b)**).

It should be emphasized that the dependence between the axial position of the emitter and the angular distribution of the emission is analogous to and the reverse of the exponential decay of a TIRF excitation intensity. In that case, there is a close relationship between the angle of incidence and the penetration depth of the evanescent light above the interface, as we have seen in the previous section (vaTIRF microscopy).

The number of photons emitted beyond the critical angle is maximized when the fluorophore is directly bound to the surface, and it equals ~34% in case of a random dipole orientation at a glass-water interface (Ruckstuhl *et al.*, 2003). Moving the molecule away from the interface leads to a steep decrease of the intensity of supercritical fluorescence (**Fig. 3(c)**), which drops by a factor of 2 when the emitter is separated by nearly one sixth of the emission wavelength.

The quantitative measurement of the fluorophore's axial position requires either the determination of the supercritical-to-undercritical angle fluorescence intensity ratio, or the measurement of the absolute intensity of the supercritical angle fluorescence. The core idea of SAF microscopy and the first technical realization of the corresponding optical system which allows for collecting the fluorescence emitted above the critical angle was proposed by the group of Stefan Seeger (Enderlein *et al.*, 1999). The fluorescence detection system consisted of a parabolic glass element (**Fig. 5(a)**), which acts as a TIR mirror that collects the fluorescence light around the angles of maximum emission. Ruckstuhl *et al.* have used this light collection scheme for simultaneous measurement of both under- and supercritical angle fluorescence (see ref. Ruckstuhl and Verdes (2004)). One of the drawbacks of the system is that the paraboloid glass segment also serves as the substrate, which however can be simplified by using a coverslip that is placed on the paraboloid's front face with index-matching immersion oil. Recently, Hill *et al.* have proposed the use of low-cost disposable biochips for supercritical angle fluorescence detection for multiplexed clinical diagnostic applications (Hill *et al.*, 2011), which simplified the application of parabolic light collectors for routine measurements.

The more critical issues of using the parabolic light collector are low compatibility with standard microscopes and the impossibility to take wide-field images (Enderlein *et al.*, 2011). In recent years, the parabolic light collector has been replaced by high NA objectives which allow also for wide field imaging. For collecting all the under-critical fluorescence, one needs an objective the numerical aperture of which is equal or larger than the critical TIR angle between the sample and the objective's immersion medium. A simple calculation shows that for emitters bound to a glass-water interface, one has to use at least a NA of 1.33 for collecting all the under-critical angle fluorescence, which is distributed within a cone of opening angle 61.1°. Collection of the supercritical angle emission requires a large value of the numerical aperture. For this reason, SAF microscopy has become

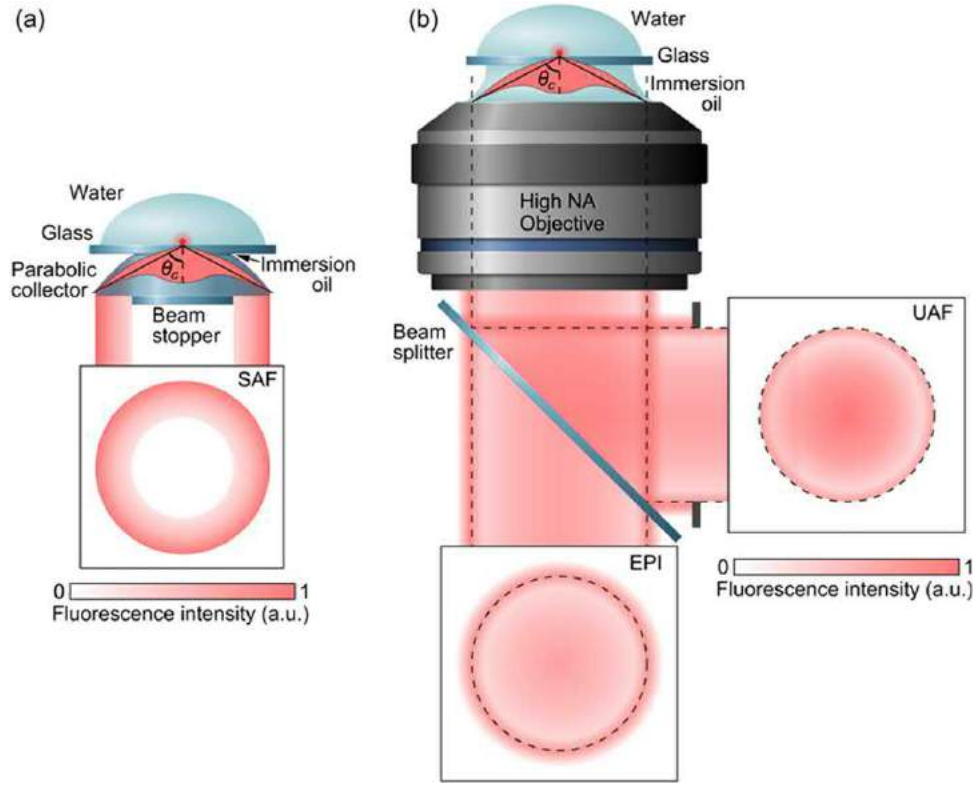


Fig. 5 (a) Schematic the parabolic collector for detection of the SAF. (b) Schematic of the high NA objective lens-based vSAF light collection scheme. Fluorescence is split in two parts: in the first detection channel, the EPI part is measured; in the second channel, only the UAF part is recorded (the SAF component is blocked in the back focal plane). As the result of the subtraction one obtains the virtual mask where only the SAF component is conserved.

widespread with the accessibility of TIRF objective lenses, which can possess NA values up to 1.49. This corresponds to a collection angle of about 79° and allows one to collect nearly all the supercritical angle fluorescence.

The first realization of SAF microscopy based on collection of both super- and under-critical fluorescence with a commercial 1.49 NA objective lens has been demonstrated in the group of Emmanuel Fort (Barroca *et al.*, 2012). A modified method that is referred to as virtual SAF (vSAF) is based on measuring fluorescence wide-field images both over all emission angles, and only over UAF emission angles (**Fig. 5(b)**). The latter was done by mechanically blocking the SAF part. As a result, the images that are obtained with the full angular distribution of emission allow for maximizing the lateral resolution, while calculating the difference of emission in the two channels results in the SAF image.

The use of a standard objective lens for SAF microscopy allows one to combine SAF microscopy which enhances axial resolution with super-resolution imaging techniques that increase the lateral resolution. By combining dSTORM and SAF microscopy, Bourg *et al*. have achieved close to 20 nm isotropic three-dimensional localization precision of fluorescent molecules in the basal cell membrane and on F-actin fibers within the first 150 nm above the substrate surface (Bourg *et al.*, 2015). Simultaneously, Ries and co-workers have used a similar experimental approach for imaging immunostained clathrin-coated pits and microtubules (Deschamps *et al.*, 2014).

Metal-Induced Energy Transfer Microscopy

As was predicted by Purcell (1946), placing a fluorescent molecule in the vicinity of a metal surface quenches its fluorescence and decreases its excited state lifetime. The mechanism of this phenomenon is similar to that of Förster resonance energy transfer (FRET): energy from the excited molecule is transferred, via electromagnetic coupling, into plasmons of the metal, where energy is either dissipated or re-radiated as light. The fluorophore-metal interaction was extensively studied in the 1970s and 1980s (Drexhage, 1974), and a quantitative theory of this interaction was developed on the basis of semi-classical quantum optics (Enderlein, 1999; Barnes, 1998). One of the key parameters that determine the character of the interaction between a quantum emitter and a metal structure is the size of the structure. If the metallic nanostructure is smaller than the wavelength of light that is emitted by the fluorophore, the fluorophore's radiation leads to a uniform oscillatory displacement of electrons inside the nanostructure, leading to strong restoring forces that act on these charges. These restoring forces become biggest at a certain

oscillation frequency, which is called plasmon resonance. Furthermore, these coherent oscillations of free electrons in metallic nanoparticles generate a highly localized electric field in close proximity to the particle's surface. Depending on the type of metal or the nanoparticle's shape and size, the plasmon resonance can be tuned to different spectral ranges for maximizing fluorophore-particle interaction. Interaction of fluorophores with localized surface plasmons has found numerous applications, with fluorescence enhancement being the most important one. Here, we will not further focus on the details of this kind of fluorphore-metal interaction and redirect the reader to the numerous existing extensive reviews.

A fundamentally different type of the fluorophore-metal interaction occurs when the fluorophore is located in close proximity to a smooth metal surface. The fluorophore's radiation creates charge density oscillations in the metal surface that are called propagating plasmons. Here, we will show how the interaction of fluorophore with a smooth metal surface can be used for axial localization of a fluorophore with nanometer accuracy. The core idea is that this interaction accelerates the return of an excited fluorescent molecule to its ground state, which manifests itself as a shortening of its excited state lifetime (also called fluorescence lifetime) (Chizhik *et al.*, 2014; Karedla *et al.*, 2014). Owing to the fact that the energy transfer rate is dependent on the distance of a molecule from the metal layer, the fluorescence lifetime can be directly converted into a distance value (**Fig. 6**). The theoretical basis for this conversion is the perfect quantitative understanding of the interaction between a quantum emitter and a metallic surface (Enderlein, 1999). It is important to emphasize that the energy transfer from the molecule to the metal is dominated by the interaction of the molecule's near-field with the metal, and is thus similar to FRET. However, due to the planar geometry of the metal film, which acts as the acceptor, the distance dependency of the energy transfer efficiency is much weaker than the sixth power of the distance, and shows a monotonous relation between lifetime and distance within roughly the first 150–200 nm above the surface for fluorescence in the visible spectral range. The distance range where a monotonous relation is observed is proportional to the wavelength of emission. Therefore, one can extend it by using a fluorophore with emission in the red or near-IR spectral region.

One of the key advantages of this method, which is called metal-induced energy transfer (MIET), is that it does not require any hardware modification to a conventional fluorescence-lifetime imaging microscope (FLIM), thus preserving its full lateral resolution. **Fig. 7** schematically shows the key elements of the microscope that are required for MIET imaging. The only additional

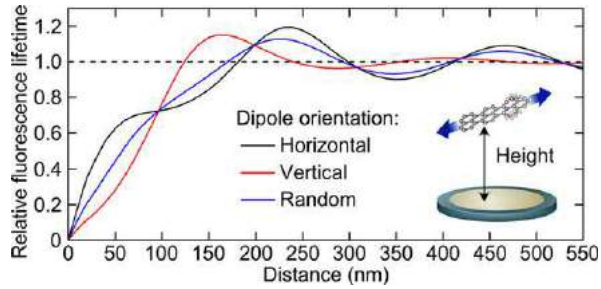


Fig. 6 Calculated dependence of molecule's excited state lifetime on its axial position over the metal film. Curves are calculated for an emission wavelength of 650 nm and a gold film thickness of 20 nm deposited on the glass cover slide. Calculations are done by the methods of Jörg Enderlein and Daja Ruhlandt, see Ref. Karedla *et al.* (2015).

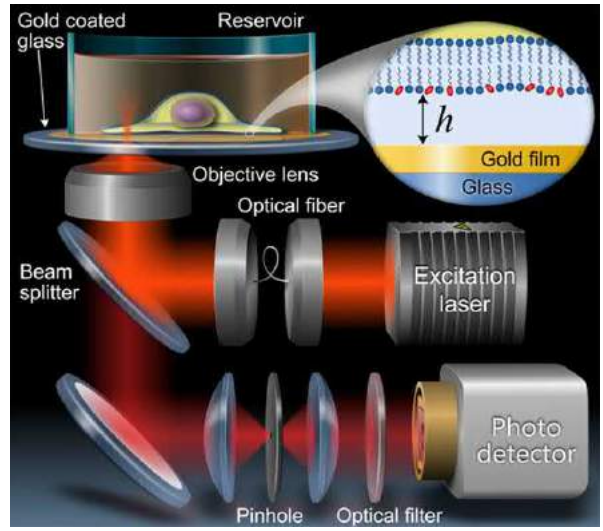


Fig. 7 Scheme of experimental setup for live cell MIET imaging.

requirement for MIET, when compared to conventional FLIM, is the presence of a thin semitransparent gold film (typically 10–20 nm thick) deposited on the glass cover slide supporting the sample.

Using a high NA objective lens (preferably at least NA = 1.4) one achieves two essential goals that are needed for MIET imaging. Firstly, since the measurements are done within a layer of ca. 150 nm height above the surface, the supercritical fluorescence constitutes a significant part of the total signal and should be collected by a high-NA objective to maximize fluorescence collection efficiency (see Section Super-Critical Angle Fluorescence Microscopy). Secondly, high NA objectives allow for minimizing the axial extension of the excitation focus, allowing for preferentially exciting molecules only within the MIET range, thus enhancing signal-to-noise ratio. As a result, when focused on the sample surface, the focused light excites only molecules within the first ~200 nm above the sample As a result, because the apical cell membrane is typically at least 500 nm away from the substrate, only dye molecules within the basal membrane are efficiently excited and detected.

For evaluating MIET measurements, one has to model the emission properties of a fluorescing molecule over a metal surface. The molecule is assumed to be an electric dipole emitter. Let us consider the emission of a single dipole emitter with orientation angles (α,β), where β denotes the inclination towards the vertical axis and α the orientation angle around that axis. The electric field amplitude of the dipole's emission into direction (θ,ϕ) is given by the general formula

$$E_{em} = e_p\left[A_\perp \cos\beta + A_{||}^c \sin\beta\cos((\varphi)-\alpha)\right] + e_s A_{||}^s \sin\beta\sin((\varphi)-\alpha) \tag{8}$$

where the $A_\perp$, $A_{||}^c$, and $A_{||}^s$ are functions of emission angle θ but not on α, β or ϕ. Explicit expressions for $A_\perp$, $A_{||}^c$, and $A_{||}^s$ can be found by expanding the electric field of the dipole emission into a superposition of plane waves, and the tracing each plane wave component through the planar structures using Fresnel's relations (for details see Enderlein *et al.* (1999), Enderlein (1999), Enderlein and Ruckstuhl (2005), Enderlein (2000)). It is important to note that the functions $A_\perp$, $A_{||}^c$, and $A_{||}^s$ depend also on the emission wavelength.

Knowing the electric field amplitude of the emission into a given direction $(\theta,(\varphi))$, one can then derive the total power of emission as

$$S_{total}(\beta,\alpha) \propto B_\perp \cos^2\beta + B_{||}\sin^2\beta \tag{9}$$

with the weight factors $B_\perp$ and $B_{||}$ that take into account the absorption of emitted energy into the metal layer (Enderlein *et al.*, 1999). Knowing the total emission power S_{total}, one can then calculate the lifetime of the emitter by

$$\tau/\tau_0 = S_0/[(\varphi)S_{total} + 1 - (\varphi)] \tag{10}$$

where (φ) is the quantum yield, τ_0 the free lifetime, and S_0 the total emission power of the emitter in free space (sample space).

For finally calculating the actual lifetime-distance curve, one has to average the result over all possible molecular orientations and also the emission spectrum of the emitter.

The applicability of MIET for live-cell imaging has been recently shown by mapping the basal membrane of living cells with nanometer accuracy (Chizhik *et al.*, 2014). Knowledge of the precise cell-substrate distance as a function of time and location with unprecedented resolution provides a new means to quantify cellular adhesion and dynamics, as is required for a deeper understanding of fundamental biological processes such as cell differentiation, tumor metastasis and cell migration.

As a biological model system three adherent cell lines were chosen: MDA-MB-231 human mammary gland adenocarcinoma cells and A549 human lung carcinoma cells, which are able to form metastasis in vivo models, as well as MDCK II from canine kidney tissue as a benign epithelial cell line. Interestingly, significant differences in the cell–interface distance between a normal epithelial cell and cancerous cell lines were observed (Chizhik *et al.*, 2014). Recently, Baronsky *et al.* have used MIET imaging for studying the epithelial-to-mesenchymal transition of NMuMG cells (Baronsky *et al.*, 2017).

Fig. 8 shows the measured intensity and lifetime images that were used to obtain the 3D reconstruction of the basal cell membrane. Because the variation of the fluorescence intensity is not only dependent on the metal-induced quenching, but also on the homogeneity of labelling, exclusively the lifetime information was used for reconstructing a three-dimensional map of the

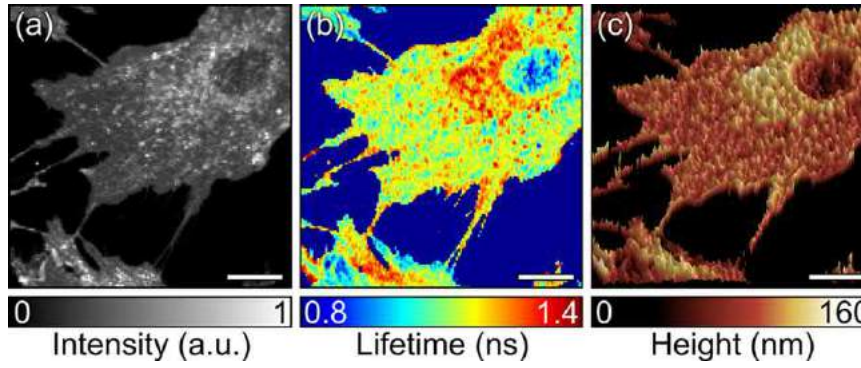


Fig. 8 Simultaneously acquired fluorescence intensity (a) and lifetime (b) images of the basal membrane of living NMuMG cells grown on a gold-coated glass cover slide. (c) Three-dimensional profile of the basal cell membrane computed from fluorescence lifetime image. Scale bars: 20 μm.

basal membrane. On the other hand, the intensity distribution was used to discriminate the membrane fluorescence against the background. Regions with no cells are difficult to identify from the lifetime images alone, as the lifetime values can become exceedingly scattered at low signal-to-noise ratios.

The axial resolution of the recorded images can be determined by calculating the standard deviation of cell-substrate distance (Chizhik *et al.*, 2014). The resolution depends on the photon rate and varies between 2 nm and 4 nm for typical fluorescence intensities measured and can be further enhanced to 1 nm by increasing the number of detected photons.

Karedla *et al.* (2014) have used MIET microscopy for axial localization of single molecules immobilized on the surface. The standard deviation for the observed single-molecule lifetime values is less than 0.1 ns, which corresponds to an axial localization accuracy of better than 2.5 nm for horizontal dipoles.

Although, we have focused on the application of MIET to map the membrane of a living cell and the single molecule axial localization, demonstrating its versatility, relative technical simplicity, and its applicability for life-science, the potential scope of applications of MIET is much greater. The distance range covered by MIET nicely bridges (and complements) the realm of conventional FRET and all the recently developed super-resolution imaging techniques. Although MIET has to rely on a perfect theoretical understanding of the fluorophore-metal interaction, which is certainly more involved than that of FRET, this is no serious obstacle in the current age of powerful desktop computers. In contrast to FRET, the infamous orientation-factor problem is greatly relaxed because one has to know only the relative orientation of one species of fluorescent molecules with respect to the planar metal film. Moreover, in contrast to FRET, one needs to label only one site of a sample with one sort of fluorophore, instead of double-labelling with a donor and acceptor. MIET is exceedingly simple to set up and neither requires modification of the FLIM system nor preparation of complex sample substrates. Coating glass cover slides with a thin metal film is the only prerequisite of the technique. Thus, the technical simplicity of MIET will allow its application in a wide range of studies where nanometer resolution is required.

Acknowledgement

The author is grateful to Jörg Enderlein and Ingo Gregor for helpful comments on this article.

See also: Optical Coherence Tomography and Its Application to Imaging of Skin and Retina

References

Ambrose, E.J., 1956. Nature 178, 1194.
Aquino, D., Schonle, A., Geisler, C., *et al.*, 2011. Nature Methods 8, 353.
Axelrod, D., 1981. The Journal of Cell Biology 89, 141.
Axelrod, D., 2001. BIOMEDO 6, 6.
Axelrod, D., Burghardt, T.P., Thompson, N.L., 1984. Annual Review of Biophysics and Bioengineering 13, 247.
Axelrod, D., Hellen, E.H., Fulbright, R.M., 2002. In: Lakowicz, J.R. (Ed.), Topics in Fluorescence Spectroscopy. Boston, MA: Springer US, p. 289.
Barnes, W.L., 1998. Journal of Modern Optics 45, 661.
Baronsky, T., Ruhlandt, D., Brückner, B.R., *et al.*, 2017. Nano Letters 17, 3320.
Barroca, T., Balaa, K., Lévêque-Fort, S., Fort, E., 2012. Physical Review Letters 108, 218101.
Boulanger, J., Gueudry, C., Münch, D., *et al.*, 2014. Proceedings of the National Academy of Sciences 111, 17164.
Bourg, N., Mayet, C., Dupuis, G., *et al.*, 2015. Nature Photonics 9, 587.
Burmeister, J.S., Truskey, G.A., Reichert, W.M., 1994. Journal of Microscopy 173, 39.
Cardoso Dos Santos, M., Déturche, R., Vézy, C., Jaffiol, R., 2016. Biophysical Journal 111, 136.
Chizhik, A.I., Chizhik, A.M., Khoptyar, D., *et al.*, 2011. Nano Letters 11, 1700.
Chizhik, A.I., Rother, J., Gregor, I., Janshoff, A., Enderlein, J., 2014. Nature Photonics 8, 124.
Deschamps, J., Mund, M., Ries, J., 2014. Optics Express 22, 29081.
Drexhage, K.H., 1974. In: Wolf, E. (Ed.), Progress in Optics 12. Elsevier, p. 163.
Enderlein, J., 1999. Chemical Physics 247, 1.
Enderlein, J., 2000. Biophysical Journal 78, 2151.
Enderlein, J., Gregor, I., Ruckstuhl, T., 2011. Optics Express 19, 8011.
Enderlein, J., Ruckstuhl, T., 2005. Optics Express 13, 8855.
Enderlein, J., Ruckstuhl, T., Seeger, S., 1999. Applied Optics 38, 724.
Fu, Y., Winter, P.W., Rojas, R., *et al.*, 2016. Proceedings of the National Academy of Sciences 113, 4368.
Gingell, D., Todd, I., Bailey, J., 1985. The Journal of Cell Biology 100, 1334.
Hell, S., Stelzer, E.H.K., 1992. Optics Communications 93, 277.
Hell, S.W., 2003. Nature Biotechnology 21, 1347.
Hell, S.W., 2009. Nature Methods 6, 24.
Hill, D., McDonnell, B., Hearty, S., *et al.*, 2011. Biomedical Microdevices 13, 759.
Huang, B., Bates, M., Zhuang, X., 2009. Annual Review of Biochemistry 78, 993.
Huang, B., Wang, W., Bates, M., Zhuang, X., 2008. Science 319, 810.
Juette, M.F., Gould, T.J., Lessard, M.D., *et al.*, 2008. Nature Methods 5, 527.
Karedla, N., Chizhik, A.I., Gregor, I., *et al.*, 2014. ChemPhysChem 15, 705.

Karedla, N., Ruhlandt, D., Chizhik, A.M., Enderlein, J., Chizhik, A.I., 2015. In: Kapusta, P., Wahl, M., Erdmann, R. (Eds.), Advanced Photon Counting: Applications, Methods, Instrumentation. Cham: Springer International Publishing, p. 265.
Kukura, P., Ewers, H., Muller, C., *et al*., 2009. Nature Methods 6, 923.
Lanni, F., Waggoner, A.S., Taylor, D.L., 1985. The Journal of Cell Biology 100, 1091.
Lassalle, H.-P., Baumann, H., Strauss, W.S.L., Schneckenburger, H., 2007. Journal of Environmental Pathology, Toxicology and Oncology 26, 83.
Limozin, L., Sengupta, K., 2009. ChemPhysChem 10, 2752.
Loerke, D., Stühmer, W., Oheim, M., 2002. Journal of Neuroscience Methods 119, 65.
Mertz, J., 2000. Journal of the Optical Society of America B 17, 1906.
Olveczky, B.P., Periasamy, N., Verkman, A.S., 1997. Biophysical Journal 73, 2836.
Pavani, S.R.P., Thompson, M.A., Biteen, J.S., *et al*., 2009. Proceedings of the National Academy of Sciences 106, 2995.
Purcell, E.M., 1946. Physical Review 69, 681.
Ruckstuhl, T., Rankl, M., Seeger, S., 2003. Biosensors and Bioelectronics 18, 1193.
Ruckstuhl, T., Verdes, D., 2004. Optics Express 12, 4246.
Shtengel, G., Galbraith, J.A., Galbraith, C.G., *et al*., 2009. Proceedings of the National Academy of Sciences 106, 3125.
Stock, K., Sailer, R., Strauss, W.S.L., *et al*., 2003. Journal of Microscopy 211, 19.

Overview: Microscopy

CJR Sheppard, National University of Singapore, Singapore

© 2005 Elsevier Ltd. All rights reserved.

Introduction

The basic construction and imaging properties of the optical microscope, one of the most important optical instruments, are described. But the restrictive meaning of a microscope as a device that the user looks down to see a magnified image is far from the present terminology that includes scanning systems (where the image is stored in a computer), nonvisible radiation, such as electrons or X-rays, and a variety of different contrast mechanisms.

According to the *Oxford English Dictionary* a microscope is 'an instrument magnifying objects by means of lenses so as to reveal details invisible to the naked eye'. Thus, basically a microscope forms a magnified image of an object. The first microscopes used visible light and formed an image showing variations in the intensity of light scattered by the object. This intensity is in general related to the optical properties of the object in a complicated way.

Nowadays there are many different types of microscope. Our understanding of a microscope must therefore be generalized in the following ways.

- The microscope may not be a conventional imaging system using lenses or mirrors. For example, it may be a scanning imaging system. A confocal system is a combination of a conventional and a scanning system. Another important category of microscopes is that of probe microscopes, including near-field optical microscopes. Some probe microscopes, for example the atomic force microscope (AFM) do not even seem at first glance to rely on the direct use of radiation.
- The microscope may not use visible light, but other electromagnetic radiation, or even other forms of radiation.
- The image can be formed using a variety of different contrast mechanisms. Some of these, such as phase contrast, are designed to image particular optical properties of the sample. Others image the generation of a form of radiation when the object is stimulated by another form of radiation. In particular, in principle, virtually any form of spectroscopy can be the basis of building up an image by measuring the spatial variations in the signal.

Different Forms of Microscopes

The Conventional Microscope

In a simple microscope, an objective lens forms a real, magnified, and inverted image of an object. In a compound microscope, an eyepiece is added, forming a virtual image that is viewed by eye to give real image on the retina. The eye can be replaced by CCD camera to record moving or still images. In early microscopes, the objective lens and eyepiece are mounted in the two ends of a brass tube. The objective screws into the tube using an RMS (Royal Microscopical Society) thread (0.8″ Whitworth 36 threads per inch), until its mounting face is flush with the end of the tube. The length of the tube is the mechanical tube length. The distance from the mounting face of the objective to the plane of the real image is the optical tube length, which varied according to different manufacturers in the range 160–210 mm. Now most objectives have infinity tube length, so that they collimate the light from the object. The collimated light is brought to a focus by an additional tube lens. An objective of correct tube length should always be used as otherwise spherical aberration is introduced. As the objective, tube lens, and eyepiece are designed together as a system, great care should be exercised when mixing components from different manufacturers.

Abbe showed that in order to form a perfect lateral image the objective must satisfy a different condition called the Herschel condition. Otherwise the image of an off-axis point will suffer from coma. An aberration-free system satisfying the sine condition is called an aplanatic system. A microscope produces a three-dimensional (3D) image of a 3D object. A point of the object closer to the lens appears further from the lens in the image. If the lateral magnification is M, the longitudinal magnification is approximately equal to M^2. However, it can be shown that it is impossible to devise an instrument that can produce a perfect 3D image of a 3D object, because to have a perfect transverse image the system must satisfy Abbe's sine condition, but to have a perfect axial image the system must satisfy the Herschel condition. These two conditions are not mutually compatible. Actually, we find that the longitudinal magnification is not exactly equal to M^2, and is not even constant in space. Different depths of the object are imaged differently: the microscope objective only produces a good image for one plane of focus, and other planes will exhibit spherical aberration. However, all of these problems can be overcome by bringing the part of the object under observation into focus, without refocusing the eye or other detector. A 3D image can thus be generated by scanning the object stage in the axial direction, and recording a stack of images from different depths in a computer. For modern objectives of infinite tube length, focusing can be alternatively achieved by piezoelectric scanning of the objective lens.

Resolution

For an object consisting of a single bright point object in a dark background, the image produced by a perfect microscope, according to paraxial diffraction theory, is the so-called Airy disk, consisting of a bright central spot, surrounded by a series of rings. The intensity in a meridional cross-section through the Airy disk is the same for any aperture of objective, or wavelength of light, but its width varies. The intensity of the first bright ring is 1.75% of that at the peak. The radius of the first dark ring of the Airy disk is

$$r_0 = \frac{0.61\lambda}{n \sin \alpha} \tag{1}$$

where λ is the wavelength, n is the refractive index of the immersion medium, and α is the angle subtended at the edge of the objective aperture. The radius depends on $n \sin \alpha$, which is called the numerical aperture and should be as large as possible for good resolution. Thus, high-magnification lenses often use an immersion fluid, usually oil with a refractive index of 1.518 (ISO 8036/1).

The optical coordinate v is defined as

$$v = \frac{2\pi}{\lambda} rn \sin \alpha \tag{2}$$

so that the dark ring of the Airy disk occurs at a value of v of $2\pi \times 0.61 = 3.83$. Resolution is sometimes expressed in terms of the full width at half maximum (FWHM) of the image of a point object, which is 3.232 in optical coordinates. A full nonparaxial theory does not give a very different figure.

Resolution of a microscope is often specified by two-point resolution, which describes whether the image of two points can be distinguished from that of a single point. According to the Rayleigh criterion of two-point resolution, two points are just resolved if the second point is placed on the first dark ring of the first. The separation is then $0.61\lambda/(n \sin \alpha)$. A cross-section through the image in an incoherent optical system of two bright point objects of equal strength and different separations is shown in **Fig. 1**. The intensity in the image between the points decreases as the separation is increased. The ratio of the intensity midway between the points to that at the points for the Rayleigh criterion to be satisfied is then found to be 0.735.

The concept of resolution should be distinguished from sensitivity or precision. An object much smaller than the resolution limit can still be detected, perhaps weakly, in a microscope: this detection of weak contrast depends on the sensitivity of the microscope rather than its resolution. The size of an object can also be measured with a precision much greater than the resolution of the microscope.

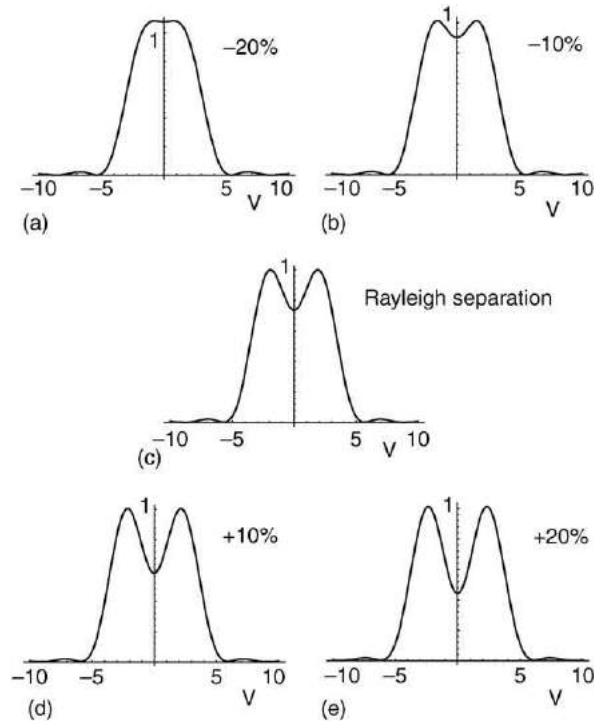


Fig. 1 A cross-section through the image of two equal point objects in an incoherent microscope. The separation of the points is that for the Rayleigh criterion to be satisfied, and for changes of ± 10, 20% of the Rayleigh separation.

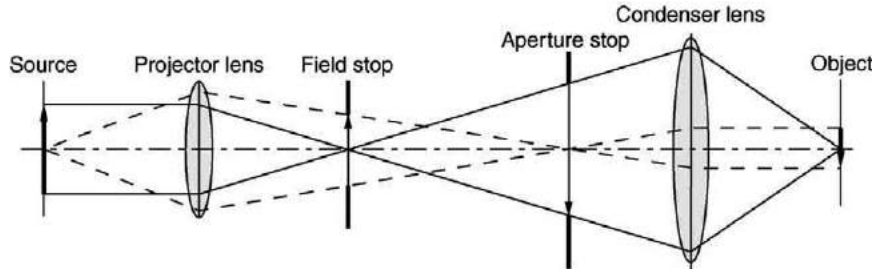


Fig. 2 Geometry of the Köhler illumination system. In practice an arrangement with a smaller number of lenses is usually used.

Illumination

If the object is not self-luminous, in order to be imaged in a microscope it must be illuminated. A semitransparent object, such as a biological slice, is illuminated in transmission. For observation of bulk objects, or surfaces, we use illumination in the reflection geometry, called epi-illumination. Either a tungsten halogen lamp or an arc source is usually used. In critical illumination, the source is focused on to the object by a condenser lens. The disadvantage of this approach is that variations in emission of the source are imaged directly into the image. Cheaper microscopes avoid this problem by using a diffuser. Better microscopes use instead the Köhler illumination system, where the source is placed in the front focal plane of the condenser lens. **Fig. 2** shows a Köhler illumination system in which the source is imaged into the front focal plane of the condenser lens by another, projector, lens. The system incorporates a separate field stop and aperture stop. In practice, the size of the field stop should be reduced to illuminate as small a region of the object as necessary in order to minimize stray light. An important part of setting up a microscope to operate properly consists in centering the aperture stop of the condenser. This is often done using a so-called Bertrand lens that allows imaging of the aperture stop.

Image formation

The Rayleigh criterion was originally specified for an incoherent optical system. It is thus applicable in fluorescence microscopy, as fluorescence is an incoherent process as two fluorescent point objects fluoresce independently. But for the image of a trans-illuminated object, the resolution depends on the coherence of the illumination. This is controlled by the numerical aperture of the condenser lens as compared with that of the objective. The ratio of these numerical apertures is called the coherence parameter, S, so that

$$S = \frac{n_c \sin \alpha_c}{n \sin \alpha} \tag{3}$$

For $S=0$ the illumination is purely coherent, while for $S \to \infty$ imaging becomes purely incoherent, thus corresponding to the Rayleigh criterion, so S should really be called an incoherence parameter. An important in-between case is when $S=1$, when the apertures of objective and condenser are equal. This is termed matched, full, or complete illumination. According to the generalized Rayleigh criterion, the points are just resolved when the ratio of the intensity midway between the points to that at the points is 0.735, which is called the generalized Rayleigh criterion. We require that the distance between the points is as small as possible when this occurs. The generalized Rayleigh separation is the same for incoherent illumination and for $S=1$, and correspondsto a distance of $2v_0=3.83$ in optical coordinates. Note, however, that for other separations of the points, the ratio is different for these two cases: it is not true, but often erroneously stated, that $S=1$ corresponds to incoherent imaging. Resolution improves as the aperture of the condenser is increased ($2v_0=5.15$ in optical coordinates for coherent illumination) reaching a maximum when $2v_0=1.46$, when resolution is 9% better than for incoherent imaging ($2v_0=3.58$). This maximum in resolution is achieved when the numerical aperture of the condenser is larger than that of the objective, which is not physically achievable if the objective has the highest possible numerical aperture. Similarly, it is impossible to achieve incoherent illumination with very large objective numerical apertures.

The effect of coherence on the resolution of an image depends on the form of the object, and on the particular resolution criterion employed. In practice, contrast also depends on the aperture of the condenser. Usually, opening the condenser improves resolution, but reduces contrast, so there will be an optimum condenser aperture size.

Abbe theory of microscope imaging

Abbe argued that for coherent illumination of a grating, the grating spectra can be observed in the back focal plane of the objective. The tube lens then forms an image from the grating components. Thus, this is an early description of Fourier optics. The strength of the grating components can be altered in the back focal plane to give various optical effects, such as phase contrast. Abbe's theory was not properly appreciated at the time because it was known that in practice, resolution could be improved by using a larger condenser aperture, which does not give coherent illumination. There was much controversy about the merits of Köhler versus critical illumination, and different sizes of condenser aperture.

We now know that Köhler and critical illumination are in principle equivalent. The aberrations of the condenser lens are not important, so that the source and condenser together behave simply as a partially coherent effective source. Imaging can still be described by Fourier optics within the framework of partially coherent imaging theory.

Although Köhler and critical illumination are equivalent in principle, Köhler illumination is in practice better because of its improved illumination uniformity.

Depth of focus

The longitudinal image of a point object is found to be approximately invariant when expressed in terms of an optical coordinate u, defined as

$$u = \frac{8\pi}{\lambda} zn \sin^2 \frac{\alpha}{2} \tag{4}$$

The axial resolution, and thus also the depth of focus, varies strongly with aperture. The FWHM for longitudinal imaging is 11.13 in optical coordinates.

Microscope objectives

Because microscope objectives often have large apertures, aberrations will be very strong, unless the objective is designed correctly. The basic design principle for a high aperture lens is the aplanatic front element (Fig. 3). It is found that all rays from a point A in a sphere of refractive index n, where A is a distance r/n from its center, appear to come from a point B, distance rn, without any aberration. This principle is used by employing a front element that has one surface of the same radius of curvature as the sphere. The front surface is a sphere centered on A (Fig. 3(b)), so that the rays are not deviated on crossing it.

A low-power achromat uses just two components with different optical dispersion to cancel chromatic aberration and correct for other aberrations (an achromatic doublet). For higher powers, two separated doublets are necessary. For the highest apertures, an aplanatic front is used. However, this can never converge the light, but only makes it less divergent. It is thus used together with an achromatic doublet. For oil immersion, the interface between the oil and the front element is not very important, so it is made planar to simplify manufacture. In practice, it is usually made planar even for a dry lens, and the resulting aberrations cancelled out elsewhere in the objective. Apochromats, corrected for three colors, use more elements, which may include two or more stages of aplanatic front. The final objective thus consists of a number of elements that must be accurately aligned relative to one another. The objective is adjusted by the manufacturer to give a good star image (image of a point object). First a spacer is selected to

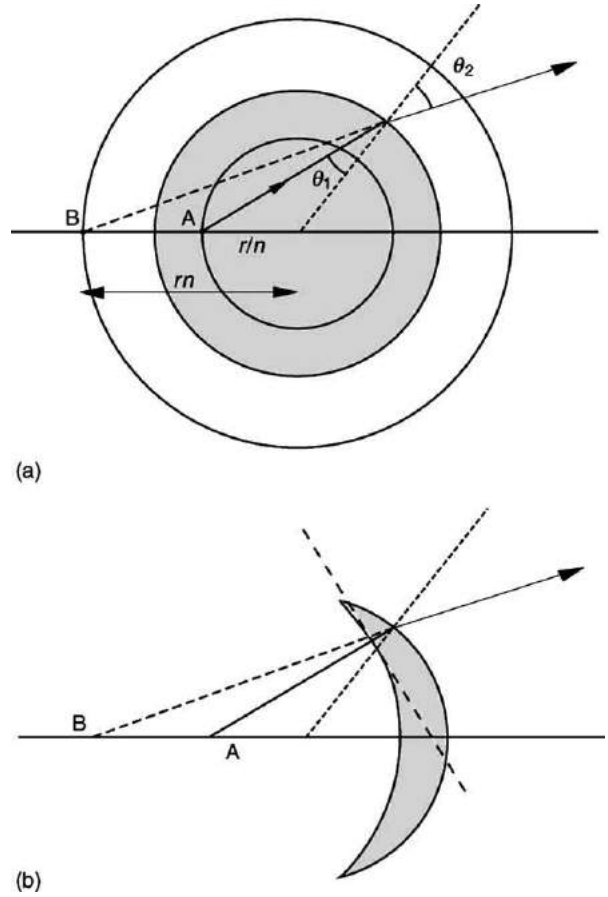


Fig. 3 The principle of the aplanatic front: (a) an aplanatic surface; (b) a meniscus lens that acts as an aplanatic system.

optimize spherical aberration. Then a sleeve is adjusted to make the objective parfocal with others. Finally a screw is used to center the assembly to remove coma.

Conventional and Scanning Microscopes

Conventional microscope

Various different types of transmission microscope are illustrated in Fig. 4. We consider image formation in a conventional microscope as illustrated schematically in Fig. 4(a), showing a microscope with critical illumination. A large area incoherent source is focused by the condenser lens on to the specimen, illuminating a comparatively large area of the specimen, corresponding to the whole field of view of the objective. Information from each illuminated point in the specimen is simultaneously transmitted by the objective lens to form the primary image. The objective is responsible for forming the image, with the condenser playing only a secondary role in determining the resolution of the system, through control of the coherence of the illumination. Fig. 4(b) shows a conventional microscope in which the image is measured point by point by a detector. In practice this could be achieved by using a CCD detector.

Scanning microscope

An image can be generated by a scanning system, as illustrated in Fig. 4(c). A probe of light is formed by demagnification of a source, and is scanned over the object in a raster. The transmitted (or reflected) light is detected by a photodetector and thus builds up an image. The size of the probe of light limits the resolution of the system, that is, the smallest detail in the object that can be seen in the image. It should be noted that the magnification of the image is given simply by the ratio of the distance scanned in the image to the distance scanned by the probe. It is thus unrelated to the demagnification of the source. The image magnification can be altered without changing the lens and is not in any way related to the resolution.

It has been shown that the imaging properties of scanning and conventional microscopes are identical under analogous conditions, this being known as the principle of equivalence. This property is based on the principle of reciprocity, which is a very general physical law that holds even with diffraction, absorption, multiple scattering, and stray light. The principle of equivalence is generally valid except if there are nonreciprocal magnetic or polarization effects, or energy losses involved (such as in fluorescence microscopy, and with inelastic scattering in electron microscopy).

Scanning systems exhibit a number of important advantages over conventional systems. Broadly, these are based on two classes of property. First, in a scanning system the image is in the form of an electronic signal. As a result, this is advantageous for quantitative measurements, as well as for image processing, including image enhancement, image restoration, and image analysis. Second, in a scanning system the object is illuminated by a focused spot, which extends the range of imaging modes available.

Confocal microscope

Finally in Fig. 4(d), we combine the arrangements of Figs. 4(b) and (c) to give a confocal scanning optical microscope, in which a point source illuminates just a small region of the object, and a confocal point detector detects light from this illuminated region.

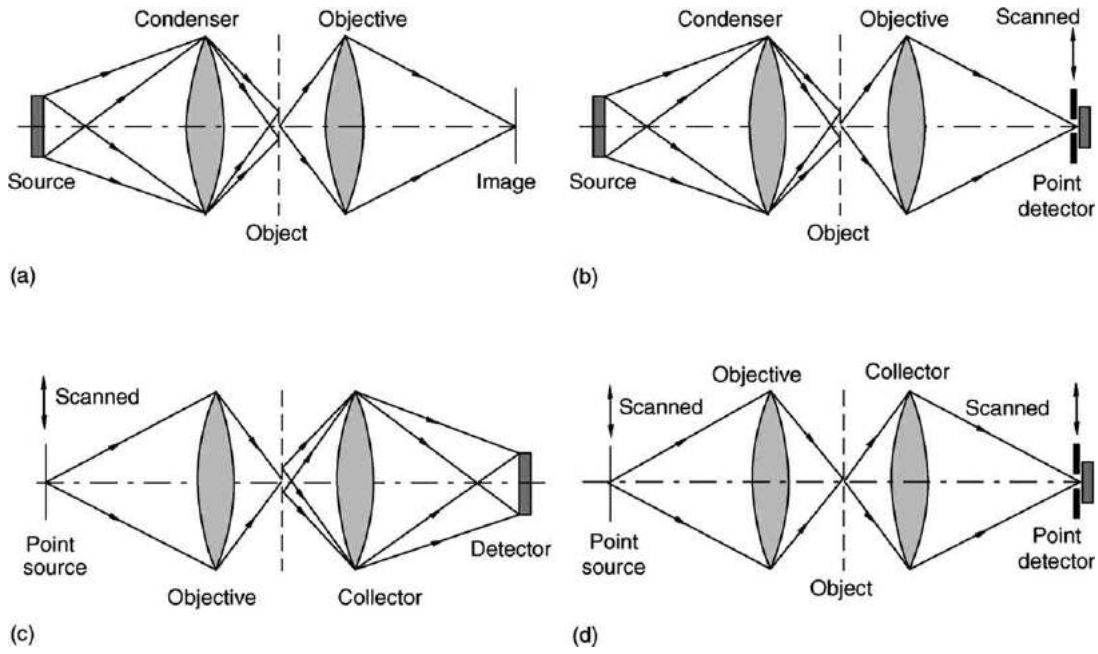


Fig. 4 Different geometries of transmission microscope: (a) a conventional microscope; (b) a conventional microscope with a point detector; (c) a scanning microscope; (d) a confocal microscope.

If the point source and detector are scanned in unison, a two-dimensional image is generated. However, this system now behaves very differently from the previous ones. The confocal microscope is thus not a special case of the general partially coherent conventional imaging system. From the symmetry of Fig. 4(d), it is clear that the two lenses play an equal part in the imaging process. This results in an improvement in resolution. In fact, the confocal system behaves as a coherent imaging system, but with a sharper effective point spread function than in a conventional coherent microscope.

Although Fig. 4 is drawn for the transmission geometry, in practice most confocal systems operate in the reflection or epi-illumination mode, in which the same objective lens is used both for illumination and detection. For a specimen placed in the focal plane, the properties of confocal transmission and reflection systems are identical. However, once the object is moved from the focal plane, certain differences arise: in particular in confocal reflection a strong optical sectioning effect occurs that allows a single section through a thick object to be imaged. This is the major advantage of the confocal microscope arrangement. Fig. 4 also applies equally well to fluorescence imaging. However, in this case, because of the incoherent nature of fluorescence emissions after excitation by coherent light, imaging is then incoherent.

Confocal microscopes can be achieved by using either a point detector, in practice performed by placing a pinhole in front of a photodetector, or by using a coherent detector. Such a coherent detector, sensitive to the amplitude of the incident radiation, is not directly available for light, but is available for acoustic radiation, as in a scanning acoustic microscope. For light, a confocal effect can also be achieved by using an interferometric method to synthesize a coherent detector. Thus, in interference microscopes using the high aperture condenser and objective lenses, an optical sectioning effect arises similar to that in the confocal microscope. Another way of producing a coherent detector is to use a single-mode optical fiber.

Probe Microscopes

Scanning tunneling microscope

The scanning tunneling microscope was the first of the family of probe microscopes, relying on a fundamentally different principle from the usual forms of microscope. A physical tip in the nanometer range is brought close, also in the nanometer range, to a conducting sample. If an electric potential is applied, electrons can tunnel across between the sample and the tip. By scanning the tip mechanically across the sample, an image can be generated with a resolution in the subnanometer range. The surface topography can also be measured with subnanometer sensitivity. While interference microscopy can measure surface topography with subnanometer sensitivity, in this case the profile is averaged over the lateral resolution of the microscope, of the order of the wavelength in dimensions. The scanning tunneling microscope can image individual atoms. The signal is related to the work function of the material. Altering the bias voltage allows the band structure of the material to be investigated.

Atomic force microscope

In the atomic force microscope, the force between the surface and the tip is measured using a cantilever beam and used to build up an image. Atomic force microscopy can be performed in either a contact or noncontact mode. It can be used with insulating specimens. Optical methods, often using a position-sensitive detector, are used to measure displacements of the cantilever.

Near-field scanning optical microscope (NSOM)

In a near-field scanning optical microscope, a very small tip or aperture is scanned relative to the specimen to attain resolution greater than the classical limit set by the wavelength of the radiation. As Fig. 5 shows, various different designs of near-field

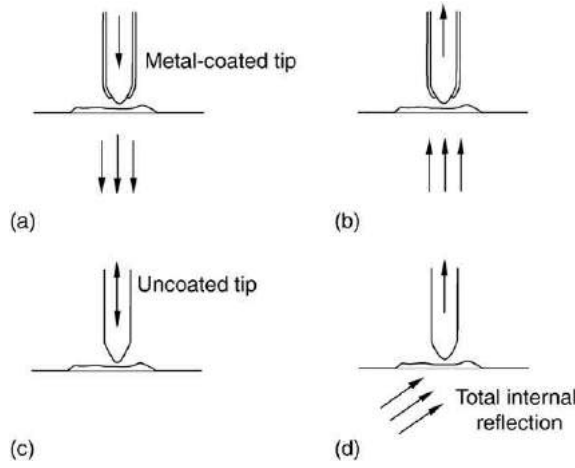


Fig. 5 Different forms of near-field microscope: (a) illumination-mode NSOM; (b) collection-mode NSOM; (c) a near-field probe used for both illumination and collection in a confocal arrangement; (d) photon tunneling microscope (PTM). Reproduced with permission from Sheppard CJR (1978) The scanning optical microscope. *The Physics Teacher* 16: 648–651. © 1978 American Association of Physics Teachers.

microscope have been proposed. It is evident that these again form into the conventional/scanning categories described earlier. The sample can be illuminated using the near-field probe, as in Fig. 5(a). This is called the illumination-mode NSOM. Or the sample can be uniformly illuminated, and a signal detected using a near-field probe as in Fig. 5(b), giving a collection-mode NSOM. Or a confocal arrangement can be used, with a near-field probe used for both illumination and collection (c). In this case, an uncoated tip can be used; as otherwise the detected signal will be very small. Finally, Fig. 5(d) shows the photon tunneling microscope (PTM), in which the sample is illuminated with evanescent waves produced by total internal reflection and an uncoated tip used to probe the evanescent field in the presence of the sample.

Different Types of Radiation

Electromagnetic Radiation

UV radiation and X-rays

The first microscopes used visible light, but, in fact, we do not need to use visible light, but can use any electromagnetic radiation, over a broad range of different available wavelengths. In Fig. 6 we show the wavelength of the electromagnetic spectrum, illustrating how the wavelength in air varies with frequency. Instead of using visible light, shorter wavelengths allow greater resolution to be achieved. Ultra-violet light is commonly used to excite fluorescence. X-rays have also successfully been used to image biological samples.

IR and microwave radiation

In the longer wavelength region, infra-red radiation is used for observation of semiconductors or for molecular spectroscopic imaging. Imaging of emitted midinfra-red radiation can show up variations in temperature, such as hot spots in semiconductors. Microwaves have also been used, but resolution is limited by the long wavelength. For this reason microwaves (and mid-IR) have also been used for near-field microscopy.

Other Radiation

Electron microscope

The other important class of radiation that can be used for illumination is matter waves. The most common of these, of course, is electrons, the wavelength of which, as a function of acceleration voltage, is shown in Fig. 7. The bend in the curve at very high

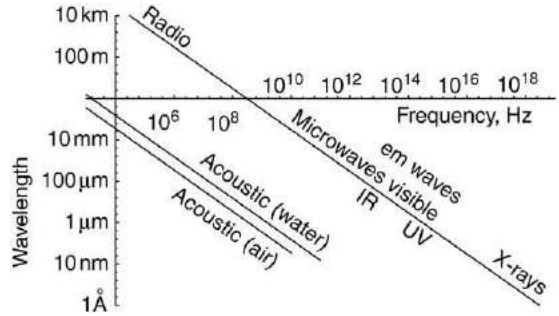


Fig. 6 The wavelength of different forms of electromagnetic radiation and acoustic radiation. Reproduced with permission from Sheppard CJR (2002) The generalized microscope. In: Diaspro A (ed.) *Confocal and Two-Photon Microscopy: Foundations, Applications and Advances*, pp. 1–18. New York: Wiley-Liss.

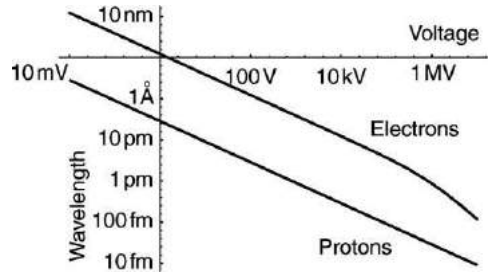


Fig. 7 The wavelength of matter waves (electrons and protons) as a function of accelerating voltage. Reproduced with permission from Sheppard CJR (2002) The generalized microscope. In: Diaspro A (ed.) *Confocal and Two-Photon Microscopy: Foundations, Applications and Advances*, pp. 1–18. New York: Wiley-Liss.

voltages is caused by relativistic effects. The wavelength of the electrons is very small: even for 100 V electrons, the wavelength is only 0.1 nm. But aberrations caused by the electron lenses limit resolution so that at present atomic resolution is only just achievable, even with much higher voltages.

In a transmission electron microscope (TEM), a beam of electrons is produced by an electron gun. The specimen is illuminated via a condenser lens (or lenses). Usually these are magnetic lenses in which a current in a coil produces a magnetic field that focuses the electrons. The electrons that are transmitted through the specimen are then focused by a series of lenses to form a final image that can be viewed directly on a phosphor screen. An X-ray detector can be used to characterize the elements in the specimen. An electron-energy-loss spectrometer, together with a detector, can measure the energy of the electrons in a particular region of the image.

Other matter radiation

Instead of electrons, other particle beams can be used for illumination. Fig. 7 shows the wavelength of a beam of protons, as function of the accelerating voltage. Because of the larger mass of protons, relativistic effects are not apparent for protons in the curve in Fig. 7. Microscope images have also been formed using ions, and even neutral particles such as neutrons. Neutral atom microscopes are also under development.

Acoustic radiation

Instead of electromagnetic waves, acoustic radiation can be used to form a scanning acoustic microscope (SAM). Ultrasonic waves are focused into a water immersion medium. Mechanical scanning is again used to build up an image. Fig. 6 shows the wavelength of the acoustic wave as a function of frequency. By using microwave frequencies, wavelengths, and therefore resolution, in the submicron range, can be generated. The SAM acts as a confocal microscope because the detector is sensitive to the amplitude of the acoustic wave. The acoustic microscope provides information on variations in the elastic properties (viscosity and elasticity) of the sample.

Different Contrast Mechanisms

The bright field microscope detects the intensity of the light transmitted through the object. A microscope with a condenser aperture of appreciable size behaves as a partially coherent system, and the image will, in general, depend on the phase of the light coming from the object as well as its intensity. Many objects are weakly scattering, so the contrast of this phase information is weak. In this case, the microscope effectively images variations in the transmittance or reflectance of the sample. Different designs of microscope can be used to image various properties of the object, thus providing new and complementary information. Phase contrast microscopy provides but one example of a different contrast mechanism. In fact, in general, any physical or chemical interaction of the illuminating radiation with the sample can be used as the basis for a contrast mechanism. These different contrast mechanisms can be performed in either a conventional or scanning arrangement, or in a confocal system.

Phase Contrast Microscopy

Phase contrast is a widely used technique in both biological microscopy (in transmission) and materials microscopy (in reflection). Its importance in biological microscopy stems, firstly, from the fact that contrast may otherwise be too weak to be visible, but secondly because the phase variations are caused by changes in optical thickness, related to physical density. In reflection microscopy, phase is related to surface height variations, but also depends on the optical material properties of the sample.

Polarization Microscopy

The polarization state of light transmitted through or reflected from a sample can also be changed. This change is detected in polarization microscopy, for example by placing the sample between crossed polarizers. The birefringence detected can be either material birefringence, or form birefringence (caused by the shape of the microstructure). Polarization microscopy is widely used in biological microscopy, and in mineralogy.

Fluorescence Microscopy

In fluorescence microscopy, electrons excited by illumination decay to the ground state and emit photons of light. Auto-fluorescence is natural fluorescence of the sample. Fluorescent dyes can be used as labels for particular biological or chemical constituents. Fluorescence microscopy is usually performed in the epi-illumination geometry to assist rejection of light from the source. Often it is performed in a confocal microscope, allowing 3D localization of the fluorescent labels.

Raman Microscopy

Raman spectroscopy can be performed on a microscopic scale to produce images of presence of particular molecular bonds. It is usually performed in a scanning system, often of the confocal type.

This is one example of the wider class of spectroscopic microscopies: in principle, any form of spectroscopy can be used as the basis for a microscope contrast mode.

Nonlinear Microscopy

Another class of contrast mechanisms is based on nonlinear optical interactions. Again, any nonlinear mechanism can be used as the basis for a contrast mechanism. These include two- (or multiphoton) fluorescence, second- (or higher-order) harmonic generation, sum or difference frequency generation, and coherent anti-Stokes Raman scattering (CARS). Probably other nonlinear optical mechanisms will be exploited in microscopy in the future.

Other Contrast Mechanisms

The contrast mechanisms described above, all rely on illumination and detection of light. But in many other modes, radiation of one form can be converted into another. These include cathodoluminescence microscopy (electrons to light), X-ray microanalysis (electrons to X-rays), photo-emission microscopy (light, usually UV, to electrons), photo-acoustic microscopy (light to ultrasonics), photothermal microscopy (light to thermal waves), optical or electron beam induced current (OBIC/EBIC). Again, in many of these, the illuminating or emitted radiation can be focused, or a combination can be used in a confocal arrangement.

Further Reading

Born, M., Wolf, E., 1999. Principles of Optics, 7th edn. Cambridge: Cambridge University Press.
Bradbury, S., Bracegirdle, B., 1997. Introduction to the Optical Microscope. Oxford: Bios Scientific Publishers.
Inoue, S., Spring, K.R., 1997. Video Microscopy: The Fundamentals, 2nd edn. New York: Plenum.
Martin, L.C., 1966. Theory of the Microscope. London: Blackie.
Paesler, M.A., Moyer, P., 1996. Near-Field Optics: Theory, Instrumentation, and Applications. New York: Wiley InterScience.
Pluta, M., 1988. Advanced Light Microscopy, Volume 1: Principles and Basic Properties. Amsterdam: Elsevier.
Sheppard, C.J.R., 1987. Scanning optical microscopy. In: Barer, R., Cosslett, V.E. (Eds.), Advances in Optical and Electron Microscopy, vol. 10. London: Academic Press, pp. 1–98.
Sheppard, C.J.R., 2002. The generalized microscope. In: Diaspro, A. (Ed.), Confocal and Two-Photon Microscopy: Foundations, Applications, and Advances. New York: Wiley-Liss, pp. 1–18.
Slayter, E.M., Slayter, H.S., 1992. Light and Electron Microscopy. Cambridge: Cambridge University Press.
Wiesendanger, R., 1994. Scanning Probe Microscopy and Spectroscopy. Cambridge: Cambridge University Press.
Wilson, T., Sheppard, C.J.R., 1984. Theory and Practice of Scanning Optical Microscopy. London: Academic Press.

Confocal Microscopy

T Wilson, University of Oxford, Oxford, UK

© 2005 Elsevier Ltd. All rights reserved.

Introduction

It is probably fair to say that the development and wide commercial availability of the confocal microscope has been one of the most significant advances in light microscopy in the recent past. The main reason for the popularity of these instruments derives from their ability to permit the structure of thick specimens of biological tissue to be investigated in three dimensions. It achieves this important goal by resorting to a scanning approach together with a novel (confocal) optical system.

The traditional wide-field conventional microscope is a parallel processing system which images the entire object field simultaneously, which is a severe requirement for the optical components. We can relax this requirement if we no longer try to image the whole object at once. The limit of this relaxation is to require a good image of only one object point at a time. The price that we have to pay is that we must scan in order to build up an image of the entire field.

A typical arrangement of a scanning confocal optical microscope is shown in **Fig. 1** where the system is built around a host conventional microscope. The essential components are some form of mechanism for scanning the light beam (usually from a laser) relative to the specimen and appropriate photodetectors to collect the reflected or transmitted light. Most of the early systems were analog in nature, but it is now universal, due to the serial nature of the image formation, to use a computer both to drive the microscope and to collect, process, and display the image.

In the beam scanning confocal configuration of **Fig. 1**, the scanning is typically achieved by using vibrating galvanometer-type mirrors or acousto-optic beam deflectors. The use of the latter gives the possibility of TV-rate scanning, whereas vibrating mirrors are often relatively slow when imaging an extended region of the specimen, although significantly higher scanning speeds are achievable over smaller scan regions. We should note that other approaches to scanning may be implemented, such as specimen-scanning and lens-scanning. These methods, although not generally available commercially, do have advantages in certain specialized applications. Since this article is necessarily limited in length much additional material may be found in other sources listed in the Further Reading at the end of this article.

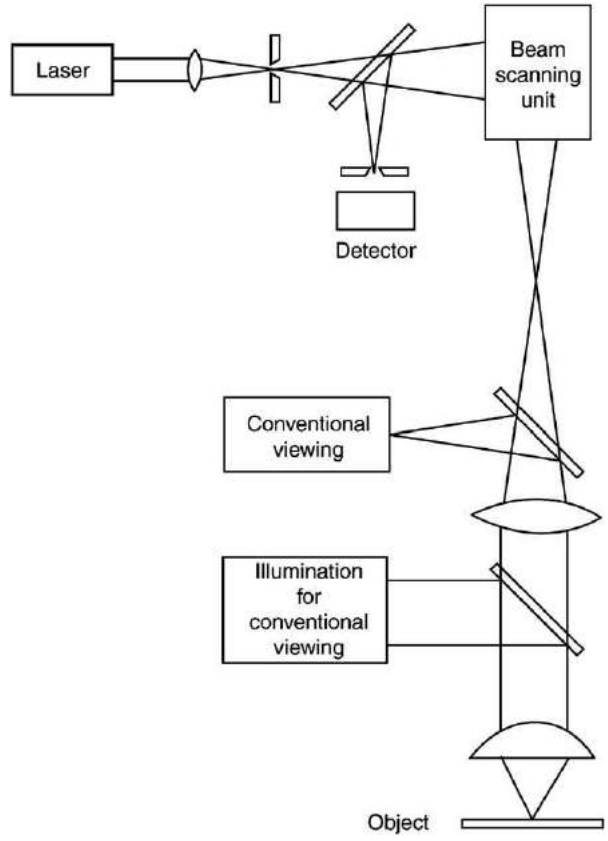


Fig. 1 Schematic diagram of a confocal microscope.

 doi:10.1016/B978-0-12-809283-5.00723-0

Image Formation in Scanning Microscopes

We will not discuss the fine detail of the optical properties of confocal systems. However, the essence is shown in Fig. 1 where we see that the confocal optical system consists simply of a point source of light which is then used to probe a single point on the specimen. The strength of the reflected or fluorescence radiation from the single object point is then measured via a point, pinhole detector. The confocal – point source and point detector – optical system therefore merely produces an 'image' of a single object point and hence some form of scanning is necessary to produce an image of an extended region of the specimen. However, the use of single-point illumination and single-point detection results in novel imaging capabilities which offer significant advantages over those possessed by conventional wide-field optical microscopes. In essence, these are enhanced lateral resolution and, perhaps more importantly, result in a unique depth discrimination or optical sectioning property. It is this latter property which leads to the ability to obtain three-dimensional images of volume specimens.

The improvement in lateral resolution may at first seem implausible. However, it can be explained simply by the principle which states that resolution can be increased at the expense of field of view, which can then be increased by scanning. One way of taking advantage of this principle is to place a very small aperture extremely close to the object. The resolution is now determined by the size of the aperture rather than the radiation. In the confocal microscope we do not use a physical aperture in the focal plane but rather use the back-projected image of a point detector in conjunction with the focused point source. Fig. 2 indicates the improvement in lateral resolution that may be achieved.

The confocal principle was introduced in an attempt to obtain an image of a slice within a thick specimen which was free from the distracting presence of out-of-focus information from surrounding planes. The confocal optical systems fulfills this requirement and its inherent optical sectioning or depth discrimination property has become the major motivation for using confocal microscopes, and is the basis of many of the novel imaging modes of these instruments. The origin of the depth discrimination property may be understood easily from Fig. 3, where we show a reflection-mode confocal microscope and consider the imaging of a specimen with an undulating surface. The full lines show the optical path when an object feature lies in the focal plane of the lens. At a later scan position, the object surface is supposed to be located in the plane of the vertical dashed line. In this case, simple ray tracing shows that the light reflected back to the detector pinhole arrives as a defocused blur, only the central portion of which is detected and contributes to the image. In this way the system discriminates against features which do not lie within the focal region of the lens. A very simple method of both demonstrating the effect and giving a measure of its strength is to scan a perfect reflector axially through focus and measure the detected signal strength. Fig. 4 shows a typical response. These responses are frequently termed the $V(z)$, by analogy with a similar technique in scanning acoustic microscopy. A simple paraxial theory

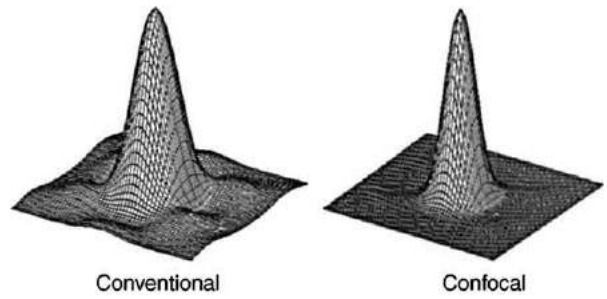


Fig. 2 The point spread functions of the conventional and confocal microscopes showing the improvement in lateral resolution which may be obtained in the confocal case.

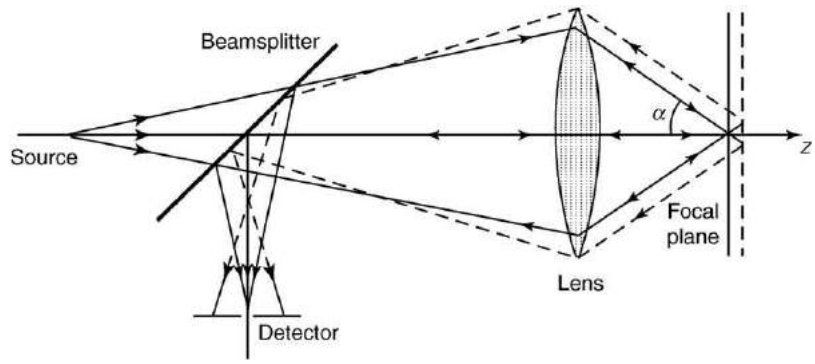


Fig. 3 The origin of the optical sectioning or depth discrimination property of the confocal optical system.

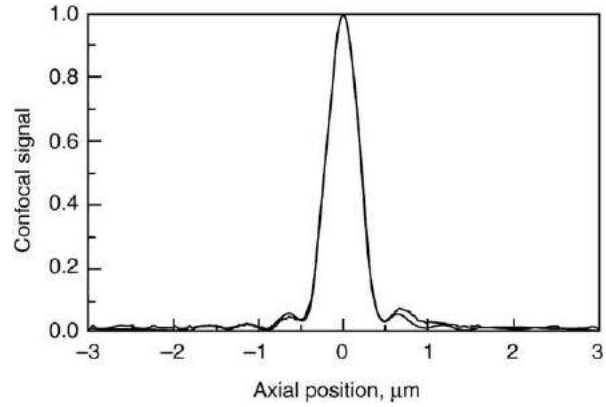


Fig. 4 The variation in detected signal as a plane reflector is scanned axially through focus. The measurement was taken with a 1.3 numerical aperture objective and 633 nm radiation.

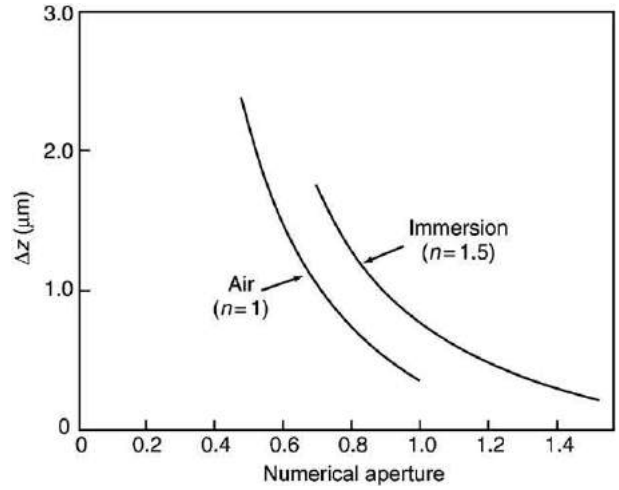


Fig. 5 The optical sectioning width as a function of numerical aperture. The curves are for red light (0.6328 μm wavelength). Δz is the full width at the half-intensity points of the curves of $I(u)$ against u.

models this response as

$$I(u) = \left[\frac{\sin(u/2)}{u/2}\right]^2 \tag{1}$$

where u is a normalized axial coordinate which is related to real axial distance, z, via

$$u = \frac{8\pi}{\lambda} nz \sin^2(\alpha/2) \tag{2}$$

where λ is the wavelength and $n \sin \alpha$ the numerical aperture. As a measure of the strength of the sectioning, we can choose the full width at half intensity of the $I(u)$ curves. Fig. 5 shows this value as a function of numerical aperture for the specific case of imaging with red light from a helium neon laser. These curves were obtained using a high aperture theory which is more reliable than Eq. (1) at the highest values of numerical aperture. We note, of course, that these numerical values refer to nonfluorescence imaging. The qualitative explanation of optical sectioning, of course, carries over to the fluorescence case but the actual value of the optical sectioning strength is different in the fluorescence case.

Applications of Depth Discrimination

Since this property is one of the major reasons for the popularity of confocal microscopes, it is worthwhile, at this point, to review briefly some of the novel imaging techniques which have become available with confocal microscopy.

Fig. 6 illustrates the essential effect: Fig. 6(a) shows a conventional image of a planar microcircuit which has deliberately been mounted with its normal at an angle to the optic axis. We see that only one portion of the circuit, running diagonally, is in focus.

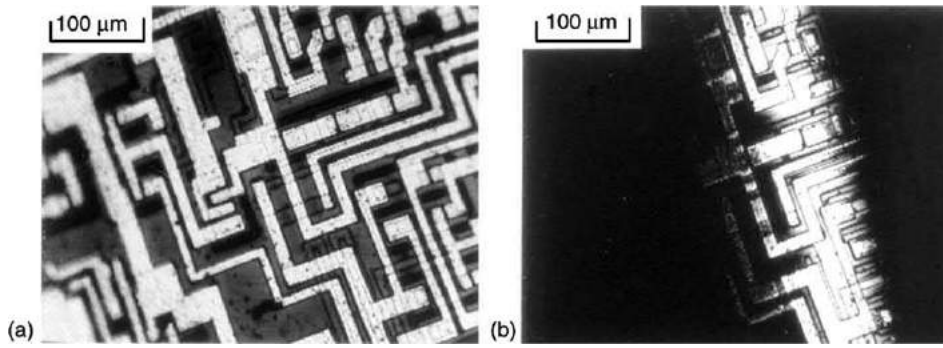


Fig. 6 (a) Conventional scanning microscope image of a tilted microcircuit: the parts of the object outside the focal plane appear blurred. (b) Confocal image of the same microcircuit: only the part of the specimen within the focal region is imaged strongly.

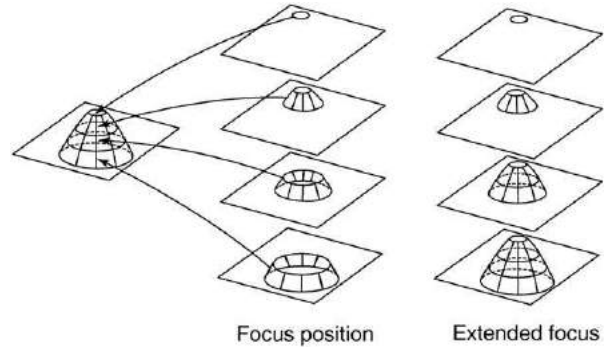


Fig. 7 An idealization of the optical sectioning property showing the ability to obtain a through-focus series of images, which may then be used to reconstruct the original volume object at high resolution.

Fig. 6(b) shows the corresponding confocal image: here the discrimination against detail outside the focal plane is clear. The areas which were out of focus in Fig. 6(a) have been rejected. Furthermore, the confocal image appears to be in focus throughout the visible band, which illustrates that the sectioning property is stronger than the depth of focus.

This suggests that if we try to image a thick translucent specimen, we can arrange, by the choice of our focal position, to image detail exclusively from one specific region. In essence, we can section the specimen optically without having to resort to mechanical means. Fig. 7 shows an idealized schematic of the process. The portion of the beehive-shaped object that we see is determined by the focus position. In this way it is possible to take a through-focus series and obtain data about the three-dimensional structure of the specimen. If we represent the volume image by $I(x,y,z)$, then by focusing at a position $z=z_1$, we obtain, ideally, the image $I(x,y,z_1)$. This, of course, is not strictly true in practice because the optical section is not infinitely thin.

It is clear that the confocal microscope allows us to form high-resolution images with a depth of focus sufficiently small that all the detail which is imaged appears in focus. This suggests immediately that we can extend the depth of focus of the microscope by adding together (integrating) the images taken at different focal settings without sacrificing the lateral resolution. Mathematically, this extended-focus image is given by

$$I_{\mathrm{EF}}(x,y) = \int I(x,y,z)\mathrm{d}z \tag{3}$$

As an alternative to the extended-focus method, we can form an auto-focus image by scanning the object axially and, instead of integrating, selecting the focus at each picture point by recording the maximum in the detected signal. Mathematically, this might be written as

$$I_{\mathrm{AF}}(x,y) = I(x,y,z_{\max}) \tag{4}$$

where $z_{\max}$ corresponds to the focus setting giving the maximum signal. The images obtained are somewhat similar to the extended focus and, again, substantial increases in depth of focus may be obtained. We can go one step further and turn the microscope into a noncontacting surface profilometer. Here we simply display $z_{\max}$.

It is clear by now that the confocal method gives us a convenient tool for studying three-dimensional structures in general. We essentially record the image as a series of slices and play it back in any desired fashion. Naturally, in practice it is not as simple as this, but we can, for example, display the data as an $x-z$ image rather than an $x-y$ image. This is somewhat similar to viewing the specimen from the side. As another example, we might choose to recombine the data as stereo pairs by introducing a slight lateral offset to each image slice as we add them up. If we do this twice, with an offset to the left in one case and the right in another, we

obtain, very simply, stereo pairs. Mathematically, we form images of the form:

$$\int I(x \pm \gamma z, y, z)\mathrm{d}z \tag{5}$$

where γ is a constant. In practice it may not be necessary to introduce offsets in both directions to obtain an adequate stereo view.

Our discussion so far on these techniques has been by way of a simplified introduction. In particular, we have not presented any fluorescence images. The key point is that, in both brightfield and fluorescence modes, the confocal principle permits the imaging of specimens in three dimensions. The situation is, of course, more involved than we have implied. A thorough knowledge of the image formation process, together with the effects of lens aberrations and absorption, is necessary before accurate data manipulation can take place.

In conclusion to this section it is important to emphasize that the confocal microscope does not produce three-dimensional images. It essentially produces very high-quality two-dimensional images of a (thin) slice within a thick specimen. A three-dimensional rendering of the entire volume specimen may then be generated by suitably combining a number of these two-dimensional image slices from a through focus series of images.

Fluorescence Microscopy

We now turn our attention to confocal fluorescence microscopy, because this is the imaging mode which is usually employed in biological applications. Although we have introduced the confocal microscope in terms of bright-field imaging the comments we have made concerning the origin of the optical sectioning, etc., carry over directly to the fluorescence case although the numerical values describing the strength of the optical sectioning are, of course, different and we will return to this point later.

If we assume that the fluorescence in the object destroys the coherence of the illuminating radiation and produces an incoherent fluorescent field proportional to the intensity of the incident radiation, $I(v,u)$, then we may write the effective intensity point spread function, which describes image formation in the incoherent confocal fluorescence microscope, as

$$I(v,u)I\left(\frac{v}{\beta},\frac{u}{\beta}\right) \tag{6}$$

where the optical coordinates u and v are defined relative to the primary radiation and $\beta=\lambda_2/\lambda_1$ is the ratio of the fluorescence to the primary wavelength. We note that $v=(2\pi/\lambda)rn \sin \alpha$, where r denotes the actual radial distance.

This suggests that the imaging performance depends on the value of β. In order to illustrate this we show in Fig. 8 the variation in detected signal strength as perfect fluorescent sheet scans through focus. This serves to characterize the strength of the optical sectioning in fluorescence microscopy in the same way that the mirror was used in the brightfield case. We note that the half-width of these curves is essentially proportional to β and so for optimum sectioning the wavelength ratio should be as close to unity as possible.

We have just discussed what we might call one-photon fluorescence microscopy in the sense that a fluorphore is excited by a single photon of a particular wavelength. It then returns to the ground state and emits a photon at the (slightly longer)

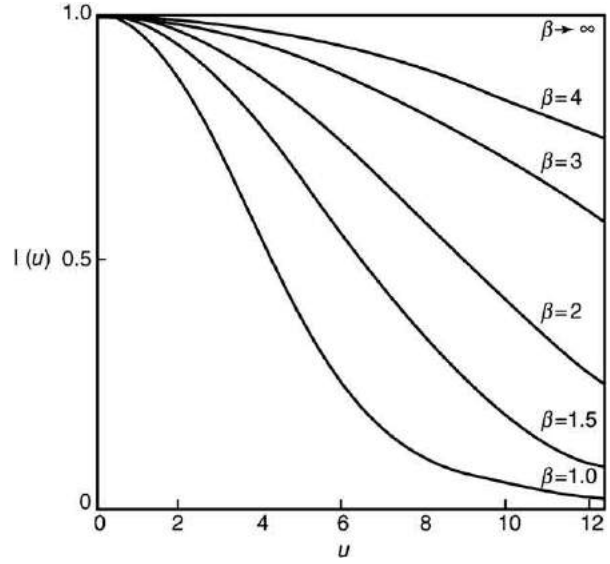


Fig. 8 The detected signal as thin fluorescent sheet is scanned axially through focus for a variety of fluorescent wavelengths. We note that if we measure the sectioning by the half width of these curves, the strength of the sectioning is essentially proportional to β.

fluorescence wavelength. It is this radiation which is detected via the confocal pinhole. Recently, however, much interest has centered on two-photon excitation fluorescence microscopy. This process relies on the simultaneous absorption of two, longer wavelength photons, following which a single fluorescence photon is emitted. The excitation wavelength is typically twice that used in the one-photon case. The beauty of the two-photon approach lies in the quadratic dependence of the fluorescence intensity on the intensity of the illumination. This leads to fluorescence emission which is always confined to the region of focus. In other words the system possesses an inherent optical sectioning property. Other benefits of two-photon fluorescence over the single photon case include the use of red or infra-red lasers to excite ultra-violet dyes, confinement of photo-bleaching to the focal region (the region of excitation), and the reduced effects of scattering and greater penetration. However, it should also be remembered that, compared with single photon excitation, the fluorescence yield of many fluorescent dyes under two-photon excitation is relatively low.

In order to make a theoretical comparison between the one- and two-photon modalities, we shall assume that the emission wavelength λ_{em} is the same, irrespective of the mode of excitation. Since the wavelength required for single-photon excitation is generally shorter than the emission wavelength, we may write it as $\gamma\lambda_{em}$ where $\gamma<1$. Since two-photon excitation requires the simultaneous absorption of two photons of half the energy we will assume that the excitation wavelength may be written as $2\gamma\lambda_{em}$ which has been shown to be a reasonable approximation for many dyes.

If we now introduce optical coordinates u and v, normalized in terms of λ_{em}, we may now write the effective point spread functions in the one-photon confocal and two-photon case as

$$I_{1p\text{-}conf} = I\left(\frac{v}{\gamma}, \frac{u}{\gamma}\right) I(v,u) \tag{7}$$

and

$$I_{2p} = I^2\left(\frac{v}{2\gamma}, \frac{u}{2\gamma}\right) \tag{8}$$

respectively. We note that although a pinhole is not usually employed in two-photon microscopy it is possible to include one if necessary. In this confocal two-photon geometry the effective point spread function becomes

$$I_{2p\text{-}conf} = I^2\left(\frac{v}{2\gamma}, \frac{u}{2\gamma}\right) I(v,u) \tag{9}$$

If we now look at **Eqs. (7)** and **(8)** in the $\gamma=1$ limit, we find that

$$I_{1p\text{-}conf} = I^2(v,u) \tag{10}$$

and

$$I_{2p} = I^2\left(\frac{v}{2}, \frac{u}{2}\right) \tag{11}$$

We now see that because of the longer excitation wavelength used in two-photon microscopy the effective point spread function is twice as large as that of the one-photon confocal in both the lateral and axial directions. The situation is somewhat improved in the confocal two-photon case but it is worth remembering that the advantages of two-photon excitation microscopy are accompanied by a reduction in optical performance as compared to the single-photon case.

From the practical point of view it is worth noting that the two-photon approach has certain very important advantages over one-photon excitation, in terms of image contrast, when imaging through scattering media apart from the greater depth of penetration afforded by the longer wavelength excitation. In a single-photon confocal case it is quite possible that the desired fluorescence radiation from the focal plane may be scattered after generation in such a way that it is not detected through the confocal pinhole. Since the fluorescence is generated throughout the entire focal volume it is also possible that undesired fluorescence radiation, which was not generated within the focal region, may be scattered so as to be detected through the confocal pinhole. In either case this leads to a reduction in image contrast. The situation is, however, completely different in the two-photon

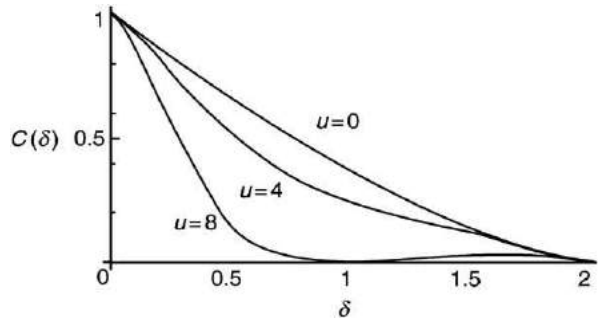


Fig. 9 The transfer function for a conventional fluorescence microscope for a number of values of defocus (measured in optical units). We notice that the response for all nonzero spatial frequencies decays with defocus.

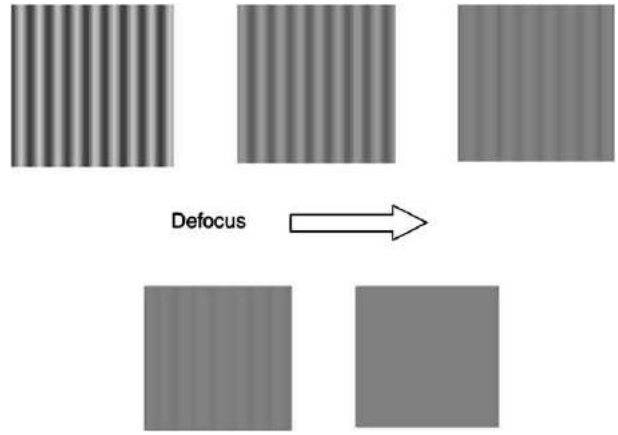


Fig. 10 The image of a one-dimensional single spatial frequency bar pattern for varying degrees of defocus. We note that for sufficiently large values of defocus the bar pattern is not imaged at all.

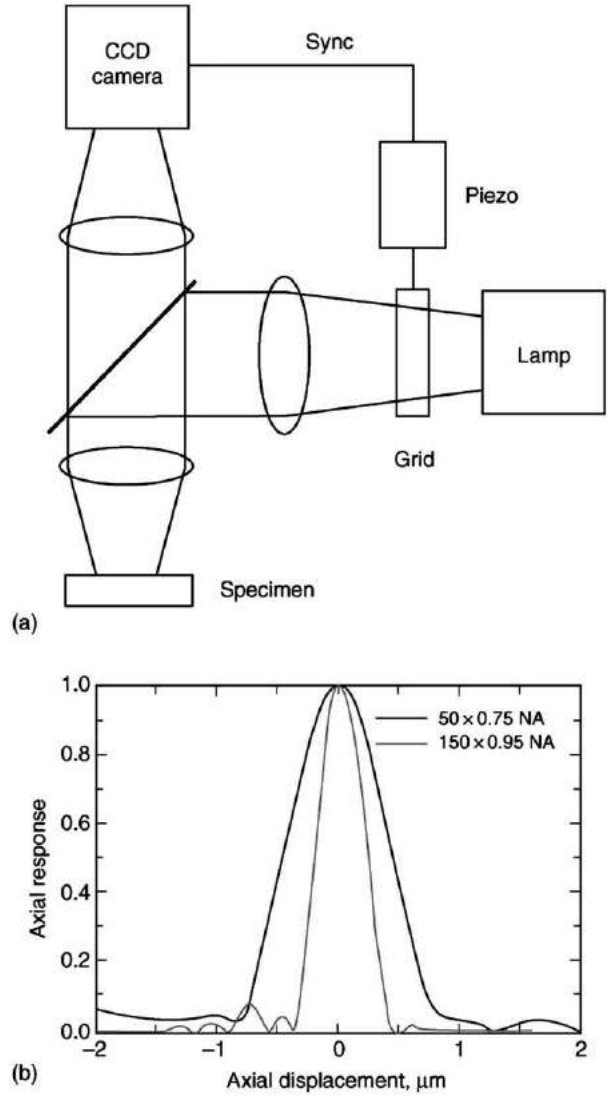


Fig. 11 (a) Shows the optical system of the structured illumination microscope together with experimentally obtained axial responses in (b) which confirm the optical sectioning ability of the instrument.

case. Here the fluorescence is generated only in the focal region and not throughout the focal volume. Furthermore since all the fluorescence is detected via a large area detector – no pinhole is involved – it is not so important if further scattering events take place. This leads to high-contrast images which are less sensitive to scattering. This is particularly important for specimens which are much more scattering at the fluorescence ($\lambda/2$) wavelength than the excitation (λ) wavelength.

The Use of Structured Illumination to Achieve Optical Sectioning

An alternative approach to obtain optical sectioning is to use structured illumination in a conventional microscope. This approach is attractive since the conventional light microscope already possesses many desirable properties: real-time image capture, standard illumination, ease of alignment, etc. However, it does not produce optically sectioned images in the sense usually understood in confocal microscopy. In order to see how this deficiency may be corrected via a simple modification of the illumination system let us begin by looking at the theory of image formation in a conventional fluorescence microscope and start by asking in what way the image changes as the microscope is defocused. We know that in a confocal microscope the image signal from all object features attenuates with defocus and that this does not happen in a conventional microscope. However, when we look closely at the image formation process we find that it is only the zero spatial frequency (constant) component which does not change with defocus (**Fig. 9**); all other spatial frequencies actually do attenuate with defocus to a greater or lesser extent. **Fig. 10** illustrates this by showing the image of a single spatial frequency one-dimensional bar pattern object for increasing degrees of defocus. When the specimen is imaged in focus, a good image of the bar pattern is obtained. However with increasing defocus the image becomes progressively poorer and weaker until it eventually disappears leaving a uniform gray level. This observation is the basis of a simple way to perform optical sectioning in a conventional microscope.

If we simply modify the illumination path of the microscope so as to project onto the object the image of a one-dimensional, single spatial frequency fringe pattern, then the image we see through the microscope will consist of a sharp image of those parts of the object where the fringe pattern is in focus together with an out-of-focus blurred image of the rest of the object. In order to obtain an optically sectioned image it is necessary to remove the blurred out-of-focus portion as well as the fringe pattern from the in-focus optical section. There are many ways to do this – one of the simplest involves simple processing of three images taken at three different spatial positions of the fringe pattern. The out-of-focus regions remain fairly constant between these images and the

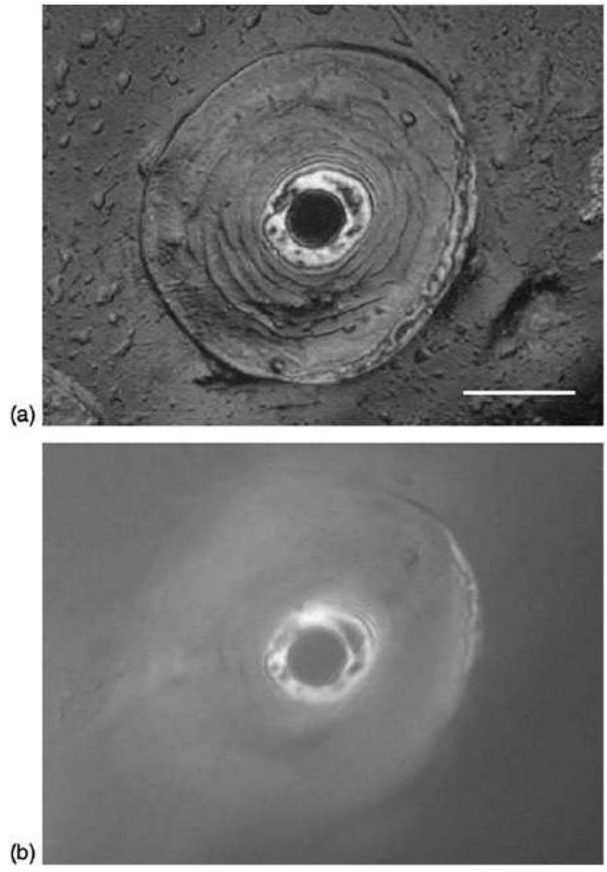


Fig. 12 Two images of the region around the spiracle of a head louse. As in the previous figure, (a) is an autofocus image and (b) shows a mid-focus conventional image. The scale bar depicts a length of 10 μm.

relative spatial shift of the fringe pattern allows the three images to be combined in such a way as to remove the fringes. This permits us to retrieve both an optically sectioned image as well as a conventional image in real time.

Since the approach involves processing three conventional microscope images, the image formation is fundamentally different from that of the confocal microscope. However, the depth discrimination or optical sectioning strength is very similar and this approach, which requires very minimal modifications to the instrument, has been used to produce high-quality three-dimensional images of volume objects which are directly comparable to those obtained with confocal microscopes. A schematic of the optical arrangement is shown in **Fig. 11(a)**, together with experimentally obtained axial responses in **Fig. 11(b)**. It will be noted that these responses are substantially similar to those obtained in the true confocal case. As an example of the kind of images which can be obtained with this kind of microscope, we show in **Fig. 12** two images of a spiracle of a head louse. The first is an auto-focus image of greatly extended depth of field constructed from a through-focus series of images. The second is a conventional image taken at mid-focus. The dramatic increase in depth of field is clear when compared with a mid-focus conventional image. We note that these images were taken using a standard microscope illuminator as light source. Indeed, the system is so light efficient that good-quality optical sections have been obtained or transistor specimens using simply a candle as light source!

Imaging using fluorescence light is also possible using this technique. However, an alternative approach that does not require a physical grid is possible if a laser is used as the light source. In this system the laser illumination is split into two beams which are allowed to interfere at an angle in the fluorescent specimen. This has the effect of directly 'writing' a one-dimensional fringe pattern in the specimen. Spatial shift of the fringe pattern is achieved by varying the phase of one of the interfering beams. As before, three images are taken from which both the optically sectioned image and conventional image may be obtained. The beauty of this approach is that no imaging optics are required at the illuminating wavelength and system.

Summary

We have discussed the origin of the optical sectioning property in the confocal microscope in order to introduce the range of imaging modes which this unique form of microscope leads to. A range of optical architectures have also been described. By far the most universal is that shown in **Fig. 1** where a confocal module is integrated around a conventional optical microscope. Other, more recent, real-time implementations have also been described. A number of practical aspects of confocal microscopy have not been discussed. This is because they are readily available elsewhere, such as advice on the correct choice of detector pinhole size or because they are still the focus of active research, such as the development of new contrast mechanisms for achieving enhanced three-dimensional resolution such as the stimulated emission depletion method, STED or 4-Pi which are still under development but offer great promise.

See also: Overview

Further Reading

Corle, T.R., Kino, G.K., 1996. Confocal Scanning Optical Microscopy and Related Imaging Systems. New York: Academic Press.
Denk, W., Strikler, J.H., Webb, W.W., 1990. Two photon laser scanning fluorescence microscopy. Science 248, 73.
Diaspro, A., 2002. Confocal and Two-Photon Microscopy. New York: Wiley-Liss.
Gu, M., 1996. Principles of Three-Dimensional Imaging in Confocal Microscopes. Singapore: World Scientific.
Hell, S., Stelzer, E.H.K., 1992. Fundamental improvements of resolution with a 4Pi-confocal fluorescence microscope using two-photon excitation. Optics Communication 93, 277.
Hell, S., Wichmann, J., 1994. Breaking the diffraction limit by stimulated emission. Optics Letters 19, 870.
Lukosz, W., 1966. Optical systems with resolving power exceeding the classical limit. Journal of the Optical Society of America 56, 1463.
Masters, B.R., 1996. Confocal Microscopy. Bellingham: SPIE.
Minsky, M., 1961. Microscopy Apparatus. United States Patent 3,013,467, Dec 19, 1961 (Filed Nov 7, 1957).
Neil, M.A.A., Juskaitis, R., Wilson, T., 1997. Method of obtaining optical sectioning by using structured illumination in a conventional microscope. Optics Letters 22, 1905.
Pawley, J.B. (Ed.), 1995. Handbook of Biological Confocal Microscopy. New York: Plenum Press.
Wilson, T. (Ed.), 1990. Confocal Microscopy. London: Academic Press.
Wilson, T., Sheppard, C.J.R., 1984. Theory and Practice of Scanning Optical Microscopy. London: Academic Press.

Atom Optics

AD Cronin and DE Pritchard, Massachussetts Institute of Technology, Cambridge, MA, USA

© 2005 Elsevier Ltd. All rights reserved.

In 1923 Louis de Broglie suggested that particles of matter propagate as waves with a wavelength

$$\lambda_{dB} = h/p \tag{1}$$

where h is Planck's constant and p is the particle's momentum. This breakthrough idea motivated Schrödinger's equation, which is the equation of motion of quantum mechanics.

Schrödinger's equation is a wave propagation equation, and therefore implies the existence of a whole new type of optics – matter wave optics – in which electron waves, neutron waves, atom waves, and entire molecule waves can be manipulated coherently. Such optics enable new measurement technologies and devices that depend on matter wave interference.

Guided by a knowledge of light waves, one can understand that the de Broglie wavelength of a particle sets the scale for focusing, diffraction, and interference. However, there are differences between matter and light. For example, the vacuum is tremendously dispersive for matter waves. In other words, the group velocity for a particle depends on its de Broglie wavelength, while for light waves the group velocity is independent of wavelength.

To illuminate the mathematical connection with light optics, we note the wave equation for light is

$$\nabla^2 \vec{E} = \mu\varepsilon \frac{\partial^2 \vec{E}}{\partial t^2} \tag{2}$$

where $\vec{E} = \vec{E}(\vec{x}, t)$ is the optical electric field, and the parameters μ and ε may vary throughout space, describing an index of refraction. The wave equation for matter waves is Schrödinger's equation:

$$\left(-\frac{\hbar^2 \nabla^2}{2m} + V\right)\psi = i\hbar \frac{\partial}{\partial t}\psi \tag{3}$$

where $\psi = \psi(\vec{x}, t)$ is the probability amplitude, or wavefunction, for a particle of mass m. Here, the potential energy V can vary throughout space, and thus control the phase and amplitude of propagating atoms. Just as density for photons is proportional to $\vec{E}(\vec{x})^2$, the probability density for particles is given by $|\psi(\vec{x})|^2$.

In a vacuum $V = 0$ and $(\mu_0\, \varepsilon_0)^{-1/2} = c$, and if we assume that both ψ and E have a time dependence described by $e^{-ik\omega}$, the wave equations become

$$\left[\nabla^2 + \frac{\omega^2}{c^2}\right]\vec{E} = 0 \tag{4}$$

and

$$\left[\nabla^2 + \frac{2m\omega}{\hbar}\right]\psi = 0 \tag{5}$$

which look similar, but have a critical difference stemming from the single time derivative in Schrödinger's equation. To see how this makes the vacuum dispersive for matter waves, but not for light, consider a propagating plane wave of either ψ or $\vec{E}$ described by $e^{i(\mathrm{kx}-\omega t)}$ (for either kind of wave, $k \equiv 2\pi(\lambda)^{-1}$). Using the wave equation for light waves, the dispersion relation is

$$\omega = ck \tag{6}$$

where c is the phase (and group) velocity of light, which is independent of k. The same plane wave substituted into Schrödinger's equation for matter waves yields the dispersion relation

$$\omega = \frac{\hbar k^2}{2m} \tag{7}$$

This is quadratic for matter waves, which means the group velocity $v_g = d\omega/dk$ is twice the phase velocity $v_p = \omega/k$, and both still depend on k.

From an engineering perspective, matter wave optics consists of lenses, mirrors, beam-splitters, and other components of an optics toolkit. The fact that electrons and neutrons can be transmitted through solid material, and that electrons can be reflected or refracted by static electromagnetic fields, has enabled optical elements to be created for these kinds of matter waves. For atoms, however, finding suitable materials for lenses or mirrors is a daunting task, since with rare exceptions (e.g., cold H on liquid He) atoms thermalize on surfaces rather than elastically bouncing off or passing through them. This was the major obstacle which delayed the blossoming of atom optics until the mid-1980s.

This obstacle has now been circumvented, but only with difficulty. Electromagnetic fields (whose spatial configurations are severely constrained by Maxwell's equations) can change the potential energy of neutral atoms, but since an atom's net charge is zero, provide only a weak and highly dispersive index of refraction based on the atom's polarizability or magnetic moment. However, these effects are tremendously enhanced if the electromagnetic fields oscillate near a transition frequency of the atom.

Hence, propagating waves and standing waves of single-frequency laser light have become standard tools in atom optics. Standing light waves are often referred to as a light crystal, because the periodic potential can diffract atom beams.

An alternative source of atom optical components is based on nanofabrication. Thin sheets of material with patterned holes serve as absorptive atom optics by transmitting atom waves only through the nanometer scale openings. A variety of techniques have been used to make physical diffraction gratings, zone plates, and holograms for atom waves. Methods such as electron beam lithography and ultraviolet photolithography both rely on sophistocated etching procedures to make the final free-standing structures. Thus, in either approach – near-resonant light, or miniature physical structures – current technologies such as the tunable laser or nanofabrication techniques have been required for the development of useful atom optics.

While coherent manipulation of atom waves is often the goal, incoherent manipulations are possible also, e.g., if photons are spontaneously scattered. Dissipative processes offer an additional class of possibilities such as increasing the brightness of an atom source, and are therefore an important part of atom optics. This article excludes atom slowing and trapping, and focuses instead on atom diffraction – a coherent process which can be used to make beam splitters for atom interferometers.

Nanofabricated Atom Optics

Because atoms stick to surfaces, mechanical structures are absorptive atom optics. Yet the de Broglie waves transmitted through slots of a mask are nearly unaffected, provided the mask is thin enough. This is because the van der Waals potential energy of interaction with nearby surfaces falls off rapidly for neutral atoms.

Consider, for example, an atom wave packet being diffracted by a mechanical grating made with physical bars and slots as shown in Fig. 1. Initially, let the atom wave packet have a slowly varying spatial envelope, $f=f(x, y, z)$, and momentum only in the $\hat{x}$-direction, $\vec{p} = \hbar\vec{k}_0 = h(\lambda_{dB})^{-1}\hat{x}$, so the wavefunction can be written as

$$\psi = f e^{i(k_0 x - wt)} \tag{8}$$

Immediately after the grating, only the portions of the wavefunction passing through slots remain nonzero, as depicted in Fig. 2. Here, the wavefunction is now periodic both due to the grating lattice vector $k_g\hat{y}$ and the initial wavevector $k_0\hat{x}$. According to the Schrödinger equation, a periodicity in any direction implies a momentum in that direction. Thus, variation of ψ in the $\hat{y}$ variation gives rise to a new momentum distribution.

The square wave modulating the envelope of the wave packet can be described by a Fourier sum times the incident wavefunction

$$\psi = f e^{i(k_0 x - \omega t)} \sum_{n=-\infty}^{\infty} a_n \cos(n k_g y) \tag{9}$$

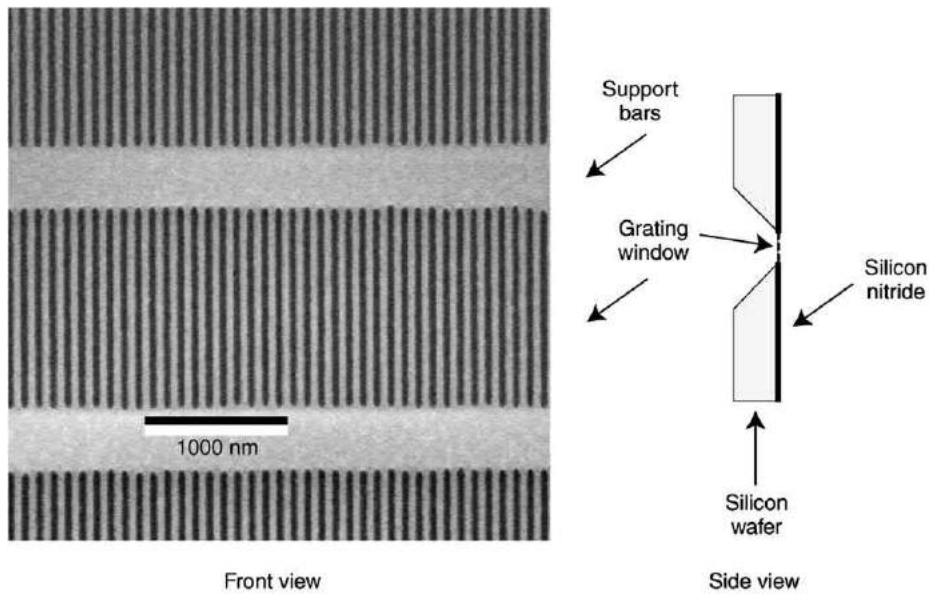


Fig. 1 Scanning electron microscope image of a silicon nitride diffraction grating for atom waves. The bars (light) absorb, and the slots (dark) transmit atom waves. The grating period is 100 nm, the open fraction is 0.67, and the free-standing bars are supported every 5 μm with a thicker strip of silicon nitride material. The grating was fabricated by Tim Savas and Henry I Smith at MIT NanoStructures laboratory.

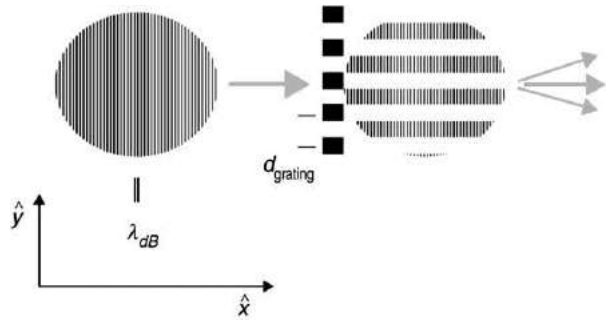


Fig. 2 Schematic diagram of an atom wavepacket passing through an absorbing grating, as seen from above. The atom wavepacket is depicted before and after passing through the grating from left to right.

where $k_g = 2\pi(d_g)^{-1}$ is the grating lattice vector. The only other physical parameter of the grating is the open fraction, γ, and this determines the Fourier amplitudes a_n

$$a_n = \frac{\sin(n\pi\gamma)}{n\pi} \tag{10}$$

From the principle of superposition (which is applicable here because the Schrödinger equation is linear) the wavefunction can be written as a sum of traveling waves with wavevectors $\vec{k}_n$:

$$\psi = f \sum_{n=-\infty}^{\infty} a_n e^{(i\vec{k}_n \cdot \vec{r} - \mathrm{wt})} \tag{11}$$

$$\vec{k}_n = \frac{k_0 \hat{x} + n k_g \hat{y}}{N} \tag{12}$$

where, just as in standard optics, the factor N serves to keep $|\vec{k}_n|$ on a spherical shell, i.e., the grating does not add energy to the atom.

Inserting this expression for the wavefunction into Schrödinger's equation we get the dispersion relation for matter waves and a different group velocity, v_n, for each k_n

$$\hbar\omega = \frac{\hbar^2 k_n^2}{2m} \tag{13}$$

$$v_n = \frac{d\omega}{dk_n} = \frac{\hbar k_n}{m} = p_n/m \tag{14}$$

Thus, diffraction through a grating puts an atom into a coherent superposition of different momenta, each separated by $\sim \hbar k_g \hat{y}$. Some time later, the atom will be in a coherent superposition of multiple locations, and the far-field probability density will be peaked at integer multiples of the diffraction angle

$$\Theta_D = \frac{k_g}{k_0} = \frac{\lambda_{dB}}{d_{\mathrm{grating}}} \tag{15}$$

where d_{grating} is the lattice spacing of the grating and the small-angle approximation for $\sin(\theta)$ has been used. Exactly as in light optics, these diffraction gratings are good momentum spectrometers, i.e., the diffraction angle is a measure of longitudinal momentum. (Contrary to light optics, group velocity can also be used to measure matter wave momentum.) Coherence between the diffraction orders remains until a perturbation occurs which would (even in principle) be sufficient to determine which path the atom took. This assertion has been tested with atoms in an interferometer (discussed below).

Atom flux in the nth diffraction order is given by

$$I_n = \left(\frac{\sin(n\pi\gamma)}{n\pi}\right)^2 \tag{16}$$

To resolve the diffracted orders the initial transverse momentum distribution of the atoms must be smaller than k_g, and the time until the far-field observation must be sufficiently large given the beam width. At intermediate times, the atom waves are in the Fresnel diffraction region where the Talbot effect can be observed. This effect causes the atom waves to form a replica of the grating in free space at integer multiples of the Talbot length, $Z_T = 2d_{\mathrm{grating}}^2 \lambda_{dB}^{-1}$.

Fig. 3 shows the far-field diffraction pattern from a beam of sodium (^{23}Na) atoms using a material grating with a period of 100 nm. The atom beam velocity peaked at 1500 ms^{-1} corresponds to a de Broglie wavelength of 0.11 Å thus, $\Theta_D \approx 10^{-4}$rad. (The beam of 3000 ms^{-1} atoms diffracts at half this angle.) The spread in longitudinal velocity of $\sigma_v/v \approx 6\%$ can be deduced from the data because it slightly increases the width for higher order diffraction peaks. The open fraction of the grating, $\gamma \approx 60\%$, can also be determined from the diffraction data, because it determines the relative intensity of the orders. Effects of the atoms' finite size and interaction with the grating bars make small corrections to this simple theory.

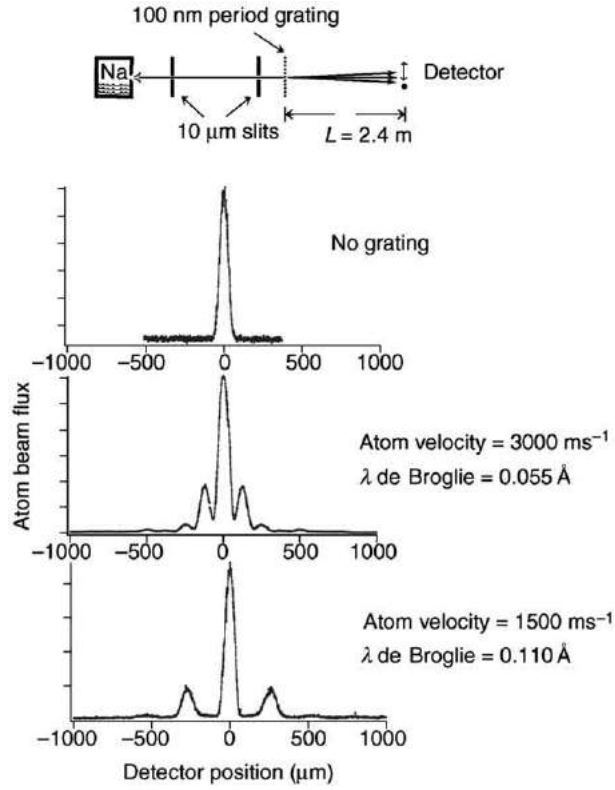


Fig. 3 Diffraction data from a beam of sodium formed by passing atoms through two collimating slits followed by a nanofabricated diffraction grating. The momentum of the atoms determines their de Broglie wavelength, and thus their diffraction angle $\sin(\Theta_D) = \lambda_{dB}/d_{\text{grating}}$. These data were obtained at MIT by the authors.

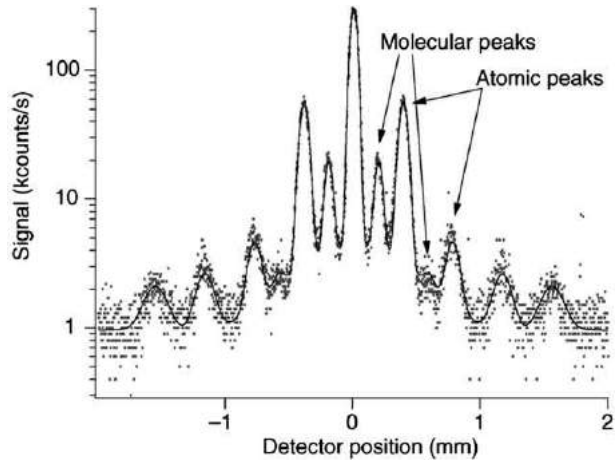


Fig. 4 Diffraction data using a mixed beam of sodium atoms (Na) and sodium dimer molecules (Na_2). From this source molecules have the same speed as atoms, thus twice the momentum. Thus, molecule waves are diffracted at half the diffraction angle compared to atom waves. These data were obtained at MIT by the authors.

Nanofabricated atom optics differ from those based on light forces in a number of ways: they are amplitude structures (with corresponding loss of transmission intensity), they are species-independent, their scale size can be several times smaller than attainable with light, and they can be arbitrarily patterned since they are fabricated by electron beam lithography. Insensitivity to species is demonstrated in Fig. 4, where a beam of Na_2 molecules and Na atoms is diffracted and separated by a nanofabricated diffraction grating. The flexibility of electron beam lithography has allowed fabrication not only of diffraction gratings, but also of spherical and cylindrical zone plates, as well as a combination of lens and a hologram that generates a focused atom image. One stunning application laid to rest a long-standing argument concerning whether a stable bound state of the $^4He_2$ dimer exists. For

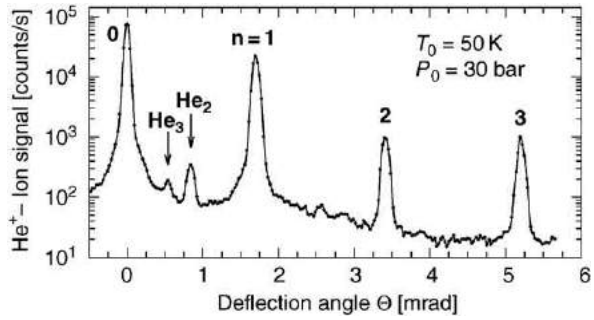


Fig. 5 Diffraction of helium atoms and helium molecules through a nanofabricated grating. These data, reproduced with permission from Wieland Schoellkopf, were obtained at the Max-Planck-Institute in Göttingen.

this a diffraction grating was used to separate and resolve $^4He_2$ and more massive clusters (**Fig. 5**). Subsequently a nano-sieve was used to estimate the size of the $^4He_2$ dimers to be 62 ± 10 Å.

Standing Waves of Light

In contrast to nanofabricated structures, standing waves of near-resonant light are phase gratings for atoms. The optical electric field dynamically polarizes the atoms and causes a shift to the ground state energy (the ac-Stark shift). For optical electric fields oscillating above (below) the atomic resonance frequency, the ac-Stark shift increases (decreases) potential energy for atoms and in either case perturbs the de Broglie wave phase.

In many respects, the interaction of an atom with a standing light wave is richer than the more familiar topic of light–atom interactions in a traveling light wave. Part of this richness reflects two ways in which a standing wave can be considered, either as two counter-propagating traveling waves or as a single, stationary standing wave. The standing wave–atom interaction is capable of transferring momentum in well-determined quantities, coherently splitting atomic wave packets, and generating forces much larger than possible with spontaneously scattered light. Not surprisingly, this interaction has many distinct facets that only appear in different regimes of the interaction parameters (intensity, detuning, and pulse duration) and atomic parameters (mass, initial momentum with respect to the standing wave, and excited state natural lifetime).

We begin with the Bragg scattering of atoms from a standing wave light grating. Although it can be difficult to realize the physical conditions that assure its occurrence, pure Bragg scattering is simpler than intermediate cases involving spontaneous decay (from light too close to resonance) or Kapitza–Dirac diffraction (from shorter interaction times).

Consider a standing wave light grating formed by two counter-propagating plane waves (traveling parallel to the z-axis) of equal amplitude, E_0, wavevector, k, frequency, ω, polarization vector, $\hat{e}$, and temporal envelope function, $f(t)$:

$$\vec{E}(z,t) = E_0 f(t)\sin(kz - \omega t)\hat{e} + E_0 f(t)\sin(kz + \omega t)\hat{e} \tag{17}$$

$$= 2E_0 f(t)\,\sin(kz)\,\cos(\omega t)\hat{e} \tag{18}$$

We would like to work with momentum states as our atomic basis, thus it is easiest to consider the description of the electric field driving the transitions in terms of two counter-propagating traveling waves of definite momentum (**Eq. (17)**), as opposed to the single standing wave they jointly form (**Eq. (18)**).

Momentum is transferred by paired stimulated absorption and emission processes, resulting in a transfer of photons between the traveling waves. An N_B^{th} order diffraction process transfers N_B photons from one traveling wave to the counter-propagating traveling wave and changes the atomic momentum by $2N_B\hbar k\hat{z}$. Furthermore, atomic population is transferred only between $|g, -N_B\hbar k\rangle$ and $|g, +N_B\hbar k\rangle$, where $|g(e), \pm N\hbar k\rangle$ denotes a two-level atom in its ground (excited) state with momentum $\pm N\hbar k$ parallel to the standing wave axis. The excited state remains nominally unpopulated so long as the temporal envelope function, $f(t)$, does not have strong frequency components near the laser detuning

$$\delta = \omega - \omega_0 \tag{19}$$

where ω_0 is the unperturbed frequency of the atomic transition. Furthermore, for a given initial state ($|g, -N_B\hbar k\rangle$) the uniqueness of the final state ($|g, +N_B\hbar k\rangle$) occurs because of the fundamental assumption that makes Bragg scattering so simple to describe; the uncertainty in the photon energy driving the transitions is small compared to the energy separation between neighboring momentum states. A quantitative discussion of the validity of this assumption will be given later.

We now calculate the probability, $P_1^B(\tau)$, of the first order ($N_B = 1$) Bragg process. Scattering transfers an atom from $|g, -\hbar k\rangle$ to $|g, +\hbar k\rangle$ when the atoms interact with a constant light intensity for a time τ (i.e., in **Eqs. (17)** and **(18)** $f(t)$ is a square wave of unit amplitude and duration τ). The geometry for Bragg diffraction from a standing wave of light is shown in **Fig. 6**, and the energy/momentum states involved in the transition are depicted in **Fig. 7**.

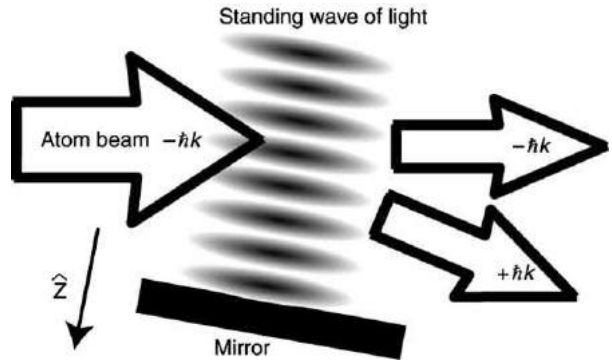


Fig. 6 Two counter-propagating running waves of light superimpose to form a standing wave of light. This 'light crystal' acts as a diffraction grating for atoms, shown here in the configuration for Bragg diffraction.

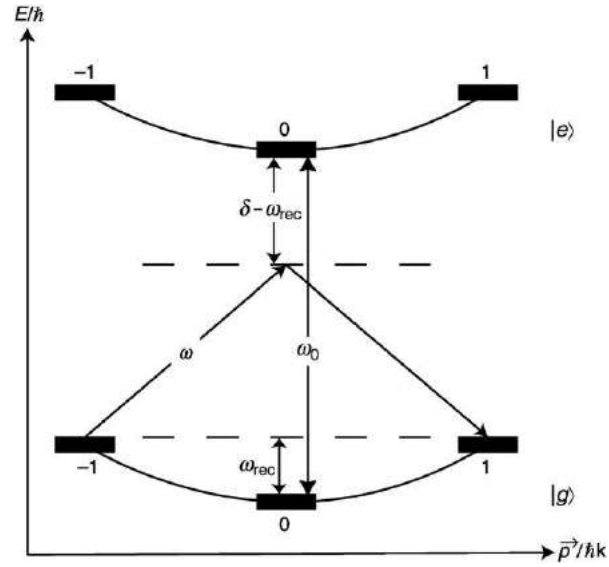


Fig. 7 Energy vs. momentum diagram describing atomic states involved in Bragg diffraction. The total energy is due to the electronic state ($|g\rangle$, $|e\rangle$) plus the kinetic energy associated with the recoil from photon emission (or absorption). In Bragg diffraction, atoms make a coherent transition from $|g, -\hbar k\rangle \leftrightarrow |g, +\hbar k\rangle$. Reprinted from Gupta S, *et al.* (2001) Coherent manipulation of atoms with standing light waves. *Comptes Rendus de L'Academie des Sciences – Series IV – Physics-Astrophysics* 2:479–495, copyright (2001) with permission from Elsevier.

Considering the electronic degree of freedom, we rewrite the Schrödinger equation as

$$(\mathcal{H}_0 + \mathcal{H}_{\text{int}})|\psi\rangle = i\hbar \frac{\partial}{\partial t}|\psi\rangle \tag{20}$$

where the total Hamiltonian $\mathcal{H} = \mathcal{H}_0 + \mathcal{H}_{\text{int}}$ is a matrix. The wavefunction is a vector of coefficients c_i in the basis $\{|g, -\hbar k\rangle, |e, 0\rangle, |g, +\hbar k\rangle\}$, with normalized population amplitudes for each component:

$$|\psi\rangle = \begin{pmatrix} c_{-1}(t) \\ c_0(t) \\ c_{+1}(t) \end{pmatrix} \tag{21}$$

In the electric dipole approximation, the interaction Hamiltonian is $\mathcal{H}_{\text{int}}(t) = -\vec{\mu} \cdot \vec{E}(t)$, where $\mu = \langle e|q\vec{r}|g\rangle \cdot \hat{e}$ is the electric dipole matrix element connecting the ground ($|g\rangle$) and excited ($|e\rangle$) states of the atom. $\hat{e}$ is the polarization vector of the light and q is the charge of the electron. By momentum conservation, only the plane wave traveling in the $\pm\hat{z}$ direction couples the $|e, 0\rangle \leftrightarrow |g, \mp\hbar k\rangle$ transitions. By using this argument, we are effectively viewing the electric field as a quantum mechanical operator. Expanding the sinusoidal variation of the electric field in terms of complex exponentials and treating the spatially dependent

complex exponential terms as quantum mechanical momentum translation operators yields the interaction Hamiltonian:

$$\mathcal{H}_{\text{int}} = \frac{\hbar\omega_R}{2}\begin{pmatrix} 0 & ie^{i\omega t} & 0 \\ -ie^{-i\omega t} & 0 & ie^{-i\omega t} \\ 0 & -ie^{i\omega t} & 0 \end{pmatrix} \tag{22}$$

For example, $e^{\pm ikz}|g, n\hbar k\rangle = |e, (n\pm 1)\hbar k\rangle$ describes absorption, and for stimulated emission, $e^{\mp ikz}|e, n\hbar k\rangle = |g, (n\pm 1)\hbar k\rangle$. This procedure includes the rotating wave approximation. In addition, we have neglected any frequency components associated with the sudden switch on of the fields and the finite duration of the light–atom interaction. In formulating $\mathcal{H}_{\text{int}}$, the strength of the light–atom interaction is parameterized by the single-photon Rabi frequency:

$$\omega_R = \frac{\mu E_0}{\hbar} \tag{23}$$

Without loss of generality, we will take μ and hence ω_R to be positive, real-valued quantities.

The total Hamiltonian follows simply by including the electronic and kinetic energy terms:

$$\mathcal{H}_0 = \hbar\begin{pmatrix} \omega_{\text{rec}} & 0 & 0 \\ 0 & \omega_0 & 0 \\ 0 & 0 & \omega_{\text{rec}} \end{pmatrix} \tag{24}$$

where the single-photon recoil energy, E_{rec}, of an atom of mass m is given by

$$E_{\text{rec}} = \hbar\omega_{\text{rec}} = \frac{\hbar^2 k^2}{2m} \tag{25}$$

Making the *ansatz* for the solution wavefunction as

$$|\psi\rangle = \begin{pmatrix} c_{-1}(t)e^{-i\omega_{\text{rec}}t} \\ c_0(t)e^{-i\omega_0 t} \\ c_{+1}(t)e^{-i\omega_{\text{rec}}t} \end{pmatrix} \tag{26}$$

and substituting into the Schrödinger equation yields three coupled first-order differential equations:

$$\dot{c}_{\pm 1}(t) = \mp\frac{\omega_R}{2}e^{i\Delta t}c_0(t), \tag{27}$$

$$\dot{c}_0(t) = \frac{\omega_R}{2}e^{-i\Delta t}(c_{+1}(t) - c_{-1}(t)), \tag{28}$$

where $\Delta = \delta + \omega_{\text{rec}} = (\omega - \omega_0) + \omega_{\text{rec}}$. Differentiating **Eq. (27)** and substituting **Eq. (28)** into the result yields two coupled second-order differential equations:

$$\ddot{c}_{\pm 1}(t) - i\Delta\dot{c}_{\pm 1}(t) + \frac{\omega_R^2}{4}(c_{\pm 1}(t) - c_{\mp 1}(t)) = 0 \tag{29}$$

With the initial conditions:

$$c_{-1}(0) = 1 \tag{30}$$

$$c_0(0) = 0 \Rightarrow \dot{c}_{\pm 1}(0) = 0 \tag{31}$$

$$c_{+1}(0) = 0 \tag{32}$$

and the assumption $\Delta^2 \gg \omega_R^2$, the solutions to **Eq. (29)** are

$$c_{-1}(t) = e^{-i\frac{\omega_R^{(2)}}{2}t}\cos\left(\frac{\omega_R^{(2)}}{2}t\right) \tag{33}$$

$$c_{+1}(t) = ie^{-i\frac{\omega_R^{(2)}}{2}t}\sin\left(\frac{\omega_R^{(2)}}{2}t\right) \tag{34}$$

where the two-photon Rabi frequency is

$$\omega_R^{(2)} = \frac{\omega_R^2}{2\Delta} \to \frac{\omega_R^2}{2\delta}, \quad |\delta| \gg \omega_{\text{rec}} \tag{35}$$

with both transitions driven at equal single-photon Rabi frequencies, ω_R.

Substituting the solution of **Eqs. (33)** or **(34)** into **Eq. (27)** yields an expression for the excited state amplitude:

$$c_0(t) = i\frac{\omega_R}{2\Delta}e^{-i\Delta t}e^{-i\omega_R^{(2)}t} \tag{36}$$

This will be important in calculating the rate of spontaneous emission events later.

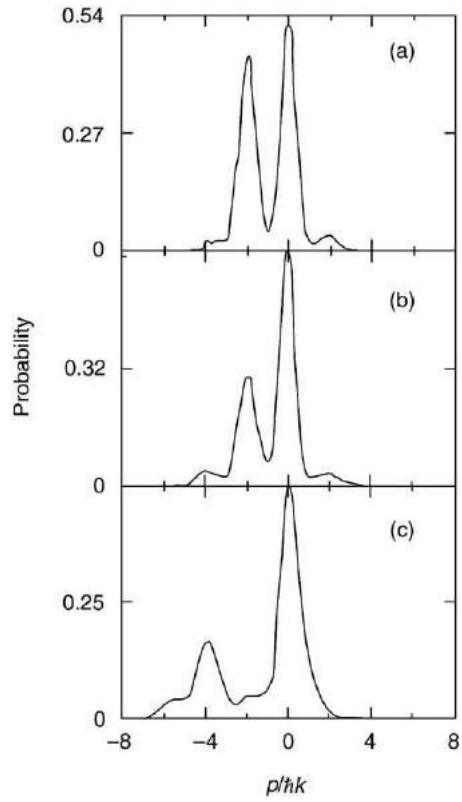


Fig. 8 Bragg scattering of an atom beam from an optical standing wave. First-order Bragg scattering at (a) lower power, (b) higher power of the laser beams (Pendellösung has set in, increasing the amplitude of the undeflected peak), (c) second-order Bragg scattering. Reprinted with permission from *Physical Review Letters* 60(6): 515–518. Copyright (1998) by the American Physical Society.

The solutions for $c_{-1}(t)$ and $c_{+1}(t)$ oscillate with the interaction duration, τ, yielding the result for the $|g, -\hbar k\rangle \rightarrow |g, +\hbar k\rangle$ transition probability:

$$P_1^B(\tau) = |c_{+1}(\tau)|^2 = \sin^2\left(\frac{\omega_R^{(2)}}{2}\tau\right) \tag{37}$$

Thus, the system oscillates between the two momentum states $|g, -\hbar k\rangle$ and $|g, +\hbar k\rangle$ in a manner analogous to the Rabi oscillation of atomic population between two resonantly coupled states. This solution with oscillatory probabilities for the two Bragg coupled states is known as the Pendellösung and has been observed for atoms, neutrons, and X-rays (**Fig. 8**). The nice feature here is that the strength of the grating can be actually controlled by the intensity of the light.

Viewing Bragg scattering as a two-photon transition from the initial ground state to the final ground state with opposite momentum, illuminates the close connection with a Raman transition between two internal sub-states of the ground state manifold, each with its own external momentum state. The formalism describing the Raman transition is basically the same as that presented here, except the two transitions can be driven at different single-photon Rabi frequencies, ω_{R1} and ω_{R2}, so that the generic two-photon Rabi frequency is given by $\omega_R^{(2)} = \omega_{R1}\omega_{R2}/2\Delta$, where Δ is the detuning from the intermediate state.

An N_B^{th} order Bragg process (similar to a $2N_B$-photon Raman process) is a coherent succession of N_B two-photon transitions from $|g, -N_B\hbar k\rangle$ to $|g, +N_B\hbar k\rangle$ with $2N_B - 1$ intermediate states of the form:

$$|e, (-N_B + 1)\hbar k\rangle, |g, (-N_B + 2)\hbar k\rangle \ldots$$

$$\ldots |g, (N_B - 2)\hbar k\rangle, |e, (N_B - 1)\hbar k\rangle$$

Such a process is characterized by a $2N_B$-photon Rabi frequency given by

$$\omega_R^{(2N_B)} = \frac{[\omega_R]^{2N_B}}{2^{2N_B-1}\Delta_1\Delta_2\cdots\Delta_{2N_B-1}} \tag{38}$$

where Δ_n is the detuning from the n^{th} intermediate state. **Fig. 9** shows what this process would look like for an N_B^{th} order Bragg transition where the intermediate state detunings are given by

$$\Delta_n = \left\{ \begin{array}{ll} \delta + (2N_B n - n^2)\omega_{\text{rec}}: & n \text{ odd} \\ (2N_B n - n^2)\omega_{\text{rec}}: & n \text{ even} \end{array} \right\} \tag{39}$$

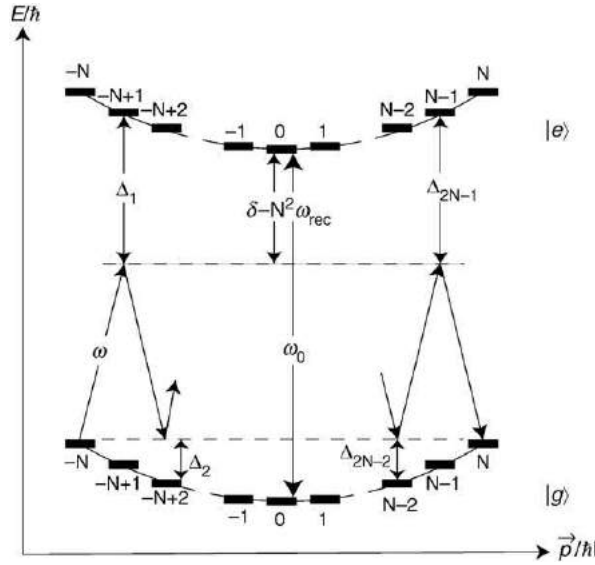


Fig. 9 Energy vs. momentum diagram describing atomic states involved in higher-order Bragg diffraction. Reprinted from Gupta S, *et al.* (2001) Coherent manipulation of atoms with standing light waves. *Comptes Rendus de L'Academie des Sciences – Series IV – Physics-Astrophysics* 2:479–495, copyright (2001) with permission from Elsevier.

Substituting these detunings into **Eq. (38)** yields the N_B^{th} order Bragg transition $2N_B$-photon Rabi frequency, $\omega_R^{(2N_B)}$:

$$\omega_R^{(2N_B)} = \frac{[\omega_R]^{2N_B}}{2^{4N_B-3}[(N_B-1)!]^2\delta^{N_B}\omega_{\text{rec}}^{N_B-1}} \tag{40}$$

where we have assumed $|\delta| \gg N_B^2\omega_{\text{rec}}$.

To ensure that the system truly undergoes Bragg scattering, and validate the assumption that only states of equal kinetic energy and opposite momentum are coupled, the overall exposure time, τ, of the atoms to the fields must be limited both from below and above.

The lower bound on τ is necessary to resolve the final momentum state ($|g, N_B\hbar k\rangle$) from neighboring momentum states ($|g, (N_B \pm 2)\hbar k\rangle$) two photon recoil momenta away. Avoiding population transfer into these states requires that the energy separation be resolvable, or

$$\tau(\delta E) \gg h \tag{41}$$

For first-order Bragg scattering processes ($N_B = 1$) the nearest lying momentum states that may be mistakenly populated are $|g, \pm 3\hbar k\rangle$, for which

$$\delta E = \frac{p_{n=3}^2}{2m} - \frac{p_{n=1}^2}{2m} = 8\hbar\omega_{\text{rec}} \tag{42}$$

Therefore

$$\tau \gg \frac{h}{8\hbar\omega_{\text{rec}}} = \frac{\pi}{4\omega_{\text{rec}}} \tag{43}$$

For sodium atoms (^{23}Na) in 590 nm light, $\tau \gg 6$ μs is the lower bound required for first-order Bragg scattering.

For all higher-order ($N_B > 1$) Bragg scattering processes, the nearest momentum states are $|g, \pm(N_B - 2)\hbar k\rangle$, which limits the interaction time to

$$\tau \gg \frac{\pi}{2(N_B-1)\omega_{\text{rec}}} \tag{44}$$

which for $N_B \gg 1$ reduces to

$$\tau \gg \frac{\pi}{2N_B\omega_{\text{rec}}} \tag{45}$$

The upper bound on the interaction duration is necessary to avoid spontaneous emission. The interaction duration must be short enough so that the expected number, N_s, of spontaneous emission events per atom during the time τ is negligible. N_s is simply given by the product of the excited state fraction (**Eq. (36)**) and the probability of spontaneous decay given that the atom is in the excited state:

$$N_s = |c_0(t)|^2\Gamma\tau = \frac{\omega_R^2}{4\Delta^2}\Gamma\tau \tag{46}$$

where Γ is the natural decay rate of the excited state. Avoiding spontaneous emission ($N_s \ll 1$) while still having a significant probability for transitions $\left(\omega_R^{(2N_B)}\tau \simeq \pi\right)$ forces one to work in the regime where $\Delta \gg \Gamma$, which is a practical requirement to avoid spontaneous emission and maintain coherence. For sodium atoms on the 590 nm transition, $\Gamma = 6.3 \times 10^7\ \text{s}^{-1}$, and a typical choice in Bragg diffraction experiments is $\Delta = 50\Gamma$ or $\Delta/2\pi = 500$ MHz.

Briefly, to relate Rabi frequency to optical intensity, the transition rate W on resonance with a Lorentzian spectral line is given by Fermi's golden rule:

$$W = \frac{\omega_R^2}{\Gamma} = \frac{\lambda_{\text{photon}}^2}{2\pi}\frac{I}{\hbar\omega} \tag{47}$$

where the last term can be regarded as the cross section for absorption multiplied by intensity in units of photon flux. Hence

$$\omega_R^2 = \Gamma\frac{\lambda_{\text{photon}}^2}{2\pi}\frac{I}{\hbar\omega} \tag{48}$$

For Na atoms in 12 mW(cm)$^{-2}$ resonant light, $\omega_R = \Gamma = 6.3 \times 10^7\ \text{s}^{-1}$. Both the probability of Bragg scattering and the spontaneous emission increase linearly with $\omega_R^2\tau\Gamma^{-1}$. However, spontaneous emission decreases as Δ^2 while the Bragg scattering probability decreases as Δ. Thus, as shown in **Fig. 10**, at sufficient detuning and laser power, Bragg scattering occurs with no spontaneous emission. For reference, 12 mW(cm)$^{-2} \times 10$ μs corresponds to $\omega_R^2\tau\Gamma^{-1} = 630$ for sodium atoms.

Bragg scattering of atoms from a standing light wave was first observed at MIT in 1988. A supersonic atomic beam was diffracted from a standing wave of near-resonant laser light as depicted in **Fig. 6**. The angle between the atomic beam (of thermal wavelength λ_{dB}) and the light grating (of periodicity $\lambda_L/2$) was tuned to the appropriate Bragg angle, θ_B, where:

$$\lambda_{dB} = \lambda_L \sin(\theta_B) \tag{49}$$

Population transfer corresponding to both first- and second-order Bragg scattering was observed (**Fig. 7**). The experiment required a sub-recoil transverse momentum spread of the atomic beam in order to resolve the different momentum states in the far field and limit the final state to only one diffracted order. The Pendellösung was observed as an oscillation in population transfer as a function of standing wave intensity, $I \propto \omega_R^{(2)}$, for a fixed interaction time, τ.

Atomic beam diffraction from an optical standing wave is a continuous-wave (CW) experiment in which the selectivity needed for the Bragg process is imposed by good angular resolution of the particle beam and a high degree of parallelism between the light crystal planes. This ensures that of the various final Bragg orders allowed by momentum conservation, only one conserves energy (energy conservation is exact in a CW experiment). For atoms scattering from a light crystal, parallelism of the crystal planes requires highly parallel photon momentum that implies a minimum width of the standing wave (the diffraction limit for the collimated photons). The transit time, τ, of the atoms across this width then exceeds the lower bound given in **Eq. (44)**.

The excellent collimation required of the atomic beam to ensure resolution of the Bragg scattered atoms reduces the intensity of the source by many orders of magnitude. A Bose–Einstein Condensate (BEC) is an attractive alternative source of atoms because its momentum spread is typically an order of magnitude below a single-photon recoil momentum. To Bragg diffract atoms initially in a stationary BEC, it is easier to move the light crystal than to accelerate the condensate. This is done by simply frequency shifting one of the traveling waves so that the resultant standing wave formed by its interference with the unshifted traveling wave moves with the proper velocity ($N_B\hbar k/m$) relative to the stationary atoms to impart the necessary momentum. The Bragg scattered atoms will then have momentum $2N_B\hbar k$ in the laboratory frame. The resonance condition thus becomes a condition on relative detuning, δ_{N_B}, between the two laser beams forming the diffraction grating. For N_B^{th}-order Bragg diffraction, the relative detuning is given by

$$\delta_{N_B} = \frac{2N_B\hbar k^2}{m} = 4N_B\omega_{\text{rec}} \tag{50}$$

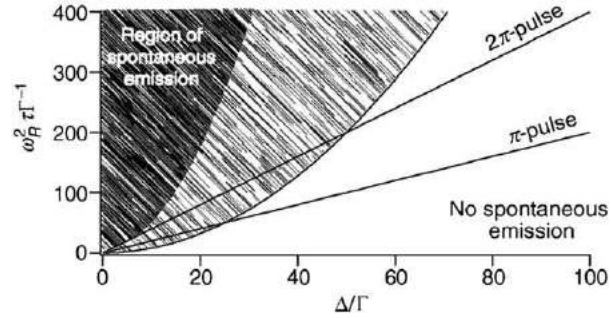


Fig. 10 The conditions for which $N_s > 0.02(0.10)$ are hashed in light(dark) gray. ω_R^2/Γ is proportional to optical intensity. The line labeled π-pulse indicates the parameters which cause complete first-order Bragg diffraction. The line labeled 2π-pulse indicates conditions where population is completely transferred back to the initial state (Pendellösung oscillation).

The first demonstration of Bragg scattering in a BEC was at NIST in 1999. They used Bragg scattering mainly as a tool to manipulate the momentum of the BEC, observing up to sixth-order processes. At MIT the interaction time was lengthened (to $\approx$ 100 times the lower bound of Eq. (44) for first-order Bragg scattering), creating a new type of spectroscopy called Bragg Spectroscopy. It is a spectroscopic measurement of the shift of the Bragg scattering frequency due to the Doppler shift ($k \cdot v$) from the atoms' motion together with any mean field interaction. (These effects can be separated by going to higher-order Bragg scattering to enhance the Doppler shift.)

Bragg Spectroscopy was used to observe the momentum distribution of a BEC in a magnetic trap. The width of the Bragg resonance curve was primarily due to a 2 kHz Doppler-broadening that yielded the momentum distribution of the condensate. The spread in the corresponding velocity distribution was very small (≈ 0.5 mm s^{-1}), even smaller than allowed by the Heisenberg uncertainty limit for a particle confined in the ground state of a harmonic trap. This reflects the increase in size of the condensate due to the mean field repulsion (^{23}Na, used in the MIT experiment, has a positive scattering length). The distribution was Heisenberg uncertainty limited at the observed size of the BEC, establishing for the first time that the coherence length of the condensate was equal to its size. In addition, the narrow Bragg resonance was shifted by the repulsive interactions within the condensate, resulting in a spectroscopic measurement of the mean-field energy.

Kapitza–Dirac Scattering

Diffraction of neutral atoms from a standing wave of near-resonant light with a short interaction time ($\tau_{KD} \ll 1/\omega_{\text{rec}}$) has come to be called Kapitza–Dirac scattering, in honor of their pioneering suggestion. In 1933, Kapitza and Dirac predicted that an electron beam propagating in a standing light wave would undergo stimulated Compton scattering and be reflected. This process has a tiny cross-section, equal to the classical electron radius squared: $\sigma_{\text{Compton}} = 8\pi/3(e^2/mc^2)^2 \approx 6 \times 10^{25}$ cm^2, and has only recently been observed using extremely high laser intensities. If the electrons are replaced by atoms, however, the scattering cross-section for resonant light $\sigma_{\text{atom}} = (1/2\pi)\lambda^2_{\text{photon}} \approx 4 \times 10^{-10}$ cm^2 is 15 orders of magnitude larger. This large cross-section, together with the ready availability of tunable lasers, has allowed stimulated scattering, both in the Kapitza–Dirac and Bragg regimes, to become the primary tool for the coherent manipulation of atoms.

In Kapitza–Dirac scattering, atomic motion during the interaction time is small compared to the characteristic dimensions of the interaction potential. This is equivalent to the eikonal approximation for scattering or the thin-lens approximation in optics. The idea is that the phase of the incident particle changes along each classical trajectory, but not the amplitude. Thus, there may be momentum transfer perpendicular to the trajectory, but the trajectory is not significantly displaced (until after the interaction is over). Mathematically, this regime can be treated by neglecting the atomic kinetic energy term in the Hamiltonian (the Raman–Nath approximation).

The standing wave interaction may be treated by considering the standing wave (ac-Stark shift) potential resulting from the applied fields given in Eq. (18):

$$V(z,t) = \frac{\hbar\omega_R^2}{\delta} f^2(t)\sin^2(kz) \tag{51}$$

where we have assumed $\delta \gg \Gamma$, because the constraint $N_s \ll 1$ (Eq. (46)) holds in this regime as well, where N_s is the expected number of spontaneous emission events per atom during the time τ. Although we neglect the kinetic energy term in the Hamiltonian, we continue to will treat z in Eq. (51) as an operator.

Given the initial atomic wavefunction in momentum space, $\psi(p_0)$, the atomic wavefunction immediately after the interaction is given by

$$\psi(p) = e^{-\frac{i}{\hbar}\int^{t} dt' U(z,t')}\psi(p_0) \tag{52}$$

$$= e^{-i\frac{\omega_R^2}{2\delta}\tau} e^{i\frac{\omega_R^2}{2\delta}\tau\cos(2kz)}\psi(p_0) \tag{53}$$

where $\tau = \int \mathrm{d}t' f^2(t')$ and the integral is over the interaction duration. With the use of the identity for Bessel functions of the first kind, $e^{i\alpha\cos(\beta)} = \sum_{n=-\infty}^{\infty} i^n J_n(\alpha) e^{\mathrm{in}\beta}$, the atomic wavefunction can be written as

$$\psi(p) = e^{-i\frac{\omega_R^2}{2\delta}\tau}\sum_{n=-\infty}^{\infty} i^n J_n\left(\frac{\omega_R^2}{2\delta}\tau\right) e^{i2nkz}\psi(p_0) \tag{54}$$

$$= e^{-i\frac{\omega_R^2}{2\delta}\tau}\sum_{n=-\infty}^{\infty} i^n J_n\left(\frac{\omega_R^2}{2\delta}\tau\right)\psi(p_0 + 2n\hbar k) \tag{55}$$

States with $2N\hbar k$ of momentum are populated with the probability:

$$P_N = J_N^2(\theta), \quad N = 0, \pm 1, \pm 2, \ldots \tag{56}$$

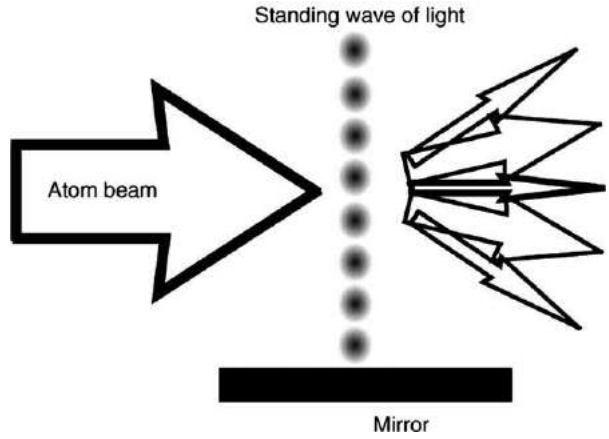


Fig. 11 Two counter-propagating running waves of light superimpose to form a standing wave of light. The more narrow beam shown here represents the configuration for Kapitza–Dirac diffraction.

where

$$\theta = \frac{\omega_R^2}{2\delta}\tau = \omega_R^{(2)}\tau \tag{57}$$

is the pulse area. This leads to a transverse rms momentum of the diffracted atoms that is linearly proportional to the pulse area:

$$p_{\mathrm{rms}} = \sum_{n=-\infty}^{\infty} (n\hbar k)^2 P_n = 2^{1/2}\theta\,\hbar\,k \tag{58}$$

The maximum and minimum bounds on the interaction time, τ, and the amount of momentum transfer to the atoms are discussed in the next section.

Kapitza–Dirac diffraction of atoms was first observed at MIT in 1986. Diffraction of a well-collimated (subrecoil) supersonic atomic beam was observed after passage through the tightly focused waist of a near-resonant standing wave (**Fig. 11**). Significant diffraction into momentum states $|g, \pm 10\hbar k\rangle$ was observed (**Fig. 12**). Even higher diffracted orders should be observable in the future using laser beams directed at small BECs for somewhat longer times.

Comparison of Atom-Standing Wave Interactions

The atomic motion induced by interaction with a standing light wave varies qualitatively with the interaction parameters. **Fig. 13** summarizes the various interaction regimes of an atom with a standing wave in terms of the two most basic parameters: the two-photon Rabi frequency, $\omega_R^{(2)} = \omega_R^2/2\delta$, and the duration of the interaction, τ. To render the plot independent of atomic species, $\omega_R^{(2)}$ is given in units of the single-photon recoil frequency, ω_{rec}, and τ is given in units of the inverse single-photon recoil frequency, $\omega_{\mathrm{rec}}^{-1}$. Thus, for ^{23}Na the point (1,1) on **Fig. 13** corresponds to (6.4 μs, $2\pi \times 25$ kHz). The product of the two-photon Rabi frequency and the duration of the interaction is the pulse area, $\theta = \omega_R^{(2)}\tau$ (**Eq. (57)**), which is likewise the product of the pair of coordinates forming a point on the plot.

The lines KD1(KD10) on **Fig. 13** show where the first maxima of $P_{1,10} = J_{1,10}^2(\theta)$ (**Eq. (56)**) occur, corresponding to the maximum possible population transfer into the first and tenth Kapitza–Dirac diffracted order respectively. Since the momentum distribution of diffracted atoms depends only on the pulse area (θ), all Kapitza–Dirac orders are parallel to each other and further offset from the origin in increasing order number.

The Kapitza–Dirac regime ends at large interaction times where the Raman–Nath approximation fails due to motion of the atoms down the slope of the standing wave potential. We show these lines dashed as the interaction time approaches the beginning of the classical oscillation regime, and terminate these lines where the oscillation produces its first focus, at the first focus line. This line corresponds to the atoms completing a quarter period of oscillation in the standing wave potential, $\tau = \tau_{\mathrm{osc}}/4$, where the oscillation time is derived from the approximation that the potential $\langle V(z,t)\rangle_t$ (**Eq. (51)**) is harmonic about the minimum:

$$\tau_{\mathrm{osc}} = \frac{\pi}{\omega_R}\left(\frac{|\delta|}{\omega_{\mathrm{rec}}}\right)^{1/2} \tag{59}$$

In the shaded region of **Fig. 13**, the atoms will oscillate classically about the potential minimum, causing a periodic focusing of the atoms alternately in position and momentum space. However, anharmonicities of the potential away from its minimum will degrade the quality of the focusing effects.

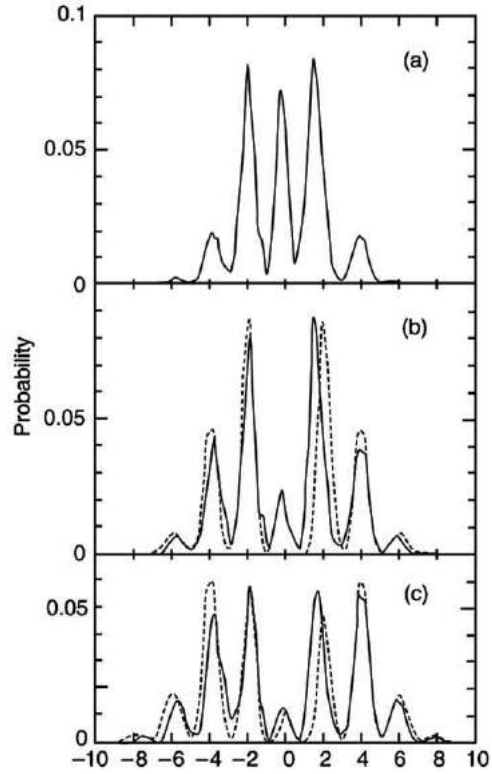


Fig. 12 Kapitza–Dirac diffraction of an atomic beam from a standing wavelight grating. The solid lines are experimental data, the dashed lines are theoretical curves. (a) $\theta = 1.69$, (b) $\theta = 2.33$, (c) $\theta = 2.84$. Reprinted with permission from *Physical Review Letters* 56(8): 827–830. Copyright (1986) by the American Physical Society.

The maximum diffracted order that can be significantly populated by the light–atom interaction is limited by energy conservation. Classically, the maximum momentum transfer to the atoms due to the sudden switch on of the standing wave is delivered to atoms that convert the full height of the standing wave potential $(\hbar\omega_R^2/\delta)$, into kinetic energy. This gives

$$\frac{p_{\max}^2}{2m} \simeq \frac{\hbar\omega_R^2}{\delta} \Rightarrow p_{\max} \simeq \omega_R \left(\frac{2\hbar m}{\delta}\right)^{1/2} \tag{60}$$

Equating the maximum absorbed momentum, $p_{\max}$, to an integer number of two-photon recoil momenta yields the maximum expected diffracted order, $N_{\max}$:

$$p_{\max} = 2N_{\max}\hbar k \Rightarrow N_{\max} \simeq \frac{\omega_R}{2}(\omega_{\text{rec}}\delta)^{-1/2} \tag{61}$$

This is just half of the square-root of the standing wave potential height measured in units of the single-photon recoil energy:

$$N_{\max} = \frac{1}{2}\left(\frac{\frac{\omega_R^2}{\delta}}{\omega_{\text{rec}}}\right)^{1/2} = \frac{1}{2}\left(\frac{\omega_R^{(2)}}{\omega_{\text{rec}}}\right)^{1/2} \tag{62}$$

As the two-photon Rabi frequency is reduced, $N_{\max}$ falls below unity. As a result, there is no longer time for the higher-order multi-photon processes to generate significant amplitudes in diffracted orders with $N > 1$ before dephasing due to the kinetic energy term (**Eq. (24)**) becomes significant and the higher-order processes become negligible. Only a small population is ever transferred to the $N = \pm 1$ orders and it does not oscillate at ω_{rec}. Therefore the classical oscillation regime does not extend below $N_{\max} \simeq 1$ where it is terminated on **Fig. 13**.

Classical oscillation would result in atoms with momentum from zero up to the maximum allowed by energy conservation. Therefore, the classical focusing of atoms must be manifest as an atomic population distribution over many of the quantized momentum states (separated by $2\hbar k$) allowed by energy conservation (**Eq. (61)**). However, as the interaction time lengthens and extends into the Bragg regime, the populated momentum states become restricted by energy conservation until only the oscillatory Pendellösung into and back from only one final state remains. Therefore, we have ended the classical oscillation regime where the Bragg condition (**Eq. (44)**) is satisfied. The Bragg regime presupposes a smooth light pulse shape. For a pulse with sharp edges, classically oscillatory behavior can still be observed at longer times than included in the shaded region of **Fig. 13**, which is why we show the large τ boundary of the classical oscillation regime as dashed.

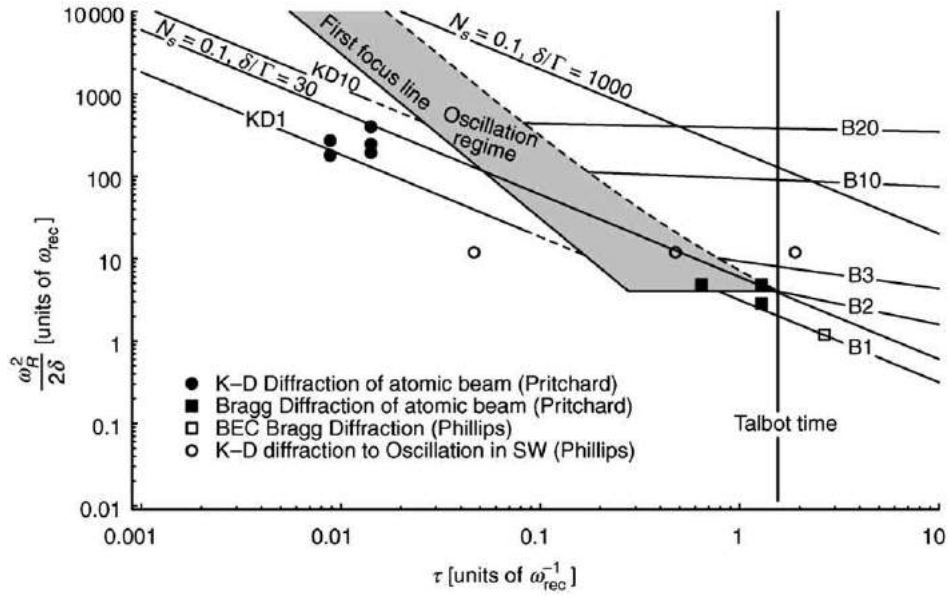


Fig. 13 Atomic diffraction from a standing light wave. The vertical axis is the two-photon Rabi frequency, $\omega_R^2/2\delta$, in units of the single-photon recoil frequency, ω_{rec}, and the horizontal axis is the pulse duration, τ, in units of the inverse single-photon recoil frequency, ω_{rec}^{-1}. The scaling is chosen to eliminate the atomic species dependence of the plot. All coherent momentum transfer processes are destroyed by spontaneous decay, which occurs with probability $N_s = 0.1$ along the lines labeled accordingly and parameterized by the given ratio δ/Γ. Lines KD1 and KD10 show conditions for the maximum transfer into the first and tenth Kapitza–Dirac diffracted order respectively. As the interaction time is increased the Raman–Nath approximation is violated (termination of Kapitza–Dirac curves) and the atoms enter the oscillatory regime, executing at least a quarter period of oscillation above the first focus line (shaded area). Cures B1, B2, B3, B10, and B20 correspond to conditions that generate complete Bragg reflection in the first-, second-, third-, tenth-, and twentieth-order respectively. Experimental conditions are shown as points. Filled circles: Kapitza–Dirac diffraction of an atomic beam (Pritchard 1986). Filled squares: Bragg diffraction of an atomic beam (Pritchard 1988). Open squares: Bragg diffraction of a BEC (Phillips 1999). Open circles: transition from Kapitza-Dirac diffraction to oscillation of a BEC in a standing wave light pulse (Phillips 1999). Reprinted from Gupta S, *et al.* (2001) Coherent manipulation of atoms with standing light waves. *Comptes Rendus de L'Academie des Sciences – Series IV – Physics-Astrophysics* 2:479–495, copyright (2001) with permission from Elsevier.

Table 1 Natural parameters and typical experimental parameters involved in standing wave diffraction. The relevant frequencies together with the corresponding times ($1/\omega$) are tabulated. The parameters for ^{23}Na have been used for system dependent quantities

ω	$\omega/2\pi$	$1/\omega$
ω_0	500 THz	0.3 fs
δ (Bragg)	500 MHz	0.3 ns
ω_R (Bragg)	100 MHz	1.6 ns
ω_R (K–D)	100 MHz	1.6 ns
Γ	10 MHz	16 ns
ω_{rec}	25 kHz	6.4 μs
ω_{osc}	1 MHz	160 ns

In the Bragg regime, transfer of population is restricted to (and back from) only one final momentum state. The allowable final states are restricted by limiting the frequency bandwidth (i.e., energy uncertainty) of the light fields in the atomic rest frame. This is accomplished by lengthening the interaction time and smoothing the rise and fall of the electromagnetic fields. The parameters for a first-order Bragg transition (**Table 1**) are typically $\delta/\Gamma \simeq 50$, $\Gamma\tau \simeq 1$, and $\omega_R/\Gamma \simeq 10$ giving $N_s \simeq 10^{-2}$ and $\omega_R^{(2)}\tau \simeq 1$. Obtaining significant population transfer with higher-order Bragg processes requires larger intensities. Various orders (1, 2, 3, 10, and 20) of Bragg diffraction are shown as lines on **Fig. 13** corresponding to $\omega_R^{(2N_B)}\tau = \pi$, where $\omega_R^{(2N_B)}$ is given in **Eq. (40)**. The lines are terminated at the appropriate interaction time determined from the final momentum state resolution condition (**Eq. (44)**). The Bragg regime extends indefinitely to larger interaction times, which might be termed the region of Bragg spectroscopy. In experiments in this regime with ^{23}Na, atomic velocity resolution below 1 mm s^{-1} was obtained at $\tau = 80\omega_{rec}^{-1}$. The study of adiabatically expanded BECs would require larger interaction times to resolve their smaller velocity spread and weaker mean field shifts.

The Kaptiza–Dirac and Bragg regimes assume a different initial atomic momentum (in the rest frame of the standing wave) parallel to the standing wave axis. Kapitza–Dirac scattering assumes no component of the initial atomic momentum along this axis. The efficiency of Kapitza–Dirac diffraction falls rapidly as the initial momentum in units of the photon momentum approaches $1/\omega_{\text{rec}}\tau$. To observe N_B^{th}-order Bragg scattering, the initial atomic momentum along the standing wave axis must have (nonzero) magnitude $N_B\hbar k$. Without adhering to this constraint, no final momentum state will be energetically degenerate with the initial state and the atomic sample will not respond to the presence of the standing wave, even if the interaction parameters are appropriate $(\omega_R^{(2N_B)}\tau \simeq 1)$ for N_B^{th}-order Bragg scattering.

The condition $N_s = 0.1$ (**Eq. (46)**), where N_s is the expected number of spontaneous emission events per atom during the light–atom interaction, is drawn on **Fig. 13** for two ratios (30 and 1000) of standing wave detuning, δ, to the atomic excited state natural lifetime, Γ. For fixed $\delta\Gamma$, we see that $N_s \propto \theta$, thus conditions with an increased pulse area (above and to the right of the $N_s = 0.1$ lines) result in a proportionally increased N_s. These $N_s = 0.1$ lines are extended across all regimes of **Fig. 13** because restricting spontaneous emission is required for both Kapitza–Dirac and Bragg scattering. As N_s approaches unity, the correct optical potential describing the light–atom interaction no longer is **Eq. (51)**, and scattering of atoms becomes an incoherent process which can lead to new possibilities such as a complex valued optical potential. Thus, while the standing wave fields in pure Bragg or Kapitza–Dirac scattering behaved as phase gratings for atoms, light gratings on resonance can effectively become amplitude diffraction gratings.

Atom Interferometry

In the 19th century, Fizeau (1853), Michelson (1881), Rayleigh (1881), and Fabry and Perot (Fabry 1899) exploited the interference properties of light waves to create the light interferometer which has since resulted in many beautiful experiments and precise measurements. Using technologies invented since the Second World War, the initial ideas of de Broglie and Schrödinger have evolved into construction of interferometers for neutrons, electrons, and atoms. These new interferometers are proving to be valuable tools for probing fundamental physics, for studying quantum mechanical phenomena, and for making inertial measurements.

The scientific value of interferometry with atoms and molecules has long been recognized. In fact, the concept of an atom interferometer was patented in 1973 and it has been extensively discussed since. Atom interferometry offers great richness stemming from the varied internal structure of atoms, the wide range of properties possessed by different atoms (e.g., mass, magnetic moment, absorption frequencies, and polarizability), and the great variety of interactions between atoms and their environment (e.g., static E–M fields, radiation, and other atoms).

Light interferometers are generally based either on achromatic beamsplitters such as half-silvered mirrors or on other semi-transparent membranes whose structure is small compared to the wavelength of the wave they are splitting. Lacking material structures that are either transparent to atoms or smaller than their de Broglie wavelength, diffraction gratings have been pressed into service both as beamsplitters and mirrors for atom waves. This means that atom interferometers are constrained to designs which somehow compensate for the dependence of diffraction angle on the wavelength of the individual atoms. In spite of this challenge, a surprising variety of atom and molecule interferometers have been built since 1991. A majority have used the three-grating configuration in which the first grating splits the incident beam, the second reverses the differential momenta given by the first, and the third recombines the two beams at the location where they overlap. Both material gratings and standing waves of light have been used in the Raman–Nath, Bragg, and adiabatic regimes to obtain interference fringes. Some designs render the interference fringes in position space, others in internal state space.

Fig. 14 shows the MIT setup for a three-grating atom interferometer which features sufficient separation between interfering paths to accommodate an interposed metal foil. This allows different fields or media to act on atom waves only in one of the two arms of the interferometer. Such an interaction region has been used to measure phase shifts due to an electric field applied to only one of the interfering paths. The phase difference between the two paths is then given by the Feynman path integral:

$$\phi = \frac{-i}{\hbar}\int V(x)dt \tag{63}$$

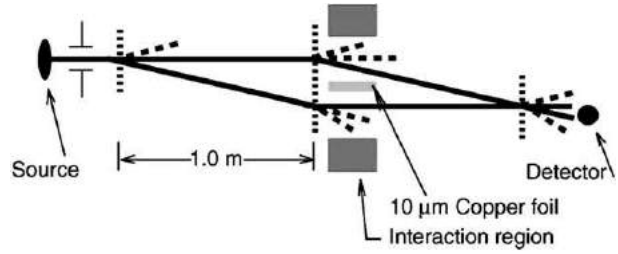


Fig. 14 An interferometer for atoms built with three nanofabricated gratings. Each atom propagates in a superposition of two paths, shown in bold. The beam of atoms is well enough collimated, and the diffraction angle is large enough, that a metal barrier can be inserted between the two paths inside the interferometer. The interference fringes are observed by translating one grating transverse to the atom beam. See for example: Berman PR (ed.) (1997) *Atom Interferometry*. San Diego, CA: Academic Press.

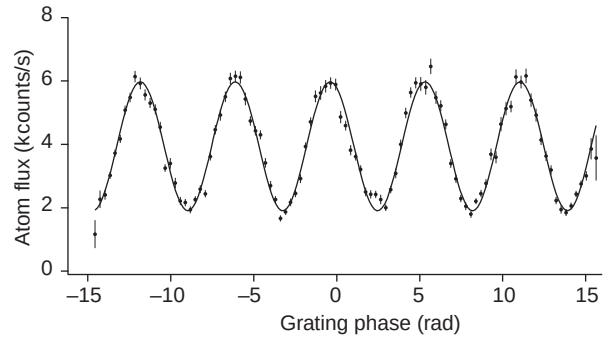


Fig. 15 Interference fringes from atoms. 2π of grating phase corresponds to translating the grating one grating period, or 100 nm. These data were obtained at MIT.

where

$$V = -\frac{1}{2}\alpha E^2 \tag{64}$$

is the potential energy due to the electric filed E, and α is the electric polarizability of the atoms. The resulting phase shift of the interference fringes (**Fig. 15**) has been used to measure the polarizability of sodium atoms to unprecedented accuracy.

Phase shifts have also been measured due a dilute target gas in one arm of the interferometer. In this case there is a complex index of refraction for the forward scattered atoms (some attenuation, and some phase shift) which depends on matter wave wavelength. Recent measurements reveal glory oscillations in the matter wave index of refraction due to passing through a dilute gas, and are a sensitive probe of interatomic potentials.

In the domain of inertial sensing, atom interferometers have been used to the local gravitational acceleration, $\vec{g}$, Newton's constant, G, gravity gradients, $\nabla\vec{g}$, and rotations Ω, each with sensitivity rivaling if not exceeding any other method. The Sagnac phase shift, due to rotations, for a two-path interferometer is

$$\phi_S = \frac{4\pi}{\lambda_{dB}v}\vec{\Omega}\cdot\vec{A} \tag{65}$$

where v is the velocity of atoms, $\vec{A}$ is the enclosed area of the interferometer, and $\vec{\Omega}$ is the rotation rate. The two factors in the denominator, λ_{dB} and v, are both $\sim 10^5$ times larger for light than for atoms, which is why atom interferometers have the potential to be 10^{11} times more accurate than optical interferometers. In practice, atom interferometers only outperform laser gyros by a small amount because they have dramatically smaller enclosed areas and particle flux than optical interferometers.

Since the first atom interferometers for Na and He* began working in 1991, others have been made for Li, Ar*, Ca, Cs, K, Mg, Ne*, Rb, and Li_2, Na_2, I_2, C_{60} and C_{70} molecules, interferometers starting with trapped atoms have been made for Cs, Ca, He*, Mg, and Rb. Interferometers using Bose–Einstein condensates have been demonstrated with Na and Rb. These lists are still growing. Diffraction from a single grating has been observed for molecules as large as C_{70} buckyballs, which may someday be used in a three-grating interferometer.

Conclusion

The manipulation of atoms using light forces from standing light waves is a rich subject. The seminal suggestion of Kapitza and Dirac laid dormant for 50 years due to lack of experimental technology. However, in the 1980s this suggestion was realized with atomic sources and considerably extended both experimentally and theoretically. In the early 1990s, coherent standing wave manipulation and nonofabricated atom optics became the two major routes to making atom interferometers. As the new century begins, these techniques are being refined further with improved sources, new detection schemes, and better atom optics. Replacing thermal atomic beams by Bose–Einstein condensates (BECs), as sources of atoms, will revolutionize the field of atom optics just as lasers did in light optics.

Conversely, stimulated light scattering and nanostructures provide new ways to study atomic and molecular properties, such as Bragg spectroscopy for BEC characterization. As progress continues, exciting developments should be forthcoming, such as definitive measurements of the fine structure constant, α, atom gyroscopes that are far superior to the best laser gyroscope technology, and improved studies of BECs. Another area that is on the brink of spectacular development is the confinement of coherent matter waves in atom waveguides and the development of the scientific and technological opportunities that these represent, in analogy to fiber optic waveguides for light.

While we have described the application of nanofabrication techniques to atom optics, it is possible to imagine technology transfer in the other direction. The fundamental problem of fabricating ever smaller structures might be tremendously advanced by

atom optics because the de Broglie wavelength of atoms is so much smaller than that of light, permitting them to be focused to directly deposit much smaller features than possible with photolithography.

See also: Coherent Lightwave Systems

Further Reading

Cohen-Tannoudji, C., Diu, B., Laloe, F., 1977. Quantum Mechanics. New York: Wiley and Sons.
Hecht, E., 1987. Optics. Reading: Addison-Wesley.
Berman, P.R. (Ed.), 1997. Atom Interferometry. San Diego, CA: Academic Press.
Mandel, L., Wolf, E.M., 1995. Optical Coherence and Quantum Optics. London: Cambridge University Press.
Balykin, V.I., Letokhov, V.S., 1995. Atom Optics with Laser Light. Chur, Switzerland: Harwood Academic Publishers.
Meystre, P., Sargent III, M., 1999. Elements of Quantum Optics. Heidelberg, Germany: Springer Verlag.
Rauch, H., 2000. Neutron Interferometry. Oxford, UK: Oxford University Press.
Meystre, P., 2001. Atom Optics. New York: Springer-Verlag.
Campargue, R. (Ed.), 2001. Atomic and Molecular Beams, the State of the Art 2000. Berlin: Springer.

Organic Semiconductors

Fang-Chung Chen, National Chiao Tung University, Hsinchu, Taiwan

© 2018 Elsevier Ltd. All rights reserved.

Introduction

Organic semiconductors (OSCs) are receiving increasing attention these days because they have many attractive properties – including light weight, low-cost production, low-temperature processing, mechanical flexibility, and abundant availability – that distinguish them from their conventional inorganic counterparts. The recent successful commercialization of active-matrix organic light-emitting diodes (OLEDs) for high-end smartphone displays suggests that organic compounds have promising prospects for use in various other electrical and optoelectric devices. For example, the fabrication of solar cells, transistors, photodetectors, and lasers with OSCs can be highly feasible and highly efficient. Another attractive property of OSCs is that they can be processed using simple solution processing techniques (e.g., ink-jet printing, reel-to-reel fabrication), making the fabrication of electronic devices much easier and cheaper. As Professor Heeger said in his Nobel lecture, "I'm convinced that we are on the verge of a revolution in 'Plastic Electronics'." We foresee rapid advances in the field of OSCs bringing increasingly more inexpensive, workable, and smart organic devices into our daily lives.

Organic materials are substances comprising mostly carbon and hydrogen atoms; they had been considered for many years to be exclusively electrically insulating. The discovery of electrical conductivity in organic compounds can be traced back to the 1950s; it has opened up a new fascinating field of research. Electroluminescence (EL) from anthracene single crystals was reported by Pope *et al.* in 1963. In the 1970s, Shirakawa, Heeger, and MacDiarmid found that the conductivity of polyacetylene could be increased tremendously – up to a level close to that of a typical metal – after exposure to vapors of chlorine, bromine, or iodine. Such high conductivity from a traditional "insulator" of electricity drew much attention and encouraged the rapid growth of the field of organic electronics. The Nobel Prize in Chemistry in 2000 was awarded to Heeger, MacDiarmid, and Shirakawa for "the discovery and development of conducting polymers."

Among the various organic electronic devices known today, the technology of OLEDs has definitely been under the spotlight. Initially, the EL observed from organic single crystals was not energy efficient and required a large voltage to drive the devices. In 1987, Tang and Van Slyke developed light-emitting devices based on amorphous organic thin films and achieved a quantum efficiency of 1% under an electrical bias of less than 10 V. In 1990, OLEDs incorporating conjugated polymers were also reported by Professor Friend at Cavendish Laboratory. Since then, relevant technologies – including new materials, device structures, and device engineering approaches – evolved rapidly, gradually establishing a new industry.

As organic-based devices have matured from scientific concepts in the laboratory to applications in the real market, there is a requirement to understand the unique properties of OSCs and determine the opportunities that this new generation of electronic materials might offer. In this article, we discuss the electronic structures of OSCs and several fundamental charge storage scenarios in OSCs. We also review the concept of doping in OSCs. We conclude with a brief overview of interesting device applications, including electrophotographic devices, thin film transistors, and light-emitting transistors.

Electronic Structures

OSCs are usually categorized into two main groups, depending on the molecular weights of their organic components: conjugated polymers (Fig. 1) and small molecules (Fig. 2). Polymers are constituted by repeated structural units (monomers) connected by covalent bonds. Because the number of repeating units usually cannot be controlled precisely, they are prepared with a distribution of molecular weights. On the other hand, small molecules have precise and much smaller molecular weights. The other distinction between the two OSC categories is in their methods of fabrication. Most conjugated polymers are soluble in organic solvents and can be processed using various solution-processing approaches. In contrast, small molecules are usually deposited through thermal evaporation under high vacuum – a deposition method that allows good control over the thickness, morphology, and other properties of the organic films. Accordingly, very thin (even down to a few nanometers), high-quality films of small molecules can be obtained quite readily. The chemical structures of the small molecules can be also tailored so that they become soluble in organic solvents, facilitating the use of solution fabrication processes. For example, pentacene (Fig. 2(d)) can be deposited only through thermal evaporation, whereas 6,13-*bis*[(triisopropylsilyl)ethynyl]pentacene (TIPS-pentacene) (Fig. 2(f)) features side chains that improve its solubility, simplify its processing while maintaining high crystallinity.

To understand the electronic structures of OSCs, we begin with the atomic orbitals (AOs) of carbon, the most important element of any organic materials. A carbon atom has six electrons; its electronic configuration is $(1s)^2(2s)^2(2p)^2$. It can be bonded to other atoms using various hybridization orbitals, including sp, sp^2, and sp^3 hybrid orbitals (Fig. 3). For example, one s and two p orbitals are superposed to form three sp^2 hybrid orbitals; the orbitals are distributed in the same plane with an angle of 120 degree between them. In a simple model molecule, ethylene, each carbon atom offers three sp^2 hybrid orbitals to bond with other atoms (Fig. 4). The 1s orbital of a hydrogen atom overlaps with one of the sp^2 hybrid orbitals to form a molecular orbital (MO),

 doi:10.1016/B978-0-12-803581-8.09538-2

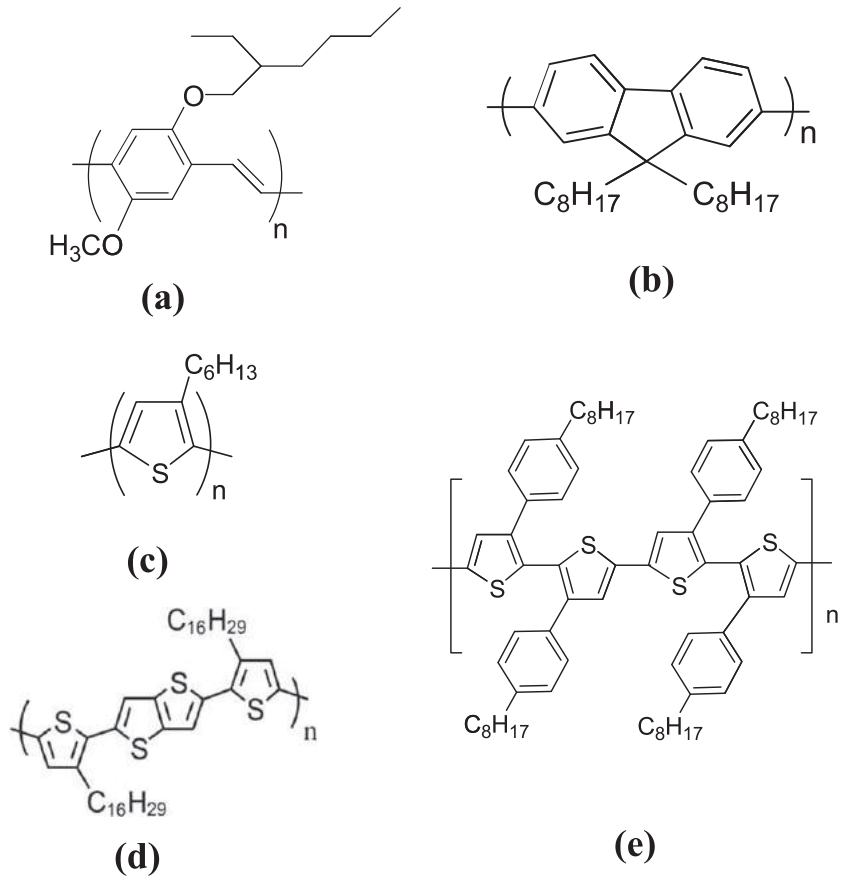


Fig. 1 Chemical structures of polymer-based OSCs: (a) poly[1-methoxy-4-(2-ethylhexyloxy)-*p*-phenylene vinylene] (MEH-PPV), (b) poly(9,9-dioctylfluorene) (PFO), (c) poly(3-hexylthiophene-2,5-diyl) (P3HT), (d) poly{2,5-bis(3-hexadecylthiophen-2-yl)thieno[3,2-*b*]thiophene} (PBTTT), and (e) poly[3-(4-octylphenyl)thiophene] (POPT).

a so-called σ-orbital; the resulting bonding is a σ-bond. The two carbon atoms are also bonded through sp^2 hybrid orbitals. Each carbon atom, however, retains one p atomic orbital, aligned orthogonal to the plane of the sp^2 hybrid orbitals. The two p_z atomic orbitals overlap side-by-side with the electron density distributed above and below the internuclear axis, forming a different type of MO called a π-orbital. Note that the π-electron cloud is delocalized between the two carbon atoms. Consequently, the carbon atoms are bonded by two bonds: a σ-bond and a π-bond; this arrangement is termed a "double bond." In view of the electron wave functions, the overlapping of two AOs produces two MOs: a bonding state and an anti-bonding state, after constructive and destructive interference, respectively. Because destructive interference results in lower electron density between the atoms, the energy of the anti-bonding state is higher than that of the bonding state. For π-orbitals, the bonding and anti-bonding states are denoted as π- and π^*-MOs, respectively.

Benzene, a larger molecule (Fig. 5), has six carbon atoms that are also bonded using sp^2 hybrid orbitals. Similarly, the six p_z AOs that remain form six π-bonding MOs: three bonding and three anti-bonding orbitals. As a consequence of interference among the six p_z orbitals, the lower bonding and upper anti-bonding states are degenerate (Fig. 5(b)). Six p_z electrons occupy the three bonding states in a neutral benzene molecule. Similar to ethylene, the π-electron cloud is delocalized over the six carbon atoms. In other words, the electrons can move from one carbon atom to another; such a delocalized structure is said to feature "conjugation."

The MO of highest energy that electrons occupy is known as the highest occupied molecular orbital (HOMO). Meanwhile, the lowest unoccupied molecular orbital (LUMO) is the MO of lowest energy that electrons do not occupy. The difference in energy between the HOMO and LUMO is the energy required to excite an electron in the molecule. In benzene, for example, Fig. 5(b), the upper bonding MOs (π_2, π_3) are the HOMOs and the lower anti-bonding MOs (π_4^*, π_5^*) are the LUMOs. For OSCs, because the energy splitting of π-bonds is usually smaller than that of σ-bonds, electronic processes (e.g., photon absorption and emission) occur energetically favorably on π-orbitals. Similarly, the charges injected from the metal contacts of organic electronic devices would tend to occupy π-MOs. In other words, the electronic functions of OSCs originate from the smaller and favorable energy levels of the frontier orbitals of the π-electron system; the σ-electrons are hardly excited because much higher energy is required for electronic transitions between σ-orbitals. Furthermore, the HOMO–LUMO energy gap decreases upon increasing the size of the π-conjugation system, because of the greater extent of π-electron delocalization.

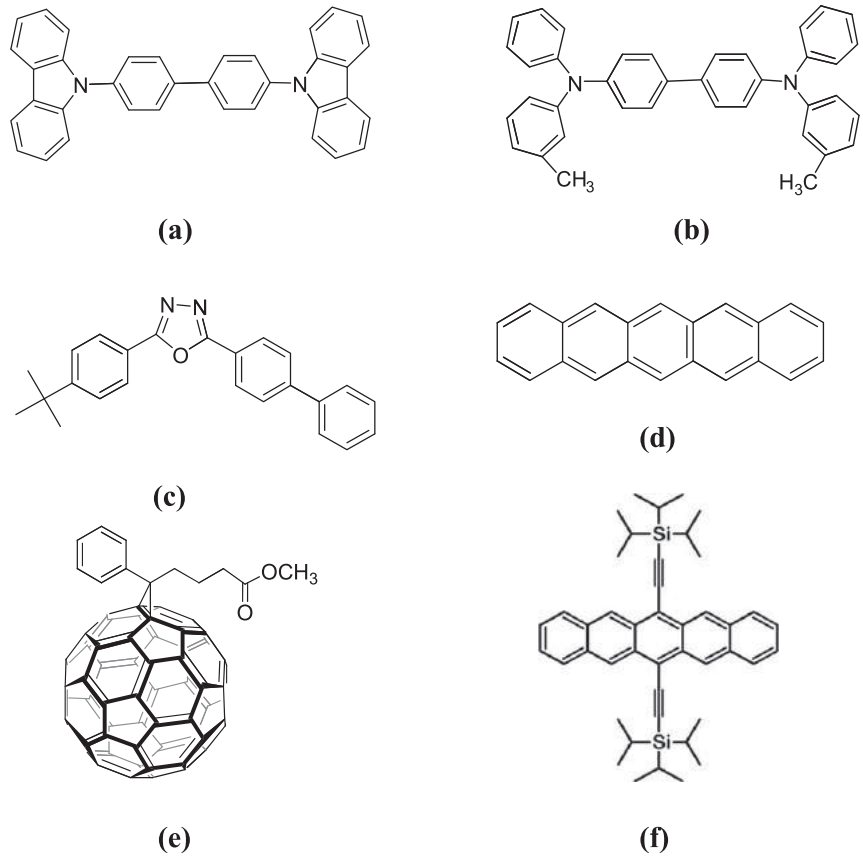


Fig. 2 Chemical structures of small-molecule semiconductors: (a) 4,4-*N,N*-dicarbazolyl-biphenyl (CBP), (b) *N,N*-diphenyl-*N,N*-*bis*(3-methylphenyl)-1,1′-biphenyl-4,4′-diamine (TPD), (c) 5-(4-biphenyl)-2-(4-*tert*-butylphenyl)-1,3,4-oxadiazole (t-PBD), (d) pentacene, (e) [6,6]-phenyl-C_{61}-butyric acid methyl ester (PCBM), and (f) 6,13-*bis*[(triisopropylsilyl)ethynyl]pentacene ((TIPS-pentacene) soluble pentacene).

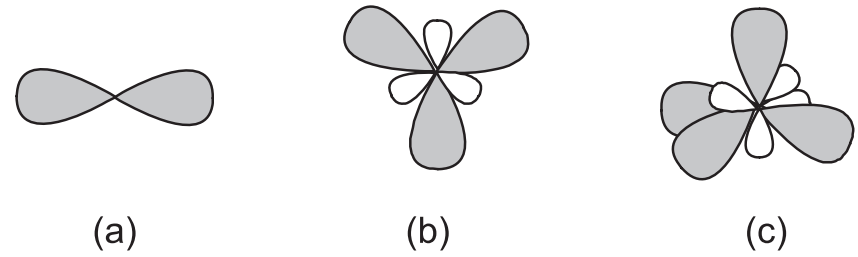


Fig. 3 Schematic representation of (a) sp, (b) sp^2, and (c) sp^3 hybrid orbitals.

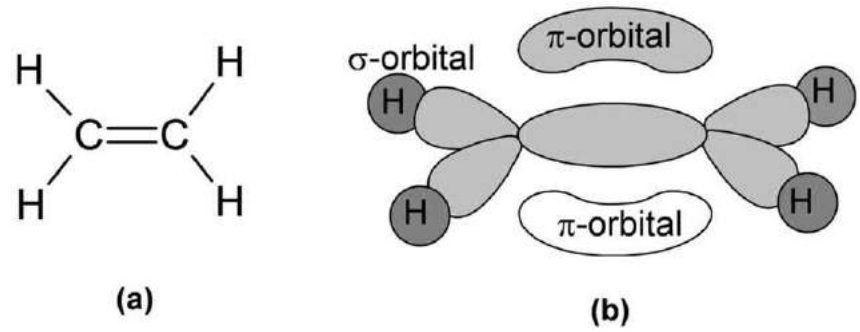


Fig. 4 (a) Chemical structure of ethylene and (b) schematic orbital diagram.

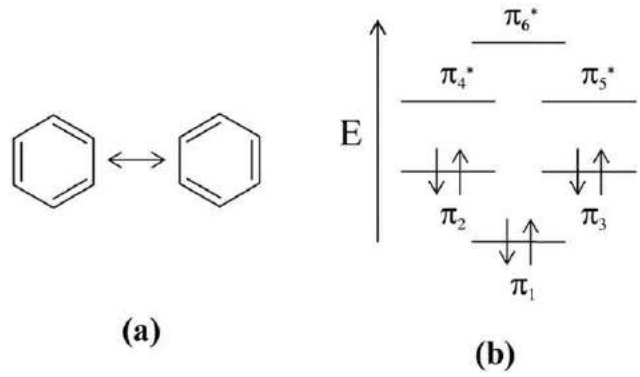


Fig. 5 (a) Chemical structure of benzene, it consists of two resonance forms and (b) energy diagram of the π-MOs in benzene.

Trans-polyacetylene was the first conducting polymer to be discovered (Fig. 6). For a single chain of neutral polyacetylene, the π-band, which can be considered to be composed of an almost infinite number of p_z orbitals, would be half-filled, resulting theoretically in metallic behavior (Fig. 6(a)). Experimental results have strongly indicated, however, that polyacetylene is a semiconductor having an energy gap of approximately 1.5 eV. In reality, the one-dimensional (1D) "metal" is unstable and the structure tends to distort, as displayed in Fig. 6(b). Accordingly, the main chain of polyacetylene actually has alternately long and short bonds. The so-called Peierls distortion converts the repeating unit of *trans*-polyacetylene to *trans*-$(-HC=CH-)_n$, instead of *trans*-$(CH)_n$. As displayed in Fig. 6(g), dimerization of the molecule opens an energy band gap. The π-band is fully occupied and the upper π^*-band is empty; this band structure is similar to that of a typical inorganic semiconductor, which features a full-filled valence band and an empty conduction band. While a 1D π-electron metal is not stable, higher-dimensional π-electron systems are not subject to such Peierls instability. For example, carbon nanotubes and graphene can be metallic or semi-metallic.

Solitons, Polarons, and Bipolarons

The electronic structure of a polymer can be described using the Su–Schrieffer–Heeger (SSH) model, based on a quasi-one-dimensional tight-binding model. It assumes that the π-electrons are strongly coupled to the polymer backbone through the electron–phonon interactions. Charge storage occurs through formation of solitons, polarons, and bipolarons. Solitons are structural defects on the polymer chains. As illustrated in Fig. 6(b) and (c), polyacetylene has two resonance forms. The soliton is a domain boundary of these two degenerate resonance configurations (Fig. 6(d)); the domain wall can actually extend over several carbon atoms (Fig. 6(e)). A soliton may be neutral or carry a charge. The energy of the solition lies between the π–π^* gap, because of its nonbonding nature. This defect state is mobile because the system energy does not depend on the position of the soliton. For non-degenerate ground-state polymers – for example, poly(phenylene vinylene) (PPV, Fig. 7(a)) and polyparaphenylene (PPP, Fig. 7(b)) – in which the interchange of single and double bonds leads to changes in energy, the solitons cannot be stable because the structure is not symmetric. Instead, double defects are required for such non-degenerate polymers. Such double defects are called polarons; they can be considered as a bound state of a charged soliton and a neutral soliton (Fig. 7(c)). Consequently, its energy levels hybridize the two states, which are split into a bonding, less energetic level and an anti-bonding, more energetic one (Fig. 7(d)). The two energy levels can be occupied by zero, one, or two electrons, resulting in the formation of positive or negative polarons. A bipolaron is a bound state of two charged solitons of equal charge; it also consists of a split pair of energy levels between the energy gap. Furthermore, solitons, polarons, and bipolarons are coupled with structural relaxation, implying strong electron–phonon interactions of the charge storage in conjugation polymers. In other words, the charges are surrounded by lattice distortions that can stabilize the system.

Excitons

Excitons are states of electronic excitations in OSCs. An exciton is a particle composed of an electron/hole pair bounded by coulombic force. The total charge of an exciton is zero. An exciton is, however, capable to move through the organic materials carrying the excitation energy. There are three types of excitons (Fig. 8): Frenkel, Wannier–Mott, and charge-transfer (CT) excitons. The main difference among them is the binding energy and/or the distance between the electron/hole pair. When the radius of the electron/hole pair is comparable with the size of a single molecule or the crystalline constant (a_L), the exciton is of Frenkel type. The small radius also implies a strong coulombic interaction. In other words, it is very difficult to overcome the binding energy and dissociate the exciton into free charges. If the radius of the exciton is much larger than a_L, it is a Wannier–Mott exciton. Therefore, the binding energy of this type of exciton is small. The intermediate case, in which the exciton extends over several molecular units, it is termed a CT exciton. The Wannier–Mott exciton is the most common one found in inorganic semiconductors. Usually it can

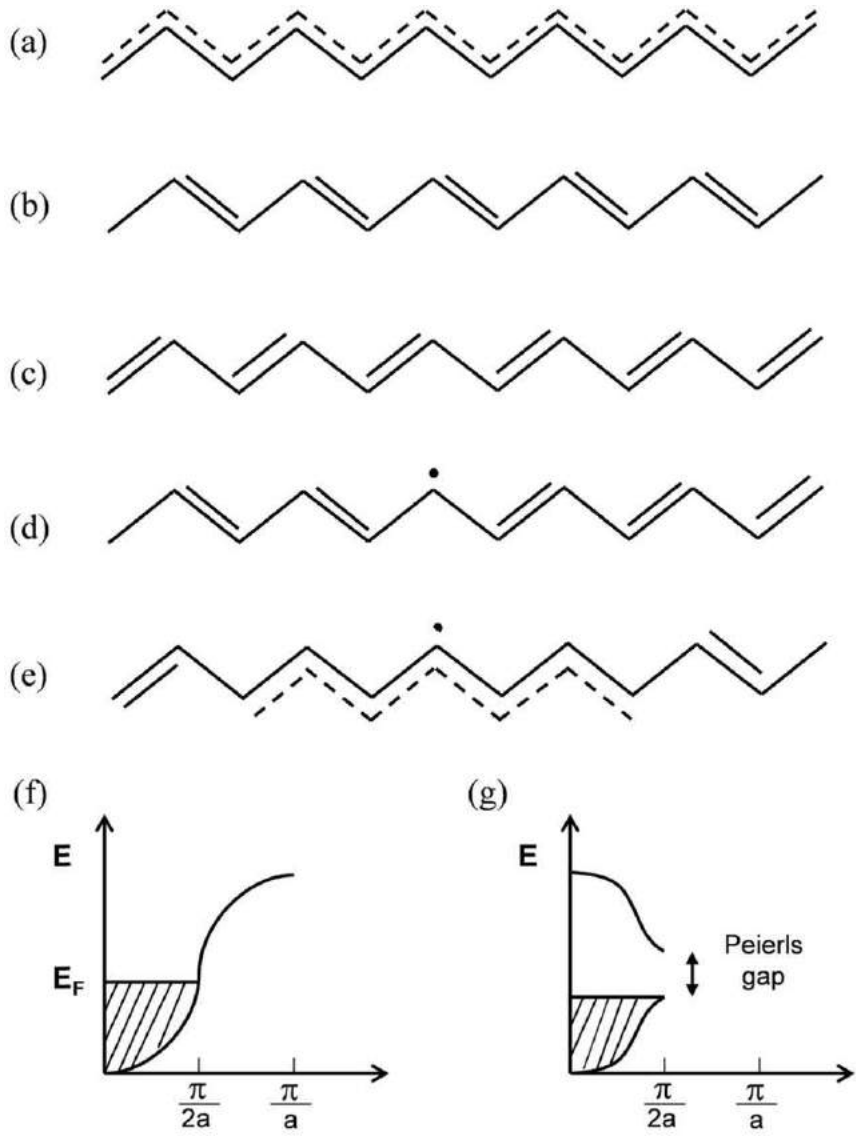


Fig. 6 (a–e) Polyacetylene: (a) undimerized structure; (b, c) two resonance forms resulting from Peierls effects; (d) soliton in *trans*-polyacetylene; (e) domain wall extension of the soliton. (f, g) Electronic band dispersion $E(k)$ plotted with respect to k for (f) non-dimerized and (g) dimerized systems. E_f is the Fermi energy; a gap appears in the dimerized system, the so-called "Peierls gap."

be detected only at low temperature, because the thermal energy at room temperature is sufficiently high to overcome its binding energy. In OSCs, most excitons are Frenkel-type because of their strong binding energy, which originates from the low dielectric constants of organic materials and their relatively localized electronic clouds. A typical binding energy for excitons in OSCs is approximately 0.5 eV.

The generation of excitons is a very important process in organic optoelectronic devices. In OLEDs, the recombination of electrons and holes results in excitons that subsequently decay to produce EL. In organic photovoltaic devices (e.g., organic solar cells), photon absorption generates the excitons, which move freely within the semiconductors, due to the strong binding energy, but are subject to effective charge dissociation at the interface between strong organic electron-donors and organic electron-acceptors. Such exciton dissociation generates free charges, eventually leading to a photocurrent after the charges have been collected by the electrodes.

Because of the strong binding energy, the directions of spin of the excitons are not likely to change readily when generated in common OSCs. Therefore, the excitons can be categorized into two different types depending on their combinations of spin directions. As displayed in **Fig. 9(a)**, the total spin angular momentum of a molecule in the ground state is a sum of the two spin vectors, equal to zero because of the opposite spin directions. In other words, the overall spin quantum number (S) is zero

$$S = |s1 + s2| = |(+1/2) + (-1/2)| = 0 \tag{1}$$

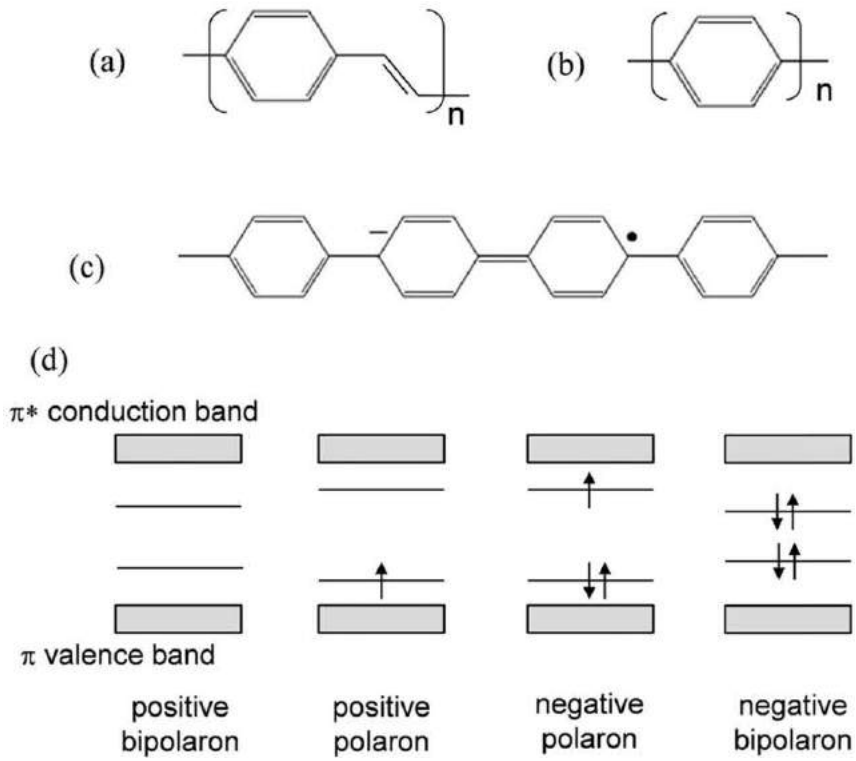


Fig. 7 Chemical structure of (a) poly(phenylene vinylene) (PPV) and (b) polyparaphenylene (PPP). (c) Schematic representation of a negative polaron in PPP. (d) Band diagram of various polarons.

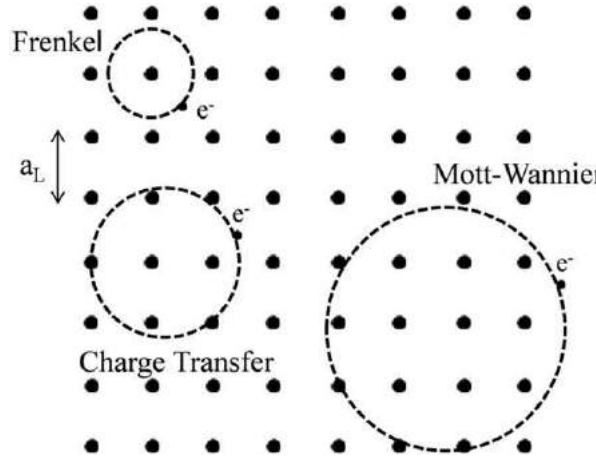


Fig. 8 Schematic representation of three different types of excitons in solid state materials; a_L is the lattice constant.

where s1 and s2 are the spin quantum numbers of the individual electron. If one electron is excited to the π-orbital, the resulting exciton is called a singlet because no net spin angular momentum exists in the molecule (Fig. 9(b)). On the other hand, if the two spin vectors have the same direction, the total spin angular momentum is now equal to 1, as revealed in the following equation

$$S = |s1 + s2| = |(+1/2) + (+1/2)| = 1 \quad (2)$$

Note that if s1 and s2 were both equal to –1/2, the sum would remain the same. Accordingly, the excited state (exciton) now exhibits a net angular moment. Assuming the presence of a magnetic field, the energy of the exciton could be split into three different energy levels. Therefore, it is called a triplet (Fig. 9(c)).

Fig. 9(d) displays possible decay processes of a typical organic molecule, where S_0, S_1, and T_1 represent the ground state, first singlet state, and first triplet state, respectively; k_{nr} and k'_{nr} are the rate constants of non-radiative decay processes and k_r and k'_r are the rate constants of radiative decay processes. The singlet exciton can flip its spin direction and transform into a triplet exciton

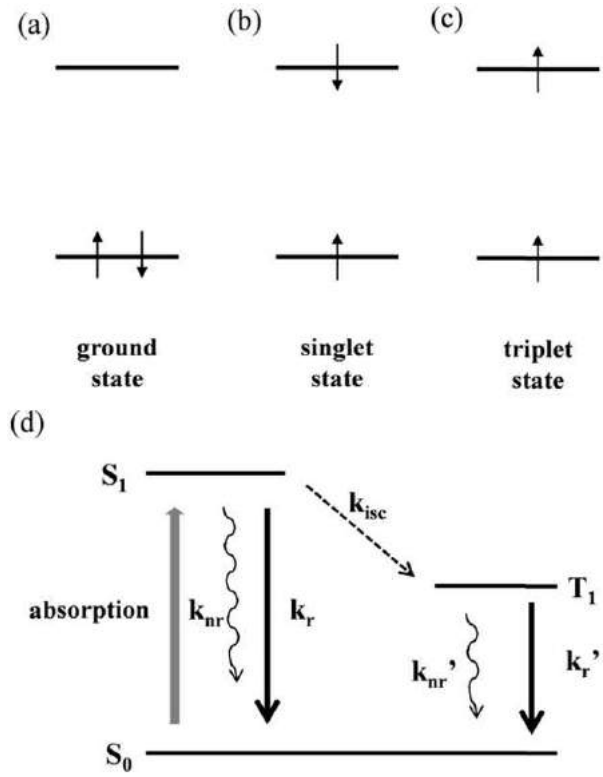


Fig. 9 Schematic representation of electron spins in the (a) ground state, (b) singlet exciton, and (c) triplet exciton of an organic molecule. (d) Excitation and possible decay processes in an OSC.

through a process called inter-system crossing (ISC); its rate constant is k_{isc}. As indicated in Fig. 9(d), the relaxation of a singlet exciton (S_1) to the ground state (S_0) is possible because the spin angular momentum is conserved. In quantum mechanics, such a transition is allowed; its radiative decay may lead to a highly efficient emission, called fluorescence (k_r). On the other hand, the transition of a triplet exciton to its ground state is forbidden. Consequently, the efficiency of the radiative decay is very low and, for most organic molecules, can be observed only at a very low temperature. The emission of triplet excitons is called phosphorescence (k_r').

Concept of Doping and p- and n-Type OSCs

Like inorganic semiconductors, OSCs can also be classified as p- and n-type semiconductors. The doping concept and process are, however, substantially different from those of inorganic materials, even though the same terminology of "doping" is used. For example, the inorganic semiconductor silicon is doped through ion implantation, in which impurities (phosphorus (P) or boron (B) atoms) are introduced. These foreign atoms substitute some of the silicon atoms and lead to new energetic levels in the band gap. Silicon becomes an n- or p-type semiconductor after the introduction of P or B atoms, respectively.

On the other hand, many different methods can be used to "dope" OSCs, including chemical doping, electrochemical doping, photo-doping, and charge injection from metal contacts. Chemical doping involves CT redox chemistry, as illustrated in the following examples for polymers

$$\text{p-type: } (\pi\text{-polymer})_n + 3/2n\ y(I_2) \rightarrow [(\pi\text{-polymer})^{+y}(I_3^-)_y]_n \tag{3}$$

$$\text{n-type: } (\pi\text{-polymer})_n + [Na^+(C_{10}H_8)^-]_y \rightarrow [(Na^+)_y(\pi\text{-polymer})^{-y}]_n + (C_{10}H_8)^0 \tag{4}$$

From a chemical point of view, p- and n-type doping is analogous to electrochemical oxidation and reduction, respectively. The doping process generates charge carriers in the OSCs. The electrical conductivity increases upon increasing the doping level and can reach a level comparable with that of a metal at a very high doping concentration. The drawback of this chemical method is that the doping level is hard to control, especially for intermediate doping levels. Fortunately, electrochemical doping can solve this problem. An electrode supplies redox charges to the semiconductor, and ions simultaneously diffuse in or out of the polymer chains from the electrolyte to compensate the charge mismatch. Through control of the voltage of the electrode, the doping level can be determined precisely. Electrochemical doping can be illustrated using the following equations:

$$p\text{-type: } (\pi\text{-polymer})_n + [Li^+(BF_4^-)]_{soln} \rightarrow [(\pi\text{-polymer})^{+y}(BF_4^-)_y]_n + Li_{electrode} \tag{5}$$

$$n\text{-type: } (\pi\text{-polymer})_n + \text{Li}_{\text{electrode}} \rightarrow \left[(\text{Li}^+)_\gamma(\pi\text{-polymer})^{-\gamma}\right]_n + [\text{Li}^+(\text{BF}_4{}^-)]_{\text{soln}} \quad (6)$$

The third method, photo-doping, is a process in which photon absorption generates an electron/hole pair, which could lead to locally oxidized (p-type doping) and nearby reduced (n-type doping) states of the material. The unique mechanism is illustrated by the following equation:

$$(\pi\text{-polymer})_n + h\nu \rightarrow [(\pi\text{-polymer})^{+\gamma} + (\pi\text{-polymer})^{-\gamma}]_n \quad (7)$$

After photon absorption, recombination to the ground state can be either radiative or nonradiative. The value of γ in the equation depends on the excitation rate in competition with the recombination rate.

The last scenario involves charge injection from metallic contacts into the OSCs. Holes and electrons are introduced into the π- and π^*-bands, respectively, as illustrated by the following equations:

$$p\text{-type: } (\pi\text{-polymer})_n - \gamma(e^-) \rightarrow [(\pi\text{-polymer})^{+\gamma}]_n \quad (8)$$

$$n\text{-type: } (\pi\text{-polymer})_n + \gamma(e^-) \rightarrow [(\pi\text{-polymer})^{-\gamma}]_n \quad (9)$$

Eq. (8) describes the injection of a hole into the filled π-band, corresponding to an oxidation reaction (removal of an electron). Eq. (9) describes the injection of an electron into an empty π^*-band, analogous to a reduction reaction. The major distinction of doping through charge injection from other doping processes (e.g., chemical doping) is the absence of counter ions to compensate the charges. Therefore, the doping process is only temporary; the states are relatively unstable. On the other hand, for chemical or electrochemical doping, the doping is permanent, unless the carriers are removed by an "undoping" process. As for photo-doping, the resulting photoconductivity is transient and limited by recombination and decay processes.

Even though OSCs can indeed be "doped" as described above and become p- or n-type semiconductors, many reports define OSCs as p- or n-type by judging whether they are good conductors for electrons or holes. For instance, pentacene is usually referred to as an excellent p-type semiconductor (**Fig. 2(d)**) because it exhibits a very high hole mobility. TPD (**Fig. 2(d)**) is often employed as a hole-transporting material in OLEDs. As a result, TPD is also considered a p-type OSC because it transports holes effectively and because holes are injected readily from the metal electrodes. Note that these OSCs are not intentionally doped and they are usually purified to as high a degree as possible to remove impurities before they are processed for device fabrication. Therefore, we cannot assume extra energy levels appear near the HOMOs, as they do for inorganic semiconductors. Another way of defining OSCs is to determine whether they function as electron donors (p-type) or electron acceptors (n-type) during device operation. For example, fullerene derivatives (**Fig. 2(e)**) are defined as n-type OSCs because they accept electrons upon photoexcitation and transport the photogenerated electrons in organic solar cells. Meanwhile, many conjugated polymers blended with fullerene derivatives are considered as p-type OSCs because they donate electrons upon photoexcitation in solar cells.

Device Applications

In this section, we review some of the most important organic electronic devices, including electrophotographic devices, OLEDs, organic thin-film transistors (OTFTs), and organic light-emitting transistors (OLETs). For practical applications, organic photoconductors were the first technology to use OSCs as a key component in commercially available products; they are often employed in offices in copy machines and laser printers (**Fig. 10**). In such an electrophotographic device, the image of a document is transferred to a photoconductive plate (photoreceptor), previously charged with static electricity, through a set of optical components. Because only parts of the photoconductive plate are discharged, as a result of its high photoconductivity, upon exposure to light, an image duplicates the original document on the surface of the photoconductive plate. The next development step involves the placement of the electrostatically charged toner particles over the partially charged surface; some of the particles are adhered to the image by the electric field. An electrostatic field then transfers the image composed of toner particles to a sheet of paper. Finally, the image is fixed through pressure and heating. After swiping out the toner particles (clean) and exposing to light to remove the remaining static electricity (erase), the photoconductive plate is ready for the next copy process.

The simplest device structure of an OLED is displayed in **Fig. 11(a)**. It typically consists of two organic layers: an electron-transport layer (ETL) and a hole-transport layer (HTL). This design obviates the need to find an OSC possessing balanced injection and transport between electrons and holes. Unlike an individual single crystal (e.g., anthracene) that allows only effective hole injection, the bilayer structure facilitates hole injection from an indium tin oxide (ITO) electrode and electron injection from a metal alloy (MgAg) electrode. The charge balance can be further finely tuned through control over the thicknesses of the HTLs and ETLs. The excitons formed after recombination of the injected electrons and holes relax to the ground states, resulting in photon emission. Because the ITO anode is transparent, a strong green emission is observed through the ITO side of this device.

In solid state organic materials, only very weak van der Waals forces exist between the molecules. Many experimental results have indicated, however, that π-electrons can be transported effectively within OSCs. Organic field effect transistors (OFETs) provide a useful platform for examining the charge transport properties of OSCs. Transistors are fundamental building blocks in modern electrical circuits; they function as either signal amplifiers or on/off switches. The phenomenon of the conductivity of a semiconductor being modulated by applying an electric field normal to its surface is called the "field effect." Most OFETs are OTFTs, implying that the active (semiconducting) layer is nearly two-dimensional. **Fig. 11(b–d)** presents the three common device structures of OTFTs; **Fig. 11(e)** illustrates the operation mechanism. The charge carriers travel in a channel at the dielectric–OSC

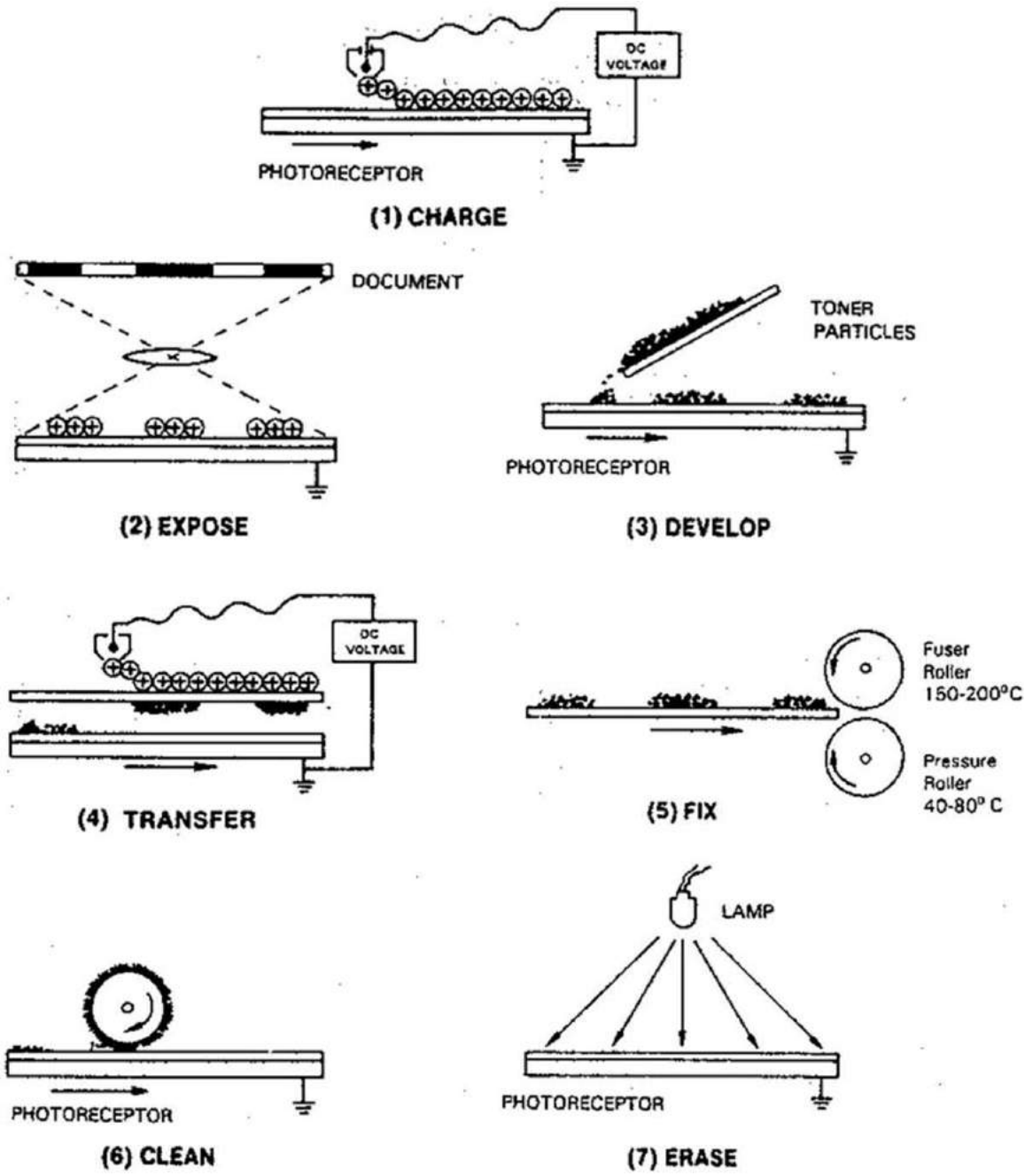


Fig. 10 Working principle of an electrophotographic device: (1) charge, (2) expose, (3) develop, (4) transfer, (5) fix, (6) clean, and (7) erase. Reproduced from Pope, M., Swenberg, C., 1999. Electronic Processes in Organic Crystals and Polymers, with permission from Oxford University Press, Copyright (1999).

interface. The source and drain electrodes provide contacts to the OSCs, and can inject and collect, respectively, the charges in the channel. The conductance of the channel can be modulated by a third gate electrode, which is separated by a layer of gate insulator. In a p-channel OTFT, for example, a negative voltage is applied to the gate (V_G), inducing holes in the channel through field effects. A negative bias is also applied between the source and drain electrodes (V_D), resulting in a driving force to flow the field-induced holes from the source to drain electrodes. The device behaves as a resistor, with the drain current (I_D) increasing linearly with respect to the increasing value of V_D. From the relationship between I_D and V_D (Fig. 11(f)), this operation region is called the linear region. While a substantial value of V_D is supplied, the magnitude of the field inducing the charges is partially canceled near the drain. When the effective voltage is lower than the threshold voltage (V_t), the concentration of induced charges drops to almost zero, forming a high resistance regime in the channel close to the drain end. The channel now pinches at one side and the value of I_D starts to saturate. This phenomenon is known as "pinch-off" and this operation region is the saturation region

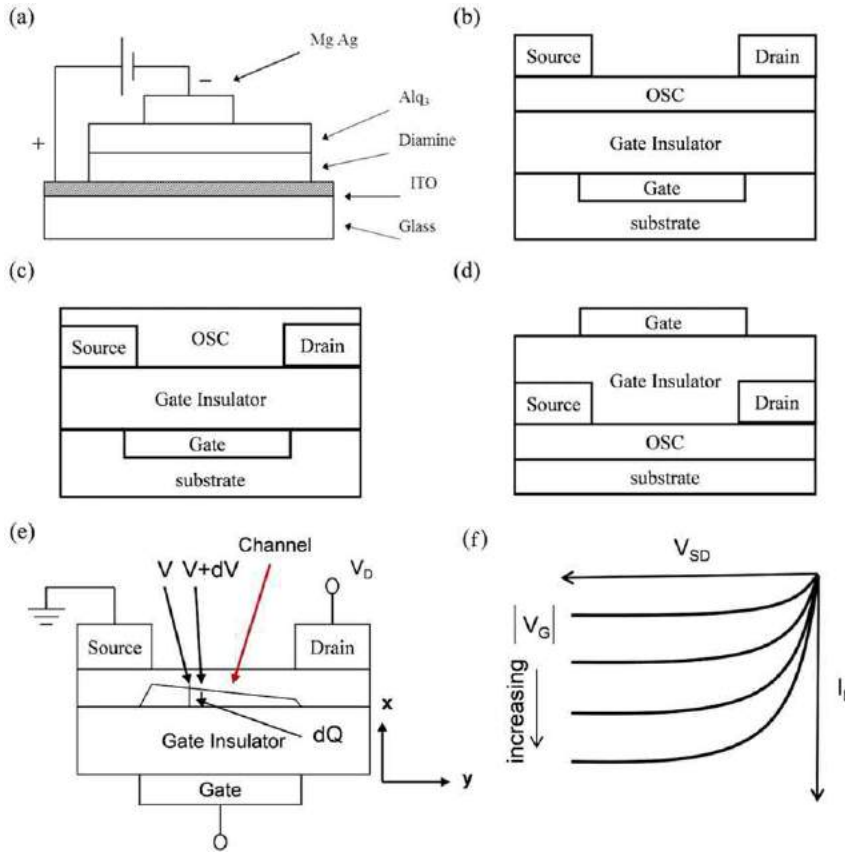


Fig. 11 (a) Device structure of a typical organic light-emitting diode (OLED); the layers of Alq_3 and diamine are the electron-transport layer (ETL) and hole-transport layer (HTL), respectively. Common structures of organic thin-film transistors (OTFTs): (b) top-contact, bottom-gate, (c) bottom-contact, bottom-gate, and (d) bottom-contact, top-gate. (e) Illustration of the operating mechanism of a typical OTFT. (f) Output characteristics (I_D–V_D) of a typical OTFT. ITO, indium tin oxide.

(Fig. 11(f)). Notably, the magnitude of the saturation current depends on the applied gate voltage. For n-channel OTFTs, the electrical behavior is similar, but the current–voltage curves are located in the first quadrant, instead of the third. The charge carriers are now electrons.

In the linear region, the drain current is described by:

$$I_D = C_{ox}\mu(W/L)\left[(V_G - V_{th})V_D - (1/2)V_D{}^2\right] \tag{9}$$

where C_{ox} is the capacitance per unit area of the dielectric layer, μ is the mobility of the OSC, and W and L are the channel length and width, respectively. In the saturation region, the value of I_D can be expressed as

$$I_D = C_{ox}\mu(W/2L)(V_G - V_{th})^2 \tag{10}$$

Therefore, fitting the curves with the above equations can allow determination of the mobilities of the OSCs in either the linear or saturation regions. The other important parameter for evaluating the performance of an OTFT is the on/off ratio, defined as I_{on}/I_{off}, where I_{on} and I_{off} are the drain currents when the channel is turn on and off, respectively. A noticeable leakage current usually exists because charges can leak through the gate and/or because some charges are stored within the semiconductors. For state-of-the-art OTFTs, the mobility can readily reach up to 1 $cm^2\ V^{-1}\ s^{-1}$. Mobilities greater than 10 $cm^2\ V^{-1}\ s^{-1}$ have also been demonstrated for solution-processed OTFTs. For example, a highly aligned metastable structure of 2,7-dioctyl[1]benzothieno[3,2-*b*][1]benzothiophene (C8-BTBT), grown from a blended solution of C8-BTBT and polystyrene, has displayed a mobility of 43 $cm^2\ V^{-1}\ s^{-1}$ (25 $cm^2\ V^{-1}\ s^{-1}$ on average), suggesting great potential for future electronic applications.

Because OLEDs are typically two-terminal devices, field-effect transistors are essential to control their luminescence levels and to switch individual OLED pixels when they serve as the elements of active-matrix display panels. In contrast, no transistors are needed when OLETs are employed for similar applications; a single OLET can perform both light-generation and electrical switching functionalities. For an unipolar OTFT, only a single type of charge carrier, electron or hole, is injected and transported along the conducting channel. Two carriers, however, are required to form excitons for light emission in OLETs. Therefore, an ideal OLET is an ambipolar device, although unipolar OLETs have also been reported. Light emission in unipolar OLETs occurs close to one of the electrodes, and the excitons are readily quenched by the metals, potentially decreasing the luminescence efficiencies.

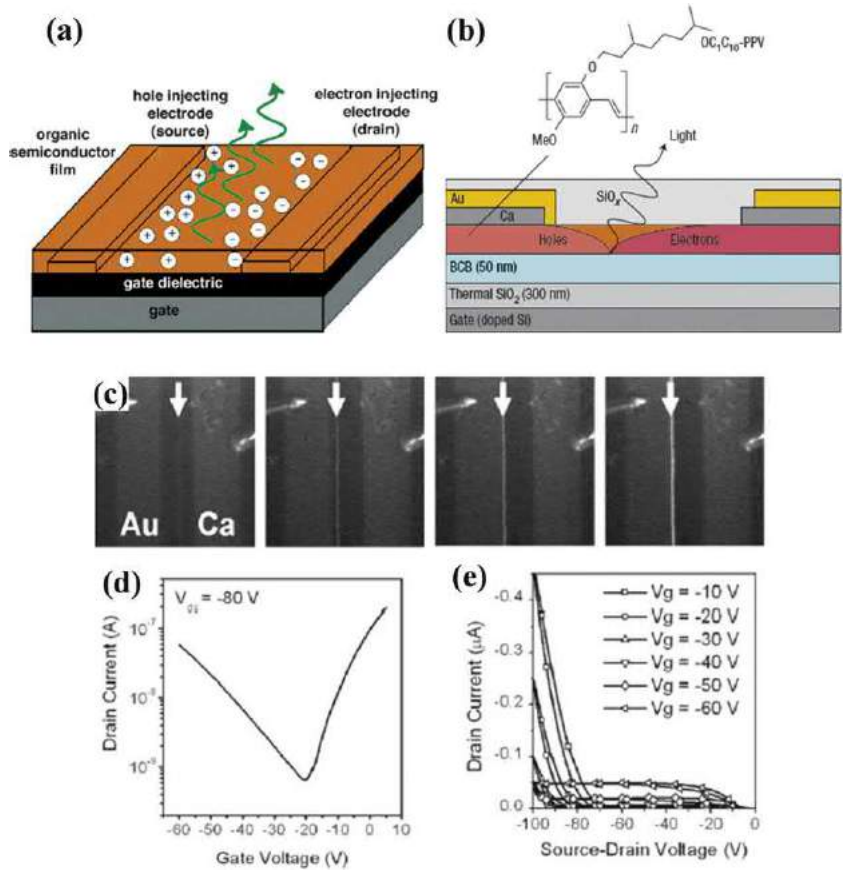


Fig. 12 (a) Schematic representation of a typical organic light-emitting transistor (OLET) device structure and its working principle. (b) Device structure of the first ambipolar OLET; the Au and Ca metal sources are positioned off-center, opposite each other, leading to two electrodes for hole and electron injection, respectively; the chemical structure of MDMO-PPV is also depicted. (c) Movement of the recombination zone as a function of drain bias: $V_G = -90$ V; $V_D = -79$, –86, –93, and –100 V (from left to right). (d) Transfer characteristics at $V_D = -80$ V. (e) Output characteristics. Reproduced from Cicoira, F., Santato, C., 2007. Organic light emitting field effect transistors: Advances and perspectives. Advanced Functional Materials 17, 3421–3434 with permission from WILEY-VCH Verlag GmbH & Co, Copyright (2007); and Zaumseil, J., Friend, R.H., Sirringhaus, H., 2006. Spatial control of the recombination zone in an ambipolar light-emitting organic transistor. Nature Materials 5, 69–74 with permission from Nature Publishing Group, Copyright (2007).

Fig. 12(a) displays the structure of a typical OLET having a bottom contact geometry; it is similar to that of a conventional OTFT. In other words, other structures, like the two other geometries in Fig. 11, are also possible choices. The source and drain electrodes are hole-injecting and electron-injecting electrodes, and the OSC should be emissive. Upon application of a reasonable gate bias (V_G), holes and electrons are injected from the source and drain contacts, respectively. The two opposite charges form excitons in the channel and, subsequently, they decay radiatively to produce light.

Ideal performance of an ambipolar device is, in practice, very difficult to achieve. First, the source and drain should be capable for injecting both holes and electrons efficiently. The OSC should also exhibit balanced hole and electrode mobilities. In 2006, Zaumseil *et al*. reported the first ambipolar OLETs incorporating poly(2-methoxy-5-(3,7-dimethyloctoxy)-*p*-phenylene-vinylene) (MDMO-PPV), a conjugated polymer displaying high photoluminescence efficiency (Fig. 12(b)). On the dielectric surface, they deposited a layer of crosslinked benzocyclobutene derivative (BCB) as a buffer dielectric to prevent the trapping of electrons at the dielectric–semiconductor interface. This approach is one of the keys to significantly improve electron (n-channel) transport on oxide dielectric surfaces. Au and Ca electrodes were then deposited for effective hole and electron injection, respectively. The use of Au electrodes only for both contacts would have led to high electron injection barrier at one side. Similarly, the use of Ca electrodes only would have led to a high hole injection barrier at one of the contacts. Fig. 12(c) illustrates the light emission from the OLET, and the movement of the light emitting zone between the two electrodes. In fact, no light emission was observed when the value of $|V_D|$ was below a certain threshold, because of limited electron injection. A narrow line of light appeared once the value of $|V_D|$ exceeded the threshold voltage. The light emission line moved toward the Au electrode upon increasing the value of $|V_D|$. The transfer characteristics of the device (Fig. 12(d)) revealed ambipolar behavior; the minimum point, at a value of V_G of approximately –20 V, indicates the transition from the electron- to hole-dominated current in the OLET. The output characteristics in Fig. 12(e) also reveal ambipolar currents. High-performance OLETs can also be fabricated by using mixed p- and n-type OSCs as the semiconducting layer. This approach can be accomplished through a bilayer structure, or co-deposition of hole and electron

transporting materials. More recent results have indicated that OLETs can outperform equivalent light-emitting diodes when using a trilayer semiconducting heterostructure.

Summary

The properties of OSCs are much different from those of inorganic semiconductors in many aspects. For example, π-electrons are responsible for the charge transport in OSCs, and the concept of doping is fundamentally different. Nevertheless, OSCs are very attractive for use in electronic devices because they are formed from inexpensive starting materials and have many useful properties, including solution-processability and flexibility. These unique properties offer many possibilities for various applications. For example, high-performance inorganic light-emitting diodes are usually fabricated through delicate crystal growth, and large-area devices are very difficult to implement. In contrast, OLEDs are readily pixelated and, therefore, can be used for flat-panel displays. We must emphasize, however, that organic electronic devices are not designed intentionally to compete with those containing inorganic counterparts. Rather, we believe that there will be many new applications in which inorganic semiconductors will not be useful; therefore, the exploration of organic devices should continue in the future.

See also: Organic Lasers. Organic Photodetectors

Further Reading

Capelli, R., Toffanin, S., Generali, G., *et al.*, 2010. Organic light-emitting transistors with an efficiency that outperforms the equivalent light-emitting diodes. Nature Materials 9, 496–503.
Cicoira, F., Santato, C., 2007. Organic light emitting field effect transistors: Advances and perspectives. Advanced Functional Materials 17, 3421–3434.
Heerger, A.J., 2001. Semiconducting and metallic polymers: The fourth generation of polymeric materials (Nobel lecture). Angewandte Chemie International Edition 40, 2591–2611.
Helfrich, W., Schneider, W.G., 1965. Recombination radiation in anthracene crystals. Physical Review Letters 14, 229–231.
Pope, M., Swenberg, C.E., 1999. Electronic processes in organic crystals and polymers. New York, NY: Oxford University Press.
Tang, C.W., VanSlyke, S.A., 1987. Organic electroluminescent diodes. Applied Physics Letters 51, 913–915.
Turro, N.J., 1991. Modern molecular photochemistry. Sousalito, CA: University Science Book.
Yuan, Y., Giri, G., Alexander, L., *et al.*, 2014. Ultra-high mobility transparent organic thin film transistors grown by an off-centre spin-coating method. Nature Communications 5, 3005.
Zaumseil, J., Friend, R.H., Sirringhaus, H., 2006. Spatial control of the recombination zone in an ambipolar light-emitting organic transistor. Nature Materials 5, 69–74.

OLED/Introduction

Dae-Gyu Moon, Soonchunhyang University, Asan-si, Chungcheongnam-do, Republic of Korea

© 2018 Elsevier Ltd. All rights reserved.

OLED Architectures

Organic light-emitting diode (OLED) is a thin film electroluminescent device that emits electromagnetic radiation from organic materials sandwiched between two electrodes to an external electric field. Since the first observation on the organic electroluminescence in 1963, Tang *et al.* made a great progress in efficiency and lifetime using a double layer structure based on small molecules in 1987. Friend *et al.* first reported polymer light-emitting devices in 1990. Baldo *et al.* made a quantum leap in efficiency of OLED using a phosphorescent molecule in 1998.

A simple OLED structure is illustrated in Fig. 1. Organic thin films are situated between the anode and cathode. At least, one of both electrodes should be optically transparent. When a sufficient forward bias is applied to the anode, electrons, and holes are injected into the organic electron and hole transport layers (HTLs) from the cathode and the anode, respectively. The injected carriers transport through the respective carrier transport layers by the internal electric field toward the electrode of opposite polarity, recombining to form excitons in the emission layer. The radiative decay of these excitons generates photons in the visible range that are extracted out of the device.

Carrier injection is improved by lowering the potential barrier height at the electrode/organic interface, which can be approximately estimated by the difference between the work function of electrode and the highest occupied (or lowest unoccupied) molecular orbital (HOMO or LUMO) energy level. ITO is widely used as a transparent anode material because it is electrically conductive and its work function is relatively high (4.5–5.0 eV). ITO surface is treated with oxygen plasma or ozone in order to increase the work function and to remove surface contaminants. Low work function metals such as Mg, Ca, Mg:Ag, or LiF/Al are used as cathode materials. The light emission processes in OLEDs provide several features such as wide viewing angle, fast response time, and current driving of luminance. OLEDs can be fabricated on many kinds of substrates including large area glasses, silicon wafers, plastic films, metal foils, and textiles. This high degree of freedom in selecting substrates makes OLEDs very promising for future optoelectronic applications.

Various functional organic layers are used to improve the efficiency and lifetime in modern OLED architectures. Typical layers are hole injection layer (HIL), HTL, electron block layer (EBL), hole block layer (HBL), electron transport layer (ETL), and electron injection layer (EIL). EBL and HBL confine the recombination and emission processes to the emission layer (EML) composed of host and guest molecules. The host molecules can be mixed with two or three kinds of molecules to control the recombination and emission processes.

Small Molecule and Polymer OLEDs

OLEDs can be prepared using small molecules or polymers. Thin film of small molecules is usually deposited by thermal evaporation in high or ultrahigh vacuum (typically 10^{-6}–10^{-7} Torr). The thermal evaporation of small molecules allows for easy deposition of multilayer devices with sophisticated architectures that precisely control all the emission processes from carrier injection to photon emission. Small molecules often have a thermal decomposition temperature much higher than the sublimation temperature so that the materials can be purified by repeated sublimation in vacuum or inert gas. High purity materials are essential in achieving high efficiency and long lifetime devices. Polymers cannot be deposited by thermal evaporation because their decomposition temperature is generally lower than their sublimation temperature. Polymer films are prepared by solution processing such as inkjet printing and spin coating. Hence, the polymer devices have advantages in simple and large area fabrication.

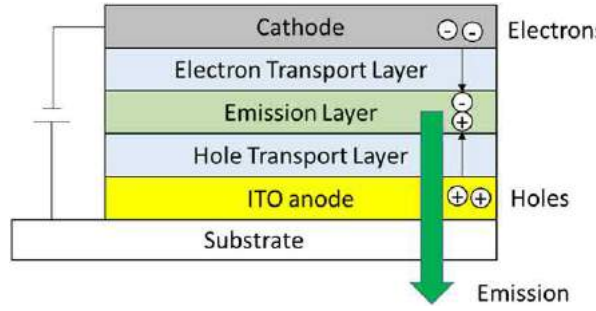


Fig. 1 Device structure of organic light-emitting diode (OLED) with triple organic layers.

 doi:10.1016/B978-0-12-803581-8.09539-4

Carrier Injection and Materials

Organic materials are regarded as insulator because they generally have very high resistance at low electric field. It means that a strong electric field is required to inject carriers from the electrodes to the LUMO or HOMO levels of organic layers. Charge carriers can be injected into the organic layers via Schottky or tunnel emission as shown in Fig. 2. Electrons or holes acquire sufficient energy at high temperature. When the energy of charge carriers is higher than the potential barrier at the interface, the carriers are thermally excited over the barrier into the organic layer. This phenomenon is called Schottky or thermionic emission. If the barrier is thin enough, electrons tunnel into the organic layer through the barrier. This mechanism is called field emission and it is expressed by Fowler–Nordheim equation assuming triangular shape of energy barrier. In both processes, small barrier height is important in improving carrier injection so that the organic materials with shallow HOMO and deep LUMO levels are preferred as the hole and electron injection layers, respectively.

Fig. 3 shows the organic materials for the HIL. Triphenylamine derivatives are widely used as a HIL material. Typical examples are 4,4′,4″-*tris*[phenyl(*m*-tolyl)amino]triphenylamine (*m*-MTDATA) (*m*-MTDATA) and 4,4′,4″-*tris*[2-naphthyl(phenyl)amino]triphenylamine (2-TNATA) (2-TNATA). copper phthalocyanine (CuPc) is also frequently used as a HIL material. HOMO levels of these materials are less than 5.2 eV. Hole injection can also be improved by using a material with a very deep LUMO level, where the holes are directly injected into the LUMO level rather than the HOMO level. For example, dipyrazino[2,3-f:2′,3′-h]quinoxaline-2,3,6,7,10,11-hexacarbonitrile (HAT-CN) has a LUMO level of 5.5–6.0 eV. poly(3,4-ethylenedioxythiophene)-poly(styrenesulfonate) (PEDOT:PSS) is widely used as a hole injecting polymer layer. This conducting polymer has a work function of about 5.2 eV. Metal oxides such as MoO_3, WO_3 are often used as inorganic buffer layer for hole injection.

The selection of electron injecting material is somewhat complicated. A low work function metal results in a small barrier for electron injection. However, they are susceptible to atmospheric oxidation and corrosion. They easily react with air, water, and organic materials. More stable metals such as Al are widely used in electronics. However, they have too high work functions to efficiently inject electrons. Therefore, very thin electron injection buffer layer is inserted between ETL and Al cathode. Alkali metal halides and metal oxides are widely used as an electron injection buffer. For example, LiF/Al is most commonly used for the cathode. Lithium quinolate (Liq) is also widely used as a small molecule EIL for Al cathode. Low binding energy between lithium and hydroxyquinoline ligand liberates lithium in the Liq complex during deposition of Liq or cathode. The interface dipole layer can be formed by charge transfer, surface rearrangement, and chemical reaction at the organic/electrode interface. The dipole layer results in the vacuum level shift at the interface so that the injection barrier is different from the simple expectation based on the work function and the HOMO or LUMO level. The sing of vacuum level shift is generally negative, attributing to the downward shift of organic energy levels. Large amount of shift is often observed at the metal/organic interface.

Carrier Transport and Materials

When the number of injected charges is higher than the equilibrium charge density in organic material, the excess charges form a space charge inducing an electric field inside the organic layer. That is, local polarization layer is formed near the electrode, which limits the charge injection from the electrode. This polarized layer is called space-charge layer. Current flow is limited by the rate at which carriers drift out of the space-charge layer, so it is called space-charge-limited current (SCLC). As the organic materials generally contain defects and impurities acting as charge carrier traps, the charge carrier transport is also limited by the number of traps. In both cases of trap-limited and space-charge-limited conduction, the current is controlled by the mobility of charge carriers. Organic molecular crystals such as anthracene exhibit band-like charge carrier transport because the charge carriers are highly delocalized. Thus, the charge carrier mobility reaches to about 1 cm^2/Vs. However, in the amorphous organic materials that are generally used in OLEDs, the charge carriers are highly localized due to weak intermolecular interaction and strong local polarization. Here, hopping process from one molecule to a neighboring molecule dominates the charge carrier transport. The resulting charge carrier mobility is low (10^{-7}–10^{-2} cm^2/Vs) in amorphous organic materials.

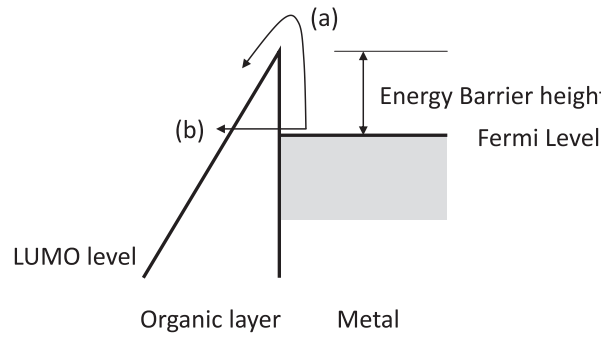


Fig. 2 Injection mechanisms of electrons from the metal into the organic layer under an applied voltage: (a) Schottky emission and (b) tunnel emission.

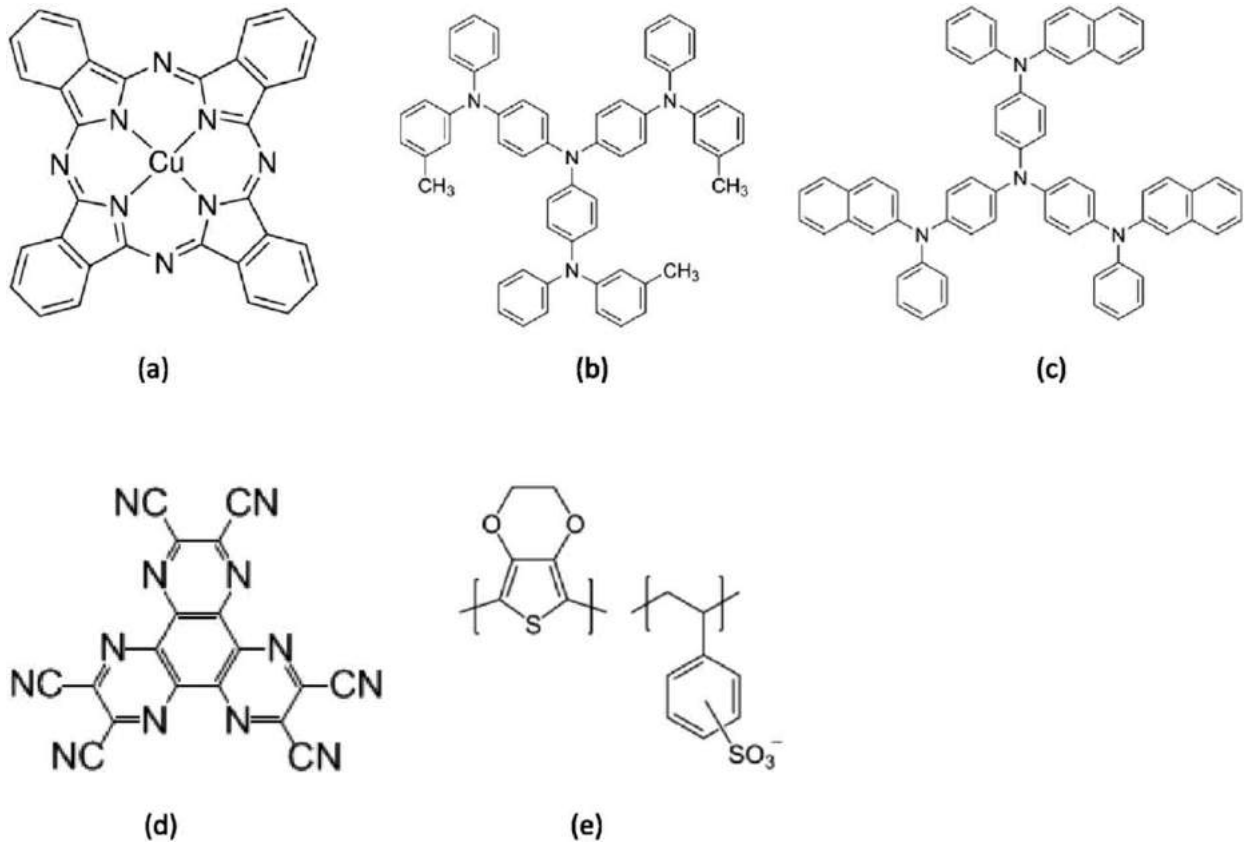


Fig. 3 Organic materials for the hole injection layer (HIL): (a) copper phthalocyanine (CuPc), (b) 4,4′,4″-*tris*[phenyl(*m*-tolyl)amino]triphenylamine (*m*-MTDATA), (c) 4,4′,4″-*tris*[2-naphthyl(phenyl)amino]triphenylamine (2-TNATA), (d) dipyrazino[2,3-f:2′,3′-h]quinoxaline-2,3,6,7,10,11-hexacarbonitrile (HAT-CN), and (e) poly(3,4-ethylenedioxythiophene)-poly(styrenesulfonate) (PEDOT:PSS).

HTL provides conductive pathway for the injected holes to migrate into the EML. The HOMO level of HTL material is designed to be slightly shallower than that of EML material for improving the charge flow into the EML with minimal hole accumulation at the HTL/EML interface. Another function of HTL is to act as electron or exciton block layer that prevents the transfer of electrons or excitons in EML to the adjacent organic or anode layer. For this purpose, the HTL material should have a shallow LUMO level and wide energy gap. Fig. 4 shows various HTL materials. Typical examples are aromatic amine-based materials such as 4,4′-cyclohexylidenebis[*N*,*N*-*bis*(4-methylphenyl) benzenamine] (TAPC), *N*,*N*′-*bis*(3-methylphenyl)-*N*,*N*′-diphenylbenzidine (TPD), and *N*,*N*′-Di(1-naphthyl)-*N*,*N*′-diphenyl-(1,1′-biphenyl)-4,4′-diamine (NPD). They have shallow HOMO levels of 5.4–5.8 eV and shallow LUMO levels of 2.4–2.7 eV. They have a small energy for hole creation and the resulting radical cation is stable. They have relatively high hole mobility of 10^{-4}–10^{-3} cm^2/Vs. However, they are easily crystallized at high temperature due to their low glass transition temperatures (T_g) of 65–96°C. Carbazole-based *tris*(4-carbazoyl-9-ylphenyl)amine (TCTA) is also widely used as HTL material. TCTA has a high T_g of 151°C and its hole mobility is about 10^{-5} cm^2/Vs. Polymers such as poly(9-vinylcarbazole) (PVK) and poly[(9,9-dioctylfluorenyl-2,7-diyl)-*co*-(4,4′-(*N*-(4-sec-butylphenyl)diphenylamine)] (TFB) are also widely used as HTL materials for solution-processed OLEDs.

ETL material should have good electron injection property, high electron mobility, high hole and exciton blocking ability. There are much smaller number of ETL materials compared with the HTL materials. The electron mobility of ETL materials is typically lower than the hole mobility of HTL materials. In operating OLEDs, it is difficult to achieve the chemical stability in ETL materials. Imidazole, siloles, boranes, and phosphine oxide, and metal complexes are used as an ETL material. Fig. 5 shows various ETL materials. *tris*(8-hydroxyquinoline) aluminum (Alq_3) is well-known electron-transporting material. The LUMO level (about 3.1 eV) of Alq_3 is sufficient to inject electrons whereas its HOMO level (<6.0 eV) is too shallow to block holes. 2,2′,2″-(1,3,5-benzinetriyl)-*tris*(1-phenyl-1-*H*-benzimidazole) (TPBi) is an important ETL material for high efficiency OLEDs. The electron mobility of TPBi is 10^{-6}–10^{-5} cm^2/Vs. TPBi has large energy gap and its LUMO level is 2.7 eV while its HOMO level is 6.2–6.7 eV. 3-(biphenyl-4-yl)-5-(4-*tert*-butylphenyl)-4-phenyl-4 *H*-1,2,4-triazole (TAZ) and BCP are wide energy gap ETL material. Pyridine-containing 2,9-dimethyl-4,7-diphenyl-1,10-phenanthroline (BCP), (e) 1,3,5-*tris*(3-pyridyl-3-phenyl)benzene (TmPyPB) has a good electron-transporting ability, exhibiting high electron mobility of about 10^{-3} cm^2/Vs. HOMO and LUMO levels of TmPyPB are 2.7 and 6.7 eV, respectively. Boron-containing 3TPYMB is also typically used as wide gap ETL material. ETL materials with wide energy gap and deep HOMO level such as TAZ, BCP, TPBi, and TmPyPB act as hole or exciton block layer. Various benzothiadiazole, pyridine, and oxadiazole polymers are generally used as an ETL material for solution-processed OLEDs.

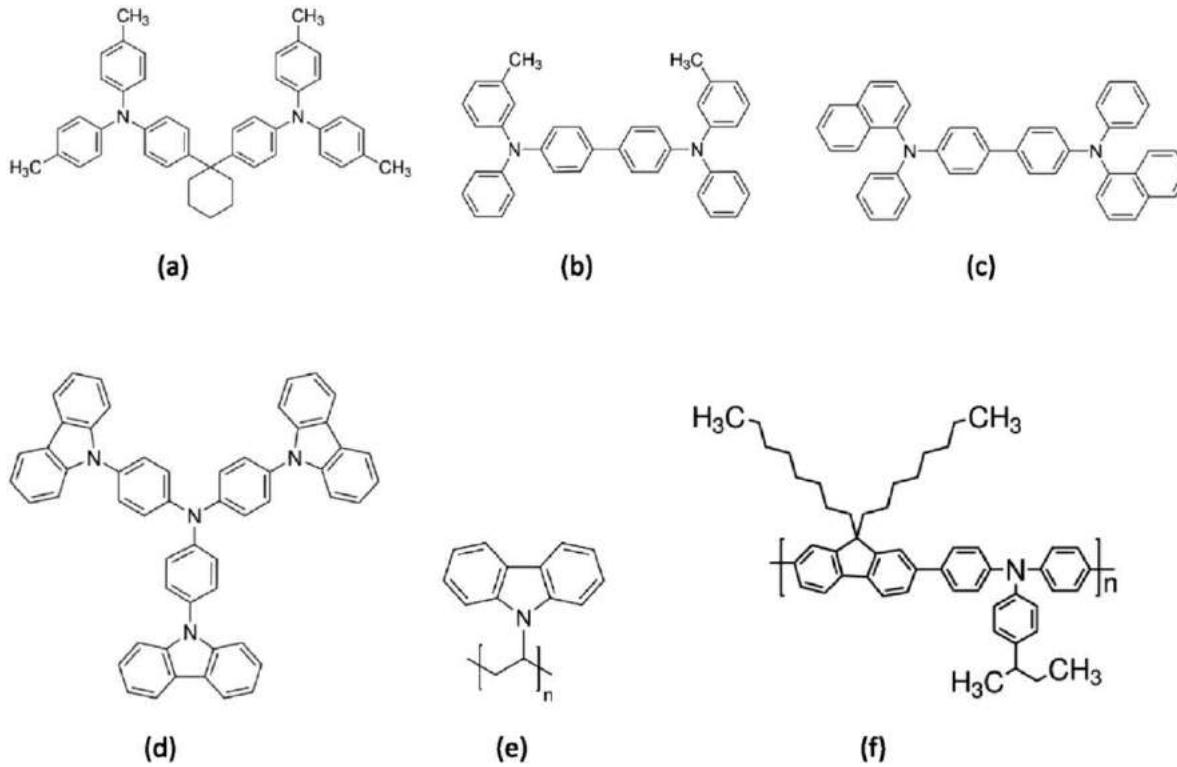


Fig. 4 Organic materials for the hole transport layer (HTL): (a) 4,4′-cyclohexylidenebis[*N,N-bis*(4-methylphenyl) benzenamine] (TAPC), (b) *N,N′-bis*(3-methylphenyl)-*N,N′*-diphenylbenzidine (TPD), (c) *N,N′*-Di(1-naphthyl)-*N,N′*-diphenyl-(1,1′-biphenyl)-4,4′-diamine (NPD), (d) *tris*(4-carbazoyl-9-ylphenyl)amine (TCTA), (e) poly(9-vinylcarbazole) (PVK), and (f) poly[(9,9-dioctylfluorenyl-2,7-diyl)-*co*-(4,4′-(*N*-(4-sec-butylphenyl) diphenylamine)] (TFB).

Doped Transport Layer

OLEDs generally require high electric field to inject charge carriers and to drive the injected carriers into the emission region because of contact barriers at the interface and low carrier mobility of organic materials. High operating voltage exceeding thermodynamic limit is typically required to drive an OLED at high luminance level. Consequently, doped transport layer is frequently used for minimizing the voltage drop in the transport layer and improving the charge carrier injection from the contacts into the neighboring organic transport materials. Hole transport or injection layer can be doped with the electron accepting atoms or molecules that releases the mobile holes in the layer (p-type doping). Fig. 6 shows the various dopant molecules for the doped transport layer. For example, if *m*-MTDATA HIL is doped with 2,3,5,6-tetrafluoro-7,7,8,8-tetracyanoquinodimethane (F4-TCNQ) molecules, electron transfer occurs from *m*-MDATA to F4-TCNQ as the electron affinity of F4-TCNQ is comparable to the ionization energy of *m*-MTDATA. It leads to negative charged F4-TCNQ molecules and positive charged *m*-MTDADA molecules, i.e., holes in the *m*-MTDATA layer that can move relatively freely throughout the *m*-MTDATA layer. F4-TCNQ molecule thus improves the electrical conductivity of the organic layer, eventually resulting in low voltage drop. HAT-CN is also widely used as a p-type dopant. The LUMO level of HAT-CN (5.7 eV) is very similar with those of typical HTL materials, thus the extra holes can be generated in the HTL by transferring electrons from HTL to HAT-CN molecules. MoO_3 is another effective p-type dopant in improving the injection efficiency and reducing ohmic losses in the transport layers. Other materials such as metals (Au, Pt), gases (Cl, Br, I), and small molecules (1,3,4,5,7,8-hexafluorotetracyanonaphthoquinodimethane – F6-TNAP) can be used as p-type dopants. Similarly, electron injection and transport can be improved by n-type dopants that donate electrons to the neighboring ETL molecules. Organic molecules (Liq, pyronine B – PyB chloride), inorganic materials (Cs_2CO_3), low work metals (Li, Cs) can modify the interface electronic structure, enhancing the conductivity of ETLs. The doped transport layer is typically separated by thin undoped organic layer from the emission region because the p-type and n-type dopants tend to provide nonradiative exciton recombination centers.

Exciton Formation and Decay

When electrons and holes recombine on organic molecules, two kinds of excitons, singlet and triplet excitons, are generated. Singlet excitons have spin antisymmetry states and their transitions to ground state are quantum mechanically allowed, giving rise to fluorescence as shown in Fig. 7. Triplet states with spin even symmetry lead to phosphorescence. Radiative transition rate of

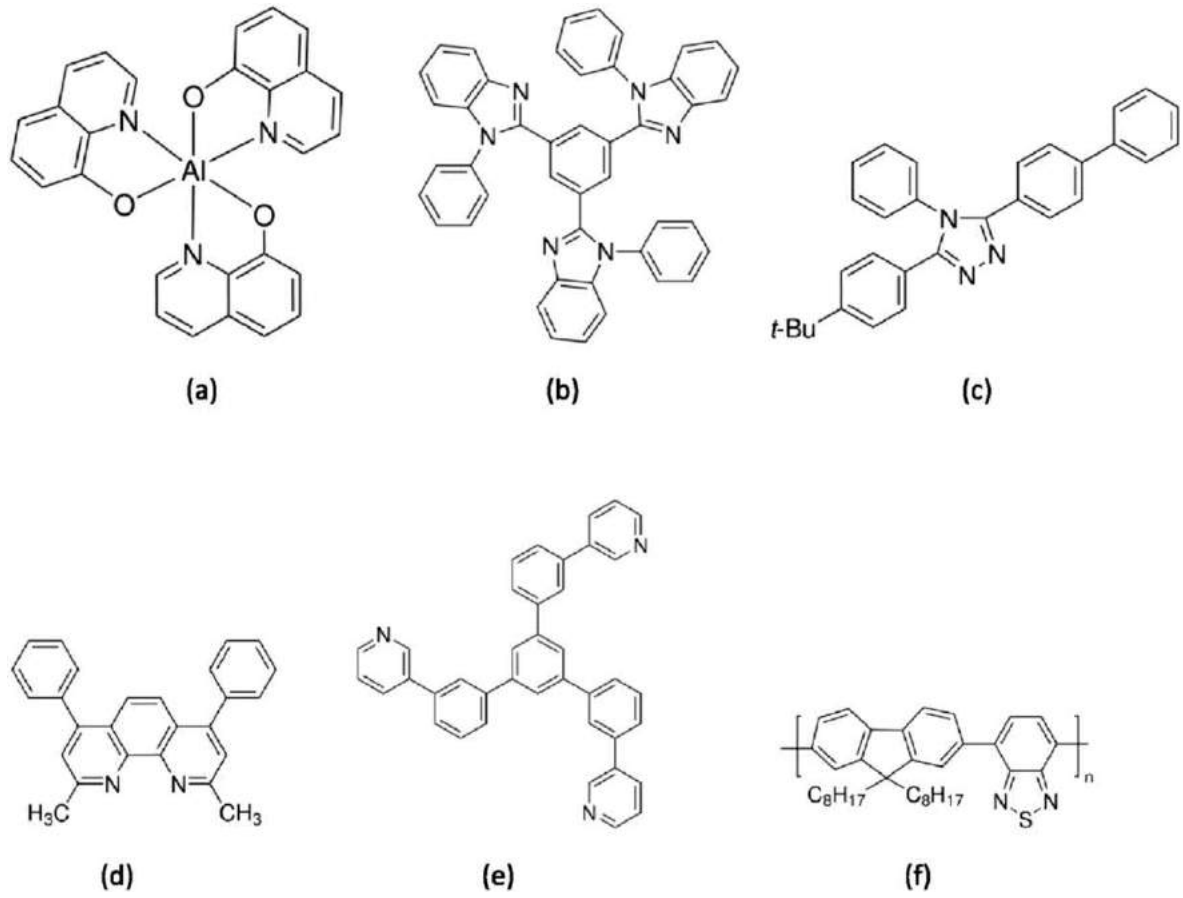


Fig. 5 Organic materials for the electron transport layer (ETL): (a) *tris*(8-hydroxyquinoline) aluminum (Alq_3), (b) 2,2′,2″-(1,3,5-benzinetriyl)-*tris*(1-phenyl-1-*H*-benzimidazole) (TPBi), (c) 3-(biphenyl-4-yl)-5-(4-*tert*-butylphenyl)-4-phenyl-4 *H*-1,2,4-triazole (TAZ), (d) 2,9-dimethyl-4,7-diphenyl-1,10-phenanthroline (BCP), (e) 1,3,5-*tris*(3-pyridyl-3-phenyl)benzene (TmPyPB), (f) poly(9,9-dioctylfluorene-*alt*-benzothiadiazole) (F8BT).

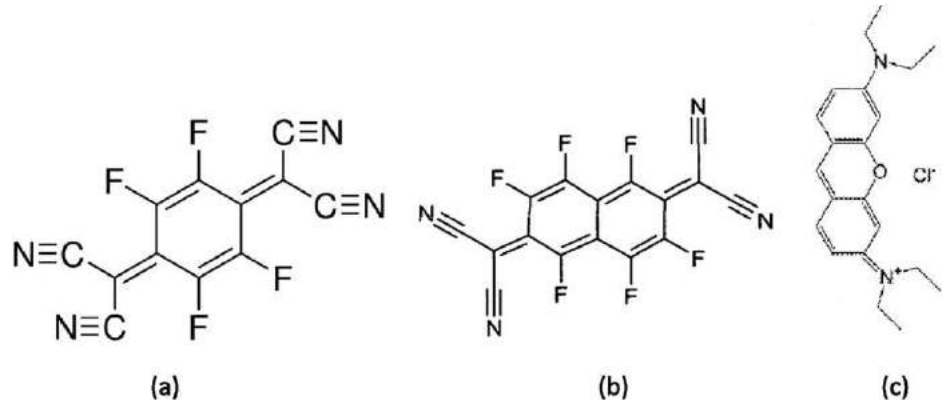


Fig. 6 Organic materials for the doped transport layer: (a) 2,3,5,6-tetrafluoro-7,7,8,8-tetracyanoquinodimethane (F4-TCNQ), (b) 1,3,4,5,7,8-hexafluorotetracyanonaphthoquinodimethane (F6-TNAP), and (c) pyronine B (PyB) chloride.

singlet exciton is fast (<10 ns), whereas the decay rate of triplet exciton is slow (100 μs–10 s) because it is a disallowed transition. Statistically 25% singlet and 75% triplet excitons are generated in the OLED due to the random nature of spin orientation when the carriers are injected into the organic materials from the electrodes. Therefore, the internal quantum efficiency (IQE) (photons/electrons) of fluorescent OLED is limited to 25%. In some fluorescent conjugated polymer or small molecules, the formation fraction of singlet excitons is higher than 25%. Triplet excitons can be converted to singlet excitons via reverse intersystem crossing (ISC) or triplet–triplet fusion in some fluorescent materials. In these cases, the IQE higher than 25% can be achieved in fluorescent OLEDs. In general, it is difficult to observe phosphorescence from fluorescent materials because the

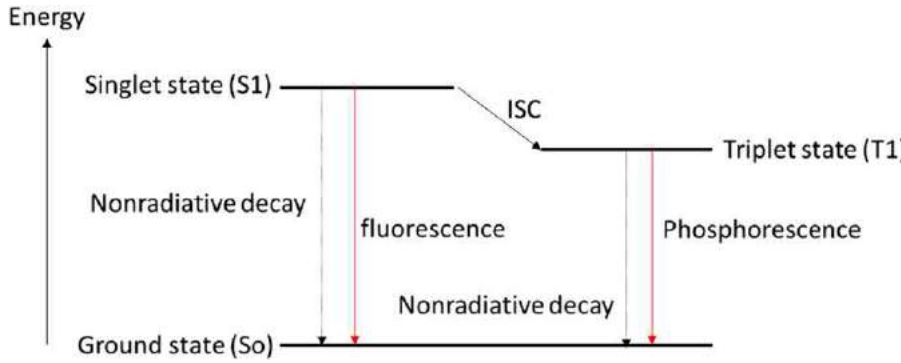


Fig. 7 Energy diagram of singlet and triplet excited states relative to the ground state, fluorescence, phosphorescence, and intersystem crossing (ISC).

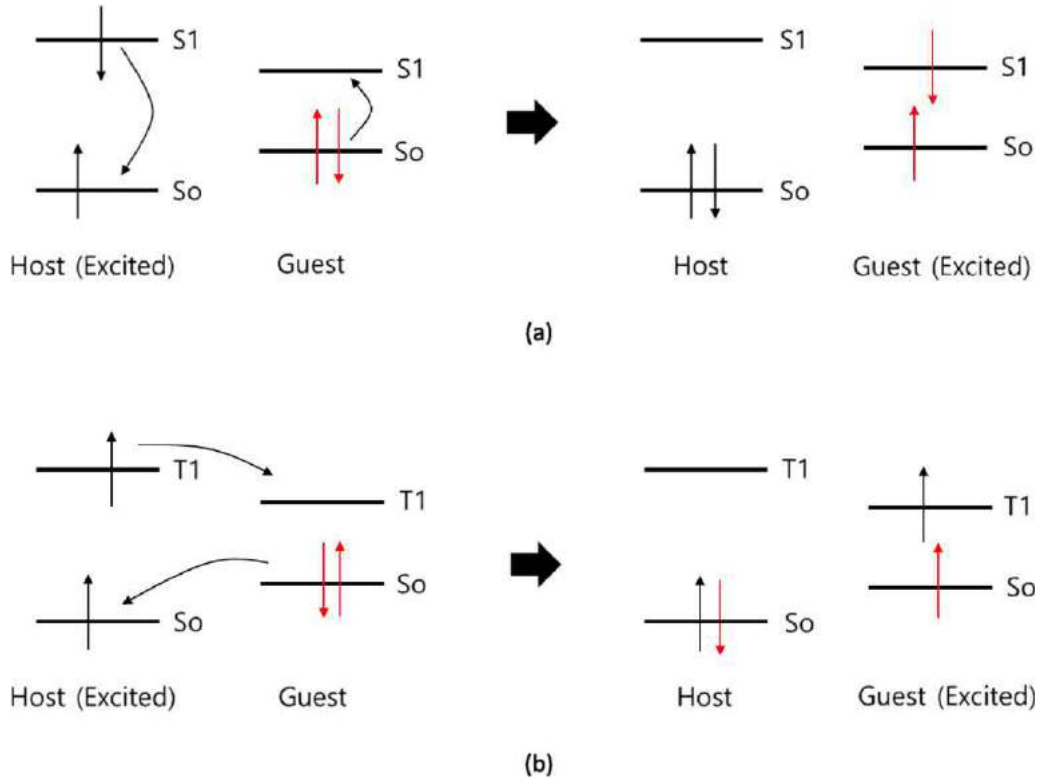


Fig. 8 Energy transfer processes from the host to the guest molecules: (a) Förster energy transfer and (b) dexter energy transfer.

radiative decay rate of triplets is much slower than that of the competing nonradiative decay process. However, phosphorescent molecules containing heavy metals such as iridium or platinum exhibit strong radiative transition from triplet excited states to ground states and fast ISC from singlets to triplet states, leading to 100% IQE device. Significant fraction of light generated by exciton decay is absorbed by surface plasmons and waveguide modes. Only about 20% of the light, i.e., roughly estimated by $0.5n^2$ where n is the refractive index of organic emitter, is coupled out of the device. Thus, the maximum achievable external quantum efficiency (EQE) is limited to 20% in OLEDs. However, high efficiency device with 20–40% EQE can be also obtained by outcoupling efficiency improvement techniques such as microlens array and horizontal dipole orientation.

Host–Guest System

Emission layer is composed of host and guest molecules in OLEDs (Fig. 8), where at least one electroluminescent emissive material is doped into the charge transporting host material. The host–guest system is an effective way to achieve high efficiency in small molecule OLEDs because most of emitters exhibit significant concentration quenching. That is, low photoluminescence

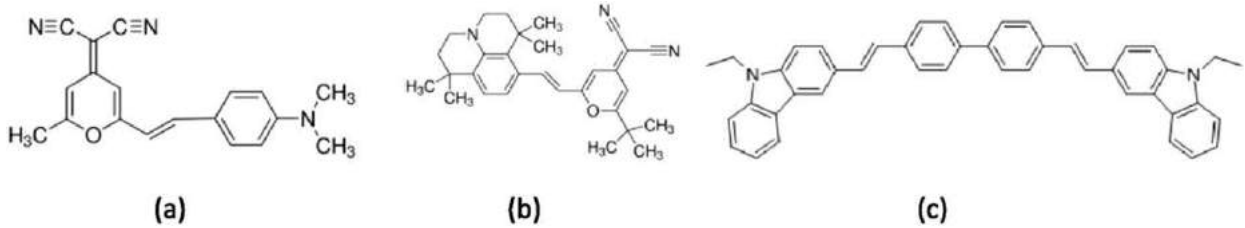


Fig. 9 Organic molecules for the fluorescent guest emitter: (a) 4-(dicyanomethylene)-2-methyl-6-(4-dimethylaminostyryl)-4 *H*-pyran (DCM), (b) 4-(dicyanomethylene)-2-*tert*-butyl-6-(1,1,7,7-tetramethyljulolidin-4-yl-vinyl)-4 *H*-pyran (DCJTB), and (c) 4,4'-*bis*(9-ethyl-3-carbazovinylene)-1,1′-biphenyl (BCzVBi).

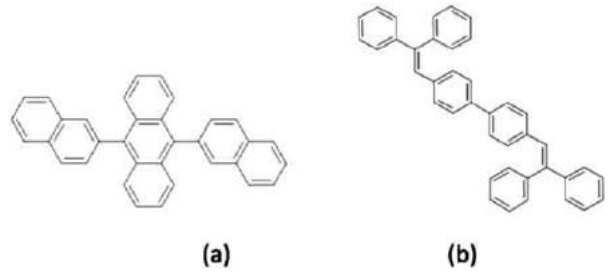


Fig. 10 Host materials for the blue fluorescent guest molecule. (a) 9,10-di(2-naphthyl)anthracene (ADN) and (b) 4,4′-*bis*(2,2-diphenylvinyl)-1,1′-biphenyl (DPVBi).

quantum yield (PLQY) is obtained in solid state even though the PLQY is about unity in gas phase or solution state. In polymer OLEDs, the EML material is often composed of a single polymer comprising multiple monomer units that provide emissive and charge transporting properties. However, the host–guest system is popular in both small molecule and polymer devices. The system also takes advantageous features of easy color tuning and operational stability. The dopant concentration in the host–guest system should be sufficiently low for avoiding nonradiative aggregate traps.

Excitons in the emission layer can be generated on the conductive host molecules. The energy of excited host molecules can be transferred to the guest molecules by Förster or Dexter mechanism. Förster energy transfer is a long range (up to about 10 nm) dipole–dipole coupling of host donor and guest acceptor molecules. This process contributes to the emission process in fluorescent OLEDs because of its singlet–singlet transfer nature. Dexter energy transfer is a short range (typically about 1 nm), intermolecular electron exchange process between donor and neighboring acceptor sites. Dexter transfer involves the triplet–triplet transfer process in phosphorescent OLEDs. Another exciton formation process is a direct recombination of electrons and holes on the guest molecules. It involves trapping of charge carriers and consequent recombination on the guest molecules.

4-(dicyanomethylene)-2-methyl-6-(4-dimethylaminostyryl)-4 *H*-pyran (DCM) and 4-(dicyanomethylene)-2-*tert*-butyl-6-(1,1,7,7-tetramethyljulolidin-4-yl-vinyl)-4 *H*-pyran (DCJTB) are widely used as fluorescent guest molecules as shown in **Fig. 9**. Coumarin and quinacridones are generally used as green fluorescent emitters. Distyrylarylene derivatives such as 4,4'-*bis*(9-ethyl-3-carbazovinylene)-1,1′-biphenyl (BCzVBi) are widely used as efficient fluorescent blue dopants. Alq_3 is the most popular electron-transporting host material for the fluorescent dopants. **Fig. 10** shows the typical blue fluorescent guest molecules. 9,10-di(2-naphthyl)anthracene (ADN) and 4,4′-*bis*(2,2-diphenylvinyl)-1,1′-biphenyl (DPVBi) are thermally stable and good phase-compatible large bandgap host for blue fluorescent guest molecules. Iridium complexes such as $Ir(piq)_3$, $Ir(ppy)_3$, FIrpic are typically doped into the wide energy gap host materials having high triplet energy levels in phosphorescent OLEDs.

Degradation of OLEDs

The luminance decreases with operating time as a result of physical, morphological, chemical degradation in OLEDs. The half-lifetime (T50 or LT50) is defined as the time the luminance drops to 50% of its initial value at the constant current density. Similarly, T70 and T97 refer to the time the luminance drops to 70% and 97% of its initial value, respectively. Typically, the lifetime becomes shorter at higher initial luminance value. The OLED luminance is approximately proportional to current density over a substantial range. Hence, the lifetime decreases in proportion to $1/(\text{current density})^n$, where n is acceleration factor of 1.2–1.9. The continuous drop of luminance under the constant current means the continuous decrease of device efficiency. This luminance degradation can be attributed to many causes such as electrochemical/photochemical reaction, crystallization, and impurities. Another common degradation phenomenon is the formation and growth of small and non-emissive regions which is called dark spots. High purity organic materials, high vacuum processes, and thorough device encapsulations are essential for long lifetime OLEDs.

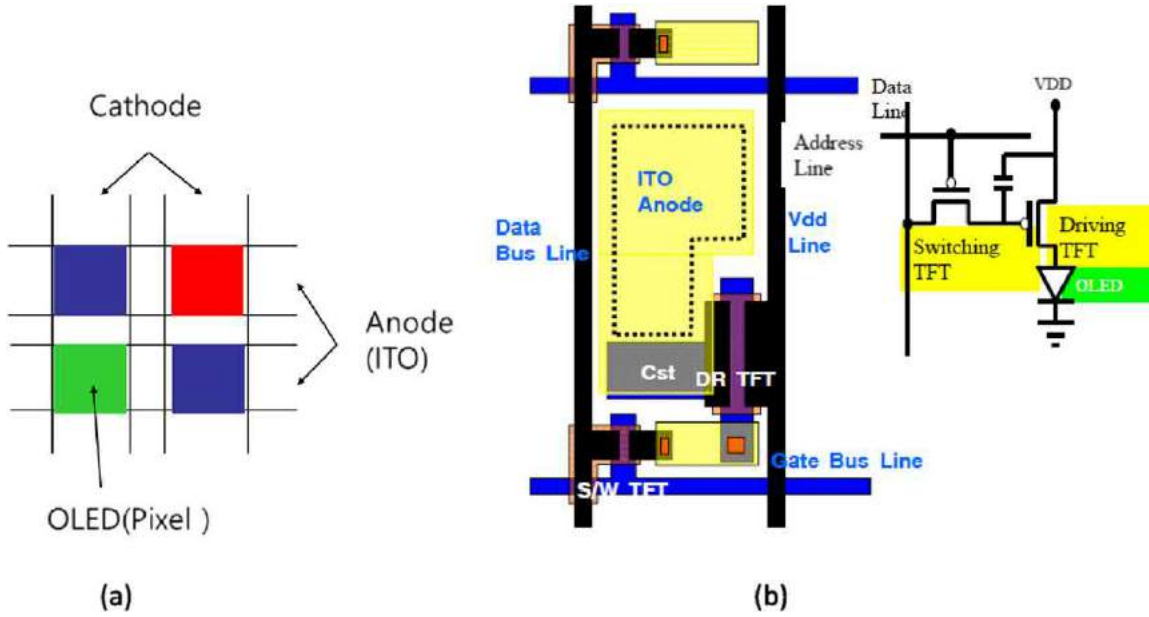


Fig. 11 Schematic pixel structures for organic light-emitting diode (OLED) displays: (a) passive matrix OLED (PMOLED) pixel and (b) active matrix OLED (AMOLED) pixel and equivalent circuit.

OLED Applications

The major applications of OLEDs are displays and lightings. OLEDs can be pixel elements in the passive matrix (PM) and active matrix (AM) displays. Vertically oriented data lines are crossed by the horizontally oriented scan bus lines in passive matrix OLED (PMOLED) displays (Fig. 11). OLED pixels are located at the crossing points. OLED pixels are fabricated by solution printing or evaporation process. PMOLED displays are limited to the low resolution and small size applications. On the other hand, active matrix OLED (AMOLED) displays are widely used for the high resolution, large size applications. AMOLED display contains thin film transistors (TFTs) for providing a constant current to an OLED pixel. Polycrystalline silicon and oxide TFTs are preferred to drive OLED pixels due to their high field effect mobility and current stability. Color pixels are fabricated by the several patterning techniques such as shadow mask process, transfer from donor substrates, and solution printing. Another method of using color filter and white OLED is widely used to fabricate high resolution and large area AMOLED displays. White OLED structure for displays is very similar with that for lightings. White OLED can be realized by various structures such as multi-emission layers, staked device, and down-conversion method. Although the display techniques are mostly applicable in lighting applications, the light sources having a high color rendering index value are preferred for the reasonable color reproduction of the illuminated objects. Therefore, the white OLED for lightings has an emission spectrum of multiple wavelength peaks.

OLEDs also offer new possibilities not accessible in other device technologies. OLEDs can be prepared on various kinds of flexible and stretchable substrates. OLEDs can provide bendable, foldable, stretchable, and rollable displays or lightings. Transparent or mirror-type displays and lightings are also possible with OLEDs. They provide widow information displays, head-mounted displays, digital speed meters, and so on. The OLED technology will open up the numerous new fields of novel applications.

See also: Organic Semiconductors

Further Reading

Baldo, M.A., O'Brien, D.F., You, Y., *et al.*, 1998. Highly efficient phosphorescent emission from organic electroluminescent devices. Nature 395, 151–154.
Burroughes, J.H., Bradley, D.D.C., Brown, A.R., *et al.*, 1990. Light-emitting diodes based on conjugated polymers. Nature 347, 539–541.
Gaspar, D.J., Polikarpov, E., 2015. OLED Fundamentals: Materials, Devices, and Processing of Organic Light-Emitting Diodes. New York, NY: CRC Press.
Li, Z.R., 2015. Organic Light-Emitting Materials and Devices. New York, NY: CRC Press.
Nalwa, H.S., Rohwer, L.S., 2003. Handbook of Luminescence, Display Materials, and Devices: Organic Light-Emitting Diodes. Valencia, CA: ASP.
Scholz, S., Kondakov, D., Lüssem, B., Leo, K., 2015. Degradation mechanisms and reactions in organic light-emitting devices. Chem. Rev. 115, 8449–8503.
Tang, C.W., VanSlyke, S.A., 1987. Organic electroluminescent diodes. Appl. Phys. Lett. 51, 913–915.
Tsujimura, T., 2012. OLED Displays: Fundamentals and Applications. Hoboken, NJ: Wiley.

Harvesting Triplet Excitons in OLED

Gufeng He, Shanghai Jiao Tong University, Shanghai, China

© 2018 Elsevier Ltd. All rights reserved.

Introduction

As early as 1960s, Pope observed an electroluminescence (EL) phenomenon from organic semiconductor, where he used a single crystal of anthracene as EL material. The driving voltage was around 400 V and the luminance was very low. Vincett brought a major step-forward in organic EL in 1982, who applied a vacuum-deposited anthracene film as the emissive layer (EML) and the driving voltages dropped to below 30 V. However, these discoveries had not drawn many attentions until Tang and VanSlyke reported a double layer heterojunction organic light-emitting diode (OLED) in 1987. The device was composed of a vacuum thermal evaporated aromatic diamine layer for hole transporting, and a tris(8-hydroxyquinoline) aluminum (Alq3) layer for electron transporting and emission. This was the first time that an organic electroluminescent device could reach a high brightness (>1000 cd/m^2) with a relatively low operating voltage (<10 V) and an external quantum efficiency (EQE) about 1%, demonstrating its exciting prospect for applications in display and lighting. Since then, OLED has attracted tremendous interests and been developed rapidly. Up to now, small size OLED displays have been widely adopted in high-end smart phones, digital cameras, mp3 players, and so on; large size OLED TVs have also entered the market. With further development of OLED, more and more OLED displays will be around us and energy saving OLED lighting will definitely shine our daily life as well.

As of a novel flat panel display technology, OLED has its remarkable advantages of wide viewing angle, high contrast ratio, fast response, large color gamut, and low power consumption, and considered as the next generation of display competing with liquid crystal display (LCD). Furthermore, because of high efficiency, large area, light and thin factors, flexibility, OLED is also an ideal diffusive light source, showing a great potential in environmental friendly lighting applications.

A simple OLED structure consists of a thin organic electroluminescent film, sandwiched between two electrodes. When an external bias is applied on the device, holes and electrons are injected from the anode and the cathode into the organic semiconductor layer, respectively, then migrate in the organic layer to the opposite side. Subsequently, they meet in the EML and recombine to form excitons. Finally, the excitons radiatively decay to the ground states and emit light. However, to improve the charge carrier injection and transport and to confine excitons within EML to achieve high performance, multilayer structure is commonly adopted in advanced OLED. A typical high efficiency OLED consists of five organic layers (**Fig. 1**): hole injection layer (HIL), hole transport layer (HTL), EML, electron transport layer (ETL) and electron injection layer (EIL), where the HTL is often used as electron blocking layer (EBL), while ETL is used as hole blocking layer (HBL).

The OLED development focuses mainly on the materials and structures. Soon after Tang's first OLED report on small molecules, in 1990, Richard Friend *et al.* successfully discovered an OLED using solvable spin-coated polymer as EML, which is usually called as polymer light-emitting diode (PLED). In their publication, a single layer of poly(p-phenylenevinylene) (PPV), sandwiched between indium tin oxide (ITO) and Al electrodes, emitted green light under applied voltages. The relatively high efficiency and low turn-on voltage promised for a large-area, low-cost solution processable commercial application. However, all these small molecule and polymer materials are fluorescent, whose emission is from singlet excited state. The electrons in organic materials are

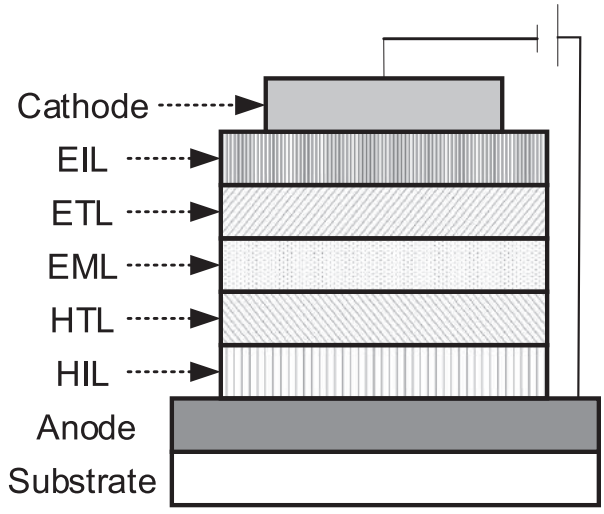


Fig. 1 Typical multilayer organic light-emitting diode (OLED) structure. EIL, electron injection layer; EML, emissive layer; ETL, electron transport layer; HIL, hole injection layer; HTL, hole transport layer.

 doi:10.1016/B978-0-12-803581-8.09540-0

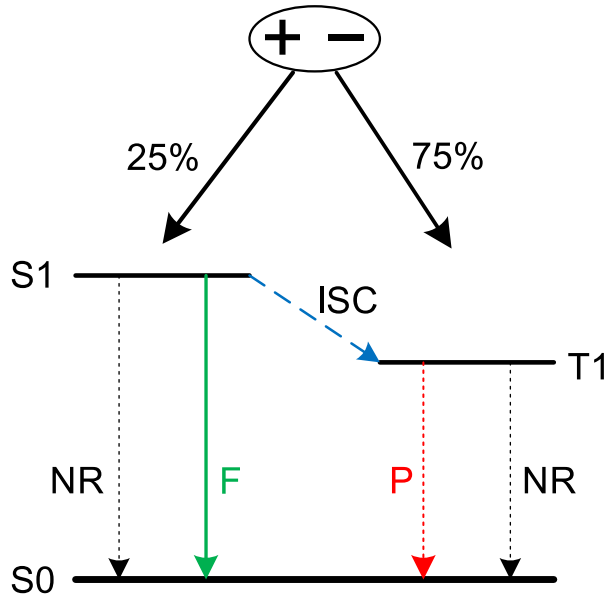


Fig. 2 Fluorescence (F) process. ISC, intersystem crossing.

mostly paired up with opposite electron spin orientations because of the Pauli Exclusion Principle. When receiving enough energy such as from light, one of the paired electrons can be excited from ground state to excited states. These two electrons have either the antisymmetric or symmetric spin orientation. Each electron spin is denoted as "s", which equals to either $+1/2$ or $-1/2$. The spin multiplicity (total spin number, S), calculated by $S=2\sum s+1$, is either 1 for singlet if the pair of electrons are spin-antisymmetric or 3 for triplet if the pair of electrons are spin-symmetric. If an organic material is excited from the ground state, the excited state usually remains as singlet due to the Wigner–Witmer selection rule in quantum mechanics for the electronic transition process. Similarly, the transition from the triplet excited state (T1) to ground state (S0) is prohibited, i.e., the phosphorescence is not observable at room temperature for normal organic electroluminescent materials. In the OLED, the excitons are generated by injected holes and electrons from the anode and the cathode, respectively, which have their own spin orientations. Therefore, the electrically generated excitons can be either singlets or triplets. According to the statistic calculation of quantum mechanics, there will be 3 triplet excitons for every singlet exciton formed. Since radiative decay from triplet excited state to singlet ground state is spin-forbidden, only a quarter of electrically generated excitons, singlets, contribute to the light emission, which limits the internal quantum efficiency of OLED at 25%, as shown in Fig. 2.

To achieve a real high efficiency, it is necessary to harvest these non-radiative (NR) triplet excitons. One strategy is to make the radiative decay possible from triplet state T1 to ground state S0 by incorporating heavy metals in the molecules to increase spin-orbit coupling, which are called phosphorescent materials. Another strategy is to make the reverse intersystem crossing (RISC) process possible by narrowing the gap between the singlet and triplet excited states. By using these two methods, all electrically generated singlets and triplets can contribute to the light emission, and the internal quantum efficiency can be up to 100% theoretically, which is four times as high as conventional fluorescence.

In 1998, Thompson and Forrest groups boosted OLED internal quantum efficiency limit from 25 to 100% by using phosphorescent electroluminescent materials. Heavy metal atoms were widely used in phosphorescent materials to mix the triplet and the singlet excited states to make the radiative decay possible from triplet state to ground state. Recently, Addachi group from Kyushu University realized 100% internal quantum efficiency via thermally activated delayed fluorescence (TADF), without using heavy metal chelate. It is another breakthrough in the development of organic electroluminescent materials. If we call fluorescent materials as the first generation, high efficiency phosphorescent materials as the second generation, then TADF materials are considered as the third generation.

Phosphorescent EL

Although the OLED had been extensively studied since the first practical OLED was invented by Kodak, a breakthrough of its development is the discovery of electro-phosphorescence by Forrest *et al.* Compared with fluorescent OLED using only singlet excitons for light emission, phosphorescent OLED can utilize both singlet and triplet excitons, which boosts the internal quantum efficiency (IQE) of OLED by a factor of 4 theoretically. Hence, phosphorescence has attracted tremendous research interests in both academia and industry for its significant performance potential. In fact, highly efficient and long living red and green phosphorescent electroluminescent materials have already been employed in commercial OLED displays. Compared with the great achievements in red and green phosphorescent materials, although the EQE of blue phosphorescent OLED has already exceeded 20%, lacking of deep color and poor lifetime still restrain its commercialization.

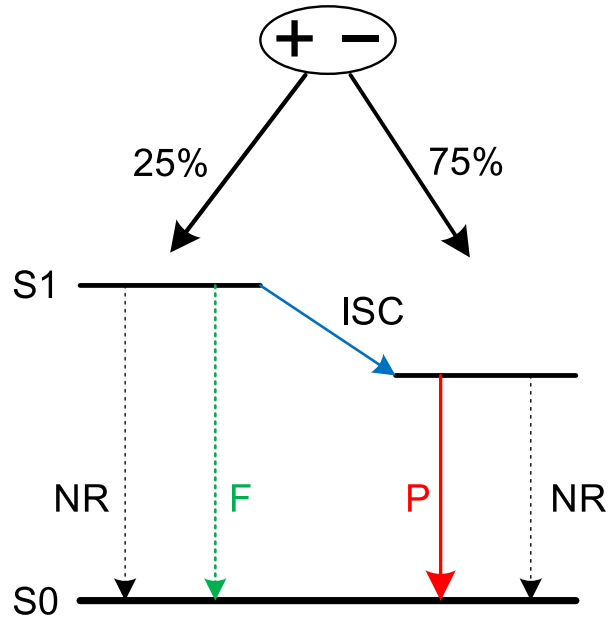


Fig. 3 Phosphorescence (P) process. ISC, intersystem crossing.

The typical lifetime of triplet excited state of organic material is usually longer than millisecond (ms), which is long enough for releasing its energy via NR decay channels such as the thermal vibration motion. There is one way to enable phosphorescence from organic materials is to suppress the thermal vibration motion by lowering temperatures down to liquid nitrogen temperature (77K). However, it is surely not practical for OLEDs, which usually operate at room temperature. A practical and effective way is to reduce the lifetime of triplet excited state so that the transition process from T1 to S0 can compete with the NR thermal vibration motion.

To enhance the phosphorescence, the most effective way is to use heavy metal atom in organic molecule, which enhances spin-orbit coupling, the interaction between spin magnetic moment and orbital magnetic moment. The strength of such coupling is proportional to the proton number in atomic nucleus, which is in turn related to the electromagnetic field generated by atomic electrons circling around. This is called as "heavy atom effect". The distinguish between triplet and singlet state becomes diminished when spin-orbit coupling constant is large. The selection rule is losing its restriction and radiative decay from the triplet excited state to singlet ground state becomes feasible, and the triplet state lifetime is shortening, faster than molecular thermal vibration motion (Fig. 3). Up to now, the heavy atoms used in phosphorescent materials are all transition metals, such as Ru, Re, Os, Ir, Pt, Au, and Hg. Among them, most phosphorescent materials focus on those group VIII B elements, Os, Ir, and Pt. Especially, Ir-containing phosphorescent materials attract the most attentions.

The presence of a heavy metal atom in complexes increases singlet–triplet mixing and adds excited states to the electronic spectrum. In addition to states localized on the organic groups (ligands), the metal atom can participate in an excited state formed by the transfer of an electron from the metal to a ligand, known as metal–ligand charge transfer (MLCT) state. The MLCT state has a larger overlap with the heavy metal atom than the ligand excited states. Therefore, the spin-orbit coupling is higher, and the mixing between singlets and triplets is greater. Consequently, the radiative decay from the MLCT triplet state to ground state is more feasible. The phosphorescence often occurs from both MLCT and ligand excited states, and the relative importance of the MLCT and ligand components depends on their relative energies. If the ligand has a significantly lower triplet energy, the MLCT component will be very small, and the phosphorescence is mainly from the ligand triplet state. In this case, the triplet experiences less spin-orbit coupling induced by the central heavy metal atom, and consequently, its lifetime may not be reduced greatly. Triplet–triplet annihilation (TTA) is more pronounced with long triplet lifetime, and the OLEDs based on such materials may experience poor efficiency at large current densities due to strong efficiency roll-off. Thus, a high efficiency phosphorescent material should preferably have a triplet lifetime of less than $\sim$10 μs, by enhancing the singlet–triplet mixing, which can be realized by ensuring that the energy of ^{3}MLCT triplet state is lower than that of ligand triplet state.

The first phosphorescent material employed in OLED was a red phosphorescent dye based on heavy metal Pt, called 2,3,7,8,12,13,17,18-octaethyl-21 H,23 H-porphine platinum(II) (PtOEP) (Fig. 4). The external quantum efficiency (EQE) reaches a maximum value of 4% with saturated red emission of (0.7, 0.3), which was not extremely high, relative to high efficiency fluorescent red emitter. However, PtOEP still attracted enough attention due to its phosphorescence nature. Firstly, PtOEP has an absorption peak at around 540 nm, and its fluorescence emission peak is at longer wavelength around 580 nm. In contrast, the observed EL peak is at 650 nm with a very nice narrow red emission band, which is much longer than the fluorescence emission of PtOEP. Furthermore, the lifetime of the emission at $\sim$650 nm in solution was measured about $\sim$50 μs, which is significantly longer than typical fluorescence lifetime of 0.1$\sim$10 ns. All these spectroscopic data infer that the EL emission at 650 nm is

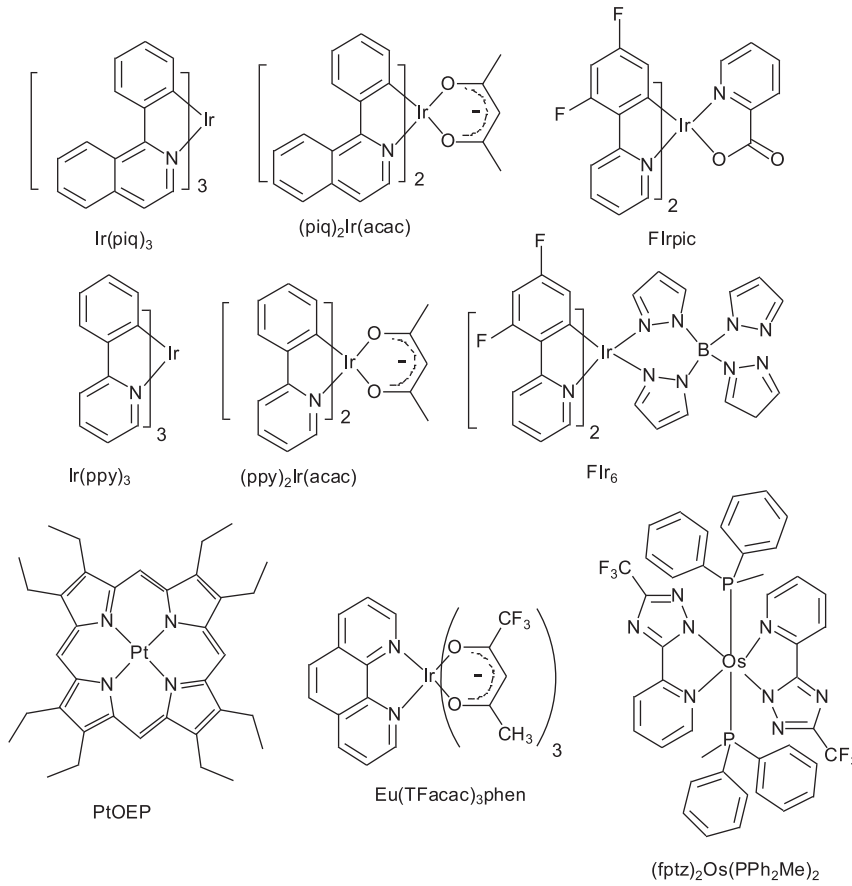


Fig. 4 Chemical structures of several typical phosphorescent materials.

phosphorescence rather than fluorescence. However, the PtOEP phosphorescent OLED shows serious efficiency roll-off, a typical EL behavior for phosphorescent OLEDs at elevated current density, which is mainly ascribed to their relatively long triplet lifetime. Furthermore, the flat square planar structure of Pt complexes often causes molecular π–π stacking that quenches the emission readily, leading to poor efficiencies in the devices.

Iridium is another mostly investigated heavy metal atom in phosphorescent materials. The $5d^6$ orbitals of Ir^{3+} provide a flexible platform for ^{3}MLCT phosphorescence. These complexes possess a chemically stable octahedral symmetry, with three bidentate ligands complexed to the central Ir atom. $Ir(piq)_3$ (tris(1-phenylisoquinoline)iridium(III)) and $(piq)_2Ir(acac)$ (bis(1-phenylisoquinoline) (acetylacetonate)iridium(III)) are two typical red phosphorescent emitters based on Iridium (Fig. 4). The common feature of these two Ir complexes is the cyclometalate ligand 1-phenylisoquinoline (piq). In fact, cyclometalate ligand piq is very powerful for red phosphorescence. Most of the red phosphorescent materials developed later are based on derivatives of piq ligand.

If the ligands are changed to ones with higher triplet energies, the phosphorescence emission can be shifted to the shorter wavelength. For example, the ligand 2-phehylpyridine (ppy) is the parent structure for many other cyclometalation ligand of green phosphorescent materials, such as $Ir(ppy)_3$ (tris(2-phenylpyridine)iridium(III)) and $(ppy)_2Ir(acac)$ (Bis[2-(2-pyridinyl-N)phenyl-C](acetylacetonato)iridium(III)) (Fig. 4). The ancillary ligand acac has a weaker ligand-field strength than ppy, leading to smaller d-orbitals splitting, which results in smaller energy of MLCT. Therefore, the emission peak wavelength of $(ppy)_2Ir(acac)$ is longer than that of $Ir(ppy)_3$ (525 vs. 514 nm). The photophysical properties of $Ir(ppy)_3$ and $(ppy)_2Ir(acac)$ are quite similar, although $Ir(ppy)_3$ is homoleptic and $(ppy)_2Ir(acac)$ is heteroleptic. The phosphorescence quantum yield of $Ir(ppy)_3$ is 0.40 and that of $(ppy)_2Ir(acac)$ is 0.34. The triplet lifetime of $Ir(ppy)_3$ is 1.9 μs and that of $(ppy)_2Ir(acac)$ is 1.6 μs. The color coordinates of $Ir(ppy)_3$ are (0.27, 0.63), whereas those of $(ppy)_2Ir(acac)$ are (0.31, 0.64). Such differences are not large, but very similar trend have been observed for other homoleptic and heteroleptic coordination complexes as well. In terms of molecular dipole moment, facial homoleptic coordination complexes are smaller than heteroleptic coordination complexes, which in turn are smaller than meridional homoleptic coordination complexes. And it is indicated by the experimental data that the molecular dipole will quench phosphorescence of the material.

Alternatively, if the ligand is made strongly electron accepting, then ^{3}MLCT emission may be blue shifted. The most famous blue phosphorescent materials are heteroleptic bis[2-(4,6-difluorophenyl)pyridinato-C2,N](picolinato)iridium(III) (FIrpic) and bis (2,4-difluorophenylpyridinato)-tetrakis(1-pyrazolyl)borate iridium(III) (FIr6) using fluoro-substituted phenylpyridine ligands

and an anionic 2-picolinic acid or poly(pyrazolyl)borate as an auxiliary ligand, respectively (Fig. 4). However, these emissions are either greenish-blue (0.17, 0.34) or sky-blue (0.16, 0.26), far from a saturated blue color as the National Television Standards Committee (NTSC) standard of (0.14, 0.08).

As the first blue phosphorescent material, FIrpic has two emission peaks at 470, 494 nm with phosphorescence quantum yield of 50–60%. The strong vibration peak at longer wavelength of main emission peak makes the color actually cyan containing a lot of green emission. With improved blue color, FIr6 has a shorter emission wavelength (λ_{max} at 457, 485 nm) and a higher phosphorescence quantum yield (96%) than those of FIrpic, but its device stability was poorer. Since the emission is mainly from the $\pi\pi^*$ state of cyclometalated ligands mixing with d-orbital of heavy transition metal via MLCT, such emission state due to the mixing of d-orbital is often inadequate, particularly for the short wavelength blue phosphorescence. Consequently, such phosphorescence usually has a longer triplet lifetime, closer to pure organic species (organic compound without containing heavy atom). Triplet state lifetime of microsecond range is required for fast emissive decay process and high phosphorescence quantum yield is desirable to achieve theoretical maximum EQE over 20%. It has been known that Ir-based organometallic compounds show short excited state lifetime due to singlet–triplet mixing and easy control of emission spectra by managing the chemical structure of ligands.

FIrpic has two fluorines on the phenyl unit to shift the highest occupied molecular orbital (HOMO) level downward for high triplet energy. The triplet energy is increased by the electron withdrawing fluorine and a bulky picolinic acid ancillary ligand. Although the emission spectrum of FIrpic is blue-shifted, it exhibits only sky blue color with y-coordinate over 0.30. The spectrum is further blue-shifted by changing the ancillary ligand from picolinate (pic) to bulky tetrakis(1-pyrazolyl)borate ligand in FIr6. The FIr6 has bulky tetrakis(1-pyrazolyl)borate ligand to reduce the conjugation of the main ligand through steric hindrance. The peak wavelength of the FIr6 is shifted to 458 nm compared with 470 nm of FIrpic.

Besides platinum and iridium, europium (Eu) is also employed as the central metal to develop phosphorescent emitters. For example, Zheng *et al.* obtains Eu(TFacac)$_3$phen using 1,1,1-trifluoroacetylacetone as ligand, and Male *et al.* demonstrates Eu(TTFA)$_3$phen using tris-(thiophenyltrifluoromethylacetylacetonate)(phenanthroline) as the ligand. The EL emission from Eu complexes is extremely sharp since the emission is from the f–f transition of Eu atom.

Os is another heavy metal atom often used in phosphorescent materials, and the emission color can be tuned by changing the ligand. Jiang *et al.* have designed a series of Os complexes. The phosphorescence lifetime is 0.6–1.9 μs, and the EL emission peak is from 620 to 650 nm, with color coordinates around (0.65, 0.33). For example, when (fptz)$_2$Os(PPh$_2$Me)$_2$ was doped into tris[4,9-phenylfluoren-9-ylphenyl]amine (TFTPA), the device exhibits red EL having EQE as high as 18% (power efficiency ~25 lm/W). It is quite remarkable that the device has minor efficiency roll-off, which is mainly attributed to the short phosphorescence lifetime of ~0.7 μs. On the other hand, symmetrical structure induces small net dipole moment and reduce dipole–dipole interaction and quench emission.

As of relatively long phosphorescence lifetime, the phosphorescent emitter materials usually need to be doped into suitable host materials to avoid severe TTA. Besides some common rules to be followed, such as excellent film-forming property, good thermal and electrochemical stability, high glass transition temperature (*T*g), there are still some special criteria to meet for host materials of phosphorescent emitters. Firstly, the host material should possess appropriate the HOMO and the lowest unoccupied molecular orbital (LUMO) levels to ensure effective hole and electron injection; secondly, the host material should have higher triplet energy than the phosphorescent emitter to prevent reverse energy transfer; Finally, the host material should possess high hole or electron transport property to reduce the operating voltages. Recently, bipolar host materials, capable of transporting both holes and electrons, have drawn more attentions. It is confirmed that employing bipolar host materials can not only reduce the operating voltages but also improve the device stabilities.

Advanced Delayed Fluorescence

After nearly 20 years development, all red, green and blue phosphorescent OLEDs have achieved extremely high EQE over 30%. However, these phosphorescent emissive materials contain heavy metals such as iridium and platinum, which are rather expensive and resource limited. To overcome this issue, a lot of studies focus on delayed fluorescent materials, which do not use heavy metals and can convert triplet excitons to singlet excitons through RISC. There are mainly two methods to achieve efficient RISC: TTA and TADF. More and more ultra-high efficiencies of fluorescent OLEDs exceeding 10%, far beyond the theoretical limitation of fluorescent emitters, have been reported recently, attracting wide research interests in both academic institutions and industry (Figs. 5 and 6).

In 2009, Kodak demonstrated some high EQE OLED devices using a fluorescent material 4,4′-bis[4-(di-p-tolylamino)styryl] biphenyl doped in 9,10-bis(2-naphthyl)-2-phenylanthracene (PADN) as EML, which are attributed to TTA contribution. Based on the assumption that spin statistics dictate 20% probability of generating a singlet exciton through TTA, they proposed a formula to estimate the maximum EQE of such system: $0.2 \times (25\% + 0.2 \times 75\%) = 8\%$. Soon later they obtained an EQE of >11% at 3 V using rubrene as emitter. This value is far beyond the theoretical limit of the fluorescent emitter imposed by spin statistics, and cannot be satisfactorily explained by previous equation. They surmise that the fluorescent OLED devices are capable of using a considerably larger fraction of triplet states than it was previously believed. With the appropriate emissive material and host material, every two triplet excitons can form one singlet exciton to contribute to the light emission, i.e., the upper limit for the singlet excited state yield in the TTA process is 0.5. Therefore the maximum internal quantum efficiency of fluorescent OLEDs is to be $25\% + 0.5 \times 75\% = 62.5\%$. The estimated maximum EQE of the fluorescent OLEDs should be revised to at least $0.2 \times 62.5\% = 12.5\%$ after considering a light out-coupling efficiency of ~20% in the device. However, in order to promote the nonlinear up-conversion TTA process, high driving voltages or concentrated sensitizers are generally essential, accompanied by proportionally increased device efficiency roll-off.

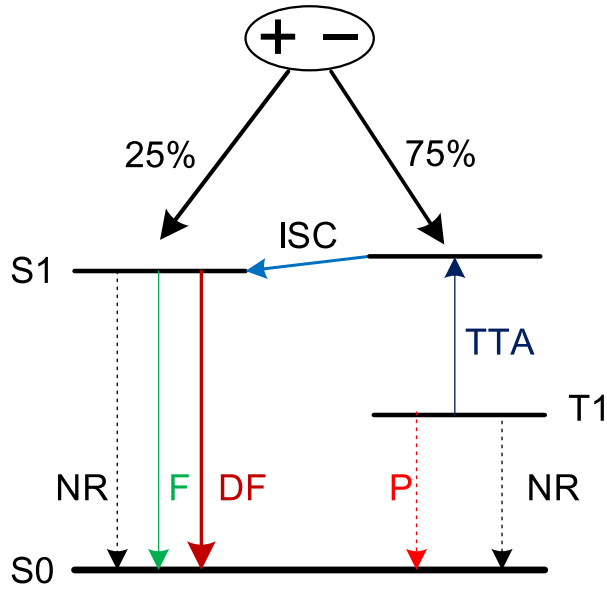


Fig. 5 Triplet–triplet annihilation (TTA) process. ISC, intersystem crossing.

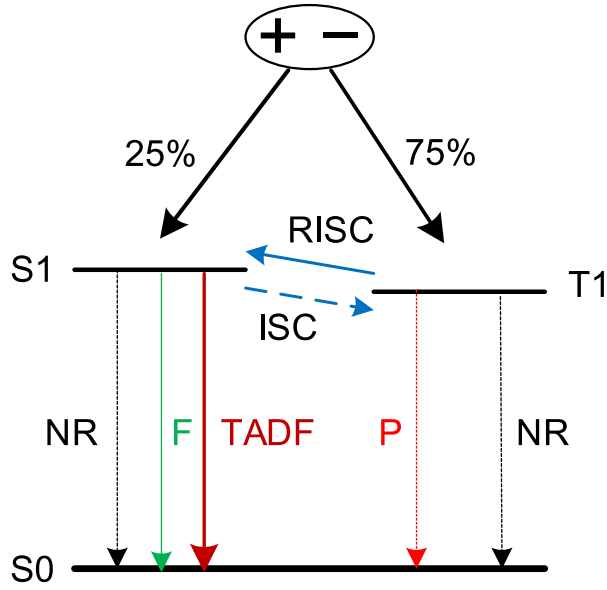


Fig. 6 Thermally activated delayed fluorescence (TADF) process. ISC, intersystem crossing; RISC, reverse intersystem crossing.

A more efficient way to harvest triplet excitons is via the direct RISC process from T1 to S1. According to Hund's rule, the energy of T1 is always lower than S1, therefore such RISC process must be stimulated or activated by external energy. If the energy difference between T1 and S1 (ΔE_{ST}) is small enough, the thermal activation of the molecules can overcome the barrier and commit the endothermic RISC process. The triplet excitons at T1 are back-transferred to S1, followed by radiative decay to the ground state S0, called TADF. There are two distinct unimolecular mechanisms involved in TADF: the prompt fluorescence (PF) from the direct electrical excited singlet S1, and the delayed fluorescence (DF) from the back-transferred singlet S1. Apparently, PF and DF have different luminescent lifetimes, which can be distinguished from the transient photoluminescence spectroscopy. And their individual fluorescence efficiency can also be calculated by integrating the intensity of each component.

In these processes, the efficient RISC from T1 to S1 is the key to harvest triplet excitons to enhance the DF. However, when the RISC process is enhanced by reducing the singlet–triplet energy splitting ΔE_{ST}, the intersystem crossing (ISC) process from S1 to T1 is also enhanced. Moreover, the RISC rate ($\sim 10^6\ s^{-1}$) is lower than the ISC rate in TADF molecules generally. In the end, there is a balance of exciton distribution between S1 and T1 states in TADF molecules. Consequently, ΔE_{ST}, rate constant of ISC and RISC are the key parameters to design efficient TADF materials.

In traditional fluorescent and phosphorescent materials, S1 energy is considerably higher than T1, and RISC hardly occurs. To facilitate RISC, a small ΔE_{ST} is particularly important. At S1 or T1 state, the unpaired two electrons are mainly distributed on the frontier orbitals of the HOMO and the LUMO, respectively. To obtain small ΔE_{ST} in the molecules, a spatial wave function separation of HOMO and LUMO need to be adopted. The general strategy is to introduce a large steric hindrance structure or a donor–acceptor system with twist/spiro/bulky connection, which can reduce the overlap between the HOMO and LUMO.

RISC process is an endothermic transition, hence it is temperature sensitive, and high temperature facilitates it. At low temperature (<100K), the fluorescence efficiency of TADF molecules are significantly suppressed and is strongly dependent on photoexcitation intensity, which are considered as characteristic features of TADF emitters.

At the early stage, such TADF materials always exhibit low fluorescence efficiencies, making it really difficult to verify the effectiveness for EML in OLED. It was not until 2009 that Adachi group at Kyushu University first introduced a series of Sn(IV) fluoride-porphyrin complexes with small ΔE_{ST} around 0.4 eV. It is demonstrated that the photoluminescence efficiency of such TADF material can be increased from $\sim$1 to 3% with an increase in temperature due to RISC. However, the activation energy of the RISC (ΔE_{ST}) was still rather high at 0.24 eV, leading to inefficient RISC, and the overall EL efficiency is still very low.

Donor–acceptor systems with pronounced intramolecular charge transfer (CT) characteristics are very suitable to realize small ΔE_{ST} through separated HOMO in donor groups and LUMO in acceptor groups for TADF emission. A steric hindrance, such as twist, bulky, or spirojunction, incorporated between the donor and acceptor groups can further effectively separates the spatial overlaps between HOMO and LUMO. For example, a typical molecule 2-biphenyl-4,6-bis(1,2-phenylindolo[2,3-a] carbazol-11-yl)-1,3,5-triazine (PIC-TRZ) has ΔE_{ST} of only 0.11 eV, which realizes a significant contribution of 30% RISC efficiency under both photoluminescence and EL processes.

Another strategy proposed again by Adachi group to realize high RISC efficiency is via exciplex of electron-donating and electron-accepting molecules, also called as intermolecular donor–acceptor system. The electron transition from the LUMO of an acceptor to the HOMO of a donor is in a large electron–hole separation distance for exciplex emission. It is possible that the hole and electron wavefunctions are spatially separated and electronic exchange energy is very small compared to that of intramolecular excited states, resulting in the triplet levels being very close to the singlet levels, i.e., a small ΔE_{ST} for efficient TADF emission via RISC. However, the limited overlap of hole and electron wavefunctions generally results in very low fluorescence efficiency of exciplex according to the Franck–Condon principle. For strong TADF emission in the exciplex, the donor and acceptor molecules should have high triplet energy levels to confine the triplet exciplex state to prevent the quenching of the triplet state via the triplet energy back transfer to the donor or acceptor. Furthermore, such intramolecular donor-acceptor system should have not only high RISC efficiency but also high fluorescence efficiency. For example, an exciplex system of 4,4′,4″-tris[3-methylphenyl(phenyl) amino]triphenylamine (m-MTDATA) as a donor and tris-[3-(3-pyridyl)mesityl]borane (3TPYMB) as acceptor has a high RISC efficiency of 86.5%. Using this emission system, the OLED achieves a maximum EQE of 5.4%, even with the rather low photoluminescence efficiency of 26%, showing a significant contribution of efficient RISC.

Within just several years' development, the EQE of TADF OLED is already over 21%, and further increased to 30% in a suitable cohost system. The device stability is significantly improved as well, with lifetimes of 2800 h at an initial luminance of 1000 cd/m^2, and of over 10,000 h at 500 cd/m^2. To take advantage of the triplet harvesting property, TADF molecules can act as host materials or singlet exciton sensitizers to harvest triplet excitons in OLEDs for fluorescent emitters. The devices show a significantly increased EQE and an enhanced device operational stability.

Although TADF materials have the potential to harvest $\sim$100% excitons, the mechanism of TADF still requires further clarification. The efficiency roll-off is quite serious for most TADF emitter based OLED, which could be attributed to pronounced triplet–triplet or singlet–triplet quenching because of slow RISC process. It is necessary to further improve the performance of TADF materials to meet the requirements of real application. Novel device configurations should be developed according to the molecular features of TADF materials, which will promote the overall device performances for advanced optoelectronic applications.

See also: Organic Semiconductors

Further Reading

Baldo, M.A., O'Brien, D.F., You, Y., *et al.*, 1998. Highly efficient phosphorescent emission from organic electroluminescent devices. Nature 395 (6698), 151–154.
Chiang, C.J., Kimyonok, A., Etherington, M.K., 2012. Ultrahigh efficiency fluorescent single and bi-layer organic light emitting diodes: The key role of triplet fusion. Advanced Functional Materials 23, 739–746.
Huang, S.H., Zhang, Q.S., Shiota, Y., 2013. Computational prediction for singlet- and triplet-transition energies of charge-transfer compounds. Journal of Chemical Theory and Computation 9, 3872–3877.
Li, Y.F., 2015. Organic Optoelectronic Materials. Switzerland: Springer.
Li, Z.G., Meng, H., 2007. Organic Light-Emitting Materials and Devices. London: Taylor & Francis.
Tao, Y.T., Yang, C.L., Qin, J.G., 2011. Organic host materials for phosphorescent organic light-emitting diodes. Chemical Society Reviews 40, 2943–2970.
Tao, Y., Yuan, K., Chen, T., *et al.*, 2014. Thermally activated delayed fluorescence materials towards the breakthrough of organoelectronics. Advanced Materials 26, 7931–7958.
Uoyama, H., Goushi, K., Shizu, K., *et al.*, 2012. Highly efficient organic light-emitting diodes from delayed fluorescence. Nature 492 (7428), 234–238.
Xiao, L.X., Chen, Z.J., Qu, B., *et al.*, 2011. Recent progresses on materials for electrophosphorescent organic light-emitting devices. Advanced Materials 23, 926–952.
Yook, K.S., Lee, J.Y., 2012. Organic materials for deep blue phosphorescent organic light-emitting diodes. Advanced Materials 24, 3169–3190.

Organic Light-Emitting Diodes/Light Extraction

Jiun-Haw Lee, National Taiwan University, Taipei City, Taiwan

© 2018 Elsevier Ltd. All rights reserved.

Introduction

Organic light-emitting diode (OLED) consists of organic thin-film stacks with different functions, sandwiched by two electrodes. When the electrical voltage applied to the OLED, electrons and holes are injected from cathode and anode, respectively, into the organic layers. Usually, there are several layers such as hole-injection layer (HIL) and hole-transporting layer (HTL) to carry holes, as well as electron-injection layer (EIL) and electron-transporting layer (ETL) to carry electrons. Electrons and holes recombine in the emitting layer (EML) and form excitons. Excitons relax the energy radiatively to generate photons. There are several optical losses when the light propagates from the OLED to the air.

Due to the difference of refractive index (n) between the organic material (typically $n \sim 1.6$–2.0) and the air ($n = 1$), part of photons emitted from the EML are trapped due to total internal reflection (TIR). Typically, the OLED was fabricated on the glass substrate ($n = 1.5$). And a transparent anode (indium tin oxide (ITO), $n = 1.8$–2.0) and a reflective cathode (Al) are used. Optical wave tends to propagate at the medium with higher refractive index. Hence, part of light is trapped inside the ITO/organic layers, which is called "waveguiding mode." And the light inside the glass substrate is called "substrate mode," to separate the TIR effects at different interfaces.

Note that the carrier mobility of the organic materials for the OLED application are pretty low (typically $< 10^{-2}$ cm^2/Vs), and hence total film thickness of the thin-film stacks in an OLED is typically less than 300 nm, which is needed to operate such a device with a reasonable driving voltage (< 10 V). Such a thickness is comparable to the visible wavelength which results in an interference effect. Typically, we can consider the OLED structure (from anode to cathode) as a "microcavity." For the case with ITO anode, reflection mainly comes from the reflective cathode (such as Al) and it is called "weak cavity." On the other hand, a semitransparent anode (such as thin metal) can be employed to replace ITO, which is formed a "strong cavity" with reflective metal cathode. By suitable tuning of the organic layer thicknesses, optical interference effect can be optimized for achieving higher extraction efficiency.

Due to the thin organic layers, the emission dipole is physically close (typically < 100 nm) to the metal electrode, which results in plasmonic loss. That is, the emission dipole excites the surface plasmon polariton (SPP), which relaxes the energy non-radiatively. A minor, but nonnegligible loss is the material coming from the organic materials and the electrodes. Fig. 1 shows the external quantum efficiency (EQE) versus the ETL thickness. The oscillatory behavior of the outcoupled mode results from the microcavity effect with ETL thickness modulation, and the substrate mode shows similar trend. Surface plasmon mode decreases with increasing the ETL thickness, because the distance between emission dipole and metal cathode increases. However, on the other hand, the substrate mode increases with thicker ETL because it supports more optical modes.

In the following, we will introduce various schemes for improving the light extraction in an OLED, starting from the enhancement of substrate mode. By applying some structures to destroy the TIR at the (glass) substrate and the air, extraction efficiency can be significantly improved. Note that OLED can be used for lighting and display applications. Image quality is an important parameter for a display, which may decrease due to these structures, and careful design should be made. Besides, enhancement ratio of the outside (substrate) mode cannot fully decoupled with the internal (waveguiding and plasmonic) modes,

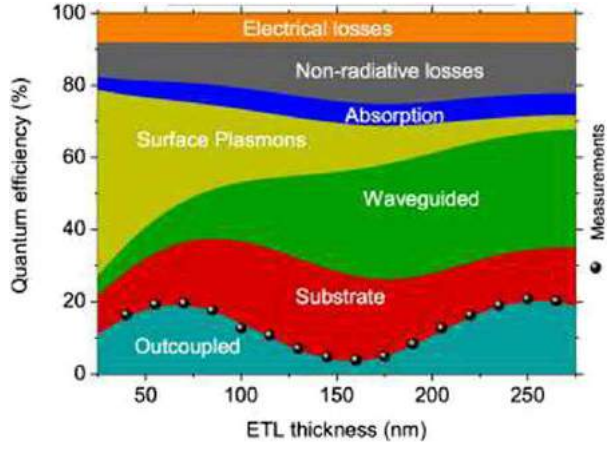


Fig. 1 Electron-transporting layer (ETL) thickness vs. distribution of different modes (outcoupled, substrate, waveguided, surface plasmons…) in an organic light-emitting diode (OLED). Black dots shows the measurement results. Maximum external quantum efficiency (EQE) (outcoupled mode) is 21% with ETL = 250 nm. Reproduced from Meerheim, R., Furno, M., Hofmann, S., Lüssem, B., Leo, K., 2010. Quantification of energy loss mechanisms in organic light-emitting diodes. Applied Physics Letters 97, 253305. Copyright (2010) with permission from American Institute of Physics.

which needs to be considered simultaneously. And we will move to the discussions of the internal modes. Again, at the ITO/organic and (glass) substrate interfaces, we can do some modulations of refractive index and structures for reducing the TIR. To reduce the plasmonic loss, a straightforward method is to keep the emission dipole away from the metal surface. And an alternative is to introduce nanostructure to couple the SPP back to the air mode.

Light Extraction of the Substrate Mode

To extract the light rays in the planar glass substrate, a straightforward method is to use a hemisphere lens structure, which has been used in semiconductor light-emitting diodes (LEDs).

Note there is a basic difference between semiconductor LED and OLED. LED was cut into a small piece, called "LED die" with the dimension ~ 1 mm $\times$ 1 mm for the following lens-like encapsulation process. On the other hand, a unique advantage for the OLED is the large-sized fabrication with the flat emission feature. For an OLED lighting panel (such as 10 cm $\times$ 10 cm), a hemisphere macro lens with radius much larger than 10 cm is not practical. Instead, miniaturized microlens is an alternative to extract the substrate mode. One may use a microlens array film (MAF) attached on the glass substrate to improve the OLED efficiency. Fig. 2(a) shows the scanning electron microscope (SEM) picture of MAF. In Fig. 2(b), MAF was applied on the top of OLED, and a brighter region was clearly seen. EQE was improved by 50% from 9.5 to 14.5%. The function of the lens structure is to redirect the light beams out of the OLED, which can be also accomplished by scattering medium. By incorporation of the material with different refractive index into the matrix film, it can be applied to the OLED which improved the light extraction with the flat out-surface, which is important for display application with touch-panel function. As shown in Fig. 2(c), a polyimide (PI) film (high-index matrix) with air voids ($n=1$) increased the EQE by 65%.

The basic idea of microlens structure for increasing light extraction of the OLED is to couple out the light at the substrate at larger incident angle. Fig. 3(a) shows the lit-on picture of an OLED pixel with the size of 100 μm $\times$ 100 μm. When applying MAF (with the pitch of 50 μm) on the OLED as shown in Fig. 3(b), photons were extracted from the surrounding of the pixel region with larger incident angle (larger than critical angle between glass substrate and the air) which increased the light outcoupling. At the same time, note that there were some dark regions at the area where the emission area and the microlenses overlapped. Because the photons with smaller incident angle can couple out of the OLED without microlenses, the incorporation of microstructure on the pixel region actually decreased the outcoupled photons at this region. Hence, a concept of patterned microlens array was proposed. By removing the pixel on the top of the pixel region, light extraction at this region was maintained, while increasing the EQE from the contribution of surrounding areas, as shown in Fig. 3(c).

For using OLED in display application, not only light extraction, but also image quality should be taken into consideration. As shown in Fig. 3(b), light extraction from the region outside the pixel implied image blurring when using as an OLED display and it decreased the image quality. Fig. 4(a) shows the Lena image on the OLED display, and Fig. 4(d) shows the enlarged picture of the left eye region. Fig. 4(b) and (e) shows the image taken with MAF attachment. Although the luminance increased by 23%, the image quality index was decreased to 74%. Fig. 4(c) and (f) are the image with patterned-MAF. One can see that the image is better with patterned-MAF, with the image quality index of 94%. Besides, the luminance of the OLED display increased by 52%.

Light Extraction of the Waveguiding Mode

To extract the waveguiding mode, it is straightforward to use some structure inside the glass substrate, close to the OLED device. Fig. 5(a) shows a low-index structure which was inserted between the ITO substrate and the organic layers. The effective refractive

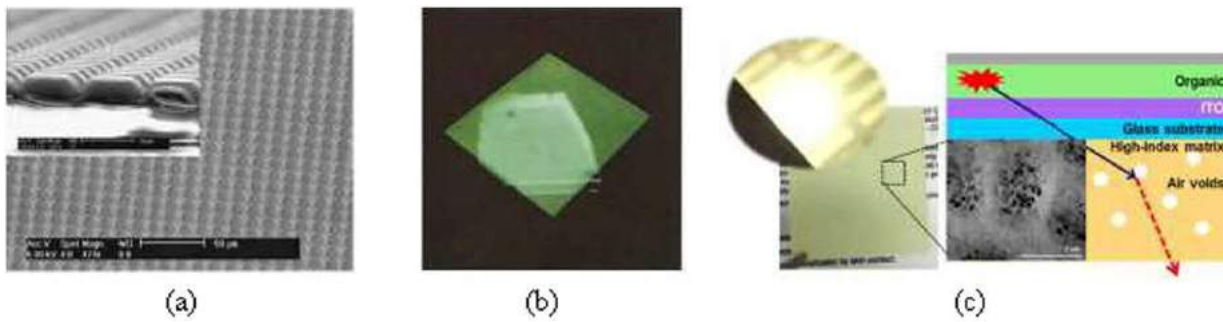


Fig. 2 (a) Scanning electron microscope (SEM) picture of the microlens array film (MAF), (b) picture of green organic light-emitting diode (OLED) emission with partially covered by MAF, and (c) light extraction by polyimide (PI) scattering film. (a,b) Reproduced from Moller, S., Forrest, S.R., 2002. Improved light out-coupling in organic light emitting diodes employing ordered microlens arrays. Journal of Applied Physics 91, 3324–3327. Copyright (2002) with permission from American Institute of Physics. (c) Reproduced from Koh, T.W., Spechler, J.A., Lee, K.M., Arnold, C.B., Rand, B.P., 2015. Enhanced outcoupling in organic light-emitting diodes via a high-index contrast scattering Layer. ACS Photonics 2, 1366 – 1372. Copyright (2015) with permission from American Chemistry Society.

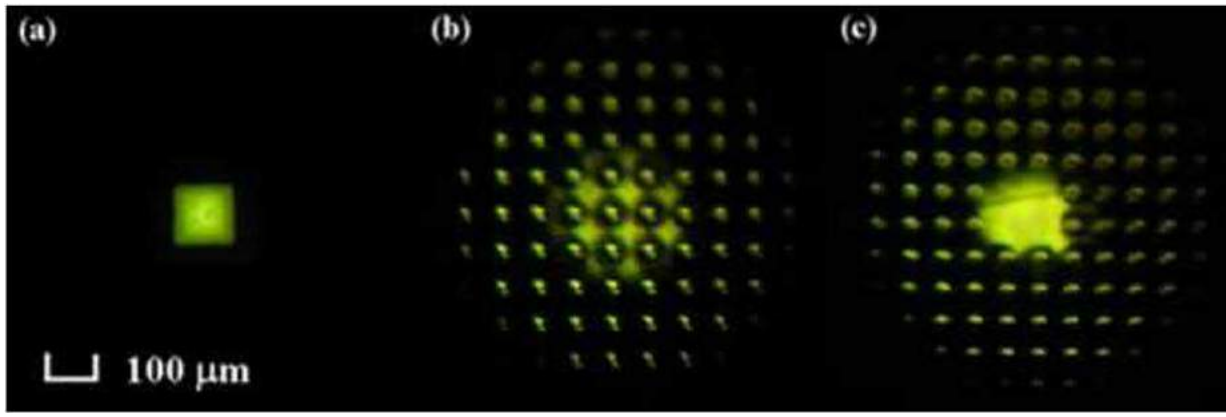


Fig. 3 (a) Optical microscope (OM) pictures of an organic light-emitting diode (OLED) emission. (b) and (c) shows the images with microlens array film (MAF) and patterned-MAF attachment on the OLED. Reproduced from Lin, H.Y., Chen, K.Y., Ho, Y.H., *et al.*, 2010. Luminance and image quality analysis of an organic electroluminescent panel with a patterned microlens array attachment. Journal of Optics 12, 085502. Copyright (2010) with permission from IOP Publishing.

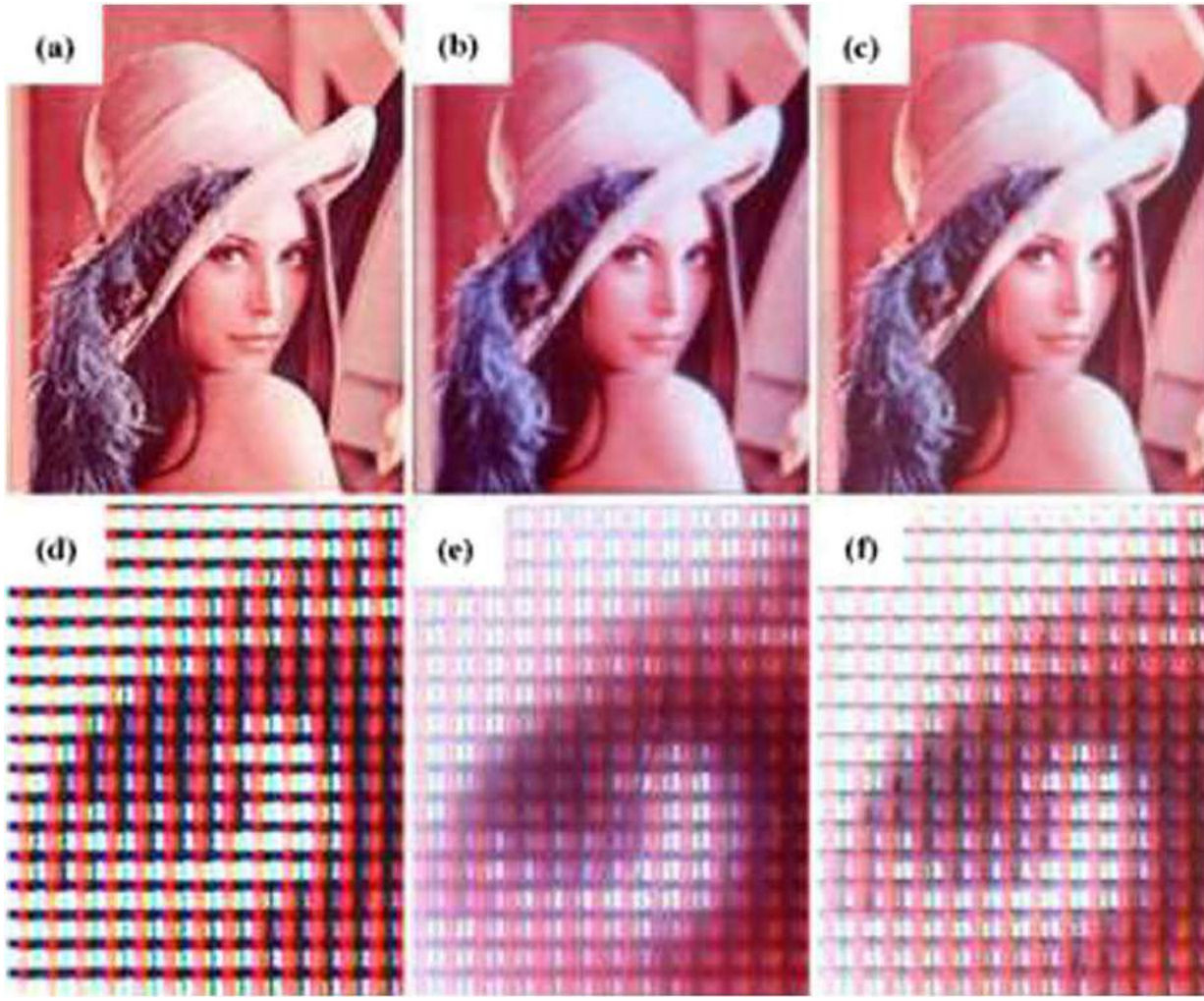


Fig. 4 (a) Lena picture on an organic light-emitting diode (OLED) display, with (b) microlens array film (MAF), and (c) patterned-MAF. (d)–(f) Are enlarged images of (a), (b), and (c), respectively. Reproduced from Lin, H.Y., Chen, K.Y., Ho, Y.H., *et al.*, 2010. Luminance and image quality analysis of an organic electroluminescent panel with a patterned microlens array attachment. Journal of Optics 12, 085502. Copyright (2010) with permission from IOP Publishing.

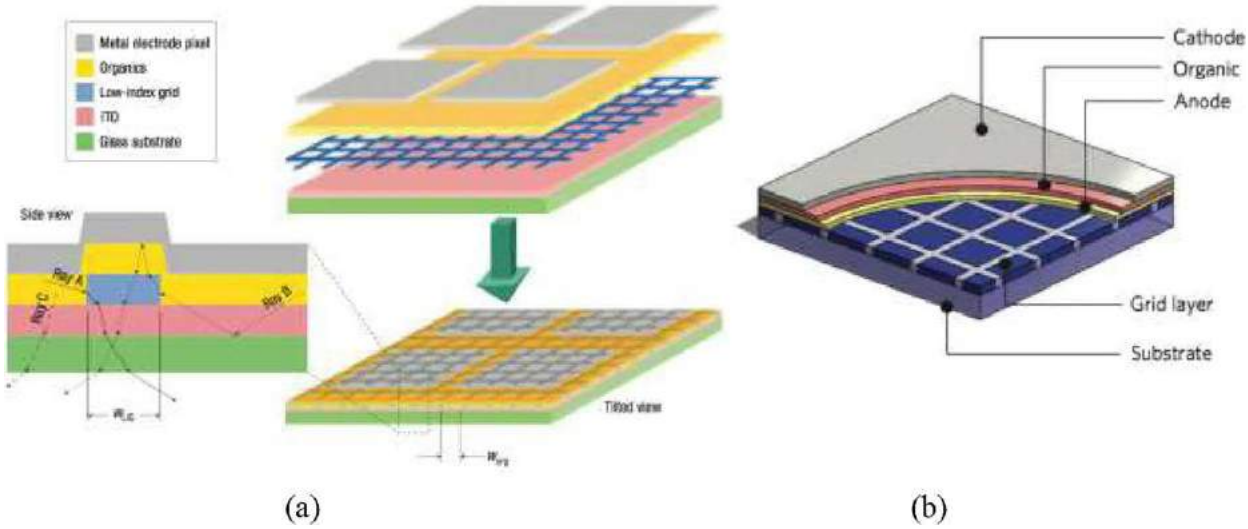


Fig. 5 (a) Schematic diagram of low-index grid (LIG) on the top of the indium tin oxide (ITO) layer and (b) planar grid layer structure between the glass substrate and the ITO. (a) Reproduced from Sun, Y., Forrest, S.R., 2008. Enhanced light out-coupling of organic light-emitting devices using embedded low-index grids. Nature Photonics 2, 483–487. Copyright (2008) with permission from Nature Publishing Group. (b) Reproduced from Qu, Y., Slootsky, M., Forrest, S.R., 2015. Enhanced light extraction from organic light-emitting devices using a sub-anode grid. Nature Photonics 9, 758–763. Copyright (2015) with permission from Nature Publishing Group.

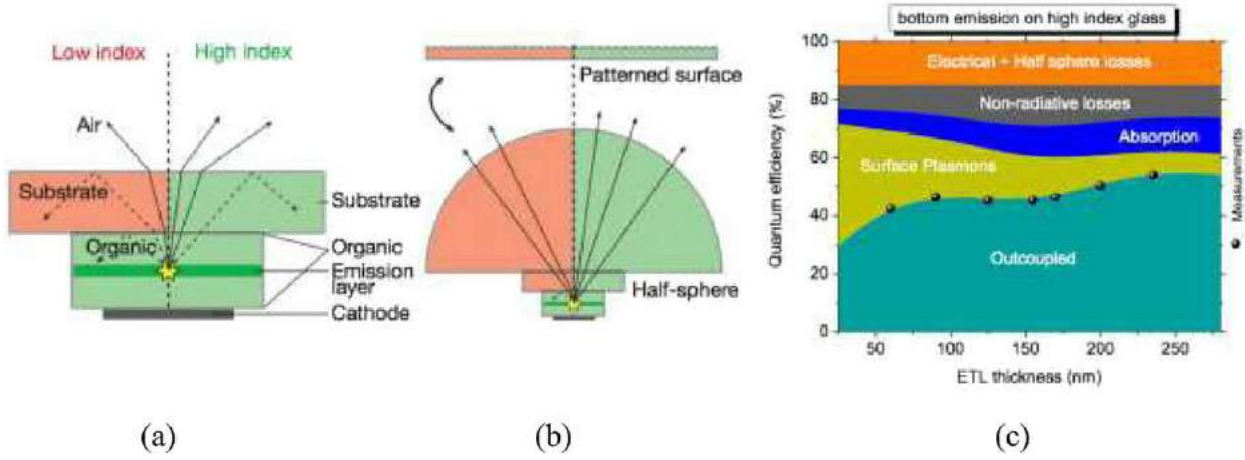


Fig. 6 (a) Schematic diagram of the organic light-emitting diode (OLED) on low- and high-index substrate, (b) with marolens and microlenses, and (c) electron-transporting layer (ETL) thickness vs. distribution of different modes in an OLED with high-index substrate and macro lens. (a,b) Reproduced from Reineke, S., Lindner, F., Schwartz, G., *et al.*, 2009. White organic light-emitting diodes with fluorescent tube efficiency. Nature 459, 234–238. Copyright (2009) with permission from Nature Publishing Group. (c) Reproduced from Meerheim, R., Furno, M., Hofmann, S., Lüssem, B., Leo, K., 2010. Quantification of energy loss mechanisms in organic light-emitting diodes. Applied Physics Letters 97, 253305. Copyright (2010) with permission from American Institute of Physics.

index of the waveguiding mode is decreased, and photons trapped in the waveguiding mode (light rays A and B in Fig. 5(a) with larger incident angle) can be effectively coupled out. By applying such low-index grid (LIG) in an OLED, 32% enhancement in EQE was observed. By using LIG and microlenses simultaneously, 130% improvement in EQE was achieved. However, the loss of contact area between ITO and organic layer reduced the luminance. Hence, one may insert such a grid structure beneath the ITO layer, as shown in Fig. 5(b). With sequential processes of deposition, etching, and planarization, embedded structure on the top of glass substrate was fabricated for extracting the waveguiding mode. Again, EQE was enhanced from 15 to 40% when using the grid structure to couple out the waveguiding mode, combined with the immersion of the OLED and photodetector inside the index-matching oil to extract all the glass substrate mode.

As discussed before, glass substrate mode and waveguiding mode both come from the TIR, with the refractive index of 1.5 and ~1.6–2.0, respectively. By using a glass substrate with high refractive index ($n = 1.8$), the waveguiding mode no longer exists. As

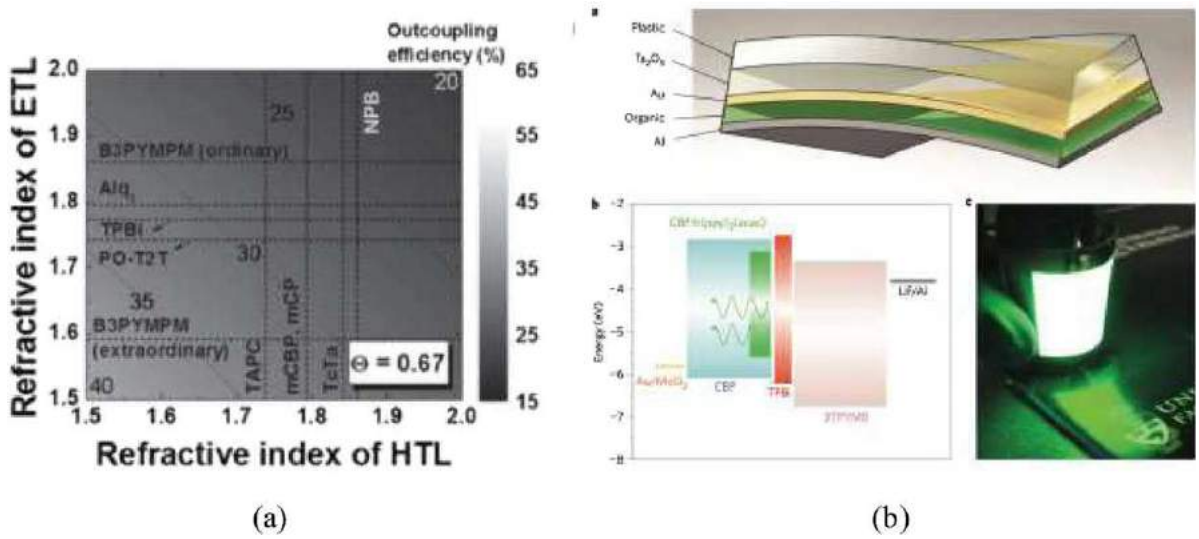


Fig. 7 (a) External quantum efficiency (EQE) values with different hole-transporting layer (HTL) and electron-transporting layer (ETL) refractive indexes and (b) indium tin oxide (ITO)-free flexible organic light-emitting diode (OLED) with Au as the anode and Ta_2O_5 to tune the optical field, together with the device structure and OLED emission pictures. (a) Reproduced from Shin, H., Lee, J.H., Moon, C.K., *et al.*, 2016. Sky-blue phosphorescent OLEDs with 34.1% external quantum efficiency using a low refractive index electron transporting layer. Advanced Materials 28, 4920–4925. Copyright (2016) with permission from Wiley-VCH Verlag GmbH & Co. (b) Reproduced from Wang, Z.B., Helander, M.G., Qiu, J., *et al.*, 2011. Unlocking the full potential of organic light-emitting diodes on flexible plastic. Nature Photonics 5, 753–757. Copyright (2011) with permission from Nature Publishing Group.

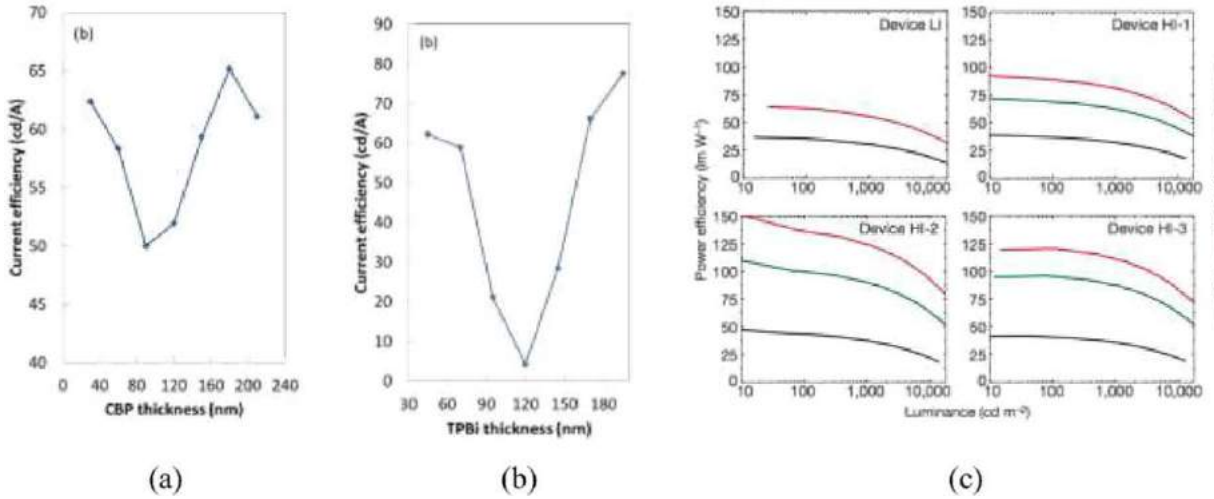


Fig. 8 Current efficiency vs. (a) hole-transporting layer (HTL) and (b) electron-transporting layer (ETL) thickness. (c) Power efficiency vs. luminance for different devices without and with outcoupling lenses. (a,b) Reproduced from Zhang, Y., Aziz, H., 2016. Insights into charge balance and its limitations in simplified phosphorescent organic light-emitting devices. Organic Electronics 30, 76–82. Copyright (2016) with permission from Elsevier. (c) Reproduced from Reineke, S., Lindner, F., Schwartz, G., *et al.*, 2009. White organic light-emitting diodes with fluorescent tube efficiency. Nature 459, 234–238. Copyright (2009) with permission from Nature Publishing Group.

shown in Fig. 6(a), one can see that the when using a high-index substrate, the there is no TIR at the OLED device and glass substrate. Then, with the incorporation of macro lens or patterned surface (such as microlenses), all the contributions from waveguiding and substrate modes can be extracted, as shown in Fig. 6(b). EQE = 54% can be achieved when ETL = 235 nm, as shown in Fig. 6(c).

Thinking from the other side, it is possible to reduce the effective refractive index of the organic materials in the OLED device for reducing the waeguiding mode. As shown in Fig. 7(a), by decreasing the refractive indexes of the HTL and ETL from 2.0 to 1.4, the EQE can be improved from 20 to 40%. One may also use a complex anode structure Ta_2O_5/Au on the flexible substrate ($n = 1.6$) to couple out the waveguiding light into the substrate mode. Then, with the use of the lens structure, 63% EQE was achieved.

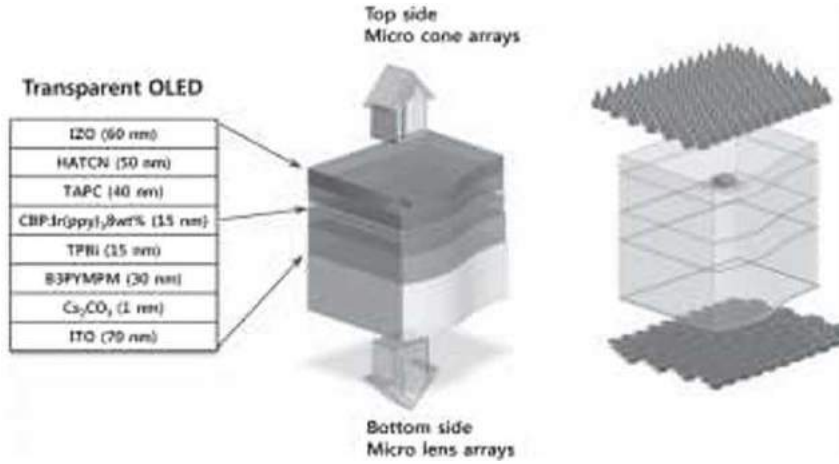


Fig. 9 Device structure of a transparent organic light-emitting diode (OLED) with metal oxide electrodes and micro-structures. Reproduced from Kim, J.B., Lee, J.H., Moon, C.K., Kim, S.Y., Kim, J.J., 2013. Highly enhanced light extraction from surface plasmonic loss minimized organic light-emitting diodes. Advanced Materials 25, 3571–3577. Copyright (2013) with permission from Wiley-VCH Verlag GmbH & Co.

Light Extraction of the Plasmonic Mode

Let us go back to the microcavity effect in an OLED in Fig. 1. For the bottom emission OLED on the glass substrate with ITO anode, the distance of the emission dipole to the reflective cathode is crucial to the light extraction efficiency. And hence modulation of ETL thickness changes the efficiency more effectively than that of HTL thickness. As shown in Fig. 8(a), when varying the thickness of HTL (CBP, 4,4′-bis(carbazol-9-yl)biphenyl), the current efficiency changed between ~50 and ~65 cd/A. On the other hand, current efficiency changed from <10 cd/A to ~80 cd/A with increasing the ETL (TPBi, 2,2′ ,2″-(1,3,5-benzinetriyl)-tris(1-phenyl-1-H-benzimidazole)) thickness, in Fig. 8(b). Besides, one can also notice that with increasing the ETL thickness, the efficiency can be higher than the first peak which was due to the reduction of plasmonic loss, as shown in Fig. 1. Fig. 8(c) shows the power efficiency versus luminance for different OLEDs. Device L1 is a common OLED structure on glass substrate. With the incorporation of half-sphere macro lens, power efficiency over 50 lm/W can be achieved. By applying a high-index substrate for coupling out the substrate mode, the efficiency can be boosted up over 80 lm/W, in device HI-1. For devices HI-2 and HI-3, thick ETL was employed, which resulted in a much higher power efficiency >150 lm/W and >110 lm/W, respectively.

Because the plasmonic loss mainly came from the metal electrode, it is possible to reduce this mode by using transparent conductive oxides as both the anode and cathode materials. Fig. 9(a) shows the device structure. ITO and indium zinc oxide (IZO) was used as the cathode and anode, respectively. Light emission from both sides and it is called transparent OLED. With the incorporation of micro- and macrostructures for extracting the substrate mode, EQE was increased from 18.1 to 47.3% and 62.9%, respectively, due to the reduction of plasmonic and substrate modes.

The origin of the non-radiative behavior of the plasmonic mode because the dispersion curve (w–k) of surface plasmon mode has no intersection with the air light cone, as shown in Fig. 10(a). However, with the introduction of the periodic nanostructure such as grating, it is possible to provide an extra in-plane wave-vector which can convert the plasmonic mode radiatively. Note that the nanostructure extracts not only the plasmonic mode, but also the waveguiding mode. To distinguish these two effects, one can use polarization dependent measurement. Emission from the surface plasmonic mode is only p-polarized. On the other hand, enhanced emission from s-polarization resulted from the outcoupling of the waveguiding mode by the nanostructure grating. Hence, a polarizer can be put in front of the detector for separating these two effects. As shown in Fig. 10(c) and (d), p- and s-polarized emission at different viewing angles were obtained, which came from the light extraction of plasmonic and waveguiding mode, respectively.

Although the uniform nanostructure provides an efficient way to extract the plasmonic and waveguiding mode, one can note that wavelength dependence is pretty strong, which means the color of this OLED is varied from different viewing angles and it is not suitable for display and lighting applications. A quasi-periodic structure was proposed by buckling fabrication. Due to different thermal expansion coefficient between poly(dimethylsiloxane) (PDMS) and Al, a quasi-periodic structure can be obtained, as shown in Fig. 11. With one-, two-, and three-times buckling, the structure with longer period (saying 900 nm) can be enhanced, with the major peak at 410 nm. 2.2- and 2.9-times improvement in power efficiency was achieved with two- and three-time bucking structure on an OLED without significantly changing the emission profile.

Thinking from the molecule viewpoint, it acts like an oscillation dipole for generating electromagnetic wave, as shown in (Fig. 12a). Here, the upper medium is metal, and surface plasmon was excited due to the electrical dipole. Depending on the Θ value, one can divide the contribution from vertical (Θ=0 degree) and horizontal (Θ=90 degree) dipoles. Note that SP mode was excited by TM waves, and hence radiation of horizontal dipoles coupled much less into plasmonic mode compared

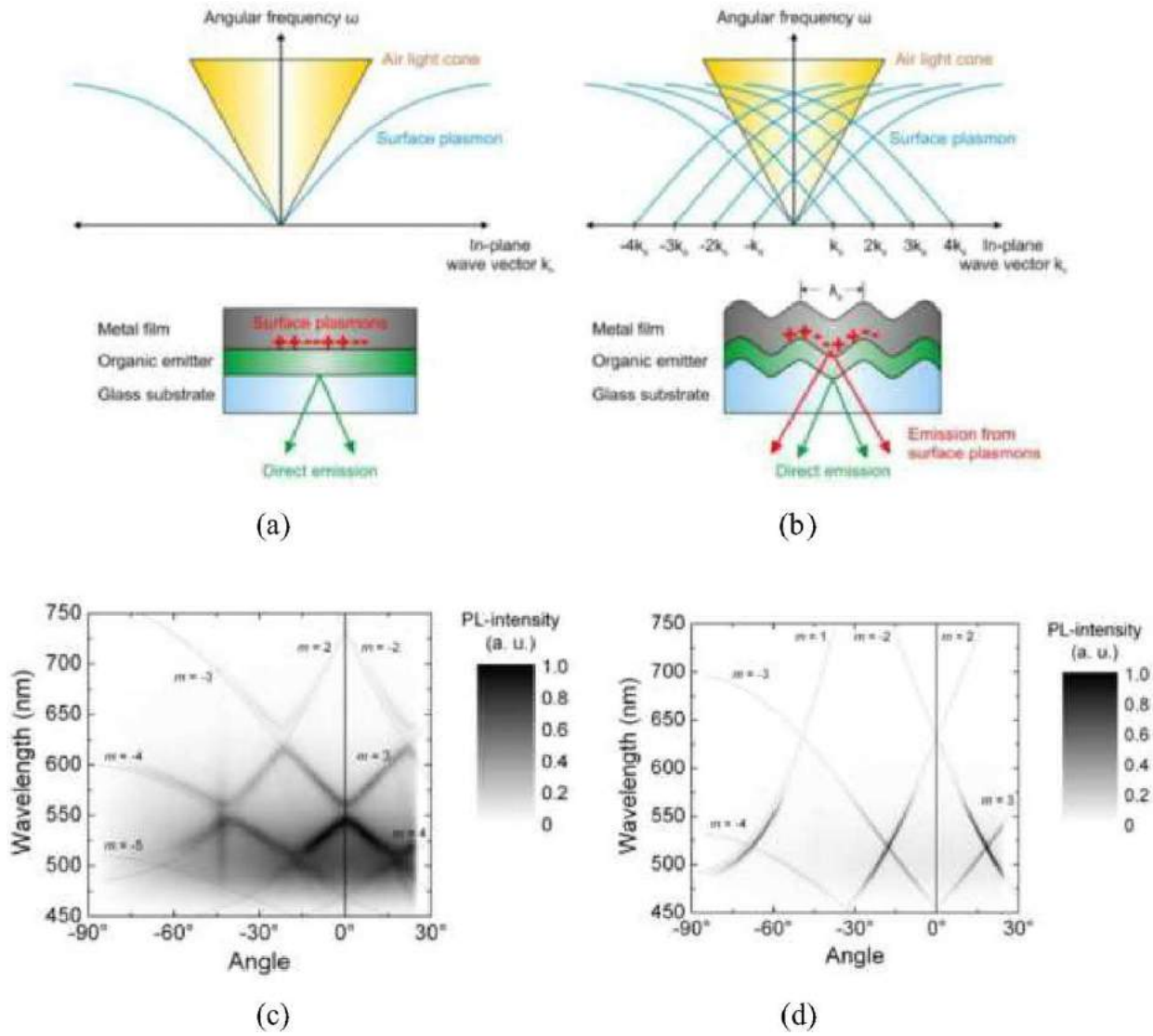


Fig. 10 Dispersion relation and device structure of a (a) planar and (b) grating structure. (c) and (d) shows the photoluminescence (PL) spectra at different viewing angles of p- and s-polarization. Reproduced from Frischeisen, J., Niu, Q., Abdellah, A., *et al.*, 2011. Light extraction from surface plasmons and waveguide modes in an organic light-emitting layer by nanoimprinted gratings. Optics Express 19, A7–A19. Copyright (2011) with permission from Optical Society of America.

to vertical dipole. By suitable choosing the organic material, it is possible to "align" the organic emitter horizontally and achieve the high EQE. Ratio between horizontal and vertical dipoles can be obtained from photoluminescence (PL) intensity at different viewing angles, as shown in **Fig. 12(b)**. Black and yellow dashed lines show the cases with pure horizontal and isotropic dipole emission, respectively. With higher horizontal dipole ratio (93% for Pt(fppz)2, Pt(II) bis(3-(trifluoromethyl)-5-(2-pyridyl)-pyrazolate)), the EQE can be as high as 38.8%, as shown in **Fig. 12(c)**. Note that it was a planar structure without any lens structure. Substrate was a typical glass. And the thin-film thickness from the emitter to the metal electrode was less than 100 nm. Hence, such a high EQE came from the reduction of plasmonic mode due to the alignment of horizontal dipole.

Summary

Here, we introduced the problem of light extraction in an OLED which limits the outcoupling efficiency ~20% in a conventional bottom emission configuration, mainly due to TIR and plasmonic loss. Various methods were introduced to improve the light extraction, with different structures and refractive index modulation. For the recent stage, experimental and simulation results show that EQE= ~60% is achievable, and further improvement is still on-going.

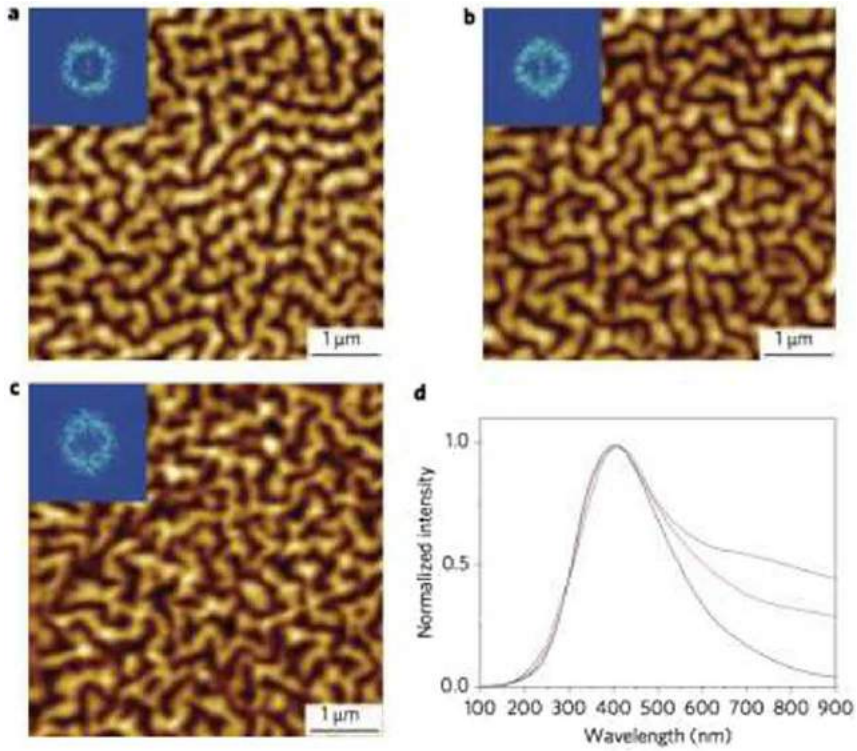


Fig. 11 Atomic-force microscopy (AFM) images for (a) one-, (b) two-, and (c) three-times buckling structure. (d) Power spectra of different buckling structures. Reproduced from Koo, W.H., Jeong, S.M., Araoka, F., *et al.*, 2010. Light extraction from organic light-emitting diodes enhanced by spontaneously formed buckles. Nature Photonics 4, 222–226. Copyright (2010) with permission from Nature Publishing Group.

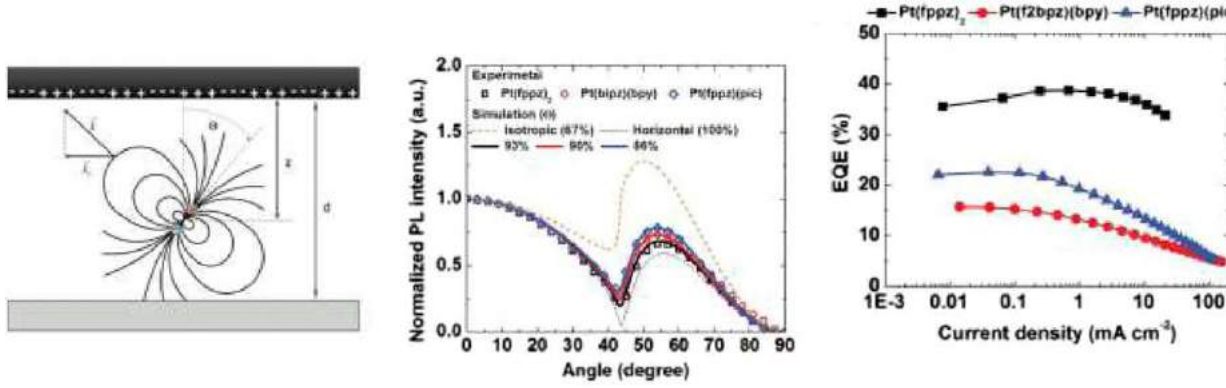


Fig. 12 (a) Schematic diagram of emission dipole in an environment. (b) Photoluminescence (PL) intensity at different viewing angles for different emitters. (c) External quantum efficiency (EQE) vs. current density of organic light-emitting diodes (OLEDs) with different emitters. (a) Reproduced from Brütting, W., Frischeisen, J., Schmidt, T.D., Scholz, B.J., Mayr, C., 2013. Device efficiency of organic light-emitting diodes: Progress by improved light outcoupling. Physica Status Solidi A 210, 44–65. Copyright (2013) with permission from Wiley-VCH Verlag GmbH & Co. (b,c) Reproduced from Kim, K.H., Liao, J.L., Lee, S.W., *et al.*, 2016. Crystal organic light-emitting diodes with perfectly oriented non-doped Pt-based emitting layer. Advanced Materials 28, 2526–2532. Copyright (2016) with permission from Wiley-VCH Verlag GmbH & Co.

See also: OLED/Introduction

Further Reading

Brütting, W., Frischeisen, J., Schmidt, T.D., Scholz, B.J., Mayr, C., 2013. Device efficiency of organic light-emitting diodes: Progress by improved light outcoupling. Physica Status Solidi A 210, 44–65.

Frischeisen, J., Niu, Q., Abdellah, A., *et al*., 2011. Light extraction from surface plasmons and waveguide modes in an organic light-emitting layer by nanoimprinted gratings. Optics Express 19, A7–A19.
Kim, J.B., Lee, J.H., Moon, C.K., Kim, S.Y., Kim, J.J., 2013. Highly enhanced light extraction from surface plasmonic loss minimized organic light-emitting diodes. Advanced Materials 25, 3571–3577.
Kim, K.H., Liao, J.L., Lee, S.W., *et al*., 2016. Crystal organic light-emitting diodes with perfectly oriented non-doped Pt-based emitting layer. Advanced Materials 28, 2526–2532.
Koo, W.H., Jeong, S.M., Araoka, F., *et al*., 2010. Light extraction from organic light-emitting diodes enhanced by spontaneously formed buckles. Nature Photonics 4, 222–226.
Lin, H.Y., Chen, K.Y., Ho, Y.H., *et al*., 2010. Luminance and image quality analysis of an organic electroluminescent panel with a patterned microlens array attachment. Journal of Optics 12, 085502.
Meerheim, R., Furno, M., Hofmann, S., Lüssem, B., Leo, K., 2010. Quantification of energy loss mechanisms in organic light-emitting diodes. Applied Physics Letters 97, 253305.
Moller, S., Forrest, S.R., 2002. Improved light out-coupling in organic light emitting diodes employing ordered microlens arrays. Journal of Applied Physics 91, 3324–3327.
Qu, Y., Slootsky, M., Forrest, S.R., 2015. Enhanced light extraction from organic light-emitting devices using a sub-anode grid. Nature Photonics 9, 758–763.
Reineke, S., Lindner, F., Schwartz, G., *et al*., 2009. White organic light-emitting diodes with fluorescent tube efficiency. Nature 459, 234–238.
Shin, H., Lee, J.H., Moon, C.K., *et al*., 2016. Sky-blue phosphorescent OLEDs with 34.1% external quantum efficiency using a low refractive index electron transporting layer. Advanced Materials 28, 4920–4925.
Sun, Y., Forrest, S.R., 2008. Enhanced light out-coupling of organic light-emitting devices using embedded low-index grids. Nature Photonics 2, 483–487.
Wang, Z.B., Helander, M.G., Qiu, J., *et al*., 2011. Unlocking the full potential of organic light-emitting diodes on flexible plastic. Nature Photonics 5, 753–757.
Zhang, Y., Aziz, H., 2016. Insights into charge balance and its limitations in simplified phosphorescent organic light-emitting devices. Organic Electronics 30, 76–82.

Conjugated Polymer-Based Solar Cells

Gang Li, The Hong Kong Polytechnic University, Hong Kong, China
Widhya Budiawan, Research Center for Applied Sciences, Academia Sinica, Taipei, Taiwan (ROC); National Tsing-Hua University, Hsinchu, Taiwan (ROC); and Academia Sinica and National Tsing-Hua University, Hsinchu, Taiwan (ROC)
Pen-Cheng Wang, National Tsing-Hua University, Hsinchu, Taiwan (ROC)
Chih Wei Chu, Research Center for Applied Sciences, Academia Sinica, Taipei, Taiwan (ROC)

© 2018 Elsevier Ltd. All rights reserved.

Nomenclature

Carrier mobility [$cm^2\ V^{-1}\ s^{-1}$]
Light intensity/power density [$W\ m^{-2}$]
Photon flux [$m^{-2}\ s^{-1}\ nm^{-1}$]
Short circuit current density [$mA\ cm^{-2}$]
Solar irradiance [$W\ m^{-2}\ nm^{-1}$]

Introduction

Photovoltaic, which directly harvest energy from sunlight into electricity, is being increasingly recognized as an important component for future global energy production. Organic semiconductor and particularly conjugated polymers-based solar cells (OPVs) have attracted world-wide attention in the past decade, because of their distinct features such as low cost production, lightweight, flexibility, electronic functional versatility from chemical synthesis, roll-to-roll compatible large area fabrication, (semi)transparency and potentially environmental friendly in fabrication, etc. The performance of OPV has been greatly improved in last decade, now reaching over 12% as shown in Fig. 1(a) (Source: National Renewable Energy Laboratory (NREL)). These achievements come from comprehensive research – from materials discovery, nanostructure morphology control in photon absorbing active layer, to interface materials innovation and device architecture engineering, device physics, to fabrication technologies. Strictly speaking, OPV can be divided into polymer and small molecule type. This article only focus on polymer solar cells and use the term OPV to represent them.

Polymer OPVs are based on organic conjugated polymers, which are carbon-based materials whose backbones are comprised of alternating C–C and C=C bonds (carbon–carbon triple bonds may also be possible in rare cases), shown in Fig. 1(b). In the alternating C–C and C=C bonds molecular structure, through sp^2 hybridization, it leads to a linear series of overlapping p_z orbitals, and creates a conjugated chain of delocalized electron density. The π electron delocalization along the conjugated backbone – i.e., the interaction of the π electrons – is responsible for their semiconducting properties. As the conjugation length (or the electron delocalization length) increases, the intrinsic material energy levels becomes closely spaced, and similar to inorganic semiconductors, a quasi "band" structure will form in organic semiconductors, including conjugated polymers. In organic semiconductors, the lowest unoccupied molecular orbital (LUMO) is equivalent to the conduction band minimum (CBM) in inorganic semiconductors, while the highest occupied molecular orbital (HOMO) is equivalent to the valence band maximum (VBM) in inorganic semiconductors (Fig. 1(c)). The primary photoexcitaion in the organic semiconductors are bounded Frenkel excitons (electron–hole pair), which is very different from the free electrons/holes in crystalline inorganic semiconductors. The excitons have a typical lifetime of $\sim$100 ps to 1 ns, decay either radiatively of non-radiatively. These differences make the working mechanism in organic polymer solar cells very different from the inorganic solar cells.

The high performance polymer solar cells are now dominated by BHJ structure, with conjugated polymer as electron donors, mixed with fullerene or nonfullerene electron acceptors.

This article aims at a concise review of polymer organics solar cell (OSC) development, and discuss the possible strategy for future improvement in polymer solar cell.

Basic Principles of OSC

The main structure of OPV is an organic material(s)-based active layer(s) sandwiched between a cathode and an anode. The active layers consist of material with low ionization potential (IP) as electron donor and material with high electron affinity (EA) as electron acceptor material. Various materials are used as either donor or acceptor including polymer, fullerene derivatives and small molecules. Furthermore, donor material is hole rich which ideally make ohmic contact with anode, whereas acceptor material contact with the cathode.

In the simplest picture of organic solar cell operation principle, the process of the photon-to-electron conversion can be divided into four basic steps (Fig. 2(a)) each with efficiencies – photon absorption (η_A), exciton diffusion (η_{ED}), charge carrier transfer (η_{CT}), and charge carrier collection (η_{CC}). The detail of every step is discussed as below.

1. Photon absorption
   The organic material semiconductor only absorbs photon that higher or equal to its bandgap. As consequence, only material with low bandgap is suitable for active layer. In this step, photon was absorbed then electrons in donor (/acceptor) material are

 doi:10.1016/B978-0-12-803581-8.09544-8

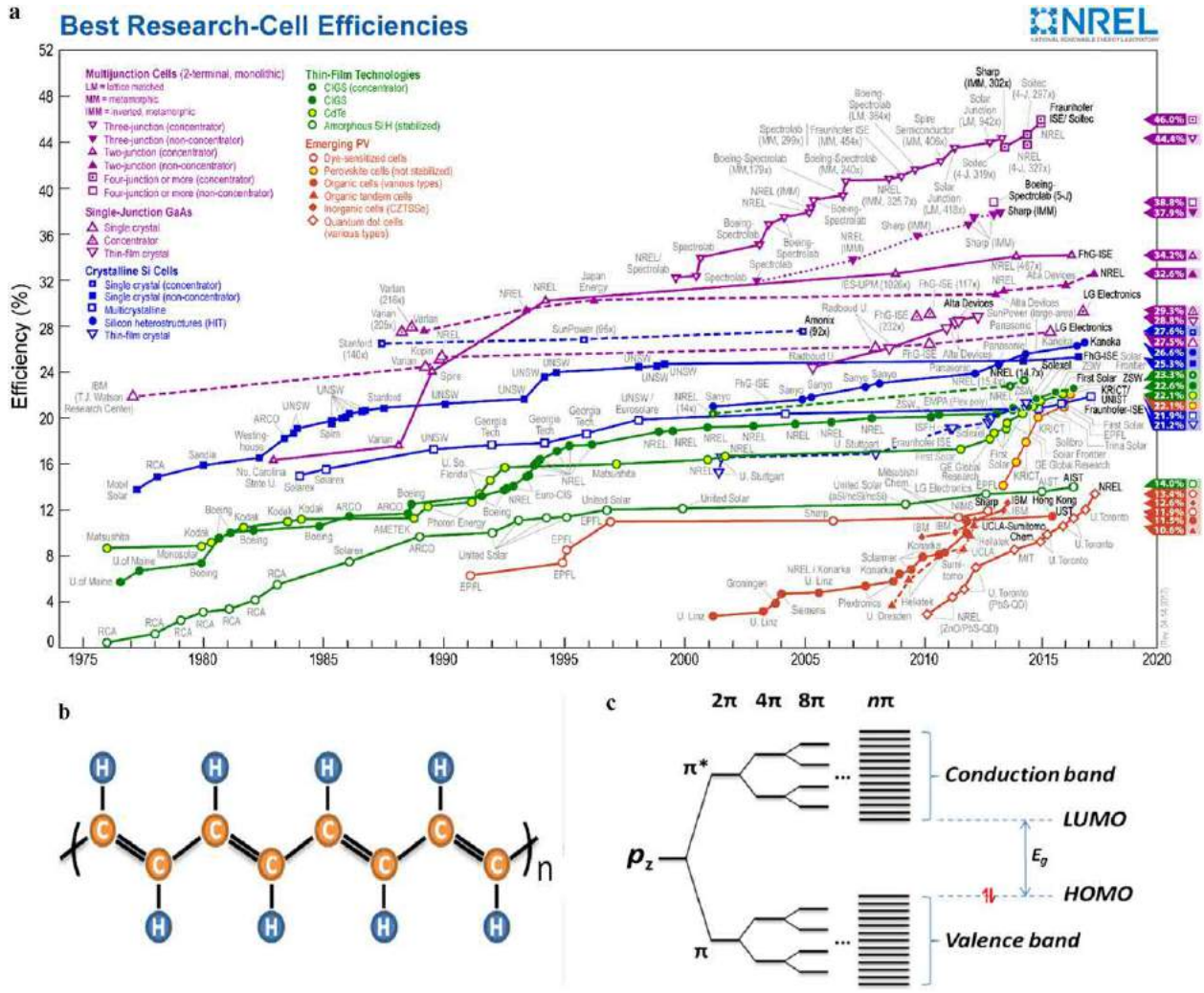


Fig. 1 (a) Efficiency-chart of best solar cell summarized by National Renewable Energy Laboratory (https://www.nrel.gov/pv/assets/images/efficiency-chart.png); (b) alternating C–C and C=C bonds in conjugated polymer backbone; (c) energy diagram in organic semiconductors via π electron delocalization $-\pi$ conjugation. HOMO, highest occupied molecular orbital; LUMO, lowest unoccupied molecular orbital.

excited to the LUMO level and created holes in the HOMO level. These electron and hole pair are bound together by attractive coulomb interaction and are called excitons. Furthermore, the absorption efficiency (η_A) of active layer is determined by the absorption spectra of the organic material, their thickness, as well as the device architecture.

2. Exciton diffusion

   The generated excitons in photon absorption process move via diffusion. This exciton should transport to the donor–acceptor interface within its lifetime to convert to charge carrier. The morphology plays significant role on exciton diffusion (η_{ED}).

3. Charge transfer

   The room temperature thermal energy of 26 meV is an order smaller than the binding energy of tightly bound Frenkel excitons in organic semiconductors. Therefore to generate "free" electron and hole polarons as charge carriers, an exciton needs to reach the donor–acceptor interface where the molecular energy level difference will provide the driving force for exciton dissociation into a geminate pair first and overcome the monomolecular process called geminate recombination. Only after this process that free charge carriers can be generated which ultimately contribute to photocurrent.

4. Charge collection

   From the D/A interface, the free charge carrier needs be transported (hole in donor, electron in acceptor material) to the organic/electrode interfaces. Again nano-morphology in BHJ configuration is critical. After the charge carriers transport to the active layer/electrode interface, they can finally be extracted from the device in order to yield photocurrent. Buffer layers (hole transport layer (HTL) and electron transport layer (ETL)) are usually necessary and critical to aid hole or electron collection by reducing the energy barriers required to transport carriers and increasing the built in electric field to help electron collections.

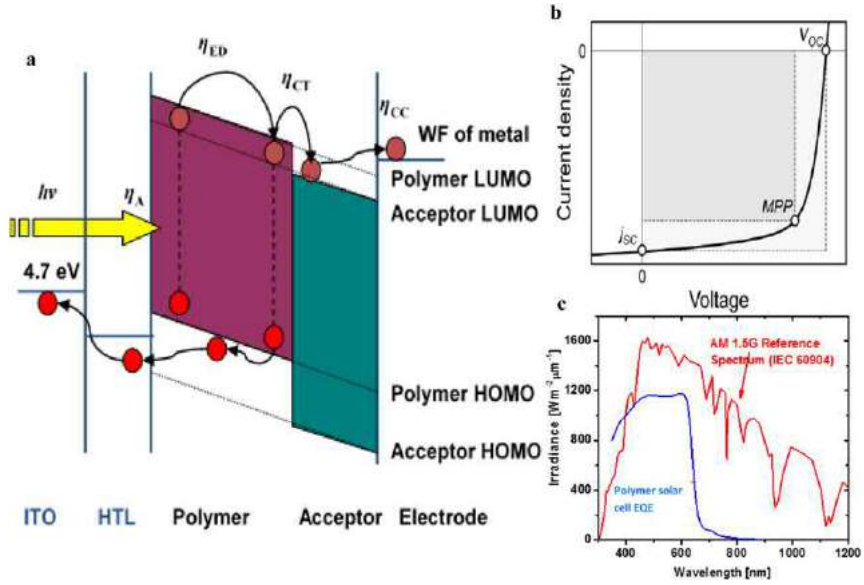


Fig. 2 (a) Simplified schematic mechanism of photocurrent generation in organic solar cells which consist of four sequence steps photon absorption (η_A), exciton diffusion (η_{ED}), charge transfer (η_{CT}), and charge collection (η_{CC}); (b) *J–V* characteristic curve of solar cell under illumination; (c) standard terrestrial AM1.5G solar spectrum (irradiance) and a typical external quantum efficiency (EQE) spectrum of polymer solar cell. HTL, hole transport layer; HOMO, highest occupied molecular orbital; ITO, indium-tin-oxide; LUMO, lowest unoccupied molecular orbital.

The overall quantum efficiency (a function of wavelength) can be calculated by following equation:

$$\eta_{EQE}(\lambda) = \eta_A(\lambda)\eta_{ED}(\lambda)\eta_{CT}(\lambda)\eta_{CC}(\lambda) \tag{1}$$

Beyond the simple model, one should realize that there are different electronic states in OPV devices – excitons, the charge transfer (CT) states/excitons, the mobile polaron transport states and localized trap states – each play a crucial role in the device operation. In particular, the CT state is an intermediate state between exciton and "free" polaron state. It comprises an electron and hole on either side of the BHJ interface, the electron and hole separation reduces the Coulomb interaction. The CT state is tightly connected with the V_{oc} limit of the solar cell.

Characterization of OSC

The *J–V* characteristics of a solar cell under illumination are shown in **Fig. 2(b)**. There are three important parameteres that combined to give the power conversion efficiency (PCE): short-circuit current density J_{sc}, open circuit voltage V_{oc}, and fill factor (FF).

1. Short circuit current density

   Short circuit current density, J_{sc}, is defined as the current when the solar cell has no external load. The J_{SC} represents the number of charge carrier that generated in active layer can collected at electrode at short circuit condition. However, not all incident light is absorbed in active layer and not all generated carriers can reach the electrodes. The magnitude of the J_{SC} depends on the absorption spectrum of the material, the morphology, and the mobility of charge carrier in the material. The high photocurrent can be achieved by selecting material with absorption spectra that overlap the photon flux density.

   The J_{sc} also depends on solar spectum. The extraterrestrial soalr spectum resembles that of a blackbody at 5760K. For terristrial solar cell application, the standard solar spectrum is AM1.5G, where the sunlight goes through 1.5 times the atmosphere, or incide from an elevation angle of 42 degree, and the label *G* means the spectrum includes both direct light and diffused light as there is scattering by the atmosphere. **Fig. 2(c)** shows the standard terrestrial AM1.5G solar spectrum (irradiance) and a typical external quantum efficiency (EQE) spectrum of polymer solar cell. In principle, the integration of the EQE with solar irradiance should be equal to the J_{sc}.
2. Open circuit voltage (V_{oc})

   Besides J_{sc}, another key parameter that determine the efficiency of PSC is the open-circuit voltage V_{OC}, which represents the maximum voltage a solar cell can provide to an external circuit. Light harvesting materials employed in OPVs have an optical bandgap of around 1.3–2.1 eV and yet the V_{OC} barely exceeds 1.0 V, i.e., significant loss of photon's original energy. In organic solar cell, the V_{OC} mainly proportional to the energy level difference between HOMO level of donor and LUMO level of acceptor, and more detialed analysis will involve the CT states tightly linked to these levels. As consequence, the selection of the

donor material and acceptor will largely determine and limit the V_{OC} value. In addition, secondary parameters affecting the V_{oc} include recombination, temperature (and thus temperature dependent mobility), work function of electrode, and morphology of active layer.

For a long period of time, fullerene derivatives such as $PC_{61}BM$ and [6,6]-phenyl-C71-butyric acid methyl ester ($PC_{71}BM$) are dominating acceptor materials in OPV reserch. In the BHJ system with fullerene derivatives acceptors, as the acceptor LUMO level is fixed, significant efforts were given to donor materials. To enhance the J_{sc}, lower bandgap polymers are the choice, and at the same time, to avoid the typical photovoltage loss, the low bandgap polymers have to have deep HOMO level.

3. FF

   FF is the ratio of the maximum power to the open and short circuit values (J_{SC} times V_{OC}) which represents the difference between a real solar cell and the ideal condition. FF shows the dependence of the photocurrent output on the internal field of device, and it's related to the series resistance (R_S) and parallel resistance (R_P). While lower R_s normally results in the higher FF value, FF is much more complex, and potential dependent recombination has to be investigated.

4. Maximum power point

   The performance of a solar cell is evaluated from an experimentally measured current–voltage characteristic curve. Maximum power point (MPP) is the point on the *J*–*V* curve that the area of resulting rectangle is largest. The MPP represent the maximum of power that can be generated by a solar cell.

5. PCE

   The PCE is define as the efficiency of the solar cell and it can be calculated as the maximum output power divided by the input power. The PCE can be calculated as follows:

$$\text{PCE}\ (\%) = \frac{P_{\text{maz}}}{P_{\text{in}}} = \frac{\text{FE} \times J_{\text{SC}} \times V_{\text{OC}}}{PP_{\text{in}}} \tag{2}$$

The current in the solar cell at any voltage is most readily understood as the sum of the dark current $J_D(V)$ and the photocurrent $J_P(V)$, where they have opposite sign in PV region.

$$J(V) = J_D(V) + J_P(V) \tag{3}$$

From $J(V_{oc}) = 0$, we know the carrier excitation rate is balanced by an equal carrier recombination rate. The photon generation rate G under 1-sun illumination in a typical organic cell is about 10^{22} cm^{-3}, and the recombination lifetime τ is about 10^{-6} s, thus the carrier concentration $N_C = G\tau$ is about 10^{16} cm^{-3}.

The dark forward current in solar cells obey the diode equation,

$$J_D(V) = J_0 \exp\left[\left[\frac{e(V - R_S J_D)}{nkT}\right] - 1\right] + \frac{V - R_S J_D}{R_P} \tag{4}$$

where n is the ideality factor, R_P is the parallel shunt resistance, and R_S is the series resistance. The J_0 is related to the barrier height and decreases with larger built-in potential V_{BI}. The ideality factor n is typically in the range 1.3–2 in good organic cells. In classic semiconductor theory, $n = 1$ is associated with band-to-band recombination, while $n = 2$ is associated with recombination through trap states by the Shockley–Read–Hall mechanism. Modeling shows that the intermediate values arise from recombination through band tails states, possibly in combination with deeper states.

OPV Device Structures

The organic polymer solar cell structure evolution is mainly for improve the interface between donor and acceptor materials, and also the polarity of the device. The development of device structure historically starts from single layer structure, to double layer structure, and bulk heterojunction (BHJ). The structure of the device discussed in sequence.

1. Single polymer layer device

   The single polymer layer OPV is the simplest structure. Polyacetylene (PA) were used in single layer organic solar cell that producing V_{OC} 0.3 V and PCE 0.3%. And poly(3-nethyl-thiophene) film sandwiched between aluminum and platinum had external quantum of 0.17% and V_{OC} of 0.4 V and FF 30%.

   Organic polymers intrinsically have large exciton binding energy. Using external electrical potential alone is very hard to provide excition dissociation, and thus the photocurrent will be very low. It has to be extremely thin to dissociate exciton, but this leads to very low light absorption – a dilemma to conquer.

2. Bilayer polymer/acceptor structure.

   In bilayer heterojunction (also known as planar heterojunction) solar cell device, film of a polymer as the electron donor (p-type), and a film of electron acceptor (n-type) are deposited on top, as shown in **Fig. 3**. The selected active layer should realize an offset in HOMO and LUMO energy level at the donor–acceptor (D/A) interface to drive exciton dissociation by CT. In the first successful of two layer organic photovoltaic device by Tang *et al.* a copper phthalocyanine (CuPC) as donor material and a perylene tetracarboxylic derivative as acceptor material were vacuum deposited to make active layer and achieved

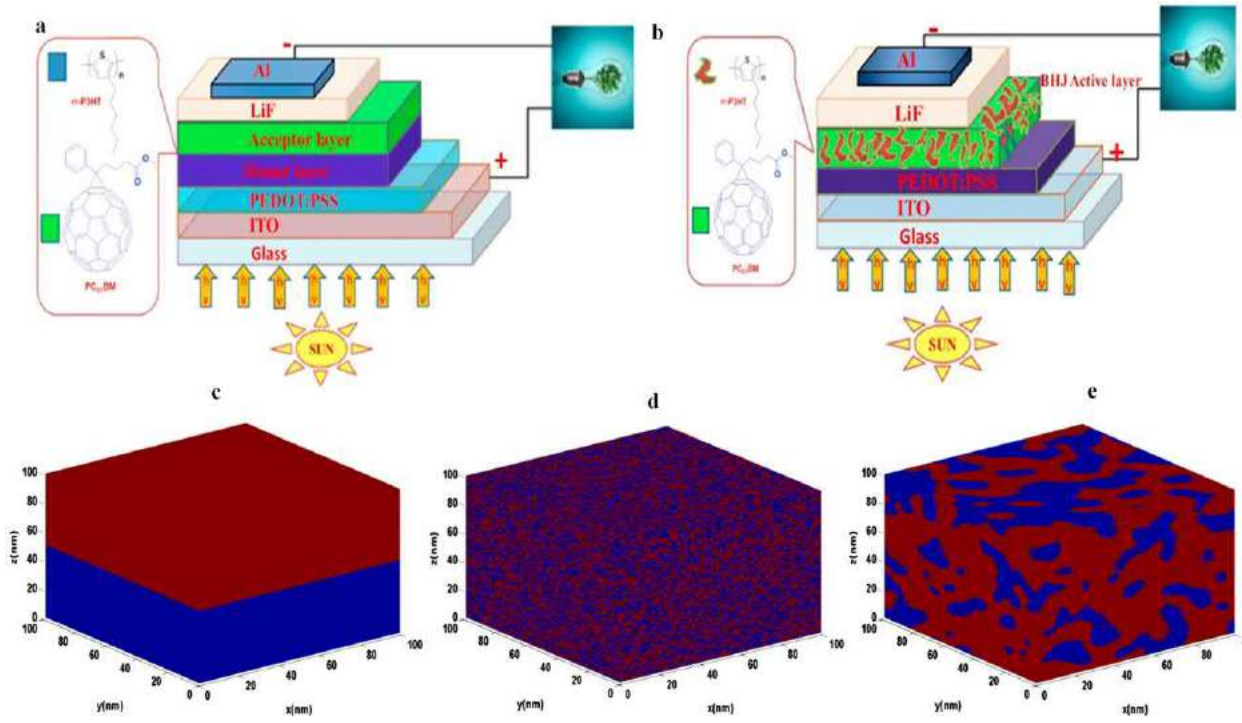


Fig. 3 Polymer solar cell in (a) bilayer structure and (b) bulk heterojunction (BHJ) structure (reproduced from Ganesamoorthy, R., Sathiyan, G., Sakthivel, P., 2017. Solar Energy Materials & Solar Cells 161, 102–148); schematic morphology in polymer solar cell (c) pure bilayer structure, (d) "uniform" BHJ structure with very small phase separation domain size, and (e) BHJ with moderately phase separation domain size (reproduced from Maqsood, I., Cundy, L.D., Biesevker, M., *et al.*, 2013. Monte Carlo simulation of Förster resonance energy transfer in 3D nanoscale organic bulk heterojunction morphologies. Journal of Physical Chemistry C 117 (41), 21086–21095). ITO, indium-tin-oxide.

efficiency around 1%. However, the drawback of bilayer structure is that the layer thickness is limited to the exciton diffusion length. Also, the bilayer structure is limited by small donor–acceptor interface area.

Since the lifetime of the exciton in most polymer films is short, the diffusion lengths are limited to less than 20 nm, which is shorter than the optical absorption pass length ($\sim$100–200 nm). Therefore only a limited part of exciton can diffuse to the interface in bilayer heterojunction. If the polymer is very thick, the excitons cannot reach the donor acceptor interface then recombine. In order to realize efficient photon conversion, this architecture must strike a balance between the relative long optical absorption length ($L_A \sim 50$ nm) and shorter characteristics length scale for exciton diffusion ($L_D \sim 10$ nm).

In evaporated small molecule solar cell, the complicated layered solar structure can be realized. IMEC group developed bilayer nonfullerene solar cell with PCE more than 6% using α-6T as donor and SubNc as acceptor. The device performance is better than using fullerene as acceptor due to broaden the absorption spectrum. The multilayer planar heterojunction to led PCE up to over 8%. The multiplayer structure, however, is difficult to realize in solution process OPV.

3. BHJ polymer solar cell structure.

Bilayer structure problem can be addressed by BHJ structure. In the BHJ device a blend or mixture of donor and acceptor molecules were used to form a bi-continual layer as shown in **Fig. 3(b).** Bicontinuous three dimensional interpenetrating network yielded an increased D–A interface, which is the necessary criteria for the effective exciton dissociation.

The first BHJ concept was introduced by Hiramoto *et al.* in evaporated small molecule through co-deposited of phthalocyanine (Pc) and perylene derivatives (PTC) as interlayer between Pc and PTC. The photocurrent enhanced due to a large number of molecular contact while in the bilayer the donor and acceptor are completely separated. The much more attractive solution processed BHJ organic polymer solar cell was realized by Heeger's group using polymer–fullerene and Friend's group in polymer–polymer blend in 1995. The BHJ concept has significantly increased the number of interfacial area of donor and acceptor phase.

Strategy to Improve BHJ Device Performance

The high performance polymer solar cell is dominated by BHJ structure. We review the progress in three key research areas: morphology, active materials, and interface and structural engineering.

BHJ Morphology Control Through Process Engineering

Bicontinuous interpenetrating active layer morphology is a pre-requisition for high organic solar cell performance. The morphology controlling is affected by many factors including crystallinity, molecular arrangement, and drying rate. In bilayer structure, interfacial area between donor and acceptor is on the planar surface (Fig. 3(c)), thus exciton dissociation efficiency into free carrier is very low. The "uniform" BHJ structure has very large donor–acceptor interface area, but the morphology become more important. As shown in Fig. 3(d), the small domain phase separation of BHJ provides a large number D–A interface, but it is not providing continuous pathway. As consequence, large number of charge generation produced but electron and hole trapped in the active layer then recombine, and cannot effectively generate J_{sc}. The right BHJ morphology will look like the excessively D–A interface in Fig. 3(e) – it has the right balance of D/A interface (for efficient exciton dissociation) and nanoscale bicontinuous pathway to enable the separated electron and hole polarons reaching the electrodes.

The reported effective approaches in tuning morphologies of the active layer in OPVs including solvent annealing (SA), thermal annealing, solvent additives, solvent (vapor) annealing, and solvent mixtures, which would be presented in the following section.

Thermal Annealing

Thermal annealing is an effective method to improve PCE discovered in the early years of OPV, when the workhorse material changed from poly[2-methoxy,5-(2′-ethyl-hexyloxy)-p-phenylene vinylene] (MEH-PPV) to soluble polythiophenes, especially regioregular poly(3-hexylthiphene) (RR-P3HT), which has lower bandgap of 1.9eV. The PCE of P3HT: fulleropyridine was enhanced by 3–4-fold with mild thermal treatment (50°C for 30 min); thermal annealing temperature, annealing time, and annealing sequence – either before (preannealing) or after (postannealing) electrode deposition, all play role in determining the performance of classical P3HT:phenyl-C61-butyric acid methyl ester (PCBM) solar cells.

The absorption of the P3HT in the P3HT:PCBM active layer, when processed in typical fast spin-coating approach, is very different from that of the pristine P3HT film. It's generally observed the P3HT absorption red shifted after thermal annealing, indicating the enhanced (or partially recovered) polymer crystallinity. Grazing incidence X-ray scattering (GIXS) become a powerful approach to investigate the polymer blend. GIXS technique gives clearly evidence of the π–π stacking orientation (orientated parallel to the substrate in P3HT:PCBM case), and enhanced crystallinity after thermal annealing above transition glass temperature (T_g). Upon thermal annealing, the PCBM molecules can freely diffuse out of these mixed regions to aggregate into PCBM cluster while enhancing P3HT crystallinity. The PCBM diffusion may induce simultaneously more ordered packing of P3HT and form bicontinuous morphology (Fig. 4(a)). In semi crystalline polythiophenes, high charge mobility occurs along the polymer main chain and parallel to the π–π stacking direction of the thiophenes rings. The increased crystallinization via thermal annealing also reduces density of the defects at the interface and in the bulk. Thermal annealing is effective beyond P3HT:PCBM. Annealing at 100°C for 20 min improves PBDTS-DTBTO (as donor) and nonfullerene ITIC (as acceptor) solar cell from 7.80 to 9.09%. Increased interchain packing with significantly intensified face-on π–π stacking indicates enhanced exciton dissociation and charge transport, thus results in enhanced current density and FF.

Solvent (Vapor) Annealing

SA is another method to control morphology of the active layer by slowing down the evaporation rate of the solvent, which slows the film formation/drying process. In P3HT:$PC_{61}BM$ system using high boiling point solvent ODCB, the slow solvent removing process provide the polythiophene chains enough time to demonstrate the self-organization capability embedded in the regioregular design of the polymer. The SA approach results in a much increased hole mobility and balanced charge transport, which lead to a more than doubled PCE of 4.4%. The thermal annealing and SA approaches improves the morphology in different way in P3HT system. Regioregular P3HT itself has excellent absorption up to 650 nm and the π–π stacking of polymer chains ensured high mobility. However the long wavelength absorption is severely suppressed with the present of acceptor PCBM when the solvent was removed quickly in traditional way. The thermal annealing approach can partially recover the polymer ordering and absorption. The SA takes another route by preserving the high degree of ordering rooted in the self-organization during the initial film formation period instead. Fig. 4(b) shows the GIXS results of the RR-P3HT:PCBM film with and without SA. This shows the polymer chain packing is dominated by edge-on orientation, and the SA not only leads to higher crystallinity, but also smaller mainchain spacing (*a*-axis). Phase image of atomic force microscopy (AFM) shows very clear polymer fibril structure with ~20–30 nm fiber diamter (Fig. 4(c)).

Dynamically, during the SA process, the BHJ blend was found swollen by solvent, which allowed PCBM acceptor to diffuse out of P3HT domains. This also improves mobility of fullerene, increases the crystallinity of P3HT, and improves phase separation between domains.

Mixed-solvent and vapor annealing can be combined to improve polymer crystallinity and inhibit intercalation into polymer side chains, shown in a poly[*N*-9′-heptadecanyl-2,7-carbazole-alt-5,5-(4′,7′-di-2-thienyl-2′,1′,3′-benzothiadiazole) (PCDTBT): $PC_{70}BM$ blend system. After solvent vapor annealing in mixed solvent tetrahydrofuran (THF) and carbon disulfide (CS_2), the out-of-of plane GIXS results show that PCDTBT crystals with larger size and higher crystallinity were formed due to enhanced π–π interaction of polymer chain as shown in Fig. 4(d). Moreover, the $PC_{70}BM$ molecules diffused out of polymer chain and formed

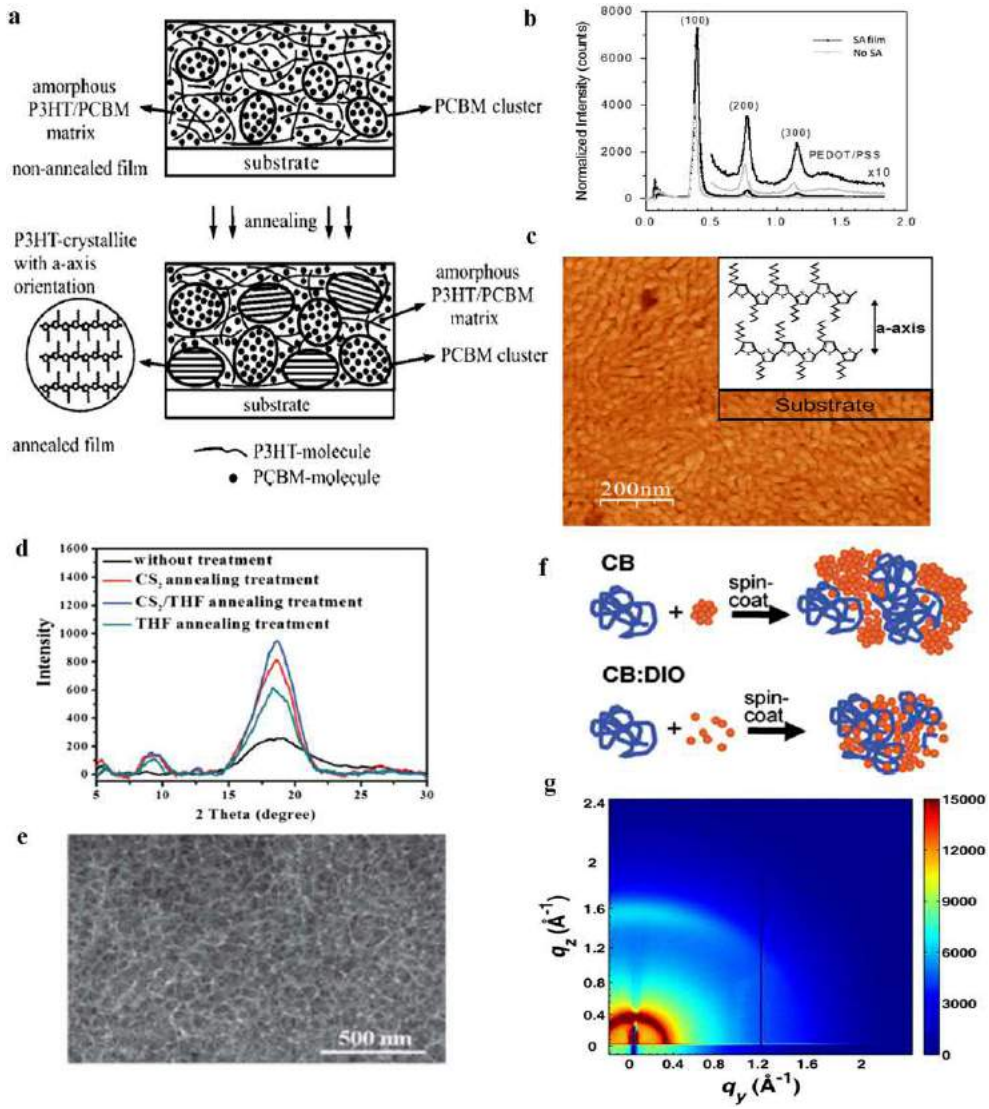


Fig. 4 (a) Schematic of structural change of P3HT:phenyl-C61-butyric acid methyl ester (PCBM) film upon thermal annealing (reproduced from Erb, T., Zhokhavets, U., Gobsch, G., *et al.*, 2005. Advanced Functional Materials 15, 1193–1196); (b) the grazing incidence X-ray scattering (GIXS) result of P3HT:PCBM films formed with and without solvent annealing (SA); (c) atomic force microscopy (AFM) image of solvent annealed P3HT:PCBM film ((b) and (c) 2007. Advanced Functional Materials 17, 1636–1644); (d) the out of plane GIXD profile shows the crystallinity of poly[*N*-9′-heptadecanyl-2,7-carbazole-alt-5,5-(4′,7′-di-2-thienyl-2′,1′,3′-benzothiadiazole) (PCDTBT):$PC_{70}BM$ films and (e) transmission electron microscopy (TEM) images of PCDTBT:PC70BM blend films with mixed solvent vapor annealing ((d) and (e) 2013. Journal of Materials Chemistry A 1, 6216). (f) Working mechanism of poly(4,8-bis-alkyloxybenzo(1,2-b:4,5-b')dithiophene-2,6-diyl-alt-(alkylthieno(3,4-b)thiophene-2) (PBDTTT):PCBM morphology formation with and without additives (reproduced from Lou, S.J., Szarko, J.M., Xu, T., *et al.*, 2011. Effects of additives on the morphology of solution phase aggregates formed by active layer components of high-efficiency organic solar cells. Journal of the American Chemical Society 133, 20661–20663); and (g) the GIXS data of PBDTTT polymer film, showing the face-on orientation of the polymer chain.

large aggregates due to the THF component, which induced phase separation. In addition, owing to the existence of the CS_2 vapor component, the migration ability of PCDTBT chains was improved, which enhanced its self-organization ability and facilitated the formation of nanofibrils (Fig. 4(e)).

Solvent Additive

The addition of small amount solvent additive during film casting is a simple and effective strategy to control morphology of polymer solar cell in many OPV systems.

The addition small amount of 1,8-octanedithiol (ODT) in poly[2,6-(4,4-bis-(2-ethylhexyl)-4H-cyclopenta[2,1-b;3,4-b′] dithiophene)-alt-4,7-(2,1,3-benzothiadia- zole)] (PCPDTBT):PCBM system effectively improve PCE from 2.8 to 5.5%. It's an important and surprising discovery. Alkanedithiol additives do not react with either the polymer or the fullerene and removed

while film drying. The alkanedithiol selectively dissolves the PCBM, but not the donor polymer. The differential solubility and boiling point provide powerful tool to achieve better ordering of donor polymer and control the phase separation. Devices without ODT addition has predominately amorphous structure, while addition 3 wt% of ODT resulted in the nucleation of crystalline PCPDTBT. Time resolved in situ wide angle (WA) GIXS experiments revealed that small amount of ODT simultaneously reduces the nucleation barrier for polymer crystallization, which facilitated reorientation and crystal growth during a prolonged film drying process.

DIO (1,8-diiodoctane) additive in main solvent chlorobenzene (CB) improves the PCE of PTB7:$PC_{71}BM$ polymer solar cell from 3.92 to 7.40%. It was found that the dramatic enhancement of the device performance due to the change in the morphology more uniform, showing good miscibility between PTB7 and $PC_{71}BM$ and form interpenetration networks. The DIO-processed blend films results more homogenous phase separation distance of 20–40 nm. The finer domain size is beneficial for charge separation and transport which enhancing FF. X-ray scattering technique shows that without DIO, the large $PC_{71}BM$ aggregates hinder $PC_{71}BM$ intercalation into the PTB7 network during film formation. DIO selectively dissolves $PC_{71}BM$ aggregates, facilitates integration of $PC_{71}BM$ into PTB7 domain and optimizing both domain sizes with improved donor/acceptor interface (**Fig. 4(f)**).

1-Chloronaphtalene (CN), diphenyl ether (DPE), 1-phenylnaphtalene (PN), 1-naphthalenethiol (SH-NA), diiodohexane (DIH) are also examples of effective additives in polymer solar cell. In fact, PN additive has enabled 11.7% PCE in OPV cell, which promotes face-on polymer backbone orientation, reduces domain size, and increases domain purity. While solvent additives show great performance in efficiency enhancement, one must try to avoid the possible drawbacks. Additives are typically high boiling point. They need to be fully removed, otherwise the film will be too weak mechanically to be used in production, and there are evidences that the remaining additives like DIO accelerates photodegradation of the active layer due to nano-morphology change. This actually leads to a new research direction of high boiling point additive free OPV toward high performance. Mixed solvent of common major organic solvents in OPV such as DCB, CB, CF, etc. sometimes can give better performance in solar cell. This approach actually already exists for over a decade. It is also a straight forward way of control the solvent remove rate.

Active Materials in Polymer Solar Cells

Polymer Active Materials

Polymer active materials are at the core of the polymer solar cell technology. The optimal morphology formation in the device is highly material system dependent. A brief review of some of the key polymer solar cells will be presented below. For detail OPV materials development, there are many excellent review publications on the topic.

One of the earliest PSCs polymers is MEH-PPV, **Fig. 5(b)**), and excellent representative PPV derivative, which is also a good light emitting polymer. MEH-PPV was further improved into poly(2-methoxy-5-(3′,7′-dimethyl-octyloxy))-*p*-phenylene vinylene (MDMO-PPV) (or OC_1C_{10}-PPV) through side chain modification, and efficiency up to 3.5% was realized in MDMO-PPV:$PC_{71}BM$. This is the best before the society figured our ways to conquer the morphology problem in regioregular RR-P3HT:PCBM in ~2005, a decade after the invention of RR-P3HT. Since then, the pace of OPV progress became much faster, and many excellent materials were invented for OPV.

Model polymer RR-P3HT has bandgap of ~1.9 eV, which only allowed about 30% of photon was absorbed. Compared to the silicon band of 1.1 eV and absorption up to 77% of the sunlight, lower bandgap material is a continuously pursuing target of the OPV society. Hsu *et al.* reviewed the low bandgap polymer design strategy for OPV shown in **Fig. 5(a)**, which still largely holds.

RR-P3HT (**Fig. 5(c)**) is an excellent example of the first strategy – stereo regularity induced interchain coupling. The interchain π–π interaction leads to increased ordering and crystallinity in the materials and red shift in absorption. Beyond RR-P3HT, several very effective synthetic strategies have been developed – (1) using alternating electron-rich (donor) and electron-deficient (acceptor) units in the backbone to form the D–A copolymers; (2) tuning the aromaticity and bond length alternation (BLA), which stabilize the lower bandgap quinoid resonance structure over aromatic structure; (3) incorporate strong electron withdrawing substitutes such as carbonyl group or fluorine atoms; (4) incorporating chemically rigid (e.g., larger planarity) unit. Thousands of new compounds have been designed and synthesized for OPV applications. Here are some representative OPV materials in the last decade.

Electron-donating carbazole unit and electron-withdrawing benzothiadiazole (BT) unit-based polymer (PCDTBT) with 1.88 eV bandgap and low lying HOMO (5.5 eV) shows promising PCE of 3.6%, which was later improved to ~7% level. Cyclopenta[2,1-b;3,4-b′]dithiophene (CPDT) and dithieno[3,2-b:2′,3′-d]silole (DTS) units with stronger electron-donating properties were copolymerized with BT unit, and two much lower bandgap polymers (**Fig. 5(d)**) – PCPDTBT (response up to 850 nm) and poly[(4,4'-bis(2-ethylhexyl)dithieno[3,2-b:2',3'-d]silole)-2,6-diyl-alt-(2,1,3-benzothiadiazole)-4,7-diyl] (PSBTBT) (response up to 820 nm) were formed due to the strong intramolecular donor–acceptor interactions. The substitution of C-atom to heavier Si-atom in PSBTBT started the heavy atom substitution approach in the OPV field. The C–Si bond is longer than the C–C bond and less steric hindrance is created in the DTS core by the side chains, leading to a better π–π stacking and enhanced crystallinity. Follow-up work shows replacing Si atom with even heavier Ge atom in carbazole unit can further improve the performance, due to the improved molecular ordering.

A beautiful example of using larger planar unit to improve carrier transport and thus OPV performance is the benzo[1,2-b;4,5-b′]dithiophene (BDT) unit. When copolymerized with thieno[3,4-b]thiophene (TT) series of building blocks, star polymers

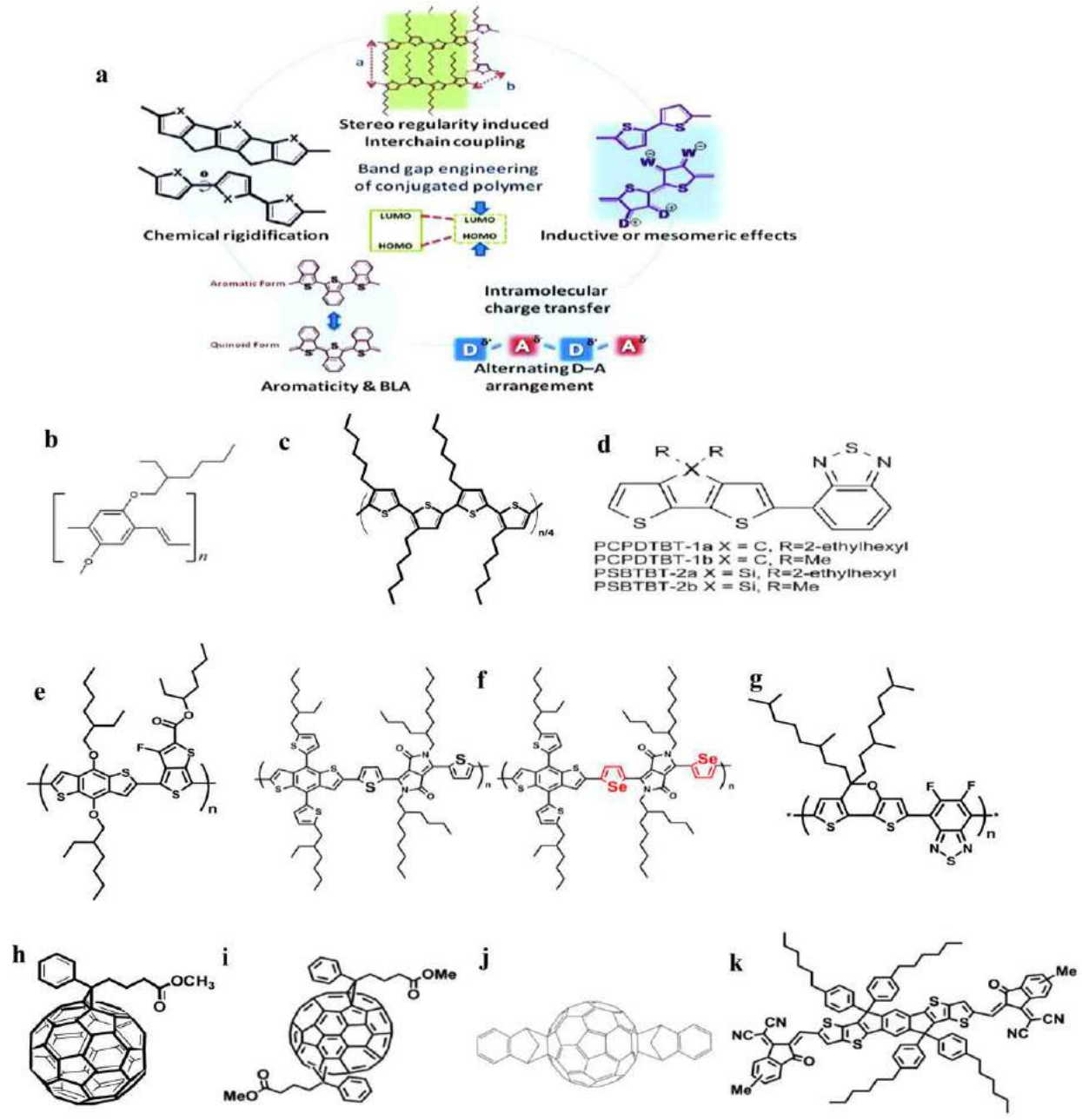


Fig. 5 (a) Design principles for energy level and bandgap tuning in conjugated polymers (reproduced from Cheng, Y.-J., Yang, S.-H., Hsu, C.-S., 2009. Synthesis of conjugated polymers for organic solar cell applications. Chemical Reviews 109 (11), 5868–5923); molecular structures of representative donor polymers; (b) poly[2-methoxy,5-(2′-ethyl-hexyloxy)-p-phenylene vinylene] (MEH-PPV); (c) regioregular poly(3-hexylthiphene) (RR-P3HT); (d) poly[2,6-(4,4-bis-(2-ethylhexyl)-4H-cyclopenta[2,1-b;3,4-b'] dithiophene)-alt-4,7-(2,1,3-benzothiadia- zole)] (PCPDTBT) and poly [(4,4′-bis(2-ethylhexyl) dithieno[3,2-b:2′,3′-d] silole)-2,6-diyl-alt-(2,1,3-benzothiadiazole)-4,7-diyl] (PSBTBT); (e) PTB-7; (f) poly(2,6'-4,8-di (5-ethylhexylthienyl) benzo[1,2-b;3,4-b]dithiophene-alt-5-dibutyloctyl-3,6-bis(5-bromothiophen-2-yl)pyrrolo[3,4-c]pyrrole-1,4-dione) (PBDTT-DPP) and poly{2,6′-4,8-di(5-ethylhexylthienyl)benzo[1,2-b;3,4-b]dithiophene-alt-2,5-bis(2-butyloctyl)-3,6-bis(selenophene-2-yl)pyrrolo[3,4-c]pyrrole-1, 4-dione} (PBDTT-SeDPP) (g) PDTP-DFBT molecular structures of representative acceptors; (h) $PC_{61}BM$; (i) Bis-$PC_{71}BM$; (j) $IC_{61}BA$ and (k) IT-M. HOMO, highest occupied molecular orbital; LUMO, lowest unoccupied molecular orbital.

PTBx, also called PBDT-TT (**Fig. 5(e)**) series of polymers were formed. Further materials improvements include adding a fluorine atom on the TT unit to lower the HOMO level, side chain engineering to tune the solubility, crystallinity, etc. This series of star polymers set the 7, 8, and 9% PCEs milestones of OPV, and still are among the best. It is also a great example that all four synthetic strategies have been used jointly to get the best result. Another example is a high V_{oc} polymer PBDT-TPD formed by copolymerizing BDT unit with strong electron accepting thieno[3,4-c]pyrrole-4,6-dione (TPD) unit.

Diketopyrrolopyrrole (DPP) unit is a strong electron-withdrawing unit, and shows its effectiveness of low bandgap OPV polymer below 1.5 eV. poly(2,6′-4,8-di(5-ethylhexylthienyl) benzo[1,2-b;3,4-b]dithiophene-alt-5-dibutyloctyl-3,6-bis(5-bromothiophen-2-yl)pyrrolo[3,4-c]pyrrole-1,4-dione) (PBDTT-DPP) polymers, a series of D–A copolymers with BDT and DPP unit, show small bandgap of ~1.46 eV, deep HOMO level, and high charge carrier mobility. The reduction of the bandgap and the enhancement of the charge transport properties of PBDTT-DPP can be accomplished by substituting the sulfur atoms on the DPP unit with selenium atoms. The resulted poly{2,6′-4,8-di(5-ethylhexylthienyl)benzo[1,2-b;3,4-b]dithiophene-alt-2,5-bis(2-butyloctyl)-3,6-bis(selenophene-2-yl)pyrrolo[3,4-c]pyrrole-1,4-dione} (PBDTT-SeDPP) (E_g ~1.38 eV, **Fig. 5(f)**) polymer gives single junction devices with PCEs of 7.2%.

Adding two fluorine atom on BT unit leads to strong electron deficient unit difluoro-benzothiadiazole (DFBT) unit. Copolymerized with less electron donating BDT unit (through side chain substitution with alky group), PBDT-DTffBT polymer of 1.7 eV bandgap gives higher V_{oc} and PCE. Asymmetric electron rich dithieno[3,2-b:2′,3′-d]pyran (DTP) unit shows even stronger electron-donating property than BDT unit, and when copolymerized with electron deficient DFBT unit, a regiorandom polymer (PDTP-DFBT) with bandgap 1.38 eV was formed. Even with this low bandgap, high V_{oc} of 0.69V, EQE over 60 and 8.0% PCE single junction device was achieved. In polymer PffBT4T, where DFBT was copolymerized with four thiophene rings, the side chains on two of the thiophene rings were found very critical for the intermolecular interaction between different polymer chains and polymer–fullerene interaction. Generally, larger side chains improve the solubility of polymer by reducing π–π interchain interaction. However, longer alkyl chains were found to be detrimental to the domain size and domain purity. This is a great example of side chain engineering in polymer design. Record 11.7% PCE was achieved in PffBT4T-C_8C_{12}:PCBM system, assisted by the sophisticated morphology control.

Acceptor Materials in OPV

Donor polymer and the acceptor together determine the device performance. The donor polymers are dominantly designed to be compatible with the fullerene derivatives ($PC_{61}BM$ (**Fig. 5(h)**) or $PC_{71}BM$) for a long time.

Fullerene bisadducts based on $PC_{61}BM$ (Bis-$PC_{61}BM$, **Fig. 5(i)**) has ~0.1 eV higher LUMO than that of PCBM, and gives higher V_{oc} and PCE in P33HT system. Indene-C_{60} or Indene-C_{60} bisadduct ($IC_{60}BA$ (**Fig. 5(j)**) or $IC_{70}BA$), via a simple one-pot reaction of indene and fullerene molecules, can achieve higher V_{oc} by over 0.2V, and PCE up to 7.4% in P3HT:ICBA system, which is due to the higher LUMO (by about 0.2 eV).

In addition, n-type polymer-based electron acceptors have also been explored such as F8TBT, CN-PPV and perylene diimide (PDI)-DTT. PDI-based acceptor perylene bisimide (PBI) has lead to 8.4% PCE polymer solar cell. Small molecule nonfullerene acceptor is a new star in the OPV research in the past a few years. Indacenodithieno[3,2-b]thiophene-based nonfullerene acceptor (ITIC), and methyl-modified nonfullerene acceptor (IT-M, **Fig. 5(k)**) are great examples. Poly[(2,6-(4,8-bis(5-(2-ethylhexyl)thiophen-2-yl) benzo[1,2-b:4,5-b′]dithiophene))-co-(1,3-di(5-thiophene-2-yl)-5,7-bis(2-ethylhexyl) benzo[1,2-c:4,5-c′]dithiophene-4,8-dione)] (PBDB-T):IT-M polymer cell reached 11.6% efficiency, while adding Bis-PCBM leads to ternary OPV with 12.2% efficiency – a record, from much preferred nonfullerene acceptor.

Interface and Architectural Engineering

The active materials and the BHJ morphology determines how efficient the active layer harvest solar irradiation, exciton conversion into free carrier, and the free carrier transport to the organic/electrodes interface. The organic/electrode contacts of OPV device determines the charge carrier extraction efficiency into the external circuit. An Ohmic electrical contact is highly desired, as a barrier height of few tens of millielectron volt can result in significant charge accumulation and thus inferior photovoltaic performance. This is true for both the anode and cathode sides of contacts for efficient charge extraction with high selectivity.

In the simplest sandwich OPV structure described by the rigid band metal-semiconductor-metal model, the difference of work function between the anode and cathode provides the driving force for the charge transport and extraction process. Sufficient metal electrodes work function difference is required for the efficient and selective charge collection in the device. Pure metal electrodes, however, are not desired, as the metal surfaces have a high density of defects causing surface recombination or strong surface dipoles at metal/organic interfaces that may harm selective charge extraction.

HTLs

Transparent conductive indium-tin-oxide (ITO) with a high work function of ~4.7 eV is the most widely used transparent electrode in organic electronics. Naturally a solution processible, water-based p-type interface layer poly(3,4-ethylenedioxythiophene):poly(styrene sulfonate) (PEDOT:PSS) (work function ~5.0 eV) was applied to form the ohmic contact with both the ITO and the organic photoactive layer for effective charge collection. Other functions including smoothing the ITO surface and removing potential pinholes, which improves the yield of the device fabrication. The PEDOT:PSS's organic, water absorbing and acidic nature are not preferred for device long-term stability.

p-Type transition metal oxide – NiO*x* is a wide bandgap (direct bandgap, E_g ~3.7 eV), transparent semiconductor with weak absorption bands due to d–d transitions of $3d^8$ electron configuration. Both vacuum sputtered and solution processed forms of

NiO*x* have been demonstrated to be effective HTL materials. With O_2-plasma treatment, the WF of NiO*x* can be increased from 4.7 to 5.3 eV, indicating a doping effect, and very suitable for HTL application. P-type copper oxides CuO*x*, and binary copper oxide such as CuGaO*x*, CuCrO*x* are also recently emerging as effective HTL materials. The binary copper oxide has larger bandgap of over 3 eV – is more suitable for window layer, as compared with visible absorbing pure CuO*x*.

V_2O_5, MoO_3, WO_3 and recently CrO*x*, are also experimental proven to be effective HTL materials in OPV. Surprisingly, it is demonstrated with direct and inverse photoemission spectroscopy measurements that Cr_2O_3, MoO_3, WO_3, and V_2O_5 are n-type materials exhibiting very deep lying electronic states. Ultrahigh vacuum (UHV) prepared MoO_3 by evaporation possesses a 6.86 eV Fermi level, a 6.70 eV EA and 9.68 eV IP. Evaporated transition metal oxides – WO_3 and V_2O_5 with even higher WFs of a $\sim$6.7 eV, and $\sim$7.0 eV, respectively. The fact that they function as HTL may be associated with the multivalence state of metal cation. It worth mentioning that the very different work function from UHV and normal high vacuum evaporation is due to the existence of oxygen in the evaporation case.

Graphene oxide (GO), also water soluble, can also function as HTL in OPVs. In addition to find the interface materials with right work function, the solution proccessibility is a much preferred research topic.

ETLs

Low work function metals are very sensitive to oxygen and moisture – good for device efficiency, but very poor stability and cost perspect. N-type transition metal oxides, such as ZnO and TiO*x*, are proven ETLs in both OLEDs and OPV devices. They have good stability, proper work function, smooth film morphology and solution processibility. TiO*x* and ZnO were also shown to function as a hole blocking layer and optical spacer to modulate the optical field inside thin device to enhance absorption, and thus may help efficiency.

Many compounds with low work-function metal such as Cs_2CO_3, CsF, LiF, $Ca(acac)_2$, etc., which have been proven to be effective ETL in OLED research, are also useful in OPV. Another class of ETL are polyelectrolyte, either conjugated (such as poly [(9,9-bis(3′-(*N*,*N*-dimethylamino)propyl)-2,7-fluorene)-alt-2,7-(9,9-dicotylfluorene)] (PFN) or nonconjugated (e.g., ethoxylated polyethylenimine (PEIE)), can enhance the electron extraction significantly in the OPV devices.

Combining the different ETLs has shown surprising performance improvement. Anatase TiO*x* with Cs_2CO_3 leads to Cs-doping of TiO*x*, and this leads more reliable electron buffer material for OPV and OLED, and it removes the UV photo-catalytic degradation disadvantage of TiO*x* alone in the device. ZnO and PFN double layer ETL was also shown to be of enhanced efficiency in OPV device.

Inverted OPV Device

Some ETL materials can convert the given high work function ITO transparent electrode into low work function contact. This provides the versatility in device polarity. Fig. 6(a) shows the 2006 UCLA work on the formation of inverted OPV by using Cs_2CO_3 ETL to convert ITO into low work function contact, and use transition metal oxide (V_2O_5) as HTL.

Different forms of TiO*x*, ZnO (sol–gel, nanoparticle), PFN, etc. were also shown to be able to enable low WF contact on transparent electrode. Ultraviolet photoemission spectroscopy gives clear evidence of the large WF reduction after these ETL applied on ITO, for example. ETLs like LiF does not have such effect. On the other side, MoO*x* is the most popular HTL used in inverted polymer solar cell.

Fig. 6(b) shows the device structure, the molecular structure of PFN ETL, and active layer polymer PTB7 in the over 9% PCE inverted polymer solar cell. Fig. 6(c) is the energy diagram of the inverted OPV device.

Tandem OPV Devices

Single junction solar cell has its theoretical limit. Shockley and Queisser proposed detailed balance model to predict the efficiency limit for p–n junction solar cells. The biggest two major losses under the S–Q assumptions (Fig. 7(a)) are (1) below bandgap loss – photons with energy higher than bandgap of absorbers can be completely absorbed, while photons below the bandgap just pass through without any absorption; (2) the thermolization loss – photons of higher energy than the bandgap energy will thermally relax, and the excess energy loses. While lower bandgap materials absorb more sunlight, and potentially higher photocurrent, the larger bandgap materials will win in the photovoltage side. Therefore a delicate balance exists in the theoretically optimization of bandgap, and $\sim$1.4 eV is the optimal bandgap of solar cell material under terrestrial illumination, with theoretical limit of $\sim$31%. The most effective way in overcoming S–Q limit is the multijunction or tandem structure, which consists of several semiconductors with different and complement bandgaps to have better coverage of the solar spectrum. The careful designed system will use the solar photons much more effectively by reducing the thermal loss. For example, theoretically three-junction solar cell design raises the ceiling to $\sim$50%.

For disordered solar cell system with lower efficiency like OPV, the tandem structure is a clear go for higher efficiency. The preferred way is the solution process tandem solar cell, as it has the potential of higher efficiency without losing the low-cost edge. The structure of tandem solar cell is more complex. Besides the two photoactive subcells, the interconnection layer connecting the two subcells is very important. In inorganic multijunction solar cells, the interconnection layer is heavy doped p–n

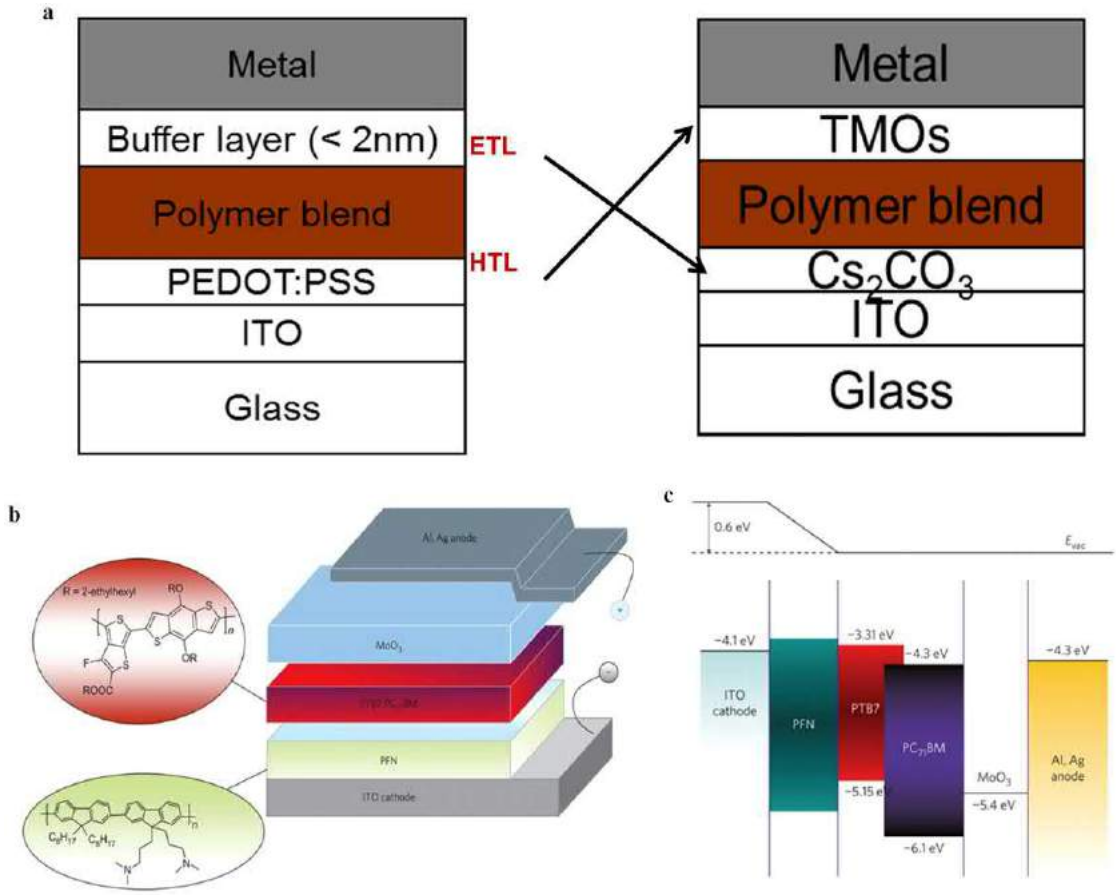


Fig. 6 (a) The formation of inverted organic conjugated polymers-based solar cells (OPVs) by switching position of electron transport layer (ETL) and hole transport layer (HTL); (b) device structure of inverted OPV using poly[(9,9-bis(3′-(*N*,*N*-dimethylamino)propyl)-2,7-fluorene)-alt-2,7-(9,9-dicotylfluorene)] (PFN) as ETL and PTB7 as active polymer; (c) energy diagram of the inverted OPV device. ITO, indium-tin-oxide; PEDOT:PSS, poly(3,4-ethylenedioxythiophene):poly(styrene sulfonate). ((b) and (c)) Reproduced from He, Z., Zhong, C., Su, S., *et al.*, 2012. Enhanced power-conversion efficiency in polymer solar cells using an inverted device structure. Nature Photonics 6, 591–595.

($p^{++}n^{++}$) tunneling junction, which has the opposite direction than that of the two subcells to produce photvoltage of the same direction.

In organic polymer solar cell, the extensive interface engineering research provide many high quality p-type and n-type interface layers to choose. In polymer tandem solar cells, the interfacial layers should also provide physical protection to the underlying subcells. Here we only provide a brief introduction on the topic.

In the beginning, the simple way of making tandem device was using semitransparent solar cell, which differ from the normal solar cell by a thin layer of thermally evaporated metal as semitransparent electrode. Tandem solar cell by stacking two or more semitransparent solar cells (allow one to be normal nontransparent cell) has four terminals, and can be connected either in series or in parallel. The configuration has clear disadvantage in optical loss, materials (substrate/TCO) cost, and was used mainly for proof of concept. Early efforts typically use subcells with same active materials, for example, P3HT:$PC_{61}BM$, PCDTBT:$PC_{61}BM$, and the efficiency was not really improved. Monolithic integrated tandem solar cell on one substrate is the more preferred way.

Heterogeneous polymer tandem solar cells with complemented spectrum coverage is the main stream research direction. In principle the complemented spectrum coverage is required for the current matching of two subcells, the high and low bandgap combination also leave the opportunity of reducing thermolization loss.

The two most important components in heterogeneous tandem polymer cells are (1) the spectrum complemented active layers in two subcells, and (2) the interconnection layer. In the spectrum complemented active layer, the classical, process well controlled P3HT is a model high bandgap polymer subcell. The 1.9 eV bandgap is similar to the high bandgap component in inorganic multijunction solar cell. It's thus a long time trend in tandem OPV field to pursue high performance polymer at ~1.4 eV bandgap, which is lower than the optimal bandgap in OPV research. In interconnection layer, there are also two major device architectures just like in single junction OPV device, i.e., conventional tandem and inverted tandem OPV device (Fig. 7(b)). A few milestones in the tandem OPV devices are the following.

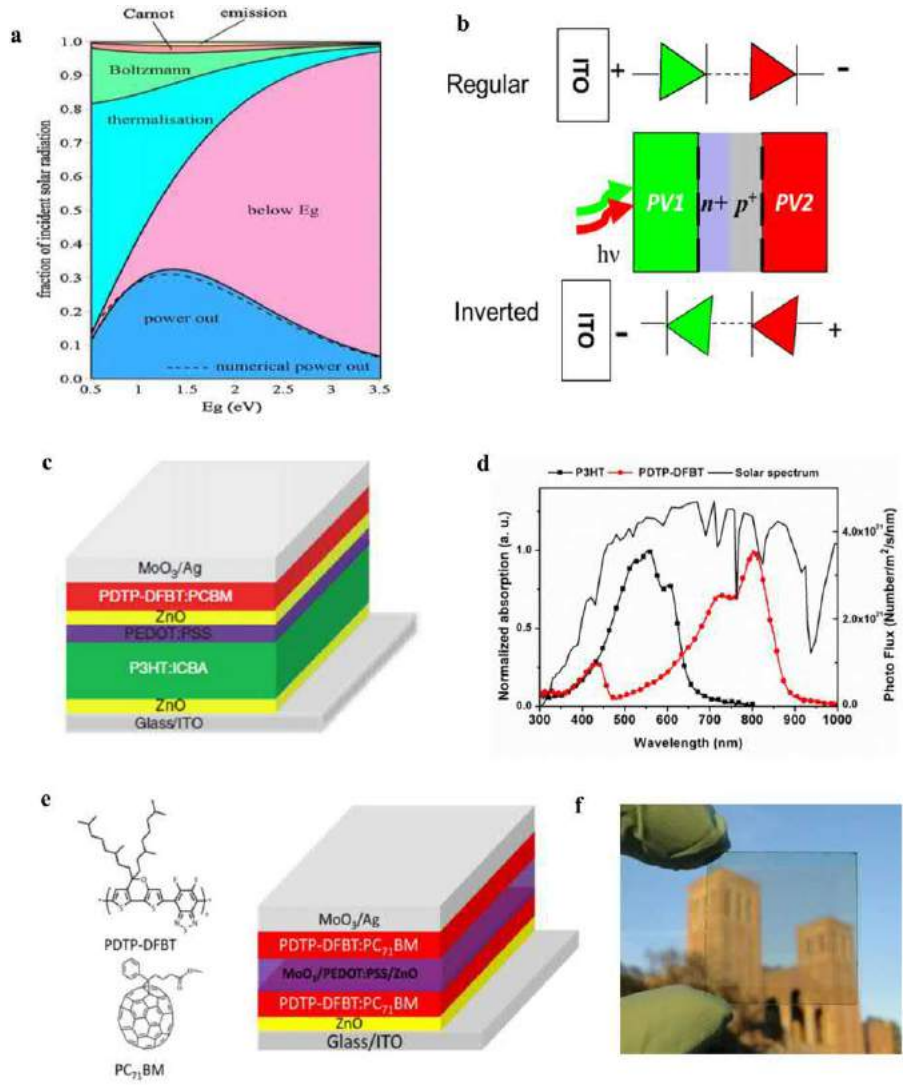


Fig. 7 (a) Loss mechanism and efficiency limitation of single junction solar cell as a function of semiconductor bandgap (reproduced from Hirst L.C., Ekins-Daukes N.J., 2011. Fundamental losses in solar cells. Progress in Photovoltaics: Research and Applications 19, 286–293); (b) diagram of conventional tandem and inverted tandem organic conjugated polymers-based solar cell (OPV) devices; (c) device structure of, and (d) wide and low bandgap polymers in the 10.6% certified tandem OPV device ((c) and (d) reproduced from You, J., Dou, L., Yoshimura, K., 2013. Nature Communications 4, 1446); (e) molecule structures and device structure of a homogeneous tandem OPV device (reproduced from You, J., Chen, C.-C., Hong, Z., *et al.*, 2013. 10.2% Power conversion efficiency polymer tandem solar cells consisting of two identical sub-cells. Advanced Materials 25, 3973–3978); and (f) picture of an all solution process visibly transparent OPV device. ITO, indium-tin-oxide.

Conventional tandem polymer solar cell – UCSB group reported solution processed TiO_2(n-type)/PEDOT:PSS (p-type) as interconnecting layer, and subcells are based on (1) low bandgap PCPDTBT:$PC_{61}BM$ front cell, and (2) wide bandgap P3HT and $PC_{71}BM$ rear cell. With the front and rear cell of 3.0% and 4.7% efficiency, respectively, a 6.5% tandem device was achieved. Improving both cells to P3HT:ICBA and PSBTBT:PCBM, and traducing MoO_3 into interconnection layer, UCLA improved the tandem efficiency to 7%. Another popular interconnection layer is based on ZnO(*n*)/pH-neutral PEDOT:PSS (p) from a Netherland group.

Inverted tandem polymer solar cells – UCLA used low bandgap polymer PBDTT-DPP ($\sim$1.44 eV bandgap):$PC_{71}BM$ as rear cell and P3HT:ICBA as front cell, modified PEDOT:PSS/ZnO as interconnection layer, 8.62% NREL certified tandem efficiency was achieved. Further reducing the bandgap of LBG polymer by replacing S to heavier atom Se, polymer PBDTT-SeDPP has bandgap of 1.38eV. The better spectrum complementation and higher hole mobility lead to 9.5% tandem PCE. PDTP-DFBT:$PC_{71}BM$ as LBG subcell gives even better performance, and the first double digit certified tandem polymer solar cell PCE of 10.6% (**Fig. 7(c)** and **(d)**).

Homogeneous tandem solar cell, in which the subcells adopt the same active materials, is not supposed to reduce thermalization loss in principle. But homogeneous tandem polymer solar cells were shown to be able to enhanced the solar cell efficiency

over single junction cell. For example, tandem cell with two identical PDTP-DFBT:$PC_{71}BM$ subcells showed a PCE enhancement of over 25% – from 8 to 10.2% (Fig. 7(e)). It is worth mentioning that when the HOMO level of polymer is deeper, such as PDTP-DFBT, PEDOT:PSS will not able to provide good enough energy alignment and hole transport function. Higher work function material MoO_3 was used to form a three layer MoO_3/PEDOT:PSS/ZnO interconnection layer for this efficient homogeneous tandem cell. Tandem cell with two identical PTB7-Th:$PC_{71}BM$ subcells showed a PCE enhancement from ~9% to over 11%. The enhancement originates from the weakness of typical polymer solar cell materials (even champion materials like PDTP-DFBT and PTB7-Th) – the limited thickness for optimal device due to the low carrier mobility. Therefore using two thinner subcells to form tandem cell can overcome the limitation and achieve higher performance.

Triple junction tandem polymer solar cell was also successfully demonstrated. Based on the 10.6% heterogeneous tandem cell, a midbandgap PTB7-Th:PCBM cell was added into the device, and the efficiency was enhanced to 11.6%. The higher work function component in interconnection layer was further improved from thermally evaporated MoO_3 into solution processed WO_3. The success of the all solution processed triple junction polymer solar cell represents an important technology progress.

The donor–acceptor type low bandgap polymers, when goes below 1.4 eV bandgap, many have the absorption spectrum that absorb in UV and near infrared (NIR), but very low absorption in visible range. This makes possible high performance visibly transparent solar cells. Fig. 7(f) shows such a cell, where the top transparent electrode is from silver nanowire ink, and the whole process is free from vacuum. Other transparent electrode techniques include thin metal layer(s), dielectric/metal/dielectric multilayer, carbon nanotube, conducting polymer, polymer-CNT, polymer-metal nanowire composites etc. Transparent tandem solar cell can be used to tune the color, and achieve higher efficiency. Currently 7% transparent tandem solar cell has been realized with relatively high visible transparency. This shows how versatile the technology is, and broad applications the technology can offer.

Polymer solar cell research is very active with continuous discoveries and breakthroughs coming out. Future new polymer donor and acceptor materials, deep understanding and control of morphology, device structure innovations will continue improve OPV performance, establish it as a nontoxic, low cost, flexible and transparent form factor clean energy solution for novel PV applications.

See also: Light Harvesting in Organic Solar cells

Further Reading

Bae, S.-H., *et al.*, 2016. Printable solar cells from advanced solution-processible materials. Chem 1, 197–219. dx.doi.org/10/1016/j.chenpr.2016.07.010.
Chen, H.Y., *et al.*, 2010. Silicon atom substitution enhances interchain packing in a thiophene-based polymer system. Advanced Materials 22, 371–375.
Cheng, Y.-J., Yang, S.-H., Hsu, C.-S., 2009. Synthesis of conjugated polymers for organic solar cell applications. Chemical Reviews 109 (11), 5868–5923.
Dou, L., *et al.*, 2015. Low-bandgap near-IR conjugated polymers/molecules for organic electronics. Chemical Reviews 15 (23), 12633–12665.
Guo, X., *et al.*, 2012. High efficiency polymer solar cells based on poly(3-hexylthiophene)/indene-C70 bisadduct with solvent additive. Energy & Environmental Science 5, 7943.
He, Z., *et al.*, 2015. Single-junction polymer solar cells with high efficiency and photovoltage. Nature Photonics 9, 174–179.
Hirst, L.C., Ekins-Daukes, N.J., 2011. Fundamental losses in solar cells. Progress in Photovoltaics: Research and Applications 19, 286–293.
Liang, Y., *et al.*, 2010. For the bright future-bulk heterojunction polymer solar cells with power conversion efficiency of 7.4%. Advanced Materials 22, 135–138.
Li, G., *et al.*, 2005. High-efficiency solution processable polymer photovoltaic cells by self-organization of polymer blends. Nature Materials 4, 864–868.
Li, N., Brabec, C.J., 2015. Air-processed polymer tandem solar cells with power conversion efficiency exceeding 10%. Energy & Environmental Science 8, 2902–2909.
Peet, J., *et al.*, 2007. Efficiency enhancement in low-bandgap polymer solar cells by processing with alkane dithiols. Nature Materials 6, 497–500.
Pope, M., Swenberg, C.E., 1999. Electronic Processes in Organic Crystals and Polymers. New York: Oxford University Press.
Shockley, W., Queisser, H.J., 1961. Detailed balance limit of efficiency of p-n junction solar cells. Journal of Applied Physics 32, 510–519.
Yu, G., *et al.*, 1995. Polymer photovoltaic cells – Enhanced efficiencies via a network of internal donor–acceptor heterojunctions. Science 270, 1789–1791.
Zhao, W., *et al.*, 2016. Fullerene-free polymer solar cells with over 11% efficiency and excellent thermal stability. Advanced Materials. 4734–4739.

Dye-Sensitized Solar Cells

Lu-Yin Lin, National Taipei University of Technology (Taipei Tech), Taipei, Taiwan
Kuo-Chuan Ho, National Taiwan University, Taipei, Taiwan

© 2018 Elsevier Ltd. All rights reserved.

History

The concept of dye-sensitized solar cells (DSSCs) based on a TiO_2 thin film originated from the year of 1972 (Fujishima and Honda, 1972). By constructing a chlorophyll-sensitized zinc oxide electrode, the photons were converted into electricity via the charge injection from the exited dye molecules into a wide band gap semiconductor for the first time (Tributsch, 1972). Numerous researchers started to study zinc oxide-based DSSCs since then. However, the relevant solar-to-electricity conversion efficiency is poor, probably due to flat surface of the semiconductor to provide only monolayer adsorption of the sensitizer. A breakthrough development was realized in the year of 1991 by Grätzel and his coworkers at the Laboratory of Photonic and Interfaces in the École Polytechnique Fédérale de Lausanne in Switzerland. They introduced nanoporous TiO_2 electrodes with rough surface to increase the light harvesting efficiency and successfully achieved a solar-to-electricity conversion efficiency (η) of 7% (O'Regan and Gratzel, 1991). Afterwards DSSCs experience a rapid growth since 2009, as shown in the annual publication number summarized in **Fig. 1**. In the year of 2011, a recorded η value of 12.3% was obtained for the DSSC composed of a zinc porphyrin dye (YD2-o-C8) co-sensitized with another organic dye (Y123) (**Fig. 2**), and $Co^{(II/III)}$ tris(bipyridyl)-based redox electrolyte (Yella *et al.*, 2011). In the year of 2014, a DSSC coupled with a zinc porphyrin dye and $Co^{(II/III)}$ tris(bipyridine)-based redox electrolyte achieved an impressive η value of 13.00% (Mathew *et al.*, 2014). Right after this achievement, a recorded η value of 14.30% was attained for a DSSC composed of the metal-free organic co-sensitizers and the redox electrolyte based on $Co^{(II/III)}$ tris(phenanthroline) in the year of 2015 (Kakiage *et al.*, 2015). These breakthroughs inspire the researchers to pursue economical photovoltaic devices based on DSSCs more eagerly for the years to come.

Mechanism and Parameters

When the light illuminated the DSSC, the incident photons are absorbed by sensitizers adsorbed on the semiconductor surface. The sensitizers are excited from the ground state (S) to the excited state (S^*). Then the excited electrons would inject into the conduction band of the semiconductor, generating the oxidation of the sensitizer (S^+). These processes can be represented as Eqs. (1) and (2).

$$S + h\nu \rightarrow S^* \tag{1}$$

$$S^* \rightarrow S^+ + e^-(\text{semiconductor}) \tag{2}$$

The injected electrons in the conduction band of the semiconductor would transport toward the conducting substrate, and then the electrons would reach the counter electrode (CE). Then the oxidized photosensitizer (S^+) would accept the electrons transported from the I^- ion redox mediator, and then be regenerated to the ground state (S), as shown in Eq. (3).

$$S^+ + e^- \rightarrow S \tag{3}$$

Simultaneously the I^- would be oxidized to I_3^- and diffuse toward the CE. Finally, it is reduced to I^- at the CE, as shown in Eq. (4).

$$I_3^- + 2e^- \rightarrow 3I^- \tag{4}$$

The energy level diagram of a DSSC and the electron transfer routes are shown in **Fig. 3**.

Like other solar cells, the performance of the DSSC can be evaluated by using the open-circuit voltage (V_{oc}), the short-circuit current density (J_{SC}), the fill factor (FF), the solar-to-electricity conversion efficiency (η), the incident photon-to-current conversion efficiency (IPCE), and the charge transfer resistances measured by using the electrochemical impedance spectroscopy (EIS).

V_{OC} is determined by the difference in energy of the electron at the semiconductor and the CE for a typical photoelectrochemical cell, or the difference in energy level of the quasi-Fermi level of the semiconductor under illumination and the Nernst potential of the electrolyte solution. V_{OC} is measured with no current flow and is the maximum voltage which the DSSC can provide to an external circuit. Eq. (5) shows the relation of photovoltaic parameters to V_{OC} for regenerative photoelectrochemical systems.

$$V_{OC} = V_T \ln\left(1 + \frac{J_{SC}}{J_0}\right) \tag{5}$$

where V_T is the thermal voltage and J_0 is the reverse saturation current density.

J_{SC} is the maximum output current of a DSSC and is measured under illumination at the zero voltage across the cell. The magnitude of J_{SC} is determined by the product of the optical absorption efficiency, charge collection, and the solar irradiance,

 doi:10.1016/B978-0-12-803581-8.09545-X

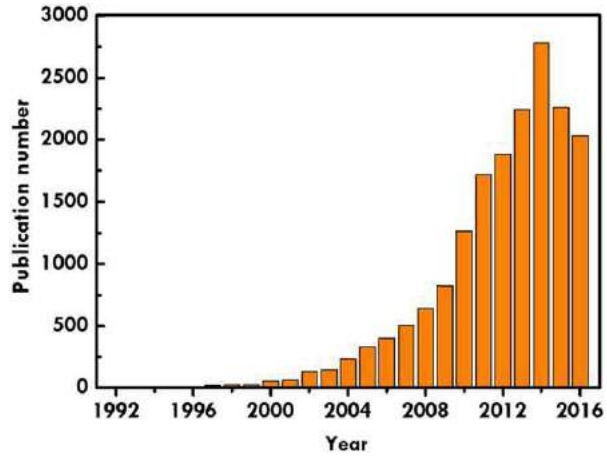
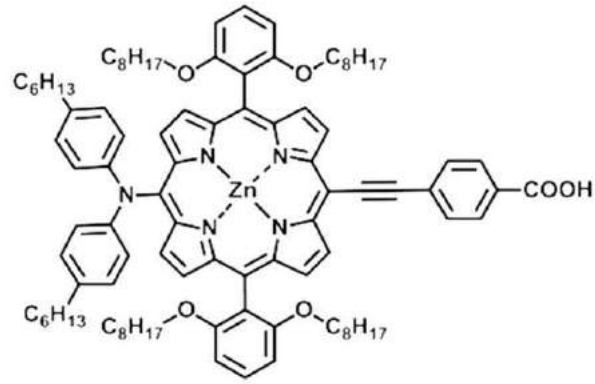
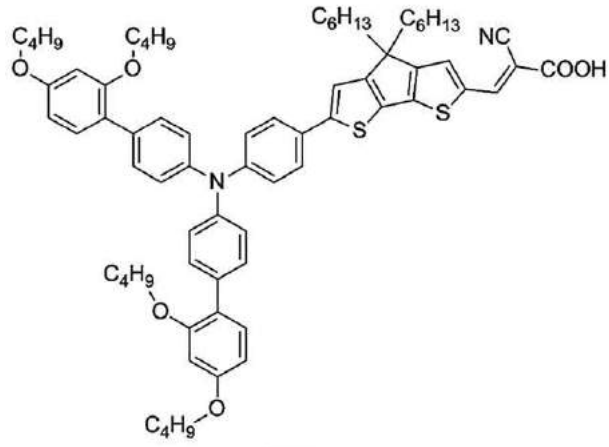


Fig. 1 Number of publications on the subject of dye-sensitized solar cells (DSSCs) from 1991 to December 2016. *Source*: Scopus.



YD2-o-C8



Y123

Fig. 2 The chemical structures of YD2-o-C8 and Y123 dyes.

integrated over the whole wavelengths of the incident light spectrum, as shown in Eq. (6).

$$J_{SC} = \int \left(1 - 10^{-\mathrm{Abs}}(\lambda)\right) \times \mathrm{IQE}(\lambda) \times e \times \Phi(\lambda) d\lambda \tag{6}$$

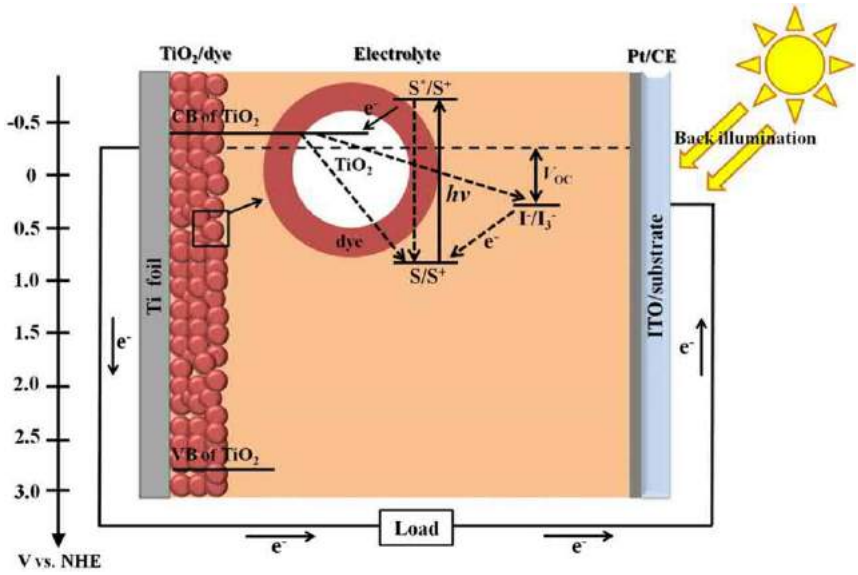


Fig. 3 The energy level diagram of a dye-sensitized solar cell (DSSC) and the illustration of the electron transfer routes in the DSSC.

where Abs(λ) is the absorbance of the sensitizer as a function of the wavelength λ, e is the elementary electron charge, and $\Phi(\lambda)$ is the standard AM 1.5 irradiance spectrum. IQE(λ) is the internal quantum efficiency for the hot electron injection, dye regeneration, and then charge collection.

FF is defined as the ratio of the maximum power output (P_{max}) from a DSSC to the product of V_{OC} and J_{SC}. The fill factor can be calculated by using Eq. (7).

$$FF = \frac{P_{max}}{V_{OC} \times J_{SC}} = \frac{V_{max} \times J_{max}}{V_{OC} \times J_{SC}} \tag{7}$$

where V_{max} and J_{max} respectively represent the photovoltage and photocurrent density corresponding to P_{max}.

η depends on the total light intensity, the intensity spectral distribution, and the DSSC temperature. The η of a DSSC is calculated as the ratio between the maximum generated power (P_{max}) and the incident power (P_{in}). The incident power is equal to the irradiance of the AM1.5 spectrum normalized to 1000 W/m^2. Hence, the η of a DSSC can be determined by the V_{OC}, J_{SC}, FF, and P_{in}, as shown in Eq. (8) as follows.

$$\eta = \frac{P_{max}}{P_{in}} \times 100\% = \frac{V_{OC} \times J_{SC} \times FF}{P_{in}} \times 100\% \tag{8}$$

A typical current density–voltage curve is shown in **Fig. 4** with the V_{OC}, J_{SC} and P_{max} indicated in the figure.

IPCE is defined as the ratio of the number of photo-generated electrons ($N_{electrons}$) flowing in the external circuit to the number of incident photons ($N_{photons}$) with a given wavelength, as shown in Eq. (9).

$$IPCE(\lambda) = \frac{N_{electrons}}{N_{photons}} \tag{9}$$

IPCE is also referred to as the external quantum efficiency (EQE). IPCE or EQE value is most often expressed as the percentage of the absorbed incident photons and the converted electrons as a function of the wavelength. The internal quantum efficiency (IQE) is also reported which represents the number of absorbed photons converted to electrons and indicates that how efficient the numbers of absorbed photons are converted into current. The IPCE value can also be calculated using Eqs. (10) and (11) as follows.

$$IPCE(\lambda) = LHE(\lambda) \times IQE(\lambda) \tag{10}$$

$$LHE(\lambda) = 1 - 10^{-Abs}(\lambda) \tag{11}$$

where LHE(λ) is the light-harvesting efficiency.

Thus, the J_{SC} can also be represented as Eq. (12) as follows.

$$J_{SC} = \int IPCE(\lambda) \times e \times \Phi(\lambda) d\lambda \tag{12}$$

where e is the elementary charge and $\Phi(\lambda)$ is the photon flux.

It is important and useful to examine the IPCE(λ) value not only in getting further information of IQE(λ) or other parameters, but also in examining the validity of the measured photocurrent. If the measured J_{SC} value showed a discrepancy from the integral IPCE results in Eq. (12), there would be a spectral mismatch or variance between the solar simulator and the true solar emission.

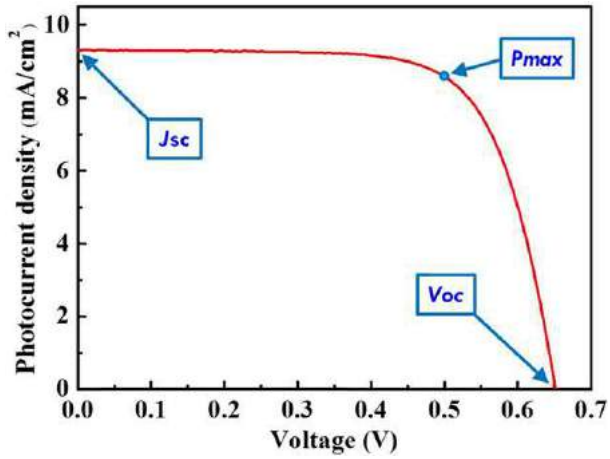


Fig. 4 A typical current density–voltage (J–V) curve with the V_{OC}, J_{SC}, and P_{max} indicated.

The steady state J–V measurements can only provide limited information about the electron transport and recombination rates. Hence, a dynamic technique like the EIS is required to study the charge transfer kinetics and therefore to get the information about the resistance and capacitance of different components in DSSCs. The primary investigated resistance at the interfaces of DSSCs from the charge transfer processes are the series resistance (R_S), the recombination resistance at the semiconductor/dye/electrolyte interface (R_{ct1}), the electron transfer resistance in the CE (R_{ct2}), and the diffusion resistance of the electrolyte causes (Z_w), which can be fitted from the Nyquist plot measured using the EIS technique. Fig. 5 shows a typical Nyquist plot for a DSSC, in which the corresponding portions for fitting to get various resistances are also labeled in this figure.

Constructions

A DSSC is composed of a photoanode, a CE, and in-between embedded an electrolyte.

Photoanode

The photoanode is one of the important components of DSSC because of its functions in adsorbing dye molecules and transferring electrons. A high electron transport rate is required to reduce electron–hole recombination rate and enhance the conversion efficiency. The photoanode is consisted of a conducting substrate, a semiconductor layer deposited on the top of the substrate, and a sensitizer adsorbed on the semiconductor layer.

Conducting substrates

The selection of suitable conducting substrates is the key factor to determine the cost and the fabrication process of DSSCs, and therefore to influence the cell performance and long-term stability. Traditionally, transparent conducting oxide (TCO) glasses were utilized as the substrate of DSSCs, for example, fluorine-doped tin oxide (SnO_2:F) (FTO), tin-doped indium oxide (In_2O_3:Sn) (ITO), and aluminum-doped zinc oxide (ZnO:Al) (AZO) glasses. Despite of their good stability against oxygen and water, the shortages of high cost, fragility, rigidity, and shape limitations restrict their practical applications. In addition, the roll-to-roll production process cannot be used for this system. Therefore, flexible substrates with light weight and easy transportation properties have become an alternative choice.

One kind of the flexible substrates is conducting plastics, for example, ITO coated polyethyleneterephtalate (ITO/PET) and ITO coated polyethylenenaphtalate (ITO/PEN). The critical challenge for conducting plastics lies in the low temperature preparation of TiO_2 layer since their maximum endurable temperature is around 150°C. Normally the TiO_2 layer is sintered at higher temperature of around 400–500°C to get good electrical contact among particles. Additionally, the typical TiO_2 paste contains organic binder and viscous solvents which should be removed in a high temperature sintering process. Mechanical compression of nanocrystalline semiconductor powder and hydrothermal synthesis of metal oxide nanocrystals have been proposed to avoid applying the high temperature sintering process. Other kind of the flexible substrates is metal foils, which possess inherent high conductivity, light scattering, and high-temperature sintering abilities, for example, stainless steel (StSt), titanium foils, and zinc foils. Among them, the best is the Ti foil-based DSSC because of its characteristics of higher conductivity and superior corrosion resistance resulted from the existence of a passive film of TiO_2 on the surface of a Ti foil. However, there remain two major challenges to overcome for metal-based DSSCs. First, metal substrates are non-transparent and the pertinent DSSCs have to be illuminated from the back side, i.e., the Pt CE side. A loss of about 25% incident solar energy is encountered because the Pt CE partially reflects light and iodine in the electrolyte absorbs photons in the near UV region. Secondly, there would be serious formation of metal oxides after sintering, leading to the increase in the interfacial resistance and therefore the cell performance is reduced.

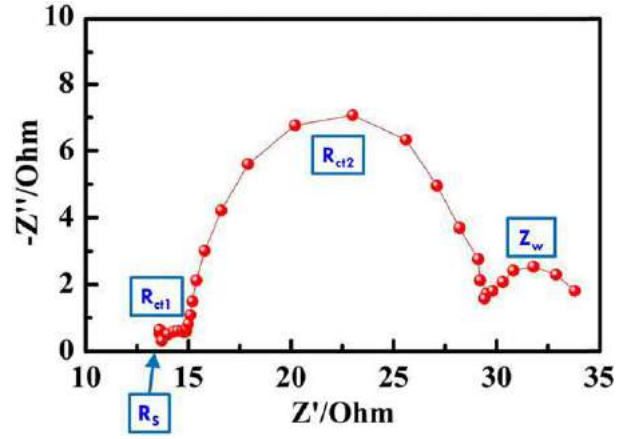


Fig. 5 A typical Nyquist plot for a dye-sensitized solar cell (DSSC).

Table 1 A partial list of the photovoltaic performance for the dye-sensitized solar cells (DSSCs) using different semiconductors on the photoanode

Semiconductor	*Dye*	V_{OC} *(V)*	J_{SC} *(mA/cm²)*	*FF (%)*	*η (%)*
TiO_2[a]NP	N719	0.85	17.7	75	11.18
TiO_2[b]NR	N719	0.74	8.9	67	4.40
TiO_2[c]NF	N719	0.77	8.7	60	4.01
TiO_2[d]NT	Orange G	0.68	7.2	61	2.91
TiO_2[a]NP/TiO_2[d]NT	CYC-B1	0.71	12.9	73	6.68
ZnO[a]NP	N719	0.56	5.1	46	1.30
ZnO[b]NR	D149	0.58	2.8	40	0.66
ZnO[c]NF	N719	0.60	3.6	62	1.34
ZnO[a]NP/ZnO[b]NR	N719	0.59	7.0	52	2.17
SnO_2 hollow spheres	N719	0.77	14.6	54	6.02
SnO_2 flowers	N3	0.63	7.2	55	2.50
SnO_2[e]NC	N719	0.56	6.7	34	1.29
SnO_2[f]NS	N719	0.65	11.5	45	3.34
Nb_2O_5[c]NF	N3	0.77	6.7	59	3.05
Nb_2O_5[e]NC	N3	0.64	17.6	40	4.48
Nb_2O_5[g]NW	N3	0.77	6.7	59	3.05
Nb_2O_5 mountains	N719	0.59	10.7	53	3.35

[a]NP = nanoparticles
[b]NR = nanorods
[c]NF = nanofibers
[d]NT = nanotubes
[e]NC = nanochanneal
[f]NS = nanosheet
[g]NW = nanowire.

Semiconductor layers

The semiconductor layer is a junction with a large contact area between two continuous networks for dye adsorption and allows electron transferring through the DSSC.

Mesoporous oxides are the most commonly used materials as the semiconductor layer, including TiO_2, ZnO, SnO_2, and Nb_2O_5. **Table 1** lists the photovoltaic performance for the DSSCs using different semiconductors on the photoanode. The nanocrystalline TiO_2 is the most applied material because of its cheap, abundant, and nontoxic characteristics. The band gap of anatase TiO_2 is 3.2 eV at an absorption edge of 388 nm and that of rutile TiO_2 is 3.0 eV at an absorption edge of 413 nm. The crystalline of TiO_2 is classified into anatase, brookite, and rutile. The illustration for the crystal structures of TiO_2 is shown in **Fig. 6** (Zhang *et al.*, 2014). Anatase and rutile phases are the main TiO_2 crystallines but the brookite TiO_2 is rarely existed, which remains stable only at the temperature higher than 600°C. Moreover, rutile TiO_2 absorbs 4% of incident light in the near-UV region, resulting in generation of holes which would reduce the long-term stability of DSSCs (Yuvapragasam *et al.*, 2015). Therefore, anatase TiO_2 is most suitable as the semiconductor layer on the photoanode of DSSCs. The high dielectric constant of TiO_2 ($\varepsilon = 80$

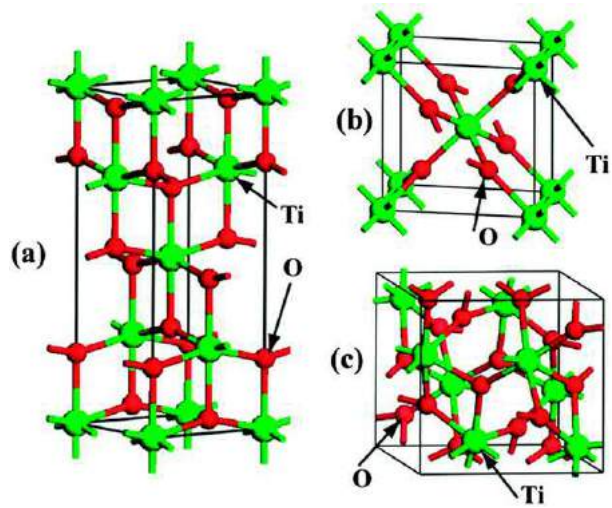


Fig. 6 TiO_2 crystallographic phases of (a) anatase, (b) brookite and (c) rutile. Reproduced with permission from Zhang, J., Zhou, P., Liu, J., Yu, J., 2014. New understanding of the difference of photocatalytic activity among anatase, rutile and brookite TiO_2. Physical Chemistry Chemical Physics 16, 20382. Copyright (2014) by Royal Society of Chemistry.

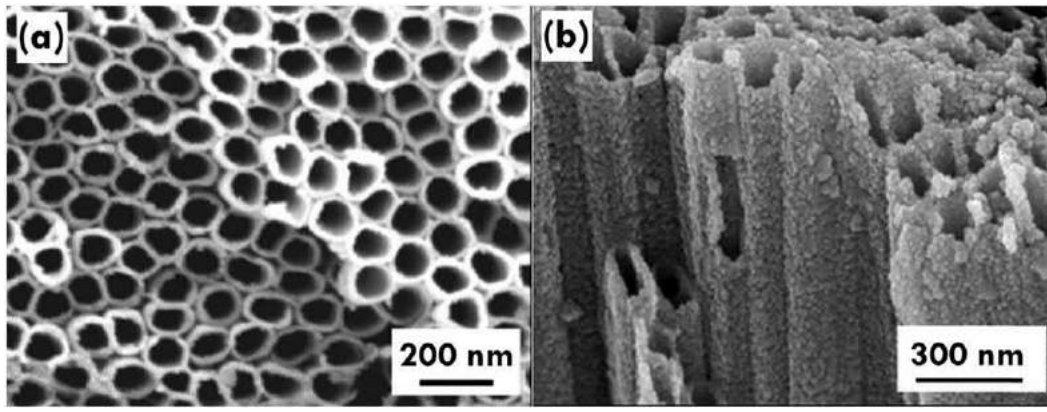


Fig. 7 (a) The top-view and (b) the side-view scanning electron microscope (SEM) images for the 1D TNT array. Reproduced with permission from Lin, L.Y., Yeh, M.H., Lee, C.P., Chen, Y.H., Vittal, R., Ho, K.C., 2011. Metal-based flexible TiO2 photoanode with titanium oxide nanotubes as the underlayer for enhancement of performance of a dye-sensitized solar cell. Electrochimica Acta 57, 270. Copyright (2011) by Elsevier.

for anatase) provides good electrostatic shielding of the injected electron from the oxidized dye molecule, thus preventing the electrons from recombination before the reduction of the dye molecule by the electrolyte. High refractive index of TiO_2 ($n=2.5$ for anatase) results in efficient diffuse scattering of light inside the porous photoanode and hence significantly enhances the light absorption.

Most photoanodes of DSSCs were based on a nanocrystalline TiO_2 film with a particle size of about 20 nm. However, the performance of the pertinent DSSCs was limited by its slow electron transport, which is in the range of a few milliseconds. The random distribution of the TiO_2 particles and the associated structural disorder of the film lead to an enhancement on the dye-injected free electrons scattering, and thereby to a reduction of electron mobility. Therefore, altering the morphology and structure of the TiO_2 film is one of the strategies for improving the efficiency of a DSSC. Several nanotubular architectures have been investigated for potential enhancement of electron percolation pathways as well as for improved ion diffusion at the semiconductor/electrolyte interface. Ordered and strongly interconnected nanoscale architecture of a TiO_2 film enables a great improvement in the electron transport in the film, for example, a vertically oriented array of one-dimensional (1D) TNTs (**Fig. 7**), which have been proved to exhibit better electron transport and therefore to reduce the loss of electrons by recombination (Lin *et al.*, 2011).

Sensitizers

The sensitizer carries out the light harvesting function and influences the electron transfer processes occurring at the semiconductor/dye/electrolyte interfaces. An efficient sensitizer has a broad and strong absorption, excellent chemical stability,

reduction potential sufficiently higher than the conduction band edge of the semiconductor, and an oxidation potential sufficiently lower than the redox potential of the electrolyte. The primary classifications of sensitizers are metal-based sensitizers and metal-free organic sensitizers.

The metal-based sensitizers comprising the chromophores of ruthenium complexes have been widely studied for DSSCs, which can achieve solar-to-electricity conversion efficiencies of around 11% under AM1.5 conditions, due to the favorable photoelectrochemical properties as well as the excellent chemical stability and intense light absorption over a wide visible range. Several efficient Ru-based complex photosensitizers were developed by Grätzel *et al*. The first famous Ru-based complex photosensitizer is cis-bis(isothiocyanato)bis-(4,40-dicarboxylic acid-2,20-bipyridine) Ru (II), denoted as N3 or red dye (Nazeeruddin *et al.*, 1993). Afterwards, the other two efficient dyes were synthesized by the same group. One is the black dye or denoted as N749 dye with the formula of tris(isothiocyanato)-2,20,2″-terpyridyl-4,40,4″-tricarbolylate Ru(II) complex, and the other is denoted as N719 dye, with the formula of di(tetrabutylammonium)cis-bis(isothiocyanato)bis-(4-carboxylicacid-40-carboxylate-2,20-bipyridine)Ru(II). The structures for these efficient sensitizers are shown in Fig. 8. Table 2 gives a partial list of the photovoltaic parameters for the DSSCs using Ru-based complex photodyes as the sensitizer. The disadvantage of the ruthenium complex dyes is that they contain a

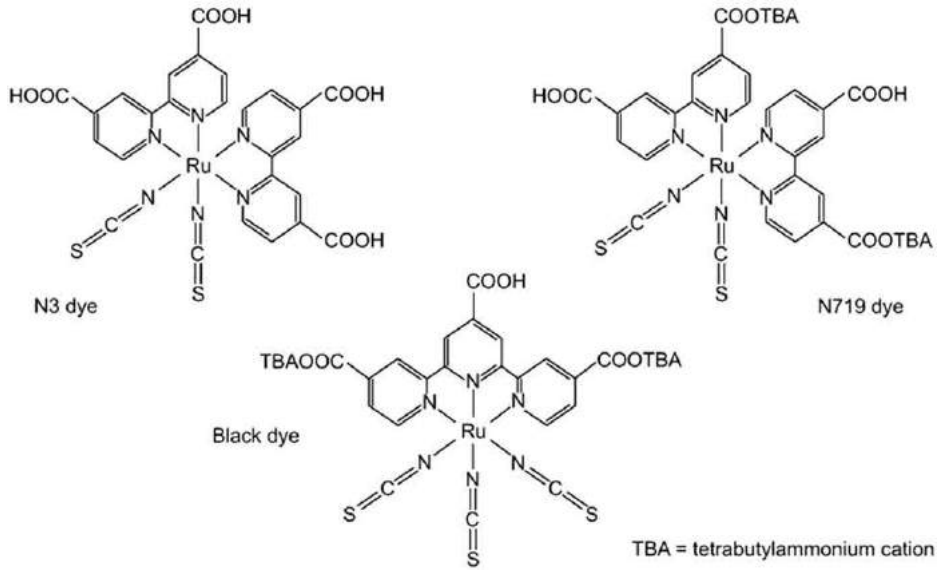


Fig. 8 The chemical structures of N3 dye, black dye, and N719 dye.

Table 2 A partial list of the photovoltaic parameters for the dye-sensitized solar cells (DSSCs) using Ru-based complex dyes as the sensitizer

Ru complex sensitizer	V_{OC} *(V)*	J_{SC} *(mA/cm²)*	*FF (%)*	*η (%)*
cis-[Ru([a]$dcbH_2$)$_2$(NCS)$_2$]	0.64	5.0	76	10.4
N719	0.85	17.7	75	11.1
N621	0.78	16.8	73	9.6
Black dye	0.74	20.9	72	11.1
cis-[Ru([a]$dcbH_2$)$_2$(NCS)$_2$]	0.70	15.0	74	7.8
[Ru([a]$dcbH_2$)$_2$([b]acac)]Cl	0.67	13.2	68	6.0
Ru([c]bmipy)([d]bpy-PO_3H_2)(NCS)	0.60	8.6	70	4.1
[Ru([a]$dcbH_2$)$_2$([e]phdmp)]Cl_2	0.42	0.60	38	3.8
Ru(bpy-(CH_2OH)$_2$)$_2$(NCS)$_2$	0.51	10.0	48	3.8
Ru([a]$dcbH_2$)$_2$([f]qdt)	0.60	11.1	70	3.7
[Ru([a]$dcbH_2$)$_2$$Cl_2$]	0.57	2.6	38	2.1
[Ru([a]$dcbH_2$)$_2$([g]aphb)]	0.58	5.5	48	1.5

[a]$dcbH_2$ = 4,4′-(CO_2H)2-2,2′-bipyridine
[b]acac = acetoacetonate
[c]bmipy = benzimidazol
[d]bpy = bipyridine
[e]phdmp = pteridinedione
[f]qdt = quinoxaline-2,3-dithiolate
[g]aphb = phenanthrolin-5-yliminomethyl-phenol.

Table 3 A partial list of the photovoltaic parameters for the dye-sensitized solar cells (DSSCs) using metal-free organic dyes as the sensitizer

Metal-free organic dyes	V_{OC} *(V)*	J_{SC} *(mA/cm^2)*	*FF (%)*	*η (%)*
C219	0.77	17.94	73	10.10
C229	0.85	15.3	73	9.40
C218	0.95	13.3	74	9.30
WS-9	0.70	18.0	72	9.04
WS-2	0.65	17.7	76	8.70
IQ2	0.77	15.7	70	8.50
WS-5	0.78	13.2	78	8.02
WS-6	0.67	15.0	77	7.76
TTZ5	0.71	18.3	59	7.71
OHexDPTP	0.77	13.8	72	7.64
BT-I	0.78	15.7	61	7.51
YCD01	0.76	13.4	73	7.43
R4	0.67	15.2	66	6.72
VP3	0.79	12.62	63	6.29
DTInDT	0.69	13.54	71	6.70
CR204	0.67	14.9	66	6.49
C278	0.84	19.6	73	12.00
C275	0.96	17.0	77	12.50

heavy metal which is expensive and harmful to the environment. Therefore, the metal-free organic dyes have been proposed as an alternative for DSSCs.

There are some advantages for the metal-free organic dyes to be used in DSSCs. First, the metal-free organic dyes are relatively inexpensive, since they can be easily synthesized and their resources are more abundant than that of the noble metals. Secondly, the extinction coefficients and the absorption coefficients of organic dyes are relatively higher than those of the noble metal-based ones. Organic dyes based on porphyrin, perylene, cyanine, xanthenes, merocyanine, coumarin, hemicyaine, indoline, diketopyrrolopyrrole, and ethylenedioxythiophene have been widely investigated for DSSCs due to their phototherapeutic and photochemical applications. **Table 3** is a partial list of the photovoltaic parameters for the metal-free organic dye-based DSSCs repeated in literatures.

Electrolytes

Electrolyte is one of the crucial parts overtaking the dye regeneration after electron injection and the electron transfer between the photoanode and the CE. The electrolyte can be classified into liquid electrolyte, quasi-solid-state electrolyte, and solid-state electrolyte.

The liquid electrolyte is composed of redox couples, additives, and solvents. The redox couple is in charge of transferring charges between the photoanode and the CE, as well as the dye regeneration. The redox couple possesses a redox potential less negative than the oxidized level of the sensitizer. Also, fast electron transfer kinetics at the CE, slow electron recombination kinetics at the sensitizer, small absorption in the visible region, as well as the noncorrosive, reasonable stability, and good diffusion properties are indispensable factors for the redox couples. The redox couple of lithium iodide/iodine was first used in DSSC by Hagfeldt and coauthors in an organic liquid electrolyte (Hagfeldt and Graetzel, 1995). However, the I_3^- is extremely corrosive toward metals such as copper or silver, and a significant part of visible light would be absorbed by the I^-/I_3^- based electrolyte. Hence, many other redox couples were proposed to replace this redox couple nowadays, for example, cobalt complexes and inorganic redox couples such as Br^-/Br_3^-, $SCN^-/(SCN)_2$, $SeCN^-/(SeCN)_2$, and S^{2-}/S, or other organic compounds. A recorded η of 12.3% was attained for the DSSC with $Co^{(II/III)}$ tris(bipyridyl)-based redox couple (**Fig. 9**) in its electrolyte. **Table 4** is a partial list of the photovoltaic parameters for the DSSCs using different redox couples in the liquid electrolytes. On the other hand, the additives were used in the electrolyte to enhance the photovoltaic performances. Specific cations like guanidium or alkali cations are typically used to increase the photocurrent density. The cations in the electrolyte would adsorb on the surface of the semiconductor layer to render the conduction band of the semiconductor shift toward more positive potentials, thus affecting the electron injection dynamics of the dye molecules in the excited state. Also, nitrogen-containing heterocyclic compounds like 4-tert-butylpyridine (4-TBP) and pyridine analogs of the N-alkylbenzimidazole derivatives are purposely used to improve the $V_{oc.}$ Lastly, the organic solvents and ionic liquids are primarily selected as the solvents for the liquid electrolyte. The organic solvents like acetonitrile (ACN), ethylene carbonate (EC), 3-methoxypropionitrile (MPN), propylene carbonate (PC), N-methylpyrrolidone (NMP) and water have been widely investigated for liquid electrolyte-based DSSCs. The ACN is the first choice organic solvent in considering of the solar-to-electricity conversion efficiency of DSSC, due to its low viscosity (0.34 cp at 25°C) and good solubility to dissolve salts and organic components. However, the encapsulation of volatile organic solvents is a critical issue owing to their high vapor pressures. Therefore, the quasi-solid-state electrolyte and solid-state electrolyte were used to enhance the encapsulation of the DSSCs.

The quasi-solid-state electrolyte is consisted of a polymer network swollen with liquid electrolytes or ionic liquid electrolytes. The quasi-solid-state electrolyte possesses both cohesive property of solid and diffusive transport property of liquid, and therefore

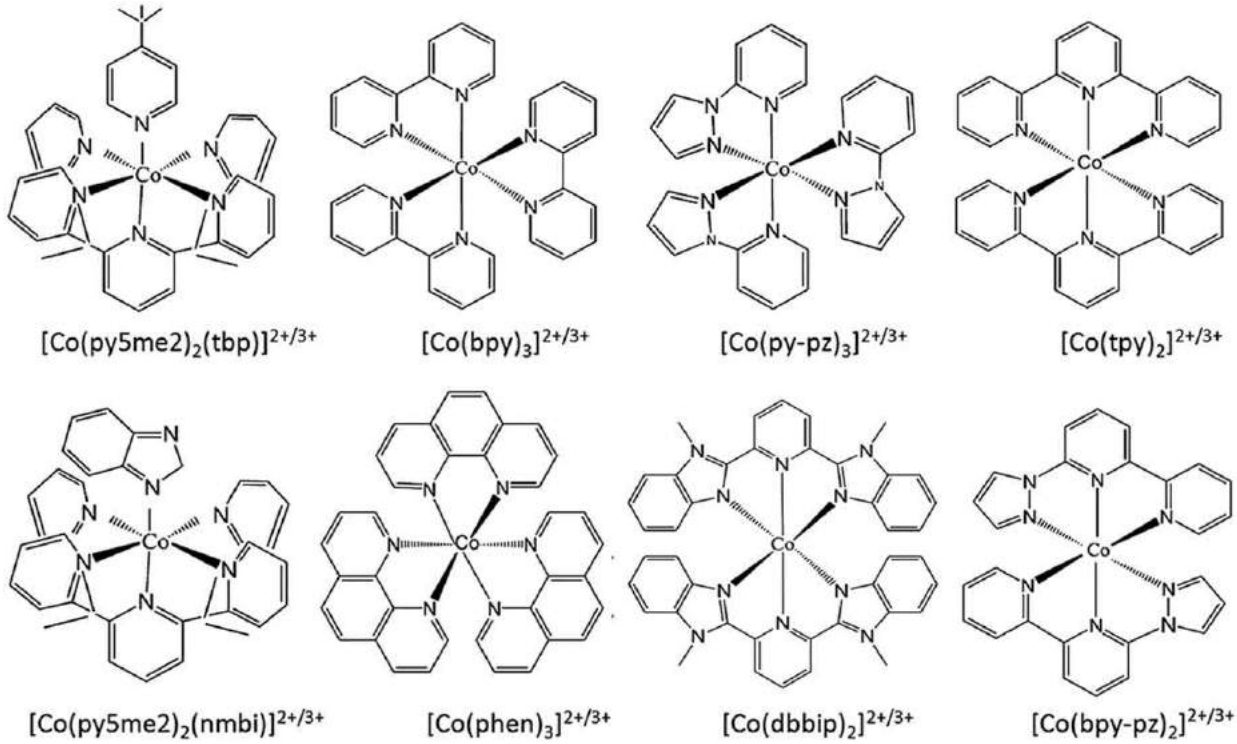


Fig. 9 The structures of the $Co^{(II/III)}$ tris(bipyridyl)-based redox couple. py5me2 = 2,6-bis(1,1-bis(2-pyridyl)ethyl)pyridine; tbp = 4-tert-butylpyridine; bpy = 4,4′-bipyridine; py-pz = 2-pyridyl pyrazolate; tpy = 2,2′:6′,2″-terpyridine; nmbi = N-methylbenzimidazole; phen = 1,10-phenanthroline; dbbip = 2,6-bis(1′-butylbenzimidazol-2′-yl)pyridine); bpy-pz = 6-(1H-pyrazol-1-yl) 2,20-bipyridine.

Table 4 A partial list of the photovoltaic parameters for the dye-sensitized solar cells (DSSCs) using different redox couples in the liquid electrolytes

Redox couple	*Sensitizer*	V_{OC} *(V)*	J_{SC} *(mA/cm²)*	*FF (%)*	*η (%)*
I^-/I_3^-	N719	0.79	17.0	77	10.29
I^-/I_3^-	C219	0.77	17.94	73	10.10
Co^{2+}/Co^{3+}	C275	0.96	17.0	77	12.50
Co^{2+}/Co^{3+}	C229	0.85	15.3	73	9.40
$[Co(bpy)_3](B(CN)_4)_2/[Co(bpy)_3](B(CN)_4)_3$	YD2-o-C8	0.97	17.3	71	11.9
$[Co(bpy)_3](B(CN)_4)_2/[Co(bpy)_3](B(CN)_4)_3$	YD2-o-C8/Y123	0.94	17.7	74	12.3
[a]TEMPO/$TEMPO^+$	D149	0.83	9.4	70	5.4
[b]T^-/[c]T_2	Z907Na	0.68	16.2	58	6.4
[d]Fc/$FcPF_6$	Carbz-PAHTDTT	0.84	12.2	73	7.5
[e]TMTU/$TMFDS^{2+}$	N3	0.66	9.45	49	3.1

[a]TEMPO = 2,2,6,6-tetramethyl-1-piperidinyloxy radical
[b]T = 1-methyl-1-H-tetrazole-5-thiolate anion
[c]T_2 = dimer of T^-
[d]Fc = Ferrocene
[e]TMTU/$TMFDS^{2+}$ = tetramethylthiourea/tetramethylformaminium disulfide.

the quasi-solid-state electrolytes offer better long-term stability than that of the liquid electrolytes. The quasi-solid-state electrolytes can be made by different methods and being classified into various sorts, for example, composite polymer electrolytes, quasi-solid ionic liquid electrolytes, and thermosetting polymer electrolytes. **Table 5** lists the used sensitizers and the photovoltaic parameters for the DSSCs based on the three types of quasi-solid-state electrolytes mentioned above.

The solid-state DSSC applied the hole transport materials (HTMs) or the solid-state electrolyte containing I^-/I_3^- redox couple as the medium to solve the solvent leakage and corrosion issues. Major research interests focus on the organic hole conductor, 2,2′7,7′-tetrakis(*N*,*N*-di-*p*-methoxyphenyl-amine)-9,9′-spiro-bifluorene (spiro-MeOTAD), which was originated in 1998 by Bach *et al.* (1998). To enhance the cell performance of the solid-state DSSC, Kojima *et al.* used two organolead halide perovskite

Table 5 A partial list of the photovoltaic parameters for the dye-sensitized solar cells (DSSCs) based on the quasi-solid-state electrolyte

Electrolyte	*Dye*	V_{OC} *(V)*	J_{SC} *(mA/cm²)*	*FF (%)*	*η (%)*
Composites polymer electrolyte					
Acetamide/[a]PEO/LiI/I_2	N3	0.74	19.81	52	9.0
[b]PEO_{13}BIm-I/[c]MPN	N719	0.73	11.61	66	5.6
[d]MPII/MPII-modified Al_2O_3	N719	0.72	17.70	60	7.6
[e]PAN/LiI/activated carbon	N719	0.77	16.82	64	8.4
[f]PMMA-EA/TiO_2	N719	0.79	12.68	68	6.9
Quasi-solid ionic liquid electrolyte					
[g]PEG/[h]EMImI	N719	0.69	20.02	52	7.1
[i]PMImI/[j]PVDF-HFP	Z907	0.67	11.29	71	5.3
[k]POEI-II/[l]MWCNT	N719	0.78	14.50	67	7.7
[j]PVDF-HFP/[a]PEO	N719	0.81	5.45	74	3.3
[m]IL/[n][PBVIm][TFSI]	N719	0.61	10.57	68	4.4
Thermosetting polymer electrolytes					
[j]PVDF-HFP	N719	0.75	16.26	68	8.4
Paa/PEG/[q]PPY	N719	0.71	13.34	71	6.3
[o]P(VA-co-MMA)/[c]MPN	N719	0.74	16.66	74	9.1
[p]PAA–PEG/graphene	N719	0.73	15.00	68	7.7

[a]PEO = poly(ethylene oxide)
[b]PEO_{13}BIm-I = dicationic bis-imidazolium diiodide salts
[c]MPN = 3-methoxypropionitrile
[d]MPII = 1-methyl-3-propylimidazolium iodide
[e]PAN = polyacrylonitrile
[f]PMMA-EA = poly(methyl methacrylate-co-ethyl acrylate)
[g]PEG = polyethylene glycol
[h]EMImI = 1-ethyl-3-methylimidazolium iodide
[i]PMImI = 1-propyl-3-Methylimidazolium Iodide
[j]PVDF-HFP = poly(vinylidene fluoride-co-hexafluoropropylene)
[k]POEI-II = poly(oxyethylene)-imide-imidazole
[l]MWCNT = multi-walled carbon nanotubes
[m]IL = ionic liquid
[n][PBVIm][TFSI] = poly(1-butyl-3-vinylimidazolium bis(trifluorome- thanessulfonyl)imide)
[o]P(VA-co-MMA) = polyvinyl(acetate-co-methyl methacrylate)
[p]PAA-PEG = poly(acrylic acid)-poly(ethylene glycol)
[q]PPy = polypyrrole.

nanocrystals, $CH_3NH_3PbBr_3$ and $CH_3NH_3PbI_3$ to sensitize TiO_2 for the visible-light conversion, and a η value of 3.8% was achieved for the photoelectrochemical cell (Kojima *et al.*, 2009). Afterwards, another type of the solid-state TiO_2 solar cell, the lead iodide perovskite ($CH_3NH_3PbX_3$) solar cell, was proposed to have promising photovoltaic performance. A recorded η value of 23% was attained for the perovskite solar cell in the year of 2016 by Chen *et al.* (2016).

Counter electrodes

The CE plays a role of transferring electrons from the external circuit to the electrolyte to reduce the oxidized redox couple used as a mediator in regenerating the sensitizer after electron injection, so as to generate the photocurrent. High electrocatalytic activity, excellent electrical and thermal conductivities, high corrosion resistance and large electrochemical surface area, as well as high exchange current densities and low charge transfer resistances are important requirements for a CE of DSSCs.

Platinum is the most commonly used catalyst in the CE, due to the high conductivity, high stability, and high catalytic activity toward I_3^- reduction. Pt can be deposited on the transparent conductive oxide (TCO) glasses by various methods, for example, spin-coating, screen-printing or sputtering. Modifying the structural characteristics and facets of Pt were verified to be useful in enhancing its catalytic activity. The high surface area and therefore the high amount of active sites available for reducing I_3 can be obtained by varying the morphology of Pt, like the Pt nanoflowers as shown in **Fig. 10**. The catalytic and photovoltaic behavior of the CE toward the I_3^- reduction also varied with different facets of Pt (Zhang *et al.*, 2013). However, since Pt is one of the expensive and rare metals in the earth, it is not suitable for the commercial production of DSSCs. Developing alternative materials to Pt as the catalyst on the CE of DSSCs is expected to decrease the cost of DSSCs.

Other cheaper materials were proposed to reduce the production cost of the cells. Conducting polymers like poly(3,4-ethylenedioxythiophene) (PEDOT), PEDOT doped with poly(4-styrene sulfonate) (PEDOT:PSS), polypyrrole (PPy), polyaniline (PANI), and poly(3,4-propylenedioxythiophene) (PProDOT) have been used as the catalyst on the CE of

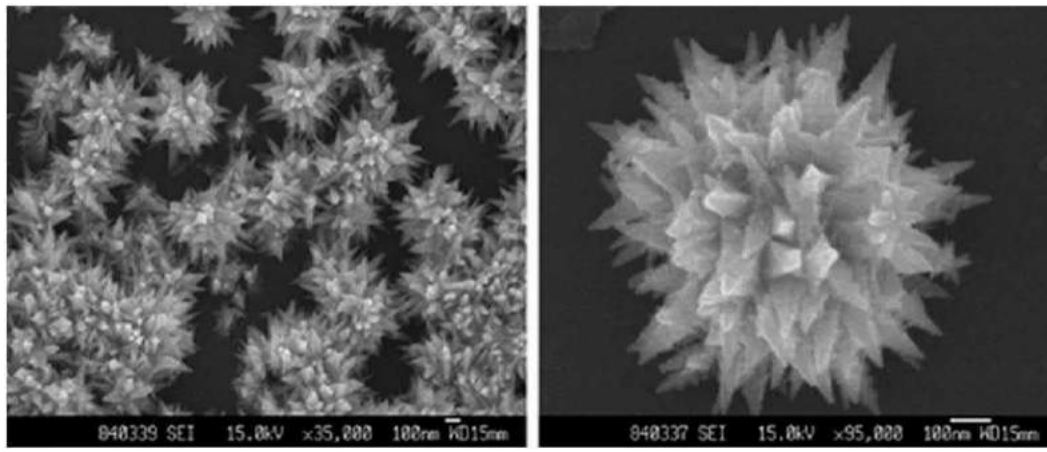


Fig. 10 The scanning electron microscope (SEM) images for the Pt nanoflowers. Reproduced with permission from He, Y.B., Li, G.R., Wang, Z. L., Ou, Y.N., Tong, Y.X., 2010. Pt nanorods aggregates with enhanced electrocatalytic activity toward methanol oxidation. The Journal of Physical Chemistry C 114 (45), 19175 Copyright (2010) by Royal Society of Chemistry.

Table 6 A partial list for the photovoltaic parameters for the dye-sensitized solar cells (DSSCs) using different catalysts on the CE

Counter electrode (CE)	*Sensitizer*	V_{OC} *(V)*	J_{SC} *(mA/cm^2)*	*FF (%)*	η *(%)*
PEDOT	N719	0.76	17.5	64	8.5
PEDOT	Y123	1.02	12.2	69	8.6
PPy	N719	0.74	15.0	68	7.7
PANI	N719	0.71	14.6	69	7.2
PANI	N719	0.71	17.2	59	7.2
PProDOT	Y123	1.00	13.1	77	10.1
PEDOT:PSS/TiN	CYC-B1	0.68	14.2	69	6.67
Glassy carbon	N719	0.71	16.5	65	7.6
Carbon nanotube (CNT)	N719	0.80	13.3	65	7.0
C60 (fullerene)	N719	0.76	11.6	32	2.8
N-doped carbon	N3	0.71	15.5	64	7.0
Graphene	Perovskite	0.70	13.1	63	5.9
[a]SWCNT	Perovskite	0.72	13.0	52	5.0
Boron-doped CNT	N719	0.70	17.1	67	8.0

[a]SWCNT = single-walled carbon nanotube.

DSSCs, due to their unique properties such as high conductivity, low cost, good stability, and high catalytic activity for I_3^- reduction. Among the conducting polymers, PANI has been one of the most intensively studied conducting polymers due to its easy synthesis, high conductivity, good environmental stability, and interesting redox properties in recent years. The performance of the conducting polymer can be enhanced by designing the morphology to achieve optimized surface roughness or doping foreign anions such as SO_4^{2-}, ClO_4^-, BF_4^-, Cl^-, and tosyl$^-$ into the conducting polymer film to increase the conductivity. However, the major problem of the conducting polymer is that the thick layer is required to achieve sufficient catalytic activities.

On the other hand, carbon materials like glassy carbon, graphene, and carbon nanotubes (CNT), are interesting low-cost alternatives to Pt. Carbonaceous materials have the advantages of high heat resistance, high electronic conductivity, high electrocatalytic activity toward I_3^- reduction, and high corrosion resistance. The power conversion efficiency and the fill factor of DSSCs are strongly dependent on the thickness of the carbon layer, which can be increased up to 10 μm to improve the fill factor of DSSCs. However, the main drawback of carbon-based CE is the requirement of large dosage to attain the targeted catalytic activity and the poor connection between the carbon film and the substrate. The photovoltaic parameters for the DSSCs using different catalysts on the CE are shown in Table 6.

Future Prospects

DSSCs have emerged as one of the cheap alternatives to the traditional silicon solar cells for harnessing the immense solar energy. Great progresses have been made for DSSCs since it was originated in 1972. The major aims are to enhance its solar-to-electricity

conversion efficiency and long-term durability. Developing efficient and novel sensitizers for conversing light with broader wavelength especially in the near IR region into multiple electrons, constructing well-defined structures of semiconductors for providing more dye-adsorbed sites and the enhancing charge transfer among the photoanode, and designing suitable catalysts on the CE for accelerating the redox reactions in the electrolyte are necessary to achieve a highly efficient DSSC. Also, gel-type or solid-state electrolytes are needed to exploit for enhancing the long-term operating stability. Eventually, the detailed studies on the charge transfer resistance at the interfaces and the electron lifetime in the electrodes should be understood for selecting more effective routes to improve the performance of DSSCs.

See also: Organic Semiconductors

References

Bach, U., Lupo, D., Comte, P., *et al.*, 1998. Solid-state dye-sensitized mesoporous TiO_2 solar cells with high photon-to-electron conversion efficiencies. Nature 395, 583–585.
Chen, B., Bai, Y., Yu, Z., *et al.*, 2016. Efficient semitransparent perovskite solar cells for 23.0%-efficiency perovskite/silicon four-terminal tandem cells. Advanced Energy Materials 6, 1601128.
Fujishima, A., Honda, K., 1972. Electrochemical photolysis of water at a semiconductor electrode. Nature 238, 37–38.
Hagfeldt, A., Graetzel, M., 1995. Light-induced redox reactions in nanocrystalline systems. Chemical Reviews 95, 49–68.
Kakiage, K., Aoyama, Y., Yano, T., *et al.*, 2015. Highly-efficient dye-sensitized solar cells with collaborative sensitization by silyl-anchor and carboxy-anchor dyes. Chemical Communications 51, 15894–15897.
Kojima, A., Teshima, K., Shirai, Y., Miyasaka, T., 2009. Organometal halide perovskites as visible-light sensitizers for photovoltaic cells. Journal of the American Chemical Society 131, 6050–6051.
Lin, L.Y., Yeh, M.H., Lee, C.P., *et al.*, 2011. Metal-based flexible TiO_2 photoanode with titanium oxide nanotubes as the underlayer for enhancement of performance of a dye-sensitized solar cell. Electrochimica Acta 57, 270–276.
Mathew, S., Yella, A., Gao, P., *et al.*, 2014. Dye-sensitized solar cells with 13% efficiency achieved through the molecular engineering of porphyrin sensitizers. Nature Chemistry 6, 242–247.
Nazeeruddin, M.K., Kay, A., Rodicio, I., *et al.*, 1993. Conversion of light to electricity by cis-X2bis(2,2'-bipyridyl-4,4'-dicarboxylate)ruthenium(II) charge-transfer sensitizers (X = Cl-, Br-, I-, CN-, and SCN-) on nanocrystalline titanium dioxide electrodes. Journal of the American Chemical Society 115, 6382–6390.
O'Regan, B., Gratzel, M., 1991. A low-cost, high-efficiency solar cell based on dye-sensitized colloidal TiO_2 films. Nature 353, 737–740.
Tributsch, H., 1972. Reaction of excited chlorophyll molecules at electrodes and in photosynthesis. Photochemistry and Photobiology 16, 261–269.
Yella, A., Lee, H.-W., Tsao, H.N., *et al.*, 2011. Porphyrin-sensitized solar cells with cobalt (II/III)-based redox electrolyte exceed 12 percent efficiency. Science 334, 629–634.
Yuvapragasam, A., Muthukumarasamy, N., Agilan, S., *et al.*, 2015. Natural dye sensitized TiO_2 nanorods assembly of broccoli shape based solar cells. Journal of Photochemistry and Photobiology B 148, 223–231.
Zhang, B., Wang, D., Hou, Y., *et al.*, 2013. Facet-dependent catalytic activity of platinum nanocrystals for triiodide reduction in dye-sensitized solar cells. Scientific Reports 3, 1836.
Zhang, J., Zhou, P., Liu, J., Yu, J., 2014. New understanding of the difference of photocatalytic activity among anatase, rutile and brookite TiO_2. Physical Chemistry Chemical Physics 16, 20382–20386.

Organic Inorganic Hybrid Perovskite Materials and Devices

Yihua Chen, Ning Zhou, and Huanping Zhou, Peking University, Beijing, P.R. China

© 2018 Elsevier Ltd. All rights reserved.

Introduction

Organic–inorganic hybrid halide perovskites have received increasing attention in the photovoltaic research community due to its remarkable optoelectronic properties, such as high carrier mobility, tunable band gap, long diffusion lengths and long lifetime. The efficiency record of perovskite solar cells has experienced a dramatic progress from 3.8% in 2009 to more than 20%, which makes perovskite one of the most competitive and promising candidate materials for solar cells. Besides, the perovskite materials have also proven to be feasible in a large variety of other optoelectronic applications, for example, light emitting diode, laser, detector, and transistors as well. In this section, the perovskite materials and the corresponding devices are reviewed regarding the progress in the crystal structure, optoelectronic property, and device working mechanism.

Crystal Structure

Organic–inorganic hybrid halide perovskite is a category of materials with the chemical formula of ABX_3, where A and B sites are often occupied with two different cations with different ionic radii. A site occupant is generally methylammonium ($CH_3NH_3^+$), formamidinium ($NH_2CH{=}NH_2^+$) or cation cesium(Cs^+) , rubidium (Rb^+), and X is halide anion, such as I^-, Br^- and Cl^- (Green *et al.*, 2014). The crystal structure of perovskites is depicted in **Fig. 1(a)**. Their crystallographic structure and pertaining stability can be guided by a tolerance factor t proposed by Goldschmidt and an octahedral factor μ. In theory, $t=(R_A+R_X)/\{\sqrt{2}\ (R_B+R_X)\}$ (Yin *et al.*, 2015) where R_A, R_B and R_X are the ionic radii of the corresponding ions, and μ is defined as the ratio R_B/R_X. To achieve stable halide perovskite, it typically requires $0.81<t<1.11$ and $0.44<\mu<0.90$. If t is lower, it is intended to form the less symmetric structures such as tetragonal (β phase) or orthorhombic (γ phase) perovskite (Lu *et al.*, 2016). In contrast, larger t ($t>1$) could result in destabilized three dimensional (3D) B–X framework, leading to a two-dimensional (2D) layered structure (Yin *et al.*, 2015). μ is directly correlated to the BX_6 octahedral structure. When $\mu>0.442$, we often observe BX_6 octahedron in a stable assembly. However, lower μ value will destabilize BX_6 octahedral assembly (Li *et al.*, 2008). A summary of both calculated tolerance factors and octahedral factors for commonly seen halide perovskites are provided in **Fig. 1(b)** (Chen *et al.*, 2015). Along with different ions and structural stabilities, different perovskites possess different transition temperatures. As the archetypal halide perovskite of $CH_3NH_3PbI_3$, the α to β, and β to γ phase transitions occur at around 330 and 160K, respectively (Ball *et al.*, 2013). Some relevant crystallographic data of different perovskite materials with phases in high, intermediate or low temperatures (e.g., α, β, and γ phases, respectively), are summarized in **Table 1** (Chen *et al.*, 2015).

It is generally believed that the cation at A site has shown no apparent effects on the electronic configurations and thus the band structure of the resultant materials, but plays the role of making charge compensation within the lattice. The A cation has been observed to influence the optical properties of perovskite by deforming the MX_6^{4-} octahedron framework when intercalating into the crystal structures. A larger (smaller) A cation can cause the entire lattice to expand (contract), and lead to the change of B–X bond lengths, which has been demonstrated to be important in determining the bandgap (Borriello *et al.*, 2008; Kulkarni *et al.*, 2014). For example, the use of formamidium($HC(NH_2)_2^+$) instead of $CH_3NH_3^+$ as A cation of the perovskite can shift the band

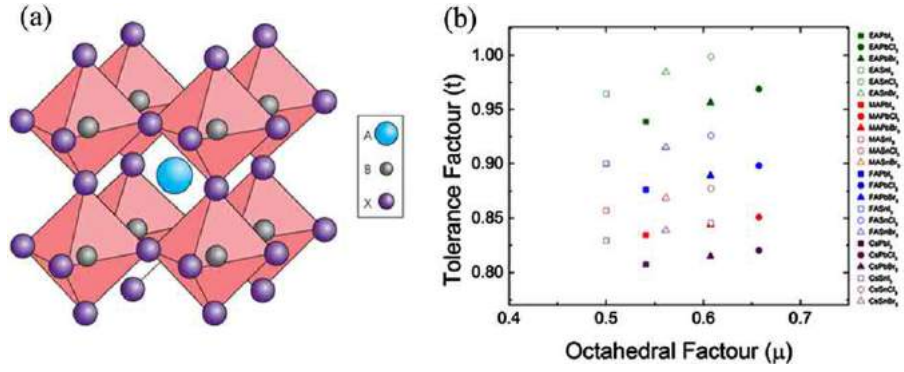


Fig. 1 (a) Cubic perovskite crystal structure; (b) calculated octahedral and tolerance factors for various combinations of commonly employed organic and inorganic hybrid perovskite components.

 doi:10.1016/B978-0-12-803581-8.09546-1

Table 1 Structural phase transformations for commonly employed hybrid perovskites

PVSK	*Phase*	*Temperature (K)*	*Structure*	*Space group*	*Lattice parameters(Å)*	*Volume (Å^3)*
$MAPbI_3$	α	400	Tetragonal	P4*mm*	*a*=6.3115; *b*=6.3115; *c*=6.3161	251.6
	β	293	Tetragonal	I4*cm*	*a*=8.849; *b*=8.849; *c*=12.642	990
	γ	162–172	Orthorhombic	P*na*2$_1$	*a*=5.673; *b*=5.628; *c*=11.182	959.6
$MAPbCl_3$	α	>178.8	Cubic	P*m*3*m*	*a*=5.675	182.2
	β	172.9–178.9	Tetragonal	P4/*mmm*	*a*=5.655; *c*=5.630	180.1
	γ	<172.9	Orthorhombic	P222$_1$	*a*=5.673; *b*=5.628; *c*=11.182	375
$MAPbBr_3$	α	>236.9	Cubic	P*m*3*m*	*a*=5.901	206.3
	β	155.1–236.9	Tetragonal	I4/*mcm*	*a*=8.322; *c*=11.833	819.4
	γ	149.5–155.1	Tetragonal	P4/*mmm*	*a*=5.8942; *c*=5.8612	
	δ	<144.5	Orthorhombic	P*na*2$_1$	*a*=7.979; *b*=8.580; *c*=11.849	811.1
$MASnI_3$	α	293	Tetragonal	P4*mm*	*a*=6.2302; *b*=6.2302; *c*=6.2316	241.88
	β	200	Tetragonal	I4*cm*	*a*=8.7577; *b*=8.7577; *c*=12.429	953.2
$FAPbI_3$	α	293	Trigonal	P3*m*1	*a*=8.9817; *b*=8.9817; *c*=11.006	768.9
	β	150	Trigonal	P3	*a*=17.791; *b*=17.791; *c*=10.091	2988.4
$FASnI_3$	α	340	Orthorhombic	A*mm*2	*a*=6.3286; *b*=8.9554; *c*=8.9463	507.03
	β	180	Orthorhombic	I*mm*2	*a*=12.512; *b*=12.512; *c*=12.509	1959.2

gap from 1.55 to 1.45 eV (Eperon *et al.*, 2014). Following FA^+, the ions such as Cs^+, Rb^+ with smaller ion radii have also been reported to be the applicable substitution for MA^+ at A site, which results in the tailored bandgap and carrier behavior in the resultant materials (Choi *et al.*, 2014; Saliba *et al.*, 2016).

The most widely reported B cations ever reported in hybrid perovskite are Pb^{2+} and Sn^{2+}, and the most efficient devices have been obtained always using Pb^{2+} based perovskite absorber. However, the toxicity of Pb^{2+} is seriously concerned which hinders the development of large-scale industrialization. To address this issue, the replacement of this heavy metal cation by an environmental friendly metal is under intense research, whereas Sn^{2+} or Ge^{2+} are investigated to be used as absorber without significant detriment to the device performance. Although $CH_3NH_3SnX_3$ possesses a more optimal band gap (1.2–1.4 eV) than $CH_3NH_3PbX_3$ (1.6–1.8 eV) does, the devices based on Sn perovskite do not appear comparable power conversion efficiency (PCE). It is mainly because the Sn based perovskite has shown a poor stability in air compared with the Pb based perovskite due to the oxidation of Sn^{2+} to Sn^{4+}, which destroys the crystal structure and thus deteriorates the device performance (Kumar *et al.*, 2014).

The halide anion exhibit the substantial influence to the optoelectronic properties in the resultant hybrid perovskites. It has been widely reported the halogen elements I, Cl and Br, and their combinations affects the performance of the perovskite solar cells significantly. The Br^- introduction into the perovskite lattice to replace I^- will produce a higher absorption coefficient in the visible range of the spectrum, and upshift the conduction band to result in a wider bandgap perovskite suitable for tandem perovskite solar cells (Noh *et al.*, 2013). However, the Br^- incorporation in $MAPbI_3$ often causes significant phase segregation upon illumination, which causes the instability issue. Introduction of Cl^- into the perovskite can extend the charge diffusion length without changing the spectrum response, but only a small percentage of Cl atoms can be tolerated in the perovskite lattice (Chen *et al.*, 2015).

Optoelectronic Properties

Hybrid perovskites demonstrate strong optical absorption, adjustable band gap, long diffusion length, high carrier mobility, ambipolar charge transport and a high tolerance of defects. We thus provide a thorough discussion regarding the origin of the above excellent optoelectronic properties in the hybrid perovskites.

Hybrid perovskites exhibit large optical density with absorption coefficient of 10^4–10^5 cm^{-1}, which allows for a reduced film thickness as the absorber in solar cells to facilitate the light harvest efficiently. Devices based on less than 500 nm perovskite film can absorb sufficient sunlight and achieve high efficiency over 15%. In comparison, the commercially available crystalline Si or other inorganic thin film GaAs or CdTe photovoltaic technology are based on the absorber with thickness of few to hundreds of μm, much thicker than those of hybrid perovskites ones. The schematic illustration for optical transition over the bandedge that contributes to the optical absorption in Si, GaAs and perovskite materials are depicted in **Fig. 2(a)**. The direct bandgaps of the halide perovskite (e.g., $CH_3NH_3PbI_3$) often exhibit optical absorption much stronger than that of silicon which possess an indirect bandgap. Compared with the GaAs semiconductor, the CB edge of the $CH_3NH_3PbI_3$ is mainly composed of degenerate Pb p orbitals. The atomic p orbital is less dispersive than s orbitals. Additionally, the edge transition in $CH_3NH_3PbI_3$ is mainly contributed from mixed-(Pb s, I p) to Pb p orbitals. It is generally believed the probability of intra-atomic Pb s to Pb p transition is high, which makes the VBM–CBM transition probability of $CH_3NH_3PbI_3$ comparable to that of GaAs. As is observed, halide perovskites show stronger optical absorption than GaAs in the visible range (Yin *et al.*, 2015). The calculated optical absorption coefficients of $CH_3NH_3PbI_3$ and GaAs are shown in **Fig. 2(b)** (Yin *et al.*, 2014).

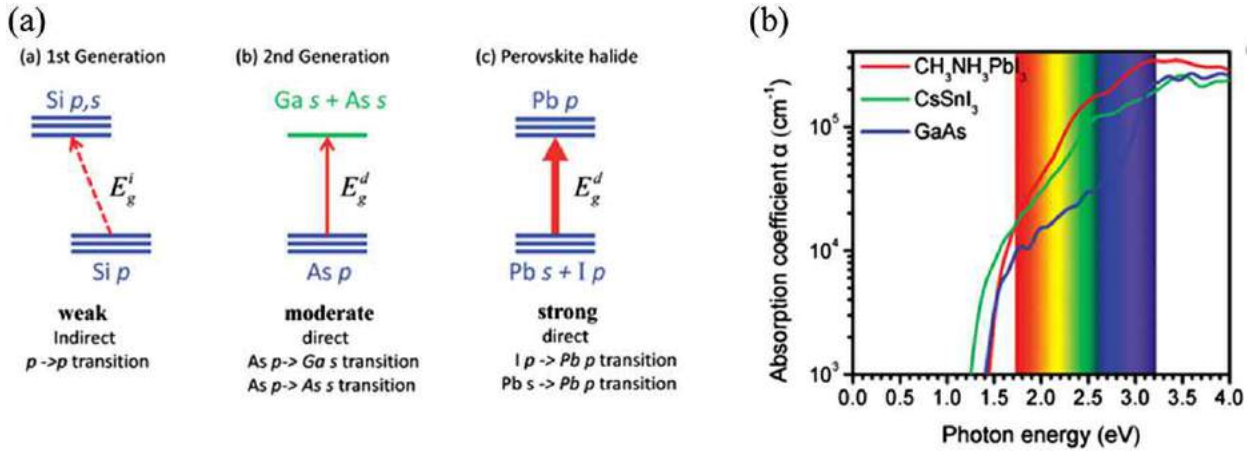


Fig. 2 (a) The schematic optical absorption of the three kinds of solar cell absorber. (b) The optical absorptions of $CH_3NH_3PbI_3$, $CsSnI_3$ and GaAs.

Table 2 DFT–PBE calculated effective masses for electrons and holes

	Electron effective mass	*Hole effective mass*
$CH_3NH_3PbI_3$	0.35, 0.32	0.31, 0.36
$CH_3NH_3PbI_3$ (SOC)	0.18, 0.23	0.21, 0.29
$CsSnI_3$	0.19	0.09
$CsSnI_3$ (SOC)	0.16	0.07
Silicon	0.26	0.29
GaAs	0.07	0.34
$CuInSe_2$	0.09	0.75
$Cu_2ZnSnSe_4$	0.1	0.26
CdTe	0.09	0.28

The electronic structure of $CH_3NH_3PbI_3$ is different from the conventional III-V (p–s) semiconductors. Its CBM is derived from Pb p orbitals, and the VBM is a combination of Pb s and I p orbitals. Even though the CBM comes from p orbitals, the p orbital of Pb^{2+} has a much higher energy level than anion p orbitals, as is usually observed in III-V (p–s) semiconductors. It leads to a more dispersive conduction band of $CH_3NH_3PbI_3$ which is lower than that of the p–s semiconductors with a higher valence band. Furthermore, the valence band of $CH_3NH_3PbI_3$ is dispersive due to strong s–p coupling over the VBM. The calculated electron and hole effective masses of $CH_3NH_3PbI_3$ via DFT–PBE, are compared with typical first and second-generation solar cell absorbers, which are listed in **Table 2**. The hole effective mass of $CH_3NH_3PbI_3$ is close to the electron effective mass, leading to ambipolar conductivity in perovskites, which facilitates to construct the p–i–n junction solar cells with versatile architectures (Yin *et al.*, 2015; Giorgi *et al.*, 2013). The carrier diffusion lengths of $CH_3NH_3PbI_3$ is up to 100 nm for both electrons and holes, and exceeding 1 μm in the mixed halide $MAPbI_{3-x}Cl_x$ have been reported via transient photoluminescence (TRPL) measurements (Xing *et al.*, 2013; Stranks *et al.*, 2013). Through the formation of hybrid perovskite single crystal, it demonstrated diffusion lengths over 175 μm in single crystals of $CH_3NH_3PbI_3$ under 1 sun illumination, owing to the reduced density of defects in the single crystal (Dong *et al.*, 2015). The defects with the relatively low formation energies are Pb^{2+} vacancies and interstitial MA^+. Consequently, both of them are able to create shallow charge-carrier trap states near the perovskite band edges as shown in **Fig. 3** (Yin *et al.*, 2014). Fortunately, the shallow defects are not responsible to nonradiative recombination centers that hampers the carrier diffusion length, which has been experimentally observed (Duan *et al.*, 2015).

Device Structures of Perovskite Solar Cell

The unprecedented rise in power conversion efficiency of perovskite solar cell, combined with the potential of cost-effective fabrication technique have stimulated the further understanding of perovskite devices (Green *et al.*, 2014; Stranks and Snaith, 2015; Park *et al.*, 2016). Two commonly employed structures for perovskite photovoltaic devices are shown in **Figs. 4(a)** and **(b)**. Both device architectures consist of a perovskite layer as the light absorber layer which is sandwiched between electron transport layer (ETL) and hole transport layer (HTL). The main difference between the two configurations is whether there is mesoporous scaffold layer or not, and accordingly they were categorized as mesoporous PSC and planar heterojunction PSC. The first adoption

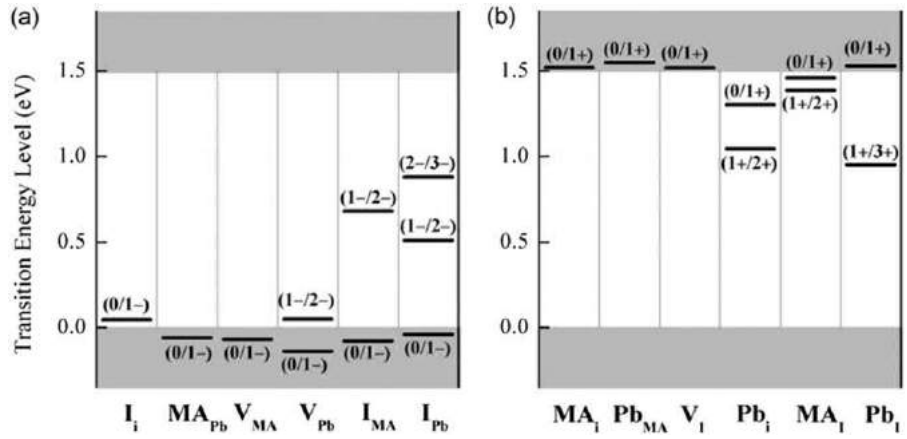


Fig. 3 The transition energy levels of (a) intrinsic acceptors and (b) intrinsic donors in $CH_3NH_3PbI_3$.

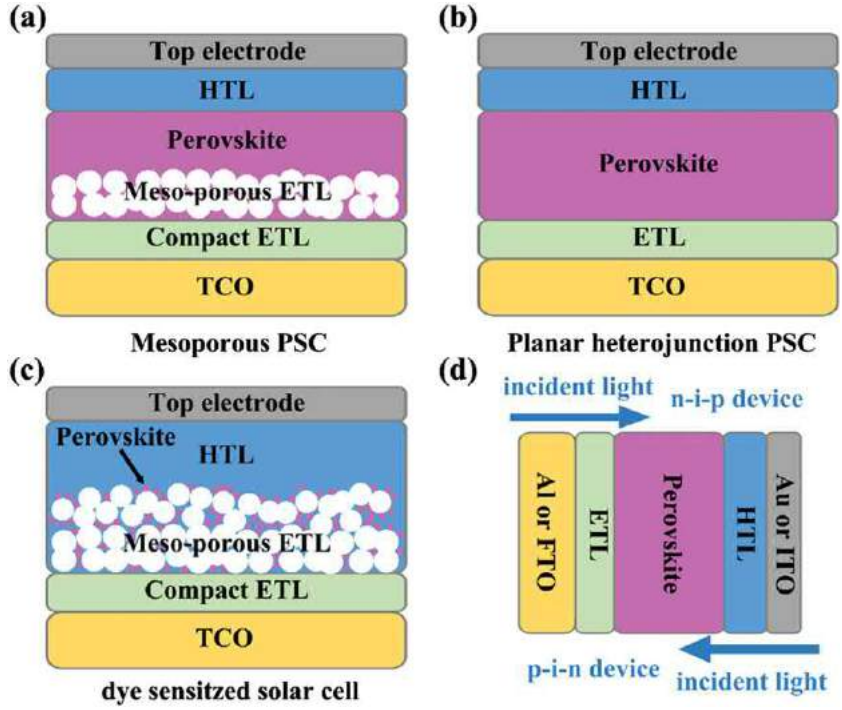


Fig. 4 The device structures of (a) mesoporous perovskite solar cell, (b) planar heterojunction perovskite solar cell, and (c) dye sensitized solar cell. (d) The n-i-p and p-i-n cell architectures.

of perovskite absorber $CH_3NH_3PbI_3$ ($MAPbI_3$) in photovoltaic device was to replace conventional dye in dye sensitized solar cell (DSSC) (Kojima *et al.*, 2009), whose structure was shown in **Fig. 4(c)**. Generally, it is considered as the archetype of mesoporous PSC. The presence of TiO_2 mesoporous scaffold layer as ETL greatly increase the contact area between perovskite and TiO_2 material, giving rise to the faster and more efficient electron transport. Further investigation has demonstrated that perovskite absorbers exhibit superior ambipolar transport ability (both electron and hole, which means that mesoporous scaffold is not necessary for perovskite photovoltaic devices, leading to the emergence of planar heterojunction PSC (Leijtens *et al.*, 2014). Compared to the mesoporous PSC, the fabrication of planar structured PSC possessed the added advantage of more simple and low-temperature processing that are attractive for mass production and flexibility. Additionally, a great deal of excellent carrier conducting layers including inorganic materials, as well as organic materials have been successfully demonstrated in the efficient planar heterojunction PSC. Depending on the relative position of the electron/hole conducting layer and incident sunlight, the planar heterojunction PSC can be simply divided into n–i–p structure devices (regular configurations) and p–i–n structure devices (inverted configurations), as shown in **Fig. 4(d)**.

To this day, the highest PCE of perovskite solar cell have reached a certified 22.1%, which is reported from National Renewable Energy Laboratory (NREL), but the detailed device structures and experiment process have not come forward yet. Moreover, Grätzel and his coworkers have realized the mesoporous PSCs with good reproducibility showing a certified PCE of 21.02% and a champion PCE of up to 21.6% under standard test condition (Bi *et al.*, 2016). The typical mesoporous PSCs device structure is FTO/compact TiO_2/mesoporous TiO_2/perovskite/spiro-OMeTAD/Au. And recently, Sargent and his coworkers reported top-performing planar heterojunction PSC using chlorine-capped TiO_2 colloidal nanocrystal film. The optimized planar photovoltaic devices have been demonstrated a certified PCE of 20.1%, which is the highest efficiency of planar heterojunction devices for now (Tan *et al.*, 2017). The reported device structure is ITO/TiO_2-Cl/Perovskite/Sprio-OMeTAD/Au.

Working Mechanism of Perovskite Solar Cell

When two types of semiconductors contact, the majority carriers in the material bulk will diffuse to each other. The movement of majority carriers will leave positive ion cores in the n-type semiconductor and negative ion cores in the p-type semiconductor, respectively, resulting in a charge depletion region with a built-in electric field, which is usually defined as a junction. When the sunlight incidence happens, the photogenerated carriers are created and the equilibrium is broken in the semiconductor absorber and in the contact region. During the subsequent diffusion process, part of the photogenerated carriers will recombine via direct recombination, Shockley-Read-Hall recombination or Auger recombination. The others will eventually diffuse to the junction and get separated assisted by the built-in electric field. The carriers will then be extracted selectively through the carrier-transport layers and reach the external circuit to generate photocurrent. When a photovoltaic devices is illuminated under sunlight, the key processes are shown in **Fig. 5**, including that (1) the incident photo with energy higher than the bandgap of light absorber layer can be absorbed in perovskite layer to generate holes and electrons, (2) the electrons transfer from perovskite to ETL, (3) the holes transfer from perovskite to HTL, which is equivalent to that of electron, (4) the electrons are recombined with photogenerated holes, (5) and (6) back charge carriers transport may occur at the interface of ETL and HTL with perovskite, (7) the electrons and holes recombine between ETL and HTL, which may occur if the quality of perovskite film is inferior so that many pinholes exist. In order to pursue high performance, process (4)–(7) must be restrained as strictly as possible, to ensure sufficient charge generation and extraction in operated perovskite photovoltaic devices.

Charge Carriers Transport Materials

Apart from the perovskite absorber, charge carriers transport layers, including ETL and HTL, also play a significant role in perovskite photovoltaic devices (Fan *et al.*, 2016; Hossain *et al.*, 2015; Zhang *et al.*, 2017; Ke *et al.*, 2015). The relative position of the valence band maximum (VBM) and conductive band minimum (CBM) of the charge carriers transport materials and perovskite provides the intrinsic motivation force for carrier separation and extraction at charge carriers transport layers/perovskite junction, which also determines the device's built-in potential of cell operation at equilibrium upon illumination. The design principles for choosing charge carriers transport materials must take two into account of two aspects. On one hand, the VBM and CBM of charge carriers transport materials are critical for appropriate energy level alignment between perovskite and charge carriers transport layers, which is essential for efficient charge carrier separation, extraction and transport to minimize open-circuit voltage loss (Cha *et al.*, 2016). On the other hand, the processibility of each functional layers should also be taken into consideration. For instance, the substrate wetting characteristics and chemical compatibility of carrier transport layers, particularly the deposition of subsequent layer upon perovskite. It has been widely reported that the processing approach can directly influence the film quality

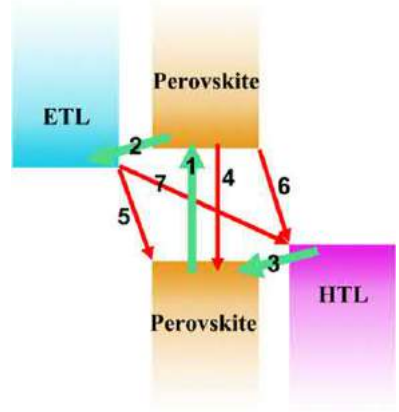


Fig. 5 Schematic of electron-transfer processes in an operated perovskite solar cell.

of perovskite solar cell, in terms of the grain size, morphology, crystallinity, surface coverage, *etc* (Song *et al.*, 2015). Therefore, rational design of carrier selective layers and the relevant processing methods determines the performance for photovoltaic devices, which has been carefully investigated in the research community.

Holes Transport Materials

Originated from the other third generation photovoltaic technologies, such as organic photovoltaics (OPV) and DSSC, 2,2′,7,7′-Tetrakis[N,N-di(4-methoxyphenyl)amino]-9,9′-spirobifluorene (sprio-OMeTAD) and Poly(3,4-ethylenedioxythiophene):poly (styrene sulfonate) (PEDOT:PSS) have become two of the most popular hole transport materials (HTM) in perovskite photovoltaic devices, whose molecular structures are shown in **Fig. 6(a)**. Owing to the excellent hole carriers mobility and appropriate VBM, CBM and Fermi energy level (**Fig. 6(b)**), both spiro-OMeTAD and PEDOT:PSS based PSC exhibit fascinating power conversion efficiency (Tan *et al.*, 2017; Meng *et al.*, 2016). However, neither of them is perfect, and they are facing a few critical challenges in way of commercialization of PSCs. Spiro-OMeTAD is too expensive to use on a large scale. In addition, it is reported pure spiro-OMeTAD exhibits weak electric conductivity, whereas chemical doping has been employed to greatly improve the carrier concentration and conductivity of the materials. However, the additive induced for chemical doping will damage the perovskite film in the solar cells. PEDOT:PSS shows acidic characteristics, which is not compatible to the perovskite film in devices and leads to long-term stability issues. Apart from that, both materials are organic species which are sensitive to moisture and oxygen. Therefore, lots of efforts are invested by research community aiming at feasible substitutions to address the current concern of inferior long-term stability in PSC devices (Bella *et al.*, 2016; Saliba *et al.*, 2016). Recently, lots of attention have been attracted to a variety of inorganic new candidates, such as NiO*x*, Cu_2O, CuSCN, CuI, and some cheaper or more stable organic HTM, whose energy level structures are shown in **Fig. 6(b)** (Hossain *et al.*, 2015). Taken as the example, NiO*x* is now under the spotlight as an inorganic p-type metal oxide hole transport material for PSCs. With the regard of valence band edge, it is demonstrated that NiO*x* can match with $MAPbI_3$ absorber (− 5.4 eV) better than that of PEDOT:PSS (5.26 eV) or spiro-OMeTAD (5.22 eV), which leads to greater open-circuit voltage and more efficient hole carriers separation and extraction. Moreover, its intrinsic stability and low-cost processing has brought forth to apparent advantages of NiO*x* among other potential HTM candidate material (Xu *et al.*, 2015).

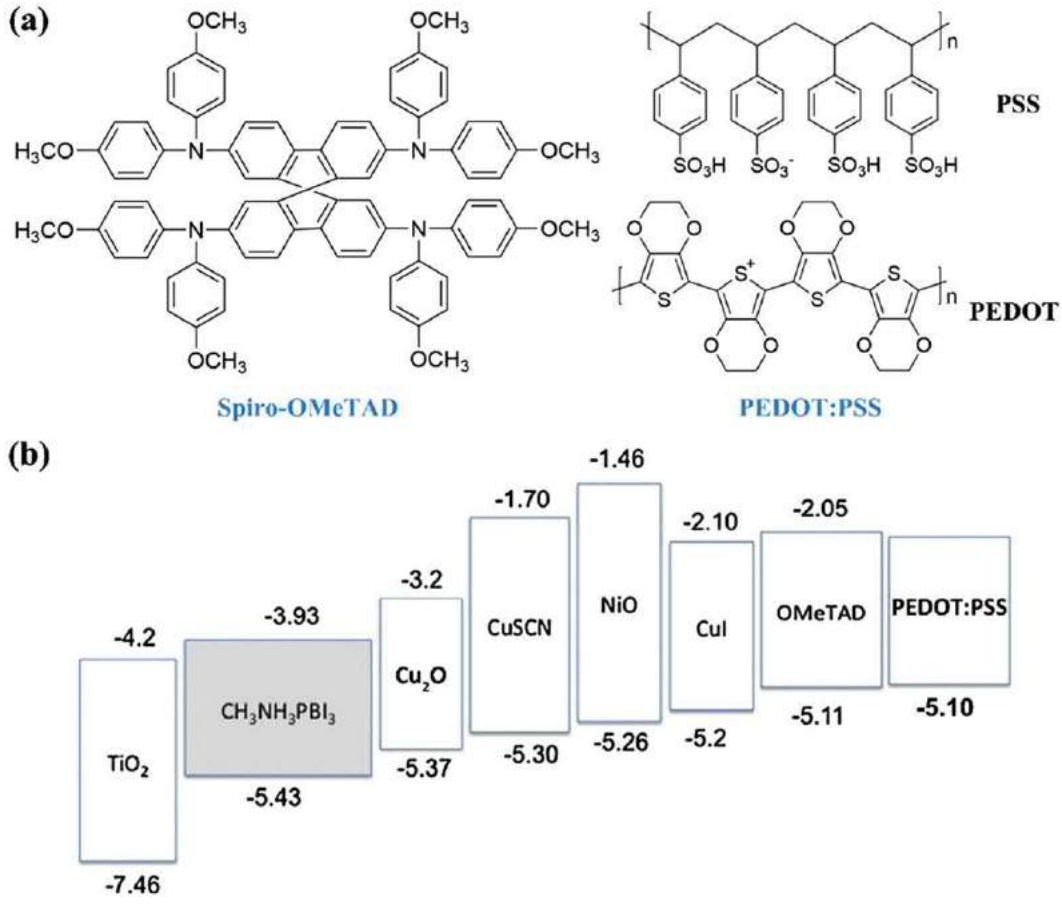


Fig. 6 (a) The molecular structures of spiro-OMeTAD and PEDOT:PSS. (b) Schematic energy level diagram of holes transport materials.

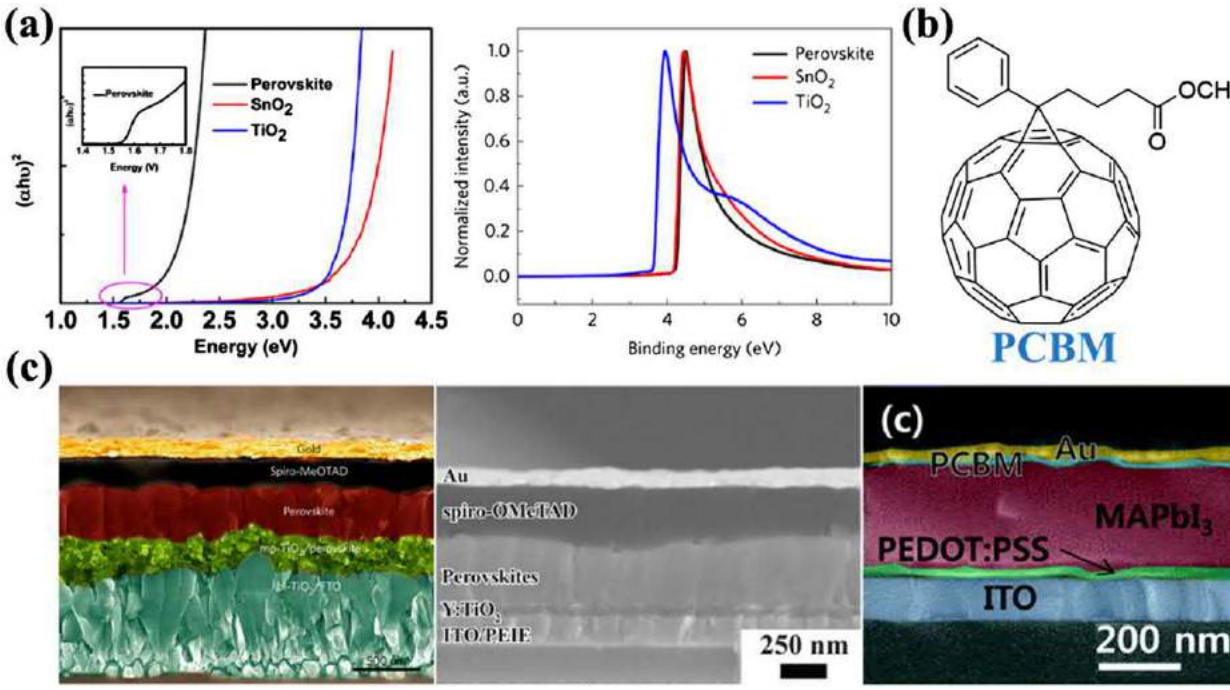


Fig. 7 (a) The left curves is the relationship of $(\alpha h\upsilon)^2$ vs. energy for perovskite, SnO_2 and TiO_2, respectively. The bandgap of materials can be determined by the linear extrapolation of the leading edges of the $(\alpha h\upsilon)^2$ curve to the base lines. The right curves are ultraviolet photoelectron spectroscopy (UPS) cutoff edges of SnO_2, TiO_2 and perovskite layer. (b) The molecular structures of PCBM. (c) The scan electron micrographs of three kinds of typical perovskite solar cells.

Electrons Transport Materials

Regarding electron transport materials (ETM), TiO_2 is the most popular choice as the electrode buffer to transfer electron from the absorber to electrode often employed in both mesoporous and planar heterojunction architectures (Tan *et al.*, 2017). This is mainly attributed to its well-aligned energy level to the perovskite absorber, as well as its well spread in DSSC/OPV. However, both compact and mesoporous TiO_2 suffer from low electron mobility and relatively high density of electronic trap states, giving rise to a high electron recombination rates. Moreover, it is reported that the TiO_2 layer is sensitive to ultraviolet exposure and oxygen, and its catalytic effects to decompose perovskite absorber is still under investigation, which may severely restrict the long-term application of perovskite photovoltaic devices. Right now, tin dioxide (SnO_2) is the most promising candidate to replace TiO_2 as electron transport material in planar heterojunction PSC with superiority of the much higher electron mobility and wider band gap than TiO_2 (**Fig. 7(a)**) (Jiang *et al.*, 2016). So with a wider bandgap of the SnO_2 as ETL, it can greatly minimize the photocurrent loss. SnO_2 also exhibits considerable stability upon ultraviolet illumination, which satisfies the requirements for commercialization. Besides these inorganic ETM, [6,6]-phenyl-C61-butyric acid methyl ester (PCBM, the molecular structure is shown in **Fig. 7 (b)**) is one of the most popular ETM usually used in inverted planar heterojunction PSC to deliver outstanding performance due to its good mobility, Fermi energy level, and particularly, the electron extraction capability. What attracts researchers most for PCBM-based perovskite devices is its negligible J-V hysteresis behavior during cell efficiency measurement.

Based on various charge carriers transport materials mentioned above, the typical devices structure of mesoporous PSC is FTO/compact TiO_2/mesoporous TiO_2/perovskite/spiro-OMeTAD/Au. As shown in **Fig. 7(c)** (Bi *et al.*, 2016), the device contains a FTO glass substrate covered by a compact TiO_2 ETL ($\sim$30 nm). A mesoporous TiO_2 scaffold ($\sim$150 nm) is deposited on the top of compact TiO_2 layer, followed with the perovskite absorber ($\sim$450 nm). Subsequently, a $\sim$200 nm thick spiro-OMeTAD as HTL is deposited by spin-coating. Finally, a thin layer of gold ($\sim$100 nm) is generally evaporated as the top electrode. As the counterpart, the typical devices structures of regular planar PSC indium tin oxide (ITO)/compact TiO_2/$MAPbI_3$/spiro-OMeTAD/Au (Zhou *et al.*, 2014), And inverted planar PSC often adopt the configuration of ITO/PEDOT:PSS/ $MAPbI_3$/PCBM/Ag (Heo *et al.*, 2015), which are shown in **Fig. 7(c)**. Moreover, the devices performance of PSC using various HTLs and ETLs are summarized in **Table 3**.

Tandem Solar Cell

For a single-junction solar cell, it achieves the limited power conversion efficiency due to the thermalization and transmission losses according to the Shockley–Queisser theory, leaving the maximum achievable efficiency close to 31% (Meillaud *et al.*, 2006).

Table 3 The device performance of perovskite solar cell with different charge carriers transport materials

Device structure	*Voc (V)*	*Jsc (mA/cm^2)*	*FF (%)*	*PCE (%)*	*References*
ITO/CuSCN/perovskite/C60/BCP/Ag	1.00	21.90	75.8	16.6	Ye *et al.* (2015)
Mesoscopic NiO/perovskite/PCBM	1.04	13.24	69.0	9.51	Wang *et al.* (2014)
FTO/NiO/$CH_3NH_3PbI_3$/PCBM/Ag	0.88	16.27	63.5	9.11	Zhu *et al.* (2014)
ITO/Cu:NiO_x/perovskite/C60	1.05	22.32	76.0	17.74	Kim *et al.* (2015)
FTO/TiO_2/perovskite/X60	1.14	24.20	71.0	19.84	Xu *et al.* (2016)
ITO/PEIE/Y:TiO_2/perovskite/spiro-OMeTAD/Au	1.13	22.75	75.1	19.30	Zhou *et al.* (2014)
FTO/NiMgLiO/perovskite/PCBM/TiNbOx/Ag	1.07	20.62	74.8	16.20	Chen *et al.* (2015)
FTO/SnO_2/perovskite/Spiro-OMeTAD/Au	1.11	23.27	67.0	17.21	Ke *et al.* (2015)
ITO/PEDOT:PSS/$CH_3NH_3PbI_3$ ($MAPbI_3$)/PCBM/Au	1.10	20.90	79.0	18.10	Heo *et al.* (2015)
FTO/WO_x/perovskite/spiro-OMeTAD/Ag	0.71	21.77	58.0	8.99	Wang *et al.* (2015)
ITO/$ZnSnO_4$/perovskite/PTAA/Au	1.05	21.6	67.0	15.3	Shin *et al.* (2015)

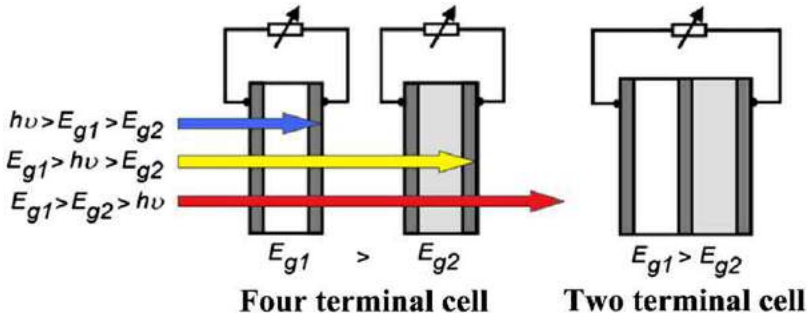


Fig. 8 Schematics of four terminal tandem solar cell and two terminal tandem solar cell.

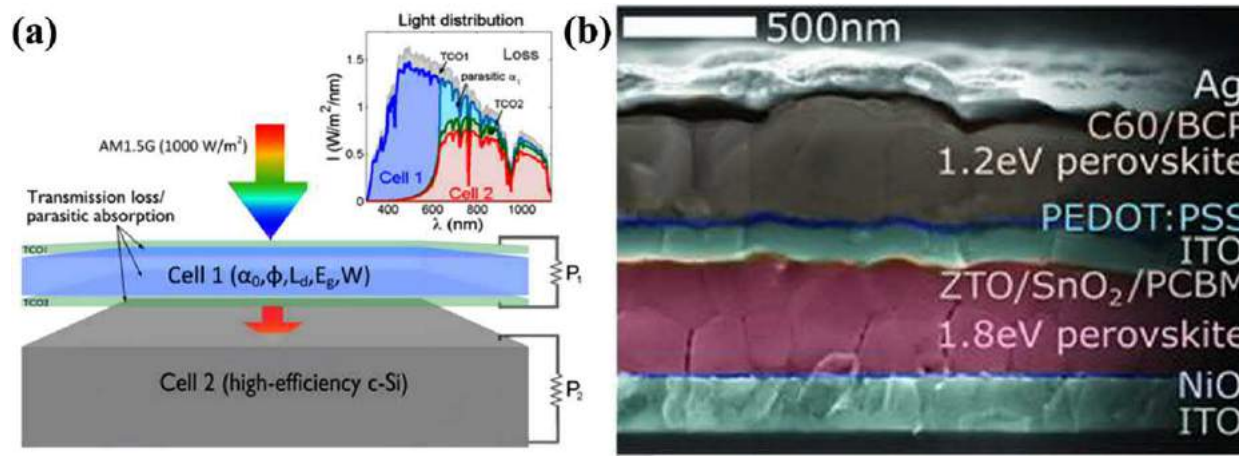


Fig. 9 (a) Schematic of a four-terminal tandem cell on silicon. (Inset) Optical distribution of absorbed sunlight (AM1.5G) through the complete tandem cell. (b) Scanning electron micrograph of the two terminal perovskite-perovskite tandem solar cell.

Different absorbers with different bandgaps will meet different theoretical PCE limits. So far, the traditional silicon solar cells are approaching their theoretical efficiency limit of ~25%. To further improve the PCE of solar cells, tandem solar cells that consists of multiple absorbers stacked in a horizontal fashion have attracted many researchers' interests. The simplest tandem solar cell, that two sub-cells are working together, can be divided into "Four terminal device" and "Two terminal device" depending on how the power output is extracted. As shown in Fig. 8, in a four terminal device, the photocurrents extracted from the two sub-cells are collected independently. In a two terminal device however, the two sub-cells are connected in series for power output (Chen *et al.*, 2015). When the incident sunlight photons reach the tandem devices, the top cell will absorb short-wavelength photons with energy higher than its bandgap E_{g1}, and the bottom cell will utilize the remaining long-wavelength photos with energy higher than its bandgap E_{g2}. In this scenario, a smart tandem design is expected to include the top photo-active layer and junction layer with

negligible absorption for long-wavelength photons to reduce the parasitic absorption as much as possible. This is essential for tandem solar cell to achieve higher efficiency. The perovskite materials are reported to exhibit negligible mid-band-gap states, which is evidenced by its low Urbach energy. Therefore, the hybrid perovskites not only exhibit very high absorption in short-wavelength spectrum range, but also display excellent transmittance over the long-wavelength spectrum range, indicating the promising potential of perovskite materials in tandem cells.

Another challenge for light activated materials in tandem solar cells application is their bandgaps. According to the theoretical calculation, the silicon-perovskite tandem solar cell can achieve an efficiency over 35%, only when the absorber with an optimized bandgap of 1.7 eV is employed in the front cell, as shown in **Fig. 9(a)** (Lal *et al.*, 2014). For this reason, the perovskite materials with tunable bandgap from 1.48 to 2.3 eV are carefully investigated, regarded as the excellent candidate as the top absorber materials. Moreover, perovskite-perovskite tandem solar cells are born sequentially and reported 20.3% efficiency for four terminal tandem cells, 17.0% efficiency for two terminal tandem cells, whose device structure is shown in **Fig. 9(b)** (Eperon *et al.*, 2016). It is believed the perovksite/c-silicon solar cell is one of the most potential technical approach toward commercialization by capitalization the well-developed crystalline silicon industry.

Summary

In summary, organic–inorganic hybrid perovskite materials as the star candidate employed in photovoltaics have made tremendous progress in decade years thanks to the intrinsic characteristics, such as high absorption coefficients, ambipolar carrier transport, long carrier lifetimes and diffusion lengths and shallow defect levels. However, there is still a long way for practical use of perovskites in photovoltaic market. In this article, we briefly review optical and electrical property for perovskite, and present the fundamental device structure and working mechanism of perovskite solar cell, whereas the relevant charge carriers transport materials are also included. Moreover, the perovskite-based tandem solar cell as a promising developing direction have been concisely discussed. Substantial efforts and researches toward the further development of perovskites photovoltaics are in progress. We confidently believe that low-cost, high performance, long-term stable and environmental friendly perovskite photovoltaic technology will be achieved in the coming years.

References

Ball, J.M., Lee, M.M., Hey, A., Snaith, H.J., 2013. Low-temperature processed meso-superstructured to thin-film perovskite solar cells. Energy Environ Sci 6, 1739.

Bella, F., Griffini, G., Correa-Baena, J.-P., *et al.*, 2016. Improving efficiency and stability of perovskite solar cells with photocurable fluoropolymers. Science aah4046.

Bi, D., Yi, C., Luo, J., *et al.*, 2016. Polymer-templated nucleation and crystal growth of perovskite films for solar cells with efficiency greater than 21%. Nat. Energy 1, 16142.

Borriello, I., Cantele, G., Ninno, D., 2008. Ab initioinvestigation of hybrid organic–inorganic perovskites based on tin halides. Phys. Rev. B 77, 235214.

Cha, M., Da, P., Wang, J., *et al.*, 2016. Enhancing perovskite solar cell performance by interface engineering using $CH_3NH_3PbBr_0$. 9I2. 1: Quantum dots. J. Am. Chem. Soc. 27, 8581–8587.

Chen, Q., De Marco, N., Yang, Y., *et al.*, 2015. Under the spotlight: The organic–inorganic hybrid halide perovskite for optoelectronic applications. Nano Today 10, 355–396.

Chen, Q., Zhou, H., Fang, Y., *et al.*, 2015. The optoelectronic role of chlorine in $CH_3NH_3PbI_3$(Cl)-based perovskite solar cells. Nat. Commun. 6, 7269.

Chen, W., Wu, Y., Yue, Y., *et al.*, 2015. Efficient and stable large-area perovskite solar cells with inorganic charge extraction layers. Science 350, 944–948.

Choi, H., Jeong, J., Kim, H.-B., *et al.*, 2014. Cesium-doped methylammonium lead iodide perovskite light absorber for hybrid solar cells. Nano Energy 7, 80–85.

Dong, Q., Fang, Y., Shao, Y., *et al.*, 2015. Solar cells. Electron-hole diffusion lengths >175 μm in solution-grown $CH_3NH_3PbI_3$ single crystals. Science 347, 967–970.

Duan, H.S., Zhou, H., Chen, Q., *et al.*, 2015. The identification and characterization of defect states in hybrid organic–inorganic perovskite photovoltaics. Phys. Chem. Chem. Phys. 17, 112–116.

Eperon, G.E., Leijtens, T., Bush, K.A., *et al.*, 2016. Perovskite–perovskite tandem photovoltaics with optimized band gaps. Science 354, 861–865.

Eperon, G.E., Stranks, S.D., Menelaou, C., *et al.*, 2014. Formamidinium lead trihalide: A broadly tunable perovskite for efficient planar heterojunction solar cells. Energy Environ. Sci. 7, 982–988.

Fan, R., Huang, Y., Wang, L., *et al.*, 2016. The progress of interface design in perovskite-based solar cells. Adv. Energy Mater. 6, 1600460.

Giorgi, G., Fujisawa, J., Segawa, H., Yamashita, K., 2013. Small photocarrier effective masses featuring ambipolar transport in methylammonium lead iodide perovskite: A density functional analysis. J. Phys. Chem. Lett. 4, 4213–4216.

Green, M.A., Ho-Baillie, A., Snaith, H.J., 2014. The emergence of perovskite solar cells. Nat. Photonics 8, 506–514.

Heo, J.H., Han, H.J., Kim, D., Ahn, T.K., Im, S.H., 2015. Hysteresis-less inverted $CH_3NH_3PbI_3$ planar perovskite hybrid solar cells with 18.1% power conversion efficiency. Energy Environ. Sci. 8, 1602–1608.

Hossain, M.I., Alharbi, F.H., Tabet, N., 2015. Copper oxide as inorganic hole transport material for lead halide perovskite based solar cells. Sol. Energy 120, 370–380.

Jiang, Q., Zhang, L., Wang, H., *et al.*, 2016. Enhanced electron extraction using SnO_2 for high-efficiency planar-structure $HC(NH_2)_2PbI_3$-based perovskite solar cells. Nat. Energy 1, 16177.

Ke, W., Fang, G., Liu, Q., *et al.*, 2015. Low-temperature solution-processed tin oxide as an alternative electron transporting layer for efficient perovskite solar cells. J. Am. Chem. Soc. 137, 6730–6733.

Kim, J.H., Liang, P.W., Williams, S.T., *et al.*, 2015. High-performance and environmentally stable planar heterojunction perovskite solar cells based on a solution-processed copper-doped nickel oxide hole-transporting layer. Adv. Mater. 27, 695–701.

Kojima, A., Teshima, K., Shirai, Y., Miyasaka, T., 2009. Organometal halide perovskites as visible-light sensitizers for photovoltaic cells. J. Am. Chem. Soc. 131, 6050–6051.

Kulkarni, S.A., Baikie, T., Boix, P.P., *et al.*, 2014. Band-gap tuning of lead halide perovskites using a sequential deposition process. J. Mater. Chem. A 2, 9221–9225.

Kumar, M.H., Dharani, S., Leong, W.L., *et al.*, 2014. Lead-free halide perovskite solar cells with high photocurrents realized through vacancy modulation. Adv. Mater. 26, 7122–7127.

Lal, N.N., White, T.P., Catchpole, K.R., 2014. Optics and light trapping for tandem solar cells on silicon. IEEE J. Photovolt. 4, 1380–1386.

Leijtens, T., Lauber, B., Eperon, G.E., Stranks, S.D., Snaith, H.J., 2014. The importance of perovskite pore filling in organometal mixed halide sensitized TiO_2-based solar cells. J. Phys. Chem. Lett. 5, 1096–1102.

Li, C., Lu, X., Ding, W., *et al*., 2008. Formability of ABX_3 (X = F, Cl, Br, I) halide perovskites. Acta Crystallogr B: Struct Sci 64, 702–707.
Lu, X., Wang, Y., Stoumpos, C.C., *et al*., 2016. Enhanced structural stability and photo responsiveness of $CH_3NH_3SnI_3$ perovskite via pressure-induced amorphization and recrystallization. Adv. Mater. 28, 8663–8668.
Meillaud, F., Shah, A., Droz, C., Vallat-Sauvain, E., Miazza, C., 2006. Efficiency limits for single-junction and tandem solar cells. Sol. Energ. Mat. Sol. C. 90, 2952–2959.
Meng, L., You, J., Guo, T.F., Yang, Y., 2016. Recent advances in the inverted planar structure of perovskite solar cells. Acc. Chem. Res. 49, 155–165.
Noh, J.H., Im, S.H., Heo, J.H., Mandal, T.N., Seok, S.I., 2013. Chemical management for colorful, efficient, and stable inorganic–organic hybrid nanostructured solar cells. Nano Lett. 13, 1764–1769.
Park, N.-G., Grätzel, M., Miyasaka, T., Zhu, K., Emery, K., 2016. Towards stable and commercially available perovskite solar cells. Nat. Energy 1, 16152.
Saliba, M., Matsui, T., Domanski, K., *et al*., 2016. Incorporation of rubidium cations into perovskite solar cells improves photovoltaic performance. Science 354, 206–209.
Shin, S.S., Yang, W.S., Noh, J.H., *et al*., 2015. High-performance flexible perovskite solar cells exploiting Zn_2SnO_4 prepared in solution below 100 degrees C. Nat. Commun. 6, 7410.
Song, T.-B., Chen, Q., Zhou, H., *et al*., 2015. Perovskite solar cells: Film formation and properties. J. Mater. Chem. A 3, 9032–9050.
Stranks, S.D., Eperon, G.E., Grancini, G., *et al*., 2013. Electron-hole diffusion lengths exceeding 1 Micrometer in an organometal trihalide perovskite absorber. Science 342, 341–344.
Stranks, S.D., Snaith, H.J., 2015. Metal-halide perovskites for photovoltaic and light-emitting devices. Nat. Nanotechnol. 10, 391–402.
Tan, H., Jain, A., Voznyy, O., *et al*., 2017. Efficient and stable solution-processed planar perovskite solar cells via contact passivation. Science 355, 722–726.
Wang, K.C., Jeng, J.Y., Shen, P.S., *et al*., 2014. p-Type mesoscopic nickel oxide/organometallic perovskite heterojunction solar cells. Sci. Rep. 4, 4756.
Wang, K., Shi, Y., Dong, Q., *et al*., 2015. Low-temperature and solution-processed amorphous WO(x) as electron-selective layer for perovskite solar cells. J. Phys. Chem. Lett. 6, 755–759.
Xing, G., Mathews, N., Sun, S., *et al*., 2013. Long-range balanced electron- and hole-transport lengths in organic–inorganic $CH_3NH_3PbI_3$. Science 342, 344–347.
Xu, B., Bi, D., Hua, Y., *et al*., 2016. A low-cost spiro[fluorene-9,9′-xanthene]-based hole transport material for highly efficient solid-state dye-sensitized solar cells and perovskite solar cells. Energy Environ. Sci. 9, 873–877.
Xu, X.B., Liu, Z.H., Zuo, Z.X., *et al*., 2015. Hole selective NiO contact for efficient perovskite solar cells with carbon electrode. Nano lett. 15, 2402–2408.
Ye, S., Sun, W., Li, Y., *et al*., 2015. CuSCN-based inverted planar perovskite solar cell with an average PCE of 15.6%. Nano lett. 15, 3723–3728.
Yin, W.J., Shi, T., Yan, Y., 2014. Unique properties of halide perovskites as possible origins of the superior solar cell performance. Adv. Mater. 26, 4653–4658.
Yin, W.-J., Shi, T., Yan, Y., 2014. Unusual defect physics in $CH_3NH_3PbI_3$ perovskite solar cell absorber. Appl. Phys. Lett. 104, 063903.
Yin, W.-J., Yang, J.-H., Kang, J., Yan, Y., Wei, S.-H., 2015. Halide perovskite materials for solar cells: A theoretical review. J. Mater. Chem. A 3, 8926–8942.
Zhang, H., Wang, H., Chen, W., Jen, A.K., 2017. $CuGaO_2$: A promising inorganic hole-transporting material for highly efficient and stable perovskite solar cells. Adv. Mater. 29, 1604984.
Zhou, H.P., Chen, Q., Li, G., *et al*., 2014. Interface engineering of highly efficient perovskite solar cells. Science 345, 542–546.
Zhu, Z.L., Bai, Y., Zhang, T., *et al*., 2014. High-performance hole-extraction layer of sol–gel-processed NiO nanocrystals for inverted planar perovskite solar cells. Angew. Chem. Int. Edit. 53, 12571–12575.

Light Harvesting in Organic Solar cells

Supriya Pillai, Matthew Wright, and Kah H Chan, University of New South Wales, Sydney, NSW, Australia

© 2018 Elsevier Ltd. All rights reserved.

Introduction

Considerable interest has evolved in the development of technologies to address the complex fabrication process and high cost of solar cells. Organic solar cells (OSCs) belong to a class of photovoltaic technology that are fabricated with organic, carbon-based semiconductors as the light absorbing active layer. OSCs offer a competitive path to realize cost-effective as well as environmentally friendly solar cells for future photovoltaic applications. They have the potential to be ultra-low cost, ultrathin, light weight and flexible (Krebs, 2009). They also offer the promise of high performance with opportunities not only in photovoltaics, but also in electronics and lighting applications. The ultrathin nature of OSC makes it transparent and allows it to be integrated into window glass or used as design elements for lighting installations. The polymers used in OSC can be easily printed and can be made in different colors.

The working principle of an organic solar cell has been discussed in the previous articles. However, to bring the need for light harvesting to context, it is important to understand that the exciton diffusion length L_D (the distance charge carriers can travel before recombining) is very short in organic semiconductors. Furthermore, L_D is significantly less than the absorption length $1/\alpha$ (distance into a material where the light intensity has dropped to 1/e or 36% of its original incident flux) for an organic solar cell. This means there is an inherent trade-off between the absorption in the organic absorber layer and the exciton diffusion length, thus forming an exciton diffusion bottleneck whereby the excitons cannot reach the donor–acceptor interface prior to dissociation into free carriers. This limits the thickness of the absorber layer d used to $\sim$100 nm so that more charge carriers can be successfully extracted before recombination occurs (Yu *et al.*, 1995; Ma *et al.*, 2005) and significantly affects the cell efficiency. The absorption efficiency within the absorber layer $\eta_A = 1 - e^{-\alpha d}$ and the exciton diffusion efficiency can be calculated as $\eta_{ED} = e_D^{-d/L}$. **Fig. 1** shows the dependence of the exciton diffusion bottleneck and the ratio of the layer thickness d to the exciton diffusion length L_D (Forrest, 2005).

The low efficiencies of OPV have hindered the commercial success of this technology. While different strategies are in place to improve either the absorption length or the diffusion length by design variations, blending polymers or improved material properties (Vezie *et al.*, 2016), this article will briefly discuss light harvesting schemes that have demonstrated or could potentially be used for increased light absorption through optical means. Conventional light trapping in silicon (Si) solar cells make use of surface textures that are on the micron scale (wavelength of light) to increase the optical pathlength. However, this is not feasible on very thin absorber layers like OSC. Moreover, texturing can induce roughness which increases the density of surface and bulk defect states, with the potential of degrading the electrical performance of cells. Hence, alternate light harnessing schemes need to be employed. They include antireflection (AR) schemes that direct more light into the absorber layer or light trapping schemes that aid the light to bounce back and forth in the active layer, thus increasing the optical path length thereby providing multiple opportunities for the light to be absorbed in the process. Other techniques include resonance/light concentration/near-field effects

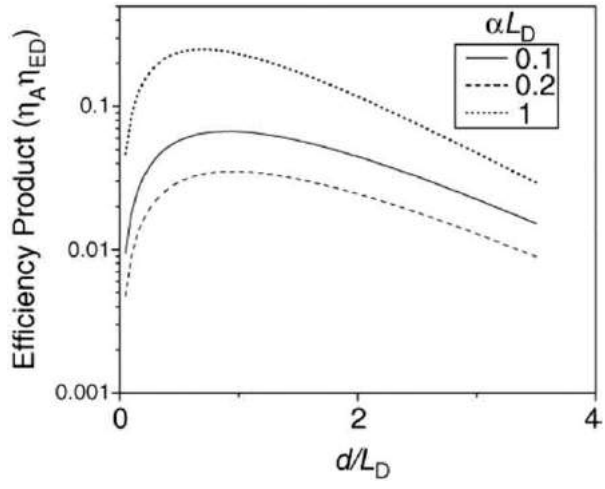


Fig. 1 Plot showing the dependence of the "exciton diffusion bottleneck" on the ratio of layer thickness d to exciton diffusion length L_D. Here α is the optical absorption coefficient within a particular layer. Taken from Forrest, S.R., 2005. The limits to organic photovoltaic cell efficiency. MRS Bulletin 30 (1), 28–32.

 doi:10.1016/B978-0-12-803581-8.09547-3

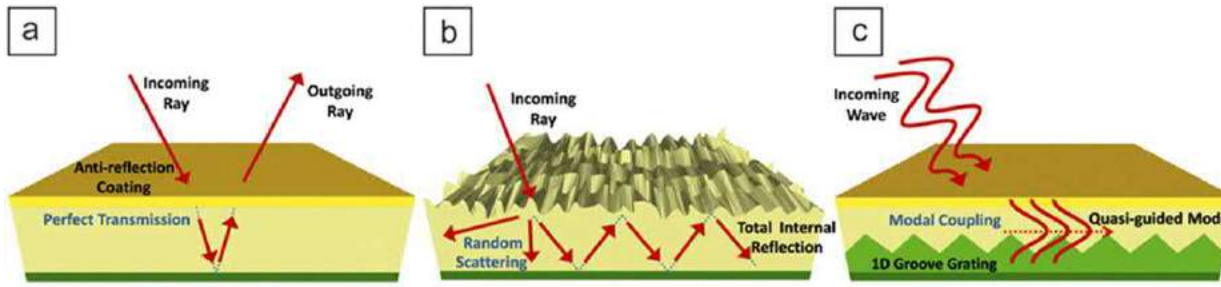


Fig. 2 Different ways of harnessing light (a) antireflection (AR) to maximize absorption, (b) light trapping where random scattering increase the path length, and (c) coherent light trapping where diffraction or electric field concentration is exploited. Taken from Mallick, S.B., Sergeant, N.P., Agrawal, M., Lee, J.-Y., Peumans, P., 2011. Coherent light trapping in thin-film photovoltaics. MRS Bulletin 36 (6), 453–460.

that can increase the optical density of states or confine the light in the absorber layer where photovoltaic conversion occurs. Approaches include graded index structures, substrate texturing, plasmonics, diffraction grating, photonic crystals, microcavities (Chen *et al.*, 2014a,b; Sergeant *et al.*, 2013) which makes use of one or more schemes. A schematic of the different light harnessing schemes is shown in **Fig. 2**. These light harvesting schemes are targeted for optical enhancement, however, some designs like plasmonics can benefit from both optical and electronic enhancement. Other approaches involve manipulating the light spectrum to be absorbed in different layers such as tandem configurations. In this work, we will discuss each of these approaches in more detail.

AR Effects

The realization of an efficient cell comes with minimization of optical losses. Since OSCs consist of stacks of different layers, the chances of reflective losses at each of the interfaces have to be eliminated to maximize in-coupling of incident light in the active layer. Hence the mitigation of optical losses has to start at the first point of incidence, which is at the front interface. This ensures that all the light that reaches the cell can be harvested in some way.

One way to achieve broadband AR properties is by using techniques seen in nature. For instance, the moth eye structures consist of nanostructured hexagonal cone shaped patterns that can substantially suppress the reflections of light at an interface of light over a broad spectral range (Bernhard, 1967) thereby increasing transmittance into the absorbing substrate over a wide angle of incidence (Huang *et al.*, 2007). Photonic structures are fabricated by mimicking moth eyes where the sub-wavelength features in the moth eye provide an effective refractive index that gradually varies and can suppress the reflection of light. The effective refractive index depends on the refractive indices of the nanostructured material and incident medium, and the angle of incidence. By tweaking these parameters the photonic structures can be optimized. Large scale fabrication of such structures is possible by interference lithography deeming it suitable for large scale production in solar cells.

Moth eye AR structures have been successfully incorporated to improve the performance of OSCs with an increase in the peak EQE by 3.5% along with making it angularly independent to oblique light (Forberich *et al.*, 2008). Another study achieved hydrophobic surfaces that enable self-cleaning properties for solar cells using a polydimethylsiloxane (PDMS) film as the AR layer on glass substrate with an encapsulated poly[(4,8-bis-(2-ethylhexyloxy)-benzo[1,2-b:4,5-b′]dithiophene)-2,6-diyl-alt-(4-(2-ethylhexanoyl)-thieno[3,4-b]thiophene)-2,6-diyl]:[6,6]-phenyl-C61 butyric acid methyl ester (PBDTTT-C:PCBM) cell increasing photocurrent efficiency. An improvement of 6.19% was reported where the nanostructures were fabricated by soft imprint lithography and the patterns formed by laser interference lithography and dry etching (Leem *et al.*, 2014). Another study using such dual-side bio-inspired nanostructures fabricated using nanoimprint lithography improved the light in-coupling efficiency of OSCs by 20%, yielding an enhanced power conversion efficiency of 9.33% (Zhou *et al.*, 2014).

Another light harnessing inspired by nature is called “flower power” that makes use of the epidermal structures of plants. Plants living in low light intensity regions make use of nanostructured surfaces need to harness light for metabolism or flowers for color saturation. These structures can not only reduce reflections like the moth eye structures, but also, in addition, can redirect incoming photons to induce light focussing effects thereby facilitating efficient light collection as well as light trapping (Hünig *et al.*, 2016). The densely packed combination of microstructures increase the chance of reflected light to bounce onto the neighboring feature especially at large angles of incidences and show only minor dependence to wavelengths. These structures also act as an imperfect lens diverging the incoupled light thereby increasing the optical path length resulting in light trapping. This double contribution has increased the power conversion efficiency of OSCs by 13% at normal incidence and 44% at an angle of incidence of 80 degree (Hünig *et al.*, 2016). The structures were fabricated by transferring the features directly from the rose petals to a PDMS stamp and then imprinting it to the cells as shown in the inset of **Fig. 3(a)** and **(b)** shows the smoothening of the Fabry–Perot resonances and reduction in the reflection on employing the rose structure on a ZnO:Al layer.

Nanowire (NW) arrays are another type of structure which has demonstrated AR and light trapping effects (Muskens *et al.*, 2008). Like in moth eye and flower structures they also exhibit broadband and omnidirectional AR properties due to the gradual

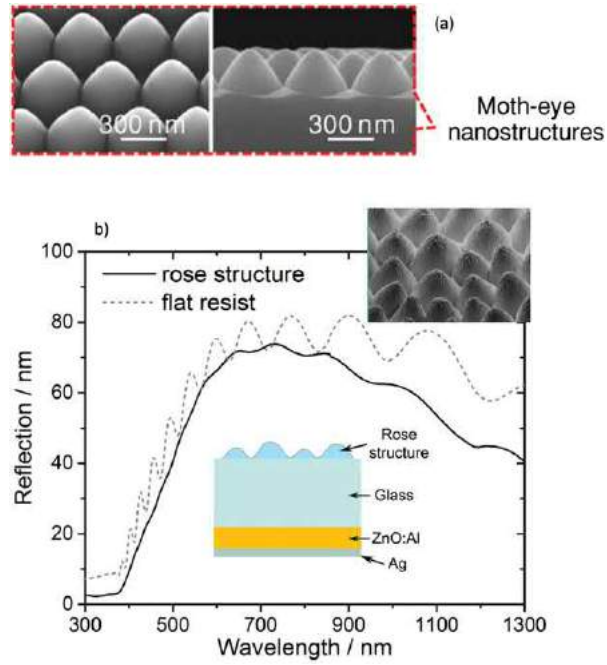


Fig. 3 (a) Scanning electron microscope (SEM) images of moth eye structures on a Si master that can be transferred to the substrate by soft imprint lithography to form inverted moth-eye structures (Reproduced from Leem, J.W., Kim, S., Lee, S.H., *et al.*, 2014. Efficiency enhancement of organic solar cells using hydrophobic antireflective inverted moth-eye nanopatterned PDMS films. Advanced Energy Materials 4 (8), 1301315) and (b) reduction in reflection and smoothening interference upon employing the "flower structure." Inset shows a 55 degree tilted SEM picture of one such structure. Taken from Hünig, R., Mertens, A., Stephan, M., *et al.,* 2016. Flower power: Exploiting plants' epidermal structures for enhanced light harvesting in thin-film solar cells. Advanced Optical Materials 4 (10), 1487–1493.

index profile. The tapered shape of the nanorod arrays leads to impedance matching between absorber and air through a gradual reduction of the effective refractive index away from the surface, resulting in low reflection particularly at longer wavelengths and eliminating interference fringes through roughening of the top interface (Lee *et al.*, 2008). Following its success on Si solar cells, ZnO NWs grown using metalorganic chemical vapor deposition have been applied on OSCs following its success on Si solar cells resulting in a 36% boost in optical absorption compared to planar devices (Hiralal *et al.*, 2014). These AR structures are particularly interesting due to the fact that the AR effect becomes more pronounced at large angles of incidence and they can exhibit self-cleaning properties due to the hydrophobic surfaces created through relevant surface treatment.

Light Trapping

While optical losses in cells can be reduced by proper choice of materials and good AR layers, inefficient light absorption in thin OSCs is a critical issue that limits cell efficiency. Traditional light trapping in solar cells consist of surface textures such as pyramids which allows randomized light paths in the cell, thus enhancing the optical path length and providing more opportunities for the light to be absorbed. However, the fragile nature and small physical dimensions of OSCs preclude such trapping schemes used in inorganic solar cells like Si which makes low cost fabrication challenging. Hence light trapping schemes have to be modified in OSCs using coherent light trapping approaches that make use of wave nature of light to make significant contributions. A good discussion on coherent light trapping can be found in Mallick *et al.* (2011).

The fundamental light trapping limit of light is $4n^2$ where n is the refractive index of the thick absorber layer. This was proposed by Yablonovitch and is known as the ray-optics limit (Yablonovitch, 1982) where the light scattered is considered to be ergodic, i.e., light will be coupled equally to all available modes. However, for thin layers where the thickness of the absorber layer is smaller or comparable to the wavelength of light, this limit does not apply as the number of modes available reduces to a set of discrete modes. Based on a rigorous electromagnetic wave approach, Yu *et al.* proposed that the standard limit can be surpassed to an absorption enhancement factor of $12 \times 4n^2$ using nanophotonic light trapping approaches (Yu *et al.*, 2011). Two such nanophotonic structures were proposed by Yu *et al.*, (2011) and (Green, 2011) where both proposed low index absorber layer sandwiched between high index layers that is ideal for OSCs. In both cases the index contrast between the cladding layer and the absorber layer provides strong nanoscale field confinement in the absorber layer with the potential to improve cell performance dramatically. Yu's structure considered a 5-nm absorber layer sandwiched between a 60 nm thick high refractive index cladding layer and a mirror. An 80-nm scattering layer consisting of groove patterns was used to couple light into the guided modes from all

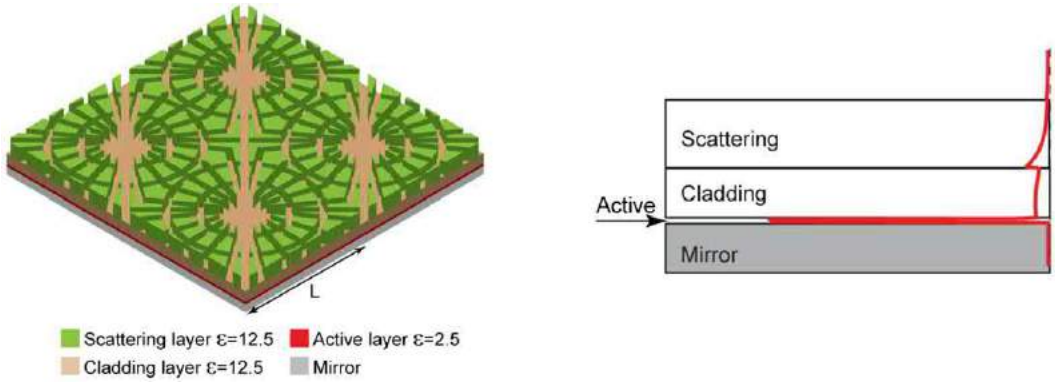


Fig. 4 (left) Schematic of a nanophotonic light trapping structure with an 80 nm thick scattering layer comprising square lattice of air grooves of periodicity 1200 nm, 60 nm cladding layer and 5 nm active layer on a mirror; (right) electric field intensity profile of the fundamental waveguide mode. Taken from Yu, Z., Raman, A., Fan, S., 2011. Nanophotonic light-trapping theory for solar cells. Applied Physics A. doi: 10.1007/s00339-011-6617-4.

angles. Green's work used a similar sandwiched structure but with the absorber layer between two high index cladding layers leading to an enhanced field in the absorber layer due to tunneling evanescent waves. While organic materials with low index are suitable and could highly benefit with active layers in these two configurations, it is crucial to identify high index cladding materials with low parasitic absorption. **Fig. 4** shows nanophotonic light trapping structure along with the electric-field intensity for the waveguide mode that is strongly confined to the active layer.

Light trapping by scattering and randomizing of light in such a way that light travels more in the plane of the absorber is difficult to realize in OSCs as the feature sizes should be larger or comparable to the thickness of the organic layer (which is the order of wavelength of light). Moreover, as mentioned earlier, nano-textures can degrade the performance of the device due to recombination losses. Hence different engineering solutions to trap light have been investigated without increasing the surface recombination. One such case is where the scattering layer is isolated from the absorber layer. The structure comprises of low absorption micro-lenses on top of reflecting mirrors with small transmitting openings for the focused light to be incident onto an OSC absorber as shown in **Fig. 5(a)**. The lens/mirror combination collimates the incident light in the forward direction and is highly reflective to both collimated and scattered light in the opposite direction. The light in this case bounces back and forth between the mirror and the back electrode increasing the probability of light absorption. More chances of photon recycling exist where absorption is weak with these light trapping elements enhancing photocurrent by as much as 25% (Tvingstedt *et al.*, 2008). One drawback of such structures is the need for accurate focusing as it is angle sensitive which may otherwise result in shading when the holes are not properly aligned.

Microlens array of closely packed hemispherical shape has been fabricated earlier using soft lithographic molding technique as shown in **Fig. 5(b)** (Myers *et al.*, 2012). Both AR and light trapping resulted in a 15–60% relative increase in efficiency. This structure did not have any mirrors, unlike the patterned mirror-and-lens light trap structure in **Fig. 5(a)**, hence a more economical structure considering that it is attached to the outer layer of glass without affecting the surface morphology of the active layer. Similar enhancements and 2.5 times longer pathlength using pyramidal rear reflectors fabricated on glass for semitransparent OSC have also been reported (Cao *et al.*, 2011).

Attempts have also been made to realize surface textures that are on a length scale much larger than the active layer thickness and that requires no modification of the device structure. The active layer and reflective metal electrode are deposited on a V or W-shaped transparent substrate coated with a transparent electrode such as indium tin oxide (ITO) (**Fig. 5(c)**) that increases photocurrent efficiency for all angles of incidence (Rim *et al.*, 2007). A 52% increase in power conversion efficiency was demonstrated using poly(3-hexylthiophene-2,5-diyl):[6,6]-phenyl-C61 butyric acid methyl ester (P3HT:PCBM) polymer blend cells that occupied the complete V shaped area. The viability of the V-shaped trap depends on the balance of the added cost of the structure and increase in active material with the reduction in installation cost of modules with high efficiencies. **Fig. 5(d)** shows a photo of the V and W-geometry cell taken from Zhou *et al.* (2008).

A photonic crystal structure is another method used for light management in OSCs. They comprise of dielectric or metallic structures that can manipulate the flow of photons. A variation to the microlens structure consist of polymer microlens on the exterior glass coupled with a photonic-plasmonic crystal at the metal cathode on the back of the cell but without mirrors (Peer and Biswas, 2014) (plasmonic structures are metal-based nanostructures with the potential to manipulate the flow of light in the adjoining absorber layer and will be discussed in more detail in a separate section). These microlens arrays focus and diffract light within the OSC which then is coupled to a periodically patterned organic layer facilitated by the periodically patterned metal cathode. Strong diffraction, waveguide modes and plasmonic light concentration effects contribute to the performance enhancement. This work demonstrated experimentally realizable solar cell structures with simulations predicting a photocurrent enhancement of $\sim$58% relative to a flat cell. The absorption approached the Lambertian limit with enhanced absorption at longer wavelengths.

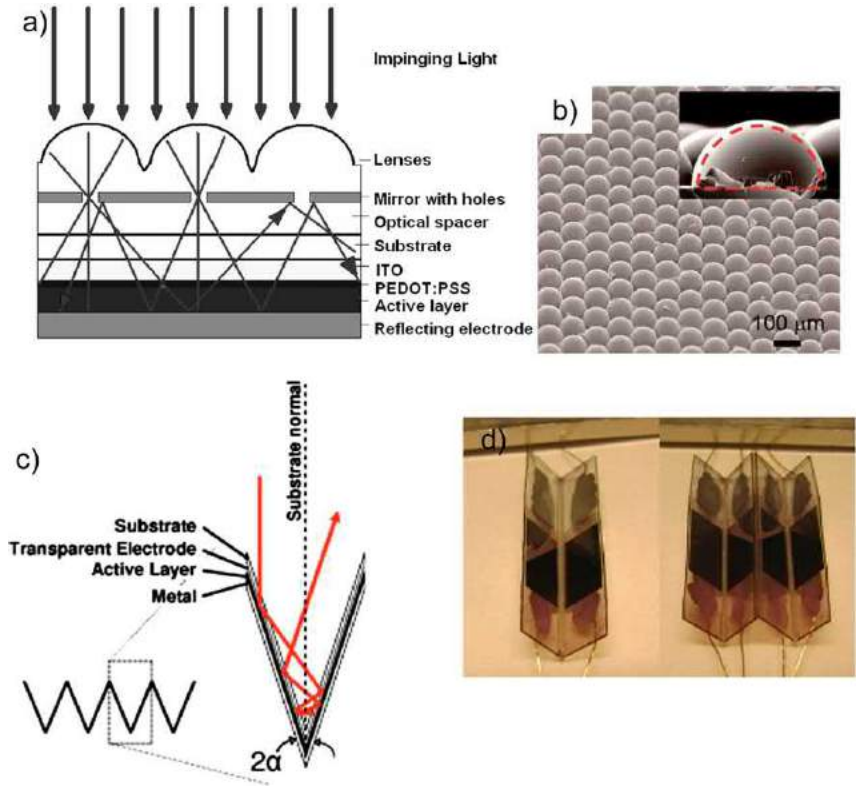


Fig. 5 (a) Schematic of an array of micro-lenses as a light trapping layer for an organic solar cell (Taken from Tvingstedt, K., Zilio, S.D., Inganäs, O., Tormen, M., 2008. Trapping light with micro lenses in thin film organic photovoltaic cells. Optics Express 16 (26), 21608–21615); (b) an scanning electron microscope (SEM) image of a microlens array (Reproduced from Myers, J.D., Cao, W., Cassidy, V., *et al.*, 2012. A universal optical approach to enhancing efficiency of organic-based photovoltaic devices. Energy & Environmental Science 5 (5), 6900–6904); (c) geometry of the V shaped light trapping structure with a very thin layer of absorber layer (Taken from Rim, S.-B., Zhao, S., Scully, S.R., McGehee, M.D., Peumans, P., 2007. An effective light trapping configuration for thin-film solar cells. Applied Physics Letters 91 (24), 243501). (d) Pictures of V and W-geometry cell (Taken from Zhou, Y., Zhang, F., Tvingstedt, K., Tian, W., Inganäs, O., 2008. Multifolded polymer solar cells on flexible substrates. Applied Physics Letters 93 (3), 033302. ITO, indium tin oxide; PEDOT:PSS, poly (3,4-ethylenedioxythiophene):polystyrene sulfonate).

A photonic substrate texturing technique, making use of folds and wrinkles, has shown to significantly enhance the incoupling of the light in OSCs (Gregg and van de Lagemaat, 2012) taking inspiration form the structure of leaves which has high light-harvesting efficiency. **Fig. 6(a)–(e)** shows the scanning electron microscope (SEM) image of the wrinkles developing into folds. Here an optically curable adhesive layer on the substrate is subject to compressive stress with a sequence of ultraviolet pulses and subsequent plasma treatment creating folds and wrinkles (Kim *et al.*, 2012). The entire folded layer was then coated with gold (Au) (anode) followed by the organic polymer P3HT:PCBM as shown in the inset of **Fig. 6(e)**. These combination of wrinkles and deep folds act as photonic structures; they increase light coupling into and trapping light by waveguiding effects. In this work although there was a 79% increase in the external quantum efficiency (EQE) in the visible region compared to devices on flat surfaces, the EQE of the polymer material was interestingly improved by more than 600% in the near-infrared (where absorption is weak), where the useful range of solar energy conversion is extended by more than 200 nm (beyond the absorption edge of P3HT:PCBM >650 nm). **Fig. 6(e)** and **(f)** show the IV and EQE of the cells with the wrinkles and wrinkle and fold combination compared to a reference cell.

Metal Nanostructures (Plasmonics)

Metal nanostructures in the form of metal nanoparticles (NPs), NWs or nanogratings have attracted a lot of attention as a means of light trapping in solar cells. Metal nanostructures in the nanoscale support plasmons which are collective oscillations of conduction electrons at a metal–dielectric interface. They support resonances that can be tuned by changing the geometry (size, shape, aspect ratio), the choice of metal or the dielectric environment around it (Raether, 1988). An entirely new field called Plasmonics is credited to the unique properties of these metallic nanostructures that can scatter, concentrate or manipulate the flow of light. Inside the device, the scattered light effectively increases the optical path length, while the near-field effect increases the electric field in the vicinity of the plasmons through the excitation of localized surface plasmon resonance (LSPR). Both effects enhance

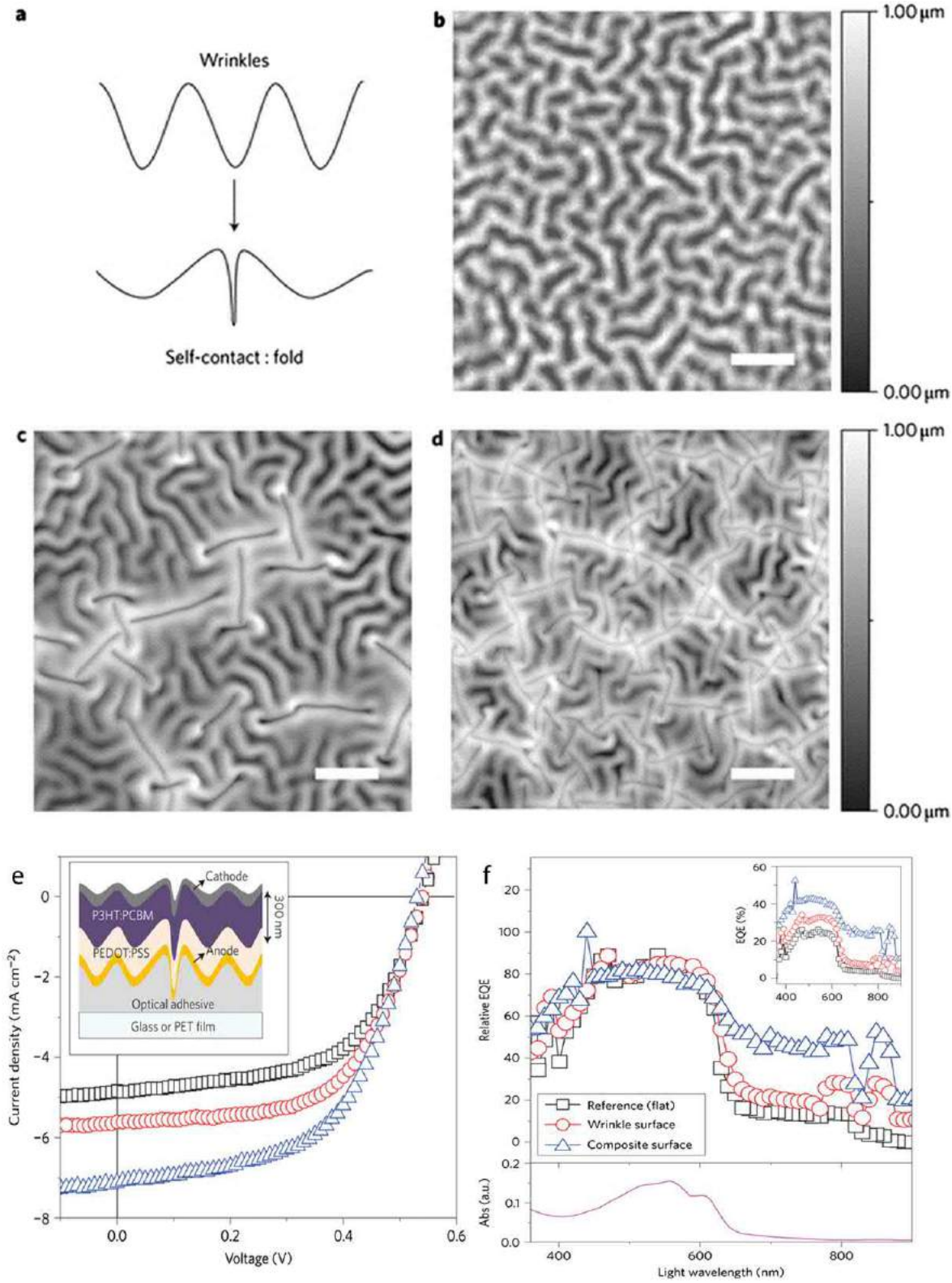


Fig. 6 (a)–(d) Scanning electron microscope (SEM) image of the morphology scan showing wrinkles developing into folds. (e) I–V characteristic of the cells with wrinkles and wrinkle and fold combination (inset) schematic of the structure with wrinkles and fold. (f) External quantum efficiency (EQE) of the polymer solar cell. The light is folded into the active layer by the folds of the adhesive and the wrinkles help localize the light through waveguiding effects. Taken from Kim, J.B., Kim, P., Pegard, N.C., *et al.,* 2012. Wrinkles and deep folds as photonic structures in photovoltaics. Nature Photonics 6 (5), 327–332.

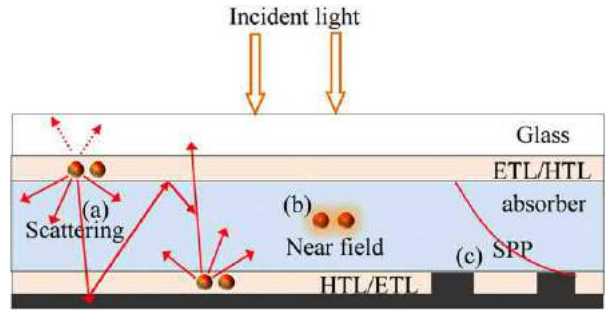


Fig. 7 Light trapping mechanisms using plasmonic effects: (a) scattering due to plasmons embedded in one of the hole/electron transport layers, (b) near field often with embedded particles in the active layer, and (c) propagating plasmons at a structured interface between metal electrode and active layer. ETL, electron transport layer; HTL, hole transport layer; SPP, surface plasmon polaritons.

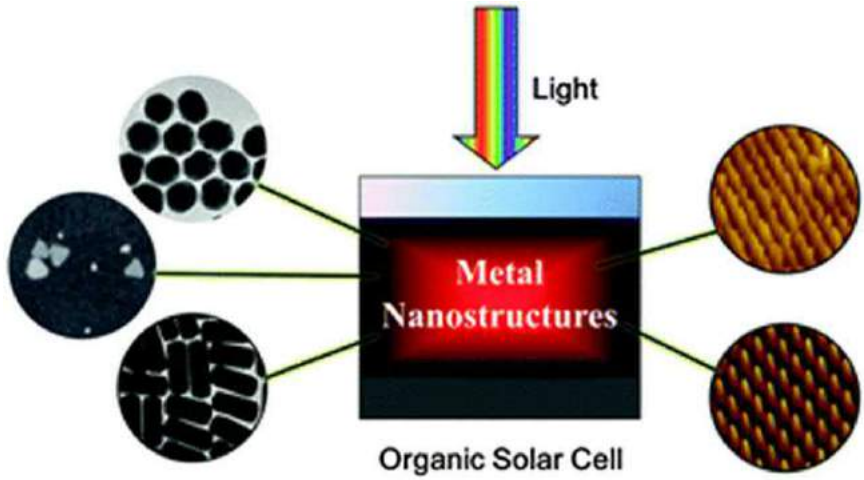


Fig. 8 Different plasmonic metal structures that can contribute to the light trapping in organic solar cells (OSCs) which includes nanoparticles (NPs), nanaorods, (NRs) and grating structures. Available online only with abstract for reference Choy, W.C.H., 2014. The emerging multiple metal nanostructures for enhancing the light trapping of thin film organic photovoltaic cells. Chemical Communications 50 (81), 11984–11993.

absorption of light in the active absorber layer in a solar cell (Pillai and Green, 2010). Structured metal interfaces can also help couple the light using surface plasmon polaritons (SPP) that are propagating plasmons at a metal dielectric interface. **Fig. 7** shows a schematic of the various plasmonic effects contributing to enhanced power conversion efficiency.

Among the metal NPs used to improve light absorption, silver (Ag) and Au are traditionally the focus of research, even though other metals also exhibit plasmonic properties (Pillai and Green 2010). In particular, aluminum (Al) NPs have been known to effectively reduce reflection losses due to their higher resonant frequency, and hence have limited metal absorption (Green and Pillai 2012). While an interband absorption in Al at 800 nm limits its use in Si solar cells (Temple and Bagnall, 2011), potential applications in organic photovoltaics (OPV) devices can be considered due to the larger bandgap of organic semiconductors.

Various plasmonic device architectures have been proposed to take advantage of the improved optical properties when plasmonic nanostructures are integrated into OSCs (Gan *et al.*, 2013; Chou and Chen, 2014; Stratakis and Kymakis, 2013) as shown in **Fig. 8**. The device structure can incorporate NPs, nanorods (NRs), nanoplatelets, nanoprisms, NWs, or nanogratings, which can be located in the active layer, the transport layers, buffer layer or at the interface between two layers (Chou and Chen, 2014). The improved optical properties in these metal nanostructures can manifest in the near field or far field, with various effects observed depending on the configuration of the plasmonic organic solar cell. A common methodology for fabricating plasmonic OSCs involves integration of plasmonic NPs (or discrete particles such as NRs) in one of the charge transport layer of the device as shown in **Fig. 7(a)**.

Rand *et al.* (2004) reported one of the earliest device architectures incorporating plasmonic nanostructures, where enhanced optical field intensity in the near-field was observed when Ag nanoclusters were utilized in OSCs. This broadband enhanced field allowed increased light absorption up to 10 nm from the clusters. More recently, Au NPs and NRs were incorporated into the poly (3,4-ethylenedioxythiophene):polystyrene sulfonate (PEDOT:PSS) layer of an organic solar cell to trigger various LSPR bands. Improvements in light absorption due to an enhanced LSPR-induced local field resulted in an increase in the device efficiency by up to 24% (Hsiao *et al.*, 2012). Transmission electron microscopy (TEM) images of the plasmonic nanostructures and the improved EQE in the 450–600 nm wavelength range are shown in **Fig. 9**. Another example of near field enhancement can be seen

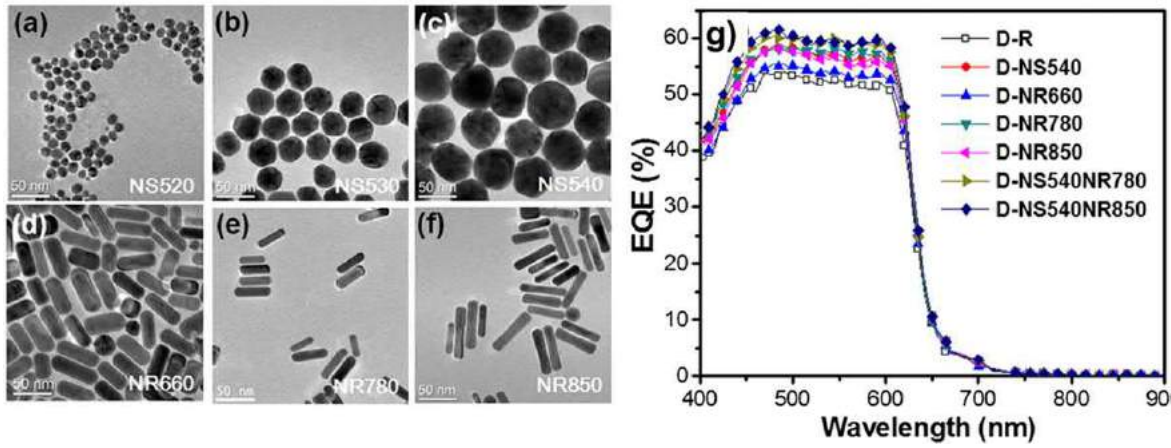


Fig. 9 (a)–(f) Transmission electron microscopy (TEM) images of different size/shape Au nanoparticle (NPs) with tunable localized surface plasmon resonance (LSPR) and (g) external quantum efficiency (EQE) spectra of poly(3,4-ethylenedioxythiophene) polystyrene sulfonate (PEDOT:PSS) layers incorporating the Au NPs at 100 mW/cm^2 illumination and EQE of devices containing various plasmonic nanostructures. Taken from Hsiao, Y.-S., Charan, S., Wu, F.-Y., *et al.,* 2012. Improving the light trapping efficiency of plasmonic polymer solar cells through photon management. The Journal of Physical Chemistry C 116 (39), 20731–20737.

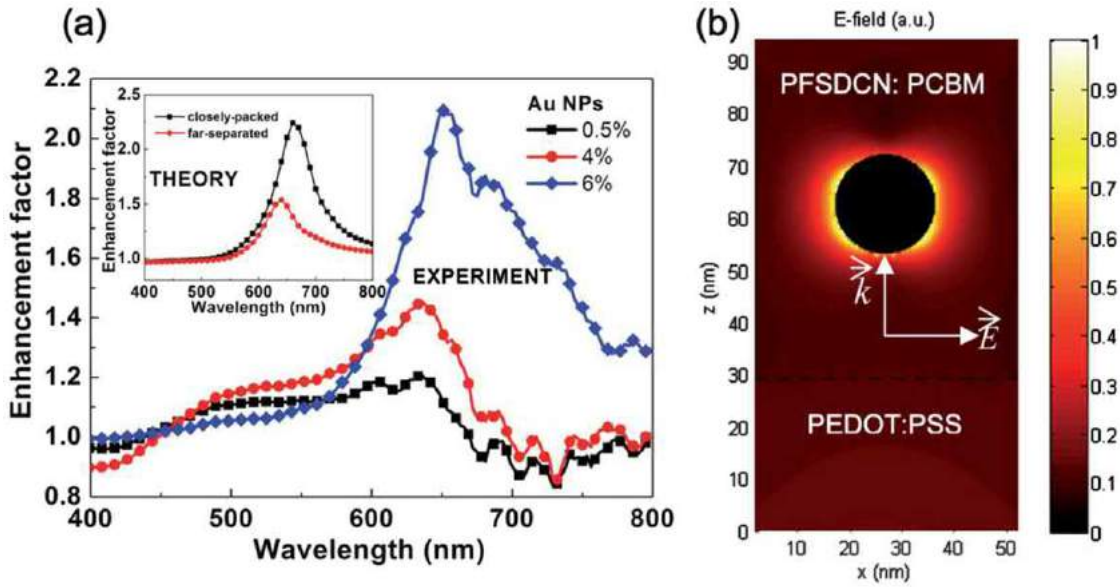


Fig. 10 (a) Experimental and theoretical demonstration of absorbance enhancement factor when Au nanoparticles (NPs) are embedded in the active layer and (b) the calculated near field enhancement around the Au NP in the active layer. PEDOT:PSS, poly(3,4-ethylenedioxythiophene) polystyrene sulfonate; PFSDCN:PCBM, poly[2,7-(9,9-dioctylfluorene)-alt-2-((4-(diphenylamino) phenyl)thiophen-2-yl)malononitrile]:[6,6]-phenyl-C61 butyric acid methyl ester. Taken from Wang, C.C.D., Choy, W.C.H., Duan, C., *et al.,* 2012. Optical and electrical effects of gold nanoparticles in the active layer of polymer solar cells. Journal of Materials Chemistry 22 (3), 1206–1211.

when Ag NPs are incorporated into the PEDOT:PSS using a pulse-current electrodeposition technique (Kim *et al.,* 2008). It was found that stronger light absorption is due to the high electromagnetic field strength in the vicinity of excited surface plasmons. While NPs can affect device performance when inadvertently contacting the active layer, there have been successful demonstrations of plasmonic nanostructures integrated in the active layer as represented in **Fig. 7(b)**. In one report, Au NPs embedded into the active layer of the polymer solar cells showed improved performance both experimentally and theoretically due to excitation of LSPR (Wang *et al.,* 2012). The strong lateral distribution of the near field in this case is cited as the reason for enhancement as shown in the results in **Fig. 10**. Plasmonic nanostructures have also been used in a dual plasmon configuration. Liu *et al.* demonstrated increased J_{sc} from a device containing Au nano-dots and Au NPs in a blend with PEDOT:PSS respectively at each interface of the active layer (Liu *et al.,* 2013). The effective optical path length was increased due to the light scattering and LSPR effects of the Au NPs. It was also reported that increased light absorption from the Au nanodots was mainly derived from near-field

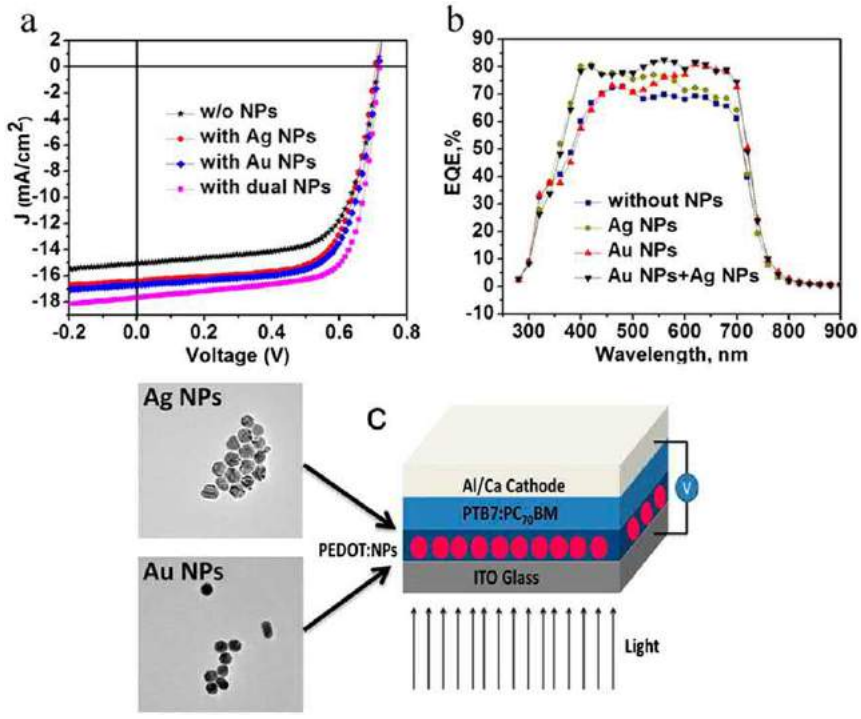


Fig. 11 (a) I–V characteristics of solar cells without and with Au and Ag nanoparticles (NPs), (b) external quantum efficiency (EQE) spectra without and with Au and Ag NPs, (c) schematic of the placement of the NP in the poly(3,4-ethylenedioxythiophene) (PEDOT) layer and the corresponding transmission electron microscope (TEM) images of the Au and Ag NPs. ITO, indium tin oxide; PTB7:$PC_{70}BM$, poly[[4,8-bis[(2-ethylhexyl)oxy]-benzo[1,2-b:4,5-b']dithiophene-2,6-diyl][3-fluoro-2-[(2-ethylhexyl)-carbonyl]thieno[3,4-b]thiophenediyl]]:[6,6]-phenyl-C70-butyric acid methyl ester. Taken from Lu, L., Luo, Z., Xu, T., Yu, L., 2013. Cooperative plasmonic effect of Ag and Au nanoparticles on enhancing performance of polymer solar cells. Nano Letters 13 (1), 59–64.

effects. Cooperative plasmonic effect using Au and Ag NP of ~40–50 nm diameter size embedded in the anode buffer layer PEDOT resulted in an 8.67% bulk heterojunction polymer cell accounting for 20% enhancement (Lu *et al.*, 2013). The observed effects were greater than any one type of the single NPs alone and were attributed to the dual resonance peaks of the two different NPs. The IV curve and the EQE of the comparative performance of poly[[4,8-bis[(2-ethylhexyl)oxy]-benzo[1,2-b:4,5-b']dithiophene-2,6-diyl][3-fluoro-2-[(2-ethylhexyl)-carbonyl]thieno[3,4-b]thiophenediyl]] (PTB7) and [6,6]-Phenyl-C70-butyric acid methyl ester ($PC_{70}BM$) blend polymer cell is shown in **Fig. 11(a)** and **(b)**, respectively, along with a schematic and TEM images of the NPs in **Fig. 11(c)**. In this work, it was concluded that the LSPR-induced local field not only helped to improve light absorption, but also aided the electrical properties like charge separation and transport thereby improving carrier density and lifetime.

There have been many observations of the near-field in plasmonic OSCs, however, far-field effects or light scattering can also significantly contribute to improved device performances. By varying the size of Ag NPs in PEDOT:PSS, a plasmonic forward scattering effect was demonstrated in PCDTBT:$PC_{70}BM$ and PTB7:$PC_{70}BM$ OSCs (Baek *et al.*, 2013). Enhanced light absorption due to plasmonic scattering by the Ag NPs led to improved EQE. Near-field scanning optical microscopy was used to probe the higher degree of light scattering in plasmonic devices. Simulations with these Ag NPs also found a high ratio of forward light scattering to total scattering, which indicates minimum backward scattered power loss.

Advanced plasmonic nanostructures, such as NWs, nanogratings and nanocomposites, have also been successfully integrated into OSCs. Kang *et al.* (2010) used a Ag NW electrode configuration to enhance power conversion efficiency by SPR and waveguide effects. Further improvements can be made to raise the efficiency by adjusting the period of the Ag grating such that the enhanced spectral range matches the peak absorption in organic semiconductors, thus demonstrating the flexibility and potential when integrating plasmonic nanostructures. Improvements in device performance extends to the application of Ag nanogratings and Au NPs in a dual plasmonic nanostructured device, which revealed broadband absorption enhancement (Li *et al.*, 2012). The improved broadband light absorption was ascribed to the simultaneous effects of LSPR (Au NPs) and hybridized SPR (Ag nanogratings).

As discussed previously, far-field effects also exist when these advanced plasmonic nanostructures are incorporated into OSCs. In one study, hole-mask colloidal lithography was used to pattern the Ag rear electrode and MoO_x hole transport layer (Niesen *et al.*, 2013). The resultant nanostructured Ag electrode as shown in **Fig. 12(a)** was tuned by varying the size of the protrusions in the MoO_x layer to maximize light scattering due to the dipole LSPR at the red absorption tail of the poly(3-hexylthiophene-2,5-diyl):indene-C60 bisadduct (P3HT:ICBA) active layer. Systematic optimization of the optical interference pattern, when changing the dimensions of the optical spacer and plasmonic nanostructure, were essential in achieving the observed enhanced absorption

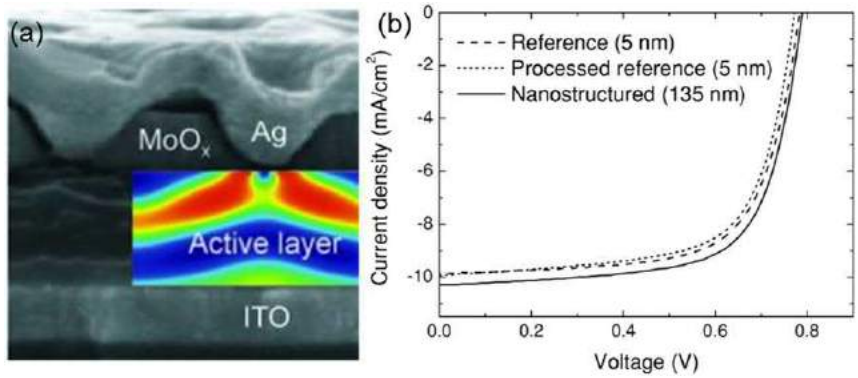


Fig. 12 (a) Scanning electron microscope (SEM) image of a nano-textured rear Ag electrode showing the different layers. Inset is the field profile in the active layer overlayed onto a section of the active layer and (b) I–V characteristics of flat reference devices with a 5-mm-thick MoO_x layer and the nanostructured device with a total MoO_x layer thickness of 135 nm with the increase attributed to light scattering.

(**Fig. 12(b)**). Importantly, it was noted that the near-field enhancement exists mainly within the MoO_x layer and, in that case, was not the cause of enhanced light absorption, rather the enhancement was the result of light scattering.

In general, it is often important to isolate the plasmonic nanostructures from the active layer. This is to avoid any metal assisted recombination or defects impacting the electrical properties of the cell. Another important consideration is also to avoid any parasitic losses in the metal that could compromise useful absorption. Plasmonic applications that rely on the near-field effect would need to address the trade-off between proximity of plasmon to the active absorber layer and electric field strength caused by SPR. The trade-off arises because it is advantageous to physically separate plasmonic nanostructures from the active layer to decrease surface recombination. However, the electric field enhancement provided by the plasmons decays exponentially with distance. Hence, there is an optimal physical separation to achieve high efficiency devices, which usually is $\sim$20 nm in the vicinity of the particle. A systematic study of the near-field interaction between excitons and plasmonic metal NPs in OSCs found that far-field light scattering was not a significant consideration for the Ag NPs used in their study (Niesen *et al.*, 2012). As expected, the enhanced absorption from the near-field rapidly decreased when a spacer layer was introduced between the active layer and the NPs. In another experiment, Morfa *et al.* (2008) found that varying Ag film thickness affects the average J_{sc} and V_{oc}. It was suggested that the film thickness of the PEDOT:PSS layer should be limited as the electric field decays with distance.

Recent efforts in utilizing core-shell NPs have found promising results that both preserves the near-field and reduce surface recombination effects (Chen *et al.*, 2013; Janković *et al.*, 2013). A unique device structure for plasmonic OPV devices, that used large sized Au@SiO_2 NPs (50 nm SiO_2 shell and 70 nm Au core) which penetrated into all layers in the device had been successfully demonstrated (Chen *et al.*, 2013). The main contribution of the Au@SiO_2 NPs was reported to be LSPR effects from the Au NP core. Au-SiO_2 core-shell NRs can also be blended within the active layer to improve performance in poly[2,6-(4,4-bis-(2-ethylhexyl)-4H-cyclopenta [2,1-b;3,4-b′]dithiophene)-alt-4,7(2,1,3-benzothia-diazole)]:[6,6]-phenyl-C70-butyric acid methyl ester (PCPDTBT:PC_{70}BM) OPV devices (Xu *et al.*, 2013).

The challenges of having the metal nanostructures incorporated into the device and the extent of understanding the physical mechanisms behind these effects have prompted many simulation studies. The studies attributed enhanced performance in plasmonic device to light concentration and redistribution of plasmons (Zhu *et al.*, 2012; Dunbar *et al.*, 2012), which can be further categorized depending on the positioning of plasmonic nanostructures: NPs dispersed in the active layer, nanostructured metallic electrode and in-scattering NPs. Simulations can be used to model light absorption and compared to a reference flat solar cell. The presence of the NPs provided an overall increase in absorption despite the reduction in absorption due to the omitted parts of the active layer. It is predicted that both scattering and near-field enhancement due to SPR are responsible for the broadband enhancement in light absorption. A simulation study has also analyzed the trade-off between absorption in the active layer as opposed to parasitic absorption in the near-field of the metal for the case of embedded spheres (Lee and Peumans 2010). The study showed that enhanced optical absorption results from strong scattering by a 10 nm Ag metal nanoparticle which locally enhances the optical electric fields. The enhancement extends to wavelengths longer than the plasmon resonance wavelength for which the losses in the metallic particles become insignificant.

A three-dimensional finite-difference time domain (FDTD) model is also commonly employed for simulation purposes. Using FDTD software, changes in metal NPs scattering cross-section, emission efficiency and far-field scattering pattern can be investigated by varying properties of a thin dielectric film around the NPs (Powell *et al.*, 2013). It is also imperative that the refractive indexes of materials within the device be considered when integrating metal NPs into OSCs. In particular, transparent conducting oxides, that frequently form the front contact in OPV devices, typically have large refractive indexes compared to the active layer. Hence, losses around the dipolar peak are expected due to the preferential light scattering into the higher index front contact.

Discussions on the progress in incorporating metallic nanostructures in OSCs and categorization of the physical mechanisms that led to improvements can be found in the literature (Choy, 2014). These improvements were found to originate from modifications of the optical or electrical properties in the OPV device. Changes in electrical properties, such as exciton dissociation,

charge carrier transport and charge extraction can also contribute to enhanced performance in plasmonic OSCs as mentioned earlier. Further discussions on the electrical effects of plasmonic OSCs can be found in the literature (Choy and Xingang, 2016; Chan *et al.*, 2016) and will not be discussed here.

Spacer Layer and Cavity Effects

Light harvesting by manipulating and optimizing the optical field can also be achieved via cavity effects or optical spacers. OSCs consist of many thin layers, each with a unique refractive index and thickness. (Burkhard *et al*, 2010). **Fig. 13** provides a schematic device structure, which includes a glass substrate, conducting oxide ITO electrode, thin electron transport layer (e.g., TiO_2), organic active layer (like P3HT:PCBM), a hole transport layer (e.g., MoO_3) and a reflective metal electrode (Ag).

As shown in **Fig. 13**, light enters the device through the glass substrate. Ideally, all the light would be absorbed in the active layer, however, in practice, this is not the case as mentioned before due to various losses. The light passes through the transparent electrode, some light is absorbed in the active layer, however, some light passes through and is reflected by the back electrode. Interference between the incoming and reflected light causes the optical field to go to zero at the reflective electrode. This leads to the formation of an optical field standing wave, of which the maximum and minimum will lie somewhere in the device. The nature of this optical field is determined by the refractive index and thickness of each layer.

It seems intuitive to simply increase the thickness of the active layer to maximize the absorption, however, the nature of the organic semiconductors places limitations on the film thickness. The optimum active layer film thickness is usually very thin, on the order of 100 nm, limited by the diffusion length of the excitons. Due to the limited film thickness, it is crucial to understand and optimize this optical interference effect.

As the maximum in the optical field is governed by the thickness and refractive index of the layers, it is possible to control the position of the maximum field by altering the device architecture. Including an additional layer to redistribute the optical field is called an optical spacer (Kim *et al.*, 2006). **Fig. 14** describes the influence of an optical spacer. As shown, the insertion of a thin layer can shift the absorption maximum to better align with the active layer. It was shown that the insertion of a TiO_2 optical

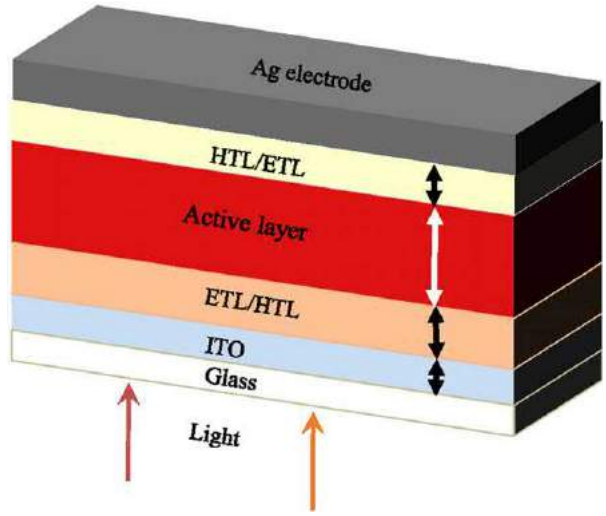


Fig. 13 Schematic diagram of a device structure showing the many layers involved. ETL, electron transport layer; HTL, hole transport layer; ITO, indium tin oxide.

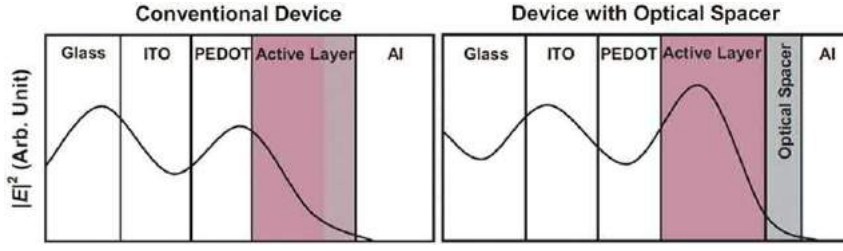


Fig. 14 Schematic representation of the optical field in an organic solar cell with and without an optical spacer. ITO, indium tin oxide; PEDOT, poly(3,4-ethylenedioxythiophene). Taken from Kim, J.Y., Kim, S.H., Lee, H.H., *et al.*, 2006. New architecture for high-efficiency polymer photovoltaic cells using solution-based titanium oxide as an optical spacer. Advanced Materials 18 (5), 572–576.

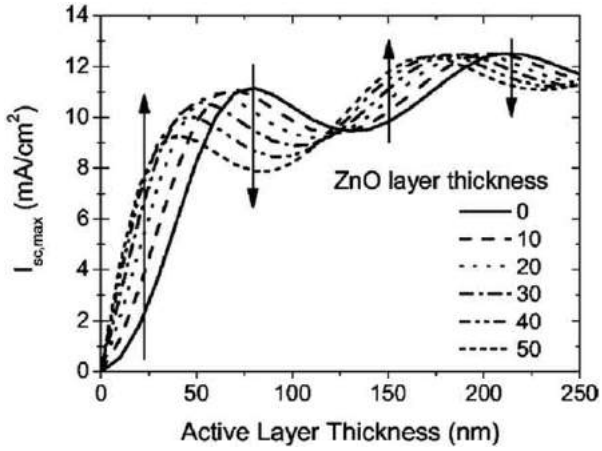


Fig. 15 Calculated short circuit current density (I_{sc}) as a function of active layer thickness for varying ZnO thicknesses. An assumption of 100% internal quantum efficiency (IQE) for all wavelengths was used. Reproduced from Gilot, J., Barbu, I., Wienk, M.M., Janssen, R.A.J., 2007. The use of ZnO as optical spacer in polymer solar cells: Theoretical and experimental study. Applied Physics Letters 91 (11), 113520.

spacer caused the power conversion efficiency to increase by 50% (relative) (Kim *et al.*, 2006). It is important to note that the optical spacer material must also serve a purpose electronically, as well as optically. For example, due to the spacer layer being part of the device, the photocatalytic property of TiO_2 under ultraviolet light can result in the breakdown of organic molecules limiting the lifetime of the device (Hiralal *et al.*, 2014). Hence the choice of the materials becomes important.

Gilot *et al.* (2007) used a ZnO layer as an optical spacer. They used transfer matrix modeling to calculate the optimum ZnO thickness, which would most effectively shift the optical field maximum into the active layer. They also calculated the maximum generated photocurrent (I_{sc}) as a function of active layer thickness, for varying ZnO layer thickness. This is displayed in **Fig. 15**. This clearly shows that the I_{sc} is not directly proportional to active layer thickness. The oscillations, causing maxima and minima, are due to the interference effects. By incorporating the ZnO optical spacer, the maxima are shifter to lower thicknesses. This positive influence of the optical spacer is more pronounced for thinner active layers.

Betancur *et al.* extend on this argument. They suggest that the position of the optical field maximum is dependent on the thickness of all layers in the device stack, not just the optical spacer (Betancur *et al.*, 2012). The device architecture, meaning the types of buffer layers used, which determines the direction of current flow, may also influence the optical field distribution. In another study it was suggested that an optical spacer will have much less impact on the photon absorption in an inverted structure device, when compared to conventional structure devices, which contain a PEDOT:PSS hole selective contact (Ameri *et al.*, 2008). In a study using ITO as spacer layer, it was found that although the degree of light absorption in inverted OPVs was not increased in such inverted structures, the favorable distribution of photogenerated excitons is expected to have decreased the level of exciton quenching near the electrodes (Chen *et al.*, 2010). Their results indicate that the inverted OPVs could still benefit from such optical effects when they had a sufficiently thick active layer. Subsequently there were studies that completely dismissed the idea of using spacer layer for increasing efficiency although the potential for increase was not ruled out for suboptimal thicknesses (Andersson *et al.*, 2009).

The nature of the interference effects also plays a role in the correct determination of the internal quantum efficiency (IQE) of an organic solar cell (Burkhard *et al.*, 2010). The IQE represents the wavelength dependent solar response for photons which are absorbed by the active layer; this parameter should be independent of the absorption profiles. Armin *et al.* showed that due to the nature of OSCs, optical interference and parasitic absorption in non-active layers must be considered to accurately determine the IQE (Armin *et al.*, 2014).

Another strategy adopted to help enhance the absorption in the thin photoactive layer is to incorporate a microcavity array into the device architecture. The concept of a microcavity design involves a resonator structure which consists of a spacer layer sandwiched between two reflectors (Chen *et al.*, 2014a,b). This allows for optical confinement due to the multiple reflections, significantly increasing the absorption path length of light with resonant frequencies. A normal OPV cell has a reflective back electrode; however, the front electrode is required to be transparent to allow light in. Such a structure behaves as an inefficient microcavity device, due to the limited reflection from the transparent electrode, which is most commonly ITO. This is made more complex as the two sandwiching layers must play a role in the electronic operation of the device, not only the optical confinement. To successfully harness this optical confinement technique, a precise trade-off between the transmission and reflection of the bottom electrode, to allow for light to enter the active layer and to enhance the multi-reflection optical confinement, respectively, must be understood.

To do so, the ITO layer was replaced. Studies have demonstrated an efficient device containing a microcavity structure by replacing the ITO with an ultrathin metal film (UTMF) and a capping layer which acted as an optical spacer (Chen *et al.*, 2014a,b; Sergeant *et al.*, 2013). The UTMF behaves as a semitransparent mirror enhancing lateral conductivity and reduce sheet resistance. One such modified device structure is shown schematically in **Fig. 16**. As shown, the light shines through the top, semitransparent

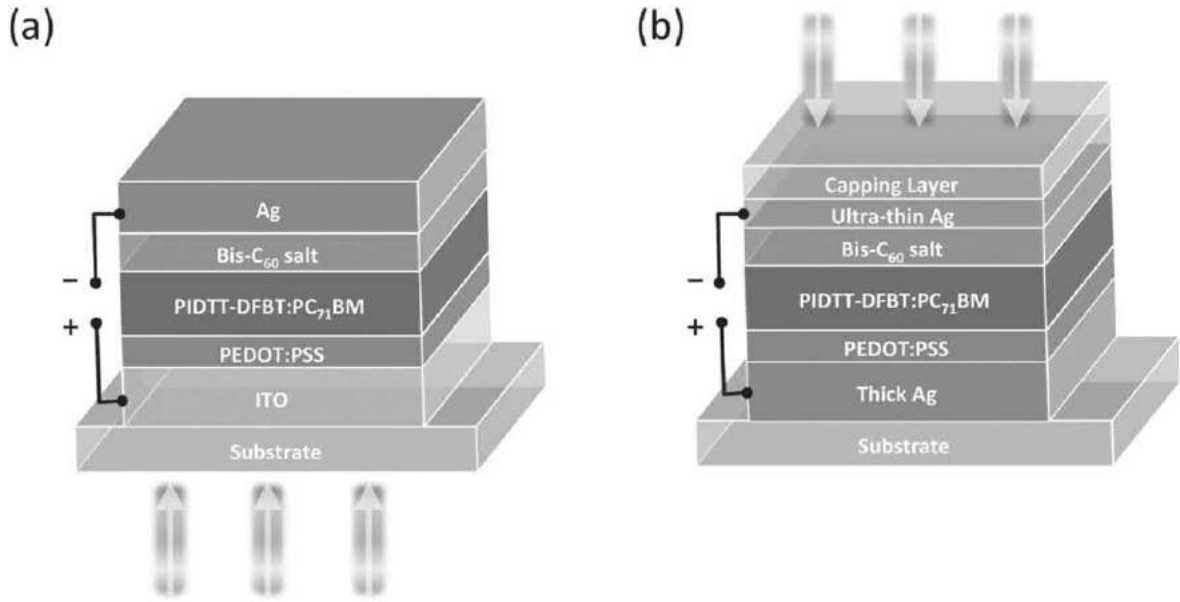


Fig. 16 Schematic depiction of (a) the traditional device structure, containing indium tin oxide (ITO), and (b) the microcavity configuration containing an ultrathin metal film (UTMF) and capping layer to increase the incoupling of light. In this device structure, the light is illuminated through the top electrode. ITO, indium tin oxide; PEDOT:PSS, poly(3,4-ethylenedioxythiophene):polystyrene sulfonate, PIDTT-DFBT, poly [(indacenodithieno[3,2 – b]thiophene)-alt-difluorobenzothiadiazole]. Reproduced from Chen, K.-S., Yip, H.-L., Salinas, J.-F., *et al.*, 2014b. Strong photocurrent enhancements in highly efficient flexible organic solar cells by adopting a microcavity configuration. Advanced Materials 26 (20), 3349–3354.

electrode. The device contained an Ag UTMF and a TeO_2 capping layer. Compared to the reference, with an ITO electrode, the average efficiency increased from 7.21 to 8.47%, which was due mainly to the J_{sc} increase. This was attributed to the increased intensity in the EQE curve, caused by the resonance effect. In addition, a device employing a variation to this architecture was fabricated using a flexible PET substrate, with an efficiency of 8.37%, only slightly lower than that for the glass substrate. Huang *et al.* achieved higher performance by coupling a microcavity structure with a high performance bulk heterojunction (BHJ) blend of poly({4,8-bis[(2-ethylhexyl)oxy]benzo[1,2-b:4,5-b′]dithiophene-2,6-diyl}{3-fluoro-2-[(2-ethylhexyl)-carbonyl]-thieno[3,4-b] thiophenediyl}) (PBDTT-F-TT):$PC_{71}BM$ (Huang *et al.*, 2015). They also used an UTMF with a TeO_2 buffer layer to achieve the microcavity resonance. The best performing device achieved an efficiency of 10.4%. The enhancement mechanism was similar to that in reference (Chen *et al.*, 2014a,b), a broadband improvement in the EQE profile correlated with improved J_{sc}. The structure was also tested on large area devices. An efficiency of more than 7% was achieved for large area devices, due to a novel semitransparent electrode containing the UTMF. This electrode was shown to be much more applicable to large device areas, when compared with ITO. Additionally, it is advantageous to replace the ITO layer, as it represents the highest cost and embodied energy in thin film solar cells.

Other Approaches for Light Harvesting

The narrow absorption band of OPV limits the use of the wider solar spectrum for energy conversion. One way to circumvent this issue is the use of multijunction or tandem solar cells in stacks with each of the cells absorbing different parts of the spectrum. The concept of tandem cells was proposed as a third generation solar cell alternative to increase light harvesting for solar applications (Green, 2001). The structure consists of a high bandgap top cell absorbing the high energy photons and thereby transmitting the low energy photons to the subsequent bottom solar cells which is arranged in the order of decreasing bandgap through a transparent interconnecting layer. For series connected cells (i.e., contact is made between the top and bottom cell), the open circuit voltage (V_{oc}) of the tandem cell is the sum of V_{oc} of the subcells, while the overall current is limited by the subcell with the smaller current. This means that the cells need to be current matched. Another approach is a three (Sista *et al.*, 2010a,b) or four terminal configuration in a two cell stack that allows separate connections, which does not require current matching. In this device configuration the two subcells are connected in parallel through a common/separate semitransparent interlayer. Hence tandem cell approach allows light harvesting of a much wider spectrum of the solar radiation than what would be possible by a single junction solar cell.

With this strategy, tremendous efforts have been devoted to the development of desirable device configurations. The lack of high performance low bandgap polymer materials along with good interconnection layer has limited the performance of tandem cells (Kim *et al.*, 2007; You *et al.*, 2013; Sista *et al.*, 2010a,b). The interconnection layers mostly used semitransparent metal layers

that added to the complexity of device fabrication and caused undesirable parasitic absorption. One of the earlier reports was that of 6.5% performance conversion efficiency at 200 W/cm^2 from fully solution processed tandem cells comprising a transparent TiO_x layer between the front and bottom cell. It made use of an inverted structure with the low bandgap polymer-fullerene composite as the charge-separating layer in the front cell and the high band-gap polymer composite as the back cell (Kim *et al.*, 2007). While tandem solar cells benefit from complementary absorption spectra by utilizing different polymer materials for the sub cells, more recently an efficiency of 6.7% was reported from identical subcells based on P2F-DO:N2200, which the authors claim is among the highest efficiencies for an all polymer tandem solar cell and attributed to the enhanced absorption of the tandem cell (Yuan *et al.*, 2016).

More understanding and development of the technology has made further improvements possible with a power conversion efficiencies exceeding 11% for a triple junction solar cell (see **Fig. 17(a)** and **(b)**) (Chen *et al.*, 2014a,b) which was greater than the first certified efficiency of 10.6% from a double junction tandem from the same group (You *et al.*, 2013).

Tremendous efforts have been devoted to the development of desirable device configurations using the tandem strategy. One such structure, unlike the sequential deposited layers, consists of a folded V-structure, like the one previously mentioned for light trapping (Rim *et al.*, 2007). It also allows an alternative solution to the problem of assembling tandem and multiple junction solar cells in the micron to centimeter range. Here the single cells are reflecting the non-absorbed light upon another adjacent cell and by folding the cells spectrally toward each other like in **Fig. 5(c)** wherein spectral broadening and light trapping are combined (Tvingstedt *et al.*, 2007).

Photon absorption and reemission in a quantum dot (QD) layer is another scattering technique capable of light harnessing in a polymer layer. Whilst only in its conceptual stage, this method has the potential to increase absorption by 28% (Xu and Munday, 2014). Here high luminescence QDs are used to absorb photons and reemit to the waveguide modes, thereby changing the directionality of the incident photons to improve coupling in the active layer. Another method of light harnessing is when

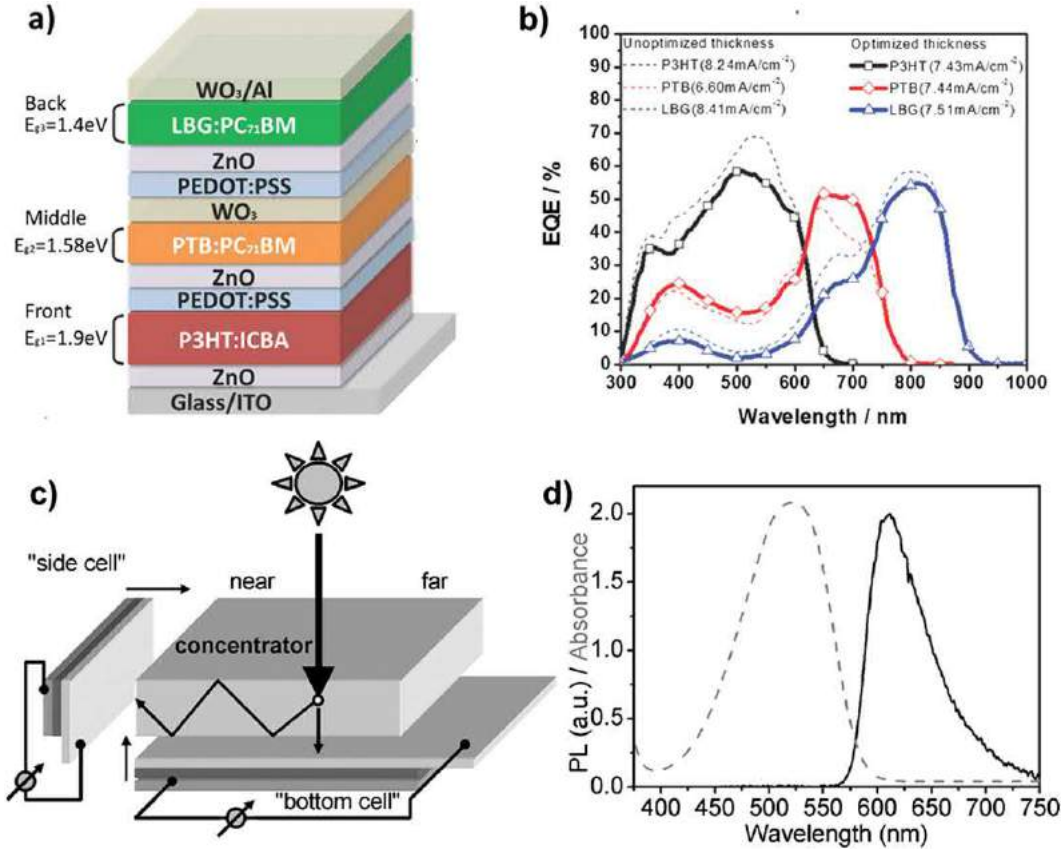


Fig. 17 (a) Layers of a triple junction organic tandem solar cell arranged in decreasing order of bandgap (light incident from glass side), (b) measured external quantum efficiency (EQE) of device in (a) showing a wider use of the solar spectrum, (c) schematic of a luminescent concentrator with cells placed either on the side or on the bottom of the concentrator plate, (d) absorbance (dashed) and photoluminescence (solid) spectra of the concentrator plate. PEDOT:PSS, poly(3,4-ethylenedioxythiophene) polystyrene sulfonate; ITO, indium tin oxide; LBG:PC71BM, low band gap:phenyl-C61-butyric acid methyl ester; P3HT:ICBA, poly(3-hexylthiophene-2,5-diyl):indene-C60 bisadduct. Images (a) and (b) taken from Chen, C.C., Chang, W.H., Yoshimura, K., *et al.*, 2014a. An efficient triple-junction polymer solar cell having a power conversion efficiency exceeding 11%. Advanced Materials 26, 5670–5677; (c) and (d) from Koeppe, R., Sariciftci, N.S., Büchtemann, A., 2007. Enhancing photon harvesting in organic solar cells with luminescent concentrators. Applied Physics Letters 90 (18), 181126.

luminescence concentrators are optically coupled to OSCs as shown in **Fig. 17(c)** where the solar cell can be placed either on the side or bottom of the concentrator plate. Luminescence concentrators use organic dyes with high photoluminescence quantum yields that concentrate and red shift the incident light (also called down conversion) and couples it to a waveguide. OSCs fabricated using zinc-phthalocyanine and C_{60} with the absorption in the 600–800 nm range, demonstrated photocurrent density increase from 8.5 to 10 mA/cm^2 by spectrally shifting the blue and green light (below 600 nm) toward the red when using such concentrators fixed to the cell (Koeppe *et al.*, 2007). Here the luminescence spectrum of the dye must overlap with the maximum in the conversion efficiency of the solar cell for optimum performance. The absorbance and emission spectrum of the concentrator plate used in the study in (Koeppe *et al.*, 2007) is shown in **Fig. 17(d)**.

The wider implementation of low-cost OSCs relies on increasing the efficiency of this technology through material improvements and optical gains. With myriad promising opportunities available for light harvesting for OSCs, the challenge is in optimizing one or more techniques into the cell without compromising on the electrical gains and at the same time keeping the fabrication cost low. In depth understanding the physical mechanisms for each of these techniques along with its dependence on the material properties is hence critical. For metal-based structures the optical properties should always be considered along with its electrical properties of OSCs. The ultimate goal of light harnessing structures should be to increase the absolute absorption in the thin film layers and not necessarily approaching the efficiency limits (Tang *et al.*, 2014). More detailed light harnessing reviews are available for those interested in further reading (Tang *et al.*, 2014; Ou *et al.*, 2016; Wang *et al.*, 2014; Fei Guo *et al.*, 2014).

Conclusion

OSCs, due to the exciton diffusion bottleneck that limits charge carrier transport in such cells, are severely limited by the thickness of the active layer. This comes with challenges in absorption of light and hence requires efficient light harvesting schemes to minimize optical losses. Different light harnessing schemes were discussed that includes AR coatings, light trapping using dielectric and metallic structures, light concentration using plasmonics, cavity effects and also the tandem structures that make use of different parts of the solar spectrum using cell stacks of different bandgaps. While the poor absorption efficiency in such cells have limited this technology to be a major player in the photovoltaics market compared to Si and other emerging thin film technologies, OSCs that can offer cheap, light weight and pliable cells may see a bright future as technology improves. It is expected that this technology may not need to be a replacement technology to Si but has the potential to find its own niche market for example, on windows or electric vehicles which require light weight structures. However, irrespective of the application, efficiency improvements will be key and it can be foreseen that light harnessing will play a major role in the development of OSCs given the potential for remarkable improvements possible as discussed in this article.

References

Ameri, T., Dennler, G., Waldauf, C., *et al.*, 2008. Realization, characterization, and optical modeling of inverted bulk-heterojunction organic solar cells. Journal of Applied Physics 103 (8), 084506.

Andersson, B.V., Huang, D.M., Moulé, A.J., Inganäs, O., 2009. An optical spacer is no panacea for light collection in organic solar cells. Applied Physics Letters 94 (4), 043302.

Armin, A., Velusamy, M., Wolfer, P., *et al.*, 2014. Quantum efficiency of organic solar cells: Electro-optical cavity considerations. ACS Photonics 1 (3), 173–181.

Baek, S.W., Noh, J., Lee, C.H., *et al.*, 2013. Plasmonic forward scattering effect in organic solar cells: A powerful optical engineering method. Scientific Reports 3 (1726), 1726.

Bernhard, C.G., 1967. Structural and functional adaptation in a visual system. Endeavour 26 (79), 79–84.

Betancur, R., Martínez-Otero, A., Elias, X., *et al.*, 2012. Optical interference for the matching of the external and internal quantum efficiencies in organic photovoltaic cells. Solar Energy Materials & Solar Cells 104, 87–91.

Burkhard, G.F., Hoke, E.T., McGehee, M.D., 2010. Accounting for interference, scattering, and electrode absorption to make accurate internal quantum efficiency measurements in organic and other thin solar cells. Advanced Materials 22 (30), 3293–3297.

Cao, W., Myers, J.D., Zheng, Y., *et al.*, 2011. Enhancing light harvesting in organic solar cells with pyramidal rear reflectors. Applied Physics Letters 99 (2), 023306.

Chan, K., Wright, M., Elumalai, N., Uddin, A., Pillai, S., 2016. Plasmonics in organic and perovskite solar cells: Optical and electrical effects. Advanced Optical Materials 5 (6), 1600698.

Chen, B., Zhang, W., Zhou, X., *et al.*, 2013. Surface plasmon enhancement of polymer solar cells by penetrating Au/SiO_2 core/shell nanoparticles into all organic layers. Nano Energy 2 (5), 906–915.

Chen, C.C., Chang, W.H., Yoshimura, K., *et al.*, 2014a. An efficient triple-junction polymer solar cell having a power conversion efficiency exceeding 11%. Advanced Materials 26, 5670–5677.

Chen, F.-C., Wu, J.-L., Hung, Y., 2010. Spatial redistribution of the optical field intensity in inverted polymer solar cells. Applied Physics Letters 96 (19), 193304.

Chen, K.-S., Yip, H.-L., Salinas, J.-F., *et al.*, 2014b. Strong photocurrent enhancements in highly efficient flexible organic solar cells by adopting a microcavity configuration. Advanced Materials 26 (20), 3349–3354.

Chou, C.H., Chen, F.C., 2014. Plasmonic nanostructures for light trapping in organic photovoltaic devices. Nanoscale 6 (15), 8444–8458.

Choy, W.C.H., 2014. The emerging multiple metal nanostructures for enhancing the light trapping of thin film organic photovoltaic cells. Chemical Communications 50 (81), 11984–11993.

Choy, W.C.H., Xingang, R., 2016. Plasmon-electrical effects on organic solar cells by incorporation of metal nanostructures. IEEE Journal of Selected Topics in Quantum Electronics 22 (1), 4100209.

Dunbar, R.B., Pfadler, T., Mende, L.S., 2012. Highly absorbing solar cells-a survey of plasmonic nanostructures. Optics Express 20, A177–A189.

Fei Guo, C., Sun, T., Cao, F., Liu, Q., Ren, Z., 2014. Metallic nanostructures for light trapping in energy-harvesting devices. Light: Science & Applications 3, e161.

Forberich, K., Dennler, G., Scharber, M.C., *et al.*, 2008. Performance improvement of organic solar cells with moth eye anti-reflection coating. Thin Solid Films 516 (20), 7167–7170.
Forrest, S.R., 2005. The limits to organic photovoltaic cell efficiency. MRS Bulletin 30 (1), 28–32.
Gan, Q., Bartoli, F.J., Kafafi, Z.H., 2013. Plasmonic-enhanced organic photovoltaics: Breaking the 10% efficiency barrier. Advanced Materials 25 (17), 2385–2396.
Gilot, J., Barbu, I., Wienk, M.M., Janssen, R.A.J., 2007. The use of ZnO as optical spacer in polymer solar cells: Theoretical and experimental study. Applied Physics Letters 91 (11), 113520.
Green, M.A., 2001. Third generation photovoltaics: Ultra-high conversion efficiency at low cost. Progress in Photovoltaics 9, 123–135.
Green, M.A., 2011. Enhanced evanescent mode light trapping in organic solar cells and other low index optoelectronic devices. Progress in Photovoltaics: Research and Applications 19 (4), 473–477.
Green, M.A., Pillai, S., 2012. Harnessing plasmonics for solar cells. Nature Photonics 6 (3), 130–132.
Gregg, B.A., van de Lagemaat, J., 2012. Solar cells: Folding photons. Nature Photonics 6 (5), 278–280.
Hiralal, P., Chien, C., Lal, N.N., *et al.*, 2014. Nanowire-based multifunctional antireflection coatings for solar cells. Nanoscale 6 (23), 14555–14562.
Hsiao, Y.-S., Charan, S., Wu, F.-Y., *et al.*, 2012. Improving the light trapping efficiency of plasmonic polymer solar cells through photon management. The Journal of Physical Chemistry C 116 (39), 20731–20737.
Huang, J., Li, C.-Z., Chueh, C.-C., *et al.*, 2015. 10.4% Power conversion efficiency of ITO-free organic photovoltaics through enhanced light trapping configuration. Advanced Energy Materials 5 (15), 1500406.
Huang, Y.-F., Chattopadhyay, S., Jen, Y.-J., *et al.*, 2007. Improved broadband and quasi-omnidirectional anti-reflection properties with biomimetic silicon nanostructures. Nature Nanotechnology 2 (12), 770–774.
Hünig, R., Mertens, A., Stephan, M., *et al.*, 2016. Flower power: Exploiting plants' epidermal structures for enhanced light harvesting in thin-film solar cells. Advanced Optical Materials 4 (10), 1487–1493.
Janković, V., Yeng, Y., You, J., *et al.*, 2013. Active layer-incorporated, spectrally tuned Au/SiO_2 core/shell nanorod-based light trapping for organic photovoltaics. ACS Nano 7 (5), 3815–3822.
Kang, M.G., Xu, T., Park, H.J., Luo, X., Guo, L.J., 2010. Efficiency enhancement of organic solar cells using transparent plasmonic Ag nanowire electrodes. Advanced Materials 22 (39), 4378–4383.
Kim, J.B., Kim, P., Pegard, N.C., *et al.*, 2012. Wrinkles and deep folds as photonic structures in photovoltaics. Nature Photonics 6 (5), 327–332.
Kim, J.Y., Kim, S.H., Lee, H.H., *et al.*, 2006. New architecture for high-efficiency polymer photovoltaic cells using solution-based titanium oxide as an optical spacer. Advanced Materials 18 (5), 572–576.
Kim, J.Y., Lee, K., Coates, N.E., *et al.*, 2007. Efficient tandem polymer solar cells fabricated by all-solution processing. Science 317 (5835), 222–225.
Kim, S.S., Na, S.I., Jo, J., Kim, D.Y., Nah, Y.C., 2008. Plasmon enhanced performance of organic solar cells using electrodeposited Ag nanoparticles. Applied Physics Letters 93 (7), 073307.
Koeppe, R., Sariciftci, N.S., Büchtemann, A., 2007. Enhancing photon harvesting in organic solar cells with luminescent concentrators. Applied Physics Letters 90 (18), 181126.
Krebs, F.C., 2009. Fabrication and processing of polymer solar cells: A review of printing and coating techniques. Solar Energy Materials & Solar Cells 93 (4), 394–412.
Lee, J.-Y., Peumans, P., 2010. The origin of enhanced optical absorption in solar cells with metal nanoparticles embedded in the active layer. Optics Express 18 (10), 10078–10087.
Lee, Y.-J., Ruby, D.S., Peters, D.W., McKenzie, B.B., Hsu, J.W.P., 2008. ZnO nanostructures as efficient antireflection layers in solar cells. Nano Letters 8 (5), 1501–1505.
Leem, J.W., Kim, S., Lee, S.H., *et al.*, 2014. Efficiency enhancement of organic solar cells using hydrophobic antireflective inverted moth-eye nanopatterned PDMS films. Advanced Energy Materials 4 (8), 1301315.
Li, X., Choy, W.C.H., Huo, L., *et al.*, 2012. Dual plasmonic nanostructures for high performance inverted organic solar cells. Advanced Materials 24 (22), 3046–3052.
Liu, C.M., Chen, C.M., Su, Y.W., Wang, S.M., Wei, K.H., 2013. The dual localized surface plasmonic effects of gold nanodots and gold nanoparticles enhance the performance of bulk heterojunction polymer solar cells. Organic Electronics: Physics, Materials, Applications 14 (10), 2476–2483.
Lu, L., Luo, Z., Xu, T., Yu, L., 2013. Cooperative plasmonic effect of Ag and Au nanoparticles on enhancing performance of polymer solar cells. Nano Letters 13 (1), 59–64.
Ma, W., Yang, C., Gong, X., Lee, K., Heeger, A.J., 2005. Thermally stable, efficient polymer solar cells with nanoscale control of the interpenetrating network morphology. Advanced Functional Materials 15 (10), 1617–1622.
Mallick, S.B., Sergeant, N.P., Agrawal, M., Lee, J.-Y., Peumans, P., 2011. Coherent light trapping in thin-film photovoltaics. MRS Bulletin 36 (6), 453–460.
Morfa, A.J., Rowlen, K.L., Reilly Ii, T.H., Romero, M.J., Van De Lagemaat, J., 2008. Plasmon-enhanced solar energy conversion in organic bulk heterojunction photovoltaics. Applied Physics Letters 92 (1), 013504.
Muskens, O.L., Rivas, J.G., Algra, R.E., Bakkers, E.P.A.M., Lagendijk, A., 2008. Design of light scattering in nanowire materials for photovoltaic applications. Nano Letters 8 (9), 2638–2642.
Myers, J.D., Cao, W., Cassidy, V., *et al.*, 2012. A universal optical approach to enhancing efficiency of organic-based photovoltaic devices. Energy & Environmental Science 5 (5), 6900–6904.
Niesen, B., Rand, B.P., Van Dorpe, P., *et al.*, 2012. Near-field interactions between metal nanoparticle surface plasmons and molecular excitons in thin-films. Part I: Absorption. The Journal of Physical Chemistry C 116 (45), 24206–24214.
Niesen, B., Rand, B.P., Van Dorpe, P., *et al.*, 2013. Plasmonic efficiency enhancement of high performance organic solar cells with a nanostructured rear electrode. Advanced Energy Materials 3 (2), 145–150.
Ou, Q.-D., Li, Y.-Q., Tang, J.-X, 2016. Light manipulation in organic photovoltaics. Advanced Science 3 (7), 1600123. -n/a.
Peer, A., Biswas, R., 2014. Nanophotonic organic solar cell architecture for advanced light trapping with dual photonic crystals. ACS Photonics 1 (9), 840–847.
Pillai, S., Green, M.A., 2010. Plasmonics for photovoltaic applications. Solar Energy Materials and Solar Cells 94 (9), 1481–1486.
Powell, A.W., Wincott, M.B., Watt, A.A.R., Assender, H.E., Smith, J.M., 2013. Controlling the optical scattering of plasmonic nanoparticles using a thin dielectric layer. Journal of Applied Physics 113 (18), 184311.
Raether, H., 1988. Surface Plasmons on Smooth and Rough Surface and on Gratings. Berlin: Springer Verlag.
Rand, B.P., Peumans, P., Forrest, S.R., 2004. Long-range absorption enhancement in organic tandem thin-film solar cells containing silver nanoclusters. Journal of Applied Physics 96 (12), 7519–7526.
Rim, S.-B., Zhao, S., Scully, S.R., McGehee, M.D., Peumans, P., 2007. An effective light trapping configuration for thin-film solar cells. Applied Physics Letters 91 (24), 243501.
Sergeant, N.P., Niesen, B., Liu, A.S., *et al.*, 2013. Resonant cavity enhanced light harvesting in flexible thin-film organic solar cells. Optics Letters 38 (9), 1431–1433.
Sista, S., Hong, Z., Park, M.-H., Xu, Z., Yang, Y., 2010a. High-efficiency polymer tandem solar cells with three-terminal structure. Advanced Materials 22 (8), E77–E80.
Sista, S., Park, M.-H., Hong, Z., *et al.*, 2010b. Highly efficient tandem polymer photovoltaic cells. Advanced Materials 22 (3), 380–383.
Stratakis, E., Kymakis, E., 2013. Nanoparticle-based plasmonic organic photovoltaic devices. Materials Today 16 (4), 133–146.
Tang, Z., Tress, W., Inganäs, O., 2014. Light trapping in thin film organic solar cells. Materials Today 17 (8), 389–396.
Temple, T.L., Bagnall, D.M., 2011. Optical properties of gold and aluminium nanoparticles for silicon solar cell applications. Journal of Applied Physics 109, 084343.
Tvingstedt, K., Andersson, V., Zhang, F., Inganäs, O., 2007. Folded reflective tandem polymer solar cell doubles efficiency. Applied Physics Letters 91 (12), 123514.
Tvingstedt, K., Zilio, S.D., Inganäs, O., Tormen, M., 2008. Trapping light with micro lenses in thin film organic photovoltaic cells. Optics Express 16 (26), 21608–21615.
Vezie, M.S., Few, S., Meager, I., *et al.*, 2016. Exploring the origin of high optical absorption in conjugated polymers. Nature Materials 15, 746–753.

Wang, C.C.D., Choy, W.C.H., Duan, C., *et al*., 2012. Optical and electrical effects of gold nanoparticles in the active layer of polymer solar cells. Journal of Materials Chemistry 22 (3), 1206–1211.
Wang, H.-P., Lien, D.-H., Tsai, M.-L., *et al*., 2014. Photon management in nanostructured solar cells. Journal of Materials Chemistry C 2 (17), 3144–3171.
Xu, X., Kyaw, A.K.K., Peng, B., *et al*., 2013. A plasmonically enhanced polymer solar cell with gold–silica core–shell nanorods. Organic Electronics 14 (9), 2360–2368.
Xu, Y., Munday, J.N., 2014. Light trapping in a polymer solar cell by tailored quantum dot emission. Optics Express 22 (S2), A259–A267.
Yablonovitch, E., 1982. Statistical ray optics. Journal of the Optical Society of America 72, 899.
You, J., Dou, L., Yoshimura, K., *et al*., 2013. A polymer tandem solar cell with 10.6% power conversion efficiency. Nature Communications 4, 1446.
Yu, G., Gao, J., Hummelen, J.C., Wudl, F., Heeger, A.J., 1995. Polymer photovoltaic cells: Enhanced efficiencies via a network of internal donor-acceptor heterojunctions. Science 270 (5243), 1789–1791.
Yu, Z., Raman, A., Fan, S., 2011. Nanophotonic light-trapping theory for solar cells. Applied Physics A. doi:10.1007/s00339-011-6617-4.
Yuan, J., Gu, J., Shi, G., *et al*., 2016. High efficiency all-polymer tandem solar cells. Scientific Reports 6, 26459.
Zhou, L., Ou, Q.D., Chen, J.D., *et al*., 2014. Light manipulation for organic optoelectronics using bio-inspired moth's eye nanostructures. Scientific Reports 4, 8.
Zhou, Y., Zhang, F., Tvingstedt, K., Tian, W., Inganäs, O., 2008. Multifolded polymer solar cells on flexible substrates. Applied Physics Letters 93 (3), 033302.
Zhu, J., Xue, M., Hoekstra, R., *et al*., 2012. Light concentration and redistribution in polymer solar cells by plasmonic nanoparticles. Nanoscale 4, 1978–1981.

Organic Lasers

Graham A Turnbull, University of St Andrews, St Andrews, United Kingdom

© 2018 Elsevier Ltd. All rights reserved.

Nomenclature

Charge mobility [$cm^2\ V^{-1}\ s^{-1}$]
Current density [$A\ cm^{-2}$]
Energy density [$\mu J\ cm^{-2}$]
Excited state densities [cm^{-3}]
Gain coefficient α ($\exp(\alpha z)$) [cm^{-1}]
Intensity/power density [$kW\ cm^{-2}$]
Optical gain [$dB\ cm^{-1}$]
Stimulated emission cross section [cm^2]
Waveguide propagation loss coefficient γ ($\exp(-\gamma z)$) [cm^{-1}]
Wavelength [nm]

Conjugated Polymers

Plastics are widely used in low-cost optical components such as lenses, diffraction gratings, optical fibers, and adhesives. Their common use derives from a combination of qualities: good optical transmission, a wide range of mechanical properties and simple fabrication via molding, extrusion, or solution processing. Functional optical polymers, including liquid crystals and photorefractives, have also been widely applied to polarization control and for nonlinear- and electro-optics. Conjugated polymers are a remarkable class of functional plastics that exhibit some quite unusual properties. Firstly, they are plastics that can conduct electricity; and in fact are electrically semiconducting. Secondly, they are plastics that can be stimulated either optically or electrically to emit visible light.

These two unusual properties derive from a particular chemical structure specific to this family of plastics. In all conjugated polymers, the backbone of the molecule is a chain of carbon atoms joined by alternating single and double covalent bonds. The simplest example is illustrated in Fig. 1(a), which shows the chemical structure of the polymer poly(acetylene). Structural integrity of the polymer is provided by a string of single σ-bonds between adjacent carbon atoms. The additional bonding electrons in the double bonds are located in π-orbitals oriented perpendicular to the polymer chain. Adjacent π-orbitals overlap, and their electrons can be widely delocalized along the polymer backbone. The delocalized electrons can move relatively freely along the chain, giving the electronic properties of the material. The π-orbitals can be transformed between bonding and anti-bonding states by the absorption or emission of light, leading to strong optical transitions. While poly(acetylene) is a very inefficient light emitter, other conjugated polymers, notably those that include phenyl rings in the backbone (Fig. 1(b)–(d)), can be highly emissive. Photoluminescence quantum efficiencies approaching unity in solution and as high as 60% in the semiconducting solid state have been realised.

Organic Semiconductor Lasers

While organic dye lasers have been widely used since the mid-1960s, the history of organic semiconductor lasers is much more recent. Other than a few early observations of lasing in molecular crystals in the 1970s by Karl and others, the field of organic

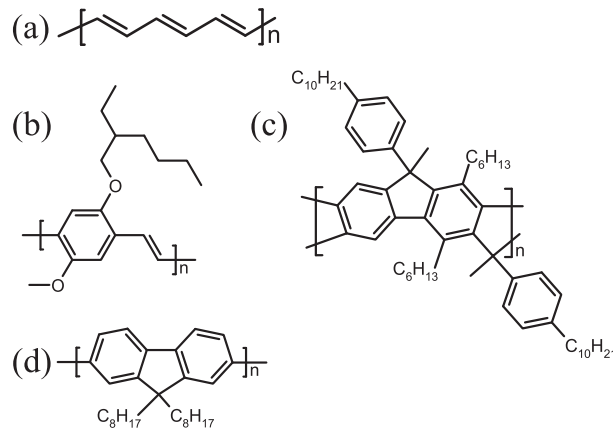


Fig. 1 Chemical structures of several conjugated polymers: (a) poly[acetylene]; (b) poly[2-methoxy-5-(2′-ethylhexyloxy)-1,4-phenylene vinylene] (MEH-PPV); (c) ladder-type poly[1,4-phenylene] (MeLPPP); (d) poly[9,9-dioctylfluorene] (PFO).

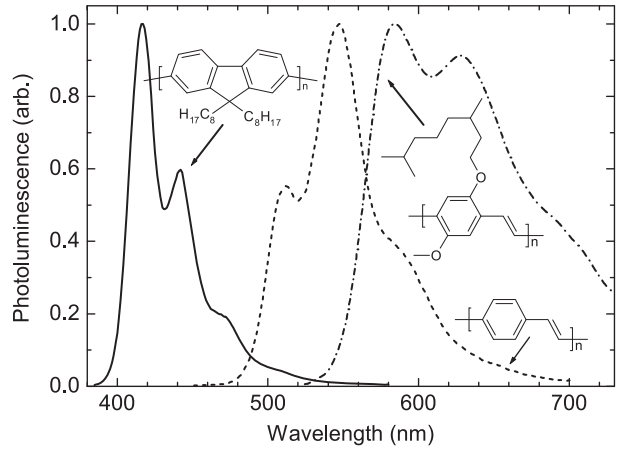


Fig. 2 Photoluminescence spectra of three common conjugated polymers. With chemical structures inset.

semiconductor lasers began in earnest following the related discovery in 1990 by Burroughes *et al.* of electroluminescence in a conjugated polymer. In 1992, Moses demonstrated lasing for the first time in a solution of the conjugated polymer poly[2-methoxy-5-(2′-ethylhexyloxy)-1,4-phenylene vinylene] (MEH-PPV) (Fig. 1(b)). However, it was another 4 years – once material synthesis had been sufficiently refined- before stimulated emission and then true laser action were observed in polymers in the semiconducting solid state. In the following year the first demonstrations were made of dye-doped small molecular semiconductor lasers. Since that time, there has been a great growth in interest in the field with an average of ~30 research papers per year. Further details of the development of the field of organic semiconductor lasers can be found in the bibliography.

So, what are the particular properties of conjugated polymers that have stimulated interest in developing organic semiconductor lasers? Firstly these materials are broadband visible emitters. Through appropriate chemical design, their emission can be tuned throughout the visible spectrum, from 400 to 700 nm (Fig. 2). The polymers exhibit large optical gain coefficients, because the optical transitions are dipole-allowed. Compared with small molecular dyes, polymers exhibit a relatively low degree of self-absorption of the emitted light, and much reduced quenching of the luminescence with increased concentration. This means that it is possible to work with much higher chromophore densities than conventional laser dyes, which is advantageous for achieving very low threshold lasing in extremely compact resonators. Furthermore, because these materials are semiconducting, they have the potential for direct electrical excitation. This could lead to semiconductor diode lasers operating throughout the visible spectrum and, in particular, in the blue and green spectral bands where currently there are few commercially-viable inorganic semiconductor sources. Finally, these materials are plastics and so are amenable to simple processing, and can be shaped and structured into complex feedback resonators.

Organic Semiconductor Gain Materials

A great advantage of organic laser media is that a very wide range of materials can be readily synthesized, and through minor changes in the molecular structure one can relatively simply tune the emission properties of the material. Many different organic semiconductors have been applied as lasers, though they fall into three major categories. These are conjugated polymers, dye-doped small molecular semiconductors and molecular single crystals. Conjugated polymers make up the most diverse materials set, most notably including derivatives of poly(paraphenylene-vinylene), poly(paraphenylene) and poly(fluorene) (Fig. 1(b)–(d)). The second category comprises small molecular semiconductors that are co-evaporated under vacuum with a dopant laser dye. In this blend of materials, the organic semiconductor functions simply as an energy transfer host for the emitting dye molecules. In the third category are organic single crystals, including materials, such as polyacenes and thiophene oligomers. These materials have the advantage of having the highest electrical mobilities of any organic semiconductors, which is important for electrical excitation. However, they can be demanding to grow into high quality single crystals, and so lack the key processing advantages of the other families of organic semiconductors.

Fig. 3(a) shows a typical energy level structure of a semiconducting polymer. Similar to a conventional laser dye, the energy levels comprise a manifold of singlet states and a manifold of triplet states, each with vibrational sublevels. The laser transition occurs from the bottom of the first excited singlet state S_1 to the vibronic overtones of the ground state S_0, so forming a classic 4-level laser system. The optical transition is dipole-allowed and so has a high oscillator strength. As a result conjugated polymers typically exhibit simulated emission cross sections in the range 10^{-16}–10^{-15} cm^2, while the population inversion lifetime is as short as a few hundred picoseconds.

There are, however, several other transitions that can compete with the stimulated emission process. There can be excited-state absorption from the S_1 singlet state into higher lying singlet states. Additionally intersystem crossing from the S_1 state to the lowest excited triplet state T_1 can subsequently lead to excited triplet absorption. Other processes in the polymer can also impede the

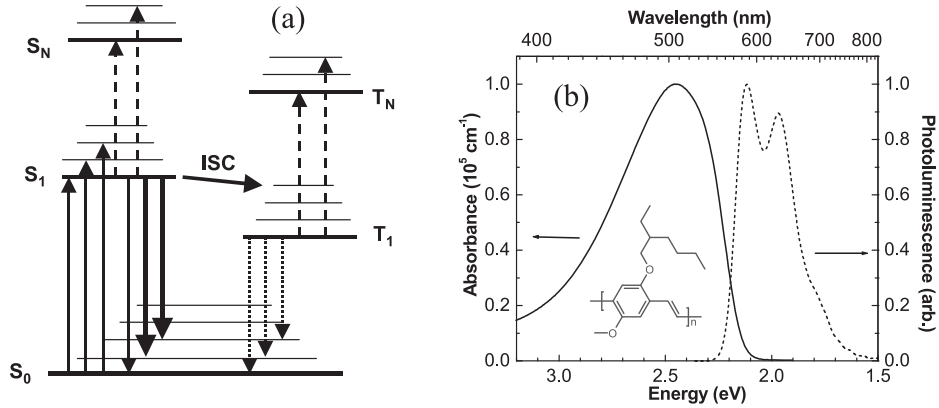


Fig. 3 (a) Generic energy level structure and optical transitions of a conjugated polymer. S_N refers to the Nth singlet state, T_N refers to the Nth triplet state; (b) absorption and photoluminescence spectra of the polymer poly[2-methoxy-5-(2′-ethylhexyloxy)-1,4-phenylene vinylene] (MEH-PPV). ISC, intersystem crossing.

stimulated emission. Firstly, charged excitations can exhibit absorption bands that overlap with the emission. Secondly, at high excitation densities, exciton–exciton annihilation can significantly deplete the excited states available for stimulated emission. Ultimately, singlet–singlet annihilation is the limiting factor for the maximum excitation density possible, and while polymer films can have a repeat-unit density of $\sim 10^{21}$ cm^{-3} the excited state density is typically limited to around 10^{18} cm^{-3}. In many materials this is not restrictive on achieving optical gain because stimulated emission can occur at densities of 10^{17} cm^{-3} and below.

An important factor that distinguishes the photo-physics of semiconducting polymers from conventional laser dyes is an internal process of exciton migration between the absorption and emission of a photon. Excitations are confined to short straight sections of the polymer between kinks or twists in the chain. These straight sections, or "sites," are typically of a few repeat units in length, though there is a statistical spread of site lengths in any given material. When formed, excitons tend to hop to the longest, lowest energy, sites before emitting a photon. The exciton migration process has two effects. Firstly it means the emission takes place from a subset of the chain segments, resulting in a lower degree of inhomogeneous broadening of the emission spectrum (vibronic peaks are better resolved than in absorption – see Fig. 3(b)). Secondly the peaks of the absorption and emission spectra tend to be widely separated in wavelength, reducing the level of self-absorption at the lasing wavelength.

As mentioned before, blending materials is a particularly attractive approach toward further reducing self-absorption in organic semiconductor lasers. In such systems, a narrow band-gap dopant chromophore is blended with a concentration of 1–2% in a wider band-gap semiconducting host. Emission from the host is strongly quenched via nonradiative Förster energy transfer to the guest molecule. The blended material exhibits an absorption profile that is dominated by the host absorption, while the emission profile is almost completely that of the guest dopant. By strongly separating the emission peak from the absorption edge of the host it is possible to achieve a substantially reduced (by perhaps an order of magnitude or more) residual absorption coefficient at the lasing wavelength. In doing so, the combined material acts much more like an ideal 4-level laser medium and can thereby have substantially lower pump thresholds for stimulated emission.

Measuring Gain

The dynamics of the excited state population in semiconducting polymers have been widely studied using femtosecond transient absorption experiments. This is a pump-probe technique in which the transmission of the broadband probe pulse is compared in the presence and absence of a pump pulse that excites molecules into the first excited state. Such measurements have the time resolution of the pump pulses used and so can typically be ~ 100 fs. By systematically delaying the arrival of the broadband probe pulse it is possible to map out the evolution of the gain dynamics across the emission spectrum of the material with very high time resolution.

Fig. 4 shows a series of snapshots of the absorption induced by a pumping pulse in a poly(thiophene) derivative. This figure shows the changing absorption of the sample between 200 fs and 400 ps after excitation. Within the absorption band of the material, one finds that the level of absorption is slightly reduced because the pump pulse has partly depleted the ground state. In the emission band there is also a reduction in the absorption that mimics in shape the photoluminescence spectrum of the polymer. This negative absorption- or optical-gain shows direct evidence for stimulated emission through much of the emission band. In the low energy tail of the emission, however, there is an increase in absorption that arises due to the excited-state absorption process mentioned earlier. Clearly, for a good laser material, the spectra of excited-state and charge-induced absorptions should overlap as little as possible with the photoluminescence.

Many other investigations of gain in semiconducting polymer films have used a phenomenon known as spectral line narrowing to explore indirectly the amplifying properties of the medium. The experimental procedure for such studies is as follows. A thin

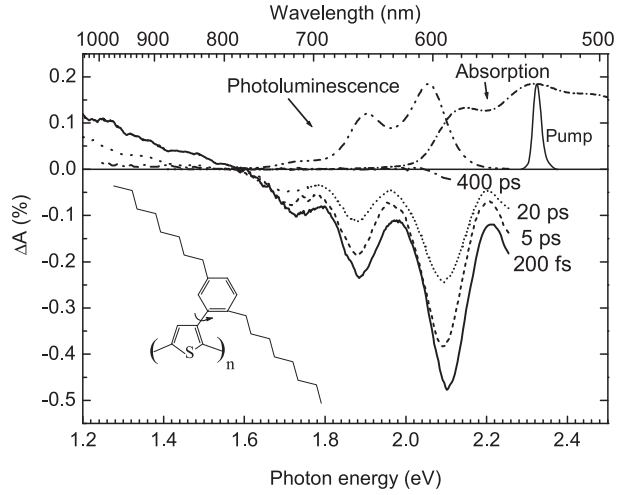


Fig. 4 Transient absorption spectra of poly[3-(2,5-dioctyl-phenyl)-thiophene]; chemical structure inset. Reproduced from Ruseckas, A., Theander, M., Valkunas, L., *et al.* 1998. Energy transfer in a conjugated polymer with reduced inter-chain coupling. Journal of Luminescence 76–77, 474–477. Copyright (1998), with permission from Elsevier.

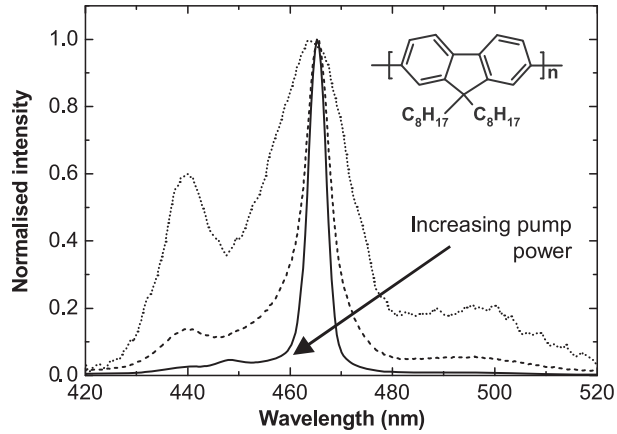


Fig. 5 The change in spectral shape with increasing excitation density (from 10 to 133 μJ cm^{-2}) of the edge emission from a PFO film – the normalized spectra show a significant spectral line narrowing at high excitation densities. Adapted from Heliotis, G., Bradley, D.D.C., Turnbull, G.A., Samuel, I.D.W., 2002. Light amplification and gain in polyfluorene waveguides. Applied Physics Letters 81, 415–417. Copyright (2002), with permission from American Institute of Physics.

film of the semiconducting material, of typically 100 nm thickness, is excited by a pulsed pump laser focused to a stripe of dimensions ~100 μm wide by a few millimeters in length. A significant fraction of the light emitted by the material is trapped in the film by total internal reflection at the polymer–air and polymer–substrate interfaces, and is thereby waveguided along the length of the excitation stripe. This waveguided spontaneous emission can be amplified by stimulated emission before being emitted out the edge of the film.

One finds that, above a particular threshold of pump energy, there is a superlinear increase in the output energy with pump intensity. Associated with this is a dramatic narrowing of the broad emission spectrum to a linewidth of typically less than 10 nm, as illustrated in Fig. 5. These two features are signatures of gain narrowing via the process of amplified spontaneous emission. The line-narrowed feature usually appears at the first vibronic overtone, of the optical transition, where the gain exceeds the losses in the material by the greatest amount. This particular wavelength experiences the greatest amplification and, above a particular pumping density, undergoes a runaway effect in which most of the light is stimulated to emit at that wavelength at the expense of the rest of the spectrum.

In the case of amplified spontaneous emission or mirrorless lasing as it is also known, the spontaneous emission guided along the length of the stripe acts as the "probe pulse." In these experiments it is therefore necessary to extract information indirectly about the net gain in the material. By integrating the spontaneous and stimulated emission along the length of the stripe one finds that the wavelength-dependent output intensity $I(\lambda)$ of the spectral line narrowed light is given by the relationship

$$I(\lambda) \propto \frac{1}{g(\lambda)} [\exp[g(\lambda)l] - 1]$$

where I_p is pumping intensity, l is the length of the stripe, and $g(\lambda)$ is the net gain coefficient. Therefore, by monitoring the intensity of the line-narrowed emission as a function of the length of the pump stripe, one can extract the value of the net gain for the material. Similarly, by progressively moving the stripe further and further away from the edge of the film, it is possible to evaluate the waveguide losses of light propagating through an unpumped region of the waveguide. Waveguide losses in conjugated polymers typically lie in the range of 3–50 cm^{-1}. Net gains can be as high as 60 cm^{-1} or 260 dB cm^{-1} at modest pumping densities of 4 kW cm^{-2}. These substantial gains in very small propagation lengths therefore highlight the attraction of waveguide-based resonators for polymer lasers. In the next section we will discuss the most commonly used feedback structures that have been used for polymer lasers.

Polymer Laser Resonators

The first demonstration of cavity lasing in a conjugated polymer was made by Moses in 1992. The resonator consisted simply of Fresnel reflections from the walls of the glass cuvette containing the polymer in solution. Lasing occurred at the peak wavelength of the gain profile. Subsequent developments in solid-state polymer lasers have involved more sophisticated resonators that exploit the capacity of these materials for very simple processing. For example, solution-processing methods such as spin-casting or dip-coating, make it possible to fabricate very high quality optical waveguides. Wavelength-scale microstructures can also be readily formed allowing the straightforward fabrication of laser microresonators.

Many different resonators have been explored for solid-state polymer lasers. Some of the key types are shown in Fig. 6, including different geometries of both microcavities and distributed feedback (DFB) structures. The first resonator used, by Tessler *et al.*, was a planar microcavity (Fig. 6(a)) in which the polymer film was sandwiched between two mirrors. The structure supported standing-wave resonances perpendicular to the plane of the film, at three wavelengths in the emission band of the polymer. Above laser threshold, light was preferentially stimulated into only one of these modes. Microcavities of other geometries have also been studied, including annular and spherical microresonators (Fig. 6(b) and (c)) in which the optical field is confined in waveguide modes, whispering gallery modes, or a superposition of the two. Such structures provide a longer interaction length in the gain medium for stimulated emission; though tend to lase on many longitudinal modes and have no directional output beam.

The final key group of resonators are DFB structures, which researchers have progressively favoured to attain the low pump threshold densities that will be required to realize electrically pumped lasing. Fig. 6(d) shows a typical DFB laser structure. The device is based on a thin polymer film that is typically 100 nm in thickness deposited on top of a silica substrate. The silica–polymer–air structure forms an asymmetric slab waveguide that supports only the lowest order transverse electric mode TE_0. To provide the feedback, the substrate is modulated with a wavelength-scale periodic grating structure. These corrugations give rise to Bragg scattering of the waveguide mode. Through careful selection of the grating period one may arrange that optical wavelengths close to the peak of the polymer gain will be Bragg scattered from the propagating TE_0 mode to the counter-propagating TE_0 mode. This is achieved when Bragg equation

$$2n_{\text{eff}}\Lambda = m\lambda_B,$$

is satisfied, where Λ is the grating period, n_{eff} is the effective refractive index of the waveguide, m is an integer and λ_B is Bragg wavelength. In so doing one may arrange that two counter-propagating waveguide modes can be coupled together thereby providing the distributed resonant feedback for the laser process. Commonly in semiconducting polymer lasers, a second order (i.e., $m=2$) Bragg grating has been favoured to provide the feedback for the laser, so that the first order scattering provides a surface-emitted output coupling, perpendicular to the plane of the guide. This surface-emitting geometry is particularly attractive in polymer lasers because it is relatively difficult to achieve a high optical quality edge to the waveguide. DFB lasers have the

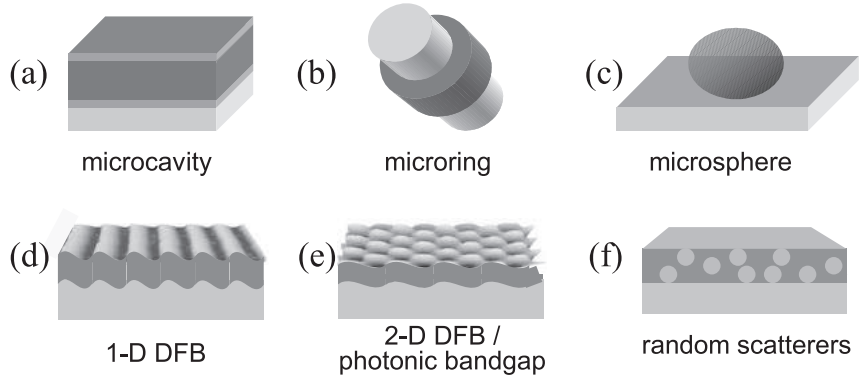


Fig. 6 Resonators used for conjugated polymer lasers. (a) Planar microcavity; (b) annular microcavity; (c) spherical microcavity; (d) distributed feedback (DFB) resonator; (e) 2-D DFB/photonic crystal resonator; (f) random laser.

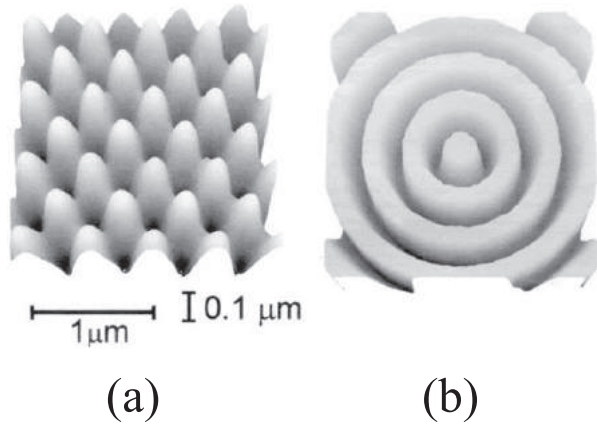


Fig. 7 Atomic force microscope images of (a) "egg-box" distributed feedback (DFB) grating and (b) circular DFB grating; grating period is 400 nm in each structure.

advantage over simple microcavity resonators in that they can combine long interaction lengths, limited by the scattering length of Bragg grating, with excellent wavelength selection, which is controlled by the grating period.

In addition to conventional 1-D DFB gratings, a number of more exotic 2-D and 3-D DFB, and photonic crystal resonators have been explored in semiconducting polymers. Even randomly located scattering sites in a polymer film have been used to provide a weak closed-loop cavity feedback. Examples of 2-D gratings are given in **Fig. 7**, which shows atomic force micrographs of an eggbox structure, formed from two orthogonal gratings, and a circular DFB grating. Such 2-D DFB structures can significantly improve the operation of surface-emitting polymer lasers compared with 1-D gratings. Improved feedback yields lower oscillation thresholds, combined with higher slope efficiencies and significantly improved beam quality. Indeed such surface emitting DFB lasers can produce nearly diffraction limited laser beams.

Typical operating characteristics of an egg-box DFB polymer laser are shown in **Fig. 8**. This laser, which is based on the material MEH-PPV, is transversely pumped with a pulsed pump laser focussed onto a small region of the waveguide; up to 90% of the incident pump light is absorbed in the 100 nm thick film. The laser has a threshold pump energy of 4 nJ and an external slope efficiency of $>7\%$, and operates on a single frequency close to Bragg wavelength of the periodic waveguide. Lasing does not occur exactly at Bragg wavelength because at this wavelength the propagation of light is suppressed by the periodic structure. This leads to a photonic stopband within which the emission is reduced. At the edges of this stopband the microstructure can support standing wave electric field patterns of the same spatial period. At these wavelengths there can be a strong interaction between the electric field and excited states in the gain medium, which leads to low threshold band edge lasing as observed in the figure.

Although DFB resonators have advantages over microcavity devices, the complicated lithographic and etching steps involved in their fabrication can detract from the key material advantage of simple processing. To address this issue several different techniques for simply replicating the complicated microstructures have been explored. These include UV embossing of flexible plastic substrates, and hot embossing and micromoulding of the active polymer itself. Such techniques can very readily reproduce structures with feature sizes as small as 100 nm and could allow future mass production of photonic microstructures in these materials.

Towards Plastic Diode Lasers

A typical experimental configuration for characterising optically pumped polymer lasers is shown in **Fig. 9**. The laser is mounted in a vacuum chamber in order to isolate the polymer from oxygen and water. A pulsed visible or ultraviolet pump laser is attenuated and then focussed onto the waveguide to transversely pump the polymer laser. The emission is collected using a charge-coupled device (CCD) spectrograph for spectral measurements and energy meter and beam profilers for other characteristics. Typical pulsed pump lasers which have been used include nitrogen laser pumped dye lasers, and spectral harmonics of regeneratively amplified Ti^{3+}-sapphire lasers or flashlamp pumped Nd^{3+}:YAG lasers. Recent advances have shown the thresholds to be low enough to be successfully pumped with a modest Nd^{3+} pulsed microchip laser.

So while optically pumped polymer lasers are now proving to be compact, functional light sources, a major motivation for research in this field remains the prospect of electrically driven plastic diode lasers. Such lasers could be very low cost, flexible light sources that would access any wavelength throughout the visible spectrum. In particular, there are exciting prospects of producing blue and green diode lasers in spectral regions currently difficult to access with inorganic semiconductors. The lowest threshold densities reported for optically pumped organic semiconductor lasers are of the order of 100 Wcm^{-2}. To achieve similar excitation densities electrically, one requires pump current densities of ~ 200 Acm^{-2}. This is substantially more than the few milliampere per square centimeter commonly used in polymer light-emitting diodes (LEDs) for display applications. Presently, such high current densities are infeasible with continuous excitation, but can be exceeded with short current pulses of a few tens of nanoseconds duration.

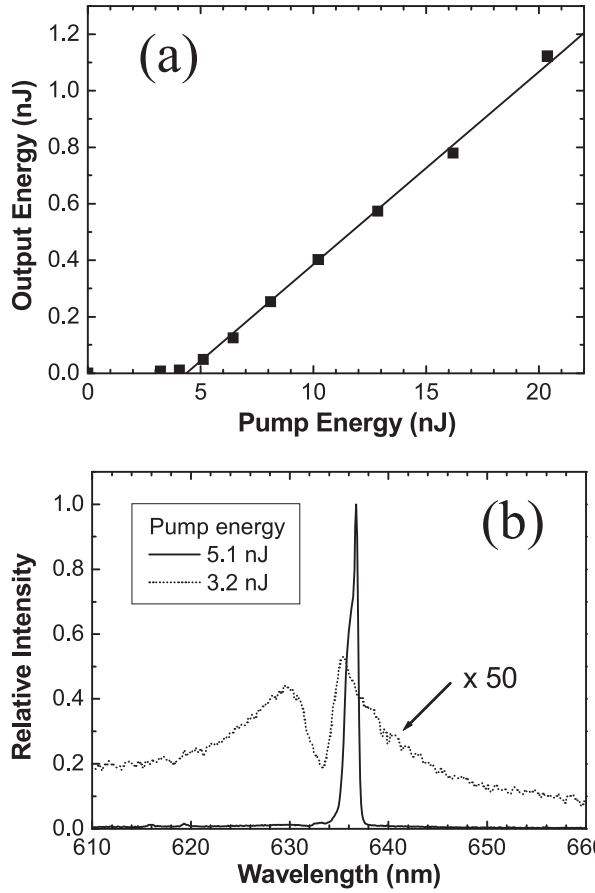


Fig. 8 (a) Energy characteristic of an egg-box distributed feedback (DFB) laser; (b) normalized emission spectra above and below lasing threshold, showing lasing in the edge of the photonic stopband. Reprinted from Turnbull, G.A., Andrew, P., Barnes, W.L., Samuel, I.D.W., 2002. Operating characteristics of a semiconducting polymer laser pumped by a microchip laser. Applied Physics Letters 82, 313–315, Copyright (2003), with permission from American Institute of Physics.

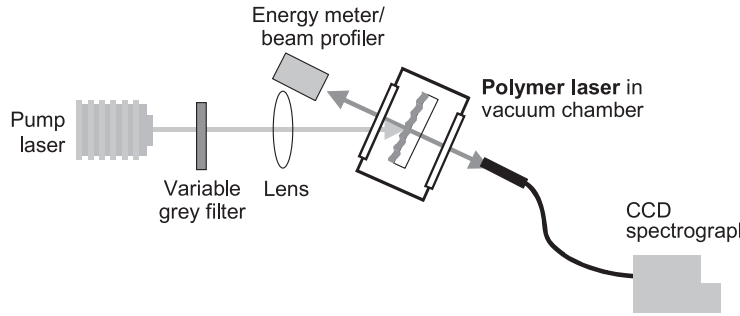


Fig. 9 Schematic of a typical experimental configuration for characterising polymer lasers. CCD, charge-coupled device.

Electroluminescence in conjugated polymers was first achieved in 1990 by Burroughes and coworkers. Since that time there has been remarkable progress made in the science and technology of organic LEDs. Commercial products are now on the market, and the feasibility of both flexible and full color light emitting displays, in which the individual pixels have been ink-jet printed, have been demonstrated in the laboratory. Despite such rapid progress in the field of organic LEDs, there have been no successful demonstrations to date of electrically pumped lasing in any organic semiconductor. In this section we highlight some of the challenges that must be faced if electrically pumped lasing is to be achieved. To understand the problems associated with electrical driving of organic semiconductor lasers it is useful first to review the generic structure of organic light emitting diodes.

A generic organic LED structure is shown in Fig. 10. The device consists of one or more organic layers sandwiched between two electrical contacts. Usually a transparent anode is used, commonly made from indium tin oxide (ITO), which allows light to be emitted from the front face of the LED. A low work-function metal such as calcium or aluminum is used as the cathode. The

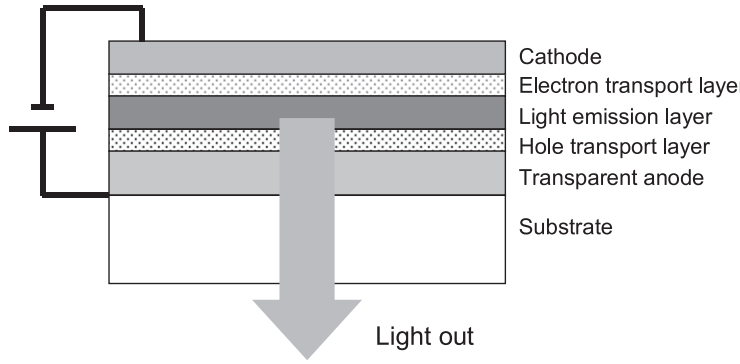


Fig. 10 Schematic structure of a generic organic light emitting diode.

organic part of the device may consist of several layers. These include one or more charge transport layers, plus a light-emitting layer in which the electrons and holes combine to form excitons before emitting light. Typically, the combined thickness of these organic layers is as little as 100 nm. Such thin devices are necessary to keep operating voltages low, to overcome potential barriers for injection and because charge mobilities in organic semiconductors are very low (10^{-5}–10^{-2} cm^2 V^{-1} s^{-1}).

The inclusion of electrical contacts into organic semiconductor laser structures can be problematic since they need to be situated very close to the emitting region. Metallic contacts can quench the luminescence and introduce losses to the waveguide mode, thereby increasing the oscillation thresholds. Furthermore, the ITO anode has a high refractive index and so can reduce the spatial overlap of the guided mode with the active medium. Such issues indicate that the design of organic LEDs needs to be somewhat modified for achieving electrically pumped lasing. In particular, there needs to be a trade-off between the optimum electronic and photonic designs. To address these issues various device structures have been proposed that distance the optical mode from metallic contacts, while reducing the thickness of the ITO layer to optimize the mode confinement in the active material.

A more demanding obstacle to electrically pumped lasing is the additional excited state absorption associated with the electrical pumping scheme. As many as three quarters of the generated excitons in an organic LED are formed in the triplet state which is non-emissive and can lead to excited-state absorption, albeit principally at lower energies than the lasing wavelength. Additionally, injected charges that have not yet formed excitons exhibit strong absorption, which overlaps significantly with the peak of the material gain. Indeed, this charge-induced absorption has so far prevented the demonstration of injection lasing in conjugated polymers, even in optimized device structures mentioned above. A possible alternative route for efficient pumping of polymer lasers could be through indirect electrical pumping. For example, an inorganic diode laser or LED, or even an organic LED, could be used as an electrically efficient optical pump for the semiconducting polymer laser. Recent advances in GaN-based LEDs and lasers provide interesting prospects for such alternative systems.

Research on semiconducting polymer lasers keenly continues, both to reduce the excitation densities needed for threshold and to investigate new material systems that could overcome the obstacle of charge-induced absorption. By building on recent developments in resonator geometries, material blends and compact pumping schemes, semiconducting polymer laser systems, whether optically or electrically pumped, should soon become practical, visible light sources for a range of applications.

See also: Organic Semiconductors

Further Reading

Burroughes, J.H., Bradley, D.D.C., Brown, A.R., *et al*., 1990. Light-emitting-diodes based on conjugated polymers. Nature 347, 539–541.
Friend, R.H., Gymer, R.W., Holmes, A.B., *et al*., 1999. Electroluminescence in conjugated polymers. Nature 397, 121–128.
Karl, N., 1972. Laser emission from an organic molecular crystal. Physica Status Solidi 13, 651–655.
Kranzelbinder, G., Leising, G., 2000. Organic solid-state lasers. Reports on Progress in Physics 63, 729–762.
Kuehne, A.J.C., Gather, M.C., 2016. Organic lasers: Recent developments on materials, device geometries, and fabrication techniques. Chemical Reviews 116, 12823–12864.
McGehee, M.D., Heeger, A.J., 2000. Semiconducting (conjugated) polymers as materials for solid-state lasers. Advanced Materials 12, 1655–1668.
Miyata, S., Nalwa, H.S. (Eds.), 1997. Organic Electroluminescent Materials and Devices. Amsterdam: OPA.
Moses, D., 1992. High quantum efficiency luminescence from a conducting polymer in solution – A novel polymer laser-dye. Applied Physics Letters 60, 3215–3216.
Pope, M., Swenberg, C.E., 1999. Electronic Processes in Organic Crystals and Polymers. New York: Oxford University Press.
Samuel, I.D.W., 2000. Polymer electronics. Philosophical Transactions of the Royal Society of London A 358, 193–210.
Scherf, U., Riechel, S., Lemmer, U., Mahrt, R.F., 2001. Conjugated polymers: Lasing and stimulated emission. Current Opinion in Solid State and Materials Science 5, 143–154.
Tessler, N., 1999. Lasers based on semiconducting organic materials. Advanced Materials 11, 363–370.
Tessler, N, Denton, G.J., Friend, R.H., 1996. Lasing from conjugated-polymer microcavities. Nature 382, 695–697.
Zhao, Z, Mhibik, O, Nafa, M, *et al*., 2015. High brightness diode-pumped organic solid-state laser. Applied Physics Letters 106, 051112.

Organic Photodetectors

Jaehoon Jeong, Hwajeong Kim, and Youngkyoo Kim, Kyungpook National University, Daegu, Republic of Korea

© 2018 Elsevier Ltd. All rights reserved.

Introduction

Organic photodetector is an optoelectronic device that can sense light with organic semiconducting materials, which typically feature pi-conjugated molecular structures, and convert it to electrical signals. The sensing range of organic photodetectors is basically dependent on the optical absorption spectra of organic semiconducting materials. Various organic semiconducting materials including small molecules and polymers can be used as a light-sensing layer in organic photodetectors.

Two types of device structures, diode and transistor, are generally employed for the fabrication of organic photodetectors. It is noted that transistors here mean "field-effect transistors." The diode structure leading to organic photodiodes has organic sensing layers (OSLs) between two electrodes, while the transistor structure leading to organic phototransistors includes additional electrode for gate control in the presence of organic layers and two counter electrodes. Therefore, organic photodiodes are in principle much simpler than organic phototransistors in terms of device structure and fabrication process. In contrast to organic photodiodes, however, organic phototransistors benefit signal amplifications by adjusting the gate voltage and enable active-matrix sensor arrays for two-dimensional images.

Organic photodetectors, both organic photodiodes and organic phototransistors, can be fabricated using wet-coating processes such as ink-jet printing, screen printing, gravure printing, spray coating, slot-die coating, etc. at low temperatures. In addition, flexible plastic films, such as poly(ethylene naphthalate) (PEN) and poly(ethylene terephthalate) (PET), can be applied as a substrate for the fabrication of organic photodetectors. These benefits enable organic photodetectors to be manufactured with continuous roll-to-roll processes leading to low-cost advantages.

Device Structure and Mechanism

Organic Photodiodes

Organic photodiodes consist of two electrodes and OSLs between the two electrodes (Fig. 1(a)). As shown in Fig. 1(b), the charges (holes and electrons) generated by incoming photons transport to corresponding electrodes due to the built-in potential made at short circuit condition. The OSLs can be composed of single materials, either p-type or n-type organic semiconductors,

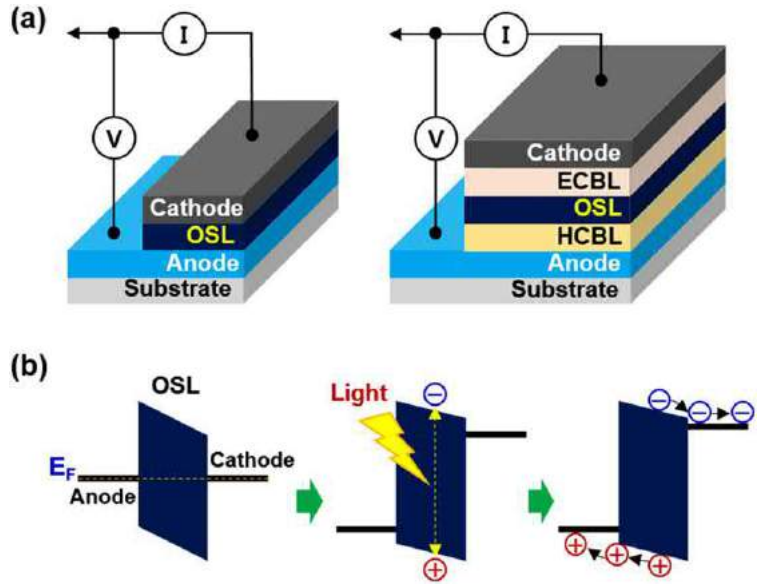


Fig. 1 (a) Typical device structures for organic photodiodes consisting of (left) single organic sensing layer (OSL) between anode and cathode and (right) with additional hole-collecting buffer layer (HCBL) and electron-collecting buffer layer (ECBL). (b) Simplified energy band diagrams for the sensing mechanism in organic photodiodes with single OSL (refer to the left structure in (a)).

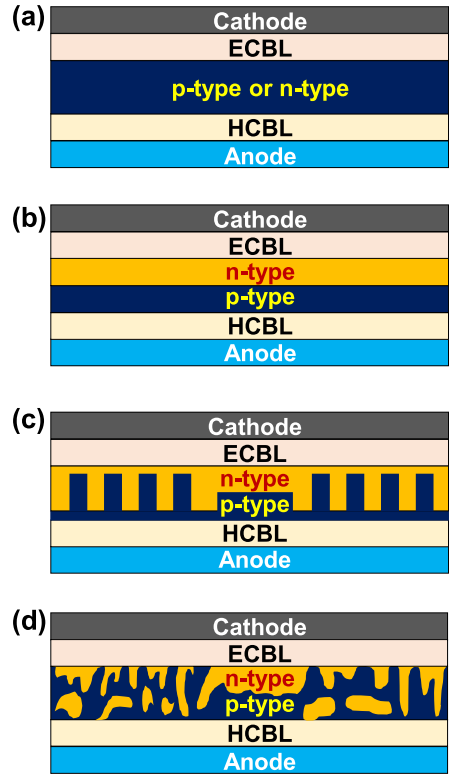


Fig. 2 Illustration for the cross-sections of organic photodiodes according to the types of organic sensing layers (OSLs): (a) single sensing layer, (b) bilayer, (c) interdigitated bilayer, and (d) bulk heterojunction layer. ECBL, electron-collecting buffer layer; HCBL, hole-collecting buffer layer.

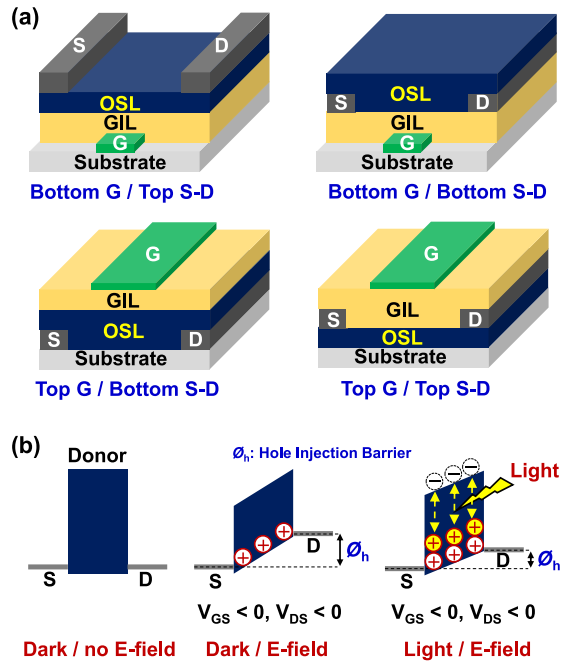


Fig. 3 (a) Representative geometry of organic phototransistors with organic sensing layer (OSL) and gate-insulating layer (GIL): (top-left) bottom gate/top source-drain, (top-right) bottom gate/bottom source-drain, (bottom-left) top gate/bottom source-drain, (bottom-right) top gate/top source-drain. (b) Energy band diagram for organic phototransistors (p-type): (left) no electric field condition in the dark, (middle) under a field-effect condition in the dark ($Ø_h$: hole injection barrier), (right) light illumination under a field-effect condition. V_{GS} and V_{DS} denote gate voltage and drain voltage, respectively.

as shown in Fig. 2(a). However, p–n junction structures are required in order to enhance the photosensitivity of devices. The simple bilayer structure can be easily prepared by employing multilayer coatings even though orthogonal solvents are essential for preparing solutions for each layer in the case of wet-coating processes (Fig. 2(b)). Considering the contact area between p-type and n-type organic semiconducting layers, the simple bilayer structure has an intrinsic limitation in the number of p–n junctions. As shown in Fig. 2(c), an interdigitated bilayer structure is expected to provide ideal p–n junctions. Unfortunately, however, the interdigitated bilayer structure on a scale of a few nanometers cannot be easily fabricated with current coating technology. Alternatively, bulk heterojunction structures are considered to deliver high photosensitivity because numerous p–n junctions are made intimately in the mixture (blend) of p-type and n-type organic semiconducting materials (Fig. 2(d)).

Organic Phototransistors

Organic phototransistors are different from organic photodiodes in the point that gate electrodes are required for the control of devices (Fig. 3(a)). Four types of organic phototransistors can be fabricated according to the position of electrodes. In general, the source and drain electrodes exist in parallel with the film plane of organic sensing channel layers. As shown in Fig. 3(b), very low charge transport (current flow) in the dark are measured when voltages (biases) are applied between source and drain electrodes in the absence of applying voltages between source and gate electrodes. Applying voltages to the gate electrodes creates field-effect charges in organic channel layers, which contributes to the increased charge transport between source and drain electrodes. Here, when light shines to the channel part of organic sensing channel layers, photons generate excitons that in turn dissociate into individual charges (electrons and holes). Therefore, the photo-generated charges are added to the field-effect charges, which are measured at the same time.

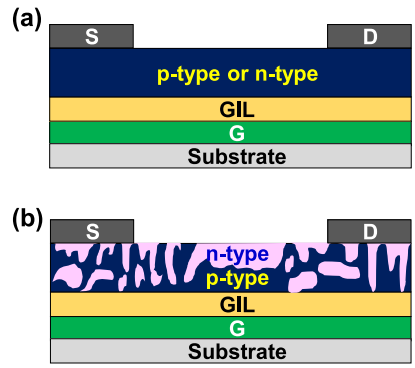


Fig. 4 Illustration for the cross-sections of organic phototransistors: (a) single sensing layer (either p-type or n-type organic semiconductors) and (b) bulk heterojunction layer (mixture of p-type and n-type organic semiconductors). GIL, gate-insulating layer.

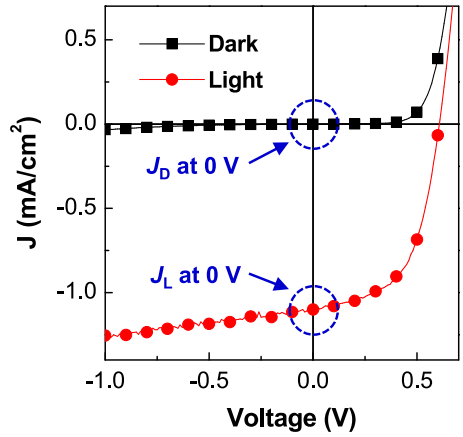


Fig. 5 Current density–voltage (*J*–*V*) curves for organic photodiodes in the dark and under light. J_D and J_L represent short circuit current density (0 V) in the dark and under light, respectively.

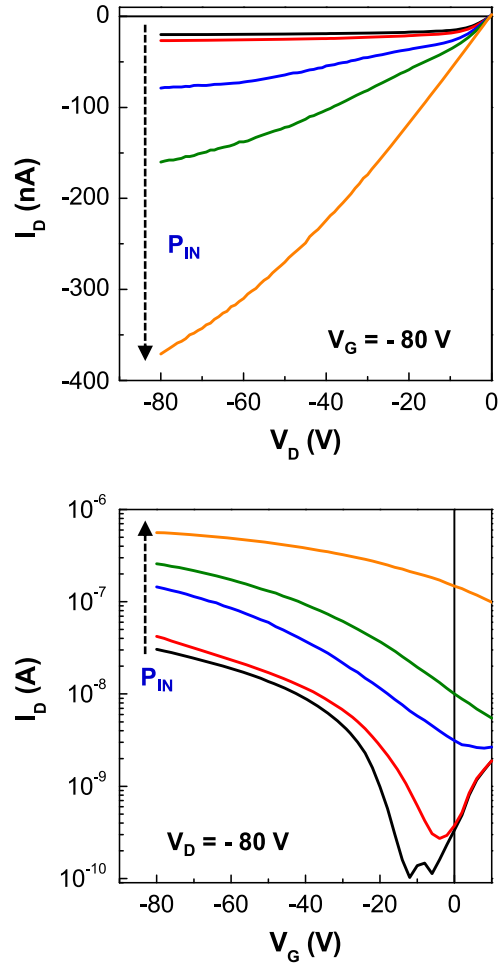


Fig. 6 Output (top) and transfer (bottom) curves for representative organic phototransistors with p-type organic sensing layers (OSLs) according to the incident light intensity (P_{IN}).

In terms of organic sensing channel layers, a variety of material combinations are possible but a single layer structure is basically applied as used for typical organic transistors. The single sensing channel layer is typically composed of one kind of organic semiconducting materials (either p-type or n-type). However, as explained for organic photodiodes, bulk heterojunction-type sensing channel layers can deliver enhanced photosensitivity because of the benefit of bulk heterojunctions leading to efficient charge separation. In addition, the bulk heterojunction-type sensing channel layers can take further advantages in tuning the sensing wavelengths by controlling the composition of p-type and n-type organic semiconducting materials with different absorption spectral ranges (**Fig. 4**).

Photosensitivity (Responsivity) of Organic Photodetectors

The photosensitivity (or responsivity, R) of organic photodetectors is defined by the ratio of net photocurrent density (J_P) to incident light intensity (P_{IN}), as given by Eq. (1). The net photocurrent density is obtained by subtracting the dark current density (J_D) from the whole current density under light (J_L) (see **Fig. 5**). It is noted that the unit of current density and incident light intensity is typically expressed as milliampere per square centimeter and watt per square centimeter, respectively. Thus the unit of responsivity becomes A/W.

$$R = \frac{J_P}{P_{IN}} [\mathrm{A/W}] \tag{1}$$

In addition, signal-to-noise (S/N) ratios are frequently used to understand the effect of background noises made in photodetectors. The S/N ratio is defined by the ratio of photocurrent density to dark current density. Further detailed approach is to

employ specific detectivity (D^*) that represents a figure of merit for photodetectors. As shown in Eq. (2), the specific detectivity is expressed by the ratio of responsivity (R and active area (A)) to noise spectral density (S_n).

$$D^* = \frac{R \cdot \sqrt{A}}{S_n} \text{ [Jones]} \tag{2}$$

The responsivity of organic photodiodes can be simply calculated using Eq. (1) from current density–voltage (J–V) curves as illustrated in **Fig. 5**. However, organic phototransistors provide two types of current–voltage curves, output and transfer curves, as shown in **Fig. 6**. Output curves are useful to get responsivity depending on drain voltage at a fixed gate voltage, while transfer curves can be employed to calculate the gate voltage-dependent responsivity at a fixed drain voltage. A particular attention needs to be paid for the measurement of photocurrent because the active area is too small to block with a shadow mask if the incident light comes directly to the sensing channel layers but the source/drain electrodes are unable to block the incident light owing to their positions.

Organic Photodiodes With Small Molecules

Organic Layer – Single Material

Various types of small molecules have been used for the fabrication of organic photodiodes with OSLs composed of single material. As shown in **Fig. 7**, pentacene and phthalocyanines were used as a p-type small molecule, while fullerene (C_{60}) and perylene derivatives were employed as an n-type small molecule. Most of small molecules have been deposited by thermal evaporation in vacuum, but soluble small molecules such as [6,6]-phenyl-C_{61}-butyric acid methyl ester ($PC_{61}BM$) can be coated from solutions. Lee *et al.* (2004) reported pentacene photodiodes (Schottky type) that could measure spectral photoresponses from 325 to 650 nm at zero bias condition. Voz *et al.* (2007) demonstrated fullerene devices of which the rectifying behavior could

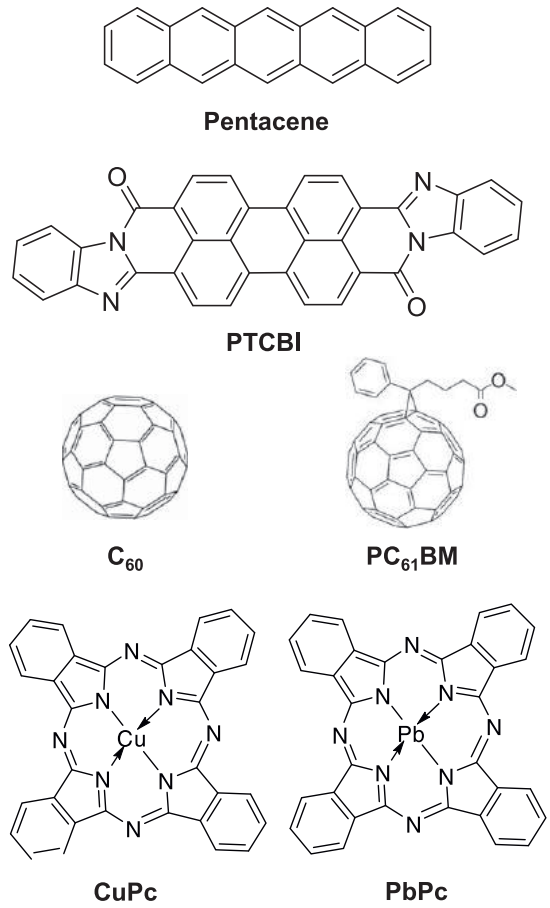


Fig. 7 p-type and n-type small molecules used for organic sensing layers (OSLs) in organic photodiodes: pentacene, 3,4,9,10-perylenetetracarboxylic bisbenzimidazole (PTCBI), fullerene (C_{60}), [6,6]-phenyl-C_{61}-butyric acid methyl ester ($PC_{61}BM$), copper phthalocyanine (CuPc), and lead phthalocyanine (PbPc).

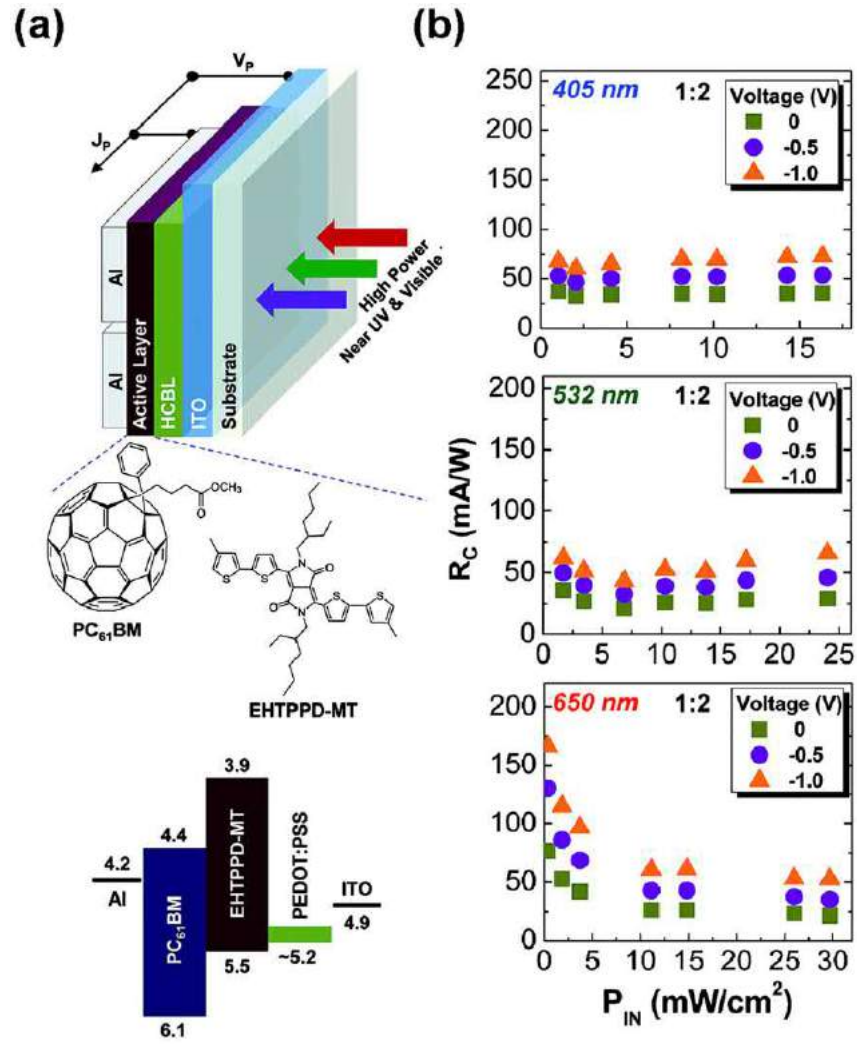


Fig. 8 (a) (top) Device structure and materials used for the fabrication of organic photodiodes with the EHTPPD-MT:$PC_{61}BM$ (1:2) BHJ layers, (bottom) flat energy band diagram for the device (note that minus " − " sign and "eV" unit were omitted for clarity). (b) Corrected responsivity (R_C) as a function of the incident light intensity (P_{IN}) under illumination with near UV (405 nm), green (532 nm), and red (650 nm) lights. (Copyright 2015 Royal Society of Chemistry).

be improved by inserting a conducting polymer interlayer. The performance of organic photodiodes was noticeably improved by employing small molecular p–n junction structures. Peumans *et al.* (2000) reported bilayer-type organic photodiodes using copper phthalocyanine (CuPc) and 3,4,9,10-perylenetetracarboxylic bisbenzimidazole (PTCBI) as a p-type and an n-type small molecule, respectively. However, the bilayer-type devices have a limitation in improving the device performances because of short exciton diffusion lengths in organic layers.

Organic Layer – Bulk Heterojunction

In this regard, organic bulk heterojunction structures were suggested as an alternative approach. Peumans *et al.* (2003) reported organic photodiodes based on CuPc:PTCBI bulk heterojunction layers, which showed controllable device performances by applying thermal annealing treatment leading to internal crystallization in bulk heterojunction films. Sullivan *et al.* (2004) demonstrated organic photodiodes based on CuPc:C_{60} bulk heterojunction films in which exciton dissociations could be improved due to the intermolecular mixing between p-type (CuPc) and n-type (C_{60}) molecules. Panchromatic organic photodiodes based on the bulk heterojunction films of lead phthalocyanine (PbPc) and fullerene (C_{70}), which can detect broadband lights from 300 to 1000 nm, have been reported by Su *et al.* (2015). As shown in **Fig. 8**, Lee *et al.* (2015) reported solution-processed all-small molecular organic photodiodes, using solutions of 2,5-bis(2-ethylhexyl)-3,6-bis(4′-methyl-[2,2′-bithiophen]-5-yl)pyrrolo[3,4-c]pyrrole-1,4(2H,5H)-dione (EHTPPD-MT) and $PC_{61}BM$, which could sense near ultraviolet (UV, 405 nm) and broad visible light (up to 650 nm).

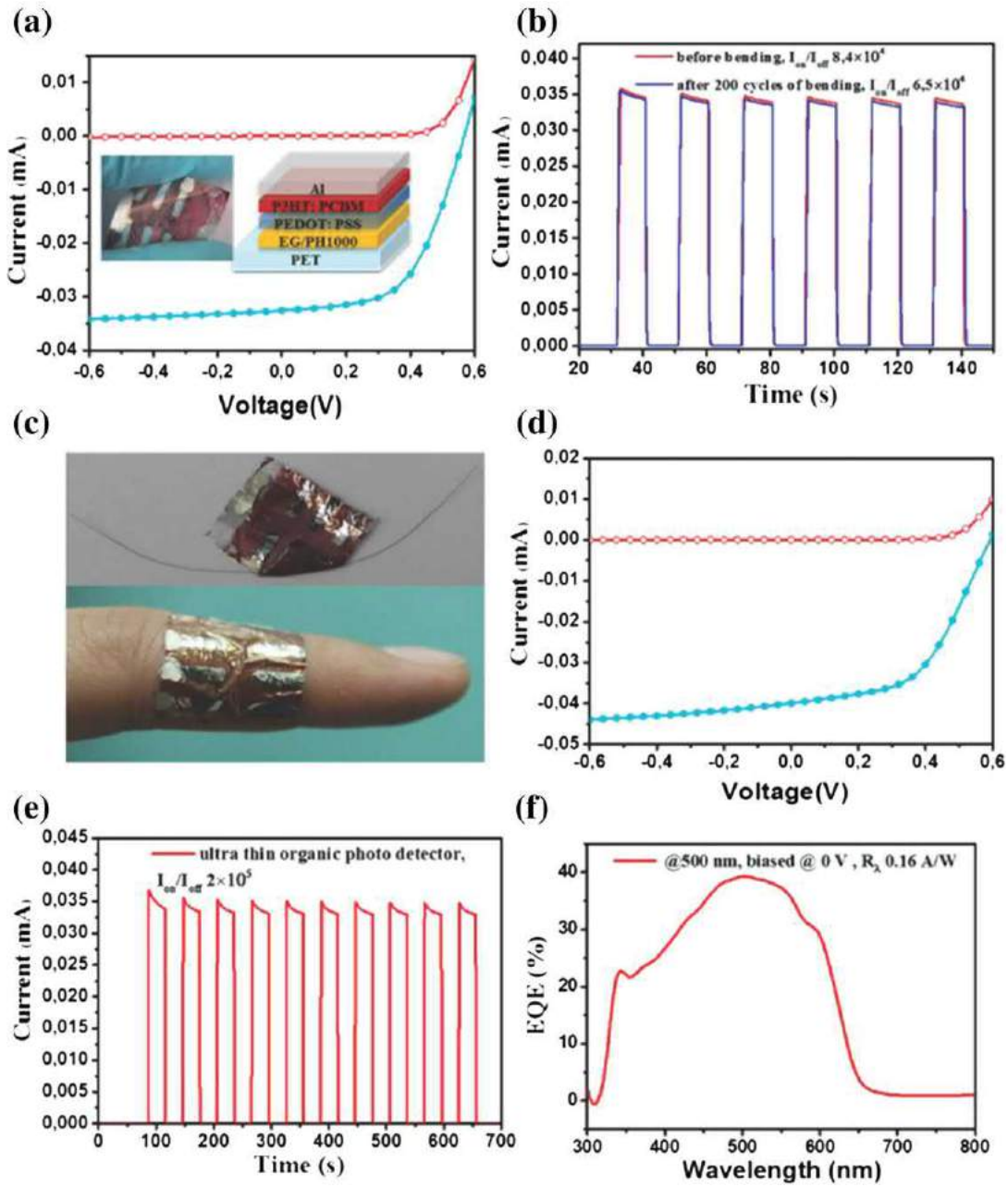


Fig. 9 (a) *I–V* characteristics of organic photodiodes fabricated on regular poly(ethylene terephthalate) (PET) (inset shows the fabricated device and schematic device structures of the organic photodiodes). (b) The on/off characteristics of the photodiodes at 0 V bias on regular PET before and after 200 cycles of bending test. (c) Ultrathin and flexibility demonstration of the fabricated photodiodes, thinner than a human hair, could be attached to the human body. (d) *I–V* characteristics of the ultrathin photodiodes. (e) The on/off characteristics of the ultrathin photodiodes. (f) External quantum efficiency (EQE) spectrum of the ultrathin photodiodes. (Copyright 2015 Wiley-VCH).

Organic Photodiodes With Polymers

Organic Layer – Single Material

Semiconducting polymers have been more extensively studied than small molecules because of their potentials for real plastic photodetectors with tough and rugged characteristics. Harrison *et al.* (1997) studied the thickness-dependent photo-generation characteristics for organic photodiodes with poly[2-methoxy-5-(2-ethylhexyloxy)-1,4-phenylenevinylene] (MEH-PPV) films.

Polymer nanowire photodiodes with poly[(9,9-dioctylfluorenyl-2,7-diyl)-*co*-(bi-thiophene)] (F8T2) films have been reported by O'Brien *et al.* (2006); Ray *et al.* (2015) tried to fabricate organic photodiodes with poly(3-hexylthiophene) (P3HT) films and tried to explain the collection-limited theory for extraordinary responses.

Organic Layer – Bulk Heterojunction

Nalwa *et al.* (2010) reported organic photodiodes based on the P3HT:$PC_{61}BM$ bulk heterojunction films and applied for chemical sensors that could sense gas-phase oxygen and glucose. The similar P3HT:$PC_{61}BM$ photodiodes, which were fabricated by Liu *et al.* (2015) who applied transparent conductive electrodes composed of graphene/PEDOT:PSS hybrid inks, exhibited excellent sensitivity in the wavelength range between 300 and 650 nm (see **Fig. 9**). Saracco *et al.* (2013) reported organic photodiodes with the bulk heterojunction layers of poly[(4,8-bis-(2-ethylhexyloxy)-benzo[1,2-b:4,5-b′]dithiophene)-2,6-diyl-*alt*-(4-(2-ethylhexanoyl)-thieno[3,4-b]thiophene)-2,6-diyl] (PBDTTT-C) and $PC_{71}BM$, which exhibited the effective role of very thin polymeric interfacial layer for achieving homogenous interfaces leading to considerably low dark current by preventing undesired charge injection from cathodes in the devices. Armin *et al.* (2015) proposed new concept called charge collection narrowing (CCN)

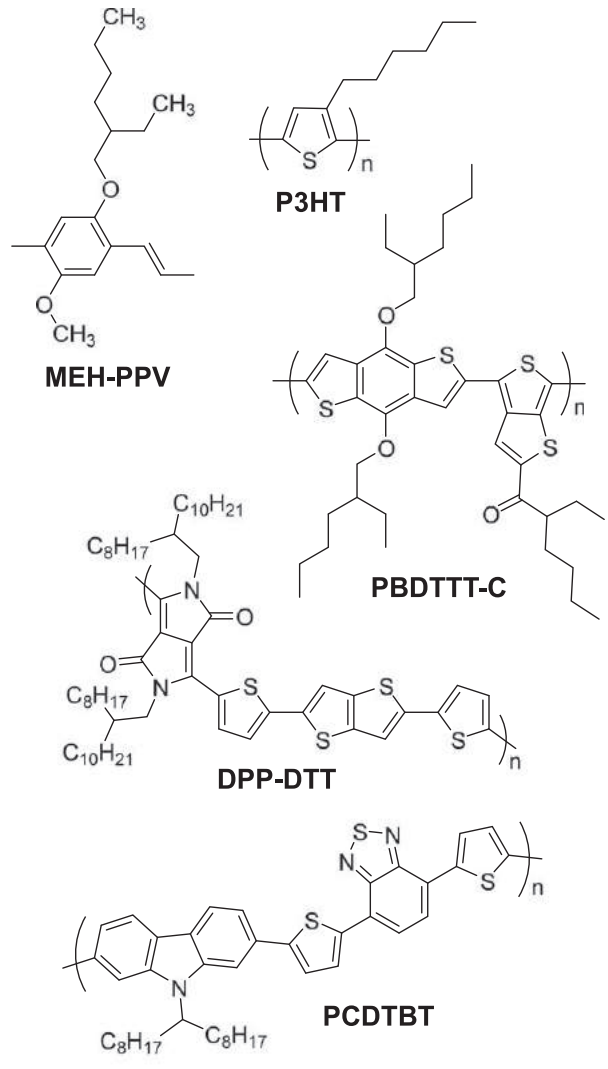


Fig. 10 Semiconducting (conjugated) polymers used for organic photodiodes: poly[2-methoxy-5-(2-ethylhexyloxy)-1,4-phenylenevinylene] (MEH-PPV), poly(3-hexylthiophene) (P3HT), poly[(4,8-bis-(2-ethylhexyloxy)-benzo[1,2-b:4,5-b′]dithiophene)-2,6-diyl-alt-(4-(2-ethylhexanoyl)-thieno[3,4-b] thiophene)-2,6-diyl] (PBDTTT-C), poly[2,5-(2-octyldodecyl)-3,6-diketopyrrolopyrrole-alt-5,5-(2,5-di(thien-2-yl)thieno[3,2-b]thiophene)] (DPP-DTT), and poly[N-9′-heptadecanyl-2,7-carbazole-alt-5,5-(4′,7′-di-2-thienyl-2′,1′,3′-benzothiadiazole)] (PCDTBT).

in organic photodiodes fabricated with the bulk heterojunction layers of poly[2,5-(2-octyldodecyl)-3,6-diketopyrrolopyrrole-*alt*-5,5-(2,5-di(thien-2-yl)thieno[3,2-b]thiophene)] (DPP-DTT) or poly[*N*-9′-heptadecanyl-2,7-carbazole-*alt*-5,5-(4′,7′-di-2-thienyl-2′,1′,3′-benzothiadiazole)] (PCDTBT) and $PC_{71}BM$. Some examples of semiconducting (conjugated) polymers for organic photodiodes are listed in Fig. 10.

Organic Phototransistors With Small Molecules

Organic Layer – Single Material

Organic phototransistors with two types of organic thin-films (pentacene and tetracene), which exhibited photoresponses in both UV and visible ranges, were reported by Choi *et al.* (2006); Qi *et al.* (2013) showed n-type organic phototransistors using core expanded naphthalene diimides fused with two 2-(1,3-dithiol-2-ylidene)malononitrile moieties (NDI-DTYM2) bears one N-alkyl chain and one aromatic phenyl group, (NDI(2OD)(4tBuPh)-DTYM2). Organic phototransistors with highly aligned crystalline 2,7-dioctyl[1]benzothieno[3,2-b][1]benzothiophene (C8-BTBT) films, which exhibited strong responses under weak UV

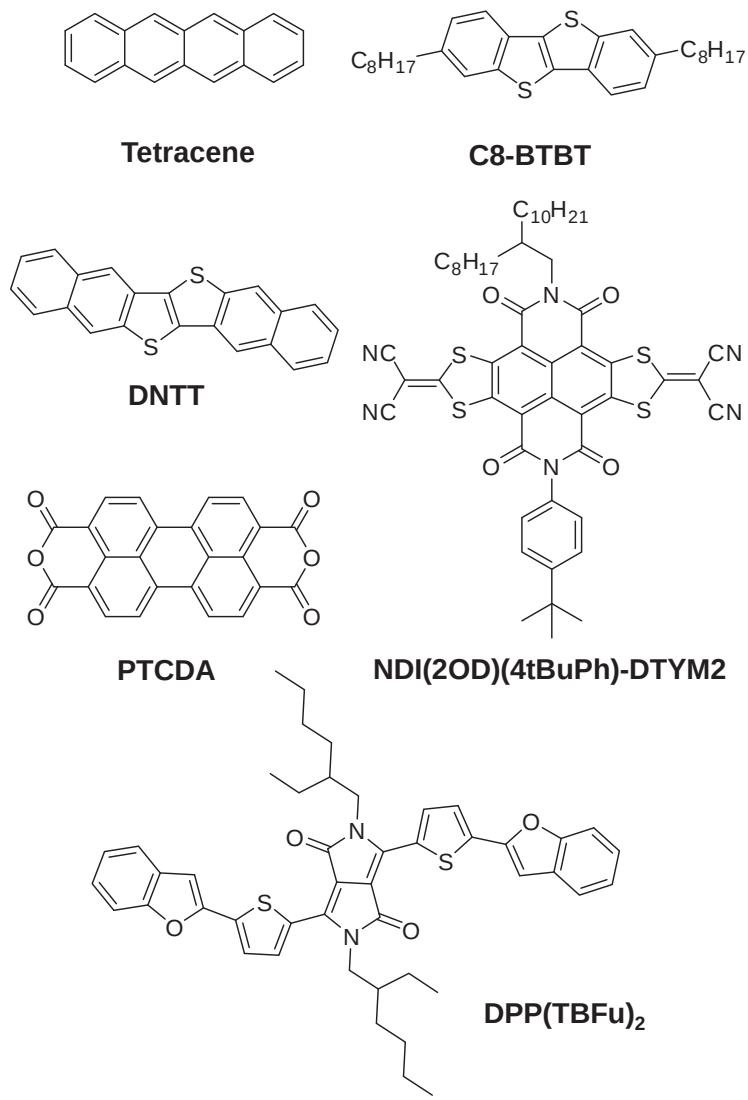


Fig. 11 Small molecules used for organic phototransistors: tetracene, 2,7-dioctyl[1]benzothieno[3,2-b][1]benzothiophene (C8-BTBT), dinaphtho[2,3-b:2′,3′-f]thieno[3,2-b]thiophene (DNTT), perylene-3,4,9,10-tetracarboxylic dianhydride (PTCDA), core-expanded naphthalene diimides fused with two 2-(1,3-dithiol-2-ylidene)malononitrile moieties (NDI-DTYM2) bears one N-alkyl chain and one aromatic phenyl group, (NDI(2OD)(4tBuPh)-DTYM2), and 3,6-Bis(5-(benzofuran-2-yl)thiophen-2-yl)-2,5-bis(2-ethylhexyl)pyrrolo[3,4-c]pyrrole-1,4(2H,5H)-dione ($DPP(TBFu)_2$).

illumination, were reported by Yuan and Huang (2016); Chu *et al.* (2016) demonstrated high photosensitivity from flexible organic phototransistors using dinaphtho[2,3-b:2′,3′-f]thieno[3,2-b]thiophene (DNTT) as an organic sensing channel layer. **Fig. 11** shows various small molecules used for organic phototransistors.

Organic Layer – Bulk Heterojunction

Peng *et al.* (2013) reported organic phototransistors with the bulk heterojunction layers of PbPc and PTCDA, which showed superior performances compared to single component-based devices and high photo-responsivity in the near infrared region. Zhang *et al.* (2013) demonstrated organic phototransistors with solution-processable bulk heterojunction layers of 3,6-Bis(5-(benzofuran-2-yl)thiophen-2-yl)-2,5-bis(2-ethylhexyl)pyrrolo[3,4-c]pyrrole-1,4(2H,5H)-dione (DPP(TBFu)$_2$) and PC$_{71}$BM and studied field-assisted charge separation in small molecular bulk heterojunction structure. It has been also reported by Xu *et al.* (2015) that solution-processed ambipolar organic phototransistors can be fabricated with microphase-separated bulk heterojunction films from solutions of p-type (silylethynylated pentacene) and n-type (silylethynylated tetraazapentacene). This study was demonstrated that photo-effects were associated with a shift of threshold voltage because of photoinduced charge carriers.

Organic Phototransistors With Polymers

Organic Layer – Single Material

Narayan and Kumar (2001) demonstrated polymer-based phototransistors with regioregular poly(3-octylthiophene-2,5-diyl) (P3OT) films for a low intensity optical detection, while wavelength-selective phototransistors with dye-doped P3HT films were also reported by Meixner *et al.* (2006); Li *et al.* (2014) showed that organic phototransistors can be fabricated by employing a

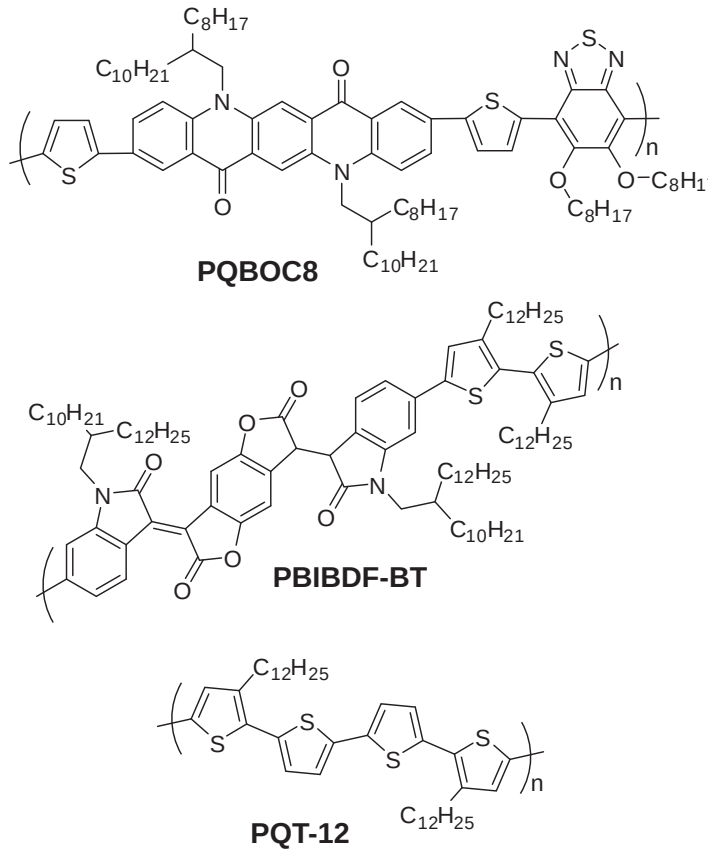


Fig. 12 Conjugated polymers used for organic phototransistors: PQBOC8 that was synthesized by Suzuki coupling reaction between 2,9-diboronic ester-N,N′-di(2-octyldodecyl)quinacridone and 4,7-bis(5-bromothiophen-2-yl)-5,6-bis(octyloxy)-benzothiadiazole, PBIBDF-BT that contains electron-rich bithiophene (BT) and electron deficient bis(2-oxoindolin-3-ylidene)-benzodifuran-dione (BIBDF), and poly(3,3-didodecylquaterthiophene) (PQT-12).

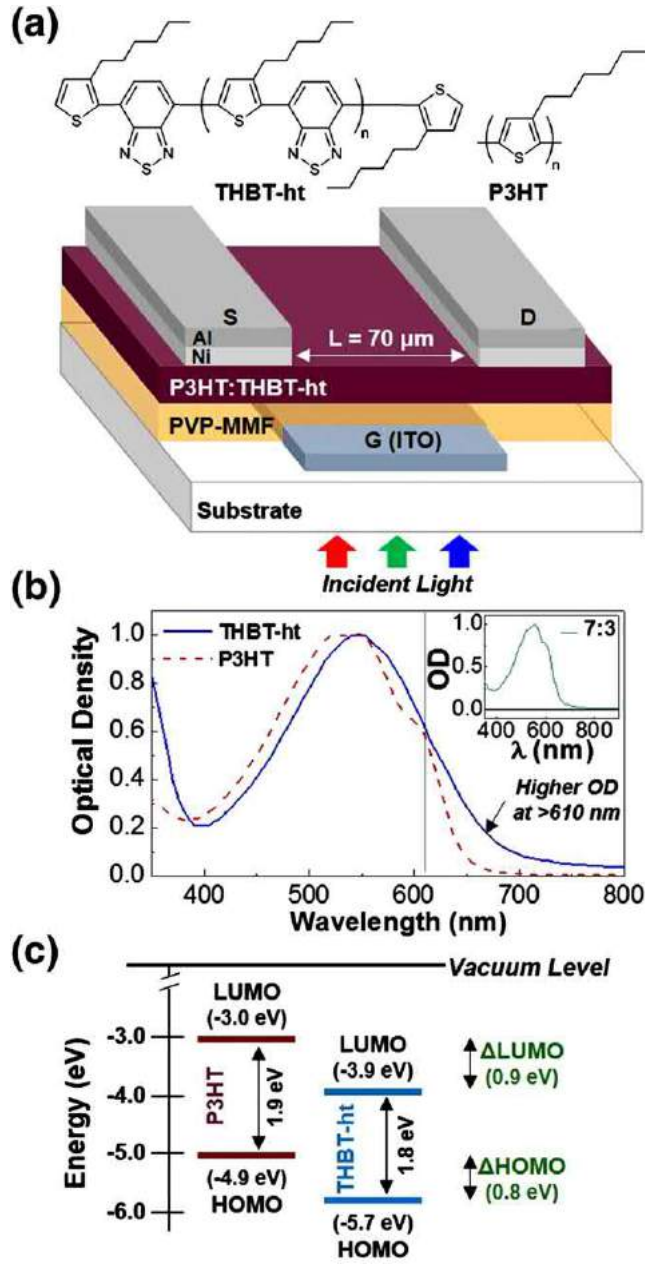


Fig. 13 (a) Materials and device structure for all-polymer phototransistors with the P3HT:THBT-ht layer. (b) Optical density (OD) as a function of wavelength (λ) for the pristine polymer and bulk heterojunction (P3HT:THBT-ht) layers. (c) Comparison of HOMO and LUMO levels for P3HT and THBT-ht. (Copyright 2016 IEEE).

simple self-assembly process in a large area at chloroform/water interface using ultrathin crystalline p-type semiconductor (PQBOC8) that was synthesized by Suzuki coupling reactions between 2,9-diboronic ester-*N*,*N*′-di(2-octyldodecyl)quinacridone and 4,7-bis(5-bromothiophen-2-yl)-5,6-bis(octyloxy)-benzothiadiazole. Lee *et al.* (2016) reported organic phototransistors with highly flexible nanofiber based on poly(3,3-didodecylquaterthiophene) (PQT-12) and poly(ethylene oxide) (PEO) as a semiconducting polymer and a processing aid component, respectively. A couple of conjugated polymers for organic phototransistors are shown in Figs. 12 and 13.

Organic Layer – Bulk Heterojunction

Hwang *et al.* (2011) demonstrated organic phototransistors with the nanoscale phase-separated polymer:polymer bulk heterojunction films of p-type P3HT and n-type poly(9,9-dioctylfluorene-*co*-benzothiadiazole) (F8BT). Han *et al.* (2015)

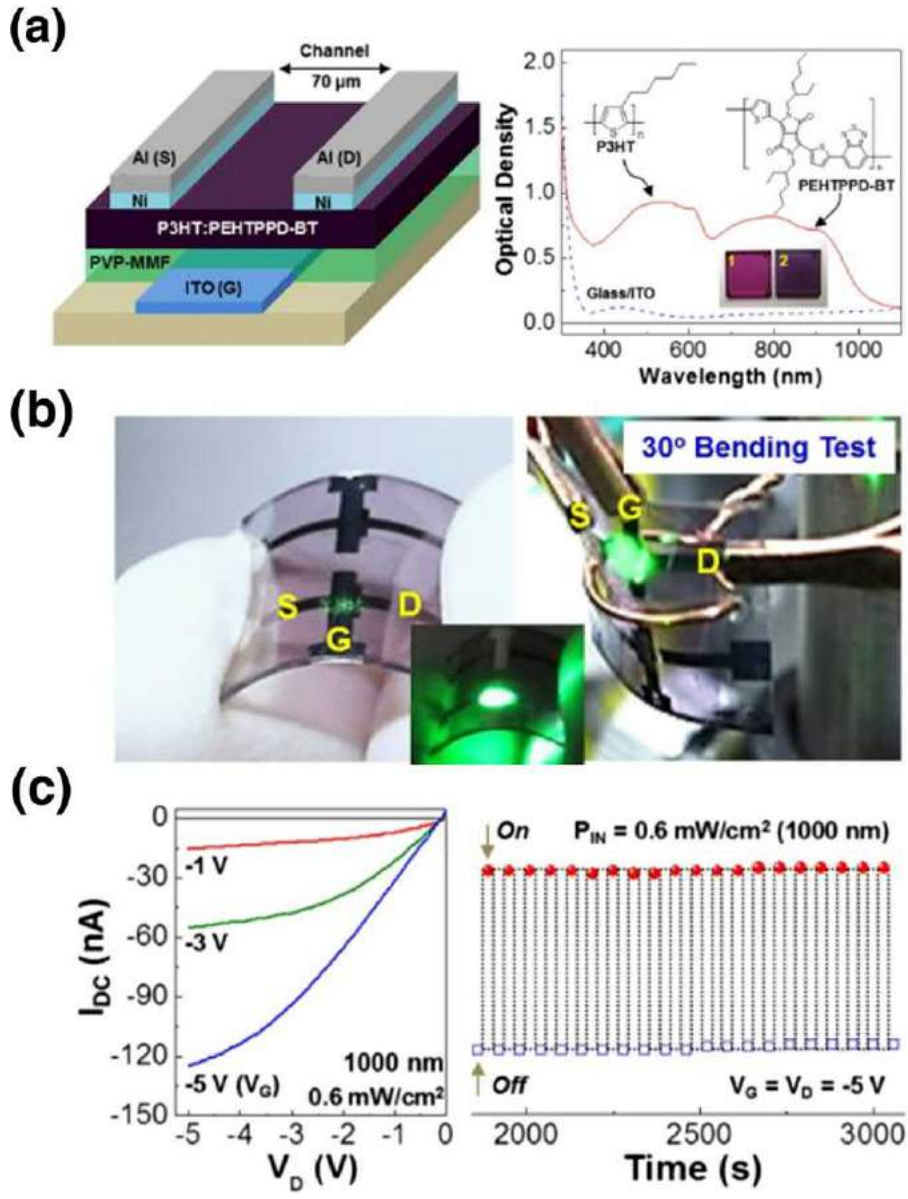


Fig. 14 (a) (left) Device structure for organic phototransistor with all-polymer bulk heterojunction (P3HT:PEHTPPD-BT) layer and (right) optical absorption spectra for the indium tin oxide (ITO) glass substrate and the P3HT:PEHTPPD-BT layer-coated ITO-glass substrate (see the photograph "2" compared with the photograph "1" of the P3HT layer-coated ITO-glass substrate). (b) Photographs for flexible plastic organic phototransistors with the P3HT:PEHTPPD-BT layers, which are bended at an angle of ~30 degree for the measurement of phototransistor performances (note that the green light was roughly illuminated as a guide for the channel part). (c) Low-voltage operation (upon bending at 30 degree) of the optimized flexible plastic organic phototransistors under illumination with near-infrared (NIR) (1000 nm) lights: (left) output curves and (right) repeated on/off modulation. (Copyright 2015 Nature Publishing Group).

demonstrated that all-polymer phototransistors, which were fabricated with the nanostructured bulk heterojunction layers of P3HT and poly[{2,5-bis-(2-ethylhexyl)-3,6-bis-(thien-2-yl)-pyrrolo[3,4-c]pyrrole-1,4-diyl}-co-{2,2′-(2,1,3-benzothiadiazole)]-5,5′-diyl}] (PEHTPPD-BT), can sense a broadband light form visible to near infrared region (see **Fig. 14**). Han *et al.* (2016) reported all-polymer phototransistors with the polymer:polymer bulk heterojunction layers of p-type P3HT and n-type hexylthiophene-end capped poly(3-hexylthiophene-co-benzothiadiazole) (THBT-ht) (see **Fig. 13**). All-polymer phototransistors with P3HT and poly[(4,8-bis(2-ethylhexyloxy)-benzo[1,2-b:4,5-b]-dithiophene)-2,6-diyl-alt-(N-2-ethylhexylthieno[3,4-c]pyrrole-4,6-dione)-2,6-diyl] (PBDTTPD) were also demonstrated by Nam *et al.* (2016). These reports support that all-polymer (polymer:polymer) bulk heterojunctions play an efficient role in improving the photosensitivity of organic phototransistors (**Fig. 15**).

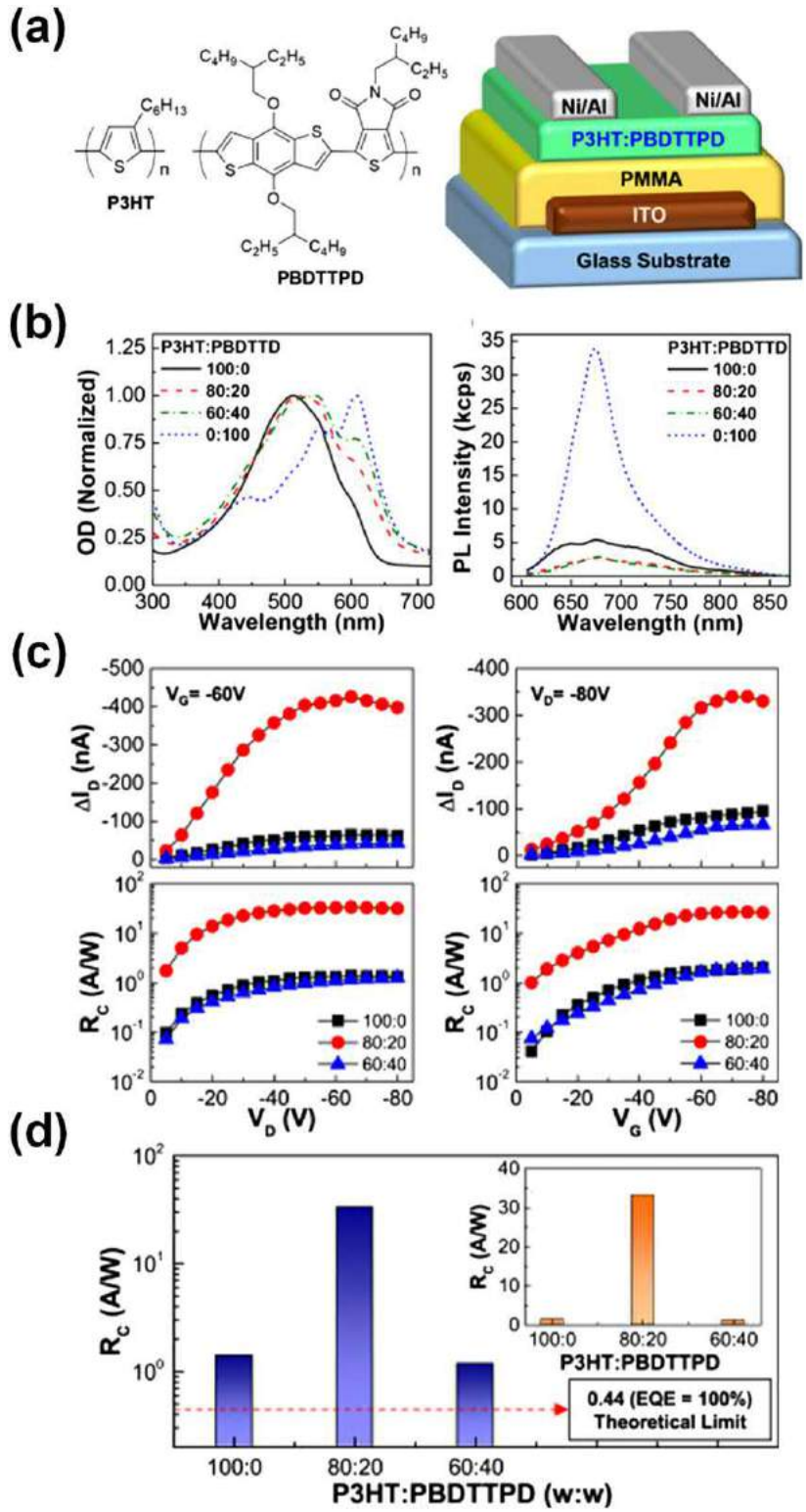


Fig. 15 (a) Chemical structure of materials and device structure for all-polymer phototransistors with the P3HT:PBDTTPD bulk heterojunction layer. (b) Normalized optical density (OD) (left) and photoluminescence spectra for P3HT:PBDTTPD bulk heterojunction layers coated on quartz substrates for different P3HT:PBDTTPD composition ratios (right). (c) Variation of drain current (ΔI_D) (top) and corrected responsivity (R_C) (bottom) as a function of drain voltage V_D, and gate voltage V_G, respectively. (d) Maximum R_C values for different P3HT:PBDTTPD composition ratios. (Copyright 2016 Elsevier).

See also: Organic Semiconductors

References

Armin, A., Vuuren, R.D.J., Kopidakis, N., Burn, P.L., Meredith, P., 2015. Narrowband light detection via internal quantum efficiency manipulation of organic photodiodes. Nature Communications 6, 6343.

Choi, J.-M., Lee, J., Hwang, D.K., *et al.*, 2006. Comparative study of the photoresponse from tetracene-based and pentacene-based thin-film transistors. Applied Physics Letters 88, 043508.

Chu, Y., Wu, X., Lu, J., *et al.*, 2016. Photosensitive and flexible organic field-effect transistors based on interface trapping effect and their application in 2D imaging array. Advanced Science 3, 1500435.

Han, H., Nam, S., Seo, J., *et al.*, 2015. Broadband all-polymer phototransistors with nanostructured bulk heterojunction layers of NIR-sensing n-type and visible light-sensing p-type polymers. Scientific Reports 5, 16457.

Han, H., Nam, S., Seo, J., *et al.*, 2016. Organic phototransistors with all-polymer bulk heterojunction layers of p-type and n-type sulfur-containing conjugated polymers. IEEE Journal of Selected Topics in Quantum Electronics 22, 6000107.

Harrison, M.G., Grüner, J., Spencer, G.C.W., 1997. Analysis of the photocurrent action spectra of MEH-PPV polymer photodiodes. Physical Review B 55, 7831–7849.

Hwang, H., Kim, H., Nam, S., *et al.*, 2011. Organic phototransistors with nanoscale phase-separated polymer/polymer bulk heterojunction layers. Nanoscale 3, 2275–2279.

Lee, H., Nam, S., Kwon, H., *et al.*, 2015. Solution-processable all-small molecular bulk heterojunction films for stable organic photodetectors: Near UV and visible light sensing. Journal of Materials Chemistry C 3, 1513–1520.

Lee, J., Hwang, D.K., Park, C.H., Kim, S.S., Im, S., 2004. Pentacene-based photodiode with Schottky junction. Thin Solid Films 451–452, 12–15.

Lee, M.Y., Hong, J., Lee, E.K., *et al.*, 2016. Highly flexible organic nanofiber phototransistors fabricated on a textile composite for wearable photosensors. Advanced Functional Materials 26, 1445–1453.

Li, H., Wu, Y., Wang, X., Kong, Q., Fu, H., 2014. A self-assembled ultrathin crystalline polymer film for high performance phototransistors. Chemical Communications 50, 11000–11003.

Liu, Z., Parvez, K., Li, R., *et al.*, 2015. Transparent conductive electrodes from graphene/PEDOT:PSS hybrid inks for ultrathin organic photodetectors. Advanced Materials 27, 669–675.

Meixner, R.M., Göbel, H., Yildirim, F.A., Bauhofer, W., Krautschneider, W., 2006. Wavelength-selective organic field-effect phototransistors based on dye-doped poly-3-hexylthiophene. Applied Physics Letters 89, 092110.

Nalwa, K.S., Cai, Y., Thoeming, A.L., *et al.*, 2010. Polythiophene-fullerene based photodetectors: tuning of spectral response and application in photoluminescence based (bio) chemical sensors. Advanced Materials 22, 4157–4161.

Nam, S., Kim, H., Bradley, D.D.C., Kim, Y., 2016. All-polymer phototransistors with bulk heterojunction sensing layers of thiophene-based electron-donating and thienopyrroledione-based electron-accepting polymers. Organic Electronics 39, 199–206.

Narayan, K.S., Kumar, N., 2001. Light responsive polymer field-effect transistor. Applied Physics Letters 79, 1891.

O'Brien, G.A., Quinn, A.J., Tanner, D.A., Redmond, G., 2006. A single polymer nanowire photodetector. Advanced Materials 18, 2379–2383.

Peng, Y., Lv, W., Yao, B., *et al.*, 2013. High performance near infrared photosensitive organic field-effect transistors realized by an organic hybrid planar-bulk heterojunction. Organic Electronics 14, 1045–1051.

Peumans, P., Bulović, V., Forrest, S.R., 2000. Efficient, high-bandwidth organic multilayer photodetectors. Applied Physics Letters 76, 3855–3857.

Peumans, P., Uchida, S., Forrest, S.R., 2003. Efficient bulk heterojunction photovoltaic cells using small-molecular-weight organic thin films. Nature 425, 158–162.

Qi, Z., Liao, X., Zheng, J., *et al.*, 2013. High-performance n-type organic thin-film phototransistors based on a core-expanded naphthalene diimide. Applied Physics Letters 103, 053301.

Ray, B., Baradwaj, A.G., Khan, M.R., Boudouris, B.W., Alam, M.A., 2015. Collection-limited theory interprets the extraordinary response of single semiconductor organic solar cells. Proceedings of the National Academy of Sciences of the United States of America 112, 11193–11198.

Saracco, E., Bouthinon, B., Verilhac, J.-M., *et al.*, 2013. Work function tuning for high-performance solution-processed organic photodetectors with inverted structure. Advanced Materials 25, 6534–6538.

Su, Z., Hou, F., Wang, X., *et al.*, 2015. High-performance organic small-molecule panchromatic photodetectors. ACS Applied Materials & Interfaces 7, 2529–2534.

Sullivan, P., Heutz, S., Schultes, S.M., Jones, T.S., 2004. Influence of codeposition on the performance of CuPc–C_{60} heterojunction photovoltaic devices. Applied Physics Letters 84, 1210–1212.

Voz, C., Puigdollers, J., Cheylan, S., *et al.*, 2007. Photodiodes based on fullerene semiconductor. Thin Solid Films 515, 7675–7678.

Xu, X., Xiao, T., Gu, X., *et al.*, 2015. Solution-processed ambipolar organic thin-film transistors by blending p- and n-type semiconductors: Solid solution versus microphase separation. ACS Applied Materials & Interfaces 7, 28019–28026.

Yuan, Y., Huang, J., 2016. Ultrahigh gain, low noise, ultraviolet photodetectors with highly aligned organic crystals. Advanced Optical Materials 4, 264–270.

Zhang, L., Wu, T., Guo, Y., *et al.*, 2013. Large-area, flexible imaging arrays constructed by light-charge organic memories. Scientific Reports 3, 1080.

Further Reading

Azzellino, G., Grimoldi, A., Binda, M., *et al.*, 2013. Fully inkjet-printed organic photodetectors with high quantum yield. Advanced Materials 25, 6829–6833.

Baeg, K.-J., Binda, M., Natali, D., Caironi, M., Noh, Y.-Y., 2013. Organic light detectors: Photodiodes and phototransistors. Advanced Materials 25, 4267–4295.

Clark, J., Lanzani, G., 2010. Organic photonics for communications. Nature Photonics 4, 438–446.

Falco, A., Cinà, L., Scarpa, G., Lugli, P., Abdellah, A., 2014. Fully-sprayed and flexible organic photodiodes with transparent carbon nanotube electrodes. ACS Applied Materials & Interfaces 6, 10593–10601.

Heeger, A.J., 2010. Semiconducting polymers: The third generation. Chemical Society Reviews 39, 2354–2371.

Vuuren, R.D.J., Armin, A., Pandey, A.K., Burn, P.L., Meredith, P., 2016. Organic photodiodes: The future of full color detection and image sensing. Advanced Materials 28, 4766–4802.

Wakayama, Y., Hayakawa, R., Seo, H.-S., 2014. Recent progress in photoactive organic field-effect transistors. Science and Technology of Advanced Materials 15, 024202.

Williams, G., Backhouse, C., Aziz, H., 2014. Integration of organic light emitting diodes and organic photodetectors for lab-on-a chip bio-detection systems. Electronics 3, 43–75.

Zhang, H., Jenatsch, S., Jonghe, J.D., *et al.*, 2014. Transparent organic photodetector using a near-infrared absorbing cyanine dye. Scientific Reports 5, 9439.

Index

Note
This index is in letter-by-letter order, whereby hyphens and spaces within index headings are ignored in the alphabetization, and it is arranged in set-out style, with a maximum of three levels of heading.

Cross-reference terms in italics are general cross-references, or refer to subentry terms within the main entry (the main entry is not repeated to save space).

Location references refer to the volume number, in bold, followed by the page number.

The page numbers suffixed by '*F*' and '*T*' refer to Figures and Tables, respectively.

A

a-axes 2:271
a-plane 2:271
A549 human lung carcinoma cells 5:182
AA stacking 4:286
AB stacking 4:286
Abbe theory of microscope imaging 5:187–188
Abbe/Rayleigh limit of two-point resolution 5:15–16
Abbott medical optics (AMO) 4:531
aberrations 5:55–58
  aberration-free
    diffraction limited systems 5:15–16
    system 5:185
  astigmatism 1:118–119
  chromatic aberrations 5:58–59
  coma 1:116–118
  contributions
    calculation at image 4:211–214
    in freeform prism 4:214–215
  curvature of field and distortion 1:119–121
  monochromatic aberrations 5:55–58
  nonspherical surfaces 1:121–122
  ray tracing in meridional plane 1:114*F*
  theories 4:205
  vector 4:207, 4:211
aberrometry 5:112–113
above threshold ionization (ATI) 2:313–314
abruptly autofocusing optical beam (AAF optical beam) 1:415–416
absolute horizontal accuracy 4:402
absolute measure of SHG 4:287–289, 4:288*T*
  models for sample 4:287–289
  role of excitonic resonances 4:289
  role of substrate 4:289
absolute vertical accuracy 4:401–402
absorbers in rare gas halide lasers 2:363*T*
absorption 2:107, 4:67, 4:310, 4:339, 5:168, 5:207
  acoustic 1:135–136
  band 4:364
  coefficient 3:221, 5:160–161, 5:161*F*
  cross-section 3:221
  edge 2:94
  efficiency 5:256–257
  experiment 1:392–393
  measurements 2:73
  spectroscopy with attosecond pulses 2:242–243
    attosecond four-wave mixing spectroscopy 2:243
    attosecond transient absorption spectroscopy 2:242–243
  spectrum 1:459, 2:107*F*, 4:88
  2D spectroscopy 2:161
"absorptive" 2DES spectrum 2:185–186
abstract imaging system 3:156
"AC apodized" Gaussian profile 1:233
ac Stark effect 4:320
ac Stark shift 4:346
Acanthamoeba keratitis 5:103–104
  two-photon imaging 5:105*F*
accelerated free electrons 1:405
acceptor
  acceptor mode 1:187
  materials in OPV 5:265
accidental cell death 3:107
accommodation 5:62*F*, 5:141, 5:150–151
  amplitude of 5:47
  restoration techniques 5:120
acetonitrile (ACN) 5:277
achievable bit-error rates 1:276–277
  comparison of modulation formats 1:280
  intensity modulation 1:277
  partial response signaling 1:278–280
  phase-shift keying 1:277
  quadrature amplitude modulation 1:277–278
achievable SNR 1:273
achromatic doublet 5:188–189
acoustic
  absorption 1:135–136
  attenuation 1:136–137
  density grating 2:4
  diffraction by acoustic waves 1:131–133
  disturbance 1:130
  frequency 1:131
  power 1:134–135
  propagation 1:131–132
  properties 2:7
  radiation 5:192
  strain amplitude 1:130–131
  wavelength 1:132–133
  wavevector 1:137
acoustic optical modulator (AOM) 3:46
acoustic radiation force (ARF) 5:147
acoustical studies and vibrometry 4:528
  laser Doppler vibrometry 4:528
  successive pulse illumination in acoustical studies 4:528
  vibration measurement of vocal folds 4:528–530
acousto-optic modulator (AOM) 1:139, 2:190, 4:98–99, 4:115, 4:435–436, 4:501–502, 4:502
acousto-optic programmable dispersive filter (AOPDF) 2:297–298
acousto-optic tunable filter (AOTF) 1:133–134, 1:137–139
  wavevector diagram for 1:138*F*
acousto-optics (AO) 1:130
  see also adaptive optics (AO)
  anisotropic bragg diffraction 1:133–134
  AOTFs 1:137–139
  beam deflectors 5:194
  birefringent scanners 1:136–137, 1:137*F*
  bragg diffraction 1:133
  devices 1:130, 1:131, 1:135, 1:135–136
  diffraction
    by acoustic waves 1:131–133
    cell 1:134*F*
    efficiency 1:134–135
    of light in Raman–Nath limit 1:132*F*
  imaging 3:226, 3:226–228, 3:227*F*
  interaction of light waves 1:131*F*
  laser cavity, acousto-optic Q-switch in 1:140*F*
  materials 1:135, 1:135*T*
  modulators 1:139–140
  momentum diagram for diffraction of light 1:133*F*
  noncollinear AOTF orientation 1:138*F*
  photo-elastic effect 1:130–131
  Q-switch 1:140

acousto-optics (AO) (*continued*)
scanners 1:135–136, 1:136*F*
spectrum of phase-modulated wave 1:132*F*
wavevector diagram for AOTF 1:138*F*
acousto-optics-optical coherence tomography (AO-OCT) 5:73
activator 2:394
activator protein-1 (AP1) 3:115–116
active cavity interferometer 2:309, 2:309*F*
active chirp laser stabilization for FMCW lidar 4:436
80 GHz distributed feedback based chirp stabilization 4:436–438
broadband (5 THz) chirp stabilization 4:436
active components 1:223–224
active dynamic holographic display devices (ADHDDs) 4:114, 4:114–115
active fiber compatible components 1:221, 1:223–226
active gain medium 2:329
active lasing materials 2:268
active locking techniques 2:453
active materials in polymer solar cells
acceptor materials in OPV 5:265
polymer active materials 5:263–265
active matrix (AM) 3:9, 3:12, 5:239
driving method 3:30*F*, 3:31
TFT driving 3:66–67
active matrix liquid crystal displays (AMLCDs) 3:1, 3:2, 3:5–6, 3:14
active matrix organic light emitting diode (AMOLED) 3:14, 5:239
active medium 2:368
active mode locked lasers (MLL) 4:38
active mode-locking of laser diodes 4:62
active optical devices 1:214
active optics 3:197, 3:198, 3:198
active Q switching 2:418–419
active regions 1:382–383, 1:382*F*
active remote sensing 2:435
active ring resonators 4:294
Active Tiling display system (AT display system) 4:116
active-passive axial waveguide integration 4:243–246, 4:244*F*
acuity 3:235–237
adaptive control 5:42
adaptive immunity 3:112–114
adaptive optics (AO) 3:197, 3:198–200, 3:278, 3:279, 5:67, 5:72, 5:72–73, 5:91, 5:119
see also acousto-optics (AO)
adaptive system design 3:201–202
applications 3:202–203, 5:81–82
correction 5:73*F*
detection schemes 5:76*F*
fast corrections 3:198–200
flood-illuminated ophthalmoscopy 5:73–74
functional assessment in conjunction with AO imaging 5:82
future development 3:202
imaging through atmosphere 3:200–201, 3:200*F*
metrics to analyze cell mosaics 5:79–81
post processing and AO image analysis 5:78–79
and post-processing 3:278–279
retinal imaging 5:73
slow corrections 3:198
in vivo multiphoton retinal imaging with 5:86–87
adaptive optics scanning laser ophthalmoscope (AOSLO) 5:64–65, 5:65*F*, 5:85, 5:86–87
erythrocyte imaging with 5:67–68
leukocyte imaging with 5:67
adaptive optics-optical coherence tomography (AO-OCT) 5:77–78
adaptive signal processing 4:333
add noise 1:263
"add-drop filter" configuration 4:216
add/drop multiplexer (ADM) 4:65
Added White Gaussian Noise (AWGN) 1:276
Addition de Photons par Transferts d'Energie' (APTE) 2:395
Additive White Gaussian Noise (AWGN) 1:299
adequate organic solvent 2:337
adiabatic pulse pairs 4:345
adjacent-channel isolation 1:266
advance cruise missile (ACM) 4:450
advance super in-plane-switching (AS-IPS) 3:60–61
advanced coherent imaging with FMCW lidar 4:439–440
advanced delayed fluorescence 5:244–246
advanced EDFA functions 1:362–363
advanced LIGO 1:432, 1:434, 1:435, 1:436*F*, 1:440*F*, 1:441*F*
advanced plasmonic nanostructures 5:300
Advanced Scientific Concepts (ASC) 4:446
advanced Virgo 1:432
aerial cables 1:333
aero-optics 3:199, 3:203
see also adaptive optics (AO); acousto-optics (AO)
age, changes with 5:60
accommodation 5:62*F*
aperture stop and iris 5:60
cornea 5:60
lens 5:60–61
light loss at retina 5:61
presbyopia 5:61
refraction 5:61
age related macular degeneration (AMD) 5:164, 5:166*F*
agency for science, technology and research system (A*STAR system) 4:117–118, 4:118*F*
aggregate nominal pulse density (ANPD) 4:401
aggregate nominal pulse spacing (ANPS) 4:401
air bands 1:171, 1:185
air periodic system 1:185
air puff corneal dynamic imaging 5:142, 5:143*F*
air puff OCT imaging 5:142–143
air puff scheimpflug imaging 5:142
clinical and experimental applications 5:145–146
corneal deformation parameters 5:143–144
corneal mechanical properties from 5:144–145
air-biased-coherent-detection matrix-optics (ABCD matrix-optics) 4:205–206
air-clad fiber 1:200–203
air-cooled argon ion lasers 4:361
air-cooled ion lasers 2:376
Air-guiding Photonic Bandgap fibers (PBG fibers) 1:263*F*
air-plasma
single-color method 1:411–412, 1:411*F*, 1:412*F*
two-color method 1:412–416
airborne targets 4:479–482
airborne topographic lidar systems, 3D metrics for 4:401
current lidar metric standards 4:401
emerging capabilities and challenges 4:402–403
accounting for relative horizontal accuracy 4:403–404
density and completeness in 3D 4:404–405
foliage penetration performance characterization 4:404
lidar error model 4:402–403
point cloud resolution measurement 4:403
airy disk 5:186
airy pattern 1:72, 5:15
albumin and other heavy proteins 3:110
Aldis calculus 4:205
Aldis theorem 4:212
AlGaAs/GaAs quantum wells, optical properties of 2:105–107
general principles 2:105–107
optical absorption 2:107–108
photoluminescence and spontaneous emission 2:108
AlGaN-based laser diodes 2:271, 2:273–277, 2:274*F*, 2:277*F*
algebra theorem 3:163
alkoxides 2:346
"all pass" arrangement 4:216, 4:216*F*
all-optical
data regeneration 1:251–252
pump–probe spectroscopy of correlated electron materials 2:133–135
switching 1:142, 4:224
all-optical signal regeneration 1:364–365, 1:366*F*, 1:370*F*
all-optical 2R/3R regeneration using optical nonlinear gates 1:367–369, 1:367*F*
optical clock recovery 1:369
optical decision element 1:367–369
optical regeneration by saturable absorbers 1:369–370
generalities on 1:365–366
principles 1:365–366
qualification of signal regenerator performance 1:366–367

synchronous modulation technique 1:370–371
allocation ID (Alloc-ID) 2:75
alternating current signal (AC signal) 3:91–92
alternating projection algorithms 3:147–148, 3:147*F*, 3:152–153
alternative coatings 1:33
alternative plasmonic materials
applications 2:261–262
case for 2:252–254
chemical sensing 2:262
conventional plasmonic materials 2:255–256
finding alternatives 2:256–257
high temperature plasmonics 2:262–263
ideal plasmonic material 2:254–255
integrated plasmonics 2:261–262
metal alloys 2:258–259
metals to "less-metals" 2:259–261
metamaterials and transformation optics 2:263–264
optical properties of materials 2:254
semiconductors to metals 2:256–257, 2:256*T*
two-dimensional plasmonic materials 2:261
altitude-resolved atmospheric Raman water spectrum signal 4:465, 4:468*F*
alumina (Al_2O_3) 1:28, 2:379
ceramic tube 2:369
thermal insulator 2:369
aluminosilicate (Al_2O_3–SiO_2) 2:347
aluminum (Al) 2:256, 2:271, 5:298
aluminum nanoparticle (Al NP) 5:298
aluminum zinc oxide (AZO) 2:257
aluminum-doped zinc oxide (AZO) 2:258, 5:273
Alzheimer's disease (AD) 3:124, 3:124–125
ambient contrast ratio (ACR) 3:73
ambient illumination and reflection 3:72–73
ambiguity function (AF) 4:164, 4:174–175
approach to AF reconstruction 4:170–171
of image of incoherent source 4:168–169
inoptics 4:164
imensity spectrum of Fresnel diffraction pattern 4:165–166
mutual intensity 4:164–165
phase-space tomography 4:169–170
propagation through paraxial optical system 4:167
propagation-based holographic phase retrieval 4:171–172
in space-invariant (isoplanatic) imaging 4:168
Ambiguity Zone Detectors (AZD) 1:279–280
American National Standards Institute (ANSI) 5:106–107
contrast ratio 3:72
American Society for Photogrammetry and Remote Sensing (ASPRS) 4:401
lidar calibration/validation Working Group 4:403–404
Amici prism 1:126, 1:126*F*
ammonia (NH_3) 1:389, 2:273
amorphous glass 2:265
amorphous oxide semiconductors (AOSs) 3:12–13, 3:13*F*
TFT 3:14–15
thin film 3:14–15
amorphous Si TFT (*a*-TFT) 3:53
amorphous silicon (*a*-Si) 3:14
amplification 1:97, 1:98, 1:223–224
factors 2:412
regenerative and multipass amplification 2:412
of spectrally narrow nanosecond or sub-nanosecond pulses 2:412
amplified laser emission 2:338
amplified spontaneous emission (ASE) 1:242–243, 1:263, 1:298–299, 1:353, 1:361–362, 1:364, 1:369–370, 2:82, 2:286, 2:410–411, 2:426–427, 4:46, 5:312–313
amplified stimulated emission (ASE) 4:362
amplifier
add noise 1:273
configurations 1:353–354, 1:354*F*
gain 1:246, 1:351–352, 1:353
noise figure 1:353
technologies 1:263*F*
amplitude 1:139, 1:231–232
of accommodation 5:47
deterministic 4:180
of diffraction wave from rectangular slit 1:70, 1:70*F*
distribution 4:182
transmittance of hologram 4:30
amplitude modulation (AM) 1:146–147, 1:367–368, 1:373, 1:392–393
radio 1:373–374
amyloid fibers 2:174
amyloid proteins 2:174–175
kinetics of amyloid formation by human amylin 2:175–176
structure of polyglutamine fibrils 2:174–175
anaglyph 3:45–46
analog signals 1:337
analog to digital converters (ADCs) 1:143, 1:278, 1:295–296, 3:175, 4:434–435, 4:509–510, 5:8
analogue holographic recording and replay 4:106–107
in-line hologram recording 4:107*F*
in-line hologram replay 4:107*F*
off-axis hologram recording 4:108*F*
real image reconstruction from off-axis hologram 4:108*F*
analyzer 2:211, 3:59
angle 1:158
analyzer-based imaging (ABI) 4:171
Anderson localization 4:278
Kerr nonlinearity in theory and experiment 4:279–281
of light 4:278
other forms of nonlinearity 4:282
theoretical considerations 4:281–282
transverse Anderson localization
of light 4:278–279
in theory and experiment 4:279–281
androgenetic alopecia (AGA) 3:120
anemometer 4:497
angle of refraction 1:153
angle-resolved photoemission spectroscopy (ARPES) 2:144–145
angled physical contact technique (APC technique) 1:337–338
angular aperture 1:133
angular dependence 1:83
angular field 1:139
angular isoplanatism 3:201
angular magnification 1:108–109
angular streaking 2:240
angular-spectrum expansion 3:140
anharmonic oscillator spectra interpretation 2:160–161, 2:161*F*
anharmonic potential 2:161
anisometropia 5:54
anisotropic Bragg diffraction 1:133–134, 1:136, 1:137
anisotropic scanner 1:136
anisotropic scattering 3:221
anisotropic waveguide-based modulators (AWM) 4:117
holographic video system 4:117*F*
annealing process 3:15
anode 5:232
anomalous dispersion 1:5, 1:6, 1:195, 1:315, 4:1–2
antenna theory 3:137–138
anterior corneal surfaces 5:45
anti-aliasing filters (AAFs) 1:299
anti-distorted beam 4:322
anti-glare surfaces (AG surfaces) 3:73
anti-reflecting surfaces (AR surfaces) 3:73
anti-Stokes waves 2:265
anti-tumor immune response induction after PDT 3:114
anti-vascular effect of PDT 3:111
anti-vascular endothelial growth factor (anti-VEGF) 5:164
antibiotic resistance, rise of 3:102–103
anticorrelation 1:453
antiferromagnetic order (AFM) 2:123
antimicrobial photodynamic inactivation (aPDI) 3:103, 3:103, 3:105, 3:106
localized infections 3:105*F*
pathogen classification and PS structure 3:103–105
PDT for infectious disease 3:105–106
rise of antibiotic resistance 3:102–103
virulence 3:105
antimissile defense (AMD) 4:445
antireflection (AR) 2:329, 2:408–409, 5:292–293
coating 2:457
AO scanning laser/light ophthalmoscopy (AOSLO) 5:73, 5:74–77, 5:77*F*, 5:78–79, 5:80*F*, 5:81*F*
aperture 3:247
mask 3:3
size 1:139
stop 5:45–46, 5:46*F*
and iris 5:60
synthesis 3:241
transmission function 1:73
aplanatic front element 5:188, 5:188*F*

aplanatic system 5:185
apochromats 5:188–189
apodization 5:16
apoptosis, PDT and 3:107
applanation-free femtosecond laser 5:133
application-specific integrated circuits (ASICs) 1:295–296, 4:418
approximate model 5:14
aquatic holography 4:106
aqueous humor 5:43
Ar II laser blue-green wavelengths 2:376–377, 2:377*T*
aramid yarns 1:331
arbitrary angle 4:178–179
arbitrary polarization 1:162
Arc gap 3:32
argon ion 2:376
  laser 2:381, 4:360–361, 4:360*T*
    oscillation 2:382
argon laser trabeculoplasty (ALT) 5:136
array illuminators *see* multiple beamsplitters
array of *N* identical apertures 1:74
array theorem 1:72–73
arrayed waveguide grating (AWG) 1:252, 1:266, 2:74, 4:222
arrayed waveguide grating routing (AWGR) 4:241
arsenic triselenide (As_2Se_3) 1:210
arsenic trisulfide 1:210
artificial reference stars 3:202
aspherical optical metrology 4:438–439
asphericity 5:44–45
astigmatism 1:118–119, 1:120*F*, 1:122*F*, 5:52–54, 5:53*F*
astronomical telescope 1:122
astronomy, high resolution imaging in 3:253–254
astrophysical molecular spectroscopy 1:396–399
Asus X-tion Pro 4:512
asymmetric cladding layers 1:186
asymmetric double quantum well (a-DQW) 2:85–86
asymmetric twin guides (ATG) 4:244
asymmetrical devices 1:340
asynchronous disk mirroring 1:281
asynchronous transfer mode protocol (ATM protocol) 2:74
Atacama Large Millimeter Array (ALMA) 1:397, 1:397*T*, 1:398*F*
athletic performance, PBM for 3:126
atmospheric/atmosphere
  coherence length
  components and contaminants 4:463–469
  profiling 4:483
  turbulence 3:272–274, 3:273*F*, 3:278
atom optics
  atom interferometry 5:217–218
  atom-standing wave interactions 5:214–217
  Kapitza–Dirac scattering 5:213–214
  nanofabricated atom optics 5:204–207
  standing waves of light 5:207–213
atom-standing wave interactions 5:214–217
atom(s) 1:224
  condensation 1:458–459
  flux in *n*th diffraction order 5:205
  interferometry 5:217–218, 5:217*F*
atomic beam diffraction from optical standing wave 5:212
atomic Coulomb potentials 2:33
atomic force microscopy (AFM) 4:419, 4:419*F*, 5:175, 5:185, 5:190, 5:261
atomic layer deposition (ALD) 2:260, 3:56
atomic orbitals (AOs) 5:220–221
atomic physics 2:40
  EIT and cross-coupling of photons in doped PCs 2:15–18
  radiative decay and photon–atom binding in PC 2:12–15
atomic QED approaches 1:458–459
atomic quantum optics 1:458–459
atomic systems 1:462
atomic vapors 2:17
atomic-like situations 1:488
attention bias modification (ABM) 3:126
attenuation 1:18, 1:255, 1:255–256, 1:308–309, 1:308*F*, 1:309*F*
  of silica material 4:1
  test methods for 1:309
    backscattering method 1:309–311, 1:310*F*
    cut-back method 1:309
    insertion loss method 1:311
  vs. wavelength approximation for silica fibers 4:14–15, 4:14*F*
attenuators 1:336, 1:342, 1:360
attosecond
  beating reconstruction by interference of two-photon transitions 2:241–242
  four-wave mixing spectroscopy 2:243
  light house 2:238, 2:239*F*
  optical pulses 2:233–234
    electric laser field in time and frequency domain 2:234
    formation of attosecond pulses 2:237
    high-order harmonic generation 2:234–235
  streak camera 2:241, 2:241*F*, 2:322, 2:323*F*
  technology 2:316–319
    gating techniques 2:319–321
    HHG 2:316–319
  transient absorption spectroscopy 2:242–243
attosecond pulses 2:311
  absorption spectroscopy with 2:242–243
  characterization 2:321–323
  formation 2:232
    attosecond pulse trains 2:237
    isolated attosecond pulses 2:237
  generation 2:234
    in water-window region 2:321
  photoelectron and ion spectroscopy with 2:240–241
    attosecond streak camera 2:241
    ion spectroscopy 2:242
    reconstruction of attosecond beating 2:241–242
  technology 2:233
  trains 2:232
attosecond spectroscopy
  see also 2D electronic spectroscopy (2DES); multidimensional THz spectroscopy
    and applications 2:238–240
    with attosecond pulses 2:242–243
    with femtosecond pulses 2:239–240
    generation of attosecond optical pulses 2:233–234
    photoelectron and ion spectroscopy with attosecond pulses 2:240–241
attractive Coulomb force 2:40
AU Optronics 3:61
Auger carrier 2:115
Auger effects 2:114–115, 2:116–117, 2:117*F*
Auger recombination 2:110, 2:463–464
augmented reality (AR) 3:48, 4:124
  devices 3:75
  display 3:48–49
  HMD 3:51, 3:51*F*
Autler–Townes effect 2:24–25
Autler–Townes splitting 4:342
auto-discovery 2:76, 2:77*F*
Auto-Recording Instrumented Environmental Sampler (ARIES) 4:112
auto-stereoscopic display 3:45
  anaglyph 3:45–46
  E-holography 3:46
  head mounted display 3:46
  integral imaging display 3:48
  LC lens for 2D/3D switchable display 3:48
  multi-planar 3:46–47
  polarizing glass 3:45
  shutter glasses 3:46
  SMV display 3:48
  spatial-multiplexed 3:48
  time-multiplexed 3:47–48
  volumetric display 3:46
autocorrelation 2:316, 3:251, 4:49–50
autocorrelator 2:316
autofluorescence 5:86, 5:97, 5:192
automatic gain control amplifier (AGC amplifier) 4:6
automatic power control (APC) 1:369–370
Autonomous Landing and Hazard Avoidance Technology project (ALHAT project) 4:450–451
autonomous underwater vehicles (AUVs) 4:110
autophagosome 3:108
autophagy, PDT and 3:108
auxiliary optical system 4:107
avalanche gain 4:423
avalanche photodiodes (APDs) 1:271, 3:98, 4:415, 4:416*F*, 4:431, 4:446–447
  comparison of false alarm rate *vs.* detection threshold profiles 4:427*F*
  dark current 4:423
  signal and noise distributions 4:427*F*
average DGD 1:257
average index 2:303–304
average modulation at optimum phase (AMOP) 3:239
average successive reflections (ASR) 3:148
axes and angles 5:47–48, 5:47*F*
axial Airy disc function 4:355
axial eye length measurement 4:500, 4:500*F*
axial shift variance 3:263
axial strain 1:216

axially symmetric imaging system 5:14, 5:14F
Axially Symmetric Vertical Alignment (ASVA) 3:61
Axis Symmetric Micro-Cell (ASM) 3:61
azaquinolone derivatives 2:346
azimuth invariant case 5:19
azimuthal acceptance angles 1:136
azimuthal circular ring of supercritical illumination 5:169
azobenzene dyes 4:95–96
azobenzene-based devices 4:114

B

Babinet and Soleil compensators 1:156–157, 1:158F, 1:159F
back focal plane (BFP) 5:168, 5:173
back reflection 1:337–338, 1:338F
back-end-of-line (BEOL) 4:219
back-projection operation 3:194, 3:195F
back-propagating conjugate wave 3:207
back-scattered Raman radiation 4:355
backchannel etched structure (BCE structure) 3:13
backlight module
  light sources 3:27–28
  optical films 3:28
  QD film 3:28–29
backlight reflector film 3:28
backscattering method 1:259, 1:309–311, 1:310F
backward phase conjugator 3:205
backward wave oscillators (BWO) 1:391
bacteriochlorophylls (BChl) 2:191–192, 2:191F
bacteriorhodopsin 4:93, 4:94F
balanced detector (BD) 1:295
ballast chamber 2:374
ballistic regime, imaging in 3:222–223
'ballistic' photons 3:219
  shallow tissue imaging 3:222–223
Balmer series of hydrogen 2:46–47
band filling effects 2:464
band gap materials 2:40
band structure 1:170
  bloch states 2:87
    density of states 2:90
    effective mass 2:89–90
    electron–photon interaction 2:90–91
    k·p theory 2:87–88
    NGSs 2:88–89
    quantum wells 2:91
    selection rules for intersub-band optical transitions 2:91–92
    three-level model of band structure 2:89F
  for multilayer fibers for external reflection applications 1:211–213
  and optical properties
  three-level model of 2:89F
band-bending regions 2:104
band-diagrams 1:233
band–band processes 2:115
bandgap 1:169, 2:269
  energy 2:33–34, 2:351
  fibers 1:203, 1:203F
  guided fibers 1:203
  renormalization 2:465
bandpass filter (BPF) 1:378, 4:46
bandpass wavelength-division multiplexor (BWDM) 1:181–183, 1:182F
bandwidth 1:135–136, 1:351–352
  bandwidth-limited frontends 4:261–263
  requirements 4:230
bare fiber connectors with direct alignment of 1:338
Bargmann transform 4:203
Bargmann's discrete representation series 4:203
barium nitrate 2:266
barium titanate ($BaTiO_3$) 4:96, 4:324
barium vapor laser 2:368–369
barrel distortion 1:120–121, 1:121F
basal cell carcinoma (BCC) 3:114, 5:162
baseband units (BBU) 1:280–281
basic fibroblast growth factors (bFGF) 3:118–119
BBU Hotels (BBUH) 1:280–281
beam coherence
  analysis 4:177
  state 4:176
beam divergence 4:358
beam intensity distribution 4:175
beam propagation method 1:197
beam pump-probe techniques 2:82
beam quality 2:407, 4:356–358
beam scanning confocal configuration 5:194
beam splitter (BS) 1:376, 4:181, 4:500, 4:507, 4:523
  gratings 1:57F, 1:58F, 1:59, 1:60F
beamsplitters 3:242
Beer's law 4:351–352, 4:352
Bell basis 1:482
bend insensitive fibers 1:195
bending lens 1:114–116, 1:116F
Benton's technique 4:104
benzalkonium chloride-ethylenediaminetetraacetic acid (BKC-EDTA) 5:148
benzene 5:221, 5:223F
benzocyclobutene derivative (BCB) 5:230–231
benzophenone (BP) 2:6–7
Berliner Elektronenspeicherring-Gesellschaft für Synchrotronstrahlung (BESY) 1:405
Bertrand lens 5:187
beryllia (BeO) 2:379, 2:381
Bessel functions 5:16
best spectacle-corrected visual acuity (BCVA) 5:133
beta-barium borate (BBO) 1:177, 1:479, 4:366
β-barium borate crystal (β-BBO crystal) 1:412, 1:413–414, 2:166, 2:296, 2:296F, 2:299F
bi-stable switches 1:214
bias-dependent collection efficiency of primary photocarriers by junction 4:423–425
bicontinuous interpenetrating active layer morphology 5:261
bidirectional reflectance distribution function (BRDF) 3:73–74, 3:74F, 4:477
biexcitons 2:97, 2:195–196
bifocal spectacles 5:120
bifunctional crystals 2:399
  up-conversion lasers based on 2:403–404
    self-frequency doubling laser 2:404, 2:404F, 2:405T
    self-sum frequency mixing laser 2:404–405, 2:405F, 2:405T
bilayer heterojunction 5:259–260
bilayer polymer/acceptor structure 5:259
bilayer-type organic photodiodes 5:321–322
bilinear operation 4:199
bilirubinometer 3:92
binary grating 1:51F, 1:52
binary modulation (OOK) 1:277
binary phase shift key (BPSK) 1:292
binocular
  adaptive optics vision simulator 5:120
  approaches to presbyopia correction 5:125
  disparity 3:208
  parallax 3:44–45, 3:45
  summation 5:125
  vision 5:44
  visual functions 5:125
biological tissues 3:95, 3:219, 3:219F
biomedical applications 3:224
  of Raman lasers 2:269
biometric parameters of lens 5:47
biophotonics 5:39
biosensing, optical techniques for 3:95
biperiodic grating 1:52, 1:53F, 1:59
bipolarons 5:223
birefringent/birefringence 1:33, 1:141–142, 5:192
  diffraction 1:133
  materials 1:150–151
  modulator functions 1:146–147
  in PCF 1:179–180
  scanners 1:136–137, 1:137F
bis(2-oxoindolin-3-ylidene)-benzodifuran-dione (BIBDF) 5:326–327, 5:326F
bispectrum algorithms 3:275–276
bistability 3:79
bistable LCDs 3:2
bit interleaved OTDM 4:35–36, 4:36F
bit interleaving *see* bit level
bit level 4:35
bit rate product 4:1, 4:1F
bit-error-rate (BER) 1:248–249, 1:273, 1:276, 1:291, 1:299, 1:364, 1:366F, 4:31–33, 4:428
  OTDM 4:45–47
  performance 4:46–47
bit-interleaving process 4:61
black box approach 4:321
black box imager 3:157
black box optical regeneration (BBOR) 1:370

black dye 5:276–277, 5:276F
blazed gratings 1:75–76, 1:78–79, 1:79F
bleaching process 4:89, 4:89F
blending materials 5:311
blind deconvolution techniques 3:276–277
blind spot 3:17
Bloch equations 2:83
Bloch oscillations 2:36
Bloch states 2:87
Bloch vector approach 2:249
Bloch waves 1:170
Bloch–floquet theorem 1:169
blocked impurity band detectors (BIB detectors) 1: 26, 1:426T
blocker 4:233–234
blood flow measurement
  in capillaries 5:65
  in retinal vessels 4:525
blown fiber 1:334–335
blue field entoptic phenomenon 5:65–66
blue InGaN laser diodes 2:271
blue lasers 2:356
blue phases (BPs) 3:10
blue-green dyes 2:345–346
blur strength 5:110
Bohr atom 2:99
Bohr radius 2:41, 2:93
Bohr-like models 2:40
bolometers 1:419
  metal films 1:427
Boltzmann distribution 2:265–266, 2:372
Boltzmann kinetic approach 2:83, 2:84
Boltzmann transport equation (BTE) 2:327, 3:257
bond length alternation (BLA) 5:263
bookkeeping method 4:350
booster amplifier 1:248
Born approximation 2:22–23, 3:137, 3:143
boron 2:271
boron oxide (B_2O_2) 1:28
Bose condensation 1:461
Bose–Einstein condensate (BEC) 4:278, 5:212
Bosonic analysis stresses 1:461
Bosonic operators 2:96–97
bottom-gate back channel etch (BCE) 3:12–13
bound electrons 2:118
bound exciton 2:93
bound-to-continuum designs (BTC designs) 1:382
box geometry 2:56, 2:156
BOXCARS geometry 2:185, 2:185–188, 2:186F
  "phasing" 2DES signal 2:188–189
  pulse-shapers 2:188
  2DES in pump–probe geometry 2:189
Bragg angles 1:133
Bragg cell 4:98
Bragg condition 2:356–357
Bragg configuration 1:139
Bragg diffraction 1:133, 5:207, 5:208F
Bragg fibers 1:263
Bragg grating 5:313–314
Bragg imaging filter 3:267
Bragg pinhole 3:270
Bragg reflection 1:229–230, 1:230F
  condition for 1:230
Bragg reflectors 2:12, 2:466
Bragg regime 4:87
Bragg scattering 1:203, 1:384, 5:207, 5:210, 5:210F
Bragg slit 3:270
Bragg spectroscopy 5:213
Bragg structure 4:266–267
Bragg wavelength 2:455–456
brain derived neurotrophic factor (BDNF) 3:123–124
brain research 3:93–94
branching devices 1:336, 1:339–341
  nonwavelength-selective 1:340–341
  WDM 1:341–342
bremsstrahlung 1:405
Brewster angle 1:153, 1:404
brief-pulse, direct-detect lidar 4:431
bright field microscope 5:192
bright-field imaging 5:198
brightness enhancement film (BEF) 3:28
Brillouin frequency shift 5:148
Brillouin microscopy 5:142, 5:148–149
  applications
    in cornea 5:149–150, 5:149F
    in crystalline lens 5:150–151, 5:150F
  Brillouin modulus and relationship with standard mechanical properties 5:149
  technique 5:148–149, 5:148F
  towarding clinical Brillouin microscopy system 5:151
Brillouin scattering 1:180, 1:259, 3:210, 5:140
Brillouin zone (BZ) 1:170, 1:170, 1:173, 2:36, 2:87
  boundary 1:185
Brillouin-assisted FWM 4:324
broad bandwidth 2:120, 2:121
broad-area striped AlGaN laser diodes 2:275–276
broadband
  chirp stabilization 4:436
  generation 2:299
  light sources 2:178
  resonator spectrometer 1:395–396
  spectroscopic ellipsometer 1:210
  spectroscopy 1:393–395
  THz detection methods 1:414–415
  THz sources 1:403
    accelerated free electrons 1:405
    air-plasma 1:411–412
    nonlinear crystals 1:405–409
    photo-Dember effect 1:404–405
    photo-induced carriers in solid materials 1:403–404
  tunability of laser sources 2:435
Broadband Passive Optical Access Networks (BPONs) 2:73, 2:74, 2:75F, 2:78T, 2:84F
Broadband Remote Access Servers (BRAS) 1:281
Bryngdahl method 4:182–183
buffer gas 2:372
building block 4:17
built-in field in semiconductor 1:404
bulk heterojunction (BHJ) 5:259, 5:260F, 5:303–304
  active materials in polymer solar cells 5:263–265
  ETLs 5:266
  HTLs 5:265–266
  interface and architectural engineering 5:265–266
  inverted OPV device 5:266
  morphology control through process engineering 5:260–261
  polymer solar cell structure 5:260
  SA 5:261–262
  solvent additive 5:262–263
  strategy to improving BHJ device performance 5:260
  tandem OPV devices 5:266–269
  thermal annealing 5:261
bulk materials 2:107–108
  electron states in 2:99–100
bulk saturable absorbers, Q switching with 2:419–421
bulk semiconductors, continuum states in 1:491
bulk SOAs 1:243–244, 1:244F, 1:245, 1:247–248
  MZI logic gates 1:251
Burgess variance theorem 4:428

C

c-axis 2:271
C-band tunable PIC *see* integrated laser Mach-Zehnder modulator PIC (ILMZ PIC)
c-plane 2:271
cable core 1:330
cable cut-off wavelength 1:312
calcite 1:150–151, 1:150F
calcium ion
  lasers 2:373
  recombination lasers 2:372–373
California Verbal Learning Test (CVLT) 3:124
cancer
  diagnostics 3:92–93
  PDT for 3:106–107
    adaptive immunity 3:112–114
    anti-vascular effect 3:111
    cellular mechanisms 3:106–107
    direct destruction of tumors 3:111
    induction of anti-tumor immune response 3:114
    innate immunity 3:111–112
    PS biodistribution 3:109–111
    PS pharmacokinetics 3:108–109
canonical evolution 4:199
canonical Fourier transform 4:202
canonical integral transforms 4:174, 4:200–201, 4:201
canonical partition function 2:111
canonical transformations 4:180, 4:199
  complex extension 4:202–203
cantilever beam 5:190
capacitance–voltage (C–V) 4:420, 4:420F

capacitive coupling 1:474–475
capacitive-feedback transimpedance amplifier (CTIA) 4:429
capillary blood flow
  blue field entoptic phenomenon 5:65–66, 5:66*T*
  erythrocyte imaging
    with AOSLO 5:67–68
    with flood illuminated adaptive optics 5:68–69
  fluorescein angiography 5:66–67
  fluorescently stained leukocytes 5:67
  leukocyte imaging with AOSLO 5:67
  measurement 5:65, 5:65*F*
capital expenditure (CAPEX) 2:74
carbon dioxide (CO_2) 1:217, 2:327, 2:442
carbon dioxide laser 1:234–235, 2:325
  see also metal vapor lasers
  characteristics 2:326
  diffusion cooled laser 2:334
  fast axial flow lasers 2:332–334, 2:332*F*
  fast transverse flow laser 2:334
  laser configuration 2:331
  molecular dynamics 2:326–327
  optical resonator 2:329–331, 2:330*F*
  sealed-off and waveguide lasers 2:331, 2:331*F*, 2:332*F*
  six level model 2:326*F*
  slow axial flow lasers 2:331–332, 2:332*F*
  TEA pressure 2:334
carbon disulfide (CS_2) 5:261–262
carbon materials 5:280
carbon nanotubes (CNT) 2:72–73, 2:308, 5:280
cardinal plane locations 1:105–106, 1:105*F*, 1:107*F*
cardinal points and planes of optical system 1:101–102, 1:102*F*
carotenoids (Car) 2:192
carrier heating (CH) 1:250–251
carrier phase estimation (CPE) 1:278, 1:284
carrier suppressed RZ (CSRZ) 1:294–295, 4:6–7
carrier to envelope phase (CEP) 2:302, 2:302*F*
carrier to frequency offset (CEO) 2:302, 2:302*F*
carrier-envelope-phase (CEP) 2:311, 2:313*F*, 2:314*F*
  stability 2:312–314
carrier-injection modulator 4:220, 4:220*F*
carrier–phonon scattering 2:84
carriers 1:489–490
  density
    coherence control 1:490–491, 1:490*F*
    dependence 2:21–23, 2:22*F*
  injection effect 4:236
  phase compensation and decoding 1:305
Cartesian coordinates 1:162, 5:14
cascade ionization 5:92
cascaded amplifiers 1:273
cascaded multiplication spectrometer 1:391–393, 1:393*F*
cascaded optical amplifiers, noise in 1:273
cascaded Raman generation 2:268
cascaded transformations 4:183–184
cat conjugator 4:324
cataphoresis process 2:374
cathode 5:232
cathode ray tube (CRT) 3:1, 3:2
  color 3:2–3, 3:3*F*
cathodoluminescence microscopy 5:193
Cauchy principal value of integral 4:317–318
causality 4:317–318, 4:320–321
caustic surface 1:114–116
cavity 1:383–384, 1:383*F*, 2:268
  cavity configurations, OPSLs 2:285
  dumping 2:412
  effects 5:302–304, 5:304*F*
    in OLEDs 1:447–448
  experiments 1:455
  lasing 5:313
  length 1:459
    change 2:306
  linewidth equation 2:344
  mode energy 1:460
  quantum electrodynamics 1:479
    effects 1:455
cavity QED 1:451
  cavity experiments 1:455
  confined space
    energy shift in 1:451–452
    modification of spontaneous transition rate in 1:451
  effects in molecular systems
    cavity effects in OLEDs 1:447–448
    modification of molecular spontaneous emission 1:445–446
    molecules in plasmonic resonators 1:446–447
    strong light–matter coupling 1:448–450
  generation of number states (Fock states) of radiation field 1:454–455
  maser operation 1:452–454
  microlasers 1:455–456
    setup of rubidium Rydberg atoms 1:453*F*
  one-atom maser or micromaser characteristics 1:454*F*
  trapping states 1:454, 1:455*F*
CD/DVD pickup head 4:507
CdTe bulk 2:58
cell death 5:91–92
cellular mechanisms of PDT 3:106–107
  and apoptosis 3:107
  and autophagy 3:108
  and necrosis 3:107–108
cellular mosaics 5:86–87
  analysis 5:100
cellulite treatment, PBM for 3:120–121
cemented doublet 1:109, 1:110*F*
cemented Glan–Thompson prism 1:151, 1:151*F*
central nervous system (CNS) 5:64
central offices (COs) 1:280–281, 2:73, 2:82*F*
centrosymmetric crystal 1:142
centrosymmetric materials 1:489–490
cerium (Ce) 4:91
cerium-doped laser host crystals 2:446
cesium (Cs) 2:361–362
cesium lithium borate (CLBO) 2:372
chalcogenide fibers 2:433
chalcogenide glass family 1:210
channel spacing 4:68
channelrhodopsins (ChRs) 3:116
charge carriers transport materials 5:286–287, 5:286*F*
charge collection narrowing (CCN) 5:324–325
charge diffusion 2:7
charge dynamics of dye-sensitized solar cells 2:168
charge neutrality 2:350
charge ordered states (CO states) 2:135
charge oscillations 2:118
charge qubits 1:471–472
charge transfer (CT) 5:223–224, 5:246, 5:257, 5:258
  in OPVs 2:194
  organic chromophores 1:144
charge-coupled device (CCD) 2:168, 3:267, 4:106, 4:110, 4:111, 5:314
  detector 5:189
charge-coupled device/complementary metal-oxide semiconductor imaging technique (CCD/CMOS imaging technique) 4:510
charge-coupled devices (CCDs) 3:86, 3:211–212, 3:214*F*, 4:98, 4:193
charge-generation layer (CGL) 3:67
CHCC process 2:115
Chebyshev functions 5:16
chemical sensing 2:262
chemical vapor deposition (CVD) 1:28–29, 2:260, 2:280, 4:284
Cherenkov radiation 1:409
CHHS process 2:115
$\chi^{(2)}$:$\chi^{(2)}$ cascaded nonlinearity 4:321
Chilla–Martinez method 4:52
chiral-nematic LCs 3:10
chiral-smectic C phase (SmC* phase) 3:10
chirp 1:142, 2:355–356
  modulation 4:499–500
  nonlinearity 4:435–436, 4:435*F*
  rate 4:434–435
chirped fiber Bragg gratings 4:27–28, 4:27*F*
chirped gratings 1:239
chirped mirrors (CMs) 2:314
chirped pulse amplification (CPA) 1:239, 1:239*F*, 2:299, 2:311, 2:324
chirped pulse THz spectrometer 1:393–395, 1:394*F*
chirped RZ (CRZ) 4:6–7, 4:8*F*
chloranil (CA) 2:7–8
chlorine 2:382
chlorobenzene (CB) 5:263
1-chloronaphtalene (CN) 5:263
chlorophyll-sensitized zinc oxide electrode 5:270
cholesteric liquid crystal display (ChLCD) 3:82, 3:84
cholesteric phase 3:10
choroid 5:130
choroidal neovascularization (CNV) 5:164
chromatic aberrations 5:58–59, 5:120
chromatic difference of refraction 5:58

chromatic dispersion (CD) 1:178–179, 1:255, 1:256, 1:294–295, 1:313–316, 1:315*F*, 1:363, 4:2, 4:9, 4:10*F*, 4:20, 4:25
  control 1:238–239
  management
    corrections to linear dispersion maps 4:25–26
    dispersion map 4:24–25, 4:24*F*, 4:24*T*, 4:25*F*
    optical nonlinearities as factors in dispersion compensation 4:22–23
  monitoring 4:31–33, 4:32*F*
  in optical fiber communication systems 4:21–22, 4:21*F*, 4:22*F*, 4:23*F*
  test methods for determination 1:315–316
chromatic microencapsulated EPD 3:80, 3:80*F*
chromatic-dispersion compensation 1:265
chromaticity diagram (CIE 1931) 3:40–41
chromatin condensation 3:107
chromium (Cr) 2:413, 2:442
  doping 2:413
  laser advances 2:440–441, 2:441*T*
  revolution 2:440–441
chromophore cytochrome c oxidase (CCO) 3:123
chromophores 1:144, 3:115
chronic mild stress 3:125
chronocyclic tomography 4:179, 4:180
chronocyclic tomography for optical pulse characterization 4:179
ciliary body 5:130
ciliary neuro-trophic factor (CNTF) 5:82
circle of least confusion 1:114–116
circular aperture 1:93–94
  diffraction from 1:70–72, 1:72*F*
circular error at 90th percentile (CE90) 4:402
circular polarization 3:45
circulators 1:336, 1:343
cladding 1:322
  center 1:322
  diameter 1:322
  of large holes 1:197
  modes 1:229
  noncircularity 1:322
cladding pumped amplifier or laser *see* double-clad amplifier or laser
classical analogue holography 4:106
classical Bohr-like description of electron 2:40
classical electromagnetism 1:458
classical motion equation 2:316–317, 2:318*F*
classical–holography 4:30, 4:109
clinical standard of care 3:91–92
clock
  multiplexing 4:45
  in OTDM 4:44–45
clock data recovery (CDR) 1:278, 4:6
clock recovery (CR) 1:301–302, 1:367, 1:369
closed form MIMO 4:408–412
closed-head injury (CHI) 3:123
closed-loop
  control methods 5:41–42
  learning control methods 5:41
  quantum learning control algorithm 5:35
  techniques 5:39
clothes-integratable-type 3:52
cloud 1:227
  mapping 4:483
CNOT gate 1:484
coarse wavelength division multiplexing (CWDM) 1:255, 4:18, 4:68
coat-debond method 3:57
coating 1:322
code division multiple access techniques (CDMA techniques) 5:6–7
  FPA read-out technique 5:8
Code *vs.* ABCD-linear system analysis 4:214
coexistence 2:78
cognitive performance enhancement, PBM for 3:126–127
coherent anti-Stokes Raman scattering (CARS) 2:244–245, 2:247, 4:315, 4:315*F*, 5:193
coherent anti-stokes Raman spectroscopy *see* coherent anti-Stokes Raman scattering (CARS)
coherent detection 1:295–296, 4:432
  heterodyne detection 1:296–297
  homodyne and intradyne detection 1:297
  phase and polarization diversity receiver 1:298
  phase diversity receiver 1:297–298, 1:298*F*
  principles 1:296
  SE and BER 1:299
  SNR 1:298–299
coherent diffraction radiation (CDR) 1:405
coherent diffractive imaging technique (CDI technique) 3:146
  defocus-based techniques 3:149–150
  Fourier measurement-based techniques 3:146–148, 3:146*F*
  transverse translation-based techniques 3:151–153
coherent edge radiation (CER) 1:405
Coherent Lidar Airborne Shear Sensor (CLASS) 4:457
coherent light 1:374, 3:96
  emission 2:63
  trapping approaches 5:294
coherent light–matter interaction 2:53–56
  double-sided Feynman diagrams 2:54*F*
  heterogeneous ensemble of two-level systems 2:56*F*
  three-level *V*-system and rephasing 2D spectrum 2:55*F*
  time-ordering for three-pulse FWM 2:54*F*
coherent lightwave systems
  coherent detection 1:295–296
  differential detection 1:295
  digital coherent receiver 1:299–300
  optical modulation 1:291–293
coherent mode-locked lasers 4:432
  dual-comb interferometry based distance measurement 4:432–434
  mode-locked laser based multi-wavelength interferometry 4:432
coherent multidimensional spectroscopy
  theory 2:150–151
  double-sided FDs 2:151–152
  Fourier transform spectroscopy 2:151
  theoretical signal origin 2:152–153
coherent population oscillations (CPOs) 1:252–253
coherent ray tracing method (CRT method) 4:123
coherent synchrotron radiation (CSR) 1:405
coherent terahertz sources 2:121–122
  coherent THz radiation 2:118
  free electron THz laser 2:119
  gas THz laser 2:118–119
  optical rectification 2:121
  semiconductor THz laser 2:119–120
  THz PCA 2:120–121
coherent transients 4:264, 4:264–265
  coherent control techniques 4:269
  coherent photocurrents 4:269–270, 4:272*F*
  destructive interference 4:267
  multidimensional Fourier transform spectroscopy 4:275–276
  optical Bloch equations 4:265
  photon echo 4:272–275, 4:275*F*
  quantum beats 4:267–269
  radiative decay 4:266
  semiconductor Bloch equations 4:265–266
  spectral oscillations 4:271–272, 4:274*F*
  superradiance 4:266–267
  transient absorption changes 4:270–271, 4:272*F*, 4:273*F*
coherent transition radiation (CTR) 1:405
coherent/coherence 1:34, 2:192–193, 2:194*F*, 2:198–199, 2:199*T*
  area of radiation 1:35–36
  beam 2:247
  coherent features, Rydberg excitons 2:47–49
  coherent illumination, PSF for 3:263
  correlation-induced spectral changes 1:45–46
  detector 5:190
  dynamics 2:82–83
  effects 4:264
  energy transfer 2:59–61
  excitons 2:37–38
  higher-order coherence 1:48–49
  homogeneity 4:176
  Innova™ ion laser 2:381
  length 1:34
  mathematical description 1:36
    analytical field representation 1:36
    degree of coherence and visibility of interference fringes 1:37
    mutual coherence 1:36–37
    spectral representation of mutual coherence 1:38
    temporal and spatial coherence 1:37–38
  mode decomposition model 3:148
  non-linear optical process 2:164
  optical
    energy 2:336
    signals 3:167
    spectroscopy 2:52
  oscillations 4:272
  parameter 5:187
  photocurrents 4:269–270, 4:272*F*
  polarization sources 2:118
  properties 3:222–223
  radiation 2:118

regime 2:82
self-imaging *see* Talbot effect
spectroscopy 4:264
systems 1:278
time of radiation 1:34
types of fields 1:40–41
cross-spectrally pure fields 1:41–42
perfectly coherent fields 1:41
quasi-monochromatic fields 1:41
types of sources 1:42–43
equivalence theorems 1:45
primary sources 1:42–43
quasi-homogeneous sources 1:44–45, 1:44F
Schell-model sources 1:43–44
secondary sources 1:43
volume 1:36
waves 4:180
coherent/coherence control 1:487, 5:39, 5:40
of carrier density, spin population, and spin current 1:490–491, 1:490F
of electrical current
using single color beams 1:491
using two color beams 1:488–490, 1:489F
experimental setup to measure steady-state voltage 1:489F
of quantum systems 2:54
in semiconductors 1:487–490
techniques 4:269
cold cathode fluorescence lamps (CCFLs) 3:25, 3:27–28
collagen 3:118–119, 5:104–105
collection-mode NSOM 5:190–191, 5:190F
colliding-pulse mode locking (CPM) 2:307–308, 2:337, 2:340
collimator lens (CL) 4:500
collinear devices 1:139
collinear multidimensional THz spectroscopy 2:197–199
collision 1:20–21, 5:40
collision-induced vibrational relaxation 2:328
colloidal self-assembly 1:175
Cologne Database for Molecular Spectroscopy (CDMS) 1:401
color encoding of OCT data 4:506, 4:506F
color filter 3:26
color formation of LCD–spatial and temporal
CMFs and tristimulus 3:17
colors in LCDs 3:17–20
dynamic color breakup 3:21–23
LPD 3:23–24
spatial color synthesis 3:19–20
static color breakup 3:21
stencil-FSC 3:22–23
structure of human eye 3:17
temporal color synthesis 3:20–21
color matching functions (CMFs) 3:17, 3:18F, 3:19F
colorless
directionless ROADMs 1:269
ROADM 4:227
colorless directionless (CD) 4:227
colorless-directionless-contentionless (CDC) 4:227
colossal magnetoresistance (CMR) 2:125
colour 3:71, 4:107
gamut and HDR 3:40–43, 3:42F
holography 4:102, 4:103, 4:103–104
pseudo colour and manipulative artist 4:104–105
red, green, blue 4:103–104
in liquid crystal displays 3:17–20
temperature 3:75–76
triangle 3:76, 3:77F
columnar mesophases 3:10–11
coma 1:116–118, 1:118F, 1:119F
comb function 4:385
commercial Hartmann–Shack aberrometers 4:530–531
commercial iTrace visual function analyzer 4:532–533, 4:532F
commercial OCT instruments for ophthalmology 4:505–506, 4:506F
color encoding of OCT data 4:506, 4:506F
multiple reference OCT for dermoscopy 4:507
OCT in cerebrovascular and cardiovascular research 4:506–507
Commission Internationale de l'Éclairage (CIE) 3:17, 3:71
common-gate amplifier 4:260, 4:260F
communication
components 4:3–6
mechanisms 4:13
OTDM 4:66T
demultiplexing of OTDM signal at receiver 4:63–65
transmission of OTDM signal over fiber 4:63
ultra-short optical pulse sources 4:62–63
commutators 4:199
compensators 1:149, 1:156–159
complementary metal-oxide-semiconductor (CMOS) 1:469, 2:168, 3:86, 4:98, 4:99, 4:106, 4:110, 4:193
cameras 3:267, 4:431
chips 4:140
CMOS-based detectors 1:422–423, 1:424F
process technology 1:419
sensor 4:112
transceiver circuits for optical interconnects
optical interconnects 4:254
receiver circuitry 4:259–261
transmitter circuitry 4:254–255
completeness 4:401
in 3D 4:404–405
complex coherence factor 4:174
complex degree of coherence 1:37
complex DSP algorithm 2:83, 2:83–84
complex field amplitude 4:176–177
complex IV *see* cytochrome C oxidase (Cox)
complex quantities 4:350
complex refractive index profile 4:291
complex-valued distributions 1:458
composite cavities 2:416
microchip lasers 2:416
compound lenses 1:109
compound microscope 5:185
compressed gases 4:322
Compton scattering 4:354
computational imaging 3:136–137, 3:136F, 3:262, 3:278
computed tomography (CT) 3:156, 3:157, 3:192, 3:256, 4:174
computer generated holograma (CGH) 4:31, 4:120–122
see also digital holography
with 64 x64 cells 4:32F
algorithms 4:33–135
from classical hologram to 4:30–131
from diffraction grating to Fourier 4:31–133, 4:31F
digital holography and 4:113–114
error reduction in 4:124
hardware aspects 4:35
ninth-order vortex 4:32F
optical filtering 4:35–136
optical vortices 4:36–137
polarization 4:37, 4:37F, 4:38F
terminology 4:37–138
computer guided treatments 5:138
computer holography 4:30
computer-based algorithms 4:108
computerized corneal topography 5:106
concentric rings 1:197
condensed matter systems 2:213
condenser lens 5:189
condition number 3:158
conducting polymers 5:279–280
conducting substrates 5:273
conduction band (CB) 1:171, 1:467, 2:33–34, 2:115, 2:116F, 4:304
conduction band minimum (CBM) 5:256, 5:286–287
cone-effect 3:202
cones 3:17, 5:43
confined space
energy shift in confined space 1:451–452
modification of spontaneous transition rate in 1:451
confocal AOSLO imaging 5:74–75, 5:74F
confocal arrangement 5:190–191
confocal diaphragms 4:355
confocal fluorescence microscopy 5:198
confocal laser scanning microscopy (CLSM) 5:98
confocal microscopy 3:270, 4:194, 5:97–98, 5:99F, 5:189–190, 5:189F, 5:194, 5:194F
applications of depth discrimination 5:196–198
of cornea 5:99–100, 5:100
in corneal pathologies 5:100–101, 5:101F
fluorescence microscopy 5:198–201
HRT-RCM 5:100, 5:100F
image formation in scanning microscopes 5:194–196
structured illumination to optical sectioning 5:201–202
confocal optical systems 5:195–196
confocal single-photon microscope 5:90
confocal system 5:185
conjugated hydrocarbons 2:345
conjugated plane (CPL) 3:202, 3:203F

conjugated polymer-based solar cells 5:256
  BHJ morphology control through process engineering 5:260–261
  characterization of OSC 5:258–259
  OPV device structures 5:259–260
  principles of OSC 5:256–258
conjugated polymers 5:220, 5:309, 5:309F, 5:310F
conjugated wave 3:205
conjugated π-electron organic materials 1:142
connectors with alignment by means ferrule 1:338
connexin 43 (C × 43) 3:118–119
conservation of momentum 1:133
consolidation lowers capital expenditure (CAPEX) 2:82
constant bit-rate (CBR) 1:287
constant lens index 5:48
constant modulus algorithm (CMA) 1:278, 1:303–304
constructive interference 3:244
constructive quantum wave interferences 5:30
contact hyperfine interaction 1:473–474
contact lenses 5:116–119, 5:118F
  material 5:126–127
contact recording technique 4:103
contentionless, ROADM 4:227
continuity condition 4:183
continuous HIO (CHOI) 3:148
continuous part of phase function 4:187
continuous phase functions 4:182, 4:188
continuous sensing 3:87
continuous variables 1:478
continuous wave (CW) 1:20–21, 1:234–235, 1:249–250, 1:352, 2:119, 2:276–277, 2:283, 2:325–326, 2:334, 2:336, 2:377–378, 2:411, 2:415, 2:440–441, 2:462, 4:108–109, 4:254, 4:257, 4:347, 5:1, 5:41, 5:212
  amplifiers 4:434
  frequency-converted 2:411–412
  lasers 2:447, 2:451, 4:110–111, 4:282, 4:302, 5:91–92
    diode lasers 5:3
    dye lasers 2:337, 2:339–340
  LIDT 4:302
  light 2:82
    radiation 4:496
  metal ion lasers 2:368, 2:373–374
  mode 1:382
  operation 1:454
  phase difference mode 4:497–500
    CW modulated signals 4:497–500
    frequency difference techniques 4:500
  pumped supercontinua 2:431–432
  Raman fiber lasers 2:268
  signal 1:367
  single-frequency 2:411
  source 4:421
continuous-director-rotation mode (CDR mode) 3:10
continuous-time linear amplifier (CTLE) 4:263
continuous-to-discrete transformation in image gathering 3:175
continuous-wave frequency modulation (CWFM) 4:499–500
contrast ratio 3:72
contrast sensitivity 5:120
contrast transfer function (CTF) 3:151, 4:166, 4:403
control field-system cooperativity principle 5:33
control knobs for frequency comb 2:305–306, 2:307F
  cavity length change 2:306
  comb control with intracavity etalon 2:306–307
  locking repetition rate 2:307–308
  repetition rate and group velocity 2:306
control laser technology 5:34
control mechanism 1:471–472, 1:471T
  charge qubits 1:471–472
  spin qubits 1:472–473
control system 3:202
controllers 4:222
controlling polarization of high-order harmonics 2:237
conventional "fundamental" resolution 3:137–138
conventional 1-D DFB gratings 5:314
conventional band (C-band) 1:357
conventional broad-area weakly-guiding single-mode lasers 4:298
conventional cold cathode fluorescence lamps (CCFLs) 3:19–20, 3:20F
conventional dielectric waveguides 1:383
conventional microscope 5:185–186, 5:189
  see also probe microscopes
  Abbe theory of microscope imaging 5:187–188
  depth of focus 5:188
  illumination 5:186–187
  image formation 5:187
  microscope objectives 5:188–189
  resolution 5:185–186, 5:186F
conventional noninterferometric imaging methods 3:241
conventional optical
  imaging 3:262
  transmission systems 1:248–249
conventional semiconductor
  device processing method 2:351
  processing methods 2:351–352
conventional single-frequency ring cavity fiber laser 2:455
conventional single-photon microscope 5:90
conventional wide-field optical microscopes 5:195
convergence 3:34
conversion efficiency (η) 1:250–251
"convex hull" method 4:488
convolution approach, numerical reconstruction by 4:144F, 4:145–146
convolution theorem 3:139–140
cool disk technology 2:381
cooled silicon bolometers 1:427
"Cooper pairs" 2:126
cooperative plasmonic effect 5:298–300
cooperativity principle 5:33–34
coordinate transformations 4:182–183
  Bryngdahl method 4:182–183
  continuity condition 4:183
copper 2:256
  twisted-pair 1:280–281
copper bromide laser (CuBr laser) 2:370
  tube construction 2:370F
copper phthalocyanine (CuPc) 5:259–260, 5:321–322, 5:321F, 5:322
copper vapor lasers (CVLs) 2:369–372, 2:370, 2:371–372
  copper bromide laser tube construction 2:370F
  excitation circuits 2:371F
  moderate peak power of 2:372
  partial energy level scheme for 2:369F
  pumped dye laser system 2:338, 2:339F
  tube construction 2:370F
core concentricity error 1:322
core noncircularity 1:322
core router growth 4:230
core-cladding index difference 1:9
cornea 4:500, 5:44–45, 5:60, 5:130
  anatomical structure 5:97, 5:97F
  confocal imaging 5:100
  confocal microscopy 5:99–100
  innervation after refractive surgery 5:102F
  Langerhans cells 5:101, 5:101F
  laser and light interaction 5:133–134
  multiphoton microscopy 5:99–100
  second harmonic imaging 5:104–105
  two-photon imaging 5:102–103
  two-photon laser scanning microscopy 5:102
corneal biomechanics 5:148
corneal birefringence 4:523
corneal collagen crosslinking 5:126
corneal cross-linking (CXL) 5:106, 5:145
  for corneal infections 5:136–138
  for refractive procedures 5:136
  two-photon imaging 5:105–106
corneal deformation parameters 5:143–144
corneal disease 5:97
corneal endothelium 5:100
corneal refractive ablations 4:533
corneal refractive surgery 5:140
corneal stroma 5:100
corneal tissue 5:142
corneal videokeratography 5:140
corneo-scleral lenses 5:119
Cornu spiral 1:88–89, 1:88F
correlated color temperature (CCT) 3:75
correlated electron materials (CEM) 2:123
  classes 2:124–126
  HF materials 2:129–130
  time-integrated optical spectroscopy 2:130–131
  time-resolved optical spectroscopy 2:132–135
  transition metal oxides 2:124–126
  typical phase diagram for hypothetical CEM 2:123F
correlated electron systems, hidden phases in 2:212–214, 2:213F

correlation 3:249
  coefficient 4:491F, 4:493
correlation-induced spectral changes 1:45–46
  experimental confirmations 1:46
  scaling law 1:45–46
  in Young's interference experiment 1:46
cortex velocity map 4:526, 4:527F
Corvis processing software 5:143
cosmetic applications, PBM for
  for fat reduction and cellulite treatment 3:120–121
  for hair regrowth 3:119–120
  skin rejuvenation 3:118–119, 3:118F
Coulomb attraction 2:93
Coulomb force 1:458–459, 2:40
Coulomb interaction 1:460, 1:461, 2:34, 2:83, 2:394, 2:465, 4:265–266
Coumarin 153 2:345–346
Coumarin 307 2:345–346
Coumarin 503 *see* Coumarin 307
Coumarin 540A *see* Coumarin 153
coumarins 2:345–346
counter electrodes (CE) 5:270, 5:279–280, 5:280F, 5:280T
coupled mode theory (CMT) 1:231–232
coupled wave equations 4:329–330, 4:329F
coupled-cavity electro-optically Q-switched microchip laser 2:419, 2:419F
coupler devices 1:341
couplers 1:339–340
coupling 5:40–41
  light and sound 3:226
  mechanisms 1:475
  optics 3:97–98
course integral holographic display system (CIH system) 4:118–119, 4:119F
course-WDM (CWDM) 4:8
CR-calculus 3:150
Cramer–Rao bound (CRB) 3:137
creatine kinase (CK) 3:126
critical angle 1:124–125
cross dichroic prism (X-prism) 3:33
cross linking of corneal collagen (CXL) 5:131, 5:133, 5:136
cross peaks 2:164, 2:165–166
cross spectrum algorithms *see* Knox–Thompson algorithms
cross-correlation technique 2:19–20
cross-coupling of photons in doped PCs 2:15–18
cross-gain modulation (XGM) 1:249–250, 1:251
cross-linking 5:145–146
cross-phase modulation (CPM) 1:16, 1:19–21, 1:21F, 1:22F, 1:180, 1:181, 1:251, 1:320, 1:321, 1:348, 1:364, 1:367–368, 4:3, 4:20–21, 4:23, 4:34
cross-spectral density 4:174, 4:180
cross-spectrally pure fields 1:41–42, 1:41–42
crossbar fabric 4:234
crossed grating geometry 2:9
crossover resonances 2:230
crosstalk attack 1:272
cryogenically cooled SBDs 1:421–422
crystal(s) 2:265, 4:328–329
  detectors 1:422
  field theory 2:436–437, 2:436F
  flakes 4:286
  lattice 2:102–103
  optic axis 1:138–139
  orientation 1:488
  second harmonic generation in 2:207–209
  SHG in 1:12–16, 1:13F
Crystalens 5:121
crystalline Raman lasers, advancements in 2:266–267
crystalline semiconductors 1:488, 2:33–34
CT-scanners 3:192–193
CT26 3:114
cubic perovskite crystal structure 5:282, 5:282F
cuprous oxide (Cu_2O) 2:40–41, 2:45–46
  basic symmetries 2:46T
  Rydberg excitons 2:41, 2:42F, 2:43F
current lidar metric standards 4:401
  absolute and relative horizontal accuracy 4:402
  absolute and relative vertical accuracy 4:401–402
  density and completeness 4:401
current nanofabrication technology 1:185
current–voltage (I–V) 4:416–417, 4:420, 4:420F
curvature sensing wavefront sensors 3:277–278
cushion layers 1:332
cut-back method 1:309
cut-off wavelength 1:311–312
Cut-off-Shifted single-mode Fibers (CSF) 1:261, 1:262
cutoff-smoothing 2:14
cyanamide 1:390
cyanines 2:344, 2:345F
cyclic adenosine monophosphate levels (cAMP levels) 3:115–116
cyclic boundary conditions 2:99
cyclic prefix (CP) 2:83
cyclic pulsed metal vapor lasers 2:368
cyclooxygenase inhibitor indomethacin 3:111
cyclotron energy 2:96
cyclotron resonance (CR) 2:75
cylinder function 4:385
cylindrical lens 4:175–176
cytochrome C oxidase (Cox) 3:115
Czokhralski method 2:404

D

D-dimensional system 4:199
'd-effective' coefficient 4:350
D-ILA display device 3:37
d-shell electrons 2:436
D_{3h} symmetry point-group 4:284
D_{6h} symmetry point-group 4:284
damage associated molecular patterns (DAMPs) 3:108–109, 3:112
damping rate of relaxation oscillations 4:69
Daniel Palanker Department of Ophthalmology 5:131–132
dark current 4:428
dark fiber 4:31
dark states 4:339–340
dark-field AOSLO 5:76–77, 5:76F
darkroom principle 3:247, 3:247F
data acquisition system (DAS) 5:6–7
data center interconnects, WDM in 1:281–282
data communications 1:226–227
  PIC 4:216
data modulation 4:21
  formats 4:6–7
data multiplexing 4:7–8
data processing algorithm for optoelectronic sensor 3:89–91
  quasi-spectral analysis 3:91
  ratiometric analysis 3:90–91
data quality measures (DQM) 4:403–404
data rate 3:182
data retrieval 4:35
data synchronization in OTDM 4:44–45
data voids 4:401
DBPSK 1:275
"DC apodized" Gaussian profile 1:233
DCI-P3 3:40–41
de Broglie wavelength 2:98–99, 2:99, 5:203
Debye–Sears diffraction 1:131–132
Debye–Sears effect 1:133
decision feedback equalizer (DFE) 4:263
decision flip-flop (DFF) 1:366–367
decoherence 5:40–41
  effects 1:487
decoherence free subspaces (DFS) 1:472
decoherence free subsystems *see* decoherence free subspaces (DFS)
deconvolution from wavefront sensing (DWFS) 3:277–278
deconvolution processing by optical methods 3:251
deep anterior lamellar keratoplasty (DALK) 5:149–150
deep ultraviolet (DUV) 2:446
deep-ridge waveguide 4:246–247, 4:247F
defect-induced damage 4:305–306, 4:306
defects 1:203, 1:214
  case 2:112
  and dislocations 2:103–104
  states 1:488
deflection angle 1:147
defocus-based techniques 3:149–150, 3:149F
  direct-inversion methods 3:151
  iterative algorithms 3:150
  recursive algorithms 3:150–151
degeneracy 2:290, 4:298–299
degenerate four wave mixing spectroscopy (DFWM spectroscopy) 1:349, 2:248
  and phase conjugation 4:313–314
degradation of OLEDs 5:238
degree, ROADM 4:227
degree of coherence 1:37
degree-4 ROADMs 1:269
degrees of freedom (DOF) 2:123
delay 4:53–54
  lines 1:193
delay interferometers (DIs) 1:295
delayed fluorescence (DF) 5:245

delayed match-to-sample memory task (DMS memory task) 3:126
delayed self-heterodyne detection 2:460–461, 2:460*F*
δ-function band shape 2:440
demultiplexers 4:39–41
  M–Z interferometers 4:40–41, 4:40*F*
  Sagnac interferometers 4:41–42
demultiplexing 4:35
  of OTDM signal at receiver 4:63–65, 4:64*F*
dendritic cells (DCs) 3:112, 3:113
Denisyuk's technique 4:103
dense wavelength division multiplexing (DWDM) 1:255, 2:81, 2:391, 4:6, 4:17–18, 4:17, 4:68, 4:221–222
  optical fiber communication systems 1:25
  transceivers 4:68
density 4:401
  density operator formalism 4:180
  phase grating 2:6, 2:7
  of states function 2:90, 2:102–103, 2:103*F*, 2:109
  in 3D 4:404–405
density functional calculations (DFT) 1:144–146, 1:145*F*
density matrix 1:164, 1:478, 2:153, 4:174
  approach 4:339
  formalism 2:56
  operator 4:180
density of modes (DOM) 2:12
density recovery profile algorithm (DRP algorithm) 5:79
dentate gyrus (DG) 3:123–124
Department of Defense (DoD) 5:3
depletion layer 1:404
depletion-mode modulators 4:258
depolarization 4:369
deposition schemes 2:258
depth discrimination applications 5:196–198, 5:197*F*
depth of focus (DOF) 4:34, 5:158, 5:188
depth perception 3:44
derivatives of phase function 4:186
dermoscopy, MR-OCT system for 4:507
Descemet's stripping endothelial keratoplasty (DSEK) 5:149–150
destructive interference 3:244, 4:267
destructive quantum wave interferences 5:30
detected laser power 4:475
detection
  of control action 5:34
  systems 3:98
detector 1:224, 3:187, 3:259
  elements 4:417–418
  sensitivity 1:419
detour phase 4:32
detuning 4:243
deuteroporphyrin (DP) 3:104
DeutschesElektronen Synchrotron (DESY) 1:405
dexter energy transfer 5:237*F*, 5:238
dextrose 1:160
DFB based chirp stabilization, 80 GHz 4:436–438
diabetic macular edema (DME) 5:138
diabetic retinopathy (DR) 5:61
Diabetic Retinopathy Vitrectomy Study Research Group trial 5:134
diabolic point (DP) 4:299
diagonal matrix 3:157, 3:159
diamagnetic term 2:65
diameter measurement 1:32
diamond-like carbon coated emitters (DLC coated emitters) 3:1
diamonds 2:267, 2:271
  Raman lasers 2:267
diatomic molecular systems 5:41
1,4-diazobicyclo[2,2,2] octane (DABCO) 2:347
dichroic absorbers 1:151–153, 1:154
dichroic materials 1:151–153
dichromated gelatin (DCG) 4:90
die-attached material, die-level chip assembled on fabricated board with 3:89
die-level chip assembled on fabricated board with die-attached material 3:89
dielectric
  bands 1:171, 1:185
  breakdown 4:303–304, 4:304
  cavity mirrors 2:415
  composition 4:13–14
  material 1:185
  media 1:346, 1:346*F*
  mirror fibers 1:213
  multi-layer mirrors 2:12
difference frequency generation (DFG) 1:385, 1:406, 2:121–122, 2:166, 2:208, 2:280, 2:291, 2:314
  OPSLs 2:287
different map (DM) 3:148
differential absorption glucose content measurement 4:522, 4:523*F*
differential absorption lidar (DIAL) 4:463, 4:467*F*, 4:469
differential dispersion parameter *see* dispersion slope
differential external quantum efficiency (DEQE) 2:274–275
differential group delay (DGD) 1:256, 1:257*F*, 1:302–303, 1:316, 4:2–3, 4:226
differential mode delay (DMD) 1:313
differential operation mode (DOM) 1:368
differential PSK (DPSK) 1:293
differential quadrature DPSK (DQPSK) 1:293, 1:294
differential quantum efficiency 2:467
differentiation filter 4:35, 4:36*F*
differentiation output 4:35, 4:36*F*
diffracted intensity 2:3
diffracted surface 1:136
diffracting aperture 1:89
diffraction 1:62, 1:65*F*, 3:264–265
  angle 5:205
  calculation of 3D PSF 3:264–265, 3:266*F*
  from circular aperture 1:70–72
  diffraction intensity 3:148
  diffraction-based scanning 3D colour video holographic display 4:119, 4:120*F*
  diffraction-propagation from spherical emitter to spherical receiver 4:157
  effects 1:10–11, 1:131, 3:205–206
  efficiency 1:134–135
  formulae 1:38–39
  Kirchhoff theory 1:62–67
  of light, theory 1:133–134
  limit 3:136–137
    of imaging system 3:264–265, 3:272
  by rectangular aperture 1:69–70
diffraction grating 1:51, 1:75–77, 1:131, 1:341
  applications 1:54–57
    beam splitter gratings 1:57*F*, 1:58*F*, 1:59, 1:60*F*
    diffractive lenses 1:56 , 1:57–59, 1:57*F*
    inductive grid filters 1:59–61, 1:61*F*
    spectroscopic gratings 1:55–57, 1:56*F*
  equations 1:51–52, 1:51*F*, 1:52*F*, 1:53*F*
  fabrication 1:54, 1:55*F*
  to Fourier CGH 4:131–133, 4:131*F*
  in optics 1:74
  theory 1:52–54
diffractive intraocular lens technology 5:120
diffractive lenses 1:56*F*, 1:57–59, 1:57*F*
diffractive multifocals design 5:123
diffractive optic (D.O.) 2:186
diffractive optical elements 4:191
diffuse correlation spectroscopy (DCS) 3:95–96
diffuse reflectance, methods for analyzing 3:89–90
diffuser 3:28
diffusing wave spectroscopy (DWS) 3:96
diffusion
  approximation equation 3:222
  coefficient 3:222
  cooled laser 2:334
  diffusion-cooled slab laser 2:331
  regime 3:221
diffusion equation (DE) 3:257
diffusive density grating 2:4
diffusive photon correlation transport 3:97
difluoro-benzothiadiazole (DFBT) 5:265
digital camera 4:174, 4:178
  display 4:177
digital coherent receiver (DCR) 1:291, 1:299–300, 1:301*F*
  carrier phase compensation and decoding 1:305
  clock recovery 1:301–302
  FO compensation 1:304–305
  group velocity dispersion equalization 1:300–301
  nonlinear impairments 1:305–306
  PMD and PDL equalization and polarization demultiplexing 1:302–304
  sampling 1:299–300
digital elevation models (DEMs) 4:401
digital Fresnel holography 4:140
digital geospatial data (2015) 4:401
digital holographic display
  see also computer generated holograms (CGH)
  and CGH 4:113–114, 4:120–122
  hardware for 4:114
    ADHDDs 4:114–115

bandwidth requirements 4:115–116
PDHDDs 4:114
selected holographic display systems 4:116
holographic display VR/AR 4:124–125
holographic stereogram for 2.5D images 4:122–123
key challenges 4:125–126
light sources 4:120
phase retrieval approach for 2D images 4:121–122
3D images 4:123–124
digital holographic microscopy (DHM) 4:106
digital holography (DH) 1:378, 4:106, 4:139, 4:407
see also computer generated holograms (CGH)
advantages 4:148–149
digital hologram setup 4:141*F*
direct phase reconstruction 4:140–143, 4:142*F*
interferometry
phase reconstruction by 4:146*F*
principle of 4:145*F*
influences of discretization 4:147–148
reconstruction principles 4:143–145
recording 4:106
and reconstruction 4:142*F*
and replay 4:107–109
temporal unwrapping 4:148*F*
digital lensless Fourier holography 4:147, 4:147*F*
digital light processing (DLP) 3:22, 3:75, 4:99
projecting engines 3:2
digital micro-mirror devices (DMDs) 3:32, 3:42–43, 4:99, 4:100*F*, 4:115, 4:120, 4:195–196
digital optical communications 1:293
digital phase-locked loop 4:498–499
digital projector *see* projection display; system
digital recording 4:109
digital scene matching area correlator (DSMAC) 4:450
digital signal processing (DSP) 1:265, 1:278, 1:291, 2:83
digital speckle pattern interferometry (DSPI) 4:140
digital subsea holocameras 4:110–112
appendicularia 4:110*F*
calenoid copepod reconstruction 4:111*F*
eHolocam 4:110*F*
jellyfish larvae reconstruction 4:111*F*
digital terrain models (DTMs) 4:401
digital-signal processing 4:369
digital-to-analog converters (DACs) 1:143, 1:294
diiodohexane (DIH) 5:263
diketopyrrolopyrrole (DPP) 5:265
dilute metals 2:259
dimension combinations 4:470–471
repetitively pulsed hypersonic flow 4:471*F*
velocity and temperature 4:470–471
diode laser locking, saturated absorption spectroscopy for
crossover resonances 2:230
Doppler free spectroscopy 2:229–230
ECDL 2:227–228
experimental setup 2:230, 2:231*F*, 2:232*F*
principles of saturated absorption spectroscopy 2:228–230
diode lasers 2:119, 2:356, 5:3
diode pumped solid state (DPSS) 4:363–364
diodes 1:422, 5:317
diopters 1:110, 5:44, 5:109
dioptric length of eye 5:109
diphenyl ether (DPE) 5:263
dipolar molecules 1:144
dipole-dipole effects 1:467
Dirac delta function 3:151, 4:202, 4:317
direct buried cables 1:333
direct cell-free light-mediated effects on molecules 3:117
direct current (DC) 3:91–92, 4:421
direct detection (DD) 1:248–249, 1:291, 4:474–475
direct digital synthesizer (DDS) 4:436–438, 5:9
direct energy gap material 2:350
direct excitation
and de-excitation 2:327
paths 2:35
direct phase reconstruction in digital holography 4:140–143, 4:142*F*
direct radiative recombination 2:41
direct transitions 2:88
direct transmitted beam 3:207
direct-inversion methods 3:151
direction of polarization 1:162
directionless, ROADM 4:227
directly modulated lasers (DMLs) 4:68–69, 4:247, 4:251–252
large-signal modulation 4:69–70
small-signal modulation 4:69
discharge technologies 2:379
discotic liquid crystals (DLCs) 3:10–11
discrepancy principle 3:189
discrete eigenvalue 5:32
discrete Fourier transform (DFT) 5:2, 5:6*F*
discrete nonlinear Schrödinger equation 4:281
discrete phase distribution 4:144
discrete sampling in digital holography 4:144
discrete states 1:488
discrete systems 1:478
discretization influences in digital holography 4:147–148
discrimination mechanism of SBS-PC 4:322–323
disk mirroring 1:281
disk module 2:409
dislocations 2:464
dismutation 3:101
disordered 1D waveguide lattices 4:280, 4:280*F*
dispersion 1:1, 1:8*F*, 1:18, 1:23–24, 1:25, 1:170, 2:304–305, 2:305*F*, 4:20, 4:25, 5:160, 5:160*F*
characteristic 4:15–16, 4:16*F*
compensation 1:195, 4:24–25, 4:29, 4:63
optical nonlinearities as factors 4:22–23
effect on optical signal 1:1–5
flattened fibers 1:33
map 4:24–25, 4:24*F*, 4:24*T*, 4:25*F*
material group velocity dispersion 1:5–6
monitoring techniques 4:20–21
in PCF 1:178–179
profiles 1:195
relation 2:88
waveguide group velocity dispersion 1:6–9
dispersion compensating fiber (DCF) 1:265, 4:10, 4:25, 4:26–27, 4:26*F*, 4:27*F*, 4:31
dispersion management (DM) 1:23–24, 1:370, 4:24–25
chromatic 4:22–23
chromatic dispersion
monitoring 4:31–33, 4:32*F*
in optical fiber communication systems 4:21–22
and compensation 4:8–11
slope mismatch 4:30–31, 4:31*F*, 4:32*F*
solutions
fixed dispersion compensation 4:26–27
tunable dispersion compensation 4:28
dispersion slope 1:195, 1:315
effects 4:20–21
management 4:20–21
mismatch 4:30–31, 4:31*F*, 4:32*F*
dispersion-compensating gratings 1:265
dispersion-shifted fiber (DSF) 1:9, 1:33, 4:2, 4:2*F*, 4:16, 4:20–21
dispersion-shifted single-mode fibers (DSF) 1:261
dispersive medium 4:179
dispersive tunable oscillator 2:338
displacement error 3:210
display(s) 3:1, 3:70
see also projection display
ambient illumination and reflection 3:72–73
BRDF 3:73–74, 3:74*F*
color 3:71
CRT 3:2–3, 3:3*F*
temperature 3:75–76
triangle 3:76, 3:77*F*
contrast ratio 3:72
CRT 3:2
electroluminescence 3:5
FED 3:4
gloss 3:71
illuminance 3:70–71
inorganic LED Displays 3:5
Lambertian surface 3:74
luminance 3:70
medium 3:53
non-Emissive Displays 3:5–6
OLEDs 3:5, 3:5*F*
optical characteristics 3:70
plasma displays 3:4–5, 3:4*F*
PPI 3:75
radiometric and photometric units 3:70
reflective LCD 3:6–7, 3:6*F*
reflectivity 3:71

display(s) (*continued*)
refresh rate and frame rate 3:77–78
resolution and image sharpness 3:75
response time 3:76–77
techniques 4:506
transflective LCD 3:6*F*, 3:7
uniformity 3:71–72
VFD 3:3–4
viewing angle 3:74–75
viewing cone 3:74–75
dissipative processes 5:204
distance measurement techniques 4:497
CW phase difference mode 4:497–500
optical ranging measurement of cornea of rabbit eye performed in vivo 4:498*F*
pulse mode 4:497
distortion 1:2, 1:119–121
analysis 4:213*F*, 4:215
distortion compensation by phase conjugation 4:331–332
distributed Bragg mirror 2:280, 2:283
distributed Bragg reflector (DBR) 2:280, 3:88, 4:18, 4:68, 4:70, 4:255, 4:293, 4:362, 4:419
lasers 2:454, 2:456–457, 2:466, 4:362, 4:362*F*
resonator 2:356–357, 2:357*F*
PWI 2:388–389, 2:389*F*, 2:390*F*
distributed Bragg reflector laser diodes (DBR-LDs) 2:81–82
distributed feedback (DFB) 1:186, 1:237–238, 1:260, 1:296–297, 1:384, 2:356–357, 2:357*F*, 4:68, 4:70, 4:293, 4:362, 5:313
dye laser 2:337
laser 1:369, 2:454, 2:455–456, 2:466, 4:3, 4:38, 4:436–438, 4:437*F*
cavity 1:233
PWI 2:389–391
solid-state dye lasers 2:337, 2:344
distributed Raman amplification (DRA) 2:83
Distributed Undercompensation (DUCS) 1:265, 1:266*F*
distribution losses 1:354
dither 1:259
DMD™ chip 3:36, 3:36*F*
donor 2:394
mode 1:187
donor–acceptor (D/A) 5:259–260
pair recombination 2:113, 2:113*F*
dopants 1:28
doped fused silica 1:224–225
doped silica fibers 1:195
doped TMD monolayers 2:59–61
doped transport layer 5:234–235, 5:236*F*
doping 2:139, 2:257, 2:412–413, 5:226–227
compensation 2:257
density 2:104
efficiency 2:257
Doppler broadened medium, propagation and wave-mixing in 4:341
Doppler broadening 2:378, 4:267, 4:342, 4:343*F*
Doppler components 5:5
Doppler effect 2:228–229, 4:98, 4:452, 4:528
Doppler free spectroscopy 2:229–230
Doppler lidar 4:450–451
Doppler OCT 5:64
Doppler principle 4:497
Doppler shift 4:344, 4:369, 4:435, 5:64–65
Doppler-free geometries 4:344
Doppler-free medium 4:345
double brightness enhancement film (DBEF) 3:28
double clad fiber 1:201
double convex lens 1:101–102, 1:101*F*, 1:102*F*, 1:103*F*
double heterostructure laser diode 2:462, 2:463*F*
double optical gating (DOG) 2:320
double prism reflectors 1:126
double quantum 2D spectra 2:155, 2:155*F*
double-clad amplifier or laser 4:504
double-grating polychromator approach 4:469
double-heterostructure Fabry–Perot laser 2:465
double-sideband (DSB) 1:429
double-sided Feynman diagrams 2:151–152, 2:153
doubled Nd:YAG laser microchip 4:447
down-conversion 1:479
cross-relaxation 2:395, 2:395*F*
DQPSK 1:275
demodulator 1:295*F*
transmitter structure 1:294*F*
Dragonfly series 2:287–288
drawing tower 1:30, 1:31*F*
Dresden protocol 5:126, 5:131, 5:133
drilling 1:196
drive power density 1:135
Drude relaxation rate (γ) 2:257
Drude–Lorentz model 2:131–132
drum vibration 4:453, 4:455*F*
dry etching 5:293
dry eye 5:126
DSI *see* time division multiplexing (TDM); T3 TDM
DSP satellite 4:488, 4:488*F*
dual coating 1:33
dual polarization (DP) 1:291
IQ transmitter PIC 4:250–251, 4:251*F*
modulation 1:275
transmission 1:293–294
dual-beam double frequency configuration 4:500–502, 4:501*F*
dual-comb approach 4:433–434, 4:433*F*
dual-comb interferometry 4:431
distance measurement 4:432–434
dual-optic IOL designs 5:121–122
dual-stage EDFA 1:273*F*
dual-view liquid crystal display 3:62
dual-wavelength optical polarimeter 4:523, 4:524*F*
duct cables 1:333
Duffendack reactions 2:373
duo-binary 4:6–7
Dyadic Green's function 1:445
dye lasers 2:336, 2:336–337, 4:347
applications 2:348
classes of 2:336*F*
emission characteristics of liquid dye lasers 2:336*T*
future of 2:348–349
laser dye survey 2:344
liquid dye lasers 2:337–338
molecular energy levels 2:337, 2:338*F*
solid-state dye laser oscillators 2:340–342
solid-state laser dye matrices 2:346–347
dye methods 5:64
dye-sensitized solar cells (DSSCs) 2:168, 5:270, 5:271*F*, 5:284–285
charge dynamics 2:168
chemical structures of YD2-o-C8 and Y123 dyes 5:271*F*
constructions 5:273
counter electrodes 5:279–280
electrolytes 5:277–279
photoanode 5:273
future prospects 5:280–281
mechanism and parameters 5:270–273
Nyquist plot for 5:274*F*
dynamic bandwidth report upstream (DBRu) 2:75–76
dynamic gain equalizing filter (DGEF) 1:362
dynamic light scattering (DLS) 3:96
dynamic spectrum analyzer (DSA) 2:459
dynamic(s)
color breakup 3:21–23, 3:21*F*
contrast ratio 3:72
dynamic range, illumination 4:88
of homogeneous catalysts 2:172
irises 3:42
linear optical effects 4:351
LPGs 1:236
optical misalignment 3:197–198
of water 2:176–177
dynamical Bloch oscillations 2:36–37, 2:37*F*
dynamical wavefront aberration 3:197–198, 3:197*F*

E

e-holography 3:46
e-paper 3:56
e-shift
device 3:37, 3:37*F*
by IVC 3:37
early supercontinuum sources 2:424–425
early transition metal lasers 2:435–436
Early Treatment Diabetic Retinopathy Study (ETDRS) 5:134
Earth Observing System (EOS) 1:379
ectasia 5:126, 5:142
edge emitters *see* edge emitting laser diode
edge emitting laser diode 2:350, 2:350*F*
density of states *vs.* energy for conduction and valence bands 2:351*F*
DFB and DBR 2:357*F*
direct current modulation frequency response for 2:355*F*
emission spectra from Fabry–Perot edge emitting laser structure 2:353*F*
energy band diagram for quantum well heterostructure 2:356*F*

energy versus momentum diagram 2:350F
Fabry–Perot resonator 2:352
gain *vs.* emission energy 2:353F
P–I curve for edge emitting laser diode 2:354F
quantum well lasers 2:354
real index guided ridge waveguide diode laser 2:352F
SCH laser 2:352F
semiconductor 2:350
edge spread function (ESF) 4:403
edge-emitting lasers (EELs) 2:466, 4:67
effective index 1:191–192
effective length 1:18
effective mass 2:87, 2:89–90
effective Poisson ratio 1:215–216
effective third-order nonlinearities 4:351
effective-index model 1:178
eHoloCam 4:110F, 4:111, 4:112
eicosanoids 3:111
eigensolutions 1:170
eigenstates 1:458
elastic regime 1:215
elastic strain 1:131
elastography 5:140
electric dipole (ED) 2:207, 2:208
approximation 1:448–449
coupling 1:474–475
electric dipole spin resonance (EDSR) 1:472
electric field (E-field) 1:172, 1:229, 4:335
amplitude 5:182
of emitting fluorophore 5:178
enhancement 5:301
influence of 2:96
poling technique 1:14
electric laser field in time and frequency domain 2:234
electric multipolar expansions 2:212
electrical current, coherence control of 1:488–490, 1:491
electrical dispersion compensation (EDC) 2:79
electrical impedance 3:196
electrical networks 4:317
electrical TDM 4:34, 4:60, 4:61F
electrically addressed SLM (EASLM) 4:116
electrically based time division multiplexing systems 4:34
electrically pumped lasing 5:316
electrically pumped VECSELs (EP-VECSEL) 2:284–285
electro absorption modulator (EAM) 4:3
electro optic effect 1:225–226
electro-absorption (EA) 4:243
electro-absorption modulated lasers (EMLs) 4:247, 4:251–253, 4:252F
electro-absorption modulators (EAM) 1:142, 1:260, 1:261F, 1:367, 4:62, 4:254, 4:256F
transmitters 4:255–257, 4:256F
electro-absorptive modulation 1:142
electro-generated excitons 3:64
electro-kinetic phenomenon 3:79
electro-luminescent display (EL display) 3:1
electro-optic detection (EOD) 2:25
electro-optic modulator (EOM) 1:141–142, 1:156–157, 1:261, 2:306, 4:3, 4:4F
electro-optic(s) (EO) 1:141, 1:141–142, 2:199, 3:232
see also nonlinear optics
design 3:181–182
devices 1:143, 1:146–147, 1:159–160
effect 1:141, 4:235
materials 1:142, 1:144–146, 1:145F, 1:146F, 1:146T
modulator 4:216
receiver 4:446–447
relationships 1:143–144
switching 1:142
technology 2:244
tensor 1:143
electro-wetting display (EWD) 3:80–82, 3:81F, 3:82F
electrochemical capacitance–voltage profiling (ECV profiling) 4:416–417
electrochemical doping 5:226
electrochemical impedance spectroscopy (EIS) 5:270
electrode array direction (EAD) 3:48
electrode structures 1:403
electrode-less discharge 2:382
electrode/organic interface 5:232
electrodynamics 3:257
electroluminescence (EL) 2:105–106, 3:5, 3:66, 5:220, 5:240, 5:315
electrolytes 5:277–279, 5:278F
electromagnetic (EM) 1:212–213, 1:217–218
field 1:451, 1:452, 2:384, 5:203–204
flux 3:229
irradiation 4:264
radiation 1:432, 1:432–433
IR and microwave radiation 5:191
UV radiation and X-rays 5:191, 5:191F
signal generators 1:143
spectrum 2:118, 2:118F
for electrical and optical communications 4:13F
wave 1:148, 2:118, 2:207–208, 3:241, 3:262, 4:13, 4:113, 4:180
interaction 4:310
propagation 1:169, 3:248–249, 3:248F
electromagnetic theory
bloch waves and brillouin zones 1:170
computational techniques 1:172
Maxwell's equations in periodic media 1:169–170
origin of photonic bandgap 1:170–172
photonic-crystal slabs 1:173–175
semi-analytical methods 1:172–173
three-dimensional photonic crystals 1:175
two-dimensional photonic crystals 1:173
electromagnetically induced transparency (EIT) 2:15–18, 2:17, 4:339
enhancement technique 4:344
nonlinear optical processes 4:342–344, 4:343F
nonlinear optics with pair of strong coupling fields 4:344–345
propagation and wave-mixing in Doppler broadened medium 4:344
pulse propagation and nonlinear optics 4:345–346, 4:345F
theoretical treatment of 4:340–342, 4:340F
three-level atomic system 4:339F
electron affinity (EA) 5:256
electron beam induced current (EBIC) 5:193
electron block layer (EBL) 5:232, 5:240
electron bombarded active pixel sensor technology (EBAPS technology) 4:445–446, 4:446F
electron energy
diagram 2:98F, 2:101F, 2:102F
distribution function 2:327F
electron injection layer (EIL) 3:64, 5:232, 5:240
electron phonon relaxation (e-ph relaxation) 2:133, 2:134F
electron spin resonance (ESR) 1:467
electron transfer (ET) 2:6–7
electron transport layer (ETL) 5:232, 5:236F, 5:240, 5:257, 5:266, 5:267F, 5:284–285, 5:286–287
electron transport materials (ETM) 5:287–288, 5:289T
electron-acoustic phonon scattering 2:464–465
electron-injection layer (EIL) 5:247
electron-transport layer (ETL) 5:227, 5:247, 5:247F
electron/hole transporting layers (ETL/HTL) 3:64
electron(s) 2:40, 2:101, 2:207, 2:464, 5:175, 5:185, 5:192
beam lithography 5:204
correlation 4:290
in large cubic sample, properties of 2:100F
microscope 4:105, 5:191–192, 5:191F
spin 1:473–474
wave 4:113
packet 2:239
electron–boson interactions effect 2:110
electron–electron
correlations 2:124
interaction
for electrons in bands 2:110
in traps 2:110–111
scattering 2:102–103
electron–hole systems (e–h systems) 1:451
polarization 2:37
recollisions 2:37–38, 2:38F
scattering 2:84–85
electronic
collimation 3:196
controller 4:224
degree of freedom 5:208
devices 4:97–98
AOM 4:98–99
EPAD 4:98
SLM 4:99
infrared imager 3:232
Kerr effect 4:53–54
recording 4:108
regime 2:119
sensor array 4:106
structures 5:220–223, 5:222F
calculations 4:289–290

electronic (*continued*)
temperature 2:164–465
wave packet 2:37
electronic spectrum analyzer (ESA) 2:458
Electronics Industries Alliance (EIA) 3:70
electron–phonon interactions, control of 1:488
electron–photon interaction 2:90–91
electrophoretic display (EPD) 3:79–80, 3:79*F*
microcup® EPD 3:80
microencapsulated 3:79–80
electrophotographic device 5:227, 5:228*F*
electroplated metal film 1:54
electroplating 1:54, 4:91
electroretinogram 5:87
electrostatic units (esu) 4:350
electrostatics 3:80–81
elementary transient holograms 2:1
ellipsometry 1:149
embossed holograms 4:91, 4:92*F*
emission
band 4:364
linewidth 4:358–359
processes 5:207
spectra 3:217
emission computerized tomography (ECT) 3:195
emission layer (EML) 5:232
emissive displays 3:1, 3:79
emissive layer (EML) 5:240
emissive OLED displays 3:72
emitted sideband radiation 2:38
emiuing layer (EML) 5:240, 5:247
emmetropia 5:51
emmetropization 5:61
empty cavity 1:459
empty-lattice approximation 2:87
emulsion swelling 4:105
enantiotropic LC mesophase 3:8
Encyclopedia 5:169–170
end-to-end WDM transmission 1:260
endlessly single-mode fiber 1:197–198, 1:198*F*
endogenous agents 3:86–87
endogenous fluorophores 5:87
energy
conservation 2:105–106, 2:115–116
conversion 2:350
dissipation rate of dipole 1:445
gap 2:87
law 2:397, 2:398*F*
level diagram 2:101
shift in confined space 1:451–452
transfers 2:394–395, 2:395*F*, 2:400, 2:401*T*
energy vs. momentum diagram (*E–k* diagram) 2:350, 2:350*F*
energy-efficient dynamic bandwidth allocation 2:79–80
energy-efficient processes 2:447
energy-recovered linac (ERL) 1:405
energy-saving techniques 2:79–80
"enhanced permeability and retention" effect (EPR effect) 3:110–111
enhanced specular reflector (ESR) 3:28
entangled state 1:479, 1:479–480
entangled wavefunctions 1:462
entanglement 1:478, 1:478
basic notions 1:478
creating entangled states experimentally 1:479–480
entangled-photon source 1:480*F*
multiqubit states and entanglement 1:478–479
optical entanglement, application of 1:484
polarization entanglement-based quantum cryptography protocol 1:482*T*
quantum key distribution 1:480–482
quantum superdense coding 1:482
quantum teleportation 1:482–484
qubits 1:478
entero-hepatic recycling 3:110
EPI-fluorescence 5:170
epi-illumination 5:187
epitaxial lateral overgrowth method (ELO method) 2:273
epsilon-near-zero (ENZ) 2:263
equi-omnidirectional ranges 1:209
equilibrium 2:103–104
equations 1:215–216
equivalence theorems 1:45
equivalently wavefunctions 1:458
erbium 1:264
erbium ions 1:362, 1:363
erbium-doped fiber (EDF) 1:355, 1:356, 4:38
erbium-doped fiber amplifier (EDFA) 1:19, 1:181–183, 1:182*F*, 1:263, 1:264*F*, 1:291, 1:351, 1:355, 2:83, 4:1, 4:4*F*, 4:5*F*, 4:17, 4:18, 4:35, 4:46, 4:68, 4:419
advanced EDFA functions 1:362–363
components 1:355–356
low-noise design 1:361–362
multiple-stage 1:358–361
single-stage amplifier 1:356–358, 1:358*F*
ergodic process 4:174
error-reduction algorithm (ER algorithm) 3:147
erythrocyte imaging
with AOSLO 5:67–68
with flood illuminated adaptive optics 5:68–69
esthetic applications, PBM for
for fat reduction and cellulite treatment 3:120–121
for hair regrowth 3:119–120
skin rejuvenation 3:118–119, 3:118*F*
etalons 2:340, 5:140
etch stop (ES) 3:13
etch stopper structure (ES structure) 3:12–13
ethylene carbonate (EC) 5:277
ethylenediamine tetra-acetic acid (EDTA) 3:104
European Society of Cataract and Refractive Surgeons (ESCRS) 5:136
europium (Eu) 5:244
eutectic LC mixtures 3:9
evanescent field
coupling technique 1:341
of TIR 5:168
evanescent spectra 3:140–142
evanescent wave coupling 1:340
evolution associated spectra (EAS) 2:192
evolutionary algorithms 5:41
Ewald limiting sphere 3:161
Ewald sphere 3:139, 3:139*F*
of reflection 3:161
ex situ approach 2:321
ex vivo techniques 5:142
exceptional points (EP) 4:291, 4:291–293
sensing at 4:298–300
exchange 1:474
gate 1:469
excimer laser crystallization (ELC) 3:14
excimer lasers 2:358–360, 2:358*F*, 5:135
absorbers in rare gas halide lasers 2:363*T*
decay paths and absorber 2:364*F*
discharge technology 2:365–367
energy and pulse rate for applications and technologies 2:359*F*
excimer wavelengths 2:360*T*
fundamentals 2:360–365
potential energy curves for rare gas halides 2:362*F*
typical formation and quenching reactions and rate coefficients 2:363*T*
typical ground and excited state densities 2:364*T*
variants on magnetic switching circuits 2:366*F*
excitation-induced dephasing (EID) 2:58
excitation(s) 4:289
excitation light, nomenclature with 4:347–349
mechanisms 2:376
properties 2:118
transport 2:7
excited ions 1:201
excited state absorption (ESA) 2:55, 2:435–436, 2:442
excited valley-orbit state 1:474
excited-state emission (ESE) 2:55
exciton lines 2:75
exciton-polaritons 1:445, 2:94
exciton(s) 2:63, 2:93, 5:223–226, 5:225*F*
binding energy 2:94–95
diffusion 5:257
formation 1:461, 5:238
and decay 5:235–237
influence of electric and magnetic fields 2:96
influence of quantum confinement 2:94–96
in magnetic fields
exciton states in magnetic fields 2:63–66
interband magneto-optical absorption 2:68–69
intraexciton magneto-optical absorption 2:73–75
many-body effects of high-density excitons in high magnetic fields 2:77–79
migration process 5:311
optical properties 2:93–94, 2:94*F*
scattering 2:96–97
exciton–exciton annihilation 5:310–311

excitonic
absorption 1:460
Auger effect 2:114–115
electronic structure and dynamics in J-aggregates 2:193–194
molecules 2:97
Mott transition 2:77–78
peak 2:107
resonance 1:459, 4:289
system 1:488
exogenous agents 3:86–87
"expanding Fourier modulus" method 3:148
experimental control of quantum phenomena 5:39
experimental implementation of coherent control 5:39
atomic systems control 5:39–40
closed-loop control methods 5:41–42
time-dependent methods 5:40–41
two-path interference methods 5:41
experimental time window 2:6–7
extended-focus method 5:197
extended-reach PONs (ER-PONs) 2:74, 2:82–83, 2:82*F*
external cavity diode lasers (ECDLs) 2:457
external cavity lasers 1:260, 2:457–458, 2:457*F*
external cavity semiconductor laser (ECSL) 4:362, 4:362–363
external modulators 1:260, 1:260–261
external optical cavity 2:280
external perturbations 1:487
external quantum efficiency (EQE) 1:448, 5:235–237, 5:240, 5:242–243, 5:247, 5:251*F*, 5:254*F*, 5:258, 5:296
external resonator 2:447
external tunability 1:172
external-cavity diode lasers (ECDLs) 2:227, 2:227–228
externally modulated lasers, requirements for 4:70
extinction ratio (ER) 1:261, 4:218, 4:218–219, 4:226
of polarizer 1:149–150
extra-terrestrial THz spectra 1:397
extracellular matrix 3:86–87
extraordinary polarization directions 2:293, 2:293*F*
extraordinary ray 1:150
extrema counting (EC) 1:318
extreme ultraviolet spectral region (XUV spectral region) 2:311
extrinsic detectors 1:418
extrinsic infrared detector arrays 1:426
extrinsic IR photodetectors 1:424
extrinsic semiconductor detectors 1:423–426, 1:425*F*
extrusion 1:196
eye
depth of focus, extending 5:122
diagrams 4:252–253, 4:252*F*
optical limitations for imaging 5:72
optical system 5:108
refractive error 5:116
refractive state 5:111

F

fabrication 1:181–183, 1:210, 1:210*F*, 1:342, 4:217, 4:218*F*
air-clad fibers 1:196
disorder 1:172
of gratings 1:54
strategies 1:175, 1:214
Fabry-Perot laser diode (FP-LD) 2:74, 2:82
Fabry–Perot cavity 1:384, 1:433–434, 1:435
resonator 2:356
storage time 1:437–439
Fabry–Perot etalon 2:386–387, 4:320–321
Fabry–Perot fibers
simulation of opto-mechanical behavior 1:215–216
structure and optical properties 1:214–215, 1:214*F*
Fabry–Perot interferometers (FP interferometers) 4:29, 5:148–149
Fabry–Perot lasers (FP lasers) 2:386–387, 2:387*F*, 4:3
Fabry–Perot resonances 5:293
Fabry–Perot resonator 2:351, 2:352, 2:465
Fabry–Perot spectroscopy 1:99
face-centered cubic lattice (fcc lattices) 1:175
Facility for Advanced Accelerator Experimental Tests (FACET) 1:405
failures integrated in time (FITs) 4:70
fanning 4:324–325
effect 4:332–333
far-field patterns (FFPs) 2:275
far-infrared (FIR) 2:73, 3:229
gas lasers 1:379, 1:379*F*
magnetoabsorption in photoexcited bulk semiconductors 2:73–75
far-infrared lasers *see* terahertz lasers
Faraday compensator (FC) 4:523
Faraday effect 1:159–160
Faraday modulator (FM) 4:523
ranging theory 5:3–6
Faraday/Kerr rotation 2:124
fast axial flow lasers 2:332–334, 2:332*F*
fast Fourier transform (FFT) 4:121–122, 4:432, 5:8
algorithm 1:300–301, 3:151
libraries 4:109
fast learning algorithms 5:34
fast pulsed electric discharge 2:368
Fast Scan Submillimeter Spectroscopic Technique (FASSST) 1:395
fast transverse flow laser 2:334
fat reduction, PBM for 3:120–121
Fe^{2+} laser advances 2:441, 2:441*T*
Federal Emergency Management Agency (FEMA) 4:404
feed-forward equalizers (FFE) 1:265, 1:278
feed-forward mode 1:369–370
feedback algorithm 5:37–38
feedback TIA 4:261, 4:261*F*
femtosecond (fs) 2:124
dye laser cavities 2:340, 2:341*F*
excitation laser 5:39–40
IR lasers 1:234–235
metrology 2:321
optical pulses 1:403
femtosecond laser 1:404, 5:135–136
effects on retina 5:91–92
induced micro incisions 5:120
IRAF reduction 5:93
mechanical damage 5:92
plasma formation 5:92
self-focusing 5:92
photochemical damage 5:92–93
in retinal imaging
artifacts and implementation of TPE fluorescence ophthalmoscopy 5:89–91
fluorophores 5:85*F*
multiphoton retinal imaging theory 5:87–89
in vivo multiphoton retinal imaging with adaptive optics 5:86–87
thermal damage 5:91–92
femtosecond laser-assisted LASIK (FS-LASIK) 5:135
femtosecond pulses 2:19–20, 2:233, 4:497, 4:497*F*, 5:39–40
attosecond spectroscopy with attoclock 2:240
recollision spectroscopy 2:239–240
pumped supercontinua 2:428–429
femtosecond-assisted cataract surgery (FLACS) 5:134
Fenna–Matthews–Olson (FMO) 2:191–192
Fermat's principle 1:96, 3:262
Fermi edge singularity 2:204–205
Fermi energy 2:103–104
Fermi functions 2:351
Fermi occupancy function 2:350–351
Fermi's Golden Rule 1:491
Fermi–Dirac statistics 2:102–103
Fermionic features 1:461
Fermions 1:460
ferroelectric LCOSs 4:115
ferroelectric materials (FE materials) 1:14, 2:128
ferroelectricity 2:123
ferroelectrics 2:128
ferrotoroidal order in $LiCoPO_4$ 2:214–216, 2:214*F*, 2:215*F*, 2:216*F*
ferrule 1:338
Feussner prism 1:151
few cycle THz spectroscopy
see also terahertz lasers
of QC heterostructures 2:25–31, 2:26*F*
amplification factor 2:31*F*
dispersion in THz broadband QCL 2:30*F*
dynamics of gain and THz pulse train formation 2:28*F*
field of THz pulse 2:30*F*
gain switching 2:27*F*
modeling time response of THz QC heterostructure 2:29*F*
of semiconductor quantum structures 2:19–21
carrier density dependence 2:21–23, 2:22*F*
linear response 2:19–21, 2:20*F*
nonlinear response 2:23–25, 2:23*F*

few cycle THz spectroscopy (*continued*)
few-cycle lasers 2:311–312
  carrier-envelope-phase stability 2:312–314
  hollow-core fiber compression 2:311–312
  OPA and OPCPA technology 2:314
  pulse 2:237
  pulse synthesis 2:314–316
  ultrashort pulse characterization 2:316
Few-Mode Fibers (FMF) 1:262
Feynman diagrams (FDs) 2:54–55, 2:151
  double-sided 2:151–152, 2:153
Feynman path integral 5:217–218
fiber 4:14–15
  coating 1:32–33, 1:221–222
  communications 4:14
  configuration 2:445
  cut-off wavelength 1:312
  diameter 1:32
  during draw 1:211
  drawing 1:30, 1:196–197, 1:211
  lasers 2:455, 4:347
  loss 1:27
  material dispersion 4:1–2
  nonlinearities 4:3, 4:4*F*
  point-to-point 1:280–281
  preform 1:218
  proof stressing 1:326
  property requirements 1:210
  sensors 1:237
  types 1:33
fiber array measurements 1:213
fiber Bragg grating (FBG) 1:230–231, 1:237*F*, 1:238–239, 1:238*F*, 1:265, 1:267, 1:267*F*, 1:341, 1:342*F*, 2:265, 2:268, 2:457, 4:11, 4:27
  mirrors 2:269
  transmission characteristic 1:342, 1:343*F*
fiber cable 1:221–222
fiber channel (FC) 1:282, 1:287
fiber characteristics measurement 1:308
  environmental characteristics 1:326
    hydrogen aging for low-water-peak single-mode fiber 1:326
    nuclear gamma irradiation 1:326–327
  fiber dimension characteristics and tests methods 1:322
    effective area 1:325–326
    fiber geometry characteristics 1:322
    mode field diameter 1:325
    NA 1:324–325
  fiber optical characteristics and tests methods 1:308–309
    attenuation 1:308–309
    chromatic dispersion 1:313–316
    cut-off wavelength 1:311–312
    DMD for multimode fibers 1:313
    macrobending sensitivity 1:311
    microbending sensitivity 1:311
    multimode fiber bandwidth for multimode fibers 1:312–313
    nonlinear effects 1:320–321
    PMD 1:316–318
    polarization crosstalk 1:318–320
  mechanical measurement and test methods 1:326
    proof stressing 1:326
    residual stress 1:326
    stress corrosion susceptibility 1:326
fiber delay lines (FDL) 4:36
fiber distributed feedback (DFB) 1:240
fiber geometry characteristics 1:322
  cladding 1:322
  coating 1:322
  core center 1:322
  measurement of fiber geometrical attributes 1:322–323
    mechanical diameter 1:324
    refracted near-field technique 1:323
    side-view technique/transverse interference 1:323
    TNF image technique 1:323–324
    transmitted near-field technique 1:323
fiber gratings 1:229, 4:29
  fabrication
    grating inscription 1:236
    photosensitivity 1:234–236
  nonlinear applications 1:239–240
  spectra 1:232–233, 1:232*F*
  stabilized diode lasers and fiber lasers 1:237–238
  theory 1:229–234
fiber optics 1:221–223, 1:221*F*
  communication systems 4:13–14
  reliability of lasers in 4:70–71
fiber polarization controller (FPC) 1:181–183, 1:182*F*
fiber Raman amplifiers (FRA) 1:19, 1:263, 1:264
fiber Raman lasers 2:265, 2:269
  advancements in 2:268–269
fiber under test (FUT) 1:309
fiber-based amplifier 2:324
fiber-based DCS measurements 3:98–99
fiber-coupled 266-nm frequency-quadrupled passively Q-switched microchip laser 2:422*F*
fiber-coupled diode lasers 2:416–417
Fiber-To-The-Home networks (FTTH networks) 1:227, 1:252
Fiber-To-The-X networks 2:73
fiberoptic telecommunications systems 2:356
fidelity 3:182–183
field 4:310–311
  control layer 4:416–417
  effect 5:227–229
  emission 5:233
  evolution dynamics 4:291–292
  fielded systems 4:16–17
  model 4:176
  phases aberration 3:278
field effect transistors (FETs) 1:419, 1:422–423, 1:424*F*
  detectors 1:420
field emissive display (FED) 3:1, 3:4, 3:4*F*
Field Imaging Far-Infrared Line Spectrometer (FIFI-LS) 1:425
field of view (FOV) 3:51, 3:152, 3:214, 3:216, 4:125, 4:475, 5:8
field sequential color (FSC) 3:20
field sequential color LCDs (FSC-LCDs) 3:20–21
field-effect transistors 5:317
Fienup algorithm 4:122
Fienup with don't-care method (Fidoc method) 4:122
fifth harmonic generation (5HG) 2:446–447
Figures of Merit (FoM) 1:286
filamentation 1:411
fill factor (FF) 4:147–148, 5:258, 5:270, 5:272
filling compounds 1:332
film casting 5:262
film patterned retarder (FPR) 3:60
filter function 4:486–488
filter polychromator 4:469
filtered back-projection (FBP) 3:194, 4:486–488
filtered back-propagation algorithm 4:177
Filtered Optical Duobinary 1:279
filters 1:336, 1:342
final-state stimulation 1:461
finite difference method 1:197
finite element modeling (FEM) 1:197, 5:142
finite impulse response (FIR) 4:255
  filter 1:300–301
finite schematic eyes 5:48
finite size incoherent radiators 3:244
finite-difference time domain model (FDTD model) 5:301
finite-dimensional quantum systems 5:30–31
Finite-Element-Models (FEM) 5:144
Fhrpic 3:64–65
first-order Bragg transition 5:216
first-order CD methods 3:150
first-order optical system 4:175
fixed analyzer (FA) 1:317, 1:318, 1:319*F*
fixed dispersion compensation 4:26–27
  see also tunable dispersion compensation
  chirped fiber Bragg gratings 4:27–28, 4:27*F*
  DCF 4:26–27, 4:26*F*, 4:27*F*
  HOM dispersion compensation fiber 4:28
fixed frequency shifter 1:140
fixed grid 4:227
flash ladar 4:446, 4:447*F*
flashlamp-pumped dye laser 2:337
flashlamps 2:336
flat panel displays (FPD) 3:2, 3:2*F*
flat photographic transparency 4:102
flat–flat cavity design 2:417
flavin adenine dinucleotide (FAD) 3:86–87
flavins 3:112
flavoproteins 5:86
flex transparent conducting film (Flex-TCF) 3:57
flex-grid 4:227
flexible display
  integrating with clothes 3:52
  integrating with human body 3:52–53
  practical processes for 3:57
flexible E-paper 3:56
flexible electrophoretic displays (EPD) 3:56
flexible liquid crystal display 3:56–57
flexible OLED (FOLED) 3:5, 3:69
flexible organic light emitting diode 3:54–56
flexible substrates 3:53
flexibleTFT 3:53–54, 3:55*F*, 3:55*T*
flexible transparent conductive film 3:57
flood illuminated adaptive optics, erythrocyte imaging with 5:68–69

flow cytometers 4:516
flow cytometry 4:514–516
flow measurement techniques 4:524–525, 4:524*F*
flower power 5:293
flowmetry 5:64–65
fluctuation as dimension 4:469–470
fluctuation vision 4:469–470
fluorescein angiography 5:66–67
fluorescein-5-isothiocyanate (FITC) 3:211
fluorescence 2:248, 4:369, 4:456, 5:241, 5:241*F*
  imaging 3:225–226, 5:85
  lifetime 5:181
  microscopy 5:175, 5:187, 5:192, 5:198–201, 5:198*F*
  multispectral imaging approaches 3:213
  rate 1:446, 1:446*F*
  spectroscopy 4:518
fluorescence correlation spectroscopy (FCS) 5:172
fluorescence lifetime imaging microscopy (FLIM) 5:172, 5:181–182
fluorescent dyes 3:211, 4:516, 5:192
fluorescent molecules 2:249, 5:88
fluorescently stained leukocytes 5:67
fluoresence recovery after photobleaching (FRAP) 5:172
fluorine (F) 1:28, 4:91
fluorine-doped tin oxide (FTO) 5:273
fluorochromes *see* fluorescent dyes
fluorophores 5:85*F*, 5:86–87, 5:169, 5:178
  fluorophore-metal interaction 5:180–181
  radiation 5:181
flux 3:234
flux-doubling model 4:304
"fly-scan" ptychography 3:153
FMCW lidar 4:434–435
focal length 2:329–331
focal plane array (FPA) 1:419, 2:167–168, 3:239, 4:369, 4:372, 4:373*F*, 4:446, 5:1
focal plane array detector (FPAD) 4:98
Fock states 1:454–455, 4:181
FOLIAdarSim sensor model 4:477
folding dynamics, protein structure and 2:173–175
  amyloid proteins 2:174–175
  membrane proteins 2:176
foliage penetration performance characterization 4:404
forced coherent population oscillations (FCPO) 1:252–253
forced swimming test (FST) 3:125
form birefringence 1:179–180
formalism 4:310–311
  properties of nonlinear susceptibilities 4:311
  relation between field and polarization 4:310–311
  wave equation in nonlinear regime 4:311–312
formamidinium ($NH_2CH{=}NH_2^+$) 5:282
Förster energy transfer 5:238
Förster resonance energy transfer (FRET) 5:180–181
forward error correction (FEC) 1:294, 2:77–78
forward looking infrared (FLIRs) 3:229, 3:232
forward problem, PDWI 3:256–258
Foscan 3:103*F*
4 f imaging 2:409
four transmitter and five aperture array 4:411–412, 4:412*F*
four wave mixing (FWM) 1:320, 1:321–322, 1:412, 3:208
four-bucket algorithm 4:509–510, 4:510*F*
four-dimensional imaging (4D imaging) 3:270, 4:526
four-level pulse amplitude modulation (PAM-4) 1:275, 1:277, 2:80, 4:242
four-wave mixing (FWM) 1:10, 1:16, 1:180, 1:250–251, 1:348, 1:348–349, 1:349*F*, 2:82, 2:156, 2:249, 4:3, 4:16, 4:20–21, 4:23–24, 4:24*F*, 4:34, 4:42–44, 4:44*F*, 4:45*F*, 4:64, 4:323, 4:342
  degenerate four-wave mixing and phase conjugation 4:313–314
  example and selected applications 4:312–313
  field 2:53
  formalism 4:310–311
  nondegenerate four-wave mixing 4:314–315
  optical Kerr effect 4:312–313
  spectroscopy 2:53
  third harmonic generation 4:313
4d phase space, extension to 4:209–211
4D-WD projection set 4:177
Fourier CGH 4:34, 4:35*F*
  diffraction grating to 4:31–133, 4:31*F*
  reconstruction setup 4:33*F*
Fourier domain OCT (FD OCT) 5:156
Fourier group 4:200
Fourier measurement-based techniques 3:146–148, 3:146*F*, 3:150
  alternating projection algorithms 3:147–148, 3:147*F*
  partial coherence algorithms 3:148–149
  three-dimensional recovery problems 3:149
Fourier modal method (FMM) 1:52–53, 1:53
Fourier optics 4:174–175, 5:16, 5:187
"Fourier Ping-Ping" 4:34
Fourier plane
  off-axis IPRG 4:374–375
  off-axis PPRG 4:377–378
Fourier projection 3:152
Fourier ptychography (FP) 3:154, 3:155*F*
  mode multiplexing algorithms 3:155
  multi-slice algorithm 3:155
Fourier space 3:137–138
Fourier sum times incident wave-function 5:204–205
Fourier theory 3:162
Fourier transform (FT) 1:69, 1:69–70, 1:318, 2:121, 3:188, 3:245, 3:249, 4:123, 4:164, 4:174–175, 4:182, 4:267, 4:272, 4:317, 4:500
  of aperture function 1:73
  domain 3:176
  methods of optical MDCS 2:53
  spectroscopy 2:151, 4:276
  theory 1:19
  2D spectroscopy 2:184
Fourier transform infrared (FTIR) 1:218, 2:131, 4:433–434
  interferometers 1:391
Fourier Transform Profilometry (FTP) 4:453
Fourier Transform Raman (FTR) 4:355
4K × 2K DMD 3:37
fourth harmonic generation (4HG) 2:446–447
fourth-order correlation function 1:48–49
"fovea centralis" 3:17
Fowler–Nordheim equation 5:233
fractional Fourier transform (FrFT) 4:176, 4:200, 4:201
fractional order Fourier transform 4:157
  see also Hough transform
  diffraction-propagation from spherical emitter to spherical receiver 4:157
  mathematical expression of diffraction through 4:157–158
  working with fractional orders 4:159–160
fractional orders
  Gaussian beams and Gouy phase 4:162
  image formation by lens 4:160–161
  optical resonator stability 4:161–162
  uncoupling variables 4:162–163
  working with 4:159–160
Fractional Talbot effect 4:166
frame rate 3:77–78
Franck–Condon principle 2:439, 5:246
Franz–Keldysh effect 2:96, 4:255–256
Fraunhofer approximation 1:67–69
Fraunhofer diffraction 1:67, 1:67*F*, 1:71*F*, 4:158
  array theorem 1:72–73
  blazed gratings 1:78–79
  diffraction
    from circular aperture 1:70–72
    grating 1:75–77
    by rectangular aperture 1:69–70
  Fourier transform 1:69
  Fraunhofer approximation 1:67–69
  grating spectrometer 1:77–78
  Kirchhoff theory of diffraction 1:62–67
  N rectangular slits 1:73–74
  Young's double slit 1:74–75
free carriers 1:403, 2:19
free electron laser (FEL) 2:119, 2:119*F*
free electron THz laser 2:119
free induction decay (FID) 1:393–395
free radicals 5:131
free space 2:12
  ECDIs 2:457–458
  free-space-based tunable dispersion compensation device 4:29
  optical communications 4:325
  optical switch technologies 4:231
    LCoS WSS 4:231
    piezoelectric moving-fiber optical switch 4:233
    2D-MEMS optical switch 4:232–233

free space (*continued*)
3D-MEMS optical switches 4:231–232
propagation in 4:167
free spectral range (FSR) 1:266, 2:81
free-carrier
plasma 4:67
theory 2:464
free-electron lasers 1:405, 1:405*F*
free-induction decay 4:266
"free" carrier absorption 4:303–304
"free" polaron state 5:258
freeform prism, aberration contributions in 4:214–215
freeform systems, visualizing aberrations in 4:208–209
French curves 1:160
Frenkel exciton 2:93
frequency 4:53–54, 4:180
chirp 1:3–4, 4:38
conversion and amplification 2:421–422
difference techniques 4:500
3D laser microvision 4:502
axial eye length measurement 4:500
dual-beam double frequency configuration 4:500–502
wavelength tuning interferometry 4:500
domain 3:87, 4:179
electric laser field in 2:234
instruments 3:259
measurement method 1:313
method 1:172, 5:147
methods 5:39
frequency-converted continuous wave 2:411–412, 2:412
frequency-dependent refractive index 1:5–6
gating 3:223–225
mode-locked laser as frequency comb generator 2:303
shifter 1:140
tuning 2:417–418
up conversions 2:398
vectors 2:198
frequency counter *see* RF spectrum analyzer
frequency division multiplexing (FDM) 1:428, 4:17
frequency domain equalizer (FDE) 1:300–301
frequency domain phase measurement (FDPM) 4:52
frequency mixing *see* heterodyning
frequency modulation (FM) 1:392–393, 5:1
frequency noise *see* phase noise
frequency offset (FO) 1:297
frequency-doubled argon ion laser 4:366
frequency-doubled krypton ion laser 4:366
frequency-doubled Nd:YAG laser 2:347, 4:111
frequency-resolved optical gating (FROG) 2:189, 2:316, 4:48, 4:52, 4:52–54, 4:53*F*, 4:56*F*
inversion algorithms 4:54–57, 4:55
measurements 4:57
simplified FROG–GRENOUILLE 4:54
trace 4:54
trace errors 4:57
frequency-resolved optical gating 2:36
frequency-shift keying 1:275
frequency-tagging 2:153–154
Fresnel approximation 4:143–145
Fresnel CDI 3:150
Fresnel diffraction 1:85–86, 1:86*F*, 1:376, 4:157, 4:157*F*
circular aperture 1:93–94
Cornu spiral 1:88–89
diffraction-propagation from spherical emitter to spherical receiver 4:157
Fermat's principle 1:96
Fresnel zones 1:89–93
images as in-line holograms 4:171–172
integral 4:371
mathematical expression of diffraction through fractional order Fourier transform 4:157–158
obliquity factor 1:82–87
opaque screen 1:94–95
pattern under coherent illumination 4:165–166
rectangular apertures 1:87–88
working with fractional orders 4:159–160
zone plate 1:95–96
Fresnel effect 1:337
Fresnel hologram 4:34
Fresnel integral 1:84–85, 1:84*F*, 1:90*T*
Fresnel reflection 1:337, 2:371–372
Fresnel transforms 4:175–176, 4:201
Fresnel zone plates (FZP) 1:377, 1:378, 3:251–252, 3:251*F*, 3:252*F*, 4:177
Fresnel zones 1:89–93, 1:90*F*, 1:92*F*, 1:94*F*, 1:96*F*
"Fresnel-type" CGH 4:31
Fresnel–Kirchhoff diffraction formula 1:66
Fresnel–Kirchhoff equation 4:109
Fresnel–Kirchhoff integral 1:67
Friis' formula 1:273
Fringe Field Switching (FFS) 3:60–61
FROG for Complete Reconstruction of Attosecond Bursts (FROG-CRAB) 2:322–323
fructose 1:160
Fubini theorem 4:162
full service access network (FSAN) 2:74, 2:77
full width at half maximum (FWHM) 1:18–19, 1:137–138, 1:188, 1:215, 1:248, 1:266, 2:277, 2:338, 2:459–460, 3:66–67, 4:218, 4:347, 4:363–364, 5:90, 5:156, 5:186
full-colour reflection hologram 4:103
full-response pulse 1:275
full-spectrum fibers 4:15, 4:18
full-width at half height (FWHH) 1:390
fullerene (C_{60}) 5:321–322, 5:321*F*
fully collinear geometry 2:189–190
functional in vivo multiphoton ophthalmoscopy 5:87, 5:87*F*, 5:88*F*
functional near-infrared spectroscopy (fNIRS) 3:94
functional optical polymers 5:309
fundamental linewidth 2:417
fundamental pulse 2:313–314
fundamental wavelength (FW) 2:295
fundus 5:50–51
camera with photoelectronic system 4:520, 4:520*F*
reflectance 5:51
furnaces 1:30–32
fused fiber WDMs 1:356
fusion
splices 1:336
technique 1:340–341

G

GaAlAs diode laser 2:400
Gaboroscopy 4:103
gadolinium scandium gallium garnet (GSGG) 2:436
gain 2:328, 2:410
coefficient 1:351–352, 1:352*F*
dependence 1:264
medium physics 2:464–465
OPSLs gain structure 2:283
saturation 1:352–353, 4:421–422, 4:422*F*
spectrum of Fiber Raman Amplifiers 1:264
gain switched modes (GS modes) 2:440–441
gain-flattening filters (GFFs) 1:358–359, 1:360, 1:361*F*
gain-switch DFB 4:38
gallium (Ga) 2:271
gallium arsenide (GaAs) 1:142, 1:489–490, 2:58, 2:350, 4:502, 4:503*F*
GaAs/AlAs multiple-quantum wells 2:68, 2:69*F*
GaAs/AlGaAs quantum well structures 2:105
quantum well
optical properties of 2:105–107
structures 2:105
Schottky barrier diode 1:422, 1:422*F*
gallium-doped ZnO (GZO) 2:258
gamma reference 3:2, 3:2*F*
GaN lasers 2:271
see also optically pumped semiconductor lasers (OPSLs)
AlGaN-based laser diodes 2:273–277, 2:274*F*, 2:277*F*
GaN-based materials 1:383
group III-nitrides 2:271–273
InGaN-based laser diodes 2:277–279, 2:278*F*
Gardner method 1:301–302
gas
dynamic lasers 2:326
lasers 1:379, 2:337
mixture 2:326
THz laser 2:118–119
gating techniques 2:319–321, 2:320*F*
Gaussian approximation 4:428
Gaussian beams 4:162, 4:348, 4:357
Gaussian constants 1:102–104, 1:105–107
Gaussian distribution 1:2–3, 1:3, 2:55–56, 4:344
Gaussian process regression-based method 3:151
Gaussian pulse 1:3*F*, 1:1–5
Gaussian statistics 4:174

Gaussian units 4:335
Gaussian-distributed random process 4:373
Gaussian-shaped spectrum resolution 5:158
Gd-Sc-Al garnet (GSAG) 2:441–442
$Gd_3Sc_2Ga_3O_{12}$ *see* gadolinium scandium gallium garnet (GSGG)
10GE-PON 2:77–78, 2:78*F*, 2:78*T*
Ge:Ga photoconductors 1:425
Geiger discharge process 3:89
Geiger-mode APD (GMAPD) 4:475
gelatin 4:90
geminate recombination 5:257
general analysis interferometry (GINTY) 1:318
general phase function 4:186
generalized Gauss lens equation 1:105–106
generalized lens 4:175–176
generalized multiple-prism dispersion theory 2:337
generalized nonlinear Schrödinger equation (GNLSE) 1:258, 2:425–426
generalized projections 4:55
  algorithm 4:55
generalized propagation 1:39
generalized Rayleigh criterion 5:187
generalized version of DOG (GDOG) 2:320
generic framing procedure (GFP) 1:287
generic mapping procedure (GMP) 1:288
generic organic LED structure 5:315–316, 5:316*F*
generic phase function 4:186
genetically encoded calcium indicators (GECIs) 5:87
geometric canonical transforms 4:199–200
geometrical laws 3:262
geometrical optics 1:62
  approximation 3:262
  transformations 3:262
Gerchberg-Saxton algorithm (GS algorithm) 3:147, 3:147*F*, 4:122
germania (GeO_2) 1:28
germanium
  intra-valence band lasers 1:380–381, 1:380*F*
  photoconductors 1:425
ghosts 1:54
Gibbs effect 3:191
Gibbs phenomenon 3:184–185
Gigabit Ethernet PON (GE-PON) 2:73, 2:76, 2:78*T*
  auto-discovery 2:76, 2:77*F*
  normal operation 2:76, 2:77*F*
Gigabit PON (GPON) 2:73, 2:74–76, 2:75*F*, 2:78*T*
  downstream GPON packet structure 2:75*F*
  upstream
    frame structure 2:75–76
    GPON packet structure 2:76*F*
glass 1:131, 1:195, 2:369, 3:25, 4:14
  casting of glass powder 1:196
  fiber transmission systems 2:468
  optical fiber preform 1:28
glass-fiber reinforced plastic (G-FRP) 1:331
glassy carbon 5:280
glaucoma 5:110
global energy production 5:256
global positioning system survey (GPS survey) 4:401–402
gloss 3:71
glucose lidars 4:522
  differential absorption glucose content measurement 4:522
  polarization-based glucose content measurement 4:522–523
glue(ing) 1:336, 2:410
Golay cells 1:420
gold (Au) 2:256, 5:296, 5:299*F*
gonioscopy lens 5:140
Gouy phase 4:162
GPON Transmission Control layer (GTC layer) 2:75
graded index fiber (GRIN fiber) 1:223, 1:356
gradient descent methods (GD methods) 3:150
gradient of singular phase function 4:187–188
gradient-rapid-assisted-pulse-echo spectroscopy (GRAPES) 2:190
granularity 4:225
graphene 5:280
graphene oxide (GO) 5:266
grating
  equations 1:51–52, 1:51*F*, 1:52, 1:52*F*, 1:53*F*
  factor 1:74
  grating-dispersion hyperspectral imaging 3:215–216
  inscription 1:236
  lattice vector 5:204–205
  spectra 1:234
  spectrometer 1:77–78, 1:77*F*
  theory 1:52–54
grating eliminated no-nonsense observation of ultrafast incident laser light e-fields (GRENOUILLE) 4:54
grating light valve (GLV) 4:100
gravitational wave detection 1:432
  gravitational wave detection GW150914 1:442–443
  GW150914 1:442–443, 1:442*F*
  interferometer configurations 1:434–437
  noise sources and interferometer sensitivity 1:437–442
gray-scale inversion 3:59
grazing incidence X-ray scattering (GIXS) 5:261
grazing-incidence grating cavities 2:337
green problem 2:411–412
Green's function 1:62–64, 1:63, 1:65, 3:138
Green's theorem 1:63
grey-to-grey (GTG) 3:77
Gross–Pitaevskii equation 4:278
ground sample distance (GSD) 4:401
ground state 5:224–225
ground state bleaching (GSB) 2:55
group conditions 4:199
group delay 1:314
group delay dispersion (GDD) 2:297
group III-nitrides 2:271–273
group index of refraction 1:315
group velocity 2:306
group velocity dispersion (GVD) 1:2, 1:4–5, 1:4*F*, 1:5, 1:5–6, 1:178, 1:179, 1:180, 1:299, 2:28, 2:294, 4:325
  equalization 1:300–301
group velocity mismatch (GVM) 2:294
GTC encapsulation method frames (GEM frames) 2:75
guided rays 1:222–223, 1:222*F*, 1:223
guided wave optics
  active fiber compatible components 1:223–226
  data communications 1:226–227
  fiber optics 1:221–223, 1:221*F*
  telecommunications technology 1:226
guided-wave optical channel 4:13, 4:14

H

Hadamard pattern 4:195–196, 4:197*F*
hair regrowth, PBM for 3:119–120
half-shade devices 1:158–159
half-V shape mode *see* continuous-director-rotation mode (CDR mode)
half-wave plate (HWP) 1:156, 1:479–480, 1:480*F*
half-width, half-maximum (HWHM) 4:347
halide anion 5:282
Hall effect measurements 4:416–417
halo photonics Doppler velocimeter 4:459–461, 4:461*F*
halogen elements 5:283
Hamilton anxiety rating scale (HAM-A) 3:126
Hamilton depression rating scale (HAM-D) 3:126
Hamiltonian(s) 2:96–97
  conservation of Hamiltonian structure 4:199
  function 4:199
  systems 4:199
Hanbury-Brown and Twiss experiment 1:49
handheld holographic video projector 4:122, 4:122*F*
Hanning window function 4:190
Hansen Experimental Physics Laboratory 5:131–132
"hard-knock" permeation 2:176
harmonic
  beams 1:490
  broadening 1:258
  conversion 2:246, 2:447
  emission 2:236, 2:317, 2:318*F*
  functions 1:2
  generation 2:234
  mode-locking EDF laser 4:38
  oscillator 2:161
hartmanngram 4:530
Hartmann–Shack ocular wavefront sensing 4:530–531
  commercial Hartmann–Shack aberrometers 4:530–531
Hartmann–Shack sensor 4:530, 4:530*F*
Hartree atomic units 2:233

harvesting triplet excitons in OLED
  advanced delayed fluorescence 5:214–246
  phosphorescent EL 5:241–244
HDR, color gamut and 3:40–43, 3:42*F*
head mounted display (HMD) 3:46, 3:48, 3:51
health issue–visual fatigue 3:45
hearing problems, PBM for 3:121
heat shock proteins (HSPs) 3:119
heat-assisted magnetic recording (HAMR) 2:262–263
Heaviside step function 4:317–318
heavy atom effect 5:242
heavy Fermion materials (HF materials) 2:129–130
HeCd laser 4:361, 4:366–367
Heidelberg retina tomograph (HRT) 5:99–100
Heidelberg retinal tomograph-Rostock cornea module (HRT-RCM) 5:100, 5:100*F*, 5:102
Heisenberg uncertainty principle 1:458, 1:463–465
helium 2:326
  buffer gas 2:373–374
  cadmium laser 2:373–374, 2:374*F*
helium-neon laser (He-Ne laser) 2:325–326, 4:359–360, 4:359*F*
hellman–feynman expression 1:172–173
Helmholtz equation 1:81
hematoporphyrin derivative (HPD) 3:110
hemoglobin (Hb) 3:91
hepatocyte growth factor (HGF) 3:120
Hermite-Gauss wavefunctions 4:161, 4:202, 4:203
Hermitian matrix 3:157
Herschel condition 5:185
Hessian matrix 3:150
heterodyne(ing) 1:373
  becomes homodyning 1:373*F*
  current 1:374–375
  in demodulation stage 1:374*F*
  detection 1:296–297, 1:374, 1:374*F*, 2:460, 2:460*F*
  holographic recording of point source object 1:376*F*
  optical direction detection 1:375*F*
  optical heterodyne detection 1:375*F*
  optical scanning holography 1:377–378, 1:378*F*
  point-object hologram 1:377, 1:377*F*
  TDFZP 1:378
  of two sinusoidal signals 1:373*F*
heterogeneous integration 4:242
hexacarbonitrile (HAT-CN) 5:233
3HG *see* third harmonic generation imaging (THG imaging)
HgCdTe detectors (MCT detectors) 2:167
HI-CLASS laser system 4:488
hidden order (HO) 2:145
hidden phases
  in correlated electron systems 2:212–214, 2:213*F*
  revealing by SHG-based techniques 2:214–216
    ferrotoroidal order in $LiCoPO_4$ 2:214–216
    magnetic quadrupole order in pseudogap of $YBa_2Cu_3O_y$ 2:220–223
    odd-parity hidden order in Sr_2IrO_4 2:217–220
    parity-broken nematic order in $Cd_2Re_2O_7$ 2:216–217
hidden symmetry of 2D magnetoexcitons 2:78–79
high aperture theory 5:195–196
high bandwidth detector arrays 4:413
high capacity TWDM-PONs 2:80–81
high delta core fiber 1:198–199, 1:199*F*
high delta core microstructure fibers (HDCMF) 1:198
high density lipoprotein (HDL) 3:110
high frequency enhancement in images 5:16
high mobility group box protein 1 (HMGB1) 3:112
high performance computer (HPC) 4:230
  switched interconnect 4:230–231, 4:230*F*
high power
  narrow linewidth CW OPSL sources 2:286
  wavelength tunable, high brightness CW OPSLs 2:285–286
high reflector (HR) 1:237–238
high resolution imaging
  in astronomy 3:253–254
    principles of Stellar interferometry 3:253–254
    two telescopes interferometer of Labeyrie 3:254
    VLTI 3:254–255
  methods 5:93
high resolution range (HRR) 4:483
high resolution range profiles (HRRPs) 4:474
high temperature plasmonics 2:262–263
high temperature poly-silicon (HTPS) 3:33
  HTPS LCD panel 3:33, 3:33*F*
high-bandwidth detectors 4:413
high-capacity transmission 1:363
high-density 2D magnetoexcitons 2:79–81
high-harmonic generation (HHG) 2:33, 2:142, 2:234–235, 2:234, 2:235*F*, 2:311, 2:316–319, 2:317*F*, 2:319*F*, 4:337
  controlling polarization 2:237
  macroscopic phase-matching aspects 2:236–237
  microscopic description 2:234–235
  microscopic quantum many-body theory 2:34
  three-step model 2:235–236
  time-resolved 2:36, 2:36*F*, 2:37*F*
  in two vs. three bands 2:35
high-intensity discharge lamps (HID lamps) 3:32
high-magnification lenses 5:186
high-order harmonics controlling polarization 2:237
high-order modulation 1:293–295
high-order photonic bandgaps 1:218–219
high-order sideband generation (HSG) 2:37–38
high-power channels 1:283–284
high-power lasers 3:199, 3:203
high-powered femtosecond laser systems 4:335
high-precision dual-comb spectroscopy 1:384
high-prf narrow-linewidth dye lasers 2:348
high-Q Fabry–Perot cavities 1:456
high-quality 3D imaging 4:510
high-resolution electronic sensors 4:110
high-resolution transmission molecular absorption database (HITRAN) 1:401
high-resolution underwater holographic imaging
  analogue holographic recording and replay 4:106–107
  digital holographic recording and replay 4:107–109
  digital subsea holocameras 4:110–112
  subsea holography and holocameras 4:109–110
high-speed
  ADC/DAC algorithm 2:83, 2:83–84
  intravascular C7XR optical coherence tomography 4:507, 4:507*F*
  phase and/or amplitude modulation 4:243
high-T_c superconductors (HTSC) 2:125, 2:126
higher-order coherence 1:48–49
  Hanbury-Brown and Twiss experiment 1:49
  Stellar intensity interferometry 1:49
higher-order mode (HOM) 1:28
  dispersion compensation fiber 4:28
higher-order nonlinear effects 1:10
higher-order spectroscopy 2:155–156, 2:249
higher-power argon ion lasers 2:381, 2:381*F*
highest occupied molecular orbital (HOMO) 3:64, 5:221, 5:244, 5:256
highly inclined and laminated optical sheet (HILO) 5:170
highly intense beams 5:39
highly nonlinear fibers (HNL fibers) 1:368
highly reflective (HR) 2:408–409
highly stabilized mode-locked lasers 4:434
Hilbert filter 4:35, 4:36, 4:36*F*
Hilbert setup 4:35, 4:36*F*
Hilbert space of square-integrable wavefunctions 4:200
Ho doping 2:413
hole block layer (HBL) 5:232, 5:240
hole burning 2:229–230, 2:230*F*, 2:231*F*
  experiment 2:167
hole injection layer (HIL) 3:64, 5:232, 5:234*F*, 5:240, 5:247
hole transport materials (HTMs) 5:278–279, 5:287, 5:287*F*
hole-mask colloidal lithography 5:300–301
hole-transport layer (HTL) 5:227, 5:232, 5:235*F*, 5:240, 5:247, 5:251*F*, 5:257, 5:265–266, 5:284–285, 5:286–287
hollow all-dielectric fibers 1:217–218
hollow core fiber 2:269
hollow optical transmission fibers 1:217
hollow-core fiber
  approach 2:311
  compression 2:311–312
hollow-core PCFs 1:263
holmium 2:413

holocameras 4:108–109, 4:109–110
hologram(s) 4:30, 4:103, 4:106, 4:120, 4:151
  amplitude transmittance 4:30
  computer generated 4:113–114
  frames 4:112
  holographic image formation 4:30*F*
  irradiance 4:372–373
  mean number of photoelectrons 4:373
  of object 1:376–377
  photoelectron density 4:373–374
  of point object 4:152
  for three-dimensional object 4:34*F*
  types 4:153–154
holographic interferometry (HI) 4:154–155
holographic optical elements (HOEs) 4:105, 4:113
holographic/holography 1:376, 3:206, 3:223, 4:30, 4:105, 4:106, 4:109, 4:113, 4:139, 4:151
  application 4:154–155
  camera 4:140
  colour recording techniques 4:104
  data storage 4:331
  display systems 4:116, 4:121*F*
  display VR/AR 4:124–125
    holographic 3D display in VR/AR HMD 4:125
    holographic 3D head-mounted display 4:125*F*
    holographic waveguide/lightguide combiner in VR/AR HMD 4:124–125
  imaging 3:168–169, 3:169*F*
  interference patterns 4:113–114
  lithography 1:175
  mechanism of PC 4:323
  perception 4:102
  phase conjugation 3:206–208
  principle 4:113, 4:151–152
  process 3:205–206, 3:206, 3:206*F*
  reconstruction 1:378
  recording 1:376–377
    electronic devices 4:97–98
    holography terminology 4:87–88
    permanent materials 4:89–90
    process in photopolymer 4:90, 4:91*F*
    and reconstruction of 3D scene 4:114*F*
    refreshable materials 4:93
  sensors 4:92–93
  simple mathematical description of 4:152–153
  stereogram for 2.5D images 4:122–123
  techniques 2:1, 4:103–104
  terminology 4:87–88
    illumination dynamic range 4:88
    illumination linearity response 4:88–89
holoscopy 4:103
holovideos 4:106, 4:109
homodyne detection 1:297
homogeneous broadening 2:52, 2:58–59, 2:93, 2:265
homogeneous catalysts, dynamics of 2:172
homogeneous dynamics 2:164–165
homogeneous Helmholtz equation 3:263–264
homogeneous lineshapes interpretation 2:157
homogeneous linewidths measurement 2:160
homogeneous medium 1:207, 4:175
homogeneous tandem solar cell 5:268–269
homogenous spectral lineshapes 2:164
homojunction device 2:462
Hooke's law 1:215–216
hopping process 5:233
horizontal depletion modulator 4:216–217, 4:216*F*
horizontal dipole orientation 5:235–237
"horizontal parallax only" systems (HPO systems) 4:118
horizontal resolution of lidar point cloud 4:403
host–guest system 5:237–238, 5:238*F*
hot carrier
  distribution 2:85
  regime 2:82, 2:84–85
hot electron bolometer (HEB) 1:421–422, 1:428
  superconducting HEB detectors 1:428–430
hot phonons 2:85
Hough transform 4:182, 4:189, 4:190*F*
  see also fractional order Fourier transform
  implicit transformation 4:189
  optical implementation 4:189–190
HSP70 3:112
Hubble Space Telescope (HST) 3:188
human amylin 2:175
  kinetics of amyloid formation by 2:175–176
human eye 5:130
  aberrations 5:55–58
  aperture stop 5:45–46, 5:46*F*
  axes and angles 5:47–48, 5:47*F*
  basic optical structure 5:43–44
  changes with age 5:60
  cornea 5:44–45
  horizontal section of right eye 5:43*F*
  Le Grand four-refracting surface schematic eye 5:44*F*
  lens 5:46–47
  light and eye 5:49–50
  pupils 5:45–46, 5:46*F*
  refractive anomalies 5:51–52
  retinal image quality 5:59–60
  schematic eyes 5:48–49
  structure 3:17, 3:17*F*
human reconstructed skin (HRS) 3:119
  human retina imaging 5:163–166, 5:164*F*, 5:165*F*
human skin imaging 5:162–163
human-in-the-loop (HITL) 3:233
Huntington's disease 2:174–175
Huygens source 1:89
Huygens-Fresnel principle 4:141–143, 4:158, 4:159*F*
Huygens' principle 1:81, 1:82*F*, 4:141
Huygens' wavelets 1:62, 1:92
Huygens–Fresnel integral 1:81
  integral for Fraunhofer diffraction 1:71
hybrid aligned nematic cell (HAN cell) 3:62
hybrid designs 1:382
hybrid EH_{11} mode 2:311–312
hybrid fiber-coaxial (HFC) 1:280–281
hybrid input–output algorithm (HIO algorithm) 3:148
hybrid multiple-prism near-grazing-incidence grating dye laser oscillator (HMPGI grating dye laser oscillator) 2:338, 2:343
hybrid perovskites 5:283
hybrid projection–reflection (HPR) 3:148
hybridizations 1:473–474
hydrogel 5:116–117
hydrogen 2:44–45
  aging for low-water-peak single-mode fiber 1:326
  atom 1:458
  loading 1:235
  model 2:44–45
hydrogen bromide in discharge (Cu HyBrID) 2:370
hydrogen cyanide (HCN) 4:436, 4:437*F*
hydrogen peroxide (H_2O_2) 3:101, 5:131
hydrogenated amorphous silicon (a-Si:H) 3:12–13
  TFT 3:13
  thin film 3:13
2-hydroxyethyl methacrylate (HEMA) 2:347
hyperfine energy level diagrams 2:228, 2:228*F*
hyperfluorescence 3:65
hyperlens 3:145
hypermetropic eye *see* hyperopic eye
hyperopic eye 5:52
hyperspectral imaging techniques 3:211
  acquisition 3:217–218
  field of view 3:214, 3:216
  grating-dispersion hyperspectral imaging 3:215–216
  image parameters 3:211, 3:213–214
  interferometric hyperspectral imaging 3:213–214
  LVF 3:216
  microarray scanning and customized excitation 3:218
  multispectral imaging 3:211–213
  software 3:216–217
  spatial resolution 3:214, 3:216
  spectral resolution 3:214–215, 3:216

I

Ianus *see* Ianus
Ianus Geminus 3:100
ideal coma 1:117–118
ideal TEM_{00} Gaussian 4:357–358
iDesign instrument 4:531
III-nitride-based semiconductors 2:271
III-V semiconductors 2:257
ill-conditioning 3:158
ill-posedness 3:162
illuminance 3:70–71
illumination
  angle scanning-based Fourier ptychography 3:154–155
  illumination-mode NSOM 5:190–191, 5:190*F*

illumination (*continued*)
level 5:45
optics 3:32
IM-DD links, capacity of 1:291
image deblurring *see* image deconvolution
image deconvolution 3:175, 3:179–180, 3:187, 3:192
image filtering 4:332
image formation 5:187
by lens 4:160–161, 4:160*F*
in scanning microscopes 5:194–196, 5:195*F*, 5:196*F*
image gathering 3:175, 3:176–178, 3:177*F*
image intensification 3:232
image magnification 5:189
image plane 4:372
image plane recording geometry (IPRG) 4:369
image processing 5:189
image restoration *see* image deconvolution
image rotator (IR) 4:176
image sensors 3:86
image space 3:158, 3:262
image-based approach 4:123–124
"image-plane" CGH's 4:31
imaging
aberrations 3:167
algorithm, PDWI 3:258–259
through atmosphere 3:200–201, 3:200*F*
in Ballistic regime 3:222–223
biological tissues 3:219*F*
computer-simulated diffraction-limited image
of binary star 3:275*F*
of point source 3:273*F*
computer-simulated long-exposure image
of binary star 3:276*F*
image of point source 3:274*F*
computer-simulated short-exposure image of point source 3:274*F*
development 4:174
using fluorescence light 5:202
Fourier amplitudes of diffraction-limited transfer function 3:275*F*
image gathering 3:176–178
image restoration 3:179–180
information theory in model 3:175–176, 3:175*F*
matrix formulation 3:156–157
measurements 5:6, 5:7*F*
in multiple scattering regime 3:225–226
optical parameters 3:219–221
process 3:136–137
radiance field 3:176
resolution 3:136–137, 3:137
through scattering media 3:219
signal coding 3:178–179
in snake-like regime 3:223–225
systems 3:262
technique 3:272–274, 4:106
between ultrafast light source and detector 3:220*F*
imbedded isolator EDFA designs 1:358, 1:359*F*
"Immediate Early Response" gene X-1 (IEX-1) 3:124
immune stimulation effect of PDT
adaptive immunity 3:112–114
innate immunity 3:111–112
"immune synapse" 3:113
impact avalanche transit time (IMPATT) 2:114
impact ionization process 2:115–116, 4:304, 4:420–421, 4:421*F*
implicit transformation 4:189
impulse function 4:385
impulse response 5:11–12, 5:11*F*
in situ approach 2:321, 2:323
in situ optical tissue diagnostics/laser speckle-based spectroscopy techniques
applications to in vivo tissue sensing 3:98–99
coupling optics 3:97–98
detection systems 3:98
diffusive photon correlation transport 3:97
experimental considerations 3:97
historical overview and background 3:96–97
light sources 3:97
modeling measured intensity correlations 3:98
in situ optical tissue diagnostics/miniaturized optoelectronic sensors
applications 3:91–92
assembly techniques 3:89
brain research 3:93–94
cancer diagnostics 3:92–93
clinical standard of care 3:91–92
data processing algorithm for optoelectronic sensor 3:89–91
die-level chip assembled on fabricated board with die-attached material 3:89
monolithic fabrication of integrated sensor 3:89
optoelectronic components 3:87–88
optoelectronic sensing system 3:86–88, 3:87*F*
small footprint components soldered on conventional PCB 3:89
in vivo
applications to in vivo tissue sensing 3:98–99
functional in vivo multiphoton ophthalmoscopy 5:87, 5:87*F*, 5:88*F*
multiphoton fluorescence ophthalmoscopy 5:93
ophthalmoscopy 5:90
structural in vivo multiphoton ophthalmoscopy 5:86–87
techniques 5:142
in vivo multiphoton retinal imaging with adaptive optics 5:86–87
in-line amplifier 1:248
in-line amplifiers 1:354
in-line holograms, Fresnel diffraction images as 4:171–172
in-line holography 4:151
in-line method 1:320
in-line reference beam hologram (ILH) 4:106, 4:107*F*, 4:109
in-line SOAs 1:249
in-line recording process 4:102
in-phase LO 2:248
in-plane switching LCDs (IPS LCDs) 3:72
in-plane-switching mode (IPS mode) 3:9, 3:59, 3:60–61
(In_2O_3:Sn) *see* tin-doped indium oxide (ITO)
incident photon-to-current conversion efficiency (IPCE) 5:270, 5:272
incident wave 1:66, 1:84–85, 3:142–143
incident wavevector 1:137
incoherence parameter 5:187
incoherent energy transfer 2:59–61
incoherent FM/CW FPA breadboard architecture 5:7–8
incoherent FM/CW ladar architecture 5:1–2, 5:2*F*
advantages 5:2–3
FM ranging theory 5:3–6
ladar block diagram 5:1–2
ladar hardware 5:6
mathematical analysis 5:3–6
incoherent illumination, PSF for 3:263
incoherent image 3:242
incoherent light holograms 3:252–253, 3:253*F*
incoherent relaxation dynamics 2:83–84
incoherent source image 4:168–169
derivation of Zernike-Van Cittert theorem from propagation of AF 4:169
partial coherence properties 4:169
pupil-AF and OTF with defocusing 4:169
pupil-AF as generalization of OTF 4:169
incubation 4:304, 4:304–305, 4:306
index dielectric slab 1:186
index guided laser 2:351–352
index guiding 1:174
index of refraction 1:141
of material medium 1:102–104
of materialsm 4:48
index-guided fibers 1:197–198, 1:263
air-clad fiber 1:200–203
endlessly single-mode fiber 1:197–198, 1:198*F*
high delta core fiber 1:198–199, 1:199*F*
TMF 1:199–200, 1:201*F*
index-weighted direction tangents 4:209–210
indicatrix 1:143, 4:512, 4:513*F*
indirect energy gap material 2:350
indium (In) 2:271
indium aluminum gallium arsenide (InAlGaAs) 4:243
indium antimonide (InSb) 1:392, 3:233
three-pulse 2D THz spectroscopy on 2:203–205, 2:203*F*
indium gallium arsenide phosphide (InGaasP) 1:224–225, 4:243
indium phosphide (InP) 1:142, 4:415–416
active-passive axial waveguide integration 4:243–246
dual polarization IQ transmitter PIC 4:250–251
electro-absorption modulated lasers 4:251–253
functional requirements 4:242–243, 4:243*F*

ILMZ PIC 4:248–249
InP waveguides 4:246–248
integration technologies 4:243–246
low loss InP waveguides 4:248
narrow linewidth high power SG-DBR laser 4:249–250
photonic integrated circuits
photonic integration 4:242
waveguides 4:246–248
indium tin oxide (ITO) 1:447, 2:257, 2:258, 3:26, 3:35, 3:57, 5:227, 5:240–241, 5:247, 5:265, 5:288, 5:295, 5:303–304, 5:304F, 5:315–316
indium zinc oxide (IZO) 5:252
indium–gold (In–Au) 3:89
individual Fourier transforms 4:145–146
indocyanine green (ICG) 5:75–76
induction furnace 1:32
inductive grid filters 1:59–61, 1:61F
inelastic light scattering 4:354
inert buffer gas 2:368
inertial navigation system (INS) 4:450
infectious disease, antimicrobial photodynamic inactivation and PDT for
history of aPDI 3:103
localized infections 3:105F
pathogen classification and PS structure 3:103–105
PDT for infectious disease 3:105–106
rise of antibiotic resistance 3:102–103
virulence 3:105
infectious keratitis 5:100–101
two-photon imaging 5:103–104
inflammation, PBM for 3:118
influenza 3:102–103
role of water in influenza M2 channel 2:176
Information and Communications Technologies (ICT) 1:285
information efficiency 3:180–181
information handling 1:130
information rate 3:180, 3:182, 3:182–183, 3:183–185, 3:183F
information theory 3:137–138, 3:175
data rate 3:182
electro-optical design 3:181–182
figures of merit 3:180
information efficiency 3:180–181
information rate 3:180, 3:182, 3:182–183, 3:183–185
maximum-realizable fidelity 3:181
model of imaging 3:175–176
performance and design trade-offs 3:181–182
theoretical minimum data rate 3:180
throughput SFR 3:182
visual quality 3:183–185
information-entropy 3:182
infrared (IR) 2:124, 2:280, 3:91–92
absorption 1:255
arrays 1:426
bolometers 1:419
light 5:85, 5:86
photon counter 2:396
radiation 3:230, 5:191
spectroscopy 2:184
spectrum 3:229
technology 1:418
wavelengths 1:217–218
Infrared Astronomical Satellite (IRAS) 1:425
infrared autofluorescence (IRAF) 5:93
reduction 5:93
infrared imager(s)
characteristics 3:234–235, 3:235F
performance 3:233–234, 3:234F, 3:235F
types 3:232–233
infrared imaging 3:233T
see also photon density wave imaging (PDWI); planar waveguide lasers (PWL)
infrared imaging 3:233T
characteristics of infrared imagers 3:234–235
history 3:232
infrared imager performance 3:233–234, 3:234F
infrared image–self-emitted energy 3:230F
Johnson's criteria 3:238T
modeling infrared imagers 3:238–239
Moser's data 3:239T
signal/dynamic range limitation in IR bands 3:232T
testing infrared imagers 3:235–237
types of infrared imagers 3:232–233
typical infrared imaging scenario 3:232F
visible and infrared spectra 3:229F
visible image–reflected energy 3:230F
infrared search and track sensor (IRST sensor) 4:447
Infrared Space Observatory (ISO) 1:425
infrared transition metal solid-state lasers
see also microchip lasers; thin disk laser (TDL)
Cr^{2+} revolution 2:440–441
early transition metal lasers 2:435–436
transition metal laser advantages and issues 2:441–442
transition metal spectroscopy 2:436–437
InGaAs linear-mode avalanche photodiodes (InGaAs LM APD) 4:415, 4:424F
device characteristics 4:420–429, 4:425F
etched mesa InGaAs APD pixel 4:418F
InP-and InAlAs-multiplier InGaAs avalanche photodiodes 4:417F
output count distributions 4:426F
room temperature band gap *vs.* crystal lattice parameter 4:416F
structure and manufacturing 4:415–420
InGaAs QW 2:284
InGaN-based laser diodes 2:271, 2:277–279, 2:278F
InGaZnO (IGZO) 3:27
inhomogeneity 2:159, 3:207
inhomogeneous broadening 2:52, 2:58–59, 2:93, 4:342, 4:343F
inhomogeneous dynamics 2:164–165
inhomogeneous Helmholtz equation 3:138
inhomogeneous linewidths 2:160
inhomogeneous spectral lineshapes 2:164
inhomogeneously-broadened systems, 2D spectra interpretation of 2:158–160
measuring homogeneous and inhomogeneous linewidths 2:160
spectral diffusion 2:160, 2:160F
injection diode laser *see* laser diode (LD)
injection laser diodes (ILDs) 1:141–142
innate immunity 3:111–112
inorganic
crystalline materials 1:142
dielectrics 3:15
glasses 2:346
and hybrid hosts 2:347–348
inorganic-based optoelectronics 3:89
inorganic–organic hybrid matrices 2:346
LED Displays 3:5
materials 4:330–331
redox couples 5:277
semiconductors 5:226
solar cells 5:294
input power (IP) 2:327
input saturation power 1:352–353
insertion loss (IL) 4:226
method 1:311
instantaneous frequency 1:3, 1:4F
instantaneous power 4:179
insulated copper conductors 1:332
integral imaging display 3:48
integral theorem of Kirchhoff 1:64
integral transform
complex extension of canonical transforms 4:202–203
exponentials of second-order differential operators 4:202
issues pertaining 4:201–202
metaplectic sign 4:201–202
operators 4:201
integrated circuits (ICs), 4:254
integrated laser Mach-Zehnder modulator PIC (ILMZ PIC) 4:248–249, 4:248F
integrated optical circuit (IOC) 1:141–142
integrated photonic circuitry 1:189–190
integrated plasmonics 2:261–262
integrating-bucket technique 4:509
intense broadband THz generation 1:411
intense pulsed laser (IPL) 3:119
intensified photodiode 4:446
intensity 4:348
autocorrelation 4:49, 4:49F, 4:50F
by axis around image/focal plane 5:22–27, 5:25F, 5:26F
of cross peaks 2:165–166
detector array 3:267
distribution 1:486, 4:164, 4:174
division multiplexing 4:45
intensity-based OCE 5:146
intensity–intensity correlation 1:48–49
of interference 3:245
on neighboring transverse planes 5:27
pattern 1:72, 5:15
reflection coefficients 1:153
transport derivation of intensity equation 4:166
on transverse image/focal plane 5:19–22
intensity and phase modulator (IM/PM) 1:370
intensity modulation (IM) 1:247–248, 1:275, 1:277, 1:291

Intensity Modulation with Direct Detection (IM/DD) 1:275
intensity spectrum of Fresnel diffraction pattern under coherent illumination
  application to simple objects 4:166
  contrast transfer functions 4:166
  derivation of transport of intensity equation 4:166
  general formulation 4:165–166
  partial Talbot effect 4:166–167
inter-aperture
  phase aberrations 4:409
  tip-tilt-piston aberrations 4:411
inter-channel crosstalk 1:271
inter-diffusion process 4:244–245, 4:245*F*
Inter-Division Interface (InDI) 1:287
inter-pulse configuration 2:314
interaction length 1:139
interaction types in OPA 2:293
interband magneto-optical absorption 2:68–69
  carbon nanotubes 2:72–73
  perovskites 2:71
  quantum wells 2:68–69
  quantum wires and dots 2:71–72
  TMDs 2:69–71
interband transitions 2:252
interband tunnelling 1:422
intercellular adhesion molecule 1 (ICAM-1) 3:118–119
interface inversion symmetry 2:246–247
interface-sensitive 2D vibrational spectroscopy 2:177–178
interfacial two-dimensional electron gases (2DEGs) 2:125
interference 1:36–37, 1:62, 1:223
  effects 1:486, 1:486–487, 1:486*F*
  methods 5:41
  microscopes 5:190
  phenomena 1:486
  polarizers 1:153–154
  spectroscopy 1:47–48
interference filter (IF) 2:211
  waveform 5:4, 5:4*F*
interference fringes 5:217–218, 5:218*F*
  visibility 1:37
interferometer 4:233
  configurations 1:434–437
  sensitivity 1:437–442
interferometric "null test" 4:35
interferometric crosstalk 1:271, 1:272
interferometric filter 2:453
interferometric hyperspectral imaging 3:213–214
interferometric imaging 3:241
  see also multiplex imaging
  distance between incoherent sources and two field points 3:242*F*
  image of two interfering wavefronts 3:243*F*
  two telescopes receive radiation from stellar object 3:243*F*
interferometric method 1:318, 4:496, 4:502–504, 5:190
  commercial OCT instruments for ophthalmology 4:505–506
  optical interferometric micro-lidar 4:502–504
  optical low-coherence tomography 4:504
interferometric modulator display (IMOD) 3:82, 3:84
interferometric multi-interferer crosstalk 1:272
interferometric multispectral system 3:213
interferometric optical switch
  Mach-Zehnder interferometer optical switch 4:236
  microring resonator optical switch 4:236
  optical phase shifters 4:236–239
interferometric PALM (iPALM) 5:176
interferometric technique 1:54, 3:146, 4:174
interferometry (INTY) 1:318, 1:318, 1:319*F*, 4:139
interferon gamma (IFN-γ) 3:120
interleavers 1:267
interleukin-1 beta (IL-1β) 3:118–119
intermediate frequency (IF) 5:2
intermodal dispersion *see* modal bandwidth
intermolecular donor–acceptor system 5:246
internal conversion process 2:337
internal quantum efficiency (IQE) 2:278–279, 5:235–237, 5:241, 5:272, 5:303
internal reflection tomography 3:144
internal rotor 1:388–389
International Organization for Standardization (ISO) 3:70
International System of Units (SI unit) 3:70
International Telecommunications Union (ITU) 1:226, 1:387, 2:74, 4:8, 4:15
  ITU-T recommendation G. 694. 1 4:17–18
internet of things (IoT) 3:52
'interrogating' beam 4:325
interstitial doping 2:257
intersubband (IS) 2:92, 2:201
  selection rules for intersub-band optical transitions 2:91–92
intersymbol interference (ISI) 1:275, 1:299, 4:218–219, 4:262–263
intersystem-crossing (ISC) 2:6–7, 3:101, 5:225–226, 5:235–237, 5:237*F*, 5:245
intervalley biexcitons 2:61–62
intra-aperture phase aberrations 4:409
intra-cavity self-Raman lasers 2:266
intra-cavity SHG 2:287
intra-cavity SHG/DFG 2:283
intra-channel crosstalk 1:271
Intra-Division Interface (IaDI) 1:287
intra-pulse schemes 2:314
intraband 2:92
"intracapsular mechanism of accommodation" 5:47
intracavity etalon, comb control with 2:306–307
intracavity Fabry-Perot 2:306–307
intracavity laser-absorption spectroscopy (ICLAS) 2:288
intracavity nonlinear spectroscopy 2:308
intracavity phase interferometry (IPI) 2:308–309, 2:309*F*
intradyne detection 1:278, 1:297
intraexciton magneto-optical absorption 2:73–75
  FIR magnetoabsorption in photoexcited bulk semiconductors 2:73–75
  semiconductor quantum wells
    optical-pump/THz-probe magnetospectroscopy 2:76–77
    optically detected FIR resonance spectroscopy 2:75–76
intraocular lens (IOL) 5:121, 5:126–127
intraocular pressure (IOP) 5:141, 5:143, 5:144
intrastromal corneal ring segments (ICRS) 5:136, 5:140
intrastromal ring segment (ICRS) 5:141
intravital microscopy of rat cremaster muscle 3:111
intrinsic
  anisotropy 2:348–349
  detectors 1:418
  factors 2:406
  laser-induced damage mechanism of wide bandgap dielectrics 4:303
INVAR 3:3
inverse Bremsstrahlung *see* "free" carrier absorption
Inverse FFT (IFFT) 1:300–301
inverse filter 3:188, 3:189*F*
inverse Fourier transform (IFT) 3:139–140, 3:245
inverse matrix 4:200
inverse piezoelectric effect 1:143
inverse problem 3:156, 3:187
  matrix formulation 3:156–157
  PDWI 3:258–259
inverse Radon transform 4:174, 4:176
inverse scattering 1:233, 1:234, 3:161
inverse source 3:137
  problem 3:159–161
inverse synthetic aperture radar imaging (ISAR imaging) 4:474
inversion
  algorithms 3:136–137
  symmetry 2:218
inverted OPV device 5:266
"invisible region" 3:141
Ioffe-Regel condition 4:278
ion
  ion permeation through K^+ ion channel 2:176
  neutralization 2:320
  spectroscopy 2:240–241, 2:242
  structure and dynamics of electrolytes 2:170–172
  traps 1:479
ionic AOS (IAOS) 3:14
ionic liquid 2:171–172
ionization gating (IG) 2:320–321
ionization potential (IP) 5:256
ionized plasma 2:372
iProfiler 4:531, 4:531*F*
IQ Modulator (IQM) 1:292–293
Ir(ppy)$_3$, organometallic-based coordination complex 3:64–65
iridium 5:243
iris 5:130

irradiance-dependent refractive index 4:350–351
ischemic diseases 5:132
is iterative Fourier transform algorithm (IFTA) 4:34, 4:35F
ISO LDT standard 4:307F, 4:308
isolated attosecond pulses 2:237
  attosecond light house 2:238
  phase matching gating 2:238
  spectral selection 2:237
  temporal gating 2:237–238
isolation loss 1:266
isolators 1:336, 1:343
isomorphic relations 4:291, 4:292T
isoplanatic angle 3:202
isothermal regime 2:82, 2:85
isotropic case 1:133
isotropic material 1:131
isotropic media 2:9
iterative algorithms 3:150
iterative inversion algorithms 2:322–323
iterative method 3:191
iterative techniques 4:174
ITO coated polyethylenenaphtalate (ITO/PEN) 5:273
ITO coated polyethyleneterephtalate (ITO/PET) 5:273
ITU-T study group 15 (SG15) 2:78–79

J

J-aggregates, excitonic electronic structure and dynamics in 2:193–194
Jablonski diagram 3:101, 5:98F
Jackson crossed-cylinder 5:109
Jacobi identity 4:199
Jahn–Teller effect (JT effect) 2:126, 2:441
Janus 3:100, 3:100F
  face of photomedicine 3:100
Janus kinase (JAK) 3:100
Jaynes–Cummings model 1:452, 1:460–461
Jet Propulsion Laboratory (JPL) 1:391, 1:392F
JFET amplifiers 1:127
Johnson–Nyquist noise 4:425
joint devices 1:336
joint time-frequency transforms 3:164
Joint-Density-of-States (JDOS) 2:254
Jones calculus 1:161, 1:168
Jones matrix Eigen analysis (JME analysis) 1:317
Jones vector 1:166–168
Josephson-junction-based qubits 1:473
Judd–Ofelt theory 2:397
jumper cable cut-off wavelength 1:312

K

K^+ ion channel, ion permeation through 2:176
Kagomé photonic crystal fibers 2:269
KAGRA, Japanese detector 1:440
Kalman filter 3:151
Kalman filter phase retrieval (KF-PR) 3:151
Kane model 2:88–89
Kapitza–Dirac diffraction 5:214, 5:214F, 5:215F
Kapitza–Dirac scattering 5:213–214
kappa (κ) 5:48
Kepler-type inverse-square law central force problem 2:441–45
keratoconus (KC) 5:100–101, 5:106, 5:118, 5:119F, 5:141
keratomileusis 5:126
Kerr effect 1:141, 1:255, 1:257, 1:258, 1:258F, 1:320, 1:368, 4:64, 5:92
Kerr lens mode-locking 5:41
Kerr nonlinear index 1:320
Kerr nonlinearity 1:239, 4:279–281
Kerr type nonlinearity 4:346
Kerr-lensing 2:412
kinetic energy 1:171
kinetic exchange interaction 1:469
kinetics of amyloid formation by human amylin 2:175–176
Kirchhoff formulation 3:265
Kirchhoff Green's function 1:63
Kirchhoff theory of diffraction 1:62–67, 1:63F
"knock-on" permeation 2:176
Knox–Thompson algorithms 3:275–276
Köhler illumination system 5:187
"Kondo liquid" state 2:129
k.p perturbation theory 2:87–88
k.p theory 2:87, 2:87–88
Kramers–Krönig dispersion relations (KK dispersion relations) 4:317
  'black box' approach 4:321
  causal linear system 4:318F
  implication of causality 4:320–321
  nonlinear absorption coefficient 4:319F
  two-photon absorption coefficient in semiconductors 4:321F
Kramers–Kronig relations 1:5
KrF^* formation kinetics 2:362
Kronecker delta 5:17
krypton ion laser 2:379, 4:361, 4:361T

L

label-free sensing 3:86–87
Labeyrie's method 3:274–275
  two telescopes interferometer 3:254
laboratory molecular spectroscopy 1:390–391
  broadband resonator spectrometer 1:395–396
  chirped pulse THz spectrometer 1:393–395
  detection and cascaded multiplication spectrometer 1:391–393
  FASSST 1:395
  sources 1:390–391
  THz lamb-dip spectroscopy 1:396
LACE satellite 4:488, 4:489F
ladar block diagram 5:1–2
ladar hardware 5:6
  imaging measurements 5:6
  point-target measurements 5:6
ladar impulse response 5:10–11, 5:11F
ladder-type poly[1, 4-phenylene] (MeLPPP) 5:309, 5:309F
Lagrange invariant 4:206
Laguerre-Gauss functions 4:203
Laguerre-Gaussian mode 4:180
"lamb dip" 2:451
lamb shift 1:452
lambda (λ) 5:48
Lambertian surface 3:74
lame's equations 1:215–216
laminated aluminum polyethylene (LAP) 1:331
land targets 4:482–483
LANDSAT satellite program 3:211
Langerhans cells 5:101, 5:101F
Large Binocular Telescope (LBT) 3:192, 3:192F
large mirrors working 3:247–248
large photonic bandgaps for CO_2 laser transmission 1:216–220
large-area (LA) 1:262
large-effective-area fibers (LEAF) 1:262
large-particle optics 4:512
large-signal modulation 4:69–70
laser 1:54, 1:99–100, 1:100, 1:201, 2:384, 2:385, 2:386F, 4:106
  ablation 2:258
  assembly 2:415
  beam 1:140, 1:487, 5:39
    divergence 4:358
    quality 4:356–358
  cavity 1:139, 1:140F, 2:331–332
  ceramics 2:411
  characteristics 4:356–358
  configuration 2:331
  cooled atoms 4:344
  cooling 1:458–459
  detection and ranging 4:444
  diffusion cooled 2:334
  Doppler flowmetry 3:95–96
  Doppler vibrometry 4:528
  dual beam method 4:523–524
  electric field 5:30
  emission linewidth 4:358–359
  fast axial flow 2:332–334, 2:332F
  fast transverse flow 2:334
  invention 1:10, 2:324
  isotope separation 2:372
  laser induced refractive index correction technique 5:126–127
  laser interference lithography 5:293
  laser-induced grating scattering 2:248
  laser-induced interference 1:487, 4:340
  laser-induced photo dissociation 5:39
  laser-pumped pulsed dye lasers 2:337–338
  laser-type amplifier 4:322
  light 3:203, 4:355
  material 4:325
  micro-radar 4:496
  phosphor 3:42
  phosphor illumination projector 3:39–40, 3:40F, 3:41F
  polarization 4:358
  pulses 2:337

laser (*continued*)
safety considerations of two-photon microscopy 5:106–107
scanners 4:483
scanning microscopy 5:99–100
sealed-off and waveguide 2:331, 2:331*F*, 2:332*F*
slow axial flow 2:331–332, 2:332*F*
sources 2:311, 4:222
spectrum 2:302
TEA pressure 2:334
transverse mode filtering 4:294–298
tube construction 2:374
ultrasonic inspection 4:332–333
velocimeter 4:497
vibrometers 4:452
laser and light interaction
application 5:137*T*
computer guided treatments 5:138
cornea 5:133–134
corneal cross linking
for corneal infections 5:136–138
for refractive procedures 5:136
lens 5:134
refractive errors 5:135
SLT and ALT 5:136
SMILE procedure 5:138
vitreoretinal disorders 5:134–135
laser crystallization (LC) 3:14
improvement from LC modes 3:60–61
lens for 2D/3D switchable display 3:48
laser diodes (LDs) 1:224, 1:260, 1:277, 2:98–99, 2:271, 2:350, 2:409, 2:446, 4:16, 4:500
laser Doppler Anemometer (LDA) 4:525
laser Doppler velocimetry (LDV) 4:525, 4:525*F*, 5:64
laser dye survey
azaquinolone derivatives 2:346
conjugated hydrocarbons 2:345
coumarins 2:345–346
cyanines 2:344, 2:345*F*
oxadiazole derivatives 2:346
pyrromethenes 2:344–345
xanthene 2:344
Laser Geodynamics Satellite (LAGEOS) 4:488, 4:489*F*
laser guide stars (LGS) *see* artificial reference stars
Laser Interferometer Gravitational-Wave Observatory (LIGO) 1:432, 1:438*F*, 1:439*F*
laser interferometer space antenna (LISA) 1:434
laser radar (ladar) 4:430, 4:474
laser range profiler (LRP) 4:447, 4:448*F*, 4:449*F*
laser range profiling (LRP) 4:474, 4:474–476
range performance for typical profiling system 4:475*F*
range profiles studies 4:477–479
signal processing techniques for range profiling and tomography 4:489–494
simulated laser radar waveforms 4:476*F*
simulating laser profiling data 4:476–477
tomography based on laser profiling 4:483–489
laser velocimetry 4:523–525
blood flow measurement in retinal vessels 4:525
two-directional velocity measurement 4:525–526
laser-assisted in situ keratomileusis technique (LASIK technique) 5:100–101, 5:126, 5:135
postsurgical assessment 5:101–102
procedures 5:142
surgery 5:150
laser-induced breakdown (LIB) 5:92
laser-induced damage (LID) 4:302
defect-induced damage 4:305–306
energy diagram of optical excitation and relaxation of dielectric materials 4:305*F*
fundamental processes 4:303–305
1-on-1 LIDTs 4:303*T*
in optical materials 4:304*F*
response of dielectric material 4:302*F*
laser-induced damage threshold (LIDT) 4:302, 4:305*F*
ISO standard for 4:307*F*
LIDT F_{th} 4:302
measuring 4:306–308
lasing cavity 2:119
last mile fibers (LMFs) 2:82–83
lateral motions 3:202
lateral spatial resolution 4:355
lateral waveguide component 2:351
latter effect 1:451
lattice
DOF 2:126
lattice-matched quantum well system 2:105
parameter 2:105
vibration 2:118
law of refraction 1:222–223
layer-based methods 4:123–124
layer-by-layer fabrication 1:175
LC alignment direction (LCAD) 3:48
3-LCD projector 3:33
LCOS *see* liquid crystal on silicon (LCoS)
Le Grand four-refracting surface schematic eye 5:44*F*
Le Grand full theoretical eye 5:48, 5:48*F*
lead iodide perovskite solar cell ($CH_3NH_3PbX_3$) 5:278–279
lead lanthanum zirconium titanate (PLZT) 4:235
lead phthalocyanine (PbPc) 5:321–322, 5:321*F*
leaky-mode coupling 4:98
least-squares sense 3:188
Lebesgue square-integrable 'wave'-functions 4:199
Leibniz rule 4:199
Leith and Upatnieks's technique 4:103
lens(es) 3:247, 3:248*F*, 5:46–47, 5:60–61, 5:134, 5:203
approximations for thin lenses 1:109–110
cardinal points and planes of optical system 1:101–102
combination 4:178
compound lenses 1:109
using Gaussian constants 1:105–107
image formation by 4:160–161, 4:160*F*
lens-scanning method 5:194
and mirrors 1:101
nodal points and planes 1:107–109
paraxial matrices 1:102–104
paraxial system for design or analysis 1:110–111
reflectors 1:111–113
lensless Fourier approach
numerical reconstruction by 4:146–147
setup 4:147*F*
lensmakers equation 1:110
lenticular lens 3:48
"less-metals", metals to 2:259–261
leukocyte
imaging with AOSLO 5:67
velocity 5:67
levulose 1:160
Lewenstein model 2:318
$LiCoPO_4$, ferrotoroidal order in 2:214–216, 2:214*F*, 2:215*F*, 2:216*F*
Lie brackets 4:199
light 1:221, 1:222, 1:223–224, 3:225–226
beam characterization 4:174–175
crystal 5:203–204
detecting devices 3:86
emitted from pinholes 1:81–82
emitting resonant cavity 2:386
harnessing 5:293
incident on aperture 3:247
interferometers 5:217
light-generation and amplification 4:243
light-guiding methodology 1:217–218
light-sensitive tissue 5:43
light-sword wavefront 5:122
light/heat sensitive ion channels 3:116–117
line 1:186
loss at retina 5:61
optics 5:203
polarization 1:488
propagation 3:219
properties 4:139
pulses 4:347
ray region 1:192
reflected from mirrors 3:205–206, 3:205*F*
scattering 1:237, 2:82
sheet microscopy 5:170
source 1:148, 3:27–28, 3:32, 3:97, 3:259, 3:267, 4:16, 4:120, 4:500
squeezing of light emission 1:463–465
substantial fraction 1:233
therapy 3:100
trapping 5:294–296, 5:295*F*, 5:296*F*
wave 1:131, 1:131*F*, 4:102, 4:113
light amplification
process 4:103
by stimulated emission of radiation (LASER) 2:329
light and eye 5:49–50
light at retina 5:50
light interaction with back of eye 5:50–51
passage of light into eye 5:49–50
light and laser therapy 5:130–131

interaction between laser and biological tissue 5:130F
photochemical interaction 5:131
photochemical relationship between oxygen, riboflavin and UVA light 5:132F
photomechanical interactions 5:132–133
photothermal interactions 5:131–132
light detection and ranging (LIDAR) 2:271, 2:451, 2:461, 4:401, 4:430
see also micro-lidars
configuration 4:512, 4:512F
error model 4:402–403
Lidar Base Specification (2014) 4:401
light emitting diodes (LEDs) 1:141–142, 1:142, 1:224, 2:82, 2:194–195, 2:271, 2:446, 3:1, 3:25, 3:88, 3:118–119, 4:3, 4:16, 4:99, 4:509–510, 5:1, 5:248, 5:314
light extraction
of plasmonic mode 5:251–253
of substrate mode 5:248
of waveguiding mode 5:248–251
light harvesting (LH) 5:292, 5:302
AR effects 5:293–294
exciton diffusion bottleneck 5:292F
LH2 2:192
light trapping 5:294–296
metal nanostructures 5:296–302
in OSCs 5:292, 5:293
other approaches for 5:304–306
spacer layer and cavity effects 5:302–304, 5:304F
ways of harnessing light 5:293F
lightfield imaging 3:169–170, 3:170F
light–matter
interaction 1:459
observation via strong light–matter interaction 1:459–461
system 1:462
lightpath 4:233
lightwave 2:384
lightwave transmitters
directly modulated lasers 4:68–69
DWDM transceivers 4:68
reliability of lasers in fiber optic systems 4:70–71
requirements for externally modulated lasers 4:70
semiconductor laser principles 4:67
structure and requirements of optical fiber communication systems 4:67–68
transmitter requirements 4:68
limbal stem cells, two-photon imaging of 5:103
limited-memory Broyden–Fletcher–Goldfarb–Shanno method (LBFGS) 3:150
limiting amplifier (LA) 4:6, 4:261
Linac Coherent Light Source (LCLS) 1:405, 2:142
$LiNbO_3$ *see* lithium niobate (LN)
line broadening effect 2:328
line spread function (LSF) 4:403
linear absorption spectrum 2:52
linear band 2:89
linear canonical transforms 4:199
canonical integral transforms 4:200–201
conservation of Hamiltonian structure 4:199
geometric canonical transforms 4:199–200
issues pertaining integral transforms 4:201–202
radial canonical transforms 4:203
linear crosstalk 1:271–272
linear defect 1:189–190
linear dispersion maps, corrections to 4:25–26
linear effects 1:255
attenuation 1:255–256
chromatic dispersion 1:256
polarization mode dispersion 1:256–257
linear electro-optic coefficient 4:330
linear electro-optic effect 4:3, 4:324, 4:351
linear error at 90th percentile (LE90) 4:402
linear feedback shift register (LFSR) 5:9
linear frequency chirp (LFC) 4:434
linear gratings 1:51, 1:51F
linear IR 2:164
linear Kramers–Krönig relations 4:317–318
linear matrix 4:210
linear optics 4:350
implementation 4:182
spectroscopy 2:82, 2:246–247
system 1:39
linear particle accelerator (LINAC) 1:405
linear perturbation analysis of rate equations 4:69
linear polarization 2:418, 4:268
optical beam 1:408
linear polarizer (LP) 1:149, 2:211
linear radiation transfer equation 3:257
linear regularization method 3:191
linear response 2:19–21, 2:20F
linear signatures 1:345–346, 1:345F
linear spectroscopy 2:244
linear susceptibility 4:339
linear variable filter (LVF) 3:216
linear-algebraic theorems 1:170
linear-mode (LM) 4:415
linearity response, illumination 4:88–89
linearly chirped grating 4:29
linearly modulated laser frequency 4:451, 4:452F
linearly polarized (LP) 1:229
optical beam 4:174
linewidth
enhancement factor 2:467–468
narrowing 2:341
Linewidth Enhancement Factor (LEF) 1:245
link layer ID (LLID) 2:76
link-level considerations 4:222
Liouville equation 4:341
Liouville space pathway 2:204–205, 2:204F
lipid peroxidation 3:102
lipofuscin 5:86
liquid and solid state systems 2:164–165
liquid crystal displays (LCDs) 3:1, 3:2, 3:18–19, 3:19F, 3:25, 3:25F, 3:31, 3:56–57, 4:99, 5:240
backlight module 3:27–28
colors in 3:17–20
controlled viewing angle 3:62
LC panel 3:25
periphery component 3:29–31
projection display 3:32–34
stripe half-wave-plate 3:34F
liquid crystal on silicon (LCoS) 1:269, 1:269F, 3:32, 3:34, 3:34F, 4:99, 4:99, 4:231
devices 4:115, 4:115F
display 3:2
projection display 3:34–35
liquid crystal technologies (LCT) 1:268, 1:269
liquid crystals (LCs) 3:8, 3:25, 3:26–27, 4:99
chiral smectic and nematic phases 3:10
color filter 3:26
discotic phases 3:10–11
glass 3:25
nematic phase 3:8–9
panel 3:25
polarizer 3:25–26
smectic phases 3:9–10
TFT 3:27
thermotropic LC phases 3:8
transparent electrode 3:26
liquid dye lasers
see also solid-state dye laser
CW dye lasers 2:339–340, 2:340F
flashlamp-pumped dye lasers 2:338–339, 2:339F
laser-pumped pulsed dye lasers 2:337–338, 2:339F
ultrashort-pulse dye lasers 2:340, 2:341F
liquid electrolyte 5:277
liquid nitrogen temperature 2:120
liquid-crystal on silicon wavelength-selective switch (LCoS WSS) 4:231
Lissajous figure 1:162
lithium niobate (LN) 1:14, 1:16, 1:144–146, 1:177, 2:294, 4:3, 4:96, 4:331
based pulse front tilting setup 1:409
technology 4:39
lithium quinolate (Liq) 5:233
lithium tantalite 1:16
lithography 1:54, 1:55F, 1:57, 1:484, 4:91
Littman configurations 4:363
Littman–Metcalf configuration 2:227, 2:228
Littrow configuration 2:227, 2:227F
Littrow type-I design 4:363
Littrow type-II design 4:363
living marine plankton recording 4:110
LiYF4 *see* yttrium lithium fluoride (YLF)
LN *see* lithium niobate ($LiNbO_3$)
local area networks (LANs) 1:354, 2:76, 4:3
local density of optical states (LDOS) 1:445
Local eXchanges (LX) 1:280–281
local oscillator (LO) 1:250, 1:374, 1:428, 2:56–57, 2:164, 2:197, 2:248, 4:45, 4:250, 4:432–433, 5:2
field 2:184
laser 1:291
local-primary-desaturation (LPD) 3:22, 3:23–24, 3:23F
localized surface plasmon applications (Q_{LSP}) 2:255
localized surface plasmon resonance (LSPR) 2:262, 5:296–298

lock-in amplifiers (LIA) 4:523
Lockheed Martin Coherent Technologies 4:458–459
long pass filter (LPF) 2:211
Long Period Grating (LPG) 1:230–231, 1:234F, 1:236
long trajectories 2:316–317
long-haul optical transmission systems 1:249
long-haul WDM systems 1:282–284
long-period FBGs 1:267
long-range WindScanner (LRWS) 4:462
long-term fluctuations 1:32
long-wave IR (LWIR) 3:232
long-wavelength-cone (L-cone) 3:17, 3:18F
longitudinal aberration 5:55, 5:56F
longitudinal acoustic waves 1:131
longitudinal chromatic aberration of eye 5:58
longitudinal modes 2:329–331, 2:386–387
longitudinal optical phonons (LO phonons) 1:382, 2:84–85
longitudinal spherical aberration (LSA) 1:114–116, 1:115F
longitudinal-optical and-acoustical differences (LO-LA differences) 1:408–409
look-up-table method (LUT method) 4:123
looping mechanism 2:396
loose jacket 1:328–330, 1:330F
Lorentz model 1:346
Lorentz oscillator 2:254
Lorentzian profile 1:352
loss factor 2:254
loss mechanisms, OPSLs 2:283–284
low bending-loss single-mode fibers (G.657 low bending-loss fibers) 1:261, 1:262
Low Cost Autonomous Attack System (LOCAAS) 4:483
low density lipoprotein (LDL) 3:110
low extinction ratio (ER) 1:252
low frequency response 1:252–253
low level light (laser) therapy (LLLT) 3:114–115
low loss InP waveguides 4:248
low noise multi-gigahertz repetition rate femtosecond pulsed OPSLs 2:286–287
low temperature poly-silicon (LTPS) 3:14, 3:27, 3:66–67
low-bandwidth feedback TIA 4:262–263, 4:262F
low-coherence interferometry 4:503–504
low-index grid (LIG) 5:248–250, 5:250F
low-index polymers 1:210–211
low-loss optical fiber 1:28
low-noise design of EDFAs 1:361–362
low-pass filter (LPF) 1:279, 1:373, 1:374, 1:378, 3:194, 4:423
low-power argon ion lasers 2:374
low-water-content fibers *see* full-spectrum fibers
low-water-peak fibers 4:15
lower exciton polaritons (LP) 1:448–449, 1:449F
lowest eigenfrequencies 1:172
lowest order mode 2:329–331
lowest unoccupied molecular orbital (LUMO) 3:64, 5:221, 5:244, 5:256
lowest-order light–matter interaction 1:458
LTPS-TFT AMOLED smartphones 3:68–69
luminance 3:70
luminance uniformity 3:72
luminescence
  process 2:105–106
  spectra 2:85
  up-conversion 2:82
luminescence mechanisms
  energy transfers 2:394–395, 2:395F
  materials 2:397
  photon avalanche 2:396–397, 2:396F
  sequential two-photon absorption 2:395–396, 2:396F
  up-conversion lasers based on 2:399–400
  up-conversion mechanisms from 2:394–395
lutetium aluminum garnet (Yb:LuAG) 2:413
Luttinger and Kohn representation (LK representation) 2:87–88

M

M-aryPSK (*m*-PSK) 1:293
M-aryQuadratureAmplitudeModulation (*m*-QAM) 1:293
m-axes 2:271
m-plane 2:271
Mach-Zehnder Interferometer (MZI) 1:146–147, 1:251, 1:193, 1:225, 1:225–226, 1:261, 1:316, 1:368, 1:68F, 4:3, 4:40–41, 4:50–51, 4:51F, 4:505
  optical switch 4:236, 4:236F, 4:242, 4:250
Mach-Zehnder Modulator (MZM) 1:144–146, 1:261, 1:261F, 1:292, 1:292–293, 1:293F, 2:80, 4:39–40, 4:259, 4:260F
  transmitters 4:258–259
macro-bending loss 1:256
macrobending sensitivity 1:311, 1:311F, 1:312F
macroscopic parameters 2:244
macroscopic phase handle 1:487
macroscopic phase-matching aspects 2:236–237
macroscopic polarization 4:264–265, 4:342, 4:349
macula 3:17
Madison Darby canine kidney II cells (MDCK II) 3:108
magnetic dipole 1:475
  coupling 1:475
  magnetic dipole-dipole interaction 1:475
magnetic fields
  exciton states 2:63–66
  influence 2:96
  three-dimensional case 2:64–66
  two-dimensional case 2:66–68
magnetic flux quantum 2:72
magnetic lenses 5:192
magnetic quadrupole order in pseudogap of $YBa_2Cu_3O_y$ 2:220–223
magnetic resonance imaging (MRI) 3:124, 3:192, 3:259
magnetically ordered oxides 2:127–128
magnetism 2:123
magneto-optic devices 1:159–160
magneto-optical Kerr effect microscopy (MOKE) 2:147
magnetoelectric coupling 2:125
magnetoelectric multiferroics (ME multiferroics) 2:128–129
magnetoresistive pyrochlores 2:135–136
magnification 1:105–106
main central office (MCO) 2:82–83, 2:82F
major histocompatibility complex class I molecules (MHC-I) 3:113, 3:114
malaria 3:102–103
manipulative artist, pseudo colour and 4:104–105
many-body effects of high-density excitons in high magnetic fields 2:77–79
  hidden symmetry of 2D magnetoexcitons 2:78–79
  superfluorescence from high-density 2D magnetoexcitons 2:79–81
mapping 4:482–483
marginal rays 1:114–116
Mark systems 4:115, 4:116–117
maser operation 1:452–454
maser patent 1:99
Massachusetts General Hospital (MGH) 4:507
mast modes measurement 4:453, 4:453F
master oscillator power fiber amplifier (MOPFA) 2:429
master oscillator/fiber power amplifier systems (MOPA systems) 4:431
  flared planar amplifier 2:286
master-oscillator laser (MO laser) 4:369
material absorption 1:172
material dispersion 1:5, 1:217–218, 1:313, 1:314F
material effective index 4:220
material group velocity dispersion 1:5–6
material sciences
  molecular electrolytes 2:170–172
  organometallic chemical catalysts 2:172
  solid state materials 2:168
materials selection criteria 1:210–211
mathematical expression of diffraction through fractional order Fourier transform 4:157–158
mathematical model of imaging 3:176
mathematical representation of optical pulse 4:48–49
matrices 4:199
matricial active triangulation 4:511–512
matricial detectors, time-of-flight principle with 4:510–511
matrix algebra 4:202
matrix analysis
  Jones calculus 1:168
  Jones vector 1:166–168
  Mueller calculus 1:165–166
  polarization ellipse 1:162–163
  Stokes parameters 1:163–166
matrix element 2:106

matrix formulation of imaging and inverse problems 3:156–157
matrix methods 1:149
  for computing polarization 1:160–161
matter interferometer 1:487
matter wave optics 5:203
maximum efficiency 4:88
Maximum Entropy Method (MEM) 3:191–192
maximum modulation 4:88
maximum permissible exposures (MPE) 5:106–107
maximum power point (MPP) 5:259
maximum-realizable fidelity 3:181
Maxwell electromagnetic theory 2:398
Maxwell's equation 1:148, 1:177, 1:458, 2:53, 2:118, 4:264, 4:266, 4:312, 4:321, 4:342–343
  in periodic media 1:169–170
Maxwell's theorem 3:262
Maxwell's wave equation 4:335
Maxwell–Boltzmann distribution 2:82
McIntyre distributions 4:426, 4:428
MDA-MB-231 human mammary gland adenocarcinoma cells 5:182
mean free paths (MFP) 3:222–223
mean time to failure (MTTF) 4:71, 4:255
mechanical diameter 1:324
mechanical flexibility 1:218
mechanical scanners 1:136
mechanical scanning 4:509–510
mechanical splices 1:336, 1:339, 1:339*F*
mechanical tuning experiment and discussion 1:216, 1:216*F*
media access control (MAC) 2:73
media parameters as dimensions 4:455–463
  atmosphere components and contaminants 4:463–469
  direct detection elastic lidar with three laser transceivers 4:466*F*
  temperature 4:469
  three components of lidar wind speed 4:466*F*
  wind and flow velocity 4:456–463, 4:457*F*, 4:458*F*
medical physics 3:199
megasample per second (MS/s) 4:434–435
MEH-PPV films 5:261, 5:309–310, 5:309*F*, 5:323–324, 5:324–325, 5:324*F*
membrane proteins 2:176
  ion permeation through K^+ ion channel 2:176
  role of water in influenza M2 channel 2:176
memory LCD 3:84
memory mechanism 1:471–472, 1:471*T*
  charge qubits 1:471–472
  spin qubits 1:472–473
memory-in-pixel (MIP) 3:84
mercury ion laser 2:376
MESA Imaging SR4000 emitters 4:510–511, 4:511*F*
meso-tetra(4-sulfonatophenyl)porphine (TPPS4) 3:108
mesogen 3:8
mesoporous oxides 5:274–275
mesostructured fibers for external reflection applications 1:209–210
  fabrication approach 1:210, 1:210*F*
  materials selection criteria 1:210–211
Metal Induced Energy Transfer (MIET) 5:176, 5:182
metal organic chemical vapor deposition (MOCVD) 2:462
metal vapor lasers 2:368
  see also carbon dioxide laser
  afterglow recombination 2:372–373
  afterglow recombination metal vapor lasers 2:372–373
  continuous-wave metal ion lasers 2:373–374
  copper bromide laser tube construction 2:370*F*
  CVLs 2:369–372
    excitation circuits 2:371*F*
    tube construction 2:370*F*
  partial energy level scheme for copper vapor laser 2:369*F*
  principal self-terminating resonance-metastable metal vapor lasers 2:369*T*
  resonance-metastable energy levels 2:368*F*
  self-terminating resonance-metastable pulsed metal vapor lasers 2:368–369
  unstable resonator configuration 2:372*F*
metal-induced energy transfer microscopy (MIET microscopy) 5:180–183, 5:181*F*
metal-induced lateral crystallization (MILC) 3:14
metal-metal waveguide (MM waveguide) 1:384
metal-organic chemical vapor deposition (MOCVD) 4:245–246, 4:416–417, 5:293–294
metal-organic-frameworks (MOFs) 2:170
metal-oxide-semiconductor (MOS) 1:468
metal-oxide-semiconductor field effect transistor (MOSFET) 3:12–13
metal-semiconductor-metal detectors (MSM detectors) 5:8, 5:10, 5:10*F*
metal(s) 5:277
  alloys 2:258–259
  electrode 5:247
  III-V semiconductors 2:257
  to "less-metals" 2:259–261
  metal-based sensitizers 5:276–277
  metal-free cables 1:331
  metal-free organic dyes 5:277, 5:277*T*
  nanostructures 5:296–302, 5:297*F*, 5:298*F*
  nitrides 2:260
  NPs 5:298
  semiconductors to 2:256–257, 2:256*T*
  TCOs 2:257–258
  vapor 2:368–369, 2:373
metal–insulator transition (MIT) 2:123, 2:126
metallic armor 1:332
metallic atoms 4:96
metallic barrier 1:331
metallic coatings 1:33
metallic counterparts 1:207
metallic silver particles 4:93
metal–ligand chargetransfer (MLCT) 5:242
metallo-dielectric waveguides 1:217–218
metallo-organic compounds 2:346
metalorganic vapor phase epitaxy (MOVPE) 2:98–99, 2:273
metamaterials 2:263–264
metaplectic group 4:202
metastable lower laser level 2:368
metasurface VECSEL 1:384
methanol 2:119
3-methoxypropionitrile (MPN) 5:277
methyl methacrylate (MMA) 2:347
1-methyl-4-phenyl-1,2,3,6-tetrahydropyridine (MPTP) 3:125
methylammonium ($CH_3NH_3^+$) 5:282
methylene blue 3:103*F*
methylnaphthalene (MNA) 2:7–8
metro and access networks, WDM in 1:280–281
metro area network (MAN) 4:17–18
metropolitan-area networks 1:281
MF concentricity error 1:322
Michelson interference rule 4:432
Michelson interferometer (MI) 1:34, 1:35*F*, 1:432, 1:433, 1:434, 1:434*F*, 1:435*F*, 4:500, 4:502–503
Michelson stellar interferometer 1:47, 1:47*F*
michrochip laser 2:454
micro electro-mechanical systems (MEMS) 1:268, 3:36, 3:84, 4:99–100
  projection display 3:35–37
Micro-Electromechanical Vertical Cavity Surface Emitting Lasers (MEM-VCSEL) 1:260
micro-interferences 4:140
micro-lidars 4:496
  see also light detection and ranging (LIDAR)
  acoustical studies and vibrometry 4:528
  devices with photonic arrays 4:507–509
  distance measurement techniques 4:497
  flow cytometry 4:514–516
  glucose lidars 4:522
  interferometric methods 4:502–504
  laser velocimetry 4:523–525
  measuring media parameters 4:512–513
  nephelometers 4:512–513
  normal and abnormal cell with fused genes 4:516*F*
  with optical doppler tomography 4:526
  oxymetry lidars 4:519–522
  Raman micro-lidars 4:516–518
  smoke detectors 4:513–514
  time-resolved fluores ence spectroscopy 4:518–519
  for velocity measurement 4:523–525
  wavefront sensing micro-lidars 4:530–531
micro-optic technologies 1:341
micro-opto-electro-mechanical systems (MOEMS) 4:99
microarray scanning and customized excitation 3:218
microbending 1:328
  loss 1:256
  sensitivity 1:311
microbolometers 1:423, 1:424*F*

microcavity 2:107, 5:313
  luminescence intensities 1:462*F*
  photoluminescence spectrum 1:461
microchip lasers 2:415
  see also thin disk laser (TDL)
  applications 2:422–423
  background 2:415–416
  composite-cavity microchip lasers 2:416
  frequency conversion and amplification 2:421–422
  monolithic microchip laser 2:415*F*, 2:416
  polarization control 2:418
  pulsed operation 2:418–419
  pumping 2:416–417
  spectral properties 2:417
  transverse mode definition 2:417
microcup® EPD 3:80, 3:80*F*, 3:81*F*
microdisplay 3:32
microencapsulated EPD 3:79–80
microlasers 1:455–456
microlens array 5:235–237, 5:295, 5:296*F*
microlens array film (MAF) 5:248
microlenses 5:250–251
micromaser 1:452, 1:454*F*, 1:455
micron scale 5:292–293
microoptical coherence tomography (μOCT) 4:507
microplasma 1:412
microring resonator (MRR) 4:29, 4:236, 4:237*F*, 4:293–294, 4:297*F*, 4:298*F*
  optical switch 4:236, 4:237*F*
microscopic/microscopy 1:484, 3:241, 4:103, 5:185
  confocal microscope 5:189–190, 5:189*F*
  contrast mechanisms 5:192
  conventional microscope 5:185–186, 5:189
  corneal deformation 5:146
  description 2:234–235
  fluorescence microscopy 5:192
  images 5:192
  interaction processes 4:264
  nonlinear microscopy 5:193
  objectives 2:249, 5:188–189
  other contrast mechanisms 5:193
  parameters 2:244
  perturbation 5:146
  phase contrast microscopy 5:192
  polarization 2:34
    microscopy 5:192
  probe microscopes 5:190
  quantum many-body theory of HHG 2:34
  quasi-particle dynamics 2:38
  radiation types 5:191
  Raman microscopy 5:192–193
  scanning microscopes 5:189
microsecond pulse emission 2:336
Microsoft Kinect play station 4:511–512, 4:512*F*
microstructure fiber(s) 1:195
  see also photonic crystal fibers (PCFs)
  air-clad fiber 1:200–203
  bandgap guided fibers 1:203
  endlessly single-mode fiber 1:197–198, 1:198*F*
  fabrication 1:195–196
  fiber draw 1:196–197
  high delta core fiber 1:198–199, 1:199*F*
  index guided fibers 1:197–198
  preform fabrication 1:195–196
  TMF 1:199–200, 1:201*F*
  tunable microstructure fiber devices 1:203–205
  types 1:197–198
microstructure tunable filter 1:205
microwave
  holography 4:155
  radiation 5:191
  spectroscopy 1:100
  tomography 3:196
microwave amplification by stimulated emission of radiation (MASER) 2:325–326
microwave kinetic inductance detectors (MKIDs) 1:428
Microwave Photonics (MWP) 1:252–253
mid infrared (MIR) 2:166, 2:197, 2:260, 2:290
  CO_2 laser 1:381
  nonlinear generation of THz radiation in mid-IR QC-lasers 1:384–385
  pulse 2:166
  THz to 2:135–139
mid-IR *see* mid infrared (MIR)
mid-to-far-infrared (IR) frequencies 2:124
mid-wavelength infrared (MWIR) 3:229, 3:232
middle cerebral artery occlusion (MCAO) 3:121–122
Middle East (ME) 4:18
middle-wavelength-cone (M-cone) 3:17, 3:18*F*
mini-scleral lenses 5:119
minimum Gibbs free energy 3:81
minimum resolvable temperature difference (MRTD) 3:234, 3:235–237, 3:237*F*
minimum resolvable temperature (MRT) 3:234
minimum temperature difference perceived (MTDP) 3:234
mirrorless lasing 5:312–313
mirrors 1:376, 5:203
  array 4:232
  fiber reflectivity 1:213
  optical characterization of mirror fibers 1:213
  planes 1:170
mitochondrial membrane potential (MMP) 3:115
modal bandwidth 1:312, 1:313*F*
modal control methods 3:202
modal dispersion 1:222–223
mode field diameter (MFD) 1:322, 1:325
mode locked fiber laser (MLFL) 4:45
mode locking 2:421
  of TDLs 2:412
mode management in PT-symmetric lasers 4:293–294, 4:295*F*, 4:296*F*
  laser transverse mode filtering 4:294–298
  single longitudinal mode lasing 4:294
mode multiplexing algorithms 3:153
mode suppression, single mode operation with 2:453–454
mode-propagation constant 1:178–179
mode-selective excitation 2:139–141, 2:141*F*
model-based methods 4:490
modeling infrared imagers 3:238–239
modelocking (ML) 2:435, 2:440–441, 2:468
  based multi-wavelength interferometry 4:432, 4:432*F*
  control knobs for frequency comb 2:305–306
  as frequency comb generator 2:303
  IPI 2:308–309
  lasers 2:302
  mode-locking as orthodoncy 2:303–304
  phase modulation and dispersion 2:304–305
  solid state lasers 2:424
  typical laser configurations 2:303, 2:303*F*
modern high-resolution CCD 4:140
modern imaging 3:144
modern optical systems 3:262
modern THz TDS 2:19
modes 1:6–7, 1:177
modest pulse energies 2:424
modified chemical vapor deposition process (MCVD process) 1:28, 1:28–29, 1:29*F*
modified Gauss–Newton methods 3:150
modified monovision technique 5:125
modified poly(methyl methacrylate) (MPMMA) 2:347
modified Schrödinger equations 2:266
modulated laser 1:141–142, 1:142
modulation 1:373, 3:242, 4:95
modulation bandwidth 1:139–140
modulation transfer function (MTF) 3:233, 3:235–237, 3:236, 3:237*F*, 4:412, 4:413*F*, 4:533, 5:16, 5:122
modulational instability (MI) 1:348, 2:426–427, 2:427
modulator 1:139–140, 4:216–217, 4:217*F*
molecular beam epitaxy (MBE) 1:422, 2:94, 2:98–99, 2:462, 4:416–417
molecular beam intensity 1:98
molecular dynamics 2:326–327
  collision-induced vibrational relaxation of upper and lower laser levels 2:328
  direct excitation and de-excitation 2:327
  electron energy distribution function 2:327*F*
  gain 2:328
  radiative relaxation 2:328
  resonant energy transfer 2:327–328
  stimulated emission 2:328–329
molecular electrolytes
  ion structure and dynamics of electrolytes 2:170–172
  time-dependent 2D IR spectral series 2:171*F*
molecular energy levels 2:337, 2:338*F*
molecular gas lasers 1:380
molecular moment of inertia 1:387
molecular orbital (MO) 5:220–221
molecular rate equations 2:329
molecular spectra 1:387

molecular spontaneous emission modification 1:445–446
molecular vibrational fingerprints 2:164
molecules in plasmonic resonators 1:446–447
Mollow triplet 2:47–48
momentum 1:487, 5:207, 5:211F
  conservation 2:115–116
  diagram for diffraction of light 1:133F
mono-mode optical fiber 4:38
monochromatic/monochrome
  aberrations 5:55–58, 5:91, 5:120
  light wave field 1:291
  material 4:68
  microencapsulated EPD 3:80, 3:80F
monocular vision 5:44
monolayer TMDs
  coherent energy transfer 2:59–61
  homogeneous broadening 2:58–59
  incoherent energy transfer 2:59–61
  inhomogeneous broadening 2:58–59
  intervalley biexcitons 2:61–62
  optical properties 2:57–58
  2DCS 2:58–59
monolayer transition metal dichalcogenides 2:53
monolithic fabrication of integrated sensor 3:89
monolithic InP PIC 4:250, 4:251F
monolithic integration 4:242
monolithic microchip lasers 2:415F, 2:416
monolithic microwave integrated circuits (MMICs) 5:1
monolithically-integrated detector arrays 1:419
monomolecular process 5:257
monotropic LC mesophase 3:8
monovision 5:54, 5:125
Monte Carlo simulations 4:422–423, 4:423F
Morpheus lander 4:450–451, 4:451F
MOS Field Effect Transistor (MOSFET) 1:468
moth eye AR structures 5:293, 5:294F
motion blur 3:77
motion parallax 3:44–45
motorized instruments 3:197
mounting 2:410, 2:411
movable digital mirror display (DMD) 3:2
moving waveguide coupler 4:233
Mueller calculus 1:160, 1:161, 1:165–166, 1:165T, 1:166T
Multi-Core Fibers (MCF) 1:262
multi-dimensional coherent spectroscopy (MDCS) 2:53
  interpreting 2D spectra 2:157
  power of 2DCS 2:150
  quantum pathway selection in 2D coherent spectra 2:153–154
  theory of coherent multidimensional spectroscopy 2:150–151
  3-pulse transient four-wave mixing 2:156–157
multi-dimensional laser radars 4:444, 4:444T
  adding velocity as dimension 4:449–452
  dimension combinations 4:470–471
  fluctuation as dimension 4:469–470
  histogram of range image 4:445F
  media parameters as dimensions 4:455–463
  ranging supplemented by two-dimensional scanning 4:444–445
  stepping up dimensionality 4:444–445
  three-dimensional description of parameters 4:444T
  2D imaging supplemented by scanning in z direction 4:445–449
  2D projections of objects 4:446F
  vibrations 4:452–455
multi-domain vertical alignment (MVA) 3:59, 3:61
multi-electrode driven (MeD) 3:48
multi-fluorescence in situ hybridization system (M-FISH system) 3:213
multi-frame blind deconvolution algorithm (MFBD algorithm) 3:276–277
multi-modal dispersion 1:178–179
multi-mode interferometers (MMI) 4:236
multi-mode THz QC-lasers 1:384
multi-order Raman sideband generation 4:345
multi-path interference 1:272
multi-planar 3:46–47
multi-point control protocol (MPCP) 2:76, 2:77F
multi-slice algorithms 3:153–154
multi-spin encodings enable initialization and measurement 1:473
multi-stage OPA system 2:166
multi-transmitter, single receive aperture system 4:409
multi-wavelength laser source 4:222
multicomponent glasses 1:27
multiconjugate adaptive optics (MCAO) 3:202
multidimensional fourier transform spectroscopy 4:275–276
multidimensional nuclear magnetic resonance (multidimensional NMR) 2:150
multidimensional spectroscopy 2:150, 2:249
multidimensional THz spectroscopy
  see also 2D electronic spectroscopy (2DES); attosecond spectroscopy
  collinear multidimensional THz spectroscopy 2:197–199
  three-pulse 2D THz spectroscopy on InSb 2:203–205
  THz-driven AC stark effect of intersubband transitions 2:200–203
  two-dimensional THz spectroscopy with three phase-locked THz pulses 2:199–200
multidrug-resistant (MDR) 3:102–103
multifaceted transmission function 4:184–185
multifiber connectors 1:338–339, 1:339F
multifocal wavefront aberrations 5:122–125, 5:124F
multilayer dielectric mirrors 1:207
multilayer preform
  fabrication sequence 1:211, 1:212F
  rod 1:211
multimode core 1:203
multimode fiber(s) 1:33, 1:223, 1:336, 1:337
  bandwidth for multimode fibers 1:312–313
multimode interference switches (MMI switches) 1:143
multimode operation 2:451–452
multipass amplification 2:412
multipass unstable resonator 2:334
multipath interference (MPI) 1:234, 4:226
multiphoton
  absorption 4:336, 5:92
  excitation 5:89
multiphoton intrapulse interference phase scan (MIIPS) 5:91
multiphoton ionization
  process 4:337
  rate 4:304
multiphoton microscopy 5:98, 5:99F
  of cornea 5:99–100
  future directions 5:107
multiphoton retinal imaging 5:87
  theory 5:87–89
multiple beamsplitters 1:59
multiple input, multiple output lidar (MIMO lidar) 4:407–408
  closed form MIMO 4:408–412
  multiple sub-aperture overlap using 3 transmitters 4:409F
  single receive aperture, light green, with three transmitter apertures 4:410F
  trade space of current MIMO 4:412–413
multiple path interference (MPI) 1:358
multiple quantum well (MQW) 2:23, 2:273–274
multiple receive apertures 4:407
multiple reference OCT system (MR-OCT system) 4:507
multiple scattering 3:136–137, 3:144
  acousto-optic 3:226–228
  coupling light and sound 3:226
  imaging in multiple scattering regime 3:225–226
  inverse source and scattering problems 3:137, 3:137F
  light 3:225–226
  photo-acoustic 3:226
  resolution in scatterer imaging 3:142–144
multiple transmitter apertures 4:407
multiple-access mechanism 1:255
multiple-inputs multiple outputs (MIMO) 1:262, 1:278
multiple-prism array 2:343
multiple-prism dispersion grating theory 2:341–342, 2:342F
multiple-prism grating cavities 2:337
multiple-prism Littrow grating laser oscillator (MPL grating laser oscillator) 2:343, 2:343F
multiple-quantum-well (MQW) 1:245, 4:243, 4:250, 4:255–256
multiple-section diode lasers 2:468
multiple-stage EDFAs 1:358–361, 1:359F, 1:360F

multiplex imaging 3:250–252
see also interferometric imaging
electromagnetic waves propagation 3:248–249
high resolution imaging in astronomy 3:253–254
spatially coherent light 3:249
spatially incoherent light 3:249–250
synthetic apertures with spatially incoherent objects 3:250–252
theta rotating interferometer 3:252–253
multiplexers 4:38–39, 4:39*F*
multiplexing techniques 4:34
multiplied shot noise 4:425
multipole method 1:197
multispectral imager 3:211
multispectral imaging systems 3:211–213, 3:212*F*
Munich interferometers 1:433–434
muscle performance, PBM for 3:126
mutual coherence 1:36–37
spectral representation 1:38
mutual intensity (MI) 1:37–38, 3:263, 4:164–165, 4:174
'mutual PC' *see* 'double PC'
Mux/DMux stages 1:370
myopia 5:51, 5:141
myopic eye 5:116

N

N rectangular slits 1:73–74
N-alkylbenzimidazole derivatives 5:277
N-atom system 1:460–461
n-butyl benzyl phtalate (BBP) 4:96–97
n-dimensional (nD) 4:174
n-doped semiconductor 3:87–88
N-ethylcarbazole (ECZ) 4:96–97
n-FFS 3:60–61
N-methylpyrrolidone (NMP) 5:277
n-type double heterostructure 2:103–104
n-type OSCs 5:226–227
N3 dye 5:276–277, 5:276*F*
N719 dye 5:276–277, 5:276*F*
NAD-phosphate, reduced form (NADPH) 3:101
nano-textures 5:295
nanocavity systems 1:460–461
nanocomposites 5:300
nanocrystalline TiO_2 5:274–275
nanofabricated atom optics 5:204–207, 5:204*F*, 5:205*F*
diffraction data from beam of sodium formed 5:206*F*
diffraction data using mixed beam of sodium atoms 5:206*F*
nanofabrication techniques 5:204
nanogratings 5:296–298, 5:300
nanoimprint lithography 5:293
nanoparticles (NPs) 5:296–298
nanophotonics 2:252
light trapping approaches 5:294–295, 5:295*F*
nanoporous TiO_2 electrodes 5:270
nanorods (NRs) 5:298
nanoscale materials 2:168–170
nanostructures 2:86
Nanowire arrays (NW arrays) 5:293–294, 5:296–298, 5:300
naphthalene diimides fused with two 2-(1,3-dithiol-2-ylidene)malononitrile moieties (NDI-DTYM2) 5:325–326
1-naphthalenethiol (SH-NA) 5:263
narrow gap semiconductors (NGSs) 2:88–89, 2:88–89
narrow laser beam 5:112–113
narrow linewidth high power SG-DBR laser 4:249–250, 4:250*F*
narrow localization 5:99
narrow viewing angle (NVA) 3:62
narrow-linewidth solid-state dye lasers 2:348
oscillator 2:332
National Geospatial Program (NGP) 4:401
National Geospatial-Intelligence Agency (NGA) 4:402
national institute of information and communications technology (NICT) 4:117, 4:117*F*
National Renewable Energy Laboratory (NREL) 5:256, 5:257*F*, 5:286
National Television Standards Committee (NTSC) 5:243–244
"NATO Maritime Target ID" 4:478–479
natural guide star (NGS) *see* off-axis reference star
natural killer cells (NK cells) 3:113
NbN HEB mixer chip 1:429, 1:430*F*
Nd doping 2:413
Nd:YLF laser 4:364
Nd:YVO_4 laser 4:364
near infrared (NIR) 2:75, 2:252, 2:394, 3:97, 3:124, 3:226, 3:229, 5:269
DBR lasers 4:362
ECSL 4:362–363
imaging systems 3:272
lasers 4:361–362
light 5:93
Nd:YAG laser 4:363–364
Nd:YVO_4 and Nd:YLF lasers 4:364
pump beam 2:121–122
radiation 5:106–107
Ti:Sapphire laser 4:364
near-field CGH 4:35
near-field light distribution *see* TNF image technique
near-field optics techniques 3:144
near-field scanning microscopy 3:144
near-field scanning optical microscope (NSOM) 5:190–191, 5:190*F*, 5:300
nearest-neighbor periodicity 1:173
necrosis, PDT and 3:107–108
necrotic cell death 3:107
negative dielectric liquid crystal in ASM (N-type ASM) 3:61
negative magnification 3:166
nematic LC modes 3:60–61
nematic liquid crystals 3:8–9
neodymium 2:413
neodymium:yttrium-aluminum-garnet (Nd:YAG laser) 2:337, 4:363–364, 4:364*F*, 5:134, 5:134–135
neon
buffer gas 2:370
ion lasers 2:379
nephelometers 4:512–513
networking issues, OTDM 4:65–66, 4:65*F*
neurodegenerative diseases, PBM for 3:124–125
Alzheimer's disease 3:124–125
Parkinson's disease 3:125
neurological severity score (NSS) 3:123
Neurothera Effectiveness and Safety Trials (NEST) 3:122–123
neurovascular coupling 5:64
neutral atom microscopes 5:192
neutral particles 5:192
neutrons 2:207, 5:192
neutrophil with fluorescent markers 4:516, 4:517*F*
New European Wind Atlas project (NEWA project) 4:461–462
next-generation PONs (NG-PON) 2:73, 2:74
coexistence 2:78
energy-efficient dynamic bandwidth allocation 2:79–80
10GE-PON 2:77–78, 2:78*F*
high capacity 2:80–81
NG-PON1 2:73, 2:74
NG-PON2 2:74
traffic flow of OFF-DWBA algorithm 2:80*F*
TWDM-PON system 2:78–79, 2:79*F*
wavelength allocation 2:78
XG-PON 2:77–78, 2:78*F*
NF-κB 3:115–116
Ni cathode 2:331
Nicol types 1:150–151
Nicolet SpectraTech NicPlan 1:215
nicotinamide adenine dinucleotide (NADH) 3:101
nicotinamide adenine dinucleotide (phosphate) (NAD(P)H) 3:86–87, 5:86
ninth-order vortex CGH 4:37*F*
NIST 4:436
nitric oxide (NO) 3:115, 3:120
nitrogen (N) 2:271, 2:327
laser 2:426
nitrogen-containing heterocyclic compounds 5:277
noble gas 2:373
noble gas ion lasers
see also up-conversion lasers
Ar II laser blue-green wavelengths 2:377*T*
energy levels in neutral and singly ionized argon 2:377*F*
4p and 4s doublet levels in singly ionized argon 2:376*F*
Krypton ion laser wavelengths 2:379*T*
operating characteristics 2:379, 2:380*F*
technology 2:379–382, 2:380*F*, 2:381*F*
theory of operation 2:376–379
ultraviolet argon ion laser wavelengths 2:378*T*
nodal points and planes 1:107–109
noise
in cascaded optical amplifiers 1:273
noise-free image 3:188

in optical transmission systems 1:272–275
sources 1:437–442
spectral intensity theorem 4:428
suppression 2:190
noise equivalent power (NEP) 1:420, 4:475
noise equivalent temperature difference (NETD) 1:419, 3:233, 3:235–237, 3:236F
noise factor (*F*) 1:242–243, 4:428
noise figure (NF) 1:242, 1:357, 1:361–362, 4:5, 4:431
nominal pulse density (NPD) 4:401
nominal pulse spacing (NPS) 4:401
non return to zero (NRZ) 1:365
non-confocal "split detection" 5:76–77
non-Doppler incoherent lidars 4:463
non-emissive display 3:1, 3:5–6
non-fiber-related effects 1:271–272
linear crosstalk 1:271–272
noise in optical transmission systems 1:272–275
non-Hermitian operators 4:291
non-integrable situation 2:65
"non-interferometric" techniques 3:146
non-invasive vision correction 5:126–127
non-orthogonal functions 4:194–195
non-parabolic bands 2:46–47, 2:88–89
non-perturbative phenomena 2:54
non-perturbative quantum interference 2:35–36, 2:35F
non-polarizing beam splitter (NBS) 4:502
non-radiative (NR) 5:241
Auger effects 2:114–115
decay processes 5:225–226
identification of Auger effects 2:116–117
impact ionization 2:115–116
processes 2:114–115
recombination 2:463–464, 2:464
relaxation 2:442–444
transition 2:3
non-relativistic classical mechanics 4:199
non-resonant
excitations 1:449, 2:33–34, 2:33
phenomena 1:452
THz detection 1:423
non-return-to-zero (NRZ) 1:247, 1:275, 1:294, 4:6, 4:7F, 4:68
data 4:21–22
modulation format 2:74
pulses 1:20–21
non-Telecentric architectures 3:36
non-zero dispersion shifted fiber (NZDSF) 1:9, 1:21, 1:23, 1:261, 1:262, 4:16, 4:24–25
noncentrosymmetric materials 1:489–490, 1:490
noncollinear AOTF orientation 1:138F
noncollinear devices 1:139
noncollinear optical gating (NOG) 2:321
noncollinear optical parametric amplifier (NOPA) 2:298–299, 2:299F
noncontact 3D metrology 4:439
noncontinuity 3:158
nondegenerate four-wave mixing 4:314–315, 4:315F
nondegenerate FWM 1:250–251, 1:349, 1:349F
nonequilibrium statistics 2:111
nonexistence 3:158
nonhyperspectral method 3:213
nonideal amplifier 1:352
nonlinear (NL) 4:311
absorption 4:351–352, 4:352T
applications of fiber gratings 1:239–240
equations 4:329–330
generation of THz radiation in mid-IR QC-lasers 1:384–385, 1:385F
impairments 1:305–306
luminescence transition 1:461
microscopy 5:193
nonlinear-fiber optics 1:177
ophthalmoscopy theory 5:85–86
phenomena 1:180–181
polarization 2:244, 4:335–336, 4:349
process 1:407
quantum electrodynamics 4:338
refraction 4:350–351
refractive index 1:177, 4:335–336
response 1:345–346, 1:368, 2:23–25, 2:23F
second-order parametric interaction 2:291
signatures 1:345–346, 1:345F
spectroscopy techniques 2:53
systems 3:144
technique 2:82
THz spectroscopy 2:197
nonlinear coefficient 1:320–321, 2:312
methods for measuring 1:321
Nonlinear Compensation (NLC) 1:278
nonlinear crystals 4:287
OR 1:405–409, 1:406F, 1:407T
organic crystals 1:409–411
tilted pulse front 1:409, 1:410F
nonlinear effect 1:255, 1:320–321, 2:15, 4:54, 4:220–221, 4:221F, 4:337–338
FWM 1:321–322
linear and nonlinear signatures 1:345–346
nonlinear coefficient 1:320–321
parametric phenomena in optical fibers 1:347–348
physical origin of optical nonlinearity 1:346–347
SBS 1:321
SPM 1:321
SRS 1:321
XPM 1:321
nonlinear fiber effects 1:257–259
dominance 1:258F
values of nonlinearity for various types of transmission fiber 1:258T
nonlinear frequency
conversion methods 2:145–146
generation 2:421–422
nonlinear optical
effects 1:491, 2:424, 4:348
frequency mixing schemes 4:339
interactions 1:10–11
phenomena 4:347
processes 4:342–344, 4:343F
techniques 2:348
nonlinear optical loop mirror (NOLM) 1:368, 4:41, 4:41–42, 4:41F, 4:42F, 4:64
nonlinear optical medium, nomenclature with 4:349–350
complex quantities 4:350
nonlinear absorption 4:351–352, 4:352T
nonlinear refraction 4:350–351
nonlinear susceptibility 4:349–350
nonlinear optical PC
collimated beam 4:322F
mechanism of double PC 4:325F
recording of hologram 4:323F
SBS 4:322F
tail-biting scheme of phase conjugation 4:324F
nonlinear optical spectroscopy 2:245
in chemistry 2:245–246
harmonic conversion 2:246
higher-order and multidimensional spectroscopy 2:249
second-order spectroscopy 2:245–246
spatially resolved spectroscopy 2:249–250
surface second-order spectroscopy 2:246–247
techniques 2:53
third-order spectroscopy 2:247–248
ultrafast time resolved spectroscopy 2:248–249
nonlinear optics 1:10, 1:345, 4:321, 4:335, 4:350
see also electro-optics (EO)
'black box' approach 4:321
causal linear system 4:318F
implication of causality 4:320–321
KK relations 4:317
nonlinear absorption coefficient 4:319F
nonlinear polarization 1:11–12
planar waveguide 1:11F
in Raman resonance 4:344–345
SHG in crystals 1:12–16, 1:13F
texts 4:317
third-order nonlinear effects 1:16–18
two-photon absorption coefficient in semiconductors 4:321F
for weak CW fields 4:345–346, 4:345F
Nonlinear Phase Noise (NLPN) 1:306
nonlinear Schrödinger equation (NLSE) 1:18–19, 1:258, 2:425–426, 4:279–280
nonlinear susceptibility 4:342, 4:349–350
properties 4:311
nonlinear tolerance (NLT) 1:283
nonlinear-optical FWM 4:323
nonlinearity 1:18, 1:172, 2:394
forms of 4:282
nonplanar ring oscillators (NPRO) 1:440–441, 2:454, 2:454–455, 2:454F
nonpolar InGaN layers 2:279
nonradiating sources 3:139, 3:160
nonreciprocal two-port optical device 1:343
nonrelativisitc Schrödinger equation 2:234–235
nonrephasing
complex signal fields 2:184–185
signals 2:185–186

nonrephasing (*continued*)
  spectrum 2:56
  2D spectra 2:154–155
nonspherical surfaces 1:121–122
nonthermal regime 2:82, 2:84
nonuniqueness in imaging 3:156
  inverse source problem 3:159–161, 3:162*F*
  matrix formulation of imaging and inverse problems 3:156–157
  nonuniqueness and prior knowledge 3:157–159
  phase retrieval 3:161–163
nonvisible radiation 5:185
nonwavelength-selective branching devices 1:336, 1:340–341
normal dispersion 1:5, 1:195, 1:315
normal operation 2:76, 2:77*F*
normal-mode coupling 1:459, 1:462
normalization 5:56
normalized shift 1:216, 1:217*F*
Normative References (N.R.) 1:286
novelty filter 4:332–333
nuclear
  gamma irradiation 1:326–327
  motion control 5:39
  shrinkage 3:107
  spin of phosphorus atom 1:474
nuclear magnetic resonance (NMR) 2:197
  spectroscopy 2:249
  spectroscopy studies 2:174
number of degrees of freedom (NDF) 3:137
numerical aperture (NA) 1:201, 1:213, 1:215, 1:223, 1:323, 1:324–325, 3:155, 5:177–178, 5:186
numerical correction (NC) 4:500
numerical reconstruction
  by convolution approach 4:144*F*, 4:145–146
  by lensless Fourier approach 4:146–147
NVTHERM model 3:239
Nyquist condition 4:432–433
Nyquist interval 4:376
Nyquist WDM 1:275

O

object plane 4:369–371
  imaging system 4:370*F*
object signal (OS) 4:500
object space 3:158
  focal length 1:101–102
object wave 1:376
object-image matrix 1:105–106
obliquity factor 1:82–87, 1:84*F*
OCT angiography (OCTA) 5:64–65, 5:161–162
1,8-octanedithiol (ODT) 5:262–263
ocular aberrations 5:108
ocular coherence tomography (OCT) 5:142
  capillary velocimetry 4:526, 4:526*F*
ocular target tissue 5:133–134
odd-parity hidden order in Sr_2IrO_4 2:217–220, 2:218*F*, 2:219*F*
OFDMA 1:255
off-axis
  geometry 4:102
  hologram 4:107, 4:108*F*
  method 3:207
  reference star 3:202
  system 4:102–103
  technique 4:151
off-axis IPRG 4:369, 4:374–375, 4:381, 4:382*F*
  estimation 4:376–377
  Fourier plane 4:374–375
  MATLAB® code to exploring 4:386–395
  sampling quotient 4:375–376
  shot-noise limit 4:377
  SNRs 4:376–377
off-axis PPRG 4:369, 4:377–378, 4:381–385, 4:383*F*
  estimation 4:378–379
  Fourier plane 4:377–378
  MATLAB® code to exploring 4:386–395
  sampling quotient 4:378
  shot-noise limit 4:379
  SNRs 4:379
off-axis reference beam hologram (OAH) 4:106, 4:107, 4:109
OFF-DWBA algorithm, traffic flow of 2:80, 2:80*F*
off-resonant interaction sequences 2:203
"off-the-shell" components of Fourier spectrum 3:139
'offset quantum-well' technology 4:244
OHD-RIKES method 2:248
omnidirectional range 1:209
omnidirectional reflectance 1:207
omnidirectional reflection 1:209
omnidirectional surfaces and fibers
  bandstructure for multilayer fibers for external reflection applications 1:211–213
  fabrication approach 1:210, 1:210*F*
  materials selection criteria 1:210–211
  mechanical tuning experiment and discussion 1:216, 1:216*F*
  mesostructured fibers for external reflection applications 1:209–210
  mirror fibers, optical characterization of 1:213
  omnidirectional reflecting mirrors 1:207–209
  preform construction process and fiber draw 1:211
  simulation of opto-mechanical behavior of fabry–perot fibers 1:215–216
  structure and optical properties of fabry–perot fibers 1:214–215, 1:214*F*
  'tunable fabry–perot' fibers 1:213–214
  wavelength-scalable hollow optical fibers 1:216–220, 1:220*F*
on-axis PSRG 4:369, 4:379–380, 4:384*F*, 4:385
  estimation 4:380
  MATLAB® code to exploring 4:386–395
  shot-noise limit 4:380–381
  SNRs 4:380
on-chip Raman lasers 2:267–268
  Feynman diagram 2:268*F*
on-off keying (OOK) 1:265, 1:275, 4:242
"on-the-shell" components of Fourier spectrum 3:139
On/Off Keying (OOK) 1:291
one dimension (1D) 2:184
  artificial molecules 1:382
  beam characterization 4:176–177
  Doppler-resolved projections 4:488
  Fourier transform spectroscopy 2:151
  laser techniques 4:474
  1D TNTs 5:275
  nonlinear spectroscopy 2:53
  photonic crystals 1:169
  PST for 4:176–177
  system 1:170
  unbounded disordered systems 4:278
  Walsh functions 5:17–18
one way phase conjugation 3:209–210, 3:209*F*
one-atom maser 1:452, 1:454*F*
one-time pad 1:481
opaque screen 1:94–95
open-circuit voltage (V_{oc}) 5:258, 5:258–259, 5:270
open-loop techniques 5:39
operational expenditure (OPEX) 2:74, 2:82
operational functionality 1:459
ophthalmic AO systems 5:72
ophthalmic lenses 5:54, 5:118
ophthalmology 3:199, 3:203
  laser and light interaction and ocular target tissue 5:133–134
  light and laser therapy 5:130–131
ophthalmoscopy 5:72
OPScan series 2:287–288
OPSilent series 2:287–288
optic axis 1:150
optical 2DCS 2:62
  coherent light–matter interaction 2:53–56
  experimental implementation of 2DCS 2:56–57, 2:57*F*
optical 3R regenerator 1:368
optical absorption 1:142, 2:105–106, 2:106, 2:107–108
  spectrum 2:107
optical addressed spatial light modulators (OASLMs) 4:114
optical amplifier (OA) 1:263–265, 1:343, 1:362
optical axis 2:329, 3:198, 5:43, 5:47–48
Optical Band-Pass Filter (OBPF) 1:277
optical beam induced current (OBIC) 5:193
optical bench metrology of IOLs 5:124–125
optical biopsy 4:516–517
optical Bloch equations (OBEs) 2:27–28, 2:53, 2:54, 2:82, 2:152, 4:265
optical carrier-level N signal (OC-N signal) 4:17
optical cavity 1:214, 2:280, 2:351
Optical Channel Data Unit (ODU) 1:287
Optical Channel Payload Unit (OPU) 1:287
Optical Channel Transport Unit (OTU) 1:287
Optical Channels (OCh) 1:287
optical characteristics of display 3:70

ambient illumination and reflection 3:72–73
BRDF 3:73–74, 3:74F
color 3:71
temperature 3:75–76
triangle 3:76, 3:77F
contrast ratio 3:72
gloss 3:71
illuminance 3:70–71
Lambertian surface 3:74
luminance 3:70
PPI 3:75
radiometric and photometric units 3:70
reflectivity 3:71
refresh rate and frame rate 3:77–78
resolution and image sharpness 3:75
response time 3:76–77
uniformity 3:71–72
viewing angle 3:74–75
viewing cone 3:74–75
optical characterization 2:258
optical circulator, principle scheme of 1:342, 1:343F
optical clock recovery 1:369
optical coherence
see also coherence
applications 1:46–47
interference spectroscopy 1:47–48
Stellar interferometry 1:47
theory 1:34
optical coherence elastography (OCE) 5:146
optical coherence tomography (OCT) 3:222–223, 3:223F, 3:224F, 4:174, 4:504, 5:64, 5:77, 5:78, 5:155, 5:156F, 5:159F, 5:163F
dispersion 5:160
FD-OCT 5:156–158
imaging of human retina 5:163–166
imaging of human skin 5:162–163
OCTA 5:161–162
principle 5:155–156
resolution 5:158–159
sensitivity 5:159–160
TD-OCT 5:155–156
wavelength range 5:160–161
optical coherent detection 1:374–375
optical communications 2:269
systems 1:291, 4:20
optical compensation film 3:59–60
optical components 5:309
optical conductivity 2:131
optical confinement technique 5:303
optical connectors 1:336, 1:338
with alignment by means ferrule 1:338
with direct alignment of bare fiber 1:338
multifiber connectors 1:338–339, 1:339F
optical coordinate 5:188
transformation 4:182
optical cycle 2:15–16
optical damage 4:336–337
optical decision element 1:367–369
optical detection devices 3:146
optical devices 4:290
optical diffraction tomography 4:174
optical disk drives 4:193
optical distribution network (ODN) 2:73
optical Doppler tomography, velocity measurement with 4:526
OCT capillary velocimetry 4:526
speckle contrast tomography 4:526
time dimension in velocity measurement 4:526
triple-beam spectral-domain OCT 4:526–528
Optical Duobinary (ODB) 1:275, 1:279
coding 1:280F
format 2:80
optical elements 4:178
optical emission 2:1–8
optical entanglement application 1:484
lithography 1:484
quantum computing 1:484
two-photon imaging and microscopy 1:484
optical fiber 1:10–11, 1:178–179, 1:221, 1:308, 1:336, 2:269, 4:1–3, 4:13
development 4:14–16
diameter measurement 1:32
fabrication 1:27, 1:28F
fiber coating 1:32–33
fiber drawing 1:30
furnaces 1:30–32
FWM 1:348–349, 1:349F
linear effects 1:255–256
nonlinear fiber effects 1:257–259
optical Kerr effect 1:348
parametric phenomena 1:347–348
preform fabrication 1:28
structure 4:14–15, 4:14F
supercontinuum generation 2:426–427, 2:426F
telecommunications 4:67
transmission effects 1:255–256
types of fiber 1:33
optical fiber amplifiers (OFAs) 1:242
optical fiber cables 1:328
blown fiber 1:334–335
cable core 1:330
components 1:330
filling compounds and other components 1:332
secondary fiber coating 1:328
sheaths 1:331–332
special cables 1:334
strength member 1:330–331
structures 1:332–333
submarine cables 1:334
types and applications 1:333–334
optical fiber communication systems 1:23, 4:67–68
chromatic dispersion 4:21–22
optical fiber gratings
applications 1:236–237
chromatic dispersion control 1:238–239
fabrication 1:234–236
fiber modes 1:229, 1:230F
fiber sensors 1:237
grating enhanced continuum 1:240F
nonlinear applications of fiber gratings 1:239–240
optical filtering 1:238
stabilized diode lasers and fiber lasers 1:237–238
theory 1:229–234
optical fill factor 4:419–420
optical films 3:28, 3:28F
optical filtering 1:238, 4:35–136
optical frequency 2:329–331, 4:1–2, 4:17
oscillations 4:341–342
optical frequency combs *see* highly stabilized mode-locked lasers
optical frequency domain imaging (OFDI) 4:504–505
optical gain 2:417
optical heterodyne detection (OHD) 2:248
optical heterodyning 1:374–375
optical holography 4:102
optical hybrid (OH) 1:297
optical imaging
systems 3:142, 3:272, 5:14
techniques 3:156
optical implementation 4:189–190
optical information 1:374
optical insulator 1:169
optical intensity 2:244
optical interconnects 4:254
optical interferometers 1:368
optical interferometric micro-lidar 4:502–504
optical isolator (OI) 4:500
optical Kerr effect (OKE) *see* self-phase modulation
optical limiting 4:332–333
optical line terminals (OLTs) 2:73
optical logic gates 1:251
optical low-coherence tomography 4:504
in cerebrovascular and cardiovascular research 4:506–507
SD-OCT 4:504–505
SS-OCT 4:505
TD-OCT 4:504
optical low-coherent tomography (OCT) 4:496
optical markers 2:82, 2:85
optical maser 1:99, 1:99–100, 2:451
optical masks 5:16
intensity distribution
along axis around image/focal plane 5:22–27
on neighboring transverse planes 5:27
on transverse image/focal plane 5:19–22
Walsh filters as 5:19
and self-similarity 5:27–28
Walsh functions 5:16–17
optical materials 5:91
optical measurements 5:64
locating eyes far point with 5:111
optical methods 5:190
optical microcavity 1:456
optical microscopy 5:175, 5:185
optical mode density 2:107
optical modulation 1:291–293
high-order modulation 1:293–295
modulators 1:292–293
optical modulator 2:262
optical multiplex section (OMS) 1:287
optical multiplexer 1:357
optical multiplexing 4:35
optical network 1:342

optical network unit (ONU) 1:252, 2:73
optical nonlinearities 1:239, 4:25–26
  as factors in dispersion compensation 4:22–23
  FWM 4:23–24
  physical origin 1:346–347
  SPM 4:23
  XPM 4:23
optical packet switching 4:227–230, 4:229F
  core router growth 4:230
  HPC switched interconnect 4:230–231
  switch core growth 4:230
optical parameters
  absorption cross-section 3:221
  photon migration in scattering media 3:221–222
  scattering cross-section 3:220–221
optical parametric amplification (OPA) 2:166, 2:290, 2:290F, 2:295F, 2:296F, 2:311, 2:314, 2:314
  architecture 2:294–295
  general OPA scheme 2:294–295
  optical parametric CPA 2:299–300
  parametric amplification 2:295–297
  phase matching 2:293
  pulse compression 2:297–298
  seed generation 2:295
  theory 2:290–292
  ultra-broadband OPAs 2:298–299
optical parametric chirped pulse amplification (OPCPA) 2:166, 2:290, 2:299–300, 2:300F, 2:311, 2:314, 2:315F
optical parametric generation (OPG) 2:295
optical path compensator (OA) 4:500
optical path difference (OPD) 3:213
optical path lengths determiniation 5:112–113
optical perturbation 4:321
optical phase 5:39
  shifters 4:236–239, 4:237F, 4:239F
  space 3:164
optical phased locked loops (PLL) 4:45
optical phonons 2:84
optical PLL (OPLL) 1:296–297
optical polarization 4:264
optical pre-amplifiers (OPA) 1:248–249, 1:273
optical processing functions 1:24
optical propagation loss 4:217
optical pulse
  chronocyclic tomography for characterization 4:179
  mathematical representation of 4:48–49
optical rectification (OR) 1:405–409, 1:406, 1:406F, 2:120, 2:121
optical regeneration by saturable absorbers 1:369–370
optical resonator 2:329–331, 2:330F, 2:371–372
  stability 4:161–162
optical response features in correlated electron materials 2:131
optical routing 4:243
  switches 1:147
optical scanning holography 1:377–378, 1:378F
optical sectioning, structured illumination to 5:199F, 5:200F, 5:201–202
optical sensing technology 3:86
optical setups for PST 4:178–179
optical signal
  dispersion effect on 1:1–5
  processing 1:130
  regeneration 1:364
optical signal to noise ratio (OSNR) 1:274, 1:274F, 1:355, 1:360, 1:361, 1:366–367, 4:5
optical solitons 1:180
  formation 2:425–426
optical sources 4:38
optical spacer 5:302–303
optical spectroscopic methods and techniques 3:95
optical spectroscopy 2:130–131
optical spectrum 1:141
optical spectrum analyzer (OSA) 2:460
optical Stark effect 4:271
Optical Supervisory Channel (OSC) 1:287
optical susceptibility tensors 2:208
optical switche(s) 1:214–215, 4:224, 4:225T
  cell 4:234
  evolution from static links to optical switching 4:224
  existing and proposed deployments of optical switches 4:224–225
  families of optical switch technologies 4:226, 4:226T
  free-space optical switch technologies 4:231
  optical packet switching 4:227–230
  packet switch capacity growth 4:225
  patch panels 4:225
  planar lightwave circuit optical switch technologies 4:233
  protection and provisioning 4:225
  reconfiguration within data center 4:225
  ROADM, using wavelength selective switch 4:226–227
  switch characteristics 4:225
  terminology of optical switching 4:224
  tunable laser optical switch technologies 4:241
optical switching in PCF 1:181
optical systems 2:329, 4:174, 4:175
  analysis and design 3:164
  for DLP 3:36
  for single-panel projection applications 3:36, 3:36F
optical technique 3:95, 4:34, 4:103, 5:39
optical time division multiplexing (OTDM) 4:34, 4:35, 4:60, 4:61F
  BER performance 4:45–47, 4:47F
  bit interleaved OTDM 4:35–36, 4:36F
  clock and data synchronization in 4:44–45
  communication system 4:61–63
  components 4:38
  networking issues 4:65–66
  packet interleaved OTDM 4:36–38, 4:37F, 4:38F
  principle 4:35, 4:35F
  TDM 4:60–61
optical time domain measurement method 1:313
optical time domain reflectometer (OTDR) 1:309, 4:438
optical transfer function (OTF) 3:173, 4:169, 5:112
  with defocusing 4:169
optical transmission systems, noise in 1:272–275
Optical Transport Hierarchy (OTH) 1:287
optical transport network (OTN) 1:287
  layering and monitoring 1:288F
  layers 1:287, 1:288F
  mapping and multiplexing 1:287–288, 1:288F
  operations and monitoring aspects 1:288–289
  tandem connection monitoring example 1:289F
Optical Transport Section (OTS) 1:287
optical vortices 4:136–137
optical waveguides 1:10–11
optical wide-gap material 4:302, 4:303F
optical-optical-optical (OOO) 4:224
optical-pump, optical-probe (OPOP) 2:133
optical-pump THz-probe (OPTP) 2:136, 2:136–137, 2:137
optical-pump/THz-probe magnetospectroscopy of semiconductor quantum wells 2:76–77
optical-to-electrical-to-optical (OEO) 4:224, 4:224F
optically compensated bend mode (OCB mode) 3:27, 3:61
optically detected FIR resonance spectroscopy of semiconductor quantum wells 2:75–76
optically detected resonance (ODR) 2:75, 2:76F
optically pumped molecular gas lasers 1:379–380
optically pumped semiconductor lasers (OPSLs) 2:280, 2:280F, 2:413–414, 2:448–450
  applications 2:287–288, 2:288F
  background 2:281
  cavity configurations 2:285
  design strategies 2:281–283
  gain structure 2:283
  high power, wavelength tunable, high brightness CW OPSLs 2:285–286
  high power narrow linewidth CW OPSL sources 2:286
  intra-cavity SHG and DFG OPSLs 2:287
  loss mechanisms 2:283–284
  low noise multi-gigahertz repetition rate femtosecond pulsed OPSLs 2:286–287
  pumping schemes 2:284–285, 2:284F
  quantum dot CW OPSL sources 2:286
optically-induced transitions 2:152
optics 3:137–138, 4:193
optimal control 1:487
optimal control experiments (OCEs) 5:31
  algorithms for implementing 5:34–38

closed-loop formulations for attaining laser control 5:37F
dissociative rearrangement 5:36F
optimal control theory (OCT) 5:31
optimal spectral 1:487
optimum energy distribution 2:334
optimum mean value 2:334
opto-acoustics *see* photo-acoustic
optoelectronic (OE) 5:6–7
applications 2:88–89
components 3:87–88
detector design 5:6–7
devices 1:141–142, 2:98–99, 2:105
LD 3:87–88
LED 3:88
OLED 3:89
OPD 3:89
optoelectronics/electronics 3:94
PLLs 4:45
properties 4:217–220, 4:218F, 5:282
regeneration 1:364–365
sensing system 3:86–88, 3:87F
silicone photodiode 3:88
SiPM 3:88–89
VCSEL 3:88
optoelectronic sensor 3:86–87
data processing algorithm for 3:89–91
quasi-spectral analysis 3:91
ratiometric analysis 3:90–91
"order" of perturbation theory 2:153
ordinary polarization directions 2:293, 2:293F
ordinary ray 1:150
organic crystalline materials 1:142
organic crystals 1:409–411
organic dielectrics 3:15
organic dye lasers 5:309–310
organic dyes 5:277
organic electro-optic
chromophore 1:144–146
materials 1:144
organic electronic devices 5:220, 5:227
organic field effect transistors (OFETs) 5:227–229
organic hosts 2:346–347
organic lasers
conjugated polymers 5:309
gain measurement 5:311–313, 5:312F
organic semiconductor gain materials 5:310–311
organic semiconductor lasers 5:309–310
plastic diode lasers 5:314–316
polymer laser resonators 5:313–314
organic layer–bulk heterojunction 5:322
organic layer–single material 5:321–322, 5:321F
organic light emitting diode (OLED) 1:445, 1:448F, 3:1, 3:5, 3:5F, 3:56, 3:64, 3:89, 5:220, 5:229F, 5:232, 5:232F, 5:240, 5:240F, 5:247, 5:249F, 5:250F, 5:252F
applications 3:67–69, 5:238–239
architectures 5:232
bottom-emission and *p-i-n* 3:65F
carrier injection and materials 5:232–233
carrier transport and materials 5:233–234
cavity effects in 1:447–448
degradation of OLEDs 5:238
devices 3:65–67
displays and lighting 3:68F
doped transport layer 5:234–235
electromagnetic modeling of light generation 3:68F
exciton formation and decay 5:235–237
host-guest system 5:237–238
materials 3:64–65, 3:66F
perspectives 3:69
small molecule and polymer OLEDs 5:232
organic light-emitting diodes/light extraction
light extraction of plasmonic mode 5:251–253
light extraction of substrate mode 5:248
light extraction of waveguiding mode 5:248–251
organic light-emitting transistors (OLETs) 5:227, 5:230F
organic macromolecular materials 1:143
organic materials 4:331
organic optoelectronics 3:89
organic PD (OPD) 3:89
organic photodetectors 5:317
organic photodiodes 5:317–319, 5:317F, 5:318F
organic phototransistors 5:319–320
with polymers 5:326–327
photosensitivity of 5:320–321
with polymers 5:322–324
with small molecules 5:321–322, 5:325–326
organic photodiodes 5:317, 5:317–319, 5:317F, 5:318F
organic layer–bulk heterojunction 5:322
organic layer–single material 5:321–322, 5:321F
with polymers 5:322–324
with small molecules 5:321–322
organic phototransistors 5:317, 5:318F, 5:319–320, 5:319F
organic layer–bulk heterojunction 5:326
organic layer–single material 5:325–326
with polymers 5:326–327
with small molecules 5:325–326
organic photovoltaics (OPV) 5:256, 5:287
acceptor materials 5:265
devices 5:224, 5:259–260, 5:298
materials 2:194
strategy to improving BHJ device performance 5:260
organic polymers 3:89
solar cell structure evolution 5:259
organic semiconductors (OSCs) 3:15, 5:220, 5:226F, 5:256
concept of doping and p-and n-type OSCs 5:226–227
device applications 5:227–231
electronic structures 5:220–223
excitons 5:223–226
gain materials 5:310–311
lasers 5:309–310
materials 5:317
p-type 5:226–227
solitons, polarons, and bipolarons 5:223
organic sensing channel layers 5:320
organic sensing layer (OSLs) 5:317–319, 5:318F
organic solar cells (OSCs) 5:256, 5:258F, 5:292, 5:293
AR effects 5:293–294
exciton diffusion bottleneck 5:292F
light harvesting 5:292
light trapping 5:294–296
metal nanostructures 5:296–302
other approaches for 5:304–306
spacer layer and cavity effects 5:302–304, 5:304F
ways of harnessing light 5:293F
characterization 5:258–259
principles 5:256–258
organic solvents 5:277
organic thin films 1:445, 3:15, 5:232
organic thin-film transistors (OTFTs) 3:15, 3:53, 5:227
organically modified ceramics (ORMOCERS) 2:346
organically modified silanes (ORMOSILS) 2:346
organic–inorganic hybrid perovskite 5:282
charge carriers transport materials 5:286–287, 5:286F
crystal structure 5:282–283, 5:282F
device structures of perovskite solar cell 5:284–286, 5:285F
ETM 5:287–288, 5:289T
HTM 5:287, 5:287F
optoelectronic properties 5:283–284, 5:284F, 5:285F
tandem solar cell 5:288–290
working mechanism of perovskite solar cell 5:286
organometallic chemical catalysts 2:172
dynamics of homogeneous catalysts 2:172
surface attached catalysts 2:172–173
orientation process 4:95–96
ORMOSIL host matrices 2:347
ortho-symplectic matrices 4:200
orthodoncy, mode-locking as 2:303–304
orthogonal frequency division multiplexing (OFDM) 1:255, 2:74, 2:83, 2:84F
orthogonal frequency division multiplexing-passive optical networks (OFDM-PONs) 2:83–84
orthogonal polarization 4:45
orthogonal superposition 4:175–176
orthoscopic real image production 4:152
out-of-resonance values 4:287
outer diameter (OD) 1:211
outer scale 3:201
output coupler (OC) 1:237–238, 2:329
outside vapor deposition process (OVD process) 1:28, 1:29
outside vapor phase oxidation (OVPO) *see* outside vapor deposition process (OVD process)
overclad tube 1:196
overcoupling/undercoupling 2:448
overlap-projection back-propagation 3:154
overlapping 4:103
oversampling smoothness (OSS) 3:148

oxadiazole derivatives 2:346
oxide disorder 1:469–471
oxide heterostructures 2:129
oximetry images from patient eyes 4:522, 4:522*F*
oxygen-dependent photobleaching 3:102
Oxymap Analyzer 4:522
Oxymap T1 instrument 4:521–522, 4:521*F*
oxymetry lidars 4:519–522, 4:519*F*

P

p-doped semiconductor 3:87–88
p-FFS 3:60–61
p-terphenyl 2:345
p-transmittance 1:153–154
p-type transition metal oxide–NiO_x 5:265–266
packet interleaved OTDM 4:36–38, 4:37*F*, 4:38*F*
packet interleaving *see* packet level
packet level 4:35
packet switch capacity growth 1:225
pain, PBM for 3:118
pair braking
  detectors 1:427–428
  photon detectors 1:427–428
panchromatic 4:88
pandrug-resistant (PDR) 3:102–103
panretinal photocoagulation (PRP) 5:131–132, 5:132, 5:134
para-magnetic (PM) 2:127
parabolic gold coated mirror 2:329–331
parabolic quantum 2:19, 2:20–21
paradoxical hypertrichosis 3:119
parallax cues 3:208–209
parallel computing 4:178
parallel fibers, array of 1:214–215, 1:214*F*
parallel resistance (R_P) 5:259
parallel-serial conversion (P/S conversion) 1:277
parallel-tangents condition 1:139
parametric (mixing) processes 1:181–183
parametric amplification of emission 1:460
parametric effects 1:345
parametric instabilities 1:442
parametric optical amplifiers 1:263
parametric superfluorescence (PSF) *see* optical parametric generation (OPG)
paraxial approximation 4:175
paraxial focal plane 1:114–116
paraxial matrices 1:102–104
paraxial optical models 4:199
paraxial optical system
  propagation in 4:168
  propagation through 4:167
paraxial ray vector 4:205–206
paraxial schematic eyes 5:48
paraxial system for design or analysis 1:110–111
paraxial transverse profile 4:180
paraxial wave state 4:180
"paraxial" schematic eyes 5:44
parity-broken nematic order in $Cd_2Re_2O_7$ 2:216–217, 2:217*F*
parity-time symmetry (PT symmetry) 4:291, 4:292*F*
  anomalous scattering properties of PT-symmetric arrangements 4:300–301
  mode management in PT-symmetric lasers 4:293–294
  sensing at exceptional points 4:298–300
  spontaneous symmetry breaking and EP 4:291–293
  three photonic PT molecules 4:299*F*
Parkinson's disease (PD) 3:124, 3:125
Parseval's theorem 4:376
partial coherence algorithms 3:148–149
partial coherence KF-PR algorithm 3:151
partial coherence properties in image of incoherent source 4:162
partial differential equations 3:258
partial mirror (PM) 4:507
partial response pulse (PR pulse) 1:275
partial response signaling 1:278–280
partial Talbot effect 4:166–167
partially coherent illumination, PSF for 3:263
partially coherent impulse response 3:263
partially coherent sources and fields 1:34
partially redundant pupil masking (PRPM) 3:279
participation number 4:282
particle image velocimetry (PIV) 4:470, 5:68–69
particle motion 1:139
particle scattering 4:317
passive component 1:223–224
passive dynamic holographic display devices (PDHDDs) 4:114
passive matrix (PM) 5:239
passive matrix driving method (PMLCD) 3:30–31, 3:30*F*
passive matrix OLED (PMOLED) 5:239
passive mode-locking 2:337
passive optical components 1:336, 1:342–343
  branching devices 1:339–341
  general considerations 1:336–338
  mechanical splices 1:339
  nonwavelength-selective branching devices 1:340–341
  optical connectors 1:338
  optical joint devices 1:336–338
  WDM 1:341–342
passive optical networks (PON) 1:280–281, 4:224
  BPONs 2:73, 2:74, 2:74, 2:75*F*
  ER-PONs 2:82–83, 2:82*F*
  GE-PON 2:73, 2:76
  GPON 2:73, 2:74–76, 2:75*F*
  NG-PON1 2:73, 2:74, 2:76–78
  NG-PON2 2:78–79
  OFDM-PONs 2:83–84
  TDM-PONs 2:74
  topology 2:73
  WDM PONs 2:74, 2:81–82
passive Q switching 2:419–421, 2:420*F*
  with bulk saturable absorbers 2:419–421
  with semiconductor saturable-absorber mirrors 2:421
passive SA-based optical regeneration 1:370
passive static optical filters 1:266
passive waveguide and guided wave optics 1:221
passive WDM filters and couplers 1:265–268
passive-matrix OLED (PM-OLED) 3:66
patch panels 4:225
path-independent loss (PILOSS) 4:235, 4:235*F*
pathogen classification 3:103–105
pattern
  effects 1:245
  pattern-projecting matricial sensors 4:511–512
  recognition and image filtering 4:332
Pattern Dependent Phase Distortion (PDPD) 1:245, 1:247–248
pattern-recognition receptors (PRRs) 3:112
patterned vertical alignment LCD (PVA-LCD) 3:62
Pauli blocking 1:460
Pauli exclusion principle 2:63, 2:84–85, 2:99, 2:106, 2:464, 3:64
Pauli-blockade mechanism 1:473
pay as you grow approach 1:361
PDM-QPSK 1:295
  transmission 1:295
2PE *see* two-photon excitation (TPE)
peak to average power ratio (PAPR) 2:83
PEDOT doped with poly(4-styrene sulfonate) (PEDOT:PSS) 5:279–280
pentacene 5:321–322, 5:321*F*
pentacene photodiodes 5:321–322
pentaprism 1:125–126, 1:125*F*, 1:126*F*
perfectly coherent fields 1:41
periodic dispersion compensation 4:24
periodic multilayer structure 1:214
periodic PT-symmetric structures 4:301
periodic structure 1:207
periodically poled $LiNbO_3$ (PPLN) 2:121, 4:39
periodically poled lithium niobate (PPLN) 1:14, 2:287
permanent materials, holographic recording media and devices 4:89–90
  DCG 4:90
  holographic sensors 4:92–93
  photopolymers 4:90–91
  photoresists and embossed holograms 4:91
  PTRG 4:91–92
  silver halide 4:89–90
perovskites 2:71, 2:72*F*
  crystals 4:235
  materials 5:282
  solar cell 5:283
    device structures 5:284–286, 5:285*F*
    working mechanism 5:286
persistent spectral hole burning 4:93–95
perturbation
  second order 2:88
  theory 1:170–171, 1:172–173
perturbed free induction decay (PFID) 2:201
perylene bisimide (PBI) 5:265
perylene derivatives (PTC) 5:260
perylene diimide (PDI) 5:265
perylene dyes 2:345, 2:345*F*

Perylene Orange 2:347
Perylene Red 2:347
perylene-3,4,9,10-tetracarboxylic dianhydride (PTCDA) 5:325–326, 5:325F
perylenes 2:345
perylimide dyes 2:345, 2:345F
Petzval curvature 1:120–121, 1:121F
pharmacological agents 5:120
phase and frequency detector (PFD) 4:436–438
phase compensators 1:413–414
phase conjugation (PC) 3:205, 3:208, 4:313–314, 4:314F, 4:322, 4:325
  formation of true and conjugate images from hologram 3:208F
  holographic mechanism of 4:323
  by holography 3:206–208
  one way phase conjugation 3:209–210, 3:209F
  phase conjugate reconstruction 4:331
  phase conjugated wave 3:205
  pseudoscopic image 3:208–209
phase conjugator 3:205–206, 3:205F
phase contrast 5:185, 5:187
  filter 4:35, 4:36F
  microscopy 5:192, 5:192
  output 4:35, 4:36F
phase control 5:39
phase cycling 2:190
phase difference 4: 98
phase diversity 3:278
  receiver 1:297–298, 1:298, 1:298F
phase factor 1:3–4
phase functions 4:183, 4:185–186, 4:185F, 4:189F
  derivatives 4:186
  general 4:186
phase gradient autofocus (PGA) 4:440
phase lock loop (PLL) 1:296–297, 4:6
phase mask (PM) 1:54, 1:236, 1:236F, 2:211
phase matching 1:11, 1:230, 1:230–231, 1:231–232, 1:231F, 2:166, 2:293
  bandwidth of OPA 2:294
  condition 1:13
  gating 2:238, 2:239F
  interaction types in OPA 2:293
  methods 2:293–294
phase modulation (PM) 1:367–368, 2:304–305, 2:305F, 4:31–33
phase modulator (PM) 1:292, 2:311
phase noise 2:458–459, 2:459F
phase plates 5:119
phase problem 3:146, 3:162
phase retrieval 3:161–163, 3:170–171
  algorithm 3:148, 3:150, 3:152, 4:55, 4:56F
  application to 4:172
  approach for 2D images 4:121–122
  problem 3:162
Phase Retrieval by Omega Oscillation Filtering (PROOF) 2:322–323
phase retrieval transform function (PRTF) 3:148
Phase Sensitive Amplifier (PSA) 1:252
phase shift 3:242–243
Phase Shift Keying (PSK) 1:245
phase shifters 4:181
phase shifting recording geometry (PSRG) 4:369
phase singularities 4:185–186
  derivatives of phase function 4:186
  general phase function 4:186
  phase functions 4:185–186
  transmission function with 4:186–187
phase space
  analysis of classical geometric optical imaging 3:167
  diagram 4:205
  in geometrical optics 4:205–206, 4:207F
  method 4:212
  optics elements 3:164–166
  rotations 4:176
  rotator 4:176, 4:177, 4:178
phase space and imaging
  elements of phase space optics 3:164–166
  holographic imaging 3:168–169, 3:169F
  imaging aberrations 3:167
  lightfield imaging 3:169–170, 3:170F
  phase-space interpretation of image formation 3:166–167
  phase-space tomography and phase retrieval 3:170–171
  pupil design for extended depth of field 3:173
  self-imaging condition 3:167–168, 3:168F
  superresolution imaging 3:171–173, 3:172F
phase space tomography (PST) 4:174
  chronocyclic tomography for optical pulse characterization 4:179
  fundamentals 4:175–176
  light beam characterization 4:174–175
  for 1D beam characterization 4:176–177
  optical setups for PST 4:178–179
  optics 4:174
  PST method 4:175, 4:176
  quantum light characterization 4:179–181
  for quantum light characterization 4:179–181
  tools 4:174
  for 2D Beam characterization 4:177–178
phase spectrum estimation methods 3:275–276
phase velocity dispersion 1:5
phase-added stereogram 4:123
phase-amplitude coupling 2:467–468
phase-conjugate mirror (PCM) 4:313–314
phase-cycling 2:153–154
phase-distorting media 3:205
phase-locked CW laser frequencies 5:41
phase-matching 2:153–154
  angle 2:294
  condition 1:349
phase-modulated wave, spectrum of 1:132F
phase-only transmission function 4:184
phase-reversal zone plate 1:95–96
phase-sensitive detection 5:146
phase-sensitive optical coherence elastography 5:146–147, 5:147F
  applications of optical coherence elastography in ocular tissues 5:147–148
  principles and implementations 5:146–147
phase-shift
  laser rangefinder 4:498, 4:498F
  phase-shifted DFB single-frequency lasers 2:455–456, 2:456F
  rangefinder using heterodyne technique 4:510, 4:510F
  technique 1:315, 1:316F
phase-shift keying (PSK) 1:275, 1:277
phase-space interpretation 3:172
  of image formation 3:166–167
  of tomographic signal recovery 3:171
phase-space optics (PSO) 3:164, 4:164, 4:170F
phase-space representations of freeform optical systems 4:205
  aberration contributions
    calculation at image 4:211–214
    in freeform prism 4:214–215
  aberration propagation in phase space 4:212F
  difference in ray positions 4:208F
  distortion analysis 4:213F
  extension to 4D phase space 4:209–211
  lens data of freeform prism of reference including additional dummy surfaces 4:210T
  phase space in geometrical optics 4:205–206
  ray-propagation and phase space trajectory in optical system 4:205F
  real ray behavior in phase space 4:207F
  transverse aberrations 4:214F
  visualization of aberrations
    in freeform systems 4:208–209
    in phase space 4:206–208
phase-space tomography 3:170–171, 4:169–170
phase-stepping technique 4:509
"phasing" 2DFS signal 2:188–189
phenyl-C61-butyric acid methyl ester (PCBM ester) 2:194, 5:261, 5:262F
[6,6]-phenyl-C_{61}-butyric acid methyl ester (PCBM) 5:288, 5:321–322, 5:321F
1-phenylnaphtalene (PN) 5:263
pheophytins (Pheo) 2:192
phosphate glasses 2:387–388, 2:392
phosphorescence 3:64
phosphorescent EL 5:241–244, 5:242F, 5:243F
phosphorous pentoxide (P_2O_5) 1:28
phosphors 3:3
phosphorus
  donors 1:469
  impurities 1:467
  system 1:469
photo activated chromophore for infectious keratitis (PACK-CXL) 5:136–138
photo diode (PD) 4:6
photo thermoplastic process 4:97, 4:97F
photo-acoustic
  imaging 3:226, 3:226F
  microscopy 5:193
photo-Dember effect 1:404–405
photo-doping process 5:227
photo-elastic coefficient 1:131
photo-elastic constant 1:130

photo-elastic effect 1:130–131, 1:144, 1:160, 1:326
photo-emission microscopy 5:193
photo-induced carriers in solid materials
  built-in field in semiconductor 1:404
  PC antenna 1:403–404
photo-orientation process 4:96
photo-physics of semiconducting polymers 5:311
photo-thermal refractive (PTR) 2:446
photo-thermo-refractive Glasses (PTRG) 4:91–92
photoacoustic spectroscopy 2:6
photoanode 5:273
  conducting substrates 5:273
  semiconductor layers 5:273–275
  sensitizers 5:275–277
photobiomodulation (PBM) 3:114–115, 3:115F
  for cosmetic and esthetic applications 3:118–119
  Cox 3:115
  direct cell-free light-mediated effects on molecules 3:117
  for enhancement of cognitive performance 3:126–127
  enhancement of performance 3:126
  flavins 3:117
  for healing of wounds and tissue damage 3:117–118
  light/heat sensitive ion channels 3:116–117
  mechanisms of action 3:115
  for muscle and athletic performance 3:126
  for neurodegenerative diseases 3:124–125
  for pain and inflammation 3:118
  for psychiatric disorders 3:125–126
  retrograde mitochondrial signaling 3:115–116
  for stroke 3:121–123
  for TBI 3:121–123
  for vision and hearing problems 3:121
photocarrier generation 4:352
photocathode 3:242
photochemical interaction 5:131
photochemical therapy 5:136, 5:136–138
photochromic glasses 4:93
photochromic materials 4:93
photoconductive antenna (PC antenna) 1:403–404, 2:120, 2:121
photoconductivity 4:324
photocurrent gain of APD 4:423
photodetection 1:291, 4:243
  mechanism 3:175
  mode 1:374
photodetector (PD) 1:378, 1:418, 4:500, 4:523, 5:189, 5:194
  photodetector-array apertures 3:177, 3:177F
Photodetector Array Camera and Spectrometer (PACS) 1:425F, 1:426
photodiodes (PD) 1:141–142, 3:88, 4:509–510, 5:2
photodisruption *see* photomechanical interactions
photodynamic alteration of tissue microcirculation 3:111
photodynamic therapy (PDT) 3:100–102, 3:101F
  antimicrobial photodynamic inactivation and PDT 3:102–103
  causes damage to biomolecules and intracellular organelles 3:107F
  mechanisms 3:101–102
  PDT for cancer 3:106–107
photoelectron 2:241
  with attosecond pulses 2:240–241
  hologram mean number of 4:373
  spectrum 2:322
photoemission electron microscopy (PEEM) 2:147
photoexcited bulk semiconductors, FIR magnetoabsorption in 2:73–75, 2:75F
photoexcited system 4:266
Photofrin 3:103F
photographic
  films 1:326
  plate 3:206–207, 3:250–251, 3:252–253
  techniques 5:64
photoinduced absorption (PIA) 2:142–143, 2:194
photoinduced phase transitions (PIPT) 2:139–141
photoionization 1:381
photoluminescence (PL) 1:461, 2:71, 2:73, 2:73F, 2:79F, 2:105–106, 2:108, 2:282, 5:252–253, 5:253F, 5:254F
  excitation 2:394
  quantum 5:309
  spectrum 2:108
photoluminescence quantum yield (PLQY) 5:237–238
photomechanical interaction 5:132–133, 5:138
photomedicine 3:100
photometric units 3:70
photomultiplier tube (PMT) 2:211, 3:86, 3:98, 4:513, 5:73, 5:74
photon density wave (PDW) 3:224, 3:256–258, 3:256, 3:258F
photon density wave imaging (PDWI) 3:256
  see also infrared imaging
  applications 3:259–260, 3:260F
  forward problem 3:256–258
  inverse problem and imaging algorithm 3:258–259
photon echo 2:54–55, 4:272–275, 4:275F
  experiment 2:162
  scheme 2:154
  spectroscopy 2:154
  spectrum 2:56
photon transport equation *see* linear radiation transfer equation
photon tunneling microscope (PTM) 5:190–191
photon(s) 1:224, 1:458, 2:63, 2:410, 3:225–226, 4:180
  absorption 1:487, 5:224, 5:256, 5:305–306
  avalanche 1:97, 2:402–403, 2:404T
  counting 4:446–447
  cutter 2:290
  detection 1:427
  detectors 1:418
  distribution 2:106
  energies 2:19, 2:446
  lifetime 4:220
  migration 3:221, 3:221–222
  photon–atom binding in PC 2:12–15
  propagation 3:97
  statistics 1:452–453, 1:453
  switches 2:18
  teleportation 1:458–459
photonic arrays, devices with 4:507–509
  focus tracking micro-lidars 4:507–509
  pattern-projecting matricial sensors 4:511–512
  range imaging with matricial light-emitting diode array 4:509–510, 4:509F
  time-of-flight principle with matricial detectors 4:510–511
photonic band diagram 1:212–213, 1:212F
photonic band gaps (PBGs) 2:12
Photonic Bandgap-guided fibers (PBG-guided fibers) 1:263
photonic bandgap(s) 1:169, 1:207
  fibers 4:30
  origin 1:170–172
photonic bandstructures 1:185, 2:13
photonic crystal fiber (PCF) 1:177, 1:178, 1:195, 1:262, 1:263, 2:427–428
  see also microstructure fiber(s)
  birefringence 1:179–180
  dispersion 1:178–179
  experiment examples 1:181
  nonlinear phenomena 1:180–181
  optical switching 1:181
  parametric (mixing) processes 1:181–183
  properties 1:178
  supercontinuum generation 1:181
  transverse mode structure 1:178
photonic crystal lasers
  electromagnetics of photonic crystals 1:185–186
  photonic band diagram for photonic crystal slab 1:186F
  photonic crystal resonant cavities and lasers 1:186–189
  photonic crystal waveguides 1:189–193
photonic crystal resonant cavities 1:187–188
photonic crystals (PCs) 1:169, 1:170, 1:185, 1:190–191, 2:12
  cavities 1:187
  defect slab waveguides 1:193T
  electromagnetics 1:185–186
  slab 1:186F, 1:187
  structure 5:295
  waveguides 1:189–193
photonic devices and circuits 4:217
photonic element 4:224
Photonic Integrated Circuits (PICs) 1:242, 1:295–296, 4:216, 4:242
photonic integration 4:242, 4:242F
photonic lattice 1:185
photonic regime 2:119
photonic substrate texturing technique 5:296
photonic switching 4:224, 4:225
photonic techniques 2:118
photonic wire lasers 1:384

photonic-crystal
devices 1:173
slabs 1:173–175
photopolymers 4:90–91, 4:154
photoreceiver input 4:429
photoreceptor(s) 3:17, 5:43, 5:86
bands 5:164
Photorefraction
adaptive signal processing 4:333
applications 4:331
basics of photorefractive effect 4:327
coupled wave equations 4:329–330
distortion compensation by phase conjugation 4:331–332
holographic data storage 4:331
inorganic materials 4:330–331
materials 4:330
optical limiting, novelty filter, and laser ultrasonic inspection 4:332–333
organic materials 4:331
pattern recognition and image filtering 4:332
photorefractive solitons 4:333–334
self-pumped phase conjugate mirrors 4:332
standard rate equation model 4:327–329
photorefractive crystals (PRC) 4:154, 4:324
photorefractive effect 4:96, 4:327
photorefractive gratings 4:331–332
photorefractive intrastromal corneal collagen cross-linking (PiXL™) 5:136
photorefractive keratectomy (PRK) 5:100–101, 5:126, 5:135
photorefractive materials 4:96–97, 4:330
photorefractive nonlinear optics 4:327
photorefractive organic compounds 4:96–97
photorefractive polymer films (PRP films) 4:114
photorefractive solitons 4:333–334
photoresistive material 1:484
photoresists 4:91
photosensitive materials 1:54
photosensitivity 1:234–236
of organic photodetectors 5:320–321
photosynthesis 2:191–192
photosystem II reaction center (PSII RC) 2:192, 2:193*F*
photothermal
cancer treatment 2:262–263
interaction 5:131–132, 5:138
microscopy 5:193
photovoltaic 5:256
effect 1:423
technologies 5:287
phthalocyanine (Pc) 5:260
physical contact solution 1:337
physical imaging system 3:136–137, 3:136*F*
physical interpretation states 1:87
Physical Layer Operation, Administration, and Maintenance (PLOAM) 2:74
physical layer operations administrations and management upstream (PLOAMu) 2:75–76
physical layer overhead (PLOu) 2:75–76
"physical processing" approach 3:137–138
physical transmission layer of worldwide telecommunications network 1:226
physical vapor deposition (PVD) 2:255, 2:260
physiological depth cue 3:44–45
π-phase shift (P_π) 4:237–238
pickup head (PUH) 4:507, 4:508*F*
pico-projector 3:32
picolinate (pic) 5:244
picosecond (ps) 2:124
pulse pumped supercontinua 2:429–431
picture/hologram 4:89
piezo-optic
devices 1:159–160
modulators 1:156–157
piezoelectric effect 2:105
piezoelectric force microscopy (PFM) 2:147
piezoelectric moving-fiber optical switch 4:233
piezoelectric optical switch 4:233
piezoelectric transducer (PZT) 4:98, 4:502
pigmented epithelium 5:130
"pinch-off" phenomenon 5:227–229
pincushion distortion 1:120–121, 1:121*F*
pinhole effect 5:122, 5:123*F*
pixels per inch (PPI) 3:75
planar heterojunction *see* bilayer heterojunction
planar laser induced fluorescence (PLIF) 4:470
planar lightwave circuit (PLC) 2:385, 4:39, 4:233, 4:234*T*
blocker 4:233–234
interferometer 4:233
interferometric optical switch 4:236
materials and physical principles 4:233
materials for planar lightwave optical switches 4:235–236
moving waveguide coupler 4:233
optical switch technologies 4:233
scaling up planar lightwave optical switch 4:234
SOA switch 4:239–240
waveguide-MEMS optical switch 4:240–241
planar lightwave optical switches materials 4:235–236
planar mirror 3:262
planar technique 1:340
planar waveguide 1:10–11, 1:11*F*, 2:384–385
planar waveguide lasers (PWL) 2:384, 2:385–387
see also infrared imaging
DBR 2:388–389
DFB 2:389–391
lasers 2:385
materials 2:387–388
planar waveguides 2:384–385
pumping 2:392–393
PWL arrays 2:391–392
stability 2:393
systems 2:393
waveguides 2:384
Planck's black-body law 3:230, 3:231*F*
Planck's constant (h) 5:89
plane of polarization 1:148, 1:162
plane wave 1:162, 1:376
approximation 1:131–132
basis 1:172
spatial structure 4:180
plasma
display 3:1, 3:4–5, 3:4*F*
double sheath 2:381–382
formation 5:92
frequency 2:132
gas dry etch processes 4:217
nonlinearities and relativistic effects 4:337–338
temperature 2:464–465
plasma-enhanced chemical vapor deposition (PECVD) 3:13
Plasmon mode 3:67
Plasmon oscillation 2:118
plasmonic(s) 5:296–302, 5:297*F*, 5:298*F*
materials 2:252
NPs 5:298
plasmonic mode, light extraction of 5:251–253
resonators, molecules in 1:446–447
structures 5:295
plastic(s) 5:309
diode lasers 5:314–316
electronics 5:220
fillers 1:332
films 5:317
plateau region 2:317
platinum (Pt) 5:279
plug and socket 1:338
plug stile attenuator 1:342
plug–adapter–plug configuration 1:338, 1:339*F*
p–n junction structures 5:317–319
pnictides 2:126
Pockel's cell 4:351
Pockels effect 1:141
pocket-projector 3:32
Poincaré sphere analysis (PSA) 1:160, 1:317
point cloud
model 4:477, 4:477*F*
resolution measurement 4:403
point object, hologram of 4:152
point response 3:253
point spread function (PSF) 3:137, 3:187, 3:263, 3:277, 4:533, 5:15*F*, 5:16, 5:59–60, 5:72, 5:90, 5:112, 5:176
for coherent, incoherent, and partially coherent illumination 3:263
diffraction calculation of 3D PSF 3:264–265
spatial frequency content of 3D PSF 3:263–264
point-based methods 4:123–124
point-by-point methods 1:236
point-object hologram 1:377, 1:377*F*
reconstruction of 1:377*F*
point-spread function (PSF) 3:149–150, 4:168, 4:370–371
point-target measurements 5:6
point-to-multipoint physical topologies (PtMP physical topologies) 2:73, 2:73*F*
point-to-point physical topologies (PtP physical topologies) 2:73, 2:73–74, 2:73*F*
points-of-presence (PoPs) 1:281

Poisson brackets 4:199, 4:200
Poisson noise 3:277
Poisson operators 4:200
Poisson statistics 1:452
Poisson-distributed random processes 4:373
Poisson's equation 2:103–104
Pokels effect 4:3
polar coordinates, 2D Walsh functions in 5:18–19, 5:19*F*
polar functional groups 3:8–9
polarimetry 1:149
polaritonic modes 1:449
polaritonic systems 2:157
polarizability 2:40
polarization 1:148, 1:346, 1:347*F*, 4:180, 4:264–265, 4:310–311, 4:310*F*, 4:311*F*, 4:358, 5:169
  CGH 4:37, 4:37*F*, 4:38*F*
  control 2:418
    of quantum pathways in 2DCS measurements 2:154
  converter 3:33, 3:33*F*
  crosstalk 1:318–320
  dependent measurements 4:285, 4:285*F*
  diversity receiver 1:298
  ellipse 1:162–163, 1:163*F*
  holograms 4:95
  interferences 4:268
  maintaining 1:195
  microscopy 5:192
  modes 1:180
  preserving fibers 1:33
  selective transient grating 2:8–10
  sensitive materials 4:95–96
  TIR 5:169
polarization beam combiner (PBC) 1:278
polarization beam splitter (PBS) 1:181–183, 1:182*F*, 1:278, 1:298, 1:479–480, 1:480*F*, 3:35
  on and off for PBS and LCoS 3:35*F*
  3-PBS/x-prism LCoS projection system 3:35*F*
  prisms 1:151, 1:152*F*
polarization dependent loss (PDL) 1:295
  equalization and polarization demultiple ing 1:302–304
polarization division multiplexed systems (PDM systems) 1:293–294
polarization gating (PG) 2:237, 2:238*F*, 2:319–320, 2:320*F*
polarization mode dispersion (PMD) 1:1, 1:256–257, 1:295, 1:316–318, 1:317*F*, 1:363, 4:2–3, 4:3*F*
  equalization and polarization demultiplexing 1:302–304
  test methods for 1:316–318
polarization switched systems (PS systems) 1:293–294, 3:101
  biodistribution 3:109–111
  pharmacokinetics 3:108–109
  structure 3:103–105
polarization-based glucose content measurement 4:522–523
polarization-dependent loss (PDL) 1:255, 4:226
polarization-gating configuration 4:53–54
polarization-insensitive modulators 1:142
polarization-insensitive NOLMs 1:368
polarization-maintaining fibers (PM fibers) 1:180
polarization-mode dispersion (PMD) 1:178–179, 1:255
polarizers 1:149–150, 2:211, 3:25–26, 4:523
  basic relations 1:149–150
  birefringent materials 1:150–151
  dichroic absorbers 1:151–153
  miscellaneous types 1:154
  reflection and transmission 1:153–154
polarizing glass 3:45
polarizing prisms 1:150–151, 1:151*F*
polarons 5:223, 5:225*F*
poly ether-imide (PEI) 1:210
poly ether-sulfone (PES) 1:210
poly-(3-hexylthiophene) films (P3HT films) 2:194, 5:323–324, 5:324–325, 5:324*F*
poly-diamond carbon coated emitters *see* diamond-like carbon coated emitters (DLC coated emitters)
poly-l-lysine chlorine(e6) (pL-ce6) 3:106
poly-methylmethacrylate (PMMA) 3:15, 5:116–117
  fiber 4:279
poly-Si thin film 3:13–14
poly-vinylephenyle (PVP) 3:15
poly(ethylene oxide) (PEO) 5:326–327
poly(2-hydroxyethyl methacrylate) (pHEMA) 4:92
poly(3-alkylthiophene) (P3AT) 3:15
poly(3-hexylthiophene) (P3HT) 3:15
poly(3-octylthiophene) (P3OT) 3:15
poly(3, 3-didodecylquaterthiophene) (PQT-12) 5:326–327, 5:326*F*
poly(3,4-ethylenedioxythiophene) (PEDOT) 5:279–280
poly(3,4-ethylenedioxythiophene):poly (styrene sulfonate) (PEDOT:PSS) 5:233, 5:287, 5:287*F*, 5:298–300
poly(3,4-propylenedioxythiophen) (PProDOT) 5:279–280
poly(9-vinylcarbazole) (PVK) 5:234
poly(9,9-dioctylfluorene-co-benzothiadiazole) (F8BT) 5:327–328
poly(acetylene) 5:309, 5:309*F*
poly(acrylamide) (paam) 4:92
poly(acrylic tetraphenyldiaminobiphenol) (PATPD) 4:96–97
poly(dimethylsiloxane) (PDMS) 4:92, 5:252
poly(ethylene naphthalate) (PEN) 5:317
poly(ethylene terephthalate) (PET) 5:317
poly(methyl methacrylate) (PMMA) 3:60
poly(N-vinylcarbazole) (PVK) 4:96–97
poly(p-phenylenevinylen) (PPV) 5:240–241
poly(vinyl alcohol) (PVA) 4:92
poly[9,9-dioctylfluorene] (PFO) 5:309, 5:309*F*
polyacetylene (PA) 5:223, 5:259
polyaniline (PANI) 5:279–280
polychromatic light 4:174
polycrystalline silicon (poly-Si) 3:12–13
polycrystalline silicon thin-film transistors (poly-Si TFTs) 3:13–14
polydimethylsiloxane film (PDMS film) 5:293
polyethylene naphthalate (PEN) 3:53
polyethylene terephthalate (PET) 3:53
polyglutamine fibrils structure 2:174–175
polygon-based methods 4:123–124
polyimide (PI) 3:56–57, 3:57, 5:248
polymer light emitting diode (PLED) 3:56, 5:240–241
polymer sustained alignment (PSA) 3:61
polymer(s) 1:195, 1:196, 5:220, 5:221*F*, 5:310–311
  active materials 5:263–265
  coating 1:201–203
  fibers 1:210
  films 5:232
  laser resonators 5:313–314, 5:313*F*, 5:315*F*
    atomic force microscope images of "egg-box" DFB 5:314*F*
  OPVs 5:256
  organic photodiodes with
    organic layer–bulk heterojunction 5:324–325
    organic layer–single material 5:323–324
  organic phototransistors with
    organic layer–bulk heterojunction 5:327–328
    organic layer–single material 5:326–327
  polymer OLEDs, small molecule and 5:232
  polymer solar cells, active materials in 5:263–265
  polymer-based phototransistors 5:326–327
polymeric photoresists 1:54
polymeric processability 1:218
polymerization 4:91
polymyxin B nonapeptide (PMBN) 3:104
polypyrrole (PPy) 5:279–280
polystyrene (PS) 3:60
  fiber 4:279
Polytec vibrometer, acoustic vibrations of violin acquired with 4:453, 4:455*F*
polyurethane 1:331
polyvinyl alcohol (PVA) 3:25–26
polyvinylchloride (PVC) 1:331
Ponderomotive force 1:411
population dynamics, investigation of 2:7–8
population inversion 2:334, 2:350–351, 2:351, 2:372
porphyrins 5:86
Porro prisms 1:126, 1:127*F*
portrait holography 4:155
position-sensitive detector 5:190
positive and negative affect schedule (PANAS-X) 3:126
positive uniaxial crystal 2:293–294
positive-intrinsic-negative (PIN) 4:6
positron emission tomography (PET) 3:192, 3:196
post-detection compensation 3:272
  blind deconvolution techniques 3:276–277
  DWFS 3:277–278
  speckle imaging techniques 3:274–276
post-processing, adaptive optics and 3:278–279
post-traumatic stress disorder (PTSD) 3:124

potassium dihydrogen phosphate (KDP) 2:190–191, 4:497
potassium titanyl phosphate (KTP) 1:16
Pouiselle's law 5:64
Pound–Drever–Hall method (PDH method) 2:227
power amplifier 1:354
power capability of laser material 2:413
power conversion efficiency (PCE) 2:355, 5:258, 5:283
power levelling sequence upstream (PLSu) 2:75–76
power management 1:283–284
power penalty (PP) 4:11
power ratio method 1:320
power recycled Michelson interferometer 1:436, 1:437F
power spectral density (PSD) 3:176, 3:176F
power times length process 2:426
power–current characteristic (*P–I* characteristic) 2:354–355
Powervision 5:121
Powervision FluidVision IOL 5:121
Poynting vector 1:164
PQBOC8 5:326–327, 5:326F
Praseodymium-doped amplifiers 1:263
pre-detection compensation 3:272, 3:278
preamplifier 1:248, 1:354
preferential pumping 2:371
preform 1:195, 1:210, 4:14–15
  construction process 1:211
  fabrication 1:28, 1:195–196
    MCVD process 1:28–29, 1:29F
    other methods 1:30
    OVD process 1:29
    VAD process 1:29–30, 1:30F
  preform-based fabrication approach 1:210
preform substrate 1:213
presbyopia 5:52, 5:61, 5:120–122, 5:121T, 5:141, 5:150–151
  binocular approaches to presbyopia correction 5:125
  extending eye's depth of focus 5:122
  multifocal wavefront aberrations 5:122–125, 5:124F
  pinhole effect 5:122, 5:123F
  restoring accommodation 5:120–122, 5:122F
primary coating 1:328
primary sources 1:42–43
primitive cell 1:170
primitive reciprocal lattice vector 1:170
principal axes 1:387
Principal Component Generalized Projections Algorithm (PCGPA) 2:322–323
principal quantum number 2:40
principal self-terminating resonance-metastable metal vapor lasers 2:369T
principal states of polarization (PSP) 1:256, 1:302–303, 1:316
principal wavelengths 2:368–369, 2:373–374
principle of equivalence 5:189
principle of reciprocity 5:189
print circuit board (PCB) 3:89
prior knowledge 3:157–159
priori information 4:176
prisms 1:124, 1:125F
  deviation 1:126–128, 1:127F
  double prism reflectors 1:126
  as instruments 1:126–128
  pre-expanded grazing-incidence grating oscillators 2:337
  prism-type devices 1:143
  single prisms as reflectors 1:124–126
  spectrometer 1:128F
pro-collagen 3:118–119
probability densities (PD) 1:365
probability density function (pdf) 3:277
probe microscopes
  see also conventional microscope
  atomic force microscope 5:190
  NSOM 5:190–191, 5:190F
  scanning tunneling microscope 5:190
probe mode decomposition model 3:153
probe modulation 1:21
probe pulse 5:312–313
probing 2:3
  ocular mechanics with light 5:141
    air puff corneal dynamic imaging 5:142
    Brillouin microscopy 5:148–149
    phase-sensitive optical coherence elastography 5:146–147
programmable optical setup 4:178, 4:178F
projected Landweber method 3:191
projection
  CRT 3:1
  re-scaling 4:178
  sets 4:177–178, 4:178
  subset 4:178
projection display 3:32, 3:32F
  see also display(s)
  color gamut and HDR 3:40–43, 3:42F
  4K × 2K 3:37
  laser phosphor illumination projector 3:39–40, 3:40F
  LCD 3:32–34
  LCoS 3:34–35
  light source 3:32
  MEMS 3:35–37
  microdisplay 3:32
  new technologies, challenges, and applications 3:37
  system 3:32
  UST 3:37–39
projection-based blind deconvolution (PBBD technique) 3:276–277, 3:277
projection-slice theorem 2:161
prolate ellipsoids 5:45
prolate spheroidal wave functions 5:16
proliferative diabetic retinopathy (PDR) 5:132
prompt fluorescence (PF) 5:245
proof stressing 1:326
propagation
  of coherence 1:38–39
    see also coherent/coherence
    generalized propagation 1:39
    Thompson and Wolf experiment 1:39–40, 1:39F
    van Cittert–Zernike theorem 1:38–39
  constant 1:6–7, 1:7F
  in Doppler broadened medium 4:344
  in free space 4:167
  holographic phase retrieval from images 4:171–172
    application to phase retrieval and X-ray holotomography 4:172
    Fresnel diffraction images as in-line holograms 4:171–172
  in paraxial optical system 4:168
  through paraxial optical system in terms of AF
    transmission through thin object 4:167–168
proportionality constant 4:351–352
propylene carbonate (PC) 5:277
prostacyclin 3:111
proteins 1:445
  function 3:102
  structure and folding dynamics 2:173–175
    amyloid proteins 2:174–175
    membrane proteins 2:176
protons 2:40, 5:192
proximity effect 1:430
pseudo colour and manipulative artist 4:104–105
pseudo image 4:152
pseudo-3D image 4:106
pseudo-Doppler range pulling 4:439
pseudogap of $YBa_2Cu_3O_y$, magnetic quadrupole order in 2:220–223, 2:222F, 2:223F
pseudoscopic conjugate image 3:209–210, 3:209F
pseudoscopic image 3:208–209, 3:209
pseudoscopic real image 4:152
pseudospin 4:265
psychiatric disorders, PBM for 3:125–126
psychological depth cue 3:44, 3:44F
psychomotor vigilance task (PVT) 3:126
psychophysics 5:87
PtP-WDM channel overlay 2:79
ptychography 3:148, 3:152
pulsatility 5:65–66
pulse amplification model 1:248
pulse characterization techniques
  autocorrelation 4:49–50
  FROG 4:52–54
    inversion algorithms 4:54–57
    measurements 4:57
  mathematical representation of optical pulse 4:48–49
  measuring pulses directly–SPIDER 4:57–58
  measuring weak pulses 4:58–59
  pulse measurement method 4:59
  simplified FROG–GRENOUILLE 4:54
  spectral interferometry–relative phase measurements 4:50–51
  time-frequency representation 4:51–52
pulse compression 2:297–298, 2:297F
  applications 1:233
pulse distortion *see* optical time domain measurement method
pulse duration 2:372–373
pulse field 4:49
pulse generation technique 4:62, 4:62F, 4:63F

pulse generator 4:45
pulse laser deposition (PLD) 3:15
pulse LID 4:302
pulse measurement techniques 4:48, 4:59
pulse mode 4:497
pulse oximeter 3:89
pulse oximetry 4:519
pulse propagation 1:18–19
  for weak CW fields 4:345–346, 4:345F
pulse repetition frequency (PRF) 2:329, 2:334, 4:479
pulse response 4:88–89
pulse sequencing to control quantum 2:154
  double quantum 2D spectra 2:155, 2:155F
  nonrephasing 2D spectra 2:154–155
  rephasing 2D spectra 2:154, 2:155F
pulse shape 2:316
Pulse shaping 5:41
pulse synthesis 2:314–316
pulse tilting technique 1:409, 1:410F
3-pulse transient four-wave mixing 2:156–157
  resolution in 2D spectroscopy 2:157
pulse width modulation (PWM) 3:81
pulse-amplitude modulation (PAM) 1:277
pulse-current electrodeposition technique 5:298–300
pulse-shapers 2:188
pulse-timing control methods 5:40
pulsed CO_2 laser 4:457
pulsed gas discharges 2:376
pulsed laser deposition (PLD) 2:258
pulsed lasers 4:347
  field 4:344
  holograms 4:102
pulsed narrow-linewidth tunable dye laser 2:337
pulsed operation 2:418–419
  active Q switching 2:418–419
  mode locking 2:421
  passive Q switching 2:419–421
pulsed pump lasers 5:314
pulsed repetition frequencies (prfs) 2:336
pulsed system 5:3
pulses
  measuring pulses directly–SPIDER 4:58–59, 4:58F
  measuring weak pulses 4:58–59
pump
  cavity 2:409
  chamber 2:409
  through design 1:358
  module 2:409
  pulse 1:181
  pump-dump control methods 5:40
pumping 2:392–393, 2:409–410, 2:410F, 2:416–417
  atoms 1:455
  of dye lasers 2:372
  OPSLs 2:284–285, 2:284F
  Ti:sapphire lasers 2:372
pump–probe
  experiment 2:3, 4:270
  geometry 2:156, 2:167
    2DES in 2:189
  pump spectroscopy 2:240–241
  Raman scattering 2:85
  techniques 2:242, 5:311
pupil plane recording geometry (PPRG) 4:369
pupil-AF 4:169
  as generalization of OTF 4:169
pupils 5:45–46, 5:46F
  design for extended depth of field 3:173
  fields 4:409, 4:410F
  plane 4:371–372
purcell factor 1:446
pure laser 3:39
pure states 1:478
pyrex glass tube walls 2:374
pyroelectric detectors 1:418, 1:420
pyrromethene 567 dye (PM567 dye) 2:345, 2:345F, 2:348
pyrromethenes 2:344–345
  dyes 2:347

Q

Q-switch(ing) 1:140, 2:412
  with bulk saturable absorbers 2:419–421
  with semiconductor saturable-absorber mirrors 2:421
Q-switched lasers 2:424, 4:351
  microchip lasers 2:422
  single-frequency lasers 2:451
QDash SOAs 1:245
QinetiQ system 4:116, 4:116F
QR-LPD™ 3:82–84
quadratic dependence of dispersion 4:9–10
quadratic optical Stark effect 4:319–320
quadrature amplitude modulation (QAM) 1:245
  2-QAM 1:293
  4-QAM 1:293
quadrature amplitude modulation (QAM) 1:245, 1:277–278
quadrature PR (QPR) 1:279
quality factor (Q factor) 1:147, 1:187–188, 1:188, 1:215, 4:218, 4:218–219
quality-of-service degradation 2:80
quantitative information 2:165
quantitative performance 4:225–226
quantized states 1:459–461
quantum beats 4:267–269
quantum bits 1:478
quantum cascade (QC) 2:19
  few cycle THz spectroscopy of 2:25–31
  heterostructure 2:25, 2:120
  lasers 1:381–382
quantum computers 1:478, 1:484
quantum computing methods 1:456–457, 1:462, 1:484, 4:174
quantum confined Stark effect (QCSE) 2:96, 2:278–279, 4:243, 4:254, 4:255–256
quantum confinement 2:19, 2:99
  influence 2:94–96
quantum control 1:487, 5:31
quantum cross-capacitance effect 1:474
quantum crytography 1:478, 1:481F
quantum dash (QDash) 1:244
quantum defect 2:46–47
quantum dots (QD) 1:242, 1:245, 1:460–461, 1:469, 1:484, 1:491, 2:99, 2:280, 3:28–29, 3:29F, 3:61–62, 3:69, 3:211, 5:305–306
  CW OPSL sources 2:286
SOAs 1:245, 1:245F, 1:247–248
quantum dynamics phenomena 5:31, 5:36
quantum efficiency (QE) 2:113–114, 4:419, 4:426F
quantum electrodynamics (QED) 1:458, 4:180
quantum information 1:456–457, 1:478
  application of optical entanglement 1:484
  basic notions 1:478
  creating entangled states experimentally 1:479–480
  entangled-photon source 1:480F
  multiqubit states and entanglement 1:478–479
  polarization entanglement-based quantum cryptography protocol 1:482T
  protocols 1:479
  quantum key distribution 1:480–482
  quantum superdense coding 1:482
  quantum teleportation 1:482–484
  qubits 1:478
quantum interference phenomenon 1:487, 4:339
quantum key distribution (QKD) 1:479, 1:481
quantum kinetics 2:83, 2:84
quantum light characterization 4:179–181
quantum lithography 1:484
quantum mechanical/mechanics 1:144–146, 1:169–170, 1:172, 1:458, 1:462, 1:479, 1:491, 4:199, 4:200, 5:30
  description of optical SHG susceptibility 2:208–209
  energy levels 2:99
  expressions 4:336
  interference 1:491
  laser field design 5:31–32
  objectives 5:34
  tunneling 2:101–102
quantum noise 1:273, 1:442
quantum optical correlations, observation of 1:461–463
quantum optics 1:458, 4:180
quantum optimal control theory for designing laser fields 5:31–34
quantum pathway selection in 2D coherent spectra 2:153–154
  polarization control of quantum pathways in 2DCS measurements 2:154
  pulse sequencing to control quantum pathways in 2DCS measurements 2:154
  quantum pathways in 3DCS and other higher-order spectroscopies 2:155–156
quantum phenomena 5:39
quantum state teleportation 1:483–484, 1:483F
quantum state tomography 1:478, 1:480
quantum system 1:487, 5:30, 5:30F, 5:35F

quantum theory 2:112
of dyes 2:337
quantum well intermixing (QWI) 4:244–245
quantum wells (QW) 1:451, 1:459, 1:459F, 1:491, 2:68–69, 2:84–85, 2:91, 2:98–99, 2:103–104, 2:104, 2:201, 2:202F, 2:278–279, 2:280, 2:281F, 2:282F, 2:462–463
electron states in 2:100–102
formation 2:103–105
and GaAs-based structures
absorption spectrum 2:107F
AlGaAs/GaAs quantum wells, optical properties of 2:105–107
electron energy diagram 2:98F, 2:101F, 2:102F
electron states in bulk material 2:99–100, 2:100–102
formation 2:103–105
GaAs/AlGaAs quantum well structures 2:105
occupancy of states in 2:102–103
properties of electrons in large cubic sample 2:100F
intersub-band transitions in 1:488
lasers 2:350
nanostructures 2:58
occupancy of states in 2:102–103
SOAs 1:245
MZI logic gates 1:251
quantum wires and dots 2:71–72
quantum-beat spectroscopy 4:269
quarter wave 1:155
quarter-wave plate (QWP) 1:479–480, 1:480F, 2:211, 2:212F, 3:35
quasi phase matching (QPM) 1:14–16, 1:14F, 1:15F
quasi-2D nature 2:69
quasi-classical action 2:318
quasi-CW
laser 2:382
mode-locked Ti:Sapphire laser 4:367
nanosecond duration laser pulses 5:39–40
quasi-DC polarization 1:406–407
quasi-equilibrium distributions 2:464–465
quasi-Fermi energy 2:81
quasi-Fermi levels 2:111, 2:355–356
quasi-free electrons in solids 2:118
quasi-homogeneous sources 1:44–45, 1:44F
quasi-monochromatic 3:263
coherent beam 4:174
fields 1:41
light 1:486
quasi-Newton's methods 3:150
quasi-periodic structure 5:252
quasi-phase-matching (QPM) 2:293, 2:399
quasi-solid-state electrolyte 5:277–278
quasi-spectral analysis 3:91
quasi-thermal equilibrium 2:94
quasi-three-level lasers 2:417
qubits 1:478, 1:478
couplings and hybridizations 1:473–474
capacitive and electric dipole coupling 1:474–475
contact hyperfine interaction 1:473–474
magnetic dipole coupling 1:475
spin qubit coupling with exchange 1:474
creating entangled states experimentally 1:479–480
multiqubit states and entanglement 1:478–479
pair 1:482
quick response liquid powder display (QR-LPD) 3:82
quinolone 2:346

R

rabbit small clot embolic model (RSCEM) 3:121–122
Rabi coupling 4:339–340, 4:340
Rabi energy 2:48–49
Rabi flopping frequency 1:452, 2:54
Rabi frequency 4:339–340
radar 4:474
radial canonical transforms 4:203
radial pumping 2:409–410
radial shift variance 3:263
radial Walsh functions 5:19
radiance field 3:176, 3:176F
radiated field, propagating and evanescent spectra of 3:140–142
radiation
acoustic 5:192
electromagnetic 5:191
electron microscope 5:191–192, 5:191F
generation of number states of radiation field 1:454–455
modes 1:229, 3:67
other matter 5:192
radiation–atom interaction 1:452
trapping 2:378
radiative decay 2:12–15, 4:266
rates 1:445, 1:447
radiative process 2:117
radiative relaxation 2:328
radiative transitions
detailed balance 2:114
donor–acceptor pair recombination 2:113
quantum efficiency 2:113–114
spontaneous and stimulated emission 2:112–113
radio frequency (RF) 1:32, 4:333, 4:431, 5:1
channel 2:73
coherent detection
32x32 pixel FPA ladar breadboard using incoherent chirped amplitude modulation 5:6–7
incoherent FM/CW ladar architecture 5:1–2
kinetic inductance detectors 1:427–428
RF-electrodes 2:334
signal power 1:139
spectrum 4:13
spectrum analyzer 2:304
radio-pharmaceuticals 3:195
radiometric units 3:70
Radon transform inversion 3:192–193, 3:194, 4:177
Radon-Wigner display (RWD) 4:177, 4:179F
Radon-Wigner transform 4:177
rainbow effect 3:33, 3:37
rainbow-colour effect 4:103–104
Raleigh–Jeans theory of cavity radiation 2:107
Raman absorption process 4:320
Raman amplification with co-and counter-propagating pumps 1:265F
Raman amplifier (RA) 1:362, 4:6
Raman lasers 2:265, 2:265–266
see also microchip lasers; thin disk lasers
advancements in
crystalline Raman lasers 2:266–267
fiber Raman lasers 2:268–269
applications 2:269
energy diagram of stimulated Raman scattering 2:265F
on-chip Raman lasers 2:267–268
Raman lasing 2:269
Raman lidar techniques 4:456
Raman micro-lidars 4:516–518
Raman microscopy 4:354, 4:354–356, 4:354F, 5:192–193
Raman optical activity (ROA) 4:358
Raman probe tip 4:517–518, 4:517F
Raman resonance, nonlinear optics with pair of strong coupling fields in 4:344–345
Raman saturation phenomena 4:366
Raman scattering 1:180, 1:258, 2:265, 2:266, 4:351, 4:467–468
Raman spectroscopy 2:164, 4:354
characteristics of laser sources 4:356–358
near infrared lasers 4:361–362
Raman microscopy 4:354–356
system 4:517–518, 4:518F
UV lasers 4:364–366
visible lasers 4:359–360
Raman-induced absorption 4:319–320
Raman-induced Kerr effect spectroscopy (RIKES) 2:247
Raman-Nath regime 4:87
Raman–Nath diffraction 1:131–132, 1:132F
Raman–Nath parameter 1:131–132
ramp-filter 3:194
Ramsey method 1:452
random and uniformly redundant arrays 3:252
random sample consensus (RANSAC) 5:79
random walk theory (RWT) 3:222
range imaging with matricial light-emitting diode array 4:509–510, 4:509F
range precision 4:430–431
range profiles studies
airborne targets 4:479–482
atmospheric profiling 4:483
dimensions and structure of small boat 4:481F
examples 4:477–479
land targets and mapping 4:482–483
naval targets 4:477–479
test vehicles for trial in Sweden 4:480F
range resolution 4:430–431, 4:430F
range responses 5:5
range-gate output 5:5, 5:5F

range-height indicator scan of absolute humidity field 4:464, 4:467*F*
range-resolved reflective tomography techniques 4:488
rapid thermal annealing (RTA) 4:245
rare gas halide lasers
  absorbers in 2:363*T*
  potential energy curves 2:362*F*
raster scanning approach 4:194–195, 4:194*F*
rate equations 4:304
ratiometric analysis 3:90–91
ray aberrations converting to wavefront aberrations 5:113–115
ray deflections, optical path lengths determining from 5:112–113
ray description of fiber propagation 1:223
ray theory 1:222
ray tracing aberrometry 4:531–533, 4:532*F*
  commercial iTrace visual function analyzer 4:532–533, 4:532*F*
  locating visual axis 4:533
  reconstructed maps and functions 4:533, 4:533*F*
ray transformation matrix 4:176, 4:178
ray-optics limit 5:294–295
Rayleigh criterion 3:137, 3:139–140, 4:403, 5:186, 5:187
Rayleigh diffusion 3:202
Rayleigh expansions *see* grating equations
Rayleigh imaging 2:409
Rayleigh lidar techniques 4:456
Rayleigh range 4:357, 4:357*F*
Rayleigh regime 3:220
Rayleigh resolution criterion 3:137–138, 4:430
Rayleigh scattering 1:149, 1:217–218, 1:255, 4:366
Rayleigh–Sommerfeld diffraction formula 3:142, 4:141–143
Raytheon Vision Systems (RVS) 1:426
Rb cell 2:229, 2:229*F*
re-amplifying, re-shaping, and re-timing (3"R") 1:364, 1:364*F*
reactive gases 2:382
reactive ion etching (RIE) 4:294
reactive oxygen species (ROS) 3:100–101, 3:115–116, 5:131
read out and integration circuit (ROIC) 4:373, 4:446
reading stones 5:120
readout
  mechanism 1:471–472
    charge qubits 1:471–472
    spin qubits 1:472–473
  points or strips 4:524
readout integrated circuit (ROIC) 4:419, 5:8
real 2D-dimensional space (R^{2D}) 4:199
real energy bands 2:87
real-time
  holography 4:327
  system 3:199
real-valued monochromatic optical wave 4:322
real-valued variant Discrete Multi-Tone 1:255
receiver circuitry 4:259–261
  see also transmitter circuitry
  bandwidth-limited frontends 4:261–263
  wideband transimpedance amplifiers 4:260–261
receivers 1:270–271
  circuits 4:222
receptor 3:250–251
recollision spectroscopy 2:239–240, 2:240*F*
recombination
  assumptions for nonequilibrium statistics 2:111
  coefficients 2:110, 2:110*F*
  effect of electron–boson interactions 2:110
  electron–electron interaction
    for electrons in bands 2:110
    in traps 2:110–111
  lasers 2:372
  nonradiative processes 2:114–115
  radiative transitions 2:112–113
  rates
    case of defects 2:112
    results and two-band case 2:111–112
reconfigurable optical add/drop multiplexers (ROADM) 1:260, 1:266, 1:268, 1:269–270, 1:269*F*, 4:225, 4:226–227, 4:228*F*
  colorless 4:227
  contentionless 4:227
  degree 4:227
  directionless 4:227
  fixed grid 4:227
  flex-grid 4:227
reconfigurable system 4:31
reconfiguration within data center 4:225
reconstructed 3D slice plot of blood flow in deep tissues 4:526, 4:527*F*
reconstruction algorithm 3:150
reconstruction of attosecond beating by interference of two-photon transitions (RABBITT) 2:241–242, 2:242*F*, 2:321–322, 2:322*F*
reconstruction principles in digital holography 4:143–145
  Fresnel approximation 4:143–145
  numerical reconstruction
    by convolution approach 4:144*F*, 4:145–146
    by lensless Fourier approach 4:146–147
reconstruction wave 1:377
recording
  emulsion 4:104
  materials 4:154
  step 3:250–251
rectangle function 4:385
rectangular apertures 1:87–88
  diffraction by 1:69–70
rectangular coordinates, two dimensional Walsh functions in 5:18
rectification process 1:421–422
recursive algorithms 3:150–151
red, green, and blue (RGB) 3:18–19, 4:103–104
red AlInGaP laser diodes 2:278–279
red laser diodes 2:356
red-green glasses *see* anaglyph
reducible time delay 1:41–42
reduction–oxidation measurements (redox measurements) 5:93
reference 5:72
  beam 4:151
  plane wave 1:374–375
  wave 1:376–377, 3:206–207
reference mirror (RM) 4:507
reference signal (RS) 4:500
reflectances 1:153
  of polarizer 1:149
reflected beam in TIR 5:170–171
reflection 1:153–154, 1:172, 2:85
  holograms 4:87
  holography 4:103, 4:104
  intensity 2:388
  microscopy 5:192
  polarizer 1:153
  spectrum 2:388, 2:389*F*, 2:391*F*
reflective display technologies 3:6*F*, 3:82–84, 3:83*T*
  EPD 3:79–80
  EWD 3:80–82
reflective LCD 3:6–7, 3:6*F*
reflective objective (RO) 2:211
reflective semiconductor optical amplifier (RSOA) 1:252, 2:74, 2:82
  based passive optical network 1:252
reflective SLMs 3:42–43
reflective tomography 4:485, 4:489
reflectivity 3:71
reflectors 1:111–113, 2:409
refracted near field technique (RNF technique) 1:322, 1:323
refracting power 1:114–116
refraction 5:61, 5:111
  diffracted beam index 1:138–139
  index 4:310
  index of refraction profile 1:207, 1:207*F*
  matrix 1:102–104
refractive anomalies 5:51–52, 5:55
  anisometropia 5:54
  astigmatism 5:52–54, 5:53*F*
  correction 5:54–55
  spherical 5:51–52
refractive anomalies, correction of 5:54–55
refractive correction 5:108–109, 5:108*F*
refractive errors 5:108, 5:111, 5:135
  aberrometry and wavefront sensing 5:112–113
  excimer laser 5:135
  femtosecond laser 5:135–136
  higher-order aberrations specification of eyes 5:110–111
  methods for determining refractive error and refractive state 5:111
    eyes refractive state 5:111
    locating eyes far point with optical measurements 5:111
    refractive state from Zernike aberration coefficients 5:111–112
  optimizing retinal image quality by correcting 5:115
  refractive correction, and physical units 5:108–109, 5:108*F*
  specification of sphero-cylindrical lenses and 5:109–110

refractive index 1:5–6, 1:27, 1:33, 2:5, 4:238–239, 4:329, 4:342, 4:358
effects 4:3
of material 1:153
refractive index profile (RIP) 1:311
refractive lens system 4:205–206, 4:206F
refractive multifocal wavefr nts 5:123
refractive state
eyes refractive state 5:111
methods for determining 5:111
from Zernike aberration coefficients 5:111–112
refractive surgery 5:125–126
refractory metal(s) 2:262–263
nitrides 2:260
refresh rate 3:77–78
refreshable materials
holographic recording media and devices 4:93
persistent spectral hole burning 4:93–95
photochromic materials 4:93
photorefractive materials 4:96–97
photothermoplastic process 4:97
polarization sensitive materials 4:95–96
regenerative amplification 2:412
regional cerebral blood flow (rCBF) 3:126
regioregular poly(3-hexylthiphene) (RR-P3HT) 5:261
regrowth integration technology 4:250
regular DFB 2:455–456, 2:456F
regularization
parameter 3:189, 3:190F
theory 3:187
regulated cascode (RGC) 4:260–261
relative horizontal accuracy 4:402
accounting for 4:403–404
relative intensity noise (RIN) 2:458, 2:458F, 4:46–47
relative vertical accuracy 4:401–402
relaxation
effects 1:216
oscillations 2:467, 4:62
relaxed averaged alternating reflectors (RAAR) 3:148
reliability of lasers in fiber optic systems 4:70–71
remote node (RN) 1:252
RN1 2:82–83
RN2 2:82–83
remotely operated vehicles (ROVs) 4:110
repetition rate 2:306
locking 2:307–308
rephrasing 2:54–55
complex signal fields 2:184–185
signals 2:185–186
time-ordering 2:57
2D spectra 2:154, 2:155F
residual stress 1:326
resistance furnace 1:31–32
resistive-feedback transimpedance amplifier (RTIA) 4:429
resolution 1:135–136, 3:137, 3:235–237, 4:430, 5:158–159, 5:185–186, 5:186F
and image sharpness 3:75
in imaging 3:136–137
computational 3:136F
inverse source and scattering problems 3:137, 3:137F
physical 3:136F
scatterer 3:142–144
source-field 3:138
limit 3:144, 5:72
superresolution 3:144–145
resolving power of zone plate 1:96
resonance
transition 2:368
upper laser level 2:368
vibration frequencies 4:455, 4:456F
wavelengths 1:231–232
resonance enhanced multiphoton ionization (REMPI) 2:248
resonance-metastable metal vapor lasers 2:372–373
resonant cavity 1:451, 2:385
APDs 4:419
resonant energy transfer 2:327–328
resonant enhancement 4:350
resonant excitation conditions 2:33
resonant periodic gain (RPG) 2:281
resonant phonon scheme (RP scheme) 1:383
resonant THz detection 1:423
resonant-phonon designs (RP designs) 1:382
resonated devices 1:143
resonator 2:465–467
spectrometer 1:395–396
types of resonator modes 2:329–331
response time 3:76–77
responsivity of organic photodetectors 5:320–321
restoring accommodation 5:120–122, 5:122F
retardation plates *see* retarders
retarders 1:149, 1:154–156
retina (R) 3:17, 3:18F, 4:500, 5:43, 5:130
femtosecond laser effects on 5:91–92
light at 5:50
light loss at 5:61
retinal blood flow measurement
capillary blood flow 5:65
clinical measurements 5:69
flow measurements 5:69
total retinal blood flow 5:64–65
retinal diseases 5:64
retinal image quality 5:59–60, 5:124–125, 5:161
optimizing by correcting refractive errors 5:115
retinal imaging 5:72
AO 5:73
femtosecond lasers in
artifacts and implementation of TPE fluorescence ophthalmoscopy 5:89–91
effects on retina 5:91–92
fluorophores 5:85F
multiphoton retinal imaging theory 5:87–89
in vivo multiphoton retinal imaging with adaptive optics 5:86–87
retinal oximeter on platform of Canon CR 6-45NM 4:520, 4:520F
retinal pigment epithelium (RPE) 5:75, 5:75F, 5:164
dark-field AOSLO 5:76F
retro-reflective targets 4:439
retro-scattering 4:456
retrograde mitochondrial signaling 3:115–116
return loss (RL) 1:337
return pulse 5:3
return-to-zero (RZ) 4:39, 4:68
format 4:21–22
pulses 1:20–21, 1:275
RZ33 1:275
RZ50 1:275
RZ67 1:275
transmission 1:294–295
reverse dispersion fiber 4:24–25
reverse intersystem crossing (RISC) 5:241
rhemoglobin 5:86
rhodamine 590 chloride *see* rhodamine 6G (Rh6G)
rhodamine 6G (Rh6G) 2:344
rhodamine dyes 2:344, 2:349
rhodopsin densitometry 5:87
ribbon cable *see* slotted core cables
riboflavin 5:126
Richardson–Lucy method 3:191–192
right sub-pixel (RSP) 3:62
rigid gas permeable contact lenses (RGP contact lenses) 5:116–117, 5:119
rigorous diffraction theory 1:52, 1:55, 1:58
rigorous electromagnetic wave approach 5:294–295
rigorous grating analysis 1:52–53
rigorous research (RIGOR) 3:122–123
ring cavity
dye lasers 2:454
fiber lasers 2:455
ring micr resonator devices 1:143, 1:147
ring modulator transmitters
controllers 4:222
fabrication 4:217
laser sources 4:222
link-level considerations 4:222
nonlinear effects 4:220–221
optoelectronic properties 4:217–220
receiver circuits 4:222
ring-based DWDM transceivers 4:221–222
transmitter circuits 4:222
ring resonant cavity 4:219
ring resonator
modulator transmitters 4:257–258, 4:257F, 4:258F, 4:259F
structure 4:218
ring-based DWDM transceivers 4:221–222, 4:221F
robustness 3:182–183
r ds 3:17, 5:43
"rogue waves" 2:429
roll-to-roll process (R2R process) 3:56, 3:57, 3:80
Ronchi grating 4:31, 4:31F
room temperature (RT) 2:441
detectors for room temperature THz imaging 1:419–422, 1:421T

room temperature (RT) (*continued*)
FET and CMOS-based detectors 1:422–423, 1:424*F*
microbolometers 1:423, 1:424*F*
SBDs 1:421–422
root mean squared difference (RMSD) 4:402
root mean squared error (RMSE) 4:401–402
root-mean square (RMS) 4:531
Rostock cornea module (RCM) 5:99–100, 5:103*F*
Roswell Park Cancer Institute (RPCI) 3:101
rotating-wave approximation (RWA) 2:12
rotation 4:176
transform 4:188
vibration spectroscopy 1:389–390
rotation anisotropy (RA) 2:207
rotational anisotropy experimental designs
generations 2:209–212, 2:210*F*, 2:211*F*
rotational spectroscopy 1:387–389
Rothwarf-Taylor equations (RT equations) 2:133–134, 2:134
rototype laser interferometric gravitational wave detectors 1:433–434
Royal Microscopical Society (RMS) 5:185
Ru-based complex photodyes 5:276–277, 5:276*T*
rubidium (Rb^+) 5:282
Rydberg atoms
energy shift of 1:452
micromaser setup 1:453*F*
Ruby laser operating 2:325–326
rule of thumb 3:272
Runge–Kutta method 2:329
Rydberg atoms 1:451, 1:452, 2:40, 2:44–45
energy shift 1:452
Rydberg excitons in Cu_2O 2:41
Rydberg series 2:33
Rydberg states in semiconductors
coherent features 2:47–49
experimental absorption spectra between resonances 2:50*F*
experimental absorption spectra of Rydberg exciton series 2:48*F*
incoherent exciton spectral redistribution function 2:49*F*
Rydberg excitons model as V-type three level system 2:49*F*
mixing of angular momentum states 2:45–46
quantum defect and non-parabolic bands 2:46–47
Rydberg blockade 2:41–44, 2:43*F*, 2:44*F*
Rydberg excitons in Cu_2O 2:41, 2:42*F*, 2:43*F*
symmetry considerations 2:44–45

S

saddle point approximation (SPA) 2:319
sagittal fan 1:118–119, 1:120*F*
Sagnac interferometers 4:41–42
NOLM 4:41–42, 4:41*F*, 4:42*F*
TOAD 4:42, 4:43*F*, 4:44*F*
salts 2:346
sampled-grating DBR (SG-DBR) 4:245
sampling 1:299–300
quotient
off-axis IPRG 4:375–376
off-axis PPRG 4:378
Sandercock's spectrometer 5:148–149
sapphire 1:186
laser 2:19–20
regenerative amplifier lasers 2:166
substrate 1:189
"satin quartz" 4:279
saturable absorbers (SA) 1:369, 1:369*F*, 2:307–308, 2:308*F*, 2:468
optical regeneration by 1:369–370
saturable absorption 2:308
crossover resonances 2:230
Doppler free spectroscopy 2:229–230
ECDL 2:227–228
experimental setup 2:230, 2:231*F*, 2:232*F*
principles of saturated absorption spectroscopy 2:228–230
spectroscopy for diode laser locking 2:227
saturation irradiance (I_{sat}) 4:349
saturation power (P_{sat}) 1:246
SAVIS laser Doppler vibrometer 4:452, 4:452*F*
scalability 4:225
scalar theory of diffraction 4:157
scalar wave
equation 2:384
model 3:138
scale invariant features transform (SIFT) 5:78
scaling 2:411
law 1:45–46, 2:371–372
up planar lightwave optical switch from small building blocks 4:234
deterministic 4:234
stages 4:234–235
symmetric 4:234
scanning
process 3:210
systems 5:185, 5:189
scanning electron microscopy (SEM) 1:211, 1:212*F*, 1:218, 1:218*F*, 1:468, 3:120–121, 5:248, 5:248*F*, 5:296
scanning laser ophthalmoscope (SLO) 5:64, 5:99, 5:163, 5:164*F*
scanning microscopes 5:189
image formation in 5:194–196
scanning near-field optical microscopies (SNOM) 2:148–149
scanning tunneling microscopy (STM) 1:468, 1:469, 2:147–148, 5:190
scatterer imaging 3:137
resolution in 3:142–144
scattering 4:67, 4:88, 5:168
amplitude 3:143
coefficients of tissues 3:220
cross-section 3:220–221
effects 1:255
objects 3:262
phenomena 1:345
photon migration in scattering media 3:221–222
problems 3:137, 3:137*F*
processes 4:270
TIR 5:171–172
scattering potential (SP) 4:500
scattering-based technique (sSNOM) 2:148–149, 2:149
Schawlow–Townes expression 4:358
Scheiner's disk 5:112
Schell-model sources 1:43–44
schematic eyes 5:48–49
Schottky barrier diodes (SBDs) 1:419, 1:421–422, 1:422*F*
Schottky emission 5:233, 5:233*F*
Schottky type photodiodes 5:321–322
Schrödinger equation 1:169–170, 1:458, 2:12–13, 2:64–65, 2:82, 2:99, 2:100, 2:103–104, 4:341, 5:30–31, 5:203, 5:205
sclera 5:130
scleral lens prosthetic device (SLPD) 5:119
scleral lenses 5:119
sealed-off
CuBr systems 2:370
and waveguide lasers 2:331, 2:331*F*, 2:332*F*
second generation of AMVA (AMVA II) 3:61
second harmonic imaging of cornea 5:104–105
second harmonics (SH) 1:412, 2:294, 2:313–314
2nd order nonlinear optical effects 1:491
2nd order perturbation theory 1:488
second ultrafast laser pulse 5:39–40
second-harmonic generation (SHG) 1:10, 1:11, 1:406, 2:121, 2:124, 2:145–146, 2:146, 2:245, 2:280, 2:291, 2:316, 2:398, 2:424, 2:446, 4:49, 4:284, 4:285*F*, 5:89
absolute measure 4:287–289
for characterization of 2D materials 4:284–285
dependence on stacking and number of layers 4:286–287
polarization dependent measurements 4:285, 4:285*F*
in crystals 1:12–16, 1:13*F*, 2:207–209
QPM 1:14–16, 1:14*F*, 1:15*F*
electronic structure calculations 4:289–290
imaging 5:74–75, 4:285–286, 4:286*F*, 5:98
of corneal collagen fibrils 5:104–105, 5:105*F*
of human cornea 5:105*F*
optical devices 4:290
spectroscopy of hidden phases
generations of rotational anisotropy experimental designs 2:209–212
hidden phases in correlated electron systems 2:212–214
hidden phases revealed by SHG-based techniques 2:214–216
second-order
correlations 1:48–49
DFB 1:384
exponentials of second-order differential operators 4:202
nonlinear polarization 4:349
spectroscopy 2:245–246

up-conversion from second-order optical nonlinearity 2:397–399
second-order dispersion *see* dispersion slope
secondary fiber coating 1:328
fiber identification 1:330
loose jacket 1:328–330, 1:330*F*
tight jacket 1:328, 1:329*F*
secondary sources 1:43
secondary wavelet 1:62
seed generation 2:295
Seidel aberration theory 4:205
selective area growth (SAG) 4:243–244
selective laser trabeculoplasty (SLT) 5:136
self Q switching 2:417
self-clutter signal 5:2
self-focusing 5:92
self-frequency doubling laser 2:404, 2:404*F*, 2:405*T*
self-imaging
condition 3:167–168, 3:168*F*
principle 3:168
self-induced Kerr effect 1:348
self-phase modulation (SPM) 1:10, 1:16, 1:16–18, 1:180, 1:245, 1:320, 1:321, 1:348, 2:311, 2:425, 4:3, 4:23
spectral broadening by 1:19, 1:20*F*
self-phase modulation 1:142, 1:348, 2:2–3, 4:278, 4:312–313, 4:320, 4:350–351, 4:351
self-phase-conjugation (SPC) 4:321
self-pumped phase conjugate mirrors 4:332
self-similarity 5:27–28
self-sum frequency mixing laser 2:404–405, 2:405*F*, 2:405*T*
self-supporting aerial cable 1:333, 1:333*F*
self-terminating
pulsed metal vapor laser 2:368–369
resonance-metastable pulsed metal vapor lasers 2:368–369
self-trapped excitons (STEs) 4:304–305
Sellmeier expansion of refractive index 1:6
semi-analytical methods 1:172–173
semi-classical
model 2:318
three-step model 2:316–317
semi-polar
InGaN layers 2:279
planes 2:271
semiconducting polymer lasers 5:310, 5:316, 5:323–324
semiconductor disk laser (SDL) 2:413–414
semiconductor laser amplifier (SLA) 4:38, 4:39, 4:40–41
semiconductor optical amplifiers (SOA) 1:242, 1:242*F*, 1:248–250, 1:263, 1:264, 1:365, 1:367–368, 1:368*F*, 4:64, 4:239, 4:250
all-optical data regeneration 1:251–252
bulk SOA 1:243–244, 1:244*F*
functional applications 1:250–251
FWM wavelength converter 1:250–251, 1:250*F*
gain mechanism in 1:242
gain-clamping 1:249–250
microwave phase shifter 1:252–253, 1:252*F*
models 1:245–247
pulse amplification 1:248
steady-state 1:245–247
time-domain model and pattern effects 1:247–248
MZI XOR
gate 1:251
logic and truth table 1:251*F*
optical logic 1:251
phase shifter transfer function 1:252–253
principles 1:242–243
reflective SOA based passive optical network 1:252
semiconductor nanostructure SOAs 1:244–245
structures 1:243–244
switch 4:239–240
semiconductor quantum structures, few cycle THz spectroscopy of 2:19–21
semiconductor saturable absorbing mirror (SESAM) 2:281, 2:412, 2:421
Q switching with 2:421
semiconductor-Bloch equations (SBEs) 1:459, 2:34, 2:83, 4:265–266
semiconductor(s) 1:224, 1:460, 2:33, 2:63, 2:83, 2:88–89, 2:98–99, 2:413–414
amplifiers 1:351
band gap 1:403
bolometers 1:426–427
cavity QED in
Heisenberg uncertainty principle 1:463–465
quantized states 1:459–461
superposition principle 1:461–463
in coherence control 1:487, 1:487–490
of electrical current 1:488–490, 1:489*F*, 1:491
of carrier density, spin population, and spin current 1:490–491, 1:490*F*
in semiconductors 1:487–490
diode edge emitting lasers 2:356
edge emitting diode laser 2:350
excitation by co-circularly polarized ω and 2ω pulses 1:490*F*
lasers 2:462, 2:462*F*
applications 2:468
dynamics 2:467–68
gain medium physics 2:464–465
resonator 2:465–467
technology 2:336
layers 5:273–275
luminescence equations 1:461
to metals 2:256–257, 2:256*T*
III-V semiconductors 2:257
TCOs 2:257–258
microcavities 1:456
nanostructures 2:19
SOAs 1:244–245
optical properties 2:99
quantum wells 2:120
optical-pump/THz-probe magnetospectroscopy 2:76–77
optically detected FIR resonance spectroscopy 2:75–76
THz-driven AC stark effect of intersubband transitions in 2:200–203
strong-field terahertz excitations in
crystalline semiconductor 2:33–34
dynamical Bloch oscillations 2:36–37, 2:37*F*
e–h recollisions 2:37–38, 2:38*F*
excitations in semiconductor 2:34*F*
HHG in two vs. three bands 2:35, 2:35*F*
non-perturbative quantum interference 2:35–36, 2:35*F*
resonant vs. non-resonant excitations 2:33*F*
SBEs 2:34
time-resolved HHG 2:36, 2:36*F*, 2:37*F*
systems 1:185, 1:462
THz laser 2:119–120
ultrafast studies
coherent dynamics 2:82–83
hot carrier regime 2:84–85
hot phonons 2:85
incoherent relaxation dynamics 2:83–84
isothermal regime 2:85
nonthermal regime 2:84
novel coherent phenomena 2:86
tunneling and transport dynamics 2:85–86
vacuum 1:467
semitransparent object 5:187
Sénarmont compensator 1:156–157
senile miosis 5:60
sensing at exceptional points 4:298–300
sensitivity 1:273, 3:235–237, 4:87–88, 5:159–160
sensitizer 2:394, 5:275–277, 5:276*F*, 5:276*T*
sensors 3:145, 3:239, 4:106
separate absorption, charge, and multiplication layer stack (SACM layer stack) 4:417
separate confinement heterostructure (SCH) 1:243, 2:351
sequential holograms 4:106
sequential two-photon absorption 2:395–396, 2:396*F*, 2:400–402, 2:401*F*, 2:402*F*, 2:402*T*
series resistance (R_s) 5:259
Shack–Hartman wavefront sensors 3:277–278, 5:72, 5:72–73, 5:113
Shack–Hartmann sensor 5:112–113, 5:113*F*
Shack–Hartmann wavefront sensing 5:124–125
shadow mask 3:3, 3:3*F*
shadowgram 3:251
shallow ridge waveguide 4:247
shallow tissue imaging through selection of ballistic photons 3:222–223
shallow waveguide etch 4:217
shape factor 1:9, 1:74
of lens 1:114–116
shearing interferometer wavefront sensors 3:277–278
sheaths 1:331–332, 1:331*F*
Shepp–Logan filter 3:194
shift variance 3:263
Shockley–Queisser theory 5:288–290

Shockley–Ramo theorem 4:422
Shor's factor-finding algorithm 1:484
short circuit current density 5:258
short pass filters (SPF) 2:211
short pulse generation 2:467–468
short trajectories 2:316–317
short wavelength infrared (SWIR) 3:229
short wire 1:244
short-circuit current density (J_{SC}) 5:270
short-exposure star images 3:274–275
short-haul transmitters 4:68
short-period FBGs 1:267
short-range WindScanner (SRWS) 4:462
short-term fluctuations 1:32
short-time-duration laser pulse 5:39
short-wavelength infrared detectors (SWIR detectors) 3:232, 4:415–416
short-wavelength-cone (S-cone) 3:17, 3:18F
shot-noise limit
  off-axis IPRG 4:377
  off-axis PPRG 4:379
  on-axis PSRG 4:380–381
shrinkage of emulsion 4:90
shutter glasses 3:46
side band technique 4:151
side mode suppression ratios (SMSR) 4:249
side pumping 2:409–410
side-looking airborne radar (SAR) 4:502
side-view technique/transverse interference 1:323
sidehands (SB) 2:321–322
signal 1:223–224
  coding 3:175, 3:178–179
  distortion 1:249–250
  fidelity 1:223–224
  interferes 4:369
  plane wave 1:374
  reflections 1:356
  regenerator 1:365, 1:365F
signal carrier phase (SC phase) 1:296–297
signal processing techniques for range profiling and tomograhy 4:489–494
signal recycling mirror (SRM) 1:436–437
signal-ASE beating 1:353
signal-to-noise ratio (SNR) 1:242–243, 1:273, 1:298–299, 1:353, 3:87, 3:274–275, 4:5, 4:34, 4:369, 4:376–377, 4:415, 4:430–431, 4:475, 5:3, 5:64, 5:146, 5:320–321
  off-axis IPRG 4:376–377
  off-axis PPRG 4:379
  on-axis PSRG 4:380
silica (SiO_2) 1:27, 1:195, 2:381
  attenuation in silica single-mode fibers 1:255
  cladding 1:229
  fibers 1:257
    fiber attenuation 4:1, 4:1F
  glass fibers 2:268
  optical fibers 1:217–218
  PCF 1:217–218, 2:433–434
  silica-on-silicon 4:235
  silica–polymer–air structure forms 5:313–314
silicate 1:186, 2:347, 4:297
silicon (Si) 1:381, 2:267, 2:350, 5:292–293
  impurity state lasers 1:381
  liquid-crystal on silicon wavelength-selective switch 4:231
  Raman lasers 2:267
silicon carbide 2:271
silicon oxynitride (SiON) 4:235
silicon photonics (SiPh) 4:236
  controllers 4:222
  fabrication 4:217
  laser sources 4:222
  link-level considerations 4:222
  nonlinear effects 4:220–221
  optoelectronic properties 4:217–220
  receiver circuits 4:222
  ring-based DWDM transceivers 4:221–222
  transmitter circuits 4:222
silicon qubits
  future 1:475
  memory, control, and readout mechanisms 1:471–472
  motivation for 1:467–468
  principal material types 1:468–471, 1:468F, 1:470–471F
  qubit couplings and hybridizations 1:473–474
silicon tetrachloride ($SiCl_4$) 1:28
silicon-germanium (SiGe) 4:254
silicon-on-insulator (SOI) 2:267, 3:14, 4:217
silicon-perovskite tandem solar cell 5:290
silicone photodiode 3:88
silicone photomultiplier (SiPM) 3:88–89
silver (Ag) 2:256, 4:91, 5:298
silver halide 4:89–90, 4:89F
  crystals 4:93
  emulsion 4:90
  photographic emulsions 4:151
simple dimensional analysis 3:160–161
simple mathematical description of holography 4:152–153
simple paraxial theory 5:195–196
simple point-to-point WDM system 4:7–8, 4:9F
simple two-band model 4:320
simplified FROG–GRENOUILLE 4:54, 4:55F
simulated and measured data 4:477, 4:478F
simulating laser profiling data 4:476–477
simulations 5:301
sinc function 1:75, 4:385
single A-scans 5:143
single active electron (SAE) 2:318
single beam technique 4:102–103
single color beams, coherence control of electrical current using 1:491
single configuration coordinate model (SCC model) 2:437–440, 2:438F
single frequency gas laser 2:454
single isotropic phase singularity 4:185
single longitudinal mode lasing 4:294
single mode connector attenuation 1:336–337, 1:337F
single mode laser 1:223
single mode operation
  with eliminated spatial hole burning 2:452–453
  with mode suppression 2:453–454
single molecules, TIRF on 5:172–173
single phosphorus impurities 1:468
single photon emission computerized tomography (SPECT) 3:124, 3:192, 3:196
single polarization transmission (SP transmission) 1:293–294
single polymer layer device 5:259
single preform 1:28
single prisms as reflectors 1:124–126
single quantum cascade 2:27–28
single spatial mode operation 4:298
single telecommunications-grade optical fiber 1:355
single-atom laser 1:455
single-color method 1:411–412, 1:411F, 1:412F
single-frequency 2:411
  DBR lasers 2:456, 2:457F
  dye lasers 2:454
  emission 4:16
  lasers 2:451, 2:451–452, 2:451F, 2:454–455
    applications 2:461
    characterization 2:458
    DBR lasers 2:456–457
    DFB lasers 2:455–456
    external cavity lasers 2:457–458
    NPRO 2:454–455
    phase noise 2:458–459
    RIN 2:458
    ring cavity fiber lasers 2:455
    single mode operation with eliminated spatial hole burning 2:452–453
    single mode operation with mode suppression 2:453–454
    spatial hole burning and multimode operation 2:451–452
    spectral linewidth 2:459–460
  operation 2:417
  ring-cavity fiber laser 2:455, 2:455F
single-hop networks 4:45
single-mode fibers (SMF) 1:21, 1:33, 1:217–218, 1:227, 1:229, 1:261–263, 1:336, 1:337, 4:1, 4:2F, 4:10F, 4:15–16, 4:17, 4:18, 4:20
single-optic accommodating IOL 5:121
single-photon
  fluorescence process 5:98, 5:98F
  Rabi frequency 5:208–209
  transitions 1:488
single-photon avalanche photodiode detectors (SPAD detectors) 4:475
single-photon excitation (SPE) 5:88, 5:98, 5:98F
single-pixel imaging using Hadamard transform
  basics 4:193–195, 4:193F, 4:194F
  Walsh-Hadamard single-pixel
    applications 4:196–197
    imaging 4:195–196
single-point detection systems 1:139
single-shot measurements 2:190
single-sideband (SSB) 1:429, 4:7
single-stage amplifier 1:356–358, 1:358F
single-wall carbon nanotubes (SWCNTs) 2:72
single-wavelength laser beams 1:136

singlet oxygen 3:102
singlet–singlet annihilation 5:310–311
singular phase function, gradient of 4:187–188
singular value decomposition (SVD) 3:157
sinusoidal structured pattern 4:453
sinusoidal surface-relief grating 1:51F, 1:52
Sjogren's syndrome 5:116–117
skew rays 3:35
skew-symmetric operation 4:199
skin lesions, treatment of 2:372
skin rejuvenation 3:118–119, 3:118F
slab coupled waveguide lasers (SCOWL) 4:293
slit scanning microscopy 5:99–100
slope tuning 4:31
slotted core cables 1:332–333, 1:332F, 1:333F
slow axial flow lasers 2:331–332, 2:332F
slow corrections 3:198
small area contrast 3:70
small footprint components soldered on conventional PCB 3:89
small incision lenticule extraction technique (SMILE technique) 5:126, 5:132, 5:133, 5:135, 5:138
small molecules
  organic photodiodes with 5:321–322
  organic phototransistors with 5:325–326
  and polymer OLEDs 5:232
small-signal modulation 4:69
smectic liquid crystals 3:9–10
smoke detectors 4:513–514, 4:514F
"smooth picture" technique 3:37
snake-like regime, imaging in 3:223–225
Snell's law 1:102–104, 1:114–116, 1:124–125
(SnO_2:F) *see* fluorine-doped tin oxide (FTO)
Society of Automotive Engineers (SAE) 3:70
soft contact lenses 5:118–119, 5:119
soft glass fibers 2:433
soft lithography techniques 1:144–146
software 3:216–217, 3:217F
sol-gel
  process 2:346
  slurry 1:196
  techniques 2:347
solar cells 2:71, 5:270
solar-to-electricity conversion efficiency 5:270
solid phase crystallization (SPC) 3:14
solid-core fibers 1:217–218, 1:263
solid-state
  devices 2:265
  DSSC 5:278–279
  lasers 2:384, 2:407
  materials 2:168
    charge dynamics of dye-sensitized solar cells 2:168
    nanoscale materials 2:168–170
  microchip lasers 2:415
  systems 2:194–196
solid-state dye laser 2:336, 2:337, 2:348–349
  see also liquid dye lasers
  DFB solid-state dye lasers 2:344
  matrices 2:346–347
    inorganic and hybrid hosts 2:347–348
    organic hosts 2:346–347
  oscillators 2:340–342
    cavity linewidth equation 2:344
    multiple-prism dispersion grating theory 2:341–342, 2:342F
    physics and architecture of 2:342–344, 2:343F
soliton(s) 2:427–428, 4:17, 5:223, 5:224F
  operation 2:304–305
  self-frequency shift 2:432–433
solution fabrication processes 5:220
solution-based deposition methods 3:15
solution-processing
  approaches 5:220
  methods 5:313
solvent additive 5:262–263
solvent annealing (SA) 5:261, 5:261–262
solvent flipping (SF) 3:148
Sommerfeld enhancement factor 2:93
Sommerfeld Green's function 1:63, 1:64F, 1:66
Sommerfeld radiation condition 1:65
sonogram 3:194, 3:194F, 4:52, 4:52F
Sony and Konica/Minolta's holographic wave guide combiners 4:125
soot 1:28
sophisticated experimental techniques 2:36
sophisticated software tools (Simulase) 2:282–283
SOPRA GES5 1:210
sound wave 4:98, 4:98F
source development lab (SDL) 1:405
source-field imaging 3:137
  resolution in
    propagating and evanescent spectra of radiated field 3:140–142
    scalar wave model 3:138
    three-dimensional resolution of far fields 3:138–140
    transverse resolution 3:142
Southeast Asia (SEA) 4:18
sp^2 hybrid orbitals 5:221, 5:222F
space bandwidth-product (SBP) 4:191
space coherence 1:35–36
space division multiplexing (SDM) 4:34, 4:45
space switches 4:34
space-bandwidth product (SBP) 3:168, 4:97
space-based far-infrared astronomy array technology (Si-As BIB array technology) 1:426
space-charge layer 5:233
space-charge-limited current (SCLC) 5:233
space-invariant (isoplanatic) imaging 4:168
spacer layer 5:302–304, 5:304F
spatial coherence 1:35–36, 1:35F, 1:37–38, 4:151
spatial color synthesis 3:19–20
spatial distribution 3:242
spatial filter (SF) 4:500
spatial Fourier domain 3:137
spatial frequency content of 3D PSF 3:263–264, 3:264F, 3:265F
spatial frequency response (SFR) 3:177–178, 3:178F, 3:181F, 3:183F
spatial gating 2:321
spatial heterodyne 4:369, 4:407
  background material 4:369–371, 4:372–373
    hologram irradiance 4:372–373
    hologram mean number of photoelectrons 4:373
    hologram photoelectron density 4:373–374
    image plane 4:372
    object plane 4:369–371
    pupil plane 4:371–372
  comparison of different recording geometries 4:381
  off-axis IPRG 4:381, 4:382F
  off-axis PPRG 4:381–385, 4:383F
  on-axis PSRG 4:384F, 4:385
  MATLAB® code to exploring off-axis IPRG, off-axis PPRG and on-axis PSRG 4:386–395
  off-axis IPRG 4:374–375
  off-axis PPRG 4:377–378
  on-axis PSRG 4:379–380
  recording geometries 4:370F
  rectangle, comb, impulse, cylinder, and sinc functions 4:385
  2-D convolution 4:386
spatial hole burning 2:340, 2:411, 2:451–452
spatial light modulator (SLM) 2:188, 3:42–43, 4:99, 4:113, 4:114, 4:115, 4:178, 4:179F, 4:191, 4:197–198, 5:91
  LCoS 4:99
  MEMSs 4:99–100
  technology 4:139
spatial modulation methods 5:41
spatial resolution 3:214, 3:216, 4:88
spatial variations 4:456
spatial-multiplexed display 3:48
spatially coherent light 3:249, 3:249F
spatially incoherent light 3:249–250, 3:249F
spatially incoherent objects, synthetic apertures with 3:250–252
spatially resolved spectroscopy 2:249–250
spatially varying complex amplitude transmittance 4:153
Spatio-TEmporally Resolved Optical Laser-Induced Damage test (STEREO-LID test) 4:307F, 4:308
special cables 1:334
special encoding techniques 4:191
specific Doppler-free configuration 4:344
specimen-scanning method 5:194
speckle contrast tomography 4:526
speckle decorrelation 5:64, 5:64–65
"speckle effects" 4:109–110
speckle imaging techniques 3:274–276
speckle interferometry *see* Labeyrie's method
speckle measurements 4:408, 4:408F
spectacles 5:116–119, 5:117F
  contact lenses 5:116–119, 5:118F, 5:119F
  spectacle-type of wearable display 3:51–52
spectral and angular Bragg selectivity 4:124
Spectral and Photometric Imaging Receiver (SPIRE) 1:427, 1:427F

spectral broadening 1:25, 1:181, 1:321, 2:424–425
by SPM 1:19, 1:20F
spectral correlation 4:468–469
spectral decomposition 3:213
spectral density 4:179
spectral diffusion 2:160, 2:160F, 2:165, 2:176
spectral dispersion 4:92
spectral efficiency (SE) 1:299
spectral fluctuations 1:283
spectral hole burning (SHB) 1:250–251, 2:468
spectral interference law 1:41–42
spectral interferogram 4:51, 4:51F, 4:52
spectral interferometry (SI) 2:82, 2:316, 4:48, 4:50, 4:51
spectral interferometry–relative phase measurements 4:50–51
Spectral Karyotyping system (SKY system) 3:213
spectral linewidth 2:459–460
delayed self-heterodyne detection 2:460–461
heterodyne detection 2:460
spectral oscillations 4:271–272, 4:274F
spectral phase interferometry for direct electric field reconstruction (SPIDER) 2:316, 2:317F, 4:48, 4:57–58, 4:58F
spectral properties
frequency tuning 2:417–418
fundamental linewidth 2:417
single-frequency operation 2:417
spectral resolution 3:214–215, 3:216
spectral selection 2:237
spectral sensitivity 4:88
spectral shear 2:316
spectral-domain optical low-coherence tomography (SD-OCT) 4:504–505, 4:505F, 5:156, 5:157F
spectral-domain Zeiss Cirrus instrument 4:506
spectrogram 4:52, 4:53F, 4:54
spectroscopic/spectroscopy 1:51, 1:139, 1:185, 2:244, 5:185
gratings 1:55–57, 1:56F
harmonic conversion 2:246
higher-order and multidimensional 2:249
information 2:244–245
microscopies 5:193
nonlinear optical spectroscopy in chemistry 2:245–246
nonlinear optics for 2:244–245
second-order 2:245–246
spatially resolved 2:249–250
surface second-order 2:246–247
third-order 2:247–248
ultrafast time resolved 2:248–249
spherical aberration 1:114–116, 1:115F, 1:117F
spherical Bessel function 3:160
spherical emitter to spherical receiver, diffraction-propagation from 4:157
spherical refractive anomalies 5:51–52
spherical wavelet 1:62
sphero-cylindrical
correcting lens 5:115
specification of sphero-cylindrical lenses 5:109–110
SPIDER 4:57, 4:58F
spin 1:475, 1:487
control
by ESR and EDSR 1:472
by kinetic exchange 1:472–473
current
coherence control 1:490–491
using two color beams 1:490–491, 1:490F
population 1:490–491, 1:490F
coherence control 1:490–491
qubits 1:472–473
coupling with exchange 1:474
spin-lattice relaxation dynamics in $HoMnO_3$ 2:138
spin–orbit interaction 1:490
spin density wave (SDW) 2:134
Spitzer-Space Telescope 1:425
splice 1:336
split-off band 2:115
splitters 1:339–340
spontaneous decay rate 1:451, 1:455
spontaneous emission (SE) 1:451, 1:456, 2:18, 2:79, 2:105–106, 2:108, 2:112–113, 2:329
spontaneous parametric down-conversion (SPDC) 1:479
spontaneous radiation rate 1:451
spontaneous symmetry breaking 4:291–293
spontaneous transition rate in confined space, modification of 1:451
sputtering 1:210–211, 2:258
square wave modulating envelope 5:204–205
square-law detector 4:347
squeezing 1:464, 1:465
Sr_2IrO_4, odd-parity hidden order in 2:217–220, 2:218F, 2:219F
stability 4:88
stacking 1:196, 4:286–287, 4:287F
stainless steel (StSt) 5:273
standard deviation (SD) 3:124, 4:429
standard Fourier optics techniques 3:278
standard Fourier transform 4:157
standard laser amplification techniques 2:324
standard perturbation–theory techniques 1:173
standard planar hybrid architecture 1:425
standard rate equation model 4:327–329, 4:328F
standard reference material (SRM) 1:316
Standard Single-Mode Fibers (SSMF) 1:255, 1:261
standing light wave 5:214, 5:216F
standing waves 2:453
interaction 5:213
of light 5:207–213
OCE 5:142
state-of-the-art
holographic recording technique 1:377–378
semiconductor manufacturing process 2:446
static color breakup 3:21, 3:21F
static contrast ratio 3:72
static links to optical switching 4:224
static OCE 5:146–147
static random access memory (SRAM) 3:84
static technique 3:95
static wave 4:98
statistical CRB 3:137
steady-state model 1:245–247
steel 1:330
Stellar intensity interferometry 1:49
Stellar interferometry principles 1:47, 3:253–254, 3:254F
stencil-FSC methods 3:22–23, 3:22F, 3:23F
step index fiber 1:33
step index optical fiber 1:222
stereo effect 3:208
stereopsis 5:44
stereoscopic display 3:45
anaglyph 3:45–46
E-holography 3:46
head mounted display 3:46
integral imaging display 3:48
LC lens for 2D/3D switchable display 3:48
multi-planar 3:46–47
polarizing glass 3:45
shutter glasses 3:46
SMV display 3:48
spatial-multiplexed 3:48
time-multiplexed 3:47–48
volumetric display 3:46
Stevens–Johnson syndrome 5:116–117
stilbenes 2:345
Stiles–Crawford effect 5:50, 5:51F, 5:124–125
stimulated Brillouin scattering (SBS) 1:320, 1:321, 4:3, 4:322, 4:322F
stimulated emission 1:97, 2:112–113, 2:325–326, 2:328–329
stimulated Raman adiabatic passage (STIRAP) 5:32–33
stimulated Raman scattering (SRS) 1:258, 1:320, 1:321, 1:357, 4:3, 4:34
stoichiometric lithium tantalite (SLT) 2:294
Stokes parameter evaluation (SPE) 1:316, 1:318, 1:318F
Stokes parameters 1:163–166
Stokes representation 1:167, 1:168T
Stokes vectors 1:160
Stokes wave 2:265
Stokes-Einstein picture 2:171–172
storage capacitor (Cs) 3:31
strain
amplitudes 1:130–131
tuning 1:237
stranded structures 1:332
Stranski-Krastanov growth technique (SK growth technique) 1:245
Straubel functions 5:16
straylight 5:50
streak cameras 4:431–432
"streaming motion" 1:380
strength member 1:330–331, 1:331F
stress
birefringence 1:160
corrosion susceptibility 1:326

stripline devices 1:143
stroke, PBM for 3:121–123
stroke therapy academic industry roundtable (STAIR) 3:122–123
strong field approximation (SFA) 2:318
strong light–matter coupling 1:448–450
strong-field terahertz excitations in semiconductors
  crystalline semiconductor 2:33–34
  dynamical Bloch oscillations 2:36–37, 2:37*F*
  e–h recollisions 2:37–38, 2:38*F*
  excitations in semiconductor 2:34*F*
  HHG in two *vs.* three bands 2:35, 2:35*F*
  non-perturbative quantum interference 2:35–36, 2:35*F*
  resonant *vs.* non-resonant excitations 2:33*F*
  SBEs 2:34
  time-resolved HHG 2:36, 2:36*F*, 2:37*F*
strontium ion laser 2:372–373, 2:373, 2:373*F*
strontium-barium niobate ($Sr_xBa_{(1-x)}Nb_2O_6$) 4:96
structural in vivo multiphoton ophthalmoscopy 5:86–87
structured illumination microscopy (SIM) 5:168–169
sub-apertures 4:407–408, 4:408*F*
sub-band energy 2:101, 2:101–102
sub-carrier multiplexing (SCM) 1:255
sub-millimeter wave lasers *see* terahertz lasers
sub-picosecond pulses 2:468
sub-Poisson statistics 1:452
sub-Poissonian atomic statistics 1:453
subcritical illumination 5:170
submarine cables 1:334, 1:334*F*
Submillimetre Common-User Bolometer Array (SCUBA) 1:430
  SCUBA-2 array 1:430
subpixel divided method 3:62
subsea holography 4:109–110
subsonic advance cruise missile AGM 129A 4:450, 4:450*F*
substantia nigra pars compacta (SNc) 3:125
substitutional doping 2:257
substrate(s) 2:464
  mode 3:67, 5:247
    light extraction 5:248
  role 4:289
successive pulse illumination in acoustical studies 4:528, 4:529*F*
sudden perturbation process 2:377–378
sum frequency generation (SFG) 1:406, 2:208, 2:247, 2:291, 2:314
sum-frequency mixing (SFM) 2:398, 2:446–447
super AMOLED products 3:67
super twisted nematic liquid crystal displays (STN LCDs) 3:2
super-heterodyne receiver 1:373
super-heterodyning 1:374
super-multi-view display (SMV display) 3:48
super-resolving method 3:190
superconducting detectors 1:427–428
superconducting HEB detectors 1:428–430
superconducting quantum interference devices (SQUIDs) 1:427–428, 1:428, 1:484
superconducting resonator 1:475
superconducting TES detectors 1:428–430
superconductivity (SC) 2:123
superconductor-insulator-normal metal (SIN) 1:427–428
superconductor-insulator-superconductor (SIS) 1:421–422, 1:427–428, 1:428, 1:428*F*
supercontinuum generation (SCG) 1:24–25, 1:25*F*, 1:181, 4:3–6
  continuous wave pumped supercontinua 2:431–432
  femtosecond pulse pumped supercontinua 2:428–429
  modeling 2:425–426
  in optical fiber 2:426–427, 2:426*F*
  picosecond pulse pumped supercontinua 2:429–431
  solitons and photonic crystal fiber 2:427–428
  spectral broadening and early supercontinuum sources 2:424–425
  wavelength extension 2:432–434
supercritical angle emission 5:171
supercritical angle fluorescence (SAF) 5:176, 5:178–180, 5:178, 5:180*F*
superfluorescence (SF) 2:63, 2:79, 2:80*F*
  from high-density 2D magnetoexcitons 2:79–81
superlens 3:145
superluminescent diode (SLD) 2:82, 4:507
superposition
  integral 3:263
  principle 1:461–463, 1:486–487
superprism structures 1:147
superradiance (SR) 2:79, 4:266–267, 4:266
superresolution 3:137–138, 3:144–145, 5:16
  depth measurements
    metal-induced energy transfer microscopy 5:180–183
    super-critical angle fluorescence microscopy 5:178–180
    variable-angle total internal reflection fluorescence microscopy 5:176–178
  imaging 3:171–173, 3:172*F*
  microscopy 5:175–176
superstructure grating (SSG) 4:502
surface attached catalysts 2:172–173
surface plasmon polariton (SPP) 2:260–261, 5:247
surface ridge *see* shallow ridge waveguide
surface second-order spectroscopy 2:246–247
surface tensions 3:80–81
surface-plasmon waveguide (SP waveguide) 1:383
surface-sensitive 2D vibrational spectroscopy 2:177–178
susceptibility tensor elements 2:210–211
Su–Schrieffer–Heeger model (SSH model) 5:223
sutures 5:47
swept source (SS) 5:157, 5:158*F*
swept source optical coherence tomography (SS-OCT) 4:436, 4:504–505, 4:505, 4:505*F*, 5:142–143
switch/switching 4:34
  characteristics
    granularity 4:225
    quantitative performance 4:225–226
    scalability 4:225
  core growth 4:230
  curves 1:181–183, 1:182*F*
symmetric topology 4:234
symmetry considerations 2:44–45
symplectic conditions 4:199
symplectic metric matrix 4:199
synchronization 4:45, 4:46*F*
synchronous digital hierarchy (SDH) 4:17, 4:17*T*, 4:60, 4:60*T*
synchronous disk mirroring 1:281
synchronous electrical detection 1:296–297
synchronous modulation technique 1:370–371
synchronous optical network (SONET) 4:17, 4:17*T*
synchronous transport module-level 1 (STM-1) 4:17, 4:60
synchronous transport signal-level 1 (STS-1) 4:17
Synopsis CodeV 4:210–211
synthetic aperture imaging lidar (SAIL) 4:431, 4:439
synthetic aperture lidar (SAL) 4:407, 4:439, 4:440*F*
synthetic aperture radar (SAR) 4:407, 4:439
synthetic apertures with spatially incoherent objects 3:250–252, 3:250*F*, 3:251*F*
  FZP 3:251–252
  random and uniformly redundant arrays 3:252
synthetic prototype 4:35
synthetic pupil 4:409
Sysmex XT-2000i and XT-1800i Automated Hematology Analyzers 4:514–515, 4:515*F*
system intensity transfer function (SITF) 3:236
system performance parameters 4:11–12
system point spread function (SPSF) 3:250–251
system-on-panel (SOP) 3:14, 3:27
systems approach to 3D imaging 3:262–263

T

tabletop
  lasers 2:324
  ultrahigh-intensity lasers 2:324, 2:324*F*
tail-biting 4:324
Talbot effect 3:168, 4:166
tandem connection monitoring (TCM) 1:289, 1:289*F*
tandem OPV devices 5:266–269
tandem scanning microscopy 5:99–100
tandem solar cell 5:288–290
tangential fan 1:118–119, 1:120*F*

taper region 1:200
tapered microstructure fiber (TMF) 1:199–200, 1:200, 1:201*F*
target acquisition model (TA model) 3:235
target of rapamycin kinase (TOR) 3:108
Taylor series 3:259, 4:21–22, 5:90
telecentric architectures 3:36
telecommunication(s) 1:142, 1:224–225, 1:459, 3:199
  fibers 4:1
  industry 1:355
  networks 1:336
  protocols 4:174
  technology 1:226
telecommunications energy-efficiency ratings (TEER) 1:285–286, 1:286*T*
Teledyne Imaging Sensors 1:426
Teledyne Optech 4:483
telephone lines 4:16–17
teleportation 1:462, 1:479
telescope 3:192, 3:241
  plane for derivation of Van Cittert–Zernike theorem 3:244*F*
  resolution 1:83, 1:83*F*
TEM00 Gaussian beam 4:348
temperature 4:469, 4:470–471
temporal analysis by dispersing pair of light E-fields (TADPOLE) 4:58–59
temporal coherence 1:34, 1:37–38, 4:151
temporal color synthesis 3:20–21
temporal gating 2:237–238
temporal heterodyne 4:407, 4:413
temporal profile 2:234
temporal unwrapping by digital holography 4:148, 4:148*F*
temporal variations 4:456
tensor
  equation 1:131
  quantity 1:139
terahertz (THz) 1:403, 1:418, 2:33–34, 2:73, 2:118, 2:124, 2:197, 2:198*F*, 2:201*F*
  emission spectroscopy 2:138–139
  gas lasers 2:119
  generation 2:121
  lamb-dip spectroscopy 1:396, 1:397*F*
  to Mid-IR 2:135–139
  molecular gas lasers 1:379–380
  molecular spectroscopy 1:387, 1:387*T*, 1:389*F*, 1:390*F*, 1:391*T*
    astrophysical molecular spectroscopy 1:396–399
    databases and verification 1:400–401
    influence of THz region on molecular spectroscopy 1:399–401
    laboratory molecular spectroscopy 1:390–391
    rotation vibration spectroscopy 1:389–390
    rotational spectroscopy 1:387–389
  output 2:121–122
  PCA 2:120–121
  photon energy 2:34
  QC-lasers 1:382, 1:383*F*
    frequency combs 1:384
  quantum cascade lasers 2:19
  radiation 1:412
  nonlinear generation 1:384–385
  source 2:121
  spectral region 2:19
  spectroscopy 2:19
  THz-driven AC stark effect of intersubband transitions 2:200–203
  THz-TDS 2:26–27
terahertz detectors 1:418
  see also organic photodetectors
  BIB detectors 1:426
  extrinsic semiconductor detectors 1:423–426
  pair braking photon detectors 1:427–428
  photon detectors 1:418
  for room temperature THz imaging 1:419–422
  semiconductor bolometers 1:426–427
  superconducting HEB and TES detectors 1:428–430
  thermal detectors 1:418–419, 1:419*F*, 1:420*T*
terahertz lasers 1:379
  see also up-conversion lasers
  active regions 1:382–383, 1:382*F*
  germanium intra-valence band lasers 1:380–381, 1:380*F*
  nonlinear generation of THz radiation in mid-IR QC-lasers 1:384–385, 1:385*F*
  optically pumped molecular gas lasers 1:379–380
  QC lasers 1:381–382
  silicon impurity state lasers 1:381
  THz QC-laser frequency combs 1:384
  waveguides and cavities 1:383–384, 1:383*F*
terahertz optical asymmetric demultiplexer (TOAD) 4:41, 4:42, 4:43*F*, 4:44*F*, 4:64
terahertz physics of semiconductor heterostructures
  few cycle THz spectroscopy
    of QC heterostructures 2:25–31
    of Semiconductor Quantum Structures 2:19–21
terahertz two-dimensional spectroscopy 2:150
terrain contour mapping (TERCOM) 4:450
Terumo OFDI system 4:507
testing infrared imagers 3:235–237
tetracene 5:325–326, 5:325*F*
tetrahydrofuran (THF) 5:261–262
texturing 5:292–293
theoretical minimum data rate 3:180
theoretical signal origin 2:152–153
Thereminvox 1:373
thermal annealing 5:261
thermal blooming effect 3:203, 3:203*F*
thermal deformation processing 1:213
thermal density phase grating 2:7
thermal detectors 1:418–419, 1:419*F*, 1:420*T*
thermal effect 3:197–198
  mitigation 2:444–445
thermal energies 2:100
thermal evaporation 1:210–211
thermal imager 3:232
thermal lens(ing) 2:6, 2:444
thermal stability 3:87
thermal tuning 1:237, 1:260
thermally activated delayed fluorescence (TADF) 3:65, 5:241, 5:245*F*
thermally-tuned SGDBR laser 4:250
Thermionic emission 5:233
thermistors 1:427
thermo-optic switch 4:237–238
thermodynamic equilibrium 2:329
thermoelectric coolers (TECs) 1:356
thermophotovoltaics (TPV) 2:262–263
thermoplastic polymers 1:210
thermotropic LC phases 3:8
theta rotating interferometer 3:252–253
theta shearing interferometer 3:252, 3:253*F*
thick grating models 1:131–132
thieno[3,4-b]thiophene (TT) 5:263–264
thieno[3,4-c]pyrrole-4,6-dione (TPD) 5:263–264
thin disk laser (TDL) 2:407, 2:408*F*, 2:409*F*
  see also microchip lasers
  amplified spontaneous emission 2:410–411
  continuous wave 2:411
  Cr doping 2:413
  examples of disks with different coating 2:407*F*
  gain 2:410
  geometry 2:407*F*
  Ho doping 2:413
  materials 2:412–413
  mode locking 2:412
  mounting 2:410
  Nd doping 2:413
  performance in different operation modes 2:411
  principle 2:408–410
  pumping schemes 2:409–410, 2:410*F*
  Q-switch and cavity dumping 2:412
  regenerative and multipass amplification 2:412
  scaling 2:411
  semiconductor 2:413–414
  temperature distribution in rod 2:408*F*
  Tm doping 2:413
  Yb:YAG 2:412–413
thin film EL displays (TFEL displays) 3:1
thin film transistor (TFT) 3:1, 3:5–6, 3:12, 3:27, 3:53, 4:99, 5:239
  a-Si:H thin film and a-Si:H 3:13
  AOS thin film and AOS 3:14–15
  devices
    with bottom-gate ES 3:12*F*
    with different semiconductor layers 3:12*T*
  driver integrated circuit 3:29–31, 3:29*F*
  LCD panel 3:5*F*
  organic thin film and OTFT 3:15
  poly-Si thin film and poly-Si 3:13–14
thin film transistor liquid crystal display (TFT-LCD) 3:25
thin grating 1:131–132
thin lenses, approximations for 1:109–110
thin phase holograms 4:154
thin-element approximation (TEA) 1:53, 2:334
thin-film transistor (TFT) 3:33
thin-film WDM filter 1:266*F*

thin-films filters (TFF) 1:266
third generation Advanced MVA III (AMVA III) 3:61
third harmonic (TH) 2:294
third harmonic generation imaging (THG imaging) 1:180, 2:218, 2:446–447, 4:313, 5:98, 5:98*F*
third order dispersion (TOD) 2:297
third-order nonlinear
  effects 1:16–18
    FWM 1:21–24, 1:24*F*
    propagation of pulse 1:18–19
    SC generation 1:24–25
    spectral broadening by SPM 1:19, 1:20*F*
    SPM 1:16–18
    XPM 1:19–21, 1:21*F*, 1:22*F*
  polarization 4:313–314
  susceptibility 4:311
  third-order nonlinearly chirped FBG 4:31
3rd order optical effects 1:491
third-order spectroscopy 2:247–248
third-order vibrational response functions 2:166
32x32 pixel FPA ladar breadboard
  32x32 pixel laboratory breadboard hardware 5:8–10
  using incoherent chirped amplitude modulation 5:6–7
  incoherent FM/CW FPA breadboard architecture 5:7–8
  laboratory ladar breadboard block diagram 5:8*F*
  MSM detector design and mounting scheme 5:10
  results of laboratory breadboard tests 5:10–13, 5:12*F*
Thomas effect 1:98
Thompson and Wolf experiment 1:39– 0, 1:39*F*
three beam spectral-domain optical low-coherence tomography 4:526, 4:527*F*
three phase-locked THz pulses 2:199–200
360 degrees holographic display 4:119–120
three transmitter and five aperture array 4:411, 4:411*F*
three-beam lidar 4:463
three-channel light-field synthesizer 2:314, 2:315*F*
three-dimension (3D) 3:267, 5:155, 5:162*F*
  case 2:64–66
  CDI technique 3:149
  completeness in 4:404–405, 4:405*F*
  density in 4:404–405
  FDTD model 5:301
  field transformations
    diffraction calculation of 3D PSF 3:264–265, 3:265*F*, 3:266*F*
    geometrical optics transformations 3:262
    PSF for coherent, incoherent, and partially coherent illumination 3:263
    spatial frequency content of 3D PSF 3:263–264, 3:264*F*, 3:265*F*
    systems approach to 3D imaging 3:262–263
  images 4:106, 4:123–124, 5:185
    systems approach to 3:262–263
  laser microvision 4:502, 4:502, 4:502*F*, 4:503*F*
  lidar scanner 4:439
  measurement 4:496
  photonic crystals 1:175
  PSF
    diffraction calculation of 3:264–265, 3:265*F*, 3:266*F*
    spatial frequency content of 3:263–264, 3:264*F*, 3:265*F*
  random wave system 4:278
  recovery problems 3:149
  resolution of far fields 3:138–140
  scattering process 3:149
  vector 5:110
three-dimensional coherent spectroscopy (3DCS) 2:53, 2:156
  quantum pathways and higher-order spectroscopies 2:155–156
three-level lasers 2:417
three-pulse
  transient FWM 2:53
  2D THz spectroscopy on InSb 2:203–205, 2:203*F*
three-step model of HHG 2:235–236
three-wave mixing (ThWM) 2:121–122, 4:325
3D displays 3:44
  see also wearable displays
  augmented and virtual reality display 3:48–49
  classification 3:47*F*
  health issue–visual fatigue 3:45
  physiological depth cue 3:44–45
  principle 3:44
  psychological depth cue 3:44, 3:44*F*
  stereoscopic and auto-stereoscopic display 3:45
3D Elevation Program (3DEP) 4:401
3D micro-electro-mechanical optical switch (3D-MEMS) 4:231–232, 4:232*F*
threshold
  energy 2:116
  fluence 4:349
  irradiance 4:349
threshold signal-to-noise ratio (SNR_{th}) 3:234
threshold voltage (V_{TH}) 3:14
thresholdless laser 1:456
thromboxane 3:111
throughput SFR 3:182
throw ratio 3:38, 3:38*F*
thulium 2:413
  doping 2:413
  thulium-doped amplifiers 1:263
THz time-domain spectroscopy (THz-TDS) 2:136
THz-air-biased-coherent-detection (THz-ABCD) 1:414–415
Tisapphire
  crystal 2:290, 5:41
  laser 4:347, 4:364, 4:365*F*
tight cables 1:334
tight jacket 1:328, 1:329*F*
tilted pulse front 1:409, 1:410*F*
tilting-plate compensators 1:156–157
time 2:184
  coherence 1:34, 1:34*F*
  diffraction limit 4:357
  dimension in velocity measurement 4:526
  domain 3:87
    electric laser field in 2:234
    expressions 2:55
    instrument 3:259
    methods 5:39
    model and pattern effects 1:247–248
  gating 3:223–225
  methods 5:40–41
  resolved optical calorimetry 2:5–7
  resolved photoemission spectroscopy 2:144–145, 2:145*F*
  time-altitude diagrams 4:467, 4:468*F*
  time-averaged intensity distribution 4:174
  time-dependent
    diffusion approximation to transport equation 3:222
    electric field 2:234
    perturbation theory 2:53
    variations of pulse 4:48
  time-to-frequency mapping 4:434, 4:434*F*
  time–bandwidth product 1:135–136
time and wavelength division multiplexed PON (TWDM-PON) 2:74, 2:78–79
time correlated single photon counting (TCSPC) 4:475
time division multiple access (TDMA) 1:255, 2:73, 2:74, 2:77
time division multiplexing (TDM) 1:226, 1:255, 1:428, 2:73, 2:77, 4:7, 4:34, 4:45, 4:60–61
  see also wavelength division multiplexing (WDM)
  T1 TDM 1:226
  T2 TDM 1:226
  T3 TDM 1:226
time-dependent Fresnel zone plate (TDFZP) 1:377–378
Time-Division Multiplexed Passive Optical Networks (TDM-PONs) 2:74, 2:78
  BPONs 2:74, 2:75*F*
  comparison of standardized 2:78*T*
  GE-PON 2:76
  GPONs 2:74–76, 2:75*F*
time-domain optical low-coherence tomography (TD-OCT) 4:504, 4:504, 4:504*F*, 5:155–156
time-domain spectroscopy (TDS) 1:418, 2:19
time-domain system (TDS) 2:25–26
time-frequency
  relationship in chirp signal 4:499–500, 4:499*F*
  representation 4:51–52
time-integrated optical spectroscopy of correlated electron materials 2:130–131
  Drude–Lorentz model 2:131–132
  general features of optical response in correlated electron materials 2:131
time-multiplexed type 3:47–48, 3:62
time-of-flight (TOF) 2:322
  camera sensor 4:510–511, 4:511*F*
  measurement 4:502–503
  principle with matricial detectors 4:510–511

time-of-flight (TOF) (*continued*)
time-resolved fluorescence spectroscopy 4:518–519, 4:519F
time-resolved HHG 2:36, 2:36F, 2:37F
time-resolved optical spectroscopy of correlated electron materials 2:132–135
  all-optical pump–probe spectroscopy of correlated electron materials 2:133–135
  angle-resolved photoemission spectroscopy 2:144–145
  mode-selective excitation 2:139–141, 2:141F
  PIPT 2:139–141
  UED 2:143–144
  ultrafast extreme UV and X-ray diffraction and spectroscopy 2:141–143
  ultrafast infrared spectroscopy 2:135–139
  ultrafast microscopy 2:146–149
  ultrafast second harmonic generation spectroscopy 2:145–146
time-resolved photoemission spectroscopy 2:144–145, 2:145F
time-resolved THz spectroscopy 2:21
time-resolved SHG (trSHG) 2:146
timing controller (T-Con) 3:29–30
tin dioxide (SnO_2) 5:288
tin-doped indium oxide (ITO) 5:273
tip/tilt correction 3:202
TIR-Fluorescence Correlation Spectroscopy (TIR-FCS) 5:172
TIR-Fluoresence Recovery After Photobleaching (TIR-FRAP) 5:172
tissue damage, PBM for 3:117–118
tissue inhibitors of metalloproteinases (TIMPs) 3:118–119
titania (TiO_2) 1:28, 5:288
Tokyo university of agriculture and technology (TAUT) 4:118, 4:118F
toll-like receptors (TLRs) 3:112
tomographic/tomography
  analysis 4:177
  examples based on laser profiling 4:483–489
  modalities 4:174
  reconstruction algorithm 4:174, 4:176
  techniques 4:174
toneburst modulation (TM) 1:392–393
top cladding 1:186
top emission OLED (TOLED) 3:5
top gate structure (TG structure) 3:12–13
Topcon TRC-50DX mydriatic retinal camera 4:521–522, 4:521F
Topcon's KR-1W 4:531
topological charge distribution 4:186–187
topology, deterministic 4:234
toricity 5:44–45
total depth (TD) 4:507
total dispersion 4:1–2, 4:2F
total internal reflection (TIR) 1:124–125, 1:124F, 4:124, 5:247
  combined with FRAP or FCS or FLIM 5:172
  polarization 5:169
  reflected beam in 5:170–171
  scattering 5:171–172
total internal reflection fluorescence (TIRF) 5:176, 5:176F
  on single molecules 5:172–173
total internal reflection fluorescence microscopy (TIRFM) 5:168
  lateral resolution 5:168–169
  qualitative basic principles 5:168
  reflected beam in TIR 5:170–171
  supercritical angle emission 5:171
  two photon TIRF 5:170
  variable polar angle illumination, including subcritical 5:169–170
total isolation 1:266
total kinetic energy 2:116
total noise factor (F_{total}) 1:249
Toyozawa lineshape 2:48–49
tracking control 5:32–33
tracking micro-lidars 4:507–509
traditional analysis interferometry (TNTY) 1:318
traditional damage tests 4:306–307
traditional double-clad fibers 1:201, 1:201–203
traditional dye lasers 2:336
traditional fiber 1:195, 1:201
traditional light trapping 5:294
traditional monovision 5:125
traditional OCT (TD-OCT) *see* time-domain optical low-coherence tomography (TD-OCT)
traditional wide-field conventional microscope 5:194
trailer effect 3:72
transcranial Doppler ultrasound (TCD) 3:126–127
transfer function 1:2
  of MZM 1:261
transfer matrix method (TMM) 1:213, 5:303
transflective LCD 3:6F, 3:7
transform-limited (TL) 2:295
  pulse duration 2:295
  single-mode laser pulse 4:344
transformation equations 4:182
transformation optics (TO) 2:252–253, 2:263–264
transient absorption changes 4:270–271, 4:272F, 4:273F
transient density phase grating technique 2:4–5, 2:7
transient grating (TG) 2:2F, 2:189
  principle 2:1F
  setup with pump–probe detection 2:3F
  signal 2:189
  techniques 2:10
transient holographic grating techniques in chemical dynamics
  applications 2:3–5
  beam geometry for transient grating 2:4F
  classification of possible contributions to transient grating signal 2:2F
  determination of material properties 2:7
  experimental setup 2:3
  investigation of population dynamics 2:7–8
  polarization selective transient grating 2:8–10
  principle 2:1–3
  principle of transient grating technique 2:1F
  time resolved optical calorimetry 2:5–7
  transient density phase grating technique 2:4–5
  transient grating setup with pump–probe detection 2:3F
transient photoluminescence (TRPL) 5:284
transient receptor potential Ankyrin (TRPA) 3:116
transient receptor potential channels (TRP channels) 3:116
transient receptor potential Melastatin (TRPM) 3:116
transient receptor potential Mucolipin (TRPML) 3:116
transient receptor potential NOMPC (TRPN) 3:116
transient receptor potential Polycystin (TRPP) 3:116
transient receptor potential Vanilloid (TRPV) 3:116
transillumination 3:225–226
transimpedance amplifier (TIA) 4:6, 4:423, 5:8
transistors 2:119, 5:317
transition amplitude 1:489–490
transition metal (TM) 2:125, 2:436
transition metal dichalcogenides (TMDs) 2:57, 2:69–71
  optical 2DCS 2:53–56
  optical properties of monolayer 2:57–58
  2DCS of monolayer 2:58–59
transition metal laser advantages and issues 2:441–442
  concentration effects 2:444
  ESA 2:442
  mitigating thermal effects 2:444–445
  nonradiative relaxation 2:442–444
  thermal lensing 2:444
transition metal oxides (TMOs) 2:124, 2:124–126
  ferroelectrics 2:128
  high-T_c superconductors 2:126
  magnetically ordered oxides 2:127–128
  ME multiferroics 2:128–129
  oxide heterostructures 2:129
  vanadium dioxide and related materials 2:126–127
transition metal spectroscopy
  crystal field theory 2:436–437, 2:436F
  SCC model 2:437–440, 2:438F
transition process 1:224, 1:486–487, 2:106
transition-edge sensor (TES) 1:428, 1:430
  superconducting TES detectors 1:428–430
transition-edge superconducting bolometers (TES bolometers) 1:428
Translating-Wedge-Based Identical Pulses eNcoding System (TWINS) 2:189
transmembrane domain of M2 channel (M2TM) 2:176
transmission 1:153–154, 1:172, 2:85
  effects in optical fibers 1:255–256
    linear 1:255–256
    nonlinear fiber 1:257–259

fiber 1:195, 1:351, 4:21–22, 4:30–31
function 1:76
continuous part of phase function 4:187
gradient of singular phase function 4:187–188
rotation transform 4:188
topological charge distribution 4:186–187
holograms 4:87
of OTDM signal over fiber 4:63
polarizers 1:153–154
through thin object 4:167–168
transmission computerized tomography (TCT) *see* X-ray tomography
transmission electron microscopy (TEM) 1:468, 3:120–121, 5:192, 5:298–300
transmissive displays 3:79
transmissive liquid crystal displays panels (transmissive LCDs panels) 3:6*F*, 3:32
transmittance of polarizer 1:149
transmitted near field technique (TNF) 1:322
image technique 1:323–324
transmitter circuitry 4:254–255
see also receiver circuitry
electroabsorption modulator transmitters 4:255–257
MZMs transmitters 4:258–259
ring resonator modulator transmitters 4:257–258
VCSEL transmitters 4:254–255
transmitter optical sub-assemblies (TOSAs) 4:252–253
transmitters
circuits 4:222
requirements 4:68
WDM 1:260
transoceanic fiber optic cable systems 4:18
transparency 2:351
transparent conducting oxides (TCOs) 2:257–258, 2:257, 5:279
transparent cornea 5:43
transparent electrode 3:26
Transparent OLED (TOLED) 3:66, 3:67*F*, 5:252
transparent polymers 2:346
transport derivation of intensity equation 4:166
transport equation (TE) 3:257
polarization 1:55
transport of intensity equation (TIE) 3:151
transpupillary thermotherapy (TTT) 5:134
transverse aberration 5:55, 5:56*F*
transverse Anderson localization
of light 4:278–279
in theory and experiment 4:279–281
transverse Cartesian coordinate 4:188
transverse chromatic aberration 5:59, 5:91
transverse coherence length 1:35–36
transverse electric (TE) 1:144, 1:173, 2:385
emission spectra 2:275
modes 1:207, 1:242
waves 1:185
transverse electromagnetic modes (TEM modes) 4:356, 4:356*F*
transverse image, intensity distribution on 5:19–22
transverse magnetic (TM) 1:144, 1:173, 2:385
emission spectra 2:275
modes 1:207, 1:242
waves 1:185
transverse mode(s) 2:329–331
definition 2:417
structure 1:178
transverse overlapping 4:322–323
transverse resolution 3:142, 5:158
transverse spherical aberration (TSA) 1:114–116, 1:115*F*
transverse translation-based techniques 3:151–153
alternating projection algorithms 3:152–153
illumination angle scanning-based Fourier ptychography 3:154–155
mode multiplexing algorithms 3:153
multi-slice algorithms 3:153–154
transverse waveguide component 2:351
transversely excited atmospheric pressure (TEA pressure) 2:334
trapping
schemes 5:294
states 1:454, 1:455*F*
trapping/cooling laser for mercury atoms 2:448–450
traumatic brain injury (TBI) 3:123–124
traveling wave 4:98
laser 2:453
OCE 5:147
SOAs 1:242
triacetyl cellulose (TAC) 3:25–26
triangle orientation discrimination (TOD) 3:235
triangular grating 1:51*F*, 1:52
triangular lattice 1:190–191, 1:196
triazole (TAZ) 5:234
trifocal intraocular lenses 5:123
trigonometric functions 5:16
trimethylaluminum (TMA) 2:273
trimethylgallium (TMG) 2:273
Trinitron CRT 3:3
trion resonance spectrum 2:62
triple-beam
configuration 4:533, 4:534*F*
spectral-domain OCT 4:526–528
triplet–triplet annihilation (TTA) 3:64, 5:242, 5:245*F*
tristimulus 3:17
trunk lines 1:226
TSI 3563 nephelometer 4:513, 4:513*F*
tuberculosis 3:102–103
tumor necrosis factor alpha (TNF-α) 3:118–119
tumor rejection antigen 3:113
tumor to normal tissue ratio 3:110
tumor-associated macrophages (TAMs) 3:110–111
tumors direct destruction by PDT 3:111
tunability 4:28, 4:28*F*, 4:29*F*
tunable attenuators 1:342
tunable device 1:203, 1:204*F*
tunable dispersion compensation
see also fixed dispersion compensation
approaches to 4:28–30, 4:30*F*, 4:31*F*
need for tunability 4:28, 4:28*F*, 4:29*F*
'tunable Fabry–Perot' fibers 1:213–214
tunable laser (TL) 1:260, 4:500
optical switch technologies 4:241
tunable microstructure fiber devices 1:203–205
tunable ONU transceivers (TRXs) 2:79
tunable thin-film filter (TTF) 2:455
tunable WDM filters 1:268
Tungstates 2:266
tuning range 2:296
tunnelling
process 1:469
and transport dynamics 2:85–86
turbine compressors 2:333, 2:334
turn around point (TAP) 1:234
"Twin Janus" *see* Janus Geminus
twin-guide technology (TG technology) 4:244
twist nematic liquid crystal displays (TN LCDs) 3:59, 3:72
"twisted-mode" laser 2:453
two color beams
coherence control of carrier density, spin population, and spin current 1:490–491
coherence control of electrical current 1:488–490
two dimension (2D) 2:197, 4:177–178
approach 1:191–192
ATR spectroscopy 2:178
autocorrelation 4:375
case 2:66–68, 2:68*F*
characterization 4:177–178
coherent spectra 2:150
convolution 3:263, 4:375, 4:386
DFT 3:150
distribution of particle velocities 4:528, 4:529*F*
EV spectroscopy 2:179
Fourier model 3:149
Fourier transform spectroscopy 4:276
fractional Fourier transform 4:157
hole crystal 1:174
imaging supplemented by scanning in z direction 4:445–449
linear canonical integral transform 4:175
magnetoexcitons 2:78–79
materials 4:284, 4:284*F*
NMR spectroscopy 2:164
phase retrieval 4:52
problem 4:54
photonic crystals 1:173, 1:185, 1:190–191, 1:384
plasmonic materials 2:261
PST for 4:177–178
ranging supplemented by two-dimensional scanning 4:414–445
SFG spectroscopy 2:178
SHG for characterization 4:284–285
simultaneous differential equations 4:201
THz spectroscopy with three phase-locked THz pulses 2:199–200, 2:200*F*

two dimension (2D) (*continued*)
time-frequency function 4:164
two-dimensionally periodic gratings 1:52
unbounded disordered systems 4:278
unit matrix 4:210
VE spectroscopy 2:179
Walsh functions 5:17
in polar coordinates 5:18–19, 5:19*F*
in rectangular coordinates 5:18
2 f-imaging 2:409
two photon TIRF 5:170
two sine modulation signals 4:499, 4:499*F*
two telescopes interferometer of Labeyrie 3:254
two-axis gimbal-less MEMS mirror 4:528
two-color method 1:412–416
peak THz electric field strength ranges 1:416*T*
phase scan 1:414*F*
THz
emission from along, two-color laser-induced filament 1:415*F*
field as function of laser intensities 1:413*F*
wave generation efficiency 1:413*F*
two-color rapid acquisition coherence spectroscopy (T-RACS) 2:192
two-dimensional coherent spectroscopy (2DCS) 2:53, 2:150
experimental implementation 2:56–57
of monolayer TMDs 2:58–59
optical 2:53–56
optical properties of monolayer TMDs 2:57–58
polarization control of quantum pathways in 2:154
pulse sequencing to control quantum pathways in 2:154
double quantum 2D spectra 2:155, 2:155*F*
nonrephasing 2D spectra 2:154–155
rephasing 2D spectra 2:154, 2:155*F*
two-dimensional infrared spectroscopy (2D IR spectroscopy) 2:150, 2:164
applications 2:168
brief theory 2:164–166
broadband light sources 2:178
delay-lines and sample chamber 2:166–167
dynamics of water 2:176–177
experimental approaches 2:166
material sciences 2:168
microscopy 2:178–179
perspective 2:177–178
protein structure and folding dynamics 2:173–175
schematic 2D IR pulse sequence and spectra 2:165*F*
signal detection systems 2:167–168
surface-and interface-sensitive 2D vibrational spectroscopy 2:177–178
2D EV spectroscopy 2:179
2D VE spectroscopy 2:179
ultrafast IR light source 2:166
two-directional velocity measurement 4:525–526
"two-faced" or "Janus effect" 3:100
two-grating compressor 4:179
two-level
model 2:89–90
quantum systems 1:478
two-path interference 5:41
two-photon absorption (2PA) 1:488, 2:267, 4:319–320, 4:320, 5:39, 5:89
two-photon excitation (TPE) 5:88, 5:98*F*
artifacts and implementation of TPE fluorescence ophthalmoscopy 5:89–91
microscopy 5:199
two-photon excited fluorescence (TPEF) 5:98
ophthalmoscopy 5:93
two-photon fluorescence microscopy method 2:249
two-photon imaging 1:484
of *Acanthamoeba* keratitis 5:104*F*
of corneal cross-linking 5:105–106
of human cornea 5:105*F*
of infectious keratitis 5:103–104
of limbal stem cells 5:103
of mice limbal stem cells 5:104*F*
of normal cornea 5:81*F*, 5:83
two-photon microscopy 5:75*F*, 5:80*F*
of enucleated rabbit eyes 5:106*F*
laser safety considerations 5:106–107
laser scanning microscopy 5:98–99, 5:102
two-photon transitions
attosecond beating reconstruction by interference of 2:241–242
excitation of 2:248
two-photonexcited fluorescence microscopy (TPEF microscopy) 5:85
two-photonexcited fluorescence ophthalmoscopy (TPEFO) 5:86–87
two-point
correlation function 4:174
resolution 5:186
two-pulse transient FWM 2:53
two-quantum spectrum 2:56
2D electron gas systems (2DEG systems) 2:261
2D electronic spectroscopy (2DES) 2:184, 2:185*F*, 2:187–188*T*
see also attosecond spectroscopy; multidimensional THz spectroscopy
applications 2:190–191
BOXCARS geometry 2:185–188
challenges 2:184–185
charge transfer in OPVs 2:194
coherence 2:192–193
early 2D studies 2:190–191
excitonic electronic structure and dynamics in J-aggregates 2:193–194
experimental implementations 2:185–188
fully collinear geometry 2:189–190
noise suppression 2:190
photosynthesis 2:191–192
single-shot measurements 2:190
solid state systems 2:194–196
2D infrared (2DIR) 2:184
microscopy 2:178–179
spectra of Q24 2:175, 2:175*F*
2D micro-electro-mechanical optical switch (2D-MEMS) 4:232–233, 4:232*F*
2D spectra/spectroscopy 2:150
connecting 2D and 1D spectra 2:161–162, 2:162*F*
of inhomogeneously-broadened systems, interpretation 2:158–160
measuring homogeneous and inhomogeneous linewidths 2:160
spectral diffusion 2:160, 2:160*F*
interpretation 2:157
anharmonic oscillator spectra interpretation 2:160–161, 2:161*F*
connecting 2D and 1D spectra 2:161–162, 2:162*F*
of coupled systems 2:157–158
homogeneous lineshapes 2:157
resolution in 2:157
2D ultraviolet (2DUV) 2:184
type-I multiferroicity 2:129
type-I reaction 3:101, 3:102
type-II multiferroics 2:129
type-II reaction 3:101, 3:102
typical LCoS pixel pitch 4:99

U

ultra violet sources (UV sources) 1:234–235
ultra-broadband
non-zero dispersion-shifted single-mode fibers 1:261, 1:262
OPAs 2:298–299
ultra-high performance (UHP) 3:40–41
ultra-realistic holographic imaging techniques 4:105
ultra-short-throw (UST) 3:37–39
US Patent 20130162957 A1 3:39*F*
US Patent 7, 009, 765B2 3:38*F*
US Patent 7441908 3:39*F*
US Patent 9, 372, 388 B2 3:40*F*
ultrafast and intense-field nonlinear optics
high-harmonic generation 4:337
multiphoton absorption 4:336
nonlinear quantum electrodynamics 4:338
nonlinear refractive index 4:335–336
optical damage 4:336–337
plasma nonlinearities and relativistic effects 4:337–338
self focusing, supercontinuum generation, and filamentation 4:336
ultrafast control of magnetization dynamics 2:141
ultrafast electron diffraction (UED) 2:143–144
ultrafast extreme UV and X-ray diffraction and spectroscopy 2:141–143
ultrafast femtosecond pulse 1:405
ultrafast infrared spectroscopy 2:135–139
ultrafast laser pulses 4:48, 4:348
ultrafast microscopy 2:146–149
ultrafast mid-IR spectroscopy 2:135
ultrafast optical fiber lasers 2:121
ultrafast optical spectroscopy (UOS) 2:124, 2:132
ultrafast second harmonic generation spectroscopy 2:145–146

ultrafast spectroscopy 2:19, 2:86
ultrafast time resolution to ARPES (trARPES) 2:144
ultrafast time resolved spectroscopy 2:248–249
ultrahigh Q microcavities 4:298–299
ultrahigh speed OTDM system 4:38
ultrahigh vacuum (UHV) 5:266
UltraQReflex™ system 5:134–135
ultrasensitive nonlinear phase-shifters 2:18
ultrashort electron pulses 2:233
ultrashort femtosecond laser pulses 1:414–415
ultrashort laser pulse technology 2:233
ultrashort optical pulse sources 4:48, 4:62–63
ultrashort pulse
  characterization 2:316
  generation 2:283
  lasers 4:348, 5:92
  ultrashort-pulse dye lasers 2:340, 2:341F
ultraslow propagation of pulses 4:345
ultrasound technology 5:155
ultrathin metal film (UTMF) 5:303–304
ultraviolet (UV) 2:290, 2:373, 4:344, 5:85
  absorption spectrum 1:235, 1:235F
  AlGaN laser diodes 2:271
  lasers 2:356, 2:446, 4:364–366, 4:366F
    dyes 2:348
    enhancement factors as function of resonator loss 2:449F
    frequency-doubled argon ion laser 4:366
    frequency-doubled krypton ion laser 4:366
    HeCd laser 4:366–367
    nonlinear optical crystals and properties 2:447T
    optical resonator with nonlinear crystal inside 2:448F
    quasi-CW mode-locked Ti:Sapphire laser 4:367
    reflected power at fundamental as function of input coupler 2:449F
    second harmonic output power as function of input coupler 2:449F
  light 5:131
  photo-emission 2:246
  photolithography 5:204
  radiation 5:191, 5:191F
  UV-excitable fluorophores 5:86
  UVA 5:136
  UV–visible spectroscopy 2:131
uncertainty principle 2:435
uncorrected myopes 5:51
uncoupling variables 4:162–163
uncyclic unsaturated hydrocarbons 2:345
under-critical angle fluorescence (UAF) 5:178
undersea optical cable systems 4:18
underwater cables 1:334
"undoping" process 5:227
unguided rays 1:222, 1:222F
unidirectional backscattering curves 1:310, 1:310F
uniform and chirped fiber gratings 1:233
uniform" BHJ structure 5:261
uniformity 3:71–72
uniformly redundant arrays 3:252
unit interval (UI) 4:263
unit vectors 4:451, 4:451F
unitary transform 4:181
United States Geological Survey (USGS) 4:401
  lidar base specification 4:401
Universal Lidar Error Model (ULEM) 4:402
  metadata 4:402–403
  sensor-space error modeling 4:403F
unmanned aerial vehicle (UAV) 4:449, 4:474, 4:484F
unsampled surface fraction (USF) 4:405
unsaturated regime 1:352
unscattered photons 3:219
up conversion mechanisms 2:394
up-conversion lasers 2:394
  see also noble gas ion lasers
  based on bi-functional crystals 2:403–404
  based on luminescence mechanisms in materials 2:399–400
    energy transfers 2:400, 2:401T
    photon avalanche 2:402–403, 2:404T
    sequential two-photon absorption 2:400–402, 2:401F, 2:402F, 2:402T
  from luminescence mechanisms 2:394–395
    energy transfers 2:394–395, 2:395F
    materials 2:397
    photon avalanche 2:396–397, 2:396F
    sequential two-photon absorption 2:395–396, 2:396F
  from second-order optical nonlinearity 2:397–399, 2:399F
upper exciton polaritons (UP) 1:448–449, 1:449F
upstream bandwidth map 2:75
uveal tract 5:43

V

V-shaped cavity 2:285
Vac-Ion® vacuum pump 2:382
vacuum fluorescent display (VFD) 3:1, 3:3–4
vacuum Rabi frequency 1:448–449
vacuum ultraviolet (VUV) 2:359–360, 2:360–361, 4:344
valence band maximum (VBM) 5:256, 5:284, 5:286–287
valence band(s) 1:171, 2:33–34
  electrodes 1:224
valence electrons 1:224
valley physics 1:467
valley superposition 1:467–468
van Cittert–Zernike theorem 1:38–39, 1:38F, 3:149, 3:245
van der Waals energy 1:452
van der Waals epitaxy (VDWE) 4:284
Vanadates 2:266
vanadium atoms 2:126–127
vanadium dioxide (VO_2) 2:126
  and related materials 2:126–127
vanilla algorithm *see* frequency-resolved optical gating (FROG); inversion algorithms
vapor-axial deposition process (VAD process) 1:28, 1:29–30, 1:30F
vapor-phase oxidation 4:14–15
variable frequency shifter 1:140
variable geometry pupil technique (VGP technique) 3:279
variable length records (VLRs) 4:402–403
variable polar angle illumination 5:169–170
variable retardation plates 1:156–159
variable-angle total internal reflection fluorescence microscopy (vaTIRF) 5:176–178, 5:177
varifocal lens(es) 4:177, 4:178–179
vascular endothelial growth factor (VEGF) 3:120, 5:132
VECSEL cavity geometries 2:285F
vector addition technique 1:93
vehicle borne laser radar 4:483
velocity 4:470–471
Velodyne Lidar 4:483
venerable algorithm 3:163
vertical alignment mode (VA mode) 3:9
vertical cavity surface emitting lasers (VCSEL) 1:186, 1:214, 1:227, 1:384, 1:459, 1:459F, 2:280, 2:281F, 2:283F, 2:413–414, 2:466, 2:466F, 2:467F, 3:88, 4:3, 4:67, 4:254, 4:293, 4:358
  transmitters 4:254–255, 4:255F, 4:256F
very high range resolution lidars 4:431
  applications 4:438–439
    advanced coherent imaging with FMCW lidar 4:439–440
    aspherical optical metrology 4:438–439
    noncontact 3D metrology 4:439
  brief-pulse, direct-detect lidar 4:431
  coherent mode-locked lasers 4:432
  FMCW lidar 4:434–435
  range precision 4:430–431
  range resolution 4:430–431
  streak cameras 4:431–432
very high resolution FMCW lidar 4:435–436
  active chirp laser stabilization for FMCW lidar 4:436
  chirp nonlinearity 4:435–436, 4:435F
very large array (VLA) 3:254–255
very large scale integration (VLSI) 1:144–146, 2:115, 2:387–388
very large telescope interferometer (VLTI) 3:245, 3:254–255, 3:254–255
very large telescopes (VLT) 3:253
very low density lipoprotein (VLDL) 3:110
vestigial singleside band (VSB) 4:7, 4:31–33
vibrating galvanometer-type mirrors 5:194
vibrational/vibration 2:328, 4:452–455
  coherence 5:40
  curve 1:92–93, 1:93F
  energy groupings 2:326
  frequency 2:217
  imensity map 4:453, 4:454F
  measurement of vocal folds 4:528–530
  mode coupling 5:39
  relaxation 2:328
  transfer rates 2:328

vibrational/vibration (*continued*)
video camera 4:107
Video Electronics Standards Association Standards (VESA Standards) 3:70
video techniques 5:64
view angles of liquid crystal displays 3:59
  controlled viewing angle of LCDs 3:62
  improvement from LC modes 3:60–61
  latest approaches of wide view angle LCDs 3:61–62
  optical compensation film 3:59–60
viewing angle 3:74–75
viewing cone 3:74–75
viewing zone-scanning holographic display system 4:118, 4:119*F*
violet InGaN laser diodes 2:278
violet laser dyes 2:348
violet wavelengths 2:373
virtual image 3:208–209, 4:107
virtual reality (VR) 3:48, 3:49*F*, 4:124
  devices 3:75
  display 3:48–49
  HMD 3:51, 3:51*F*
virtual SAF (vSAF) 5:180
virtually imaged phased array (VIPA) 4:29, 4:432, 5:149
virulence 3:105
viscoelastic effect 5:145–146
visibility of interference fringes 1:37
visible and near-infrared light 2:150
visible lasers 4:359–360
  argon ion laser 4:360–361
  He-Ne laser 4:359–360
  HeCd laser 4:361
  krypton ion laser 4:361
visible light 5:86
"visible region" 3:141
vision correction methods
  chromatic aberration 5:120
  future of 5:126–127
  presbyopia 5:120–122
  refractive surgery 5:125–126
  spectacles 5:116–119
  visual benefit of correcting higher order aberrations 5:119–120
vision problems, PBM for 3:121
visual analog scale (VAS) 3:125
visual benefit of correcting higher order aberrations 5:119–120
visual quality 3:183–185
visual stimulus 5:64, 5:111
visual Strehl ratio 5:115
visual tasks 5:119
visualization of aberrations
  in freeform systems 4:208–209
  in phase space 4:206–208
vitreoretinal disorders 5:134–135
vitreous humor 5:43
vocal folds, vibration measurement of 4:528–530, 4:529*F*
voice coil actuator (VCA) 4:507
voice coil motor (VCM) 3:37
Voigt profile 2:55–56
voltage controlled oscillator (VCO) 4:6, 4:45
voltage standing wave ratio (VSWR) 4:69
volume Bragg grating (VBG) 2:416
volume diffraction theory 3:267
volume holographic imaging (VHI) 3:267, 3:267*F*
volume turbulence 4:413
volumetric display 3:46
Voronoi diagram 5:79–80, 5:80*F*
voxels 4:404
vulval intraepithelial neoplasia (VIN) 3:114

W

wall-plug power efficiencies (WPE) 1:382
Walsh filters 5:27–28
Walsh functions
  Azimuth invariant case 5:19
  intensity distribution
    along axis around image/focal plane 5:22–27
    on neighboring transverse planes 5:27
    on transverse image/focal plane 5:19–22
  one dimensional Walsh functions 5:17–18
  in optical masks 5:16, 5:16–17
  radial Walsh functions 5:19
  two dimensional Walsh functions
    in polar coordinates 5:18–19
    in rectangular coordinates 5:18
  Walsh filters as optical masks 5:19
Walsh-Hadamard single-pixel
  applications 4:196–197
  imaging 4:195–196, 4:195*F*
Wannier excitons 2:93
Wannier–Mott exciton 5:223–224
warehouse scale computer (WSC) 1:227, 1:227*F*
watch-type of display 3:53
water 5:277
  attosecond pulse generation in water-window region 2:321
  cooled ZnSe lens 2:329–331
  dynamics 2:176–177
  role in influenza M2 channel 2:176
  vapor profiles 4:456
  water-soluble dyes 2:349
wave 4:199
  aberration 5:55, 5:56*F*, 5:59–60
  equation 4:335
    in nonlinear regime 4:311–312
  field 4:139
  front
    difference 4:410, 4:412*F*
    errors 4:410
    'reversal' beam 4:322
  optics 4:200
  propagation 1:169–170, 3:142
    equation 5:203
    process 3:139
  theory 1:222
  vector 4:180
wave plate (WP) 2:211
wave recording plane technique (WRP technique) 4:123
wave-mixing in Doppler broadened medium 4:344
wave-vector mismatch 2:291
wavefield 3:205
wavefront aberrations
  ray aberrations converting to 5:113–115
  time-scale and associated aberrations 3:197–198, 3:198*F*
wavefront aberrometers 5:111–112
wavefront distortion 3:200
wavefront healing 3:207, 3:207*F*
wavefront reconstruction 4:531
wavefront sensing micro-lidars 4:530–531
  Hartmann–Shack ocular wavefront sensing 4:530–531
  ray tracing aberrometry 4:531–533
  wavefront reconstruction 4:531
wavefront sensing technique 3:198, 5:112–113
  optical path lengths determining from ray deflections 5:112–113, 5:113*F*
  optimizing retinal image quality by correcting refractive errors 5:115
  ray aberrations converting to wavefront aberrations 5:113–115
wavefront sensor system (WS system) 3:198
wavefront sensors and control
  hybrid techniques
    adaptive optics and post-processing 3:278–279
    PRPM 3:279
  imaging and atmospheric turbulence 3:272–274
  post-detection compensation 3:274–276
  pre-detection compensation 3:278
wavefunctions 1:462, 2:66, 2:91, 2:99, 2:100–101, 2:102*F*, 5:204
waveguides (WG) 1:383–384, 1:383*F*, 2:384, 2:385*F*, 2:445
  configuration 2:445
  dispersion 1:6–7, 1:313, 1:314*F*, 4:1–2, 4:2*F*
  group velocity dispersion 1:6–9
  laser materials 2:387–388
  mode 1:190–191, 3:67
  waveguide-MEMS optical switch 4:240–241, 4:240*F*
waveguiding mode 5:247
  light extraction 5:248–251
wavelength division multiple access (WDMA) 1:255
wavelength division multiplexed PONs (WDM-PONs) 1:252, 1:252*F*, 2:74, 2:81–82, 2:81*F*
wavelength division multiplexing (WDM) 1:23, 1:143, 1:147, 1:214–215, 1:226, 1:237*F*, 1:245, 1:255, 1:291, 1:336, 1:339–340, 1:341–342, 1:341, 1:355, 1:356, 1:364, 1:371*F*, 2:81, 2:455, 4:1, 4:17, 4:20–21, 4:20, 4:34, 4:45, 4:60, 4:254
  see also time division multiplexing (TDM)
  achievable bit-error rates 1:276–277
  amplifier technologies 1:263*F*
  chromatic-dispersion compensation 1:265
  components and sub-systems 1:259–260

in data center interconnects 1:281–282
demultiplexer isolation 1:272F
development of WDM systems transport capacity over time 1:255F
entrance 4:17–18
long-haul WDM systems 1:282–284
in metro and access networks 1:280–281
mixed 10 Gb/s/100 Gb/s design 1:284, 1:285T
modulation
formats 1:275–276
of WDM signals 1:275–276
networks 4:18
non-fiber-related effects 1:271–272
optical amplifiers 1:263–265
optical multiplex section 1:263
optical transport network 1:287
passive WDM filters and couplers 1:265–268
receivers 1:270–271
ROADMs 1:269–270, 1:269F
single-mode fibers 1:261–263
superchannels 1:275
sustainability 1:284–287
system realization 1:280–281
transmission effects in optical fibers 1:255–256
transmitters 1:260
external modulators 1:260–261
LD 1:260
tunable WDM filters 1:268
wavelength switching devices 1:268–269
wavelength-selective switches (WSS) 1:269, 4:225, 4:226–227, 4:231F
wavelength(s) 1:99, 1:139
allocation 2:78
conversion 1:250–251
extension 2:432–434
filters 1:341
of light measurement 1:486
range 5:160–161
reuse schemes 2:82
scalability 1:218
scale 1:193
switching devices 1:268–269
tuning interferometry 2:265, 4:500, 4:501F
versatility and tenability 2:280
wavelength-blocking 1:270
wavelength-scalable hollow optical fibers 1:216–220, 1:220F
wavelength-scale microstructures 5:313
wavelength-selective
branching device 1:341
directional couplers 1:266
wavepacket propagation methods 5:39
WaveScan model 4:531
WDM-PON Central Office (WDM-PON CO) 1:252
weak cavity 5:247
weak-coupling regime 1:460
wearable displays
see also 3D displays
clothes-integratable-type 3:52
flexible displays integrating
with clothes 3:52
with human body 3:52–53
flexible E-paper 3:56
flexible liquid crystal display 3:56–57
flexible organic light emitting diode 3:54–56
flexible substrates 3:53
flexible TFT 3:53–54, 3:55F, 3:55T
flexible transparent conductive film 3:57
practical processes for flexible display 3:57
spectacle-type 3:51–52
watch-type 3:53
welding 2:329–331, 2:334
Western Europe (WE) 4:18
wet-coating processes 5:317
Weyl-symplectic group 4:202
whisker technology 1:422
white light emitting diodes (W-LEDs) 3:19–20, 3:27–28
"white light" spectrum 2:426
white-light continuum generation (WLC generation) 2:295
wide angle (WA) 5:262–263
schematic eyes 5:48
wide area network (WAN) 4:17–18
wide bandgap semiconductors types 2:271
wide view film (WV film) *see* optical compensation film
wide viewing angle (WVA) 3:62
wideband amplifiers 1:362
wideband transimpedance amplifiers 4:260–261
Wien's displacement law 3:230, 3:231F
Wiener filter 3:181, 3:184F, 3:185F
wiggler 2:119
Wigner distribution (WD) 4:174–175, 4:177F, 4:178F
parallel data processing for WD reconstruction 4:177–178, 4:177F
projections 4:176–177
Wigner distribution function (WDF) 3:164, 3:165, 3:166, 3:167, 4:161, 4:174
wind and flow velocity 4:456–463, 4:457F, 4:458F
Wind INfrared Doppler lidar (WIND) 4:457
Windcube 200S 4:459–461, 4:461F
Windcube of Doppler lidar 4:459–461
WindScanner system 4:461–462, 4:462, 4:462F, 4:463
windshear 4:457, 4:458F, 4:459F
WindTracer 4:458–459, 4:460F
WindTracer Terminal Doppler Solution (WTDS) 4:458–459
wire grid polarizer 1:153
WKB method 2:91
WOLED lighting 3:68–69
wound healing, PBM for 3:117–118
wurtzite material 1:491

X

X-ray absorption spectroscopy (XAS) 2:142–143
X-ray diffraction (XRD) 2:124, 2:142–143
X-ray free electron lasers (XFEL) 2:142
X-ray magnetic absorption dichroism (XMLD) 2:147
X-ray(s) 2:207, 5:175, 5:185, 5:191, 5:191F
analyzer-based imaging 4:171, 4:171F
crystallography studies 2:174, 3:8
CT principle 3:192–193
detector 5:192
free electron lasers 2:233
holotomography 4:172, 4:172F
microanalysis 5:193
photoelectron spectroscopy 2:246
tomography 3:187, 3:193F, 3:195
X-tion Pro Live 4:512
xanthene 2:344
xanthophyll 5:50–51
Xe^* 2:360–361, 2:361–362
Xe_2 2:360–361, 2:361F
XeI^* 2:361–362
xenon ion lasers 2:379, 2:379T
XG-PON 2:77–78, 2:78F, 2:78T
XG-PON2 2:77
XPM-induced intensity interference 1:21
XPM-induced Nonlinear Phase Noise (X-NLPN) 1:284

Y

Y123 dyes chemical structures 5:270, 5:271F
$Y_3Al_5O_{12}$ *see* yttrium aluminium garnet (YAG)
Yb:YAG 2:412–413
$YBa_2Cu_3O_y$, magnetic quadrupole order in pseudogap of 2:220–223, 2:222F, 2:223F
Yb–Pr-doped fiber up-conversion laser 2:402–403, 2:403F
YD2-o-C8 dyes chemical structures 5:270, 5:271F
Young's double slit interferometer 1:74–75, 1:75F, 1:486F, 1:487
Young's double-hole experiment 1:36–37, 1:36F
Young's interference experiment, spectral changes in 1:46, 1:46F
young's modulus 1:216
ytterbium ion 2:413
ytterbium laser ion (Yb laser ion) 2:408
yttrium aluminum garnet (YAG) 2:386, 2:412–413, 2:436, 4:363
Yttrium Iron Garnet (YIG) 1:356
yttrium lithium fluoride (YLF) 2:436, 4:364
Yttrium OrthoVanadate wedge (YVO_4 wedge) 1:356, 2:436

Z

Zeeman term 2:65
Zernike aberration
coefficients 5:110
estimating refractive state from Zernike aberration coefficients 5:111–112

Zernike aberration (*continued*)
function profile 4:438–439
Zernike phase contrast 3:146
Zernike polynomials 4:409, 4:411, 4:531, 5:16, 5:57, 5:110, 5:111–112
Zernike-Van Cittert theorem derivation from propagation of AF 4:169
zero delay 5:157
zero dispersion wavelength 1:179, 1:195
zero-dimension (0D) 2:72
zero-phonon donor-bound exciton transitions 1:467
zinc oxide-based DSSCs 5:270
ZnCdSe quantum well, absorption spectrum of 2:94, 2:95F
ZnO layer 2:271, 5:303
(ZnO:Al) *see* aluminum-doped zinc oxide (AZO)
ZnSe 2:94, 2:271
ZnTe 1:407, 1:407F
zonal presentation 4:531
zone plate 1:95–96, 1:95F
zonules 5:47